Lecture Notes in Civil Engineering

Joel P. Conte
Rodrigo Astroza
Gianmario Benzoni
Glauco Feltrin
Kenneth J. Loh
Babak Moaveni *Editors*

Experimental Vibration Analysis for Civil Structures

Testing, Sensing, Monitoring, and Control

Springer

Lecture Notes in Civil Engineering

Volume 5

Lecture Notes in Civil Engineering (LNCE) publishes the latest developments in Civil Engineering - quickly, informally and in top quality. Though original research reported in proceedings and post-proceedings represents the core of LNCE, edited volumes of exceptionally high quality and interest may also be considered for publication. Volumes published in LNCE embrace all aspects and subfields of, as well as new challenges in, Civil Engineering. Topics in the series include:

- Construction and Structural Mechanics
- Building Materials
- Concrete, Steel and Timber Structures
- Geotechnical Engineering
- Earthquake Engineering
- Coastal Engineering
- Hydraulics, Hydrology and Water Resources Engineering
- Environmental Engineering and Sustainability
- Structural Health and Monitoring
- Surveying and Geographical Information Systems
- Heating, Ventilation and Air Conditioning (HVAC)
- Transportation and Traffic
- Risk Analysis
- Safety and Security

More information about this series at http://www.springer.com/series/15087

Joel P. Conte · Rodrigo Astroza
Gianmario Benzoni · Glauco Feltrin
Kenneth J. Loh · Babak Moaveni
Editors

Experimental Vibration Analysis for Civil Structures

Testing, Sensing, Monitoring, and Control

Springer

Editors
Joel P. Conte
Department of Structural Engineering
University of California at San Diego
La Jolla, CA
USA

Rodrigo Astroza
Faculty of Engineering and Applied Sciences
Universidad de los Andes
Las Condes, RM - Santiago
Chile

Gianmario Benzoni
Department of Structural Engineering
University of California at San Diego
La Jolla, CA
USA

Glauco Feltrin
Swiss Federal Laboratories for Materials Science and Technology (EMPA)
Zürich
Switzerland

Kenneth J. Loh
Department of Structural Engineering
University of California at San Diego
La Jolla, CA
USA

Babak Moaveni
Department of Civil and Environmental Engineering
Tufts University
Medford, MA
USA

ISSN 2366-2557 ISSN 2366-2565 (electronic)
Lecture Notes in Civil Engineering
ISBN 978-3-319-67442-1 ISBN 978-3-319-67443-8 (eBook)
https://doi.org/10.1007/978-3-319-67443-8

Library of Congress Control Number: 2017953432

© Springer International Publishing AG 2018
This work is subject to copyright. All rights are reserved by the Publisher, whether the whole or part of the material is concerned, specifically the rights of translation, reprinting, reuse of illustrations, recitation, broadcasting, reproduction on microfilms or in any other physical way, and transmission or information storage and retrieval, electronic adaptation, computer software, or by similar or dissimilar methodology now known or hereafter developed.
The use of general descriptive names, registered names, trademarks, service marks, etc. in this publication does not imply, even in the absence of a specific statement, that such names are exempt from the relevant protective laws and regulations and therefore free for general use.
The publisher, the authors and the editors are safe to assume that the advice and information in this book are believed to be true and accurate at the date of publication. Neither the publisher nor the authors or the editors give a warranty, express or implied, with respect to the material contained herein or for any errors or omissions that may have been made. The publisher remains neutral with regard to jurisdictional claims in published maps and institutional affiliations.

Printed on acid-free paper

This Springer imprint is published by Springer Nature
The registered company is Springer International Publishing AG
The registered company address is: Gewerbestrasse 11, 6330 Cham, Switzerland

Preface

Research, development, and applications in Experimental Vibration Analysis for Civil Engineering Structures are being fed by the continuous progress in the fields of sensor and testing technologies, instrumentation, data acquisition systems, computer technology, and computational modeling and simulation of large and complex civil infrastructure systems. The objectives and challenges are to understand the behavior and state of health of structural, geo-structural, and soil–foundation–structural systems as well as predicting their remaining useful life using vibration data collected from these systems when subjected to operational and extreme loads. Advanced data analysis (e.g., system and damage identification) methods are required to extract the needed information from the data and to gain from the information the knowledge required to support decision making related to maintenance and inspection, retrofit, upgrade, and rehabilitation of these systems as well as in case of emergency response. These data analysis methods are developed using numerically simulated structural response data, experimental data from small-scale physical structural models, experimental data from large- or full-scale physical structural specimens tested under laboratory conditions, or field data collected from civil structures under in-situ conditions.

EVACES, the International Conference on Experimental Vibration Analysis for Civil Engineering Structures, is a premier venue where recent progress in the field is presented and discussed by experts from all over the world. After the first six successful editions of EVACES which took place in Bordeaux, France (2005); Porto, Portugal (2007); Wroclaw, Poland (2009); Varenna, Italy (2011); Ouro Preto, Brazil (2013); and Dübendorf, Switzerland (2015), EVACES 2017 was organized by the University of California at San Diego and held on the main campus of the University in July 12–14, 2017.

The papers presented at EVACES 2017 are subdivided into the following subareas: (1) keynote papers; (2) damage identification and structural health monitoring; (3) testing, sensing, and modeling; (3) vibration isolation and control; (4) system and model identification; and (5) coupled dynamical systems (including human–structure, vehicle–structure, and soil–structure interactions).

We express our sincere thanks to the members of the Organizing Committee, the members of the Scientific Committee, and, in particular, all the authors and participants for their essential and valuable contributions.

Joel P. Conte
Rodrigo Astroza
Gianmario Benzoni
Glauco Feltrin
Kenneth Loh
Babak Moaveni

Organization

Editors/Organizing Committee

Joel P. Conte
Professor, Ph.D.
Department of Structural Engineering
University of California, San Diego
USA
jpconte@ucsd.edu

Rodrigo Astroza
Assistant Professor, Ph.D.
Faculty of Engineering and Applied Sciences
Universidad de los Andes
Chile
rastroza@miuandes.cl

Gianmario Benzoni
Research Scientist, Ph.D.
Department of Structural Engineering
University of California, San Diego
USA
gbenzoni@ucsd.edu

Glauco Feltrin
Senior Researcher, Ph.D.
Swiss Federal Laboratories for Materials Science and Technology (EMPA)
Switzerland
glauco.feltrin@empa.ch

Kenneth Loh
Associate Professor, Ph.D.
Department of Structural Engineering
University of California, San Diego
USA
kjloh@ucsd.edu

Babak Moaveni
Associate Professor, Ph.D.
Department of Civil and Environmental Engineering
Tufts University
USA
babak.moaveni@tufts.edu

Scientific Committee

A. Emin Aktan	Drexel University, USA
Rodrigo Astroza	Universidad de los Andes, Chile
Flavio Barbosa	Federal University of Juiz de Fora, Brazil
Jan Bien	Wroclaw University of Science and Technology, Poland
Elsa Caetano	University of Porto, Portugal
Joel P. Conte	University of California San Diego, USA
Christian Cremona	Bouygues Construction, France
Alvaro Cunha	University of Porto, Portugal
Alexandre Cury	Federal University of Juiz de Fora, Brazil
Guido De Roeck	KU Leuven, Belgium
Glauco Feltrin	EMPA, Switzerland
Alain Fournol	AVLS, France
Carmelo Gentile	Politecnico di Milano, Italy
Raid Karoumi	KTH Royal Institute of Technology, Sweden
Mieszko Kuzawa	Wroclaw University of Technology, Poland
Antonino Morassi	University of Udine, Italy
Alex Pavic	University of Exeter, UK
Patrick Paultre	University of Sherbrooke, Canada
Luis F. Ramos	University of Minho, Portugal

Contents

Keynote Papers

Assessment of Small Damage by Direct Modal Strain Measurements 3
G. De Roeck, E. Reynders, and D. Anastasopoulos

Flexible Architectures for Full-Scale Performance Evaluation of Tall Buildings: Burj Khalifa and Beyond 17
Tracy Kijewski-Correa and Andrew Bartolini

Information-Driven Modeling of Structures Using a Bayesian Framework 38
Costas Papadimitriou, Costas Argyris, and Panagiotis Panetsos

Development of a High Accuracy and High Sampling Rate Displacement Sensor for Civil Engineering Structures Monitoring 62
Hoon Sohn, Kiyoung Kim, Jaemook Choi, Gunhee Koo, and Junyeon Chung

Damage Identification and Structural Health Monitoring

A New Approach to Damage Detection in Bridges Using Machine Learning 73
A.C. Neves, Ignacio González, John Leander, and Raid Karoumi

Vibration Based Damage Identification Method for Cantilever Beam Using Artificial Neural Network 85
Putti Srinivasa Rao and N.V.D. Mahendra

Advanced Statistical Techniques Applied to Raw Data for Structural Damage Detection 94
Alan S. Torres, Vinicius N. Alves, Alexandre A. Cury, and Flavio S. Barbosa

Virtual Laboratory for Leveraging Technology for Bridges and Constructed Systems 104
Emin Aktan, Ivan Bartoli, Franklin Moon, Marcello Balduccini, Kurt Sjoblom, Antonios Kontsos, Hoda Azari, Matteo Mazzotti, John Braley, Charles Young, Shi Ye, and Andrew Ellenberg

Radio-Frequency Identification Triggering System for Structural Health Monitoring of Highway Bridges 118
Johnn Judd, Richard Schmidt, McKenzie Danforth, James Branscomb, and Michael Jung

Evaluating Vibration Serviceability Using Experimental Modal Testing 126
Anthony R. Barrett, D. Bradley Davis, and Thomas M. Murray

Damage Detection by Experimental Modal Analysis in Fiber-Reinforced Composites 138
C.A. Geweth, F. Saati Khosroshahi, K. Sepahvand, C. Kerkeling, and S. Marburg

Retrofitting of Damaged Structure Using Vibration Monitoring Technique 146
Vishisht Bhaiya, Shiv Dayal Bharti, Mahendra Kumar Shrimali, and Tushar Kanti Datta

Experimental Damage Identification Using SVD-Based Sensitivities of Truncated Transfer Function 156
Mohammad Rahai, Ali Bakhshi, and Akbar Esfandiari

Vibration-Based Support Vector Machine for Structural Health Monitoring 167
Hong Pan, Mohsen Azimi, Guoqing Gui, Fei Yan, and Zhibin Lin

Structural Health Monitoring of a Curved Segment of an Elevated Railroad 179
Carlos H. Huerta-Carpizo, David Murià-Vila, Gerardo Aguilar, and Abraham R. Sánchez

Performance Evaluation of Hinges in Cantilever Steel Truss Bridges by Temperature Induced Strain 192
Takeshi Miyashita, Eiji Iwasaki, and Masatsugu Nagai

Vibration-Based SHM of Railway Bridges Using Machine Learning: The Influence of Temperature on the Health Prediction 200
Elisa Khouri Chalouhi, Ignacio Gonzalez, Carmelo Gentile, and Raid Karoumi

Finite Element Model Calibration of a Historic Wiegmann–Polonceau Truss Based on Experimental Modal Parameters 212
Hoa T.M. Luong, Werner Lorenz, Rolf G. Rohrmann, Volkmar Zabel, and Samir Said

General Conditions for Full-Field Response Monitoring in Structural Systems Driven by a Set of Identified Equivalent Forces 225
Eliz-Mari Lourens and Dominik Fallais

Experimental Vibration Tests in Fatigue Evaluation of a Riveted Truss Bridge 237
Mieszko Kużawa, Tomasz Kamiński, and Jan Bień

Damage Sensitivity Evaluation of Vibration Parameters Under Ambient Excitation 249
John James Moughty and Joan Ramon Casas

Operational Damage Localization of Wind Turbine Blades 261
Yaowen W. Ou, Vasilis K. Dertimanis, and Eleni N. Chatzi

Study on the Vibration Feature of Concrete Deck Slabs Under Fatigue Wheel Loading 273
Chen Xu and Hiroshi Masuya

Fuzzy Pattern Recognition in Vibration-Based Structural Health Monitoring 283
Mohammad Azarbayejani

Efficient Finite Elements Model Updating for Damage Detection in Bridges 293
M. Saidou Sanda, O. Gauron, N. Turcotte, C.-P. Lamarche, P. Paultre, M. Talbot, and J.-F. Laflamme

A Comparison of Damage Detection Methods Applied to Civil Engineering Structures 306
Szymon Gres, Palle Andersen, Rasmus Johan Johansen, Martin Dalgaard Ulriksen, and Lars Damkilde

A Displacement Reconstruction Strategy for Long, Slender Structures from Limited Strain Measurements and Its Application to Underground Pipeline Monitoring 317
Mayank Chadha and Michael D. Todd

Testing, Sensing and Modeling

Displacements Monitoring of Suspension Bridge Using Geodetic Techniques 331
Wojciech Anigacz, Damian Beben, and Jacek Kwiatkowski

Modelling of Pot Bearings – A Preliminary Study 343
Mahir Ülker-Kaustell, Gabriel F. Boschmonar, Pablo B. Isusi, Stefan Trillkott, Claes Kullberg, and Raid Karoumi

Full-Scale Dynamic Testing of a Railway Bridge Using a Hydraulic Exciter 354
Andreas Andersson, Johan Östlund, Mahir Ülker-Kaustell, Jean-Marc Battini, and Raid Karoumi

A Practical Multi-cross-line Model for Simulating Nonlinear Cyclic Behavior of Reinforced Concrete Shear Wall in Super High-Rise Buildings 364
Baoyin Sun, Quan Gu, Peizhou Zhang, and Jinping Ou

Dynamic Shake-Table Tests on Two Full-Scale, Unreinforced Masonry Buildings Subjected to Induced Seismicity 376
Gabriele Guerrini, Francesco Graziotti, Andrea Penna, and Guido Magenes

Utilising an Advanced Technology of People Tracking in Vibration Serviceability Application 388
Ahmed S. Mohammed and Aleksandar Pavic

Forced-Vibration Tests of the Daniel-Johnson Multiple-Arch Dam 397
O. Gauron, Y. Boivin, S. Ambroise, P. Paultre, J. Proulx, M. Roberge, and S.-N. Roth

Experimental Vibration Analysis of Composite Bridge Superstructure with Excessive Deformations 409
Mieszko Kużawa and Jan Bień

Real-Time Structural Instrumentation as an Emergency Response and Business Continuity Tool 420
Erik Bishop, Kenny O'Neill, Drew Nielson, Dave Swanson, David Gonzalez, and Derek Skolnik

A Comparison of Two Data Acquisition Techniques for Modal Strain Identification from Sub-microstrain FBG Data 432
Dimitrios Anastasopoulos, Kristof Maes, Guido De Roeck, and Edwin Reynders

Strong Motion Structural Monitoring in Practice 445
K. O'Neill, E. Bishop, D. Swanson, D. Aveyard, D. Skolnik, and M. Fraser

A Bio-inspired Framework for Highly Efficient Structural Health Monitoring and Vibration Analysis 455
Maria-Giovanna Masciotta, Alberto Barontini, Luís F. Ramos, Paulo Amado-Mendes, and Paulo B. Lourenço

Development of the UPRM Hybrid Simulation Facilities: Substructuring Techniques Coupled Numerical Simulations 469
Maria D. Cortes-Delgado and Lemuel González Hernández

Shake-Table Testing and Performance Assessment of a Partially Grouted Reinforced Masonry Building 480
Andreas Koutras and P. Benson Shing

Vibration Isolation and Control

Vortex-Induced Vibration of Stay Cables, Verification on the Footbridge 497
Shota Urushadze and Miroš Pirner

Vertical Vibration Mitigation of a Bridge Cable Using a Non Smooth Absorber Under Gravity 505
Mathieu Weiss, Bastien Vaurigaud, A. Ture Savadkoohi, and C.-H. Lamarque

An Assessment of a Fractional Derivative Model Applied to Simulate the Dynamic Behavior of Viscoelastic Sandwich Beam 514
Waldir Felippe and Flavio Barbosa

Modal Phase Compensation for Application of Direct Velocity Feedback to Active Control of Floor Vibration Under Impact Excitation 523
Kai Xue, Akira Igarashi, and Takahiro Kachi

Application of a 240 Metric Ton Dual-Use Tuned Mass Damper System 536
Christian Meinhardt

Mitigate Seismic Response of Three-Span Bridge Using MR Damping System 547
G. Heo, C. Kim, S. Jeon, C. Lee, and S. Seo

An Analytic Comparison Regarding Steady-State Damping Performance Between the Twin Rotor Damper and a Dynamic Vibration Absorber 557
Richard Bäumer, Richard Terrill, and Uwe Starossek

Design of Test Setup for Prototype Testing of Base Isolators 568
Shiv Dayal Bharti, Mahendra Kumar Shrimali, Arnav Anuj Kasar, and Tushar Kanti Datta

Comparison of State-of-the-Art Methods of Estimating & Controlling Floor Vibrations 577
Austin Devin and Paul J. Fanning

Optimal Design of Active Tuned Mass Dampers for Mitigating Translational–Torsional Motion of Irregular Buildings 586
Mohsen Azimi, Hong Pan, Mehdi Abdeddaim, and Zhibin Lin

Active Vibration Control of a Three Degree of Freedom Oscillator Using Two Eccentrically Rotating Masses 597
R. Terrill, R. Bäumer, and U. Starossek

System and Modal Identification

Experimental Evaluation of the Effect of Geometric Nonlinearities on Structural Resonances 611
Reyolando M. Brasil and Alexandre M. Wahrhafitg

The Selection of a Dynamic Model of a RC Chimney Based on In Situ Research 619
Tadeusz Tatara and Bartłomiej Ratajewicz

A New System Identification Method Operated in the Pole Domain . . . 631
Qianying Cao, Bin Gao, Huajun Li, and Sau-Lon James Hu

Discussion of Several "RSID" Algorithms to Linear Time-Varying System and System with Abrupt Change of Joint Failure 644
Chin-Hsiung Loh and Jun-Da Chen

Dynamic Characteristics of a 55-Story Building Before and After Retrofit 656
Mehmet Çelebi, Toshihide Kashima, S. Farid Ghahari, Shin Koyama, Ertuğrul Taciroğlu, and Izuru Okawa

Time-Frequency Analysis of Suspension Bridge Response for Identification of Vortex Induced Vibrations 667
Daniel Cantero, Ole Øiseth, and Anders Rønnquist

Dynamic Characteristics of Layered Stone Pagoda System 676
Byeong Hwa Kim

Identification of Symmetrical Structures with Fabrication and Damage Induced Asymmetry 683
Abhineet Gupta, Wei Zhao, Chris Regan, Peter Seiler, and Rakesh K. Kapania

Experimental Incremental System Identification Method Using Separate Time Windows on Basis of Ambient Signals 694
Simon Schleiter, Okyay Altay, and Sven Klinkel

Effect of Cross-Section and Discontinuities on Damping Enhancement in Composites: An Experimental Study 705
Komal Chawla and Samit Ray. Chaudhuri

Modal Strain Energy Based Structural Parameter Identification from Limited Vibration Measurement 714
D. Bandyopadhyay and J.S. Ali

Experimental Modal Properties of a Steel Arch Bridge During the Static Load Test 725
Fabrizio Gara, Vanni Nicoletti, Davide Roia, and Andrea Dall'Asta

Evaluation of Vibration Problems in Existing Office Buildings 736
Matthew A. Pavelchak

Post-earthquake Field Measurement-Based System Identification and Finite Element Modeling of an 18-Story Masonry-Infilled RC Building 746
Mohammed A. Mohammed, Hanshun Yu, Andre Furtado, Andre R. Barbosa, Babak Moaveni, Humberto Varum, Hugo Rodrigues, Nelson Vila-Pouca, and Richard L. Wood

Study of the Environmental Influence on the Dynamic Behavior of Adobe Walls: Preliminary Test in Laboratory Specimens 758
Rick Delgadillo, Giacomo Zonno, Rubén Boroschek, Paulo B. Lourenço, and Rafael Aguilar

Assessing the Performance of a Heavy Haul Railway Viaduct Through Monitoring Traffic Loads and Dynamic Effects 770
Fulvio Busatta and Pilate Moyo

Specific Dynamic Properties of SFRC Based on Waste Ceramic Aggregate 781
Jacek Katzer and Jacek Domski

Parametric Estimation of Wave Dispersion for System Identification of Building Structures 791
Hamed Ebrahimian, Monica Kohler, Anthony Massari, and Domniki Asimaki

Coupled Dynamical Systems (Includes Human-Structure, Vehicle-Structure and Soil-Structure Interaction)

Experimental Testing of Soil-Steel Railway Bridge Under Normal Train Loads 805
Damian Beben

Analysis of Records from Downhole Arrays 816
Erdal Şafak and Eser Çaktı

Effect of Soil-Structure Interaction on Low to Medium-Rise Steel Frames Through Shake Table Experiments 822
B. Vivek and Prishati Raychowdhury

Natural Vibration Characteristics and Seismic Response Analysis of Train-Bridge Coupling System in High-Speed Railway 831
Zhi Liu, Hui Jiang, Lanfang Zhang, and Endong Guo

Simulation of Human Induced Vibration of a Lively Footbridge 839
Eleonora Lai and Maria G. Mulas

Vibrations in Multilayered Soils: A Simplified and Robust Prediction Equation 851
Abdul Karim Jamal Eddine, Luca Lenti, and Jean-Francois Semblat

The Effect of Traffic Modeling on Damage Detection Procedure of Bridges 860
A.H. Hadjian Shahri and A.K. Ghorbani-Tanha

Soil-Foundation Compliance Evidence of the "Chiaravalle Viaduct" . . . 871
Marco Regni, Fabrizio Gara, Francesca Dezi, Davide Roia, and Sandro Carbonari

Experimental Analysis of Arroyo Bracea II Bridge in Madrid – Sevilla High-Speed Railway Line: Dynamic Response of the Structure and Effect of Soil Properties 882
Pedro Galvín, Antonio Romero, Emmanuela Moliner, and María D. Martínez-Rodrigo

Dynamic Modeling of Train and Bridge with Stepped-Beam Cross-Sections 893
Hani Nassif, Yingjie Wang, and Peng Lou

Nonlinear Stay Cable – Bridge Deck Interaction 902
Benedikt Weber

Author Index 915

Keynote Papers

Assessment of Small Damage by Direct Modal Strain Measurements

G. De Roeck(✉), E. Reynders, and D. Anastasopoulos

Department of Civil Engineering,
KU Leuven, Kasteelpark Arenberg 40, 3001 Leuven, Belgium
guido.deroeck@kuleuven.be

Abstract. Vibration based Structural Health Monitoring was and is still a hot topic in research. Much progress has been made both from the theoretical as well as the practical side. Vibration-based SHM traditionally makes use of uniaxial/triaxial accelerometers or velocity meters. Also sometimes inclinometers are installed. Recent trends in SHM are the use of high-rate GPS receivers [1], wave propagation-based piezoelectric ceramic sensing technology and optical fiber sensors for dynamic strain and temperature measurements [2].

A particular challenge for structural health assessment is the discovery of small local damage. It is well known that for small damages, the changes in natural frequencies remain very low. Moreover, they are considerably influenced by environmental conditions (mainly temperature) [3], which influence has to be eliminated on beforehand [4, 5]. Also modal displacements are rather insensitive to small stiffness perturbations. On the contrary, modal strains (or curvatures) are very receptive to small stiffness changes. Additionally, they immediately spot the damage location. Some authors have tried to derive curvatures from modal displacements but this procedure is very prone to even slight measurement and/or identification errors. Therefore, the key issue is the direct measurement of (modal) strains. However, the development of a distributed strain sensor network able to cope with the very low strain intensities during ambient excitation is still a challenge. In this paper by recent experiments on steel and concrete beams the extreme accuracy of dynamic measurements with optical FBG strain sensors is demonstrated.

Another possibility to obtain precise modal strains would be the development of a transducer that amplifies the strains. In a recent research project, by using Topology Optimization [6], a transducer was developed that measures differential axial displacements over a sufficient long distance and at the same time is upscaling the strains. Results obtained with this transducer are reported.

In this context, a new challenge for Optimal Sensor Placement [7] is to deal with different sensor types, e.g. displacement transducers, accelerometers and strain sensors.

For localization and quantification of damage, the most powerful method is FE-model updating based on minimizing differences between measured and calculated modal parameters [8]. The addition of modal strains to the objective function of the minimization problem will improve the damage identification process.

Keywords: Modal analysis · Modal strains · Damage assessment · Structural health monitoring · Optical strain fibers

© Springer International Publishing AG 2018
J.P. Conte et al. (eds.), *Experimental Vibration Analysis for Civil Structures*,
Lecture Notes in Civil Engineering 5, https://doi.org/10.1007/978-3-319-67443-8_1

1 Introduction

Vibration-based structural health monitoring (SHM) is based on the principle that modal parameters of a structure are like a signature of structural behaviour. Output-only or operational modal analysis (OMA) became very popular as no artificial vibration source is needed which is anyhow impossible in many cases. Powerful time domain system identification algorithms like Stochastic Subspace Iteration (SSI) have replaced the obsolete "peak-picking" method [9, 10].

Vibration-based SHM traditionally makes use of uniaxial/triaxial accelerometers or velocity meters. Also sometimes inclinometers are installed. Recent trends in SHM are the use of high-rate GPS receivers [1], wave propagation-based piezoelectric ceramic (PZT) sensing technology and optical fiber sensors (OFS) for dynamic strain and temperature measurements [2].

Because of the omission of cables, wireless networks (WNs) have a lot of evident advantages, like the ease of system setup, the largely reduced installation time, the possibility of local data processing, data interpretation and anomaly detection. In a recent project a wireless measurement with high time-synchronization accuracy was developed [11]. Spatial jitter was reduced to 125 ns, far below the 120 μs required for high-precision acquisition systems and much better than the 10-μs current solutions, without adding complexity. Moreover, the system is scalable to a large number of nodes to allow for dense sensor coverage of real-world structures.

In most of modal testing campaigns, there are more degrees-of-freedom (DOFs) to be measured than sensors available. The whole measurement grid then needs to be covered in several phases by different measurement setups. A number of reference locations are then selected and transducers at these points are often kept fixed in all setups. The ideal location for a reference sensor is a position where all modes have relatively large modal amplitudes. However, there exists no guidelines or general principles for evaluating whether a chosen number of reference sensors leads to sufficiently accurate mode shape estimates. In practice, even when measuring large structures, often a very limited number of reference sensors is allocated. The other transducers are roved in successive setups, hence these transducers are often termed `roving' sensors, so that by the end of the last setup, vibration responses at all grid points will have been recorded. So for any measurement campaign, the following questions have to be answered: (i) the location of the reference sensors, (ii) their number, (iii) the location of the roving sensors in the different setups. Answers can be given by applying Optimal sensor location (OSL) approaches. In [7] their practical applicability has been illustrated on a large-scale operational modal test of a five-span steel truss railway bridge. The measurement layout was designed according to intuitive reasoning, based on the modal results of a preliminary Finite Element analysis. Afterwards, this test design has been reviewed using OSL. A new challenge is to deal with different sensor types, e.g. displacement transducers, accelerometers and strain sensors.

Results can be used for calibration of numerical FE-models inherently containing uncertainties especially related to boundary conditions, joint stiffnesses, structural contribution of non-bearing parts, material parameters, damping, …

Subsequently, properly calibrated FE-models can be used to derive from response measurements the actual excitation like moving loads on road or railway bridges and wind forces on tall structures. Moreover, these models can be used to obtain from the response measurements in a limited number of sensors information in otherwise difficult to assess points, like strains close to weldings or forces in bolts [12].

Other interesting applications relate to the follow-up of critical phases during erection of constructions.

Moreover, changes in modal parameters (i.e. natural frequencies, damping ratios, mode shapes and modal strains) can be used as features to detect and to identify damage. Compared to other approaches for structural damage identification, vibration-based damage identification has the advantages of (1) being nondestructive, (2) being able to identify damage that is invisible at the surface, (3) being 'global' because no a priori location of the damage needs to be assumed as opposed to local methods such as ultrasonic testing. A good overview of recent trends is given in [13].

Unfortunately, modal parameters are not only sensitive to damage, but also to changing environmental conditions such as temperature variations, and moreover, their estimation from vibration response data is also prone to experimental errors. This is well known for natural frequencies but less observed and understood for mode shapes and modal strains. Challenge is to eliminate the environmental influences by prediction models that just rely on estimated modal properties (i.e. output-only models [4]) or on the measured environment as input and the estimated modal parameters as output (i.e. input-output models [5]). These models are trained by using data gathered in undamaged condition.

2 Small Local Damage

2.1 Background

A particular challenge for structural health assessment is the discovery of small local damage. Not only natural frequencies and mode shapes will hardly be affected but also its influence hidden in the uncertainty blur. Therefore, the development of a distributed strain sensor network able to cope with the very low strain intensities during ambient excitation is a challenge. Optical fiber sensors with Bragg grating technology permanently attached to the structure could be a good choice in this respect. Interrogation units are still quite expensive but can be coupled and uncoupled when adopting a periodic monitoring maintenance strategy. An additional advantage of the measured strain field is that it can be directly related to the stress field. Such a system will also be able to measure quasi-static deformation as occurs in case of shrinkage, creep, thermal expansion and very slowly applied dynamic loads. The idea of directly measuring accurate strains is explored in the next sections.

2.2 Upscaling Strain Transducer

During ambient excitation strains are very small so extracting modal strains is rather cumbersome. Moreover, in concrete structures when mean strains are measured over a long enough stretch, the classical Bernoulli assumption that plane sections remain plane

is still reasonably well fulfilled. This also implies that (modal) curvatures can be used for damage assessment.

Therefore a transducer that measures differential axial displacements over a sufficient long distance and at the same time amplifies the strains would be of great benefit. In a recent research project such transducer was developed by using Topology Optimization [14]. The transducer is connected by bolts to the test structure (Fig. 2: points 1 and 2). The actual strain is the one between the two bolts. The goal of the Topology Optimization is to amplify the strain occurring between points A and B (Fig. 1), which is measured by a Bragg grating on an optical fiber between these two points.

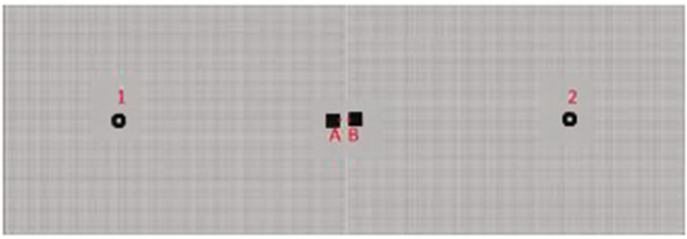

Fig. 1. Grid used in the topology optimization.

In Topology Optimization, a design is obtained by optimizing the distribution of a certain amount of material in the design domain. This design domain (grid) is displayed in Fig. 2. Note that some elements of this design domain are filled with material in advance. This due to the way the transducer and optical fiber will be mounted. The objective of the optimization is to minimize the horizontal displacement at the fixation point of the fiber, in case a positive horizontal force is applied at the fixation bolt of the transducer. This obtained by defining a minimum compliance optimization function as described in Wang (2011) [19]:

$$\min_{x} c(\boldsymbol{x})$$

$$\textit{subject to} : \boldsymbol{KU} = \boldsymbol{F}; \quad \frac{V}{V_0} \leq f_v; \quad 0 \leq x_e \leq 1 \tag{1}$$

In this equation, **x** is the vector with the element densities x_e, ranging from 0 (void) to 1 (solid). These element densities will be altered to obtain an optimal objective value c. **K** is the global stiffness matrix, **U** is the global displacement vector containing the displacements in all degrees of freedom and **F** is the global force vector. V is the material volume and V_0 is the total volume of the design domain. The ratio of these parameters must be smaller than a prescribed volume fraction f_v. This volume constraint is applied to this optimization, ensuring the total amount of material remains below a certain amount. Through calibration a volume constraint of 50% was selected, as a higher volume would not result in a higher objective value but would have a negative influence on the natural frequencies of the transducer.

The optimum of the objective function is calculated using the Method of Moving Asymptotes [6]. This algorithm will iteratively calculate the optimum. Convergence will be assumed when a change in material distribution of less than 5% occurs. This standard optimization approach results in one node hinges and bending in the optical fiber. To obtain a more robust design, extra constraints are applied. The first constraints ensured a local length scale control, preventing one node hinges. Another constraint was added, ensuring the mounting platforms of the optical fiber will not rotate, preventing bending of the fiber. This algorithm will iteratively calculate the optimum. Convergence will be assumed when a change in material distribution of less than 5% occurs.

The result of the optimization is shown in Fig. 2. A strain amplification by a factor 120 can theoretically be obtained.

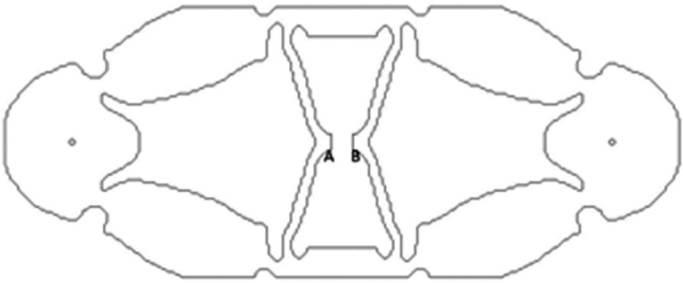

Fig. 2. Strain transducer from Topology Optimization.

Figure 3 shows a displacement plot by ANSYS for the right half of the sensor. A compression between 1 and 2 results in an elongation of AB. A prototype of this

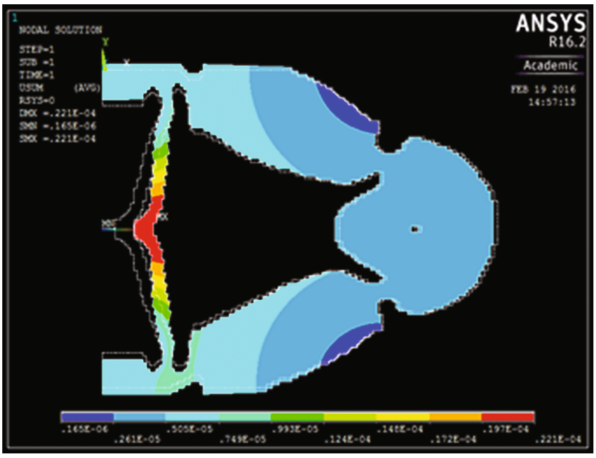

Fig. 3. Displacement plot.

sensor has been produced by laser cutting and its upscaling factor tested in the laboratory [14].

2.3 Strain Optical Fiber Network

To demonstrate the high accuracy that can be obtained from optical fiber strain sensors, an extensive experimental modal analysis test has been performed on a steel I-beam IPE 100 (Fig. 4) at the Structural Mechanics Laboratory of KU Leuven [15, 16]. The length of the beam is 3.0 m and steel plates are welded at its ends. The boundary conditions are set to approximate free-free conditions. For that purpose, the beam was

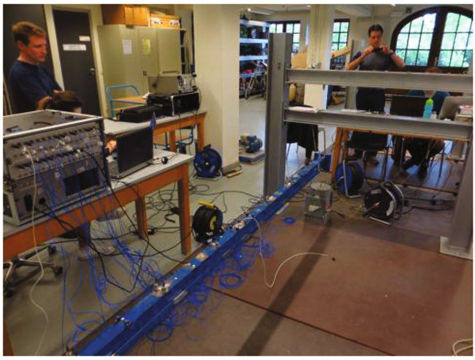

Fig. 4. Instrumented steel beam.

suspended on flexible springs. The beam was excited through a shaker located at the left end (Fig. 5) with various force amplitudes (2.3–13.5 N) and excitation signals (pure random, swept sign, periodic random) from [0:200] Hz and from [0:500] Hz. The low forces produce strain RMS values below one micro-strain.

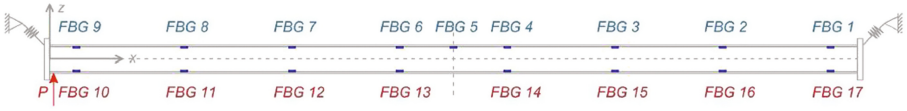

Fig. 5. FBGs setup - front view.

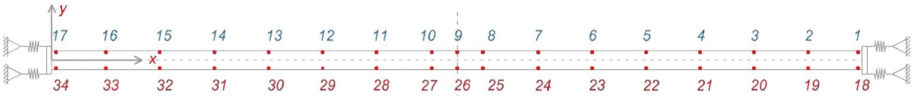

Fig. 6. Accelerometers setup - top view.

The beam was instrumented with a chain of multiplexed Bragg Grating (FBG) strain sensors glued at the top and the bottom flange of the beam (Fig. 5) and accelerometers (Fig. 6). The sampling frequency was f_s = 20000 Hz for the accelerometers and f_s = 950 Hz for the FBGs.

FBG based sensing relies on tracking the Bragg peak wavelength as it shifts with a change in the measured peak. Recently a fast and accurate peak detection algorithm has been recently proposed [17]. The fast phase-correlation (FPC) algorithm determines the wavelength shift from the phase shift between the undisturbed FBG spectrum and the perturbed spectrum.

Three modal analyses were performed by applying the Matlab toolbox MACEC [18] with two algorithms, SSI-cov and CSI [10]: (1) using FBG strain data; (2) using accelerometer data; (3) using both data. In the latter case, the accelerometer data were down-sampled at 950 Hz.

In the interval [0:200] Hz 2 bending modes and 3 torsional modes could be identified. An excellent correspondence with FE calculated modal properties is observed [16]. Moreover, the obtained modal characteristics from the combined modal analysis show a high consistency with the ones obtained from the separate analyses. The differences in modal displacements are less than 5%. The combined analysis, using data from both FBG strain sensors and accelerometers, allows to obtain mass normalized modal strains. Mass normalization is possible because acceleration was measured at the same location and direction as the applied force. Figure 7 shows the

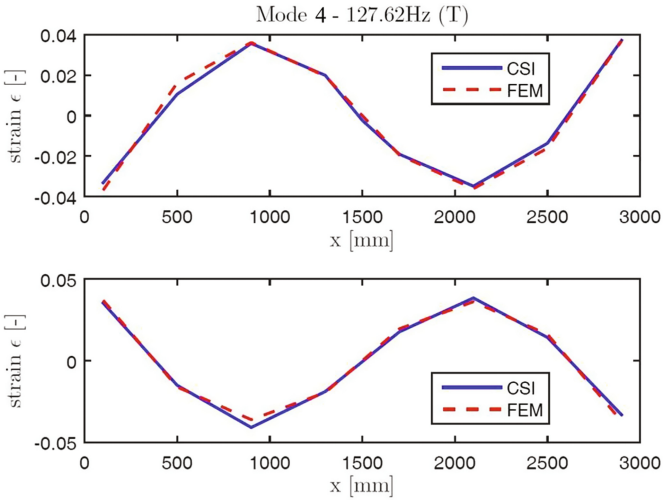

Fig. 7. Normalized modal strains of the third torsional mode T3.

comparison between calculated and measured mass normalized strains. Remarkable is the excellent agreement, taken into account the very low strain levels and the longitudinal orientation of the FBG strain fibers. They sense the torsional modes because of the restrained warping effect.

2.4 Damage Identification by Modal Strains

In a very recent experiment the ability of modal strains to identify more accurately structural damage in reinforced concrete beams is investigated. In order to comply with the Bernoulli assumption for beams, mean strains have to be measured over a suffi-

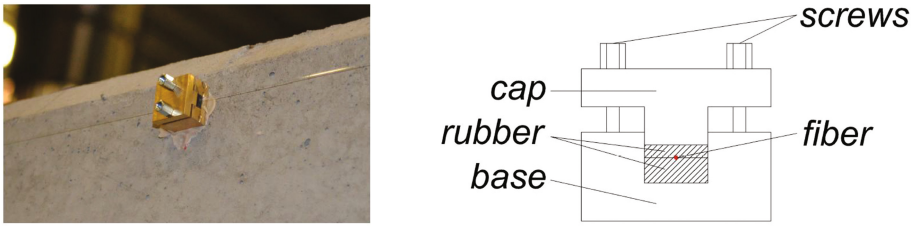

Fig. 8. Connector system for optical strain fiber.

ciently long length (e.g. typically one or two crack distances). Small measurement lengths will show a clear discontinuous behavior, depending on the location of the strain sensor: above a crack or between cracks.

A connector (Fig. 8) has been developed to clamp an optical glass fiber containing

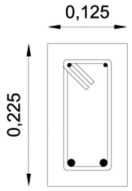

Fig. 9. Beam cross section.

several Bragg gratings at discrete points with proper spacing.

The experiment is aiming to identify the dynamic characteristics of a reinforced concrete beam at increasing damage levels. The beam has a length of 1.7 m and a rectangular cross section with dimensions 125 × 225 mm (Fig. 9). Steel reinforcement consists of 2 bars of 12 mm diameter at the tensile side and 2 bars of 8 mm at the compression side.

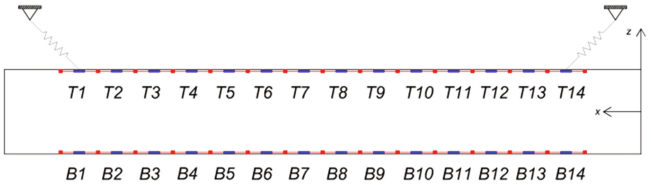

Fig. 10. FBG sensors setup - front view.

Shear reinforcement is by stirrups of 6 mm diameter. Concrete cover of these stirrups is 25 mm.

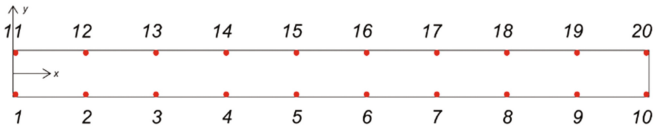

Fig. 11. Accelerometers setup - top view.

Two chains of multiplexed FBG strain sensors were attached: one on the front side at the bottom and on the back side at the top (Fig. 10). Each chain contains 14 FBG

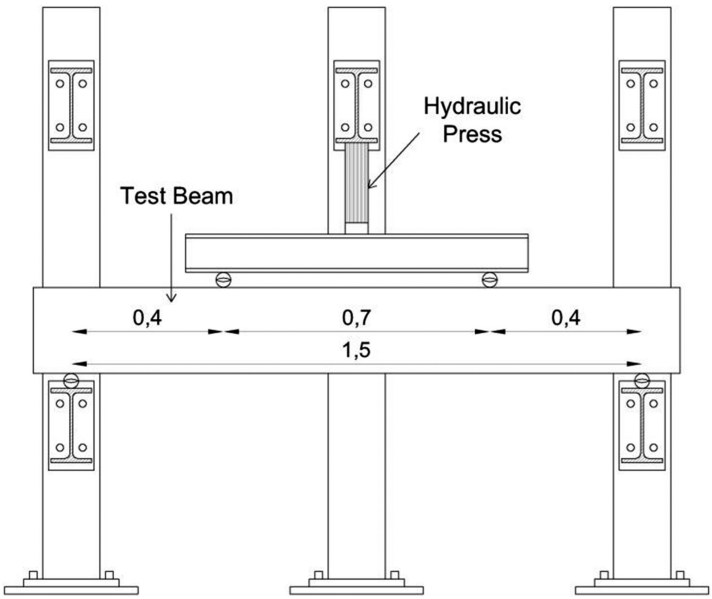

Fig. 12. Four point bending static test setup.

sensors which measure the average strain along a length of 100 mm. The chains measure the strains of the beam at a distance of about 1 cm from its edges.

At the top side of the beam 20 accelerometers were installed (Fig. 11). The distance between the accelerometers was about 20 cm.

Prior to the dynamic tests, damage is induced by static loads in a four point bending configuration (Fig. 12).

After each static test producing progressive damage, the beam is suspended from flexible springs, approaching dynamic free-free boundary conditions, to perform a modal identification. Dynamic response is provoked by hammer impacts and by a

shaker, exciting both the bending and the torsion modes. Input signal to the shaker is a sine sweep. The sampling frequency of the FBG strain acquisition system (FAZT I4) is f_s = 1000 Hz and 10000 Hz for the acceleration acquisition system (NI PXI-1050 chassis with NI PXI-4472B modules).

In the initial state, by using the acceleration data in MACEC, three vertical bending

Table 1. Natural frequencies

Mode	Type	f (Hz) ANSYS	f (Hz) measured	Difference (%)
1	L1	172	168	2.5
2	B1	304	301	1.3
3	L2	460		
4	T1	589	590	−0.2
5	B2	767	761	0.7
6	L3	865		
7	A1	1175		
8	T2	1179	1184	−0.4
9	B3	1356	1371	−1.1
10	L4	1360		
11	T3	1771	1766	0.3

modes (B1, B2, B3) and three torsional modes (T1, T2, T3) are identified (Table 1). When applying system identification to the strain data, only one lateral bending mode (L1) and one vertical bending mode (B1) could be extracted due to the limited sampling frequency of the FBG strain acquisition system. No axial modes (A) are found. In Table 1 also a comparison is made with a FE model (ANSYS) consisting of solid elements for the concrete and truss elements for the reinforcement.

Table 2 gives a view of the corresponding experimental mode shapes.

Damage is applied at different static loads (Fig. 12) till failure. Dynamic tests are performed after each unloading and change of boundary conditions to free-free, by attaching the beam to flexible springs. The extensive dataset is currently analyzed. Some preliminary results obtained after applying a static load P of 80 kN are presented. This load exceeds the crack load (about 30 kN). Table 5 resumes the frequency shifts. Despite the clear decrease of natural frequencies, the changes in mass normalized mode shapes are rather small, as shown in Table 3 for the first bending mode B1 and the third bending mode B3. The changes for the higher mode B3 are more pronounced, but still small.

The simultaneous measurement of accelerations (at the location of the applied load) and strains also allows to obtain mass normalized modal strains.

Table 4 shows for mode B1 the mass normalized modal strains at the top (left column) and at the bottom (right column). Results are given at initial undamaged state and at P equal to 80 kN. The initial modal strains, measured over a length of 10 cm) show a very good correspondence with the mass normalized strains from the FE model.

For the damaged beam the modal strains are more irregular. One of the reasons could be the short measurement length (10 cm) compared to the mean crack spacing, which is about 9 cm. Integrating over a longer length (by summing up over several

Table 2. Mode shapes

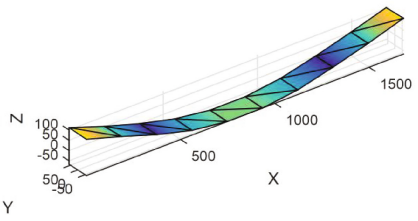	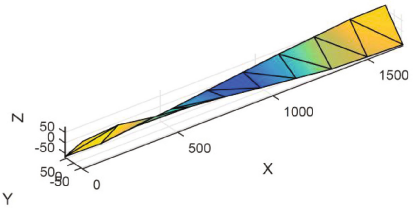
Mode shape B1 – 301 Hz	Mode shape T1 – 590 Hz
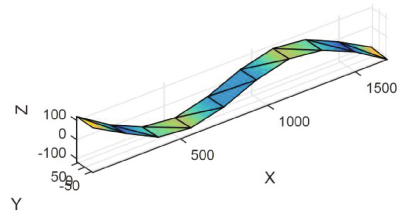	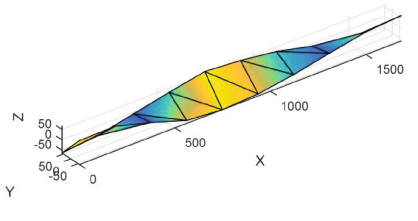
Mode shape B2 – 761 Hz	Mode shape T2 – 1184 Hz
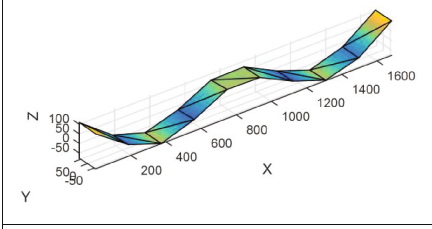	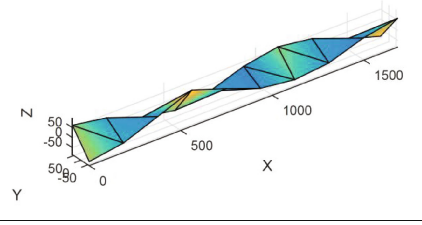
Mode shape B3 – 1371 Hz	Mode shape T3 – 1766 Hz

Table 3. Mass normalized mode shapes B1 and B3, before (blue) and after damage (red).

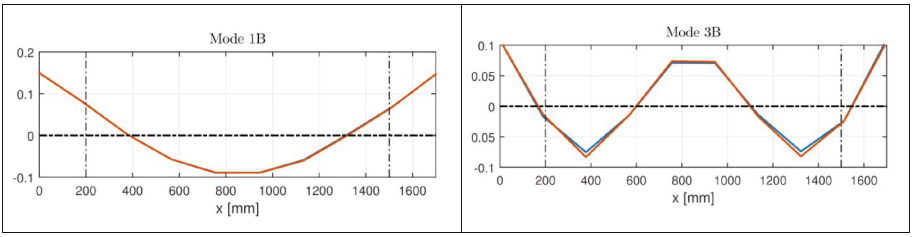

Table 4. Changes in mass normalized modal strains of mode B1: measured versus FE simulated

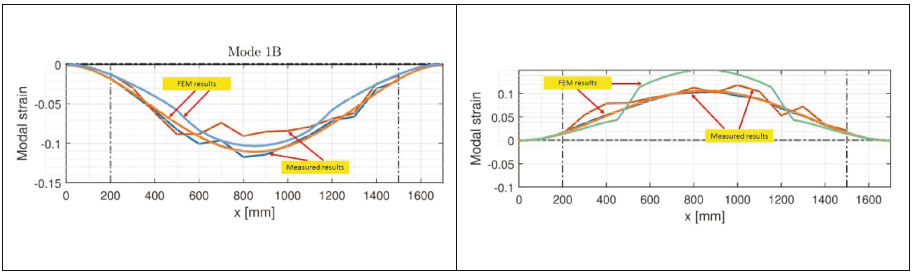

Table 5. Change of natural frequencies (at P = 80 kN)

	Acceleration data - CSI		
	Undamaged beam	Damaged beam (80KN)	Percentile difference
Mode	frequency (Hz)	frequency (Hz)	%
B1	300.50	248.20	-17.4
T1	590.30	501.50	-15.0
B2	761.30	629.30	-17.3
T2	1183.70	1019.10	-13.9
B3	1371.40	1132.70	-17.4
T3	1765.90	1564.00	-11.4
	Strain data - SSI-cov		
	Undamaged beam	Damaged beam (80KN)	Percentile difference
Mode	frequency (Hz)	frequency (Hz)	%
L1	168.00	139.20	-17.1
B1	300.60	249.70	-16.9
	Combined data - CSI		
	Undamaged beam	Damaged beam (80KN)	Percentile difference
Mode	frequency (Hz)	frequency (Hz)	%
B1	300.60	249.70	-16.9

sensors) will result in a smoother behavior. Comparison is also made with an approximate FE model in which the E-modulus of the tensile zone of the central, most damaged part of the beam (zone of 0.7 m in Fig. 12) is reduced in a way that the calculated natural frequencies are close to the measured values of Table 5. From this simulation it can be concluded that the observed changes in mass normalized modal strains go in the right direction: a reduction at the top (compression) side and an increase at the tensile (bottom side). However, quantitatively there are important differences that need further investigation.

Much more information will be available when the measured static and dynamic results of the different loading steps will be treated. The strain results will be opposed to the observed crack patterns at successive loads. The suitability of the designed clamping system will be investigated, e.g. by carefully analyzing the elastic strains at low load levels.

3 Conclusions

The ability to discover small damage by vibration monitoring is driven by the development of new sensor types, especially those that measure very low dynamic strains, and their application at proper locations by using optimal sensor location algorithms. A laboratory test shows that accurate mode shapes and modal strains can be obtained from acceleration and FBG measurements, even at very low excitation levels. The very low strain levels during ambient excitation can be amplified by a proper transducer design. For reinforced (and prestressed) concrete structures a system has been developed that allows to measure small modal strains (and curvatures) over a length which is in correspondence with classical theory for (cracked) reinforced beams.

Acknowledgments. The research presented in this paper has been performed within the framework of the project G099014N "Identification and modeling of structural damage", funded by the Research Foundation Flanders (FWO), Belgium. Their financial support is gratefully acknowledged.

References

1. Yi, T.H., Li, H.N., Gu, M.: Experimental assessment of high-rate GPS receivers for deformation monitoring of bridge. Measurement **46**(1), 420–432 (2013)
2. Lopez-Higuera, J.M., Cobo, L.R., Incera, A.Q., Cobo, A.: Fiber optic sensors in structural health monitoring. J. Lightwave Technol. **29**(4), 587–608 (2011)
3. Deraemaeker, A., Reynders, E., De Roeck, G., Kullaa, J.: Vibration based structural health monitoring using output-only measurements under changing environment. Mech. Syst. Signal Process. **22**(1), 34–56 (2008)
4. Reynders, E., Wursten, G., De Roeck, G.: Output-only structural health monitoring in changing environmental conditions by means of nonlinear system identification. Struct. Health Monit. **13**(1), 82–93 (2014)
5. Reynders, E., De Roeck, G.: Robust structural health monitoring in changing environmental conditions with uncertain data. In: Proceedings of the 11th International Conference on Structural Safety and Reliability, ICOSSAR, 2003, New York, NY, USA, 16–20 June 2013 (2013)
6. Bendsoe, M.P., Sigmund, O.: Topology Optimization: Theory Methods and Applications. Springer, New York (2003)
7. Bui, T.T., Reynders E., Lombaert G., De Roeck, G.: Ambient vibration testing of a large truss bridge with optimal sensor placement. In: Gao, G., Tutumluer, E., Chen, Y. (eds.) Recent Advances in Environmental Vibration; Proceedings of the 6th International Symposium on Environmental Vibration. China Scientific Book Services (2013)

8. Teughels, A., De Roeck, G.: Damage detection and parameter identification by finite element model updating. Arch. Comput. Methods Eng. **12**(2), 123–164 (2005)
9. Peeters, B., De Roeck, G.: Reference-based stochastic subspace identification for output-only modal analysis. Mech. Syst. Signal Process. **13**(5), 855–878 (1999)
10. Reynders, E., De Roeck, G.: Reference-based combined deterministic-stochastic subspace identification for experimental and operational modal analysis. Mech. Syst. Signal Process. **22**(3), 617–637 (2008)
11. Araujo, A., García-Palacios, J., Blesa, J., Tirado, F., Romero, E., Samartín, A., Nieto-Taladriz, O.: Wireless measurement system for structural health monitoring with high time-synchronization accuracy. IEEE Trans. Instrum. Meas. **61**(3), 801–810 (2012)
12. Lourens, E., Papadimitriou, C., Gillijns, S., Reynders, E., De Roeck, G., Lombaert, G.: Joint input-response estimation for structural systems based on reduced-order models and vibration data from a limited number of sensors. Mech. Syst. Signal Process. **29**, 310–327 (2012)
13. Cunha, A., Caetano, E., Magalhães, F., Moutinho, C.: Recent perspectives in dynamic testing and monitoring of bridges. Struct. Control Health Monit. **20**(6), 853–877 (2013)
14. Jonckers, T.: Development of High-accuracy Strain Sensors using Topology Optimization, MSc Thesis, KU Leuven (2016)
15. Anastasopoulos, D., Moretti, P., Geernaert, T., De Pauw, B., Nawrot, U., De Roeck, G., Berghmans, F., Reynders, E.: Modal strain identification from low-amplitude FBG data using an improved wavelength detection algorithm. In: Bakker, J., Frangopol, D.M., van Breugel, K. (eds.) Proceedings of the 5th International Symposium on Life-Cycle Civil Engineering, IALCCE 2016, pp. 319–326. Delft, The Netherlands, Taylor & Francis (2016)
16. Anastasopoulos, D., Moretti, P., Geernaert, T., De Pauw, B., Nawrot, U., De Roeck, G., Berghmans, F., Reynders, E.: Identification of modal strains using sub-microstrain FBG data and a novel wavelength-shift detection algorithm. Mech. Syst. Signal Process. **86**, 58–74 (2017)
17. Lamberti, A., Vanlanduit, S., De Pauw, B., Berghmans, F.: A novel fast phase correlation algorithm for peak wavelength detection of fiber bragg grating sensors. Opt. Express **22**(6), 7099–7112 (2014)
18. Reynders, E., Schevenels, M., De Roeck, G.: MACEC 3.3: a Matlab toolbox for experimental and operational modal analysis, BWM-2014-06, KU Leuven, internal report (2014)
19. Wang, F., Lazarov, B.S., Sigmund, O.: On projection methods, convergence and robust formulations in topology optimization. Struct. Multidisciplinary Optim. **43**, 767–784 (2011)

Flexible Architectures for Full-Scale Performance Evaluation of Tall Buildings: Burj Khalifa and Beyond

Tracy Kijewski-Correa[1(✉)] and Andrew Bartolini[2]

[1] Department of Civil and Environmental Engineering and Earth Sciences/Integration Lab, Keough School of Global Affairs, University of Notre Dame, Notre Dame, IN, USA
tkijewsk@nd.edu

[2] Department of Civil and Environmental Engineering and Earth Sciences, University of Notre Dame, Notre Dame, IN, USA
abartoli@nd.edu

Abstract. While the benefits of full-scale monitoring of civil infrastructure have been widely motivated, uptake and adoption within the building sector has been minimal due to a variety of practical barriers. These benefits are particularly noteworthy for the design, operation and maintenance of tall buildings, whose predicted responses are rarely verified by any formal feedback mechanism, despite their life safety and economic implications. This paper takes the first steps toward establishing these feedback loops and encouraging greater uptake by exploring the sensing architecture that was deployed in Burj Khalifa. Its modular hardware design and creative use of the building's local area network delivered a plug-and-play solution. Units could be readily deployed by non-experts to measure the building's accelerations and displacements as well as on-site meteorological conditions – encouraging local ownership of the system. These modules are coordinated by an on-site server, supporting efficient and scalable integration of a robust array of sensing modalities. The use of local servers overcomes many of the challenges of data acquisition in large-scale distributed sensing, while also automating data processing and web-based visualization. Given the growing emphasis on real-time displacement monitoring in tall buildings, the paper further explores how tiltmeters can be integrated into these modular sensor arrays to more effectively capture low-frequency displacements and the overturning action of core-based systems. The paper closes by considering how the development of modular sensing hardware for this signature application can be scaled to benefit a wider array of buildings. This democratization of sensing technology in the form of low-cost, re-deployable sensing modules can facilitate design feedback through community monitoring campaigns that directly engage building management as end users of this instrumentation, fostering uptake through exposure.

Keywords: Full-scale monitoring · Tall buildings · Global positioning systems · Accelerometers · Tiltmeters

© Springer International Publishing AG 2018
J.P. Conte et al. (eds.), *Experimental Vibration Analysis for Civil Structures*,
Lecture Notes in Civil Engineering 5, https://doi.org/10.1007/978-3-319-67443-8_2

1 Introduction

While the benefits of full-scale monitoring of civil infrastructure have been widely motivated, at minimum by the applications showcased at this conference, uptake and adoption within the buildings sector has been minimal, particularly outside of seismic zones due to a variety of practical barriers [1, 2]. These benefits are particularly noteworthy for the design, operation and maintenance of tall buildings. Design of these structures is reliant upon a myriad of simplifying assumptions whose implications are rarely verified by any formal feedback mechanism despite their life safety and economic implications [3]. Considering that the scale, cost and complexity of civil structures limits full-scale testing or prototyping in the design stage, the only viable feedback loops come from full-scale monitoring once a tall building is commissioned. Particularly in designs that push the envelope of structural typologies and construction technologies, this lack of feedback into the design process not only results in over-conservatism, but also limits the ability to formalize performance-based design processes for this critical class of structure. The detrimental impacts to the practice have been acknowledged by international professional organizations, who have called for an effort to generate databases of full-scale properties that could be used to inform future designs [4].

A number of urban zones around the globe such as Hong Kong, Shanghai, Chicago, Dubai, Seoul and Tokyo have responded by serving as living laboratories for the observation of tall building performance under wind and occasionally earthquakes [5–10]. The first author and her collaborators have been a part of this effort, instrumenting and/or analyzing the response of over seventy buildings in three different countries, beginning with the Chicago Full-Scale Monitoring Program [3] and culminating most recently with the first SmartSync installation on Burj Khalifa in 2008 [8]. What is noteworthy about these global monitoring efforts is the fact that these deployments were largely driven by the research community and not the building owners and management themselves. Thus while they represent successes in demonstrating a technology and even in securing permission to install it on private property, if post-commission monitoring is to truly proliferate, it must be viewed as an essential component of long-term building maintenance and operations. Making the transition to owner-driven monitoring programs necessitates a clear demonstration of the value-added through full-scale monitoring, requiring reductions in the cost and intrusion of these installations, as well as allowing ownership to interact with the monitoring process and benefit from data products that truly support their decision making [11].

Hardware design and system architecture thus become starting points to re-imagine monitoring systems that are less intrusive and costly to employ. The majority of these urban monitoring efforts have relied on wired instrumentation arrays in “hub and spoke” architectures with centralized data acquisition units (often data loggers). While these platforms have proven reliable and stable for long-term deployments (the Chicago Full-Scale Monitoring Program’s arrays have been in continuous operation since 2002), lengthy cables are prone to noise contamination and are difficult and expensive to install, particularly over the heights needed for tall buildings. This has resulted in an inherently rigid system that cannot be easily redeployed or expanded, thus relegating these installations to the highest unoccupied floor.

Certainly a number of recent technology advancements have challenged these limitations. By taking advantage of wireless communications, multi-hop radio or cellular relays have replaced cables to ease installation and maintenance burdens [12]. While the challenges of transmitting and synchronizing large amounts of data wirelessly with minimal packet loss and interference are well documented, a number of workarounds have been proposed. Applications, such as the four-story Four Seasons Building in Sherman Oaks, California affirm the ability to eliminate significant cost, while also increasing the ability to conduct rapid deployments [13]. However, tall buildings present a uniquely dense communications environment, as the mechanical floors where these sensors are often placed have a variety of noise sources, including transmission equipment belonging to local radio, television and cellular companies. This poses an interesting design requirement for sensor arrays in these buildings, one that delivers the reliability of a wired connection with the flexibly and ease of a wireless system to minimize cost and intrusion to building ownership and management.

2 Conceiving a Modular Sensing Architecture

The ownership of the Burj Khalifa (Dubai, UAE) recognized not just the value of their investment, but the fact that it was the tallest building ever constructed and was exposed to a wind climate that was unique in comparison to other urban zones around the world. Therefore, they solicited bids for a comprehensive Building Movement Monitoring System (BMMS) to assist in the building's operations and maintenance and even monitor the building during construction, scaling the sensor array up as the building rose. Given the cost and feasibility constraints, this would require a modular hardware design with minimal demands for dedicated runs of instrumentation cables. The result was a system called SmartSync, conceived by the first author and her collaborators at Notre Dame. SmartSync's first analog and digital prototypes (four modules in total) were deployed in Burj Khalifa during the late stages of its construction in July 2008 [14]. As a test of its scalability principles, this system was later expanded when the building was completed (summer of 2010) in partnership with the wind tunnel consultants at Cermak Peterka Petersen (CPP) to monitor acceleration responses within its core at six points along the height: Levels (L) 73, 123, 155 and 160, Tier (T) 23A, and the top of pinnacle [15]. The array also included displacement and meteorological condition monitoring at Level 160, as well as acceleration responses in the B2 sublevel at each of the three wings of the tower. This array is visualized in Fig. 1.

To subvert the need for dedicated instrumentation cabling and facilitate non-expert installation, the SmartSync concept relies upon the building's existing Internet backbone as a system of "virtual" instrumentation cables. Given the reliability of modern local area networks (LAN) in tall buildings and the sampling rate necessary to capture the dominant vibration modes, these networks have more than ample bandwidth for data transmission and an inherent ability to synchronize communications from distributed sensor nodes. A centralized server operating on the same network performs basic data acquisition (DAQ), event triggering, post-processing, and curation, while also providing an interface for data visualization. Note that the system does not rely on the clocks and

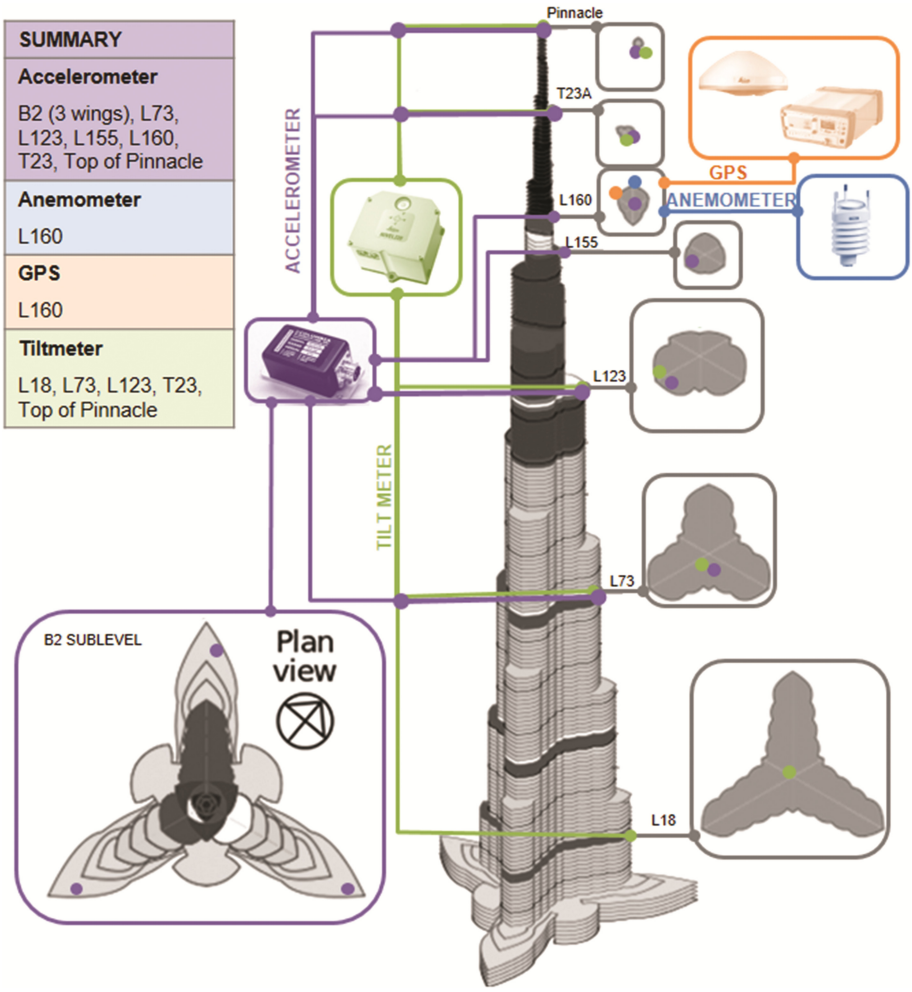

Fig. 1. Schematic representation of sensor modules on Burj Khalifa with approximate positions of installation on floorplan at instrumented levels.

time stamps from individual sensor modules for synchronization. Instead, the server executes a call to sample data simultaneously across the distributed devices, thereby linking all data delivered by this request to the same server timestamp. Certainly there exists some potential network latency, usually less than 1 ms in a reliable LAN environment, but this latency, if anything, affects only the delivery time since unified time stamping occurs at the moment data delivery is requested. To insure reliability of this data delivery, TCP/IP (Transmission Control Protocol/Internet Protocol) is invoked, with a forcible override of the Nagle algorithm. This stable stream delivery service guarantees transmission of data sent from one host to another without duplication or loss, ideally suited for data from variable sensors coordinated over LAN.

This centralization of all data acquisition functions at the server implies that only basic network interfacing is required at the location of each sensor, thus placing no restriction on the sensor type (analog or digital) and accommodating variable sampling rates. This has proven especially advantageous, as the system initially installed has been expanded over time, integrating various third party sensors into a single integrated BMMS. Moreover, as the configuration and triggering operations are all software-enabled at the server level, the system can be used concurrently for wind or seismic monitoring, with dual triggering mechanisms (top-down vs. bottom-up, respectively) designed to record continuous time histories in the event of significant responses driven by either hazard. Using this backbone, the sensor modules were designed with a "plug-and-play" philosophy, delivering units that could be moved to any location with access to power and Internet. This essentially places monitoring hardware directly in the hands of those best suited to advocate for it (building owners and management).

2.1 SmartSync Sensing Modules

While a detailed account of SmartSync's development is presented in Kijewski-Correa et al. [8], a summary of the hardware now follows. Dynamic response monitoring is delivered by an accelerometer module using low-noise, force-balance analog accelerometers from Columbia Research Laboratories (<1 μg resolution, 15 V/g sensitivity) with the capability of measuring down to DC, a critical consideration for a tall building like Burj Khalifa with fundamental modes under 0.1 Hz. In order to provide a stable interface for long-term monitoring in especially harsh desert environments, the accelerometers at upper elevations interface with a Campbell Scientific datalogger that samples at 20 Hz, in lieu of a lower-cost DAQ over LAN interface. Unfortunately, acceleration responses are insufficient to characterize structural performance of this class of structure. Considering the implications of $P-\Delta$ effects and the ensuing performance of drift-sensitive mechanical and cladding systems, total drifts of tall buildings must also be resolved. This includes capturing responses in the static and quasi-static frequency ranges under wind, which are often non-negligible for tall, flexible structures [16]. Capturing mean, background (quasi-static), and resonant displacements requires the accelerometers to be supplemented by alternate technologies like global positioning systems (GPS) [17], specially designed to accommodate the continuous variation in satellite visibility and orientation, as well as the potential for multipath distortions common in urban deployments [18]. Thus the design of a GPS-based displacement module requires the installation of an antenna outside of the building (Leica AT504 GG choke ring GPS antenna) connected by a short length of coaxial cabling with in-line surge protection to a Leica GRX1200 GG receiver acquiring data at 10 Hz. Additionally, the need to produce high accuracy displacement measurements (sub-centimeter accuracy) requires a second GPS displacement module to be installed on a nearby stationary structure (called the reference GPS station). Measurements taken on the primary structure are processed against these reference measurements to reduce atmospheric interferences that degrade the accuracy of GPS-calculated displacements.

The anemometer module offers direct measurement of on-site weather conditions (wind speed and direction) to evaluate the dynamic response against wind tunnel

predictions. In this case, the sensor again must be external to its electronics enclosure and with sufficient durability to withstand the harsh winds in this desert climate. This necessitated a compact, ultrasonic anemometer without moving parts (Vaisala WXT520 Met Station). This digital sensor streams wind velocity data, as well as temperature, humidity and barometric pressure, at a rate of 1 Hz through the same ruggedized Campbell Scientific datalogger used in the accelerometer module. The supporting hardware for each of these three sensors (and in the case of the accelerometers, the sensor itself) is housed in a ventilated, NEMA certified enclosure (Fig. 2), with an uninterruptible power supply and remote power regulator to provide control of power and reboot functions in event of a system failure.

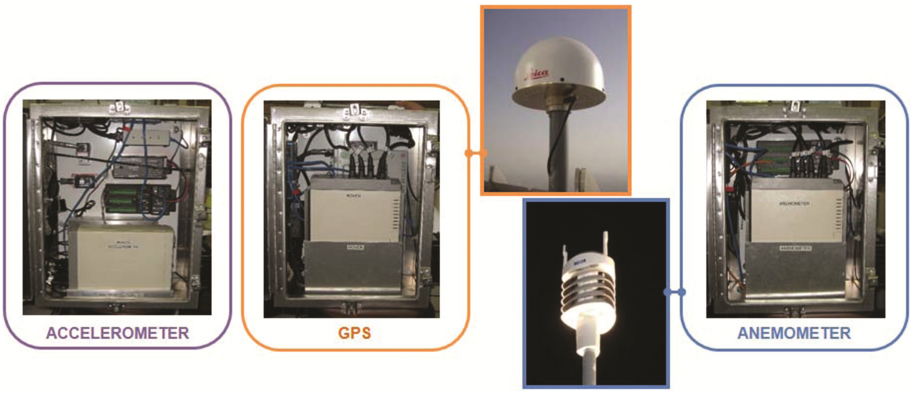

Fig. 2. Sensing modules initially deployed in Burj Khalifa: accelerometer, GPS and anemometer, with latter two modules linked to their external sensing element (GPS antenna and meteorological station, respectively).

2.2 Enhanced Displacement Monitoring

It became apparent that the ownership of Burj Khalifa had a drift-sensitive mindset. Displacements were an easier response quantity to comprehend (vs. accelerations) and most of the criteria for building operations or the interaction between structural and non-structural components were defined with respect to displacement. Thus the reliability of displacement monitoring for this building became critical. It is well understood that comprehensive displacement monitoring would always require a hybrid approach: an appropriate low frequency monitoring technology and an appropriate high frequency monitoring technology. The latter is of course best met by the high-precision accelerometers, while the former historically relied on GPS [8, 19–21]. As the previous section suggests, this was the approach initially adopted for Burj Khalifa. However, the requirement for unobstructed views of the sky and minimization of multipath effects caused by reflected signals [22–24] have proven difficult to overcome. Specifically, the installation at Level 160 produces significant obstruction of satellites and reflection of signals off the upper elevations of the tower. This renders the GPS displacements during these times highly unreliable. This prompted an exploration of alternative displacement sensors that

could diversify the array such that error sources unique to each sensor type can be corrected algorithmically through cross validation against the other data streams.

Fortunately, inclination sensors such as tiltmeters are able to capture the static and quasi-static components of a structure's overall response without the concerns over signal obstructions and distortions. Like GPS, tiltmeters are already commonly used for ongoing static monitoring during the construction of tall buildings like 432 Park Avenue and Freedom Tower in New York City, as well as the Burj Khalifa in Dubai [25–27]. Unfortunately, none of these projects retained this hardware for ongoing monitoring once the buildings were commissioned. More recently, tiltmeters have been used in two short-term dynamic monitoring studies (up to one day): the 600 m Canton Tower, formally known as the Guangzhou New TV Tower [23, 28] and a 30-story building in Turkey [29]. The study conducted on the Canton Tower demonstrated good agreement between tiltmeter data and the derived tilts from strain gauges along the height of the tower, assuming pure Euler bending of the structure [23, 28]. Conversely, the study on the 30-story building in Turkey assumed a shear-dominated behavior for the structure, with a linear increase of drift with height, resulting in significant differences between the tiltmeter-derived displacements and GPS data [29]. Thus the reliability of tiltmeter-derived displacements depends greatly on the consistency of assumptions made about the vertical distribution of quasi-static deformations and the actual building deformation profile and the type of sensors it will interact with in a hybrid array. The former point must acknowledge that no building will manifest a deformed shape that is solely flexure or shear-dominated. Thus, while showing promise as part of hybrid arrays, greater investigation into the long-term stability of these devices is required to accurately project displacements from inclination measurements and to enable the development of protocols to correct error sources inherent to the technology.

Leica Geosystem's high precision biaxial tiltmeters (NIVEL210) were evaluated for inclusion in Burj Khalifa's SmartSync array. These devices use a patented electro-optical concept to achieve a resolution is 0.001 mrad, with a ±3 mrad range. The frequency range of this digital instrument is dependent on the query rate of the supporting DAQ system, with laboratory validations confirming output rates up to 2 Hz, though 1 Hz is recommended for long-term monitoring campaigns. A series of tests discussed in Bartolini and Kijewski-Correa [30] benchmarked the device warm-up and drift characteristics, dynamic precision, temperature compensation, and corrections for lateral distortions induced by inertial sloshing of the liquid plane. These findings are briefly summarized herein:

- Drift characteristics are established through 45-day static operation of a pair of biaxial tiltmeters in a vibration-isolated room two stories below ground. The results in Fig. 3 illustrate that tiltmeter channels generally manifest negligible drifts, remaining within the manufacturer's stated accuracy limits for the entire 45-day period. Channels that do drift (see Tiltmeter #2 – Y Direction in Fig. 3) tend to manifest a persistent linear trend that can be removed in post-processing.

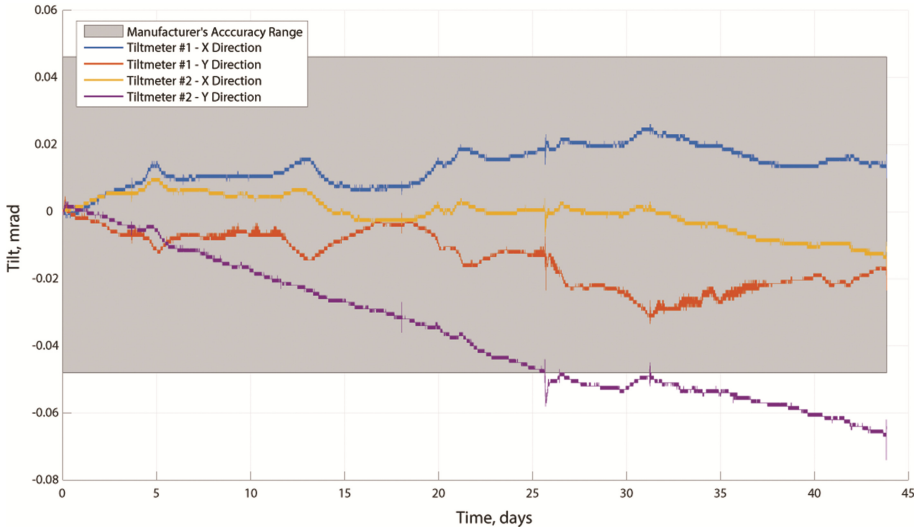

Fig. 3. Static test results for pair of biaxial tiltmeters in vibration-isolated room establishing drift characteristics.

- The dynamic range of the devices was experimentally established by inclining the devices on a rigid lever cyclically pivoting on a frictionless pin. Repeated trials on this assembly affirmed average peak inclination remains within 3% of the theoretical peak inclination (Fig. 4).

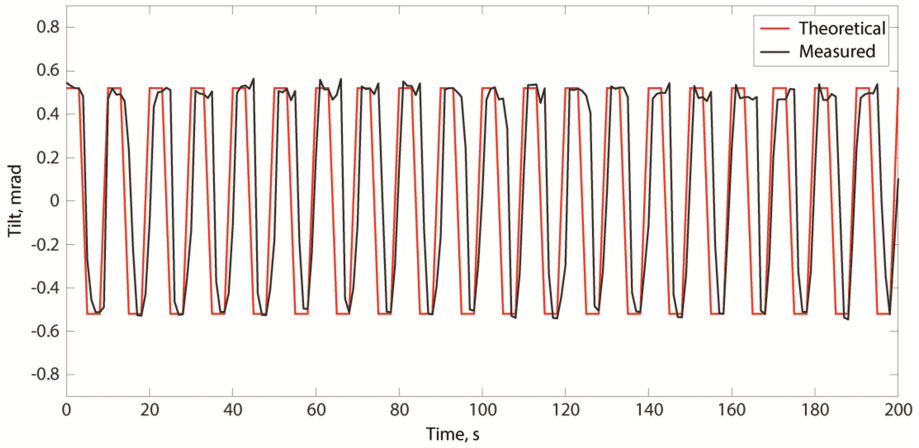

Fig. 4. Oscillating lever experimental results establishing tiltmeters' dynamic precision.

- To document temperature sensitivity, two tiltmeters were placed alongside each other and exposed to a period of controlled heating. The tiltmeters output their internal temperature, which is plotted in Fig. 5 to illustrate the effect of environmental heating

on internal device operations. Manufacturer-stated thermal error and ambient accuracy ranges are shaded in Fig. 5, encompassing the inclination outputs for the duration of the test. As the device's internal temperature lags the external temperature, inclination outputs particularly in the x-direction demonstrate the effects of heating before the rise in internal temperature. Empirical formula for temperature compensation are not available from the manufacturer, which is perhaps unsurprising since the devices manifest inconsistent nonlinear behavior during their stabilization in the cooling

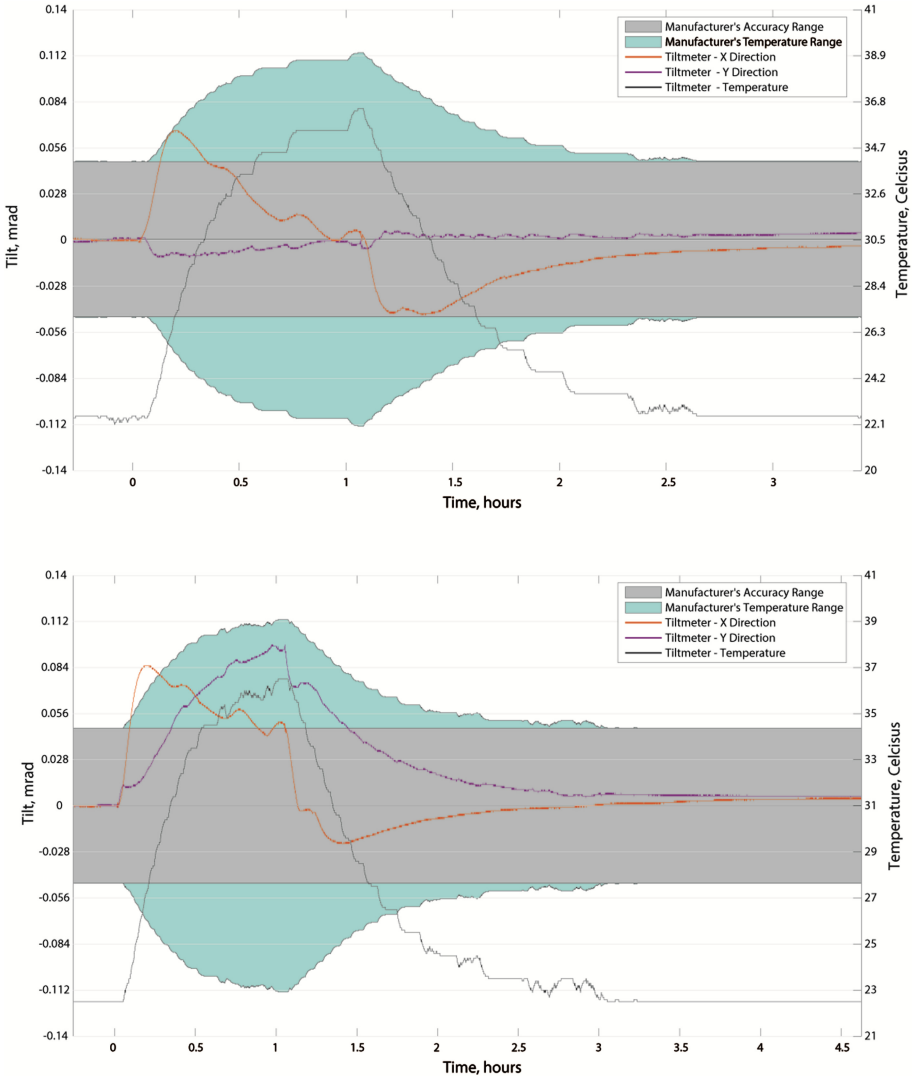

Fig. 5. Effect of temperature gradients on tiltmeter performance: tiltmeter #1 (top) and tiltmeter #2 (bottom).

period. However, correlations between the perceived tilts on both axes of the device and the internal temperature curve suggest that these effects can be de-trended from the data, particularly over the temperature ranges and time scales of the gradients anticipated during their deployment.

- In post-commissioning monitoring, tiltmeters will be exposed to dynamic sway responses in addition to inclinations. To investigate this effect, the devices were mounted on a portable shake table (in a non-inclined position). The table was then driven uni-axially with sinusoidal motion having an amplitude of ±1.0 cm and a frequency of 0.1 Hz (peak acceleration of 0.4 mg). Figure 6 demonstrates the detected dynamic inclination due to lateral sway, a result of the sloshing of the liquid film within the device. Thus the effect of lateral sway responses will have to be similarly post-processed using collocated acceleration measurements and retaining only the tiltmeter data that characterizes the sub-resonant behavior of the structure.

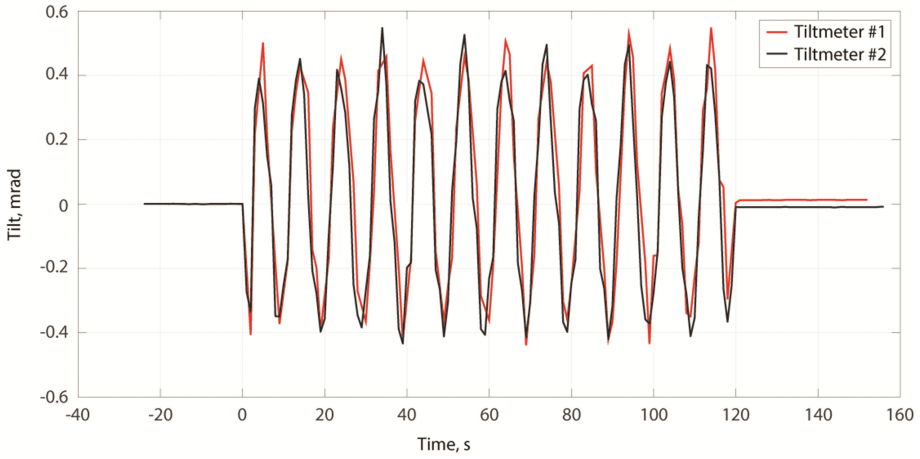

Fig. 6. Inclination outputs detected during simulated lateral sway responses on portable shake table.

2.3 Derived Displacement Data

In order to derive sub-resonant displacements from measured inclinations, it is assumed that displacements $v(h, t)$ of the structure at height h and time t will distribute according to the fundamental mode:

$$v(h, t) = V(t) * \varphi(h) \tag{1}$$

where $V(t)$ is the time-varying component of the structure's displacement, and $\varphi(h)$ is the structure's fundamental mode shape (normalized to one at the full height of the building). Taking the derivative with respect to height, the spatially-varying slope ($\theta(h, t)$) at height h and time t can be defined as:

$$\theta(h,t) = \frac{dv(h,t)}{dz} = V(t) * \frac{d\varphi(h)}{dz} = V(t) * \beta(h) \tag{2}$$

which is partitioned into time varying $V(t)$ and spatially varying $\beta(h)$ components. After low pass filtering to isolate the sub-resonant response, the tiltmeter's inclination data $\gamma\left(h_i,t\right)$ at the instrumented height h_i is used to determine the time-varying component of the structure's displacement:

$$V(t) = \frac{\gamma\left(h_i,t\right)}{\beta(h_i)} \tag{3}$$

With this, the sub-resonant (static and quasi-static) displacement response can be determined using Eq. (1). Meanwhile, accelerometer data is bandpass filtered to retain only the dynamic responses of the participating modes by removing sub-resonant trends and high frequency noise and is then double integrated to determine the resonant displacements, $\Delta\left(h_i,t\right)$. The total displacement at the instrumented levels is then determined by combining both these derived sub-resonant $\gamma\left(h_i,t\right)$ and resonant $\Delta\left(h_i,t\right)$ displacement responses from the tiltmeters and accelerometers, respectively. Note that displacements at non-instrumented locations can readily be projected to other floors using modal superposition [11].

These components contributing to these derived sub-resonant $\gamma\left(h_i,t\right)$ and resonant $\Delta\left(h_i,t\right)$ displacement responses are visually depicted in Fig. 7, reinforcing the fact that the response of tall buildings is generally a complex combination of cantilever overturning, particularly in systems with internal cores or exterior tubes, and frame racking from the transfer of interstory shears at each level of the building. Each of the sensors used to derive the total displacements are inherently disposed to capture one of these deformation components, with accelerometers better equipped to capture the lateral sway responses dominated by racking, while the tiltmeter records the plane by plane rotations of the building, i.e., its degree of overturning. Together, the relative proportions of these two different types of responses provides a number of critical insights, e.g., influence dynamic properties such as damping [31]. However, in order to use tiltmeters as a primary indicator of such system-level overturning under lateral loads, units must be installed in regions with sufficient rigidity to isolate this behavior and minimize the recording of other subsystem inclinations, e.g., secondary heaving of the floor plates. For practical purposes, this is generally achieved by mounting the units on the core walls of buildings with primarily internal reinforced concrete lateral systems or at the beam-column interfaces of exterior framed or braced tube systems (generally made of steel).

Finally, returning to the need to minimize costs in owner-driven monitoring programs, the optimal placement of tiltmeters becomes an important consideration. An optimization study was executed to identify which levels of Burj Khalifa should be instrumented to minimize errors in displacement estimation, based on the first four observed mode shapes [30]. Locations already instrumented by accelerometers were preferred so the units could share common network infrastructure and deliver collocated

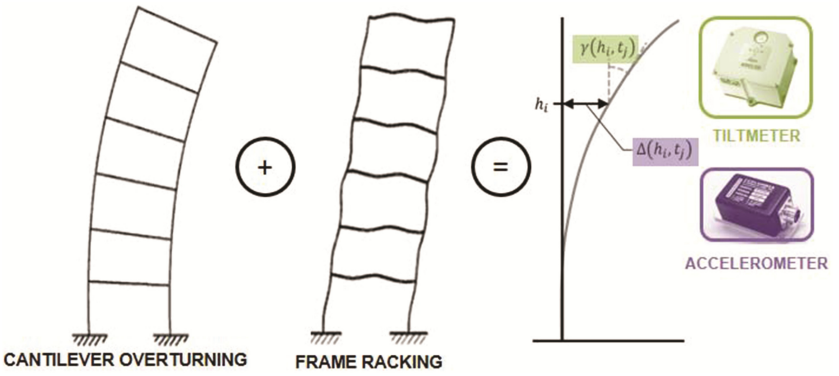

Fig. 7. Schematic depiction of the contributions of overturning and racking to overall displacement response of tall buildings as measured by accelerometer and tiltmeter modules.

observations of both the sub-resonant and resonant response. Thus tiltmeters are optimally placed at Levels 73, 123, Tier 23 and the top of pinnacle. A lower elevation installation point is also required to initialize the derived displacement algorithm that tracks the cumulative displacements [30]. As the sublevel (B2) installations are not in the core region, the algorithm initializes with a new installation at mechanical level L18. These locations are visually depicted in Fig. 1.

2.4 Server-Side Data Management

As discussed in Kijewski-Correa et al. [8], the initial SmartSync deployment established a Data Acquisition (DAQ) server on the building LAN that simultaneously supported real-time visualization and on-demand data analysis for authorized users through a secure web portal. The extent to which these processes were automated to minimize human interventions was an important design consideration that furthers the uptake of monitoring systems by building ownership and management. As the sensor array continues to expand, the approach to data management has partitioned the server architecture to further improve performance. In its current conception, an Analysis Server runs Leica Geosystem's SPIDER Software to calculate building displacements from the relative positions of approximately ten satellites received by the primary antenna on L160 and the adjacent reference station, at a precision of under 1 cm (in real-time kinematic mode). This server is also responsible for processing the raw inclination data from the tiltmeters to estimate the sub-resonant displacements of the tower according to the methodology in the previous section. The DAQ Server used the aforementioned TCP/IP-based sampling strategy to acquire these displacement feeds from the DAQ server, along with 21 channels of acceleration data (from 9 locations installed by the lead author's team at Notre Dame [ND] and by CPP), the SmartSync anemometer (at Level 160), and 22 distributed sonimometers installed by Honeywell (as part of an existing array to support building operations). The DAQ Server plays a central role in the architecture, as visualized in Fig. 8, providing five essential data functions:

1. **Data collecting:** All data acquisition operations are programmed in National Instruments LabVIEW, so that data can be collected in its various formats and even at different sampling rates. When the LabVIEW code executes a call for sampling data, it is collected simultaneously across all the distributed devices. All data captured at the time of this request is thereby tied to the same timestamp, that of the central server itself to minimize synchronization issues. This operation also includes transforming the data to physical engineering units, adjusting accelerometer orientations to yield results on the primary building axes, and correcting any bias or drift in the sensor outputs. In the case of GPS measurements, this includes removal of the GPS baseline position of the building, locked down by international positioning services using multiple regional reference stations.
2. **Displacement processing:** The DAQ server calculates the displacement composite (discussed previously) using the data from the GPS, tiltmeters and accelerometers, a process aided by the use of such low-noise hardware. At each instrumented level, the sub-resonant displacements (produced by the Analysis Server) are aggregated with the high frequency displacements derived from the accelerometer data, generating a composite displacement that more reliably estimates the mean, quasi-static and dynamic responses of the building.
3. **Statistical analysis and archiving:** As the data are received at the DAQ server at variable sampling rates, buffers accumulate the data over 10-minute intervals. Summary statistics are calculated from the buffered data every ten minutes, time stamped and stored in the Visualization (Viz) Server's Data Warehouse.
4. **Triggering and archiving:** One early consideration in system design was whether to retain all data, 24 hours a day, seven days a week sampled as frequently as 20 Hz. Certainly the cost of data storage need not drive such decisions; instead the ability to efficiently identify and display events of interest within vast stores of ambient data led to the adoption of an event-triggered acquisition strategy. The decision to trigger is instigated by a moving analysis window that evaluates the data buffered from the network's master modules to determine if their statistics (RMS values) have exceeded a pre-defined threshold. When this occurs, one-hour time histories (at the full sampling resolution of each module) are continuously recorded from all the sensing modules for as long as these thresholds are surpassed. For wind events, the master module is at the uppermost floor (top of pinnacle); for seismic events, the sublevel (B2) modules are used. Acquired time histories are stored in LabVIEW's binary format.
5. **Data pushing:** The DAQ server will intermittently push to the Data Warehouse on a dedicated Viz Server at multiple intervals. Every minute, the latest buffered and time stamped data is pushed for real-time visualization as separate packets for each sensor type. Every ten minutes, latest archival statistics are pushed, while triggered time histories are pushed on an hourly basis (when available). The Data Warehouse is backed-up daily off-site via FTP.

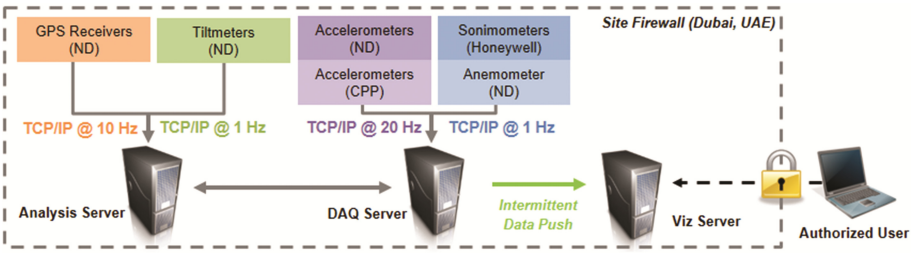

Fig. 8. Conceptualization of interactions between distributed sensor modules and servers partitioning data analysis, acquisition and visualization functions.

The introduction of a dedicated Viz Server in the latest iteration of the system architecture permits more robust end user-facing data query, annotation and visualization capabilities for this continually expanding sensor array. The project's new visualization environment provides users with a single secure dashboard, similar to that developed in the lead author's CyberEye project [32]. Authorized users can customize personal dashboards, controlling their sizing, placement and arrangement of the dashboard's windows within the web browser as they interact with two workflows. The first (Archived Data Exploration) uses the archived 10-minute statistics as the primary relational database for user queries. Since users can augment database entries with defined key-value pairs, this metadata can be queried using logical joint search operators to identify records that fall within specific ranges of dates, statistical properties, or even assigned attributes. For example, by taking advantage of software previously developed for data intake and discovery [33], a user can search "Shamal" events (metadata tag), that occurred in 2014 (exact year), with RMS accelerations greater than 10 mg at the pinnacle (data value range) and would then receive a list of the Data Warehouse entries meeting these joint criteria. Furthermore, any queried time history can be fed into the on-demand system identification tool to estimate dynamic properties or downloaded for additional offline analysis. These higher-level on-demand analyses are conducted by Matlab scripts running on the Viz Server, accessed by end users through web-accessible graphical user interfaces (Fig. 9).

The second workflow (Dynamic Visualization) creates a scalable visualization system for the growing number of sensor types and displays preferences for real-time (buffered) or queried (archival) data (see Table 1). Users simply go to the options tab of their dashboard and select the desired data type, location, variable, display type and preferred units (SI, English) from drop down menus encompassing the response selections available (Table 1). It is important to emphasize that by adopting this approach, the options within Table 1 can be expanded in the future without having to completely redesign the visualization environment. A number of standard displays (configurations) are also stored as defaults in the dashboard that meet the most common end user needs, e.g., real-time derived time histories or power spectra at all instrumented levels. These are visually summarized in Fig. 9, grouped by type. The real-time visualization suite displays current statistics, displacement/acceleration time histories and x-y loci plots,

meteorological conditions, and spectra derived from the latest data streams buffered in the server [8].

Table 1. Summary of visualization options for response data streams.

Data types	Locations	Variables	Display	Modality
Acceleration	B2 (Wing A), B2 (Wing B), B2 (Wing C), L73, L123, L155, L160, T23, top of pinnacle	X, Y	Statistics summary	Buffered data, Archived data (Query)
			Time history, Response locus, Power spectrum	Buffered data, Archived data (Query)
Derived displacements	L18, L73, L123, T23, top of pinnacle	X, Y (Mean, Quasi-Static, Dynamic)	Time history, Response locus, Power spectrum	Buffered data, Archived data (Query)
			Statistics summary	Buffered data, Archived data (Query)

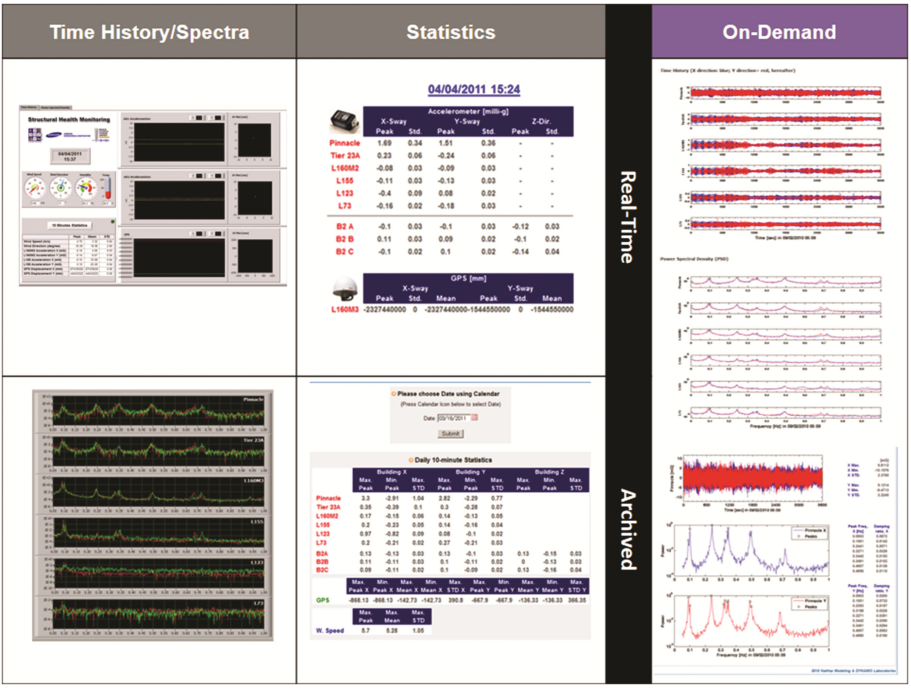

Fig. 9. Screenshots of default views in web-interfaces for Burj Khalifa.

3 Beyond Burj: Democratizing Sensing

Unfortunately, Burj Khalifa represents an extreme application of such value that it warranted long-term instrumentation and the owner's personal investment to develop and expand its scalable, modular architecture. Most building owners do not find themselves in this financial position and, perhaps even more importantly, with a mindset that recognizes the value of full-scale monitoring for not just their property, but as that much needed feedback to the design community on as-designed vs. as-built performance [4]. Given the diverse combinations of structural system [34], construction materials, soil conditions, and loading environments possible in practice, this feedback is needed from a large number of tall buildings. This reality prohibits the deployment of long-term traditional hub and spoke wired systems and favors a rapidly deployable, cost-effective, minimally intrusive sensing approach amenable to short-term monitoring campaigns on a large inventory of buildings [35].

While the SmartSync system invested significantly in server-side capabilities for real-time data acquisition and visualization using ruggedized hardware (necessitated by long-term deployments in harsh desert environments), there are viable hardware alternatives for short-term, batch processed data collection in benign environments. In fact, the commercial market has generated a number of microprocessors suitable for cost-effective sensor modules that can be rapidly deployed. This has enabled the design and fabrication of a prototype self-contained, re-deployable sensor module, shown schematically in Fig. 10. The prototype uses an Arduino UNO microprocessor to sample data from the same force-balance biaxial accelerometer used in Burj Khalifa (Columbia Model SA-207LN), though other lower cost accelerometers could be used since most buildings won't have fundamental modes near DC. Accelerations, processed by analog anti-aliasing filters, are stored on an SD card using a data logging shield. A supplemental custom op-amp circuit manages the signal conversions between this accelerometer and the Arduino UNO. In order to achieve higher resolution, the 10-bit ADC on the Arduino UNO is bypassed by a 16-bit A/D converter, resulting in an estimated resolution of less than 0.01 milli-g. A key point of emphasis is the reduced cost of the data acquisition

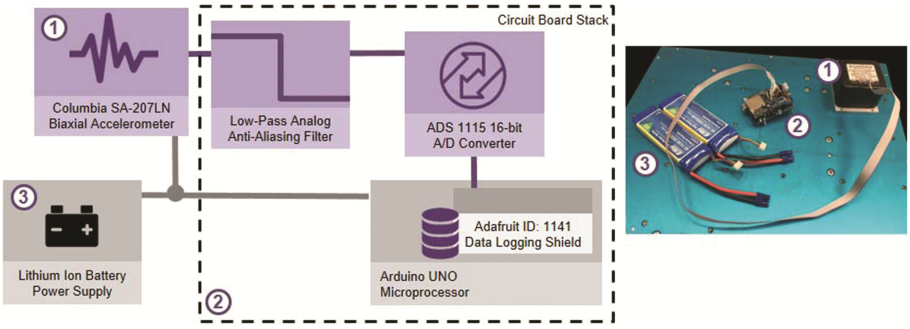

Fig. 10. Schematic of the re-deployable accelerometer module with numbered references to photographed components.

elements: approximately $100 (USD), which is an order of magnitude less than the ruggedized data loggers used in Fig. 2.

The implications of using low-cost hardware were explored through a comprehensive experimental validation using a series of static and dynamic (controlled shake table motions) tests [35]. Four independent static tests experimentally documented the RMS noise floor of the device as 0.01 milli-g. Dynamic testing then used a portable Quanser shake table to simulate three types of motions: sine waves of varying amplitudes and frequencies, sinusoidal chirps, and simulated multi-modal response of a tall building under wind. The sine wave tests confirmed the sensor module's ability to reliability capture low-amplitude accelerations as the errors associated with peak accelerations of 0.45 milli-g were under 3%. The sinusoidal chirp tests verified the sensor's ability to capture modulations in frequencies as shown in Fig. 11, with RMS errors from the entire suite of 12 tests consistently under 4%. Finally, the simulated tall building motion, which included modal responses at 0.10 Hz, 0.25 Hz, and 0.41 Hz, is shown in Fig. 12, achieving an RMS error of less than 1.5% over 18 experiments with RMS responses of over 1 milli-g.

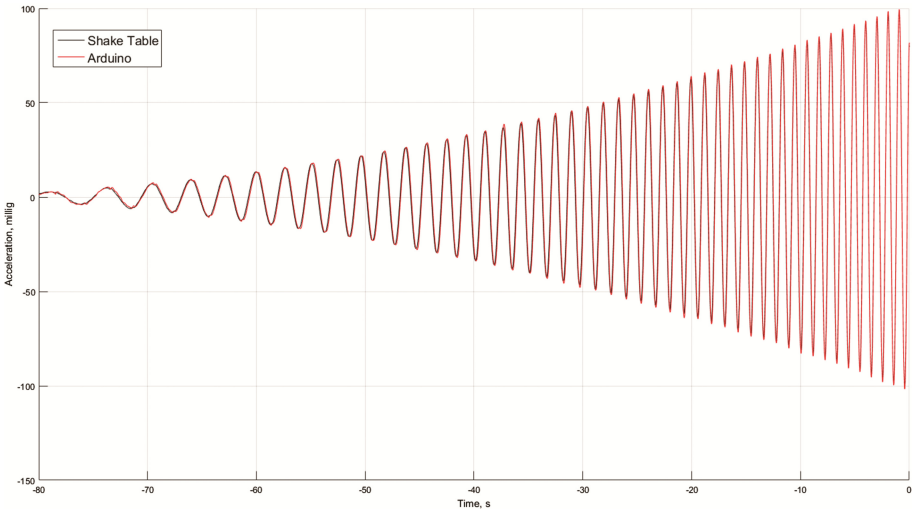

Fig. 11. Validation of rapidly deployable accelerometer module: sinusoidal chirp with recorded accelerations (red) plotted on top of experimentally simulated motion (black).

Even with a suitable technology that is cost-effective and easy to deploy, widespread monitoring of commissioned buildings will only proliferate if owners become advocates and see value in participating. For this reason, five units of this prototype have been fabricated and are slated to deploy for short-term monitoring campaigns on tall buildings in collaboration with partnering firms. These contacts (or the building management, typically building engineers) will receive the re-deployable monitoring units by mail and will install them as instructed to collect response data over a two day period. As all data acquisition and power requirements are met by the self-contained units, this will

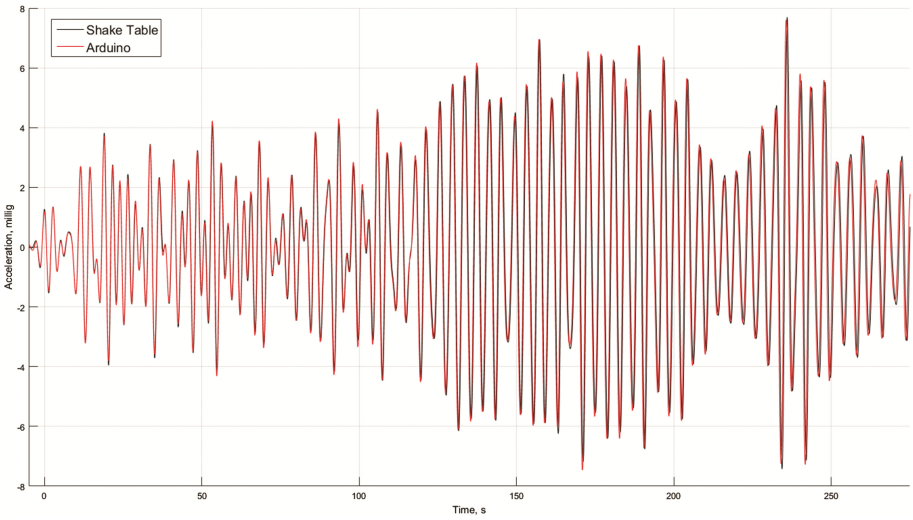

Fig. 12. Validation of rapidly deployable accelerometer module: simulated wind-induced response of tall building with recorded accelerations (red) plotted on top of experimentally simulated motion (black).

require no access to building networks or power sources. Once the short-term deployment completes, the units are shipped back to the research team for data retrieval and then sent off to another building in the community monitoring program. Meanwhile, the research team processes the data and generates a report on in-situ dynamic properties and response characteristics of the building, stylized to deliver salient features back to the owner and engineer of record that demonstrate the value of post-commissioning monitoring, while the wider research community receives anonymized parameters derived from this data to inform communal database-enabled design tools [4].

4 Conclusions

The many scaled and analytical models used in the design of civil infrastructure are rarely verified by any formal feedback mechanism, despite their life safety and economic implications. As discussed in this paper, tall buildings are especially primed to benefit from post-commissioning monitoring due to the fact that their designs are often driven by loadings derived from wind tunnel testing and highly sensitive to dynamic properties that have yet to be consistently predicted in the design stage. This paper provoked the question: How can we encourage owners and management to embrace monitoring after commissioning as a way to generate these critical feedback loops? Doing so will require not only minimizing cost and intrusion, but also encouraging greater buy-in among building owners and management by engaging them actively in the monitoring process. This paper chronicled steps toward this aim achieved by first introducing a modular sensing architecture that was initially deployed in the Burj Khalifa, the current world's tallest building. Emphasis was placed on how a modular hardware design and the

creative use of a building's local area network enables a plug-and-play solution that could be readily deployed by non-experts to measure the building's responses, literally placing the monitoring program in the hands of the building ownership. These modules are coordinated by local servers through TCP/IP, allowing the system to scale efficiently, to integrate a robust array of sensing modalities, and to overcome many of the challenges of distributed sensing in large-scale civil infrastructure. The story of this application further emphasized the need to develop systems that communicate information in a manner that owners and management understand – in many cases, real-time displacements. This necessitates hybrid sensor arrays of accelerometers to derive resonant displacements along with GPS, or as further motivated by this study tiltmeters, which not only measure sub-resonant response but also directly quantify the degree of overturning in core-based structural systems. Regardless of the sensor selected, these technologies are never truly "off the shelf," requiring experimental validation as well as algorithmic strategies to remove drifts, compensate for temperature effects, understand the effect of lateral motions on inclination sensing, and integrate measurements from different sensor types to offset errors inherent to each. Furthermore, all these operations must be automated to reduce human interventions so that building ownership, management and engineers can seamlessly interact with the data and data products through secure web interfaces to support their decision making. The paper closes by considering how the lessons learned in the development of modular sensing hardware for a signature application like Burj Khalifa can be scaled to benefit a wider cross section of buildings. This democratization of sensing technology in the form of low-cost, re-deployable sensing modules can facilitate design feedback through community monitoring campaigns that directly engage building management as end users of this instrumentation in-short term deployments on their buildings. By cycling sensors across portfolios of buildings with the help of engineers and building management, vital data on as-built performance can be mined to inform database-assisted design, while providing participating owners and engineers with a rare glimpse of their building's in-situ performance, hopefully fostering more open mindsets towards monitoring through the value delivered by this engagement.

Acknowledgments. The author gratefully acknowledges the generous support of Samsung Corporation (and a joint venture with Besix and Arabtec JV in collaboration with Turner Construction International) and Emaar Properties who have continued to support long-term monitoring on Burj Khalifa. The support of the US National Science Foundation (NSF) through Grants CMS 00-85109 and CMS 06-01143 that founded our full-scale monitoring programs in Chicago and scaled them to encompass Burj Khalifa. Of course, this work is only made possible through the collaborative efforts of my colleagues in the NatHaz laboratory led by Prof. Ahsan Kareem and assisted by Dr. Dae Kun Kwon, our new collaborations at the Center for Research Computing guided by Dr. Charles Vardeman, and the engineers at Samsung C&T under the leadership of Mr. Ahmad Abdelrazaq. I am also indebted to my former graduate students Jennifer Cycon and Jeff Loftus, who respectively assisted with the design and installation of the SmartSync modules on Burj Khalifa, and to undergraduate researchers Abelardo Corral, Eric Lifka, and Peter Rymsza and electrical engineering PhD student Michael McConnell who assisted with the fabrication and experimental validations of the new hardware platforms discussed herein.

References

1. Kijewski-Correa, T.L.: The case for full-scale monitoring of wind-sensitive structures: how to capitalize on the mutual benefits for structural designers and wind engineers. In: INVENTO 2014: XIII Conference of the Italian Association for Wind Engineering, Genoa, Italy (2014)
2. Catbas, F.N., Kijewski-Correa, T.: Structural identification of constructed systems: a collective effort toward an integrated approach that reduces barriers to adoption. J. Struct. Eng. Spec. Issue State-of-the-Art Struct. Ident. **139**, 1648–1652 (2013)
3. Kijewski-Correa, T., Kilpatrick, J., Kareem, A., Kwon, D.K., Bashor, R., Kochly, M., Young, B.S., Abdelrazaq, A., Galsworthy, J., Isyumov, N., Morrish, D., Sinn, R.C., Baker, W.F.: Validating the wind-induced response of tall buildings: a synopsis of the Chicago full-scale monitoring program. J. Struct. Eng. **132**, 1509–1523 (2006)
4. Oldfield, P., Trabucco, D., Wood, A.: Roadmap on the Future Research Needs of Tall Buildings. CTBUH, Chicago (2014)
5. Li, Q.S., Xiao, Y.Q., Wong, C.K.: Full-scale monitoring of typhoon effects on super tall buildings. J. Fluids Struct. **20**, 697–717 (2005)
6. Lu, X., Guo, X., Shi, W., Liu, J.: Vibration control and site measurement on Shanghai World Financial Center tower. China Nat. Struct. Eng. **4**, 63–70 (2009)
7. Kijewski-Correa, T., Kilpatrick, J., Kareem, A., Kwon, D.K., Bashor, B., Kochly, M., Young, B.S., Abdelrazaq, A., Galsworthy, J.K., Isyumov, N., Morrish, D., Sinn, R.C., Baker, W.F.: Validating wind-induced response of tall buildings: synopsis of the Chicago full-scale monitoring program. ASCE J. Struct. Eng. **132**, 1509–1523 (2006)
8. Kijewski-Correa, T., Kwon, D.K., Kareem, A., Bentz, A., Guo, Y., Bobby, S.: SmartSync: an integrated real-time structural health monitoring and structural identification system for tall buildings. J. Struct. Eng. Spec. Issue State-of-the-Art Struct. Ident. **139**, 1675–1687 (2013)
9. Satake, N., Suda, K., Arakawa, T., Sasaki, A., Tamura, Y.: Damping evaluation using full-scale data of buildings in Japan. J. Struct. Eng. **129**, 470–477 (2003)
10. Yoon, S.W., Ju, Y.K., Kim, S.B.: Vibration measurements on tall buildings in Korea. In: Proceedings of the 11th International Conference on Wind Engineering, Lubbock, TX (2003)
11. Weigand, T., Kijewski-Correa, T.: Automated habitability assessment and performance based design of tall buildings. In: Proceedings of ICWE 14, 14th International Conference on Wind Engineering, Porto Alegre, Brazil (2015)
12. Kijewski-Correa, T., Su, S., Cycon, J.: System identification in wired, wireless and hybrid architectures. In: Proceedings of 5th International Engineering and Construction Conference (IECC'5), Irvine, CA (2008)
13. Chintalapudi, K., Fu, T., Paek, J., Kothari, N., Rangwala, S., Caffrey, J., Govindan, R., Johnson, E., Masri, S.: Monitoring civil structures with a wireless sensor network. IEEE Internet Comput. **10**, 26–34 (2006)
14. Abdelrazaq, A.: Design and construction planning of the Burj Khalifa, Dubai, UAE. In: Structures Congress, Orlando, FL (2010)
15. Abdelrazaq, A.: Validating the dynamics of the Burj Khalifa. CTBUH J. **2**, 18–23 (2011)
16. Williams, T., Kareem, A.: Performance of building cladding in urban environments under extreme winds. In: Proceedings of 11th International Conference on Wind Engineering, Lubbock, TX (2003)
17. Kijewski-Correa, T., Kareem, A., Kochly, M.: Experimental verification and full-scale deployment of global positioning systems to monitor the dynamic response of tall buildings. J. Struct. Eng. **132**, 1242–1253 (2006)

18. Kijewski-Correa, T., Kochly, M.: Monitoring the wind-induced response of tall buildings: GPS performance and the issue of multipath effects. J. Wind Eng. Ind. Aerodyn. **95**, 1176–1198 (2007)
19. Cazzaniga, N.E., Pinto, L., Forlani, G., Abruzzi, P.: Monitoring oscillations of slender structures with GPS and accelerometers. In: From Pharaohs to Geoinformatics, FIG Working Week 2005 and GSDI-8, Cairo, Egypt (2005)
20. Li, X., Ge, L., Ambikairajah, E., Rizos, C., Tamura, Y., Yoshida, A.: Full-scale structural monitoring using an integrated GPS and accelerometer system. GPS Solut. **10**, 233–247 (2006)
21. Smyth, A., Wu, M.: Multi-rate Kalman filtering for the data fusion of displacement and acceleration response measurements in dynamic system monitoring. Mech. Syst. Signal Process. **21**, 706–723 (2007)
22. Nickitopoulou, A., Protopsalti, K., Stiros, S.: Monitoring dynamic and quasi-static deformations of large flexible engineering structures with GPS: accuracy, limitations and promises. Eng. Struct. **28**, 1471–1482 (2006)
23. Xia, Y., Zhang, P., Ni, Y., Zhu, H.: Deformation monitoring of a super-tall structure using real-time strain data. Eng. Struct. **67**, 29–38 (2014)
24. Yi, T., Li, H., Gu, M.: Recent research and applications of GPS-based monitoring technology for high-rise structures. Struct. Control Health Monit. **20**, 649–670 (2013)
25. Leica Geosystems: The vertical alignment system: Building tall and straight, World Trade Center One (2014)
26. Abdelrazaq, A.: Validating the structural behavior and response of Burj Khalifa: synopsis of the full-scale structural health monitoring programs. Int. J. High-Rise Build. **1**(1), 37–51 (2011)
27. Stocking, A.: Standing tall, with very good posture, 12 Aug 2014. http://cenews.com/article/9843/standing-tall-with-very-good-posture
28. Ni, Y.Q., Xia, Y., Liao, W.Y., Ko, J.M.: Technology innovation in developing the structural health monitoring system for Guangzhou new TV tower. Struct. Control Health Monit. **16**, 73–98 (2009)
29. Yigit, C.O., Li, X., Inal, C., Ge, L., Yetkin, M.: Preliminary evaluation of precise inclination sensor and GPS for monitoring full-scale dynamic response of a tall reinforced concrete building. J. Appl. Geod. **4**, 103–113 (2010)
30. Bartolini, A., Kijewski-Correa, T.: Capturing the total displacement of tall buildings: use of tiltmeters in full-scale monitoring arrays. In: 2017 ASCE Structures Congress, Denver, CO (2017)
31. Williams, S., Bentz, A., Kijewski-Correa, T.: A typology-driven damping model (TD2M) to enhance the prediction of tall building dynamic properties using full-scale wind-induced response data. In: Proceedings of the 12th Americas Conference on Wind Engineering (12ACWE), Seattle, WA (2013)
32. Kijewski-Correa, T., Smith, N., Taflanidis, A., Krusche, M., Liu, C., Vardeman, C., Kennedy, A.: CYBER-EYE: development of integrated cyber-infrastructure to support rapid hurricane risk-assessment. In: Proceedings of the 12th Americas Conference on Wind Engineering (12ACWE), Seattle, WA (2013)
33. Bartolini, A., Kijewski-Correa, T., Smith, N., Kennedy, A., Krusche, M., Vardeman, C.: CyberEye data intake and discovery cyberinfrastructure for post-event reconnaissance. In: 14th International Conference on Wind Engineering, Porto Alegre, Brazil (2015)
34. Bartolini, A., Kijewski-Correa, T.: A uniform vernacular for structural systems in modern tall buildings. In: CTBUH 2015 New York Conference, New York City, NY (2015)
35. Bartolini, A., Kijewski-Correa, T.: A predictive model for damping in tall buildings based on structural system behavior. In: 2017 ASCE Structures Congress, Denver, CO (2017)

Information-Driven Modeling of Structures Using a Bayesian Framework

Costas Papadimitriou[1(✉)], Costas Argyris[1], and Panagiotis Panetsos[2]

[1] Department of Mechanical Engineering,
University of Thessaly, 38334 Volos, Greece
costasp@uth.gr
[2] Capital Maintenance Department, Egnatia Odos S.A., 57001 Thermi, Greece

Abstract. This work presents a comprehensive Bayesian framework for integrating information from data and models of civil infrastructure systems. In the proposed framework, modeling uncertainties are quantified and propagated through simulations using probability tools. Bayes theorem is used to select the most appropriate model among alternative competing ones, to estimate the parameters of a model and the uncertainties in the parameters, and to propagate the uncertainties in output quantities of interest that are important for evaluating structural performance and safety. The framework is developed using as data the modal characteristics estimated from response time history measurements. Theoretical challenges associated with the selection of the model prediction error equation introduced to build up the likelihood are pointed out. Bayesian tools such as Laplace asymptotic approximations and sampling algorithms require a moderate to very large number of system re-analyses to be performed, often resulting in excessive computational demands. Computationally efficient techniques are presented to drastically speed up computations within the Bayesian uncertainty quantification framework. These techniques include model reduction techniques based on component mode synthesis, surrogate models and parallelized Bayesian algorithms to exploit HPC environments. Bayesian optimal experimental design methods constitute a major component of the proposed framework for cost-effectively selecting the most informative data. A computationally efficient asymptotic approximation is proposed to simplify information-based utility functions used for optimizing the placement of sensors in a structure. The structure of the approximation provides insight into the use of the prediction error spatial correlation to avoid sensor clustering, as well as the effect of the prior uncertainty on the optimal sensor configuration. The framework is illustrated by integrating vibration measurements and high fidelity models for (a) a reinforced concrete bridge to update stiffness related model parameters, and (b) a circular hanger to estimate the axial tension required in structural safety evaluations.

Keywords: Bayesian inference · Parameter estimation · Model selection · Optimal sensor placement · Structural dynamics

© Springer International Publishing AG 2018
J.P. Conte et al. (eds.), *Experimental Vibration Analysis for Civil Structures*,
Lecture Notes in Civil Engineering 5, https://doi.org/10.1007/978-3-319-67443-8_3

1 Introduction

Computational science tools for handling uncertainties in structural dynamics simulations, based on experimental/monitoring data, are conceptually and computational much more challenging that conventional computing tools. Bayesian analysis provides a logical framework for quantifying and propagating uncertainties in system simulations, integrating physics-based models and available data. Bayesian inference is used for quantifying and calibrating uncertainty models in structural dynamics based usually on vibration measurements, as well as propagating these uncertainties in structural dynamics simulations for updating robust predictions of system performance, reliability and safety [1]. The Bayesian framework is also used to guide the design of experiments in order the cost-effectively collect the most informative data for parameter estimation. The process of data-driven modeling and uncertainty quantification is important for finite element model updating, structural health diagnosis, and decision making for cost-effective system design and maintenance actions that meet performance/safety requirements. Thus, exploiting knowledge from data to develop confidence in the model predictions is expected to improve the resilience of engineering infrastructure systems against hazardous events.

Predictions of uncertainties within the Bayesian framework depend on the selection of the structure of the error terms in the model prediction error equations [2]. Bayesian tools such as Laplace methods of asymptotic approximation [3] and sampling algorithms such as Markov Chain Monte Carlo (MCMC) [4, 5] are used to represent the posterior distribution of the model parameters, as well as compute multidimensional integrals over high-dimensional spaces of the uncertain model parameters, manifested in the formulations for model class selection, robust predictions and model averaging [6–8]. The asymptotic approximations involve solving optimization problems as well as computing the Hessian of certain functions in a small number of points in the parameter space. The sampling algorithms involve generating samples for tracing and then populating the important uncertainty region in the parameter space, as well as evaluating integrals over high-dimensional spaces of the uncertain model parameters. These tools require a moderate to very large number of system re-analyses to be performed over the space of uncertain parameters. For complex models of engineering systems, for which one simulation may require a significant amount of time, the overall computational demands involved in the Bayesian tools may be substantial. For finite element models involving hundreds of thousands or even million degrees of freedom and nonlinear actions activated during system operation, the computational demands in the Bayesian framework may be excessive.

Selected theoretical and computational developments of a Bayesian inference framework for structural dynamics are addressed in the present paper. The framework is presented for data consisting of modal frequencies and mode shapes. The importance of the selection of the model prediction errors are pointed out by comparing two different prediction error models. For large-order finite element (FE) models of hundreds of thousands or millions degrees of freedom, and/or localized nonlinear actions activated during system operation, efficient techniques are presented to drastically speed up computations. The optimal experimental design problem is also addressed.

An efficient asymptotic approximation is used to simplify information-based utility functions introduced for measuring the useful information contained in the data. It is shown that the approximation provides valuable insight into the importance of the prediction error spatial correlation, as well as the effect of the prior uncertainty on the optimal sensor placement. Applications are mainly focus on the use of the framework for FE model selection/calibration, as well as structural health monitoring using vibration measurements from civil infrastructure.

2 Bayesian Framework for Uncertainty Quantification and Propagation

In this section we present the Bayesian framework for uncertainty quantification, parameter estimation, model selection and uncertainty propagation.

2.1 Parameter Estimation and Model Selection

The Bayesian framework for parameter estimation [3, 6] and model selection [7] is used to estimate the parameters of a structural model along with their uncertainties, and choose the best model among alternative competing ones utilizing data. The inference is based on certain characteristics of the measured response time histories. Herein we illustrate the method using modal characteristics (modal frequencies and modeshapes). Let m be the experimentally identified modal frequencies and mode shapes $D = \{\hat{\omega}_r, \hat{\phi}_r \in R^{N_0}, r = 1, \cdots, m\}$ of the structure, where N_0 is the number of measured DOFs. Consider also a parameterized model class M and let $\underline{\theta} \in R^{N_\theta}$ be the set of free structural model parameters to be identified using the estimated modal properties. Depending on the model class used, the model parameters may include material properties, structural stiffness and mass related characterisitcs, conditions at joints between structural elements or at boundaries, as well as geometrical properties such as equivalent beam length(s) used in simplified models of structures. The predictions of the modal frequencies and mode shapes obtained for a particular value of the parameter set are denoted by $\omega_r(\underline{\theta})$ and $\phi_r(\underline{\theta})$, respectively.

Probability density functions (PDF) are used to quantify uncertainties in the parameter set $\underline{\theta}$. Using Bayes' theorem, the posterior PDF $p(\underline{\theta}|D, M)$ of the model parameters $\underline{\theta}$ based on the measured data D and the modeling assumptions, is obtained as follows:

$$p(\underline{\theta}|D, M) = \frac{p(D|\underline{\theta}, M)p(\underline{\theta}|M)}{p(D|M)} \tag{1}$$

where $p(D|\underline{\theta}|M)$ is the probability of observing the data (likelihood function) from a model M corresponding to a particular value of the parameter set $\underline{\theta}$, $p(\underline{\theta}|M)$ is the prior

PDF of the model parameters, and $p(D|M)$ is the evidence of the model class given by the multi-dimensional integral

$$p(D|M) = \int_{\Theta} p(D|\underline{\theta}, M) p(\underline{\theta}|M) d\underline{\theta} \tag{2}$$

where Θ is the domain of variation of the model parameters.

The likelihood $p(D|\underline{\theta}, M)$ is derived by using a probability model for the prediction error for the modal frequencies and mode shapes. One such model is mathematically postulated as follows:

$$\hat{\omega}_r = \omega_r(\underline{\theta}) + \hat{\omega}_r e_r \tag{3}$$

$$\widehat{\underline{\phi}}_r = \beta_r \underline{\phi}_r(\underline{\theta}) + \left\| \widehat{\underline{\phi}}_r \right\| \underline{\varepsilon}_r \tag{4}$$

for all modes $r = 1, \ldots, m$ where $\beta_r = \widehat{\underline{\phi}}_r^T \phi_r / \underline{\phi}_r^t \underline{\phi}_r$, with $\underline{\phi}_r \equiv \underline{\phi}_r(\underline{\theta})$, is a normalization constant that accounts for the different scaling between the measured and the predicted mode shape. The model prediction errors e_r and $\underline{\varepsilon}_r$ are due to modeling error and measurement noise. Modeling the prediction errors as $e_r \sim N(0, \sigma_\omega^2)$ and $\underline{\varepsilon}_r \sim N(0, \sigma_\phi^2 I)$ zero-mean Gaussian variables, assuming that the prediction errors are independent, and including the prediction error parameters σ_ω and σ_ϕ into the uncertain parameter set $\underline{\theta}$, the likelihood $p(D|\underline{\theta})$ takes the form

$$p(D|\underline{\theta}, M) \sim \frac{1}{(\sqrt{2\pi})^m \sigma^m} \exp\left[-\frac{m}{2\sigma^2} J(\underline{\theta}) \right] \tag{5}$$

where $J(\underline{\theta})$ is given by

$$J(\underline{\theta}) = \frac{1}{m} \sum_{r=1}^{m} \frac{[\omega_r(\underline{\theta}) - \hat{\omega}_r]^2}{\hat{\omega}_r^2} + \frac{\sigma_\omega^2}{\sigma_\phi^2} \frac{1}{m} \sum_{r=1}^{m} \frac{\left\| \beta_r \phi_r(\underline{\theta}) - \hat{\phi}_r \right\|^2}{\left\| \hat{\phi}_r \right\|^2} \tag{6}$$

Using the prediction error introduced in Eq. (4), each mode shape component is taken as an independent data point. The mode shape data can be used as correlated or uncorrelated data, depending on the choice of the covariance matrix. Introducing correlation between the mode shape components is more realistic [2], but requires the choice of a suitable correlation function. Herein the mode shape data are treated as uncorrelated. An alternative approach is to use the modal assurance criterion (MAC) value between the predicted and experimental mode shape. Specifically, the non-negative numbers $1 - MAC_r^2$ for all modes $r = 1, \ldots, m$ are assumed to follow a lognormal distribution whose parameters are included in the uncertain parameter set. This approach actually reduces the number of data from a full vector to a scalar measure of discrepancy between two vectors (experimental and model predicted mode

shapes). The effect of the two prediction error models in estimating model parameter uncertainties will be examined later in the application section.

The Bayesian framework can also be used to select the best model class among a family of alternative competitive model classes $M_1, \ldots, M_\mu$ [7], used to represent the dynamics of the structure. Using the Bayes theorem, the posterior probability $P(M_i|D)$ of the model class M_i given the data D is obtained from

$$P(M_i|D) = \frac{p(D|M_i)P(M_i)}{p(D)} \tag{7}$$

where $p(D|M_i)$ is the evidence of M_i, $P(M_i)$ is the prior probability of M_i and $p(D) = \sum_{i=1}^{\mu} p(D|M_i)P(M_i)$ is a normalizing constant that guaranties that the sum of the probabilities over all model classes considered in the selection equals one. Assuming that the model classes are equally probable prior to the use of the data, then the most probable model class based on the data corresponds to the model class with the highest evidence.

Bayesian computational tools are used to estimate the uncertainty in the model parameters, select the best model class and propagate the parameter uncertainties to useful quantities of interest. Herein we use the Transitional Markov Chain Monte Carlo (TMCMC) [8] algorithm and its parallelized extended version [9] in order to sample from the posterior PDF of each model class, estimate uncertainties in the model parameters, as well as propagate uncertainties to compute output quantities of interest such as modal frequencies and MAC values. One more merit of using the TMCMC algorithm for Bayesian purposes is the calculation of the evidence as a by-product of the algorithm [8]. Alternative Gaussian asymptotic approximations can also be used to approximate the posterior PDF and carry out the model selection and uncertainty propagation. For details the reader is referred to reference [10].

2.2 Uncertainty Propagation

The main interest in updating the uncertainty in the model parameters through measured data lies in propagating this uncertainty through the model to quantify the uncertainty in output quantities of interest (QoI). Specifically, given a scalar output QoI $g(\underline{\theta})$ which depends on the uncertain parameters $\underline{\theta}$, the objective is to evaluate its uncertainty given the uncertainty in $\underline{\theta}$ which is quantified by the posterior PDF in (1). Simple measures of uncertainty in $g(\underline{\theta})$ are the mean, given by

$$Mean[g(\underline{\theta})] = E[g(\underline{\theta})] = \int g(\underline{\theta})p(\underline{\theta}|D)d\underline{\theta} \tag{8}$$

and the variance, given by $Var[g(\underline{\theta})] = E[g^2(\underline{\theta})] - E^2[g(\underline{\theta})]$, where $E[g^2(\underline{\theta})] = \int g^2(\underline{\theta})p(\underline{\theta}|D)d\underline{\theta}$ is the second moment of $g(\underline{\theta})$. Stochastic simulation algorithms are used to provide sample estimates of the integrals. Specifically, the Transitional Markov Chain Monte Carlo (TMCMC) algorithm [8] is used. The samples $\underline{\theta}^{(j)}, j = 1, \ldots, N$

drawn from the posterior PDF $p(\underline{\theta}|D)$ can be used to approximate the integrals (8) with the sample estimate

$$E[g(\underline{\theta})] \approx \frac{1}{N}\sum_{j=1}^{N} g\left(\underline{\theta}^{(j)}\right) \tag{9}$$

The samples $\underline{\theta}^{(j)}, j = 1, \ldots, N$ are dependent, but are used for statistical averaging as if they were independent, accepting a reduced accuracy in the sample estimate.

2.3 Techniques for Reducing Computational Demands

Bayesian inference techniques are computationally very demanding operations due to the large number of FE model re-analyses required. An outline of effective methods for drastically reducing the computational demands at the system, algorithm and hardware levels within the aforementioned Bayesian tools is next presented. Specifically, at the system level, component mode synthesis (CMS) techniques [11–13], consistent with the parameterization scheme, are integrated with Bayesian techniques to efficiently handle linear structural components of large-order models of hundreds of thousands or millions degrees of freedom and localized nonlinear actions activated during system operation. These techniques are used to carry out the re-analyses efficiently in a substantially reduced space of generalized coordinates using exact component modes and characteristic interface modes computed only once from a reference FE model. The re-assembling of the reduced-order system matrices from components and interface modes is avoided. The effectiveness of the theoretical and computational developments have been demonstrated with model updating applications for a number of structures in references [11–13]. At the algorithmic level, surrogate models such as kriging techniques are adopted within the TMCMC algorithm to drastically reduce the number of computationally expensive full model runs [14]. Finally, parallel computing algorithms implemented within TMCMC [9, 15] are proposed to efficiently distribute the computations in available multi-core CPUs. Due to space limitation, the reader is referred to the cited papers for the details and effectiveness of these techniques to reduce the computation effort for a number of structural dynamics problems.

3 Optimal Experimental Design

The objective of an experiment is to maximize the information contain in the data for estimating the parameters of the model. Lindley [16] has introduced the expected utility function $U(\underline{\delta})$ to reflect the usefulness of the experiment in estimating the model parameters, where $\underline{\delta}$ are design variables. The expected utility function has the form

$$U(\underline{\delta}) = \int_{\mathrm{Y}} \int_{\Theta} u(\underline{\delta}; \underline{\theta}, \underline{y})\, p(\underline{\theta}, \underline{y}|\underline{\delta})\, d\underline{\theta}\, d\underline{y} \tag{10}$$

where $u(\underline{\delta};\underline{\theta},\underline{y})$ is the utility function given a particular value of the model parameter set $\underline{\theta}$ and the outcome $\underline{y}$ from the experiment, $p(\underline{\theta},\underline{y}|\underline{\delta}) = p(\underline{\theta}|\underline{y},\underline{\delta})\,p(\underline{y}|\underline{\delta})$, $p(\underline{\theta}|\underline{y},\underline{\delta})$ is the posterior uncertainty in the model parameters given the outcome $\underline{y}$ and $p(\underline{y}|\underline{\delta})$ is the uncertainty in the data. The utility function is chosen to be related to the information gained by the experiment. Based on information theory, it can be chosen to be the relative entropy or the Kullback-Leibler divergence between the prior and posterior probability distribution given an outcome $\underline{y}$ obtained from an experimental design $\underline{\delta}$. The expected utility function is an average of the utility function over all possible values of the model parameters as they are inferred from the data, and all the possible outcomes of the experiment. Using the relative entropy in (10) in place of the utility function, the expected utility function takes the form

$$\begin{aligned} U(\underline{\delta}) &= \int_{\Upsilon}\int_{\Theta} p(\underline{\theta}|\underline{y},\underline{\delta})\ln\frac{p(\underline{\theta}|\underline{y},\underline{\delta})}{\pi(\underline{\theta})}\,d\underline{\theta}\,p(\underline{y}|\underline{\delta})\,d\underline{y} \\ &= \int_{\Upsilon}\int_{\Theta} p(\underline{\theta}|\underline{y},\underline{\delta})\ln p(\underline{\theta}|\underline{y},\underline{\delta})\,d\underline{\theta}\,p(\underline{y}|\underline{\delta})\,d\underline{y} - \int_{\Theta}\int_{\Upsilon} p(\underline{\theta}|\underline{y},\underline{\delta})\,p(\underline{y}|\underline{\delta})\,d\underline{y}\ln\pi(\underline{\theta})\,d\underline{\theta} \end{aligned} \tag{11}$$

Introducing the information entropy of the posterior PDF of the model parameters

$$H(\underline{y},\underline{\delta}) = -\int_{\Theta} p(\underline{\theta}|\underline{y},\underline{\delta})\ln p(\underline{\theta}|\underline{y},\underline{\delta})\,d\underline{\theta} \tag{12}$$

for a given outcome of the experiment $\underline{y}$ obtained from design $\underline{\delta}$, substituting (12) into (11) and noting that the second integral is a constant, say a, the expected utility function takes the form

$$\begin{aligned} U(\underline{\delta}) + a &= -\int_{\Upsilon} H(\underline{y},\underline{\delta})\,p(\underline{y}|\underline{\delta})\,d\underline{y} = -\int_{\Theta}\int_{\Upsilon} H(\underline{y},\underline{\delta})\,p(\underline{y}|\underline{\theta},\underline{\delta})\,d\underline{y}\,p(\underline{\theta}|\underline{\delta})\,d\underline{\theta} \\ &= -\int_{\Theta} \bar{H}(\underline{\theta},\underline{\delta})\,\pi(\underline{\theta})\,d\underline{\theta} \end{aligned} \tag{13}$$

where $\bar{H}(\underline{\theta},\underline{\delta})$ is a function of the parameters $\underline{\theta}$ given by

$$\bar{H}(\underline{\theta},\underline{\delta}) = \int_{Y} H(\underline{y},\underline{\delta})\,p(\underline{y}|\underline{\theta},\underline{\delta})\,d\underline{y} \tag{14}$$

which is the average information entropy over all outcomes, conditioned on the value $\underline{\theta}$ of the model parameters.

The optimal experimental design is formulated as finding the optimal values $\underline{\delta}_{opt}$ of the design variables $\underline{\delta}$ that maximize the utility function $U(\underline{\delta})$, i.e.

$$\underline{\delta}_{opt} = \arg\max_{\underline{\delta}} U(\underline{\delta}) \tag{15}$$

Optimal experimental design problems involving the design of the position of sensors often results in multiple local and local solutions. Also, the gradient of the objective function with respect to the design variables in most cases of practical interest cannot be evaluated analytically. To avoid premature convergence to a local optimum and the evaluation of sensitivities of the utility function with respect to the design variables, stochastic optimization algorithms can be used to find the optimum. Herein the CMA-ES algorithm [17] is used for solving the optimization problem, requiring only evaluation of the objective function at different values of the design variables. Alternatively, sequential sensor placement algorithms (forward-FSSP and backward-BSSP) have also been proposed to provide computationally efficient estimates of near optimum solutions [18].

3.1 Sampling Method

In general, it should be noted that the objective function of Eq. (11) cannot be calculated analytically even for simple models. Sampling approaches have been proposed to approximate the integrals. Specifically, the following estimator has been introduced [19] which uses the two sums estimate

$$U(d) \approx \frac{1}{N}\sum_{i=1}^{N}\left\{\ln\left[p\left(y^{(i)}|\theta^{(i)},d\right)\right] - \ln\left[\frac{1}{N}\sum_{j=1}^{N}p\left(y^{(i)}|\theta^{(i,j)},d\right)\right]\right\} \tag{16}$$

It can be shown that the first term of the sum can be evaluated analytically and therefore the estimator simplifies considerably to:

$$U(d) \approx -\frac{1}{2}log\{(2\pi e)^k|\Sigma_e(d)|\} - \frac{1}{N}\sum_{i=1}^{N}\ln\left\{\frac{1}{N}\sum_{j=1}^{N}p(y^{(i)}|\theta^{(j)},d)\right\} \tag{17}$$

where $\theta^{(i)}$ are N model parameter samples from the prior and $y^{(i)}$ are N data samples from the likelihood for the corresponding prior samples and design variables. To substantially reduce the number of model runs, without significantly sacrificing estimation accuracy, the samples $\theta^{(i,j)}$ in the nested (double) sum are selected to be the same as the samples $\theta^{(i)}$.

3.2 Asymptotic Approximation

The PDF $p(\underline{y}|\underline{\theta},\underline{\delta})$ is Gaussian with respect to $\underline{y}$ with mean $\underline{g}(\underline{\theta},\underline{\delta})$, the predictions from the model given the value of the parameters $\underline{\theta}$. Using Laplace asymptotic

approximation [20], the integral in (14) can be asymptotically approximated, for small prediction error variance, by

$$\bar{H}(\underline{\theta}, \underline{\delta}) = H(\underline{g}(\underline{\theta}, \underline{\delta}), \underline{\delta}) \tag{18}$$

Substituting in (13), the expected utility function is given by

$$U(\underline{\delta}) + a = -\int_{\Theta} H(\underline{g}(\underline{\theta}, \underline{\delta}), \underline{\delta})\, \pi(\underline{\theta})\, d\underline{\theta} \tag{19}$$

which is an integral of the information entropy of the posterior PDF of the model parameters corresponding to the outcome $\underline{y} = \underline{g}(\underline{\theta}; \underline{\delta})$ conditioned on the values of the model parameters over the support of the prior PDF, weighted by the prior distribution of the model parameters. The integral (19) represents the robust information entropy over all possible values of the model parameters quantified by the prior PDF.

Using Monte Carlo simulations or sparse grid techniques [21, 22], the integral of (19) can be evaluated in the form

$$U(\underline{\delta}) + a \approx -\sum_{j=1}^{n} w_j \bar{H}(\underline{\theta}^{(j)}, \underline{\delta}) \sim -\sum_{j=1}^{n} w_j H(\underline{g}(\underline{\theta}^{(j)}, \underline{\delta}), \underline{\delta}) \tag{20}$$

where $\underline{\theta}^{(j)}, j = 1, \ldots, n$, are either the samples drawn from the prior $\pi(\underline{\theta})$ or the sparse grid points in the parameters space, and w_j are weights equal to $w_j = 1/n$ for the Monte Carlo technique or, for sparse grid techniques, their values depend on the sparse grid order and the prior distribution selected [21, 22].

For sufficiently large number of data, the posterior PDF can be asymptotically approximated by a Gaussian PDF $N(\underline{\theta}; \hat{\underline{\theta}}, Q^{-1})$ centered at the most probable value $\hat{\underline{\theta}} \equiv \hat{\underline{\theta}}(\underline{y}; \underline{\sigma}, \underline{\delta})$ that is obtained by minimizing the function $J(\underline{\theta}; \underline{y}, \underline{\sigma}, \underline{\delta})$, i.e.

$$\hat{\underline{\theta}}(\underline{y}; \underline{\sigma}, \underline{\delta}) = \arg\min_{\underline{\theta}} [J(\underline{\theta}; \underline{y}, \underline{\sigma}, \underline{\delta}) - ln\pi(\underline{\theta})] \tag{21}$$

and covariance matrix $C = C(\hat{\underline{\theta}}; \underline{y}, \underline{\sigma}, \underline{\delta})$ equal to the inverse of the Hessian of $-\ln p(\underline{\theta}|\underline{y}, \underline{\sigma}, \underline{\delta})$, given by

$$C^{-1}(\underline{\theta}; \underline{y}, \underline{\sigma}, \underline{\delta}) = \nabla_{\theta} \nabla_{\theta}^{T} [-\ln p(\underline{\theta}|\underline{y}, \underline{\sigma}, \underline{\delta})] = Q(\underline{\theta}; \underline{y}, \underline{\sigma}, \underline{\delta}) + Q_{\pi}(\underline{\theta}) \tag{22}$$

and evaluated at the most probable value $\hat{\underline{\theta}}(\underline{y}; \underline{\sigma}, \underline{\delta})$, where

$$Q(\underline{y}, \underline{\sigma}, \underline{\delta}) = \frac{1}{2} \nabla_{\theta} \nabla_{\theta}^{T} J(\underline{\theta}; \underline{y}, \underline{\sigma}, \underline{\delta}) \tag{23}$$

is the Hessian of $J(\underline{\theta};\underline{y},\underline{\sigma},\underline{\delta})$ and $Q_\pi(\underline{\theta}) = \underline{\nabla}_\theta \underline{\nabla}_\theta^T[-\ln \pi(\underline{\theta})]$ is the Hessian of the prior PDF. Both the most probable value and the covariance or Hessian depend on the data $\underline{y}$, the values of the prediction error parameter set $\underline{\sigma}$ and the design variables $\underline{\delta}$.

Using the Bayesian asymptotic approximation for the posterior PDF, valid for large number of data, the information entropy for the outcome $\underline{y} = \underline{g}(\underline{\theta}^{(j)};\underline{\delta}) \equiv \underline{g}_j(\underline{\delta})$ is given by

$$H(\underline{g}(\underline{\theta}^{(j)},\underline{\delta}),\underline{\delta}) \equiv H(\underline{g}_j(\underline{\delta}),\underline{\delta}) = \frac{1}{2}N_\theta \ln(2\pi) - \frac{1}{2}\ln\det[\hat{Q}_j(\underline{\sigma},\underline{\delta}) + Q_\pi(\hat{\underline{\theta}}_j)] \tag{24}$$

where, $\hat{Q}_j(\underline{\sigma},\underline{\delta}) \equiv Q(\hat{\underline{\theta}}_j;\underline{g}(\hat{\underline{\theta}}_j;\underline{\delta}),\underline{\sigma},\underline{\delta}) = \underline{\nabla}_\theta \underline{g}^T(\underline{\theta}^{(j)};\underline{\delta})\,\Sigma^{-1}(\underline{\sigma})\,\underline{\nabla}_\theta^T \underline{g}(\underline{\theta}^{(j)};\underline{\delta})$, $\hat{\underline{\theta}}_j = \hat{\underline{\theta}}(\underline{g}(\underline{\theta}^{(j)},\underline{\delta});\underline{\sigma},\underline{\delta}) \sim \underline{\theta}^{(j)}$, and $\Sigma(\underline{\sigma})$ is the covariance matrix of the prediction error, that depends on the parameter set $\underline{\sigma}$. The matrix $\hat{Q}_j(\underline{\sigma},\underline{\delta})$ is the Fisher information matrix (FIM) evaluated at the sampling point $\underline{\theta}^{(j)}$. The optimal design maximizes a measure of the sensitivity of the response quantities of interest with respect to the model parameters, weighted over all points covering the support of the prior in the parameter space.

In the special case of a linear model with respect to the model parameters, i.e. $\underline{g}(\underline{\theta};\underline{\delta}) \equiv \underline{a}_0 + A\underline{\theta}$, and Gaussian prior $\pi(\underline{\theta}) = N(\underline{\theta};\underline{\mu},S)$ with mean $\underline{\mu}$ and covariance S, the information entropy in (24) is independent of $\hat{\underline{\theta}}_j$ and is given by

$$H(\underline{g}(\underline{\theta}^{(j)},\underline{\delta}),\underline{\delta}) \equiv H(\underline{g}_j(\underline{\delta}),\underline{\delta}) = \frac{1}{2}N_\theta \ln(2\pi) - \frac{1}{2}\ln\det[A\Sigma^{-1}A + S^{-1}] \tag{25}$$

The asymptotic estimate requires the first derivatives of the model prediction with respect to the model parameters, evaluated at the sample points of the sparse grid method. The asymptotic approximation is useful in the sense that it provides useful insight into the properties of the objective function (utility function or information entropy). Specifically, using the mathematical structure of the asymptotic approximation it can be shown that

- The information entropy decreases as more sensors are added [18].
- Including spatial correlation between the prediction errors has the effect of placing the sensors away from each other [23]. Spatially uncorrelated prediction errors often result in sensor clustering.
- Otherwise unidentifiable problems involving less sensors than number of parameters can be solved by utilizing the information from a non-uniform prior [24].
- The variances of Gaussian prior PDF for the model parameters act as weighting factors for the identification of the corresponding parameters in the optimal experimental design [24]. The variance of a model parameter, say θ, weigh the contribution of the sensitivity of the output quantities of interest $\underline{g}(\underline{\theta};\underline{\delta})$ to the parameter θ. The higher the variance of the prior of the parameter θ, the higher the contribution of the sensitivity of the output quantities with respect to this parameter to the information entropy.

3.3 Implementation for Modal Identification

The optimal experimental design methodology is implemented for estimating the optimal sensor locations for identifying a number of modes in a structure using response time history measurements. Using modal analysis, the response vector $\underline{u} \equiv \underline{g}(\underline{\theta}) \in R^N$ is given with respect to the parameter set $\underline{\theta}$ in the form $\underline{u} = \Phi\underline{\theta}$, where $\Phi \in R^{N\times m}$ is the mode shape matrix for m contributing modes, and $\underline{\theta} \equiv \underline{\xi} \in R^m$ ($m \leq N_d$) is the modal coordinate vector. The objective is to design the sensor configuration that provides the most information in order to estimate the modal coordinate vector $\underline{\xi}$. Noting that $\underline{\nabla}_\theta \underline{g}(\underline{\theta}) = \Phi$ and substituting into (25), the expected utility function takes the form

$$U(\underline{\delta}) = \frac{1}{2}\ln\det[\hat{Q}(\underline{\sigma},\underline{\delta}) + S^{-1}] - a - \frac{1}{2}N_\theta \ln(2\pi) \tag{26}$$

where

$$\hat{Q}(\underline{\sigma},\underline{\delta}) = \{L_{\underline{\delta}}\Phi\}^T\{L_{\underline{\delta}}\Sigma(\underline{\sigma})L_{\underline{\delta}}^T\}^{-1}\{L_{\underline{\delta}}\Phi\} \tag{27}$$

which is independent of the model parameters. The information matrix $\hat{Q}(\underline{\sigma},\underline{\delta})$ in (27) has exactly the same form as the one proposed in [23] for designing the optimal sensor locations.

Using (27), the Fisher information matrix $\hat{Q}(\underline{\sigma},\underline{\delta})$ is non-singular if the number of sensors N_0 is at least equal to the number of contributing modes m ($N_\theta = m$). For $N_0 < m$, $\hat{Q}(\underline{\sigma},\underline{\delta})$ is singular and for uniform prior PDF the determinant of the FIM will be zero for any sensor configuration. This means that the information content in the measured data and the prior is not sufficient to estimate all the parameters simultaneously. The problem is critical for the FSSP algorithm where one performs the optimization by starting with no sensors placed on the structure and sequentially adding at the optimal location one sensor at a time on the structure. Previous formulations on the subject based only on the FIM [23, 25] failed to address this problem. Moreover, FSSP algorithms could not be used due to the singular $\hat{Q}(\underline{\sigma},\underline{\delta})$. A non-singular matrix $\hat{Q}(\underline{\sigma},\underline{\delta}) + S^{-1}$ is obtained by using a non-uniform prior distribution. The non-uniform prior yields a Hessian S that is added to the Fisher information matrix $\hat{Q}(\underline{\sigma},\underline{\delta})$ and makes the combined matrix $\hat{Q}(\underline{\sigma},\underline{\delta}) + S^{-1}$ non-singular.

Assuming a Hessian matrix $S = diag(1/\rho_k)$ for the prior PDF, the utility function is given by

$$U(\underline{\delta}) = \frac{1}{2}\sum_{k=1}^{N_\theta}\log(\lambda_k + \rho_k) \tag{28}$$

where $k = 1, \ldots, N_\theta$, are the eigenvalues of the Fisher information matrix. Note that when one takes the limit when $\rho_k \to 0$ for all k, the optimal experimental design is equivalent to the one proposed in [23], obtained by maximizing the product of the

non-zero eigenvalues in the FIM, instead of maximizing the product of all eigenvalues. The information contained in the prior allows to systematically place the sensors optimally in the structure even for the cases where the data provide no information along certain directions in the parameter space.

4 Application 1: Model Updating of Metsovo Bridge

4.1 Description

The Metsovo bridge of Egnatia Motorway, shown in Fig. 1, is crossing the deep ravine of Metsovitikos river, 150 m over the riverbed. This is the highest bridge of the Egnatia Motorway, with the height of the tallest pier equal to 110 m. The total length of the bridge is 537 m. The bridge has 4 spans of length 44.78 m, 117.87 m, 235 m, 140 m and 3 piers of which the pier M1(45 m) supports the boxbeam superstructure through pot bearings (movable in both horizontal directions), while the piers M2(110 m) and M3(35 m) piers connect monolithically to the structure.

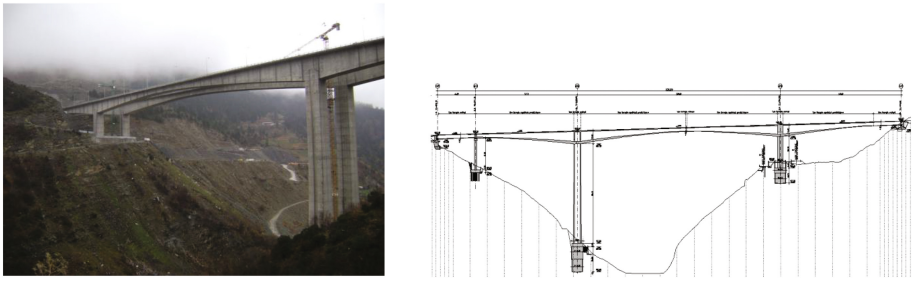

Fig. 1. (a) General view and (b) schematic diagram of Metsovo bridge.

4.2 Finite Element Model

A high fidelity finite element model of the bridge was constructed using COMSOL Multiphysics. The soil-structure interaction was taken into account by modeling the soil with large blocks of material and embedding the piers and abutments into these blocks. The domain of the superstructure and the soil was meshed using tetrahedral Lagrange solid elements. Several mesh sizes were tried, and an accuracy analysis was performed in order to find a reasonable trade-off between the number of degrees of freedom of the model and the accuracy in modal frequencies and mode shapes. The resulting mesh had approximately 800,000 DOFs and was found to cause errors of the order of 0.1–0.5% in the first 20 modal frequencies, compared to the smallest possible mesh sizes which had approximately 3 million DOFs. In that way the model was optimized with respect to the number of DOFs using a variable element size in each part of the bridge, as shown in Fig. 2.

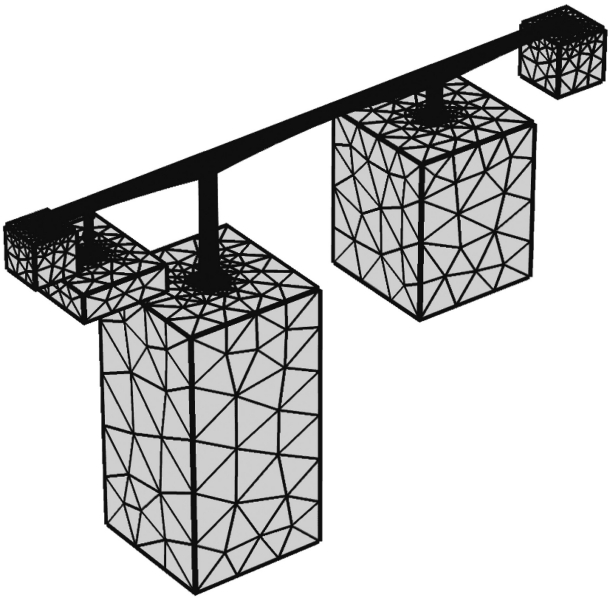

Fig. 2. Mesh of the bridgel FE model.

4.3 Optimal Placement of Reference Sensors

Next, optimal sensor locations results are presented using (26) and (27) as the objective function. The design variables were selected such that they describe not only the locations of the sensors in the bridge, but its type as well (vertical or transverse sensor). In order to demonstrate the effectiveness of the optimal sensor placement methodology, note from Fig. 3 that the first 4 sensors are selected to be vertical and the next 5 are transverse, in locations where we have significant contribution from as many modes as possible. Figure 4 shows the effect of the Gaussian prior variances in the optimal design by increasing the prior variance for the 1st mode which is transverse. The transverse sensors become optimal because more weight is given to them through the Gaussian prior. The one sensor moves closer and closer to the peak of the 1st transverse mode when we increase the Gaussian variance of the first mode. The weights were finally selected so that one transverse and one vertical sensor are optimally placed on the structure so that the lowest 20 modes are identified using reference and roving sensors.

4.4 Experimental Modal Analysis

Acceleration measurements were collected under normal operating conditions of the bridge in order to identify the modal properties of the structure (natural frequencies, mode shapes, damping ratios). The measured data were collected using 5 triaxial and 3 uniaxial accelerometers paired with a 24-bit data logging system and an internal SD flash-card for data storage. The synchronization of the sensors was achieved by using a GPS module in each of the sensors, hence they could be programmed to start and stop

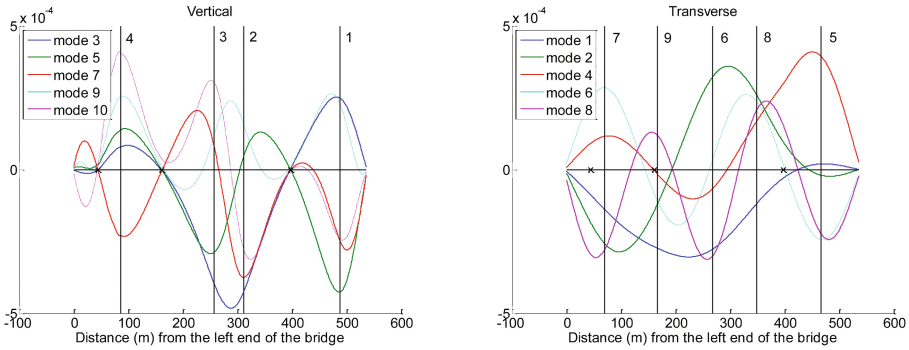

Fig. 3. Optimal sensor locations for vertical and transverse sensors

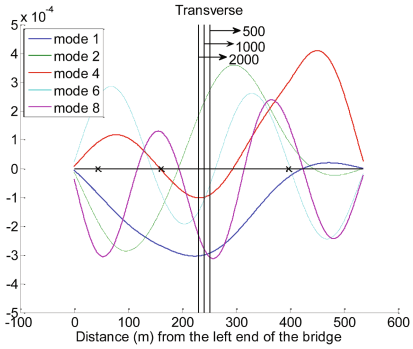

Fig. 4. Optimal locations for 1st sensor for prior variance of 1st mode equal to 500, 1000 and 2000. All other prior variances equal to 100.

recording at exactly the same time for the desired duration. Due to the small number of available sensors, the measurements were conducted using reference and roving sensors. The entire length of the deck was covered in 13 sensor configurations with each configuration recording for 20 min at a sampling rate of 100 Hz. One tri-axial and three uniaxial sensors (one vertical and two horizontal), one at each side of the bridge, remained at the same position, in order to provide common measurement points along different configurations so as to enable the procedure of mode shape assembling. The optimal position of the reference sensors was estimated using the Bayesian optimal experimental design methodology.

The excitation of the bridge during the measurements was primarily due to road traffic, which ranged from motorcycles to heavy trucks, and environmental excitation such as wind loading and ground micro-tremor, which classifies this case as output-only or ambient modal identification. For the extraction of modal properties from the ambient acceleration data, a Bayesian methodology [26] was followed based on the fast Fourier transform of the acceleration time histories in a specific, user-defined frequency band of interest. More than twenty five modal frequencies were

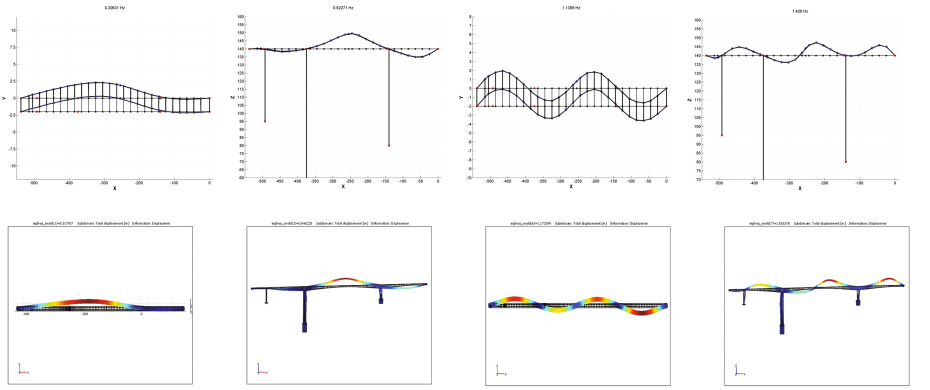

Fig. 5. Identified and model predicted mode shapes: left to right: first transverse, first bending, fourth transverse, third bending.

estimated. However, due to the sparsity of the sensors, only 10 mode shapes were reliably estimated in terms of their type. Figure 5 presents some illustrative modal identification results of identified mode shapes compared with the corresponding ones from the FE model.

4.5 Model Updating Results

The stiffness properties of the finite element model were updated using the modal frequencies and modeshapes estimated from the acceleration measurements. For demonstration purposes the following parameterization was used. The stiffness of the finite element model was parametrized by one parameter for the deck, one for the piers and one for the soil stiffness. The parameters multiply the nominal values of the modulus of elasticity of the corresponding part, so they are expected to lie close to 1. A value of the parameters equal to 1 would imply that the modulus of elasticity is equal to the nominal value. Model reduction techniques using CMS, consistent with the employed parameterization, were used to drastically reduce the finite element model from approximately 800,000 degrees of freedom (DOF) to as low as several hundred DOFs, without sacrificing the accuracy in computing the lowest 20 modal frequencies and modeshapes. Details are presented in [10].

The estimation of the parameters values and their uncertainties was performed using two prediction error models. The first model is based on Eq. (4) for the prediction error for the mode shapes and assumes that the error term is Gaussian with spatially uncorrelated covariance matrix, while the second prediction error model assumes that the non-negative terms $1 - MAC_r^2$ for all modes $r = 1, \ldots, m$ follow a lognormal distribution. The parameters of the distribution are included in the uncertain parameter set. As it was mentioned, the second prediction error model reduces the number of data per mode shape from a full vector per mode to a scalar measure of discrepancy between two vectors (experimental and model predicted mode shapes).

Results are obtained using TMCMC to generate samples from the posterior PDF of the structural model and prediction error parameters and then the uncertainty is propagated to estimate the uncertainty in the predicted modal frequencies of the bridge. Surrogate models were not employed due to the small size of the reduced model obtained using the CMS algorithm. The prior distribution of the parameters was assumed to be uniform with bounds in the domain [0.2,2] $\times$ [0.2,2] for the deck and pier parameters, in the domain [0.01,10] for the soil parameter and in the domain [0.001,1] $\times$ [0.001,1] for the prediction error parameters σ_ω and σ_ϕ. The domain for the soil parameter was deliberately chosen larger in order to be able to explore the full effect of the soil stiffness on the model behavior and its comparison with the experimentally identified modal frequencies and mode shapes. The calibration is done using the lowest eight modal frequencies and mode shapes identified for the structure.

For the case of the first prediction error model for which the entire mode shape vectors being used as uncorrelated data, the posterior marginal distributions for the stiffness parameters of the deck, pier and soil are shown in Fig. 6, and the uncertainty propagation for predicting the modal frequencies and MAC values are shown in Fig. 7.

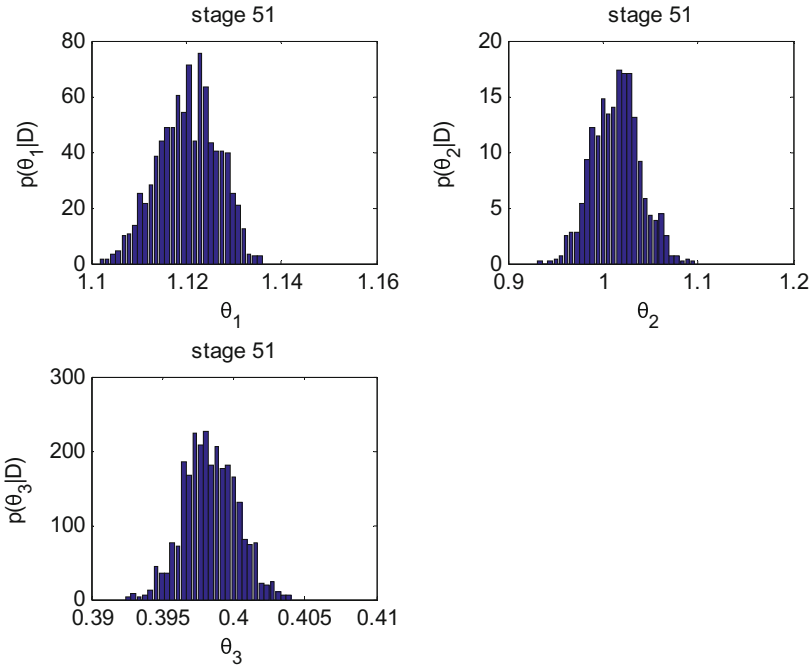

Fig. 6. Posterior marginal distributions (1st prediction error model). Top Left: deck, Top Right: pier, Bottom Left: soil.

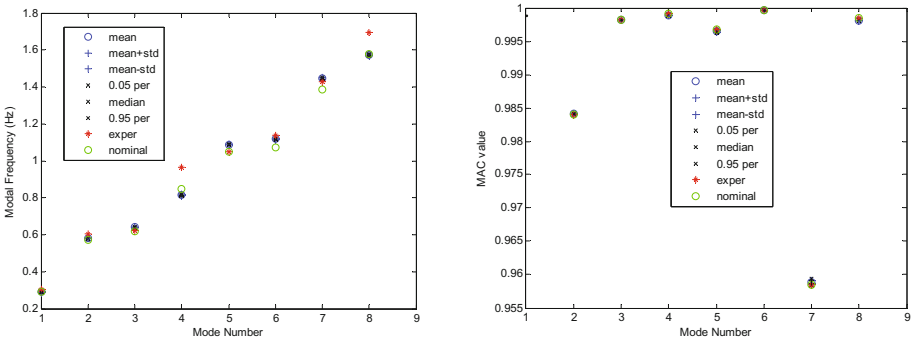

Fig. 7. Uncertainty propagation to modal frequencies and mode shapes for the first prediction error model.

For the case of the second prediction error model where the likelihood (for the mode shapes) is built by assuming that $1 - MAC_r^2$ follow a lognormal distribution, the posterior marginal distributions of the model parameters are presented in Fig. 8, and the uncertainty propagation results for the modal frequencies and the MAC values are shown in Fig. 9. It should be noted that both prediction error models give consistent predictions for the most probable value of the stiffness parameters. The second prediction error model, however, predict substantially larger uncertainties than the first prediction error model. The small uncertainties predicted from the first prediction error model are due to the fact that correlation between neighborhood measurements was ignored, treating the large number of identified mode shape components as independent. Also it should be noted that the stiffness of the soil is predicted with significantly higher confidence, corresponding to small uncertainty, than the stiffness of the deck and the pier. It can be concluded that the selection of the model for the prediction error is important in estimating the uncertainty in the model parameters and the propagation of this uncertainty to output response quantities of interest. Finally, from the uncertainty propagation results in Figs. 7 and 9 it can be concluded that the finite element model of the bridge is overall an adequate representation of the bridge dynamics for most of the modes. However, there is a discrepancy between predictions and measurements for the fourth and eighth modal frequency, consistently observed for both models of the prediction errors. In addition, the worst MAC value is observed for the seventh mode. Improvements in predictions are expected if more stiffness parameters are introduced to be updated in the Bayesian inference formulation. Also, the discrepancies observed give an indication of the adequacy of the finite element model and/or parameterization scheme considered.

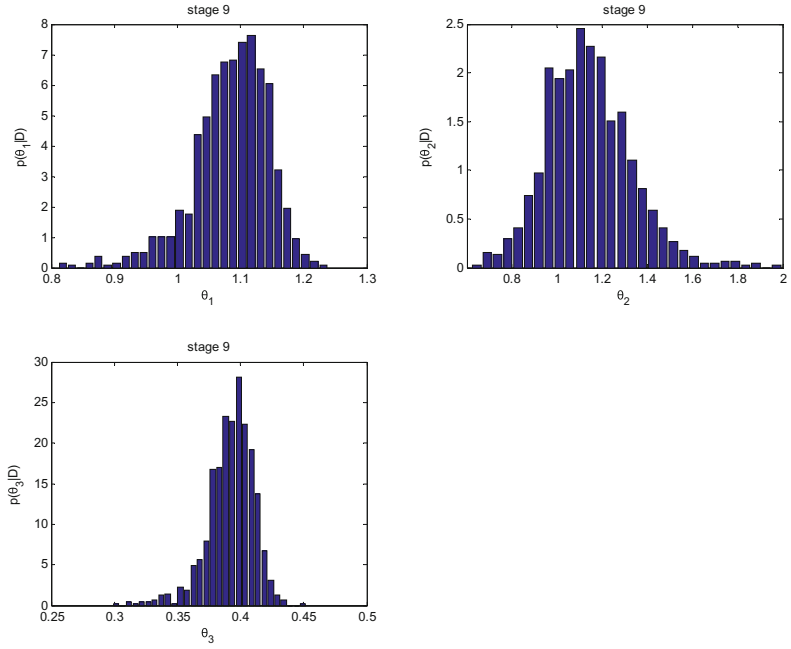

Fig. 8. Posterior marginal distributions (2nd prediction error model). Top Left: deck, Top Right: pier, Bottom Left: soil.

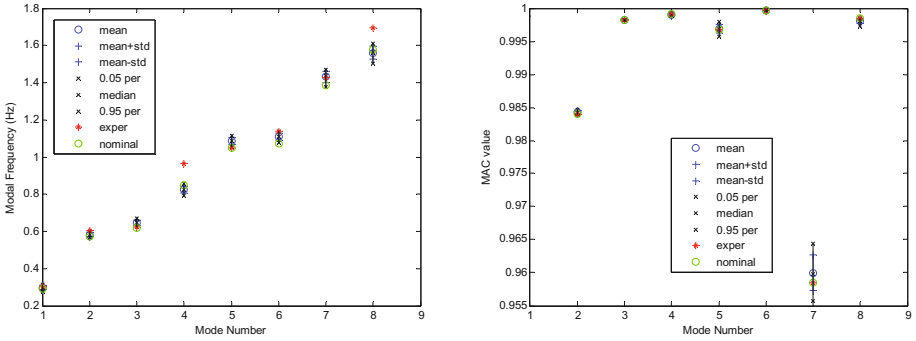

Fig. 9. Uncertainty propagation to modal frequencies and mode shapes for second prediction error model.

5 Application 2: Estimation of Hanger Tension in Arch Bridges

5.1 Description of Hanger

The hanger under investigation is hanger 3 of the 20 hangers used to support the deck of an arch bridge located in Athens, Greece. The arch bridge is shown schematically in Fig. 10. The hangers are made out of steel and they are connected to the deck and the arch substructures with edge plates. The connections of the hanger with the deck or the arch with end plates are approximately 1 m long and affect the hanger flexibility at the two ends. The plate that connects the hanger with the deck has its orientation along the longitudinal direction of the bridge deck, while the plate that connects the hanger to the arch has its orientation along the transverse direction of the bridge deck. The boundary conditions at the plate surface that connects to the arch or the deck substructures depend on the flexibility of the deck and the arch.

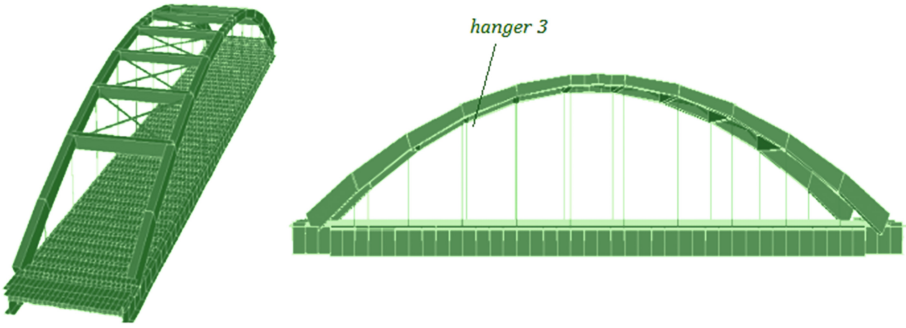

Fig. 10. The arch bridge with the hangers.

The hangers are made of steel with modulus of elasticity 200 GPa, mass density 7800 kg/m^3 and Poisson ratio 0.3. The total length of the hanger including the connections is 12 m, while the clear length of the circular section of the hanger is 9.82 m. The diameter of the circular section of the hanger is 0.13 m.

Based on the design plans, the geometry of the hanger, its material properties and the connection details of the two edge plates of the hanger are identical. The only difference is the orientation of each edge plate. Assuming that the end conditions of the edge plates are fixed, the modal frequencies of vibration of the hanger along the longitudinal and transverse direction bridge are expected to be identical. Impulse hammer tests performed on the hanger 3 of the bridge are used to estimate the modal frequencies of the hanger. In predicting the modal frequencies, the bending stiffness of the present hanger cannot be ignored. In addition the plate elements installed in the hangers to connect the circular section to the bridge arch and deck also affect the bending stiffness.

5.2 Estimation of Hanger Tension

The axial tension in the hanger axial is estimated using two types of models classes: detailed FE model classes and simple beam model classes. Estimation is based on the lowest twelve experimentally identified modal frequencies of the hanger, six along the transverse and six along the longitudinal direction of the bridge deck. The parameter estimation and the model class selection is performed for the model classes reported in Table 1. The FE model classes *FEfix* and *FEflex* are used to identify whether or not the flexibility in the end conditions of the hanger, arising from the flexibility of the arch and the deck, is important. The *FEfix* assumes that the end conditions are fixed, while *FEflex* assumes flexible end conditions modelled by attaching a proper arrangement of springs. The simple beam model classes *Bfix* and *Bflex* are used for the purpose of identifying which one of them is capable of predicting adequately the hanger tension based on the results obtained from the FE model classes which are considered to contain the more accurate information for the hanger tension. Depending on the type and number of parameters, the beam model classes are further classified as follows.

- $Bfix(T, L)$: two-parameter model class. The parameters include the hanger tension T and the equivalent hanger length L. The model uses the equivalent length concept [27] to provide the necessary flexibility of adjusting the length of the uniform cross-section of the beam to fit the modal frequency data. This flexibility arises from the end plate connections and the boundary conditions between the hanger and the arch or the deck.
- $Bfix(T, L_t, L_l)$: three-parameter model class. The parameters include the hanger tension T and the equivalent hanger lengths L_t and L_l assumed to be different for deflections of the hanger in the (x, z) (longitudinal direction) and (y, z) (transverse direction) planes. This model has freedom to provide different beam flexibilities along the transverse and longitudinal directions of hanger deflection.
- $Bfix(T|L_i)$: a family of μ one-parameter model classes. Eah model class includes only a single parameter, the hanger tension given the value of the hanger length to be L_i, $i = 1, \ldots, \mu$.
- $Bflex(T, L, \underline{k})$: three- to six-parameter model classes. The parameters include the hanger tension, the equivalent length, as well as the rotational stiffnesses $\underline{k}$ at the two ends which may vary from one to four.

Table 1. Log evidence and estimates of hanger tension for all model classes

Model class	$\mathbf{N}_{\underline{\theta}}$	Log Evidence	Tension quantiles [5%, 50%, 95%]	Tension Mean	Tension Standard Dev.	Tension MPV	Fit
FEflex	5	24.03	[0.75, 0.92, 1.04]	0.909	0.0897	0.822	0.0103
FEfix	1	22.24	[0.59, 0.70, 0.80]	0.701	0.0627	0.701	0.0263
$Bfix(T, L)$	2	20.72	[0.68, 0.86, 1.06]	0.867	0.114	0.854	0.0248
$Bfix(T, L_t, L_l)$	3	22.49	[0.73, 0.86, 0.98]	0.856	0.0731	0.856	0.0115
$Bflex(T, L, k_3)$	3	20.90	[0.70, 0.88, 1.08]	0.883	0.1215	0.888	0.0112
$Bflex(T, L, k_1, k_3)$	4	20.10	[0.70, 0.94, 1.35]	0.974	0.1905	0.888	0.0112
$Bflex(T, L, \underline{k})$	6	19.23	[0.77, 1.19, 1.44]	1.144	0.2196	0.968	0.0115

Table 1 presents the most probable value (MPV), the mean, the standard deviation, and the 5%, 50% and 95% quantiles of the hanger tension estimated from all model classes. TMCMC is used to carry out the estimation of the parameters of each model class. The number of samples per TMCMC stage is 1000 for *FEflex*, 500 for *FEfix*, 5000 for *Bfix* and *Bflex* model classes. The number of samples per TMCMC stage used for each case is chosen as a trade-off between computational effort and solution accuracy. A large number of samples is used for the analytical beam model due to the small time-to-solution, of the order of a few minutes, in relation to the time-to-solution required for estimating the hanger force using the finite element model classes. A smaller number of 500 samples per TMCMC stage is used for the FEfix model class due to a small number of two parameters involved as opposed to six parameters involved in the FEflex model class. Representative times-to-solution obtained in a dual 4-core computer using the parallelized versions of TMCMC algorithm are of the order of 60 h for *BEflex*, 12 h for *BEfix* and several minutes for the *Bfix* and *Bflex* model classes. The number of TMCMC stages, which affect the time-to-solution is approximately 4 to 7, depending on the model class and the individual run. Further details are presented in reference [28]. Due to geometrical nonlinearity assumed for estimating the hanger tension, model reduction strategies are not applicable in this example. Also, surrogate models can not be used either due to the fact that modeshape components were not measured so the correspondence between measured and model predicted modes (in the transverse and longitudinal direction of hanger deflection) was not readily available. The only option to reduce the time-to-solution is to use as many computer workers available to run simultaneously the large number of parallel chains in TMCMC.

Comparing the evidence values for the two FE model classes *FEflex* and *FEfix* it can be seen that the *FEflex* is the preferred model class with probability $Pr(FEflex|D) = 0.86$, against $Pr(FEfix|D) = 0.14$ for the *FEfix* model class. The *FEflex* is found to give a significantly better fit to the data which is equal to 1.03 % as compared to the fit 2.63% for the *FEfix* model. The prediction of the hanger tension obtained from the two FE models are substantially different. *FEflex* predicts the most probable value at 0.91 with uncertainty bounds in the range $[0.75, 1.04]$, while *FEfix* predicts the most probable value to be 22% lower at 0.70 with uncertainty bounds in the range $[0.60, 0.80]$.

Based on the 5% and 95% quantiles estimated for the hanger tension from the *FEflex* model, it is concluded that the uncertainty in the hanger tension is 10%. This uncertainty is due to the inability of the model class *FEflex* to fit exactly all 12 modal frequencies. This uncertainty could affect predictions of structural safety when the hanger stresses are close to yield stresses. Taking into account that the nominal hanger tension value is $T_0 = 922KN$ and the hanger cirular cross-sectional area has diameter $D = 0.130m$, the 5% and 95% credible intervals for the hanger stresses range between $[0.16, 0.22]\sigma_y$, where $\sigma_y = 330MPa$ is the yield stress of the hanger material. Thus, the safety factor for this particular hanger is relative high and well within the safe domain, assuming that the mode of failure corresponds to stresses in the hanger exceeding material yield stresses.

From the results in Table 1 it can also be observed that the simplified beam models predict the value of the hanger tension and its uncertainty to be significantly closer to the

predictions made from the *FEflex* model than the predictions made from the *FEfix* model. This suggests that the simplified beam models are effective in predicting the hanger tension. The model class $Bfix(T, L_t, L_l)$ is selected by the Bayesian framework as the most preferred model class among all the beam model classes. It provides accurate estimates of the hanger tension and the uncertainties, close to the ones provided by the *FEflex* model with flexible supports. The dynamics of the hanger in the longitudinal and transverse directions of the bridge is thus well approximated by the three-parameter simplified beam model $Bfix(T, L_t, L_l)$ using the concept of two independent equivalent lengths in the transverse and longitudinal direction. The beam model $Bfix(T, L)$ with a single equivalent length provides less accurate estimates of the tension due to different modal frequencies arising from the asymmetry of the boundary conditions. The simplified beam model $Bflex(T, L, \underline{k})$ provides fairly accurate results with higher uncertainty in the values of the hanger tension. This model is less preferred than the $Bfix(T, L_t, L_l)$ model class. The model $Bfix(T|L_i)$ with fixed length value selected arbitrarily does not provide an adequate fit the measured frequency data due to the fact that the dynamics of the beam is sensitive to the value of the length of the beam.

6 Conclusions

A Bayesian framework was presented for integrating information from data and models of civil infrastructure systems. Although the framework was developed for the case where data consist of modal characteristics estimated from vibration measurements, it can be generalized to account for other response characteristics and model nonlinearities. Using Bayesian tools such as asymptotic approximations and sampling algorithms, the framework ranks alternative competing model classes introduced to model the structural behavior, and furnishes estimates of the model parameters along with their uncertainty. Computationally efficient techniques were outlined for reducing the large computational burden associated with the Bayesian framework due to the large number of model simulations when applied to complex models of structural behavior. A Bayesian optimal experimental design framework was also presented for optimally selecting the locations of sensors in order to acquire data that are most informative for parameter inference. Sampling and asymptotic approaches were presented to estimate the information-based utility functions introduced to evaluate the information provided by a design. It was demonstrated that the asymptotic estimate provides useful insight into the dependence of the optimal sensor configuration on the number and location of sensors, the effect of spatially correlated prediction errors on sensor locations, and the effect of prior uncertainty in the model parameters on the optimal sensor configuration estimates.

The framework was demonstrated on two case studies involving civil infrastructure systems located in Greece, using experimentally identified modal data. The first structure was a reinforced concrete bridge where the stiffness parameters were estimated using modal data identified from acceleration measurements. In particular, the effect of the selection of the prediction error in the uncertainties of the parameters was investigated and certain deficiencies were identified. The second structure was a hanger of an arch bridge. High fidelity, geometrically nonlinear, finite element model classes, as well as simplified beam model classes were introduced as competing models to

estimate the hanger tension using modal data. The effect of the flexibility of the supports on the reliable estimation of the hanger axial tension and its uncertainty was pointed out. It was also recognized that certain beam model classes that fully take into account the flexibility of the supports are capable of providing reliable hanger force estimates with minimal computational effort compared to high fidelity finite element model classes.

Acknowledgments. This research has been implemented under the "ARISTEIA" Action of the "Operational Programme Education and Lifelong Learning" and was co-funded by the European Social Fund (ESF) and Greek National Resources.

References

1. Papadimitriou, C., Beck, J.L., Katafygiotis, L.S.: Updating robust reliability using structural test data. Probab. Eng. Mech. **16**(2), 103–113 (2001)
2. Simoen, E., Papadimitriou, C., Lombaert, G.: On prediction error correlation in Bayesian model updating. J. Sound Vib. **332**(18), 4136–4152 (2013)
3. Beck, J.L., Katafygiotis, L.S.: Updating models and their uncertainties. I: Bayesian statistical framework. J. Eng. Mech. ASCE **124**, 463–467 (1998)
4. Metropolis, N., Rosenbluth, A.W., Rosenbluth, M.N., Teller, A.H., Teller, E.: Equation of state calculations by fast computing machines. J. Chem. Phys. **21**(6), 1087–1092 (1953)
5. Hastings, W.K.: Monte-Carlo sampling methods using Markov chains and their applications. Biometrika **57**(1), 97–109 (1970)
6. Yuen, K.-V.: Bayesian Methods for Structural Dynamics and Civil Engineering. Wiley, Chichester (2010)
7. Beck, J.L., Yuen, K.V.: Model selection using response measurements: Bayesian probabilistic approach. J. Eng. Mech. ASCE **130**, 192–203 (2004)
8. Ching, J., Chen, Y.-C.: Transitional Markov Chain Monte Carlo method for Bayesian model updating, model class selection and model averaging. J. Eng. Mech. ASCE **133**, 816–832 (2007)
9. Angelikopoulos, P., Papadimitriou, C., Koumoutsakos, P.: Bayesian uncertainty quantification and propagation in molecular dynamics simulations: a high performance computing framework. J. Chem. Phys. **137**, 103–144 (2012)
10. Chatzi, E.N., Papadimitriou, C. (eds.): Identification Methods for Structural Health Monitoring. Series: CISM-International Centre for Mechanical Sciences. Springer, New York (2016)
11. Papadimitriou, C., Papadioti, D.C.: Component mode synthesis techniques for finite element model updating. Comput. Struct. **126**, 15–28 (2013)
12. Jensen, H., Muñoz, A., Papadimitriou, C.: An enhanced substructure coupling technique for dynamic re-analyses: application to simulation-based problems. Comput. Methods Appl. Mech. Eng. **307**, 215–234 (2016)
13. Jensen, H., Munoz, A., Millas, E., Papadimitriou, C.: Model-reduction techniques for reliability-based design problems of complex structural systems. Reliab. Eng. Syst. Saf. **149**, 204–217 (2016)
14. Angelikopoulos, P., Papadimitriou, C., Koumoutsakos, P.: X-TMCMC: adaptive kriging for Bayesian inverse modelling. Comput. Methods Appl. Mech. Eng. **289**, 409–428 (2015)

15. Hadjidoukas, P.E., Angelikopoulos, P., Papadimitriou, C., Koumoutsakos, P.: Π4U: a high performance computing framework for Bayesian uncertainty quantification of complex models. J. Comput. Phys. **284**(1), 1–21 (2015)
16. Lindley, D.V.: On a measure of the information provided by an experiment. Ann. Math. Stat. **27**, 986–1005 (1956)
17. Hansen, N., Müller, S.D., Koumoutsakos, P.: Reducing the time complexity of the derandomized evolution strategy with covariance matrix adaptation (CMA-ES). Evol. Comput. **11**, 1–18 (2003)
18. Papadimitriou, C.: Optimal sensor placement methodology for parametric identification of structural systems. J. Sound Vib. **278**, 923–947 (2004)
19. Ryan, K.J.: Estimating expected information gains for experimental designs with application to the random fatigue-limit model. J. Comput. Graph. Stat. **12**, 585–603 (2003)
20. Bleistein, N., Handelsman, R.A.: Asymptotic Expansions of Integrals. Courier Corporation, New York (1975)
21. Gerstner, T., Griebel, M.: Numerical integration using sparse grids. Numer. Algorithms **18**, 209–232 (1998)
22. Bungartz, H., Griebel, M.: Sparse grids. Acta Numer. **13**, 147–269 (2004)
23. Papadimitriou, C., Lombaert, G.: The effect of prediction error correlation on optimal sensor placement in structural dynamics. Mech. Syst. Signal Process. **28**, 105–127 (2012)
24. Argyris, C., Papadimitriou, C., Panetsos, P.: Bayesian optimal sensor placement for modal identification of civil infrastructures. J. Smart Cities **2** (2016)
25. Kammer, D.C.: Sensor placement for on-orbit modal identification and correlation of large space structures. J. Guid. Control Dyn. **14**(2), 251–259 (1991)
26. Au, S.-K.: Fast Bayesian ambient modal identification in the frequency domain, Part I: Posterior most probable value. Mech. Syst. Signal Process. **26**, 60–75 (2012)
27. Bellino, A., Marchesiello, S., Fasana, A., Garibaldi, L.: Cable tension estimation by means of vibration response and moving mass technique. Mech. Ind. **11**, 505–512 (2010)
28. Papadimitriou, C., Giakoumi, K., Argyris, C., Spyrou, I., Panetsos, P.: Bayesian estimation of tension in bridge hangers using modal frequency measurements. Struct. Monit. Maint. **3** (4), 349–375 (2016)

Development of a High Accuracy and High Sampling Rate Displacement Sensor for Civil Engineering Structures Monitoring

Hoon Sohn(✉), Kiyoung Kim, Jaemook Choi, Gunhee Koo, and Junyeon Chung

Department of Civil and Environmental Engineering,
Korea Advanced Institute of Science and Technology (KAIST), Daejeon, Republic of Korea
hoonsohn@kaist.ac.kr

Abstract. Displacement is one of the key physical quantities that are necessary to understand characteristics and behaviours of civil engineering structures. In this study, a new displacement sensor module is developed by integrating GPS-RTK and accelerometer sensors into a single unit so that dynamic and pseudo-static displacements of various civil engineering structures can be measured with high accuracy, precision and sampling rate. Displacement is estimated by fusing GPS-RTK and accelerometer measurements using a two-stage Kalman filter. The two-stage Kalman filter improves accuracy, precision, and sampling rate by recursively integrating the acceleration measured by the accelerometer and correcting the integration error using the displacement intermittently measured from the GPS-RTK sensor. The proposed displacement sensor offers the following advantages over the existing GPS-RTK sensors commonly used for civil engineering structures monitoring: (1) The proposed displacement sensor can achieve a better accuracy (around 2 mm) and a better sampling rate (up to 100 Hz) compared to the conventional GPS-RTK sensors, and (2) The performance is less affected by weather conditions, multipath problems and signal blockage, which typically deteriorate the performance of conventional GPS-RTK sensors. To validate the performance of the proposed displacement sensor, a series of lab scale tests were conducted.

Keywords: Displacement estimation · Sensor data fusion · Two-stage Kalman filter · Civil engineering structures monitoring · GPS-RTK · Accelerometer

1 Introduction

Displacement is one of the important physical quantities to understand characteristics and behaviors of civil structures, since displacement response of the structures implies useful information such as velocity, acceleration and deflection [1–3]. Hence, interest in displacement measurement for civil structures has been increasing in many areas of structural health monitoring, safety/condition assessment, and system identification [4]. Despite of strong motivation of displacement information, precise displacement measurement for civil structures is still challenging and unwieldy.

© Springer International Publishing AG 2018
J.P. Conte et al. (eds.), *Experimental Vibration Analysis for Civil Structures*,
Lecture Notes in Civil Engineering 5, https://doi.org/10.1007/978-3-319-67443-8_4

LVDT (linear variable differential transformer) is one of the most traditional method for measuring displacement. LVDT measures displacement with high precision around submillimeter and high sampling rate. [5] However, installation of LVDT spends much time since it requires direct contact with target structure and need a fixed scaffold or support for reference [6].

LiDAR (light detection and ranging) is commonly used to construct 3D coordinates of the objects, but it can be used to measure the displacement [7, 8]. LiDAR measures distance using time of flight or phase shift information of the laser back from the target with high precision of 3 to 5 mm and sampling rate up to 120 Hz [9]. However, the noise level is easily affected by weather condition and obstacle between the LiDAR and target structure can deteriorate the accuracy and generates noise [10, 11].

Vision sensor can measure displacement of multiple points simultaneously by tracing the pixel of the target structure's consecutive images. Displacement resolution is totally dependent on resolution and spatial area of the image. Vision sensor suffers from the similar problem with LiDAR in that a moving object or an obstacle between camera and the target structure cause difficulty of measuring precise displacement [12–15].

With the advent of real-time kinematic (RTK) technology, GNSS (Global Navigation Satellite System) has been widely used for measuring displacement of civil infrastructures [16–18]. GPS-RTK has a precision of 1 to 3 cm in plane direction and 5 to 7 cm in vertical direction with sampling rate up to 20 Hz [16–18]. Although GNSS is generally used in structural health monitoring for civil structures, there are still some limitations: (1) performance of the GNSS is heavily affected by weather conditions and the number of available satellite (2) measurement from GNSS can be disturbed by multipath problem [19].

Displacement can be acquired by double-integrating acceleration measured from accelerometer, which is fixed to the target structure. The integration error is generated and accumulated when estimating displacement by integrating measured acceleration [20]. There are some techniques to eliminate this type of error by using baseline correction [21]. However, baseline correction technique is not proper for real-time displacement estimation since post-processing is essential [22].

Displacement estimation techniques based on multi-rate data fusion of acceleration data and intermittent displacement measurement have been developed to minimize bias accumulation and numerical integration errors during integration of acceleration. Chan et al. [23] measures displacement by merging acceleration and displacement from GPS. Firstly, adaptive filter removes noise of displacement measured by GPS using the noise characteristics. Then, high frequency sampled acceleration is combined to de-noised displacement by using EMD (Empirical mode decomposition) to estimate displacement with better accuracy. However, EMD generally has a problem in that the high level of error occurs at the starting and end of the processed time signal.

Moschas and Stiros [24] introduced supervised-type learning filter, which is designed from acceleration measured by accelerometer to de-noise displacement measurement from GPS. However, the filter is not proper real-time and autonomous dynamic displacement estimation since the parameter of the filter is determined with the time duration and frequency range of the actual response of the accelerometer.

Smyth and Wu [25] firstly applied multi-rate Kalman filter by fusing high frequency sampled acceleration and low frequency sampled displacement in displacement estimation. The method estimates displacement in the state-space model in terms of acceleration and intermittently measured displacement. In the state-space model, displacement is estimated by double integrating acceleration, correcting the integration error with intermittently measured displacement. However, the error due to large bias of accelerometer cannot be corrected since the bias cannot be considered in the state-space model.

This paper presents development of a new displacement sensor by fusing an accelerometer and GPS-RTK with low price. The proposed sensor can be applied to monitoring the displacement of civil infrastructures such as bridges, dams and buildings. The proposed displacement sensor offers the following advantages over the existing GPS-RTK sensors commonly used for civil engineering structures monitoring: (1) The proposed displacement sensor can achieve a better accuracy (around 2 mm) and a better sampling rate (up to 100 Hz) compared to the conventional GPS-RTK sensors, and (2) The performance is less affected by weather conditions, multipath problems and signal blockage, which typically deteriorate the performance of conventional GPS-RTK sensors.

This paper is organized as follows: Sect. 2 presents a detail configuration of the developed displacement sensor. In Sect. 3, a lab scale experiment is described to verify the precision and accuracy of the developed sensor. The concluding remarks are provided in Sect. 4.

2 Description of Developed Displacement Sensor

The developed displacement sensor consists of 3 modules: (1) Sensor module, (2) GPS base module, (3) Computation module. Three force-feedback accelerometers in the sensor module measure tri-axial acceleration with 100 Hz, and a GPS rover in the sensor module measures tri-axial displacement with 10 Hz by communicating a GPS base module. While the measured displacement and acceleration are acquired, the timestamps of all the sensors are synchronized, since displacement and acceleration data have different sampling rate. Then, synchronized displacement and acceleration data are transmitted to a computational module. In the computational module, the acceleration and displacement data from the sensor module are processed to eliminate noise through a moving average filter. Then they are fused to produce displacement with a better accuracy and a better sampling rate than conventional GPS-RTK by using a two-stage Kalman filter proposed by Kim et al. [26].

2.1 Sensor Module

The sensor module consists of a GPS rover, three force-feedback accelerometers and a data acquisition system. The GPS rover measures displacement with sampling rate of 10 Hz communicating with the GPS base module, and the force-feedback accelerometers measure acceleration with sampling rate of 100 Hz. Then, the sampled acceleration and

displacement measurements are synchronized in the data acquisition system and transmitted to the computational module.

The force-feedback accelerometers can measure DC and low frequency acceleration, which corresponds to the frequency range of responses of civil infrastructures. When the force-feedback accelerometers face with a vibratory motion, force is exerted on the mass pendulum and the pendulum would attempt to move from the null position. When the null detector detects motion, the coil current is increased for the pendulum to maintain null position. The coil current provides the restoring force required to maintain the null position and this current is in direct proportion to the applied acceleration. For the development of the displacement sensor, force-feedback accelerometers have been newly developed by Poongsan FNS Co. Ltd.

In consideration of cost effectiveness, Swift Navigations Piksi GPS-RTK chipsets have been selected as GPS base and rover modules, since it is less than USD 500 per module but shows reasonable accuracy as low as 2–3 cm. Also, Tallysman TW3870 antenna has been adopted for both GPS rover and base antenna. The base and rover modules communicate information in satellite signals each other so that calculating the phase of the signal's carrier wave and optimal ambiguity integer. After the optimal ambiguity integer is converged, the accuracy of displacement measurement by GPS-RTK is maximized.

The data acquisition system controls the simultaneous digitization in 24 bits ADC with 100 Hz and synchronizes the 3-axis acceleration and displacement measurement. Additionally, it transmits the synchronized heterogeneous data to the computation module for estimating displacement precisely by using several data fusion techniques (Fig. 1).

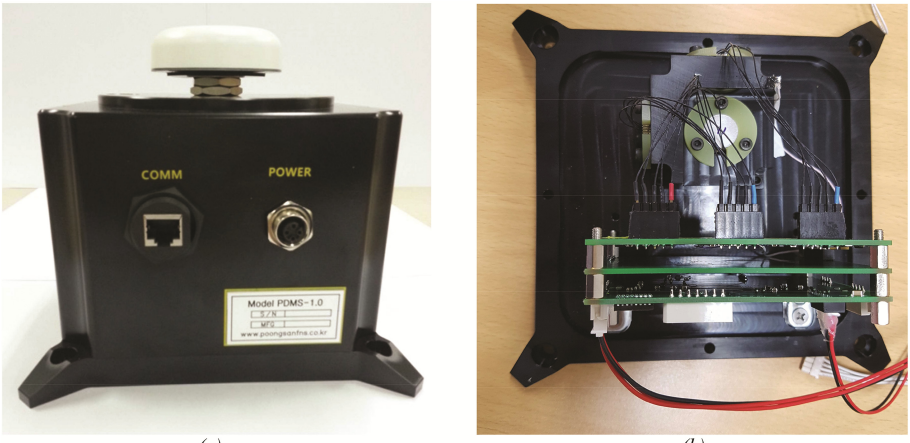

(a) *(b)*

Fig. 1. Configuration of the developed displacement sensor: (a) Developed displacement sensor, (b) Inside of the developed displacement sensor

2.2 GPS Base Module

The GPS base module simply consists of a GPS-RTK chipset and a GPS antenna. Since the precision and accuracy of measurement from the GPS base module affect the quality of displacement measurement of the GPS rover, the GPS base antenna typically has better performance than the GPS rover antenna. The measured data from the GPS base module are transmitted to the GPS rover for operating GPS-RTK.

2.3 Computation Module

After the received acceleration and displacement data from the sensor module are collected at the computational module, 3 axis displacements are estimated through several data fusion techniques. The data fusion scheme is a combination of different filters including a moving average filter and a two stage Kalman filter.

Usually, civil structures vibrate within a low frequency band, so the high frequency signals can be assumed to be noise which needs to be eliminated. Then, a moving average filter removes high frequency noise in measured acceleration and displacement.

In addition, displacement data from the GPS rover are obtained on the base of three direction (north, east, and down), and acceleration is obtained on the base of three direction (x, y, z) of the accelerometer. Because the coordinate systems of the accelerometer and the GPS rover are different, it is needed to be aligned so that all the measurements can be represented on the base of the same coordinate system.

After the noise is eliminated through a moving average filter and the coordinate is aligned, the filtered data is implemented to a two-stage Kalman filter proposed by Kim et al. [26] in order to estimate the precise and accurate displacement. The two-stage Kalman filter fuses displacement and acceleration by recursively integrating measured

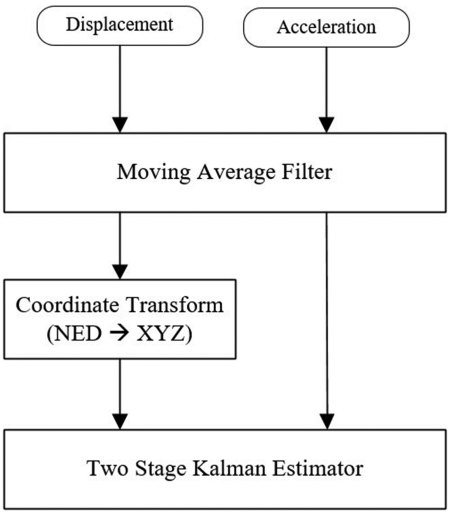

Fig. 2. Overall data fusion scheme

acceleration and correcting integration error using measured displacement to estimate displacement which has a better accuracy, precision and sampling rate (Fig. 2).

3 Experimental Verification

A series of laboratory tests were performed to validate the performance of the developed displacement sensor. An overview of the test configuration is shown in Fig. 3. The target displacement is measured from the aluminum plate located on the modal shaker (APS 400 EIELCTRO-SEIS), which is vertically vibrated. On the top of the aluminum plate, the developed displacement sensor module is attached to measure the displacement of the aluminum plate. The GPS base module is placed on the 2 story structure 3 m away from the displacement sensor module. The computation of the measured data is processed at real time in the laptop computer. Also, the reference displacement is measured by aiming an Optex-FA CD5-W500 laser triangulation sensor (LTS) to top of the aluminum plate. The modal shaker vibrates with 1 Hz for 20 s and stops for 5 s repetitively.

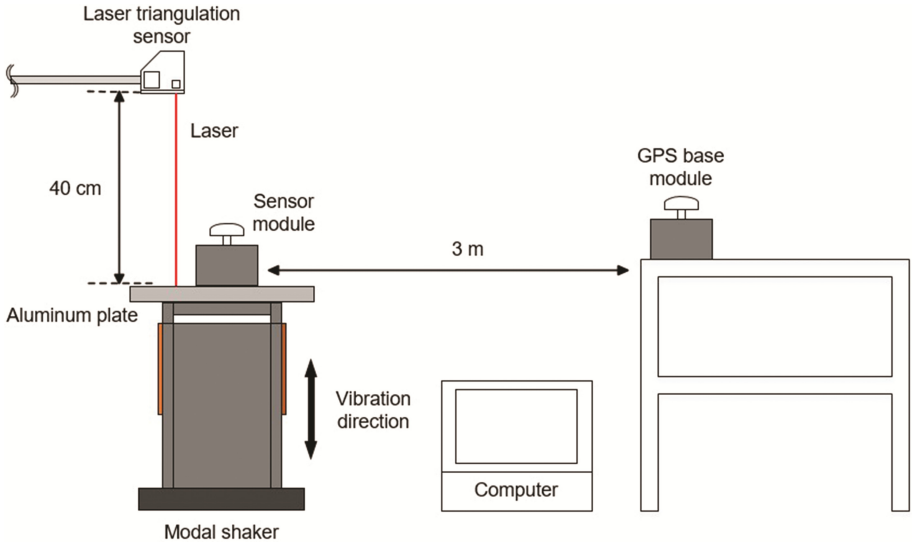

Fig. 3. Overview of a plate vibration test.

Figure 4 shows an example of the acceleration and displacement measured by the sensor module before computation. The measured acceleration is smaller than 1 m/s^2 and is contaminated with a high level of noise, as shown in Fig. 4(a). The GPS-RTK displacement measurement in Fig. 4(b) shows noise-contaminated sinusoidal responses.

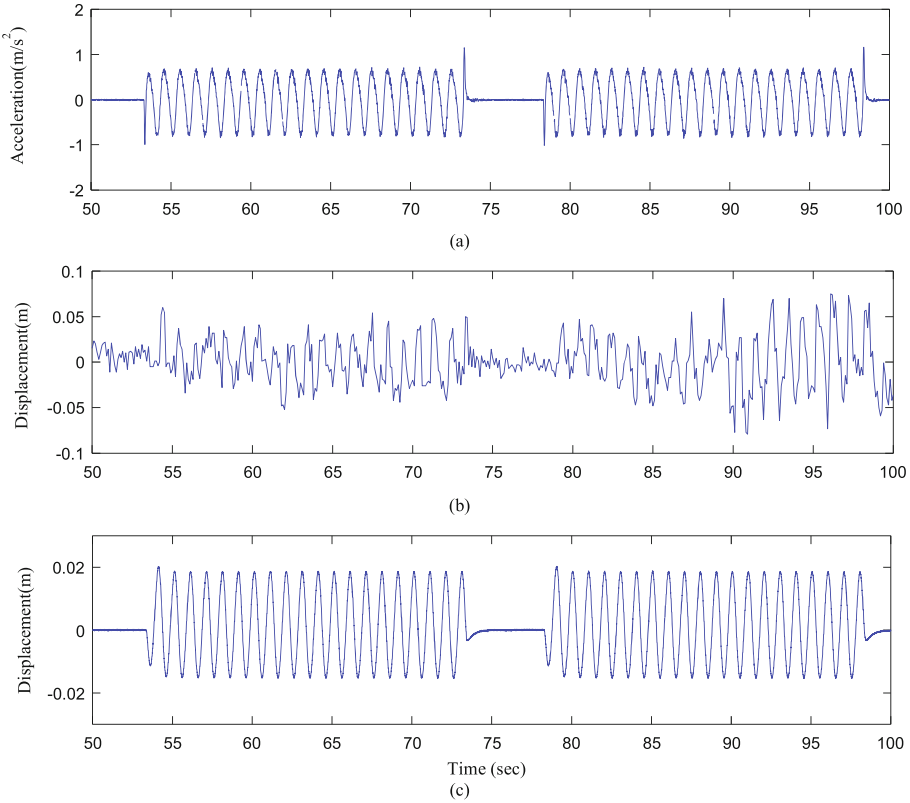

Fig. 4. Measured responses of the aluminum plate on the modal shaker: (a) acceleration measured by accelerometer, (b) displacement by GPS-RTK, and (c) displacement by LTS.

Firstly, the moving average filter is implemented to the measured data to eliminate the noise in computational module. Then, two-stage Kalman filter is used to estimate displacement with high precision, high accuracy, and a high sampling rate. Comparison between the estimated displacement and reference (LTS) are shown in Fig. 5. The average RMSE with respect to the reference is 2.9 mm. Considering that the RMSE of

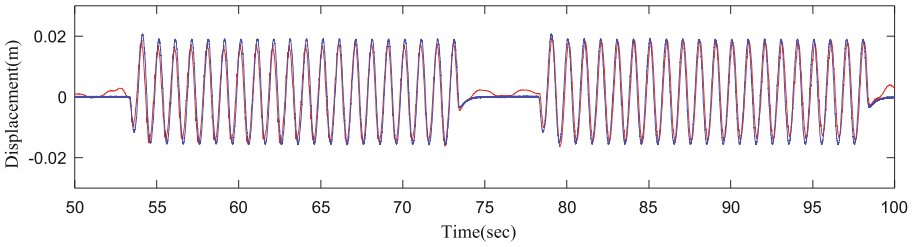

Fig. 5. Displacement estimation using the developed displacement sensor

the GPS RTK displacement measurement (Fig. 4(b)) is 20.1 mm, an 85% reduction of RMSE is achieved.

4 Conclusion

Displacement measurement is crucial for understanding and characterizing the behavior of civil infrastructure. GPS-RTK is the most widely used for displacement measurement of large-scale civil infrastructure. Typically, GPS-RTK has an accuracy of about 5 to 7 mm in the vertical direction at a sampling rate of 20 Hz for measuring displacement. However, it is easily affected by weather conditions, multipath error, and blockage of satellite signals. The developed displacement sensor overcomes some of the drawbacks of GPS-RTK by incorporating acceleration from an accelerometer, displacement from GPS-RTK. The developed sensor improves the accuracy, precision, and sampling rate of displacement compared to GPS-RTK, and estimates displacement at real-time. The lab scale test presents that the root mean square error (RMSE) of displacement with respect to a reference measurement obtained by a LTS was improved from 20.1 mm with GPS-RTK to 2.9 mm with the developed sensor.

Acknowledgements. This research was supported by a grant (15CTAP-C097371-01) from Technology Advancement Research Program (TARP) funded by Ministry of Land, Infrastructure and Transport of Korean government.

References

1. DiMassa, G., Russo, R., Strano, S., Terzo, M.: System structure identification and adaptive control of a seismic isolation test rig. Mech. Syst. Signal Process. **40**, 736–753 (2013)
2. Kim, J., Kim, K., Sohn, H.: Data-driven physical parameter estimation for lumped mass structures from a single point actuation test. J. Sound Vib. **332**, 4390–4402 (2013)
3. Kim, J., Kim, K., Sohn, H.: In situ measurement of structural mass, stiffness, and damping using are action force actuator and a laser Doppler vibrometer. Smart Mater. Struc. **22**, 085004 (2013)
4. Kim, J., Lynch, J.P.: Subspace system identification of support excited structures-Part II: gray-box interpretations and damage detection. Earthquake Eng. Struct. Dynam. **41**, 2253–2271 (2012)
5. Moreu, F., Jo, H., Li, J., Kim, R.E., Cho, S., Kimmle, A., Scola, S., Le, H., Spencer, B.F., LaFav, J.M.: Dynamic assessment of timber rail road bridges using displacements. J. Bridge Eng. **20**, 04014114 (2014)
6. Merkle, W.J., Myers, J.J.: Use of the total station for loading test of retro fitted bridges with limited access. In: Proceeding of SPIE, Smart Structures and Materials 2004: Sensors and Smart Structures Technologies for Civil, Mechanical and Aerospace Systems, vol. 5391, pp. 687–694 (2004)
7. Gordon, S.J., Lichti, D.D., Stewart, M.P., Franke, J.: Modeling point clouds for precise structural deformation measurement. In: Proceedings of International Society for Photogrammetry and Remote Sensing Congress, Istanbul, Turkey, pp. 1014–1019, July 2004
8. Park, H.S., Lee, H.M., Adeli, H., Lee, I.: A new approach for health monitoring of structures: terrestrial laser scanning. Comput. Aided Civil Infrastruct. Eng. **22**, 19–30 (2007)

9. Blais, F.: Review of 20 years of range sensor development. J. Electron. Imaging **13**, 231–240 (2004)
10. Moschas, F., Stiros, S.: High accuracy measurement of deflections of an electricity transmission line tower. Eng. Struct. **80**, 418–425 (2014)
11. Moschas, F., Stiros, S.: Three dimensional dynamic deflections and natural frequencies of a stiff footbridge based on measurements of collocated sensors. Struct. Control Health Monit. **21**, 23–42 (2014)
12. Kamiyama, K., Vlack, K., Mizota, T., Kajimoto, H., Kawakami, N., Tachi, S.: Vision based sensor for real-time measuring of surface traction field. IEEE Comput. Graph. Appl. **25**, 68–75 (2005)
13. Lee, J.J., Shinozuka, M.: A vision based system for remote sensing of bridge displacement. NDTE Int. **39**, 425–431 (2006)
14. Park, J.W., Lee, J.J., Jung, H.J., Myung, H.: Vision-based displacement measurement method for high-rise building structures using partitioning approach. NDTE Int. **43**, 642–647 (2010)
15. Kim, S.W., Kim, N.S.: Multi-point displacement response measurement of civil infrastructures using digital image processing. Procedia Eng. **14**, 195–203 (2011)
16. Nakamura, S.: GPS measurement of Wind-induced suspension bridge girder displacement. ASCE J. Struct. Eng. **126**, 1413–1419 (2000)
17. Breuer, P., Chmielewski, T., Górski, P., Konopka, E.: Application of GPS technology to measurements of displacements of high-rise structures due to weak wind. J. Wind Eng. Ind. Aerodyn. **90**(3), 223–230 (2000)
18. Tamura, Y., Matsui, M., Pagnini, L.C., Ishibashi, R., Yoshida, A.: Measurement of wind-induced response of buildings using RTK-GPS. J. Wind Eng. Ind. Aerodyn. **90**, 1783–1793 (2002)
19. Grewal, M.S., Weill, L.R., Andrews, A.P.: Global Positioning Systems, Inertial Navigation, and Integration. Wiley, Hoboken (2007)
20. Thong, Y.K., Woolfson, M.S., Crowe, J.A., Hayes-Gill, B.R., Jones, D.A.: Numerical double integration of acceleration measurement in noise. Measurement **36**, 73–92 (2004)
21. Moore, D.M.: Effect of baseline corrections on response spectra for two recordings of the 1999 Chi-Chi, Taiwan, Earthquake. U.S. Geological Survey Open-File Report, pp. 99–545 (1999)
22. Moore, D.M.: Effect of baseline corrections of displacement and response spectra for several recordings of the 1999 Chi-Chi, Taiwan, Earthquake. Bull. Seismol. Soc. Am. **91**(2001), 1199–1211 (1999)
23. Chan, W.S., Xu, Y.L., Ding, X.L., Dai, W.J.: An integrated GPS-accelerometer data processing technique for structural deformation monitoring. J. Geod. **80**, 705–719 (2006)
24. Moschas, F., Stiros, S.: Measurement of the dynamic displacements and of the modal frequencies of a short-span pedestrian bridge using GPS and an accelerometer. Eng. Struct. **33**, 10–17 (2011)
25. Smyth, A., Wu, M.: Multi-rate Kalman filtering for the data fusion of displacement and acceleration response measurement in dynamic system monitoring. Mech. Syst. Signal Process. **21**, 706–723 (2007)
26. Kim, K., Choi, J., Koo, G., Sohn, H.: Dynamic displacement estimation by fusing biased high-sampling rate acceleration and low-sampling rate displacement measurements using two-stage Kalman estimator. Smart Struct. Syst. **17**, 647–667 (2016)

Damage Identification and Structural Health Monitoring

A New Approach to Damage Detection in Bridges Using Machine Learning

A.C. Neves[1(✉)], Ignacio González[2], John Leander[1], and Raid Karoumi[1]

[1] Structural Engineering and Bridges, KTH-Royal Institute of Technology, Stockholm, Sweden
acneves@kth.se
[2] Sweco AB, Stockholm, Sweden

Abstract. At the same time that civil engineering structures are increasing in number, size and longevity, there is a conforming increasing preoccupation regarding the monitoring and maintenance of such structures. In this sense the demand for new reliable Structural Health Monitoring systems and damage detection techniques is high. A model-free damage detection approach based on Machine Learning is presented in this paper. The method performs on the collected feature measurements on a railway bridge, which for this study were gathered in a numerical experiment using a three dimensional finite element model. The first step of the approach consists in collecting the dynamic response of the structure, simulated during the passage of a train over the bridge, in both the healthy and damage states of the structure. The next step consists in the design and unsupervised training of Artificial Neural Networks that use as input accelerations and axle loads and compute a novelty index, called prediction error, based on a novelty detection approach. The distribution of the obtained prediction errors is statistically evaluated by means of a Gaussian Process and, after this process, damage indexes can be defined. Finally, the efficiency of the method is assessed in terms of Type I (false positive) and Type II (false negative) errors using Receiver Operating Characteristic curves. The promising results obtained in the case study demonstrate the capability of the presented method.

Keywords: Structural Health monitoring · Machine Learning · Damage detection · Model-free based method · Artificial Neural Networks

1 Introduction

1.1 General

Civil engineering structures are aging and being used past their life expectancy, at the same time carrying heavier traffic loads due to the increasing demand for transport capacity. Bridges in particular are a critical link in modern transport networks and, thus, this is probably the most appropriate time for the development of robust and reliable structural damage detection systems that ensure the operation of bridges in safe conditions.

© Springer International Publishing AG 2018
J.P. Conte et al. (eds.), *Experimental Vibration Analysis for Civil Structures*,
Lecture Notes in Civil Engineering 5, https://doi.org/10.1007/978-3-319-67443-8_5

Structural Health Monitoring (SHM) consists in the implementation of a damage detection and classification strategy for engineering structures, making it a concept shared in many areas of research such as Aerospace, Civil and Mechanical engineering. The aptitude to monitor a structure and eventually detect damage at the earliest possible stage supports clever maintenance strategies and provides accurate remaining life predictions.

A review of some of the most recent developments within SHM divulged in published articles is here presented. A topic of relevant research interest is the optimal sensor location, when done adequately provides the maximum information with the least number of sensors, thus allowing for cost reduction. Regarding this topic, some works worth mentioning are [1–3]. One of the dominant research topics within SHM is the discrimination of the changes in structural response caused by operational and environmental variability (e.g. temperature fluctuation) from the changes caused by damage. An efficient way to make this distinction of sources of variability in structural behavior is by applying algorithms such as Artificial Neural Networks [4]. Machine Learning has highly contributed to most of the new advances in the field of SHM. These algorithms normally belong to the outlier detection category, which considers training data coming exclusively from the normal condition of the structure (unsupervised learning), exposing structural abnormalities from monitoring data. It is worth pointing out the important work done by Worden and Farrar [5] in monitoring of structures using machine learning techniques such as neural networks, genetic algorithms and support vector machines. Not surprisingly, the newest proposed methods that show superior performance, with improved accuracy and stability, result from the integration of several techniques that may already exist but that were not previously used in combination with others. Some examples are: a novel damage identification technique combining Proper Orthogonal Decomposition (POD) with time–frequency analysis using Hilbert Huang Transform (HHT) and Dynamic Quantum Particle Swarm Optimization (DQPSO) [6]; a structural damage detection method based on posteriori probability Support Vector Machine (PPSVM) and Dempster-Shafer (DS) evidence theory [7]. Finally, the performance of the damage detection method based on machine learning techniques, often so-called classifier, should be evaluated. Some commonly tools used to perform that evaluation are the Receiver Operating Characteristic curves [8] or Probability of Detection curves [9].

Based on the work of González [10], a model-free damage detection approach using Machine Learning techniques is presented in this paper. The method performs on the collected feature measurements on a railway bridge, which for this study consists of vertical linear accelerations gathered in a numerical experiment using a three dimensional finite element model. The first step of the approach consists in collecting the dynamic response of the structure, simulated during the passage of a train over the bridge, in both the healthy and damage states of the structure. The next step consists in the design and unsupervised training of Artificial Neural Networks that use as input accelerations and axle loads and compute a novelty index, called prediction error, based on a novelty detection approach. The distribution of the obtained prediction errors are statistically evaluated by means of a Gaussian Process and, after this process, damage indexes can be defined. Finally, the efficiency of the method is assessed in terms of Type I (false positive) and Type II (false negative) errors using Receiver Operating

Characteristic curves. The promising results obtained in the case study demonstrate the capability of the presented method.

1.2 Structural Health Monitoring

Structural Health Monitoring is a powerful instrument to ensure structural integrity and safety and it has become vastly popular over the past few decades. SHM consists in the implementation of a strategy to detect damage in infrastructures, combining a variety of sensing technologies with an embedded measurement system to capture, log, and analyze real-time data.

Implied in Axiom II of SHM [5], the damage identification process involves the comparison between two distinct states of the system, the baseline case and the atypical case. Therefore, SHM can be seen as a problem of statistical pattern recognition which is composed of four parts: operational evaluation; data acquisition, normalization and cleansing; feature extraction and data compression; statistical-model development for feature discrimination. Table 1 depicts a general scheme of the SHM process and what is involved in each of the parts.

Table 1. Parts of a SHM system

1. Operational Evaluation	➔	**2.** Data Acquisition, Normalization and Cleansing	➔	**3.** Feature Extraction and Data Compression	➔	**4.** Statistical model Development
- Life-safety and economic justifications to perform SHM; - Definition of damage to be detected; - Operational and Environmental conditions; - Data Acquisition limitations.		- Type and amount of data to be collected; - Periodicity in data acquisition; - Data normalization procedures; - Sources of variability.		- Selection of the best features of the data from damage detection; - Statistical distribution of the features; - Data condensation.		- Damage or not damaged; - Damage location; - Damage extension; - Damage Type; - Remaining useful life of the structure; - Incorrect diagnosis of damage (FP and FN).

Diagnosis of damage in structural systems primarily involves the identification of damage, followed by the identification of its location, type and severity. A robust SHM system is composed of the following stages of damage identification, accordingly to [5]:

- Level 1: Is there damage present in the structure?
- Level 2: What is the geometric location of the damage?
- Level 3: What is the type of damage?
- Level 4: What is the severity of the damage?
- Level 5: What is the prediction of the remaining service life of the structure?

The idea behind this hierarchy is that the higher the level of assessment the more information one will have about the structural condition but it also raises the difficulty in acquiring that information. Hence, the several levels will have different requirements on the types of sensors, the type of algorithm used for monitoring damage and number of model parameters.

The first stage of damage identification uses methods that provide a qualitative indication of the presence of damage in the structure, which can be accomplished without prior knowledge of how the system behaves when damaged – unsupervised learning. These algorithms are referred as outlier or novelty detection methods and to solve the task of novelty detection one can use learning algorithms such as Artificial Neural Networks (ANNs).

2 Method

2.1 Artificial Neural Networks

Artificial Neural Networks are a family of mathematical models that is inspired by the structure of biological neural networks in which the basic processing unit of the brain is the neuron (Fig. 1). Neurons interact with each other by summing stimuli from connected neurons (Fig. 2). Once the total stimuli exceed a certain threshold, the neuron fires - a phenomenon called activation - and it generates a new stimulus that is passed on into the network. Knowledge is encoded in the connection strengths between the neurons in the brain.

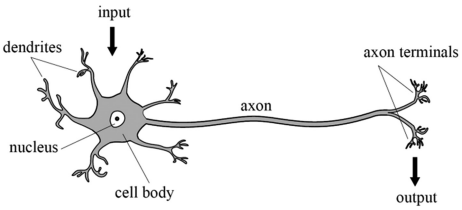

Fig. 1. The biological neuron.

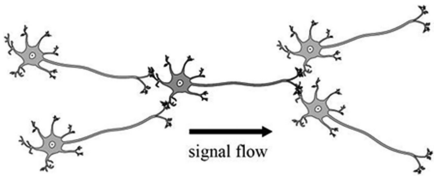

Fig. 2. Small network of neurons: the dendrites receive the input signals, the body of the cell (nucleus) is responsible for processing the input signals and the axon sends the signal from the body of the cell towards the neighbor neurons.

Mundane examples of applications of ANNs are: speech recognition and generation, optimization of chemical processes, manufacturing process control, cancer cell analysis, transplant time optimizer, recognition of chromosomal abnormalities, solution of optimal routing problems such as the Traveling Salesman Problem, etcetera. ANNs are a powerful tool for SHM in the aid of problems in sensor data processing that require parallelism and optimization due the high complexity of the variables' interactions. Generally, the ANNs offer solutions to four different problems: auto association, regression, classification and novelty detection.

The idea behind using ANNs for SHM is to use a data set of signal parameters obtained from a reference structure, such as an undamaged structure or a numerical model of a structure, and to use soft computing methods to warn about damage and its characteristics. Only the data from normal operating condition of the structure is used as training data – unsupervised learning. This is normally what happens in reality as concerning civil engineering structures one lacks the data for damaged condition of the structure of interest due to costs and practicality constraints. The downside of using such unsupervised methods is that they do not have much diagnostic ability beyond simple detection. With these methods, a reference model of the normal condition is first created and then the newly acquired data (e.g. from measurements of the structure) is compared with the data obtained from the model. If there are significant deviations, the algorithm is said to indicate novelty, meaning that the structure has departed from its normal condition and damage is probably present.

2.2 Receiver Operating Characteristic Curve

One approach that enables the statistical evaluation of the errors related with false detection is the Receiver Operating Characteristic (ROC) curve [11]. A ROC curve is a two-dimensional graphic in which the True Positive rate (TPr) is plotted in the y axis and the False Positive rate (FPr) is plotted in the x axis and the graphic demonstrates relative trade-offs between these benefits and costs, respectively, depending on a threshold that is selected, for example comparing a damage index (DI) with it. Recalling the definition of DI, one that surpasses the threshold will make the system warn for damage, whereas one that falls behind the threshold makes the system to not warn for damage. It is then understandable that a very high threshold will never indicate damage since the classifier finds no positives (resulting in 0% of False and True Positives), whereas a very low threshold will always indicate damage since everything is classified positive (resulting in 100% of False and True Positives). Figure 3 illustrates the Probability Density Functions (PDFs) of the null (structure is undamaged) and alternative (structure is damaged) hypotheses, which are in the basis of the process with which the ROC curve is created. When the threshold is placed to the right of the null distribution, damage is not detected and therefore both probabilities of TP and FP are zero. By translating the threshold to the left, the area under the null distribution increases (and thus does the probability of true detection) but so will the area under the alternative distribution increase (and thus does the probability of false detection). If the threshold is pulled to the extreme left, the TP and FP probabilities will approximate the unity. Using the distributions of Fig. 3 as an example, for the fixed threshold depicted the ROC registers approximately 70% TPs (shaded area) against 15% FPs (shaded area). Well-known characteristics of the ROC curve are:

- the trade-off between sensitivity and specificity (Fig. 4). An increase in sensitivity is achieved by moving the cutpoint to a higher value – making the criterion for a positive test less strict. An increase in specificity is achieved by moving the cutpoint to a lower value – making the criterion for a positive test more strict;
- the closer the curve comes to the left and the top borders of the ROC space, the more accurate is the damage detection method (– ROC curve in Fig. 4); the closer

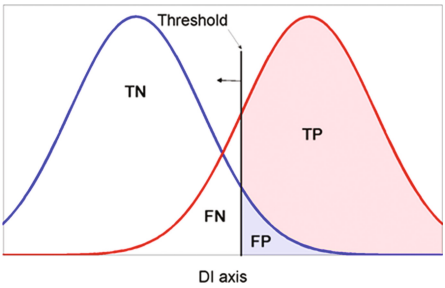

Fig. 3. ROC curve construction. – Null (Normal condition) and – Alternative (Abnormal condition) PDFs along with the detection threshold moving from the right (higher threshold) to the left (lower threshold). TP – True Positive; FP – False Positive; FN – False Negative; TN – True Negative.

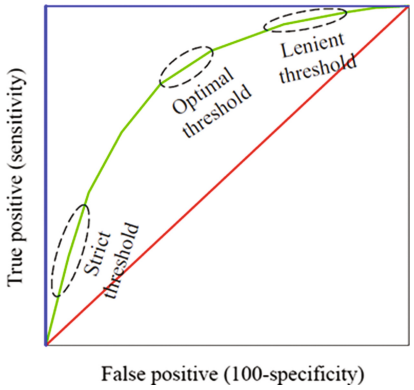

Fig. 4. ROC curves: – excellent; – good; – worthless.

the curve comes to the 45-degree diagonal of the ROC space, the less accurate is the damage detection method (– ROC curve in Fig. 4);

- the area under the curve is a convenient way of comparing the classifier methods' accuracy: an ideal perfect one as a value of 1.0 whereas a random worthless one has a value of 0.5;
- the slope of the tangent line at a certain threshold gives the likelihood ratio for that value of the test;

3 Bridge and Finite Element Model

A numerical 3D model of a single-track railway bridge was developed in the FEM software ABAQUS [12]. The structure consists of a concrete deck, two steel girder beams that support the deck and steel cross bracings that connect the girders. The deck and the girder beams were modelled as shell elements and the cross bracings were modelled as truss elements. All the elements of the bridge are assumed to be rigidly connected to each other.

Damage in the bridge is simulated considering two damage scenarios: in damage case 1, a section of the bottom flange of one girder beam is removed (Fig. 5), in an attempt to represent a damage situation where a fatigue crack exists. The cut out section has the dimensions of some longitudinal length l by the flange width, reflecting a situation when a propagating crack has reached its critical depth (about 30% of the flange's width or less) causing the sudden rupture through the whole flange width; in damage case 2 one bracing is removed (Fig. 6), which equivalently corresponds to reducing to approximately zero its Elastic modulus in the model. Assuming that girder

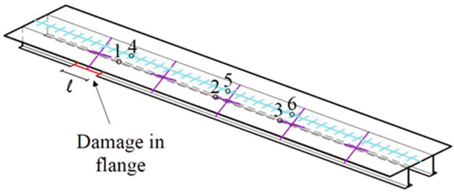

Fig. 5. Damage Case 1 (DC1). – Track alignment; – Bracing; – Damage location; **1-6** Sensor numbering and location.

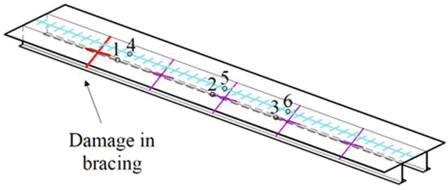

Fig. 6. Damage Case 2 (DC2). – Track alignment; – Bracing; – Damage location; **1-6** Sensor numbering and location.

beam and bracings are connected by high-tension bolts, this can reflect a situation where there is looseness in the bolted connection [13] yielding the bracing to become inefficient in its function. The numbers 1 to 6 in the figures below represent the locations of the accelerometers that are installed on the top of the bridge deck: three aligned with the train track and three aligned with the girder beam in which damage in *DC1* takes place.

The proposed method for structural assessment is intended to identify existing damage from the measured vibration of the bridge. Dynamic loads typically come from traffic, which is expected to be continuous while the bridge is in service. Traffic induced vibration was simulated in the numerical model by means of the passage of a train with a fixed configuration, crossing the bridge with a speed within the range [70–100] km/h, in increments of 0.1 km/h. A total of 300 different train passages were simulated and the corresponding measurement data sets were gathered and saved. The moving axle loads were modelled as series of constant moving forces with short time steps conforming to vehicle motion.

4 Results

Figure 7 illustrates the Root Mean Squared Error (RMSE) of the predicted accelerations by the six sensors, in the presence of an undamaged structure (in blue) and for a damaged structure (in red), reflecting Damage case 1 with the removal of a $0.9 \times 0.4\,m^2$ section from the flange. For each sensor and each train passage, in a similar way for both healthy and damaged scenarios, one can estimate the RMSE as

$$RMSE = \sqrt{\frac{\sum_{i=1}^{T}(output_i - target_i)^2}{T}} \tag{1}$$

where, for a certain instant i, $target_i$. is the expected acceleration in healthy condition of the bridge, $output_i$ is the acceleration predicted by the network and T is the time interval during which the accelerations were recorded. The train passages in the x axis are ordered by increasing speed and it is, thus, possible to observe a tendency for the error to increase with increasing train speed. Moreover, for the highest speeds (96–

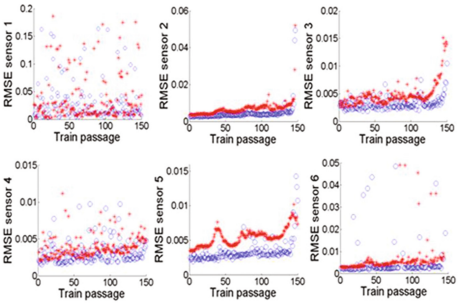

Fig. 7. RMSE against increasing speed of the train. Damage case 1: damage extension of $0.9 \times 0.4\,m^2$. o Data from healthy structural condition; * Data from damaged structural condition.

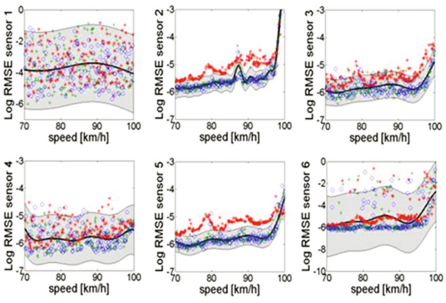

Fig. 8. GP fitted by prediction errors against increasing train speed. A Log-Normal Distribution of the error is considered. — Mean; Standard deviation; + Data to fit the GP; o Data from healthy condition; * Data from damaged condition, considering Damage Case 1 with a $0.9 \times 0.4\,m^2$ section reduction.

100 km/h) it seems like even the response for healthy structural condition is poorly predicted, yielding large errors. This phenomenon can be explained by the fact that the maximum considered speeds excite the structure to frequencies close to its natural frequencies. As a consequence of that, the behavior of the structure may depart from its expected normal behavior and the trained network is not able to correctly predict the resulting accelerations anymore. Also noticeable is that the sensors positioned closer to the geometric middle of the bridge (sensors 2 and 5) seem to perform damage detection more efficiently, whilst sensors placed nearby the end supports (sensors 1 and 4) are not as efficient in the detection. This may be due to the fact that the dynamic response of the structure is more accentuated in the middle of the span than in its extremities and, accordingly, measurements registered in the middle of the span are expected to enable the network to make a clearer distinction between structural states.

It should be noted that the non-linear input-output relating function that the network uses can become quite complex and for that reason training an ANN that covers all the train load cases and speeds is extremely difficult. Fortunately, bridges are designed to be normally crossed by trains of the same configuration, very similar axle load and moving consistently within a limited range of speeds. Therefore the ANN is trained to predict accelerations only for those specific cases of speed and train type. In fact, the range of speeds (70–100 km/h) considered to train the network could actually be reduced, most likely yielding further accurate predictions of accelerations and, for example, reducing the disorder observed in the plots of sensors 1 and 4 in Fig. 7. In any case, even not making this adjustment, the results turned out to be very satisfactory.

Throughout the testing phase and after the errors in the predictions are determined, one has already qualitative indication that the network can successfully discriminate between structural states. However, making inferences based only on the plot from Fig. 7 would constitute a subjective way of judging what degree of separation is enough to suspect that damage is indeed present in the structure. Even if the bridge is

found to be in good condition, the recorded dynamic response will be different for each train passage, as the magnitude of the response depends on the speed and axle load of the train plus other variations such as the operational and environmental settings. In short, this means that the prediction errors will oscillate for each train passage, even within the normal condition of the bridge. Hence there is a distribution of the errors that needs to be characterized stochastically and it is the errors that significantly deviate from this distribution that will work as a warning that damage in the structure may exist.

The prediction errors from 150 randomly selected train passages in healthy condition of the bridge are used to fit a statistical distribution that will work as a baseline for each sensor [10]. The Gaussian process (GP) [14] consists in assigning a normally distributed random variable to every point in some continuous domain. For each train speed the associated predicted errors are normally distributed and the mean and standard deviation of the error can differ between speeds. New data is then compared against the baseline: 150 other train passages in healthy condition and 150 in damaged condition. The idea is to compute discordancy measures for data and then compare the discordancy with a threshold, from which one is able to discriminate between healthy and damaged structural condition.

After the outcome of the prediction error is characterized by a GP (Fig. 8), damage detection can be performed by checking predictions that differ significantly from the expected values. A discordancy measure for normal condition data is the deviation statistic

$$z = \frac{|x_\xi - \bar{x}|}{\sigma_x} \tag{2}$$

where x_ξ is the candidate outlier and $\bar{x}$ and σ_x are, respectively, the mean and standard deviation of the data sample. The Mahalanobis distance [15] is one common measure of novelty in data and can be used in standard outlier analysis to provide a Damage Index (DI). To take into account only the train passages that give high prediction errors the distance to the mean is given in standard deviations and the error's differences, $(RMSE_n(v) - \mu_n(v))$, are signed. The DI for each train speed v is then defined as

$$DI(v) = \sum_{n=1}^{6} \frac{RMSE_n(v) - \mu_n(v)}{\sigma_n(v)} \tag{3}$$

where for each sensor n, $RMSE_n$ is the predicted error, μ_n is the mean predicted error and σ_n is the standard deviation of the predicted error. If the feature vector is related to undamaged condition, then $DI \approx 0$; otherwise, $DI \neq 0$. With the determined DIs for different train passages, the Receiver Operating Characteristic (ROC) curve can be constructed for each situation. Figure 9 depicts several ROC curves, each corresponding to a different damage severity within damage case 1. One point in the ROC space is considered better than another if it is associated to a higher TPr for the same FPr. Based on this conviction, as expected and in general, one verifies that more severe damage is related to a better detection. For example, for a fixed FPr of 8% we have

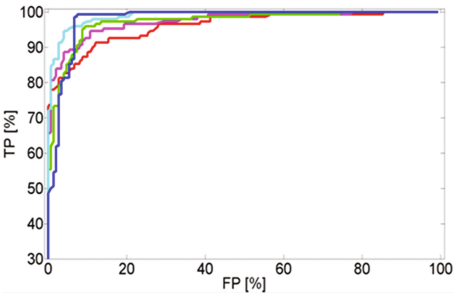

Fig. 9. ROC curves for different damage extensions l of Damage Case 1: damage resulting from cutting off a section of extension l from the bottom flange of one girder beam. – 20 cm; – 40 cm;– 70 cm; – 100 cm; – 160 cm.

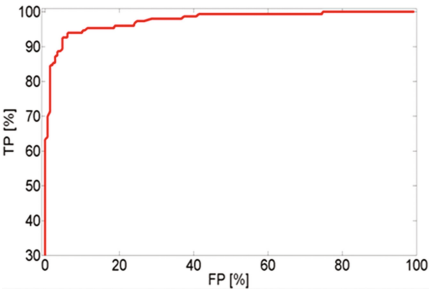

Fig. 10. ROC curve for DC2: damage resulting from a malfunctioning intermediate bracing.

associated 86, 90.7, 92, 96 and 99.3% TPr with damage severities of 20, 40, 70, 100 and 160 cm, respectively. Similarly, Fig. 10 depicts the ROC curve of the system in the presence of damage case 2. The improvement in detection capability with increasing damage is, however, not always verified as expected, since there are some operating points of DI that actually make the system more apt to detect damage in the presence of smaller rather than larger damage. For instance, we can see in Fig. 8 that the performance of the classifier for very low values of *FPr* is worse in the presence of the largest damage (160 cm), since it is related to a lower *TPr* when compared with any other smaller damage. The fact that some ROC curves respecting different amounts of damage intersect each other at certain thresholds, when ideally they should be separable over all the ROC space, may be partially explained by the fact that when the ROC curve is generated many assumptions and simplifications concerning parameters had to be previously made. Furthermore the process encompasses statistical analysis, thus yielding slightly different results every time it is repeated.

5 Conclusions

The novel methodology here proposed, based on the work presented in [10], provides a rational fashion for enhancing the damage diagnosis strategy for damaged structures, allowing for both improvements in safety and reduction of maintenance cost. The method proposes the use of past recorded deck accelerations in the bridge as input to an Artificial Neural Network that, after effectively trained, is able to predict an acceleration at a certain time in the future. The nonconformity between the measured value and the value predicted by the network will work as a primary indicator of damage. This study comprises the statistical evaluation of the prediction errors of the network by means of a Gaussian Process, after which one can select the optimal detection threshold.

From the attained results it is possible to derive some general conclusions:

- the outcome revealed to be noise sensitive, as expected, but the method seems to be robust and to perform well within typical levels of noise. It is a general conclusion that damage is more prone to be noticed in the presence of weaker noise and severer damage;
- lower vehicle speeds seem to overall provide measurements that enable better predictions by the trained network, in the sense that the prediction errors in both healthy and damaged structural condition are lower;
- the two sensors placed in the middle of the bridge seem to be the most efficient in the damage detection process, apparently disregarding where in the bridge damage takes place. This may be explained by the fact that the dynamic response of the bridge is more emphasized at half-span.
- ROC curves associated with scenarios where damage is more severe generally present a superior relation TP/FP, since for the same probability of TP one has to accept an inferior probability of FP when compared to less evident damage.

The method has although some weaknesses that can be tackled with additional research. This could concern the study of environmental and operational effects on the proposed damage detection method - other relevant parameters than accelerations may be given as input to the neural networks, such as temperature measurements. The consideration of these will most likely produce networks with higher accuracy in the prediction of the structural response, making the algorithm more shielded against the influence of other factors unrelated to damage that can induce significant changes in the behavior of the structure. The study presents a limited number of damage scenarios: a wider range of possible locations for damage in the bridge should be considered, including the impact of multiple damage scenarios, i.e. situations where damage events occur simultaneously in different parts of the structure. It would also be interesting to understand what are the limitations of the proposed method in terms of the smallest damage it can detect.

References

1. Huang, Y., Ludwig, S.A., Deng, F.: Sensor optimization using a genetic algorithm for structural health monitoring in harsh environments. J. Civ. Struct. Health Monit. **6**, 509–519 (2016)
2. Li, J., Zhang, X., Xing, J., Wang, P., Yang, Q., He, C.: Optimal sensor placement for long-span cable-stayed bridge using a novel particle swarm optimization algorithm. J. Civ. Struct. Health Monit. **5**(5), 677–685 (2015)
3. Yi, T.-H., Li, H.-N., Wang, C.-W.: Multiaxial sensor placement optimization in structural health monitoring using distributed wolf algorithm. Struct. Control Health Monit. **23**(4), 719–734 (2016)
4. Jin, C., Jang, S., Sun, X., Li, J., Christenson, R.: Damage detection of a highway bridge under severe temperature changes using extended Kalman filter trained neural network. J. Civ. Struct. Health Monit. **6**, 545–560 (2016)
5. Farrar, C.R., Worden, K.: Structural Health Monitoring. A Machine Learning Perspective. Wiley, New York (2013)

6. Rao, A.R.M., Lakshmi, K.: Damage diagnostic technique combining POD with time-frequency analysis and dynamic quantum PSO. Meccanica **50**(6), 1551–1578 (2015)
7. Zhou, Q., Zhou, H., Zhou, Q., Yang, F., Luo, L., Li, T.: Structural damage detection based on posteriori probability support vector machine and Dempster-Shafer evidence theory. Appl. Soft Comput. **36**, 368–374 (2015)
8. Figueiredo, E., Figueiras, J., Park, G., Farrar, C.R., Worden, K.: Influence of the Autoregressive Model Order on Damage Detection. Comput.-Aided Civ. Infrastruct. Eng. **26**(3), 225–238 (2011)
9. Deeb, M., Zabel, V.: The application of POD curves to damage detection in civil engineering structures – a numerical and experimental study. In: International Conference on Noise and Vibration Engineering ISMA 2012, Leuven, Belgium (2012)
10. Gonzalez, I., Karoumi, R.: BWIM aided damage detection in bridges using machine learning. J. Civ. Struct. Health Monit. **5**(5), 715–725 (2015)
11. Fawcett, T.: An introduction to ROC analysis. Pattern Recogn. Lett. **27**, 861–874 (2005)
12. Abaqus FEA: ABAQUS Inc. http://www.3ds.com/products-services/simulia/products/abaqus/. Accessed May 2017
13. White, K.: Bridge Maintenance Inspection and Evaluation. CRC Press, Boca Raton (1992)
14. Rasmussen, C., Williams, C.: Gaussian Processes for Machine Learning. The MIT Press, Cambridge (2006). ISBN 026218253X
15. Worden, K., Manson, G., Fieller, N.: Damage detection using outlier analysis. J. Sound Vib. **229**(3), 647–667 (2000)

Vibration Based Damage Identification Method for Cantilever Beam Using Artificial Neural Network

Putti Srinivasa Rao(✉) and N.V.D. Mahendra(✉)

Department of Mechanical Engineering, Andhra University College of Engineering (A), Andhra University, Visakhapatnam 530003, India
s_putti@rediff.com, mahendra.nelaparthi@gmail.com

Abstract. This paper presents the use of Artificial Neural Networks (ANN) techniques to identify the damage in cantilever beams. We consider two cantilever beams of different materials i.e. aluminum and stainless steel. Different crack lengths are introduced on the beams from 0–10 mm with 2 mm interval. 0 mm, 2 mm, 4 mm, 6 mm, 8 mm and 10 mm cracks denotes damage level 0, 1, 2, 3, 4 and 5 respectively. The undamaged cantilever structure is treated as damage level 0. Experimental modal analysis is conducted for each case using impact hammer test. To validate the experimental values modal analysis is conducted in ANSYS software. From the modal analysis results it is observed that, for lower modes there is no change in frequencies but for higher modes the natural frequencies are decreasing with the increase in crack length. The FRFs obtained from experimental modal analysis are used as inputs to train the ANN. In the present paper, two types of networks are considered. One is Radial Basis Function (RBF) network and other is feed forward network. For each material total of 60 sets of data were collected. Part of the data is used to train the ANN and remaining data is used to test the trained ANN. From the results, the ANN is capable of identifying the damage and its severities.

Keywords: ANN · Vibration · Damage identification · Cantilever beam · ANSYS

1 Introduction

Mechanical components fail in many modes such as fatigue, creep, resonance structural defects may experience dynamic loads, prior to fail due to presence of cracks. Cracks in machine or any engineering systems may lead to catastrophic failure of the machine and must be detected early. For this reason, methods allowing early detection and localization of cracks have been the subject of intensive investigation. The cracks present in the system may be considered to develop the analytical model to study the effect of cracks on the modal response of the system. The damage [1] in the beam member introduces the stiffness, which can be used along with the prevailing boundary conditions to formulate the vibration characteristic equation to obtain the mode shape, natural frequency of vibration, crack parameters such as relative crack severities and relative crack positions. Utilization of the dynamic response of the member is one of

© Springer International Publishing AG 2018
J.P. Conte et al. (eds.), *Experimental Vibration Analysis for Civil Structures*,
Lecture Notes in Civil Engineering 5, https://doi.org/10.1007/978-3-319-67443-8_6

the technique which has been widely accepted for crack diagnosis in different engineering systems. The structural health monitoring (SHM) [2] technique provides information on the life expectancy of structures simultaneously detects and locates structural damage. Vibration-based damage identification techniques are based on the principle that damage alters both the physical properties as well as its dynamic characteristics of the structure. Therefore, by analyzing a structure's dynamic properties from structural vibration, any damage, including its location and severity, can be identified. Among the Vibration-based damage identification methods, the ANNs as a very effective tool and have proven to be robust in the presence of noise. Many methods have been developed and studied to detect damage through the changes in the dynamic response of a structure. Due to its capability to recognize pattern and to correlate non-linear and non-unique problem, ANN have received increasing attention for use in detecting damage in structures based on vibration modal parameters.

Rytter [3] presented the four level classification of damage identification system. Cawley and Adams [4] have developed a technique based on experiment to estimate the location and depth of the crack from changes in the natural frequencies. Sahin and Shenoi [5] examined the effectiveness of using natural frequencies and mode shape curvatures as inputs for ANNs. Lee et al. [6] presented an ANN-based damage detection method using three different types of mode-shape-based parameters as inputs for the networks. Mayes and Davies [7] proposed a method for the prediction of the magnitude of a rotating cracked and rotor crack location, from analytically obtained mode shapes and frequency measurements. Wu et al. [8] applied FRF data as an input to represent the undamaged and damaged condition of each member in a simulated three-storey building. Povich [9] verified the application of FRF as the input parameters to detect damage condition in a 20-bay planar truss composed of 60 structure. Ghate et al. [10] have proposed a multi-layer perceptron neural network based classifier for fault detection in induction motors which is inexpensive, reliable by employing more readily available information such as stator current. Liu et al. [11] use an autoregressive with exogenous inputs (ARX) model of a cantilever aluminum beam to extract vibration signatures, and employ multilayer, feed-forward neural networks (MFFNN) to locate damage and estimate its size. Narkis [12] developed a closed-form solution for the damage detection of a single crack in a simply supported beam by measuring the change in natural frequencies of the bending vibrating modes and the axial vibration modes. Masri et al. [13] carried out a study regarding the effect of different lengths of vibration signature to ANN performance.

The main aim of this paper is to develop ANN-based damage detection methods for severity estimation of cantilever beam by conducting laboratory investigations to validate experimentally and verify numerically with the finite element models.

2 Artificial Neural Network

The creation of neural networks was originally inspired by the human brain and the way it processes information. The human brain consists of about 10^{11} electrically active cells called neurons, which are heavily interconnected. The biological neural system provided the basis for a great deal of research into artificial neural network models.

This research was driven by the desire to build better pattern recognition and information processing systems. By definition, 'artificial neural systems, or neural networks, are physical cellular systems which can acquire, store, and utilize experiential knowledge'. To model such a system requires, first, a model of the network's basic building block, the single neuron.

ANN is composed of several processing elements, namely, neurons that are interconnected with each other. Figure 1 shows the model of an artificial neuron which consists of a neuron that receives weighted inputs (w) that are summed and passed through an activation function (f) to produce a single output.

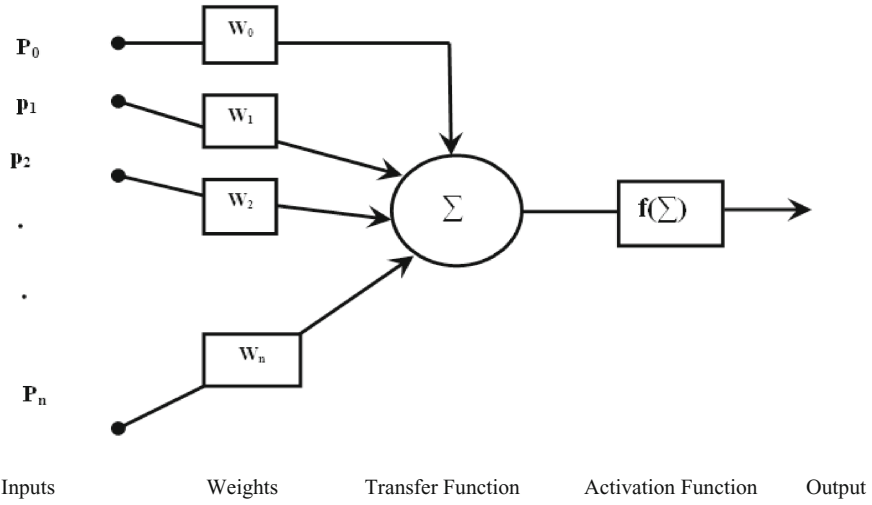

Fig. 1. Schematic structure of an artificial neuron.

A typical neural network has three layers, namely, the input layer, the hidden layer and the output layer. Signals are received at the input layer, pass through the hidden layer and reach the output layer. Each layer can have a different number of neurons and activation functions, such as sigmoid and linear functions. All neurons are interconnected to the neurons in the next layer through their weights.

3 Damage Identification Using ANN

The main use of the two vibration-based damage identification schemes for Artificial Neural Network (ANN) is pattern recognition and noise reduction. One scheme is a modal parameter method (based on the damage index (DI) method), and the other scheme is a frequency response function (FRF) method. To enhance damage signatures and to reduce the size of input data to neural networks, curve fitting techniques (CFT) are employed. Damage Identification Methods are:

Method 1: Damage identification method based on Damage Index (DI) method
Method 2: Damage identification method based on Frequency Response Functions (FRF)

In the present work, damage identification method based on FRF is used. FRF data are directly measured data and are one of the easiest to obtain in real-time as they require only a small no of sensors and very little human involvement. FRFs are normalized complex quantities that specify how vibration is transmitted as a function of frequency between points on the structure. Measured FRF data are usually the most compact form of data obtained from vibration tests of structures. As FRF data are sensitive to structural changes, they have been used as indicators in various forms to detect damage.

4 Modal Testing and Experimental Modal Analysis

Modal testing and experimental modal analysis [14] is the process of characterizing the dynamic properties of a test structure by exciting the structure artificially and identifying its modes of vibration. When a structure is damaged, e.g. its geometrical properties change, its boundary conditions modify or its material properties alter the dynamic characteristics of the structure change. These changes are the basis for the presented damage identification methods, and modal testing and experimental modal analysis serves as a means to extract the dynamic properties for the given structures. Modal analysis is used to determine the vibration characteristics such as natural frequencies and mode shapes of a structure or a machine component while it is being designed. It can also be a starting point for another more detailed analysis such as a transient dynamic analysis, a harmonic response analysis or a spectrum analysis. The natural frequency depends on specific stiffness and the length of particular components. Experimental modal analysis is based on the use of experimentally collected data from modal testing using transfer function method. This method involves the acquisition of point to point Frequency Response Functions (FRF's) at a set of points defined as dynamic model.

In the present work, two cantilever beams of aluminum and stainless steel are considered. The dimensions of the beams were 3 mm $\times$ 25.4 mm $\times$ 250 mm (ASTM standards). According to the manufacturer's specifications the modulus of elasticity of aluminum beam was 71 $\times$ 10^9 N/m^2, the Poisson's ratio was 0.33 and the density was 2770 kg/m^3 and for stainless steel beam young's modulus was 190 $\times$ 10^9 N/m^2, the Poisson's ratio was 0.305, and the density was 7861 kg/m^3. Using a C clamp, one end is fixed to a vice. To study damage scenarios of various intensities, a total of 5 single damage cases were investigated. These relate to damage at same location having five levels of severity. Damage was gradually inflicted by a saw cut from the 50 mm from free end of the beam. The five damage severities are 2, 4, 6, 8 and 10 mm depth with 1 mm width. Impact hammer test is performed to capture the FRF data. Total test setup is shown in Fig. 2.

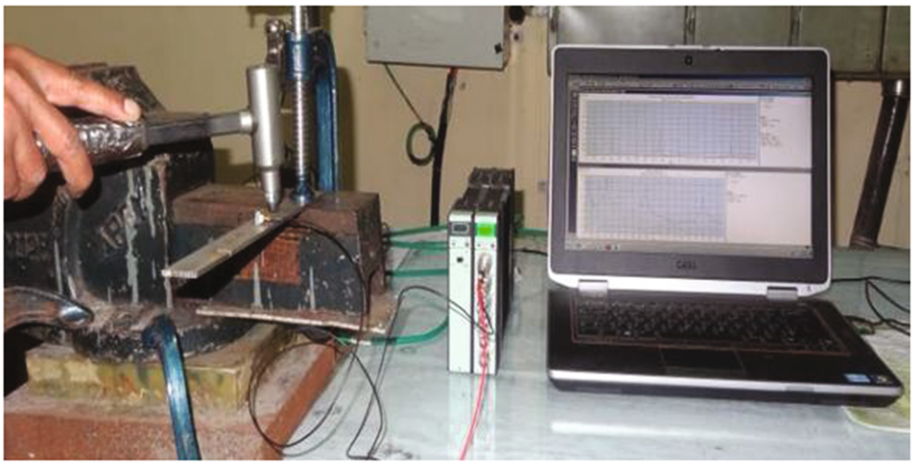

Fig. 2. Total test set up of modal testing and experimental modal analysis.

5 Finite Element Modelling

Finite Element Method (FEM) is a numerical method for solving a differential or integral equation. It has been applied to a number of physical problems, where the governing differential equations are available. The method essentially consists of assuming the piecewise continuous function for the solution and obtaining the parameters of the functions in a manner that reduces the error in the solution. It uses subdivision of a whole problem domain into simpler parts, called finite elements, and variation methods from the calculus of variations to solve the problem by minimizing an associated error function.

To perform finite element modeling for Cantilever beam with and without cracks for two different materials, ANSYS 15 is used. Modal Analysis was performed for same proposed models to validate experiment results. The geometric models for Modal Analysis were developed using CATIAV5R20 package. The modal parameters results were compared with the natural frequencies obtained from experimental modal analysis.

6 ANN Training and Testing

In the present work, ANN is trained by using Radial Basis Function Network method. The arrows in the Fig. 3 symbolize parameters in the network. The RBF network consists of one hidden layer of basis functions, or neurons. At the input of each neuron, the distance between the neuron center and the input vector is calculated. The output of the neuron is then formed by applying the basis function to this distance. The RBF network output is formed by a weighted sum of the neuron outputs and the unity bias.

There are total 6 cases (1 undamaged and 5 damaged cases). For damaged cases, width of the crack is 1 mm and depth of the crack is 2, 4, 6, 8 and 10 mm.

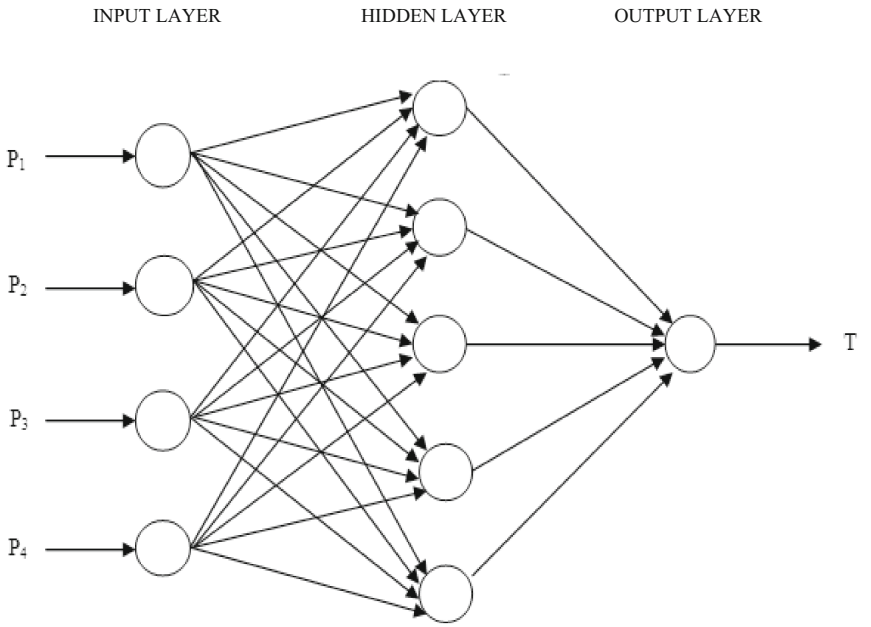

Fig. 3. RBF network with one output.

For each case 10 sets of data was collected. So 60 sets of data each for both aluminum beam and stainless steel beam. Total 120 sets of data was collected. Two separate neural networks are trained each for aluminum beam and stainless steel beam. 60 sets of data are used to train each neural network and 60 sets of noise polluted data are used for testing the trained neural network.

After assigning inputs and outputs to ANN the relations between input and output data was established by using Radial Basis Function Network, "newrbe" function. Testing the trained data using "sim" function and "reverse" function. Testing the trained data using "sim" function.

7 Results and Discussion

From modal analysis natural frequencies are obtained and compared theoretically, experimentally and ANSYS for undamaged case for both aluminum and stainless steel beams and the same is shown in Table 1. From the table we can observe that there is a change in natural frequency with change in crack size.

Similarly, natural frequencies are compared experimentally and ANSYS for all damaged cases, for both aluminum and stainless steel beams and the same is shown in Table 2. From the table we can observe that there is a change in natural frequency with change in crack size.

From the testing of the trained ANN results are obtained. FRF data of each set of a particular damage state is given as input and corresponding damage in mm is obtained

Table 1. Comparison of natural frequencies (Hz) for undamaged case from modal analysis.

Type of beam	Modal analysis	Aluminum beam			Stainless steel beam		
		Mode 1 (Hz)	Mode 2 (Hz)	Mode 3 (Hz)	Mode 1 (Hz)	Mode 2 (Hz)	Mode 3 (Hz)
Un-damaged (0 mm Crack)	Theory	53.05	332.79	931.91	51.56	323.16	904.94
	Experiment	52.5	323.75	927.5	51.25	317.5	906.25
	ANSYS	53.585	335.43	938.92	51.95	325.26	910.35

Table 2. Comparison of natural frequencies (Hz) of all damaged cases from modal analysis

Type of beam	Modal analysis	Aluminum beam			Stainless steel beam		
		Mode 1 (Hz)	Mode 2 (Hz)	Mode 3 (Hz)	Mode 1 (Hz)	Mode 2 (Hz)	Mode 3 (Hz)
Damaged beam 2 mm crack	Experiment	52.5	321.25	930	51.25	316.25	902.5
	ANSYS	53.64	335.76	940.08	52.01	325.53	911.3
Damaged beam 4 mm crack	Experiment	52.5	321.5	927.5	51.25	315	895
	ANSYS	53.66	335.39	936.95	52.02	325.17	908.28
Damaged beam 6 mm crack	Experiment	51.25	322.5	928.75	51.25	315	893.75
	ANSYS	53.67	334.85	932.26	52.03	324.6	903.55
Damaged beam 8 mm crack	Experiment	51.5	321.25	918.75	51.25	313.75	886.25
	ANSYS	53.69	334.02	925.12	52.05	323.86	896.92
Damaged beam 10 mm crack	Experiment	51.25	318.75	912.5	51.25	313.75	873.75
	ANSYS	53.69	333.07	917.41	52.06	322.97	889.32

Table 3. Results obtained from ANN training using RBF for aluminum beam.

Sl. no.	Crack length (mm)					
	0	2	4	6	8	10
1	0.0034	1.9966	3.9993	5.9994	7.9851	9.9991
2	0.0047	1.9940	4.0004	5.9999	7.9998	10.0003
3	0.0065	1.9977	4.0057	6.0007	8.0004	9.9993
4	0.0097	1.9982	3.9979	6.0109	8.0025	9.9995
5	0.0003	1.9967	3.9995	5.9994	8.0006	10.0014
6	0.0080	1.9998	3.9940	5.9998	7.9971	10.0020
7	0.0048	1.9986	3.9923	5.9908	7.9938	10.0008
8	0.0073	1.9990	3.9887	5.9977	7.9828	9.9998
9	0.0021	1.9943	3.0044	5.9997	7.9939	10.0013
10	0.0002	1.9990	3.9976	6.0114	7.9992	9.9988

Table 4. Results obtained from ANN training using RBF for stainless steel beam.

Sl. no.	Crack length (mm)					
	0	2	4	6	8	10
1	−0.0018	1.9967	4.0890	5.9637	7.9782	9.9547
2	−0.0083	1.9964	3.9734	5.9803	7.9488	9.9374
3	0.0000	1.9919	4.1906	5.9726	7.9716	10.0006
4	0.0000	1.9961	3.9902	5.9795	7.9557	9.9560
5	0.0000	1.9959	4.1789	5.9856	7.9859	9.9367
6	0.0000	1.9965	4.1959	5.9980	7.9809	9.9801
7	0.0000	1.9996	4.1716	5.9833	7.9964	9.9481
8	0.0000	1.9996	3.9689	5.9822	7.9899	9.9133
9	0.0000	1.9960	4.1818	6.0753	7.9585	9.9488
10	0.0000	1.9961	3.9657	5.9919	7.9852	9.9578

as output. For example, if FRF data of a damaged beam with 2 mm crack size is given as input for the trained ANN, then the output obtained is damage 2. Similarly, for damaged beams with 4, 6, 8 and 10 mm crack sizes the output obtained is damage 4, 6, 8 and 10 respectively for both aluminum and stainless steel beams. For all the sets of input corresponding outputs are shown in Tables 3 and 4 for aluminum and stainless steel beams.

8 Conclusions

1. The modal analysis for undamaged cantilever beam is conducted experimentally and it is validated with the theoretical values for both aluminum and stainless steel beams. The modal analysis is conducted for undamaged cantilever beam using ANSYS software for both aluminum and stainless steel. From this it is concluded that, for the first three modes the natural frequencies are coinciding and is shown in Table 1.
2. The modal analysis is also conducted for damaged cantilever beams experimentally and validated using ANSYS software for both aluminum and stainless steel. From this it is concluded that, for the first mode the natural frequencies are not varying much and for higher modes the natural frequencies are gradually decreasing with increase in crack length and is shown in Table 2.
3. Crack with larger crack depth imparts greater reductions in natural frequency than that of the smaller crack depth ratio. Hence, the accuracy of results improves as crack depth increases.
4. From the obtained experimental FRF data, the ANN is trained using RBF and feed forward networks. The trained network is tested and the results are tabulated in Tables 3 and 4 for aluminum beams and Tables 5 and 6 for stainless steel beams. From these results it is concluded that both RBF and feed forward networks are identifying the damage and its severity.

5. It is also concluded from the ANN results, the RBF network is giving more accurate results than feed forward network for the experimental data considered in this study. Hence RBF network is more suitable for this experimental data considered in this paper work.
6. From the above results, it is concluded that ANN is capable of identifying the damage and its severity for the cantilever beam considered in the experimental work based on the vibration FRF data.
7. The proposed approach has the ability to detect a crack in a cantilever beam using natural frequencies.

References

1. Rao, P.S., Ratnam, Ch.: Vibration based damage identification using Burg's algorithm and Shewhart charts. J. ASTM Int. **8**(4), 1–12 (2011)
2. Rao, P.S., Ratnam, Ch.: Health monitoring of welded structures using stastical process control. Mech. Syst. Signal Process. **27**, 683–69512 (2012)
3. Rytter, A.: Vibration based inspection of civil engineering structures. PhD thesis, Aalborg University, Aalborg (1993)
4. Cawley, P., Adams, R.D.: The location of defects in structures from measurements of natural frequencies. J. Strain Anal. **14**(2), 49–57 (1979)
5. Sahin, M., Shenoi, R.A.: Quantification and localization of damage in beam-like structures by using artificial neural networks with experimental validation. Eng. Struct. **25**, 1785–1802 (2003)
6. Lee, J.J., Yun, C.B.: Damage diagnosis of steel girder bridges using ambient vibration data. J. Eng. Struct. **28**, 912–925 (2006)
7. Mayes, I.W., Davies, W.G.R.: Analysis of the response of a multi-rotor-bearing system contacting a transverse crack in a rotor. J. Vib. Acoust. Stress Reliab. Des. ASME **106**(1), 139–145 (1984)
8. Wu, X., Ghaboussi, J., Garret, J.H.: Use of neural networks in detection of structural damage. Comput. Struct. **41**(4), 649–659 (1992)
9. Povich, C., Lim, T.W.: An artificial neural network approach to structural damage detection using frequency response function. In: Proceeding of the AIAA Adaptive Structures Forum, USA (1994)
10. Ghate, V.N., Dudul, S.V.: Cascaded neural-network based fault classifier for three phase induction motor. IEEE Trans. Ind. Electron. **58**(5), 1555–1563 (2011)
11. Liu, P., Sana, S., Rao, V.S.: Structural damage identification using time-domain parameter estimation techniques. Structural health monitoring 2000, pp. 812–820. Stanford University, Palo Alto (1999)
12. Narkis, Y.: Identification of crack location in vibrating simply supported beams. J. Sound Vib. **172**(4), 549–558 (1994)
13. Masri, S.F., Nakamura, M., Chassiakos, A.G., Caughey, T.K.: Neural network approach to detection of changes in structural parameters. J. Eng. Mech. ASCE **126**(7), 666–676 (1996)
14. Rao, P.S., Ratnam, Ch.: Experimental and analytical modal analysis of welded structure used for vibration based damage identification. Glob. J. Res. Eng. Mech. Mech. Eng. **12**(1), 631–642 (2012)

Advanced Statistical Techniques Applied to Raw Data for Structural Damage Detection

Alan S. Torres[1], Vinicius N. Alves[2], Alexandre A. Cury[3(✉)], and Flavio S. Barbosa[3]

[1] Federal University of Juiz de Fora, Juiz de Fora, Brazil
[2] Federal University of Ouro Preto, Ouro Preto, Brazil
[3] Department of Applied and Computational Mechanics, Federal University of Juiz de Fora, Juiz de Fora, Brazil
alexandre.cury@engenharia.ufjf.br

Abstract. Structural Health Monitoring is one of the most promising and challenging areas of research in the field of Civil Engineering. Over the last decades, researchers have focused on the development of consistent and reliable indicators aiming to detect, locate, quantify or even predict damage. More recently, some researchers are focusing on the use of raw time histories extracted from structural dynamic monitoring to build damage indicators. In this sense, this paper has as its main interest the use of high-order statistics (HOS) coupled with clustering techniques i.e. the k-means and c-means algorithms to detect structural modification (damage). The approach is applied directly to dynamic measurements (accelerations) obtained on site. The efficiency of such methodology is attested by means of a numerical study performed on a model of a simply supported beam and a study based on a real case railway bridge, in France. Results show that HOS coupled with clustering techniques are able to differentiate damage scenarios with adequate classification rates.

Keywords: Damage detection · High-order statistics · Clustering methods · Raw data · SHM

1 Introduction

Structural Health Monitoring (SHM) is of great importance to Civil Engineering, once it allows the detection of modifications in the physical properties of structures. SHM permits, if possible and/or necessary, the use of recovery procedures in suitable time. These procedures are often based on evidence collected from tests performed on the structure that would ideally allow 'detecting, locating, quantifying, and even predicting damages'. Recently, researches have focused on the dynamic evaluation as part of structural diagnoses [1, 2], by the extraction of modal parameters or data built from these parameters that, so far, have provided promising results. However, some problems remain unsolved, such as the sensitivity of the damage identification methods, their need of a reference state and their reliability when it comes to the detection of false alarms [3].

© Springer International Publishing AG 2018
J.P. Conte et al. (eds.), *Experimental Vibration Analysis for Civil Structures*,
Lecture Notes in Civil Engineering 5, https://doi.org/10.1007/978-3-319-67443-8_7

Historically, damage detection techniques were developed under the premise that structural damage could be detected by observing the variation of the structure's vibration characteristics, i.e. natural frequencies, damping ratios, and mode shapes. This premise was and is correct, since these parameters are directly affected by modifications in the structure's mass and stiffness. However, the identification of modal parameters usually demand time and, ultimately, represent some sort of filtering process, yielding a loss of information compared to the raw acceleration data. This "filtering" process might erase any small tendencies, which could represent a structural modification. Moreover, modal components usually describe an equivalent linear structural behavior, which is not always the case after a damage occurs. On the other hand, raw data may contain thousands of accelerations values measured by numerous sensors. Thus, examining all of these data directly may take time or even be prohibitive, despite the current computers' processing power [4]. In this sense, it is imperative to transform these substantial amounts of data into a more compact yet rich descriptive type of data.

To this end, this paper proposes the use of Higher-Order Statistics (HOS). HOS refer to functions that use the third and higher cumulants of a given sample. This definition comes as the opposite of "Low-Order Statistics", which use linear and quadratic cumulants (arithmetic mean and variance, respectively). The third and higher cumulants of a sample are given by its skewness and kurtosis, respectively.

In this paper, raw data obtained from dynamic tests (acceleration measurements) are transformed into a more compact arrangement by computing HOS for each sensor e.g. accelerometer used. Then, these quantities are applied to two clustering algorithms in order to discriminate different structural states or, in other words, to detect damage. This paper is based on the conjecture that the HOSs are sensitive to damage, meaning that they can provide information regarding variations on the physical properties of structures that could indicate the existence of damage. Thus, the clustering algorithms would eventually be able to identify different structural scenarios.

The key objective of this paper is to develop a methodology capable of detecting structural damage by clearly differentiating physical states that correspond to an "undamaged" configuration from a "damaged" configuration. It is important to emphasize that such a methodology is original, since it uses HOS coupled with clustering techniques. However, it must also be reminded that this is a rather complex problem, since the proposed methodology is applied directly to the raw data i.e. the raw dynamic measurements.

2 Methodology

This section presents the main concepts within the framework of this paper. First, a brief description of HOS is presented. Then, a short explanation about k-means and c-means clustering algorithms is given (more details can be found in [5]).

2.1 High-Order Statistics

As previously explained, HOS refer to statistics that use the third and higher cumulants of a given sample. The HOS used in this paper are summarized in Table 1 where the variable "y_i" represents each sensor (accelerometer) measuring "n" acceleration values for each dynamic test.

Table 1. High order statistics used as damage sensitive characteristics. Adapted from [6].

Statistic	Formula
Peak value	$y_{peak} = \max\|y_i\|$
Mean	$\bar{y} = \frac{1}{n}\sum_{i=0}^{n} y_i$
Mean square	$\bar{y}_{sq} = \frac{1}{n}\sum_{i=0}^{n} y_i^2$
Root mean square (rms)	$rms = \sqrt{\frac{1}{n}\sum_{i=0}^{n} y_i^2}$
Variance	$\sigma^2 = \frac{1}{n}\sum_{i=0}^{n} (y_i - \bar{y})^2$
Standard deviation	$\sigma = \sqrt{\frac{1}{n}\sum_{i=0}^{n} (y_i - \bar{y})^2}$
Skewness	$\gamma = \frac{\frac{1}{n}\sum_{i=0}^{n} (y_i - \bar{y})^3}{\sigma^3}$
Kurtosis	$k = \frac{\frac{1}{n}\sum_{i=0}^{n} (y_i - \bar{y})^4}{\sigma^4}$
Crest factor	$X_{CF} = \frac{y_{peak}}{rms}$
K-Factor	$X_K = y_{peak} \cdot rms$

2.2 k-Means Clustering Algorithm

This clustering method was developed over a generalization of the classical dynamic clusters method. Clustering of a dataset is the partition of that data into groups, named clusters, so that the data inside a cluster has the highest degree of similarity among all possible combinations. What defines this 'similarity' is the clustering algorithm. In this paper, the chosen algorithm - k-means - uses the spatial distance between a data point (a dynamic test) to the centroid of the cluster. The idea is to identify the best combination of data that produces the clusters with the highest degree of similarity, that is, the smallest data-centroid sum of distances. The k-means algorithm has several metrics to calculate those spatial distances. In this paper, the metrics used are the square Euclidean and the cityblock, shown in Eqs. (1) and (2), respectively:

$$d(E_i, E_j) = \sqrt{\sum_{k=1}^{n} (E_{ik} - E_{jk})^2} \tag{1}$$

$$d\left(E_i, E_j\right) = \sum_{k=1}^{n} \left|E_{ik} - E_{jk}\right| \tag{2}$$

Once the statistics were extracted, the resulting datasets were analyzed through clustering algorithm k-means.

2.3 C-Means Clustering Algorithm (FCM)

As fully described in [8], "A fuzzy set is a class of objects that has a continuum of grades of membership. Such a set is characterized by a membership (characteristic) function that assigns a grade of membership that ranges between zero and one to each object. The FCM is an iterative algorithm clustering method that produces optimal c-partitions by minimizing the weighted dissimilarity function [7].

Let $T_i(i = 1, 2, \ldots, n)$, which represents a m-dimensional vector (m is the number of categories of each dynamic test transformed into symbolic data). This notation is used to determine the cluster centers CC_{qr} for the q^{th} cluster and its r^{th} dimension by using the expression given below:

$$CC_{qr} = \frac{\sum_{i=1}^{n} U_{iqr}^{f} T_{ir}}{\sum_{i=1}^{n} U_{iqr}^{f}} \tag{3}$$

where C is the number of the cluster to be made $(2 \leq C \leq N)$, and f is an appropriate level of cluster fuzziness $f > 1$. U is the membership matrix, which has the size $n \times C \times m$ and is first initialized randomly such that $U_{iqr} \in [0, 1]$ and $\sum_{q=1}^{C} U_{iqr} = 1$ for each i and a fixed value of r.

Then, the Euclidean distance is evaluated between the i^{th} data point and the q^{th} cluster with respect to the r^{th} dimension with the equation below:

$$D_{iqr} = \left\|T_{ir} - CC_{qr}\right\| \tag{4}$$

In the following step, CC_{qr} is updated in Eq. (4) by recalculating the fuzzy membership matrix U according to D_{iqr}(if $D_{iqr} > 0$), as follows:

$$U_{iqr} = \frac{1}{\sum_{c=1}^{C} \left(\frac{D_{ir}}{D_{icr}}\right)^{f^2 - 1}} \tag{5}$$

This updating iteration is repeated until the changes in U are sufficiently small such that $(U \leq \varepsilon)$, where ε is a predefined termination criterion.

The main difference between hard clustering (k-means) and soft-clustering (FCM) relies on the fact that hard-clustering methods can only assign a given object to a unique cluster. Conversely, soft-clustering methods allow classifying a given

object as a part of different the clusters. This allows defining the so-called pertinence values. The higher these values are, more likely a given object is to be classified into a cluster. In this paper, the aforementioned procedure is coupled with symbolic data transformation within Matlab® software framework. In fact, fuzzy c-means procedures are built-in in the Fuzzy Toolbox. The Euclidian distance was used and the level of fuzziness was set to 2."

3 Results

It should be noted that the above-mentioned clustering methods were already applied to structural modal parameters (natural frequencies and mode shapes) obtaining very good results [1]. Thus, the main purpose of this paper is to explore the improvements/drawbacks of the proposed techniques when dealing with raw accelerations measurements directly.

Hence, the methodology follows two steps:

1. Evaluation of HOS for each accelerometer;
2. Use HOS (step 1) as inputs to the clustering techniques (k-means and c-means).

It is worth mentioning that these steps strongly depend on the quality of the input data. In other words, if measured data are poorly sampled, or have missing or even incorrect values, the results obtained by the proposed approach will be surely compromised.

In this paper, two sets of data were used for the validation of the proposed methodology. In both cases, it was previously known which data corresponded to the 'undamaged' and 'damaged' states. Therefore, the goal for both clustering algorithms is to allocate the 'undamaged' tests into one cluster and the 'damaged' tests into another. Thus, it would show that this technique is able to distinguish between two groups related to two different physical structural conditions.

3.1 Numerical Application – Simply Supported Beam

The first dataset corresponds to a numerical simulation of the vibration response of a 6-m simply supported steel beam. The beam is discretized into 200 finite elements using Matlab. A random force is applied at 0,69 m from the right support as shown in Fig. 1. The beam has the following physical and geometric properties:

- Elastic modulus – 210 GPa;
- Volumetric mass – 7850 kg/m^3;
- Cross-sectional area – $2{,}81 \times 10^{-3}$m^2;
- Moment of inertia – $2{,}81 \times 10^{-4}$m^4.

Dynamic measurements are taken at 10 equidistant points of the beam during 100 s. The sampling frequency is 0.01 Hz, which corresponds to 10.000 acceleration measurements per sensor. Damage is simulated as the reduction of the elastic modulus of the beam in three progressive states, yielding three damage levels:

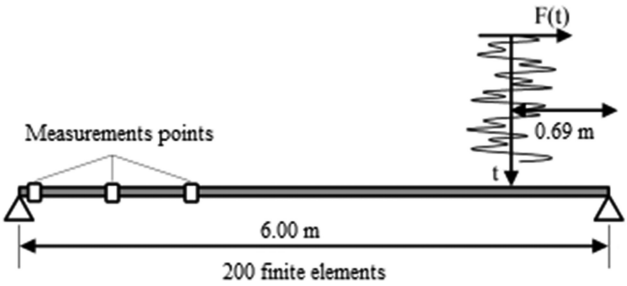

Fig. 1. Discretized beam.

- Undamaged (D0): unaffected beam;
- Level 1 (D1): reduction of 20% in the elastic modulus of elements 96–105;
- Level 2 (D2): same as level 1 + reduction of 10% in the elastic modulus of elements 146–155.

Additionally, three levels of white noise (0, 5 and 10%) are added to the data.

The main objective here is to separate two different damage levels at a time (D0 from D1 and D0 from D2) for each noise level. Each dataset of the numerical simulations contains measurements from 10 accelerometers and, for each accelerometer, 10 HOSs are calculated (as shown in Table 1). Thus, each dataset yields a 20×100 matrix (20 tests by 100 HOS). Tables 2 and 3 present the results obtained for the k-means method.

Table 2. Percentages of correctly classified data (levels D0 and D1, k-means).

	No noise		5% noise		10% noise	
	Sqeuclidian	Cityblock	Sqeuclidian	Cityblock	Sqeuclidian	Cityblock
D0	80%	80%	80%	80%	80%	80%
D1	70%	70%	70%	70%	70%	70%

Table 3. Percentages of correctly classified data (levels D0 and D2, k-means).

	No noise		5% noise		10% noise	
	Sqeuclidian	Cityblock	Sqeuclidian	Cityblock	Sqeuclidian	Cityblock
D0	80%	80%	80%	80%	80%	80%
D2	60%	60%	60%	60%	60%	60%

It is possible to notice that the proposed methodology is rather capable of distinguishing both damage levels, although the correct rates were lower for the second case. Tables 4 and 5 present the results obtained using the c-means technique.

From Tables 4 and 5 one notices that the c-means algorithm yields better results compared to the k-means method. Furthermore, it is important to remark that both

Table 4. Percentages of correctly classified data (levels D0 and D1, c-means).

	No noise		5% noise		10% noise	
	Sqeuclidian	Cityblock	Sqeuclidian	Cityblock	Sqeuclidian	Cityblock
D0	100%	100%	100%	100%	100%	100%
D1	70%	70%	70%	70%	70%	70%

Table 5. Percentages of correctly classified data (levels D0 and D2, c-means).

	No noise		5% noise		10% noise	
	Sqeuclidian	Cityblock	Sqeuclidian	Cityblock	Sqeuclidian	Cityblock
D0	90%	90%	90%	90%	90%	90%
D2	70%	70%	70%	70%	70%	70%

methods are completely insensitive to noise, since all rates remained unchanged throughout the simulations.

3.2 Experimental Application – TGV Viaduct

The second application comprehends the measurements taken in the PK 075 + 317 viaduct in Southeast France, between Paris and Lyon, over which passes high-speed rails for TGV (*Train à Grande Vitesse*) trains. The viaduct is 17.5 meters wide (Fig. 2).

Fig. 2. Side view of viaduct.

This bridge was built in the early eighties; the increase of the operating speed of TGVs has moved the excitation frequency of the trains close to the first natural frequency of the bridge. This risk of resonance was furthermore increased by the uncertainties in the mass of the ballast disposed on the bridge. The first natural frequency was 5.86 Hz and the excitation frequency was around 4.0 Hz. The French railways SNCF

Fig. 3. Tightening procedure.

considered that this difference was not enough and ballast recharging in connection with new operating speeds could reduce it even more. Therefore SNCF set up a system of rods near the bearings tightened by torque wrench (Fig. 3); this strengthening brought stiffness and increased the natural frequencies. In 2003, a strengthening intervention was scheduled and led to a change in natural frequencies.

In order to assess the efficiency of the tightening procedure, eight vertical accelerometers were installed under the bridge's deck, having the sampling frequency fixed at 4096 Hz. 28 dynamic tests were carried out i.e. 15 tests before and 13 after the procedure. Thereby, this dataset can be represented by a 28 $\times$ 80 matrix containing 10 HOS for each accelerometer.

Table 6 presents the results obtained by both clustering techniques. It is possible to observe that such approaches were not able to differentiate the two structural scenarios adequately. Therefore, it was necessary to enhance the analysis. This was achieved by performing a series of combinations of the HOS, two at a time, for each accelerometer. The goal was to find the best combination i.e. the one that yields the smallest within cluster sum of distances. This criterion was adopted, since it is believed to provide the most accurate classification. Results are shown in Table 7.

Table 6. Percentages of correctly classified data within cluster.

	k-Means		c-Means	
	Sqeuclidian	Cityblock	Sqeuclidian	Cityblock
Before	67%	67%	80%	80%
After	23%	23%	38%	38%

From Table 7, it is clear to observe a significant improvement in the classification rates. Moreover, for the c-means method using the cityblock metric, 100% of the tests were correctly classified into cluster "before".

Table 7. Percentages of correctly classified data within cluster.

	k-Means		c-Means	
	Sqeuclidian	Cityblock	Sqeuclidian	Cityblock
Before	79%	79%	100%	100%
After	85%	100%	85%	85%

4 Conclusions

This paper introduced a novel approach based on the coupling of High-Order Statistics with k-means and c-means clustering algorithms. The main goal was to discriminate different structural behaviors using only raw information for feature extraction.

In order to assess the efficiency of the proposed approach, two applications were studied: the cases of a FEM beam model and of a real-case railway viaduct. For the first case, different damage and noise levels were simulated. It was noticed that although the procedure was insensitive to noise, it was not properly capable of distinguishing and separating the structural states. For the experimental application, the same methodology was applied, yielding poor results. Thus, the combination of the HOS, 2 at a time, proved itself rather suitable for the TGV, since it made possible for the clustering algorithms to identify two different states in the dataset, as shown in Table 7. Moreover, the c-means presented a better performance compared to the k-means.

It is important to highlight the complexity of such an analysis, since it deals directly with raw data measurements. However, the authors are aware that results must be improved before using this methodology to untested structures.

Acknowledgements. The authors would like to thank UFJF (Universidade Federal de Juiz de Fora - Federal University of Juiz de Fora), CAPES (Coordenação de Aperfeiçoamento de Pessoal de Nível Superior), CNPq (Conselho Nacional de Desenvolvimento Científico e Tecnológico - "National Council of Technological and Scisentific Development") and FAPEMIG (Fundação de Amparo à Pesquisa do Estado de Minas Gerais) for the financial support.

References

1. Alves, V., Cury, A., Roitman, N., Magluta, C., Cremona, C.: Structural modification assessment using supervised learning methods applied to vibration data. Eng. Struct. **99**, 439–448 (2015)
2. Cury, A., Cremona, C.: Assignment of structural behaviors in long-term monitoring: application to a strengthened railway bridge. Struct. Health Monit. **11**, 422–441 (2012)
3. Cury, A., Cremona, C., Diday, E.: Application of symbolic data analysis for structural modification assessment. Eng. Struct. **32**(3), 762–775 (2010)
4. Santos, J.P., Cremona, C., Orcesi, A.D., Silveira, P.: Multivariate statistical analysis for early damage detection. Eng. Struct. **56**, 273–285 (2013)
5. Madhulatha, T.S.: An overview on clustering methods. IOSR J. Eng. **2**(4), 719–725 (2012)

6. Farrar, C., Worden, K.: Structural health monitoring: a machine learning perspective. Wiley, Chichester (2013)
7. Bezdek, J.C.: Pattern recognition with fuzzy objective function algorithms. Plenum, New York (1981)
8. Alves, V., Cury, A., Roitman, N., Magluta, C., Cremona, C.: Novelty detection for SHM using raw acceleration measurements. Struct. Control Health Monit. **22**, 1193–1207 (2015)

Virtual Laboratory for Leveraging Technology for Bridges and Constructed Systems

Emin Aktan[1], Ivan Bartoli[1], Franklin Moon[2], Marcello Balduccini[3], Kurt Sjoblom[1], Antonios Kontsos[4], Hoda Azari[5], Matteo Mazzotti[1], John Braley[2(✉)], Charles Young[1], Shi Ye[1], and Andrew Ellenberg[4]

[1] Civil, Architectural and Environmental Engineering Department, Drexel University, Philadelphia, PA, USA
[2] Civil and Environmental Engineering Department, Rutgers University, Piscataway, NJ, USA
jbbraley@gmail.com
[3] Computer Science Department, Drexel University, Philadelphia, PA, USA
[4] Mechanical Engineering and Mechanics Department, Philadelphia, PA, USA
[5] Federal Highway Administration, Mclean, VA, USA

Abstract. The writers are exploring the development of an innovative and adaptive resource for highway bridge owners, managers, engineers as well as technicians from non-destructive testing (NDT) and structural health monitoring (SHM) industries and the public. The primary objective is an official Federal Highway Administration (FHWA) website offering guidance and training on how technology tools may be selected and applied with sufficient depth to generate reliable and actionable information. Currently a large number of technology tools in the realm of "information, communication, computing and data technology," "software for modelling and analysis of multi-physics phenomena and civil engineering systems," "sensing, imaging and non-destructive probing," and, "uncertainty and risk analysis and decision-making" are available for off-the-shelf purchase or applications by consultants. However, there are very few institutions that offer an ability for an integrative leveraging of such tools and the resulting data in conjunction with engineering heuristics for meaningful, feasible and effective solutions to infrastructure performance problems.

Users will be exposed to the challenges of designing field experiments, integrating, visualizing and interpreting data, information, simulation results as well as heuristic knowledge for identifying and understanding the root causes of condition defects and deterioration as well as performance shortcomings. Explanations will feature both case studies and computational simulation tools that employ multi-physics software to generate more interactive and in-depth visualizations than possible with field data alone. How various probes may offer information regarding invisible defects and deterioration will be shown along with training exercises for aspiring NDT and SHM engineers.

Given that vibration analysis is a common approach to SHM, and that many NDT techniques leverage vibrations caused by different physics at multiple scales, this paper will focus especially on vibration analysis case studies that are being developed as content for the website.

Keywords: Virtual laboratory · Bridge assessment · Vibrations · Structural health monitoring · Non-destructive testing · Training

© Springer International Publishing AG 2018
J.P. Conte et al. (eds.), *Experimental Vibration Analysis for Civil Structures*,
Lecture Notes in Civil Engineering 5, https://doi.org/10.1007/978-3-319-67443-8_8

1 Introduction

There is a growing consensus on the need to make a transition to data driven objective decision making in the realm of managing highway infrastructures. Achieving this will require the use of sensing, simulation, and information technologies to obtain, visualize and interpret quantitative performance data. Furthermore, robust and effective leveraging of technology demands proper policy, best practice standards, and also presupposes a profession with the requisite education/training. Along with these prerequisites, there is also an opportunity for a "gathering place" to help develop a community of highway infrastructure researchers, practicing engineers and professionals in technology to exchange ideas and contribute to best practices.

Within this context, the FHWA Exploratory Advanced Research Program has sought the development of an interactive Virtual Nondestructive Evaluation Laboratory for Highway Structures with the following overarching goals:

- Permit users to explore various NDT and SHM technologies in a holistic manner - inclusive of fundamentals of field experiment design, data collection and archival logistics, data processing, visualization, and interpretation.
- Offer realistic NDT and SHM case studies that expose users to decision scenarios related to the design and deployment of various NDT and SHM applications following best practices.
- Provide a platform for the development of training and certification programs for the deployment of NDT and SHM technologies.

2 Background

The authors are particularly interested in how constructed systems such as bridges should be inspected and their condition and performance measured objectively by technology leveraging. Objective data will enable condition and load capacity evaluation, maintenance, repair, retrofit or renewal decisions and designs to be integrated in the context of asset management. However, decision making by objective data from technology leveraging can be challenging and requires a systems approach and integration of more than one technology domain (for instance knowledge in bridge behavior, NDT, field testing using sensing and imaging, information technology, modelling and simulation, decision theory, organizational and consultant qualifications).

From the authors' perspective, the following items are offered as a set of prerequisites needed for comprehensive applications of technology:

(a) **Bridge heuristics** – i.e. observation-based understanding of how bridges are loaded, behave, carry their loads, and how various elements of a bridge work as a system. It takes a solid engineering education followed by many years of apprenticeship in design and field inspections to accumulate reliable heuristics. In the last several decades the community has lost many engineers whose heuristic knowledge was not captured and archived by proper applications of knowledge engineering.

(b) **Experimental arts, information technology, and logistics** – To deploy technology, inspectors must have the physical and engineering skills required for climbing a bridge safely, and the ability to install sensors and cameras for capturing critical responses over various time scales to understand the operational responses and live load environment. Current developments with wireless sensing and imaging appear likely to offer reliable measurements of loads and responses over days and even years within the near future.

Progress in Digital Image Processing (DIP) in mapping deterioration and cracks invisible to naked eye and attempts to integrate such advances in robotic platforms (unmanned aerial systems) will affect bridge assessment in the near future. Similarly, inspectors will have increasing access to portable technology (google glass or other advanced tools) and be able to share in real time information on the deterioration and defects they are observing to discuss possible causes and implications with an experienced engineer with heuristics.

The prerequisites to perform the next generation of bridge inspections include a grounding in experimental arts in the laboratory, and an ability to collect measurement data from the correct members and locations. Ideally, inspectors should be engineers, likely with an advanced degree. However, since it will be hard to have such qualifications for each bridge inspector, it would be desirable to take advantage of bridge "type-specific" inspections once every five years, unless warranted by the importance, design and construction details of a structure. Type-specific inspections would be designed and executed after collecting information on bridges that carry their loads by similar structural systems and mechanisms, such as "simply-supported" or "continuous multi-span" or "integral-abutment" RC deck on steel-girders.

(c) **Modeling and Simulation** – Current bridge engineering applications are not always grounded in a correct understanding of how structures should be modeled, and how these models may be calibrated by a number of images and strategically measured responses from the field. However, it is expected that every bridge engineer in the near future will be able to perform 3D FE modeling and analysis, which is essential for design of sensing, and interpretation of measured responses. Software for quick and complete 3D geometry capturing of actual as-built bridge geometry (LIDAR, Photogrammetry, etc.) is also becoming widely available, and this should make having a virtual twin of every bridge possible even today.

(d) **Decision Theory** – Decision theory includes reliability, uncertainty and risk analysis as well as optimization and decision-making under uncertainty. Engineering design skills are critical and necessary in addition to decision theory for making sound and prudent decisions involving economics and public safety.

(e) **Business Case, Organizational and Consultant Qualification** – Organizational leadership and culture are especially critical if the community wishes to transition from the current empirical approaches to one that properly leverages heuristics and relies on objective measurements for bridge management. Currently there are signature bridges that cost billions of dollars and with many performance concerns that are not leveraging technology, while other structures are monitored without a valid business case, and without any value to the bridge owner.

The principal objective of the Virtual Laboratory is therefore to facilitate technology leveraging by proper integration of the domains discussed above and by providing scenarios including a business case. The integration may be carried out by considering the framework represented in Fig. 1.

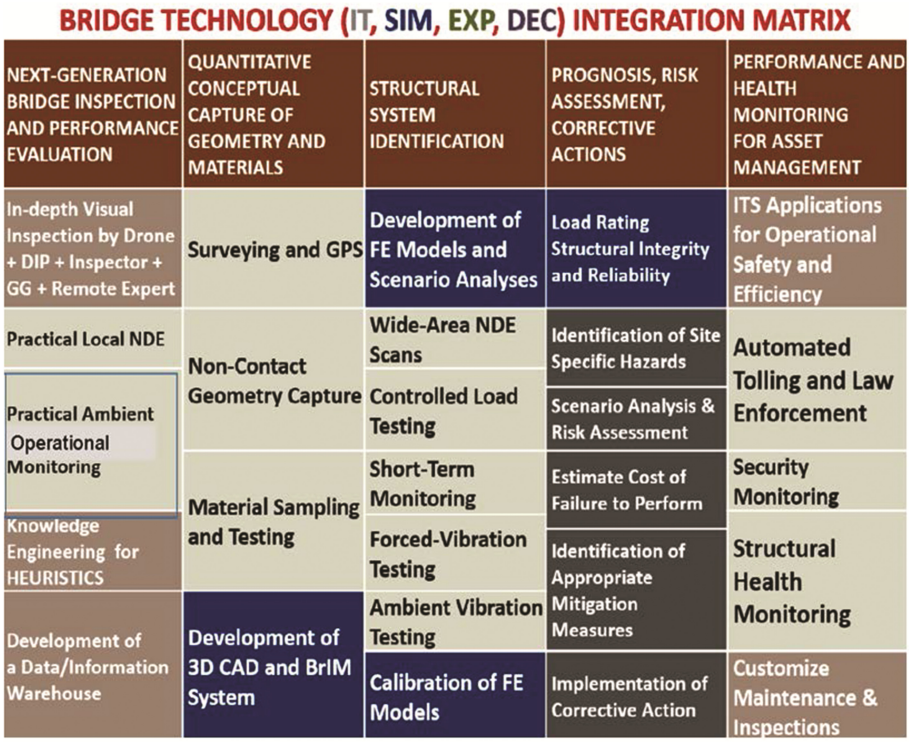

Fig. 1. Integration of technology to support the decision making process for highways structures preservation (this figure outlines the proposed framework in a chronological order (from left to right))

The primary fields of the framework (Table columns) are:

1. **Objective + Heuristic inspection and evaluation of condition and performance** of a bridge. Clear understanding of operational loads and responses, in addition to boundary conditions and continuity between spans, superstructure and substructures. If warranted, foundation diagnostics should be included.
2. Objective and Quantitative Capturing of **Geometry and Material Properties**.
3. Structural-Foundation-Soil Modeling and **System Identification (i.e. model validation and calibration)** by leveraging measured data from operational monitoring, NDT and controlled testing.
4. Prognosis, Condition, Capacity and **Risk Assessment and Design of Corrective Actions**.

5. **Performance and Health Monitoring** – including Operational, Serviceability, Durability, Security, Safety and Resilience Monitoring.

Each application may require some or all of the steps illustrated in Fig. 1, depending on the business case. If a Department of Transportation (DOT) is interested in a bridge type-specific study on a sample of a large population of bridges, each and every step may be justified. A one-time application to a one-of-a-kind bridge may not require many of the steps. A major toll crossing may justify the investment into the application of the entire set of steps in Fig. 1.

The writers have explored the challenges and advantages of technology leveraging by applications to both long-span signature crossings as well as bridge type-specific applications [1–7], and aim to design and construct the proposed virtual laboratory based on these experiences.

3 Virtual Laboratory for Leveraging Bridge Assessment Technology

A mock-up of the envisioned gateway to the Virtual Laboratory website is shown in Fig. 2. To provide some structure the website is organized into three areas that represent the different users and their distinct ways of interacting with the website. First, decision-makers would enter the website through the "decision scenarios" pathway that would present realistic scenarios (inclusive of goals, constraints, etc.) to illustrate the potential trade-offs and strategies that can be employed when contemplating a technology deployment. Second, the technical details associated with the four primary categories of Non Destructive Evaluation (NDE) approaches and their integration is provided. This will include general descriptions of various methods within each category with references to the NDE Web Manual (see fhwaapps.fhwa.dot.gov/ndep/) [8], interactive lab experiments, and interactive field applications. Third, the "Simulation and Sensor Lab" pathway will provide technical details for the various tools and methods as a reference for all users.

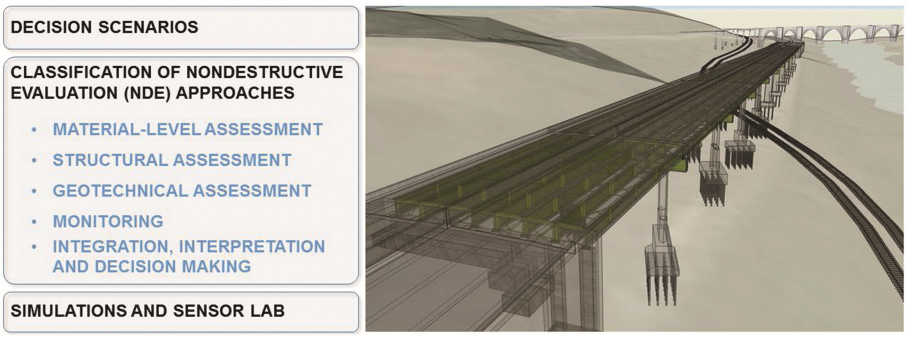

Fig. 2. Mock-up portal of the Virtual Laboratory

Case studies with applications of SHM and NDE will be included in the Virtual Laboratory. An example is provided here showing the Operational Monitoring Application to a Reinforced Concrete (RC) Deck-on-Steel Girders Viaduct.

3.1 Decision Scenario: Operational Monitoring Application to a RC Deck-on-Steel Girders Viaduct

The viaduct carrying I-76 approaching Philadelphia (Fig. 3) was first constructed in 1952, and the superstructure was replaced in 1986. The structure has 11 spans running alongside the banks of the Schuylkill River, carrying two lanes of traffic in each direction. The viaduct is congested during daytime, and it has been reported to carry about ~100,000 vehicles per day with ~4% being trucks. The DOT has been exploring whether it is possible to reconfigure the lanes and shoulders to fit 6 traffic lanes during rush hour. Meanwhile, there have been many calls from motorists reporting unusual levels of vibration on the viaduct. The District Bridge Engineer has been concerned about the performance of the viaduct and when the opportunity arose, requested the research team to evaluate the structure.

Fig. 3. Operational monitoring application to a RC deck-on-steel girders viaduct

3.2 Structural System

The Viaduct was designed to leverage existing piers (from a previous bridge) which were supported on piles except for some directly supported by pre-existing masonry structures underneath. Pier heights were adjusted by pouring extensions where needed, and rectangular closed steel box cross-girders were placed on piers to serve as pier-caps. Each traffic direction is carried by 4 built-up steel girders that are supported on the cross-girders as shown in Fig. 4, while the two directions of the bridges feature separate RC composite decks that are NOT laterally connected. The girders are continuous over every

other pier but are simply supported at the other piers, creating a sequence of two span continuous sections (Fig. 4).

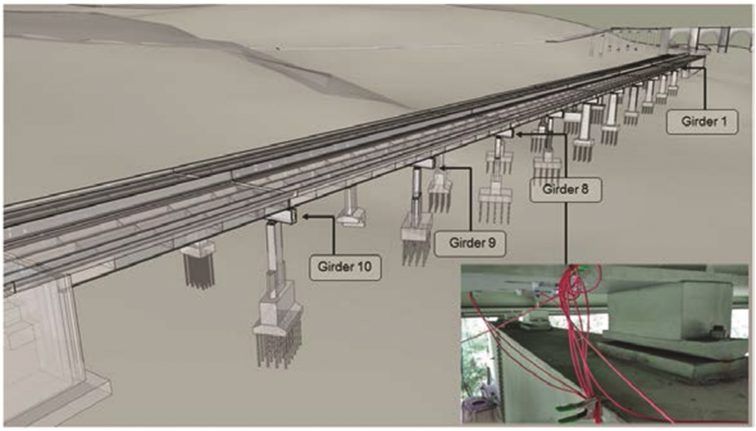

Fig. 4. RC Deck-on-steel girders viaduct geometry

3.3 Structural Assessment

Given the difficulty of accessing the driving lanes of the viaduct which could not be closed to traffic during the day, researchers decided on monitoring the operational responses of the superstructure, cross-girders and piers to identify the spans with the largest vibration. This study indicated that the superstructure elements (deck and girders), the cross-girders and the piers all exhibited varying levels and nature of vibration. The largest vertical vibrations at the cross-girder and superstructure were measured under Spans 7 and 8 exceeding 0.1 g at the cross-girder and about 0.3 g under the

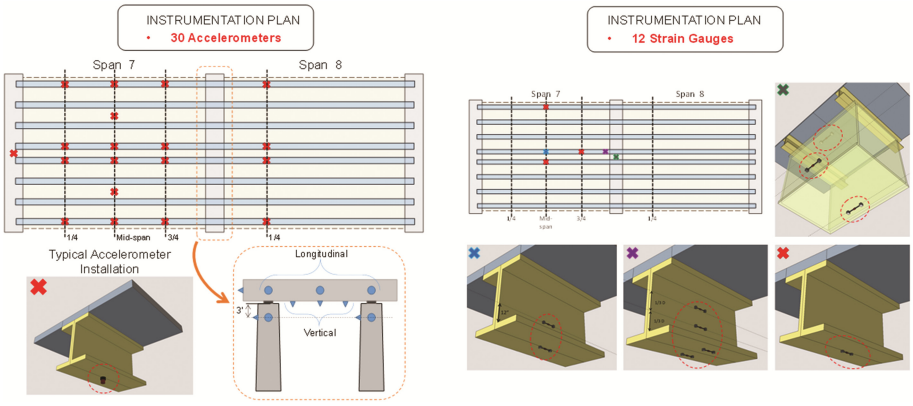

Fig. 5. Viaduct vibration study instrumentation plan consisting of dense array of accelerometers and strain gages

superstructure. Therefore, a longer duration of monitoring with a dense array of 30 accelerometers under Spans 7 and 8 as well as 12 Vibrating-wire strain gages was undertaken. The instrumentation plan is shown in Fig. 5.

A finite element (FE) model of the bridge was constructed to assist in the design of the sensing system. Locations of maximum acceleration for the structure's natural modes of vibration were determined by running a linear dynamic solver on the model. The sensor layout was designed based on these locations so that the major modes of vibration could be uniquely captured. This resulted in a dense sensor layout on one of the instrumented spans. A power line running beneath the other span restricted access to much of the span, and thus a sparse sensor layout was employed.

Several sensors were also installed on the piers and box cross girder to investigate any relationship between the substructure and superstructure motion (Fig. 5).

Acceleration data was sampled at 200 Hz which allows for identification of modes of vibration as high as 100 Hz. The acceleration data was analyzed using Fourier transformation methods to extract information about the acceleration at specific frequencies. Several modes of vibration were found at frequencies below 5 Hz.

Figure 6(a) shows the power of each frequency. The peaks in the plots are poles where a mode of vibration is located, and for this structure, a natural frequency. In some instances, poles are at very similar frequencies and the separate peaks cannot be easily distinguished. This is due to the geometry of the structure (high degree of symmetry) and the fact that there are essentially two identical bridges adjacent to one another. The main modes identified consisted of bending and torsional modes. For these modes, the mid-span degrees of freedom are experiencing the greatest acceleration.

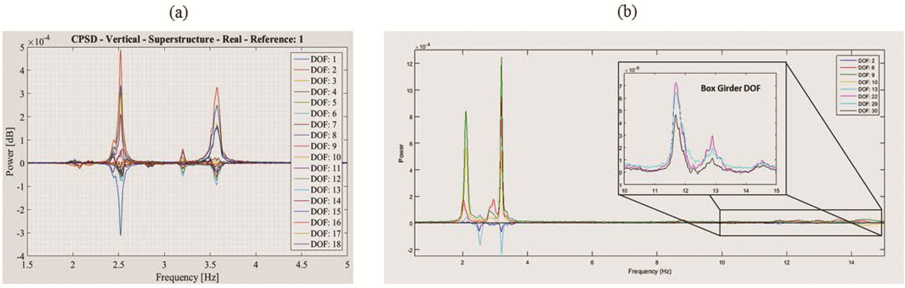

Fig. 6. (a) Cross power spectral density of superstructure degree of freedoms (DOFs); (b) CPSD of box girder DOF and select superstructure DOF

The vibration of the box cross girder shown in Fig. 6(b), which is of principle concern due to its fracture critical designation, experiences several modes of vibration between 10 and 15 Hz. However, the magnitude of vibration is much less than that experienced by the superstructure, and the box girder participates very little at the superstructure modes of vibration.

A total of 12 strain gauges were installed and data recorded for more than 24 h. Gauges were sampled at 50 Hz which allowed us to characterize the dynamic strain that the structure experiences under operational conditions.

Strain gauges located at the center of the span frequently recorded strain levels in excess of 100 microstrain (~3 ksi) throughout the 24 h recording session, even during the middle of the night. Occasional responses as high as 200 microstrain (~6 ksi) were recorded in the bottom flange of longitudinal girders at mid-span. In comparison, the expected strain from an AASHTO HL-93 truck (with lane load) is 150 microstrain (~4.5 ksi), based upon finite element modeling and analysis of the structure.

The maximum response recorded on the box cross girder was −92 microstrain (~2.7 ksi) on the top and 92 microstrain (~2.7 ksi) on the bottom. While no gauges were installed on the concrete deck, in two locations multiple gauges were installed at varying heights on the girder cross section, allowing the strain profile to be captured to extrapolate the deck strains assuming composite behavior. It was found that the deck in the positive moment region may be frequently experiencing tension as high as 100 microstrain which would correspond to a stress in excess of 300 psi. This level of frequent and cyclical stress in concrete could potentially cause cracking. These cracks would allow faster chloride ion intrusion, hastening corrosion of the reinforcement.

The strain data was further analyzed by applying a low pass filter to remove the response associated with frequencies above 1.5 Hz, thus permitting the dynamic response of the bridge to be removed from the data and only the static response of the bridge to be estimated. The plot of both the full response and the static (filtered) response is provided in Fig. 7. The portion of strain due to the dynamic response of this structure is significant. Figure 7 time history was recorded during a large event. The static response accounts for over 100 microstrain, but the vibration of the structure causes the total response to exceed 200 microstrain. For this event, an amplification of the static response by approximately 75% is observed. In comparison, the amplification applied for bridge design is, at most, 33%. This level of amplification is on the upper end of what researchers

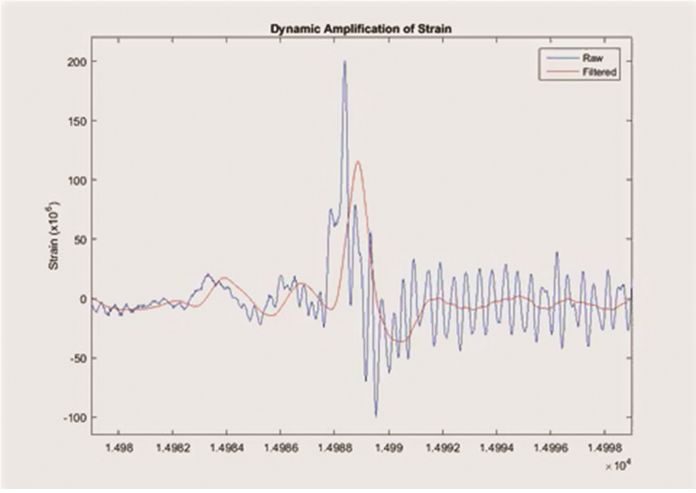

Fig. 7. Dynamic amplification of strain

and transportation organizations have measured. However, the fact that the high amplification occurs regularly and even with large events, makes the nature of this bridge's response quite novel.

4 Discussion

The relatively high magnitude of vibration experienced by this structure is likely due to a number of factors. The long span length and continuity create a flexible bridge that can be excited for a longer period of time by the vehicles crossing it. The dynamic characteristics of the structure may also be playing a role, where the loading frequency applied by the traffic is close to some of the bridge's natural modes of vibration. Furthermore, the viaduct spans leading up to the monitored spans may be experiencing an amplifying vehicle-bridge interaction, effectively conditioning the frequency of the vehicle loading to be in tune with the structure.

The high levels of vibration are not considered a safety concern unless they impact drivers. The operational strains, while larger than predicted and greatly magnified by dynamic effects, are still well below stress and fatigue limit states. However, even though the bridge has sufficient capacity, the long term durability of the structure is questionable. The tensile stresses in the concrete deck at mid-span are close to the tensile capacity of the material, and thus may be causing cracking, accelerating corrosion and degradation.

Visual inspection of the viaduct was performed in May 2017 and researchers performed NDE scans to check the deck for cracks and possible delamination during the inspections. The NDE results will be presented in the Virtual Laboratory as a case study.

4.1 Material Level Assessment

In the presentation of NDE methods and results obtained from field applications as discussed in the previous section, the Virtual Lab will often refer to the FHWA NDE Web Manual (see fhwaapps.fhwa.dot.gov/ndep/) that provides a powerful way to select NDE technology based on type of material, structure element and target of investigation as well as a description of the different NDE techniques [8].

The NDE portion of the virtual lab will give the users a progressive exposure to the concepts and physics behind each relevant NDE method using Multiphysics simulations, experiments executed in the laboratory and NDE data collected in the field. An additional component of the lab will also look into strategies to perform NDE data integration/fusion (meaning the fusion of data coming from different NDE methods), to facilitate asset management strategies and asset owners decision making.

Simulations of NDE applications often require the solution of complex sets of differential equations with numerical techniques such as Finite Element Method (FEM), Finite Difference method (FDM) and others. Any simulation that will appear on the Virtual Laboratory will be validated with ad hoc experimental testing following strategies similar to the ones used in structural identification.

As an example, finite element method simulations have been used to demonstrate the effect of heat transfer in bridge structural elements such as bridge decks to observe the presence of damage (i.e. delaminations). For instance, to introduce the concept of heat transfer and infrared (IR) thermography to Virtual Laboratory users, the heat transfer is predicted using Abaqus on a 20 cm thick square concrete specimen (60×60 cm^2) including delaminations simulated by 3 mm thick foam inserts (15×15 cm^2 in plan dimensions) subject to controlled heat radiation (similar to sun radiation). Figure 8 shows the reinforced concrete block with the 3 foam delaminations depicted (Fig. 8a).

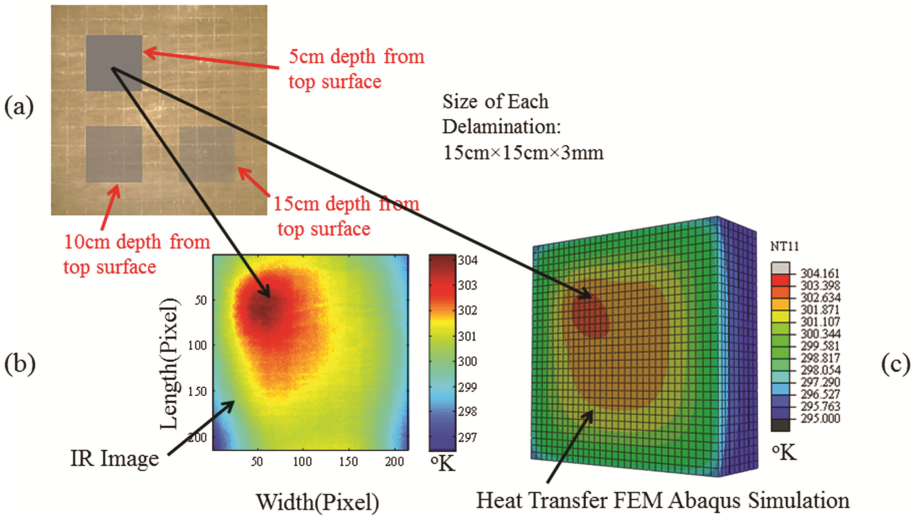

Fig. 8. NDE Simulations: IR and Heat Transfer (FEM simulation example and experimental validation)

After 2 h of heating provided by a set of heat lamps, only the shallow delamination is visible in both the validation experiment, where heat maps are extracted using a FLIR SC325 infrared camera (Fig. 8b) and in the Abaqus FEM simulation (Fig. 8c). The effect of the shallow delamination (5cm deep) is a small increase of the surface temperature above the foam inclusion (that slows the heat transfer process occurring inside the block). From this experiment and simulation, the Virtual Laboratory user can: (1) begin to understand the difficulty to observe deep delaminations within such a specimen using IR, (2) appreciate the delay between the initiation of the heating process when the lamps are turned on (or when the sun begins irradiating the surface of the bridge deck), and the appearance of temperature gradients on the deck surface, and (3) comprehend the 3D nature of the heat transfer process.

Another NDE approach that is commonly considered to unveil delaminations in bridge decks is the impact echo (IE) method. In this approach, a small impactor generates high frequency vibration in the concrete material (few tens of kHz). The stress waves induced are a combination of surface waves, P waves and S waves traveling within the

material [8]. A sensor placed in the impact position is used to record the local displacement or acceleration. The presence of delaminations significantly alter such responses since the principle resonance observed, caused by the repeating reflection of the P (longitudinal wave), and observed in the frequency domain, changes. In fact, due to the mismatch in impedances at the delamination locations, the wave scatters when it reaches the delamination and the P wave path increases, increasing the round trip of the P wave (and decreasing its resonance frequency). Also, a P wave reflected by the delamination (with a short round trip time) causes a higher frequency peak to appear in the frequency domain. Furthermore, for large delaminations, a plate mode (where the plate is the region of concrete between the delamination and the surface) is excited, and appears in the frequency domain as low frequency resonance.

These phenomena are the core of the IE method and while it is well accepted by the industry and researchers, the Virtual Laboratory will attempt to introduce it to DOT personnel. To achieve this goal, simulations such as the one shown in Fig. 9 will be leveraged to explain the physics behind the approach and gradually introduce the users to approach. Specifically in Fig. 9 the response of a displacement sensor during an IE test is simulated together with the stress distribution created by the IE wave travelling within the thickness of a concrete slab that has a 10 cm delamination at 5 cm from the deck surface.

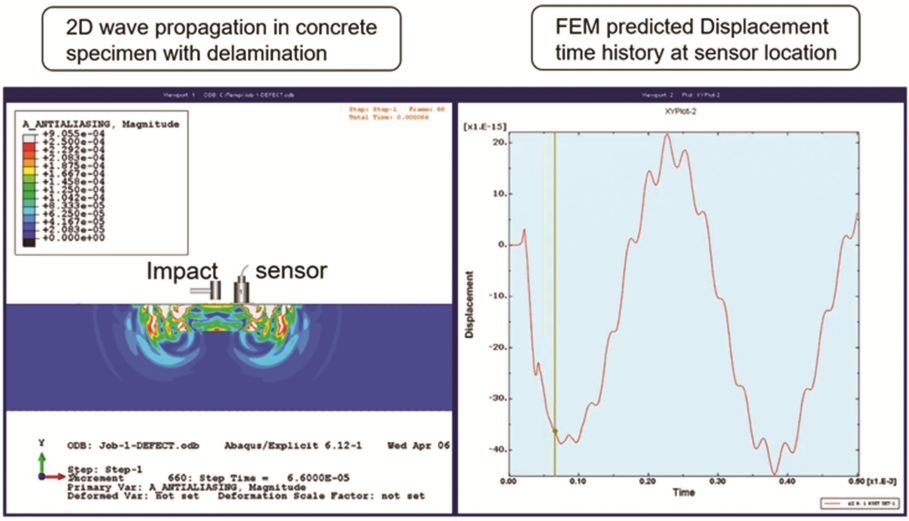

Fig. 9. FEM simulation showing the response of a displacement sensor during an IE test (right plot) and acceleration amplitude induced by the IE wave travelling within the thickness of a concrete slab that has a 10 cm delamination at 5 cm from the deck surface

A large number of simulations such as the one shown here, will allow the users to comprehend the IE approach, get familiar with common signals recorded during a test, visualize the effect of geometry, size and location of the delaminations, and appreciate the effects of different probes and their location.

Simulations will be only a portion of the Material Level assessment NDE Virtual laboratory and will be extended to a number of methods such as the ground penetrating radar [8] and other NDE techniques. For each NDE method, after an introduction to simulated ideal NDE scenarios created using FEM tools, the user will be exposed to experiments of progressively increased difficulty in the laboratory. In the laboratory, specimens of known characteristics with defects of known properties will be used and actual NDE signals will be recorded. Finally, Virtual Laboratory users will be exposed to NDE data collected in the field, where the presence of operational variability and environmental factors can make the application of any NDE technique increasingly complicated and reduce its effectiveness.

5 Conclusions

This paper discusses the development of a Virtual Laboratory to expose its users to the application of NDE and SHM into asset management of highway bridges. If successful, the resulting Virtual Laboratory website will serve infrastructure stakeholders such as highway asset owners, DOTs, industry users and researchers.

A "decision scenarios" pathway will present realistic scenarios (inclusive of goals, constraints, etc.) to illustrate the potential trade-offs and strategies that can be employed when contemplating a technology deployment in highway bridges. Second, the technical details associated with four primary categories of NDE approaches (material, structural and geotechnical assessments as well as monitoring strategies) will be provided in the Virtual Laboratory. This will include general descriptions of various methods within each category, interactive lab experiments, and interactive field applications. Finally, the "Simulation and Sensor Lab" pathway will provide technical details for the various tools and methods as a reference for all users.

In this paper an introduction to the Virtual Laboratory concept is provided, by first showing an example of decision scenario where a DOT may leverage technology to assess vibrations on a viaduct, presenting the results from the vibration monitoring of the structure and finally introducing selected NDE approaches that could assess the consequences of deterioration as well as performance deficiencies in bridges.

The virtual lab will provide an environment to train and educate the direct users of NDE technologies (technicians, engineers, etc.) as well as guide the decision-makers that will integrate technology deployments within their management practices (to better meet agency goals). In addition to these distinct, but related, educational objectives, the Virtual Lab could offer the base to develop universal certification programs to enhance QC related to technology applications.

Acknowledgments. This project is supported by the Federal Highway Administration Exploratory Advanced Research Program (Cooperative Agreement DTFH6115H00007). The opinions expressed in this paper are those of the authors and do not necessarily reflect the opinions of the sponsors. Writers are grateful to Drs. Azari, Director of the NDE Lab, Mr. Kuehn, Director of EARP, and other former and present FHWA and State DOT engineers and academics providing guidance, overview, insight and content.

References

1. Aktan, A.E., Catbas, F.N., Grimmelsman, K.A., Pervizpour, M.: Development of a model health monitoring guide for major bridges. Report submitted to Federal Highway Administration Research and Development for Contract DTFH61-01-P-00347, Drexel Intelligent Infrastructure and Transportation Safety Institute, Drexel University, Philadelphia (2002)
2. Aktan, A.E., Faust, D.: A holistic integrated systems approach to assure the mobility, efficiency, safety and integrity of highway transportation. In: 1st International Conference on Structural Health Monitoring and Intelligent Infrastructure, Tokyo, Japan (2003)
3. Catbas, F.N., Ciloglu, S.K., Aktan, A.E.: Strategies for load rating of infrastructure populations: a case study on T-beam bridges. Struct. Infrastruct. Eng. **1**(3), 221–238 (2005)
4. Catbas, F.N., Ciloglu, S.K., Hasancebi, O., Grimmelsman, K., Aktan, A.E.: Limitations in structural identification of large constructed structures. J. Struct. Eng. **133**(8), 1051–1066 (2007)
5. Catbas, F.N., Aktan, A.E.: Development of a monitoring system for a long-span cantilever truss bridge. In: Encyclopedia of Structural Health Monitoring (2009)
6. Glisic, B., Yarnold, M.T., Moon, F.L., Aktan, A.E.: Advanced visualization and accessibility to heterogeneous monitoring data. Comput. Aided Civ. Infrastruct. Eng. **29**(5), 382–398 (2014)
7. Yarnold, M.T., Moon, F.L., Aktan, A.E.: Temperature-based structural identification of long-span bridges. J. Struct. Eng. **141**(11), 04015027 (2015)
8. Gucunski, N.: Nondestructive testing to identify concrete bridge deck deterioration. Report S2-R06A-RR-1, Transportation Research Board (2013)

Radio-Frequency Identification Triggering System for Structural Health Monitoring of Highway Bridges

Johnn Judd[1(✉)], Richard Schmidt[1], McKenzie Danforth[2], James Branscomb[3], and Michael Jung[4]

[1] University of Wyoming, Laramie, WY, USA
jjudd5@uwyo.edu
[2] Martin/Martin, Inc., Lakewood, CO, USA
[3] Wyoming Department of Transportation, Cheyenne, WY, USA
[4] Felsburg Holt & Ullevig, Centennial, CO, USA

Abstract. One challenge with structural health monitoring (SHM) for highway bridges is managing large amounts of response data. This paper discusses a proposed SHM system that was developed to collect, store, and prioritize excitation data caused by traffic loads, especially overweight trucks. In the proposed system, a microcontroller is used to trigger the release of data. A radio-frequency identification (RFID) reader and antenna combinations are installed on the truck and at the bridge of interest. The truck information, including axle weights and configuration, is assigned to the RFID tag and placed on the windshield. The transponder at the bridge detects the approaching RFID tag and triggers the data acquisition system to release the response (strain) data from a sensor interrogator through a microcontroller to a network portal (such as a cellular modem or Ethernet radio) while the truck passes over the bridge. Field tests were conducted to validate the proposed system. The optimal position of the vehicle relative to the transponder, the height and horizontal position of the transponder, and the location of the RFID tag were investigated for a vehicle travelling at 105 kph (65 mph). The tests results indicated that the triggering system was successful, but it was sensitive to the position of the tag relative to the transponder.

Keywords: New technologies · Structural health monitoring · Bridges · Traffic excitation · Radio-frequency identification

1 Introduction

Structural health monitoring (SHM) of highway bridges has several purposes. SHM can be used to detect and evaluate the extent of structural damage, estimate the remaining service life of an existing structure in use, assist in making decisions related to maintenance, among other applications [1]. For highway bridges, SHM can also be used to evaluate bridge load ratings [2], to assess the impact of overweight vehicles, and to determine appropriate routing for overweight vehicles [3]. However, there are several challenges with the application of a SHM system on highway bridges. One challenge is

© Springer International Publishing AG 2018
J.P. Conte et al. (eds.), *Experimental Vibration Analysis for Civil Structures*,
Lecture Notes in Civil Engineering 5, https://doi.org/10.1007/978-3-319-67443-8_9

that SHM systems on highway bridges may be exposed to harsh environmental conditions. Another challenge is that a continuous SHM system is capable of producing large amounts of response data.

A fiber optic sensor SHM system for highway bridges was developed to overcome these challenges. Techniques for installation and protection of fiber optic sensors on concrete and steel host structures were developed [2, 4], and instrumentation and a fiber optic interrogator for the SHM system were established [3]. The objective of the study reported in this paper was to develop and validate a radio-frequency identification (RFID) triggering system for managing response data from the fiber optic sensors. The triggering system is a critical component of the SHM system because the continuous data can become unmanageable and may not be feasibly passed through a cellular modem.

2 Concept

The RFID system operates by transferring information using radio-frequency electromagnetic fields and a transponder to wirelessly transmit data to and from RFID tags. The concept is to install RFID reader and antenna combinations, or transponders, at a port of entry weigh station and at a bridge of interest. At the port of entry, the permitted truck information, including the axle weights and configuration, is assigned to an RFID tag with an identification code. The tag is then placed on the windshield of the vehicle. At the bridge, a second transponder detects the presence of the RFID tag when the vehicle is within range and triggers the data acquisition system to store the bridge response (strain) data while the permitted vehicle passes over the bridge. Finally, the strain data is transmitted through the cellular network to a database. The RFID identification number assigned to the permitted vehicle at the weigh station (with the axle loads and configuration) is used to correlate the vehicle with the strain data.

2.1 Port of Entry

The first transponder is located at a port of entry (Fig. 1). All permitted vehicles are required to stop at the ports of entry when crossing over a state line to assure that they remain in compliance with their specified axle loads and gross vehicle weight requirements. In the proposed concept, when a permitted vehicle is weighed, it is assigned a tag encoded with a vehicle identification number. At the weigh station, the axle weights, gross vehicle weight, and axle configuration are determined. The information is then logged into a database and associated with its assigned vehicle identification number. This enables a transponder to read the data from the tag at a subsequent point in time. The vehicle traverses the highway with the tag inside the vehicle.

Photo of typical truck scale (weigh in motion system (www.mt.com)

Photo of typical RFID tag (www.engadget.com)

Fig. 1. Instrumentation scheme at Port of Entry (adapted from [5]).

2.2 Bridge

The second transponder is located at a bridge with the SHM system (Fig. 2). When a tagged vehicle approaches the bridge and the tag is within range of the transponder, the transponder will send a signal to the data acquisition unit on the bridge to activate the data storage. The transponder will read the vehicle identification number written on the tag and send its information and the bridge's response to a database.

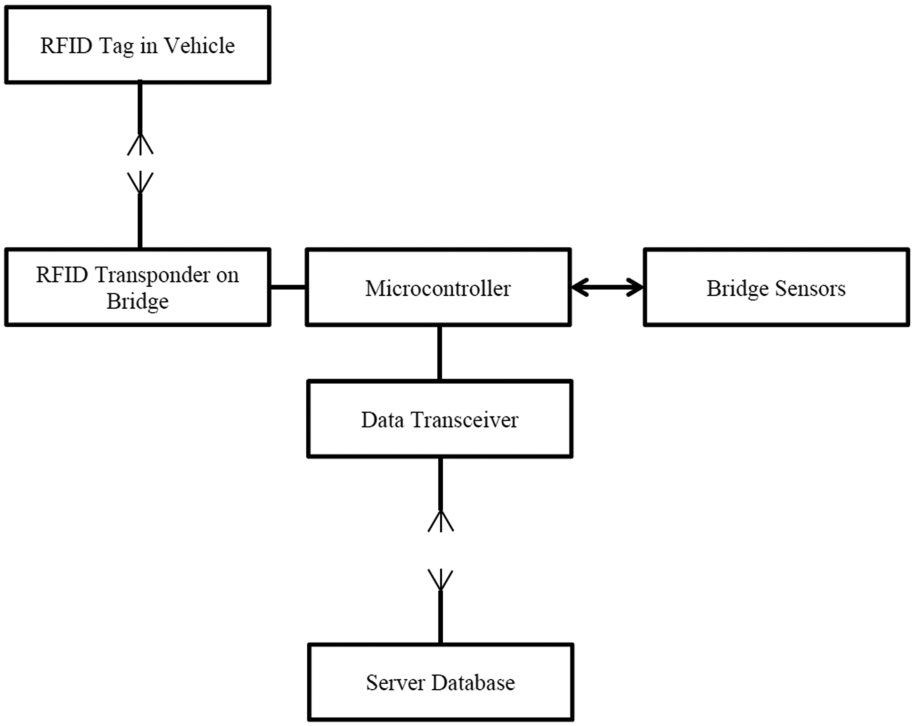

Fig. 2. Instrumentation scheme at Bridge [5].

2.3 Instrumentation

Hardware for interrogation and instrumentation of the SHM system was developed using a commercially available fiber optic network interrogator and a custom designed microcontroller unit. A two-channel SmartScan 02 Lite FBG interrogator produced by Smart Fibres was purchased to collect data from the sensors. The interrogator type was selected based on a study of commercially available fiber optic network interrogators. Compared to a custom-developed interrogator, commercially-developed interrogators provided lower cost, more compact form-factor, and were more energy-efficient, which is important for application of the concept in remote locations. A microcontroller unit was custom-designed to convert serial peripheral interface (SPI) signals back to the Ethernet so that strain data can be directed through a cellular network. The microcontroller consists of a printed circuit board containing two Ethernet controllers, a microcontroller, a PDI programming port, voltage supply and regulator, LED indicators, and general purpose input/output pins included for future programming. A detailed description and images of the printed circuit board are provided in the associated report [5].

The RFID triggering system consists of three primary components: an RFID reader, antenna, and tags. The CS203ETHER Integrated RFID reader was used to read and write information to the tags and to transmit data. It was designed to withstand extreme

weather conditions, including water and dust, with a high read rate. The RFID antenna communicates with the tags using radio frequency signals. The antenna has a range of approximately 9 m (30-ft). The range may be extended by using an additional IP67 antenna. The reader and antenna together are referred to as the "transponder," because the two components are physically enclosed in one unit that can be powered through an Ethernet connection. In this study, the unit was $0.3 \times 0.3 \times 0.08$ m (1 ft by 1 ft by 3 in.). The CS6710 Windshield RFID tags are each assigned a unique identification number, and store data transmitted from one transponder that can be read by another transponder at a different location. The tags are designed to be coupled with the CS203 integrated reader and placed on the inside of vehicle windshields. The tags are passive: they do not require batteries in order to communicate with the reader and antenna. The tag is approximately 6.4×11.5 cm (2.5 in. tall by 4.5 in. wide).

3 Validation

Field tests for the triggering mechanism validated the performance of the RFID system components. The validation procedure was considered successful when the RFID transponder recognized the presence of the RFID tag in an approaching vehicle, recorded the tag identification number, and triggered the storage of SHM strain data for a predetermined amount of time. This procedure was designed to test the system for a possible deployment project, so the focus was to demonstrate the capabilities of the triggering mechanism to provide a basis for future work.

Two operational modes were developed for the system: software and hardware. The software mode required use of a laptop computer that commands the microcontroller to store strain sensor data. This mode was utilized for field tests. Having a laptop in the field is not ideal, because it cannot handle extreme weather conditions, requires additional space in a weatherproof enclosure, and calls for an increase in power supply. The hardware mode was developed to prevent this scenario, and if the hardware mode is used, the laptop is not needed in the field. The hardware mode was under development at the time of testing; therefore, the software mode was used for field tests. However, the hardware mode has since been systematically validated, and it will be functional for field tests in the future.

3.1 Test Configuration

The field tests were performed on a rural highway (Highway 17, "Roger Canyon Road") north of the University of Wyoming (about a 2.5-hour drive north of Denver). The equipment was powered by means of a vehicle using a power convertor. The highway has two lanes that are each 3.4 m (11-ft) wide, which is slightly more narrow than a typical interstate lane width (3.7 m). The distance from the edge of the lane to the transponder was 1.8 m, and the distance from the ground to the bottom of the transponder was 1.8 m. The transponder was on the south side of the highway facing west. The RFID tag that was placed in the vehicle was 1.5 m above the ground.

The tests were organized so that the initial positioning of each RFID component was established prior to testing the system at full speed, including the position and direction of the RFID transponder, RFID vehicle, and RFID tag. For all tests, the vehicle was driven in the east direction toward the transponder. Each time the transponder detected the tag, the SHM strain data from three sensors were recorded for the allotted 30-second time frame.

3.2 Direction of RFID Transponder

The tag was placed in the upper left-hand corner of the windshield, and the vehicle travelled at 105 kph (65 mph). The horizontal direction most effective for detecting the tag was investigated for three arrangements (Fig. 3). First, the transponder was faced parallel to the oncoming vehicle. This method was successful when the vehicle travelled in the closest lane, however the transponder did not detect the tag when the vehicle was in the farther lane. Second, the transponder was directed perpendicular to the road. This angle was effective for the vehicle in the farthest lane, however it did not trigger when the vehicle was in the closest lane. Third, the transponder faced the northwest direction at a 45-degree angle. When the vehicle was located in the closest and farthest lanes, the transponder identified the tag and triggered the data storage.

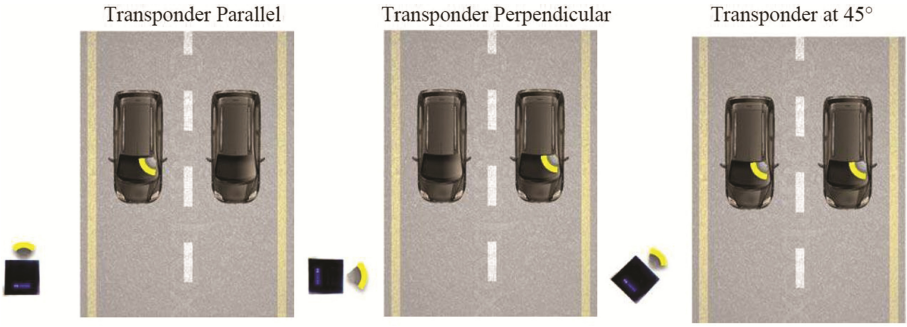

Fig. 3. Direction of transponder with respect to the vehicle [5].

The position of the transponder from the ground also varied throughout testing. It was determined that the system was triggered occasionally at a height of 1.5 m (5 ft), consistently at 1.8 (6 ft), and rarely at 2.1 m (7 ft). Additionally, the transponder was initially located at a distance of 2.4 m (8 ft) from the edge of the lane, however the distance was decreased to 1.8 m (6 ft) to obtain a reliable detection. The vertical angle that the transponder was directed was not investigated.

3.3 Lane Position of Vehicle

To determine the range from the transponder to the tag, the tag was placed in the upper left-hand corner of the vehicle windshield (Fig. 4). The transponder was directed at a 45-degree angle northwest. The vehicle was located in the lane closest to the transponder

and travelled at a speed of 16 kph (10 mph). The transponder detected the presence of the tag when the vehicle was approximately 3 m (10 ft) from the reader, measuring parallel on the road. The vehicle then travelled in the farthest lane, again headed east. With the tag farther away, the transponder detected the tag when the vehicle was in line with the reader.

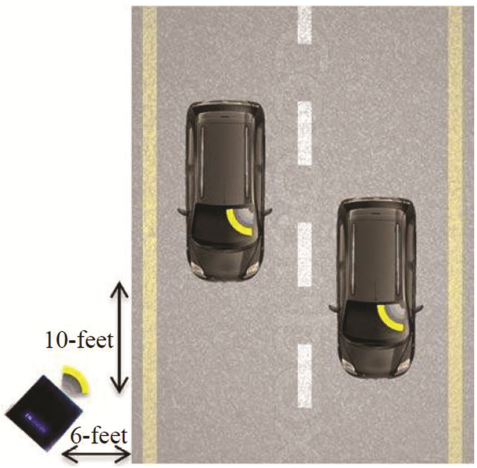

Fig. 4. Lane position of vehicle with respect to transponder [5].

The tags were designed to be placed on the inside of a vehicle's windshield. For the field tests, the tag was initially placed on the upper left-hand corner of the windshield. The vehicle was driven at 105 KPH (65 MPH) in the closest lane, and the transponder detected the tag six out of six times consecutively. The vehicle was then driven in the farthest lane with the same tag positioning, and the tag was identified in two out of four runs. As a result, an additional tag was added to the upper right-hand corner of the vehicle. The transponder then detected the tag two out of two times while the vehicle was in the farthest lane. This test suggests that the maximum perpendicular distance for consistent triggering is approximately 5.5 m (18 ft), and inconsistent triggering occurs at a distance of 8.5 m (28 ft) for a system using one antenna.

Up to this point, the positions of the transponder, vehicle, and tag were established, and the outcome of the three tested parameters had to be confirmed. The transponder was angled at 45-degrees facing the northwest direction; the vehicle was located in the farthest lane to test the worst-case scenario for vehicle placement; and the tag was placed in the upper right-hand corner of the windshield. The vehicle was driven at 105 kph (65 mph), and the transponder recognized the tag, triggering the data saving system six out of six times. These tests indicated that the RFID triggering system was successful.

After the vehicle event was triggered, the SHM strain measurement data automatically saved to a file onto the computer hard drive. The file included the wavelength readings, tag identification number, date, and time, respectively. The wavelength readings were recorded from three of the four available interrogator channels, where one sensor was located on each channel. The sensors were not the focus of the field tests nor

were they adhered to a host material affected by traffic events, so the readings fluctuated only slightly due to noise and marginal temperature variations.

4 Conclusions

A radio-frequency identification (RFID) reader and antenna combination system was developed in order to manage strain data from a SHM on a highway bridge. Field tests were conducted to validate the proposed system. The optimal position of the vehicle relative to the transponder, the height and horizontal position of the transponder, and the location of the RFID tag were investigated. The field tests indicated that the RFID triggering system was successful, but was sensitive to the position of the tag relative to the transponder.

Several aspects of the concept need to be studied before implementation of the RFID triggering system can occur. The installation of the system at the port of entry needs to be developed, and larger transponder range capabilities and cellular data transmission capabilities need to be explored. The selection of an RFID transponder needs to be evaluated. (One option is the E-ZPASS system.) Moreover, during the proof of concept tests, the transponder did not have a large enough detection range to trigger the system consistently when the tag was located on the left-hand corner of the windshield. An additional antenna may need to be added to the system on the opposite side of the highway for consistent and confident triggering.

Acknowledgments. The research was supported by the Wyoming Department of Transportation and the Mountain Plains Consortium.

References

1. Web, G.T., Vardanega, P.J., Middleton, C.R.: Categories of SHM deployments: technologies and capabilities. J. Bridg. Eng. ASCE **20**(11), 04014118 (2015)
2. Jung, M.A.: Development of a fiber optic based load testing system for highway bridges. M.S. Thesis, Department of Civil and Architectural Engineering, University of Wyoming, Laramie, Wyoming (2014)
3. Danforth, M.: Laramie River bridge load-testing plan with sensor verification and RFID feasibility of permitted vehicles. M.S. Thesis, Department of Civil and Architectural Engineering, University of Wyoming, Laramie, Wyoming (2015)
4. Maurais, D.T.: Strain transfer behavior of notch embedded Fiber Bragg Gratings. M.S. Thesis, Department of Civil and Architectural Engineering, University of Wyoming, Laramie, Wyoming (2012)
5. Schmidt, R.J.: Structural health monitoring of highway bridges subjected to overweight trucks, Phase I – Instrumentation development and validation. Final Report, Department of Civil and Architectural Engineering, University of Wyoming, Laramie, Wyoming (2016)

Evaluating Vibration Serviceability Using Experimental Modal Testing

Anthony R. Barrett[1(✉)], D. Bradley Davis[2], and Thomas M. Murray[3]

[1] Department of Civil and Environmental Engineering, United States Air Force Academy, Colorado Springs, CO, USA
anthony.barrett@usafa.edu
[2] Civil Engineering Department, University of Kentucky, Lexington, KY, USA
[3] Department of Civil and Environmental Engineering, Virginia Tech, Blacksburg, VA, USA

Abstract. Predicting the dynamic response of pedestrian structures such as building floors and footbridges to human-induced activity is a complex problem that involves estimation of the dynamic properties of the structure and estimating its response to a loading that varies in intensity and location with respect to time. Even though the problem is complex, researchers have developed guides to aid designers in avoiding vibration serviceability issues by providing simple analytical tools for evaluating a proposed design. The strength of these guides lies in prevention of serviceability problems at the design stage, although they also serve as an informative measure when in-service floors or pedestrian bridges are reported to have excessive vibrations.

Current methods of on-site serviceability evaluation typically involve heel-drop tests to determine natural frequencies and walking tests to record sinusoidal peak acceleration response, generally as response-only single channel measurements. A general understanding of the floor response is achieved this way by looking at the resulting acceleration traces and autospectra resulting from these unmeasured excitations. The most accurate method for estimating the dynamic properties of a structure is experimental modal testing to acquire accelerance frequency response functions (FRF).

This paper proposes a method for evaluation of vibration serviceability using the mid-bay/span driving point accelerance FRFs of low-frequency (<9 Hz) pedestrian structures derived from experimental modal testing. The method proposes using an accelerance limit curve generated from a contemporary design guide to represent a tolerance limit of vibration serviceability. On-site evaluation can be performed with modal testing by comparing the peaks of a measured accelerance FRF with the accelerance limit curve. The method is demonstrated using a set of mid-bay driving point accelerance FRF measurements from an in-situ building floor and comparing with a widely recognized design guide-based accelerance limit curve.

Keywords: Modal analysis · Floor · Human-induced vibration · Evaluation · Serviceability

© Springer International Publishing AG 2018
J.P. Conte et al. (eds.), *Experimental Vibration Analysis for Civil Structures*,
Lecture Notes in Civil Engineering 5, https://doi.org/10.1007/978-3-319-67443-8_10

1 Introduction

Evaluating the vibration serviceability of low-frequency (<9 Hz) pedestrian structures such as building floors and pedestrian bridges subjected to human-induced activity is a complex problem. The first step is the estimation of the static and dynamic properties of a relevant portion of a structure. The second step involves estimating a structure's response to a human loading that varies in both intensity and location with respect to time. Lastly, the predicted response is compared to a human tolerance threshold, which can also vary with frequency, to determine whether or not the vibration level is acceptable. Even though the problem is complex, researchers have developed guides to aid designers in avoiding vibration serviceability issues by providing simple analytical tools for evaluating a proposed design. The strength of these guides lies in prevention of serviceability problems at the design stage, although they also serve as an informative measure when the occupants of an in-service building floor or other pedestrian structure report excessive vibrations and a consultant is asked to evaluate.

Current methods of on-site serviceability evaluation typically involve a series of heel-drop tests to determine natural frequencies and walking tests to record sinusoidal peak acceleration response. This testing is generally accomplished using response-only single channel measurements, from which a general understanding of the floor response is achieved by looking at the resulting acceleration traces and autospectra from these unmeasured excitations. The most accurate method for estimating the dynamic properties of a structure, however, is experimental modal testing. Experimental modal testing measures both the input force and resulting acceleration response to develop an accelerance frequency response function (FRF). This paper proposes a direct method for evaluation of vibration serviceability by comparing measured FRFs of low-frequency pedestrian structures derived from experimental modal testing to an acceleration response tolerance threshold derived from contemporary design guidance.

2 On-Site Evaluation Using Response-Only Testing

The second edition of AISC's *Steel Design Guide Series 11*: *Vibrations of Steel-Framed Structures Due to Human Activity* [1], hereafter referred to as DG11, has a chapter on evaluation of vibration problems, including recommended vibration measurement techniques. Though experimental modal testing is discussed in the chapter, the nature of on-site serviceability evaluation lends itself to portable testing equipment, and consequently most on-site evaluation is accomplished using equipment that typically only measures the acceleration response to some human-induced excitation such as a heel drop or paced walking. Davis et al. [2] demonstrated a simplified procedure using a portable response-only measurement system for evaluating a problem floor and developing a retrofit solution. A heel drop is an impact force caused by a person assuming a natural stance, maintaining straight knees, shifting their weight to the balls of the feet, rising approximately 65 mm on their toes, and then suddenly relaxing to allow their full weight to freefall and strike the floor with their heels. As a human-induced impulse load requiring no equipment other than sturdy shoes, a heel drop serves as naturally portable and effective input force to a pedestrian structure from

which the acceleration response can be analyzed to determine the natural frequencies. Knowing the frequencies from the heel drop tests, paced walking tests using a metronome at a subharmonic of the structure's dominant frequencies can incite a resonant response from which the accelerations are compared to human tolerance limits. The time-history decay from a heel drop (or bouncing at a resonant frequency) can also be used to estimate damping in the structure, although it has been shown this can result in misleading damping estimates in floors with closely spaces modes [3]. The cost of equipment required for response-only testing is lower than other methods; however a proper serviceability evaluation involving walking tests often requires more than one person and is still time and labor intensive.

3 Experimental Modal Testing

Experimental modal testing, which measures both the input force and acceleration response to construct the accelerance FRF, is unmatched in estimating the dynamic properties of a structure. For low-frequency floors or pedestrian bridges, modal testing allows estimation of the most relevant dynamic parameters such as dominant natural frequencies, damping, and with a set of measurements, the mode shapes of vibration over a tested area. Using modal analysis software, these parameters can be estimated even when modes are very closely spaced, which is often the case in continuous-slab multi-bay floors. Modal testing is typically accomplished to validate or tune finite element (FE) models, as measured frequencies and mode shapes can be used to guide FE model adjustments to bring predicted frequencies and mode shapes into agreement with measured values. Much of DG11's new chapter on FE modeling of floors is based on techniques refined through this type of experimental testing [3–5].

Input force is often applied using an electrodynamic shaker, which provides the most controllable source of dynamic loading to a structure. An electrodynamic shaker has the ability to provide an input force at a relatively constant magnitude and within a very specific frequency range of interest by using a swept sine signal. A swept sine signal, also known as a chirp signal, is a sinusoidal function with a changing frequency over time to provide force input to the floor or pedestrian bridge structure over the specified range of frequencies. The input force generated by the shaker is measured either indirectly or directly. Attaching an accelerometer to the armature mass allows an indirect computation of input force by multiplying the armature's measured acceleration by its mass. Davis et al. [6] cautioned against this indirect method for measuring input force due to shaker-structure interaction, especially for light structures, which can lead to lower quality FRFs that inaccurately predict the peak accelerance values. The preferred method for directly measuring input force from the shaker is accomplished by placing a force transducer between the shaker and the structure. Acceleration response is measured using one or more accelerometers, and with the input force measured as described above, a digital signal processor analyzes the signals to estimate the accelerance FRF.

One of the distinct advantages of experimental modal testing is the ability to estimate the mode shapes of a structure, though this typically requires a considerable number of measurements, leading to extended times required for testing. Obtaining mode shapes

are generally of most interest for validating FE models and not required for the evaluation method presented here. For evaluating vibration serviceability using modal testing, a focus on just acquiring driving point FRF measurements from the middle of each bay/span significantly reduces the time required on site for testing. A driving point FRF is the measurement taken with an accelerometer at the same location as the input force. A mid-bay/span driving point FRF is acquired by exciting the structure at the center of a bay of a floor or span of a pedestrian bridge and has been shown to be the most informative measurement for parameter estimation [9]. The dominant peaks of the driving point FRFs identify frequencies most susceptible to a harmonic of walking excitation, and the magnitude of those peaks directly represent the expected acceleration response per input force applied at that frequency. The mid-bay/span location is the point that most design guides use for their estimation of peak acceleration response for comparison to a human tolerance limit, making the mid-bay/span driving point FRF the ideal experimental modal testing measurement for directly evaluating vibration serviceability.

Contemporary design guidance is not easily compared to modal measurements in the field. The following section develops an accelerance limit curve based on the tolerance limits and walking force representation in DG11, whose evaluation accuracy has been vetted extensively against a large database of problem floors [10]. Once established, an accelerance limit curve could serve as a convenient threshold for direct on-site evaluation using experimental modal testing.

4 Developing an Accelerance Limit

In North America, the leading publication used for evaluation of vibration serviceability of structures due to walking excitation is the previously discussed AISC DG11, which is used to demonstrate the proposed evaluation method in this paper. Though there are various other design guides currently in use throughout the world [11–13], they address vibration serviceability in the same general manner as DG11:

(1) Estimate the dynamic properties of the floor.
(2) Estimate a dynamic loading to simulate the applied forces of human activities.
(3) Compute the acceleration response of the floor for comparison with an established level of acceptability.

Like DG11, other publications offer similar simplified methods for manually computing the dynamic properties of fundamental frequency and effective mass/weight of the floor and provide recommended values of damping. These publications recognize the complexity of representing the forces from human activities such as walking and take the approach of representing this complex loading as a Fourier series. Using the computed properties of the floor and assumed loading, the publications compute an acceleration response to compare to acceptability criteria. For office floors, the acceptability criteria suggested by DG11 is a constant 0.005 g for frequencies between 4 Hz and 8 Hz, although this level can also be conservatively applied to frequencies outside that range. Most publications recognize the stepped nature of the dynamic load coefficients within certain frequency ranges (corresponding to the various harmonics of

step frequency). DG11 offers a simplified exponentially decreasing curve fit expression, $0.83e^{-0.35f}$.

The computed acceleration using DG11 applies at the fundamental frequency, and no consideration is given for the response at (or contribution from) other frequencies. In this respect, using the accelerance FRF differs because it describes the response (and allows evaluation) over a range of frequencies and includes the contribution of other modes.

The fundamental premise of the presented evaluation method, and its ability to represent an acceleration response tolerance limit (serviceability threshold) over a range of frequencies, lies within the definition of the accelerance frequency response. The value of accelerance is best described by:

$$\textit{Measured}\ \text{Accelerance FRF Magnitude} = \frac{\textit{measured}\ \text{steady state acceleration response}}{\textit{measured}\ \text{input force}} \tag{1}$$

Because DG11 defines a steady state acceleration limit for human comfort and estimates the applied loading from walking excitation as a steady state harmonic force, a design accelerance magnitude is defined:

$$\textit{Design}\ \text{Accelerance FRF Magnitude} = \frac{\text{steady state acceleration response tolerance limit}}{\textit{design}\ \text{input force}} \tag{2}$$

The accelerance FRF is a function of frequency, f. The acceleration response tolerance limit can be taken as a constant value over the frequency range of interest. The input force from walking excitation is a function of frequency and the magnitude of the simulated sinusoidal force is based on the harmonic of walking that will likely correspond with frequency of the floor. Thus, an accelerance limit as a function of frequency, $A_o(f)$, is defined in general terms as

$$\begin{aligned} A_o(f) &= \frac{\text{steady state acceleration response limit}}{\textit{design}\ \text{input force}} \\ &= \frac{a_o}{F(f)}\ (\text{acceleration units})/(\text{force units}) \end{aligned} \tag{3}$$

Using the form of Eq. (3), an accelerance limit can be developed from design guidance to accommodate both the suggested acceleration tolerance limits and the curve-fit harmonic force representation of walking excitation. In this form, the design guide-based accelerance limit is directly comparable to on-site accelerance measurements from modal testing.

For DG11, the general form of the accelerance limit is:

$$A_o(f) = \frac{a_o}{R\alpha_i P} = \frac{a_o}{P_o e^{-0.35f}} = \left(\frac{a_o}{P_o}\right) e^{0.35f} \tag{4}$$

where:

$A_o(f)$ = accelerance limit as a function of frequency, f, in units of acceleration per unit of input force

a_o = acceleration limit for human comfort

= $0.005g$ $(0.5\%g)$ for office floors

= 0.05g (5%g) for outdoor pedestrian bridges

$\alpha_i = 0.83e^{-0.35f}$ (DG11 simplified dynamic load coefficient)

P = person's weight (taken as 698 N for DG11)

R = reduction factor (taken as 0.5 for office floors, 0.7 for footbridges in DG11)

$P_o = 0.83RP$

The DG11 accelerance limit for an office floor is then:

$$A_{o,\text{ office floor}}(f) = \frac{a_o}{R\alpha_i P} = \frac{0.5\%\text{ g}}{(0.5)(0.83e^{-0.35f})(698\text{ N})} = \left(\frac{0.5\%\text{ g}}{290\text{ N}}\right)e^{0.35f}$$
$$= 0.00173e^{0.35f}\ \%\text{ g/N} \tag{5}$$

Accelerance limits can also be developed for pedestrian bridges using the same approach, though DG11 suggests using a reduction factor R = 0.7 and an acceleration tolerance limit of 0.015 g or 0.05 g for indoor and outdoor pedestrian bridges, respectively. For an outdoor pedestrian bridge, the DG11 accelerance limit is:

$$A_{o,\text{ outdoor footbridge}}(f) = \frac{a_o}{R\alpha_i P} = \frac{5\%\text{ g}}{(0.7)(0.83e^{-0.35f})(698\text{ N})} = \left(\frac{5\%\text{ g}}{406\text{ N}}\right)e^{0.35f}$$
$$= 0.0123e^{0.35f}\ \%\text{ g/N} \tag{6}$$

The DG11-based accelerance limit curves of Eqs. (5) and (6) are plotted in Fig. 1.

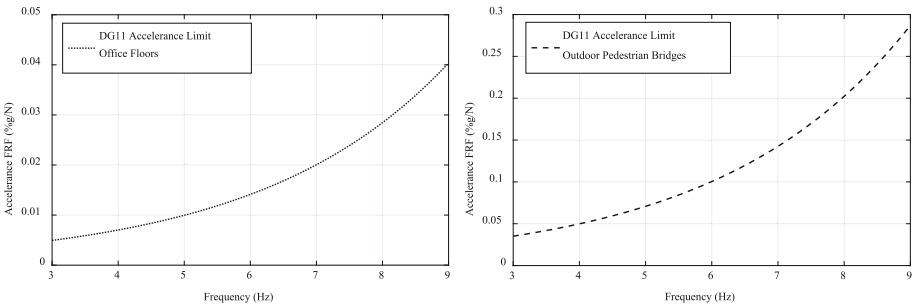

Fig. 1. DG11-based accelerance limit curves

The acceleration limit a_o and forcing terms $\alpha_i P$ presented in DG11 are based on established theories of human tolerance to vibration and the effective harmonic force due to walking, however R represents a catch-all reduction factor used to account for less-than-full steady state resonant response and because the individual walking and the individual subject to vibration are not located at the point of maximum response within a bay. The subjective nature of its suggested value means that other values of R may be considered.

Although the variables a_o, R, and $\alpha_i P$ in the basic expression of Eq. (4) are from DG11, they represent the general terms used in some form within all of the evaluation methods (acceleration limit, reduction factor, and effective forcing amplitude, respectively). The simplified dynamic load coefficient term used by DG11 makes each accelerance limit curve a smooth increasing exponential. Some other methods of evaluation use a stepped dynamic load coefficient (or stepped function with slight slope), and thus the form of the design accelerance "curve" would also be stepped. Although specific terms of the other methods differ from DG11, they are highlighted to demonstrate that they are not insurmountable for developing accelerance limits based on the evaluation method fundamentals.

5 Evaluating Vibration Serviceability Using Experimental Modal Testing

This section demonstrates the evaluation of vibration serviceability of an in-situ building floor using measurements obtained by experimental modal testing and the above-developed accelerance limit curve. Originally presented by Davis [4], the tested floor is part of a four story, 5,100 m^2 building that was under construction at the time of testing (Fig. 2(a)). Though under construction at the time of testing, the floor was mostly clear of construction material (Fig. 2(b)) and the underside supported only minimal piping and ductwork.

The framing plan for the tested floor is shown in Fig. 2(c). Most bays of the building are 9.14 m square, and the floors were constructed using conventional steel framing beneath 325 mm total thickness composite slabs comprised of normal weight concrete on 50 mm metal deck. Experimental modal testing was accomplished using a 108 kg electrodynamic shaker atop a force transducer to measure input force and an array of accelerometers measuring acceleration response. Driving point measurements (accelerometer and force input at same location) were taken with the shaker located at mid-bay of each of the four numbered bays shown in Fig. 2(c).

Presented elsewhere in detail [4], FRF curve-fitting of measurements taken with the shaker located in these four bays identified six mode shapes with frequencies ranging from 6.4 Hz to 8.2 Hz and viscous modal damping ratios between 0.51% and 0.61% of critical. The driving point FRFs for the shaker located at the center of each of the four bays are shown in Fig. 3. Also shown on each plot is the DG11-derived accelerance limit curve. A comparison of the accelerance FRF peaks and tolerance limit curve forms the basis of modal testing-based evaluation of vibration serviceability. Peaks that exceed the accelerance limit curve provide an immediate indication of a serviceability problem for the condition of the building at the time of testing.

(a) As-Tested Building Condition

(b) As-Tested Floor Condition

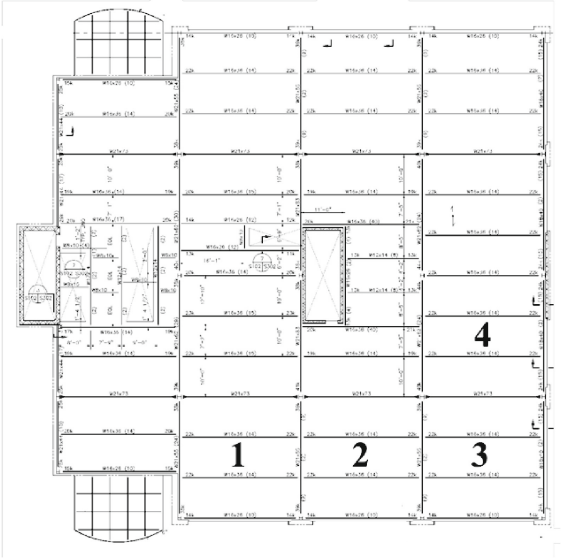

(c) Tested Floor Framing Plan

Fig. 2. Evaluated building

As shown in plots of Fig. 3, this floor is anticipated to have serviceability issues because peaks within the mid-bay driving point FRFs exceed the accelerance limit curve in three out of the four bays.

- Bay 1's 0.0339% g/N FRF peak exceeds the 0.0297% g/N serviceability limit at 8.125 Hz (Fig. 3(a)).
- Bay 2's 0.0172% g/N FRF peak exceeds the 0.0163% g/N serviceability limit at 6.40 Hz (Fig. 3(b)).
- Bay 3's 0.0265% g/N FRF peak exceeds the 0.0201% g/N serviceability limit at 7.00 Hz (Fig. 3(c)).
- Per Fig. 3(d), Bay 4 should not have a serviceability issue as no FRF peak exceeds the accelerance limit curve. The highest FRF peak, 0.0173% g/N, is below the 0.0233% g/N serviceability limit at 7.425 Hz.

An unsatisfactory serviceability evaluation should not be surprising given the extremely low levels of damping that were measured for this floor under construction (0.5 to

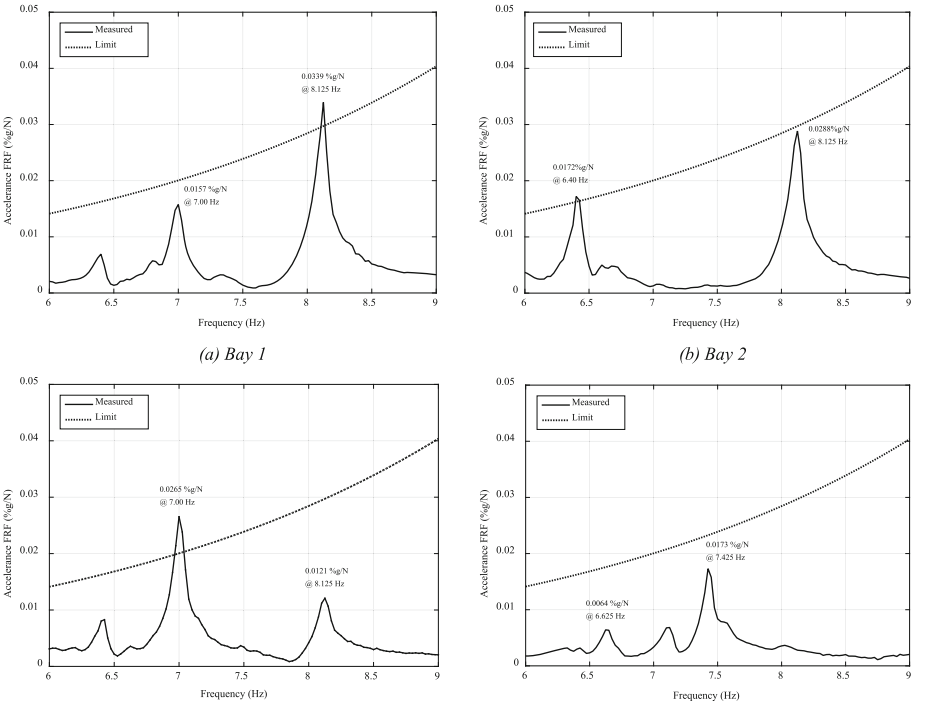

(a) Bay 1 *(b) Bay 2*

(c) Bay 3 *(d) Bay 4*

Fig. 3. Mid-bay driving point accelerance FRF magnitudes with accelerance limit curve overlays

0.6% of critical), which was essentially a bare structural system. Even though the approach presented is meant for evaluating serviceability of in-service structures, the floor presented here that was tested while under construction still serves as a useful demonstration of the evaluation method.

6 Comparison of Accelerance-Based Evaluation Results with Walking Tests

In addition to modal testing, walking tests were conducted in each of the four bays by an individual using a metronome set at a pace within the normal range of human walking speeds corresponding to an integer division of a natural frequency identified from the FRF. The upper limit of the normal range of human walking speeds is around 2.2 Hz [1]. The 6.4 to 8.2 Hz range of identified frequencies for the tested floor indicates it could experience a resonant response due to walking at a pace corresponding to the third or fourth subharmonic of one of these frequencies. For Bays 1, 2, and 3, the walking pace frequency selected corresponded to the frequency of the FRF peaks shown to exceed the 0.5% g accelerance limit in Fig. 3(a)–(c). For Bay 1,

a walking pace of 122 beats per minute (bpm) was selected, corresponding to the fourth subharmonic of the 8.125 Hz frequency. For Bay 2, a walking pace of 128 bpm was selected, corresponding to the third subharmonic of the 6.425 Hz frequency. For Bay 3, a walking pace of 105 bpm was selected, corresponding to the fourth subharmonic of the 7.00 Hz frequency. For Bay 4, which did not have an FRF peak exceeding the accelerance limit, a 133 bpm walking pace frequency was selected to correspond with the first notable peak in Fig. 3(d) at 6.625 Hz even though it had a lower magnitude than the dominant peak at 7.425 Hz. This frequency was selected because it could be tested by an achievable pace corresponding to the third subharmonic.

The acceleration response time histories were recorded at mid-bay during each walking test and are shown for each of the four bays in Fig. 4. Tolerance limits of DG11 are in terms of sinusoidal peak accelerations, thus single peak accelerations in measured waveforms are not directly comparable. The calculation procedures for estimating the peak acceleration due to walking in DG11 are based on a single degree of freedom system subjected to a steady state excitation. Thus, a single peak in a measured acceleration record is not the same as was assumed in the development of the criterion. To evaluate typical measured building floor acceleration waveforms, the waveforms are first filtered to 1 Hz to 15–20 Hz (the range that humans feel accelerations). A rolling two-second root mean square (RMS) acceleration is then computed and the center acceleration for each interval converted to peak acceleration by multiplying the RMS value by $\sqrt{2}$ times 100%. The resulting acceleration is referred to as the equivalent sinusoidal peak acceleration (ESPA), which is then compared to the specified tolerance limit for evaluation. The computed ESPA values for each bay are annotated in their respective plots in Fig. 4.

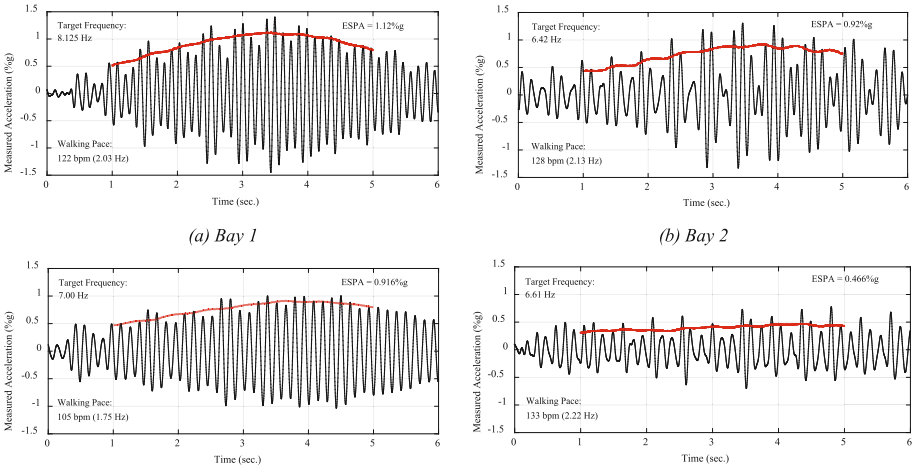

Fig. 4. Paced walking test acceleration time histories

As shown in the paced walking test acceleration waveforms in Fig. 4(a) through (c), Bays 1, 2 and 3 each experienced a resonant build-up, resulting in ESPA values exceeding the 0.5% g serviceability limit. For Bay 4, the walking pace of 133 bpm, corresponding to the third subharmonic of 6.625 Hz, did not result in an ESPA exceeding the 0.5% g tolerance limit as shown in Fig. 4(d). Though not shown, walking tests were performed at a 105 bpm pace, corresponding to the fourth subharmonic of the dominant 7.425 Hz frequency, however these tests resulted in accelerations less than those shown in Fig. 4(d). For all four bays, the results of walking tests agreed with evaluation results obtained by comparing the DG11-derived accelerance limit curve to the mid-bay driving point FRFs obtained using modal testing. Note that the results of these walking tests were only presented to support validity of the accelerance-based evaluation method. In practice, accelerance-based evaluation would alleviate the need to perform walking tests, potentially even making experimental modal testing evaluation quicker than traditional response-only testing and evaluation.

7 Conclusions

This paper described the formulation of an accelerance limit based on a contemporary design guide's acceleration tolerance limits and estimated dynamic loading from human activities. Establishing a tolerance limit in terms of accelerance allows direct on-site serviceability evaluation using the high-quality accelerance FRFs acquired with modal testing. A demonstration evaluating serviceability using an accelerance limit was presented using the floor system of an in-situ building. By comparing of the accelerance limit to experimental modal testing-derived mid-bay driving accelerance FRFs, the floor was shown to exceed recommended limits, which was confirmed from the results of paced walking tests.

It should be noted that there is currently a limited database of high quality modal testing-derived driving point FRF measurements for in-situ floor and pedestrian bridge structures in the published literature. Although the database of floors and pedestrian bridges with these accelerance measurements is limited, the methods of DG11 have been successfully vetted against an extensive database of problem floors evaluated using response-only testing. The accelerance limit presented in this paper is based on DG11 and capitalizes on its prediction accuracy. Though modal testing has traditionally been prohibitive for on-site evaluation, testing focused on only acquiring mid-bay/span driving point FRFs significantly reduces testing time, making this evaluation method comparable to traditional response-only testing. It is possible that future research could make modal testing more accessible, from which the database of pedestrian structures with FRF measurements and their corresponding subjective serviceability evaluations (human surveys of whether the vibration levels are acceptable or unacceptable) would expand. The strength in the evaluation method lies in its ability to be verified by field measurements. As more lively floors are evaluated via modal testing, the calibration of the presented accelerance limit can be verified or adjusted.

References

1. Murray, T.M., Allen, D.E., Ungar, E.E., Davis, B.: Steel Design Guide Series 11: Vibrations of Steel-Framed Structures Due to Human Activity. American Institute of Steel Construction (AISC), Chicago, Illinois (2016)
2. Davis, B., Liu, D., Murray, T.M.: Simplified experimental evaluation of floors subjected to walking-induced vibration. J. Perform. Constr. Facil. **28**, 04014023 (2014). doi:10.1061/(ASCE)CF.1943-5509.0000471. ASCE
3. Barrett, A.R.: Dynamic testing of in-situ composite floors and evaluation of vibration serviceability using the finite element method. Ph.D. Dissertation, Virginia Polytechnic Institute and State University, Blacksburg, VA (2006)
4. Davis, D.B.: Finite element modeling for prediction of low-frequency floor vibrations due to walking. Ph.D. Dissertation, Virginia Polytechnic Institute and State University, Blacksburg, VA (2008)
5. Davis, D.B., Murray, T.M.: Simplified finite element method for predicting low-frequency floor vibration due to walking. In: Proceedings of the 2010 North American National Steel Construction Conference. American Institute of Steel Construction, Chicago, IL (2010)
6. Davis, B., Barrett, A.R., Murray, T.M.: Use of a force plate versus armature accelerometer for measuring frequency response functions. Exp. Tech. **35**, 73–79 (2011)
7. Blakeborough, A., Williams, M.S.: Measurement of floor vibrations using a heel drop test. Proc. Inst. Civ. Eng. Struct. Build. **156**, 367–371 (2003)
8. Hanagan, L.M., Raebel, C.H., Trethewey, M.W.: Dynamic measurements of in-place steel floors to assess vibration performance. J. Perform. Constr. Facil. **17**(3), 126–135 (2003). ASCE
9. Barrett, A.R., Murray, T.M.: Dynamic testing and behavior of in-situ composite office floors. In: Experimental Vibration Analysis for Civil Engineering Structures 2011, vol. I, Varenna, Italy, pp. 347–355, 3–5 October 2011
10. Pabian, S., Thomas, A., Davis, B., Murray, T.M.: Investigation of floor vibration evaluation criteria using an extensive database of floors. In: Proceedings of the ASCE Structures Congress, pp. 2478–2486. ASCE, Reston (2013)
11. Smith, A.L., Hicks, S.J., Devine, P.J.: Design of Floors for Vibration: A New Approach, SCI P354. The Steel Construction Institute, Silwood Park, Ascot, Berkshire, England (2007)
12. RFCS: Human Induced Vibrations of Steel Structures, Vibration Design of Floors, Guideline. European Commission Research Fund for Coal and Steel, Brussels, Belgium (2007)
13. Willford, M., Young, P.: CCIP-016: A Design Guide for Footfall Induced Vibration of Structures. The Concrete Centre, Surrey, United Kingdom (2006)

Damage Detection by Experimental Modal Analysis in Fiber-Reinforced Composites

C.A. Geweth[1(✉)], F. Saati Khosroshahi[1], K. Sepahvand[1], C. Kerkeling[2], and S. Marburg[1]

[1] Chair of Vibroacoustics of Vehicles and Machines, Technical University of Munich, 85748 Garching bei München, Germany
christian.geweth@tum.de
[2] Honda R&D Europe GmbH, 63073 Offenbach, Germany

Abstract. Uncertainties during the manufacturing process or due to unexpected load variations in the course of operation can cause damages or faults in structures. These deviations from the original or intended properties can impact the durability and the application for the component. Destructive testing methods are often impractical since the investigated component becomes unfeasible. Instead, a non-destructive testing method, which is based on the change of the dynamic behaviour caused by the faults in the structures, allows examining the produced or built-in component. Experimental investigation of the changes can be employed to detect and quantify the damages to some extent, if the relationship between the properties and the damage is not known. The non-destructive vibrational testing methods, in particular, are based on the relation between the material properties of a structure and its measured vibrational behaviour, e.g. natural frequencies and mode shapes.

The structural responses of several FRC structures are investigated in this paper by using the experimental modal analysis. To measure the structural responses without changing the dynamical behaviour, a laser-scanning vibrometer is used. Two different sets of measurements are performed. In the lower frequency range a shaker is used for excitation. In the higher frequency range a loudspeaker is used as excitation with a microphone as phase reference. In order to extract the eigenfrequencies and modal data from the measurement, a modal analysis is performed afterwards. For identifying the changes in the natural frequencies and mode shapes, specimens without and with several different kinds of artificial faults are tested. The experimental results are compared with a finite element simulation of the structures. The advantages and merits of this method as well as its limits and drawbacks are discussed in this study.

Keywords: Fiber-reinforced composites · Damage detection · Experimental modal analysis · Structural health monitoring · Non-destructive testing

1 Introduction

The possibility to detect and localize damages in structures without damaging them in the process offers plenty of applications and opportunities. Such methods allow, for

© Springer International Publishing AG 2018
J.P. Conte et al. (eds.), *Experimental Vibration Analysis for Civil Structures*,
Lecture Notes in Civil Engineering 5, https://doi.org/10.1007/978-3-319-67443-8_11

instance, to verify the quality of produced component in a manufacturing line or to monitor the conditions of a single component in entire assemblies. Therefore, they open the opportunity to use a structure to its actual end of its lifetime. Also, the methods help to reduce the cost and efforts of maintenance, hence specific information about the location and type of defect can be obtained. One possibility to recognize defects in a structure is to measure the deviation in the structural dynamic behavior of a structure. The change of the structural response of the specimen results out of the shift of the geometrical and material properties caused by the defect. Since the different properties cause a change in the global behavior of the structure, this method is able to detect faults in inaccessible areas of the specimens. Furthermore, they allow a faster investigation than local methods like for example ultrasonic testing. One usually mentioned drawback of such a global method is the possible ambiguous results. Hence several possible reasons can contribute in the shift of frequency [1–3]. One additional disadvantage of such a method is that it requires knowledge about the distribution of the natural frequencies and structural response of the non-damaged components. Without information on the influence off manufacturing tolerances and uncertain material properties on the eigenfrequencies [4], a clear conclusion can hardly be reached. Those data could either be obtained by measuring a statistical significant number of specimens or by precise simulations, taking the variation of the material and geometrical parameters into account [5]. For structural health monitoring, the necessary information about the structural dynamical behavior can be obtained by measurements in the beginning of the lifetime of the structure.

The feasibility of non-destructive testing on fiber-reinforced components is investigated in this study. The method has received increasing attention in recent years for damage detection for such material and structures, cf. [6, 7] and references therein. Those structures and materials are especially critical, owning to the fact that they possess a more complicated structural component, which can have under invisible delamination. Therefore measurements were performed on five test specimens. Three of those samples were produced with different kinds of artificial defects. The possibility to identify defected specimen from the change of the natural frequencies is investigated. The experimental results then are compared to simulation results simulation.

The paper is organized as follows: After the description of the used samples and the experimental setup, the experimental results are discussed. The finite element model is introduced and a comparison between the experimental and numerical results is conducted. The final section contains the conclusion.

2 Test Specimens and Experimental Setup

2.1 Samples

For the experimental part of this study, five specimens made out of fiber-reinforced composites were investigated. The five samples were seemingly identical and could not be clearly distinguished by shape, appearance or - with the exception of the specimen “Pressure” - by weight. The orientation and material for the fibers and resin is identical within the manufacturing tolerances as well as the number of the layers. Three of those samples were produced with artificial defects as listed in Table 1.

Table 1. Overview of the specimens.

Specimen	Defect characterization
Pr 1 ok	Manufactured without artificial damages
Pr 2 ok	Manufactured without artificial damages
Del10mm	10 mm wide area of delamination
Del25mm	25 mm wide area of delamination
Pressure	Insufficient pressure for injecting the resin

For the production of the samples "Del10mm" and "Del25mm", a layer of polytetrafluorethylene (PTFE) was added between the layers. Due to the chemical properties of this thermoplastic polymer, the lamination of the neighboring layers is prevented. Therefore in the area of the PTFE-foil, the sandwich structure is delaminated. As depicted in Fig. 1, the foil is placed over the entire length of the structure. The width of the delaminated area differs for each of the samples. The width of the PTFE-foil for the two specimens with delamination are listed in Table 1. In the production process of the sample "Pressure", the pressure for injecting the resin was significantly reduced. Therefore, the resin was unable to infiltrate the fibers completely. This also results in a slightly low weight of that sample.

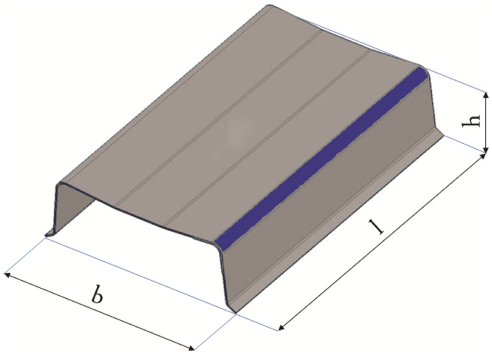

Fig. 1. Geometry of test specimens (yellow area of delamination) [8]

Two specimens were produced as reference without artificial defects. Allow samples had a length of $l = 600$ mm, a width of $b = 395$ mm and a height of $h = 130$ mm. With the exception of the sample "Pressure", the mass was determined as $m = 1.86$ kg. As mentioned above, the mass of the specimen "Pressure" is about $\Delta m \approx 80$ g lower than the mass of the other samples [8].

2.2 Experimental Setup

The structural dynamic behavior of the specimens was investigated in a wide frequency range. In order to get good results over the entire frequency range, two series of measurements were performed on all samples. The two series of measurements differ in

excitation method, number of measured points and obviously the frequency range. In both cases, the measurements were done in an anechoic chamber in order to prevent disturbance from other sources. Rubber strings were used to suspend the specimens to approximate free-free boundary conditions during the measurements. To keep the influence of the strings as little as possible, the strings were connected at positions on the structures, which coincident with nodal lines for most of the modes. To gather the structural response to the excitation, a laser-scanning-vibrometer (LSV) was used. The control unit of the LSV includes a data acquisition unit, which was used to record the signal from the reference sensor. The excitation signal was generated by the build-in signal generator. For the first series of measurement the structures were excited by a shaker. In that case a pseudo-random signal was generated. As phase reference, a force transducer between the shaker and the specimens was used. This measurement was done up to a frequency of $f_{max} = 400$ Hz and a total of 92 equal distributed measurement points. In order to meet the Shannon theorem for the second series of measurements the spatial resolution was increased to 299 measurement points on the same area. Furthermore, the source of excitation was changed to a speaker with a microphone as phase reference. The investigated frequency band was set from $f_{min} = 150$ Hz to $f_{max} = 1300$ Hz. Since the frequency range of both series of measurement is overlapping, it is possible to compare and verify the quality of the results of both measurements with each other. The excitation signal was changed to a white noise. In order to reduce leakage, a hanning window was used in the second set of measurements [8].

A modal analysis was performed on the measured and to the frequency-domain-transferred data with the software ME'ScopeVES™. Afterwards, the extracted modal data were sorted based on their mode shapes. The mapping of the mode shapes from one sample to another was done by utilization of the modal assurance criterion (MAC). The number assigned to the modes in this paper is therefore not necessarily based on the frequency or the number in the simulation. Instead, the compared mode shapes are highly similar.

3 Experimental Results

As already mentioned in the previous section, the two overlapping series of measurements can be used to verify the results of each excitation methods. By comparing the modes in that frequency range, it can be shown that the average frequency deviation between both setups is within the range of 0.6% and is therefore quite small. Since the natural frequencies of the shaker measurement are lower, it can be assumed that the additional mass of the force transducer is the main reason for that deviation [9, 10]. The compared mode shapes were seemingly identical.

In order to compare the change of the natural frequencies due to the damage, the eigenfrequencies of each mode of the two specimens "Pr 1 ok" and "Pr 2 ok" was averaged. The deviation of each sample to that average natural frequency is investigated in order to detect modes affected by the artificial defects. For most identified modes, the natural frequency of the specimens "Del25mm" and "Pressure" is lower than the average

frequency of the modes. For the sample "Del10mm", this effect can be observed for a fewer number of modes.

As an example, this is shown in Fig. 2 for the sixth and eleventh mode. The averaged eigenfrequency for the sixth mode is determined with $f_{06} = 178.9$ Hz and for the $f_{11} = 355.2$ Hz. In the case of Fig. 4, the 12th and 20th modes correspond to the averaged natural frequencies of $f_{12} = 371.4$ Hz and $f_{20} = 588.5$ Hz. In both figures, the grey area shows the frequency spread of the two not artificially damaged samples. For all four modes, it is clearly visible that natural frequencies of the specimens "Pressure" and "Del25mm" are about 2% lower than the average frequency. This can be interpreted as the result of a reduced stiffness due to the delamination or due to the incomplete infiltration of the resin. A comparison between the mode shapes of the 6th and 11th respectively the 12th and the 20th shows that the number of nodal lines and loops increases by one over the width of the investigated area. Since those two pairs of modes show a similar deviation to the average eigenfrequency, this could be an indication that a localization of the delaminated area is possible (Figs. 2 and 3).

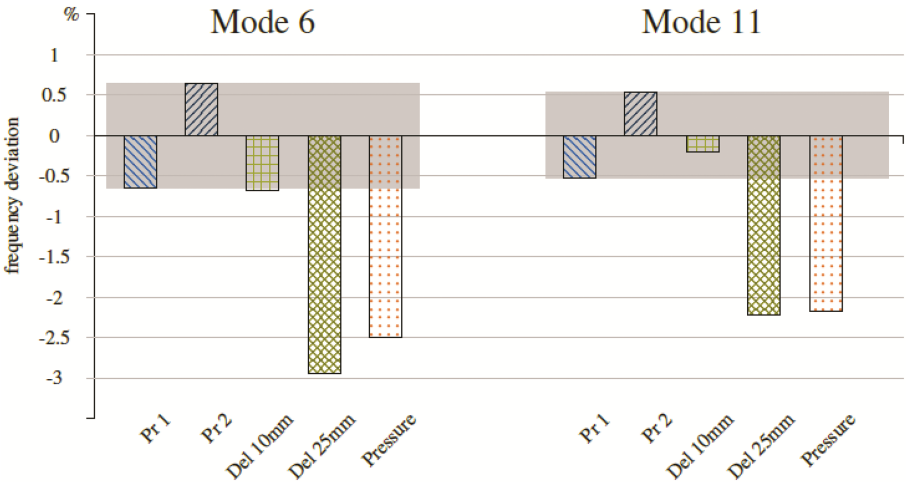

Fig. 2. Frequency deviation between specimens for sixth and eleventh mode

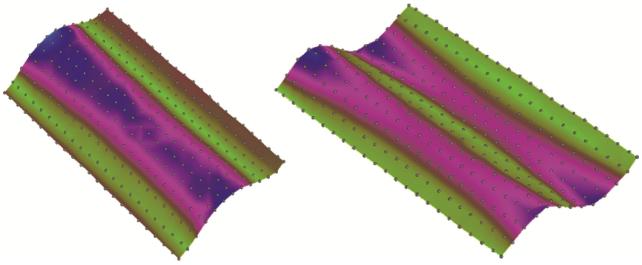

Fig. 3. Mode shape of sixth and eleventh mode

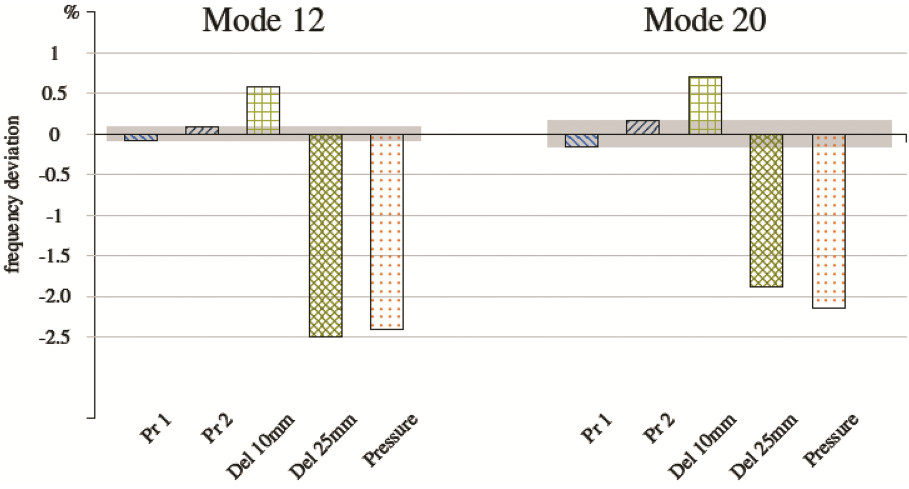

Fig. 4. Frequency deviation between specimens for 12th and 20th mode

The reasons for the deviation of specimen "Del10mm" are not obvious. For the 6th and 11th mode the decrease in frequency is smaller than the deviation of the two not artificially damaged samples. A possible explanation could be that the damage is placed on a nodal line for both modes and therefore hardly affects these two modes. For the modes 12 and 20, the natural frequency differs clearly from the two reference samples. The reasons for the higher frequency could not be conclusively clarified.

Finally, it should be noted that for all determined modes, the natural frequency of sample "Pr 2 ok" is higher than the natural frequencies of "Pr 1 ok". However, the absolute and relative difference in the frequency for those two specimens are not constant.

4 Finite Element Modeling

The FEM model for extracting the normal modes of structures ignoring damping involves solving the following eigenvalue problem as

$$\left[-\omega_i^2\mathbf{M}+\mathbf{K}\right]\left\{U_i\right\}=0$$

In which **M** and **K** are mass and stiffness matrices, receptively, ω_i and $\left\{U_i\right\}$ are the natural frequency and the mode shape of the i-th mode. The finite element model of the component samples having delamination is constructed in ANSYS® APDL. The APDL code uses parametrized model to include nominal values of geometry and material properties. Due to the small thickness of the plate respect to other dimensions, the simulation employs element "*shell181*" to capture the bending and membrane characteristics. The element has four nodes with six degrees of freedom at each node, i.e. translations in the x, y, and z directions, and rotations about the x, y, and z axis. The modal analysis

using Block Lanczos method is performed to get the natural frequencies and mode shapes.

The results are shown in Fig. 5 for modes no. 12 and 20 compared to identified experimental modes. As demonstrated, considering the complex geometry of the plate, the natural frequencies and the mode shapes for the considered modes show a good agreement. Some disagreements, however, can be detected which may be due to the presence of mismatch between material model of the implemented artificial layer with real one. A more accurate numerical model can be developed considering the material model update for the delaminated layer.

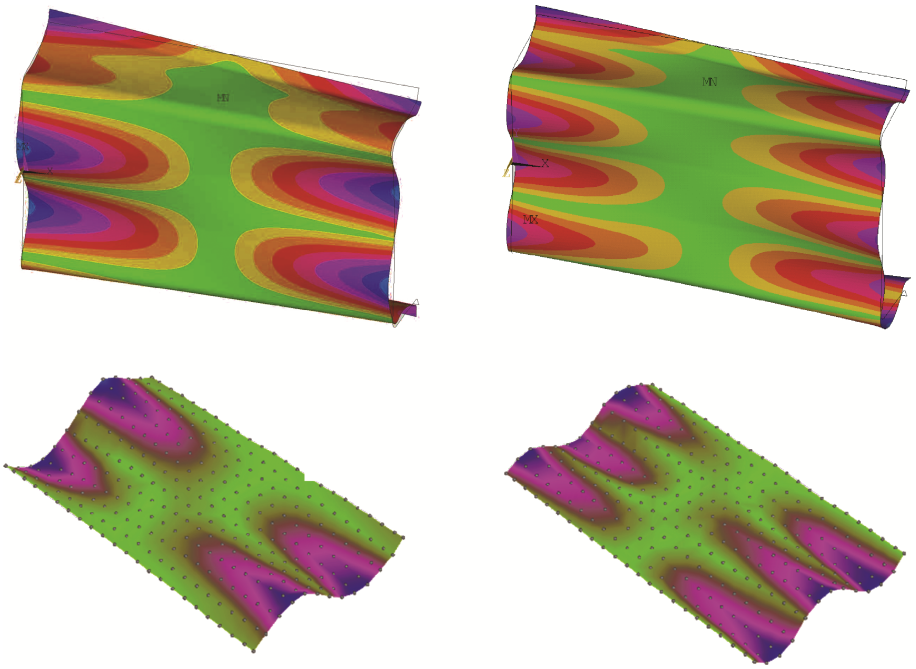

Fig. 5. Comparison of Mode shapes; left, 12th mode FEM = 345 Hz, exp. = 371.4 Hz; right: 20th mode FEM = 530 Hz, exp. = 588.5 Hz

5 Conclusions

As shown in the previous sections, it is possible to perform non-destructive testing with a vibration based method. Nevertheless, it is necessary to conduct further research in order to evaluate the precision and limitations of this method. Furthermore, it is shown that a simulation of the mode shapes is possible. Although the difference in frequency between the experimental results and the finite element model shows a good agreement, a more accurate FE-model, especially for the delamination could reduce the effort for further studies. A precise numerical model could help, taking the delamination into

account, in order to clarify the possibility of a damage localization. Further experimental studies could resolve the open questions about the precision of this method.

Acknowledgments. The research on which this paper is based on the support of Honda R&D Europe (Germany), both financially and technically. We thank them for their interest in this topic, the supply with test specimens and their support of this research.

References

1. Gladwell, G.M.L.: The inverse problem for the vibrating beam. Proc. R. Soc. Lond. **393**, 277–295 (1984)
2. Morassi, A.: A uniqueness result on crack location in vibrating rods. Inverse Probl. Eng. **4**, 231–254 (1997)
3. Stache, M., Guettler, M., Marburg, S.: A precise non-destructive damage identification technique of long and slender structures based on modal data. J. Sound Vib. **365**, 89–101 (2016)
4. Geweth, C.A., Sepahvand, K., Marburg, S.: Stochastic radiated sound power of structures with uncertain parameters. In: Proceedings of NOVEM (2015)
5. Sepahvand, K., Marburg, S., Hardtke, H.-J.: Stochastic free vibration of orthotropic plates using generalized polynomial chaos expansion. J. Sound Vib. **331**(1), 167–179 (2012)
6. Mook, G., Pohl, J., Michel, F.: Damage detection and characterization in smart CFRP composites. In: Proceedings of SPIE—The International Society for Optical Engineering, San Diego, pp. 120–128 (2002)
7. Cheikh, M.: Reanalysis of structures with modification of the stiffness, application to the modeling of damage in unidirectional composites. Comput. Struct. **78**(5), 725–736 (2000)
8. Geweth, C.A., Saati Khosroshahi, F., Sepahvand, K., Kerkeling, C., Marburg, S.: Damage detection of fibre-reinforced composite structures using experimental modal analysis. In: Procedia Engineering, X International Conference on Structural Dynamics, EURODYN 2017(2017)
9. Langer, P., Sepahvand, K., Krause, M., Marburg, S.: Simple vibroacoustic systems—influence of uncertainties in simulation and experiment. In: Proceedings of NOVEM (2015)
10. Matthews, D., Sun, H., Saltmarsh, K., Wilkes, D., Munyard, A., Pan, J.: A detailed experimental modal analysis of a clamped circular plate. In: Proceedings of 43rd Internoise (2014)

Retrofitting of Damaged Structure Using Vibration Monitoring Technique

Vishisht Bhaiya[1(✉)], Shiv Dayal Bharti[1], Mahendra Kumar Shrimali[1], and Tushar Kanti Datta[2]

[1] Department of Civil Engineering, Malaviya National Institute of Technology, Jaipur, India
vishishtbhaiya@gmail.com
[2] National Centre for Disaster Mitgation and Management, Malaviya National Institute of Technology, Jaipur, India

Abstract. Health monitoring of structures has become a popular research subject in recent years. The technique is mostly utilized for system identification through dynamic testing. System identification is required for a number of reasons like continuous monitoring of the state of the existing structures, evaluation of damages in the structure and assessment of residual strength. In this study, the evaluation procedure of the damages in the existing structure through dynamic testing is described and a suitable retrofitting strategy is proposed based on the experimental results. For this purpose, the results of the dynamic test of a five story building model representing properties on scaled prototype structure are collected to obtain its fundamental mode and fundamental frequencies of vibration. With the help of the above experimental data, a retrofitting strategy is developed to rehabilitate the structure to a desired lateral strength. The methodology consists of following steps: (i) recreating the same building model in computer to define a target strength and (ii) a static procedure for increasing the lateral stiffness of the damaged building is described from the measured mode shape and frequency of the damaged structure and those of the recreated structure. For verification of the accuracy of the retrofitting strategy, free vibration test of the retrofitted building is also carried out. The results of the study show that it is possible to design additional lateral resisting elements to increase the lateral strength of a damaged structure to target strength from the free vibration test results of the damaged structure.

Keywords: System identification · Retrofitting · Free vibration test · Damaged building

1 Introduction

A number of research studies are available on structural health monitoring and system identification techniques using the experimental data. The studies can be classified under two categories, namely classical technique and recently developed technique using sophisticated experimentation. The classical techniques include non-destructive testing (NDT), ambient vibration test and forced vibration test. These entire tests are aimed at evaluating lateral resistance of the structure to withstand lateral forces

© Springer International Publishing AG 2018
J.P. Conte et al. (eds.), *Experimental Vibration Analysis for Civil Structures*,
Lecture Notes in Civil Engineering 5, https://doi.org/10.1007/978-3-319-67443-8_12

produced due to earthquake and other sources creating lateral vibration to the structure. NDT test is used to evaluate the material strength of the materials at strategic point for evaluating the current strength of the materials used for constructing the structure, with the help of measured dimensions of the structure and current strength of material lateral resistance of the overall structure is determined. With the development of dynamic testing facilities dynamic test are favored to determine the overall lateral resistance of the structure to dynamic forces. A number of techniques are reported in the literature to identify both global and local damages using the information derived from mode shapes.

System identification is generally divided to linear and nonlinear system identification according to global characters of the structure. Nowadays, most of the structural health monitoring methods employ linear system identifications and damage detection techniques, however some research have been done in the nonlinear field. Many linear system identification methods have been introduced in the past four decades, such as: Ibrahim time domain method [1], Eigen system realization algorithm [2], poly-reference least-squares complex frequency domain method [3], peak picking method, wavelet transform [4, 5], Hilbert Huang transform [6], Parametric System Identification [7] etc. Loh and Lin [8] analyzed the dynamic characteristics of a seven-story reinforced concrete building during four earthquakes, and determined the modal frequencies and damping ratios of the building, and the time-varying properties of the parameters were also detected by using the online identification method. Sanli and Çelebi [9] studied the dynamic characteristics of a 13-story building during four earthquakes, and the natural frequency and normalized mode shape of the building were identified using the transfer functions between different channels of each earthquake record, then the damage was detected by the variation of the modal parameters. Lin and Betti [10] identified the time-varying structural parameters for damage detection purposes, and the least-square (KalmanFilter) based identification algorithm was adopted in their study. Gong and Xie [11] had presented a method to identify the time-invariant and time-varying modal parameters including the frequencies and damping ratios based on earthquake response data of a 7-story reinforced concrete building which suffered moderate damage in Chi-Chi Earthquake.

More complete information regarding the lateral resistance of the structure to the dynamic forces can be derived using forced vibration test in which the frequency response function of the structure corresponding to lateral degrees of freedom are obtained in complex domain. One of the shortcomings of the forced vibration technique is that only a limited number of measurements are possible in practice and therefore, full state of the system is estimated using different types of filter such as Kalman filter, particle filter etc. The estimation of the full state from the measured one introduces some approximation in the estimation of the frequency response function corresponding to all dynamic degrees of freedom. The advantage of this method is the ability to predict dynamic response of the structure to any future excitation producing lateral vibration. Recent techniques for system identification consist of analysing the time history of responses of the structure to any arbitrary dynamic excitation. For this, wavelet theory and Hilbert transformation are used to analyze the signals for system identification such as derivation of frequency response function.

Retrofitting strategies to be adopted for rehabilitating the structure to a target level using the information derived from the dynamic testing as stated above are not well documented in the literature. Different types of retrofitting strategies specifically for building the structures is well established and being implemented in practice. However, most of these methods are based on heuristic approach, knowledge based and expert opinion. Retrofitting of a building structure to a target level of lateral strength is difficult to implement in practice. It involves a trial and error approach method. In this paper, a simple technique of retrofitting a damaged building to achieve approximately a target lateral strength is described using experimental data obtained from ambient vibration test for a five storey building. The building strength deteriorated due to environmental effects and other factors over the passage of time. The fundamental time period of the building model and its fundamental mode shape were obtained by the ambient vibration test. This information is utilized to obtain the additional lateral stiffness to be provided in the building in the form of bracings. Ambient vibration test on the retrofitted building model was then carried out to determine its fundamental frequency and mode shapes and are compared with those of the recreated computer model of the building structure providing the target lateral strength to be achieved.

1.1 Retrofitting Strategy

Damaged building is a five storey reinforced concrete building square in plan as shown in Fig. 1. It is an old building which got damaged due to environmental effects and aging. It was decided to retrofit the building with bracings with steel joists as shown in a typical elevation of a frame (Fig. 2). It was intended to retrofit the building with bracings for achieving as close as possible to a target lateral strength to resist earthquake lateral forces. For this purpose, a prototype new building is recreated in the computer having the same dimensions of different elements of the damaged building. Fundamental mode shape and frequency of the building is theoretically determined. Ambient vibration test of the damaged building is carried out. Sensors are placed on the central frame at each storey. The building is made to vibrate by creating impact on the ground adjacent to the building. The fundamental mode shape and frequency of the building are determined from the experimental test.

Let the condensed stiffness matrix of the recreated building corresponding to sway degree of freedom be $[K_d]$ and the mass matrix without live loads be denoted by [M]. With these matrices the fundamental frequency and mode shape are obtained as ω and ϕ respectively. Let the measured frequency and mode shape of the damaged building be ω_1 and ϕ_1 respectively.

The following modal equations hold good for the two systems.

$$\left[K_d - M\omega^2\right]\phi = 0 \tag{1}$$

$$\left[\bar{K} - M\omega^2\right]\phi_1 = 0 \tag{2}$$

In Eq. (2), it is assumed the mass of the damaged building remains nearly the same as that of the recreated building. Further $\bar{K}$ is assumed to be the stiffness matrix of the

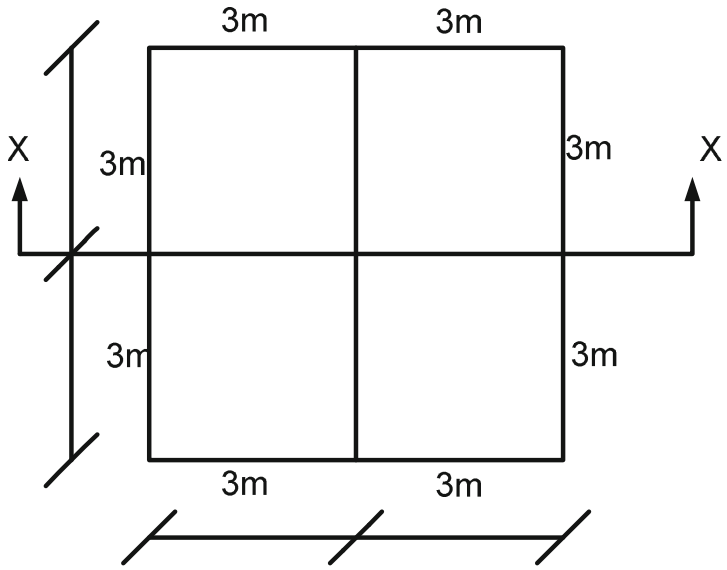

Fig. 1. Plan of the 5 story prototype building

damaged building corresponding to the sway degree of freedom which is not known. From Eqs. (1) and (2), it is easy to obtain the following equation

$$K_d\phi - \bar{K}\phi_1 = M\phi\omega^2 - M\phi_1\omega_1^2 \tag{3}$$

As a first approximation, it is assumed that the fundamental mode shapes of the damaged and recreated buildings remain nearly the same. With this assumption

$$(K_d - \bar{K})\phi = M\phi\left(\omega^2 - \omega_1^2\right) = P \tag{4}$$

Since M, ϕ, ω, ω_1 are known, P is known. Thus Eq. (4) represents a matrix equation involving the difference in lateral resistance between the two systems namely, the recreated building and the damaged building, the bracings in the damaged building are to be designed to meet this difference. Note that the procedure allows an approximate design of the bracings to be made to achieve a target lateral resistance of the damaged building without having the direct knowledge of the existing strength of the building. The mode shape and the fundamental frequency of the building derived from the ambient vibration test are sufficiently utilized to retrofit the building to target strength.

The design of the bracings meeting the difference in lateral resistances between the two systems are given by Eq. (4) is explained with the help of an example of a five storey building frame. Consider the frame in Fig. 2. Five bracings are provided in five

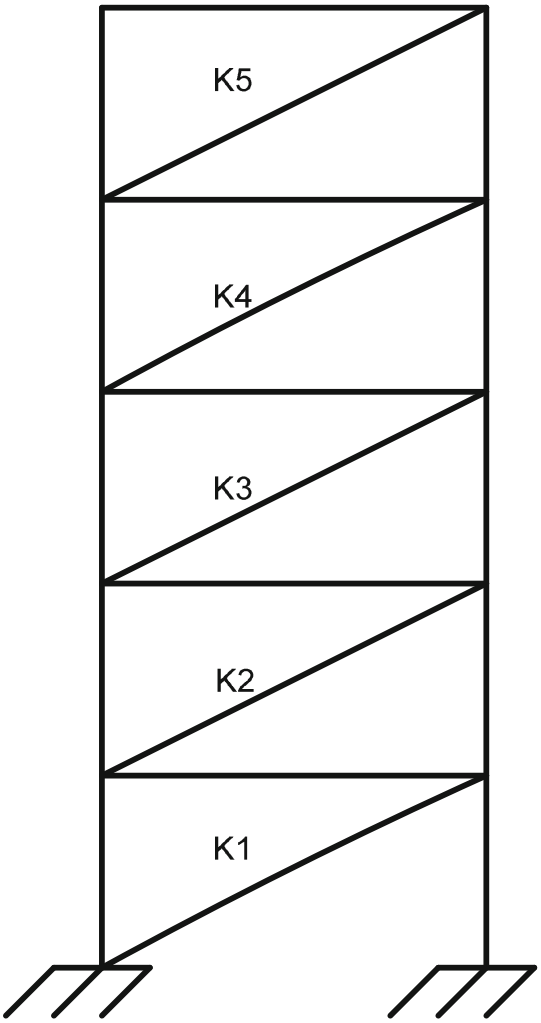

Fig. 2. Elevation of the 5 story prototype building

storey's as shown in the Fig. 2. Let K_i(i = 1,…,5) be the lateral stiffness provided by each bracing. Equation (4) may be extended in matrix form as

$$\begin{bmatrix} (\Delta K_1 + \Delta K_2) & -\Delta K_2 & 0 & 0 & 0 \\ -\Delta K_2 & (\Delta K_2 + \Delta K_3) & -\Delta K_3 & 0 & 0 \\ 0 & -\Delta K_3 & (\Delta K_3 + \Delta K_4) & -\Delta K_4 & 0 \\ 0 & 0 & -\Delta K_4 & (\Delta K_4 + \Delta K_5) & -\Delta K_5 \\ 0 & 0 & 0 & -\Delta K_5 & \Delta K_5 \end{bmatrix} \begin{matrix} \phi_1 \\ \phi_2 \\ \phi_3 \\ \phi_4 \\ \phi_5 \end{matrix} = \begin{Bmatrix} P_1 \\ P_2 \\ P_3 \\ P_4 \\ P_5 \end{Bmatrix} \quad (5)$$

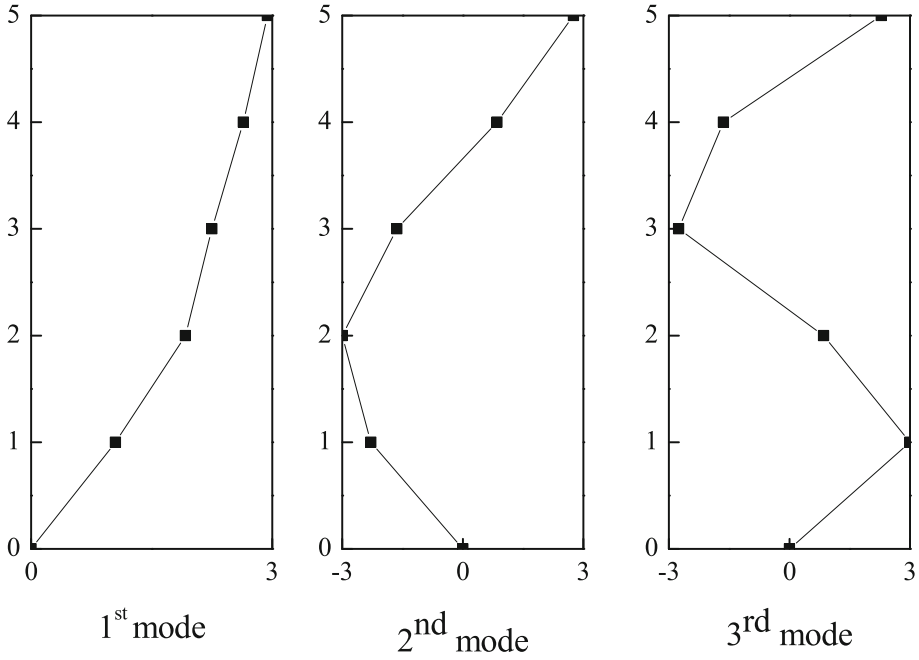

Fig. 3. Theoretical mode shapes of the recreated building'

in which ΔK_i represents the difference in the lateral stiffness of the ith floor between the two systems. It is clear from the above equation that $\Delta K_i = K_i$.

Equation (5) can be expanded in the following form after substituting ΔK_i by K_i.

$$\begin{aligned}
&(K_1 + K_2)\phi_1 - K_2\phi_2 = P_1 \\
&- K_2\phi_1(K_2 + K_3)\phi_2 - K_3\phi_3 = P_2 \\
&- K_3\phi_2(K_3 + K_4)\phi_3 - K_4\phi_4 = P_3 \\
&- K_4\phi_3(K_4 + K_5)\phi_4 - K_5\phi_5 = P_4 \\
&- K_5\phi_4 + K_5\phi_5 = P_5
\end{aligned} \tag{6}$$

The set of algebraic equations (Eq. 6) can be rearranged in the following form:

$$\begin{aligned}
&- K_1\phi_1 + K_2(\phi_1 - \phi_2) = P_1 \\
&K_2(\phi_2 - \phi_1) + K_3(\phi_2 - \phi_3) = P_2 \\
&K_3(\phi_3 - \phi_2) + K_4(\phi_3 - \phi_4) = P_3 \\
&K_4(\phi_4 - \phi_3) + K_5(\phi_4 - \phi_5) = P_4 \\
&K_5(\phi_5 - \phi_4) = P_5
\end{aligned} \tag{7}$$

When the set of equations (Eq. 7) are written in matrix form, it takes the form

$$\begin{bmatrix} \phi_1 & (\phi_1-\phi_2) & 0 & 0 & 0 \\ 0 & (\phi_2-\phi_1) & (\phi_2-\phi_3) & 0 & 0 \\ 0 & 0 & (\phi_3-\phi_2) & (\phi_3-\phi_4) & 0 \\ 0 & 0 & 0 & (\phi_4-\phi_3) & (\phi_4-\phi_5) \\ 0 & 0 & 0 & 0 & (\phi_5-\phi_4) \end{bmatrix} \begin{Bmatrix} K_1 \\ K_2 \\ K_3 \\ K_4 \\ K_5 \end{Bmatrix} = \begin{Bmatrix} P_1 \\ P_2 \\ P_3 \\ P_4 \\ P_5 \end{Bmatrix} \quad (8)$$

Equation 8 is an upper triangular matrix. Hence, K_i i = 1, 2, …, 5) can be easily obtained by solving the above matrix.

With computed values of K_i (i = 1, 2, …, 5) the cross sectional area of the bracings is obtained using Eq. (9)

$$A_i = \frac{K_i L}{E} \quad (9)$$

where E is the modulus of elasticity of steel and L is the length of the bracing.

2 Numerical Study

2.1 Damaged Structure

Beam sizes: 250 mm × 450 mm in longitudinal direction and 250 × 350 mm in transverse direction.
Column sizes: 250 mm × 450 mm
Infill wall: 250 mm thick in longitudinal and 150 mm in transverse direction.
Slab thickness: 100 mm

2.2 Recreated Structure

Same dimensions are retained with M40 concrete

2.3 Design of Bracings

Using Eq. 4, P_1 to P_5 and Eq. 8, K_1 to K_5 are calculated as:

P_1 = 1478, P_2 = 2993, P_3 = 4584, P_4 = 13040, P_5 = 157440

K_1 = 30242 kN/m, K_2 = 31200 kN/m, K_3 = 32362 kN/m, K_4 = 35800 kN/m, K_5 = 38252 kN/m

The area required for bracing is given as using Eq. 9,

A_1 = 696 mm^2, A_2 = 719 mm^2, A_3 = 745 mm^2, A_4 = 825 mm^2, A_5 = 881 mm^2

ISA angles of size 60 × 60 × 8 mm are used for bracings at each floor.

The ambient vibration test results of the damaged building are shown in Fig. 4. Records of the damped free vibration of two floors obtained from the sensors are shown in the Fig. 4. The fundamental mode shapes are normalized within a maximum value of three in order to match the fifth floor sensor record of the fifth floor with amplitude of 3 V. All the mode shapes are theoretically calculated and are also normalized with respect to

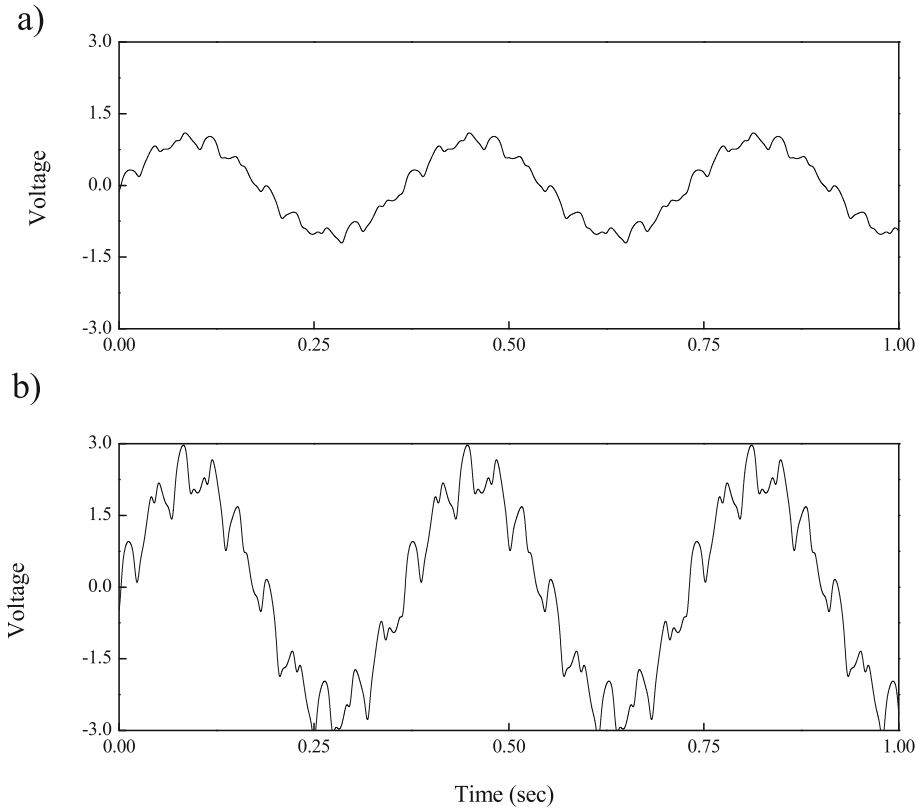

Fig. 4. Ambient vibration test results for (a) sensor at 2nd floor and (b) sensor at 5th floor for the damaged building

fifth floor value of three. For the purpose of comparison, the first three mode shapes of the recreated building are shown in Fig. 3. The fundamental time period of the recreated building is obtained as 0.4 s. It is seen that the fundamental period of the damaged building model is about 1.4 times of that of recreated building. The bracings provided to retrofit the damaged building are shown in Fig. 2. The bracings are designed as explained earlier. The bracings are connected as diagonal members in the frame in both directions. The bracings were connected to the beam column joints with the help of suitable connections in the panel.

Table 1. Comparison of time periods

Time period	T_1 (sec)	T_2 (sec)	T_3 (sec)
Damaged	0.58	0.18	0.12
Recreated	0.4	0.15	0.09
Retrofitted	0.42	0.16	0.1

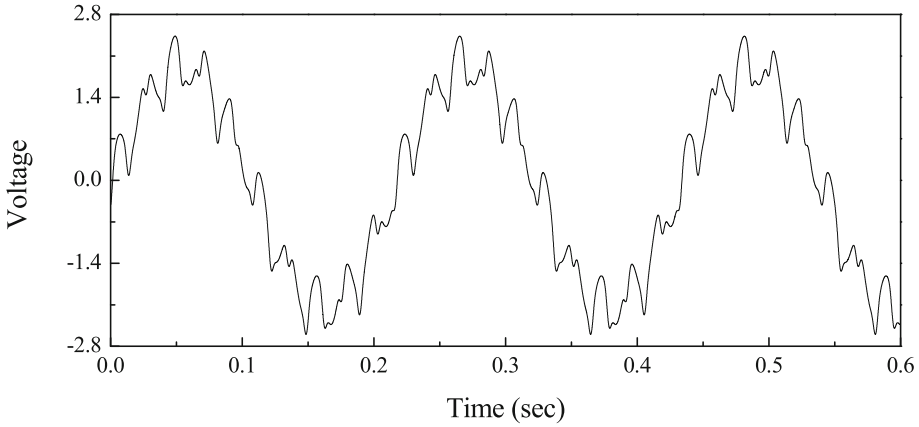

Fig. 5. Ambient vibration test results for the sensor placed at fifth floor of the retrofitted building

Ambient vibration of the retrofitted building was carried out. Table 1 shows a comparison of the first three time periods of the damaged, recreated and retrofitted building. In Fig. 5, the free vibration record of the fifth floor is shown. In the Fig. 6, the fundamental mode shapes of the damaged, recreated and retrofitted building were compared. It is seen from the figure that there is no significant difference in the

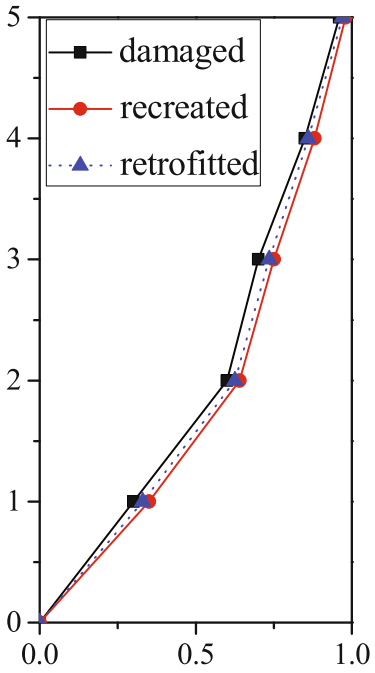

Fig. 6. First mode shapes of the damaged, recreated and retrofitted building

fundamental mode shape of the three building models. However, fundamental time period of the three buildings are different. The periods of the retrofitted building and recreated building are quite closed, indicating that retrofitting strategy is adequate to achieve the target lateral strength for the damaged building.

3 Conclusions

A simple retrofitting strategy is presented to strengthen the damaged building for achieving target strength. For this purpose, ambient vibration test of damaged and retrofitted building models are carried out in order to determine their fundamental mode shapes and time periods. Recreated building is designed and analyzed in order to define the target strength to be achieved. Results of the study indicate that the retrofitting strategy is quite satisfactory to achieve a target strength using a simple technique of retrofitting by the way of providing diagonal bracings in the frame of the damaged building.

References

1. Ibrahim, S.R.: A Time Domain Vibration Test Technique. University of Calgary, Calgary (1973)
2. Juang, J.-N., Pappa, R.S.: An eigensystem realization algorithm for modal parameter identification and model reduction. J. Guid. Control Dyn. **8**(5), 620–627 (1985)
3. Peeters, B., Lowet, G., Van der Auweraer, H., Leuridan, J.: A new procedure for modal parameter estimation. Sound Vib. **38**(1), 24–29 (2004)
4. Daubechies, I.: Ten Lectures on Wavelets, vol. 61. SIAM, Philadelphia (1992)
5. Graps, A.: An introduction to wavelets. IEEE Comput. Sci. Eng. **2**(2), 50–61 (1995)
6. Huang, N.E., Shen, Z., Long, S.R., Wu, M.C., Shih, H.H., Zheng, Q., Yen, N.-C., Tung, C. C., Liu, H.H.: The empirical mode decomposition and the Hilbert spectrum for nonlinear and non-stationary time series analysis. In: Proceedings of the Royal Society of London A: Mathematical, Physical and Engineering Sciences. The Royal Society (1998)
7. Ljung, L.: Model Validation and Model Error Modeling. Linköping University Electronic Press, Linköping (1999)
8. Loh, C.H., Lin, H.M.: Application of off-line and on-line identification techniques to building seismic response data. Earthq. Eng. Struct. Dyn. **25**(3), 269–290 (1996)
9. Sanli, A., Çelebi, M.: Earthquake damage detection of a thirteen story building using recorded responses. In: Proceedings of 3rd International Workshop on Structural Health Monitoring, Stanford University, Stanford, CA (2002)
10. Lin, J.W., Betti, R.: On-line identification and damage detection in non-linear structural systems using a variable forgetting factor approach. Earthq. Eng. Struct. Dyn. **33**(4), 419–444 (2004)
11. Gong, M., Xie, L.: Structural damage identification under strong earthquake excitation. In: The 2nd International Conference on Structural Health Monitoring of Intelligent Infrastructure (2005)

Experimental Damage Identification Using SVD-Based Sensitivities of Truncated Transfer Function

Mohammad Rahai[1], Ali Bakhshi[1(✉)], and Akbar Esfandiari[2]

[1] Department of Civil Engineering,
Sharif University of Technology, Tehran, Iran
bakhshi@sharif.edu
[2] Department of Marine Engineering,
Amirkabir University of Technology, Tehran, Iran

Abstract. In this paper, the application of SVD-based Principal Component Analysis (PCA) performed on truncated form of transfer function is demonstrated. Damage scenarios with light severity and distributed locations could be detected, localized and quantified using a one-step model updating. The objective of this study is to demonstrate the application of SVD-based Principal Component Analysis performed on moving windows of transfer function. It uses the sensitivities of measured responses in frequency domain, its singular values and right eigenvectors for FE model updating in an efficient way, by developing a quasi-linear sensitivity equation of structural response. The benefit of applying PCA for dynamical systems comes from its ability to detect and rank the dominant coherent spatial and frequency-dependent information of dynamic response. An experimental study on a concrete beam has been validated to show the ability of this technique for damage detection.

Keywords: Finite element method · Structural model updating · Singular value decomposition · Sensitivity equation · Damage detection

1 Introduction

Most of technical literature in the SHM context has been dedicated to feature extraction and parameter estimation [1]. In this regard, there are two main approaches in parameter estimation: (a) model-free techniques and (b) model-updating techniques [1]. Many model-based approaches generally utilize frequency domain data. These, indeed, give a clearer picture of modal characteristics of structures, such as: natural frequency, mode shapes and frequency response functions etc. Modal-based damage identification methods often use damage equations based on sensitivities of structural parameters. In this regard, robust sensitivity equations would improve the updating algorithms against existing errors. Sensitivities of natural frequency was evaluated by [2, 3] which cannot provide enough information for localization of damage. Hence, mode shapes were have been utilized to enhance spatial information of damage [4, 5]. Modak et al. [6] used experimental frequency response function data to update model of structure in direct and iterative method. Esfandiari et al. [7] proposed a new method based on quasi-linear

© Springer International Publishing AG 2018
J.P. Conte et al. (eds.), *Experimental Vibration Analysis for Civil Structures*,
Lecture Notes in Civil Engineering 5, https://doi.org/10.1007/978-3-319-67443-8_13

sensitivity equation of FRF without using derivative of FRF and using measurement of some data, not all of them. Yuan and Yu [8] developed a complex form of FRF with respect to base excitation. They tried to handle damping issue by explaining the idea of "step by step" model updating. Esfandiari et al. [9] presented a damage detection algorithm for linear structures using Fisher Information Matrix and stored strain energy concepts. Pedram et al. [10] introduced the spectral density of strain as a high-sensitive parameter to structural changes under random excitation. Sipple and Sanayeie [11] studied parameter grouping and ungrouping schemes for FRF-based FE model updating of link stiffness of UCF grid structure.

The central idea of the PCA was appeared in Beltrami [12], while it is commonly reported that the first implicit form of the PCA was suggested by Pearson [13] in the biological field. PCA is a powerful tool for analyzing high-dimensional data which can express their similarities and differences by describing it compactly. It reduces the number of dimensions by transforming the original data to a new uncorrelated dataset, the principal components [14]. Da Silva et al. [15] proposed an Autoregressive moving average model by data compressing in time domain using of PCA. Then, fuzzy clustering techniques was applied to classify damage in Benchmark frame structure. Papadopoulo and Lourakis [16] utilized an exact analytic technique for estimating the Jacobian of the SVD components of a matrix with respect to the matrix itself. Ahmdian et al. [17] outlined SVD as a useful way to regularize ill-conditioned equations required for parameter estimation. De Boe and Golinval [18] was applying PCA on sensors time response and compared it with the intact structure to diagnosis damage.

2 Theoretical Development

For a linear time invariant structure, the transfer function of the structure is defined as

$$H(\omega) = (-\omega^2 M + j\omega C + K)^{-1} \tag{1}$$

Where K, M and C are stiffness, mass and damping matrices, respectively. ω is the frequency of the excitation load and $j = \sqrt{-1}$.

For a single input force at the location s, a subset of the FRFs is expressed as

$$H^s = \begin{pmatrix} h_1(\omega_1) & \dots & h_1(\omega_n) \\ \vdots & \ddots & \vdots \\ h_m(\omega_1) & \cdots & h_m(\omega_n) \end{pmatrix}_{m \times n} \tag{2}$$

m is the number of DOFs equipped with sensors for response measurement and n is the number of excitation frequencies.

Using the SVD technique, the modified FRF matrix, H^s can be expressed as

$$H^s = U \Sigma V^T \tag{3}$$

Where U and V are $m \times m$ and $n \times n$ orthogonal matrices, representing left and right singular matrices, respectively. Σ is the $m \times n$ diagonal matrix containing singular

values in descending order. The singular values can be interpreted geometrically as the projections of the observations onto the PCs. The following properties are attributed to left and right singular matrices as

$$UU^T = 1 \tag{4}$$

$$VV^T = 1 \tag{5}$$

Damage location and severity can be determined by the sensitivity equation derived from both the columns of V and non-zero entries of Σ. They represent frequency-dependent information of measurement data and factor scores, respectively. Therefore, Eq. (3) has been rewritten as

$$\Sigma = U^T H^s V \tag{6}$$

For the damaged structure, Eq. (6) is expressed as

$$\Sigma + \delta\Sigma = (U + \delta U)^T (H^s + \delta H^s)(V + \delta V) \tag{7}$$

Where δU, $\delta\Sigma$, δV, and δH^s represent changes of the corresponding matrices due to damage. Using the FRF matrix of the damaged structure, U_d, Σ_d, V_d are obtained from the SVD of modified H^s_d. Therefore, δU, $\delta\Sigma$, and δV can be calculated as

$$\delta\Sigma = \Sigma_d - \Sigma \tag{8}$$

$$\delta U = U_d - U \tag{9}$$

$$\delta V = V_d - V \tag{10}$$

Neglecting high-order changes, Eq. (11) can be obtained by expanding Eq. (7) and subtracting it from Eq. (7)

$$\delta\Sigma_k - (U_{:k})^T H^s \delta V_{:k} - (\delta U_{:k})^T H^s \delta V_{:k} - (\delta U_{:k})^T H^s \delta V_{:k} \cong U^T_{:k} \delta H^s V_{:k} \tag{11}$$

Where, $U_{:k}$ and $V_{:k}$ are the k^{th} column of U and V matrices, respectively, and Σ_k is the k^{th} entry of Σ. The value of k is between 1 to maximum required PCs and should not exceed the minimum of m and n. Equation (11) relates the change of each PC to the change of the modified FRF matrix which is inherently a function of changes of structural parameters. For the k^{th} PC, Eq. (11) can be rewritten as

$$\delta r^k_\Sigma \cong S^k_\Sigma \delta P \tag{12}$$

Where δr^k_Σ is the left side of Eq. (11). Therefore, the value of δr^k_Σ is known. S^k_Σ is the sensitivity matrix and relates the changes of the k^{th} singular values to the changes of mass, stiffness and damping parameters. δP is a vector which contains unknown damage percentage of all structural elements. δH^s illustrates the changes of the

modified FRF matrix and can be extracted from changes of the measured FRFs. Therefore, the change of the snapshot FRF matrix (δH^s) is expressed as:

$$\delta H^s = \begin{pmatrix} \delta h_1(\omega_1) & \cdots & \delta h_1(\omega_n) \\ \vdots & \ddots & \vdots \\ \delta h_m(\omega_1) & \cdots & \delta h_m(\omega_n) \end{pmatrix}_{m \times n} \tag{13}$$

(l, q) entry of δH^s expresses the change of FRF at the l^{th} measurement location for the q^{th} excitation frequency. Perturbed FRF response of the structure can be expressed as [7]

$$\delta H(\omega) = -H^d(\omega)(\delta K + j\omega\delta C - \omega^2 \delta M)H(\omega) \tag{14}$$

Where, superscript d indicates the damaged state of the structure. Assuming that damage only causes changes in the stiffness matrix, the (l, q) entry of δH^s is evaluated as

$$\delta H^s_{lq}(\omega) = -H^d_l(\omega_q)(\delta K)H_s(\omega_q) \tag{15}$$

$H^d_l(\omega_q)$ is the l^{th} row of the transfer function of the damaged structure and $H_s(\omega_q)$ is the s^{th} column of the transfer function of the intact structure. The perturbed global stiffness matrix of the structure is constructed by assembling the elemental stiffness matrix as [19]

$$\delta K = A\delta P A^T \tag{16}$$

Where, $\delta P(\mathrm{n}_e \times \mathrm{n}_e)$ is the changes of elemental stiffness parameters caused by the damage. $A(\mathrm{n} \times \mathrm{n}_e)$ is defined as the stiffness connectivity matrix. Substituting Eq. (20) into Eq. (15), with some mathematical manipulations, $\delta H^s_{lq}(\omega)$ converts to be a function of damage as

$$\delta H^s_{lq}(\omega) = -H^d_l(\omega_q) A diag\left(A^T H_s(\omega_q)\right)\delta P = S^s_l(\omega_q)\delta P \tag{17}$$

Where, $S^s_l(\omega_q)$ is the sensitivity equation for the change of frequency-domain response at the l^{th} measurement location with respect to the q^{th} excitation frequency subjected to the excitation at the s^{th} location. Therefore, using Eq. (23), the sensitivity equation for the matrix δH^s, is obtained as

$$\delta H^s = \begin{bmatrix} \left[S^s_1(\omega_1)\delta P\right] & \cdots & \left[S^s_1(\omega_n)\delta P\right] \\ \vdots & \ddots & \vdots \\ \left[S^s_m(\omega_1)\delta P\right] & \cdots & \left[S^s_m(\omega_n)\delta P\right] \end{bmatrix}_{m \times n} \tag{18}$$

Using the above definition for δH^s, sensitivity of the k^{th} singular value is expressed as

$$S^k_\Sigma = \sum_{l=1}^{m}\sum_{q=1}^{n} U^d_{lk} S^s_l(\omega_q) V^d_{qk} \tag{19}$$

3 Model Updating Procedure

3.1 Incomplete Measurements

The exact sensitivity of the Principal Components (PCs) necessitates full measurement of the FRF of the damaged structure, $H_d(\omega)$, which is quite impractical. The full measurement of this matrix is impossible due to practical and technical limitations. Furthermore, the excitation and measurement of rotational and embedded DOFs are technically difficult and needs special devices. In order to avoid the need for full measurement of FRF, it is approximated using the decomposed form of the transfer function. It can be estimated Using the measured natural frequencies and damping loss factors of the damaged structure, Ω_{di} and ξ_{di}, and numerical mode shapes, natural frequencies and damping loss factor of the intact structure, ϕ, Ω_i and ξ_i, respectively as

$$H_d(\omega) \cong \sum_{i=1}^{nm} \frac{\phi_i \phi_i^T}{\Omega_{di}^2 - \omega^2 + 2j\xi_{di}\Omega_{di}\omega} + \sum_{i=nm+1}^{m} \frac{\phi_i \phi_i^T}{\Omega_i^2 - \omega^2 + 2j\xi_i\Omega_i\omega} \tag{20}$$

where nm is the number of the measured natural frequencies and m is the number of DOFs. The second term is considered to alleviate the adverse effect of incompleteness in higher frequency ranges. This term in the approximate formula accelerate the rate of convergence. It also helps the sensitivity equation to be more precise during the model updating process, by incorporating the updated natural frequency and mode shapes of the higher modes to the successive iteration of model updating.

The damping effect on the response rapidly decreases by moving away from the resonance frequencies. In this paper, modeling and updating of damping is ignored because exciting frequencies are considered far from resonance frequencies. Equation (20) results in a proper approximation of $H_d(\omega)$, provided that excitation frequencies is close to the natural frequencies, as considered in this paper. By considering the exciting frequencies near the natural frequencies, the denominator of Eq. (20) is dominated, therefore taking the mode shapes of the intact structure instead of the damaged one can be neglected. However, the exciting frequencies should not be very close to the natural frequencies to prevent resonance phenomena.

3.2 Updating Frequency Ranges

For parameter estimation, it is necessary to have the highest value of change in the response due to changes in the unknown structural parameters. In this regard, updating frequency points should be located around resonant frequencies, where the amplitude of vibration is relatively large and changes rapidly by damage. At frequency ranges corresponding to low vibration amplitude, structural response may highly be affected by noise levels. It proves the incapability of these points for a robust model updating. On the other hand, using excitation frequency close to resonant frequency makes the model sensitive to damping factors and its errors, as illustrated in Fig. 1. This idea has been applied to the updating process, not to update the damping matrix and avoid facing a non-monotonous objective function.

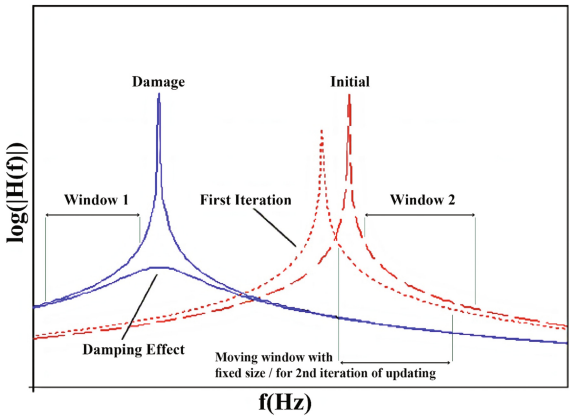

Fig. 1. Updating region of frequencies adopted from [20]

As shown in Eq. (11), singular vectors and their changes play an important role in obtaining large amounts of sensitivities of PCs and neglecting high-order terms. Hence, for a specific excitation location, the percentage of change of right and left singular matrices after damage can be considered as a scale to adopt the best updating frequency points. The response data of the intact structure have almost the same spatial data as that of the damaged one when they correspond to the same updating frequencies (windows 1 and 2, Fig. 1). When two classes of data related to both windows are used for applying SVD, PCs can't describe the major trends of variations of vectors. Hence, low amounts of changes in left and right eigenvectors have been obtained and neglecting high-order terms in Eq. (11) is meaningful.

4 Experimental FE Model Updating

In order to investigate the ability of the proposed method to predict stiffness parameters for cases of extensive damage as well as its robustness against measurement errors, a laboratory beam was tested. Figure 2 shows the experimental setup for a reinforced concrete beam. The laboratory beam was dynamically tested in the intact stage. FE model of concrete beam was calibrated using measured FRFs and the proposed model updating method. Then, it is damaged using a two-point static loading, dynamically tested again, and updated using the FRFs for the damaged beam. Finally, distributed damage caused by static load of 65 kN was detected and quantified in the form of changes in bending parameters of the beam.

Figure 3 shows the details of the FE model of the concrete beam and excitation and measured points. Since during the extreme damage, concrete cracks are expected to propagate along the depth of the beam, element lengths are chosen to be close to the depth of the beam to capture changes in bending rigidities. The FE model of the beam consists of 28 beam elements with two DOFs at each node, a transverse translation and a rotation. Two vertical springs were considered to model boundary conditions at the supports.

Fig. 2. Concrete beam with a two-point static loading setup [21]

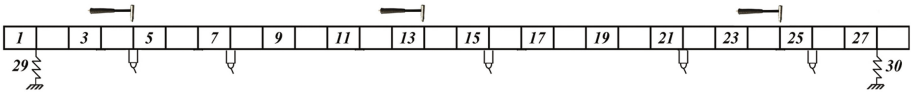

Fig. 3. Finite element model of the concrete beam

Only stiffness parameters were calibrated because damage is not severe enough to change the whole mass of the structure.

The concrete beam was excited at DOFs 9, 29, 51 and acceleration responses were measured at DOFs 9, 15, 43, 51, 31. The sampling rate was 4096 Hz. Since the 731A Wilcoxon accelerometers behave linearly below 200 Hz, model updating can be performed only below 200 Hz. This is an acceptable range for this application.

Two springs at the supports were considered to model the effect of the rubber pads on the stiffness of the beam and the beam's response. The stiffness of springs at the supports should be calibrated to match the FE model with the measured data. Initial values for the stiffness parameter of the rubber pads were considered as 70 MN/m. This value was used to update the model roughly and better match the natural frequencies of the initial FE model and experimental natural frequencies. Updated numerical and experimental natural frequencies for the initial model were compared to the experimental natural frequencies and given in Table 1.

This Table shows the percentage differences of natural frequencies of the initial FE model with respect to the experimental. The % Difference w.r.t Experimental natural frequencies is calculated as 100*(Initial Numerical − Experimental)/Experimental). For the initial model updating and also damage cases that follow, the frequency ranges were selected based on the data selection guidelines stated above and the quality of the experimental FRFs. The range of selected excitation frequencies were used for FE model updating as shown in Table 2. In these frequency ranges, FRFs are sensitive to changes in structural parameters, and optimization algorithms exhibit smooth and monotonous behavior. Such frequency points are located around the natural frequencies of the intact and damaged structures. Window 1 and 2 are starting frequency points

Table 1. Intact stage: experimental and updated frequencies of concrete beam

Mode number	Analytical model (updated) (Hz)	Experimental beam (Hz)	Relative difference % (with respect to exp.)	
1	13.097	13.088	−0.122	0.069
2	49.915	49.803	0.244	0.225
3	97.920	97.873	0.317	0.048
4	138.600	140.734	−2.403	−1.516
5	173.578	177.805	0.256	−2.377

Table 2. Updating frequency ranges

	Around mode 1 (Hz)	Around mode 2 (Hz)	Around mode 3 (Hz)
Window 1	5–10	35–40	90–97
Window 2	14–18	53–58	118–125

for model updating around considered mode shapes. They may change during further updating iterations with a fixed size to make the model converge to realistic results.

Using the proposed method of parameter estimation for FE model calibration, all of the beam parameters, including flexural rigidities of the beam elements and axial stiffness of the spring elements were updated in a single updating process. Predicted values for the stiffness of springs at the left and right side of the concrete beam were estimated at 44.8 MN/m and 46.4 MN/m, respectively. Figure 4(a) shows updated bending rigidities of the intact concrete beam elements.

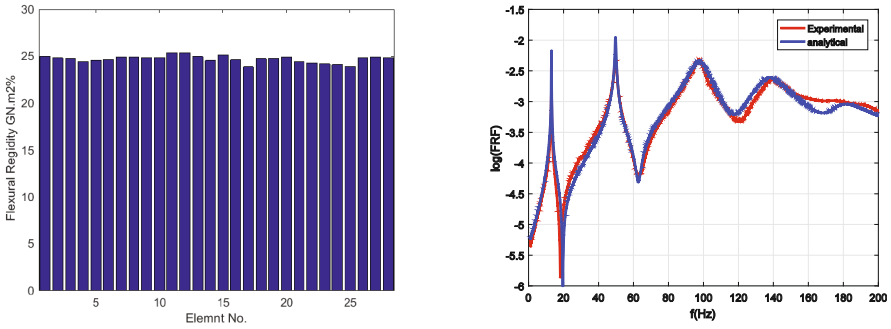

Fig. 4. (a) Intact stage: updated flexural rigidities of concrete beam FEM. (b) Intact stage: measured and updated FRF at DOF 9 with excitation at DOF 9

Figure 4(b) shows great match between the updated and experimental FRFs of the beam at DOF #9 subjected to the excitation at DOF #9, indicating a well-calibrated FE model of the intact beam. Differences between the FRFs at higher excitation frequencies are related to measurement and modeling error, especially those related to the

damping modeling. After calibration of the FE model of the intact beam, the concrete beam underwent the loading stage of 65 kN to induce distributed cracks in concrete and consequently decreases the effective bending rigidities EI. During the static loading process, the rubber pads were removed to prevent any damage to the pads and were replaced during the next stage of vibration testing. After causing damage by static loading, a new set of impact tests were performed. Table 3 shows the measured natural frequencies of the damaged beam. The last two columns show the relative difference between the intact initial FE model and the experimental FRFs (100*(initial − experimental)/experimental), and between the updated FE model and the experimental FRFs (100*(updated − experimental)/experimental). As this table shows, there was a close match between first three natural frequencies. The bending rigidity of all beam elements and the axial spring stiffness of two support were updated simultaneously. The percentage of stiffness reduction with regard to the initial values for bending rigidity along the beam length is plotted in Fig. 5(a). This Damage case shows about 23% damage compared the intact condition between the two point loads near the center and gradually reduced on the sides of the concrete beam. At this stage of updating, stiffness parameters of elements number 1 and 28 in Fig. 3 were not considered in model updating because they are located beyond the supports and do not contribute to major curvatures of the structural responses. Figure 5(b) compares a sample of the

Table 3. Natural frequencies of initial, updated and experimental models- loading stage

Mode number	Analytical model (intact) (Hz)	Analytical model (updated) (Hz)	Exp. beam (damaged) (Hz)	Relative difference % (with respect to exp.)	
				Initial	Updated
1	13.097	12.21	12.1	8.24	0.91
2	49.915	46.45	46.2	8.04	0.54
3	97.920	93.58	92.8	5.52	0.84
4	138.600	134.63	130.19	6.46	3.41
5	173.578	167.78	165.56	4.84	1.34

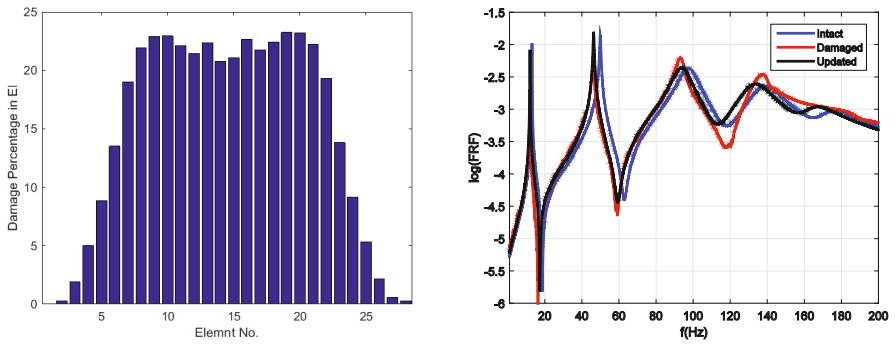

Fig. 5. (a) Loading stage: updated flexural rigidities of concrete beam FEM. (b) Loading stage: measured and predicted FRF at DOF 9 with excitation at DOF 9

predicted FRF at DOF 9 with respect to excitation at DOF 9. Predictions for this stage of model updating show a close match between the predicted and experimental resonances and anti-resonances of beam model. It demonstrates the ability of the proposed method to locate and quantify extensive distributed damage in the concrete beam using the proposed SVD-based method.

5 Conclusions

In this paper, a new sensitivity equation is obtained for estimating location and severity of structural damage at the element level by principal components analysis of the incomplete frequency response functions (FRFs). In order to drive the sensitivity equation, only PCs of the FRFs and measured natural frequencies. The proposed SVDD-based method is presented as a one-step model updating technique. Hence, it does not need to predict the potential damage locations at the beginning to narrow the search space for better damage quantification in the next step. The selected frequency windows of FRFs used for FE model updating is based on making large differences between objective functions of the damaged and intact structures for successful model updating. After calibrating the intact model, loading stage of 65 KN resulted in distributed 23% damage in the middle of the beam. Closeness of the main modal features of updated FE and experimental models confirms the accurate results of damage severity and location. Future work could extend the model updating approaches to incorporate more dependencies between sensor data interpretation in the frequency domain. The main contribution of the results of this loading stage is that this method can firmly detect and quantify distributed low-level damages occurring in noisy conditions of the laboratory. Low-level frequency ranges are selected for model updating which is practical for real situations.

References

1. Farrar, C.R., Worden, K.: An introduction to structural health monitoring. Philos. Trans. R. Soc. Lond. A **365**(1851), 303–315 (2007)
2. Salawu, O.: Detection of structural damage through changes in frequency: a review. Eng. Struct. **19**(9), 718–723 (1997)
3. Khiem, N., Toan, L.: A novel method for crack detection in beam-like structures by measurements of natural frequencies. J. Sound Vib. **333**(18), 4084–4103 (2014)
4. Zhang, Y., Wang, L., Xiang, Z.: Damage detection by mode shape squares extracted from a passing vehicle. J. Sound Vib. **331**(2), 291–307 (2012)
5. Li, H., Wang, J., Hu, S.-L.J.: Using incomplete modal data for damage detection in offshore jacket structures. Ocean Eng. **35**(17), 1793–1799 (2008)
6. Modak, S.V., Kundra, T.K., Nakra, B.C.: Prediction of dynamic characteristics using updated finite element models. J. Sound Vib. **254**(3), 447–467 (2002)
7. Esfandiari, A., Bakhtiari-Nejad, F., Rahai, A., Sanayei, M.: Structural model updating using frequency response function and quasi-linear sensitivity equation. J. Sound Vib. **326**, 557–573 (2009)

8. Yuan, Z.X., Yu, K.P.: Finite element model updating of damped structures using vibration test data under base excitation. J. Sound Vib. **340**, 303–316 (2015)
9. Bakhtiari-Nejad, F., Rahai, A., Esfandiari, A.: A structural damage detection method using static noisy data. Eng. Struct. **27**(12), 1784–1793 (2005)
10. Pedram, M., Esfandiari, A., Khedmati, M.R.: Finite element model updating using strain-based power spectral density for damage detection. Struct. Control Health Monit. **23** (2), 286–302 (2016)
11. Sipple, J.D., Sanayei, M.: Finite element model updating of the UCF grid benchmark using measured frequency response functions. Mech. Syst. Signal Process. **46**(1), 179–190 (2014)
12. Beltrami, E.: Sulle funzioni bilineari. Giornale di Matematiche ad Uso degli Studenti Delle Universita **11**(2), 98–106 (1873)
13. Peason, K.: On lines and planes of closest fit to systems of point in space. Philos. Magn. **2** (11), 559–572 (1901)
14. Jolliffe, I.: Principal Component Analysis. Wiley, New York (2002)
15. da Silva, S., Junior, M.D., Junior, V.L., Brennan, M.J.: Structural damage detection by fuzzy clustering. Mech. Syst. Signal Process. **22**(7), 1636–1649 (2008)
16. Papadopoulo, T., Lourakis, M.I.: Estimating the jacobian of the singular value decomposition: theory and applications. In: European Conference on Computer Vision, pp. 554–570. Springer, Berlin (2000)
17. Friswell, M.I., Mottershead, J.E., Ahmadian, H.: Finite–element model updating using experimental test data: parametrization and regularization. Philos. Trans. R. Soc. Lond. A **359**(1778), 169–186 (2001)
18. De Boe, P., Golinval, J.C.: Principal component analysis of a piezosensor array for damage localization. Struct. Health monit. **2**(2), 137–144 (2003)
19. Peterson, L., Doebling, S., Alvin, K.: Experimental determination of local structural stiffness by disassembly of measured flexibility matrices. In: 36th Structures, Structural Dynamics and Materials Conference, p. 1090 (1995)
20. Esfandiari, A., Sanayei, M., Bakhtiari-Nejad, F., Rahai, A.: Finite element model updating using frequency response function of incomplete strain data. AIAA J. **48**(7), 1420–1433 (2010)
21. Esfandiari, A., Rahai, A., Sanayei, M., Bakhtiari-Nejad, F.: Model updating of a concrete beam with extensive distributed damage using experimental frequency response function. J. Bridge Eng. **21**(4), 04015081 (2016)

Vibration-Based Support Vector Machine for Structural Health Monitoring

Hong Pan[1,2,3], Mohsen Azimi[3], Guoqing Gui[1], Fei Yan[3], and Zhibin Lin[3(✉)]

[1] School of Architecture and Civil Engineering, Jinggangshan University, Ji'an 343009, Jiangxi, China
[2] College of Civil Engineering, Tongji University, 1239 Siping Road, Shanghai, China
[3] Department of Civil and Environmental Engineering, North Dakota State University, Fargo, ND, USA
zhibin.lin@ndsu.edu

Abstract. There are ever-increasing interests to determine effectively structural diagnosis and conditional assessment for structural health monitoring (SHM). Although research has been extensively conducted in the conventional physical-based vibration analysis, advancement in sensor technologies and complexity in structural systems post great challenges in the effectiveness of these techniques. Alternatively, various data-driven based machine learning techniques are recently emerging tools to data clarification. In this study, a new vibration-based machine learning was proposed for condition assessment and damage detection in SHM. Three vibration-based feature extraction methods, autoregressive, vector autoregressive and singular value decomposition methods, were used as damage sensitive features. A kernel function based support vector machine was used to facilitate the identification between damaged and undamaged cases. A benchmark with varying environment and operational conditions in the literature was selected to verify the effectiveness of the proposed methods. The results showed that three feature methods could effectively map damage features in a high dimensional feature space, thereby dramatically improving the effectiveness and accuracy of data classification. Moreover, comparisons of results revealed that the singular value decomposition methods exhibit higher sensitivity to damage states as compared to other two approaches.

Keywords: Vibration · Machine learning · Damage feature extraction · Structural health monitoring · Damage detection

1 Introduction

The success of structural health monitoring (SHM) requires techniques that could effectively diagnose the structural conditions and identify any damages/defects experienced in many engineering fields, including aerospace, civil and mechanical engineering. Dynamic responses of structural systems collected by various sensors are usually used as the basis for structural diagnosis in the physical-based analytical models and simulation techniques [1–7]. Advanced development of sensor technologies not

© Springer International Publishing AG 2018
J.P. Conte et al. (eds.), *Experimental Vibration Analysis for Civil Structures*,
Lecture Notes in Civil Engineering 5, https://doi.org/10.1007/978-3-319-67443-8_14

only allows big progress in these methods, but also posts big challenges when facing ever-increasingly complex systems or different interferences.

Data-driven machine learning attracts high interest in large-scale structural systems [8–14]. The key of these data-driven methods for structural diagnosis is to select proper damage features. Although some attentions have been paid to vibration-based feature extraction methods, such as autoregressive model or singular value decomposition methods, it is still a big challenge to assess methods that could better serve as sensitive features. From a systematical standpoint, few attempts are made to address data-driven structural diagnosis and damage detection in terms of applicability of feature extraction techniques. As a result, findings from these previous studies may not fully account for data process. Thus, integration of these new methods in structural diagnosis is necessary to large-scale structural systems.

Therefore, this study aims to develop a data-driven framework for structural diagnosis and damage detection using support vector machine integrated with enhanced feature extraction techniques. Three feature extraction methods were selected. A benchmark was used to calibrate the developed concept and demonstrate the effectiveness and sensitivity of the data-driven damage detection in the SHM.

2 Data-Driven Approaches for Structural Diagnosis in SHM

Data-driven machine learning methods [12] are the statistical strategy for implementing data mining process, as schematically shown in Fig. 1. The data-driven approaches for structural diagnosis in SHM could mainly include four stages: (a) data acquisition and preprocessing of collected sensor data; (b) feature extraction; (c) support vector machine learning for data training and model development for data classification; and (d) conditional assessment and decision making, as shows in the following flow chart in Fig. 1.

The success of the structural diagnosis in SHM is highly dependent of potential sensitive features, such as damages/defects/abnormality. Three vibration-based feature extraction approaches, autoregressive, vector autoregressive and singular value decomposition methods, are selected herein as damage sensitive features and addressed below.

2.1 Features Extraction and Supervised Machine Learning

Feature extraction is crucial to identify potential sensitive features for structural diagnosis. The three different extraction approaches herein are presented to compress and extract the data for potential damage-sensitive features [15].

2.2 Autoregressive Model (AR)

The AR model [15–17] is the time-series based analysis using the linear combination with p parameters:

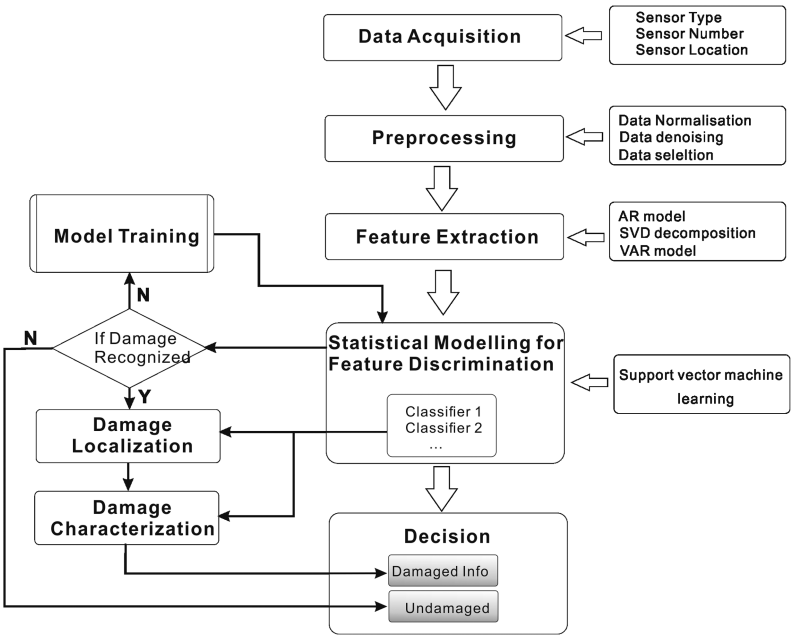

Fig. 1. Flow chart of data-driven approach for SHM.

$$x_i = \sum_{j=1}^{p} \phi_j x(i-j) + e_i \tag{1}$$

where x_i denotes the discrete signal, i denotes the time step, and e_i denotes an error. ϕ_j is unknown AR parameters. The order of the AR model is determined by the Akaike information criterion (*AIC*) method [18]:

$$AIC(p) = N \cdot \ln\sigma_p^2 + 2p \tag{2}$$

where, N is the samples number; and σ_p^2 is the prediction variance of p order model. In [12], the order of AR models ($p = 15$) is sufficient for the convergence.

2.3 Multivariate Vector Autoregressive Model (VAR)

The VAR model is a powerful model to use for multivariate time series [19]. The VAR (p) model can be written as:

$$y_t = a_0 + \sum_{j=1}^{p} A_j y_{t-j} + \varepsilon_t, \tag{3}$$

where y_t is an $M \times 1$ vector on M data acquisition sensor, y_t for $t = 1, \ldots, T$, ε_t is an $M \times 1$ vector of errors which coming from the zero-mean Gaussian distribution with covariance parameter Σ. A_j is an $M \times M$ matrix a_0 is an $M \times 1$ intercepts vector.

The matrix form of VAR model can be written as:

$$\boldsymbol{Y} = \boldsymbol{XA} + \boldsymbol{E}, \tag{4}$$

where $\boldsymbol{Y}$ is a $T \times M$ matrix which stacks the T times of observations data; $\boldsymbol{A}$ is a $(1 + Mp) \times M$ matrix and defined by $\boldsymbol{A} = \left(a_0 A_1 \ldots A_p\right)'$; and $\boldsymbol{X}$ is a $T \times (1 + Mp)$ matrix. The vector form of Eq. (4) could be rewritten by

$$\boldsymbol{Y} = (\boldsymbol{I} \otimes \boldsymbol{X})\hat{\boldsymbol{\alpha}} + \boldsymbol{\varepsilon} \tag{5}$$

where $\hat{\boldsymbol{\alpha}} = vec\left(\hat{\boldsymbol{A}}\right)$ and $\hat{\boldsymbol{A}} = \left(\boldsymbol{X}'\boldsymbol{X}\right)^{-1}\boldsymbol{X}'\boldsymbol{Y}$ are determined by the ordinary least squares estimation. Vector $\hat{\boldsymbol{\alpha}}$ is to define a relation between the own lag and different variable lag and has been reported as the damage sensitive feature. It is different from AR model, as they have different variable lag coefficients.

2.4 Singular Value Decomposition (SVD)

The singular value decomposition is a mathematical method [14], which seeks an orthogonal basis for representation of the linear data space. Assume $\boldsymbol{X}$ is a $M \times N$ matrix. The relationship between the rank of a matrix and the independent hidden variables of the data is closed. In the context of the SVD, it is possible to find the approximate data by using some main hidden variables. Hence, the SVD can be seen as a linear method to separate the main signal and noise from others. The decomposition of the matrix $\boldsymbol{X}$ can be express as:

$$\boldsymbol{X} = \boldsymbol{U\Sigma V}' = \sum\nolimits_{i=1}^{\gamma} \sigma_i \mu_i \upsilon_i' \tag{6}$$

where the $\boldsymbol{U}$ and $\boldsymbol{V}$ are the orthonormal matrix with a dimension of $M \times M$ and $N \times N$;

$$\boldsymbol{U} = [\boldsymbol{\mu}_1 \boldsymbol{\mu}_2 \ldots \boldsymbol{\mu}_m], \boldsymbol{V} = [\upsilon_1 \upsilon_2 \ldots \boldsymbol{\upsilon}_n], \boldsymbol{U}'\boldsymbol{U} = \boldsymbol{I}_{\mathrm{m}} \text{ and } \boldsymbol{V}'\boldsymbol{V} = \boldsymbol{I}_{\mathrm{n}} \tag{7}$$

and the $\boldsymbol{\Sigma}$ is a $M \times N$ diagonal matrix and the signaler nonzero diagonal values of the matrix $\boldsymbol{\Sigma}$ are arranged by

$$\sigma_1 \geq \sigma_2 \geq \cdots \geq \sigma_\gamma = \cdots = \sigma_{min} = 0 \tag{8}$$

It is common to assume that, $\gamma \leq \mathrm{N}$, that it is, the number of data space variables is bigger than the number of independent data variables. The vectors $\mu_i(\upsilon_i)$ adjacent to the i_{th} singular value σ_i can span an orthonormal n-dimensional space $\mathbb{R}^n$.

$$\boldsymbol{X} = \boldsymbol{U\Sigma V}' = \begin{bmatrix} \boldsymbol{U}_\Upsilon & \boldsymbol{U}_\Upsilon^\perp \end{bmatrix} \begin{bmatrix} \boldsymbol{\Sigma}_\gamma & 0 \\ 0 & 0 \end{bmatrix} \begin{bmatrix} \boldsymbol{V}_\gamma' \\ \left(\boldsymbol{V}_\gamma^\perp\right)^H \end{bmatrix} \tag{9}$$

where

$$\boldsymbol{U}_{\gamma} = \left[\boldsymbol{\mu}_1 \boldsymbol{\mu}_2 \ldots \boldsymbol{\mu}_{\gamma}\right], \text{ and } \boldsymbol{U}_{\gamma}^{\perp} = \left[\boldsymbol{\mu}_{\gamma+1} \boldsymbol{\mu}_{r+2} \ldots \boldsymbol{\mu}_m\right] \tag{10a}$$

$$\boldsymbol{V}_r = \left[\boldsymbol{\upsilon}_1 \boldsymbol{\upsilon}_2 \ldots \boldsymbol{\upsilon}_{\gamma}\right], \text{ and } \boldsymbol{V}_{\gamma}^{\perp} = \left[\boldsymbol{\upsilon}_{\gamma+1} \boldsymbol{\upsilon}_{\gamma+2} \ldots \boldsymbol{\upsilon}_n\right] \tag{10b}$$

$$\boldsymbol{\Sigma}_{\gamma} = diag(\sigma_1, \ldots, \sigma_{\gamma}) \tag{10c}$$

The singular vector μ_i or υ_i are treated as the dominant singular vectors. For signal $\boldsymbol{X}$, the number of dominant orthonormal dimensional can be selected based on the Forbenius-norms as:

$$\|\boldsymbol{X}\|_F = \sqrt{\sum_{i=1}^{n} \sum_{j=1}^{m} \left|x_{ij}\right|^2} = \left\|\boldsymbol{U}\boldsymbol{\Sigma}\boldsymbol{V}'\right\|_F = \|\boldsymbol{\Sigma}\|_F = \sqrt{\left(\sigma_1^2 + \ldots + \sigma_n^2\right)} \tag{11}$$

The energy of the data is preserved in the singular value spectrum σ_i [14]. For noise-corrupted signals the denoising process can be treat like a delete of some minima σ_i. In general decomposition process, one needs reshape the signal to a Hankel matrix, and then uses SVD to decompose the Hankel matrix, determine the number p of singular value spectrum σ_i selected and finally generate the denoised signal and noise:

$$\boldsymbol{X} = \boldsymbol{X}_0 + \boldsymbol{X}_{noise} \tag{12}$$

where $\boldsymbol{X}_0$ is the first raw of $\boldsymbol{H}_{X_0}$. $\boldsymbol{X}_{noise}$ is the residual of the denoised signal. The statistical residual of the signal $\boldsymbol{X}$ is also selected as a damage feature vector, as addressed in the following section.

2.5 Three Feature Extraction Techniques and Their Residual Errors

The residual error (RE) has been found as high sensitivity as statistical damage features [12, 21–23]. In this study, the REs for the three feature extraction techniques, AR, SVD and VAR models, are also computed:

$$e_i = x_i - \hat{x}_i \tag{13}$$

where $\hat{x}_i$ is the predicted signal value and the measured signal x_i. A total of sixteen statistical features from the residual errors were summarized from the literature [12, 21–23], as listed in Table 1.

2.6 Supervised Machine Learning Using Support Vector Machine

The SVM, as one of supervised machine learning techniques, is herein used for data classification [12, 24]. By applying Gaussian radial basis function Kernel function, the SVM is defined by the variable ξ_i and the error penalty C:

$$\min\left(\frac{1}{2}\left\|w^2\right\| + C\sum\nolimits_{i=1}^{N}\xi_i\right) \tag{15a}$$

$$\text{subject to } y_{i(w.X)} + b \geq 1 - \xi_i, \xi_i \geq 0 \tag{15b}$$

where w and b refer to the vector and scalar to define the position of the hyperplane. ξ_i denotes a distance measured between the hyperplane.

Table 1. Definition of statistical features [12]

Feature	Formulations	Feature	Formulations
Maximum	$RE_1 = \max(e_i)$	RMS	$RE_9 = rms = \sqrt{\frac{1}{N}\sum_{j=1}^{N} e_i^2}$
Minimum	$RE_2 = \min(e_i)$	Form factor	$RE_{10} = \frac{rms}{\frac{1}{N}\sum_{j=1}^{N}\lvert e_i\rvert}$
Mean	$RE_3 = \mu = \frac{1}{N}\sum_{j=1}^{N} e_i$	Crest factor	$RE_{11} = \frac{\max(e_i)-\min(e_i)}{rms}$
Maximum-minimum	$RE_4 = \max(e_i) - \min(e_i)$	kurtosis factor	$RE_{12} = \frac{\sum_{i=1}^{N} e_i^4}{\sqrt{\sum_{i=1}^{N} e_i^2}}$
Mean of absolute value	$RE_5 = \frac{1}{N}\sum_{j=1}^{N}\lvert e_i\rvert$	Pulse factor	$RE_{13} = \frac{\max(e_i)-\min(e_i)}{\frac{1}{N}\sum_{j=1}^{N}\lvert e_i\rvert}$
Standard deviation	$RE_6 = \sigma = \sqrt{\frac{\sum_{j=1}^{N}(e_i-\bar{e}_i)}{N}}$	Margin factor	$RE_{14} = \frac{\max(e_i)-\min(e_i)}{\left[\frac{1}{N}\sum_{j=1}^{N}\lvert e_i\rvert\right]^2}$
Skewness	$RE_7 = \sqrt{\frac{1}{6N}\sum_{j=1}^{N}\left(\frac{e_i-\mu}{\sigma}\right)^3}$	Upper control limit	$RE_{15} = UCL = \mu + 3\frac{\sigma}{\sqrt{n}}$
Kurtosis	$RE_8 = \sqrt{\frac{N}{24}\left[\frac{1}{N}\sum_{j=1}^{N} -3\right]}$	Lower control limit	$RE_{16} = LCL = \mu - 3\frac{\sigma}{\sqrt{n}}$

3 Case Study

3.1 Benchmark for Calibration of the Proposed Concept

A three-story frame aluminum structure found in the literature [23] was selected as a benchmark to demonstrate the effectiveness of the proposed concept. As shown in Fig. 2(a), the structure consists of an electro-dynamic shaker mounted to the base for excitation, and the extra plate at top of the 3rd floor separated by columns to form an adjustable gap (Fig. 2(b)). Noted that the contact of the bumper and column result in non-linearity to simulate the cases in actual situation, where structures could experience the crack opening and closing or loose of bolt connection. Four sensors (accelerators), as marked by Sensors 1 to 4 in Fig. 2(a), were installed at the floors to capture the dynamic response during the excitation.

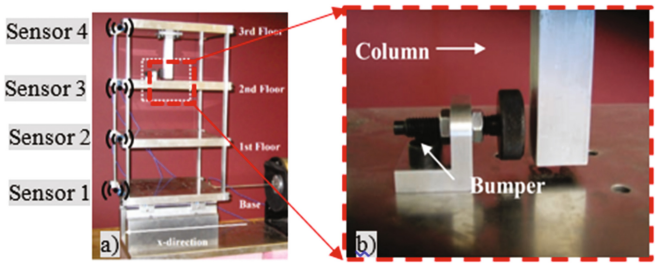

Fig. 2. Three-story frame structure [23]: (a) overview and test setup and (b) adjustable bumper and column

3.2 Scenarios Designed for Data-Driven Structural Diagnosis

Table 2 shows the designed 17 different scenarios, as documented in the literature. Each scenarios has 10 times testing and each floor has been installed with an acceleration sensor. The parameters AR and RE have been selected as damage features.

Table 2. Test matrix of the structural state conditions [12]

Label	State condition	Description
Undamaged states (# 1 to 9)		
State#1	Undamaged	Baseline condition
State#2	Undamaged	Added mass (1.2 kg) at the base
State#3	Undamaged	Added mass (1.2 kg) on the 1st floor
State#4	Undamaged	States 4–9: 87.5% stiffness reduction at various position to stimulate temperature impact (more detail in the reference)
State#5	Undamaged	
State#6	Undamaged	
State#7	Undamaged	
State#8	Undamaged	
State#9	Undamaged	
Damaged states (# 10 to 17)		
State#10	Damaged	Gap (0.20 mm)
State#11	Damaged	Gap (0.15 mm)
State#12	Damaged	Gap (0.13 mm)
State#13	Damaged	Gap (0.10 mm)
State#14	Damaged	Gap (0.05 mm)
State#15	Damaged	Gap (0.20 mm) and mass (1.2 kg) at the base
State#16	Damaged	Gap (0.20 mm) and mass (1.2 kg) on the 1st floor
State#17	Damaged	Gap (0.20 mm) and mass (1.2 kg) on the 1st floor

4 Results and Discussions

4.1 Effectiveness of Various Feature Extraction Methods and Sensitivity

As stated in the case study, the nonlinear damage was induced by the impact of the bumper and column (see Fig. 2(b)) at the the 2nd and 3rd floors near Sensors 3 and 4, as schematically shown in Fig. 3. These three feature extraction techniques, AR, VAR, SVD and their residuals (RE), exhibit the different levels of the effectiveness for pattern recognition. As shows in Fig. 3, the statistical analysis of dynamic response at each floor through sensors were displayed using the SVD feature extraction, where the blue lines mean the undamaged states (Cases 1–9) and the pink lines represent the damaged states (Case 10–17). For each state, residual has been selected with 1000 times steps, as shown in the x axis. Two dash lines in red shown in Fig. 3 are the maximum and minimum residual values from undamaged state, respectively. Clearly, all of the residual plots are on the same scale for the undamaged states, while it is apparent that all damaged states exhibit much higher response for all sensors.

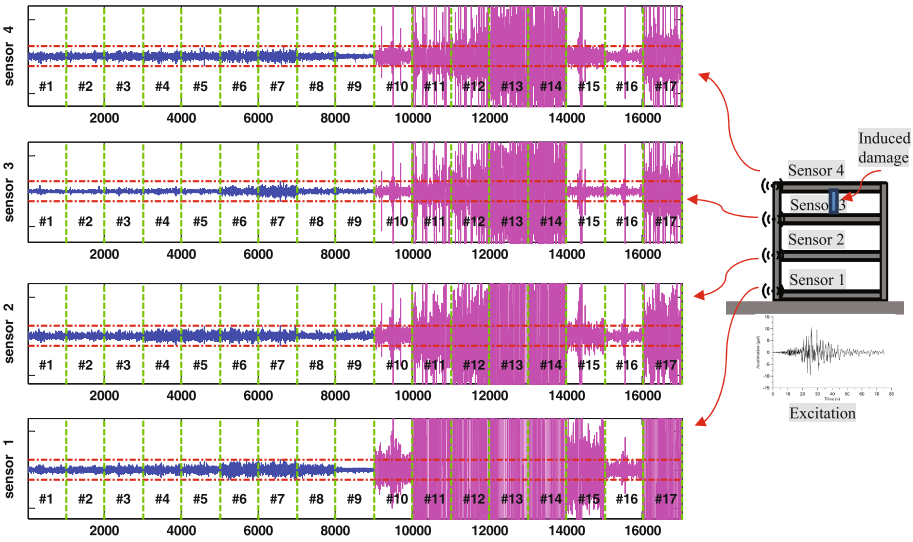

Fig. 3. Residuals from SVD for each state (undamaged state 1–9, damaged state 10–17)

Moreover, each residual of damaged state exhibits some singularities, which was responsible for the impact of the column and the bumper, and the time domain residual method can capture each individual impact. Also, Fig. 3 shows that the SVD method has the high sensitivity to allow identifying conditions between damage and undamaged states, even for data from Sensor 1, which is far away from the damage resources.

Figure 4 was plotted to demonstrate the effectiveness of each feature extraction approach. Clearly, the AR model could effectively identify the presence of damage conditions (Cases 10–17) using data from Sensor 3, but apparently such capability

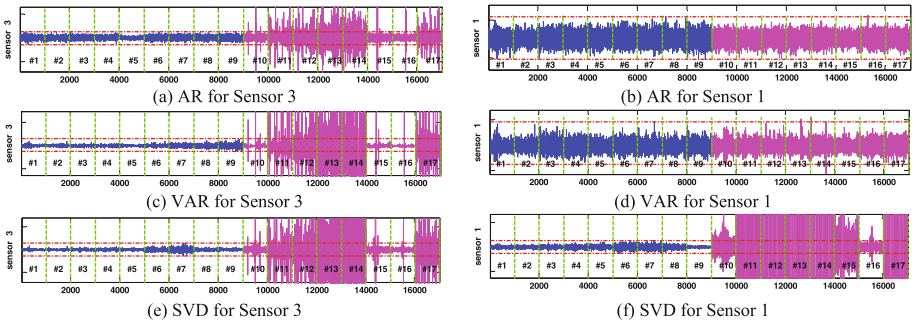

Fig. 4. Residuals from three techniques for each state at Sensors 1 and 3 (undamaged state 1–9, damaged state 10–17)

diminishes when processing data from Sensor 1 (or 2). Furthermore, although the VAR residual shows a few difference between damage and undamaged states for Sensor 1, such identification could not be valid if there are more interference. Differently, the SVD method exhibits much higher sensitive to damage as compared to other two approaches. It is mainly because the SVD uses the block Hankel matrix (see Eq. (13)), where information of all sensors are captured and in turn, enhance the sensitivity. It should be noted that since there are singularities in the cases for damage states, the SVD could demand much longer computation time than other two methods.

4.2 Damage Detection and Their Effectiveness

The residual of probability of designed states, including state 1 (original undamaged state) and state 10 (0.2-mm gap), are plotted in Fig. 5. The probability plot is a method to evaluate the data which is fit for some distribution. We assume the residual fits the Normal distribution. The probability is generated from an estimated cumulative distribution function (CDF) from the sample, and then scales are used to make the ideal distribution to a straight line. As clearly illustrated in Fig. 5, each method residuals (AR, VAR or SVD) of original state (state 1) shows a good fit for normal distribution. A good distribution fit is one where the observation is near the fitted dash line. Differently, in the context of damaged states (see state 10), probability curves are not straight line anymore, as shown in Fig. 5, that it is, there are some abnormal points from the normal distribution due to damages. Hence, the estimated CDF could aid to

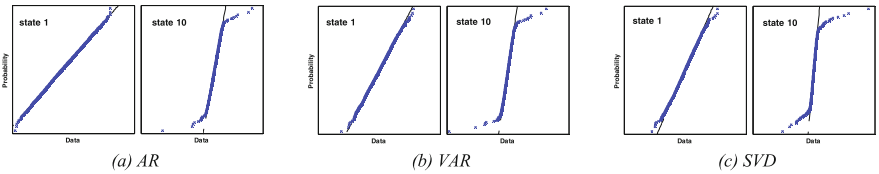

Fig. 5. Normal probability distribution of residual for three features at sensor 4

identify potentially early damages. The comparison of three approaches also confirmed that the SVD residuals have more sensitivity to damage, as identified in Fig. 4.

The SVM maps the feature space to a nonlinear space to get a better pattern recognition. In this study, 50 experiments data have been selected for each state, the total sample is 850. The samples have been separate as training group and testing group with equal number. Figure 6 plots the receiver operating characteristic (ROC) curves for three features and their associated residuals for the accomplishment of the machine learning. Clearly, the ROC curves showed that all features identified in this study has an almost perfect discrimination ability, even with different operational and environmental states.

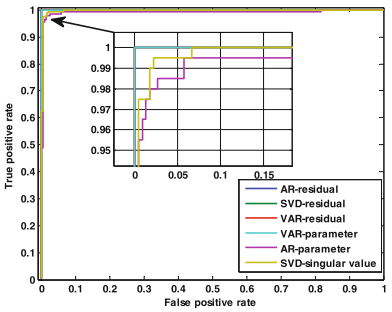

Fig. 6. The ROC curves of different feature extraction method

5 Conclusions

This study presented new data-driven structural diagnosis and damage detection with three feature extraction techniques for facilitating the pattern recognition and improving the identification between damaged and undamaged cases. Results have demonstrated the SVD model has significantly higher accuracy and sensitivity as compared to other two approaches, as it has higher sensitivity to the local fluctuation. Furthermore, the probability curves of three feature extraction approaches further confirm that the damaged states behave nonlinear as compared to original undamaged ones, and thus lead to a higher reliable data identification.

Acknowledgments. The authors gratefully acknowledge the financial support provided by Ozbun Economic Development Award, National Natural Science Foundation of China (No. 51468023), ND Department of Commerce, US DOT and US DOT CAAP Pipeline and Hazardous Materials.

References

1. Zou, Y., Tong, L., Steven, G.P.: Vibration-based model-dependent damage (delamination) identification and health monitoring for composite structures: a review. J. Sound Vib. **230**, 357–378 (2000)

2. Kopsaftopoulos, F.P., Fassois, S.D.: A functional model based statistical time series method for vibration based damage detection, localization, and magnitude estimation. Mech. Syst. Signal Process. **39**, 143–161 (2013)
3. Magalhães, F., Cunha, A., Caetano, E.: Vibration based structural health monitoring of an arch bridge: from automated OMA to damage detection. Mech. Syst. Signal Process. **28**, 212–228 (2012)
4. Masciotta, M.G., Ramos, L.F., Lourenço, P.B., Vasta, M.: Damage detection on the Z24 bridge by a spectral-based dynamic identification technique. In: Dynamics of Civil Structures, vol. 4, pp. 197–206. Springer, Berlin (2014)
5. Comanducci, G., Magalhães, F., Ubertini, F., Cunha, Á.: On vibration-based damage detection by multivariate statistical techniques: application to a long-span arch bridge. Struct. Health Monit. **15**(5), 505–524 (2016)
6. Ge, R., Pan, H., Lin, Z., Gong, N., Wang, J.: RF-powered battery-less wireless sensor network. In: 5th International Symposium on Next-Generation Electronics Hsinchu, Taiwan (2016)
7. Lin, Z., Yan, F., Azimi, M., Azarmi, F., Al-Kaseasbeh, Q.: A revisit of fatigue performance based welding quality criteria in bridge welding provisions and guidelines. In: International Industrial Informatics and Computer Engineering Conference (IIICEC), Shaanxi, China (2015)
8. Gerist, S., Maheri, M.R.: Multi-stage approach for structural damage detection problem using basis pursuit and particle swarm optimization. J. Sound Vib. **384**, 210–226 (2016)
9. Jang, J.: Development of Data Analytics and Modeling Tools for Civil Infrastructure Condition Monitoring Applications. Columbia University, Columbia (2016)
10. Ko, J.M., Ni, Y.Q.: Technology developments in structural health monitoring of large-scale bridges. Eng. Struct. **27**, 1715–1725 (2005)
11. Rashedi, R., Hegazy, T.: Capital renewal optimisation for large-scale infrastructure networks: genetic algorithms versus advanced mathematical tools. Struct. Infrastruct. Eng. **11**, 253–262 (2015)
12. Gui, G., Pan, H., Lin, Z., Li, Y., Yuan, Z.: Data-driven support vector machine with optimization techniques for structural health monitoring and damage detection. KSCE J. Civil Eng. **21**(2), 523–534 (2016)
13. Pan, H., Ge, R., Wang, J., Gong, N., Lin, Z.: Integrated wireless sensor networks with uas for damage detection and monitoring of bridges and other large-scale critical civil infrastructures. In: NDE/NDT for Highway and Bridges: Structural Materials Technology, Portland, OR, USA (2016)
14. Yan, F., Chen, W., Lin, Z.: Prediction of fatigue life of welded details in cable-stayed orthotropic steel deck bridges. Eng. Struct. **127**, 344–358 (2016)
15. Widodo, A., Yang, B.-S.: Application of nonlinear feature extraction and support vector machines for fault diagnosis of induction motors. Expert Syst. Appl. **33**, 241–250 (2007)
16. Gersch, W.: Estimation of the autoregressive parameters of a mixed autoregressive moving-average time series. IEEE Trans. Autom. Control **15**, 583–588 (1970)
17. Yao, R., Pakzad, S.N.: Autoregressive statistical pattern recognition algorithms for damage detection in civil structures. Mech. Syst. Signal Process. **31**, 355–368 (2012)
18. Figueiredo, E., Figueiras, J., Park, G., Farrar, C.R., Worden, K.: Influence of the autoregressive model order on damage detection. Comput. Aided Civil Infrastruct. Eng. **26**, 225–238 (2011)
19. Zivot, E., Wang, J.: Modeling Financial Time Series with S-PLUS®. Vector autoregressive models for multivariate time series, pp. 385–429. Springer, New York (2006)
20. Ouali, M.A., Chafaa, K.: SVD-based method for ECG denoising. In: 2013 International Conference on Computer Applications Technology (ICCAT), pp. 1–4 (2013)

21. Sharma, A., Amarnath, M., Kankar, P.: Feature extraction and fault severity classification in ball bearings. J. Vib. Control **22**, 176–192 (2016)
22. Boldt, F.D.A., Rauber, T.W., Varejao, F.M.: Feature extraction and selection for automatic fault diagnosis of rotating machinery
23. Figueiredo, E., Park, G., Figueiras, J., Farrar, C., Worden, K.: Structural Health Monitoring Algorithm Comparisons Using Standard Data Sets, Report (2009)
24. Suykens, J.A.K., Vandewalle, J.: Least squares support vector machine classifiers. Neural Process. Lett. **9**, 293–300 (1999)
25. Furey, T.S., Cristianini, N., Duffy, N., Bednarski, D.W., Schummer, M., Haussler, D.: Support vector machine classification and validation of cancer tissue samples using microarray expression data. Bioinformatics **16**, 906–914 (2000)

Structural Health Monitoring of a Curved Segment of an Elevated Railroad

Carlos H. Huerta-Carpizo[1], David Murià-Vila[1(✉)], Gerardo Aguilar[1,2], and Abraham R. Sánchez[1]

[1] Department of Structural Engineering, Institute of Engineering, Universidad Nacional Autónoma de México (UNAM), México City, México
dmv@pumas.ii.unam.mx
[2] WSP | PB, New York City, USA

Abstract. A new Metro line was opened in 2012 in Mexico City. The elevated portion of this line is located in an area of high seismic risk with compressible soft soil. The monitoring and analysis of the structural response has been done for both transitory events and long-term conditions using two interdependent systems and two sets of sensors. Structural health is estimated using a set of key parameters calculated from sensors installed on a curved portion of the elevated railway.

The structural health has been assessed by defining four damage levels that are delimited by two load states: service and design. Since the installation of the monitoring system, 14 seismic events, more than 50,000 train passes and four years of long-term effects have been recorded.

This paper presents the damage level observed and criteria used for its assessment. Also, the main observations derived from the analysis of data recorded by the monitoring systems over a four-year period are described. Structural properties and their change in time have been analyzed through a set of health indicators defined from the available sensors. Changes to these structural performance indicators have been also correlated to ambient temperature. Finally, the overall condition of the structure is assessed in light of the data recorded by the structural health monitoring systems.

Keywords: Structural health monitoring · Elevated railway · Damage levels · Environmental effects · Structural response

1 Introduction

In an effort to address the problems of public transportation, a new Metro line in the south west area of Mexico City was opened to the public in 2012. A portion of this line has an elevated superstructure supported by compressible soft soils in an area of high seismic risk, which is also characterized by significant regional subsidence. The geotechnical and structural characteristics of the Metro line and its evident importance to the city made it a perfect target for structural health monitoring, which started in August 2012 and continues to date.

The monitoring has been done through observations of the structural response for both transitory events and long-term conditions, which has been achieved using two

© Springer International Publishing AG 2018
J.P. Conte et al. (eds.), *Experimental Vibration Analysis for Civil Structures*,
Lecture Notes in Civil Engineering 5, https://doi.org/10.1007/978-3-319-67443-8_15

interdependent sets of recording systems and two sets of sensors. The network for transitory events includes accelerometers fixed to the columns and to the ground, linear variable displacement transducers (LVDTs) between neighboring beams and at the beam–column joints, and strain gages attached to the girders at midspan. The long-term monitoring comprises biaxial inclinometers mounted on the footings and capitals of the columns, and the same set of LVDTs used for transitory events.

Average displacements, rotations and ambient temperature have been obtained through continuous data recording every 15 min. Peak accelerations measured at the base and capital of columns, as well as on the ground, including the fundamental lateral frequency of the structural system, peak displacements between beams and columns, and deformations at midspan have been estimated from recordings taken during rush hours.

The structural health has been assessed by defining four distinct damage levels that are delimited by the service and design load states. The threshold between the service and design loads states was established on the basis of the campaign of field tests carried in 2012 [1], which was confirmed during a similar campaign of 2014. Fourteen seismic events and more than 50,000 train passes have been recorded during the four years of operation of the system.

This paper presents the main observations derived from the analysis of data gathered by the monitoring systems over a four-year period. Structural properties and their change in time are studied through the analysis of the variation of lateral frequencies, capital and footing rotations, deformations at midspan, and the relative displacements between columns and beams. Changes to these structural performance indicators have been also correlated to ambient temperature. Finally, the overall condition of the structure is assessed in light of the data recorded by the structural health monitoring systems.

2 Instrumented Section of the Elevated Railway

The location of the site to deploy the structural health monitoring system was based on the most unfavorable soil conditions along the metro line, and also taking into account the feasibility of conducting vehicular load tests and building a control room to house the recording equipment. The instrumented portion of the superstructure is located in a geotechnical zone showing a transition between firm and soft soils [2].

The structure is built with precast prestressed concrete members. The typical portion of the elevated railway consists of a simply supported beam resting on cantilevered columns. The beams are composed of several segments assembled on site and supported on fixed bearings at their ends. The cross section of the beam comprises three ribs integrally joined to a bottom slab forming a W shape. The distance between columns centerlines is 30 m and their clear height is 8 m. The columns and their footings were prefabricated and cast integrally at the prestressing plant. The foundation of each column consists of a single footing connected to four 37-m long piles of 1.2 m of diameter, which were cast on site (Fig. 1).

Figure 1 show the location of instruments of the permanent monitoring system, which included nine accelerometers (red dots with labels starting with an “A” in Fig. 1),

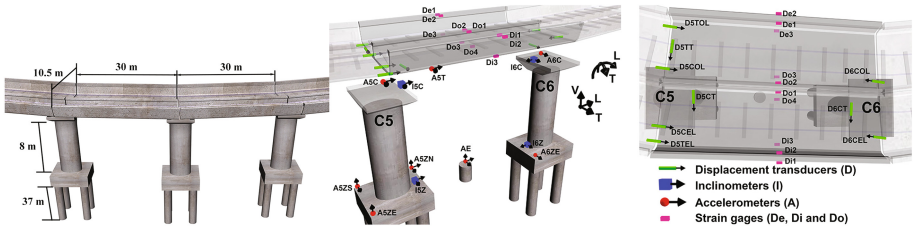

Fig. 1. Instrumented portion of the elevated railway.

four inclinometers/thermometers (blue squares with labels starting with an "I") and 15 displacement transducers (long rectangles with labels starting with a "D"). Also, ten surface strain gages where installed at midspan (small pink rectangles with labels starting with "De", "Di", or "Do"), which have allowed for measuring concrete strains within the depth of the W-shaped cross section, in particular while train loads are present in the span. Surface strain gages are not part of the permanent structural health monitoring system. However, readings are taken periodically with these strain gages to aid in the assessment of the condition of the instrumented section of the railway.

3 Assessment of Structural Health

The structural health monitoring system was conceived with two main objectives in mind: (a) To determine the structural state and performance of the instrumented region by means of a quick inspection and fast analysis of data [1, 3, 4], and (b) to develop computational tools for data analysis [5] while optimizing location and number of instruments for the most complete estimation possible of structural behavior [3, 6]. The monitoring of the structure started in August of 2012, about two months before the Metro line was open to the public.

Two distinct procedures were devised to analyze the data recorded by the monitoring system, one was focused on the short-term effects associated with short-duration events such as earthquakes and train traffic, while the second aimed at determining the long-term behavior of the structure.

In order to assess the structural condition and its changes with respect to time, key variables recorded by the structural health monitoring system were compared with eight limiting values of structural performance and two indicators of the severity of damage. The key parameters were established during the first months of monitoring using both basic design considerations and the results of field load tests [1] and correspond to the "reference state". Some of the key parameters were later adjusted to reflect the cumulative effect of a 4-year long monitoring program, including train traffic and the occurrence of seismic events. The test program used to determine the key parameters consisted on subjecting the structure to static and dynamic load tests with the use of actual Metro trains. Seven cars of the two Metro trains used for the tests were loaded using water-filled containers to apply the design service load. It was envisioned that such load imposed the maximum service-level load on the structure.

Ten key parameters or structural-performance indicators were derived from the collection of instruments deployed: peak ground acceleration (PGA), Arias horizontal intensity (I_{hArias}) [7], fundamental frequency of vibration in the radial direction of the curve (f_r), relative displacement between girders (D_{bb}), relative displacement between girder and column (D_{bc}), tangential rotation of the foundation (RF_t) and the column capital (RC_t), radial rotation of the foundation (RF_r) and the column capital (RC_r), and, lastly, the relative rotation between the top of the column and the footing in both tangential ($\Delta_t = RCt - RF_t$) and radial directions ($\Delta_r = RC_r - RF_r$).

As discussed in [8–10], the long-term analysis of recorded data, show variations associated with ambient temperature and humidity, soil and structure mechanical properties and condition at a given time, and instrument-related noise. These changes were clearly identified within the long-term data recordings by using statistical analysis in which data dispersion and confidence levels are studied. Consideration of ambient effects in long-time records was made by determining the statistical confidence level for which the data recorded may vary due to ambient effects alone. Confidence intervals for each of the eight key parameters was determined from the mean value of recorded data points obtained for a given time frame. Using a normal probability distribution, the limiting values for the confidence interval were set using the mean value of the data points (μ) and two times the standard deviation of the data (σ), so that 95.4% of the distribution is within the interval.

All confidence intervals were determined with respect to a given "reference state" associated with both the mean value of a data set within a selected time frame and the dispersion of the data, which means that all changes and variations of the eight key structural parameters are relative to said "reference state". When the mean value of a key structural parameter exceeds the limit associated with a given damage state, the structure is reclassified accordingly.

A relevant variable of the statistical analysis of the data available through the structural health monitoring system is the time frame or window of analysis, as selecting the wrong time interval may result in the unintended elimination of relevant data. In order to prevent this, various options of time intervals were evaluated, which allowed for the study of short-duration events in which the acceleration-based threshold was not triggered.

In order to estimate the effect of the window of analysis in the calculation of the confidence interval, several durations ranging from 1 h to 120 days were analyzed. The results of the analysis show that confidence intervals of the eight key parameters remain essentially the same for windows of analysis between 1 and 24 h. The study also showed that windows of analysis in excess of 60 days are useful in describing seasonal changes but are ineffective in determining structural changes. In consideration of this parametric analysis and the characteristics of the monitoring system, it was decided to use a 1-day long window of analysis for short-term, transitory events, and a 30- to 60-day time frame for long-term, cumulative effects.

The parametric analysis of time frames allowed to confirm the coincidence between the recording of maximum values of the key parameters and the occurrence of clearly identifiable activities or physical phenomena. For instance, paving works, casting of concrete sidewalks and the installation of underground piping were all detected and identified by the structural health monitoring system. These events, in addition to

relevant adjustments to the monitoring system, were helpful as reference points for the long-term analysis of the elevated railway. The trends and limiting values of the confidence intervals identified for each of the eight key parameters for various durations of the window of analysis are presented in the results section of this paper.

3.1 Evaluation Criteria

Four stages of damage or categories of structural performance were defined in order to evaluate and classify the ten key parameters. These stages are delimited by two load conditions, namely service-level and design-level conditions. The four level for key parameters was defined as follows:

- **Level 1** – If the key parameter do not exceeds the limits of the confidence interval nor the Level 1limiting value.
- **Level 2** – The key parameter exceeds the limits of the confidence interval, but such key parameters show values that are less than 50% of the design limiting values. Also when a sudden change in trend with respect to that of Level 1 is observed.
- **Level 3** – The key parameter exceeds both the limits of the confidence interval and 50% of the design limiting values, but they are less than 85% of the design limiting values. Also when a sudden change in trend with respect to that of Level 2 is observed. This level indicates that service-level conditions have been exceeded.
- **Level 4** – If the key parameter exceeds both the limits of the confidence interval and 85% of the design limiting values. Also when a sudden change in trend with respect to that of Level 3 is observed.

The analysis to assign a level of damage or structural performance is carried for each of the ten key parameters after the occurrence of every event, and also when the long-term cumulative effects have exceeded either the upper or lower boundaries of the confidence interval, or if a sudden change in the trend of the key parameter is observed. Note that with each re-categorization of a given key parameter to a higher level, there is an intrinsic change in the limiting boundaries of the confidence interval, and the associated design values.

In addition to the 4-level classification for each key parameter described above, four color-based categories were used to describe the structural health condition. These categories were developed using various combinations of the ten key parameters initially selected. The four categories of structural health were:

- **Green** – Low impact to structural integrity where there are not significant changes with respect to the original properties and physical condition of the structure.
- **Yellow** – Probable low impact to structural integrity with potential to impact structural integrity adversely. When the structure falls in this category, a visual inspection may be required to gather additional evidence of structural performance. If the visual inspection determines that poor structural behavior has occurred a corrective intervention will be necessary. The structure is classified in this category if any of the following combinations is observed:
  - Fundamental radial frequencies of vibration, rotation of the foundation, rotation of column capital, or the difference between rotation of column capital and

rotation of the foundation exceed the values associated with the Level 1 of structural performance.
  - PGA exceeds the limiting value associated with Level 1 of structural performance, and the rotation of the foundation exceeds 85% of the limiting value associated with Level 1 of structural performance.
  - Relative displacement between column and girder exceeds the limiting value associated with Level 1 of structural performance.
  - Cumulative long-term relative displacement between column and girder or the rotation of the foundation exceeds the limiting value associated with Level 1of structural performance.
  - Rotation of the foundation exceeds the limiting values associated with Level 1 of structural performance after a short-duration event (0.0004 rad).
- **Orange** – Medium impact to structural integrity where key parameters exceed 50% of the limiting design values, but are less than 85% of those values. The structure requires a visual inspection to determine its condition. The structure is classified in this category if any of the following combinations is observed:
  - PGA exceeds the limiting value associated with Level 2 of structural performance, and the rotation of the foundation exceeds the limiting value associated with Level 2 of structural performance.
  - Cumulative long-term relative displacement between column and girder or the rotation of the foundation exceeds the limiting value associated with Level 2 of structural performance.
- **Violet** – High impact to structural integrity where key parameters exceed 85% of the limiting design values. The structure requires an immediate and thorough inspection to determine its condition. The structure is classified in this category if any of the key parameters exceeds the limiting values associated with Level 3 of structural performance.

3.2 Threshold for Structural Health and Structural Performance Classification

The limiting values for the Level 1 of structural performance were derived from the analysis of recorded data over a 4-year period. Both transitory, short-duration events associated with both train traffic and seismic sources, and long-term cumulative effects were considered. For short-duration seismic events, the maximum amplitude for each key parameter was determined for recordings after which the structure showed no damage. For train-associated demands, the maximum amplitude for each key parameter was determined from the *in-situ* load tests carried in 2012 [1]. Limiting values for long-term events in Level 1 of structural performance were based on the specified allowable deformation of the encapsulated neoprene supports, which was 0.45 mm for the relative displacements between column and girder. The limiting values for Level 1 of structural performance between girders in the tangential and radial direction were 1.50 mm and 0.90 mm, respectively. The limiting values for rotation of the foundation and for the relative rotation between column capital and footing were determined on the basis of the rotation associated with the first flexural cracking of the column without consideration of post-tensioning forces.

During the time of service of the monitoring system, none of the key parameters has reached the design limits. Thus, limiting values for Level 2 and Level 3 of structural performance under both transitory and long-term cumulative effects have been determined using a linear finite element model of the instrumented section of the structure [11] in which the material and structural properties have been calibrated using the results of *in-situ* load tests aimed at measuring elastic deformations and determining the dynamic properties of the structure [1]. The mean values for the key structural parameters determined after four years of monitoring, including their dispersion within a confidence interval and the corresponding limiting values for the three levels of structural performance described earlier are presented in Table 1.

4 Results of Four Years of Health Monitoring

The main observations for both transitory, short-duration events and long-term cumulative effects on the elevated railway after four years of structural health monitoring are presented next.

4.1 Short-Term Transitory Events

The structural health monitoring system has recorded 14 short-duration seismic events [3]. The event with the largest Arias intensity took place on April 18, 2104 ($I_{h\ Arias}$ = 15.7 cm/s). Table 2 lists the main characteristics of the twelve most recent seismic events recorded, including the corresponding PGA, the calculated fundamental frequency of the structure in the radial (transverse) direction of the railway, and the observed dominant period of the ground.

In order to determinate the fundamental and additional relevant vibration frequencies of the structure, a spectral analysis of all the recorded seismic events was conducted. A cumulative analysis of the data shows that the fundamental frequency in the radial or transverse direction of the railway has remained practically constant during the four years of monitoring (Fig. 2a). Also, the response spectrum derived from all seismic events recorded in the four-year span points to a dominant ground period that has remained in the range of 0.82 to 1.34 s (0.75 to 1.21 Hz), with predominant values between 0.97 and 1.08 s (0.93 and 1.03 Hz) (Fig. 2b).

Noting that the various dynamic demands imposed on the structure are triggered by two very distinct sources –the ground movement and acceleration for seismic events, and girder movement and vibration for train-traffic events– it is expected that their records also present distinct differences. Figure 3 shows a clear distinction between the short duration of train-traffic events in comparison with earthquake events using, for illustration purposes, the largest Mw = 7.2 record of April 18, 2014 (event 14-1 in Table 2). Note, however, that the corresponding Fourier spectra at the column capital shows that train-traffic demands resulted in frequency amplitudes in excess of 2 Hz. The analysis of the spectral quotients between the column capital ("C" in Fig. 3) and ground acceleration ("G" in Fig. 3) show that train-traffic events triggered structural frequencies not observed for seismic events, which is an indicator of the wider frequency content of the train-traffic events.

Table 1. - Current mean, dispersion and limiting values for Level 1, 2 and 3 of structural performance considering long-term effects

Parameter	Location	Direction	Long-Term Cumulative		Level 1 Reference Values			Limiting Values		
			Mean Value (October, 2016)	Confidence interval	Train-Traffic Events	Seismic Events	Long-Term Effects	Level 1	Level 2	Level 3
Frequencies, in Hz	Columns	Radial (T)	2.18	±0.09	2.05–2.30	2.05–2.30	2.05–2.30	2.05	1.90	1.76
Rotation, in rad	Capital	Radial (T)	−0.0011	±0.0004	Not Applicable	Not Applicable	0.0060	0.0060	0.009	0.013
	Footing	Radial (T)	0.0025	±0.0002	0.0004	0.0001	0.0035	0.0035	0.005	0.007
Relative Rotation, in rad	Capital-Footing	Radial (T)	−0.0036	±0.0004	Not Applicable	Not Applicable	0.0025	0.0025	0.004	0.006
Relative Displacement, in mm	Girder-Girder	Longitudinal	0.19	±0.31	0.45	0.40	1.5	1.5	2.00	2.40
	Girder-Girder	Transverse	−0.58	±0.08	0.20	0.10	0.8	0.8	1.20	1.50
	Column-Girder	Longitudinal	−0.25	±0.05	0.30	0.10	0.45	0.45	0.60	0.80
	Column-Girder	Transverse	0.36	±0.06	0.10	0.10	0.45	0.45	0.60	0.80
PGA, in cm/s^2	Ground	Transverse or Longitudinal	Not Applicable	Not Applicable	10	40	40	40	85	200
$I_{h\ Arias}$, in cm/s	–	Transverse plus Longitudinal	Not Applicable	Not Applicable	1	16	Not Applicable	16	120	190

Table 2. - Characteristics of seismic event recorded by the monitoring system, estimated structural frequency and ground dominant period

Event	Date	Location	M_w	Epicentral Distance, in km	Arias Intensity $I_{h\ Arias}$, in cm/s	PGA, in cm/s^2	Maximum Acceleration of Column Capital, in cm/s^2	Fundamental Radial Frequency, in Hz	Dominant Period of the Ground, in s
12-3	05-01-12	Guerrero	5.6	237	0.28	6.1	11.2	2.20	0.97–1.08
12-4	11-15-12	Guerrero	6.1	197	0.96	8.4	19.1	2.19	0.97–1.08
13-1	04-21-13	Michoacán	5.8	364	0.33	6.1	8.6	2.19	0.99–1.08
13-2	06-16-13	Guerrero	5.8	144	3.47	30.0	36.0	2.19	0.97–1.09
13-3	08-21-13	Guerrero	6.0	286	0.68	10.1	45.6	2.18	0.99–1.08
14-1	04-18-14	Guerrero	7.2	325	15.66	35.1	53.5	2.18	0.98–1.07
14-2	05-08-14	Guerrero	6.4	310	4.34	25.1	30.9	2.19	0.97–1.08
14-3	05-10-14	Guerrero	6.2	319	0.79	10.3	11.2	2.19	0.99–1.08
14-4	07-29-14	Veracruz	6.4	408	0.23	5.2	8.3	2.18	0.98–1.07
15-1	03-20-15	Puebla	5.4	161	0.17	5.5	15.3	2.19	0.98–1.07
15-2	11-23-15	Guerrero	5.6	275	0.16	4.4	5.5	2.19	0.97–1.09
16-1	05-08-16	Jalisco	4.5	685	0.11	3.0	5.6	2.19	0.99–1.08

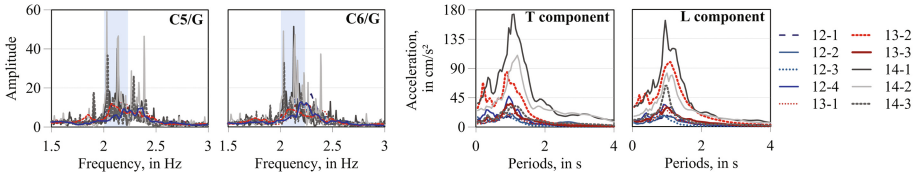

a) Spectral Quotient *b) Response Spectrum*

Fig. 2. Spectral quotient and response spectrum derived from the recorded seismic events

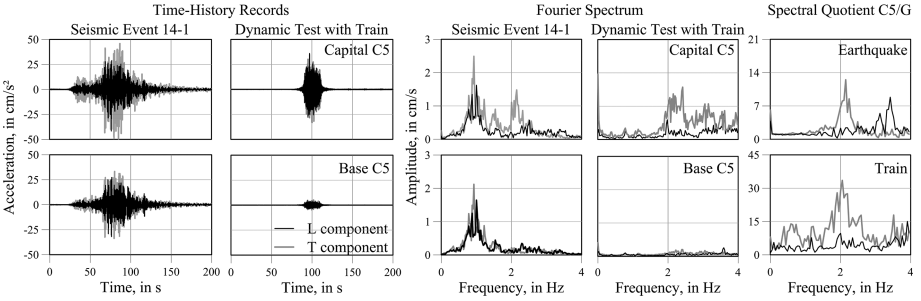

Fig. 3. Comparison of records, Fourier spectrum and spectral quotients of seismic events and train-traffic events

The mean value of the fundamental frequency of the structure calculated on the basis of train-traffic events is 2.18 Hz in the radial or transverse direction. This value has good agreement with the one obtained after the *in-situ* load tests carried out in 2012 [1] and 2014, which showed a fundamental frequency in the range of 2.1 to 2.2 Hz.

The associated dispersion of this key parameter is 4.8% of the mean value. The cumulative effect of the 14 seismic events recorded to date has been negligible in terms of the fundamental frequency of the structure, which is consistent with the visual inspections carried out periodically.

During the load test campaigns of 2012 and 2014, the strain gages installed on the webs of the W-shape girder were used to determine the strain distribution in the cross-section of the girder. Additionally, the data provided by these instruments has been gathered periodically and immediately after the occurrence of the most intense earthquakes. Figure 4 shows selected strain gage records from 2012 to 2016 for instruments Do3 ("Intrados") and Do4 ("Extrados"). Note that the maximum measured strains have remained under 40 με throughout the service life of the railway, including the *in-situ* load tests.

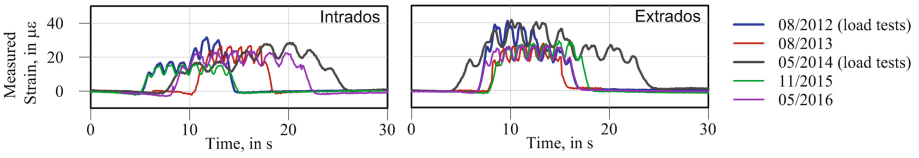

Fig. 4. Selected strain gage records for instruments Do3 (Intrados) and Do4 (Extrados) from 2012 to 2016

4.2 Long-Term Cumulative Effects

Figure 5 shows data of selected key parameters at relevant locations of the structure along the 4-year monitoring campaign. In each plot, the mean value corresponding to 1, 7, 30 and 60 days and the corresponding boundary values for the confidence interval of 30 days are also included. Clearly identifiable construction and maintenance events are shown as vertical light blue lines at their dates of occurrence. Paving work, casting of concrete sidewalks and installation of underground piping are identified by the W1 and W2 markers. The replacement of ballast and rails, which took place between September and November of 2015 while the Metro service was suspended, is identified with the W3 marker. Improvements to the recording equipment of the structural health monitoring system have been carried out two times and are represented by the vertical red lines with the I1 and I2 markers in Fig. 5. The horizontal green broken lines in the plots of Fig. 5 depict the threshold values delimiting the Level 1 of structural performance.

The first row of plots in Fig. 5 presents the evolution in time of the rotation at the base of columns C5 and C6 (inclinometers I5Z and I6Z in Fig. 1), which show a steady increase during the first five and eight months of the monitoring campaign, respectively. This increase has been associated with the local rearrangement of soil layer and foundation, which has been previously observed in an elevated viaduct located in a geologically similar area of Mexico City, which is supported by an identical foundation system [12]. After the initial increase, the mean rotation values have remained more or less the same, with a modest decreasing trend. In consideration of the rotation at the base of column C5, which exceeded 0.0032 rad for the key parameter RF_t calculated

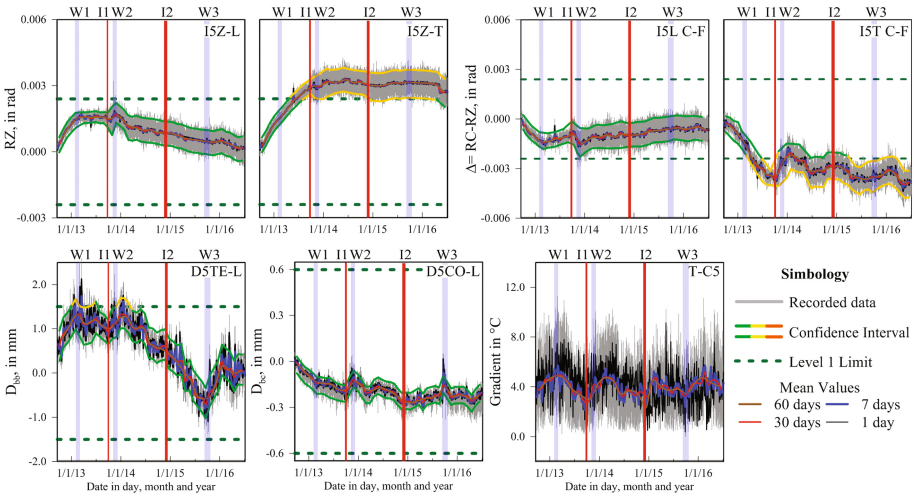

Fig. 5. Results of the long-term monitoring system

from the recordings of inclinometer I5Z-T and marked the threshold of Level 1, the railway has reached the Yellow classification in terms of structural health. As the structure reached the Level 2 condition, the mean value for rotation at the base of columns was 0.0025 rad with a variation of only 0.26% with respect to the mean value.

Since the classification of the structural health in the Yellow category, the mean value of the rotation at the base of the columns has slowly reduced, but not reaching the point to change the assessment of the structural health from Yellow to Green. The small change in displacements recorded along the time suggest a plausible correlation with seasonal changes of ambient temperature and humidity.

An important observation is that all construction and maintenance works (W1, W2 and W3 markers in Fig. 5) resulted in measurable changes to the rotations of both the base (RF) and capital (RC) of the columns. However, these changes were only temporary and the mean values after the works concluded returned to those observed prior to the start of construction or maintenance activities. A similar effect was observed for the relative displacement between girders D_{bb} (transducers D5TE, D5TO, and D5T), and for the relative displacement between columns and girders D_{bc} (transducers D5CE and D6C). However, the relative displacements between girders D_{bbt} (instruments D5TE and D5TO) did not go back to the mean values prior to the start of construction and maintenance works. The lack of recovery in the man values of D_{bbt} was particularly evident after the replacement of ballast and rails, identified with the W3 marker in Fig. 5.

The general trends for key parameters D_{bb}, D_{bc}, RF_t (inclinometers I5Z and I6Z) and RC_r (inclinometers I5C and I6C) show correlation with seasonal changes in ambient temperature.

The periodic calculation of the fundamental frequency of the structure in the radial direction, which is done daily at 3 a.m. from the readings of instruments A5C, A6C and AE, has resulted in a mean value of 2.18 Hz, with a variation of less than 5% of the

mean value. In the 4-year period of monitoring, there has not been a measurable change of the fundamental frequency of the structure due to train traffic, seismic events, or construction and maintenance activities.

5 Conclusions

The set of criteria used to classify the structural health and performance on the basis of ten key parameters have been proven very successful to provide relevant information at a glance. Furthermore, the key parameters have been validated through statistical analysis, and clear correlations have been established between them and both relevant construction and maintenance activities, and seasonal temperature changes.

During the first eight months of structural monitoring, it was observed that the rotation at the base of both instrumented columns exceeded the limits set for the Level 1 of structural performance, resulting in a Yellow category of structural health. Both structural performance and structural health categories remain the same to date. However, a slowly decreasing trend for the key parameters has been observed during the last three years, which has been associated with the rearrangement of soil layers around and below the foundation.

The trend exhibited by the relative displacements between columns and girders in the tangential direction (along the axis of the railway) is of a slow decrease bringing the mean value closer to the Level 1 threshold. Relative displacements between girders, and between columns and girders have shown daily and seasonal changes that have been correlated with the gradient of ambient temperature.

Fourteen seismic events of low and moderate intensity have been recorded during the four years of monitoring campaign and their effects on the structure have been studied. The results of the analysis show no significant changes to structural response, which is also an indicator of the absence of structural damage.

The use of a well-calibrated linear model representing the structure has been adequate to estimate the overall structural performance. However, it is recognized that the use of a nonlinear model might be necessary to confirm the observations to date, especially as the structure incurs into the range of non-linear behavior during its service life, or the properties of the soil-structure system change with time. A nonlinear model is expected to be developed in order to better estimate the structural degradation associated with the Orange and Violet categories of structural health.

The structural health monitoring system, including its data management policy, data analysis methodology, and maintenance and updating policy have been able to provide good quality information on a consistent basis without interruption during over four years of monitoring. The results of the data analysis have provided valuable information to support the operation and maintenance of the Metro line. The current monitoring campaign, complemented with periodic inspections to the structural members of the instrumented region of the elevated railway has been recommended to continue in the future with the goal of detecting structural damage in a timely manner to prevent not only temporary suspension of the Metro service, but also extreme conditions pointing to structural failure.

Acknowledgments. The support of Mexico City's government and the active involvement of the Institute of Engineering of the National Autonomous University of Mexico (IIUNAM) to design, deploy and maintain the monitoring system of the railway for more than four years is recognized. The collaboration of José M. Riobóo, Juan C. Arce, Luis Cabrera and Arturo Padilla in providing information on the design of the project and for their valuable comments is appreciated. The participation of the following IIUNAM researchers, technicians and students is gratefully appreciated: Alberto Vásquez, José Camargo, Luis A. Aguilar, Daniel Aldama, Miguel A. Mendoza, Yoatzin López, Mauricio Ayala, Alejandro Mora, and José M. Velasco.

References

1. Murià-Vila, D., Sánchez-Ramírez, A.R., Huerta-Carpizo, C.H., Aguilar, G., Camargo, J., López, Y.: Field tests of a curve in an elevated urban railroad. In: Proceedings of the 9th International Conference on Structural Dynamics, EURODYN 2014, Porto, Portugal (2014)
2. NTCDF: Normas Técnicas Complementarias para Diseño por Sismo. of the Reglamento de Construcciones para el Distrito Federal, Gaceta Oficial del Gobierno del Distrito Federal, 103-BIS, October 6 (2004)
3. Murià-Vila, D., Huerta-Carpizo, C., Sánchez-Ramírez, A., Pérez, J., Cruz, C.: Seismic monitoring on the curved portion of an elevated railway. In: Proceedings of the 10th NCEE, Anchorage, Alaska (2014)
4. Aktan, E., Chase, D., Inman, D., Pines, D.: Monitoring and managing the health of infrastructure systems. In: Proceedings of the 2001 SPIE CHMHTI-2001 (2001)
5. Bradford, S., Heaton, T., Beck, J.: Structural monitoring and evaluation tools at caltech: instrumentation and real-time data analysis. In: Proceedings of the 2004 ANCER AMNYEERP-2004, Honolulu, Hawaii (2004)
6. Xiang, Y.Q., Weng, S.L.: Health monitoring and assessment management system of Wenhui Bridge. In: Proceedings of the 1st ICSHMII, Tokio, Japan, pp. 913–920 (2003)
7. Arias, A.: A measure of earthquake intensity. In: Hansen, R.J. (ed.) Seismic Design for Nuclear Power Plants. MIT Press, Cambridge (1970)
8. Clinton, J., Bradford, S., Heaton, T., Favel, J.: The observed wander of the natural frequencies in a structure. Bull. Seismol. Soc. Am. **96**(1), 237–257 (2006)
9. Boroschek, R., Tamayo, F., Aguilar, R.: Evaluación de los efectos ambientales en un edificio de media altura. Memorias del Congreso Chileno de Sismología e ingeniería Sísmica Achisina 2015, Santiago, Chile, Paper 63 (2015)
10. Peters, B., De Roeck, G.: One-year monitoring of the Z24-Bridge: environmental effects versus damage events. Earthquake Eng. Struct. Dynam. **30**(2), 149–171 (2001)
11. Vázquez, A.: Representación de la respuesta de una vía elevada en la ciudad de México. Masters Dissertation, Posgrado de Ingeniería, UNAM, México (2013)
12. Murià-Vila, D., Sánchez-Ramírez, A., Huerta-Carpizo, C., Aguilar, G., Pérez, J., Carrillo, R.: Field tests of elevated viaducts in Mexico city. J. Struct. Eng. **141** (2015). SPECIAL ISSUE: Field Testing of Bridges and Buildings

Performance Evaluation of Hinges in Cantilever Steel Truss Bridges by Temperature Induced Strain

Takeshi Miyashita[1(✉)], Eiji Iwasaki[2], and Masatsugu Nagai[2]

[1] Department of Civil and Environmental Engineering, Nagaoka University of Technology, Nagaoka, Niigata, Japan
mtakeshi@vos.nagaokaut.ac.jp
[2] Nagaoka University of Technology, Nagaoka, Niigata, Japan

Abstract. In this study, short-term monitoring using more than a hundred sensors was carried out for an existing long-span bridge, which has been administrated by a local government, with the aim of evaluating its present performance toward planning future maintenance strategy. The bridge studied is a cantilever (Gerber) steel through truss bridges that was completed and opened to the traffic in 1937. Consequently, the performance of Gerber hinges were evaluated, then information for prior repair was obtained.

Keywords: Structural health monitoring · Steel truss bridges · Strain · Temperature

1 Introduction

Due to bridges aging progression in Japan, an effective and efficient maintenance has been demanded [1]. Until now, visual inspection is the most effective maintenance method. However, work optimization for this kind of inspections is difficult, and the quantitative information about stress properties, which is necessary for an effective maintenance, cannot be obtained. On the other hand, aiming an efficient maintenance, it is though that the use of ICRT (ICT: Information and Communication Technology + IRT: Information and Robot Technology) technologies will continue increasing in the near future [2].

Problems related with visual inspections can be solved effectively performing an on-site loading test. One example related with the initiative for the use of ICRT technologies is bridge monitoring, which consists in a large number of sensors disposed along the bridge in order to monitor its condition and make a diagnosis about its soundness [3]. One of the problems that have arisen is that there are only a few applications of both inspections in long-span bridges administrated by local governments.

Of course, cost represents a big problem for its application, but this is not the only obstacle. There is also a technical difficulty to arrange sensors in the whole bridge, to construct a measurement system, and to analyze a big quantity of data. Notwithstanding these difficulties, since July of 2014, bridge inspection every 5 years has become mandatory in Japan. Henceforth, it is expected that the demand for methods to evaluate current conditions and methods for bridge monitoring will continue increasing.

© Springer International Publishing AG 2018
J.P. Conte et al. (eds.), *Experimental Vibration Analysis for Civil Structures*,
Lecture Notes in Civil Engineering 5, https://doi.org/10.1007/978-3-319-67443-8_16

In this research, aiming the establishment of a strategy for future maintenance of long-span bridges administrated by local governments, a short-term monitoring is carried out. Here, more than one hundred sensors are installed along the bridge in order to evaluate its current performance.

2 Bridge of Study

On this research, the bridge of study is Chosei Bridge, an 850.8 m-long bridge build over Shinano River, located in Niigata Prefecture. It is a 13 span (67.50 + 11@65.00 + 67.50 m) cantilever (Gerber) steel through truss bridge completed and opened to traffic in 1937 (Fig. 1). Road width corresponding to this bridge is 7.50 m. The pedestrian bridge adjacent to Chosei Bridge was constructed in 1972.

Fig. 1. Bridge of study.

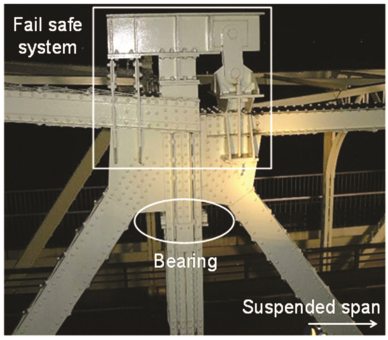

Fig. 2. Current condition of hinges.

From 1995 to 1996, movable supports and bridge fail safe system corresponding to Gerber hinge section were replaced and installed, respectively. In 2003, construction works to implement non-drain expansion devises in all Gerber hinges were carried out. Figure 2 shows current condition of Gerber hinges.

In 2006, during the execution of repainting works of the 2nd span, remarkable corrosion in lower chords of the main structure was found, and it was determined that it was necessary to repair those damaged sections. Based on the corrosion condition examination performed that year, a repair design was carried out. Then, from 2007 to 2011, lower chords repair (patch of steel plates, members' replacement) was carried out. However, a loading test was not performed after the repair, so stress and others current properties of the bridge were not grasped.

3 Short-Term Monitoring

3.1 Outline

The measured items are: each span strain, acceleration, vertical deflection, and temperature in span center vicinity as a representative point. Additionally, since the adjacent

pedestrian bridge shares the same pier with Chosei Bridge, for reference, acceleration measurements of 3 spans corresponding to the pedestrian bridge were carried out. In total, 130 points were measured. Measurement location is shown in Fig. 3. In order to classify vehicles type, a previously installed web camera, originally used to monitoring the snow condition, is used.

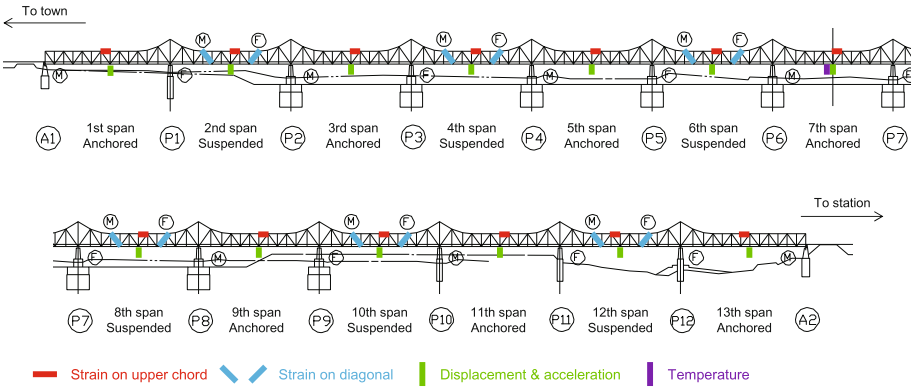

Fig. 3. Measurement location.

A free flow traffic monitoring was carried out, starting at 2:00 of June 13th, finishing at 14:00 of June 17th, with a total of 108 h (388,800 s) of monitoring. After completing the measurements, all the measurement systems were removed. For the monitoring period, a file text of approximately 18.8 GB was obtained. In this research, attention is focused on strain data that helps to grasp stress properties.

Since the bridge of study is quite long, 850.8 m, it was difficult to gather together all the sensor's wiring in the same place. Then, it is also difficult to close the road to traffic for long periods of time, so the bridge was divided into 3 blocks, and a measurement system was constructed for each block.

3.2 Strain Measurement

To measure the strain, self-temperature compensation type uniaxial strain gauges for general use were used. Strain was measured in the upper chord located at the vicinity of each span's center on the downstream side. Additionally, in the cantilever span, measurement points were provided at the 2 diagonal bracing members that connect from the Gerber hinge to the span center. In order to consider the influence of axial force and bending moments, 4 strain gauges are attached at each cross-section of each element. To calculate the section force from the measured strain, member's coordinate system shown in Fig. 4, steel Young's modulus E (= 200 GPa), cross-sectional area A, cross-sectional coefficients W_{yi} and W_{zi} ($i = 1, 2, 3, 4$), axial force N_x, bending moments around y and z axis M_y and M_z, measured strain ε_i, and the next formula are used.

$$\frac{1}{E}\begin{bmatrix} 1/A & 1/W_{z1} & 1/W_{y1} \\ 1/A & 1/W_{z2} & 1/W_{y2} \\ 1/A & 1/W_{z3} & 1/W_{y3} \\ 1/A & 1/W_{z4} & 1/W_{y4} \end{bmatrix} \begin{Bmatrix} N_x \\ M_z \\ M_y \end{Bmatrix} = \begin{Bmatrix} \varepsilon_1 \\ \varepsilon_2 \\ \varepsilon_3 \\ \varepsilon_4 \end{Bmatrix} \tag{1}$$

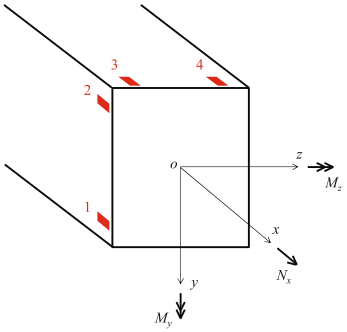

Fig. 4. Coordinate system of members.

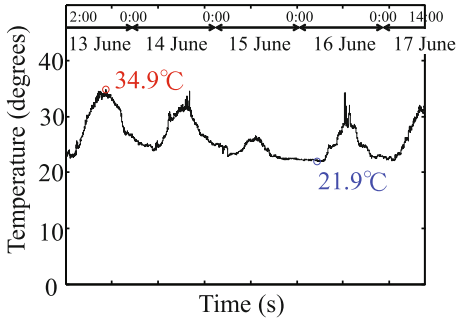

Fig. 5. Temperature during monitoring period.

3.3 Temperature Measurement and Web Camera

The vicinity of 7th span's center was selected as the representative point to measure the temperature. The temperature measurement was carried out using a thermocouple T-GF-0.65. It was installed above the pedestrian bridge, in a place out of the sun. In order to classify vehicles type, a previously installed web camera (Panasonic BB-HCM381), originally used to monitoring the snow condition, is used. It was installed above the upper lateral bracing located in the vicinity of P1 in 2nd span.

4 Monitoring Results

4.1 Temperature Measurement

Temperature variation corresponding to the vicinity of 7th span's center measured with the installed thermocouple is shown in Fig. 5. During the measurement period, maximum temperature was 34.9°, and the minimum temperature was 21.9°. The temperature when the initial measurement was carried out, on May 22nd of 2013, was 21 degrees.

4.2 Strain Measurement

Figure 6 shows upper chord's normal stress for each span. Black solid line represents the normal stress, which is the sum of the static stress component originated by temperature influence, and the dynamic stress component originated by live load. To separate both components, a moving average is carried out. Here, 20,000 data items for each time are considered. From this moving average, static stress component is determined and represented by the blue solid line. Then, the blue solid line's value is subtracted from black solid line's value in order to obtain the dynamic stress component.

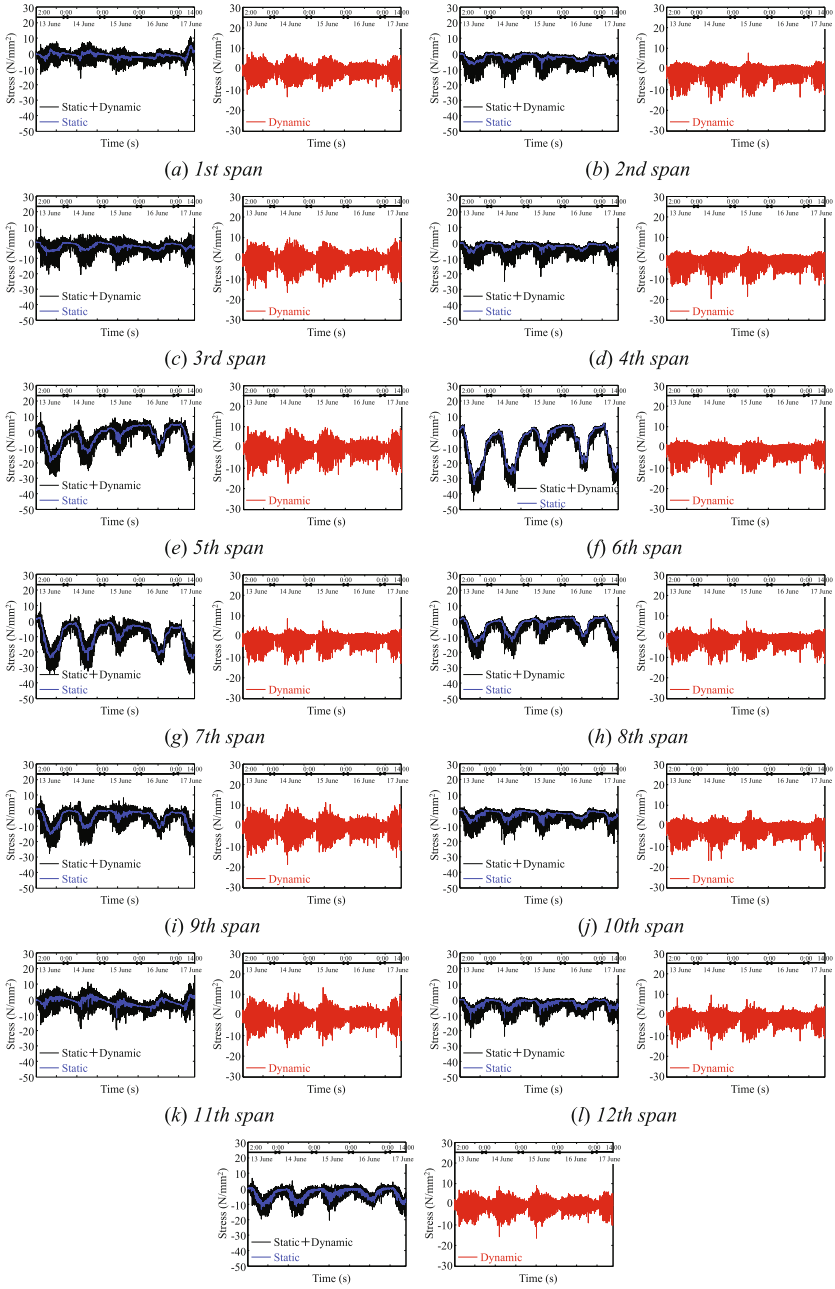

(*a*) *1st span* (*b*) *2nd span*

(*c*) *3rd span* (*d*) *4th span*

(*e*) *5th span* (*f*) *6th span*

(*g*) *7th span* (*h*) *8th span*

(*i*) *9th span* (*j*) *10th span*

(*k*) *11th span* (*l*) *12th span*

(*m*) *13th span*

Fig. 6. Upper chord's normal stress for each span.

Table 1 shows each component of the minimum normal stress for each span during the monitoring period. As is shown Table 1, 6th span is the span which presented the minimum value of normal stress, this is −44.6 MPa. An analysis of the data corresponding to this stress, and a vehicle identification using the web camera is shown in Fig. 7. From Fig. 7(c), it is determined that the dynamic stress component when the normal stress reached its minimum value is −11.6 MPa.

Table 1. The minimum normal stress during the monitoring period.

Span	1	2	3	4	5	6	7	8	9	10	11	12	13
Static + dynamic	−15.8	−21.9	−20.5	−24.8	−28.8	−44.6	−34.1	−24.4	−28.5	−21.9	−19.6	−24.6	−20.4
Static	−5.4	−9.8	−8.2	−7.4	−19.5	−33.7	−25.5	−16.3	−15.4	−10.1	−11.8	−13.0	−13.2
Dynamic	−13.3	−16.9	−16.5	−19.7	−17.3	−18.0	−17.7	−13.8	−18.8	−17.1	−16.0	−16.7	−16.3

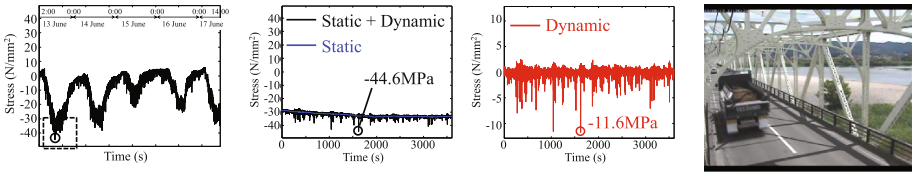

(*a*) *Whole figure* (*b*) *Static component* (*c*) *Dynamic component* (*d*) *Identified vehicle*

Fig. 7. The minimum normal stress during monitoring period (Upper chord in 6th span).

As is shown Table 1, the dynamic stress component on 4th span is −19.7 MPa. An analysis of the data corresponding to this stress, and a vehicle identification using the web camera is shown in Fig. 8. Then, from Table 1, it is known that the dynamic stress component on 6th span is −33.7 MPa. Now, using the temperature variation during the period of monitoring: 34.9–21.9 = 13.0 degrees, steel coefficient of linear expansion: 12×10^{-6}/degrees, and steel Young's coefficient: 200 GPa, the temperature stress is calculated. Its value is –31.2 MPa. Because this stress is of the same magnitude that the static stress component presented in 6th span, it is inferred that the Gerber hinge movable part is not working, that it is fixed. Considering this, the relationship between temperature and the static stress component is shown in Fig. 9. In 5th, 6th and 8th spans, the coefficient of determination R^2, 0.9, is exceeded. Among these 3 spans, 6th and 8th spans are cantilever spans, and it is found a high correlation between temperature and static stress component correspondent to the upper chord of both spans. Therefore, it is though that the Gerber hinges of these spans should be repair preferentially.

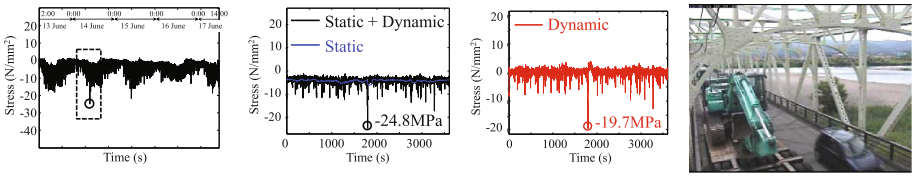

(*a*) *Whole figure* (*b*) *Static component* (*c*) *Dynamic component* (*d*) *Identified vehicle*

Fig. 8. The minimum normal stress during monitoring period (Upper chord in 4th span).

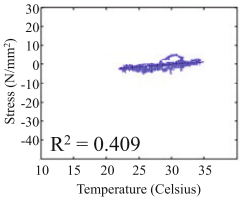

(*a*) *1st span*

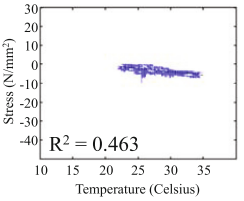

(*b*) *2nd span*

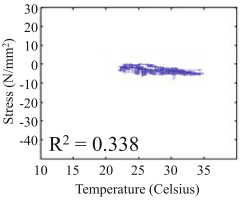

(*c*) *3rd span*

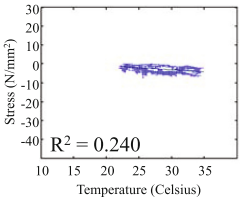

(*d*) *4th span*

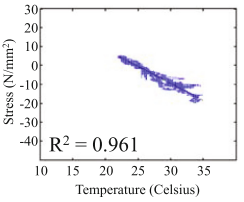

(*e*) *5th span*

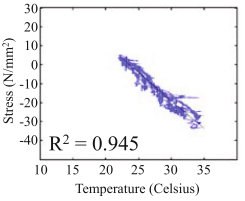

(*f*) *6th span*

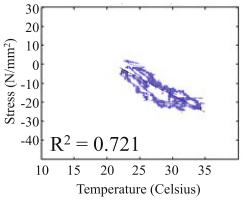

(*g*) *7th span*

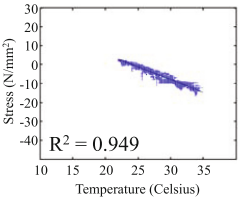

(*h*) *8th span*

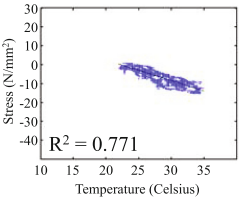

(*i*) *9th span*

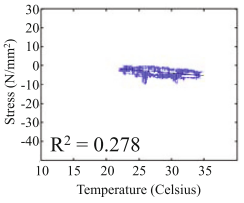

(*j*) *10th span*

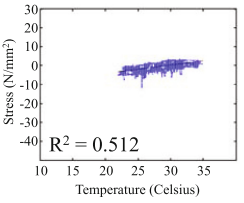

(*k*) *11th span*

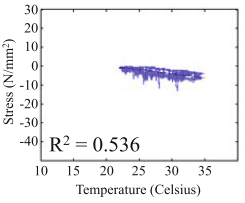

(*l*) *12th span*

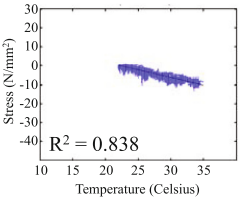

(*m*) *12th span*

Fig. 9. The relationship between temperature and the static stress component.

5 Conclusions

In this research, aiming the establishment of a strategy for future maintenance of long-span bridges administrated by local governments, a short-term monitoring was carried out. Here, more than one hundred sensors are disposed along the bridge in order to evaluate its current load-carrying capacity and performance. The bridge studied is a 13 span Gerber (cantilever) steel through truss bridge completed and opened to traffic in 1937.

Results after 4.5 days of monitoring showed that, in the case of upper chord's normal stress, the minimum dynamic stress component originated by live load minimum value was −19.7 MPa, and the corresponding minimum static stress component originated by temperature variation was −33.7 MPa. From this, it was deduced that static stress component fluctuation is bigger than dynamic stress component fluctuation. The minimum static stress component resulted to be of the same magnitude that the temperature stress, which was calculated using the temperature variation during the period of monitoring, steel coefficient of linear expansion, and steel Young's coefficient. Since this time on-site measurements related with the Gerber hinge movable part were not carried out, a future examination will be necessary. However, based on the obtained results, it was inferred that the Gerber hinge movable part is not working, that it is fixed. Additionally, based on the relationship between each span temperature and the static stress component, it was found a high correlation between temperature and static stress component correspondent to the upper chord of 6th and 8th spans. Therefore, it is though that the Gerber hinges of these spans should be repair preferentially.

References

1. Nagai, M., Miyashita, T.: Recent topics on steel bridge engineering in Japan - design and maintenance. In: 10th Korea-China-Japan Symposium on Steel Structures, Seoul, South Korea (2009)
2. Cross-ministerial Strategic Innovation Promotion Program: Homepage of Cross-ministerial Strategic Innovation Promotion Program. http://www.jst.go.jp/sip/k07.html. Accessed Jun 2016
3. Boller, C., Chang, F.K., Fujino, Y.: Encyclopedia of Structural Health Monitoring. Wiley, New Jersey (2009)

Vibration-Based SHM of Railway Bridges Using Machine Learning: The Influence of Temperature on the Health Prediction

Elisa Khouri Chalouhi[1(✉)], Ignacio Gonzalez[2], Carmelo Gentile[3], and Raid Karoumi[2]

[1] Department of Structural Engineering and Bridges, Royal Institute of Technology, Stockholm, Sweden
elisakc@kth.se
[2] KTH Royal Institute of Technology, Stockholm, Sweden
[3] Politecnico di Milano, Milan, Italy

Abstract. Civil engineering structures continuously undergo environmental conditions changes that can lead to temporary variations of their dynamic characteristics. Therefore, damage detection techniques have to be able to distinguish abnormal changes in the response due to damage from those normally related to environmental conditions variability.

This paper addresses this issue by presenting a damage detection method that uses machine learning to detect and localize damage in railway bridges under varying environmental conditions (i.e. temperature). Results of the application to simulated data are shown with validation purposes.

The first stage of the proposed algorithm consists in training a set of Artificial Neural Networks (ANNs) to predict deck accelerations during train passages assuming the bridge to be undamaged (or in a known state of preservation). In the second stage, the currently measured response is compared with that predicted by the trained ANNs. Since possible changes in the bridge state of preservation (damage) decrease the predictive accuracy of the ANNs, this comparison allows for the damage detection. During both stages, air temperature is given as input to the networks together with the train characteristics (i.e. speed and load per axle).

The application results in the paper prove the ability of the algorithm to detect and localize damage. Furthermore, when the same procedure was applied neglecting the environmental factor, a noticeable decrease of the prediction power was met. This proves that changes in structural properties due to temperature variation can mask the damage occurrence and prevent its detection. The importance of accounting for environmental variations in damage detection is thus highlighted.

Keywords: Structural Health Monitoring · Environmental conditions · Machine learning · Damage detection · Artificial Neural Network

1 Introduction

After the economic crisis of 2009, a steady growth in railway traffic for most of the EU countries was registered from 2011 on. This aspect, together with a lot of railway bridges

© Springer International Publishing AG 2018
J.P. Conte et al. (eds.), *Experimental Vibration Analysis for Civil Structures*,
Lecture Notes in Civil Engineering 5, https://doi.org/10.1007/978-3-319-67443-8_17

approaching the end of their design life, could result in structures no more functional for their intended use. In order to recognize in time such situations and avoid catastrophic consequences, several condition-based maintenance philosophies have been developed; they are based on the idea of taking a quick corrective action if a sensing system installed on the structure has notified the presence of damage.

Due to the need of developing such philosophies, *Structural Health Monitoring* (SHM) has become an active field of research in civil engineering applications. SHM, as defined in [1], is the process of detecting damage by (i) measuring the structure response under various operational and environmental conditions, (ii) extracting damage-sensitive features and (iii) analysing them to assess the system health. In order to make a diagnosis based on these features, it is necessary to find the relation between them and the structure state of health. In this context, the discipline of *machine learning* consists in learning this relation during the *training period* from a set of recorded data. When only data from the normal operating conditions are used during the training, one can speak about *unsupervised learning*; *supervised learning*, instead, refers to the case in which data sets in several health conditions are recorded and used during the training to identify several classes the structure health could belong to. In both cases, *pattern recognition* can be used to detect damage by comparing the current recorded response with that/those learned during the training phase. In the case of unsupervised learning, since the comparison is made only with one typical structure condition, it is not possible to identify the exact current class but only to detect possible anomalies with respect to the normal condition. Anomalies in the response are then flagged as damage. However, if the training phase does not take into account all factors defining the normal response of the structure, there is the risk of identifying as damaged a structure that is only experiencing environmental and/or operational conditions different from those considered in the training phase. Civil engineering structures, such as bridges, inevitably experience environmental condition variability; therefore, it is of main importance to distinguish between changes in the structure behaviour due to damage and those related to other causes, such as temperature variation.

During the last years, several approaches (*data normalization* procedures) have been used to solve this issue. One solution can be finding damage-sensitive features insensitive to environmental variations. In [2], principal component analysis (PCA) is employed to identify these features; however, in the case of unsupervised learning where data from the damaged system are not available, this approach is not completely reliable. Therefore, in the field of SHM using modal parameters, the influence of environmental variability on the common damage-sensitive features has been largely studied. Data collected on Bridge Z24, Switzerland, has been used in [3] to quantify the variance in eigen-frequencies due to temperature changes; it has been shown to be of the same order of magnitude of that due to damage. Therefore, it is important to filter the environmental influence before proceeding with the damage detection. In [4], indeed, a linear adaptive filter has been developed for the Alamosa Canyon Bridge, New Mexico, in order to distinguish changes in the modal parameters due to damage from those due to temperature changes. Finally, in [5], while identifying damage based on natural frequencies shifts and mode shapes changes, the linear correlation between temperature and modal frequencies has been shown again for the case study of San Michele Bridge, Italy.

The approach proposed in this paper to solve the environmental variability issue is different from the above mentioned. First of all, deck accelerations are used instead of the common modal parameters of [3–5]. Accelerations are sensitive both to damage and temperature variability; however, the influence of the latter is not modeled in order to filter data before proceeding with the damage detection. Instead, the environmental parameter is treated in the same way as loads applied to the structure (i.e. traffic); they are given as input to the algorithm, which is taught to predict the deck accelerations for such operational and environmental conditions in the healthy stage. Assuming a training phase covering most of the environmental and operational conditions the bridge commonly experience, any discrepancy between predicted and measured accelerations can be flagged as damage. Indeed, the influence of temperature is already considered both in the predicted behavior and in the measured one; therefore, the discrepancy can only be caused by parameters that are not considered in the prediction, i.e. structural changes due to damage.

2 Methodology

The aim of this work is to expand an existing [6] damage detection method for railway bridges. With respect to the original version, the expanded algorithm takes into account the inevitable environmental conditions variability (i.e. air temperature changes) bridges are subject to. Moreover, indications about the best usage of the algorithm are given based on results obtained in a case study.

Three main stages can be recognized in the method: (1) data collection, (2) training of Artificial Neural Networks (ANNs) and Gaussian Processes and (3) health classification of the structure.

For the first stage, the installation on the bridge of a monitoring system composed of accelerometers, thermocouples and a Bridge Weight In Motion (BWIM) system is required. During each train passage, the accelerations of the deck at several locations along the bridge are recorded together with the air temperature. The BWIM system, instead, provides information about the crossing vehicle, such as axle loads and their position. These data have to be collected during two phases: a *reference period* and the moment when the bridge state of health has to be classified (*testing period*). The first set of data refers to a moment in which the structure state of preservation is known: it can be damaged or not but at a known degree. Indeed, the proposed one can be classified as *novelty detection method*; the algorithm does not detect damage as deterioration of the bridge properties, but as change in the structure behaviour with respect to the reference one.

In stage 2, data in reference condition are used to train one ANN and one Gaussian process per accelerometer.

In [7], ANNs are intuitively defined as universal approximators; indeed, through an initial period called *training*, they learn to approximate whichever function by knowing the values (*targets* t) it reaches for given sets of independent variables (*inputs* **x**). The aim of the training phase is to find the parameters of the ANN that minimize the prediction error for the given inputs. The prediction error for the s-th ANN (pe^s), given n sets

of inputs ($\mathbf{x}_i^s$) and corresponding targets (t_i^s), is computed as in Eq. (1), where ANN($\mathbf{x}_i^s$) are the approximations of the function (*outputs*) in correspondence of the given inputs.

$$pe^s = \frac{1}{n}\sum_{i=1}^{n}[ANN(\boldsymbol{x}_i^s) - t_i^s]^2. \tag{1}$$

In the present study, one ANN per accelerometer is trained using targets and inputs recorded during several train passages with a time step defined by the sampling frequency of the monitoring system. Deck accelerations play the roles of targets and outputs, while the input vector contains: the air temperature (T) recorded by the thermocouple closest to the considered accelerometer, the speed (v) of train crossing the bridge, the location on the bridge of the first axle of the vehicle and the acceleration values at the k previous time steps.

After training the ANNs with data collected in reference condition during several train passages, the prediction errors over each train passage are computed: in the case study, a strong dependence on the train speed and the air temperature has been noticed. Therefore, a Gaussian Process [8] is used to find a normal distribution of the prediction error for each ANN using train speed or air temperature as independent variables. Drawing an analogy with that of ANNs, the training of a Gaussian Process in this study has as targets the prediction errors of the corresponding trained ANN computed over each train passage, while the input is represented by the train speed or the air temperature.

In the end of stage 2, each ANN is able to predict acceleration time histories in a bridge section (i.e. where the accelerometer is located) during a train passage given as input, for each time step, train speed, load magnitude, first axle position, air temperature and previous accelerations in the same section. Due to the nature of data used for the training, such prediction is realistic as long as the bridge state of health remains as in reference condition. Moreover, for each accelerometer, the mean values ($\mu_s(v)$ and $\mu_s(T)$) and the standard deviations ($\sigma_s(v)$ and $\sigma_s(T)$) of pe^s as function of air temperature and train speed are known. Once again, such normal distributions for prediction errors are realistic as long as reference conditions are valid.

In the third and last stage, data collected in testing condition are given as inputs to the trained ANNs, who predict the accelerations the deck would have if reference conditions were still valid. One pe^s is then computed as in Eq. (1) for each train passage and each sensor, using the recorded accelerations as targets and the predicted ones as outputs. Finally, a *damage index* (DI) taking into account all the n_s accelerometers is computed as in Eq. (2) for each train passage:

$$DI = \frac{1}{n_s}\sum_{i=1}^{n_s}\frac{pe^s - \mu_s(v)}{\sigma_s(v)}. \tag{2}$$

In case the bridge, due to damage, undergoes structural changes with respect to reference condition, the recorded accelerations differ from the predicted ones, leading to high prediction errors and high damage indices. Therefore, comparing the DI of a single train passage with a discriminating threshold, it is possible to classify the bridge as damaged or not. The choice of this threshold is of great importance; indeed, a low value would lead to high probability of false positive (i.e. the bridge is erroneously classified as

damaged), while a high one to high probability of false negative (i.e. the bridge is erroneously classified as undamaged). Of course, undetected damage is the most dangerous case; however, lowering the threshold too much would make the proposed method useless, ending up in bridges always classified as damaged. Therefore, the best threshold should be chosen based on considerations about the probability of damage and the costs related to false positives and negatives. As previously mentioned, a single train passage allows the computation of DI and thus the classification of the bridge state of health. However, it is recommended to use more than one passage in order to make the diagnosis more reliable.

3 Case Study

A case study has been analyzed in order to validate the proposed method and highlight the improvement with respect to the original one. A simple two-dimensional model of a beam bridge has been used to simulate data that would a monitoring system of the type described above would record.

3.1 The Bridge and the Train

In order to reproduce a realistic case, dimensions resembling those of the Banafjäl Bridge in Sweden have been used. A uniform mesh made of Euler-Bernoulli beam elements, characterized by six degrees of freedom each, has been considered. Geometric and material properties of the model are summarized in Table 1, while a schematic illustration of the FEM model is shown in Fig. 1.

Table 1. Material and geometric properties of the FEM model.

Bridge span length (L)	42 m
Cross sectional area (A)	7.11253 m^2
Mass per unit meter (ρ)	18066 kg/m
Moment of inertia of the cross section (I)	0.62 m^4
Number of elements of the mesh (n_{el})	150
Length of each element (L_{el})	0.28 m

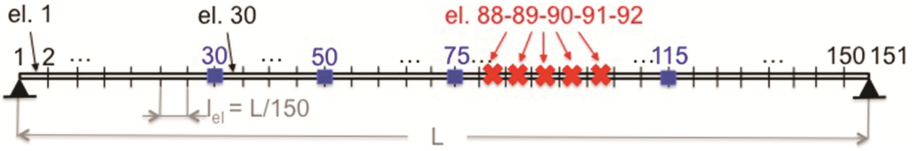

Fig. 1. Schematic illustration of the FEM model.

It has been assumed that the structural members of the modelled bridge are made of steel. Metals have a Young modulus (E) that varies with temperature: an approximated relation [9] between the modulus of elasticity and temperature is shown in Eq. (3):

$$E(T) = E_{15\,^{\circ}\mathrm{C}}[1 - \alpha_E * (T - 15\,^{\circ}\mathrm{C})]. \tag{3}$$

The influence of temperature is also taken into account through the thermal expansion experienced by materials such as steel. In case of prevented elongation (i.e. the beam bridge is assumed to be hinged at both end points), this phenomenon leads to the onset of an axial force (Eq. (4)) that affects the system stiffness.

$$N(T) = \sigma * A = \varepsilon * E(T) * A = \frac{\Delta L_{el}}{L_{el}} * E(T) * A = \frac{L_{el} * \alpha_L * (T - T_{construction})}{L_{el}} * E(T) * A. \tag{4}$$

A construction temperature of 15 °C has been assumed during the simulation, while Table 2 shows common values of the thermal characteristics of construction steel in the temperature range ±35 °C [9].

Table 2. Thermal characteristics of the assumed bridge material.

Young modulus at 15 °C ($E_{15\,^{\circ}\mathrm{C}}$)	210 GPa
Temperature coefficient for Young modulus (α_E)	2.4e−41/°C
Coefficient of thermal expansion (α_L)	10.7e−61/°C

The dissipation in the bridge, instead, has been modelled as Rayleigh damping with modal damping ratio (ξ) of 6% for both the first and the second bending modes.

The considered crossing vehicle is as a single locomotive with four axles running always in one direction (from element 1 towards element 150 of Fig. 1) with constant speed during the passage. The distance between the axles is equal to 2, 3 and 2 m. During the simulation, the train is then modelled as four moving point loads, which represent the only external loads applied to the structure.

3.2 The Monitoring System and the Simulated Data

For what concern the BWIM system, the axle position is assumed to be provided without errors, while load magnitudes are accurate to 5%. For the sake of this simulation, assuming that the first axle of the crossing vehicle is above the first node of the bridge at the beginning of the passage, its position can be easily computed at each time step by knowing the constant value of the train speed. Both the train speed and each axle load have been obtained from uniform random distributions respectively in the ranges 20–23 m/s (ca. 72–83 km/h) and 100–120 kN (the total weight of a common wagon is around 40 tons).

Due to the limited dimensions of the bridge and the consequent short duration of each train passage, the air temperature can be assumed constant along the structure and during each passage. This condition, in a real case, would correspond to the installation of only one thermocouple, i.e. only one temperature value for all the accelerometers. Unlike train speed and axle loads, air temperature can't be randomly selected from a range assuming uniform probability distribution; therefore, an ad hoc distribution was created by fitting a set of temperature data collected in Bromma, Sweden, during one year.

Finally, for what concern the set of accelerometers, four of them with sampling frequencies of 300 Hz have been ideally placed in correspondence of the nodes number 30, 50, 75 and 115 (blue squares in Fig. 1).

In the numerical simulation, the accelerations of those nodes have been obtained by numerically integrating the equation of motion. The method used in this integration is the Newmark-beta method with the Trapezoidal Rule and zero initial displacement and speed of the considered points. Finally, in order to mimic those that a real set of accelerometers would record, the simulated acceleration time histories were corrupted with an artificial white noise of 0 mean and 0.5 mg standard deviation.

Data due to 650 train passages have been simulated in undamaged conditions (bridge and train characteristics as mentioned above), while 200 in damaged ones. For the second set of data, damage has been modelled as a 30% reduction of the value of $E_{15\ °C}$ in Table 2 in elements number 88, 89, 90, 91 and 92 (red crosses in Fig. 1).

Undamaged conditions have been used as reference ones; 300 and 150 train passages have been used for training, respectively, the ANNs and the Gaussian Processes. The method, then, has been tested with the remaining data: namely, two different sets (200 train passage in undamaged conditions and 200 in damaged ones) have been used as testing data in order to prove that the algorithm is able to differentiate the two cases, i.e. detect damage.

4 Results

Figure 2 shows prediction errors (pe) referring to data in testing conditions plotted in ascending order (for the sake of readability). As previously mentioned, 200 train passages in undamaged conditions and 200 in damaged ones, respectively blue circles and red asterisks in Fig. 2, have been used as testing data.

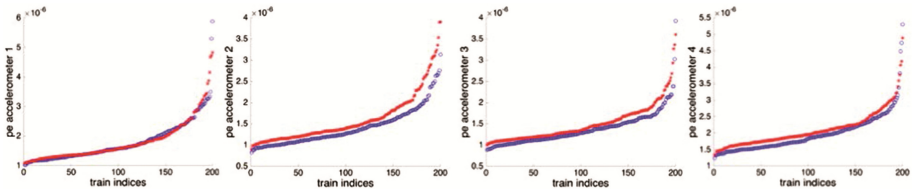

Fig. 2. Prediction errors for all accelerometers plotted in ascending order. Passages marked with red asterisks correspond to damaged conditions, those with blue circles to undamaged ones.

For each accelerometer, except for the first one, the two curves are clearly separated giving a first hint to the ability of the proposed method of identifying changes in the structural behavior due to damage. More precisely, since the ANNs have been trained with a set of passages in undamaged conditions, Fig. 2 confirms what expected: pe in damaged conditions have higher values than those in undamaged ones.

Figures 3 and 4 show pe plotted respectively against train speed and air temperature. The meaning of the blue circles and red asterisks is the same as in Fig. 2, while black crosses come from the train passages in undamaged conditions used to train the Gaussian

Processes. The latters have been trained using as independent variable the speed for Fig. 3 and the temperature for Fig. 4. The black thick line is $\mu_s(v)$ (or $\mu_s(T)$) and the grey area is limited by the two curves $\mu_s(v) \pm 2\sigma_s(v)$ (or $\mu_s(T) \pm 2\sigma_s(T)$).

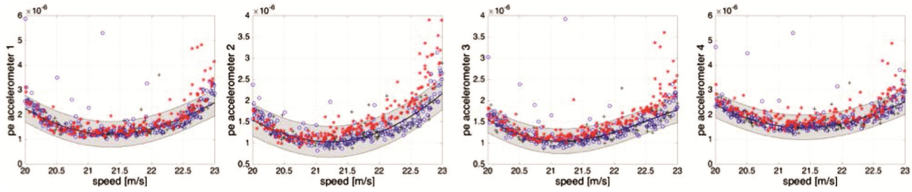

Fig. 3. Prediction errors for all accelerometers plotted against speed, which is the independent variable for the Gaussian Processes. Passages marked with black crosses have been used to train the Gaussian Processes, the black thick line is the mean μs(v) and the grey zone is the that delimited by μs(v) ± 2σs(v). Passages marked with red asterisks correspond to damaged conditions, those with blue circles to undamaged ones.

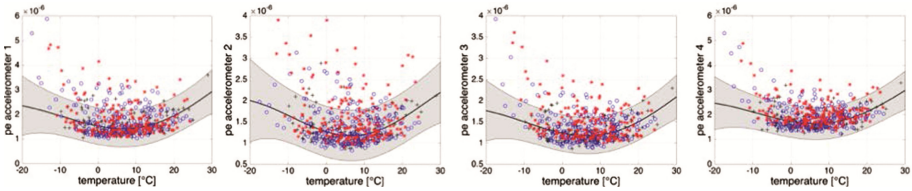

Fig. 4. Prediction errors for all accelerometers plotted against air temperature, which is the independent variable for the Gaussian Processes. Passages marked with black crosses have been used to train the Gaussian Processes, the black thick line is the mean $\mu_s(v)$ and the grey zone is the that delimited by $\mu_s(v) \pm 2\sigma_s(v)$. Passages marked with red asterisks correspond to damaged conditions, those with blue circles to undamaged ones.

Remembering Chebyshev's inequality, most (at least 75%) pe values in undamaged conditions, which are the training conditions for the Gaussian Processes, should belong to the grey area; Figs. 3 and 4 confirm it. Instead, pe in damaged conditions tend to escape that area from above; indeed, pe increase whenever testing conditions are different from reference ones. This phenomenon and, as a consequence, the separation between the damaged and undamaged sets of data is much more visible in Fig. 3 than in Fig. 4. Moreover, pe in Fig. 4 are much more widespread and with a less clear trend than in Fig. 3.

It can be concluded that, despite depending on both train speed and air temperature, the prediction errors have to be stochastically characterized using only the speed as independent variable in order to be a reliable indicator of damage. This explains why only $\mu_s(v)$ and $\sigma_s(v)$ appear in the damage index of Eq. (2).

Moreover, having a careful look at the four graphs of Fig. 3, it can be noticed that the separation between damaged and undamaged sets is: almost undetectable for the first accelerometer (except for very high speed values), clear in the second and third ones for $v > 21$ m/s and visible for the last one in correspondence of all speed values.

Accelerometers 2 and 3 are the closest to the center of the span, where the bridge can vibrate more freely, while accelerometers 3 and 4 are the closest to the damaged area.

It can be concluded that placing sensors far from constrained areas allows for better damage detection, but also information about the possible location of the damage can be collected through these graphs. Moreover, trains crossing the bridge at higher speeds give a clearer indication of damage when present; therefore, it is recommended to use them as testing passages instead of others at lower speeds.

Figure 5a shows the damage indices (DI) computed considering all four sensors for the two sets of testing data. Once again, blue circles and red crosses represent respectively undamaged and damaged conditions, while the continuous lines have been placed at the mean values height for both sets.

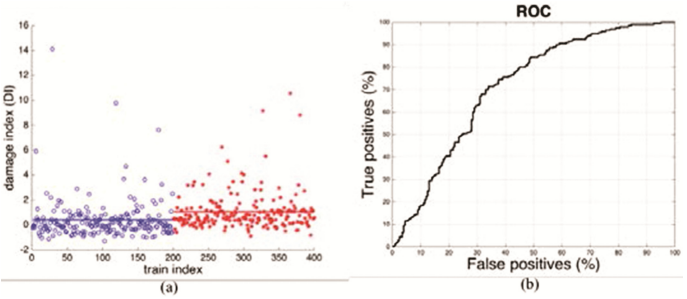

Fig. 5. (a) Damage indices for 400 train passages (200 in undamaged and 200 in damaged conditions). Passages marked with red asterisks correspond to damaged conditions, those with blue circles to undamaged ones. The continuous lines represent the mean values of the two sets. (b) Receiver Operator Curve based on the results of (a).

As expected DIs in damaged conditions are generally higher than those in reference (here undamaged) ones.

A quantitative indication of the detection power of the present method is given by the *Receiver Operating Characteristics* (ROC) curve of Fig. 5b. Indeed, given two sets of data (called *positives* and *negatives*) belonging to two different classes and using a classifier to guess the class they belong to, it is possible to compute the two performance metrics TP (*true positive rate*) and FP (*false positive rate*). TP represents the ratio between the number of positives correctly classified and the total number of positives, while FP that between the number of negatives incorrectly classified (i.e. classified as positives) and the total number of negatives. In the present study, negatives are associated to reference conditions and positives to damaged ones. The classifier is the proposed damage detection method and, as previously mentioned, it is based on a DI threshold value; indeed, for each value it is possible to classify data and thus compute one value of TP and one of FP. The ROC curve comes from varying the value of such threshold. The more the curve looks like a reversed L (i.e. 100% TP corresponds to 0% FP), the better the classifier works. Another indicator of the classificatory prediction power is the *area under the curve* (AUC): the closer to 1, the higher prediction power.

For the curve of Fig. 5b, AUC = 0,7138 and the following couples of values can be identified: TP = 90%, FP = 58% and TP = 70%, FP = 33%. A DI threshold value corresponds to each couple TP-FP; therefore, if one uses the value corresponding to the couple 70–33%, evaluating the state of health of the bridge using only one train passage, there is 30% (100% - TP) probability of being unable to detect damage if present. However, as shown in Table 1, the prediction becomes much more reliable increasing the number of passages and using the Bayesian inference to compute the *conditional/posterior probability of damage* (Table 3).

Table 3. Posterior probability of damage.

A priori probability of damage	TP [%]	FP [%]	Train passages resulting in healthy classification	Train passages resulting in damaged classification	Posterior probability of damage [%]
1e−06	70	33	19	1	42
			26	4	93
			35	10	99

In order to show the improvement with respect to the original method, the simulated data have been used again following the same procedure but removing the air temperature from the input of the ANNs. Moreover, other data have been simulated neglecting the influence of temperature on the bridge behavior (i.e. constant Young Modulus and no attempted elongation due to temperature variation) and training the ANNs without the environmental factor; Fig. 6 shows the three obtained ROC curves. The red dotted one refers to ANNs trained without temperature and simulated data independent on

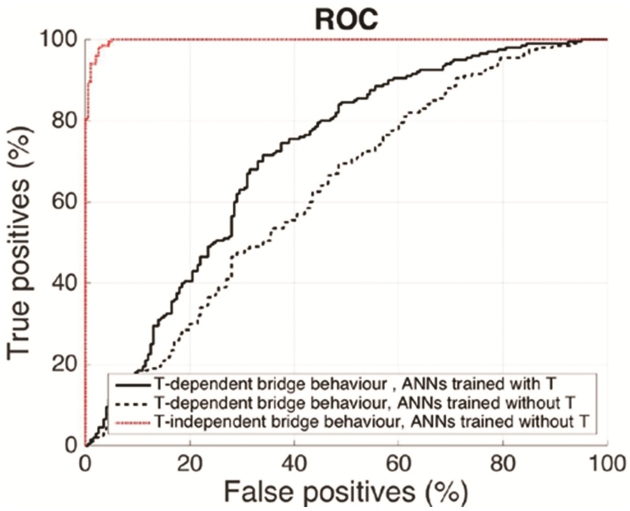

Fig. 6. ROC curves.

temperature as well. It has the ideal shape (i.e. reversed L) and AUC = 0,9974; however, a behavior unrelated to environmental conditions variability is unreal. When it comes to data simulated considering temperature effect, it is clear how neglecting it in the ANNs training (black dashed line) leads to a less reliable classification; indeed, the black dashed line is almost straight and has a AUC of only 0,6265.

5 Conclusions

In this paper, a model-free damage detection method for railway bridges has been presented and validated on a case study. The algorithm uses acceleration time histories recorded on the bridge deck during train passages as damage-sensitive quantities. A set of Artificial Neural Networks (ANNs) is trained to predict the bridge response to railway traffic in normal conditions. The comparison between predicted and measured responses, in terms of accelerations, allows for the classification of the state of health of the structure; indeed, any relevant change in the bridge behavior is associated to damage. Since air temperature is known to strongly affect structures response to external loads, the novelty of the present study is the addition of this quantity to the inputs of the ANNs. Doing so, the environmental condition is taken into account in the prediction of the bridge behaviour in normal conditions; therefore, its effect neither can be misinterpreted as damage nor can hide damage presence.

A simple two dimensional finite element model of a railway beam bridge has been used to validate the proposed method. Results show the ability of the algorithm of detecting damage and giving information about its location. An improvement in the detection power given by the introduction of the air temperature is clearly shown as well. The FE model has been exclusively used to simulate data a set of accelerometers would record on an actual bridge; indeed, in order to apply this damage detection method, no FE model of the examined bridge is required (*model-free*). This consideration increases even more the reliability of the case study results leading to assume that the method would work also for different types of bridges. The authors, indeed, are currently applying it to data recorded on real bridges obtaining promising results.

Air temperature has been proved to be of main importance in the ANNs training, i.e. in the prediction of the bridge response. Instead, for what concern the stochastic characterization of the ANNs performance (in term of prediction errors), the fundamental parameter is train speed. Indeed, as shown in Figs. 3 and 4, damage can be much easily detected when ANNs prediction errors are stochastically characterized using train speed as independent variable instead of temperature.

When applying this method, better performances can be reached under some conditions.

Figure 3 shows that damage is easier to detect for trains running at higher speeds; therefore, those should be used in the testing phase to detect the possible damage. Moreover, accelerometers placed far from constraints give a clearer indication of damage presence than those placed in their proximity. Therefore, when choosing the sensors location, it is recommended to place most of them in areas of the bridge free to vibrate. Finally, once damage has been detected, information about its location can be gathered

comparing pe plots for all sensor; those in which damage is recognizable for all tested speeds are the closest to the damaged area. However, such information is not so easily readable; therefore, additional studies are needed to have a more reliable damage localization.

Acknowledgement. This research has been carried out at the Department of Civil and Architectural Engineering, at the Division of Structural Design and Bridges, at the Royal Institute of Technology (KTH), in Stockholm.

Partners in the project were:
Royal Institute of Technology, Stockholm, Sweden,
Politecnico di Milano, Milan, Italy.

References

1. Farrar, C.R., Worden, K.: Structural Heath Monitoring: A Machine Learning Perspective. John Wiley & Sons, Chichester (2013)
2. Manson, G.: Identifying damage sensitive, environmental insensitive features for damage detection. In: 3rd International Conference on Identification in Engineering Systems, Swansea, UK (2002)
3. De Roeck, G., Peeters, B., Maeck, J.: Dynamic monitoring of civil engineering structures. In: Computational Methods for Shell and Spatial Structures IASS-IACM, Chania, Crete (2000)
4. Sohn, H., Dzwonczyk, M., Straser, E.G., et al.: An experimental study of temperature effects on modal parameters of the Alamosa Canyon Bridge. Earthq. Eng. Struct. Dyn. **28**, 879–897 (1999)
5. Gentile, C., Saisi, A.: Continuous dynamic monitoring of a centenary iron bridge for structural modification assessment. Front. Struct. Civ. Eng. **9**, 26–41 (2015)
6. Gonzalez, I., Karoumi, R.: BWIM aided damage detection in bridges using machine learning. J. Civil Struct. Health Monit. **5**, 715–725 (2015)
7. Braspenning, P.J., Thuijsman, F., Weijters, A.: Artificial Neural Networks: An Introduction to ANN Theory and Practice. Springer, Heidelberg (1995)
8. Rasmussen, C.E., Nickisch, H.: Gaussian processes for machine learning (GPML) toolbox. J. Mach. Learn. Res. **11**, 3011–3015 (2010)
9. NPL (National Physical Laboratory). http://www.kayelaby.npl.co.uk

Finite Element Model Calibration of a Historic Wiegmann–Polonceau Truss Based on Experimental Modal Parameters

Hoa T.M. Luong[1,2(✉)], Werner Lorenz[2], Rolf G. Rohrmann[3], Volkmar Zabel[4], and Samir Said[5]

[1] Division 7.3 Fire Engineering,
Bundesanstalt für Materialforschung und -prüfung (BAM), Berlin, Germany
mai.luong@bam.de
[2] Chair of Construction History and Structural Preservation,
Brandenburg University of Technology (BTU) Cottbus-Senftenberg,
Cottbus, Germany
[3] SABM Strukturanalyse & Bauwerksmonitoring, Berlin, Germany
[4] Institute of Structural Mechanics,
Bauhaus-Universität Weimar, Weimar, Germany
[5] Division 7.2 Buildings and Structures, BAM, Berlin, Germany

Abstract. This paper describes the experimental calibration of an existing Wiegmann–Polonceau roof truss based on modal parameters. Dynamic tests allowed the determination of the natural frequencies and mode shapes of the global truss and of individual truss members. The global and local modal configurations as well as coupled vibration of truss members are discussed. In addition, as truss members are axially loaded, the effect of stress stiffening on the modal parameters is considered. Moreover, several finite element models with different modelling assumptions for the details of the connections and member geometrical characteristics such as gusset plates and turnbuckles were developed. A suitable numerical model was chosen to represent the truss structural behavior. This paper focuses on the local measurement and analysis strategies applied to single truss members. The possibility of using a local analysis method, namely methods that consider individual members as part of a structure, is demonstrated to assess the behavior of the global truss structure. The comparison of the results after calibration reveals a very good correlation between the experimentally identified and numerically estimated modal parameters of the historic truss.

Keywords: Historic truss structures · Coupled vibration · Stress stiffening · Modal analysis · Finite element model calibration

1 Introduction

Truss structures are used in various constructions such as roof trusses in railway stations, market halls, industrial buildings or truss girders in bridges. Particularly, iron and steel trusses supporting the roof of buildings are of interest. A number of these

© Springer International Publishing AG 2018
J.P. Conte et al. (eds.), *Experimental Vibration Analysis for Civil Structures*,
Lecture Notes in Civil Engineering 5, https://doi.org/10.1007/978-3-319-67443-8_18

lightweight truss structures are still in use to support historic and heritage monuments. Examples of significant historic truss structures are the iron roof trusses of the State Hermitage Museum in Saint Petersburg. In terms of volume, variety of constructive prototypes and richness of details, they are outstanding evidence of early European structural steelwork [1, 2]. Preservation of historic truss structures has been becoming increasingly important.

Due to presence of damages, change in intended use, increase in service loads or accidental actions, safety evaluation of existing trusses is essential. The structural assessment requires the knowledge of the axial forces or corresponding stresses in truss structures. In addition, the application of non-destructive assessment methods is required. For truss structures, the axial forces can be estimated by static calculations, given information about parameters such as external loads, prestress conditions, boundary and joint connections are known accurately. However, information about these parameters is difficult to be acquired precisely in practice. This is especially true for historic constructions, where uncertainties relating the end constraints, prestress of turnbuckles, geometrical properties due to corrosion damages, as well as varied mechanical properties of historical materials, cannot be adequately taken into account into static calculations [3]. As a result, inverse identification of the input parameters, in particular the loads, have been proposed based on the output parameters such as natural frequencies and mode shapes [4–7].

Concerning the dynamic behavior of trusses, the constituted truss members vibrate interactively with each other in a coupling manner, resulting in similar modes of vibration. Moreover, as multiple load patterns exist in trusses, compressive and tensile forces have countering effects on the modal parameters. Based on the state of research with limited work relating to the structural parameter estimation of historic Wiegmann–Polonceau trusses using modal parameters, this paper discusses the finite element (FE) model calibration applied to existing trusses. Particularly, the global versus local measurements and analysis strategies that consider a global truss model or a single beam model representing individual truss members are addressed. Furthermore, uncertainties related to the geometrical and mechanical properties of historic truss structures are examined.

2 Investigated Wiegmann–Polonceau Roof Truss

The Wiegman–Polonceau truss structures, proposed by the German engineer, Rudolf Wiegmann (1804–1865), and the Frenchman, Camille Polonceau (1813–1859), were popular support systems of iron building constructions in the second half of the 19th century [8]. The structural efficiency of these types of trusses is demonstrated by their characteristics as lightweight structures with impressive weight-to-span ratio and slender tension members. The simplified design of the trusses assumed all hinged joints. In individual truss members, mainly compressive and tensile forces are assumed.

The investigated historic Wiegman–Polonceau truss is located at a formerly horse riding building that was constructed between 1885 and 1891 in the city of Potsdam, Germany [9]. The roof system of the building consists of eight individual trusses at a distance of about 4.2 m from each other and connected with each other by horizontal tie-bars.

The dimension of the whole building is approximately 18 m wide and 38 m long. The trusses are positioned at about 5.8 m above the ground level. From 2000 to 2013, renovation works were planned and carried out for the heritage protected building within a residential project, in which the building's exterior walls and the iron roof trusses were preserved.

Considering one single truss system, the truss is approximately 18 m wide and 6 m high (see Fig. 1). Several tension members of the truss have turnbuckles to allow compensation for differences in manufacture, i.e. the member dimensions can be adjusted during erection. In addition, preloading could be applied to achieve a desired deformation or prestress state of the truss. The shape of the strut members in compression is thickened in the middle is to avoid buckling. This shape was assumed to be optimal and economical form for small cast iron compression members of the Wiegmann–Polonceau trusses.

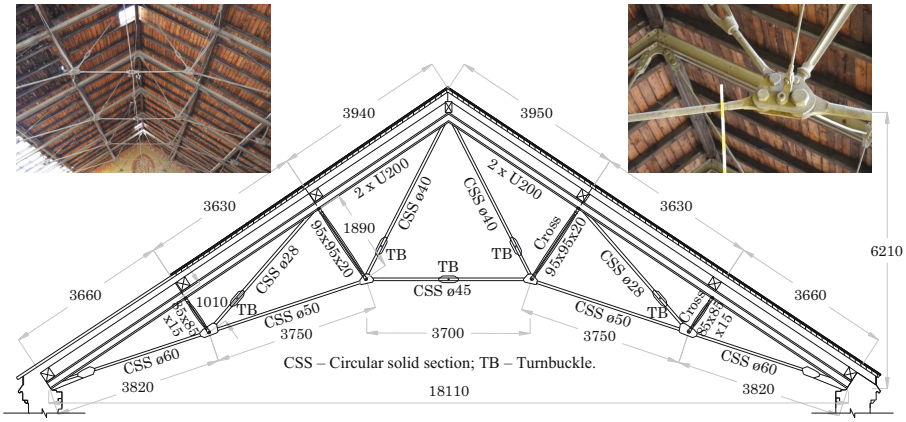

Fig. 1. Investigated historic iron Wiegmann–Polonceau truss in the city of Potsdam, Germany.

3 Finite Element Modelling

Static and dynamic analyses were carried out using the finite element method to examine the structural behavior of the truss. Based on a literature research of the historical materials, the mechanical properties of the truss were assumed as the modulus of elasticity of the wrought iron of 195 000 N/mm^2 for all truss members, except the four compression struts. The four struts with the optimal shape were assumed to have the modulus of elasticity of the cast iron of 90 000 N/mm^2. The value of the mass density was chosen as 7850 kg/m^3 and the Poison ratio of 0.3. The FE models were created using the program ANSYS [10]. The shear deformation and rotational inertia were taken into account based on Timoshenko beam theory.

During the process of building the FE models, different simplifications were considered to evaluate appropriate assumptions as well as meaningful simplifications for the numerical models that approximate the behavior of the structure. In total, four different FE models were created, considering whether both the inertia and mass or only the mass of the gusset plates at the connections and the turnbuckles were included.

In addition, different types of elements were examined. The first model is referred to as a simplified FE model including the mass of the gusset plates and turnbuckles, being modeled as point mass elements. The second model is also a simplified FE model but more detailed than the first one, including the inertia and mass of the gusset plates as beam elements with rectangular cross-sections, and the mass of the turnbuckles. The third model is a more detailed FE model taking into account the inertia as well as mass of both the gusset plates and turnbuckles; the gusset plates were modeled as beam elements with rectangular cross-sections, while the turnbuckles as beam elements with circular hollow cross-sections. The fourth model is similar to the third one, except that shell elements were chosen for the gusset plates.

3.1 Preliminary Analysis of the Axial Force and Axial Stress Distribution

All FE models were subjected to the loads of the roof, applying as point loads at five joints on the top chords. The roof loads are resulted from the timber roof above the truss, including the main timber beams, secondary timber beams, timber claddings and bitumen sealing sheets. A manual estimation of the roof loads was made. The total point load applied to each joint of the four joints on the top chords was calculated as 5.60 kN, whereas a point load on the remaining joint was estimated at a lower value of 4.06 kN due to the missing timber claddings and bitumen sealing sheets on one section of the roof (see Fig. 2).

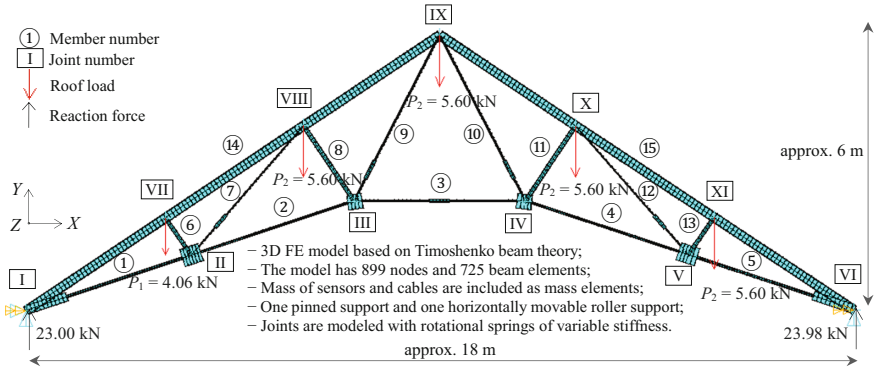

Fig. 2. Global FE model of the truss with assumed applied roof loads.

At first, static analyses were performed for all models. An initial basic check of the generated models was made by checking the reaction forces, which are consistent for all models. The sum of the resistant forces applied at the supports was also checked to be equal the total applied dead loads and live loads. A further check of the model was done by analyzing the vertical deflections. The maximum deflection of the truss was obtained similarly by all FE models of approximately 8.9 mm. After that, dynamic analyses were conducted. The results of the natural frequencies and mode shapes show some differences between the models. It demonstrates that modeling assumptions and

modeling simplifications affect the dynamic results of the truss. The details of the results for all models can be found in [9]. In this paper, the third FE model will be presented in details.

Figure 2 shows the third model together with the assumed roof loads. In total, the model was divided into 725 elements. The left support was modeled as pinned, whereas the right support as roller to be movable in horizontal direction. The masses of the sensors are included in the truss model. The experiments will be described in the next section of the paper. Figure 3 presents the static axial force and corresponding stress distribution of the FE model. Because the truss geometry is not absolutely symmetric as well as the asymmetric applied roof loads, the resulted axial forces and corresponding stresses are different for the members of similar characteristics. The relatively low state of stress of the truss was because some parts of the roof components were disassembled during the construction work of the building for the renovation project. In addition, at the time of the investigation of the truss, seasonal loads such as snow loads were not present.

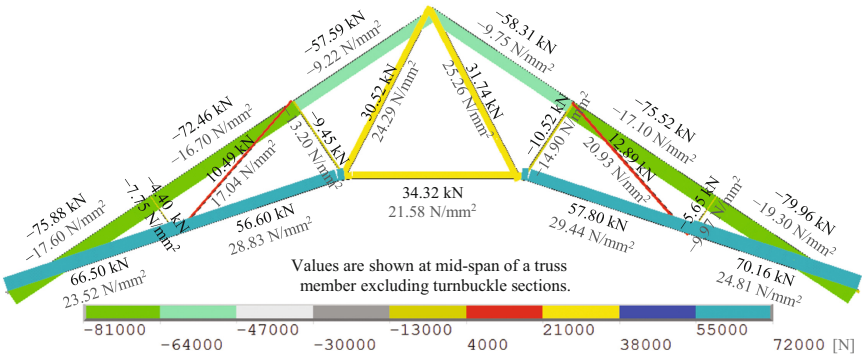

Fig. 3. Numerical static analysis showing the axial force distribution of the global FE model of the truss.

3.2 Stress Stiffening Effects on the Modal Parameters

Axial forces and thus axial stresses in truss structures cause changes in the structural stiffness, which in turn, modify the dynamic properties. This influence has been clearly recognized in the case of an axially loaded tie-bar, inducing a shift in the frequency spectrum [5]. The second-order effect of the axial force on the transversal stiffness of structural members has been utilized by researchers for the inverse identification of the axial forces in the members based on modal parameters. Relevant publications for members as part of a structure are for instance [4, 6, 7]. While [4, 7] concerned the multiple axial force identification of truss-like structures using FE modeling coupled with model updating techniques, [6] developed an analytical-based algorithm to determine the axial forces of single bars with unknown boundary conditions. Considering the different approaches in the literature, global analysis is referred as analysis of a truss structure as a whole, while local analysis is associated with single truss members. The local analysis based on the algorithm proposed by [6] will be explained in later part

of the paper. In the scope of this paper, only the results of the local measurements and analysis of a single truss member are included. The numerical modeling and analysis strategy applied to individual members as part of a structure is discussed.

When analyzing a single member of the truss, a FE model based on Timoshenko beam theory was built with rotational as well as translational springs at the beam ends, as shown in Fig. 4. The common assumptions for joints of truss structures are pinned-jointed. However, as examined in [7], the assumptions of the joint rigidity can have significant effects on the dynamic behavior of a structure. Thus, for correct approximation of the structural dynamics, the numerical model should consider the unknown joint stiffness. For practical evaluation of the joint flexibility, constraint parameter in the form of percentages of semi-rigid connection has been introduced [11]. The non-dimensional fixity factor representing the semi-rigid connection is expressed as

$$\gamma_i = \frac{k_{ri}L}{3EI + k_{ri}L} \tag{1}$$

where k_{ri} is the rotational spring stiffness of the member end i, EI is the bending stiffness and L is the length of the member. The value of the fixity factor$^{\gamma}$ is bounded between zero to one, corresponding to pinned to rigid condition.

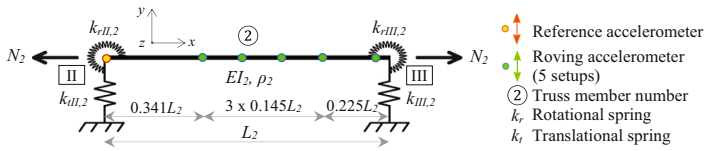

Fig. 4. Local measurement and analysis of the second truss member as part of the global truss structure.

4 In-Situ Dynamic Experiment

The in-situ experiments were conducted considering two types of measurements. The global measurements of the vibration behavior of the whole truss were carried out with ambient vibration and hammer excitations using geophones. The geophones were placed at selected connection nodes and mid-spans of the truss members. Regarding the local measurement, a single member of the truss, i.e. the second truss member, was selected. For this member, the geometrical property of the cross-sections can be considered uniform symmetric with no presence of turnbuckle elements. Therefore, it facilitated the numerical modeling of the member. In addition, a relative uniform axial stress distribution could be expected. Moreover, the vibration characteristics of the member subjected to an axial tensile force can be studied without concerning the member's buckling behavior. The vibration measurements for the member were performed with hammer excitation. Two accelerometers were used, which measured in the vertical direction perpendicular to the local longitudinal direction of the member.

One accelerometer was attached to the member as reference, while the other one was roving accelerometer in five setups (see Fig. 4). Due to the on-going renovation work on-site at the time of testing, there were several restrictions as follows. The allowable time to set up and carry out the tests was strictly limited. Furthermore, there were limitations with respect to the number of accessible members for measurements as well as the number and positions of the sensors to be installed on the truss member.

The results of the local measurement of the single truss member are presented next. The modal analysis for the second truss member was performed adopting the stochastic subspace identification (SSI) [12]. Figure 5(a) shows the stabilization diagram of one test setup based on state models of order between 1 and 200. Stable poles are seen corresponding to the natural frequencies.

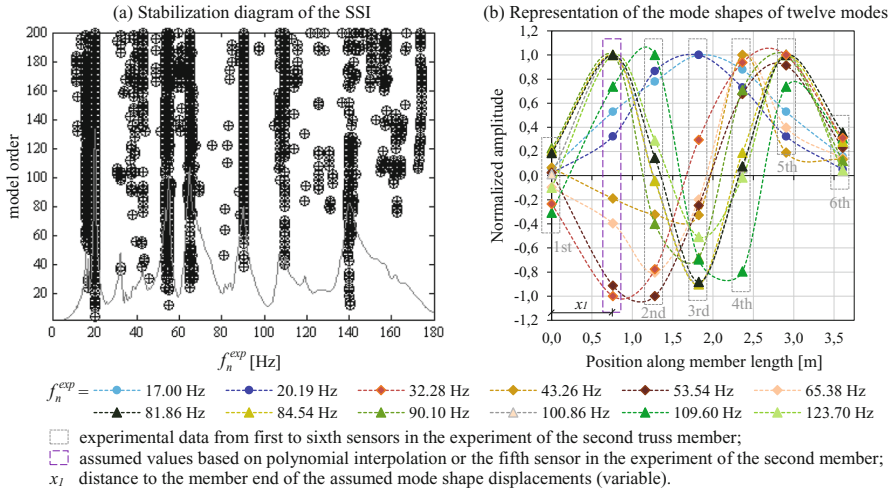

Fig. 5. Experimentally identified modal parameters from local measurement of the second truss member.

Figure 5(b) presents the experimentally identified frequencies and mode shapes of the first twelve modes of the second truss member. The mode shapes are normalized to a maximum modal displacement equal to one. It is noted that the plotted mode shapes are based on not only the experimental measurements but also assumption of an additional mode shape displacement at each frequency, whose values are by polynomial interpolation of the experimental data or equal to those from the fifth sensor in the experiment. The additional location is to create a better representation of the mode shapes, because the experimental data for this location was not available. It is noticed that the number of modes for a member of a truss system increases significantly compared to that of a single beam. Similar mode shapes appear, for example the mode shape in the form of the first vibration mode of a single beam appears at 17.00 Hz as well as 20.19 Hz, indicating coupled vibration behavior of the truss members.

5 Analysis Strategy and Results

Two analysis directions for the truss structure were considered, i.e. global analysis of the whole truss and local analysis of single truss members. The results of the local analysis of the second truss member will be summarized.

5.1 Parametric Study of Uncertain Parameters

The FE model as shown in Fig. 4 was used. The model has uncertain input parameters. The first uncertain parameter is the member axial force, considering that the loads of the roof were manually estimated. The second uncertain parameter is the rotational spring stiffness of the connections, as the joint flexibility was unknown. For simplification, the two member ends are assumed to have identical rotational spring stiffness. Beside the axial force and joint flexibility, other uncertain parameters include the modulus of elasticity of the wrought iron, the cross-sectional area and member length. Table 1 provides an overview of the assumed variations of the parameters. The aim was to examine the effects of the parameters on the frequencies. After that, it was aimed to calibrate the parameters of the numerical model based on the experimentally identified modal parameters.

The results of the numerically calculated frequencies using the FE model of the second truss member are shown in Table 2. For the case of the investigated single truss member, the parameters of the axial force, modulus of elasticity and cross-sectional area have less influences on the frequency values than the joint rigidity and member length, while the joint rigidity has the most significant effect. The numerically calculated frequencies in the range that are closest to the experimentally identified frequencies based on the vibration mode in the form of the first vibration mode of a single beam were identified. When taking into consideration that other combinations of the

Table 1. Assumed variations for the parameters of the FE model of a truss member as single beam.

Parameter	Designation	Initial value	Variation	Limits (lower/upper)	Distribution	Unit
N	Member axial force	56.60	±17.9%*	46.47/66.77	Uniform	kN
σ	Member axial stress	28.83		23.67/34.01	Uniform	N/mm^2
γ	Joint fixity factor	0.50	Pinned to rigid	0.00/1.00	Uniform	–
E	Modulus of elasticity	195 000	±5%	185 000/205 000	Uniform	N/mm^2
A	Cross-sectional area**	1963.50	−11.64%/ +12.36%	1734.94/2206.18	Uniform	mm^2
L	Length***	3500	+8.70%	3500/3750***	Uniform	mm

*Based on the static analysis of the global truss model with ±30% of the applied point loads of the roof;
**Of solid circular cross-sections; d – diameter of circular cross-sections; initial value d = 50 mm, variations of d of ± 3 mm;
***Depending on the embedded length of the member ends at connections, maximum distance from bolt-to-bolt connections.

Table 2. Numerically calculated natural frequencies based on the FE model of the second truss member.

σ [N/mm^2]	N [kN]	$^{\gamma}$ [–]	E [N/mm^2]	A [mm^2]	L [mm]	f_1 [Hz]	Δ_1 [%]	f_2 [Hz]	Δ_2 [%]	f_3 [Hz]	Δ_3 [%]
0.00*	0.00**	0.000	185 000	1734.94	3750	6.70	–	26.79	–	60.22	–
23.67	46.47	0.000	195 000	1963.50	3750	10.10	50.75	31.41	17.25	66.20	9.93
					3500	11.19	67.01	35.55	32.70	75.44	25.27
		0.999			3750	**17.73**	164.63	46.14	72.23	87.97	46.08
					3500	**20.07**	199.55	52.56	96.19	100.48	66.85
28.83	56.60	0.000	195 000	1734.94	3750	10.80	61.19	31.27	16.72	64.13	6.49
			185 000	1963.50	3500	11.64	73.73	35.57	32.77	74.48	23.68
			195 000	2206.18		11.76	75.52	37.55	40.16	79.81	32.53
			205 000	1963.50		11.91	77.76	37.00	38.11	77.94	29.43
		0.999	195 000	1963.50	3750	18.11	170.30	46.70	74.32	88.51	46.98
			185 000		3500	**20.07**	199.55	51.93	93.84	98.70	63.90
			195 000			**20.48**	205.67	53.14	98.36	101.14	67.95
			205 000			**20.89**	211.79	54.33	102.80	103.51	71.89
34.01	66.77	0.000	195 000	1963.50	3750	11.20	67.16	32.87	22.70	67.77	12.54
					3500	12.33	84.03	37.03	38.22	77.02	27.90
		0.999			3750	18.52	176.42	47.30	76.56	89.28	48.26
					3500	**20.88**	211.64	53.73	100.56	101.80	69.05
			205 000	2206.18	3500	21.98	228.06	57.35	114.07	109.42	81.70

*Approximate value; **zero–applied load, only self-weight; calculated differences Δ_i to the frequencies of zero–load model; Bold numerical frequencies in most similar range with the experimentally identified frequencies based on the mode in the form of the first vibration mode of a single beam.

parameters were also possible, a relatively diverse possibility of the sets of parameters was found. Based on the parametric study, no unique set of parameters, which provides the numerical frequencies to match with the experimentally identified frequencies, was recognized. However, for the joint rigidity, the results of the frequencies show a consistent trend that the joint flexibility to be closer to the rigid condition than the common assumption of hinged condition. A possible explanation is the inherent presence of friction or corrosion damages to historic truss structures.

5.2 Vibration-Based Axial Force Estimation for Single Truss Members

The parametric study gives useful preliminary estimation of the parameters. For more accurate identification of the parameters, the analytical-based algorithm based on [6] was used to determine the axial force in members of the truss, i.e. the second member. It requires the installment of five or more sensors on the member, whose positions should cover a sufficient length of the member and be not too near the end constraints. The identified axial force is obtained from each experimentally identified frequency and five mode shape amplitudes of the member. In addition, the knowledge of the characteristics of the members, among which the modulus of elasticity, bending stiffness and cross-sectional area, is required. From the analysis of the truss model and the parametric study, the initial values and assumed variations of the parameters of the truss member were chosen (see Table 3). Because at least five sensors are required for the use of the analytical-based algorithm, a first mode shape displacement was assumed at the position x_1, whose value was based on polynomial interpolation or the fifth

Table 3. Assumed values and variations of the parameters for the use of the analytical-based algorithm.

Parameter	Designation	Assumed value	Variation	Assumed limits (lower/upper)	Distribution	Unit
E	Modulus of elasticity	195 000	±5%	185 000/205 000	Uniform	N/mm^2
A	Cross-sectional area	1963.50	−11.64%/ + 12.36%	1734.94/2206.18	Uniform	mm^2
x_1	Distance to bolt connection*	760	−3.95%/ + 2.63%	730/780	Uniform	mm

*Of the assumed mode shape displacement; the other four distances, i.e. x_2 to x_5, are from the second to fifth sensors in the experiment of the second truss member. At 738 m, the five locations on the mode shapes are equally distributed.

Table 4. Identified member axial forces and corresponding stresses based on the analytical-based algorithm.

E [N/mm^2]	A [mm^2]	x_1 [m]	N^a [kN]	σ^a [N/mm^2]
185 000	1963.50 (d = 50 mm)	760	61.75	31.45
195 000	**1963.50 (d = 50 mm)**	760	**55.48**	28.26
205 000	1963.50 (d = 50 mm)	760	49.22	25.07
195 000	1734.94 (d = 47 mm)	760	61.59	35.50
195 000	2206.18 (d = 53 mm)	760	45.37	20.57
195 000	1963.50 (d = 50 mm)	730	34.40	17.52
195 000	1963.50 (d = 50 mm)	780	72.15	36.75

sensor in the experiment. The knowledge of the member length is not necessary, but only the distance of the sensors to an assumed end point of the member is required. The end of the member was assumed at the point of the bolt connection. The mode used in the analytical-based algorithm was chosen as the experimentally identified frequency of 20.19 Hz. The four amplitudes of the corresponding mode shapes displacements were from the second to fifth accelerometers. This mode was used based on recommendations to select the modes given in [9]. The results of the identified axial forces are provided in Table 4. The identified force of 55.48 kN and the corresponding set of input parameters are relevant compared to the values in Table 2. Although the variations of the input parameters cause varied identified forces, but when considering the relevance of the input parameters at the corresponding axial forces compared to that in Table 2, the identified force of 55.48 kN is most reasonable.

5.3 Results of the Calibration

Based on the local analysis of the second member of the truss that is the focus of this paper, the parameters of the FE model of the truss after calibration have the following characteristics: the loads P_1 of 4.04 kN and P_2 of 5.40 kN corresponding to a tensile force of about 55.52 kN and tensile stress of 28.28 N/mm^2 in the second truss member; the fixity factor of approximately 0.99, the modulus of elasticity of 195 000 N/mm^2

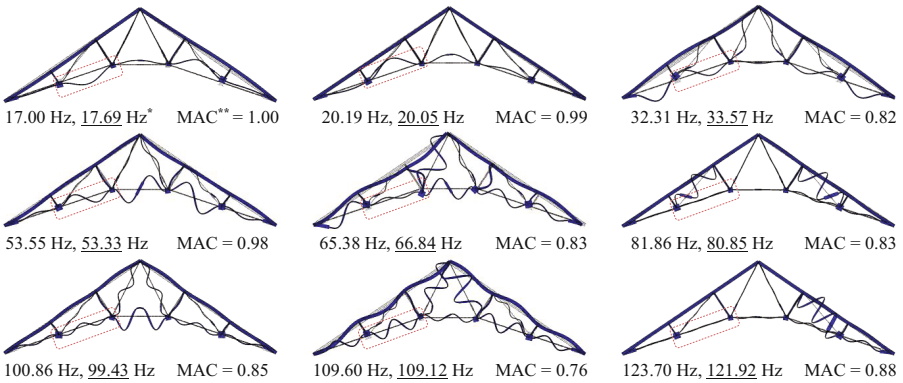

Fig. 6. Numerically computed modes of the truss model after calibration based on the mode pairing with the experimentally identified modes of the second truss member.

and the cross-section of the second truss member of 1963.50 mm^2. The fixity factor or the stiffness of the rotational spring at supports and joints after calibration disagrees to the common assumption of hinged joints for trusses. It illustrates the accuracy of the results is affected if the assumption for joints is not properly considered. For the investigated truss, the applied loads could be manually estimated reasonably well, because the condition of the renovation work on-site allowed a relatively clear view of the load components as well as a good accessibility to the structure. However, this is usually not the cases for historic structures. Figure 6 shows the nine modes of vibration of the calibrated numerical model of the truss in comparison with the experimentally identified modal parameters by the local measurement of the second truss member. The natural frequencies and the modal assurance criteria (MAC) are provided, whose values indicate the consistency of the numerical and experimental mode shapes. The results with a MAC value of at least 0.75 are presented. A good agreement between the experimentally identified and numerically calculated modal parameters is observed.

The results of the local analysis were based on an assumed additional mode shape displacement, due to the limitation of the positions of the instrumented sensors on the investigated truss member. Thus, the results can vary depending on the assumptions of the location as well magnitude of the additional mode shape displacement. For in-situ tests on existing truss structures, it is highly recommended to install at least five sensors on truss members, if the design of experiments using more sensors is allowed. It should be emphasized that the local analysis of single truss members does not allow a comprehensive evaluation of the truss dynamic responses. An example of similar modes of vibration at closely-spaced modes of the truss structure is given in Fig. 7. The MAC values for both the numerical modes to the experimentally identified mode of the second truss member are similarly close to one. However, when concerning the global mode shapes of the truss, the two modes differentiate themselves by the in-phase or out-of-phase vibration of the member at symmetric location with respect to the second member of the truss.

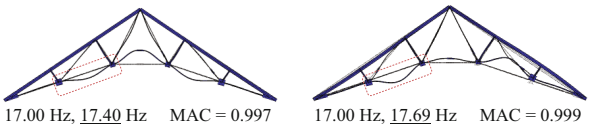

Fig. 7. Closely-spaced numerically computed modes of the truss structure.

6 Conclusions

The in-situ dynamic tests were performed on a historic Wiegmann–Polonceau roof truss in the city of Potsdam, Germany. The truss was chosen as it sets a good example of a historic lightweight iron and steel truss characterized primarily by axial forces. The modal parameters of the existing truss could be identified reasonably well. The numerical modeling of the truss recommends accurate modelling of the connection details and turnbuckle elements. The inertia and weight of the gusset plates and turnbuckles should be included. Moreover, the joints should be modelled with rotational springs to account for the uncertain degrees of joint rigidity. The modal parameters of the calibrated FE model are in good agreement with the experimental results.

In this paper, the local vibration measurement and analysis strategies were described. The presented results illustrate the possibility of using a local analysis method concerning individual members of a truss to estimate the structural parameters and structural behavior of the global truss. Useful results can be obtained from the local analysis. It has the advantages of a practical testing procedure as well as simplified analysis process that can save time and cost. Nevertheless, for insightful interpretation and comprehensive assessment of the dynamic behavior of the truss, a global analysis of the structure is required.

References

1. Lorenz, W.: Modern museums in world heritage monuments—structural challenges, structural solutions (in Russian). In: Proceedings of the International Conference on Museums of the 21st Century—Restoration, Reconstruction, Renovation, 20–22 October 2008. The State Hermitage Publishers, St. Petersburg (2010). S.28–36. ISBN 978-5-93572-392-7
2. Lorenz, W., Heres, B.: Archäologie des Konstruierens - Untersuchungen zur Entstehung von Konstruktions-sprachen an den Eisentragwerken der Eremitage St. Petersburg. In: Forum der Forschung 10 (2006). H.19, S.163–170
3. Luong, H.T.M.: Development of standard charts to determine the tensile stress in historic metallic tie-bars. In: Joint International Symposium on Experimental Mechanics and Society for Experimental Mechanics Fall Conference (ISEM-ACEM-SEM-7th ISEM 2012-Taipei), Taiwan (2012)
4. Bahra, A.S., Greening, P.D.: Identifying multiple axial load patterns using measured vibration data. J. Sound Vib. **330**(15), 3591–3605 (2011)

5. Luong, H.T.M., Ramos, L.F., Aguilar, R.: Identification of the tensile force in tie-rods of historical constructions. In: Proulx, T. (ed.) Civil Engineering Topics, Volume 4: Proceedings of the 29th IMAC, A Conference on Structural Dynamics, pp. 71–81. Springer, New York (2011)
6. Maes, K., Peeters, J., Reynders, E., Lombaert, G., De Roeck, G.: Identification of axial forces in beam members by local vibration measurements. J. Sound Vib. **332**(21), 5417–5432 (2013)
7. Luong, H.T.M., Zabel, V., Lorenz, W., Rohrmann, R.G.: Vibration-based model updating and identification of multiple axial forces in truss structures. In: 6th Asia Pacific Workshop on Structural Health Monitoring. Procedia Engineering, vol. 188, pp. 385–392. Hobart, Australia, 7–9 December 2016. doi:10.1016/j.proeng.2017.04.499
8. Kurrer, K.-E.: The History of the Theory of Structures: From Arch Analysis to Computational Mechanics. Ernst & Sohn (2008). ISBN 978-3-433-01838-5
9. Luong, H.T.M.: Identification of the state of stress in iron and steel truss structures by vibration-based experimental investigations. Ph.D. thesis, Brandenburg University of Technology Cottbus-Senftenberg (under preparation) (2017)
10. ANSYS®: Academic Research, Release 13.0. Bundesanstalt für Materialforschung und -prüfung (BAM) (2012–2017)
11. Türker, T., Kartal, M.E., Bayraktar, A., Muvafik, M.: Assessment of semi-rigid connections in steel structures by modal testing. J. Constr. Steel Res. **65**(7), 1538–1547 (2009)
12. Peeters, B., De Roeck, G.: Stochastic system identification for operational modal analysis: a review. J. Dyn. Sys. Meas. Control **123**(4), 659–667 (2001)

General Conditions for Full-Field Response Monitoring in Structural Systems Driven by a Set of Identified Equivalent Forces

Eliz-Mari Lourens(✉) and Dominik Fallais

Faculty of Civil Engineering and Geosciences, Delft University of Technology, Delft, The Netherlands
E. Lourens@tudelft.nl

Abstract. Kalman-type filters are being increasingly used to estimate the full-field dynamic response of structures from a limited set of vibration measurements. Various coupled input-state and coupled input-state-parameter estimation algorithms have been developed in this context, ranging from an initial formulation for use with linear reduced-order structural systems to alternative filters for dealing with acceleration-only data and recently also nonlinear model descriptions. The use of these algorithms allows for response prediction to be performed in the absence of any knowledge of the excitation forces, where often a set of *response-driving equivalent forces* is identified from the measurements. Up to now, the success of response estimation based on the identification of equivalent forces has been related only to whether these forces satisfy the so-called controllability requirements. In this contribution, controllability is shown to be an insufficient criterion for guaranteeing the accuracy of response estimates based on equivalent loading. Instead, the need for a new criterion is advocated, which would allow for a proper assessment of the applicability of equivalent force based monitoring to various engineering problems. Concepts are illustrated using simple numerical examples where a comparison is made between the true and assumed noise statistics and the response prediction accuracy for a number of distinct cases. These include situations where (a) the applied and equivalent loads are concentrated and collocated, (b) the applied and equivalent loads are concentrated and non-collocated, and (c) modal equivalent forces are used. Results are applicable to any Kalman-type coupled input-state estimator derived using the principles of minimum-variance unbiased estimation.

Keywords: Kalman filter · Equivalent forces · Controllability · Response prediction · Structural health monitoring

1 Introduction

Commonly employed vibration sensors, e.g. accelerometers and strain gauges, provide only local information on the dynamic response of a structure. In many situations, however, knowledge of the full-field structural response is required. Consider for instance the monitoring of accumulated fatigue damage at critical locations that are

© Springer International Publishing AG 2018
J.P. Conte et al. (eds.), *Experimental Vibration Analysis for Civil Structures*,
Lecture Notes in Civil Engineering 5, https://doi.org/10.1007/978-3-319-67443-8_19

inaccessible for measurement, e.g. the location just below the seabed on an offshore wind turbine foundation [1, 2]. Monitoring of the full-field response of a structure in conjunction with the forces applied to it can also be used to obtain insights into complex interaction phenomena, e.g. ice-induced vibrations [3, 4].

In recent years, a number of inverse methodologies for the extrapolation of structural response to unmeasured locations have been proposed. These methodologies can roughly be divided into two categories, namely those that assume that the numerical model used for the extrapolation is free from errors, and those that do account for modelling errors. Belonging to the former category are the modal expansion algorithms [1, 5], where modal coordinates are identified through a pseudo-inversion of the mode shape matrix. The second category consists of various Kalman-type filters, where modelling as well as measurement errors are included in the estimation process as stochastic processes of which only the variances are known. This second category can again be divided into two groups: filters that rely on some assumptions regarding the loading on the structure (e.g. white noise) [6], and filters that are able to observe full-field structural response in the absence of any knowledge of the dynamic evolution of the applied loading [7]. In this contribution, we will focus on the latter, and more specifically on cases in which also the spatial distribution of the loading is assumed unknown, and a set of response-driving equivalent forces is identified from the measurements. Through careful analysis of the assumptions forming the basis for the derivation of these algorithms and their possible violation in various real-life applications, the limitations of response estimation based on equivalent loading is exemplified. The presented situations include those in which the locations of the forces are only known approximately, and those in which modal equivalent forces are assumed.

2 Coupled State and Input Estimation

Consider the equations of motion for a linear structural system discretized in space:

$$\mathbf{M}\ddot{\mathbf{u}}(\mathrm{t}) + \mathbf{C}\underline{\mathbf{u}}(\mathrm{t}) + \mathbf{K}\mathbf{u}(\mathrm{t}) = \mathbf{S}_{\mathrm{p}}\mathbf{p}(\mathrm{t}) \tag{1}$$

where $\mathbf{M}$, $\mathbf{C}$, and $\mathbf{K} \in \mathbb{R}^{n_{\mathrm{DOF}} \times n_{\mathrm{DOF}}}$ denote the mass, damping, and stiffness matrices, respectively. In what follows it is assumed that the response of the system can be accurately described by means of a limited number of n_{m} modes as $\mathbf{u}(\mathrm{t}) = \boldsymbol{\Phi}\mathbf{z}(\mathrm{t})$ with $\boldsymbol{\Phi} \in \mathbb{R}^{n_{\mathrm{DOF}} \times n_{\mathrm{m}}}$ and $n_{\mathrm{m}} \ll n_{\mathrm{DOF}}$. By defining a modal state vector $\mathbf{x}(t) = [\mathbf{z}(t) \quad \dot{\mathbf{z}}(t)]^{\mathrm{T}}$, Eq. (1) can be transformed to first-order state-space form:

$$\dot{\mathbf{x}}(t) = \mathbf{A}_{\mathrm{c}}\mathbf{x}(t) + \mathbf{B}_{\mathrm{c}}\mathbf{p}(t) \tag{2}$$

$$\mathbf{d}(t) = \mathbf{G}_{\mathrm{c}}\mathbf{x}(t) + \mathbf{J}_{\mathrm{c}}\mathbf{p}(t) \tag{3}$$

where $\mathbf{x}(t) \in \mathbb{R}^{n_s}$, and:

$$\mathbf{A}_c = \begin{bmatrix} 0 & \mathbf{I} \\ -\boldsymbol{\Omega}^2 & -\boldsymbol{\Gamma} \end{bmatrix},\ \mathbf{B}_c = \begin{bmatrix} 0 \\ \boldsymbol{\Phi}^T \mathbf{S}_p \end{bmatrix},\ \mathbf{G}_c = \begin{bmatrix} \mathbf{S}_d\boldsymbol{\Phi} - \mathbf{S}_a\boldsymbol{\Phi}\boldsymbol{\Omega}^2 & \mathbf{S}_v\boldsymbol{\Phi} - \mathbf{S}_a\boldsymbol{\Phi}\boldsymbol{\Gamma} \end{bmatrix},\ \mathbf{J}_c = \mathbf{S}_a\boldsymbol{\Phi}\boldsymbol{\Phi}^T\mathbf{S}_p. \tag{4}$$

The matrices $\boldsymbol{\Omega}^2$ and $\boldsymbol{\Gamma}$ are defined as $\boldsymbol{\Omega}^2 = \boldsymbol{\Phi}^T\mathbf{K}\boldsymbol{\Phi} = diag\left\{\omega_j^2\right\}$ and $\boldsymbol{\Gamma} = \boldsymbol{\Phi}^T\mathbf{C}\boldsymbol{\Phi} = diag\left\{2\xi_j\omega_j\right\}$. Discretization of Eqs. (2) and (3) assuming constant intersample behaviour of the inputs, and the addition of stochastic noise processes $\{\boldsymbol{w}_k\}_{k=1}^{\infty}$ and $\{\boldsymbol{v}_k\}_{k=1}^{\infty}$ for representing respectively process and measurement errors, leads to:

$$\mathbf{x}_{k+1} = \mathbf{A}\mathbf{x}_k + \mathbf{B}\mathbf{p}_k + \boldsymbol{w}_k \tag{5}$$

$$\mathbf{d}_k = \mathbf{G}\mathbf{x}_k + \mathbf{J}\mathbf{p}_k + \boldsymbol{v}_k \tag{6}$$

where

$$\mathbf{A} = e^{\mathbf{A}_c\Delta t},\ \mathbf{B} = [\mathbf{A} - \mathbf{I}]\mathbf{A}_c^{-1}\mathbf{B}_c, \mathbf{G} = \mathbf{G}_c, \text{and } \mathbf{J} = \mathbf{J}_c. \tag{7}$$

In recent years a number of Kalman-type filters have been proposed for jointly estimating the states $\mathbf{x}$ and input $\mathbf{p}$ on the basis of a set of measurements $\mathbf{d}$ and the system of equations presented above. Due to space limitations these algorithms will not be presented; instead we refer to [8] for a recent comparison. The results presented in the following sections were all generated with the joint input-state estimator [7], but the conclusions are valid for any Kalman-type coupled input-state estimator derived using the principles of minimum-variance unbiased estimation.

2.1 Noise Process Assumptions

The noise processes are in general characterized as zero-mean, white noise signals with known covariance matrices:

$$\mathbb{E}\{\boldsymbol{w}_k\} = \mathbb{E}\{\boldsymbol{v}_k\} = 0 \tag{8}$$

$$\mathbb{E}\left\{ \begin{bmatrix} \boldsymbol{w}_k \\ \boldsymbol{v}_k \end{bmatrix} \begin{bmatrix} \boldsymbol{w}_l^T & \boldsymbol{v}_l^T \end{bmatrix} \right\} = \begin{bmatrix} \mathbf{Q} & \mathbf{S} \\ \mathbf{S}^T & \mathbf{R} \end{bmatrix} \delta_{kl} \tag{9}$$

In the remainder of the paper, the focus will be on the effect of having discrepancies between the theoretical assumptions above and the physical situation, especially focusing on the consequences hereof with regard to the uniqueness of the estimates.

3 Response Prediction Using Equivalent Forces

The state and force estimates – $\hat{\mathbf{x}}$ and $\hat{\mathbf{p}}$ – obtained with these Kalman-type filters can be used to estimate the full-field response of a structure on the basis of limited sensor data. The idea was first presented in [7], and involves reformulating a new observation equation as follows:

$$\hat{\mathbf{d}}_{e,k} = \mathbf{G}_e \hat{\mathbf{x}}_k + \mathbf{J}_e \hat{\mathbf{p}}_k \tag{10}$$

where a hat denotes an estimated quantity, and the subscript 'e' abbreviates extrapolated. When a set of equivalent forces $\hat{\mathbf{p}}$ is identified, the process and measurement noise $\boldsymbol{w}_k$ and $\boldsymbol{v}_k$. in Eqs. (5) and (6) can be divided into contributions from force location errors, modelling errors, and sensor noise. For reduced-order systems constructed using Eq. (4), modelling errors consist of specifically eigenfrequency, eigenmode, and damping errors, i.e. errors on the dynamic properties. One can write:

$$\boldsymbol{w}_k = \{\boldsymbol{w}_k\}_{\text{force}} + \{\boldsymbol{w}_k\}_{\text{prop}} \tag{11}$$

$$\boldsymbol{v}_k = \{\boldsymbol{v}_k\}_{\text{force}} + \{\boldsymbol{v}_k\}_{\text{prop}} + \{\boldsymbol{v}_k\}_{\text{sensor}} \tag{12}$$

where 'prop' abbreviates properties. Defining $\blacksquare_{\text{real}}$ and $\blacksquare_{\text{eq}}$ as the matrices/vectors corresponding to respectively the real and equivalent force locations, the contributions from errors on these locations can be further specified as:

$$\{\boldsymbol{w}_k\}_{\text{force}} = \mathbf{B}_{\text{real}} \mathbf{p}_{k,\text{real}} - \mathbf{B}_{\text{eq}} \hat{\mathbf{p}}_k \tag{13}$$

$$\{\boldsymbol{v}_k\}_{\text{force}} = \mathbf{J}_{\text{real}} \mathbf{p}_{k,\text{real}} - \mathbf{J}_{\text{eq}} \hat{\mathbf{p}}_k \tag{14}$$

where $\mathbf{B}_{\text{eq}}$ and $\mathbf{J}_{\text{eq}}$ is constructed according to Eq. (4) using the assumed locations of the equivalent forces. Note that the two stochastic error processes become correlated – $\mathbf{S} = \mathbb{E}\{\boldsymbol{w}_k \boldsymbol{v}_k^{\mathrm{T}}\} \neq 0$; cf. Eq. (9) – and are possibly no longer white. Recalling again that $\mathbf{Q} = \mathbb{E}\{\boldsymbol{w}_k \boldsymbol{w}_k^{\mathrm{T}}\}$ and $\mathbf{R} = \mathbb{E}\{\boldsymbol{v}_k \boldsymbol{v}_k^{\mathrm{T}}\}$, an additional distinction is made between *real* and *assumed* covariances:

$$\mathbf{Q}_e = \mathbf{Q}_{\text{real}} - \mathbf{Q}_{\text{as}}, \mathbf{R}_e = \mathbf{R}_{\text{real}} - \mathbf{R}_{\text{as}}, \mathbf{S}_e = \mathbf{S}_{\text{real}} - \mathbf{S}_{\text{as}} \tag{15}$$

where the subscripts 'e' and 'as' denote error and assumed, respectively, and the real covariances are those specifed in Eqs. (11) and (12). These matrices can be further decomposed into blocks representing the (co)variances between the modal displacements $\mathbf{z}$, the modal velocities $\dot{\mathbf{z}}$, and the data $\mathbf{d}$, respectively:

$$\mathbf{Q}_e = \begin{bmatrix} \mathbf{Q}_{e,\mathbf{zz}} & \mathbf{Q}_{e,\mathbf{z}\underline{\mathbf{z}}} \\ \mathbf{Q}_{e,\dot{\mathbf{z}}\mathbf{z}} & \mathbf{Q}_{e,\dot{\mathbf{z}}\underline{\mathbf{z}}} \end{bmatrix}, \mathbf{S}_e = \begin{bmatrix} \mathbf{S}_{e,\mathbf{zd}} \\ \mathbf{S}_{e,\dot{\mathbf{z}}\mathbf{d}} \end{bmatrix} \tag{16}$$

where $\mathbf{Q}_{e,\mathbf{zz}}, \mathbf{Q}_{e,\mathbf{z}\underline{\mathbf{z}}}, \mathbf{Q}_{e,\underline{\mathbf{z}}\underline{\mathbf{z}}} \in \mathbb{R}^{n_s/2 \times n_s/2}$ and $\mathbf{S}_{e,\mathbf{zd}}, \mathbf{S}_{e,\dot{\mathbf{z}}\mathbf{d}} \in \mathbb{R}^{n_s/2 \times n_d}$.

4 Numerical Examples

A 21-node cantilever beam model is constructed based on Euler-Bernoulli beam theory and subsequently reduced to 10 DOF's on the basis of the first 10 modes. The properties of the beam are as follows: length $L = 1$ m, mass $m = 1$ kg/m, and bending stiffness $EI = 1$ Nm^2. A modal damping ratio of $\xi = 2\%$ is assumed for all modes. The first three natural frequencies of the beam are 0.56, 3.51, and 9.82 Hz, respectively. The excitation is chosen as a superposition of two harmonic forces with frequencies equal to 2.03 Hz and 6.66 Hz, and is applied at the tip of the beam. These frequencies are chosen as the average of respectively the first and second, and second and third natural frequency of the structure. A sampling frequency of 1000 Hz is used in all the following examples, satisfying the Nyquist-Shannon sampling criterion with respect to the highest load frequency and all structural frequencies up to the 6$^{\text{th}}$ mode. It is mentioned that when the coupled input-state estimation is performed based on real data, the selected time step size should also be chosen with regard to the physical delay in the system, in order to ensure that causality is respected [9, 10].

Simulated data from 4 accelerometers and 1 strain gauge is used for the estimation, as shown in Fig. 1. The data set and chosen (equivalent) force locations satisfy the observability, controllability and direct invertibility criteria as formulated in [11] for all cases analyzed.

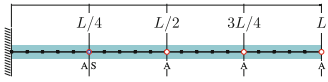

Fig. 1. Cantilever beam instrumented with 4 accelerometers (A) and a strain gauge (S).

To analyze the effect of specifically the equivalent force assumptions, no modelling errors will be included in all examples presented in the following sections, implying that $\{\boldsymbol{w}_k\}_{\text{prop}} = \{\boldsymbol{v}_k\}_{\text{prop}} = \boldsymbol{0}$ in Eqs. (11) and (12), whereby the error processes reduce to $\boldsymbol{w}_k = \{\boldsymbol{w}_k\}_{\text{force}}$ and $\boldsymbol{v}_k = \{\boldsymbol{v}_k\}_{\text{force}} + \{\boldsymbol{v}_k\}_{\text{sensor}}$. Each measurement signal is corrupted with a white noise signal whose standard deviation is proportional to the standard deviation of the measurement signal itself: $\{\boldsymbol{v}\}^i_{\text{sensor}} = \zeta \sigma_{\mathbf{d}_i} \mathbf{r}$, with ζ the noise level, $\sigma_{\mathbf{d}_i}$ the standard deviation of the considered output i, and $\mathbf{r} \in \mathbb{R}^{\text{N}}$ a vector of random values drawn independently from a normal distribution with zero mean and unit standard deviation. In order to minimize the effect of noise, the applied noise level is set to 1e^{-6}. The assumed noise matrix $\mathbf{R}_{\text{as}}$ is constructed so as to be consistent with the true added sensor noise, so that $\mathbf{R}_{\text{e}}$ of Eq. (15) is related solely to the force positions: $\mathbf{R}_{\text{e}} = \mathbb{E}\left\{\{\boldsymbol{v}_k\}_{\text{force}}\{\boldsymbol{v}_k\}^{\text{T}}_{\text{force}}\right\}$. By also assuming $\mathbf{Q}_{\text{as}} = 0$ and $\mathbf{S}_{\text{as}} = 0$ in all of the presented analyses, $\mathbf{Q}_{\text{e}}$ and $\mathbf{S}_{\text{e}}$ can be similarly related solely to the force positions: $\mathbf{Q}_{\text{e}} = \mathbb{E}\left\{\{\boldsymbol{w}_k\}_{\text{force}}\{\boldsymbol{w}_k\}^{\text{T}}_{\text{force}}\right\}$ and $\mathbf{S}_{\text{e}} = \mathbb{E}\left\{\{\boldsymbol{w}_k\}_{\text{force}}\{\boldsymbol{v}_k\}^{\text{T}}_{\text{force}}\right\}$ – cf. Eq. (15). In order to rule out the effect of potential initialization errors or different convergence speeds, the first 10 s of each data trace will be neglected during the post processing.

4.1 Collocated Nodal Force

First a situation is considered where the force location is known exactly, and no use is made of the concept of equivalent forces: $\{\boldsymbol{w}_k\}_{\text{force}} = \{\boldsymbol{v}_k\}_{\text{force}} = \mathbf{0}$, and consequently $\mathbf{Q}_e = \mathbf{R}_e = \mathbf{S}_e = \mathbf{0}$. A nodal force applied at the tip of beam is identified in conjunction with the 10 modal states from the strain and acceleration data specified in Fig. 1. As expected, all modal states and forces are identified with high accuracy, allowing for an error-free extrapolation of the response of the beam to any location by means of Eq. (10). Results are omitted due to space limitations.

4.2 Nodal Equivalent Force at 3L/4

For the next analysis an equivalent force is considered to act at $3L/4$, representing a situation where only some uncertain information on the force location is available. In this case $\{\boldsymbol{w}_k\}_{\text{force}}$ and $\{\boldsymbol{v}_k\}_{\text{force}} \neq \mathbf{0}$, and consequently all error matrices – $\mathbf{Q}_e$, $\mathbf{R}_e$, $\mathbf{R}_e$ – will become populated. Figure 2 shows, on the left, the true (simulated) and estimated modal states (top) and modal velocities (bottom) for the first 3 modes. Although the first modal displacement is identified relatively accurately, the discrepancies between the simulated and estimated modal states become larger for the higher modes. To quantify these errors an RMS error measure for each modal state $\mathbf{z}^i$ is defined as follows:

$$\text{RMS}_{\mathbf{z},i} = \sqrt{\frac{1}{\text{N}} \sum_{k=1}^{\text{N}} \left(\frac{\mathbf{z}_k^i - \hat{\mathbf{z}}_k^i}{\max(|\mathbf{z}^i|)} \right)^2} \tag{17}$$

where i is the mode number. To disregard the effect of having large differences in orders of magnitude between the different states, the simulated states are first normalized to unity and subsequently the corresponding scale factors are used to scale also the estimates. The difference between the scaled versions of the simulated and estimated state is finally used to compute the normalized RMS error defined in Eq. (17). Table 1 presents these values for the modal displacements in the current problem,

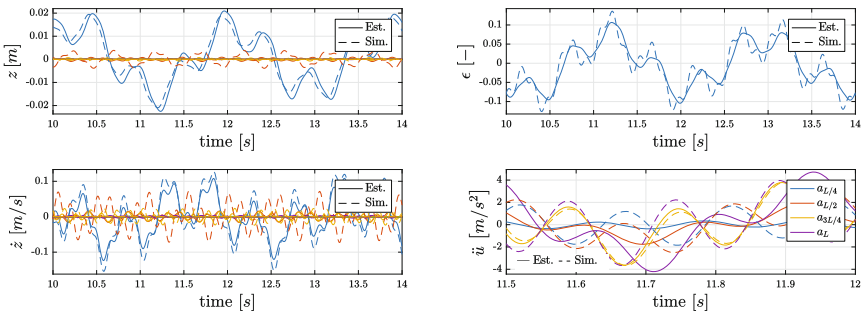

Fig. 2. True (dashed lines) and estimated (solid lines) time histories of the modal states (left) and the predicted strain and accelerations at the measurement locations (right). Nodal equivalent force at 3L/4.

Table 1. RMS modal displacement errors in the case of a nodal equivalent force at 3L/4.

State i	1	2	3	4	5	6	7	8	9	10
$\mathrm{RMS}_{\mathbf{z},i}$	$8.63e^{-2}$	$6.65e^{-1}$	$6.00e^{-1}$	$\mathbf{9.53e^{-1}}$	$6.92e^{-1}$	$3.19e^{-1}$	$2.80e^{-1}$	$2.38e^{-1}$	$2.96e^{-1}$	$7.26e^{-1}$

clearly showing an increased error for the higher-order modes, with a maximum occurring in mode 4.

Figure 2 and Table 1 show that the modal states and forces cannot be reconstructed uniquely, an effect caused by a violation of various assumptions used in the derivation of the estimator. Since the identified modal estimates are incorrect, the data reconstructed on the basis of these estimates – see Eq. (10) – will also be incorrect, as shown on the right in Fig. 2. Note that here we are not even attempting to reconstruct at locations other than those measured, and still there exists a clear discrepancy between measured and reconstructed data.

To analyze further the effect of assuming an erroneous force location, the matrices $\mathbf{Q}_{\mathbf{e},\mathbf{zz}}$ and $\mathbf{S}_{\mathbf{e},\mathbf{zd}}$, defined in Eqs. (15) and (16), are plotted in Fig. 3. These matrices are particularly interesting to consider since they can most easily be related to the uniqueness of the modal state estimates on the one side, and the uniqueness of the coupled input-state estimates on the other.

It is clear from the nonzero off-diagonal elements in $\mathbf{Q}_{\mathbf{e},\mathbf{zz}}$ that the force error correlates the state errors, especially between modal displacements 2, 3, 4, 5 and 10. Note that the effect hereof is clearly visible in the results presented in Table 1, where the largest error was found in modal state 4, corresponding to the location of the largest entry on the diagonal of $\mathbf{Q}_{\mathbf{e},\mathbf{zz}}$ in Fig. 3. Due to these unaccounted-for correlations, the algorithm is not able to uniquely identify the states. Similar conclusions can be drawn with regard to the uniqueness of the state versus force estimates on the basis of the matrix $\mathbf{S}_{\mathbf{e},\mathbf{zd}}$ in Fig. 3 (right). The force error strongly correlates the state error on modal displacement 4 with the measurement error on the tip acceleration, implying that it will be difficult to distinguish between (and thus uniquely identify) the force and modal state 4 on the basis of this measurement.

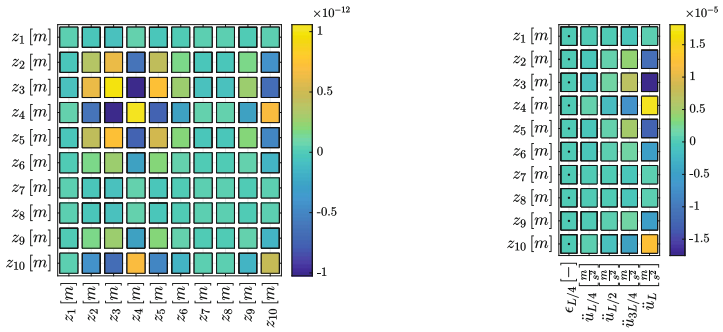

Fig. 3. Error covariance matrices $\mathbf{Q}_{\mathbf{e},\mathbf{zz}}$ (left) and $\mathbf{S}_{\mathbf{e},\mathbf{zd}}$ (right) for a nodal equivalent force at 3L/4.

A final note on Fig. 3 (right): the direct transmission terms $\mathbf{J}\mathbf{p}_k$ in Eq. (16) do not influence strain outputs since all corresponding entries in $\mathbf{S}_a$ are zero, and thus all error covariance terms related to strain outputs are zero (denoted by a dot in the figure).

4.3 Nodal Equivalent Force at L/4

Next a case is considered in which the equivalent force is located at $L/4$ from the support, while the true applied force is still acting at L. As expected, the accuracy of the state estimates drastically decreases, as shown in Fig. 4 and Table 2.

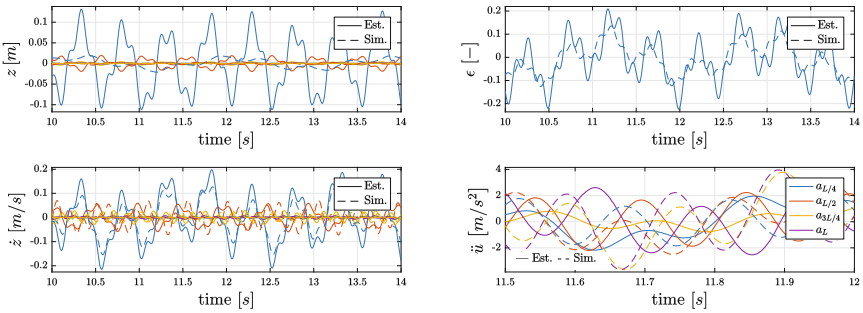

Fig. 4. True (dashed lines) and estimated (solid lines) time histories of the modal states (left) and the predicted strain and accelerations at the measurement locations (right). Nodal equivalent force at L/4.

Table 2. RMS modal displacement errors in the case of a nodal equivalent force at L/4.

State i	1	2	3	4	5	6	7	8	9	10
$\text{RMS}_{\mathbf{z},i}$	2.78	3.83	3.76	**8.22**	7.38	3.93	1.33	5.62	8.00	7.07

Compared to excitation at L, the placement of an equivalent force at $L/4$ correlates more modal errors – see matrix $\mathbf{Q}_{\text{e,zz}}$ in Fig. 5. The correlations are also much stronger, as can be concluded from the order of magnitude of the components of $\mathbf{Q}_{\text{e,zz}}$ in this figure compared to those in Fig. 3. The normalized RMS state errors are an order of magnitude larger (Table 2), and the sizes of these errors again correlates well with the amplitudes on the diagonal of $\mathbf{Q}_{\text{e,zz}}$ in Fig. 5, with the largest error again occurring in mode 4. In order to quantify the relative size of the error $\{\boldsymbol{w}_k\}_{\text{force}}$ with respect to the modal state $\mathbf{z}^i$, the following additional error measure is defined:

$$e_{\mathbf{z}}^i = \frac{\max\left(\left\{\boldsymbol{w}_{k,\text{force}}^i\right\}_{k=1}^{\text{N}}\right)}{\max\left(\left\{\mathbf{z}_k^i\right\}_{k=1}^{\text{N}}\right)} \tag{18}$$

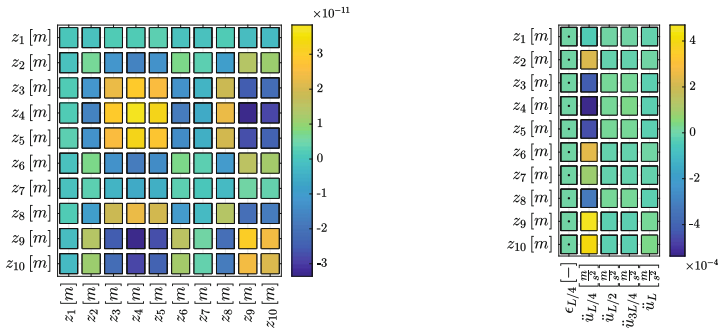

Fig. 5. Error covariance matrices $\mathbf{Q}_{\mathrm{e,zz}}$ (left) and $\mathbf{S}_{\mathrm{e,zd}}$ (right) for a nodal equivalent force at L/4.

For the current problem the largest modal displacement state error due to the erroneous assumption on the force location amounts to $e_{\mathbf{z}}^4 = 7.41\mathrm{e}^{-2}$, i.e. $\pm 7\%$, resulting in a normalized RMS state error of ± 8. These values can be compared to an $e_{\mathbf{z}}^4$ of 1.4% in the previous case (nodal force at $3L/4$), which resulted in a maximum normalized RMS error of 0.95. It additionally becomes increasingly difficult to distinguish between the effects of the force and those of the states on the measurements, due to the strong correlations in $\mathbf{S}_{\mathrm{e,zd}}$ (Fig. 5).

4.4 Modal Equivalent Forces

A simple way to ensure that the states can be related to the forces in a unique way, is the identification of modal equivalent forces [1]. Choosing the modal forces is crucial for an accurate response prediction, since the chosen modes must be able to represent the (dynamic and static) response of the structure. Two conflicting requirements arise in this regard: on the one side a sufficient number of modal forces is required in order to assure an accurate response prediction over a possibly broad range of frequencies and operational deflection shapes, whereas the number of equivalent modal forces is simultaneously restricted by the number of acceleration and strain/displacement measurements through the direct invertibility criterion and uniqueness/stability conditions [11]. For the results presented in this section, four modal forces were identified in order to drive the modal response of the first four modes.

For a system consisting of n_{m} modes and n_{p} modal forces, this is achieved by defining:

$$\boldsymbol{\Phi}^{\mathrm{T}}\mathbf{S}_{\mathrm{p}} = \begin{bmatrix} \mathbf{I}_{n_{\mathrm{p}}\times n_{\mathrm{p}}} & 0_{n_{\mathrm{p}}\times(n_{\mathrm{m}}-n_{\mathrm{p}})} \end{bmatrix}^{\mathrm{T}}$$

and then proceeding to construct $\mathbf{B}_{\mathrm{c}}$, $\mathbf{J}_{\mathrm{c}}$, $\mathbf{B}$ and $\mathbf{J}$ as in Eqs. (4) and (7). Results are presented in Fig. 6 and Table 3.

As expected, the modal states and velocities are identified more accurately than in the previous two cases, allowing an almost perfect reconstruction of the measured data – see Fig. 6 (right). The RMS state errors (Table 3) for some of the dominant modes in the response – especially mode 2 and 3 – are also significantly less than with nodal

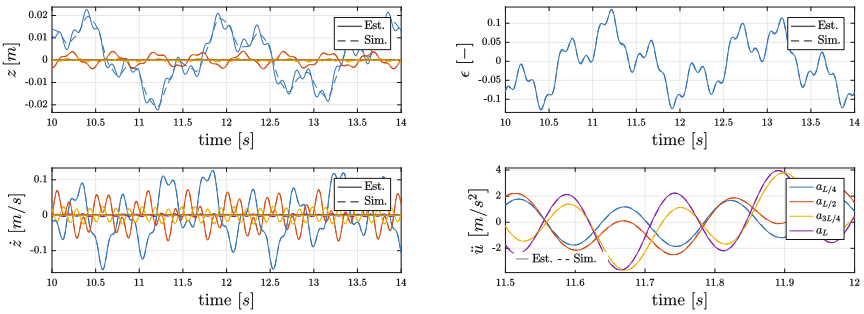

Fig. 6. True (dashed lines) and estimated (solid lines) time histories of the modal states (left) and the predicted strain and accelerations at the measurement locations (right). Modal equivalent forces.

Table 3. RMS modal displacement errors in the case of modal equivalent forces.

State i	1	2	3	4	5	6	7	8	9	10
$\text{RMS}_{\mathbf{z},i}$	$5.27e^{-2}$	$3.29e^{-2}$	$6.77e^{-2}$	$2.79e^{-1}$	$4.99e^{-1}$	$5.00e^{-1}$	$5.00e^{-1}$	$5.00e^{-1}$	$5.00e^{-1}$	$5.00e^{-1}$

equivalent forces (cf. Tables 1 and 2). The largest relative error on the states – see Eq. (18) – amounts to $\pm 2\%$ and occurs, as expected, in those modes that are not excited by equivalent forces, i.e. modes 5–10.

It is interesting to note, though, that some spurious high-frequency components are present in the first identified modal displacement at the top left of Fig. 6. These can be attributed to the existence of marginally stable zeros in the system. To satisfy the stability and uniqueness criteria [11], 3 additional strain sensors should in this case have been added to the measurement system in order to compensate for the 3 additional forces that are to be identified. Since this was not done, the identified forces and states cannot be reconstructed uniquely. Instead, an amplitude modulation of the 1st modal displacement, to which the acceleration measurements are least sensitive, is observed in Fig. 6 (left).

It is important to realize that the resulting error, being on the mode most dominant in the displacement and strain response, will have a significant influence on the accuracy of any strain or fatigue damage predictions (Fig. 6).

To conclude, it can be stated that even though the use of modal forces guarantees a unique relation between the states and the forces, it does not necessarily lead to unique solutions for the coupled input-state estimation problem. In order to ensure the latter, the effects on the measured data of the states as opposed to the forces should be uniquely distinguishable. In practice this requires an increase in the number of strain sensors to have them equal to the number of excited modes, which is not always feasible.

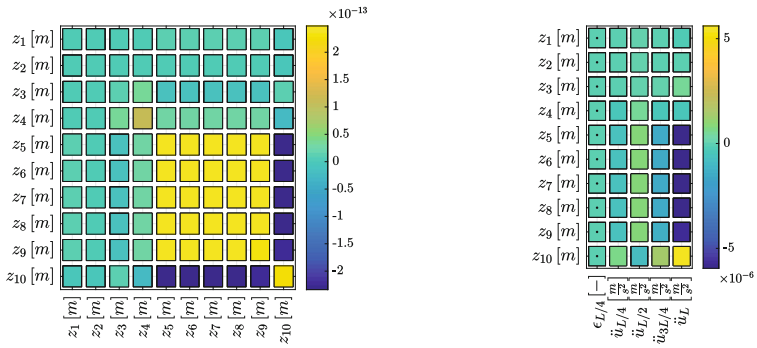

Fig. 7. Error covariance matrices $\mathbf{Q}_{\mathbf{e},\mathbf{zz}}$ (left) and $\mathbf{S}_{\mathbf{e},\mathbf{zd}}$ (right) for the case of modal equivalent forces.

5 Conclusions

Modal state and force estimates obtained with Kalman-type filters can be used to estimate the full-field response of a structure on the basis of limited sensor data. In this contribution, the focus was on situations where no knowledge on the applied loading is available, neither in terms of its dynamic content, nor its spatial distribution. In these situations response-driving equivalent forces are often identified, where it is generally assumed that an accurate response prediction can be achieved by simply ensuring that these equivalent forces meet the controllability requirements. It has been shown, however, that controllability is an insufficient condition for ensuring the accuracy of the full-field response estimates, and that they remain, in fact, very sensitive to a correct assumption on the force locations. This is mainly due to a violation of various assumptions regarding the correlation between the assumed noise processes, which directly influences the uniqueness of the estimated states and forces. The identification of modal equivalent forces can partly solve this problem, but will in many cases require a possibly drastic increase in the number of (strain) sensors, depending on the number of modes contributing to the response.

Acknowledgements. The research presented in this paper has been performed within the framework of the project "SHM2.0 – Smart monitoring of bridge performance", funded by *3TU. Bouw*. Their financial support is gratefully acknowledged.

References

1. Maes, K., Iliopoulos, A., Weijtjens, W., Devriendt, C., Lombaert, G.: Dynamic strain estimation for fatigue assessment of an offshore monopile wind turbine using filtering and modal expansion algorithms. Mech. Syst. Signal Process. **76**, 592–611 (2016)
2. Van der Male, P., Lourens, E: Operational vibration-based response estimation for offshore wind lattice structures. In: Structural Health Monitoring and Damage Detection, vol. 7, pp. 83–96. Springer, New York (2015)

3. Nord, T.S., Lourens, E., Määttänen, M., Øiseth, O., Høyland, K.V.: Laboratory experiments to study ice-induced vibrations of scaled model structures during their interaction with level ice at different ice velocities. Cold Reg. Sci. Technol. **119**, 1–15 (2015)
4. Nord, T.S., Øiseth, O., Lourens, E.: Ice force identification on the Nordströmsgrund lighthouse. Comput. Struct. **169**, 24–39 (2016)
5. Iliopoulos, A., Shirzadeh, R., Weijtjens, W., Guillaume, P., Van Hemelrijck, D., Devriendt, C.: A modal decomposition and expansion approach for prediction of dynamic responses on a monopile offshore wind turbine using a limited number of vibration sensors. Mech. Syst. Signal Process. **68**, 84–104 (2016)
6. Papadimitriou, C., Fritzen, C.-P., Kraemer, P., Ntotsios, E.: Fatigue predictions in entire body of metallic structures from a limited number of vibration sensors using Kalman filtering. Struct. Control Health Monit. **18**(5), 554–573 (2011)
7. Lourens, E., Papadimitriou, C., Gillijns, S., Reynders, E., De Roeck, G., Lombaert, G.: Joint input-response estimation for structural systems based on reduced-order models and vibration data from a limited number of sensors. Mech. Syst. Signal Process. **29**, 310–327 (2012)
8. Azam, S.E., Chatzi, E., Papadimitriou, C., Smyth, A.: Experimental validation of the Kalman-type filters for online and real-time state and input estimation. J. Vib. Control (2015). doi:10.1177/1077546315617672
9. Bernal, D., Ussia, A.: Sequential deconvolution input reconstruction. Mech. Syst. Signal Process. **50**, 41–55 (2015)
10. Bernal, D.: Non-recursive sequential input deconvolution. Mech. Syst. Signal Process. **82**, 296–306 (2017)
11. Maes, K., Lourens, E., Van Nimmen, K., Reynders, E., De Roeck, G., Lombaert, G.: Design of sensor networks for instantaneous inversion of modally reduced order models in structural dynamics. Mech. Syst. Signal Process. **52**, 628–644 (2015)

Experimental Vibration Tests in Fatigue Evaluation of a Riveted Truss Bridge

Mieszko Kużawa(✉), Tomasz Kamiński, and Jan Bień

Department of Civil Engineering,
Wroclaw University of Science and Technology, Wroclaw, Poland
mieszko.kuzawa@pwr.edu.pl

Abstract. The paper presents a practical implementation of experimentally supported fatigue life prediction of an 80-year old riveted truss bridge. The bridge is an unique road structure crossing the Vistula River in Puławy in Poland. Its main part is composed of 5 large spans with Gerber beam static system. In the previous decades the bridge played an important role in the transportation system of the whole region and despite of its advanced age and historic value it was intensively exploited by heavy vehicles. Thus, taking into account the age of the structure and intensity of the traffic crossing the bridge in the past, some doubts about the remaining fatigue resistance of bridge critical members − defined by the fatigue safety level and damage indicator − were formulated.

Fatigue evaluation of the old riveted truss structure was performed according to general assumptions of the Eurocodes [1, 2] and the *European Recommendations for Estimation of Remaining Fatigue Life of Existing Steel Structures* [3]. Essential input data used for estimation of fatigue damage accumulation in critical bridge components as well as for prediction of residual lifetime of the whole structure was based on experimental vibration tests performed under real live loads.

Keywords: Riveted road bridge · Experimental vibration test · Fatigue analysis

1 Bridge Structure and Objectives of the Study

The investigated structure called the Ignacy Mościcki Bridge is located over the Vistula River in Puławy in Poland. The bridge is a unique road structure in the form of a continuous beam with hinges – the so-called Gerber system – made of truss girders. The main part of the bridge is composed of 5 spans with the lengths: 85 + 88 + 110 + 88 + 85 meters. The bridge truss girders, bracings as well as deck grillage are riveted and the steel components of the bridge are made of mild steel. Top part of the deck is constructed in the form of an RC slab. Massive supports are made of concrete with stone facade. The structural form including basic dimensions of the investigated bridge is presented in Figs. 1 and 2.

© Springer International Publishing AG 2018
J.P. Conte et al. (eds.), *Experimental Vibration Analysis for Civil Structures*,
Lecture Notes in Civil Engineering 5, https://doi.org/10.1007/978-3-319-67443-8_20

Fig. 1. The Ignacy Mościcki Bridge over the Vistula River in Puławy

During the World War II the structure was damaged twice: in 1939 and in 1944. After the war it has been rebuilt and opened for traffic in 1949. Since then, until the construction of the bypass of the Puławy city in 2008, the bridge was a part of a national road playing an very important role in the transportation system of the whole region. Despite of its advanced age and historic value it was intensively exploited neglecting compliance with any particular restrictions related to total weight of vehicles crossing the bridge. Since 2008 intensity of the traffic on the bridge has significantly decreased as the admissible weight of vehicles was limited to 12 tonnes.

In the course of special inspection [4] some defects of the bridge superstructure were observed, however no fatigue cracks were directly detected. Anyway, considering the age of the structure and intensity of heavy traffic crossing the bridge in the previous decades, some doubts about the remaining fatigue resistance of bridge critical members appeared. Thus, the main goal of the presented investigation was to estimate the level of the fatigue damage already accumulated in the critical bridge components as well as to predict the remaining life time of the whole structural system.

2 General Procedure of Fatigue Evaluation

The fatigue analysis and prediction of the remaining life of the Ignacy Mościcki Bridge is performed following the general assumptions of the European design codes [1, 2] and recommendations [3]. The assessment is aimed at providing evidence that the bridge will function safely over a specified residual service life. The approach is based on a step-by-step procedure of different precision levels and various input data defining considered loads. In the presented case study the method includes three phases described below.

Phase I – a preliminary evaluation – aimed at identification of critical members in the structure for which a fatigue hazard exists. It was performed by means of a Finite Element model of the bridge developed on the basis of data coming from the structural drawings supplemented by a site investigation. Within the initial calculations the Fatigue Load Model 3 (FLM3) of the Eurocode 1 [1] was applied and its effects in bridge riveted steel members were referred to the S-N curve corresponding to detail fatigue category of 71 MPa according to [2]. The initial evaluation of the fatigue safety level is carried out according to the formula:

$$\mu_{fat} = \frac{\Delta\sigma_C}{\gamma_{Mf} \cdot \gamma_{Ff} \cdot \Delta\sigma_{E,2}} \geq 1 \tag{1}$$

where: μ_{fat} – fatigue safety level; $\Delta\sigma_C$ – reference value of the fatigue strength corresponding to $N_c = 2 \times 10^6$ cycles; $\Delta\sigma_{E,2}$ – equivalent constant amplitude stress range related to $N_c = 2 \times 10^6$ cycles; γ_{Mf} – partial factor for fatigue strength $\Delta\sigma_C$; γ_{Ff} – partial factor for equivalent constant amplitude stress ranges $\Delta\sigma_{E,2}$;

Rules defining values of the above-mentioned parameters are given in [2]. The equivalent constant amplitude stress range $\Delta\sigma_{E,2}$ can be calculated as follows:

$$\gamma_{Ff} \cdot \Delta\sigma_{E,2} = \lambda_1 \cdot \lambda_2 \cdot \lambda_3 \cdot \lambda_4 \cdot \Delta\sigma\left(\gamma_{Ff}, Q_k\right) \tag{2}$$

where: $\Delta\sigma(\gamma_{F,\ f},\ Q_k)$ – the maximum stress range generated by fatigue loads in an analysed bridge member; λ_i – damage equivalent factors determined according to [2]; Q_k – characteristic value of a single variable action generated by FLM3 [1].

When the calculated fatigue safety level $\mu_{fat} < 1$ for any of structural members then the member safety needs to be further assessed following subsequent steps of higher precision of the procedure.

Phase II – a detailed investigation – is a refined assessment carried out only for those members whose fatigue safety level determined in the Phase I was not ensured (i.e. when $\mu_{fat} < 1$). This can be done by application of a more complex load model as well as more precise numerical representation of the structure itself. Within step (a) of this phase FLM4 load model can be utilised consisting of 5 different vehicles given in [1]. If the obtained results are still not satisfactory step (b) of the Phase II is introduced by correction of the FLM4 model values of load on the basis of strain measurements carried out in bridge critical members under real traffic loads. In both steps (a) and (b) of the Phase II the already accumulated fatigue damage in the selected structural members is evaluated. It is calculated using the Palmgren-Miner damage summation rule, simply stated as follows:

$$D_d = \sum \frac{n_{Ei}}{N_{Ri}} \leq 1 \tag{3}$$

where: D_d – the total damage accumulated during the elapsed lifetime in an analysed spot of an evaluated riveted member, n_{Ei} – number of cycles occurring at stress range $\gamma_{Ff}\Delta\sigma_i$, for band i in the factored spectrum; N_{Ri} – the endurance (expressed in cycles) obtained from the factored $\Delta\sigma_c/\gamma_{Mf}\,N_R$ curve corresponding to a stress range of $\gamma_{Ff}\Delta\sigma_{i.}$

In case of the Phase IIb the values of loads defined in FLM4 are modified by factor χ, which is calculated individually for each structural component and is expressed by formula:

$$\chi = \gamma_f \cdot \eta \tag{4}$$

where: γ_f – partial factor for loads; η – ratio of extreme strain range generated by real traffic loads to extreme strain range generated by vehicles of FLM4.

Phase III – a remaining fatigue life estimation – is aimed at estimation of its remaining fatigue life considering present and future operation conditions of a structure. The main input data at this phase are results of stress/strain measurements carried out on site in bridge critical members under real traffic loads covering a longer (minimum one-day) period of the structure typical operation. The measured strain history in consecutive steel components is directly used to create a real stress range spectrum which may be used for representation of present and future operation conditions of a bridge. Additionally some expected external conditions may be included influencing future changes of the traffic on the bridge. Then, considering all periods of the structure operation including past and future traffic conditions leading to damage accumulation within structural members the remaining fatigue life time may be determined.

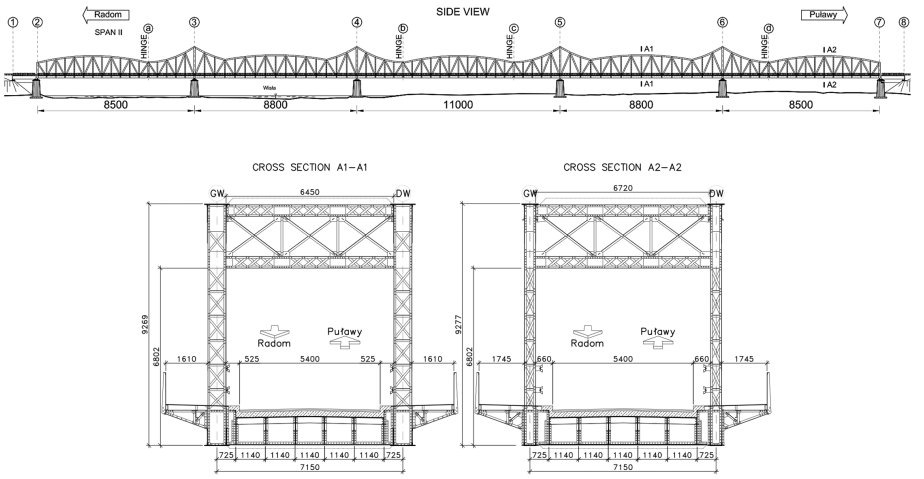

Fig. 2. Structural form of the investigated bridge: (a) side view, (b) cross-sections

For the purpose of theoretical fatigue evaluation of the analysed bridge in Phase I and IIa the truss superstructure was modelled by means of one- and two-dimensional finite elements. One-dimensional beam type elements were utilised for representation of all riveted components of spatial superstructure including bracings. Two-dimensional shell type elements were used for modelling of prefabricated RC deck slab and steel sidewalk decks. The finite element model of the truss spans (Fig. 3) was created and applied within ROBOT Structural Analysis system.

In Phase I the stress ranges in steel members caused by FLM3 load model of Eurocode 1 [1] were analysed. The preliminary theoretical analysis pointed out critical components of spans potentially exposed to fatigue phenomenon and made a detailed examination of those members necessary. The identified elements exposed to fatigue are some of the diagonals of main girders and deck components, especially stringers.

In Phase IIa, stress ranges induced by the theoretical live load model FLM4 defined in code [1] and recommended for fatigue analysis of existing road bridges in Europe [3] were evaluated. To determine the intensity of heavy traffic on the investigated structure in the previous years of its operation, data from the General Measurements of Traffic performed on national roads in Poland since 1975 were used. Estimated the total number of heavy vehicles N_{obs}, which crossed the bridge so far during its almost 80 years of operation is about 25.6 millions.

Calculated in Phase IIa values of fatigue damage indicator D_d occurred to be greater than 1 for most of the selected critical components of structure identified in Phase I. So high values of the damage level D_d indicates that remaining fatigue life of the bridge critical members have already expired and thus indicated the need of experimental confirmation of the bridge remaining fatigue life under real traffic loads.

3 Methodology of Experimental Vibration Tests

On site testing of the bridge in Puławy provided evidence that the structure may function safely over its specified service life. The experimental verifying of the bridge remaining fatigue life was based on measurements of structure response in selected points to various live loads. Choice of the points' location was based on numerical analysis in Phase I using the described FE model of the bridge which indicated the members with insufficient fatigue safety level (where $\mu_{fat} < 1$). Dynamic tests of the structure were executed according to recommendations specified in [5–8] and experience from previous similar tests, e.g. [9–12].

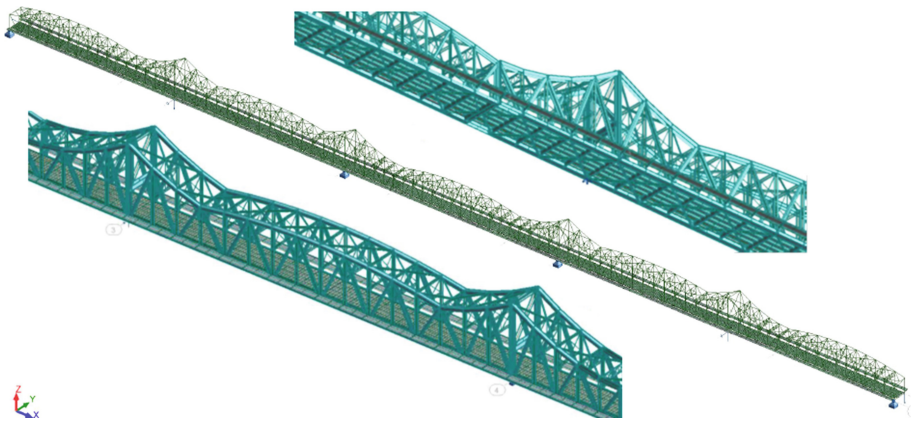

Fig. 3. General view of FE model of the Ignacy Mościcki Bridge

The whole-day special testing of the structure response to live loads included measurements of:

– strains in diagonal members of the main truss girder (points 00-03),
– strains in steel members of the deck within span no. VI, i.e. a cross-beam (point 04-05) and stringers (points 06-09),
– vertical displacements (points 10-12) close to cross-section A3-A3 (see Fig. 4).

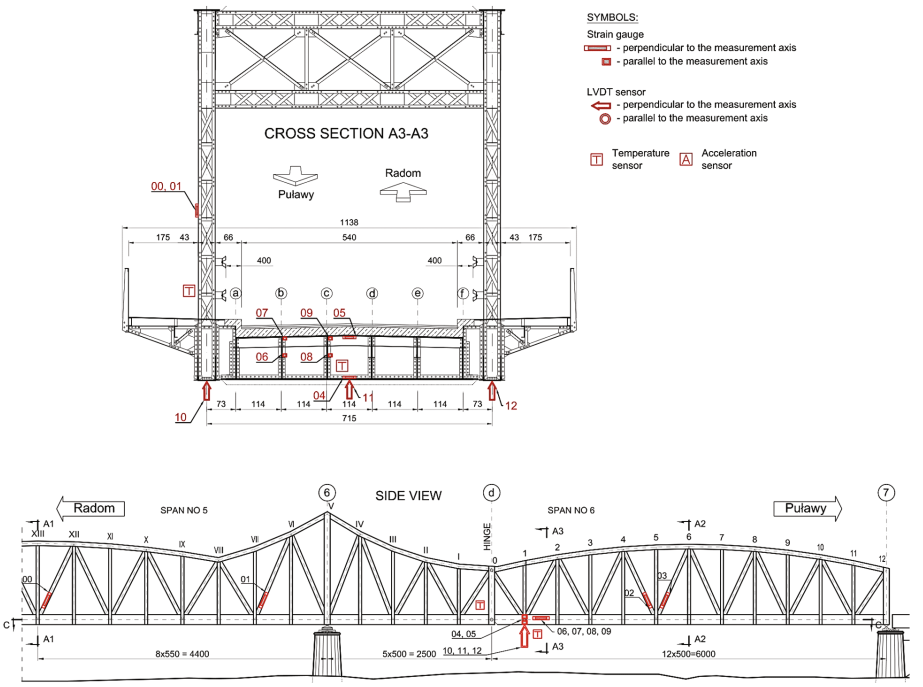

Fig. 4. Arrangement of gauges during the tests: (a) in cross section, (b) in lateral view

Location of the measurement points and types of gauges applied in tests is given in Fig. 4. The measurements were carried out during a one-day session under quasi-static and dynamic live loads including designed and controlled load scenarios as well as under natural operation conditions.

The obtained results were used twofold. Firstly, they enabled initial calibration of the numerical model applied in Phase I of the procedure and its enhancement introduced in Phase II related to improvement of numerical representation of a connection of the deck to the truss girder. Secondly, the measured response provided data on real stress ranges within the structural members and in this way allowed modification of the fatigue load models applied in Phase IIb as well as gave a direct input to remaining fatigue life estimation at real present and future operation conditions.

4 Results of the Vibration Tests

Measurements under live loads were carried out to get real-time information of the superstructure performance subjected to a live load of designed and controlled parameters (i.e. axle loads and spacing, vehicle velocity and location) as well as under natural traffic loads occurring at present time during regular operation of the bridge. Selected results of measurements of physical quantities caused by different types of vehicles in investigated bridge critical members are presented in Figs. 5 and 6.

Tests under dynamic loads of designed and controlled parameters consisted of a series of passages of a single 40-tonne truck along the bridge at the following speeds: 5, 20, 40, 60 km/h. Parameters of the applied truck (see Fig. 5a) have been selected in such a way to get a higher effect in the analysed bridge components than an effect induced by any truck meeting the regulatory requirements for admission to traffic in Poland. Eventually utilised 4-axle vehicle weighing 40 tonnes, due to its actual exceedance of the permissible axle loads, caused in the superstructure slightly larger effects than typical heavy vehicles being in service in Poland which meet regulatory requirements.

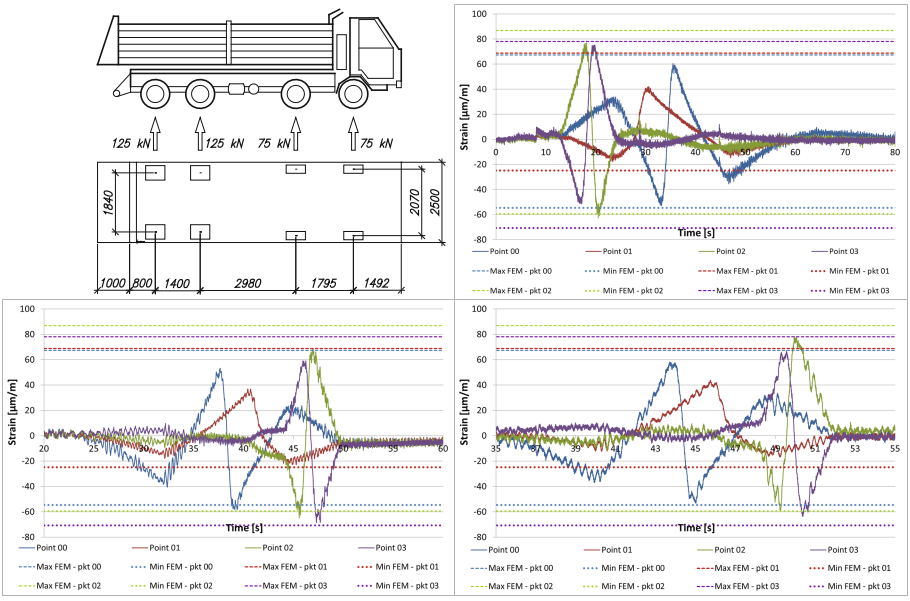

Fig. 5. History of strains induced in the main girders by a single 40-tonne 4-axle vehicle (a) crossing the bridge with various speed: (b) v = 20 km/h, (c) 40 km/h, (d) 60 km/h

Exemplary history of strains induced in diagonal members of the truss main girders by the applied vehicle (Fig. 5a) crossing the bridge with speed varying between 20–60 km/h is shown in Fig. 5b–d. In the diagrams the results of strain measurements were also compared with extreme static effects of loading with a moving theoretical vehicle of the same type determined by means of the applied numerical model. As it can be seen the experimentally determined peak values of strains related to real vehicle load

proved to be consistent with the results of the theoretical analysis. The theoretical strains based on FE analyses are very close to the experimentally identified values – maximum of measured strains was equal 78,26 μm/m (point 02) and corresponding calculated one amounts to 86,83 μm/m. The differences between the experimental and theoretical results are relatively small and do not exceed 5% on average. Therefore it can be concluded that the obtained results confirm high precision of applied numerical model as well as a proper modelling approach utilised in Phases I and II of the theoretical fatigue evaluation procedure. Besides the measurements showed low dependence of extreme internal effects occurring in the main truss members to the speed of a vehicle, while indicated larger fragility to dynamic excitation of short members of the deck. Thus phenomenon is predicted also in some design codes in the form of the dynamic factor being reduced to 1.0 for longer members.

Measured strains caused by the single 40-tonne truck provided data on extreme real stress ranges occurring in critical components of the bridge superstructure induced by heavy traffic crossing the bridge in the previous decades, until 2008. The obtained maximum values of strain ranges caused by the utilised single vehicle was equal to $\Delta\varepsilon_{max}$ = 139.68 μm/m (point 02) which confirmed a risk of fatigue failure in the studied structural members.

Dynamic testing of the bridge truss superstructure under regular operating conditions aimed also at identification of the contemporary loads which may affect the fatigue durability of bridge critical components. The measured history of strains caused by the actual traffic constituted essential input for the prediction of the bridge remaining fatigue life.

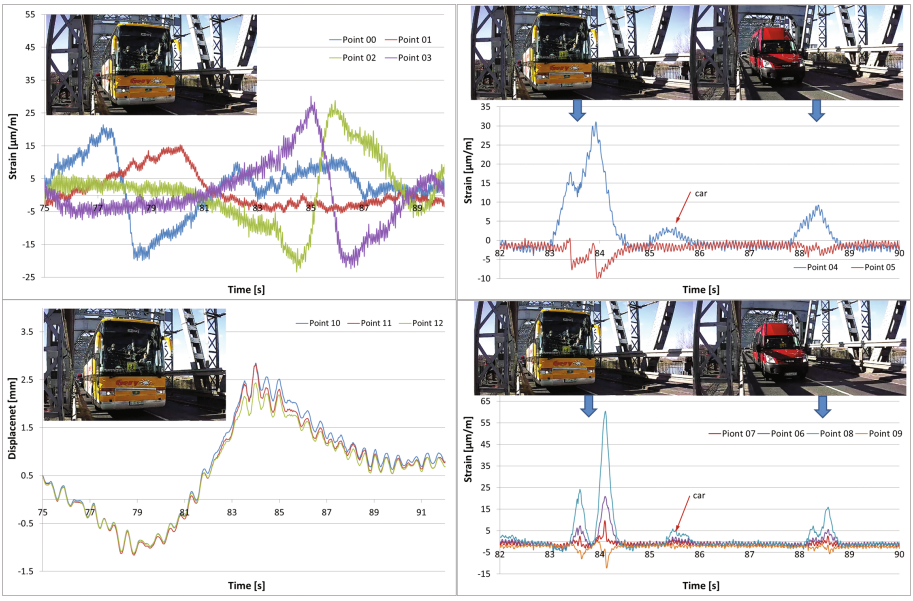

Fig. 6. History of physical quantities induced by selected actual traffic loads during regular operation of the bridge in analysed bridge members: (a) strains in main girders, (b) strains in cross-beam, (c) strains in stringers, (d) displacements of span

It was found that the highest values of measured physical quantities at present time of bridge operation are essentially related to the passing of 2-axle buses with total weight usually varying between 14–16 tonnes. Exemplary history of physical quantities induced by such vehicles are presented in Fig. 6. However it should be underlined that during preparation to the load test, in particular on the day preceding the measurements, a few 5-axle trucks of permissible weight of 40 tonnes were also identified.

The presented data in Fig. 6 show that at the current operating conditions (i.e. since 2008 when bypass of city was build) the highest strains occurring in bridge critical members caused by the actual traffic are relatively small. Maximum value of measured strains in diagonals of the truss girders and in deck components are equal 37,53 μm/m (7,69 MPa) and 60,35 μm/m (12,37 MPa), respectively.

5 Fatigue Damage Accumulation Assessment and Remaining Fatigue Life Estimation

Experimental tests performed using a single 40-tonne vehicle revealed that maximum values of strain ranges caused by such vehicles, which intensively exploited the bridge over the previous decades until 2008, in the light of current knowledge (e.g. according to [2, 3]) can affect fatigue life of some diagonals of truss girders and stringers of the deck system. Assuming detail category of 71 MPa (defined in [2] and suggested in [3]) for bridge riveted components the corresponding fatigue cut-off limit below which micro-damage does not accumulate in material is 103.8 μm/m (21.28 MPa) considering safety factor $\gamma_M = 1.35$. Meanwhile the maximum strain range taken from the measured strain history (see Fig. 7a) for selected elements equals $\Delta\varepsilon_{max} = 139.68$ m/m (28.63 MPa).

It was also concluded that effects caused by purely theoretical load model FLM4 [1] substantially differ from those induced by the real live loads crossing the bridge, both at present as well as also during intensive operation of bridge in the past. In particular, axle loads and total weights of FLM4 trucks, which were adopted in [1] with a considerable safety margin, do not meet the regulatory requirements relating to the technical conditions of vehicles operating in Poland. Therefore extreme stress ranges generated by fatigue load model FLM4 was modified by factor χ calculated individually for each structural component according to formula (4). Obtained values of factor χ, are varying between 0.63-0.75 for different members.

In Phase IIb, based on modified FLM4 axle loads, the calculated fatigue damage D_d was less than 1 for all investigated members. The estimated level of fatigue damage D_d for the considered critical members of the riveted bridge superstructure is diverse and ranges from 0.13 to 0.90. The greatest fatigue damage (D_d = 0,87–0,9) have already accumulated in diagonals of the suspended span (points 02-03), while the relatively low level of damage occurred in deck members. This means that the fatigue life of critical components of the bridge has not been completely exhausted so far.

Maximum strain ranges registered in analysed bridge members induced by current regular traffic loads are presented in Fig. 7b.The maximum value of the calculated strain range $\Delta\varepsilon$ from among all performed measurements is 66,10 μm/m. Obtained value of $\Delta\varepsilon$ is significantly less than the fatigue threshold value accounting for

103,8 μm/m ($\gamma_{Ff}\Delta\sigma_L$ = 21.28 MPa) below which the occurring strain ranges potentially do not contribute to fatigue durability of bridge riveted members.

It was concluded that when the limitation related to the total weight of a single vehicle crossing the bridge is respected by bridge users than the fatigue damage does not accumulate in critical bridge members and in that case there is no risk of superstructure failure associated with it.

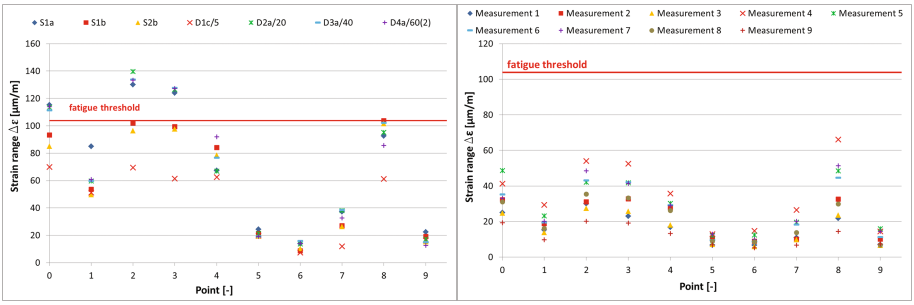

Fig. 7. Maximum strain ranges [μm/m] registered in analysed bridge members by means of experimental tests, caused by: (a) the single 40-tonne vehicle representing the loading acting on the structure until 2008, (b) current regular traffic loads

6 Summary

Fatigue evaluation procedure of the old riveted bridge in Puławy in Poland was described in this paper. The applied procedure of structure evaluation was performed following the general assumptions of the European design codes [1, 2] and recommendations [3]. The collecting of basic input data used for bridge assessment was based on experimental vibration tests carried out using real live loads of designed and controlled parameters as well as under natural (random) operation conditions.

Taking into account the results of the theoretical analysis and experimental load tests the following general conclusions may be formulated:

- Applied numerical modelling and analysis approach of riveted superstructure of the Ignacy Mościcki Bridge enabled precise representation of strain/stresses in all structural members taking into consideration both, global and local effects of loads.
- Fatigue evaluation supported by results of the experimental vibration tests provided information on actual loads acting on the structure and enabled refinement of theoretical load models of the European design codes [1] suggested also in [3], allowing a more detailed assessment of the level of fatigue damage of the bridge critical members.

- The estimated maximum level of fatigue damage is quite high ($D_{d,\ \max} = 0.9$) but indicates that the remaining life of the critical structural components has not yet been fully exhausted.
- Measured strain ranges induced by actual traffic, with the total weight of vehicles limited to 12 tonnes, are relatively low. This allows to conclude that according to the present knowledge in the analysed members fatigue damage does not accumulate and there is no risk of superstructure failure associated with it.
- Determined low dependence of extreme internal effects occurring in the main truss members to the speed of a vehicle (contrary to the effects occurring in short members of the deck) confirmed such a phenomenon expressed by the dynamic factor being reduced to 1.0 for longer members given by some design codes.
- Overall maintenance of the considered bridge is satisfactory. However, localised corrosion pits in any members need a special attention because simultaneous acting of corrosion and fatigue will dangerously accelerate degradation mechanism.

The applied method of testing planning and execution as well as measuring system confirmed practicability of the solutions in identification of bridge characteristics as well as in determination of real load spectra acting on a structure. All that is of great importance in condition evaluation of existing old structures.

References

1. EN1991-2: Eurocode 1: Actions on structures – Part 2: Traffic loads on bridges. European Standard, Brussels: CEN (2003)
2. EN1993-1-9: Eurocode 3: Design of steel structures – Part 1-9: Fatigue. European Standard, Brussels: CEN (2003)
3. Kühn, B., Lukić, M., Nussbaumer, A., Günther, H.-P., Helmerich, R., Herion, S., Kolstein, M.H., Walbridge, S., Androic, B., Dijkstra, O., Bucak, Ö.: Assessment of Existing Steel Structures: Recommendations for Estimation of Remaining Fatigue Life. Background documents in support to the implementation, harmonization and further development of the Eurocodes prepared under the JRC-ECCS Cooperation (2008)
4. Kamiński, T., Bień, J., Hildebrand, M., Kużawa, M., Rabiega, J.: Ocena kondycji mostu kratownicowego przez Wisłę W Puławach, Wrocławskie Dni Mostowe – Duże mosty wieloprzęsłowe. Projektowanie, technologie budowy, monitoring, Wrocław, pp. 475–485, 29–30 November 2016. (in Polish)
5. Alampalli, S.: Effects of testing, analysis, damage, and environment on modal parameters. Mech. Syst. Signal Process. **14**(1), 63–74 (2000)
6. Ewins, D.J.: Modal Testing: Theory, Practice and Application. Research Studies Press Ltd., Baldock (2000)
7. Cunha, A., Caetano, E., Magalhaes, F.: Output-only dynamic testing of bridges and special structures. Struct. Concr. **8**(2), 67–85 (2007)
8. Wenzel, H.: Health Monitoring of Bridges. John Wiley & Sons Ltd., Chichester (2009)
9. Kużawa, M., Bień, J., Rawa, P., Kamiński, T., Zwolski, J.: Static and dynamic load tests of cable-stayed bridge over Odra River in Wrocław. In: 6th International Conference on Bridge Maintenance, Safety and Management "IABMAS", Stresa, Italy, pp. 3344–3351 (2012)

10. Bień, J., Kużawa, M., Zwolski, J., Banakiewicz, A., Rabiega, J., Rawa, P., Adamcewicz, S.: Fatigue life assessment of Grunwaldzki Bridge based on experimental vibration tests. In: 3rd International Conference on Experimental Vibration Analysis for Civil Engineering Structures "EVACES 2009", Wrocław, pp. 569–580 (2009)
11. Bień, J., Kużawa, M., Kamiński, T.: Validation of numerical models of concrete box bridges based on load test results. Arch. Civ. Mech. Eng. **15**(4), 775–1202 (2015)
12. Kużawa, M., Bień, J.: Experimentally validated nonlinear analysis of bridge plate girders with deformations. Stud. Geotech. Mech. **37**(3), 53–61 (2015)

Damage Sensitivity Evaluation of Vibration Parameters Under Ambient Excitation

John James Moughty(✉) and Joan Ramon Casas

Department of Civil and Environmental Engineering,
Technical University of Catalonia (BarcelonaTech), Campus Nord,
Calle Jordi Girona, 1-3, 08034 Catalonia, Spain
john.james.moughty@upc.edu

Abstract. Traditionally, damage detection techniques in bridges have focused on the use of modal-based damage features as they are supported by a well established theoretical base and can be directly related to changes in stiffness. However, modal-based damage features can also be difficult to extract from noisy data and thus their application may require initial large amplitude excitation, in the form of impact tests on closed bridges, to extract an accurate and full modal response. Furthermore, as damage detection and identification methodologies evolve to account for more and more variables, yet still fail to make the breakthrough into industrial applications, there may be an argument to reassess the selection of features used as inputs to these methodologies. Following some recent investigations that discovered a correlation between certain vibration parameters and bridge condition, the present study expands this inquiry by examining the level of damage sensitivity exhibited by various vibration parameters under more scrutiny. Initial sections of this paper outline the vibration parameters to be assessed and the damage detection algorithms employed. The paper finishes with the assessment of the chosen vibration parameters by using vibration data from a progressively damaged bridge subjected to ambient excitation. The paper also suggests a methodology that can be implemented to reduce uncertainty regarding ambient excitation sources.

Keywords: Damage detection · Damage features · Vibration parameters · Structural health monitoring · Outlier detection

1 Introduction

Damage detection and identification methods are increasingly considered to be a more objective approach to assessing bridge condition than visual inspections, which suffer inconsistencies due to inspector competency and differ in methodology from country to country [1]. Although there are many advanced methods of damage detection now available, there still seems to be poor agreement on the optimal damage feature to use. Many damage features suffer from over sensitivity to external conditions, while others are difficult to extract accurately in ambient conditions. The optimal damage feature should be easily extracted, sensitive to damage and insensitive to external variability. The socio-economic value of the bridge is also a factor, as more valuable structures may be assessed using many sensors coupled with advanced analysis methodologies.

© Springer International Publishing AG 2018
J.P. Conte et al. (eds.), *Experimental Vibration Analysis for Civil Structures*,
Lecture Notes in Civil Engineering 5, https://doi.org/10.1007/978-3-319-67443-8_21

However, the vast majority of bridge structures are of lower socio-economic value and thus require a simple and effective methodology that is cost effective. The present study investigates the level of damage sensitivity of a number of vibration parameters that are relatively simple to extract and assess. Data from a progressive damage test conducted on the S101 Bridge in Austria is used to test the damage sensitivity of the chosen vibration parameters. The associated uncertainty related to ambient excitation load sources is also addressed within by the incorporation of the Minimum Covariance Determinate estimator to the outlier detection algorithms.

2 Damage Features: Vibration Parameters

This study aims to explore the possibility of utilizing vibration parameters as damage features in ambient conditions. A number of vibration parameters have been identified that may attain some degree of damage sensitivity. The chosen vibration parameters assessed herein are: RMS Acceleration; Cumulative Absolute Acceleration; Arias Intensity; Peak-to-Peak Acceleration; and Vibration Intensity measured in Vibrars.

For the parameters RMS Acceleration and Cumulative Absolute Acceleration, they are measures of vibration amplitude across a specified time scale. The RMS Acceleration is simply the root mean square of the acceleration time history, and may attain some degree of damage sensitivity when a bridge is subjected to ambient excitation, as a persistent increase in the acceleration RMS may indicate that the structure is having to dynamically resist ambient loading more often due to the fact that it is losing the structural ability to resist the ambient sources of load in a more static and stable manner. Likewise, the Cumulative Absolute Acceleration, being the sum of all absolute acceleration values over a time window, may also indicate the structure's need to act in a more dynamic manner due to structural decline. It should be noted that these parameters are most likely to be of value in ambient conditions, where the sources of loading are Gaussian in nature.

Arias Intensity, defined by Arias [1], is a vibration parameter that is generally used to describe an earthquake's vibrational energy over its total duration. As the energy content of an earthquake is proportional to the square of the acceleration, Arias Intensity incorporates this by calculating the scaled integral of the squared acceleration response. Arias Intensity is commonly used as an indicator of an earthquake's damage potential both from its total cumulative value and also via the max slope of its cumulative series. In the present study, the total Arias Intensity will be used to assess the bridge vibration energy over time and if this changes with damage.

$$I_A = \frac{\pi}{2g} \cdot \int_0^{\infty} a(t)^2 dt \tag{1}$$

In the case of current investigation into the damage sensitivity of vibration intensity measured in vibrars, this stems from previous literature by Casas and Rodrigues [3], who discussed the relationship between vibration intensity and structural condition of bridges. The variable "vibration intensity" was first proposed by Koch [4] to be correlated to the degree of damage in buildings. The rationale behind this connection lies

in the fact that the mean-square value of the acceleration varies with frequency $\{a^2(\mathrm{f})\}$ and damage potential of the vibration falls off with frequency, therefore, it is reasonable to assume that damage caused by inertia forces is proportional to $\{a^2(\mathrm{f})/f = \mathrm{I}(\mathrm{f})\}$. In a simply harmonic motion with an acceleration of amplitude $\mathrm{a_o}$, the term $\{\mathrm{a_o^2/f}\}$ is called vibration intensity. The SI units are $\mathrm{mm^2/s^3}$ and its non-dimensional (decibel) form is presented in Eq. (3), where I_S is a standard value, arbitrarily chosen to be 10 $\mathrm{mm^2/s^3}$. Additionally, vibration intensity can be determined via displacement vibration though the relationship presented in Eq. (4). The units of V defined in this way are called '*Vibrars*'.

$$I = \mathrm{a_0^2}/f \tag{2}$$

$$V = 10 \log 10(I/I_S) \left(\text{where } I_S = 10 \text{ mm}^2/\text{s}^3\right) \tag{3}$$

$$V = 10 \log\left(160\pi^4 a^2 f^3\right) \tag{4}$$

Results from the aforementioned study by Casas and Rodrigues [3], and subsequently revised in Moughty et al. [5], found that the correlation between maximum vibration intensity measured in Vibrars and bridge condition was weak, however, the authors noted that the damage index, developed via FEA calibration, may have accounted for the poor correlation, as much of the data used to calibrate the FEA models was dated or unavailable. Conversely, the same study found a relatively strong correlation between max Peak-to-Peak accelerations and bridge condition. In the same sense that RMS acceleration and Cumulative Absolute Acceleration may indicate structural decline through increased dynamic behavior, max Peak-to-Peak acceleration may demonstrate likewise.

Unlike the other vibration parameters assessed in this study, vibrars are a function of not only vibration amplitude, but frequency as well. This allows for greater depth of assessment, as specific frequency ranges can be targeted for analysis. In the study by Casas and Rodrigues [3], only the max vibrar values were extracted, however the present study expands this to include the vibrar values associated with the first four natural frequencies also, specifically, the first two bending modes and the first two torsional modes. The vibrar extraction process entails the conversion of the acceleration time histories to the frequency domain and subsequently scaling the values based on the relationship expressed in Eq. (3). For improved accuracy of extraction, Hanning windows were employed in two stages; firstly, a low number of long windows with an overlap of 50% were applied to improve frequency resolution and extraction, while a larger number of windows were employed to optimize the amplitude resolution and extraction. However, caution is advised with this approach as the number of windows chosen may affect results, as too few windows makes for noisy amplitude values, while too many will raise the noise floor and thus the amplitude values also.

3 Outlier Detection Methodologies

For the purposes of demonstrating the raw damage sensitivity associated with each vibration parameter, the standard Mahalanobis Squared-Distance (MSD) outlier detection algorithm is employed for its simplicity which will allow for a better examination of the vibration parameters' damage sensitivity, without enhancement from more advanced pattern recognition techniques. However, in addition to assessing the damage sensitivity of certain vibration parameters, the present study also assesses the performance of some other outlier detection techniques, namely Principle Component Analysis (PCA) and Singular Value Decomposition (SVD).

A further addition to the present study is the incorporation of the Minimum Covariance Determinate (MCD) estimator to the aforementioned outlier detection methodologies to increase performance robustness and mitigate the uncertainty surrounding the sources of ambient excitation.

3.1 Mahalanobis Squared-Distance

The MSD [6] is a common technique used to detect outliers in multivariate data by using the mean and covariance of a training dataset, which in the present study is that of the undamaged condition. The MSD is determined as shown in Eq. (5), where $\{X\}_\zeta$ is the potential outlier, $\{\bar{X}\}$ is the mean of the training data and $[\Sigma]$ is the covariance matrix of the training data.

$$D_\zeta = \left(\{X\}_\zeta - \{\bar{X}\}\right)^T [\Sigma]^{-1} \left(\{X\}_\zeta - \{\bar{X}\}\right) \tag{5}$$

3.2 Principle Component Analysis

PCA is a technique used primarily to reduce the dimensionality of complex data sets while retaining a high level of relevant detail that can be more easily observed and quantified. PCA works by initially finding the maximum variance of the dataset, which it uses as its first principle component, and continuing in an orthogonal manner to associate subsequent principle components to the next largest variance. By doing this, PCA can discard the linear combinations of the data that contribute least to the overall variance of the data set. As an outlier detection technique, a covariance matrix $[\Sigma]$ is obtained for the training data and subsequently decomposed using the calculated principle components $[\Lambda]$ as shown in Eq. (6). Test data $\{x\}_i$ can be scored using the transformation matrix $[A]^T$ and the component-wise means of the training data $\{\bar{x}\}$, as shown in Eq. (7) [7].

$$[\Sigma] = [A][\Lambda][A]^T \tag{6}$$

$$\{z\}_i = [A]^T(\{x\}_i - \{\bar{x}\}) \tag{7}$$

3.3 Singular Value Decomposition

SVD is a technique used to transform rectangular matrix of the undamaged training data [M] into two orthogonal matrices [U] and $[V]^H$ and a vector containing the singular values [Λ], as shown in Eq. (8), which is the same decomposition method as used in Eq. (6). For outlier detection, a new matrix [M′] is obtained by inserting a vector of data from a damaged or unknown condition state $\{y\}_i$ at the end of an undamaged matrix [X] (Eq. (9)). Equation (8) is repeated for [M′] and damage is assessed by finding the difference between the original and updated singular values [7].

$$[\mathrm{M}] = [U][\Lambda][V]^H \tag{8}$$

$$[M'] = [[X], \{y\}_i] \tag{9}$$

3.4 Minimum Covariance Determinate

A further addition to the present study is the incorporation of the Minimum Covariance Determinate (MCD) estimator to the aforementioned outlier detection methodologies to increase performance robustness and mitigate the uncertainty surrounding the sources of ambient excitation by finding outliers within the training data and removing them. As the environment conditions remained constant through the damage test on the S101 Bridge and the bridge was no longer in use, it would be generally considered acceptable to assume a Gaussian distributed source of ambient loading and that all recorded vibrations were due to this load source. However, due to the fact that one lane under the bridge was still in operation throughout the test and construction work was in progress nearby, this cannot be assumed. This leaves a case where the undamaged vibration data used to train the various outlier detection algorithms may contain outliers itself due to passing traffic or construction vehicles. The inclusion of these outliers in the training data may have a substantial negative impact on the subsequent test/damaged data results, particularly if the outliers are significantly dissimilar to the majority of data.

The MCD is employed in the present study via the FAST MCD algorithm [8] which accomplishes its objective of removing erroneous data by first determining the subset of data whose covariance matrix has the lowest possible determinant to that of the total dataset. This process takes multiple iterations to complete and requires each subset assessed to contain at least 50% of the overall dataset, although in the present study the limit was increased to 75% for conservatism. Once the MCD finds the data points that contribute most to abnormal variance compared to the remaining data, it returns newly updated mean and covariance values that can be used directly in the MSD, as Dervilis et al. [9] demonstrated. Additionally the new covariance matrix from the MCD can be used in the training phase of PCA via Eq. (6), in addition to updating the component-wise means $\{\bar{x}\}$ in Eq. (7). Furthermore, as the MCD identifies the erroneous data points, the latter can be removed before training the SVD.

4 Test Data: Progressive Damage Test of the S101 Bridge

The S101 Bridge was a post-tensioned three-span flyover near Vienna in Austria that was constructed in the early 1960's. The main span had a length of 32 m, while the two side spans had lengths of 12 m each. The cross-section of the bridge deck was 7.2 m wide and was designed as a double-webbed t-beam, whose webs had a width of 0.6 m. The height of the beam varied from 0.9 m in the mid-span to 1.7 m over the piers, as can be seen in Fig. 1. In 2008, it was decided to replace the S101 Bridge due to insufficient carrying capacity and deteriorating structural condition being identified from visual inspection data. Additionally, the bridge did not meet its service requirements, as the structure did not fit into the overall traffic and infrastructure concept for its location anymore.

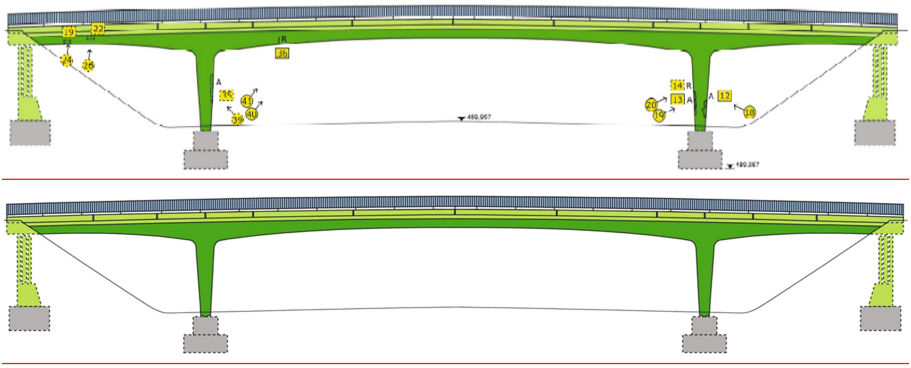

Fig. 1. S101 Bridge longitudinal section [10]

A progressive damage test was conducted on the S101 Bridge across three days in 2008 (December 10th to December 13th). The artificial damage was imposed though the completion of a number of sequential actions, which are presented in Table 1. Overall, the damage applied can be divided into two main stages, with the first comprising of a simulated pier foundation settlement conducted on the bridges north side only, and the second comprising of a bridge deck stiffness loss through the severing of four pre-stressed tendons.

The bridge was closed to traffic during the progressive damage test, meaning that excitation was mainly ambient, although one traffic lane beneath the bridge was in use throughout the test which resulted in vibrations being transmitted through the foundations. Additionally, construction work was also in progress nearby that used heavy machinery and affected the vibratory response of the bridge at times, particularly during the cutting of the first pre-stressed tendon when it was noted that a vibrating impact roller was in operation close by. These additional sources of excitation add a level of uncertainty to the vibration data as no specific information on traffic volume was recorded. As for environment sources of excitation, very little temperature variation was observed throughout the test duration as sub-zero temperatures were kept within a 3–4° range due to heavy cloud cover that did not clear during daylight hours.

It is worth noting that prior to the artificial pier settlement stage of the damage test, the deck was hydraulically supported by a temporary supporting pier that was loaded to the original pier's supporting force of 120t. This allowed for greater control and safety when cutting through the pier, while also allowing the pier to be lowered quickly in 1 cm stages. The initial plan was to lower the pier in 5 steps to a maximum of 5 cm, however, due to increased cracking in the supporting t-beam, the pier settlement was halted at 3 cm, after which compensating plates were inserted under the pier before being hydraulically lifted back to its original position. Although subsequent damage actions were performed on the bridge, which entailed the severing of four pre-stressed tendons (see Table 1), the present study focuses only on the pier settlement damage actions.

Vibration data was recorded by numerous accelerometers located on the bridge deck, with a sample rate of 500 Hz. Vibration recordings from the sensors did not cease throughout the progressive damage test, even recording during the night. For the present study, the measured data was discretized into 66 s time-segments of 33,000 samples each.

Table 1. List of measurements recorded during the S101 Bridge progressive damage test

Damage state	Start time	End time	Description of damage actions
1[a]	10.12.2008 05:16 PM	11.12.2008 07:13 AM	Undamaged
2[a]	11.12.2008 07:13 AM	11.12.2008 10:21 AM	North-western column cut through
3[a]	11.12.2008 10:21 AM	11.12.2008 11:49 AM	First step of lowering bridge pier (1 cm)
4[a]	11.12.2008 11:49 AM	11.12.2008 01:39 PM	Second step of lowering bridge pier (2 cm)
5[a]	11.12.2008 01:39 PM	11.12.2008 02:45 PM	Third step of lowering bridge pier (3 cm)
6[a]	11.12.2008 02:45 PM	12.12.2008 05:52 AM	Compensating plates are inserted
7[a]	12.12.2008 08:04 AM	12.12.2008 01:12 PM	Column returned in original position
8	12.12.2008 01:12 PM	12.12.2008 03:03 PM	First tendon severed
9	12.12.2008 03:03 PM	13.12.2008 05:44 AM	Second tendon severed
11	13.12.2008 05:44 AM	13.12.2008 10:08 AM	Third tendon severed
12	13.12.2008 10:08 AM	13.12.2008 11:14 AM	Fourth tendon partially severed

Note[a]: Damage states highlighted in BOLD were chosen for damage detection assessment as part of this paper's work.

5 Results

Results of the present study are divided into two sections: (1) results of the damage sensitivity assessment of chosen vibration parameters, (2) comparison of outlier detection algorithm performance with and without the incorporation of MCD as an initial step to remove outliers from the training data for the purposes of reducing uncertainty regarding ambient loading.

5.1 Vibration Parameter Damage Sensitivity Assessment

The following results have been obtained via the MSD outlier detection algorithm which used random selection of 70% of the undamaged data as a training set and 30% for validation before being applied to the damaged data. A threshold value of 95% was chosen throughout. Vibration parameters were extracted from four sensor locations on the main span of the bridge deck, specifically, from the quarter point, center point, three-quarter point and from next to the damaged pier. Parameters were combined across all four sensor locations to increase damage sensitivity and outlier detection robustness. As previously mentioned, the data assessed is from the pier settlement damage actions only, which entail the cutting, lowering and returning of the pier in stages that can be clearly identified in the following plots. Note that the last stage in the plots represents two stages as denoted in Table 1, which contain vibration parameters associated with the insertion of compensatory plates and with the pier being returned to its original position.

Figures 2, 3 and 4 present the results of the five vibration parameters: RMS Acceleration; Cumulative Absolute Acceleration; Arias Intensity; Peak-to-Peak Acceleration; and Maximum Vibration Intensity measured in Vibrars (Max across all frequencies). All parameters demonstrate some degree of damage sensitivity, with Cumulative Absolute Acceleration and Arias Intensity performing best, as can be seen from the MSD values on the Y-axis. Interestingly, the Max Vibrars (Fig. 4) performed worst, however, as Vibrars are a function of frequency, a more refined assessment can be made by targeting specific frequency ranges.

Figures 5(a), (b) and 6(a), (b) each present the results of the Vibration Intensity measured in Vibrars associated with the first four natural frequencies for each sensor location. The damage sensitivity of Vibrars is considerably improved in this manner, as clear definition between damage actions is visible.

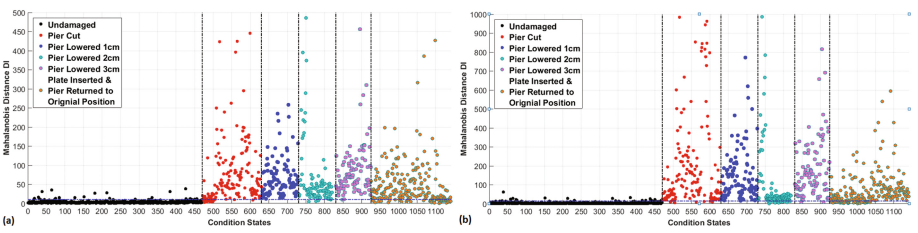

Fig. 2. RMS acceleration (a) and cumulative absolute acceleration (b) from four sensor locations combined

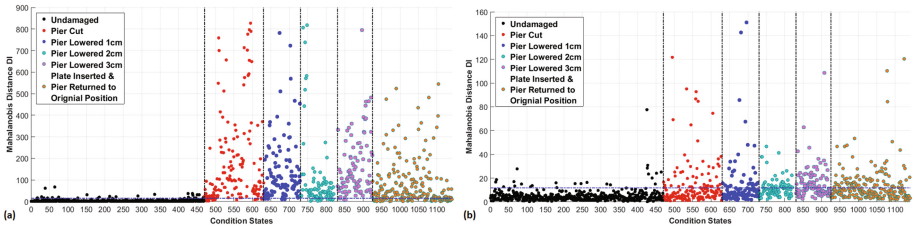

Fig. 3. Arias intensity (a) and max peak-to-peak acceleration (b) from four sensor locations combined

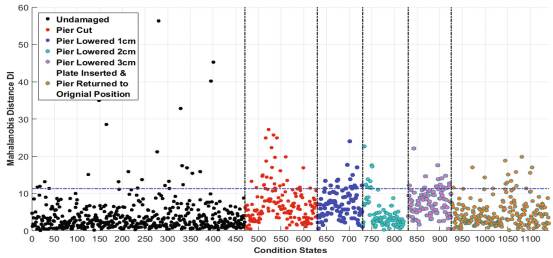

Fig. 4. Maximum vibration intensity (vibrars) from four sensor locations combined

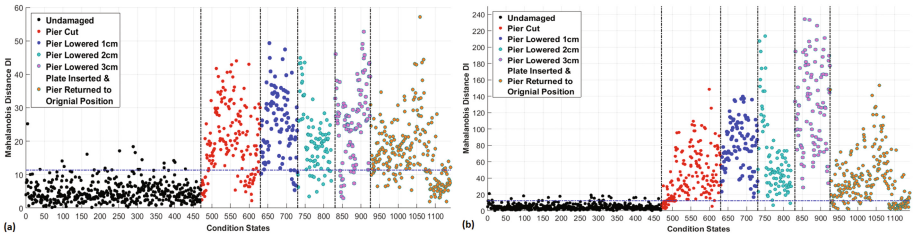

Fig. 5. Vibration intensity (vibrars) associated with the first four natural frequencies for sensors located at south quarter point (a) and center point (b)

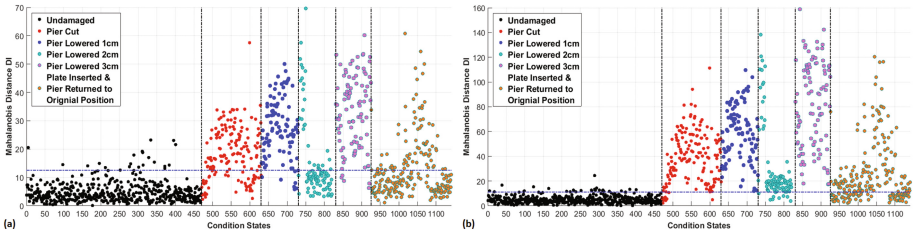

Fig. 6. Vibration intensity (vibrars) associated with the first four natural frequencies for sensors located at north quarter point (a) and next to damaged pier (b)

Figure 7 presents the results of the Vibration Intensity measured in Vibrars associated with the first four natural frequencies combined across all four sensor locations, resulting in a total of 16 damage features. Excellent condition separation is achieved in this manner, with additional detail becoming visible, for instance, one can observe when the pier was fully cut through by the stepped separation in the red data, also when the pier was fully returned to its original position in the final section of data. Additionally, the individual lowering steps are amplified.

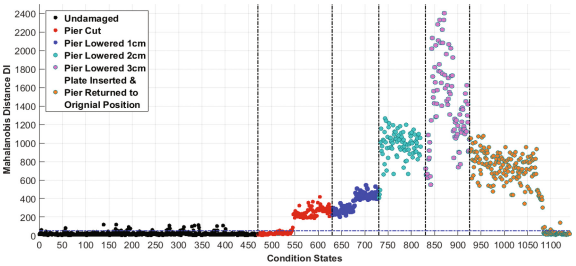

Fig. 7. Vibration intensity (vibrars) associated with the first four natural frequencies for all 4 sensor locations combined

5.2 Outlier Detection Performance and Robustness Assessment

The following results demonstrate the ability of the outlier detection algorithms MSD, PCA and SVD for discerning changes in structural condition. Additionally, the incorporation of the MCD estimator applied to the training data to remove outliers that may be associated with unknown eternal excitation sources is assessed also. All results herein are for the Vibration Intensity measured in Vibrars associated with the first four natural frequencies combined across all four sensor locations. Figure 8(a) and (b) present the MSD results for the standard MSD method (same as Fig. 7 but different scale) and the robust MSD method incorporating the MCD estimator. It is clear that the removal of outliers from the training data enhances the MSD performance. The removed outliers from the training data were reintroduced in the test data, and can now clearly be identified in Fig. 8(b) as outliers.

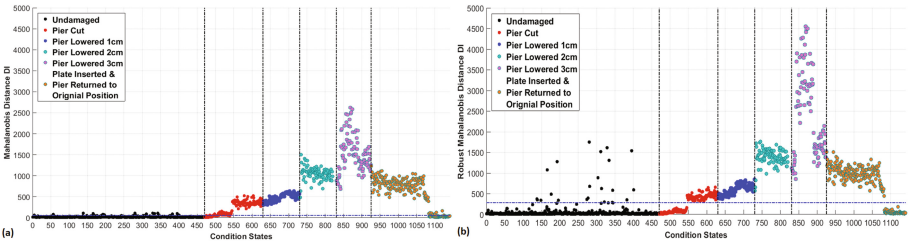

Fig. 8. Vibration intensity (vibrars) associated with the first four natural frequencies for all 4 sensor locations combined using standard MSD (a) and robust MSD incorporating MCD (b)

Figures 9(a), (b) and 10(a), (b) present the results from the PCA and SVD method, respectively. It can be seen that both methods are successful in determining condition variation, although not to the same level of clarity as conveyed by the MSD method. Also of note is that the incorporation of the MCD estimator improved the PCA performance significantly, but only slightly improved that of the SVD.

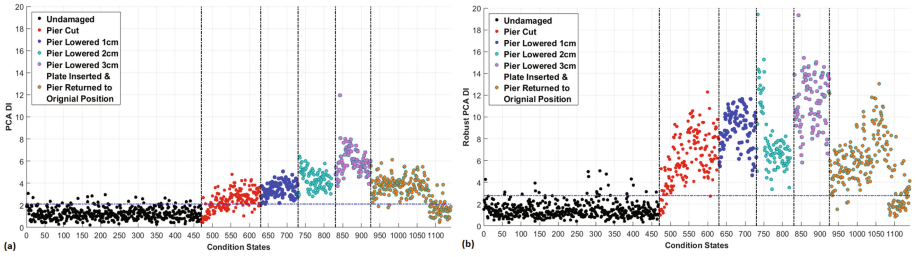

Fig. 9. Vibration intensity (vibrars) associated with the first four natural frequencies for all 4 sensor locations combined using standard PCA (a) and robust PCA incorporating MCD (b)

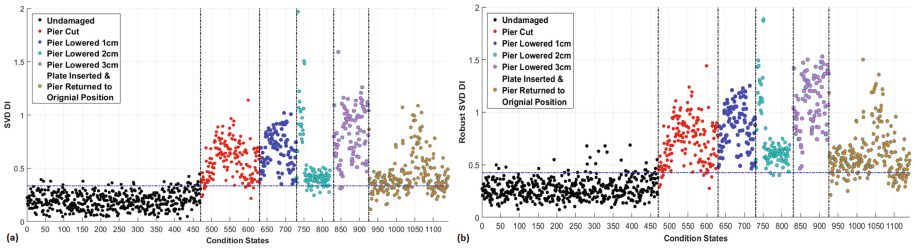

Fig. 10. Vibration intensity (vibrars) associated with the first four natural frequencies for All 4 sensor locations combined using standard SVD (a) and robust PCA incorporating SVD (b)

6 Conclusions

The present study investigated the damage sensitivity of a number of vibration parameters and determined that vibration parameters that are associated with vibration energy (squared amplitude of vibration) perform best, namely; Cumulative Absolute Acceleration, Arias Intensity and Vibration Intensity. This is presumably due to the fact that as the bridge is damaged, it needs to resist external loads using more kinetic energy as it attains less potential energy.

Vibration intensity assessed was calculated using the vibrar scale which weights the intensity magnitude depending on frequency. It was assessed by both extracting the overall maximum vibrar and by targeting specific narrow frequency ranges whereby the vibrar scale no longer had much effect. Judging by the significant difference in results between the max vibrars and the targeted narrow frequency range vibrars, it can be determined that the vibrar scale does not lend itself well to enhancing damage detection, and may in fact inhibit it.

As vibration intensity is a function of frequency and vibration energy, it attains a level of adaptability greater than the other vibrations parameters assessed that allows for multiple vibration intensity damage features to be extracted per time history. The results obtained from the targeted frequency ranges associated with the first four modes demonstrated that vibration intensity also attains a high level of damage sensitivity. It was also demonstrated that combining damage features across multiple modes and sensors considerably improves results.

All assessed outlier detection methodologies performed well, although MSD produced the highest resolution of structural condition variation. Additionally, the incorporation of the MCD estimator to the outlier detection algorithms successfully improved results by identifying and removing erroneous data from the training sets and helped to mitigate the uncertainty regarding external sources of excitation.

Acknowledgments. This project has received funding from the European Union's Horizon 2020 research and innovation programme under the Marie Skłodowska-Curie Grant agreement No. 642453.

References

1. Federal Highway Administration: Bridge Evaluation Quality Assurance in Europe, Technical report Document, FHWA-PL-08-016, March 2008
2. Arias, A.: A measure of earthquake intensity. In: Hansen, R.J. (ed.) Seismic Design for Nuclear Power Plants, pp. 438–483. MIT Press, Cambridge (1970)
3. Casas, J.R., Rodrigues, F.: Bridge condition and safety based on measured vibration level. In: International Association for Bridge and Structural Engineering. Proceedings of Workshop, Helsinki, 11–12 February 2015
4. Koch, H.W.: Determining the effects of vibration in buildings. V.D.I.Z. **25**(21), 744–747 (1953)
5. Moughty, J.J, Casas, J.R., Rodrigues, F.: Assessment of vibration intensity as a condition and safety indicator for short-span bridges. In: Proceedings of the Fifth International Symposium on Life-Cycle Civil Engineering, IALCCE 2016, Delft, The Netherlands, 16–19 October 2016
6. Mahalanobis, P.C.: On the generalized distance in statistics. Proc. Nat. Inst. Sci. India **2**(1), 49–55 (1936)
7. Farrar, C.R., Worden, K.: Structural Health Monitoring - A Machine Learning Perspective, 1st edn. John Wiley & Sons, Ltd., Chichester (2013)
8. Rousseeuw, P.J., Van Driessen, K.: A fast algorithm for the minimum covariance determinant estimator. Technometrics **41**(3), 212–223 (1999)
9. Dervilis, N., Worden, K., Cross, E.J.: On robust regression analysis as a means of exploring environmental and operational conditions for SHM data. J. Sound Vib. **347**, 279–296 (2015)
10. Vienna Consulting Engineers (VCE): Progressive Damage Test S101 Flyover. Internal Report, No. 08/2308, Vienna, Austria (2009)

Operational Damage Localization of Wind Turbine Blades

Yaowen W. Ou, Vasilis K. Dertimanis, and Eleni N. Chatzi(✉)

Department of Civil, Environment and Geomantic Engineering,
ETH Zurich, Zurich, Switzerland
chatzi@ibk.baug.ethz.ch

Abstract. This study tackles the challenge of operational damage identification on wind turbine blades and proposes a novel framework for damage detection and localization. A vibration-based scheme is proposed, which tracks the variability of the mode shape curvatures (MSCs) of the blade along its plane direction. The method consists of a training and a diagnostics stage. In the former, MSC information for a number of predefined modes is extracted over varying operational conditions in the healthy state of the blade and, via the implementation of the principal component analysis (PCA), a statistical characterization of each blade's node is estimated. Then, during the diagnostics stage, the MSCs are assembled and the same PCA mapping is enforced. A corresponding damage index is established, in order to detect and localize damage, if it exists. In both stages, MSC extraction is based on the successful estimation of vector autoregressive moving average (VARX) models that rely on pressure excitation and distributed strain measurements.

Keywords: Wind turbines · Operational conditions · Damage localization · Principal component analysis · Mode shape curvatures

1 Introduction

Structural damage detection and localization forms a scientifically difficult and technologically important issue that has, over the past years, attracted the attention of researchers, engineers, as well as infrastructure stakeholders and insurance companies. Among other candidate approaches, vibration-based structural health monitoring methods have been extensively investigated, as a result of their sound theoretical basis, and the further support provided through well-established and cost effective instrumentation schemes [1, 2].

Focusing on structures that operate on harsh and diverse conditions, such as wind turbine blades, an important aspect of this problem pertains to decision-support, for powering off or intervening for inspection/repair of these components, in light of the variability of the environments they are exposed to. A major challenge lies in the notable influence exerted on damage-sensitive features, such as natural frequencies and mode shapes, by the aforementioned environmental influences [3, 4]. These effects are more extensively documented on bridge structures, with an approximately 5% frequency variation on the Alamosa Canyon bridge reported in Farrar et al. [5] due to changing

© Springer International Publishing AG 2018
J.P. Conte et al. (eds.), *Experimental Vibration Analysis for Civil Structures*,
Lecture Notes in Civil Engineering 5, https://doi.org/10.1007/978-3-319-67443-8_22

environmental conditions, while Alampalli [6] reports an up to 50% variation in natural frequencies of an abandoned bridge in Claverack (NY) as a result of freezing of the supports.

Available methodologies for incorporating or discarding operational variability from structural models and associated indicators may be cast in two prominent categories [7]: (i) output-only methods, relying on response data alone, which seek to remove environmental influences from extracted vibrational features [8, 9], and (ii) input-output methods, which instead aim to determine a functional relationship between the response features and the measured operational conditions [10, 11]. In the first class of methods, PCA [12] or its nonlinear ramifications (kernel PCA [13], Factor Analysis), holds a prominent role in solving the unsupervised learning problem by identifying patterns that are indicative of the effects of the unobserved inputs.

Powered by PCA on modal frequencies, Yan et al. [14, 15] detect damage in both experimental and simulated data under varying environments. Bellino et al. [16] propose a PCA approach suitable for time-varying systems, a topic of particular interest for wind turbine facilities. Nguyen and coworkers [17] suggest a temporal and spectral implementation of PCA for treatment of eigenfrequency and modal shape features respectively, extracted from a bridge in Luxemburg for the purpose of damage detection and localization.

Surprisingly, while the MSCs have been extensively used for damage detection and localization, they have not been exploited to such an end under the influence of changing operational and environmental conditions. For instance, Limongelli et al. [18] employ PCA and MSCs to localize artificial damage on a cantilever aluminum beam tested in the laboratory, under the premise however of invariant environmental conditions. In incorporating such a consideration, Shokrani et al. [19] recently introduced a framework for exploiting MSCs for damage localization, demonstrated on the numerical case study of a bridge system. The present study advances this approach for implementation with simulations of dynamic strain data, extracted from an operational wind turbine blade under temperature variations. For this purpose and under normal operating conditions, the variation of MSCs is tied to the independent sources of operational variability. Thus, during a training stage, the MSCs formulated across a representative operational period, a residual matrix is calculated and a statistical characterization of each node of the blade is derived. Accordingly, in every diagnostic stage, the corresponding MSCs are decomposed using the PCA information established at the training stage and an induced damage index is utilized for achieving damage detection and localization. It is noted that the method uses pressure excitation and distributed strain responses. The latter are deemed preferable when fatigue analysis is of interest, they do not take much space, while recent sensor technologies (e.g. Fiber Bragg Grating) indicate that strain sensors can be embedded into composite materials and integrated into several arrays, which imply structural information from a large number of points [20]. The method can be directly applied, however, to other types of excitation response pairs as well.

2 Blade Description

2.1 Finite Element Model

Figure 1(a) displays the FE model geometry of the wind turbine blade considered, which is 1750 mm long and weighs approximate 5 kg. It consists of woven materials by E-glass and Polyurethane resin matrix, as well as four shear webs in root region. The finite element (FE) model is constructed using shell elements for the outer surfaces of the blade with orthotropic material of equivalent mechanical properties (relying on the specifications provided by the manufacturer).

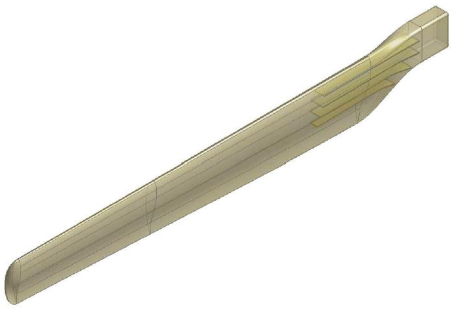

(a) ANSYS Workbench® FE model geometry

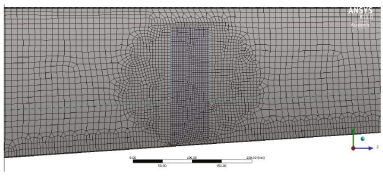

(b) ANSYS Workbench® FE model damage detail

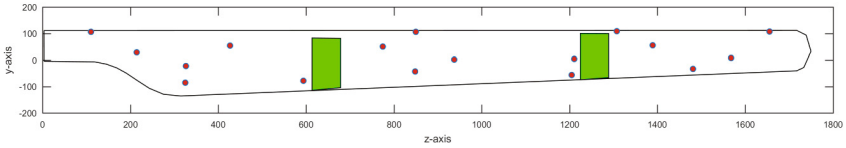

(c) Blade's plane view, showing the axes, the boundary, the damage areas and the sparse data configuration

Fig. 1. Details of the blade's numerical model.

Accurate simulation of the blade in its healthy and damaged states is ensured by careful meshing of the associated geometry, especially with respect to the contact regions among the different blade constitutive materials and elements. This applies specifically to the contact regions between (i) the shell surface and the core foam, (ii) the shear webs' edges and the outside shell surface, (iii) the shear webs' edges and the core foam, and (iv) the shear webs' faces and the core foam. A bonded contact type has been realized for these regions, implying no relative movement (with or without friction) among the edge-surface contacts during simulation.

Following the work described in Ou et al. [21], the FE model is subsequently updated using nonlinear optimization. This is accomplished by minimizing the relative error between the first six natural frequencies and those obtained through the experimental modal analysis data on the actual blade. The reference temperature of the updating process is 20 °C.

In order to include a realistic operational framework, the working temperature of blade is arranged from −15 °C to 40 °C and it is decomposed into 12 uniform intervals of 5 degrees. As temperature changes, the Young's modulus and the shear modulus in all directions are reduced in accordance to existing thermal constitutive equations [22–24]. The Poisson ratios remain constant, while the thermal energy conduction time is ignored, since the analysis is carried out in the steady-state.

2.2 Damage Areas

As Figs. 1(b) and (c) indicate, two typical damage locations at approximately 35% (location A) and 70% (location B) along the z-axis in the flapwise direction of the blade are considered [25]. These are realized as a percentage reduction in the associated material properties within two areas of sizes [210 × 65] mm and [185 × 65] mm. The mesh (obtained by applying shell elements) of the 35% damage area (closer to blade root) is illustrated in Fig. 1(b).

2.3 Wind Pressure Excitation

Blade excitation adopts the model described in Ou et al. [26], according to which the dynamic pressure applied is provided by

$$P_w(t) = \frac{1}{2} C_p \rho u_w^2(t) \tag{1}$$

where C_p and ρ denote the pressure coefficient (assumed constant) and the density of air, respectively, while u_w is the wind speed load, given by the sum of an average speed (u_a), a wind speed ramp ($u_r(t)$), a wind gust ($u_g(t)$) and a turbulence ($u_t(t)$), as

$$u_w(t) = u_a + u_r(t) + u_g(t) + u_t(t) \tag{2}$$

The ramp and the gust components evolve over specific intervals, $[T_{sr}, T_{er}]$ and $[T_{sg}, T_{eg}]$, respectively, and they are calculated by

$$u_r(t) = \begin{cases} A_{ramp} \frac{t - T_{sr}}{T_{er} - T_{sr}}, & t \in [T_{sr}, T_{er}] \\ 0, & \text{otherwise} \end{cases} \tag{3}$$

$$u_g(t) = \begin{cases} A_{gust}\left(1 - 2cos\left(2\pi \frac{t - T_{sg}}{T_{eg} - T_{sg}}\right)\right), & t \in [T_{sg}, T_{eg}] \\ 0, & otherwise \end{cases} \tag{4}$$

with A_{ramp} and A_{gust} corresponding to the ramp and gust amplitudes, respectively. The turbulent component is given by

$$u_t(t) = \sqrt{2} \sum_{k=1}^{N} \left[P_D(\omega_k) \Delta\omega\right]^{1/2} cos(\omega_k t + \varphi_k) \tag{5}$$

where ω_k are frequencies in rad/s, φ_k are random phases in $[0, 2\pi]$ and $P_D(\omega_k)$ is a spectral density function calculated by

$$P_D(\omega_k) = lu_a \left(ln\left(\frac{h}{z_0}\right)\right)^{-1} \left(1 + 1.5\frac{\omega_k l}{u_a}\right)^{-\frac{5}{3}} \tag{6}$$

In Eq. (6), h (m) is the height of the hub from the ground, l (m) is the turbulence length scale and z_0 (m) is the roughness length. The spectral density values to be used in Eq. (5) are sampled by evenly discretizing $P_D(\omega_k)$ at N_ω frequency points, $\omega_k = k\Delta\omega$, for a resolution $\Delta\omega$ and a cutoff frequency $\omega_c = N_k\Delta\omega$.

3 The Operational Damage Localization Framework

The proposed method consists of two interrelated steps that take on (i) the acquisition of sufficient information describing the healthy operational regime of the blade, during a *training stage*; and (ii) the establishment of a robust hypothesis test, which provides information on where a damage has occurred, during a *diagnostics stage*. The method currently assumes the availability of pressure excitation and strain response data, but it can be easily adapted to any type of available vibration excitation-response pairs. Both stages are based on the effective identification of a representative number of blade's vibration modes and the subsequent estimation of a function that approximates the curvature of each vibration mode's shape. To this end, an *estimation module* is integrated to the method, which accepts vibration excitation-response data recorded at distinct operational points (either training, or diagnostics) and returns the curvature functions of the vibration modes.

3.1 The Estimation Module

During each operational point, a VARX model of the form

$$\boldsymbol{\varepsilon}[t] + \sum\nolimits_{k=1}^{na} \mathbf{A}_k \boldsymbol{\varepsilon}[t-k] = \sum\nolimits_{m=0}^{nb} \mathrm{B}_m P_w[t-m] + \mathbf{e}[t] \tag{7}$$

is fitted to the data, where $\boldsymbol{\varepsilon}[t]$ is the $[s \times 1]$ vector of recorded strains at the monitored locations on the blade, $P_w[t]$ is the excitation pressure, $\mathbf{A}_k$, $\mathbf{B}_m$ are the $[s \times s]$ and $[s \times 1]$ coefficients of the associated AR and exogenous matrix polynomials, respectively, and $\mathbf{e}[t]$ is a zero mean vector Gaussian white noise with covariance matrix $\boldsymbol{\Sigma}_{ee}$.

VARX model estimation is quite standard and it reduces to a typical linear regression problem that is solved through ordinary linear least squares. The interested reader is referred to Ljung [27] for further details. Upon availability of a VARX model, the next step pertains to the derivation of its state-space realization [21, 28, 29]

$$\boldsymbol{\xi}[t+1] = \mathbf{F}\boldsymbol{\xi}[t] + \mathbf{G}P_w[t] + \mathbf{K}\mathbf{e}[t] \tag{8a}$$

$$\boldsymbol{\varepsilon}[t] = \mathbf{H}\boldsymbol{\xi}[t] + \mathbf{M}P_w[t] + \mathbf{e}[t] \tag{8b}$$

in which $\boldsymbol{\xi}[t]$ is the $[s \cdot na \times 1]$ state vector and **F**, **G**, **K**, **H**, **M** are the matrices of the state and the output equations, of appropriate orders. For the purposes of the current study, only **F** and **H** are of particular interest. The former is of size $[s \cdot na \times s \cdot na]$ and corresponds to the block companion matrix of the VAR matrix polynomial. By solving the eigenvalue problem of **F**

$$\mathbf{F}\Pi = \Pi\Lambda \tag{9}$$

the eigenvectors $\boldsymbol{\Pi}$ and the eigenvalues $\boldsymbol{\Lambda} = diag\{\lambda_1, \lambda_2, \ldots\}$ are extracted and the vibration modes of the blade are estimated [21]. Accordingly, "mode shape"-type information at the measurement locations may be retrieved by $\boldsymbol{\Phi} = real\{\mathbf{H}\Pi\}$.

Based on the calculated values for $\boldsymbol{\Phi}$ and the boundary conditions of the blade, a "mode shape"-type function $f(y, z)$ is approximated using biharmonic spline interpolation [30] on a denser scattered data grid within the shape of the blade. Then, the MSCs along the two directions can be computed by

$$\Psi_{j,y}(y,z) \equiv \frac{\partial^2 f(y,z)}{\partial y^2} = \frac{f(y+\delta y,z) - 2f(y,z) + f(y-\delta y,z)}{\delta y^2} \tag{10a}$$

$$\Psi_{j,z}(y,z) \equiv \frac{\partial^2 f(y,z)}{\partial z^2} = \frac{f(y,z+\delta z) - 2f(y,z) + f(y,z-\delta z)}{\delta z^2} \tag{10b}$$

with $j = 1, 2, \ldots, n$ denoting vibration mode.

3.2 The Training Stage

It is herein assumed that excitation-response data can be acquired from the blade in a distinct number of operational points $\tau_1, \tau_2, \ldots, \tau_q$, during the *healthy state* of the blade. At each such point, a VARX model is identified and the MSCs of Eqs. (10a), (10b) are extracted for n vibration modes. By denoting all available grid nodes by $k = 1, 2, \ldots, p$ (a unique grid node corresponds to any (z, y) point on the surface of the blade), a $[p \times q]$ matrix is defined for every mode and along each direction as

$$\mathbf{D} = \begin{bmatrix} \Psi[\tau_1, 1] & \cdots & \Psi[\tau_q, 1] \\ \vdots & \ddots & \vdots \\ \Psi[\tau_1, p] & \cdots & \Psi[\tau_q, p] \end{bmatrix} \tag{11}$$

where the bracket notation implies MSC information in a specific operational point and at a specific node. Application of the PCA maps **D** by

$$\mathbf{K} = \mathbf{TD} \tag{12}$$

where $\mathbf{K} \in \mathbb{R}^{d \times q}$ and $\mathbf{T} \in \mathbb{R}^{d \times p}$ is an orthogonal matrix. Both **T** and d are calculated by the singular value decomposition of the covariance matrix of **D** [14, 19], while $d << p$ corresponds to the number of all individual sources that affect the MSC under normal operating conditions and its choice is, in general, not critical.

The loss of information from the mapping of Eq. (12) can be quantified by truncating the mapped data back to the original space

$$\widehat{\mathbf{D}} = \mathbf{T}^T\mathbf{K} = \mathbf{T}^T\mathbf{T}\mathbf{D} \tag{13}$$

and by defining a residual matrix

$$\mathbf{R} = \mathbf{D} - \widehat{\mathbf{D}} \tag{14}$$

each row of which, say $[\mathbf{R}]_{l,*}$, evaluates the loss of information at a specific node. The aim of the training stage is thus to estimate the matrix $\mathbf{T}$, as well as to fit a statistical distribution to $[\mathbf{R}]_{l,*}$. For the current study it is assumed that the normal distribution is sufficient in characterizing the row samples of $\mathbf{R}$. It must be noted, however, that this assumption is not restrictive; it just determines the outlier detection method to be used during the diagnostics stage.

3.3 The Diagnostics Stage

Consider now the acquisition of excitation-response data at an arbitrary operational point τ_{I}. As before, the MSCs associated with this point are extracted via the estimation module, leading to a column vector $\mathbf{w}$ (for every mode and every direction considered) of the form

$$\mathbf{w} = (\Psi[\tau_{\mathrm{I}}, 1], \Psi[\tau_{\mathrm{I}}, 2], \ldots, \Psi[\tau_{\mathrm{I}}, p])^T \tag{15}$$

To decide if the new data comes from a healthy or a damaged state of the blade, the vector $\mathbf{w}$ is appended to the matrix $\mathbf{D}$ to define

$$\mathbf{D}_{\mathrm{I}} = [\mathbf{D}\mathbf{w}] \tag{16}$$

Just as in the training stage, projection and remapping of $\mathbf{D}_{\mathrm{I}}$ implies

$$\widehat{\mathbf{D}}_{\mathrm{I}} = \mathbf{T}^T\mathbf{T}\mathbf{D}_{\mathrm{I}} \tag{17}$$

and the updated residual matrix is

$$\mathbf{R}_{\mathrm{I}} = \mathbf{D}_{\mathrm{I}} - \widehat{\mathbf{D}}_{\mathrm{I}} \tag{18}$$

The latter residual matrix contains one additional sample in every row. Thus, a simple hypothesis test can be established, in order to determine if this new sample belongs to the estimated normal distribution of that row, implying that the new operational point comes from a healthy state of the blade, or if it does not, implying that this point likely comes from a damaged state of the blade. Under the assumption of normality, the adopted hypothesis test pertains to the classical Grubbs' test, where the statistic G is compared against the critical value G_{cr} at a certain significance level a.

If $G < G_{cr}$ the null Hypothesis (e.g. no damage) is adopted, otherwise the alternative Hypothesis (e.g. damage) is adopted instead. Based on this test, a damage index is defined in terms of the distance of the new sample from the mean value of the corresponding distribution

$$\beta_k = \begin{cases} 0, & G < G_{cr} \\ \frac{\left|[\mathbf{R}]_{k,\tau_1}\right|}{\sigma_k}, & G < G_{cr} \end{cases} \tag{19}$$

for k = 1,2,…, p. According to Eq. (19), a non-zero damage index not only implies the presence of the damage, but also indicates the exact position (or a set of positions), where this damage has occurred. It must be emphasized that there is no guarantee that under a specific damage the same index is "excited" in all monitored modes. Indeed a damage may be sensitive in only a subset of modes, or may not be captured at all.

4 Results

The proposed damage localization method is now applied and assessed via the small-scale wind turbine blade previously described. To this end, the blade is simulated within the selected temperature range in its healthy state, as well as in distinct damage states that pertain to both single and multiple damages. In every simulation, the excitation consists of the same mean wind (12 m/s), ramp and gust components, and different realizations of the turbulent component. All numerical values for the associated quantities of the excitation are adopted from Ou et al. [26, Table 1].

Using the sparse data grid of Figs. 1(c), Figs. 2 and 3 display the performance of the damage index (Eq. (19)) when a 30% damage in location A is induced, for the first six mode shapes of the blade and for MSCs calculated along both z and y axis. It is apparent that the damage index has been activated only in the first mode, maintaining almost negligible values in all other ones. Moreover, even if significant values are returned for the first mode of the y axis (Fig. 3, top plot), these are located in very narrow areas for away from the one of the actual damage. Such narrow areas are also

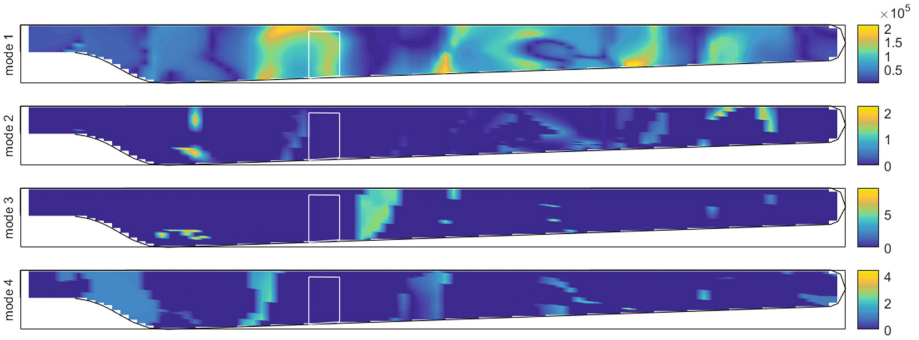

Fig. 2. Damage index for 30% stiffness reduction in location A (sparse grid, MSCs along z direction).

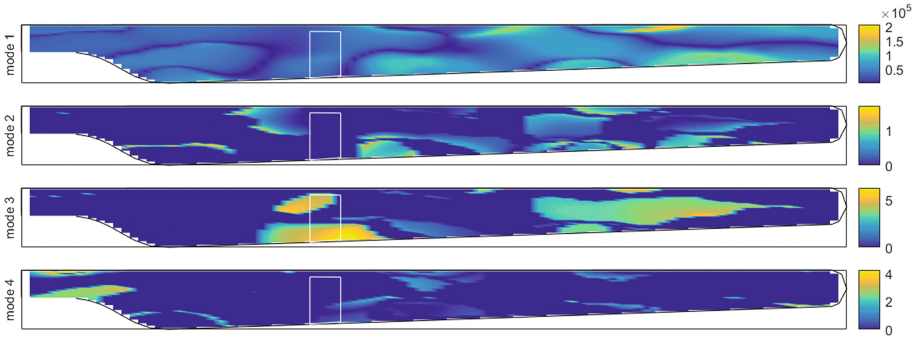

Fig. 3. Damage index for 30% stiffness reduction in location A (sparse grid, MSCs along y direction).

visible in the first mode of the z axis (Fig. 2, top plot) and they deserve further attention, especially in respect to the underlying effects of the blade damage mechanisms. In any case, it is, however, obvious that the damage index has successfully detected and localized a significant area that lies exactly very close to the damage location A. Following these results, only the first mode shape's MSC along the z axis is considered for further analysis and Fig. 4 illustrates the values of the damage index for 50% damage in location A. The damage has been successfully localized, while "false alarm" areas are sufficiently suppressed.

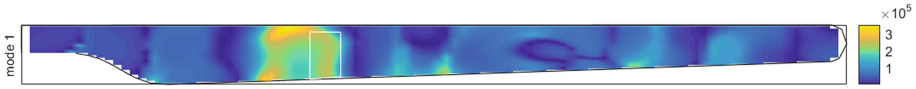

Fig. 4. Damage index for 50% stiffness reduction in location A (sparse grid, MSC along z direction).

The case of simultaneous damages at locations A and B is shown in Fig. 5, from which similar remarks can be made. Interestingly, the damage index is activated along the z axis before the two locations, a feature that is rather attributed to the finite difference approximation of the MSCs. Notice also that difference damage levels may mask damages in other locations. This is apparent in Figs. 5(b)–(c), where the damage levels are different between locations and the index of the lower damage level is masked by the one of the higher damage level. An adaptive strategy for handling such cases, maybe through the use of structure-based information, is currently under investigation.

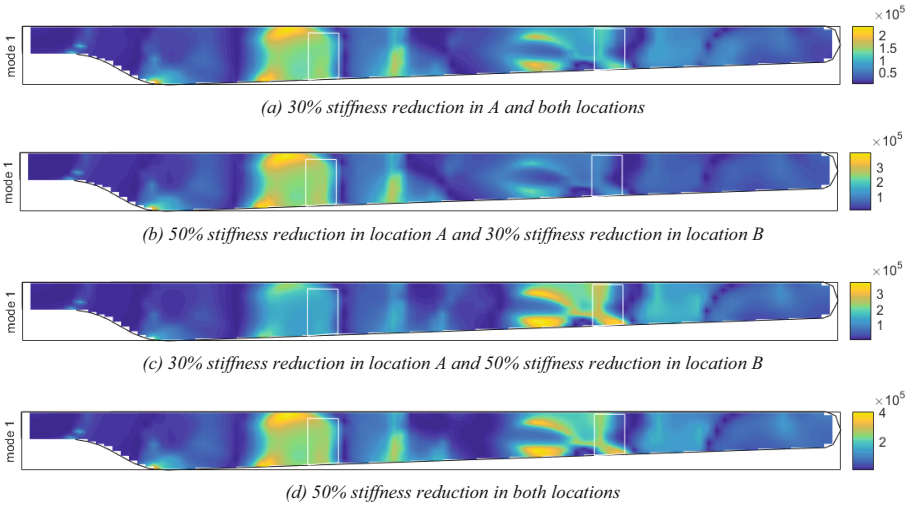

Fig. 5. Damage index for multiple damages along the blade (MSCs along z direction).

5 Conclusions

A novel vibration-based damage detection and localization method for wind turbine blades is outlined in this paper. The method accounts for environmental variability and explores the behavior of the blade's MSCs along distinct operational points. Based on an estimation module, during which a VARX model is estimated and the MSCs are extracted for a number of predefined modes, the proposed scheme constructs MSC data matrices and applies the PCA, in order to estimate all individual sources of variability. At a training level, this allows a statistical characterization of each individual node of the blade in its healthy state. Then, during a diagnostics stage, new data is appended to each node and the procedure is repeated using the quantities extracted at the training stage. A simple and effective hypothesis test and an associated damage index assigned to each node provide indications on whether damage has occurred, or if the new samples belong to the estimated distributions, implying that the blade is still undamaged.

As the numerical results indicate, the method seems capable in identifying and localizing both single and multiple damages at various levels. This encouraging performance suggests further consideration of the method as a potential candidate for damage localization under environmental variability. To this end, a number of important issues are currently under systematic investigation by the authors. These include the effects of data type and locations, the performance of the method in higher modes, its adaptation to output-only schemes (through the use, for example, of simple VAR models), the behavior of the underlying interpolation, as well as the validation of the method through laboratory and field data.

Acknowledgments. Professor E. Chatzi would like to gratefully acknowledge the support of the ERC Starting Grant award ERC-2015-StG #679843 on the topic of "Smart Monitoring, Inspection and Life–Cycle Assessment of Wind Turbines".

References

1. Farrar, C.R., Worden, K.: An introduction to structural health monitoring. Philos. Trans. R. Soc. Lond. A: Math. Phys. Eng. Sci. **365**(1851), 303–315 (2007)
2. Carden, E.P., Fanning, P.: Vibration based condition monitoring: a review. Struct. Health Monit. **3**(4), 355–377 (2004)
3. Cornwell, P., Farrar, C.R., Doebling, S.W., Sohn, H.: Environmental variability of modal properties. Exp. Tech. **23**(6), 45–48 (1999)
4. Liu, C., De Wolf, J.T.: Effect of temperature on modal variability of a curved concrete bridge under ambient loads. J. Struct. Eng. **133**(12), 1742–1751 (2007)
5. Farrar, C.R., Doebling, S.W., Cornwell, P.J., Straser, E.G.: Variability of modal parameters measured on the Alamosa Canyon Bridge. In: Proceedings of SPIE, Orlando, FL, USA, pp. 257–263 (1997)
6. Alampalli, S.: Effects of testing, analysis, damage, and environment on modal parameters. Mech. Syst. Signal Process. **14**(1), 63–74 (2000)
7. Limongelli, M.P., Chatzi, E., Döhler, M., Lombaert, G.: Towards extraction of vibration-based damage indicators. Quantifying the Value of Structural Health Monitoring, COST Action TU1402 (2015)
8. Kullaa, J.: Elimination of environmental influences from damage-sensitive features in a structural health monitoring system. In: Proceedings of the 1st European Workshop on SHM, Paris, France, pp. 742–749 (2002)
9. Spiridonakos, M., Chatzi, E., Sudret, B.: Polynomial chaos expansion models for the monitoring of structures under operational variability. ASCE-ASME J. Risk Uncertain. Eng. Syst. Part A: Civ. Eng. **2**(3), B4016003 (2016)
10. Yuen, K., Kuok, S.: Ambient interference in long-term monitoring of buildings. Eng. Struct. **32**(8), 2379–2386 (2010)
11. Peeters, B., Maeck, J., De Roeck, G.: Vibration-based damage detection in civil engineering: excitation sources and temperature effects. Smart Mater. Struct. **10**(3), 518–527 (2001)
12. Magalhães, F., Cunha, A., Caetano, E.: Vibration based structural health monitoring of an arch bridge: from automated OMA to damage detection. Mech. Syst. Signal Process. **28**, 212–228 (2012)
13. Reynders, E., De Roeck, G.: Vibration-based damage identification: the Z24-bridge benchmark. In: Beer, M., Kougioumtzoglou, I.A., Patelli, E., Au, I.S.K. (eds.) Encyclopedia of Earthquake Engineering. Springer, Berlin (2015)
14. Yan, A.M., Kerschen, G., De Boer, P., Golinval, J.C.: Structural damage diagnosis under varying environmental conditions—part I: a linear analysis. Mech. Syst. Signal Process. **19**(4), 847–864 (2005)
15. Yan, A.M., Kerschen, G., De Boer, P., Golinval, J.C.: Structural damage diagnosis under varying environmental conditions—part II: local PCA for non-linear cases. Mech. Syst. Signal Process. **19**(4), 865–880 (2005)
16. Bellino, A., Fasana, A., Garibaldi, L., Marchesiello, S.: PCA-based detection of damage in time-varying systems. Mech. Syst. Signal Process. **24**(7), 2250–2260 (2010)

17. Ngyen, V.H., Mahowald, J., Maas, S., Golinval, J.C.: Use of time-and frequency-domain approaches for damage detection in civil engineering structures. Shock Vib. (2014). doi:10.1155/2014/872492
18. Limongelli, M.P.: An experimental evaluation of the reliability of a damage localization algorithm based on FRF interpolation. J. Civil Struct. Health Monit. **5**(4), 427–439 (2015)
19. Shokrani, Y., Dertimanis, V., Chatzi, E., Savoia, M.: Structural damage localization under varying environmental conditions. In: 11th HSTAM International Congress on Mechanics, Athens, Greece (2016)
20. Dos Santos, F.L.M., Peeters, B., Van Der Vorst, R., Desmet, W., Góes, L.C.S.: The use of strain and mixed strain/acceleration measurements for modal analysis. In: 9th International Conference on Structural Dynamics, EURODYN 2014, Porto, Portugal (2014)
21. Ou, Y., Chatzi, E.N., Dertimanis, V.K., Spiridonakos, M.D.: Vibration-based experimental damage detection of a small-scale wind turbine blade. Struct. Health Monit. **16**(1), 79–96 (2017)
22. Wang, Z., Zhou, Y., Mallick, P.K.: Effects of temperature and strain rate on the tensile behavior of shod fiber reinforced polyamide-6. Polym. Compos. **23**(5), 858–871 (2002)
23. Guo, Z.S., Feng, J., Wang, H., Hu, H., Zhang, J.: A new temperature dependent modulus model of glass/epoxy composite at elevated temperatures. J. Compos. Mater. **47**, 3303–3310 (2012)
24. Walsh, R.P., McColskey, J.D., Reed, R.P.: Low temperature properties of a unidirectionally reinforced epoxy fibreglass composite. Cryogenics **35**(11), 723–725 (1995)
25. Sörensen, F.B., Jørgensen, E., Debel, P.C., et al.: Improved design of large wind turbine blade of fibre composites based on studies of scale effects (Phase 1)—summary report. Report no. Risø-R-1390(EN), Risø National Laboratory, Roskilde, Denmark (2004)
26. Ou, Y., Dertimanis, V.K., Chatzi, E.N.: Experimental damage detection of a wind turbine blade under varying operational conditions. In: Proceedings of USD2016, Leuven, Belgium (2016)
27. Ljung, L.: System Identification: Theory for the User. Prentice-Hall Inc., New Jersey (1999)
28. Lütkepohl, H.: New Introduction to Multiple Time Series Analysis. Springer, Berlin (2002)
29. Dertimanis, V.K., Koulocheris, D.V.: VAR based state–space structures: realization, statistics and spectral analysis. Lecture Notes in Electrical Engineering, vol. 85, pp. 301–315. Springer, Heidelberg (2011)
30. Sandwell, D.T.: Biharmonic spline interpolation of GEOS-3 and SEASAT altimeter data. Geophys. Res. Lett. **14**(2), 139–142 (1987)

Study on the Vibration Feature of Concrete Deck Slabs Under Fatigue Wheel Loading

Chen Xu[1(✉)] and Hiroshi Masuya[2]

[1] Department of Bridge Engineering, Tongji University, Shanghai, China
xuchenprc@hotmail.com
[2] Department of Environmental Design,
Kanazawa University, Kanazawa, China

Abstract. The concrete deck slab is an important part in the concrete bridge, which supports the traffic load directly. However, the damages due to the fatigue, corrosion, etc. in the concrete slabs have not been restrained fully at all. It can be usually observed in the aging bridges all around the world, significantly influencing the structure safety and durability. Particularly, the fatigue induced concrete cracks can be viewed as a very serious problem that needs to be dealt with in both of the structure maintenance and health monitoring stages. But precisely detecting such cracks is still not an easy work currently since the slab is usually underneath the traffic pavement. One thing for sure is that the cracks may lead to the stiffness variations, and in this sense a study on the vibration feature variation due to the fatigue concrete cracks was carried out for the purpose of trying to relate the vibration characteristics to the fatigue damage concrete cracks. In detail, a fatigue wheel load test were carried out to initiate and develop concrete cracks, in which two full scale concrete deck slab test specimens were designed and manufactured. During the wheel loading test, the impact vibration tests were carried out on these specimens at certain wheel load cycles, in which a newly developed lightweight impact vibration equipment was introduced for the vibration excitation. Based on the test results, it can be found the vibration frequencies and modes appeared observable variations due to the concrete cracks. Moreover, a discussion of using the vibration feature to assess the fatigue damage levels of the concrete deck slab was made through Modal Assurance Criterion (MAC) evaluation.

Keywords: Concrete deck slab · Wheel loading · Concrete cracks · Vibration feature · Modal assurance criterion · Bridges

1 Introduction

The concrete deck slab is an important part in the concrete bridge, which directly supports the traffic load and transfer it to the bridge girders. The damage on the concrete slab can actually influence the bridge safety and durability significantly. It includes the fatigue cracks, corrosion cracks and material chemical reaction induced damages (such as alkali-silica reaction). These damages haven't been full restrained, which can be usually observed on the aging bridges around the world. In particular, the fatigue induced concrete cracks can be viewed as a very serious problem that needs to

© Springer International Publishing AG 2018
J.P. Conte et al. (eds.), *Experimental Vibration Analysis for Civil Structures*,
Lecture Notes in Civil Engineering 5, https://doi.org/10.1007/978-3-319-67443-8_23

be dealt with in both of the structure maintenance and health monitoring stages. But precisely detecting such cracks is still not an easy work since the slab is usually underneath the traffic pavement. One thing for sure is that the cracks may lead to the stiffness variations, resulting to the variations of the slab vibration feature. This was the fundamental idea of the developed non-destructive damage detecting techniques.

The vibration based structural damage identification method has been concerned for years. In particular, the variation of the structural natural frequency [1], vibration mode shape [2], modal shape curvature [3] have been researched for the damage localization. Moreover, the element modal strain energy change [4], etc. has been applied to improve the damage quantification. Later, it was demonstrated that the natural frequency, mode shape and damping ratio are the structural invariants. In other words, the variation of the modal parameters can tell the structural mechanical change.

In this sense, the impact vibration-based fatigue damage assessment on the concrete deck slab under the wheel loading was considered in this study. Particularly, the modal parameters such as the natural frequency, vibration mode, etc. were observed through the impact tests during the fatigue damage development. Moreover, the Modal Assurance Criterion (MAC) was used for concerning the relationship between the vibration modes and fatigue induced damages. These observations were expected to indicate the fatigue damages.

2 Test Setup

2.1 Specimen Layout

There were two identical full-scale concrete deck slab specimens (N1 and N2) designed and manufactured for the wheel loading test. The layout the specimens was shown in Fig. 1. The slab longitudinal length, parallel with the wheel routine, was 3.0 m and the transverse length was 2.8 m. The slab thickness was 0.19 m. The diameter of the embedded reinforcement was 10 mm, and the longitudinal reinforcement ratio was 0.32% while the transverse reinforcement ratio was 0.44%. In addition, there were two whole on the slab specimens filled by the carbon fiber mortar. This was for other research purposes. The hole dimension was small and it was believed to perform little effect on the concrete slab fatigue cracks. Based on the material tests [5], the 28-days tested concrete compressive strength and Young's modulus of N1 specimen were 42.4 and 33500 MPa while those of N2 specimen were 40.4 and 33500 MPa.

2.2 Load Setup

The wheel loading setup was shown in Fig. 2. A rubber wheel ran on the aligned concrete slabs at the middle back and forth. The slabs were supported at the transverse positions which had a 150 mm distance to the edge through being fixed to the red steel beam by rebars (Fig. 2). The wheel load was 160kN and the contact width between the wheel and the slab surface was around 35 cm. The wheel running speed was about 2 km/h. Each of the slab specimens experienced 135,000 running cycles. Moreover, the 160 kN static and impact load tests were also carried out at certain numbers of wheel

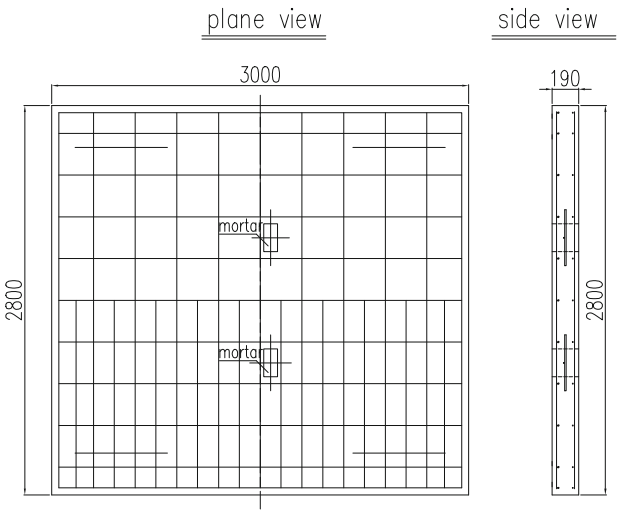

Fig. 1. Mode shapes of the building.

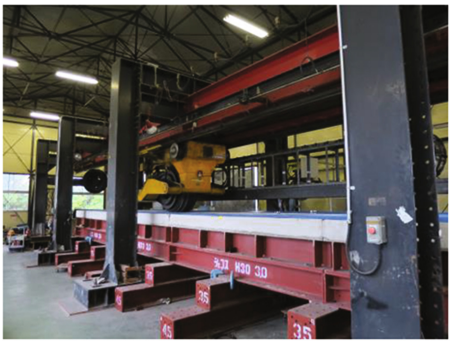

Fig. 2. Wheel loading setup.

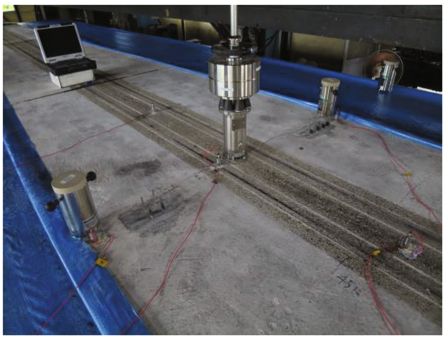

Fig. 3. The self-development lightweight impact equipment.

running cycles, which were for inspecting the fatigue induced deflections and the vibration features, respectively. Concerning the impact test, the impact force was driven by a self-developed lightweight impact equipment (Fig. 3). In detail, a 25 kg falling weight was lifted up to 100 cm high to excite an impact force.

2.3 Sensors

A number of sensors, including the deflection meters, vibration accelerators, strain gauges, etc., were mounted on the specimens for the experimental investigation. In particular, Figs. 4 and 5 respectively show the distributions of the mounted deflection meters underneath the slab specimens and the vibration accelerators on the slab

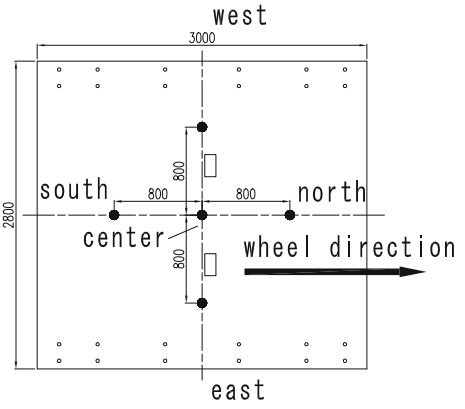

Fig. 4. The deflection sensors underneath the slab specimen.

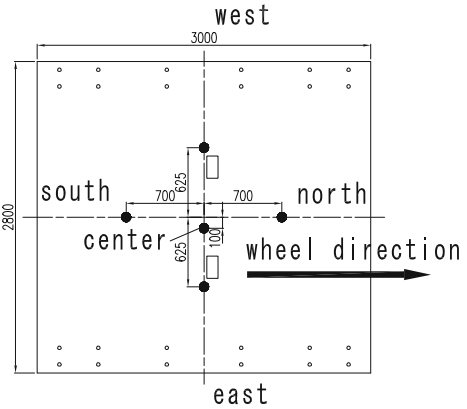

Fig. 5. The accelerators on the slab specimen surfaces

surfaces. Generally, the sensors were distributed along with both of the wheel running direction and the transverse direction. Concerning the positions of the vibration accelerators, they were at the 1/4, 2/4, 3/4 of the longitudinal running span and the transverse span. It was noteworthy that the accelerator at the center was deviated from the slab geometrical center, about 10 cm, for the impact force application.

3 Test Results

3.1 The Fatigue Crack Feature

The distributions of the concrete cracks underneath the slab specimens after the 135000 running cycles were shown in Fig. 6. It was in common that the crack distributed like the grids. It can be seen the cracks appeared obviously at early 5000 wheel running cycles. These crack were marked by red. Afterwards, the cracks kept developing with the wheel running cycles, becoming denser and wider though the range of the crack distributions was relatively constant. However, the cracks development was not always symmetrical to the slab center during the test, sometimes deviated to the left and sometimes right. This indicated the variation of the fatigue damage position. Moreover, the maximum crack width was also measured in the test, which were 0.25 mm in N1 and 0.40 mm in N2 at 135,000 cycles.

3.2 The Fatigue Induced Deflection

The fatigue induced deflections at the slab centers were summarized in Fig. 7. The wheel load running cycles were reflected in the horizontal axis and the deflections were reflected in the vertical axis. There were two lines in each figure in Fig. 7, reflecting the deflection developments when the static load were 160 kN and 0 kN respectively. It can be seen the deflection increased rapidly only at the early running cycles and then

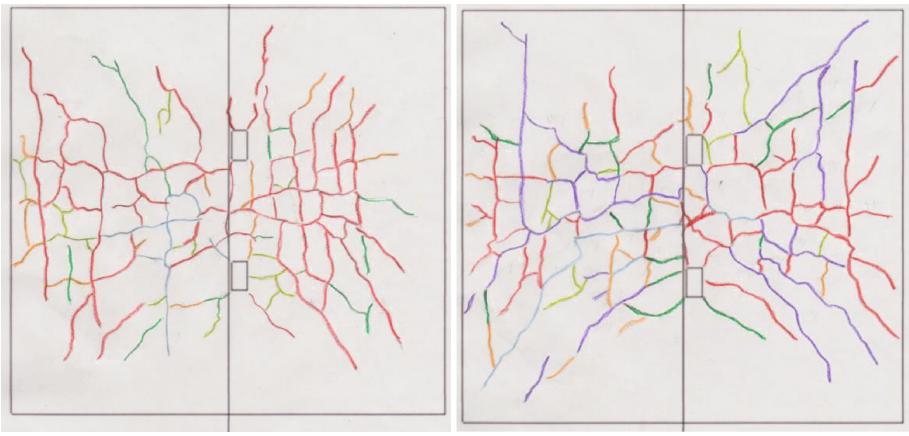

a) N1 specimen. *b) N2 specimen.*

Fig. 6. The crack distributions at the 135000 running cycles.

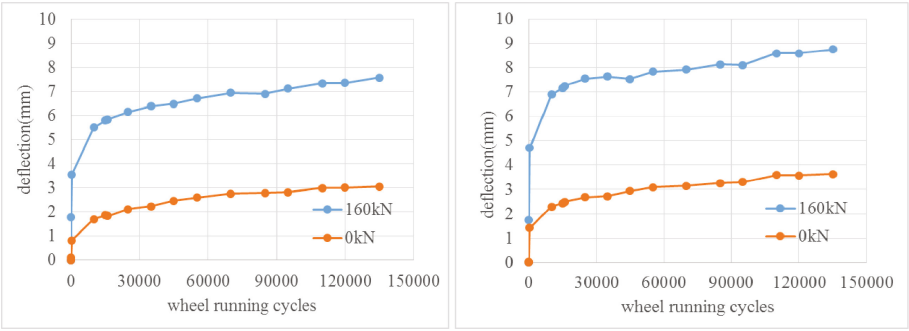

a) N1 specimen. *b) N2 specimen.*

Fig. 7. The fatigue induced slab deflection at the center.

the increase became much slower. The defections of N1 and N2 at 25,000 cycles attained around 7–9 mm. In general, the deflection at the slab center was the largest, but its development seemed to be not so sensitive to the fatigue induced concrete cracks. In other words, measuring the slab deflection may not be efficient to assess the fatigue damage of the concrete deck slab.

3.3 The Frequency Domain Spectrum

The measured time accelerations induced by the constant impact energy were transformed to the frequency domain spectrums as shown in Fig. 8 through FFT. Concerning the frequency spectrum of N1 as shown in Fig. 8(a), there were two frequency spectrum peaks at the initial conditions. When the running cycles started, the afterwards vibration frequency spectrum peaks became more and more. The fatigue induced

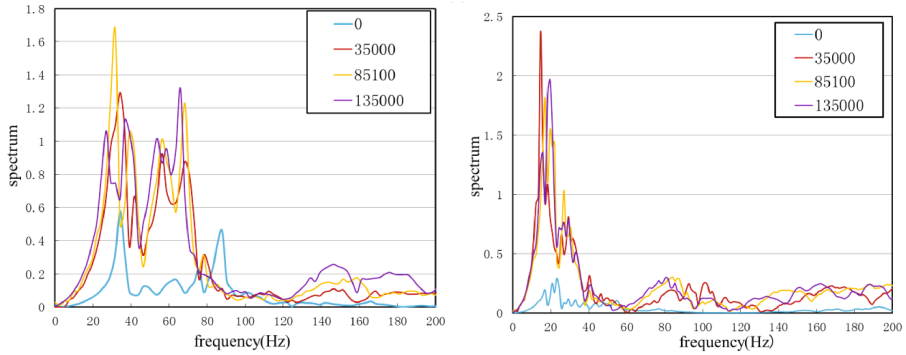

a) N1 specimen. *b) N2 specimen.*

Fig. 8. The impact frequency spectrum at the slab center.

concrete slab cracks can be the main reason. The same situation can be summarized by Fig. 8(b) as well, showing the frequency domain spectrum of N2.

Moreover, Fig. 9 summarized the specific frequencies corresponding to the first spectrum peaks. Such frequencies were actually the ones of the first vibration mode. According to Table 1, there is a tendency that the frequency of the first vibration mode decreased with the running cycles. In this sense, the vibration frequency appeared to be more sensitive than the center fatigue induced deflections to the fatigue damage on the concrete deck slab.

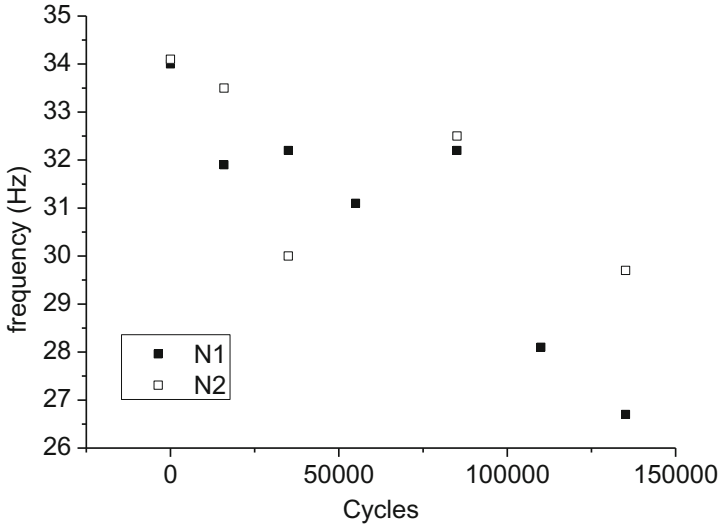

Fig. 9. Frequencies of the first spectrum peak in Fig. 7 vs. wheel running cycles.

3.4 The Vibration Mode Variation

Furthermore, the slab longitudinal vibration modes of N1 and N2 specimen were calculated by ERA method [6] and summarized in Figs. 10, 11 and 12. The horizontal axis shows the positions of the accelerators in the longitudinal direction and the vertical axis shows the normalized vibration mode amplitude. The 1st, 2nd and 3rd vibration modes of N1 and N2 were respectively shown in Figs. 10, 11, and 12. And the mode variation with the wheel running cycles were summarized as well. It can be found that the mode changed obviously during the fatigue wheel loading process. And such variation becomes even much more significant at the higher order vibration modes. Such phenomenon meant that the high order vibration mode should be more sensitive to the fatigue damage on the concrete deck slab.

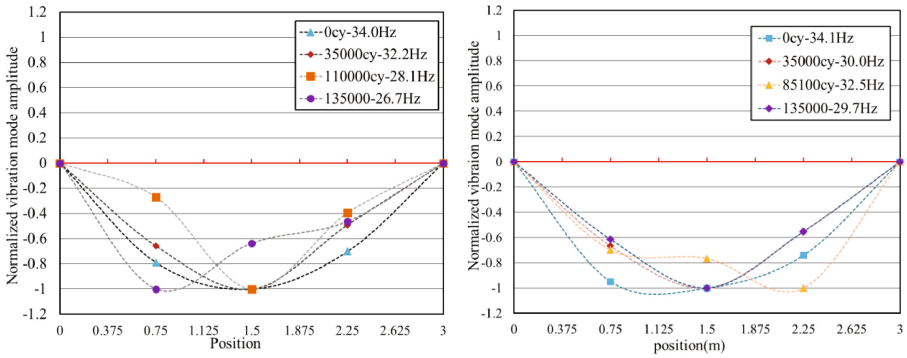

a) N1 specimen. *b) N2 specimen.*

Fig. 10. The 1st impact vibration mode in the transverse direction.

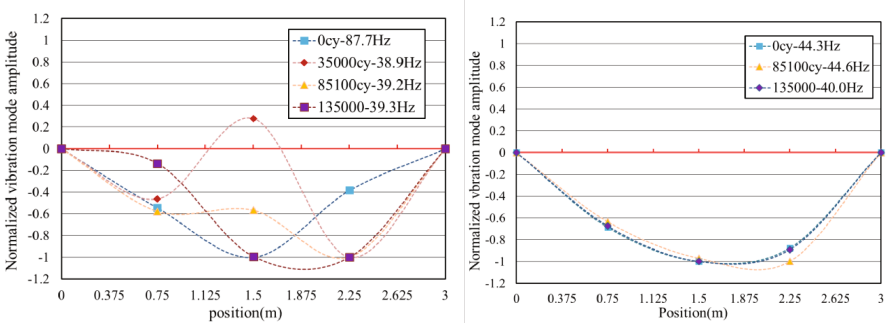

a) N1 specimen. *b) N2 specimen.*

Fig. 11. The 2nd impact vibration mode in the transverse direction.

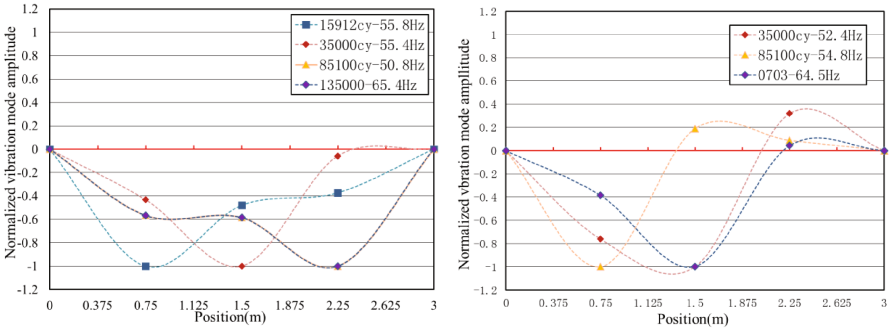

a) N1 specimen. *b) N2 specimen.*

Fig. 12. The 3rd impact vibration mode in the transverse direction.

3.5 The MAC Based Fatigue Damage Assessment

For the purpose of verifying the vibration modes and studying the relationship between the vibration mode and the fatigue damage on the concrete slab deck, the Modal Assurance Criterion (MAC) as expressed in Eq. (1) was introduced. In Eq. (1), ϕ_T was the vibration mode vectors at the 0 load cycle status, ϕ_E was vibration mode vectors after fatigue test started and n was the number of the observation points.

$$MAC = \frac{\left(\sum_{j=1}^{n} \phi_{Tj}\phi_{Ej}\right)^2}{\sum_{j=1}^{n} \phi_{Tj}^2 \sum_{j=1}^{n} \phi_{Ej}^2} \tag{1}$$

The MAC matrix results of the slab vibration modes during the fatigue loading process with reference to the vibration mode at 35000 running cycles were contoured in Figs. 13 and 14, respectively for N1 and N2. Since the 3rd vibration mode at 0cy was not available, the vibration modes at 35000 cycles was considered as the reference. The horizontal axis shows the order of the vibration modes at certain running cycles, and the vertical axis shows the order of the vibration mode at 35000 running cycles. The MAC value of 1 means the two corresponding vibration modes are identical while the value of 0 means the modes are not correlated. Accordingly, it can be seen that the 1st vibration modes (matrix element 1-1) appeared to have good correlation, while the 2nd and 3rd vibration modes (matrix element 2-2) were comparatively less correlated. This confirmed that the vibration mode were sensitive to the fatigue damage of concrete deck slab, especially the high order vibration mode.

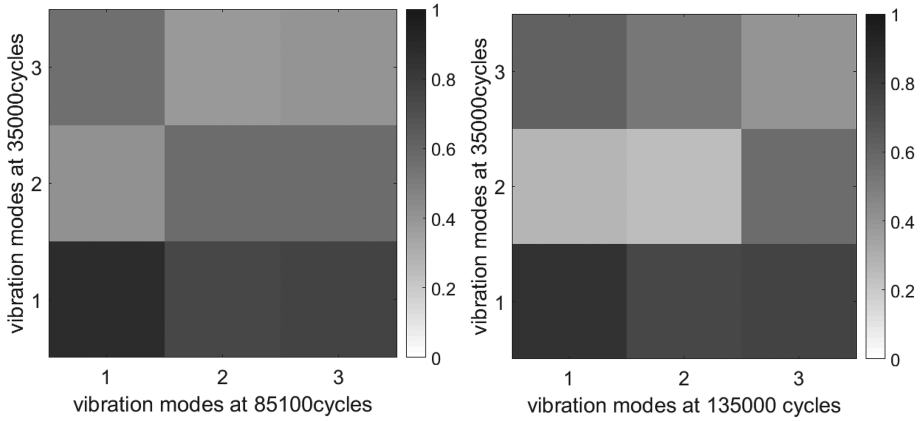

Fig. 13. N1 Vibration mode shape variation assessment by MAC.

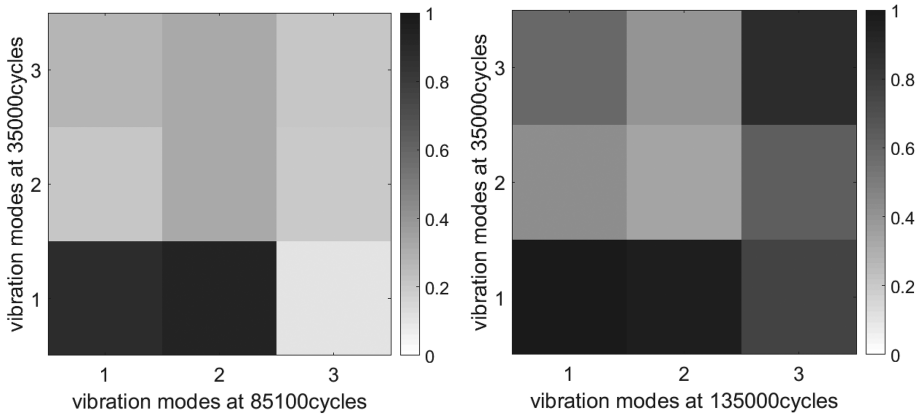

Fig. 14. N2 Vibration mode shape variation assessment by MAC.

4 Conclusion

The wheel loading fatigue test on two full-scale concrete deck slabs was carried out to investigate the efficiency of vibration based assessment method. The following summations were derived based on the test results.

The final condition of the fatigue test appeared as the concrete slab fatigue cracks and vertical deflections. The maximum concrete crack width was 0.25 mm in N1 and 0.40 mm in N2. The crack distributions were like girds, and the cracks developed with the wheel running cycles. However, the range of the cracks was relatively constant during the running cycles.

The vertical deflections of the slabs developed rapidly only at early running cycles, and afterwards it developed much slower. It was not easy to assess the fatigue damage through the deflection variation.

The impact test results showed that the vibration modal parameters such as the frequency spectrum, vibration mode could be sensitive to the local fatigue damage. And these was in line with the Modal Assurance Criterion (MAC) evaluations on the vibration mode shape variation caused by the fatigue damage.

Acknowledgments. The test in this research were carried out in the structural laboratory of Osaka Institute of Technology. The assistance from Mr. Nakahumi YAMAGUCHI and Mr. Hiroshi Yokoyama are appreciated. Meanwhile, thanks for the kind help from all of the fellows in the structural mechanics laboratory of Kanazawa University.

References

1. Sophia, H., Garrett, D.J.: Identification of stiffness reductions using natural frequencies. J. Eng. Mech. ASCE **121**(10), 1106–1113 (1995)
2. Yong, X., Hong, H., James, M.W.B., Xia, P.-Q.: Damage identification of structures with uncertain frequency and mode shape data. Earthq. Eng. Struct. Dyn. **31**(5), 1053–1066 (2002)
3. Pandey, A., Biswas, M., Samman, M.: Damage detection from changes in curvature mode shapes. J. Sound Vib. **145**(2), 321–322 (1991)
4. Shi, Z.Y., Law, S.S., Zhang, L.M.: Damage localization by directly using incomplete mode shapes. J. Eng. Mech. ASCE **126**(6), 656–660 (2000)
5. Japan Industry Standard: Method of test for compressive strength of concrete. JIS A 1108 (1998). Japan [in Japanese]
6. Juang, J.N., Pappa, R.S.: An eigensystem realization algorithm for modal parameter identification and model reduction. J. Guid. **8**(5), 620–627 (1985)

Fuzzy Pattern Recognition in Vibration-Based Structural Health Monitoring

Mohammad Azarbayejani(✉)

Civil and Environmental Engineering Department,
New Mexico Institute of Mining and Technology, Socorro, NM, USA
mohammad.azarbayejani@nmt.edu

Abstract. In this paper, fuzzy sets are established for different states of a reinforced concrete bridge based on finite element model of the bridge. This bridge has been monitored continuously using vibrational signals obtained from accelerometer and strain gauge sensors installed on girders of the bridge. A Finite element model of the bridge is calibrated based on real data gathered from the bridge to be a close representation of the real structure. The calibrated finite element models of the bridge are then constructed for healthy, medium damaged and severe damaged states of the bridge. Using fuzzy set principles, the healthy, medium and severe damage states of the bridge are constructed with fuzzy bell functions. Fuzzy pattern recognition using similarity between fuzzy sets is then utilized to identify any unknown states of the bridge that can give authorities an unbiased tool for efficient maintenance of the bridge.

Keywords: Structural health monitoring · Bridges · Fuzzy sets · Fuzzy pattern recognition · Finite element model

1 Introduction

Structural health monitoring (SHM) is an ongoing field of research mainly focus on detecting and locating damage in structures. The main goal of SHM systems is to increase the safety and reliability of infrastructure with minimum human intervention and more efficiency. Since defining damage is a challenging task, researchers agreed that damage cannot be measured but its influence on the structure's response might be sensed/observed [1]. Based on Farrar et al. [2] damage is defined as "*Intentional or unintentional changes to the boundary conditions and system connectivity, which adversely affect the current or future performance of that system.*" Other definitions of damage such as decrease in stiffness, crack growth and strain thresholds exist in the SHM literature [3–5].

Much effort has been done to probe damage in a structure, before it reaches a critical state. Damage reduces the structure stiffness and hence affects the performance of the structure. Identifying a proper feature that can be observed to realize changes that occur in the structural response due to presence of damage has been the focus of most research efforts. Most current damage features rely on dynamic characteristics of the structure such as natural frequency, modes shapes, etc., because vibration characteristics

© Springer International Publishing AG 2018
J.P. Conte et al. (eds.), *Experimental Vibration Analysis for Civil Structures*,
Lecture Notes in Civil Engineering 5, https://doi.org/10.1007/978-3-319-67443-8_24

demonstrate the degradation in stiffness and are relatively easy to measure in the time domain [6]. Using vibration signals, it has been shown that some damage features can be identified in the frequency domain or the wavelet domain [7, 8]. The size and complexity of civil infrastructure play a major role in developing efficient SHM systems. For some structures, the measurements of interest might not be limited to strain and vibration measurements. For instance, in cable-stayed bridges, measuring force and the condition of strands are a major focus in monitoring the health of the cables. In pipeline structures, corrosion of pipelines is of major interest for its health monitoring [9].

Bridges are among the most important infrastructure of any nation and they play a key role in transportation system. One of the major responsibilities of Departments of Transportation and the Federal Highway Administration is to maintain high standards in safety and reliability of bridges. Based on a recent report of ASCE bridges received a grade of C^+ and it mentioned that one in nine of the nation's bridges are rated as structurally deficient which necessitates $20.5 billion investment annually. This cost covers not only the shoring up of bridges, but also includes keeping a watchful eye on bridges with degrading performance, thereby helping the U.S. Departments of Transportation (DOTs) to make efficient decisions on future maintenance, repair or full replacement of the nation's bridge infrastructure. This will open great opportunities to implement SHM systems on civil infrastructure for researchers. It became obvious to the public that if a simple monitoring system was installed on the I-35 Bridge in Minneapolis, the significance of the disaster of the total failure of this bridge would have been lessened or prevented. After this tragedy, researchers utilized more SHM systems on bridges [10–15]. On the other hand, SHM systems can be incorporated in a great number of civil infrastructure under construction. Deploying efficient monitoring systems on bridges can provide early warning about potential damage. Moreover, continuous monitoring of bridges and critical infrastructure may enable us to move from the current schedule-based maintenance to condition-based maintenance. This should save millions of dollars and allow for the focusing of resources. Furthermore, using new advances in sensing technology and wireless systems made the remote monitoring of bridges a reality.

In this paper, a monitoring system consisting of accelerometers and strain gauges was designed and installed on a reinforced concrete (RC) bridge. Then a finite element (FE) model of the bridge was developed and calibrated based on the real vibration data from the monitoring system. Fuzzy sets are established using the real data and data from the FE model of the bridge for healthy and damaged states of the bridge. These fuzzy sets are then used to identify the current state of the bridge based on the principles of fuzzy pattern recognition. Proper identification of the current state of the bridge will help authorities to make effective decision in maintenance planning and/or replacing the existing bridge.

2 Bridge Description and the Designed SHM System

An RC bridge on Interstate 40 in New Mexico was selected for installation of the monitoring system. This three span bridge consists of five RC K-frame girders with a total

length of about 200 feet. Figures 1 and 2 shows the RC bridge which is located in the City of Tucumcari in NM.

Fig. 1. Bridge 7937 in Tucumcari NM.

Fig. 2. K-frames of Bridge 7937.

The monitoring system that was used for this bridge consists of twenty PCB 333B50 accelerometers (5 installed on each girder) and Vishay electromechanical strain gauges. Accelerometer sensors were used to acquire vibrational data from the bridge. These sensors are connected to a Compact Rio data acquisition device that consists of two important parts: (1) a real-time controller that has volatile memory and nonvolatile memory for data storage. The real-time controller also encompasses an Ethernet port with built-in file servers allowing access by HTTP and FTP, and (2) a multi-slot reconfigurable chassis that contains FPGAs and a Peripheral Component Interface (PCI) bus interface that connects between the FPGA and the real-time controller. This built-in data transfer protocol is used to communicate data to the controller where post processing, data logging and communication to a host computer can take place. The FPGA chip connects directly to the analogue input modules using FPGA functions. Different types

of sensors can be connected to different types of analogue modules. Figure 3 shows the Compact Rio data acquisition device with the modules connected to the chassis.

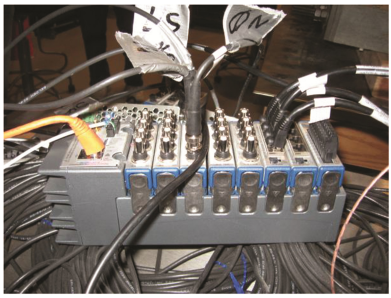

Fig. 3. Compact Rio data acquisition device.

Before installing the SHM system on the RC bridge, all the sensors, FPGA modules and data acquisition device were tested and no error were found in the monitoring system (Fig. 4). The following figures show the installed monitoring system on the bridge:

Fig. 4. Steel box used for the data acquisition device housing.

3 Finite Element Model of the Bridge and Fuzzy Damage Classification

A three dimensional finite element (FE) model of the bridge was developed using SAP2000 software. The FE model was calibrated using the real signals received from accelerometer and strain gauge sensors on the bridge. This model simulates the variable cross sections of girders along with the RC slab on top of them and presents the behavior of the bridge under traffic loadings. Since the bridge is in a healthy state, we used the calibrated 3D FE model to introduce different damage states to the bridge (Fig. 5). The damage states were developed by decreasing the flexural stiffness (EI) of different elements. Figure 6 illustrates the 3D FE model of the bridge.

Fig. 5. Accelerometer sensors installed on the bridge.

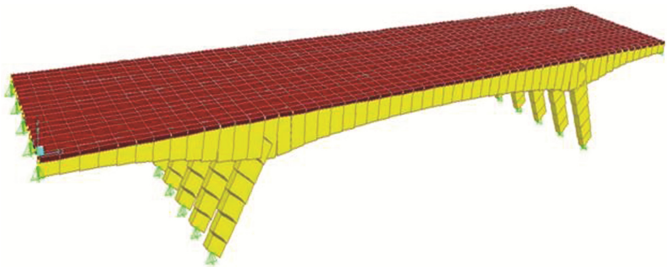

Fig. 6. 3D FE model of the bridge.

Once the FE model of the bridge was established, damage features, which were the energy of acceleration signals in wavelet domain, were extracted at each node of the FE model. Here, we utilized fuzzy set theory in order to represent damage features. Different damage states in structures are defined by different fuzzy sets that are established by principles of inductive reasoning. The vagueness and uncertainties associated with the damage definition and the significant overlap between different damage states in structures make damage-state description amenable to fuzzy definitions and fuzzy pattern recognition. Inductive reasoning or inductive inference is the process of extracting general rules from limited and specific sets of information [16]. Inductive reasoning is considered a cognitive activity that integrates probabilistic and non-probabilistic uncertainty for approximate reasoning of observations. The damage definition process is always based on limited and uncertain information. Damage detection and damage pattern recognition is therefore a proper field for utilizing principles of inductive reasoning [17]. Our method aims at classifying damage states in the structure by establishing fuzzy sets. Since different damage states in the structure have significant overlap and vague boundaries, fuzzy sets are used to describe these damage states. Using fuzzy set theory, the two kinds of uncertainties (i.e. aleatoric and epistemic) associated with defining damage states in structures are considered.

The use of inductive reasoning for classification is based on the fact that the process of induction is associated with minimum uncertainty. Shannon [18] introduced entropy as a measure of disorder in classifying data in 1948 to describe uncertainty or to quantify the information content in a dataset. The uncertainty associated with the value of a discrete random variable (ξ) can be measured by the entropy (S) as

$$S(\zeta) = -\sum_{\zeta \in Z} p(\zeta) \log p(\zeta) \tag{1}$$

where $p(\xi)$ is the probability of the occurrence of ξ. In order to minimize uncertainty, the entropy $S(\xi)$ should be minimized. The minimized entropy $S(\xi)$ will partition the domain into two classes [19, 20]. This entropy can be used as a reasoning basis to obtain generalized classes for a specific set of limited observations. Fuzzy categories are formulated based on the premise of an argument regardless of the fact that such categories are not certain [21].

In order to establish fuzzy sets to describe damage states of the structure, the threshold values defining the boundaries of these fuzzy sets need to be identified. First, two fuzzy sets can be established as a two class partitioning problem, then other fuzzy sets describing other damage states of the structure can be established by generating subclasses for each individual class. Based on inductive reasoning principles the first threshold partitions a domain into two classes. This point (x^0) that minimizes entropy in the interval [x_1, x_2] can be used to partition this domain. The entropy of point (x^0) on the damage feature domain (x) can divide the interval [x_1, x_2] into two intervals [x_1, x^0] and [x^0, x_2]. The entropy S can be calculated as

$$S(x) = \sum_i p^i(x) S_i(x) \tag{2}$$

$$S_i(x) = -\sum_j p_j^i(x) \ln p_j^i(x) \tag{3}$$

where $p_j^i(x)$ is a conditional probability that the class j sample is in the region [x_i, $x_i + x$] and [$x_i + x$, x_{i+1}] and $p^i(x)$ are probabilities that all samples are in the region [x_i, $x_i + x$] and [$x_i + x$, x_{i+1}]. The values $p_j^i(x)$ and $p^i(x)$ are calculated as

$$p_j^i(x) = \frac{n_j^i(x) + 1}{n^i(x) + 1} \tag{4}$$

$$p^i(x) = \frac{n^i(x)}{n}, \sum p^i(x) = 1 \tag{5}$$

where $n_j^i(x)$ is the number of class j samples located in the ith interval [x_i, $x_i + x$], $n^i(x)$ is the total number of samples located in the ith interval and n is the total number of samples in the interval [x_i, x_{i+1}].

By choosing the type of membership function (MF) (triangular, bell shape and etc.), fuzzy sets are established in the damage feature domain. To consider the fuzziness in the damage detection process, some degree of overlapping between two adjacent fuzzy sets needs to be achieved. To establish secondary fuzzy sets accounting for other damage states of the structure, the secondary threshold values are obtained based on the primary threshold value. In other words, the damage feature with the highest membership value in an intermediate fuzzy set corresponds to the minimum membership value in the two

neighbouring fuzzy sets. That enables a significant overlap between the damage fuzzy sets which directly correlates to the level of fuzziness (uncertainty) in the damage states [22].

For Tucumcari Bridge, one primary threshold value and two secondary threshold values were identified to establish three fuzzy sets describing three damage states in the bridge: healthy, medium damage and severe damage. It is important to note the importance of correlating that fuzzy level of damage to mechanical damage in the structure. A few methods have been recently proposed for establishing such correlation [23, 24].

The process of classifying an unknown fuzzy set based on known fuzzy sets is called fuzzy pattern recognition. As the fuzzy damage sets are established as explained above, using fuzzy pattern recognition, datasets of damage feature can be classified to one of the damage classes already defined by fuzzy sets on the damage feature domain. Such classification can be developed using the degree of similarity approach. The degree of damage similarity (DM) between two fuzzy damage vectors $\underset{\sim}{D^i}$ and $\underset{\sim}{D^j}$ is defined as

$$DM = (\underset{\sim}{D^i} \circ \underset{\sim}{D^j}) \wedge (\overline{\underset{\sim}{D^i} \oplus \underset{\sim}{D^j}}) \tag{6}$$

Where $(\underset{\sim}{D^i} \circ \underset{\sim}{D^j})$ is the inner product of the two fuzzy vectors D^i, D^j and $(\overline{\underset{\sim}{D^i} \oplus \underset{\sim}{D^j}})$ is the complement of the outer product of the two vectors. When the value of $\widetilde{DM}$ approaches 1, the two fuzzy vectors are similar and when DM approaches 0, the two fuzzy vectors are dissimilar.

Assuming the current state of the bridge 7937 as healthy, all of the acceleration data obtained from the bridge using installed sensors can be used to calculate the energy of the signals in wavelet domain as a damage feature for healthy state. Since high correlation was observed between signals obtained from the calibrated FE model and the signals from accelerometers on the bridge, the FE model can be used to generate acceleration signals for different damaged states of the bridge. The damage is defined on the FE model as reductions in stiffness of the frame elements in the locations that are more prone to be cracked. For this reason three elements located on the joint of the K-frame on Girder 3 of the FE model are selected as damaged elements. These elements are located at the location of maximum negative moment. By reducing the flexural stiffness in these three elements by 10% to 50% in the FE model, the damage feature is calculated from the nodes of the FE model. Using the principles of inductive reasoning and a bell function for establishing fuzzy membership functions, three fuzzy damage states in the

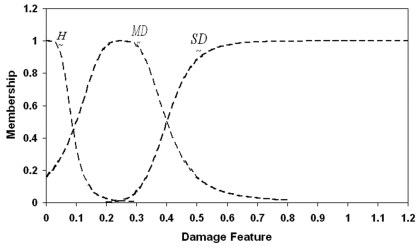

Fig. 7. Healthy, medium damage and severely damage states fuzzy sets for the bridge.

structure: healthy (H), medium damage (MD) and severe damage (SD) were developed as shown in Fig. 7.

4 Results and Discussions

After establishing fuzzy sets representing different states of the bridge, an unknown data set from the real signals from the bridge was obtained. Figure 8 shows the unknown data set A in comparison with the known states of healthy, medium damage and severely damage states of the bridge.

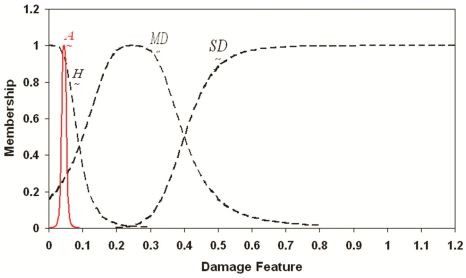

Fig. 8. An unknown data set A in comparison to the known states of the bridge.

Using the similarity degree (DM) described by Eq. (6), the similarity between the unknown dataset and the established fuzzy damage states of the RC bridge can be calculated by the means of fuzzy pattern recognition. Based on this equation, the known fuzzy set A has 95% degree of similarity with the healthy state and 33% degree of similarity with the medium damage and no degree of similarity with severe damage state. These results confirm that the accelerometer data were obtained from the healthy state of the bridge. Using fuzzy pattern recognition and comparing data with the known established states of the bridge will give authorities a good feedback about the current state of the bridge. This feedback would certainly inform the decision making for efficient maintenance of the bridge.

5 Conclusions

In this paper, a fuzzy pattern recognition method was introduced and utilized on a real bridge to identify the current and future states of the bridge with respect to the known healthy, medium and severe damage states of the bridge. The RC bridge already had an installed monitoring system consisting of accelerometers and strain gauge sensors connected to an FPGA data acquisition device. The 3D FE model of the bridge was developed and calibrated using real data from the bridge. The calibrated FE model was used to provide the data for the medium and severe damage states of the bridge. Using these data along with the principles of inductive reasoning, a group of fuzzy sets for healthy, medium damage and severe damage states of the bridge were established. An

unknown state of the bridge created using the acceleration data from the bridge was used to confirm the efficiency of the method in identifying the current state of the bridge. It was shown that the unknown state of the bridge has 95% similarity to the healthy state, using the degree of similarities between fuzzy sets. The fuzzy pattern recognition would be an effective tool for authorities to make better decisions on the safety and maintenance needs of the bridge.

References

1. Lemaitre, J., Desmorat, R.: Engineering Damage Mechanics: Ductile, Creep, Fatigue and Brittle Failures. Springer, New York (2002)
2. Farrar, C.R., Lieven, N.A.J., Bement, M.T.: An Introduction to Damage Prognosis. In: Inman, D.J., Farrar, C.R., Lopes, V., Steffen, V. (eds.) Damage Prognosis for Aerospace, civil and Mechanical System. Wiley, West Sussex, England (2005)
3. Broek, D.: Elementary Engineering Fracture Mechanics. Martinus Nijhoff Publishers, Dordrecht (1986)
4. Worden, K., Dulieu-Barton, J.M.: An overview of intelligent fault detection in systems and structures. Struct. Health Monit. **3**(1), 85–98 (2004)
5. Lemaitre, J., Desmorat, R.: Engineering Damage Mechanics: Ductile, Fatigue and Brittle Failures. Springer, New York (2002)
6. Neild, S.A., McFadden, P.D., Williams, M.S.: A review of time-frequency methods for structural vibration analysis. Eng. Struct. **25**, 713–728 (2003)
7. Chang, C.-C., Chen, L.-W.: Damage detection of cracked thick rotating blades by a spatial wavelet based approach. Appl. Acoust. **65**, 1095–1111 (2004)
8. Reda Taha, M., Noureldin, A., Osman, A., El-Sheimy, N.: Introduction to the use of wavelet multi-resolution analysis for intelligent structural health monitoring. Can. J. Civ. Eng. **31**(5), 719–731 (2004)
9. Thein, A.: Pipeline structural health monitoring using macro-fiber composite active sensors. Master Thesis, Department of Mechanical, Industrial, and Nuclear Engineering, University of Cincinnati (2006)
10. Hu, X., Wang, B., Ji, H.: A wireless sensor network-based structural health monitoring system for highway bridges. Comput. Civ. Infrastruct. Eng. **28**(3), 193–209 (2013)
11. Catbas, F.N., Susoy, M., Frangopol, D.M.: Structural health monitoring and reliability estimation: long span truss bridge application with environmental monitoring data. Eng. Struct. **30**(9), 2347–2359 (2008)
12. Yang, C., Wu, Z., Zhang, Y.: Structural health monitoring of an existing PC box girder bridge with distributed HCFRP sensors in a destructive test. Smart Mater. Struct. **17**(3), 035032 (2008)
13. Torres, B., Payá-Zaforteza, I., Calderón, P.A., Adam, J.M.: Analysis of the strain transfer in a new FBG sensor for structural health monitoring. Eng. Struct. **33**(2), 539–548 (2011)
14. Bao, Y., Beck, J.L., Li, H.: Compressive sampling for accelerometer signals in structural health monitoring. Struct. Health Monit. **10**, 235–246 (2010)
15. Ooijevaar, T.H., Loendersloot, R., Warnet, L.L., De Boer, A., Akkerman, R.: Vibration based structural health monitoring of a composite T-beam. Compos. Struct. **92**(9), 2007–2015 (2010)
16. Feeney, A., Heit, E.: Inductive Reasoning: Experimental, Developmental and Computational Approach. Cambridge University Press, UK (2007)

17. Tenenbaum, J.B., Griffiths, T.L., Kemp, C.: Theory-based Bayesian models of inductive learning and reasoning. Trends Cogn. Sci. **10**(7), 309–318 (2006)
18. Shannon, C.E.: A mathematical theory of communication. Bell Syst. Tech. J. **27**, 379–423 (1948)
19. Kim, C.J., Russell, B.D.: A learning method for use in intelligent computer relays for high impedance faults. IEEE Trans. Power Delivery **6**(1), 109–115 (1991)
20. Ross, T.J.: Fuzzy Logic with Engineering Applications. Wiley, West Sussex (2004)
21. Applebaum, D.: Probability and Information: An Integrated Approach. Cambridge University Press, NY (2003)
22. Klir, G.J., Yuan, B.: Fuzzy Sets and Fuzzy Logic, Theory and Application. Prentice Hall, Upper Saddle River (1995)
23. Zhang, J., Sato, T., Iai, S., Hutchinson, T.: A pattern recognition technique for structural identification using observed vibration signals: nonlinear case studies. Eng. Struct. **30**(5), 1417–1423 (2008)
24. Sheyka, M.: Analytical and Experimental Investigations of Photonic Crystals for Sub-Micron Damage Detection. M.Sc. Thesis, Department of Civil Engineering, University of New Mexico, NM, USA (2008)

Efficient Finite Elements Model Updating for Damage Detection in Bridges

M. Saidou Sanda[1], O. Gauron[2], N. Turcotte[3], C.-P. Lamarche[2], P. Paultre[2(✉)], M. Talbot[4], and J.-F. Laflamme[4]

[1] CIMA+, Sherbrooke, QC, Canada
[2] Department of Civil Engineering, University of Sherbrooke, Sherbrooke, QC, Canada
patrick.paultre@usherbrooke.ca
[3] WSP Canada Inc., Brossard, QC, Canada
[4] Structures Department, Ministry of Transportation of Quebec, Quebec, QC, Canada

Abstract. The study presented in this paper is part of a global research project aiming to detect damage in bridges with modal analyses of traffic-induced ambient vibrations by updating a detailed 3D finite element (FE) model. The commercial software FEMtools is used to solve the resulting largely underdetermined problem. The paper presents the case study of the Rivière-aux-Mulets Bridge located on Highway 15 in Ste-Adèle north-west of Montreal (QC, Canada). The reference 3D FE model of the bridge is first briefly presented. Then, four numerically-simulated damage cases to deck regions, piers or bearings were considered by modifying the stiffness of the elements in the model. The effects of these damages on the vibration frequencies and mode shapes were studied. It appeared that the mode shapes are very poor indices for local damages and that severe damages are not necessarily linked to high reductions of the vibration frequencies. The basic application of the FE model updating algorithms did not provide good estimates of the simulated damage. Thus, an improved procedure is proposed that has three main elements: (i) to control the unknowns-to-equations ratio in the inverse problem within a recommended range; (2) to use an iterative procedure in which update parameters are progressively discarded; (3) to prevent the algorithms from increasing the stiffness of concrete elements. The results obtained on all cases showed good accuracy in localizing and quantifying the simulated damage. The high sensitivity of vibration modes to the bearings parameters seems to be the source of most detection errors. Finally, the proposed methodology is shown to be robust with the accurate detection of combined damage with opposite effects on the natural frequencies of the bridge.

Keywords: Damage detection · Bridges · Finite element model updating · Modal analyses · Traffic-induced vibrations

© Springer International Publishing AG 2018
J.P. Conte et al. (eds.), *Experimental Vibration Analysis for Civil Structures*,
Lecture Notes in Civil Engineering 5, https://doi.org/10.1007/978-3-319-67443-8_25

1 Introduction

Damage detection methods using model updating are based on the modification of mass, stiffness and damping matrices of finite element (FE) models to minimize the discrepancies between experimentally measured responses of the structure and the same responses of the numerical model. The application of the method between two periods of time allows for damage identification, localization and quantification by comparing the updated matrices to the original correlated matrices. Although update calculations are performed automatically by algorithms, the application of the model updating method is not straightforward and depends on many user-defined parameters [1]. The user should also be aware of numerous sources of errors [2, 3], including modelling errors and experimental errors in the target modal responses.

Most civil engineering case studies of model updating in the literature have been applied for damage detection purposes only on small laboratory structures [4], on real-scale structures that can be idealized with stick models [5] or were used for reduced problems using simplified damage functions [6, 7]. In this paper, the commercial software FEMtools [8] is used for direct damage detection by FE model updating on a real bridge using a detailed 3D FE model where the number of update parameters of the model largely exceeds the number of experimental data. The study presented is part of a global research project lead by the University of Sherbrooke and the Ministry of Transportation of Quebec aiming to detect damage in bridges with modal analyses of traffic-induced ambient vibrations using FE model updating. The paper presents the case study of the Rivière-aux-Mulets Bridge located on Highway 15 in Ste-Adèle north-west of Montreal (QC, Canada). The bridge is first briefly presented together with modal analysis results. Then, the reference FE model used for damage detection is briefly presented, resulting from a challenging work of tuning based on experimental modal analyses. Four numerically-simulated damage cases to either deck regions, piers or bearings are considered by modifying the stiffness of the elements in the model. The effects of these damages on the vibration frequencies and mode shapes are studied. The basic application of the FE model updating algorithms of FEMtools is shown not to provide good estimates of the simulated damages. Thus, an improved step-by-step application procedure of the model updating methods dedicated to bridge damage detection with detailed 3D FE models is then established to obtain systematically reliable damage detection results for all damage cases, including combined damage cases.

2 Rivière-Aux-Mulets Bridge

The bridge under study in this paper is the Rivière-aux-Mulets Bridge located on Highway 15 (East direction) in Ste-Adèle, north-west of Montreal (Quebec, Canada). The bridge was built in 1964 together with a twin bridge in the West direction and was one of the first post-tensioned concrete box girder bridge built by balanced cantilever method in North America. Figure 1 presents an elevation view of the bridge and the typical cross-section of the concrete box girder. The twin bridges underwent several increasing damage mainly related to this erection method. The west bridge was

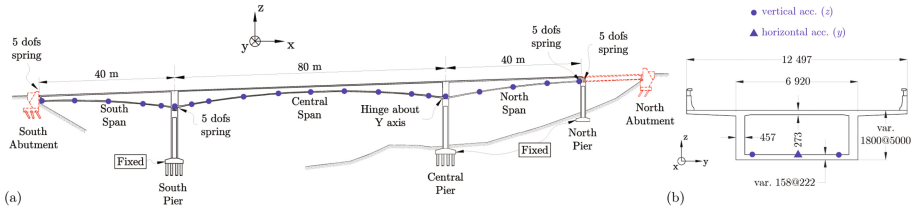

Fig. 1. Rivière-aux-Mulets Bridge and measurement locations: (a) elevation view; (b) cross-section of the box girder.

replaced in 2006 and major repairs were done on the east bridge including addition of post-tensioning cables and of monitoring systems.

Several modal identification tests under traffic-induced ambient vibrations were performed on the bridge by the Ministry of Transportation of Quebec at regularly spaced intervals since 2004, including a much detailed modal analysis in November 2013 performed with the University of Sherbrooke. This former test was used as a basis for the damage detection study presented in this paper. Figure 1a shows the 20 measurement locations instrumented with accelerometers along the deck of the bridge for this test. Figure 1b shows the location of the three accelerometers used at each location in the box girder (1 in y direction, 2 in z direction), resulting in 60 recorded degrees of freedom (DOF) on the whole structure. Table 1 presents the first eight natural frequencies identified using the Frequency Domain Decomposition method (FDD) for the bridge in 2004 and 2013 together with the type of each mode (flexural, lateral or torsional). Figure 2 illustrates the mode shapes of three modes.

Table 1. Natural frequencies of the bridge.

Exp. mode	Type*	2004	2013	Δf_{exp}	FEM	Δf_{num}	MAC_{num}
1	1st F	1.534 Hz	1.563 Hz	+1.89%	1.568 Hz	+0.30%	0.998
2	1st L	1.987 Hz	2.036 Hz	+2.47%	2.035 Hz	−0.04%	0.954
3	2nd F	3.335 Hz	3.330 Hz	−0.15%	3.337 Hz	+0.23%	0.985
4	3rd F	4.559 Hz	4.616 Hz	+1.25%	4.595 Hz	−0.45%	0.925
5	2nd L	5.005 Hz	5.209 Hz	+4.08%	5.206 Hz	−0.04%	0.974
6	4th F	5.583 Hz	5.644 Hz	+1.09%	5.640 Hz	−0.06%	0.957
7	1st T	6.252 Hz	6.185 Hz	−1.07%	6.185 Hz	+0.00%	(0.432)
8	5th F	8.067 Hz	8.182 Hz	+1.43%	8.194 Hz	+0.16%	0.882

*Note: F = Flexural L = Lateral T = Torsional

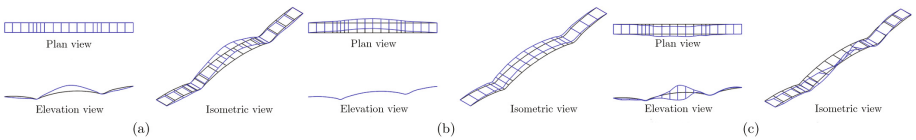

Fig. 2. Mode shapes of the bridge: (a) 1st flexural (mode 1); (b) 1st lateral (mode 2); (c) 1st torsional (mode 7).

3 Updated Finite Elements Model of the Bridge

A 3D detailed numerical model of the bridge was developed using the FE software Abaqus [9] and it was then directly exported into FEMtools to perform model updating tasks. Elements in red in Fig. 1 were not modeled and their interaction with the rest of the bridge was considered by using spring elements. Figure 3a illustrates the 3D FE model. The final detailed model is made of 4484 hexahedral C3D20R elements for the concrete box girder (length of the elements is similar to the mean length of the segments), 414 hexahedral C3D20R elements for the piers and 20 spring elements for the boundary conditions. The boundary conditions used are shown in Fig. 1a and mainly consist in fixed conditions at the base of the piers and five-DOF spring elements (all DOF except rotation about *y*-axis that is free) either for piers-to-deck or abutments-to-deck interactions.

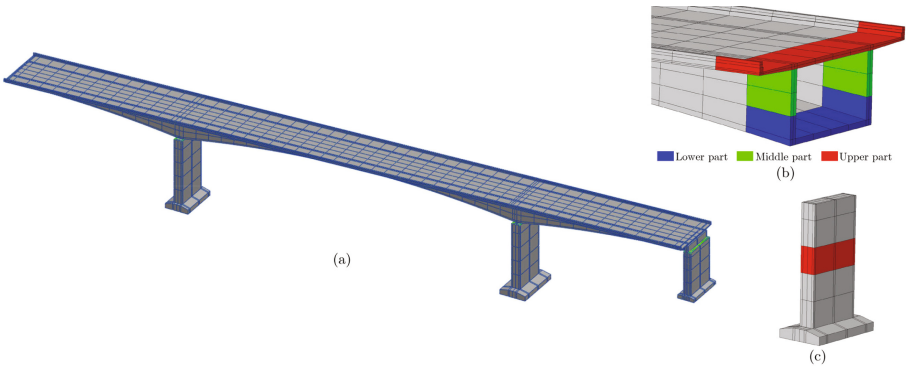

Fig. 3. Detailed 3D FE model of the bridge: (a) mesh; (b) box girder update parameters; (c) piers update parameters.

The fine tuning of such a detailed and complete FE model based on experimental modal properties is a very challenging task that represents as much work as the damage detection analyses themselves. Model updating algorithms of FEMtools were used to update the model with the experimental modal properties of the bridge extracted in 2013. By doing this, the authors proposed a systematic practical updating procedure dedicated to bridge structures that leads to a well-tuned FE model in five steps. This methodology is out of the scope of this paper and only information needed for the rest of the paper is presented. Update parameters were defined as the Young's moduli of the elements of the segments and of the piers grouped in layers as illustrated in Fig. 3b and 3c, resulting in 199 update parameters including the stiffness of the 20 springs for the boundary conditions. A sensitivity analysis performed on the eight identified natural frequencies allowed to discard not-detectable parameters (middle part of the box girder and several springs) to finally keep 133 update parameters (including 8 springs). Natural frequencies and mode shapes of the eight identified modes in Table 1 (except the inaccurate shape of the torsional mode 7) were used as target responses of the structure for the model updating process. Thus, the unknowns-to-experimental equations ratio in the model

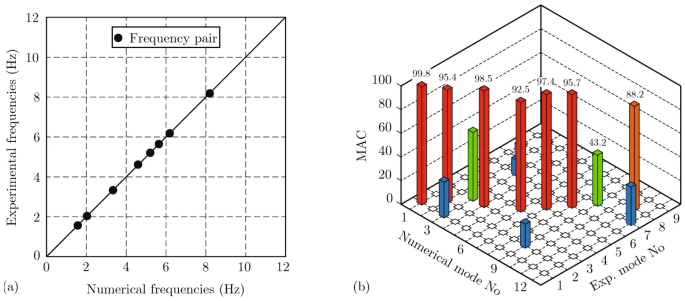

Fig. 4. Correlation between updated numerical and 2013 experimental (a) natural frequencies; (b) mode shapes (MAC)

updating inverse problem is r_p = 133/15 = 8.87, corresponding to a largely underdetermined problem. Mode shape target responses were considered through MAC values. Figure 4 and last columns of Table 1 illustrate the accuracy of the updated FE model, which will be used as a reference for the damage detection study.

4 Effects of Simulated Damage Cases on Modal Properties

Numerically simulated damages to the bridge were considered in this damage detection study by model updating rather than real damages. Apart from the fact that real cases of significantly damaged structures with modal properties available before and after the damage occurred are difficult to find, the main reason for simulated damage cases is that the damage detection process using FEMtools with a detailed 3D FE model had to be first evaluated on reference cases where the solution is known exactly. Simulated cases were thus required to develop a practical, systematic and efficient methodology able to provide reliable results in such largely underdetermined model updating problems.

Four damage cases are presented in this paper and are illustrated in Fig. 5. First case (Fig. 5a) consists in a loss of stiffness up to −50% spread in a realistic manner through several elements of the underside of the north span of the bridge deck. In a similar manner, the second case (Fig. 5b) consists in a progressive stiffness reduction at the base of the south pier up to −50%. The third case (Fig. 5c) corresponds to the deterioration of the south pier-to-deck bearing in the lateral direction with an increase of stiffness of +50%. The last case (Fig. 5d) is a combination of damage to the central span of the bridge deck (−50% loss of stiffness) and to the rotation bearing around *x*-axis at the south pier (+50% gain of stiffness).

When using model updating damage detection methods based on damage-induced evolutions of natural frequencies and mode shapes, it matters to understand the orders of magnitude of these modifications related to the kind and intensity of the damages. Table 2 compares the natural frequencies and mode shapes (through MAC values) of the original model to those of the damaged models for each of the four damage cases considered. MAC values between mode shapes were computed by using only the same DOF available in the experimental modal analysis presented in Fig. 1. For synthesis

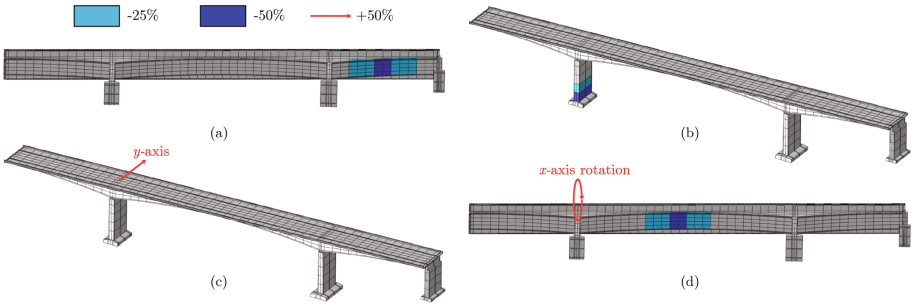

Fig. 5. Simulated damage cases: (a) north span; (b) south pier; (c) lateral bearing at south pier; (d) combined damage.

purpose a cumulative damage index is presented in the last line of Table 2 for frequencies and MAC that corresponds to the square root of the quadratic sum of the evolutions over all modes. Table 2 shows that local damages such as those presented have only slight effects on the mode shapes of the structure, which translates into MAC values always near or equal to unity. Thus, MAC cannot be considered as valuable damage indices. If we focus on natural frequencies, it is important to note that even significant damages do not necessary lead to large evolutions. The order of magnitude of the cumulative frequency damage index between 3% and 5% (up to 7% for the case of combined damage) makes any concerned engineer appreciate that the generally low evolutions of experimentally measured frequencies on a real structure (as those obtained between 2004 and 2013 in Table 1) can be in fact related to non-negligible damages. This result also points out the need for model updating damage detection methods to be very sensitive and the obvious problem caused by experimental uncertainties.

Table 2. Damage-induced evolutions of the modal properties for each damage case.

Exp. mode	f_{num}	North span		South pier		y-south bearing		Combination	
		Δf	MAC	Δf	MAC	Δf	MAC	Δf	MAC
1	1.568 Hz	−3.29%	0.999	−0.18%	1.000	+0.00%	1.000	−2.74%	1.000
2	2.035 Hz	−0.14%	1.000	−3.57%	0.999	+3.21%	0.997	+0.24%	1.000
3	3.337 Hz	−2.38%	0.996	−0.04%	1.000	+0.00%	1.000	−1.91%	0.999
4	4.595 Hz	−1.60%	0.993	−0.34%	1.000	+0.00%	1.000	−0.84%	0.999
5	5.206 Hz	−0.37%	1.000	−0.27%	1.000	+0.15%	0.999	−0.31%	0.999
6	5.640 Hz	−1.34%	0.995	−0.51%	0.999	+0.00%	1.000	−1.34%	0.999
7	6.185 Hz	−0.00%	1.000	−0.36%	1.000	+2.66%	0.998	+5.26%	0.988
8	8.194 Hz	−0.68%	0.998	−0.65%	0.999	+0.00%	1.000	−3.30%	0.996
Cumulative damage index		4.63%	1.0%	3.71%	0.2%	4.17%	0.4%	7.24%	1.3%

5 Detection of Simulated Damage Cases Using Model Updating

FEMtools model updating algorithms were used to detect the simulated damage cases presented in Fig. 5. The study consisted in extracting for each damaged model the eight natural frequencies and mode shapes corresponding to those available through an experimental modal analysis and to use them as target responses to update the undamaged reference model. The same 133 update parameters defined to tune the reference model and the same target modal properties were used in the damage detection study, i.e. eight natural frequencies and seven mode shapes defined only at DOF available in the experimental modal analysis.

5.1 Direct Application of the Model Updating Process

Like most model updating algorithms, FEMtools allows the user for setting different computing options that can greatly influence the results of the analysis. Particularly, several convergence criteria can be used and their acceptance value can be chosen, and weighting factors (namely, *scatters* in FEMtools) on both target responses and update parameters can be set. All of these parameters (scatters particularly) are not easy to define at optimal values even for experienced users, and they often relies on non-evident considerations that depend on each case study or on trial-and-error analyses. A direct model updating calculation was first performed to detect the simulated damages by using standard computing options of FEMtools. By experience, the authors set the convergence criterion to $CC_{TOT} = CC_{ABS} + CC_{MAC} < 0.2\%$ (this low limit value is justified by the numerical nature of the study without uncertainties) or maximum 20 update iterations. Criteria CC_{ABS} and CC_{MAC} correspond to the weighted mean relative differences of all natural frequencies and mode shapes (through MAC values), respectively, between the target responses and the FE model responses. Values of scatters were set to FEMtools default values, which give more importance to the tuning of the natural frequencies than to mode shapes (due to higher uncertainties in usual experimental studies) and which consider that all update parameters have the same uncertainty.

Figure 6a presents in a graphical form the stiffness modification applied to the update parameters by the model updating analysis for the case of damage in the north span. Even if the analysis identifies non negligible damage mainly to the bridge deck, the results of such an analysis are obviously not useful to localize accurately the concerned span of the bridge nor the upper or lower part of the girder, nor to quantify the damage. For academic purpose, another analysis was performed by using all natural frequencies and mode shapes of the first 20 modes of the FE model (Fig. 6b). In such conditions, localization and quantification results are highly improved, although results are still not perfect with non-negligible damage identified in both other spans and on the vertical bearing of the north pier. These last results are of course practically not available since only eight modes were identified experimentally. However, they show that the main challenge of damage detection by updating detailed 3D FE models is the lack of experimental data compared to the number of unknowns.

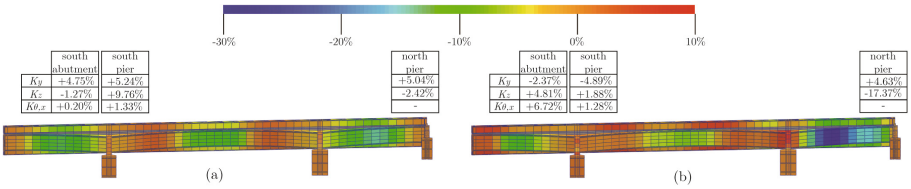

Fig. 6. Direct model updating results for damage detection of the north span case using: (a) 8 modes; (b) 20 modes.

5.2 Step-by-Step Application of the Developed Procedure for the North Span Damage Case

For illustration purpose, the previous model updating procedure is applied and described in details in this section using the north span damage case, which proved to be the one that required the largest number of iterations. Although the procedure implies subjective decisions of the user concerning the parts of the structure to discard from one iteration to the other, the authors' choices always relied on clear evidences.

Figure 7a presents the modifications to the update parameters after the first iteration, which was performed by using all 133 update parameters and for targets the eight natural frequencies, seven mode shape MAC and all experimentally available DOF of the first flexural mode. Considering instrumented DOF shown in Fig. 1, 60 new target responses were added by using individual DOF of mode 1, which results in a reduction of the unknowns-to-equations ratio r_p from 8.87 to 1.77. The comparison of Fig. 7a with Fig. 6a shows a great improvement of the detection results, even before any iteration is done. The probable main damage is clearly identified on the lower part of the north span with −25% stiffness reduction (compared to −15% in Fig. 6a), but some doubts remain about eventual damage to the central span and to at least the vertical bearing of the south pier. All piers, the south span of the deck and most of the bearings are obviously not affected by the analysis. Hence, a second iteration was performed, which started from the undamaged model and used only update parameters from the central and north spans and two remaining bearing springs that were modified by more than 5% during iteration 1. In order to ensure a slightly underdetermined problem instead of an overdetermined one, only additional target DOF of mode 1 from the downstream side of the bridge were used (which does not affect the global definition of this flexural mode), resulting in a ratio r_p = 1.49. Figure 7b presents the detection results (discarded update parameters in gray). The results obtained are already sufficient for damage detection purpose and the analyses could have been stopped at iteration 2. The localization of the damage is obvious in the underside only of the north span and the quantification is valuable with up to −35% in stiffness. Nevertheless, a third iteration was performed in order to get the most accurate updated model suitable for eventual further analysis of the bridge. Figure 7c presents the results of iteration 3, where only update parameters of the north span and the vertical bearing of the south pier were kept and no additional target DOF were required (r_p = 1.93) in order not to get a largely overdetermined problem. The results show that the remaining spring is unaffected, but the stiffness reduction in the north span is surprisingly not as accurate as

for iteration 2. Considering the fact that springs elements at boundary conditions have a huge sensitivity for the bridge modes, a final iteration was performed by only discarding the now useless spring parameter (r_p = 1.87). Figure 7d presents the results that give a nearly perfect detection of the damage location and intensity.

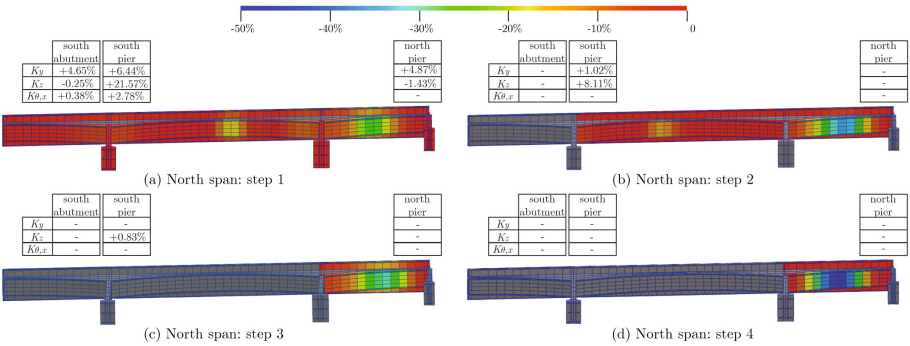

Fig. 7. Application of the proposed model updating iterative procedure to detect damages for the north span case.

5.3 Efficient Model Updating Procedure for Damage Detection in Bridge Structures

Considering the results of the previous section, the authors focused on the development of a practical, systematic and efficient model updating procedure dedicated to bridge structures that allows for reliable results when a detailed FE model is used that makes the inverse problem largely underdetermined. Since the objective was to get a user-friendly procedure, the authors developed the methodology to be efficient with FEMtools default values of all weighting factors. The proposed methodology relies on three points aiming to control the unknowns-to-equations ratio r_p and to guide the analysis to the most probable solution:

1. Use of selected individual DOF of one mode shape as target modal responses in the model updating process in addition to the natural frequencies and mode shapes MAC. By doing this, the determination ratio r_p of the inverse problem can be controlled in a recommended range from 1.0 to 2.0 (slightly undetermined problem) defined according to the authors' experience. The first flexural mode is a good candidate for these additional responses because it is generally experimentally well-defined and it is sensitive to almost all update parameters in a bridge. The choice of the DOF used should ensure that the mode shape is globally well-defined over the whole structure.
2. Proceed with iterative analyses by progressively discarding the update parameters that remain unmodified and that are obviously not involved in the sought damage. Whole regions of structure should be discarded instead of individual update parameters. By doing this, the excessive number of unknowns can be reduced at each step. At each iteration, the updating process should start from the undamaged FE model and the user should also choose adequately the additional target DOF in

order not to get a largely overdetermined problem, which generally causes the algorithms to diverge.

3. Avoid concrete elements from stiffening over the update process by imposing a zero upper limit to the allowed variation of the related update parameters. Even if not essential, this strategy proved to be useful to get more accurate results. The authors acknowledge that it is a kind of bias assuming that concrete components can only loose stiffness over the time, which is an acceptable assumption at least for non-brand-new concrete structures.

5.4 Results of Other Damage Cases

Model updating damage detection analyses were performed on the three other damage cases presented in Fig. 5 by using the proposed iterative procedure. Since the proposed methodology is systematic, the first model updating iteration always consisted in updating all 133 parameters by using 75 experimental target data (eight natural frequencies, 7 mode shape MAC and 60 individual DOF of mode 1) resulting in a ratio $r_p = 1.77$.

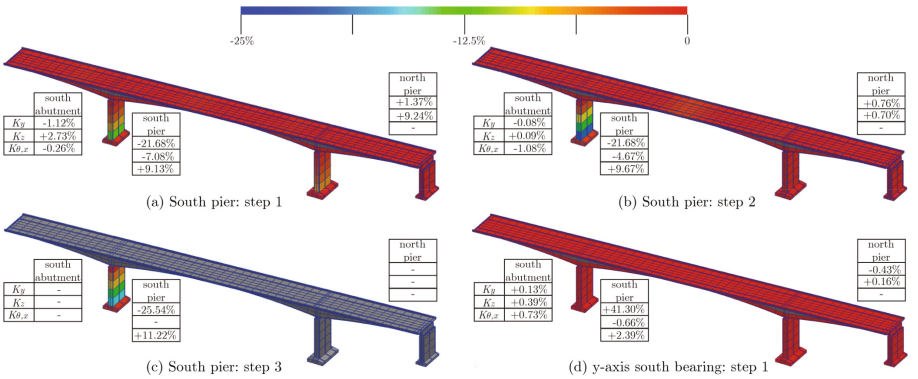

Fig. 8. Damage detection results for cases: (a) to (c) south pier; (d) lateral y-axis south bearing.

Figure 8a–c present the three iteration analyses required to detect the damage case on the south pier. This case is particularly interesting in the fact that the authors had to introduce some sophistication in the method to solve it. Iteration 1 (Fig. 8a) shows clearly that the damage comes from either the south or central piers or from some bearings. A new iteration using only these parameters and no additional DOF as required by the procedure led to inaccurate localization of the damage to the wrong pier. That is why in Fig. 8b, iteration 2 reproduced the same analysis as iteration 1 ($r_p = 1.77$) but by substituting additional DOF of mode 1 (flexural mode) by those of mode 2 (lateral mode). Such a substitution should indeed always be done when the first iteration shows that the whole deck is not involved in the damage, considering the fact that lateral modes are much more sensitive to piers stiffness than flexural modes. Results in Fig. 8b provide now an accurate localization of the damage to the base of the south pier or to the lateral or rotational springs of the south bearing. The final iteration in Fig. 8c was then performed with only one pier, two bearing springs and without

additional target DOF (r_p = 0.53), but it did not improve the results. It matters to note that even if the location of the damage was accurately identified, the accuracy of the damage intensity is not as good in this case. The algorithms had obviously some problem to differentiate the effects of the pier and those of the corresponding bearing. The overdetermination of the problem at iteration 3 (r_p = 0.53) is another probable explanation.

Figure 8d presents the detection results for the damage case on the *y*-axis spring of the south bearing, which only required a single iteration to localize and to quantify perfectly the damage. Damage to the bearings is in fact the most detectable type of damage because of the high sensitivity of the modes to the boundary conditions of the model.

Figure 9 presents the detection results of the combined damage case, involving damage to both the lower part of the central span and the rotation spring about *x*-axis of the south bearing. This combined case was studied to challenge the robustness of the proposed methodology when several parts of the bridge are damaged simultaneously. In addition, both applied damages have opposite effects on the main target responses (natural frequencies) of the model updating process. Also, to get an objective review of the proposed model updating procedure for damage detection, this case was developed by one of the authors, but the analysis was performed blindly by another one. After iteration 1 (Fig. 9a), only update parameters related to the central span and three spring elements were kept, and additional DOF of mode 1 from only the downstream side of the bridge were used for iteration 2 (r_p = 1.12). Figure 9b shows that two iterations were enough to identify both damages accurately (location and intensity), hence validating the procedure for bridge structures.

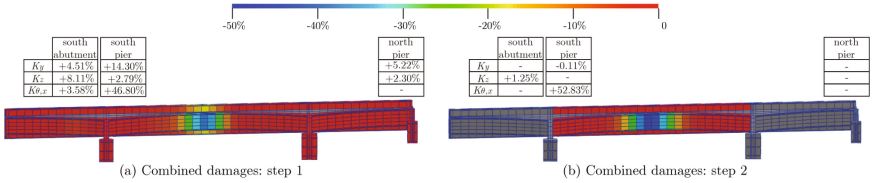

Fig. 9. Damage detection results for the combined damage case (central span and x-axis rotation of the south bearing)

6 Conclusions

This paper presented a damage detection study based on the case study of the Rivière-aux-Mulets Bridge located on Highway 15 in Ste-Adèle north-west of Montreal (QC, Canada). The commercial software FEMtools was used to perform FE model updating analyses to detect simulated damage cases by using a detailed 3D FE element model of the bridge. Such a study results in a largely underdetermined inverse problem

where the number of update parameters is much higher than the number of target natural frequencies and mode shapes available from experimental modal analyses.

Four numerically-simulated damage cases to either deck regions, piers or bearings were considered by modifying the stiffness of the elements of the reference 3D FE model, which was originally updated on experimental modal analysis results. The effects of these damage on the vibration frequencies and mode shapes were studied. It appeared that the mode shapes are very poor indices for local damage and that severe damage are not necessarily linked to high evolutions of the vibration frequencies. The basic application of the FE model updating algorithms did not provide good estimates of the simulated damages. Thus, an improved procedure was proposed, which uses the default values of all FEMtools weighting parameters and that has three main elements: (i) the addition of selected individual DOF from an adequately selected mode shape to control the unknowns-to-equations ratio of the inverse problem within a recommended range from 1.0 to 2.0; (2) iterative analyses in which update parameters are progressively discarded if they are not modified in the previous iteration; (3) the prevention of the algorithms from increasing the stiffness of concrete elements. This practical and systematic methodology was illustrated in details with the damage case on the north span of the bridge and results of the other cases were more briefly presented. All results obtained showed good accuracy in localizing and quantifying the simulated damage in only two or three iterations. The damage to the pier was the most difficult case to identify, because the model updating algorithms seem to be confused by the high sensitivity of the spring elements of the corresponding bearing. On the contrary and for the same reason, the damage case performed on a bearing spring element was the easiest case, requiring no iteration. The robustness of the proposed procedure was finally blind-tested by the authors with a combined damages case, where opposite modifications to both a span stiffness and a spring element stiffness were applied. Even in this case the model updating procedure showed very good performance to localize and to quantify both damages.

Real damage cases that include experimental uncertainties on the target modal properties were not discussed in this paper. Such studies would obviously require additional improvements in the proposed methodology, because individual DOF of mode shapes always contain significant experimental errors. Different approaches have to be studied for this problem, including the adequate use of the available weighting factors or the use of convergence data from the model updating process as a source of evidences to trust the results obtained or not.

Acknowledgments. The authors gratefully acknowledge the Ministry of Transportation of Quebec for its financial support in the project and for the access to the Rivière-aux-Mulets Bridge and its related data. The authors also acknowledge the Fonds de Recherche du Québec Nature et Technologie (FRQNT) for its indirect support through the funding of CEISCE research center.

References

1. Friswell, M.I., Mottershead, J.E.: Finite Element Model Updating in Structural Dynamics. Kluwer Academic Publishers, Boston (1995)
2. Simoen, E., De Roeck, G., Lombaert, G.: Dealing with uncertainty in model updating for damage assessment: a review. Mech. Syst. Signal Process. **56–57**, 123–149 (2015)
3. Weber, B., Paultre, P., Proulx, J.: Consistent regularization of nonlinear model updating for damage identification. Mech. Syst. Signal Process. **23**(6), 1965–1985 (2009)
4. Weber, B., Paultre, P.: Damage identification in a truss tower by regularized model updating. ASCE J. Struct. Eng. **136**(3), 307–316 (2010). ASCE
5. Paultre, P., Weber, B., Mousseau, S., Proulx, J.: Detection and prediction of seismic damage to a high-strength concrete moment resisting frame structure. Eng. Struct. **114**, 209–225 (2016)
6. Teughels, A., Maeck, J., De Roeck, G.: Damage assessment by FE model updating using damage functions. Comput. Struct. **80**(25), 1869–1879 (2002)
7. Fanga, S.E., Perera, R., De Roeck, G.: Damage identification of a reinforced concrete frame by finite element model updating using damage parameterization. J. Sound Vib. **313**, 544–559 (2008)
8. Dynamic Design Solutions (DDS), FEMtools v3.9 (2016). http://www.femtools.com/
9. Dassault Systèmes Simulia Corp, Abaqus software v6.12 (2012). http://www.3ds.com/products-services/simulia/products/abaqus/

A Comparison of Damage Detection Methods Applied to Civil Engineering Structures

Szymon Gres[1(✉)], Palle Andersen[2], Rasmus Johan Johansen[3], Martin Dalgaard Ulriksen[3], and Lars Damkilde[4]

[1] Department of Structural Engineering, Aalborg University, Universal Foundation A/S, Aalborg, Denmark
sg@civil.aau.dk
[2] Structural Vibration Solutions, Aalborg, Denmark
[3] Department of Structural and Offshore Engineering, Aalborg University, Esbjerg, Denmark
[4] Department of Structural Engineering, Aalborg University, Aalborg, Denmark

Abstract. Facilitating detection of early-stage damage is crucial for in-time repairs and cost-optimized maintenance plans of civil engineering structures. Preferably, the damage detection is performed by use of output vibration data, hereby avoiding modal identification of the structure. Most of the work within the vibration-based damage detection research field assumes that the unmeasured excitation signal is time-invariant with a constant covariance, which is hardly achieved in practice. In this paper, we present a comparison of a new Mahalanobis distance-based damage detection method with the well-known subspace-based damage detection algorithm robust to changes in the excitation covariance. Both methods are implemented in the modal analysis and structural health monitoring software ARTeMIS, in which the joint features of the methods are concluded in a control chart in an attempt to enhance the damage detection resolution. The performances of the methods and their fusion are evaluated in the context of ambient vibration signals obtained from, respectively, numerical simulations on a simple chain-like system and a full-scale experimental example, namely, the Dogna Bridge. The results reveal that the performances of the two damage detection methods are quite similar, hereby evidencing the justification of the new Mahalanobis distance-based approach as it is less computational complex. The control chart presents a comprehensive overview of the progressively damaged structure.

Keywords: Structural health monitoring · Ambient excitation · Damage detection · Control chart-based algorithm fusion

1 Introduction

In the field of damage diagnosis, the vibration-based methods have proven effective in detection of structural deterioration solely based on the operational data from the structure [1]. The practical aspect of using only the output measurements cause several difficulties due to the variations in the ambient excitation, which can be due to variability in environmental conditions, for example, wind, temperature and precipitation,

© Springer International Publishing AG 2018
J.P. Conte et al. (eds.), *Experimental Vibration Analysis for Civil Structures*,
Lecture Notes in Civil Engineering 5, https://doi.org/10.1007/978-3-319-67443-8_26

and operational conditions [2]. This issue is addressed in several detection techniques available in the literature [2–7] and used for the condition-based maintenance and the early damage detection in practice [5]. A general review of different damage detection strategies is presented in [8, 9].

The concept of vibration-based damage detection relates to identification of the damage-induced deviations in the damage-sensitive features of the collected output data. The deviations are defined by a relative comparison of the reference and operational states of the system. The commonly used features for the detection are the modal parameters (natural frequencies, mode shapes and damping ratios) identified from the data. However, some research questions the use of the modal parameters, arguing that the modal data itself is not sensitive enough to detect the local faults [9], especially when in practice the structure is excited by low-frequency inputs. One workaround for the system identification when estimating the features is to use the statistical properties of the data. The statistical methods use the probability distributions of the deviations, which differ between the damaged and the undamaged states, hence indicating faults in the system.

The focus of this work is twofold. One is to present a simple statistical approach for the damage detection based on the Mahalanobis distance featured with the Hankel matrices. The distance metric is calculated on the output vibration data processed in the framework similar to subspace-based methods [12], hereby providing an approach that is robust to changes in the excitation covariance. As such, damage is detected as deviations of the distance from the reference test state. The deviations are compared with the χ^2-test build on the residual from the subspace-based methods [13]. The second objective is to present a complete, practical overview of the damage indicators combined from both methods in the Hotelling control chart [18].

The performance of both methods is tested on numerical simulations and data from a full-scale bridge. The numerical, academic example is a coupled spring-mass system, excited by white noise of random variance. The full-scale case is the Dogna Bridge, Italy. The bridge is artificially progressively damaged and excited by the wind.

The structure of the paper is as follows. The basic principles of the robust subspace-based damage detection method and the methodology based on the Mahalanobis distance calculated on the Hankel matrices are presented in Sect. 2. The two test examples are described in Sect. 3. Both the comparison and joint performance of the methods on the numerical and full scale detection cases are presented in Sect. 4. The results are concluded in Sect. 5.

2 Methodology

In this section we recall the basic principles of the subspace-based damage detection [7] and present the algorithm for the Mahalanobis distance-based damage detection. Both methods are data-driven.

2.1 Subspace-Based Damage Detection

The damage detection consists of monitoring the deviations of the current system from its reference state, characterized by some nominal property repeatable for every

healthy conditions. The deviations are defined by a residual that, theoretically, differs between the healthy and the damaged states [13]. Consider the discrete state space model

$$\begin{aligned} \mathbf{x}_{k+1} &= \mathbf{F}\mathbf{x}_k + \mathbf{v}_k \\ \mathbf{y}_k &= \mathbf{H}\mathbf{x}_k + \mathbf{w}_k \end{aligned} \tag{1}$$

with the state transition matrix $\mathbf{F} \in R^{nxn}$, the observation matrix $\mathbf{H} \in R^{rxn}$, the states $\mathbf{x_k} \in R^n$ and the outputs $\mathbf{y_k} \in R^r$, where r is the number of sensors and n denotes the order of the system [6]. The unmeasured white noise input $\mathbf{v_k}$ drives the dynamics of the system and $\mathbf{w_k}$ is the measurement noise. Any perturbation in the structural properties of the system, manifested in the stiffness or mass, leads to deviations in the state matrices and are subsequently reflected in $\mathbf{y_k}$. As a consequence, damage changes the eigenstructure of the state space model. Hence, the damage-sensitive system property relates to $\mathbf{F}$.

Let $\mathbf{\Sigma}_s = \mathrm{E}\left(\mathbf{x}_{k+1}\mathbf{x}_{k+1}^{\mathbf{T}}\right)$ be the state covariance matrix and $\mathbf{G} = \mathrm{E}\left(\mathbf{x}_{k+1}\mathbf{y}_k^{\mathbf{T}}\right) = \mathbf{F}\mathbf{\Sigma}_s\mathbf{H}^T$ the cross-covariance between the states and the outputs [6]. The output covariance yields $\mathbf{\Lambda}_i = \mathrm{E}\left(\mathbf{y}_{k+i}\mathbf{y}_k^{\mathbf{T}}\right) = \mathbf{H}\mathbf{F}^{i-1}\mathbf{G}$ and can be structured in the block-Hankel matrix

$$\mathbf{H}_{p+1,q} = \begin{bmatrix} \mathbf{\Lambda}_1 & \mathbf{\Lambda}_2 & \cdots & \mathbf{\Lambda}_q \\ \mathbf{\Lambda}_2 & \mathbf{\Lambda}_3 & \cdots & \mathbf{\Lambda}_{q+1} \\ \vdots & \vdots & \ddots & \vdots \\ \mathbf{\Lambda}_{p+1} & \mathbf{\Lambda}_{p+2} & \cdots & \mathbf{\Lambda}_{p+q} \end{bmatrix} = \mathrm{Hank}(\mathbf{\Lambda}_i). \tag{2}$$

$\mathbf{H}_{p+1,q} \in R^{(p+1)r\,x\,qr}$ where p and q are parameters such $q = p + 1$. The $\mathbf{H}_{p+1,q}$ can be factorized into the observability and controllability matrices such

$$\mathbf{H}_{p+1,q} = \mathbf{O}_{p+1,q}\mathbf{C}_q \tag{3}$$

where the observability matrix, $\mathbf{O}_{p+1,q} \in R^{(p+1)r\,x\,n}$, and controllability matrix, $\mathbf{C}_q \in R^{n\,x\,qr}$, are given by

$$\mathbf{O}_{p+1,q} = \begin{bmatrix} \mathbf{H} \\ \mathbf{HF} \\ \vdots \\ \mathbf{HF}^p \end{bmatrix}, \mathbf{C}_q = \begin{bmatrix} \mathbf{G} & \mathbf{FG} & \ldots & \mathbf{F}^{q-1}\mathbf{G} \end{bmatrix}. \tag{4}$$

The subspace-based damage detection test detects if the residual of the characteristic property of the reference (healthy) state of the system based on $\mathbf{O}_{p+1,q}$, or subsequently $\mathbf{H}_{p+1,q}$ (Eq. 5), is significantly different from zero. Consider the space, or a property of the reference state, where

$$\mathbf{S}^T\hat{\mathbf{H}}_{p+1,q} \approx 0. \tag{5}$$

$\hat{\mathbf{H}}_{p+1,q}$ is the empirical output block-Hankel matrix and $\mathbf{S}$ is the left kernel $\mathbf{U}_0$ of the reference state $\hat{\mathbf{H}}_{p+1,q}$, hence

$$\hat{\mathbf{H}}_{p+1,q}^{ref} = \begin{bmatrix} \mathbf{U}_1 & \mathbf{U}_0 \end{bmatrix} \begin{bmatrix} \Delta_1 & 0 \\ 0 & \Delta_0 \end{bmatrix} \begin{bmatrix} \mathbf{V}_1^T \\ \mathbf{V}_0^T \end{bmatrix}, \tag{6}$$

where Δ_1 contains non-zero singular values. The reference and the subsequently tested states share the same left null space only when no damage occurs. Bearing that in mind, the residual vector is defined as

$$\boldsymbol{\xi} = \sqrt{N} vec\left(\mathbf{S}^T \hat{\mathbf{H}}_{p+1,q}\right). \tag{7}$$

Note that the excitation of the system is ambient, which leads to changes in the cross-covariance matrix, $\mathbf{G}$, (recall $\mathbf{G} = \mathrm{E}\left(\mathbf{x}_{k+1}\mathbf{y}_k^{\mathbf{T}}\right) = \mathbf{F}\Sigma_s\mathbf{H}^T$), and consequently in the output block Hankel matrix $\hat{\mathbf{H}}_{p+1,q}$. That results in non-zero residuals (Eq. 7) between the healthy states. To avoid that, [13] use the fact that $\hat{\mathbf{H}}_{p+1,q}$ shares the same null space with its principal left singular vectors $\mathbf{U}_1$, so for each healthy state it holds that $\mathbf{S}^T\mathbf{U}_1 \approx 0$. Matrix $\mathbf{U}_1$ contains n independent column vectors that span the column space of $\hat{\mathbf{H}}_{p+1,q}$ and are principal directions of the data, invariant to the change in excitation covariance [19]. The robust residual is defined as

$$\boldsymbol{\xi} = \sqrt{N} vec\left(\mathbf{S}^T\mathbf{U}_1\right), \tag{8}$$

which is tested for being significantly different from zero by use of the χ^2-test,

$$\chi_\xi^2 = \boldsymbol{\xi}^T \boldsymbol{\Sigma}_\xi^{-1} \boldsymbol{\xi}, \tag{9}$$

where $\boldsymbol{\Sigma}_\xi$ is the empirical covariance of the residual calculated as in [7].

2.2 Mahalanobis Distance-Based Damage Detecion

The Mahalanobis distance, MD, is a metric used in multivariate statistics to calculate the distance between a point and a distribution. The formulation of the metric takes into account the correlations between different data dimensions by the covariance matrix of the data. For the multivariate normally distributed variables, the squared MD follows the χ^2-distribution [20]. One of its practical uses is detection of outliers [16] and recently detection of structural damages based on the transmissibility functions or AR-coefficients as a feature [14, 15].

The square Mahalanobis metric of the observations in the data vector $\mathbf{x}_i$, from the reference data vector with the sample mean $\boldsymbol{\mu}$ and the covariance matrix $\boldsymbol{\Sigma}$ is defined as

$$MD_i = (\mathbf{x}_i - \boldsymbol{\mu})^T \boldsymbol{\Sigma}^{-1} (\mathbf{x}_i - \boldsymbol{\mu}). \tag{10}$$

In this paper the Mahalanobis distance is calculated on the empirical block-Hankel matrices with the output correlations between a reference and damaged states and used

directly as a damage indicator. The proposed metric is robust towards the variations of the excitation covariance and can therefore be used with the operational measurements. Consider m reference data sets and i tested states, so that

$$MD_i \leq T_m \rightarrow healthy$$
$$MD_i > T_m \rightarrow damaged.$$

where T_m is a threshold calculated for the reference state. The MD increases as the system is subjected to any change that affects its vibration characteristics. The modified version of the squared MD featured with the Hankel matrices is defined as

$$MD_i = vec\left(\hat{\mathbf{H}}_{p+1,q}^{corr}\right)^T \left(\boldsymbol{\Sigma}_{\hat{\mathbf{H}}_{p+1,q}^{corr,ref}}\right)^{-1} vec\left(\hat{\mathbf{H}}_{p+1,q}^{corr}\right). \tag{11}$$

Let $Y \in R^{r\ x\ mN}$ where Y is the output response, m is the number of the reference sets and N is the length of one data set. The formulation of the empirical block-Hankel matrix yields

$$\hat{\mathbf{C}}_i = \frac{1}{mN}\sum\nolimits_{k=1}^{mN} \frac{\mathbf{Y}_k \mathbf{Y}_{k-i}^T}{\sigma_k \sigma_{k-i}}; \hat{\mathbf{H}}_{p+1,q}^{corr,ref} = \text{Hank}\left(\hat{\mathbf{C}}_i\right). \tag{12}$$

Consequently, $\hat{\mathbf{H}}_{p+1,q}^{corr}$ is determined using Eq. 12 for each tested data set with $m = 1$. The covariance of the empirical, vectorized Hankel matrix is estimated from the covariance of the sample mean with the methodology recalled from [7]. The threshold above which the data set is considered damaged is defined as one standard deviation above the mean value of the reference state, which theoretically should approach zero.

2.3 Simple System Simulation

For the numerical test, we considered a coupled spring-mass system with 15 DOF, Fig. 1. Output accelerations are simulated using white noise input of variance taken randomly from the normally distributed vector in between [1 50], acting on the last DOF. The acceleration data is recorded in all DOF along the system. To challenge the robustness of the damage detection methods, different amounts of white noise, namely, 3%, 10% and 30%, are added to the response signals.

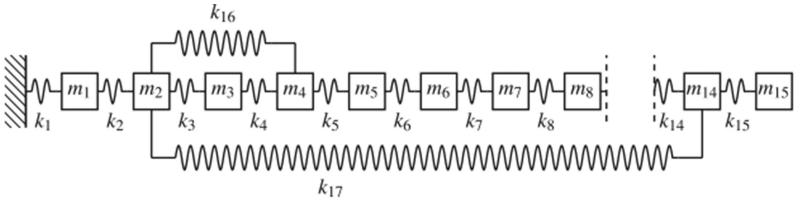

Fig. 1. Simple system scheme.

The damage is simulated as a progressive reduction in the stiffness of the 8th spring by 2%, 5%, 10% and 30%. The sampling frequency is 50 Hz. The system is excited for 1000 s in blocks of 50 data sets for each simulated case. That results in 250 data records per sensor per noise level with a random variance in between each set.

3 Results

The damage is detected for the three noise levels present in the response of the simple system. 30 out of 50 healthy data sets are used to establish the reference state. The thresholds for both of the methods are defined as a number of standard deviations above the mean metric of the reference state. One standard deviation for the unsafe zone, and two standard deviations for the damaged zone.

The comparison of the damage indicators for the case of 3% and 30% of white noise added to the response data is illustrated in Figs. 2 and 3. The percentage of the detected damage sets with respect to the simulation case and degree of the damage is summarized in the Table 1.

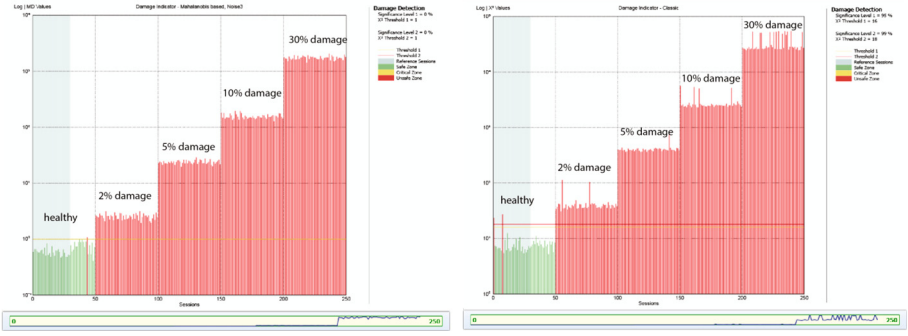

Fig. 2. Damage detection in simple system. Case-3% of noise in the response. Damage indicators for the Mahalanobis-based (left) and robust subspace-based (right).

Both methods are robust towards the change in variance of the excitation and detect each degree of the damage present in the response data containing 3% of white noise, Fig. 2. While increasing the noise level to 30%, the Mahalanobis-based approach performs more accurate in detecting the smaller deviations, see Fig. 3 and Table 1. The fusion of the methods in a control chart, created for the 30% noise case, results in detection of all the 5% damage sets and half of the 2% damaged sets; what was not possible with a single method, see Fig. 4.

4 Dogna Bridge

The Dogna bridge, Fig. 5, crosses the River Fella and connects the villages of Crivera and Valdogna (Dogna) in Friuli Venezia Giulia, a region located in the North East of Italy.

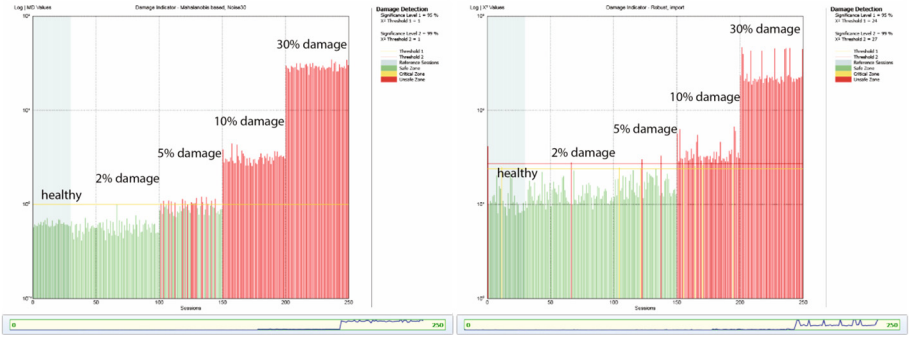

Fig. 3. Damage detection in simple system. Case-30% of noise in the response. Damage indicators for the Mahalanobis-based (left) and robust subspace-based (right).

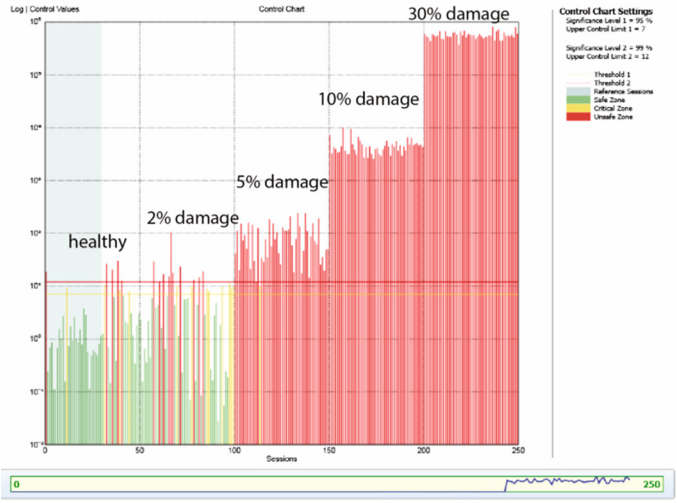

Fig. 4. Hotelling T^2 control chart for simple system. Robust subspace and Mahalanobis-based detection. Case: noise 30%.

Table 1. Comparison of the detection methods. Ability to detect damage in the simple system for different noise levels.

Case	Method	Damaged sets detected			
		2% damage	5% damage	10% damage	30% damage
Noise 3%	Subspace-based	100%	100%	100%	100%
	Mahalanobis-based	100%	100%	100%	100%
Noise 10%	Subspace-based	10%	26%	100%	100%
	Mahalanobis-based	40%	100%	100%	100%
Noise 30%	Subspace-based	2%	8%	100%	100%
	Mahalanobis-based	0%	40%	100%	100%

The bridge is a four-span, single-lane concrete bridge. The span is 16 m, with a 4 m lane. The deck is made of a 0.18 m reinforced concrete (RC) slab, supported by three longitudinal simply supported RC beams with a rectangular cross-section of 0.35 × 1.20 m. The beams are connected to the supports with the rectangular RC

Fig. 5. Dogna bridge, Italy.

diaphragms 0.3 × 0.7 m. The piers are RC walls 1.5 m thick, 4.5 m deep, and 3.6 m high. The pylons are fixed in a piled foundation that consists of a 1 m thick RC slab supported by a drilled RC piles of 1 m in diameter and 18 m in length.

For traffic safety reasons, the Dogna bridge was demolished on May 2008 and has been replaced by a new bridge built about 200 m downstream. A test campaign was carried out from April 02 to 11 2008 and consisted of a series of tests progressively damaging one of the bridge spans. The tests were carried out under similar environmental conditions so the influence of temperature and humidity on the structure is insignificant. Figure 6 shows the artificially damaged bridge span during the tests.

The bridge was equipped with ten accelerometers mounted on its deck. The samples were taken with the frequency of 400 Hz. The measurement campaign lasted 50 min in total while the reference state was measured for 20 min. The damage was introduced in three blocks: the first cut, the second cut and the third cut with the damaged center span.

5 Results

For the general overview of the measurements, the first six singular values of the cross-spectral densities from the output acceleration data for the reference state are plotted in Fig. 7.

A total number of 22 data sets are analyzed. Each measurement lasts 147.5 s. In the frequency range of 0–40 Hz there are three modes excited at 10.2 Hz, 14.2 Hz and 27.2 Hz, Fig. 7.

Fig. 6. Artificially damaged beams. The cuts introduced progressively during the tests, along with the damage in the centerline of the span.

The reference measurement model for the damage detection is built from 6 out of 8 healthy data records. Data sets between 9 and 14 are the measurements from the damaged state corresponding to the cuts in the beams. Damaged in the centerline was introduced in data sets from 15 to 22. The comparison of the subspace-based and Mahalanobis-based detection methods and the control chart combining the methods is illustrated in Fig. 8.

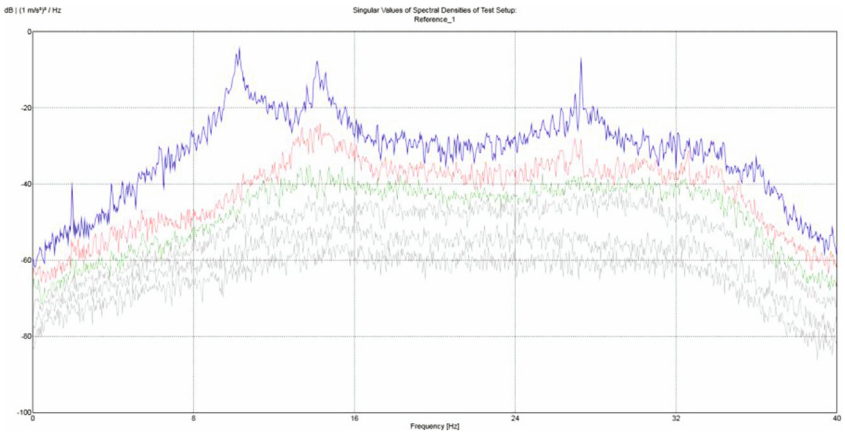

Fig. 7. First six singular values of the cross spectral densities of the output acceleration data for the reference state.

Both the subspace-based and Mahalanobis-based damage indicators do not increase with the number of the cuts in the beams in sets 9–14, see Fig. 8. However, each method clearly distinguishes the healthy data from the damaged and detects the last stage of the damage (the damage of the centerline of the span), see Figs. 6 and 8. In this case, the fusion of the detection methods in the control chart does not enhance the damage detection, however results in similar indicators as obtained from the robust subspace and Mahalanobis distance-based methods.

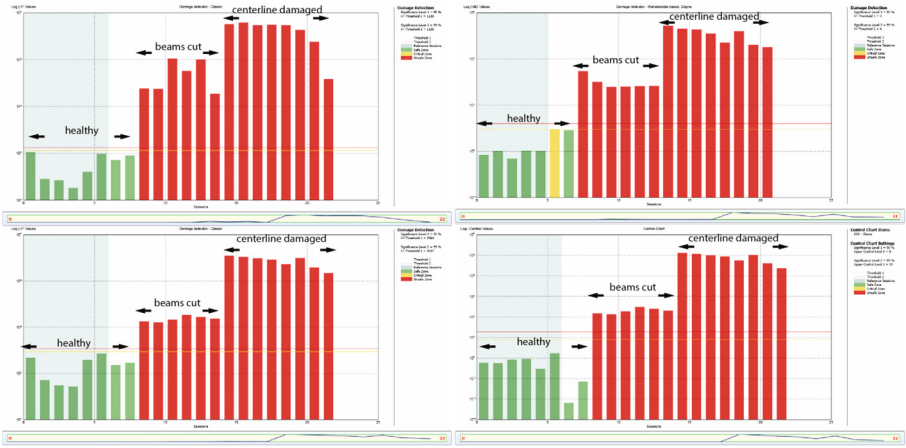

Fig. 8. Damage detection in Dogna bridge. Damage indicators from top: Robust subspace (left). Mahalanobis-based (right). From bottom classical subspace (left), Hotelling control chart (right).

6 Conclusions

In this paper a recently developed Mahalanobis distance-based damage detection method was presented and compared to well-known and proven subspace-based damage detection approaches. The methods were tested on noisy simulation data and a full-scale bridge example. Both test cases were excited by ambient excitation with a changing intensity.

The performance of the new Mahalanobis distance-based detection method appears similar to the subspace-based methods for the low-noise numerical and experimental cases. As well as the subspace-based methods, the proposed algorithm is robust to changes in the excitation covariance. The new method reveals advantage over the subspace-based methods regarding detection of the damages based on the noisy simulations. The combination of the methods in the control chart was successful and resulted in the most effective detection of the damages both for simulations and the full-scale test.

The research regarding the detection methods will continue with focus on testing the algorithms on more extensive full-scale experimental campaigns with different types and extent of damages. The fusion of the methods enhanced the performance of the combined damage indicators, hence research on this subject will proceed. The use of empirical block-Hankel matrices as damage sensitive features will be further examined and compared with different transformation of the output data.

References

1. Farrar, C., Doebling, S., Nix, D.: Vibration-based structural damage identification. Philos. Trans. R. Soc. A Math. Phys. Eng. Sci. **359**(1778), 131–149 (2001)
2. Balmès, E., Basseville, M., Mevel, L., Nasser, H.: Handling the temperature effect in vibration-based monitoring of civil structures: a combined sub- space-based and nuisance rejection approach. Control Eng. Pract. **17**(1), 80–87 (2009)
3. Bernal, D.: Kalman filter damage detection in the presence of changing process and measurement noise. Mech. Syst. Signal Process. **39**(1–2), 361–371 (2013)
4. Döhler, M., Hille, F.: Subspace-based damage detection on steel frame structure under changing excitation. In: Proceedings of 32nd International Modal Analysis Conference, Orlando (2014)
5. Döhler, M., Hille, F., Mevel, L., Rücker, W.: Structural health monitoring with statistical methods during progressive damage test of S101 bridge. Eng. Struct. **69**, 183–193 (2014)
6. Döhler, M., Mevel, L.: Subspace-based fault detection robust to changes in the noise covariances. Automatica **49**(9), 2734–2743 (2013)
7. Döhler, M., Mevel, L., Hille, F.: Subspace-based damage detection under changes in the ambient excitation statistics. Mech. Syst. Signal Process. **45**(1), 207–224 (2014)
8. Doebling, S., Farrar, C., Prime, M.: A summary review of vibration-based damage identification methods. Shock Vib. Dig. **30**(2), 91–105 (1998)
9. Carden, E., Fanning, P.: Vibration based condition monitoring: a review. Struct. Health Monit. **3**(4), 355–377 (2004)
10. Worden, K., Farrar, C., Manson, G., Park, G.: The fundamental axioms of structural health monitoring. Proc. R. Soc. A Math. Phys. Eng. Sci. **463**(2082), 1639–1666 (2007)
11. Worden, K., Manson, G., Fieller, N.: Damage detection using outlier analysis. J. Sound Vib. **229**(3), 647–667 (2000)
12. Van Overschee, P., De Moor, B.: Subspace identification for linear systems: theory, implementation, applications. Kluwer Academic Publisher, Boston (1996)
13. Basseville, M., Abdelghani, M., Benveniste, A.: Subspace-based fault detection algorithms for vibration monitoring. Automatica **36**(1), 101–109 (2000)
14. Zhou, Y., Maia, N.M., Wahab, M.A.: Damage detection using transmissibility compressed by principal component analysis enhanced with distance measure. J. Vib. Control (2016). doi:10.1177/1077546316674544
15. Cheung, A., Cabrera, C., Sarabandi, P., Nair, K.K., Kiremidjian, A.: The application of statistical pattern recognition methods for damage detection to field data. Smart Mater. Struct. **17**, 1–12 (2008)
16. Filzmoser, P.: A multivariate outlier detection method. In: Proceedings of State University Conference, 18 (2004)
17. ARTeMIS Pro. 5.1: Structural Vibration Solutions A/S. NOVI Science Park, Aalborg (2016)
18. Lowry, C.A., Montgomery, D.C.: A review of multivariate control charts. IIE Trans. **27**(6), 800–810 (1995)
19. Yan, A.M., Golinval, J.C.: Null subspace-based damage detection of structures using vibration measurements. Mech. Syst. Signal Process. **20**, 611–626 (2006)
20. Hardin, J., Rocke, D.M.: The distribution of robust distances. J. Comput. Graph. Stat. **14**(4), 928–946 (2005)

A Displacement Reconstruction Strategy for Long, Slender Structures from Limited Strain Measurements and Its Application to Underground Pipeline Monitoring

Mayank Chadha(✉) and Michael D. Todd

Department of Structural Engineering, University of California San Diego, La Jolla, CA 92093-0085, USA
machadha@eng.ucsd.edu

Abstract. In this paper, we discuss about reconstructing the global deformed shape of slender structures such as pipelines, tethers, or cables from a limited set of scalar surface strain measurements. We present a comprehensive approach that captures the effect of curvature, shear, torsion, and axial deformation. Our primary focus is to demonstrate the applicability of the approach to aid in damage detection algorithms. This theory utilizes Cosserat rod theory and exploit localized linearization approach that helps to obtain local basis function set for the displacement solution in director frame. The uniaxial strain vector and the surface strain for the Cosserat beam incorporating the above-mentioned effects are obtained and used to develop the reverse algorithm to reconstruct global shape of the structure. Error analysis due to noise in measured strain values is performed and results are discussed.

Keywords: Cosserat rod theory · Shape reconstruction · Local basis function · Director frame · Underground pipelines

1 Introduction

This paper discusses the formulation of global shape sensing algorithm that captures the effect of curvature, shear, torsion and axial deformation focusing on the applicability of the shape sensing methodology in civil structures. The theoretical framework for shape sensing using finite strain measurements are laid by the work of Todd et al. [1] and Chadha and Todd [2]. The formulation holds the Euler-Bernoulli rigid cross-section assumption primarily because Poisson's effect and warping of the cross-section are not the dominant effects in slender structures.

The global shape sensing of slender structures is desirable in many instances like pipelines, oil exploration, tethers, cables, and even non-civil applications like cardiac catheters, surgical tubing, and others. This theory is geometrically exact and fully nonlinear; hence it can capture large deformations. The mechanics developed for this problem is rooted to the work of Cosserat and Cosserat [3], Simo [4], Simo and Vu-Quoc [5], Iura and Atluri [6], and Reissner [7–9].

© Springer International Publishing AG 2018
J.P. Conte et al. (eds.), *Experimental Vibration Analysis for Civil Structures*,
Lecture Notes in Civil Engineering 5, https://doi.org/10.1007/978-3-319-67443-8_27

As mentioned in [2], the distributed strain sensing may be grouped into non-contact and contact methods. The technique illustrated here assumes a contact sensing method. This technique focus on obtaining the local uniaxial surface strain measures through any type of multiplexed sensing approach, including fiber Bragg gratings (FBGs), Rayleigh backscatter, or conventional resistive strain gauges.

The remainder of the paper is arranged as follows: Sect. 2 briefs the kinematics of the problem, develops the surface strain measurement incorporating the aforementioned deformation effects, and presents a locally-exact solution basis on which a global deformed shape is built. Section 3 presents the application of the techniques to underground pipeline monitoring in case of seismic events. Section 4 culminates the discussion with conclusions and observations.

2 Kinematic Description

2.1 Geometry of the Beam-Midcurve and the Directors

We briefly discuss about the theoretical framework developed in [2] as a matter of completion. The global shape of the structure is defined by a midcurve (the locus of cross-sectional geometric centroids), and the director triad attached to the midcurve. Therefore, in a pure geometric sense, the problem is a single manifold problem with the arc length ξ_1 being the manifold parameter. We define the initial unstrained reference configuration by $\Omega_o \subset \mathbb{R}^3$. We assume that the initial shape is known (in which the strain gauges are attached to the object in a zero-strain state), which we assume is straight for simplicity. The geometric description of the configuration of the beam is same as defined in [2], which we shall briefly discuss.

We define an orthogonal frame $\{\mathbf{E_i}\}$. The domain of the beam is defined by the material point $\{\xi_1, \xi_2, \xi_3\}$, such that the origin of the frame $\{\mathbf{E_i}\}$ is at $\{\xi_i = 0\}$ with $i = 1, \ldots, 3$. Let L_o represent the length of midcurve in the undeformed reference state $\Omega_o \subset \mathbb{R}^3$, such that $\xi_1 \in [0, L_o]$. Any configuration of the structure is defined by the mid-curve. The position vector $\varphi(\xi_1) = \varphi_i \mathbf{E_i}$, parametrized by the undeformed arclength ξ_1, represents the midcurve. The orientation of any cross-section in the deformed configuration $\Omega \subset \mathbb{R}^3$ is defined by the set of orthogonal Cosserat director triad $\{\mathbf{d_i}(\xi_1)\}$, such that $\mathbf{d_i}(\xi_1) = d_{ij}(\xi_1)\mathbf{E_j}$. The vector $\mathbf{d}_1(\xi_1)$ is perpendicular to the cross-section and the vectors $\{\mathbf{d}_2(\xi_1), \mathbf{d}_3(\xi_1)\}$ spans the cross-section of the beam at ξ_1. We note that

$$\mathbf{d_i}(\xi_1) = \mathbf{Q}(\xi_1)\mathbf{E_i}. \tag{1}$$

Here, $\mathbf{Q}(\xi_1)$ represents family of orthogonal matrices that belongs to $SO(3)$ rotational groups. Hence, they satisfy $\mathbf{Q}\mathbf{Q}^{\mathrm{T}} = \mathbf{I}$ and $\det \mathbf{Q} = 1$. $\mathbf{Q}(\xi_1)$ being a curve on the manifold $SO(3)$, the tangent vector to this curve in $SO(3)$ is expressed as $\mathbf{Q}_{,\xi_1}$ that represents the tangent space of $SO(3)$. It can be easily obtained that $\mathbf{Q}_{,\xi_1}\mathbf{Q}^{\mathrm{T}} = \mathbf{K}(\xi_1)$ such that $\mathbf{K}(\xi_1)$ is the linear space of skew symmetric matrices. Therefore, there exists an axial vector $\boldsymbol{\kappa} = \bar{\kappa}_i \mathbf{d_i}$ associated with $\mathbf{K}(\xi_1)$ such that $\mathbf{K}(\xi_1)\mathbf{g} = \boldsymbol{\kappa} \times \mathbf{g}$. Here, $\mathbf{g} = \bar{g}\mathbf{d_i}$ represents any vector in $\mathbb{R}^3$. Therefore, from (1),

$$\mathbf{d}_{\mathbf{i},\xi_1} = \left(\mathbf{Q}_{,\xi_1}\mathbf{Q}^{\mathrm{T}}\right)\mathbf{d}_{\mathbf{i}} = \mathbf{K}\mathbf{d}_{\mathbf{i}} = \boldsymbol{\kappa} \times \mathbf{d}_{\mathbf{i}}. \tag{2}$$

The vector $\boldsymbol{\kappa} = \bar{\kappa}_i \mathbf{d}_{\mathbf{i}}$ represents a Darboux vector associated with the infinitesimal rotation tensor $\mathbf{K}$, parametrized by ξ_1. Equation (2) represents the differential equation that governs the evolution of the directors and hence the cross-sections.

To define the position vector $\boldsymbol{\varphi}$ and the governing differential equation corresponding to $\boldsymbol{\varphi}$, we define the following:

1. Let $\theta(\xi_1)$ and $\phi(\xi_1)$ represent the pitch and yaw angle of the mid-curve. We define another triad $\{\mathbf{T}, \mathbf{V}, \mathbf{H}\}$ that originates from the centroid of each cross-section such that the vector $\{\mathbf{T}, \mathbf{V}\}$ spans the pitch angle plane. The vector $\mathbf{T}(\xi_1)$ is the tangent vector to the midcurve. Thus, $\mathbf{H} = \mathbf{T} \times \mathbf{V}$. If there is no shearing in the beam, the triad $\{\mathbf{T}, \mathbf{V}, \mathbf{H}\}$ coincides with $\{\mathbf{d_i}\}$. The definition is made clear in the Fig. 1 below. Therefore,

$$\begin{bmatrix} \mathbf{T}(\xi_1) \\ \mathbf{V}(\xi_1) \\ \mathbf{H}(\xi_1) \end{bmatrix} = \begin{bmatrix} \cos\theta(\xi_1)\cos\phi(\xi_1) & \sin\theta(\xi_1) & \cos\theta(\xi_1)\sin\phi(\xi_1) \\ -\sin\theta(\xi_1)\cos\phi(\xi_1) & \cos\theta(\xi_1) & -\sin\theta(\xi_1)\sin\phi(\xi_1) \\ -\sin\phi(\xi_1) & 0 & \cos\phi(\xi_1) \end{bmatrix} \begin{bmatrix} \mathbf{E}_1 \\ \mathbf{E}_2 \\ \mathbf{E}_3 \end{bmatrix} = \mathbf{W}_1 \begin{bmatrix} \mathbf{E}_1 \\ \mathbf{E}_2 \\ \mathbf{E}_3 \end{bmatrix}. \tag{3}$$

2. Assume that the deformed arc length coordinate is given by s. The infinitesimal length of the undeformed mid-curve $\mathrm{d}\xi_1$ deforms to $\mathrm{d}s$ causing infinitesimal axial strain $e(\xi_1)$. If the object is subjected to shear and torsion, the orientation of the cross-section changes. The tangent vector is no longer perpendicular to the cross-section. The shearing effect is quantified by the angles $\gamma_{11}(\xi_1)$, $\frac{\pi}{2} - \gamma_{12}(\xi_1)$ and $\frac{\pi}{2} - \gamma_{13}(\xi_1)$ subtended by the directors $\mathbf{d}_1, \mathbf{d}_2$ and $\mathbf{d}_3$ with the tangent vector $\mathbf{T}(\xi_1) = \frac{\partial \boldsymbol{\varphi}}{\partial S}$, as shown in Fig. 1. Hence following relation can be noted:

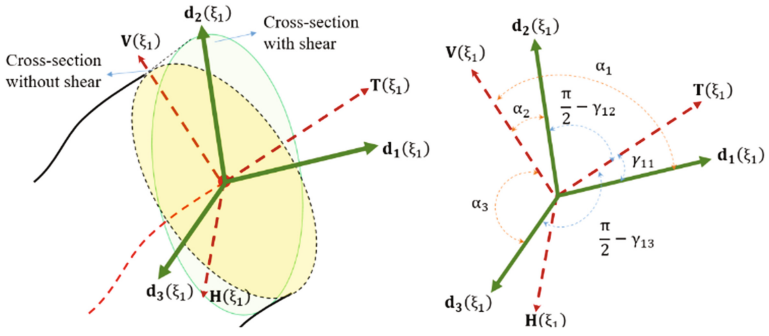

Fig. 1. Relationship between $\{\boldsymbol{d}_1, \boldsymbol{d}_2, \boldsymbol{d}_3\}$ and $\{\boldsymbol{T}, \boldsymbol{V}, \boldsymbol{H}\}$ material frame of reference (Color figure online)

$$e = \frac{\mathrm{d}s - \mathrm{d}\xi_1}{\mathrm{d}\xi_1}; \frac{\partial \xi_1}{\partial s} = \frac{1}{1+e},$$

$$\boldsymbol{\varphi}_{,s} \cdot \mathbf{d_i} = \frac{1}{1+e}\boldsymbol{\varphi}_{,\xi_1} \cdot \mathbf{d_i} = \left\{ \begin{matrix} \cos\gamma_{1i}, & \text{when } i = 1 \\ \sin\gamma_{1i}, & \text{when } i = 2,3 \end{matrix} \right\}. \tag{4}$$

Therefore,

$$\boldsymbol{\varphi}_{,\xi_1} = (1+e)\cos\gamma_{11}\mathbf{d}_1 + (1+e)\sin\gamma_{12}\mathbf{d}_2 + (1+e)\sin\gamma_{13}\mathbf{d}_3 = (1+e)\mathbf{T}. \tag{5}$$

3. It is necessary to define the parameters $\alpha_1(\xi_1)$, $\alpha_2(\xi_1)$ and $\alpha_3(\xi_1)$ as the angles subtended by the directors $\mathbf{d}_1, \mathbf{d}_2$ and $\mathbf{d}_3$ with the vector $\mathbf{V}$ respectively. This is done to define the relation between $\{\mathbf{T}, \mathbf{V}, \mathbf{H}\}$ and $\{\mathbf{d_i}\}$. Therefore, from the expression of tangent vector in Eq. (5), we can express,

$$\begin{bmatrix} \mathbf{T}(\xi_1) \\ \mathbf{V}(\xi_1) \\ \mathbf{H}(\xi_1) \end{bmatrix} = \mathbf{W}_2 \begin{bmatrix} \mathbf{d}_1 \\ \mathbf{d}_2 \\ \mathbf{d}_3 \end{bmatrix}. \tag{6}$$

Therefore, from Eqs. (3) and (5) we have,

$$\begin{bmatrix} \mathbf{d}_1 \\ \mathbf{d}_2 \\ \mathbf{d}_3 \end{bmatrix} = \mathbf{W}_2^{-1}\mathbf{W}_1 \begin{bmatrix} \mathbf{E}_1 \\ \mathbf{E}_2 \\ \mathbf{E}_3 \end{bmatrix}. \tag{7}$$

The component of the orthogonal tensor $\mathbf{Q}$ in Eq. (1) can be obtained from Eq. (7) in terms of the parameters $(\theta(\xi_1), \phi(\xi_1), \gamma_{1i}(\xi_1), \alpha_i(\xi_1))$ such that $\left[\mathbf{Q}^{\mathbf{T}}\right]_{\mathbf{d_i} \otimes \mathbf{E_i}} = \mathbf{W}_2^{-1}\mathbf{W}_1$. Note that the following orthogonality constrains hold,

$$|\mathbf{T}| = |\mathbf{V}| = |\mathbf{H}| = 1; \quad |\mathbf{T}|_{,\xi_1} = |\mathbf{V}|_{,\xi_1} = |\mathbf{H}|_{,\xi_1} = 0. \tag{8}$$

Therefore, the component of the Darboux vector can be obtained from the Eq. (2) in terms of the deformation parameters $(\theta(\xi_1), \phi(\xi_1), \gamma_{1i}(\xi_1), \alpha_i(\xi_1))$ and their derivatives, satisfying the constraints in Eq. (8). The expressions for $\bar{\kappa}_1, \bar{\kappa}_2$ and $\bar{\kappa}_3$ can be referred to Appendix A.1 in [2]. From Eqs. (2) and (5) we arrive at an important equation that governs the evolution of the system as,

$$\begin{bmatrix} \boldsymbol{\varphi}_{,\xi_1} \\ \mathbf{d}_{1,\xi_1} \\ \mathbf{d}_{2,\xi_1} \\ \mathbf{d}_{3,\xi_1} \end{bmatrix} = \begin{bmatrix} 0 & (1+e)\cos\gamma_{11} & (1+e)\sin\gamma_{12} & (1+e)\sin\gamma_{13} \\ 0 & 0 & \bar{\kappa}_3 & -\bar{\kappa}_2 \\ 0 & -\bar{\kappa}_3 & 0 & \bar{\kappa}_1 \\ 0 & \bar{\kappa}_2 & -\bar{\kappa}_1 & 0 \end{bmatrix} \begin{bmatrix} \boldsymbol{\varphi} \\ \mathbf{d}_1 \\ \mathbf{d}_2 \\ \mathbf{d}_3 \end{bmatrix}. \tag{9}$$

2.2 The Strain Vector

The position vector of any material point (ξ_1, ξ_2, ξ_3) in the deformed configuration Ω is given as,

$$\mathbf{R}(\xi_1, \xi_2, \xi_3) = \boldsymbol{\varphi}(\xi_1) + \xi_2 \mathbf{d}_2 + \xi_3 \mathbf{d}_3. \tag{10}$$

The strain vector ϵ for this problem is obtained as,

$$\epsilon = \sum_{\mathrm{i}=1}^{3} \left(\frac{\partial \mathbf{R}}{\partial \xi_i} - \mathbf{d_i} \right) = \frac{\partial \mathbf{R}}{\partial \xi_1} - \mathbf{d}_1. \tag{11}$$

Using Eq. (10), following expressions can be obtained,

$$\frac{\partial \mathbf{R}}{\partial \xi_i} = \begin{cases} \left(\boldsymbol{\varphi}_{,\xi_I} - \mathbf{d}_1 + \boldsymbol{\xi_2} \mathbf{d}_{2,\xi_I} + \boldsymbol{\xi_3} \mathbf{d}_{3,\xi_I} \right) + \mathbf{d}_1 = \boldsymbol{\epsilon} + \mathbf{d}_1, & \text{when } i = 1; \\ \mathbf{d_i}, & \text{when } i = 2, 3. \end{cases} \tag{12}$$

Equations (11) and (12) represent the fact that only the first component of any infinitesimal vector in the undeformed state Ω_o gets strained to $\boldsymbol{\epsilon} + \mathbf{d}_1$. Any vector on the cross-section plane of the beam rotates and is not strained. Using Eqs. (9), (11) and (12), the expression of strain vector in terms of deformation parameters $(e, \gamma_{1i}, \bar{\kappa}_i)$ becomes

$$\boldsymbol{\epsilon} = \{((1+e)\cos\gamma_{11} - 1) - \xi_2\bar{\kappa}_3 + \bar{\kappa}_2\xi_3\}\mathbf{d}_1 + \{(1+e)\sin\gamma_{12} - \bar{\kappa}_1\xi_3\}\mathbf{d}_2 + \{(1+e)\sin\gamma_{13} + \bar{\kappa}_1\xi_2\}\mathbf{d}_3. \tag{13}$$

Consider a point q on the surface of the undeformed section on which the strain gauge is attached. If p represent the midcurve point, the vector $\mathbf{r}_{pq} = \xi_2\mathbf{E}_2 + \xi_3\mathbf{E}_3$ represents the position vector of the strain gauge with respect to the midcurve for the given section. We represent the magnitude of the vector $\mathbf{r}_{pq}$ as $r = \sqrt{\xi_2^2 + \xi_3^2}$. The vector $\mathbf{r}_{pq}$ makes an angle σ with $\mathbf{E}_2$. Hence, $\xi_2 = r\cos\sigma$ and $\xi_3 = r\sin\sigma$.

To find the scalar value of strain in the strain gauge, we need the orientation of the strain gauge. If μ is the angle subtended by the strain gauge with the vector $\mathbf{E}_1$ in undeformed configuration or $\mathbf{d}_1$ in the deformed configuration, the direction of the strain gauge in the deformed configuration is obtained as $\mathbf{n} = \cos\mu\mathbf{d}_1 - \sin\mu\sin\sigma\mathbf{d}_2 + \sin\mu\cos\sigma\mathbf{d}_3$ as obtained in [2]. We define the following strain parameters

$$S_1 = ((1+e)\cos\gamma_{11} - 1); S_2 = (1+e)\sin\gamma_{12}; S_3 = (1+e)\sin\gamma_{13}$$

$$S_4 = r\bar{\kappa}_1; S_5 = r\bar{\kappa}_2; S_6 = r\bar{\kappa}_3;$$

$$e = \sqrt{(S_1+1)^2 + S_2^2 + S_3^2} - 1. \tag{14}$$

The scalar strain is obtained as a function of the strain parameters S_i using Eqs. (13) and (14) as

$$\begin{aligned}\varepsilon &= \boldsymbol{\epsilon} \cdot \mathbf{n} \\ &= \{S_1 - \cos\sigma \cdot S_6 + \sin\sigma \cdot S_5\}\cos\mu \\ &\quad - \{S_2 - \sin\sigma \cdot S_4\}\sin\mu\,\sin\sigma + \{S_3 + \cos\sigma \cdot S_4\}\sin\mu\,\cos\sigma\end{aligned} \tag{15}$$

2.3 Solution Approach

We demonstrate the solution for the circular section such that $|\mathrm{r}_{pq}|$ is constant for all the strain gauges. The solution may be easily extended to the non-circular section based on the theory discussed above. Solution of Eq. (9) requires 6 strain parameters $(S_1, \ldots, S_6)$. This requires 6 strain gauges per cross-sections. Equation (15) can then be inverted to obtain the strain parameters $(S_1, \ldots, S_6)$. To obtain the approximate structure, we discretize the object into N segments. At the n^{th} discretized cross-section $\left(\xi_1 = \xi_{1_n}\right)$, we attach 6 strain gauges with angles $\sigma_{n,m}$, at a distance of $r_{n,m} = r$ from the centroid, where $m = 1, \ldots, 6$. Thus, the scalar strain at the n^{th} cross-section is obtained by,

$$\begin{aligned}\varepsilon_{\mathrm{n,m}} &= \left\{S_{1_n} - \cos\sigma_{n,m} \cdot S_{6_n} + \sin\sigma_{n,m} \cdot S_{5_n}\right\}\cos\sigma_{n,m} \\ &\quad - \left\{S_{2_n} - \sin\sigma_{n,m} \cdot S_{4_n}\right\}\sin\mu_{n,m}\sin\sigma_{n,m} + \left\{S_{3_n} + \cos\sigma_{n,m} \cdot S_{4_n}\right\}\sin\mu_{n,m}\cos\sigma_{n,m}\end{aligned} \tag{16}$$

Therefore, the discretized form of Eq. (9) becomes,

$$\begin{bmatrix} \varphi_{\mathbf{n},\xi_1} \\ \mathbf{d}_{1_\mathbf{n},\xi_1} \\ \mathbf{d}_{2_\mathbf{n},\xi_1} \\ \mathbf{d}_{3_\mathbf{n},\xi_1} \end{bmatrix} = \begin{bmatrix} 0 & S_{1_n}+1 & S_{2_n} & S_{3_n} \\ 0 & 0 & \frac{S_{6_n}}{r} & -\frac{S_{5_n}}{r} \\ 0 & -\frac{S_{6_n}}{r} & 0 & \frac{S_{4_n}}{r} \\ 0 & \frac{S_{5_n}}{r} & -\frac{S_{4_n}}{r} & 0 \end{bmatrix} \begin{bmatrix} \boldsymbol{\varphi}_\mathbf{n} \\ \mathbf{d}_{1_\mathbf{n}} \\ \mathbf{d}_{2_\mathbf{n}} \\ \mathbf{d}_{3_\mathbf{n}} \end{bmatrix}. \tag{17}$$

We use a localized linear approach, linearizing the coefficient in Eq. (17) locally in each n^{th} segment, which is then solved analytically. We use the boundary and continuity condition to solve for the constants of integration. The midcurve position vector $\varphi_\mathbf{n}(\xi_1)$ and the directors $\mathbf{d}_{\mathbf{i_n}}(\xi_1)$ are obtained as Eq. (19) in [2]. In the next section, we demonstrate some application of the shape sensing algorithm to damage detection in underground pipelines.

3 Application to Damage Detection in Underground Pipelines

The underground pipelines are prone to severe damage due to seismic activities like earthquake, liquefaction- induced lateral spreading, landslide, and others. These events have global effect on the pipeline configuration. Hence, monitoring the performance of

underground pipelines during these seismic events and in real time is equally important as developing resilient design methodologies for the same.

Earthquakes causes transient ground deformation and permanent ground deformations. In the simplest sense, the primary cause of underground pipeline deformation is the movement of soil mass associated with the seismic activities. There is abrupt ground deformation at the margin of landslide.

The paper by O'Rourke et al. [10] describes a large-scale test conducted on high density polyethylene pipelines that were subjected to 1.22 m of strike-slip displacement at a vertical fault crossing an angle of 65°. We simulate a similar kind of pipe deformation except that we do it for a much longer circular pipeline of 500 m with a diameter of 800 mm. The schematic diagram of the strike-slip fault effecting the underground pipeline is shown in Fig. 2.

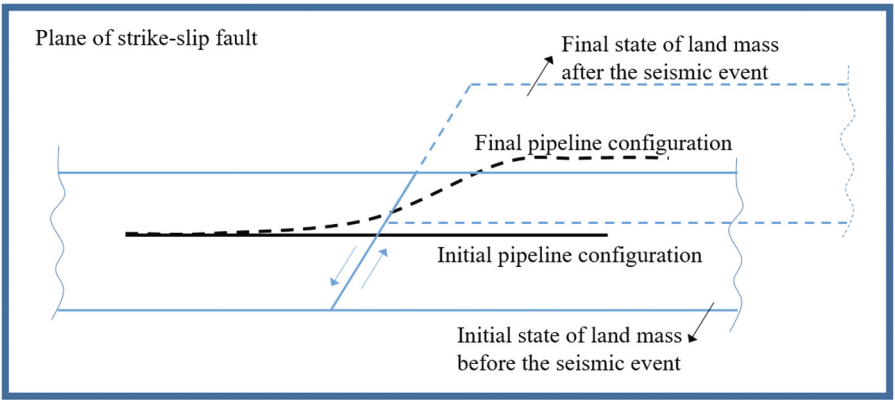

Fig. 2. Schematic diagram of strike-slip fault (Color figure online)

Since we ignore Poisson's effect, the algorithm is material-independent. We impart the pipeline with the axial strain shown in Fig. 3. We model the pipeline such that the left end is fixed. This represents the case where the portion of pipeline to the left of the considered portion is not effected by the seismic event. The scalar surface strain values for a given deformed shape at the set cross-sections for a strain gauge is obtained analytically using Eq. (15). The values of the strain parameters for the n^{th} section $\{S_{1_n}, \ldots, S_{6_n}\}$ (as required in Eq. (17)) is obtained by solving 6 simultaneous equations in Eq. (16). Note that if we include the Poisson's effect, we will have 7 unknown strain parameters. But excluding Poisson's effect simplifies the Eq. (16) to depend on $\{S_{1_n}, \ldots, S_{6_n}\}$. We fix the angles for 6 strain gauges at n^{th} cross-section as $\sigma_n = \left\{\frac{\pi}{4}, \frac{\pi}{2}, \frac{3\pi}{4}, \pi, \frac{5\pi}{4}, \frac{3\pi}{2}\right\}$ and $\mu_n = \left\{\frac{\pi}{4}, -\frac{\pi}{4}, \frac{\pi}{4}, -\frac{\pi}{4}, \frac{\pi}{4}, -\frac{\pi}{4}\right\}$. The set of angles σ_n and μ_n must be such that Eq. (16) is invertible.

The curvature is the dominant deformation for the pipeline with this geometric conditions. Hence, we primarily consider the deformation to consist of $\bar{\kappa}_2, \bar{\kappa}_3$, and the axial strain e. We run the simulation for 6 cases varying the number of equally spaced cross-sections N = (5, 10, 20, 50, 100), about which the strain gauges are attached.

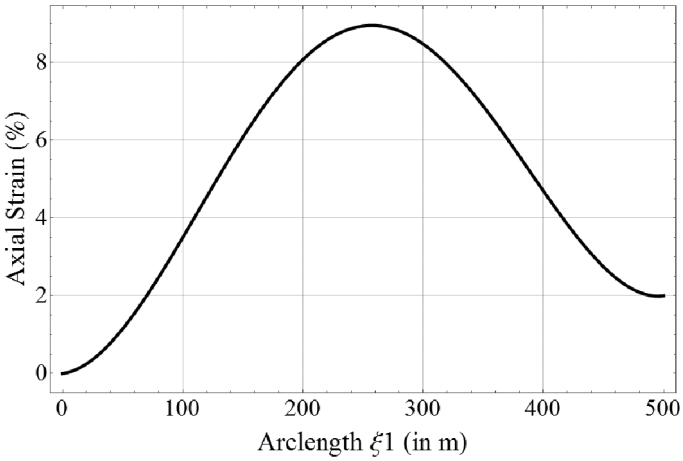

Fig. 3. Axial strain along the pipeline

Each section has 6 strain gauges. Hence there are $6N$ number of total strain gauges in the problem. The displacement of the distal end is $51.75\mathbf{E}_2 + 51.1\mathbf{E}_2$ (in m).

Figure 4 compares the reconstruction of the midcurve result (dotted black) for three cases of N = (5, 10, 100), with the exact deformed shape (orange). Figure 5 compares the reconstruction of the cross-sections by plotting the exact directors obtained using forward model ($\mathbf{d}_1$ in red, $\mathbf{d}_2$ in blue, $\mathbf{d}_3$ in green) with the directors predicted by the shape sensing algorithm (represented by dotted vectors). It is observed that the error is recognizable for 5 sensor locations (spacing of 100 m) with root mean error of 44 m. An excellent convergence is observed in the shape sensing with increase of sensor locations. For $N = 10$ and 100, the rms error is merely 2.354 and 0.015 m, respectively, which justifies an excellent shape reconstruction. Figure 6 compares the exact component of position vector of midcurve φ and the director $\mathbf{d}_1$ with the predicted components for N = 5, 10, and 50.

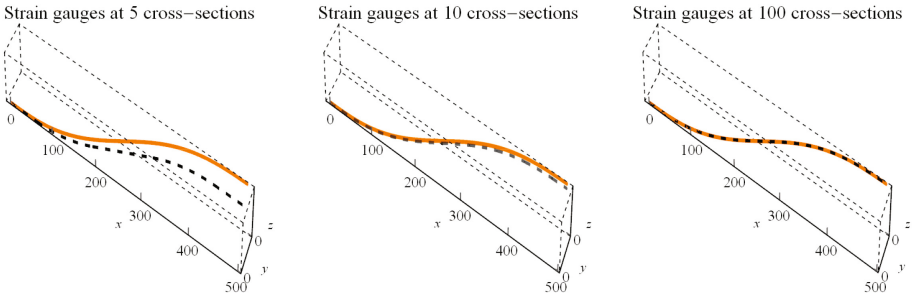

Fig. 4. Exact deformed shape (*orange curve*) of pipeline vs. the reconstructed shape of the pipeline (*dotted black*) (Color figure online)

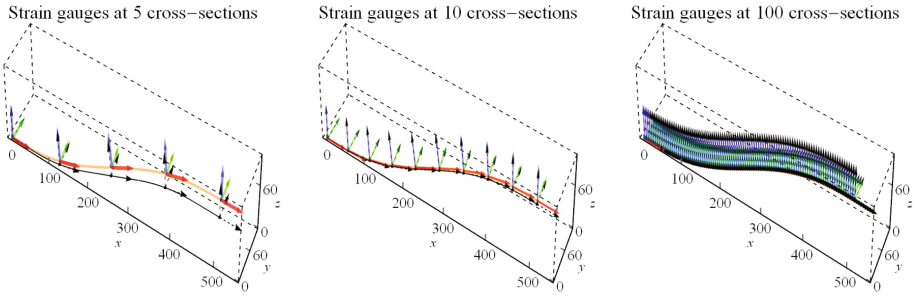

Fig. 5. Exact directors ($\mathbf{d}_1$ in *red*, $\mathbf{d}_2$ in *blue*, $\mathbf{d}_3$ in *green*) compared to the predicted directors (*dotted arrows*) (Color figure online)

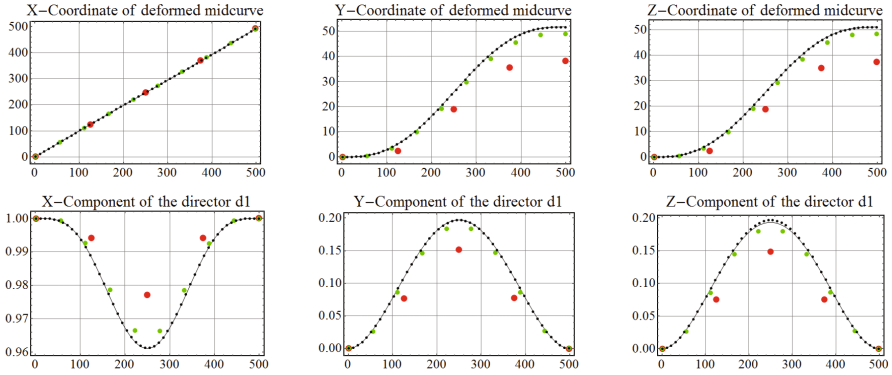

Fig. 6. Comparison of the component of exact (*solid black curve*) vectors $\boldsymbol{\varphi}$ and $\mathbf{d}_1$ with the predicted components for five, ten and fifty strain gauge locations (*red dot*, *green dot*, *black dot* respectively). (Color figure online)

In the ideal case, the strain gauge reading is noise-free. However, practicality dictates that an uncertainty/error analysis be performed, as real strain gages have noise. As in [1, 2], to examine these influences for a first-order assessment of robustness, we add uniformly distributed random noise to the strain values at a [−5, 5] microstrain level and at a [−50, 50] microstrain level before inputting these values into the shape sensing algorithm. We run fifty such realizations in the Monte-Carlo sense and evaluate the average rms error for different numbers of sensor counts. In fact there are three primary sources of error: the first is the error due to approximations in solving Eq. (17), the second is the error due to noisy strain gauge readings, and the third is the uncertainty in the boundary conditions. Figure 7 represents the average rms error for the position vector at various noise levels. The black curve represents the error for the no noise or the ideal case, where the primary cause of deviation is the approximations in the algorithm. The red and blue curves represent the error due to [−5, 5] and [−50, 50] microstrain noise, respectively. It is observed that the error depends on the noise level and the complexity of deformation. The error reduces at a rate greater than exponentially with the increase of sensor count.

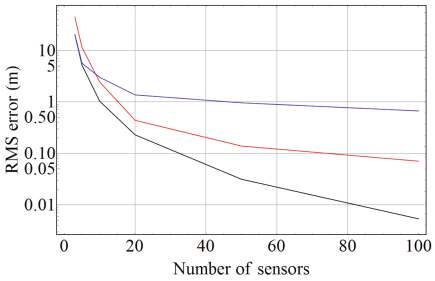

Fig. 7. Root mean square error for no noise (*black curve*), [−5, 5] micro strain noise (*red curve*) and [−50, 50] micro strain noise (*blue curve*) (Color figure online)

4 Conclusion

In this paper, we discussed about the shape sensing algorithm useful for the general three-dimensional shape reconstruction of slender structures. The problem bears the nature of a single manifold problem where the configuration of the structure is defined by the midcurve and the director triad. The methodology presented uses geometrically exact and nonlinear Cosserat rod theory, thereby making the method appropriate to capture large deformation involving finite strain. The formulation captures the effects due to elongation, shear, and curvatures $(e, \bar{\kappa}_1, \bar{\kappa}_2, \bar{\kappa}_3, \gamma_{11}, \gamma_{12}, \gamma_{13})$ assuming Euler-Bernoulli's rigid cross-section assumption.

We established the expression for the surface strain measure in terms of the strain parameters. The discretized form of the governing differential equations for the mid-curve position vector and director are obtained, and the global solution to the set of differential equations obtained is determined using the continuity conditions and the boundary conditions.

The primary purpose of this paper is to demonstrate the ability of this shape sensing methodology to monitor the deformed shape of underground pipelines, important for seismic monitoring applications. It is known that the underground pipelines are severely affected due to seismic activities like earthquake, landslide, and liquefaction.

We simulated a deformed shape for a portion of pipeline 500 m long and 800 mm in diameter and attempted to reconstruct its shape by our algorithm. Excellent reconstruction is obtained for as low as 10 sensor locations (50 m spacing, 60 sensors in total). We observed that the rms error decays with increase in sensor count. Therefore, the shape reconstruction method discussed above can serve as a useful aid in a damage detection strategy that involves knowing the displacement shifts in the pipeline.

References

1. Todd, M.D., Skull, C.J., Dickerson, M.: A local material basis solution approach to reconstructing the three-dimensional displacement of rod-like structure from strain measurements. ASME J. Appl. Mech. **80**, 041028 (2013). doi:10.1115/1.4023023

2. Chadha, M., Todd, M.D.: A generalized approach for reconstructing the three-dimensional shape of slender structures including the effects of curvature, shear, torsion and elongation. ASME J. Appl. Mech. **84**, 041003 (2017). doi:10.1115/1.4035785
3. Cosserat, E., Cosserat, F.: Theorie des Corps Deformable. Herman, Paris (1909)
4. Simo, J.C.: A finite strain beam formulation. The three-dimensional dynamic problem. Part 1. Comput. Methods Appl. Mech. Eng. **49**, 55–70 (1985)
5. Simo, J.C., Vu-Quoc, L.: A geometrically exact rod model incorporating shear and torsion-warping deformation. Int. J. Solids Struct. **27**, 371–393 (1991)
6. Iura, M., Atluri, S.N.: On a consistent theory, and variational formulation of finitely stretched and rotated 3-d space-curved beam. Comput. Mech. **4**, 73–88 (1989)
7. Reissner, E.: On one-dimensional finite-strain beam theory: the plane problem. J. Appl. Math. Phys. **23**, 795–804 (1972)
8. Reissner, E.: On one-dimensional large displacement finite beam theory. Stud. Appl. Mech. **52**, 87–95 (1973)
9. Reissner, E.: On finite deformation of space curved beams. J. Appl. Math. Phys. **32**, 734–744 (1981)
10. O'Rourke, T.D., Jung, J.K., Argyrou, C.: Underground pipeline response to earthquake-induced ground deformation. Soil Dyn. Earthq. Eng. **91**, 272–283 (2016)

Testing, Sensing and Modeling

Displacements Monitoring of Suspension Bridge Using Geodetic Techniques

Wojciech Anigacz[1], Damian Beben[1(✉)], and Jacek Kwiatkowski[2]

[1] Faculty of Civil Engineering and Architecture, Opole University of Technology, Opole, Poland
d.beben@po.opole.pl
[2] J&L Consulting, Opole, Poland

Abstract. The objective of the study was to compare and assess suitability of three methods of geodetic measurements used to dynamic testing of suspension bridge. Tachymetry, photogrammetric and laser scanning methods were tested. The above-mentioned methods were tested at the main span of the suspension bridge of 165 m on the Oder River, Poland. Information on the change in the shape of bridge structure under the influence of service load are very significant concerning maintenance (exploitation). The examined bridge comprises 5 spans – four outmost flood spans and the main river span of suspended structure. The structure serves as a technological bridge. Through the bridge passes a belt conveyor connecting lime quarry with a cement factory. Weight of the output transported through the bridge is 900–1100 Mg/h, and the speed of the belt conveyor movement was 2 m/s. The scope of examinations included performing measurements of the changes in the bridge and bearing cable deflection values during the belt conveyor operation and stoppage, using the above-mentioned methods. The most accurate among the used methods was the tachymetry and laser scanning methods, thus the results obtained with these methods were considered as the reference data. The tachymetry measurements were conducted using precise tachymetry TC2002 manufactured by Leica. In the photogrammetric method, digital photography was used, i.e. a Canon 650D camera with high resolution, photographic turntable and the newest software. In the case of the laser scanning, a Trimble TX8 scanner was used. As a result of conducting the experimental tests, the obtained displacements of the bridge did not exceed 49.1 mm and 60 mm for tachymetry (and laser scanning) and photogrammetric method, respectively, thus being lower than the limit values calculated in accordance with the bridge standard. Besides, the bridge displacements obtained under static load were higher than results received from dynamic load.

Keywords: Bridge · Displacements · Photogrammetric · Tachymetry · Laser scanning

1 Introduction

In order to validate structural specifications, or to provide diagnostic surveys for planning maintenance and modernization of bridges and other engineering structures, dynamic and static tests are often conducted. Typical experimental tests are usually

© Springer International Publishing AG 2018
J.P. Conte et al. (eds.), *Experimental Vibration Analysis for Civil Structures*,
Lecture Notes in Civil Engineering 5, https://doi.org/10.1007/978-3-319-67443-8_28

carried out using accelerometers, strain, inductive [1, 2] and wireless sensors and levelling [3]. However, installation of the most of these sensors require direct contact with the structure. Therefore, examining structures can cause accessibility problems, often requiring using the scaffolds. That is why, authors decided to analyze three measurement methods intended for non-destructive monitoring of the construction displacements.

Fast developing measurement techniques, especially geodetic, and in particular the mass measurements, in theory and practice, enable to obtain full information on the structure and changes in the bridge structure geometry. The importance of the undertaken issue is proven by the fact that the global-company (NineSigma) organized a tender. The task concerned developing an innovative technology of Non-Contact Mobile Inspection of Concrete Degradation. The authors of the article have such technology, the latest equipment (often prototype-pre-production), the latest software, and adequate knowledge and experience [4].

Most of the current researchers [3, 5–8] have a classic approach to the structure testing, which means that they put a reference measurement grid outside the tested object and on the object itself. They mark (signalize) points that are measured. Such approach is fully correct in the case of conducting long-term tests. The reference points outside the tested structure allow to determine changes of the bridge structure geometry in the absolute frame of reference comprised of the reference points, with coordinates determined, for instance, using the GPS method. In the presented case, the preparatory works on the bridge structure were minimized. It was decided to use well-visible details of the bridge structure as the measurement points and additionally a dozen of measurement targets and white balls (on magnets) were temporarily installed. The tachymetry method was the reference method. Such approach required especially careful approach to the measurement processes, which means that the two measurement stations were stable through the whole period of examinations to make it possible to compare the measurement sequences at later time. The interesting way of measuring displacements of bridges using the microwave interferometry method was presented by Beben and Anigacz [9].

Setting up a measurement grid is associated with passing its errors onto the controlled points. Thus, the authors [10, 11] used sophisticated mathematical apparatus to minimize these errors. Such problems, however, did not occur in the presented case. In the photogrammetric and scanning measurements, the bridge was measured from one station and the binding points were the well-visible details of the bridge. Yu et al. [8] reported an interesting comparison of the various measurement methods, measurement accuracy, measurement type, bridge type and measurements costs. However, the presented information, e.g. in regards to the laser scanning turned out to be too optimistic because obtaining accuracy below 1 mm is in practice limited to small bridges only (where the distance between the scanner and the bridge is small). Tang et al. [7] compared potential of the tachymetry method and laser scanning in the measurements of bridges. They reported values of the measurement errors on real objects.

First attempt to examinations of the geodetic methods on the suspension bridge was presented by Anigacz et al. [12]. The results clearly show that the laser scanning method using the Faro Focus 3D X130 scanner proved to be the least accurate in the

case of the bridge. It was a result of too high distance from the bridge and too little resolution of the scanner (points density).

The objective of this study was to compare and assess the suitability of different geodetic measurement methods for monitoring displacements of the suspension bridge. Information on the change in the shape of the bridge load-carrying structure under static and service loads are very important for a number of reasons. Knowing the changes in the structure shape, the correctness of the project and/or modernization assumptions can be evaluated. Besides, the obtained experience can be used in the similar projects. Additionally, after some period of exploitation one can obtain information if the bridge displacements do not exceed the code limit. In the current research work, three independent measurement methods were used: (i) tachymetry, (ii) photogrammetric, and (iii) laser scanning. The main span of the monitored suspension bridge was 165 m. Every method has some specific properties, more or less useful in measurements of such type of bridge. In the article, exemplary results of the measurements of changes in displacements of the main span of a bridge were presented. Advantages and disadvantages of individual methods were also described.

2 Short Bridge Description

The studied structure is a two-pylon steel suspension bridge over the Oder River intended for connecting the marl mine with cement factory with the transport line (Fig. 1). The bridge comprises five spans – four outmost flood spans and the river span. The structure of the transport gallery is suspended with hangers under the main bearing cables distributed over two pairs of pylons. The pylons are 26.50 m high each, and the total length of the entire bridge structure is 285.00 m. The load-carrying structure with span of 165.00 m is suspended on cables. The flood part of the bridge consists of spatial truss galleries of the span of 30.00 m each, with the upper roadway (as extension of the suspended galleries), two on each side of the river span. The galleries are supported with the pinned-pinned steel column. The bridge was designed as a structure suspended on two steel pylons, through which a set of 2×6 bearing cables of 48 mm diameter. To secure the horizontal stability (e.g. from excessive rocking of the bridge caused by the aerodynamic influence of the wind), in its lower part, a set of two correction cables was used crossed in 1/3 of the river span. In the river part, the truss structure of the bridge of the width of 5.80 m and height of 3.00 m consists of repeating elements of the length of 15.00 m. The cables are connected to the pylon in a fixed manner through a head and screwed connections that enable moving the cables on the pylon tip. The ends of cables (stays) are mounted to the reinforced concrete anchor blocks on both sides of the objects. Possible horizontal displacements of the bearings were expected on the outmost poles by the entrance to the bridge. In the pylon, tangent bearings were used.

The bridge is intended for transporting the limestone output with a belt conveyor placed in the transport gallery. Weight of the output transported through the bridge is 900–1100 Mg/h, and the speed of the belt conveyor movement was 2 m/s. Recently the bridge were modernized in the range of: (i) replacement of the steel bridge deck on the composite deck, (ii) replacement of one hanger, (iii) repair of cracks of pylons. Currently,

Fig. 1. View of the suspension bridge from the measurement position.

any signs of deformation, cracks and perforations were not noticed in the monitored bridge. Overall rating of the bridge structure according to the field inspection [13] was "satisfactory". Detailed description of the bridge was presented by Anigacz et al. [12].

3 Measurements Methodology

3.1 General Notes

The geodesy has a large range of measurement methods, from which it is necessary to choose the most useful ones for measuring the displacements of the suspension bridge of the span of 165 m. One of the most significant factors influencing the selection of the method is the geometric specificity of the bridge. In the analyzed case, it is a linear structure with the span of 165 m (the main span of bridge).

The experimental tests were carried out after forty years of service of the bridge and after one year from the bridge modernization. The bridge displacements were registered during four different stages: (i) static load (without limestone and the belt conveyor was stopped – it was the reference stage with which other results were compared), (ii) dynamic load (without limestone, the conveyor was moving), (iii) dynamic load - normal service (with limestone, the conveyor was moving), and (iv) static load (with limestone, the conveyor was stopped). The testing was taken continuously for 12 h. On the examined bridge structure, three measurement methods were tested, i.e.: (i) tachymetry, (ii) photogrammetric, and (iii) laser scanning. Based on this methods, the displacements of the river span of the bridge were determined.

3.2 Tachymetry Method

The tachymetry method depends on the field determination of the spatial polar coordinates, i.e. distances and vertical and horizontal angles from the set of chosen directions. The accuracy of the determination of the point's position is described by Eq. (1):

$$m_n = \sqrt{m_x^2 + m_y^2 + m_h^2} \tag{1}$$

where m_p – spatial error; m_x – error of the coordinate $x = d \times \sin z \times \sin \alpha$; m_y – error of the coordinate $y = d \times \sin z \times \cos \alpha$; m_h = error of the coordinate $h = d \times \cos z$; α – horizontal angle; z – vertical angle (zenithal); d – slant distance.

Tachymeters are available theoretically measuring the distances with the accuracy of 1 mm and the directions with the accuracy of 0.5″ (0.15 mgon). The accuracies obtained under the field conditions are usually much lower and oscillate within the range of 1–5 mm for the distances and 3–10″ for the determination of the directions.

The angular resolution of the measurement device has high significance especially for the identification of details, e.g. edges in the case of big distances [14, 15]. In the analyzed case, the stations of the tachymeter were placed on both sides of the river in order to lower the target lengths, i.e. distances between the tachymeter station and the measurement point. In the presented case the distances did not exceed 100 m (Fig. 2).

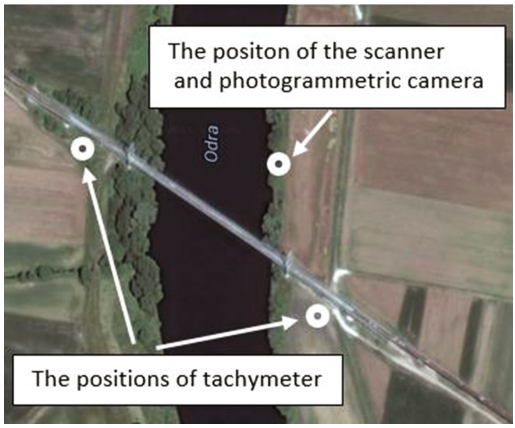

Fig. 2. Positions of the tachymeter, scanner and photogrammetric camera during testing.

Despite of such a significant difference between the accuracies obtained in the laboratory conditions and in the field conditions, the tachymetry method is currently the most accurate method of determining the position of the points in space [15]. For this studies, the total station TC2002 manufactured by Leica was used and dozen or so different measurement targets (Fig. 3). Calculations of the displacements were conducted using the authors' programs.

The results obtained with this method were adopted as the reference data for the remaining measurement methods. The correctness of the obtained results of displacements were verified by a measurement from the second station. In order to identify the measured displacements of the bridge, two-sided telemeter targets were used that enabled measurement of the distance from both sides of the target. The measurement targets were placed in the node points of the transport gallery over the transverse beam (in the middle of the span, 1/4 and 3/4 of the span). The opening in the middle of the target has 5 m diameter. On that basis, it can be concluded that the accuracy of aiming (measurement the direction) was between 1–2 mm.

Fig. 3. View on (a) the Tachymeter TC 2002 during testing, (b) one of the measurement targets.

3.3 Photogrammetric Method

In this method, the Canon 650D camera with the lens of fixed focus of 85 mm and the GigaPano turntable were used (Fig. 4). The level of spherical aberrations, confirmed in the laboratory on the test rectangle (Graph paper 420 × 297 mm), did not exceed 3 columns of the matrix pixels (5184 × 3456 pixels). To process the pictures, Kolor AutoPano Giga 4.0 software was used. To calibrate the generated panorama through rescaling for defining the "size" of individual pixel, the Photoshop CC computer software was used. The Photoshop CC software enables linear rescaling of the pixel size. In order to obtain the displacement results during the dynamic testing, the camera was set in such a way to perform a sequence of photographs at a given time, for example 5 photographs per second. This approach enabled to obtain the distribution of displacements of the bridge.

To scale the panorama of the bridge to the set pixel size, the characteristic distances were used. In this study, the additional elements, i.e. measurement targets (Fig. 5b) and white reference spheres (Fig. 5a) were temporarily installed using neodymium magnets. Segments of the span that previously were measured with the tachymetry method were also monitored. The photogrammetric method has the following advantages, among others: short time of making measurements (time of taking a picture, sequence), possibility of visualization with the elements of specialization, and possibility of multiple interpretations of the measurement. It is a relatively cheap method, and commonly available. The final analytical data illustrating the effects of the measurement session depend on three main factors: (i) resolution of the matrix of the digital camera, (ii) quality of the optics (resolution, reduction of the spherical aberration), (iii) software ability of assessing the process of interaction with the user, e.g. in stitching.

Fig. 4. The Canon 650D camera with the lens 85 mm situated on the GigaPano turntable.

Fig. 5. View on the additional reference elements installed on the bridge: (a) white ball, (b) measurement target.

3.4 Laser Scanning Method

Laser scanning method is a relatively new measurement method allowing to obtain the quasi-constant, spatial representation of the area of the examined structure seen in the central view. The accuracy of the results depend mainly on the distance between the scanner and the examined structure. In the last several years, fast development of the laser scanning has been observed [4, 5, 10]. Scanner uses a laser beam that, after being reflected from the measured structure, comes back to the scanner. The distance is determined on the basis of a difference of phases of the generated and reflected beam. During the measurement, scanner can be turned by 360° horizontally. Horizontal and vertical angle of the scanner mirror set, information on the measured distance and quality of the reflected signal are calculated in real time into the coordinates.

During first attempt of checking the possibility of using the laser scanning method to the bridge displacement monitoring, the other scanner was used (Anigacz et al. [12]). However during elaboration of the test results it turned out that applied scanner do not

allows to obtain the correct results. The quality of the scan of the bridge span was in the upper limit of the scanner coverage, i.e. 100–120 m. During the analysis of the results, it turned out that the quality (point density) of the scan is too low.

Taking into account the above experience, the authors decided to use for the bridge examinations a Trimble TX8 scanner (Fig. 6). This scanner measures up to 1 million of points per second and allows to create clouds of over a billion of points. The maximum scan range is 120 m, but it can be increased to 340 m. The wavelength of the laser is 1.5 μm and the scan frequency is equal 1 MHz. The declared accuracy of the measurement of the distance was ±2 mm, and angle resolution is 80 μrad. The standard unit of resolution is dpi, so it means a dot per inch of the length. In the technical applications where the elements of the studied structures are located in different distances from the scanner, the angle resolution is the more convenient to use than the dpi which constantly changing with the change of the distance.

For the results analysis and point cloud processing, specifically designed the Trimble RealWorks 10.2 program [16] was used. The software provides a complete solution to efficiently register, analyze, model and create deliverables using data from virtually any source. The software also allows for the automatic interpolation of the markers center, which in this study constituted the measurement targets and white reference spheres (the same as in the photogrammetric method – see Fig. 5).

Fig. 6. The Trimble TX8 scanner during bridge testing.

Data from a scanner of such type are obtained in the .fls format. Conversion to the .rcs format was conducted with the ReCap360 software. Files with the extension .rcs are read by all the AutoDesk applications. The subsequent scans are matching to characteristic points (measurement targets and white reference spheres) in such a way that the next measurement sessions can be topologically consistent. This allows for significantly reduction of the working time on the measurement object.

From the presented measurement methods, the equipment and software connected with the laser scanning are the most expensive. It would be ideal to use three methods at the same time when the bridge is examined. Then the information on the bridge structure geometry would be a synthesis of all the used methods [15].

4 Results and Their Analysis

Altogether, during the measurements, at least of 3 different points of the bridge (i.e. in 1/4, 1/2 and 3/4 of the bridge span where the targets and white reference spheres were installed) were analyzed as well as the two pylons were monitored. It needs to be noted that the tachymetry measurement of a few measurement points was spread over time. Thus, it is most probable that the differences in the values of the deflection were caused by the lack of full synchronization of measurements conducted with different methods.

Table 1. Comparison of the maximum registered displacements of the suspension bridge.

Measurement method	Load scenarios	1/4 of span (mm)	1/2 of span (mm)	3/4 of span (mm)
Tachymetry	Dynamic, without load	0.3	2.1	1.7
	Dynamic, with load	19.7	35.4	24.1
	Static, with load	24.0	49.1	37.7
Photogrammetric	Dynamic, without load	0	3	2
	Dynamic, with load	15	43	29
	Static, with load	18	60	46
Laser scanning (previous results)	Static, with load	*	*	*
Laser scanning (Trimble)	Dynamic, without load	**	**	**
	Dynamic, with load	**	**	**
	Static, with load	19	49	38

* Previous results obtained with the laser scanning using other scanner [12] have been regarded as uncertain (too high discrepancy in comparison to other methods)

** On this stage of measurements, authors do not able to extract displacements during dynamic testing (further works are needed)

The results of the displacements for the main span of the suspension bridge for the chosen three measurement points (1/4, 1/2, and 3/4 of the span) are shown in the Table 1. The results presented in Table 1 mean difference between displacements in given load scenarios and reference stage (static load, i.e. without limestone and conveyor belt was stopped). The maximum values of displacements amounted to 49.1, 60 and 49 mm, for the tachymetry, photogrammetric and laser scanning method, respectively. Such quite large difference between the photogrammetric and tachymetry (and laser scanning) method is associated with the pixel size (4 mm). The highest displacements of the bridge were noted in the middle of the bridge span. Results presented in Table 1 clearly showed that the bridge displacements during static load (the belt conveyor with the limestone was stationary) were higher than results obtained

during dynamic loads (the belt conveyor with limestone in motion). These differences were in the range of 17–37% and it depended on the measurement points of the bridge. This is related to the way of load action on the bridge, i.e. linear load acting stationary, but the long-term (during static measurements it was about 40 min). The bridge displacements during movement of the belt conveyor without limestone were very low (on the limit of measurement error). The obtained maximum values of displacements are significantly lower than the limit value (l/500 = 330 mm) according to the bridge standard PN-82/S-10052 [17] calculated like for the steel road bridges.

Figure 7 illustrates the selected results of displacements obtained with the photogrammetric method. The analysis of the obtained results consisted of overlapping two photographs. The first one was taken without the load – stopped belt conveyor without limestone, and the second one shows the overlap of two sequences of photographs – without the load and with the load (limestone). On the joint pictures one pixel was scaled to 10 mm, and then it was calculated by how many pixels the measured elements were shifted against one another. In effect, quite accurately, the change in the deflection of the bridge under the influence of the service load – belt conveyor with the limestone (weight ranging from 900–1100 Mg/h) moving with the speed of 2 m/s, was determined.

Fig. 7. Bridge displacements of the bridge obtained from the photogrammetric method.

As can be seen in Table 1 the displacements obtained from the tachymetry and laser scanning methods during the static loads are almost the same. While the bridge displacement values obtained with the photogrammetric method are ca. 18% higher than those received from the tachymetry and laser scanning methods. Figure 8 presents the selected scan of the displacements bridge during static loads using the laser scanning method. Unfortunately at this stage of operation of the laser scanning, possibilities to obtain the bridge displacements during dynamic test are not fulfilled. The authors have an idea to conduct further research works with the laser scanning, for example with using of the line scan mode. It is possible to scan a line repeatedly and dynamic displacement of the bridge can be determined from the scan data.

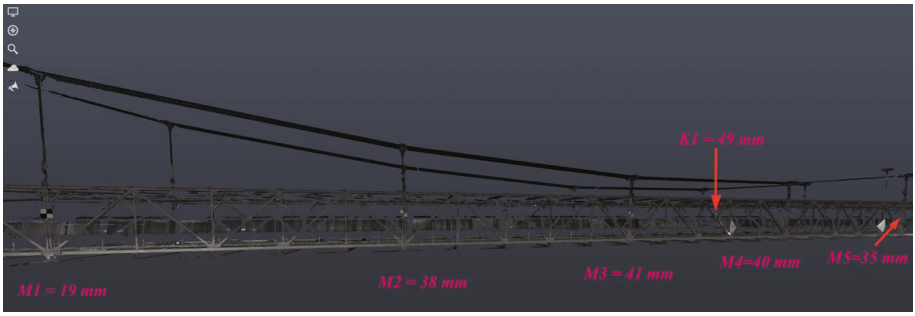

Fig. 8. Bridge displacements in selected points using the laser scanning method.

5 Final Conclusions

As a result of displacements monitoring of the suspension bridge with span of 165 m under static and dynamic load scenarios, conducted with using three methods: tachymetry, photogrammetric, and laser scanning, the following conclusions can be drawn:

1. The maximum displacements of the bridge obtained using the tachymetry method (reference method) were observed in the middle of the span and were 49.1 mm. The biggest displacements of the bridge caused by the influence of the service load need to be considered relatively small. It should be also noted that the bridge displacements obtained under static load are higher than results received from dynamic load. Displacements obtained from all applied methods were significantly lower than the limit value for the bridge-type in every case. Based on the photogrammetric method, the results obtained for the values of the bridge displacements under static loads were generally underestimated in comparison to the tachymetry and laser scanning methods (in the case of this bridge ca. 18%).
2. In the case of the photogrammetric method the camera's focus needs to be chosen in such a way that the value of a pixel was higher, for example 2 mm. Higher scale of the photograms will allow to obtain additional information on the surroundings of the measured point, e.g. permanent deformations, cracks, etc.
3. Currently, the laser scanning method only allows to obtain the bridge displacements under static loads with the same accuracy like with using tachymetry method. Further research works for laser scanning method are needed in order to determine the structures behavior under dynamic loads, for example with using of the line scan mode.
4. In the case of the tachymetry and photogrammetric methods measurements with several tachymeters and cameras of the same points would need to be conducted at the same time, in order to fulfil the quality requirements. In this way properly accurate information on the subject of displacement of certain measurement points would be obtained. Such approach would make full synchronization of measurements possible, however, such measurements are difficult to perform from the practical point of view.

References

1. Beben, D.: Corrugated steel plate (CSP) culvert response to service train loads. J. Perform. Constr. Facil. ASCE **28**(2), 376–390 (2014)
2. Cantero, D., Ülker-Kaustell, M., Karoumi, R.: Time–frequency analysis of railway bridge response in forced vibration. Mech. Syst. Signal Process. **76–77**, 518–530 (2016)
3. Anigacz, W., Kokocinska-Pakiet, E.: Long-term monitoring of earth dam settlement. In: Proceedings of the 4th International Symposium on Life-Cycle Civil Engineering, Tokyo (2014)
4. Kwiatkowski, J.L.: Construction life cycles monitoring of industrial installations verified by hybrid bulk measurement techniques. Doctoral dissertation, Opole University of Technology, Opole, Poland (2014)
5. Jauregui, D.V., White, K.R., Woodward, C.B., Leitch, K.R.: Noncontact photogrammetric measurement of vertical bridge deflection. J. Bridge Eng. ASCE **8**(4), 212–222 (2003)
6. Schofield, W., Breach, M.: Engineering Surveying, 6th edn. Elsevier, Amsterdam (2007)
7. Tang, P., Akinci, B., Garrett J.H.: Laser scanning for bridge inspection and management. In: IABSE Symposium Weimar (2006)
8. Yu, Y., Liu, H., Li, D., Mao, X., Ou, J.: Bridge deflection measurement using wireless mems inclination sensor systems. Int. J. Smart Sens. Intell. Syst. **6**(1), 38–57 (2013)
9. Beben, D., Anigacz, W.: Interferometric radar application for dynamic testing of bridge structures. In: Proceedings of the 7th International Conference on Bridge Maintenance, Safety & Management, Shanghai (2014)
10. Beshr, A.A.A.: Structural deformation monitoring and analysis of highway bridge using accurate geodetic techniques. Engineering **7**, 488–498 (2015)
11. Osada, E.: Geodesy, 2nd edn. Wroclaw University of Technology Press, Wroclaw (2002)
12. Anigacz, W., Beben, D., Kwiatkowski, J.: Analysis of suitability of new measurement technologies to examine changes in geometric parameters of a suspension bridge. In: Proceedings of the 8th International Conference on Bridge Maintenance, Safety & Management, Foz do Iguaçu (2016)
13. Janas, L., Michalak, E.: Rules for the application of a grading scale of technical condition and usability to service of road engineering structures. General Directorate for National Roads and Motorways, Warsaw (2008)
14. Berenyi, A., Lovas, T., Barsi, A., Dunai, L.: Potential of terrestrial laser scanning in load test measurements of bridges. Period. Polytech. **53**(1), 25–33 (2009)
15. Luhmann, T., Müller, Ch.: Photogrammetrie Laserscanning Optische 3D-Messtechnik. Herbert Wachman, Heidelberg (2007)
16. Trimble Realworks 10.2 User Guide. https://www.trimble.com/3d-laser-scanning/realworks.aspx
17. PN-82/S-10052: Bridge Structures, Steel Structures, Design. Polish Committee of Standardization, Warsaw, Poland

Modelling of Pot Bearings – A Preliminary Study

Mahir Ülker-Kaustell[1(✉)], Gabriel F. Boschmonar[2,3], Pablo B. Isusi[2,3], Stefan Trillkott[2], Claes Kullberg[2], and Raid Karoumi[2]

[1] Tyréns AB, Stockholm, Sweden
mahir.ulker-kaustell@tyrens.se
[2] KTH, Royal Institute of Technology, Structural Engineering and Bridges, Stockholm, Sweden
[3] Polytechnic University of Madrid, E.T.S.I., Caminos, Canales y Puertos, Madrid, Spain

Abstract. Previous research indicates that roller and pot bearings may give rise to considerable non-linear effects in certain bridges. These effects appear as variations in natural frequency, mode shape and modal damping ratio, depending on the amplitude of vibration. At small amplitudes of vibration, it seems reasonable to assume that the rolling or sliding mechanism is inactive, thus yielding a stiffer structure and no additional dissipation of energy due to friction. At slightly larger amplitudes of vibration, although still remaining small with respect to geometrical non-linearity, the rolling or sliding mechanism activates, whereby the corresponding constraints are relieved. At the same time, because of the rolling or sliding friction, a certain amount of energy dissipates to the surroundings. In order to improve our understanding of these mechanisms and their practical implications, a preliminary experimental study has been performed with the aim of developing a simple model of these mechanisms, which can be included in theoretical models of bridges and other structures. In this paper, we give a short description of the outcome of our laboratory tests and the status of our model development process.

Keywords: Bridges · Pot bearings · Friction · Laboratory tests · Non-linear modes of vibration

1 Introduction

This preliminary study was motivated by an analysis of the free vibrations after passing trains. Rebelo et al. [1] found a shift in the natural frequency of a ballasted railway bridge when they used the short time Fourier transform to analyze their free vibration data. A faster analysis, including an estimate of the instantaneous equivalent viscous damping ratio was obtained by applying the wavelet transform to the free vibration signals [2]. This analysis revealed that the natural frequency of the fundamental mode of vibration was reduced as the amplitude of vibration increased, while the modal damping ratio increased.

© Springer International Publishing AG 2018
J.P. Conte et al. (eds.), *Experimental Vibration Analysis for Civil Structures*,
Lecture Notes in Civil Engineering 5, https://doi.org/10.1007/978-3-319-67443-8_29

The dynamic properties of civil engineering structures are often analyzed under the assumption that the structural response is linear. This holds true in most applications in the serviceability limit state, but there are conditions under which this assumption does not hold true. One such condition is the presence of friction mechanisms such as pot bearings, spherical bearings, disk bearings and roller bearings. These mechanisms all have in common that there exists a limit force, which must be overcome in order to activate the sliding or rolling mechanism. Thus, for responses which are too small to activate the sliding or rolling motion over moveable bearings, the dynamic properties may differ substantially from those obtained under responses which are large enough to activate the motion.

A simply supported beam bridge will serve as an example. Figure 1(a) shows a model of a simply supported bridge consisting of an Euler-Bernoulli beam, resting on some form of (more or less) flexible supports. Due to the eccentricity between the elastic line of the beam and the bearings, the dynamic properties of the beam will be highly dependent on the ability of the moveable bearing to move [3, 4]. If the friction force in the bearing is not overcome by the internal forces, the beam will be clamped and if it is, the beam will be (close to) simply supported. This will influence the modes of vibration and their frequencies. Furthermore, when the motion over the bearings is active, a certain amount of frictional damping will contribute to the overall damping of the structure. That this contribution to the overall damping is in fact relevant can be shown by simple calculations, e.g. by comparing the strain energy in the beam, at given amplitude of vibration, to the work performed by the friction forces in the sliding bearings. Figure 1(b) shows a photo of a continuous 3-span post-tensioned concrete beam bridge. From the free vibrations, only very small variations in the dynamic properties were found. However, when a simple hysteretic bearing model based on the Bouc-Wen model, was used to simulate free vibrations of larger amplitudes of vibration, the results shown in Fig. 1(c) where obtained. Case 3 is the best fit of the Bouc-Wen model used model the bearings to the available experimental data. The rest of the curves in Fig. 1(c) are the result of a small parametric study, reported in reference [4]. These results have justified further studies within this field and have the following implications when analyzing experimental data from existing structures:

1. Estimates of natural frequencies can be overestimated since we often use free vibrations from traffic loads or ambient sources of excitation, which only produce relatively small amplitudes of vibration.
2. Estimates of the mode shapes may deviate substantially from the expected.
3. Estimates of modal damping ratios can be underestimated.

In model updating procedures, one may need to compensate for these effects. In terms of stiffness, the extreme cases of either sliding or not sliding may serve as useful approximations. However, in order to quantify the additional damping and exploit it, in a safe and robust way, for assessments of existing bridges and in design of new bridges, more detailed knowledge is required. Therefore, this investigation aims at defining a simple bearing mechanism element, suitable for use in finite element models of bridges and other structures. A non-linear spring-dashpot element based on the Bouc-Wen model [5, 6] has been chosen as the basis for such a bearing mechanism element.

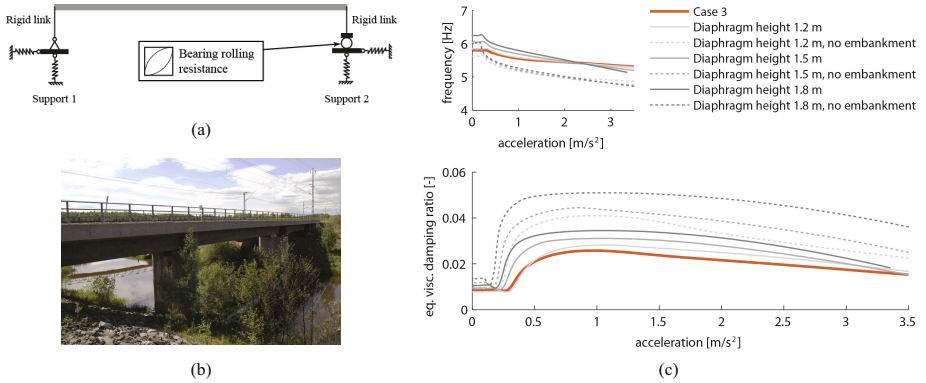

Fig. 1. (a) Principles for 2D models of beam bridges. (b) The Sagån bridge. (c) Theoretical natural frequency and equivalent viscous damping ratio of the fundamental mode of the Sagån bridge (see reference [4]).

2 Steel-PTFE Contact Interfaces

Most modern bearing types, i.e. pot bearings, spherical bearings and disk bearings, rely on Polytetrafluoroethylene (PTFE), to provide bearings with a translational capacity either in one or in two directions. Bridge bearings have not been studied so much in the context of structural dynamics, but naturally, seismic devices have been studied rather extensively in this context. In particular, Dolce et al. [7] have performed some rather extensive studies on the kinetic coefficient of friction of steel—PTFE interfaces. From these studies, one may conclude that the steel-PTFE contact interface is highly dependent on the following three factors:

1. Sliding speed (the coefficient of friction increases asymptotically with increasing sliding speed).
2. Contact pressure (the coefficient of friction decreases with increasing contact pressure).
3. Contact temperature (the coefficient of friction decreases with increasing contact temperature).

Apart from the above listed factors, there exist some cyclic effects which tend to reduce the coefficient of friction as the number of cycles increase. This effect is more pronounced for higher sliding speeds which imply that it is somehow related to the heat generated at the steel-PTFE interface. More recently, Lomiento et al. [8] have provided a friction model which accounts for the cyclic effects reasonably accurately. In the present context however, it is assumed that the cyclic effects can be discarded. The influence of break-away and stick-slip is also discarded.

3 Laboratory Tests

We have performed some preliminary tests with the purpose of obtaining a direction for the development of a model of bearing mechanisms with steel-PTFE sliding contacts.

The test rig (see Fig. 2) was designed for the smallest available commercial pot bearing (provided by KB Spennteknikk, www.spennteknikk.no). We mounted the bearing in a stiff box, facilitating three vertical load cells under the box to measure the vertical force and the retaining moment of the bearing and one horizontal load cell to measure the friction force. A number of displacement transducers were used to measure the horizontal displacement of the bearing and the vertical displacements at two different locations to measure the rotation of the bearing. The vertical load was applied using a 250 kN hydraulic cylinder and a 50 kN hydraulic cylinder was used to apply the motion in a displacement-controlled cyclic test-procedure.

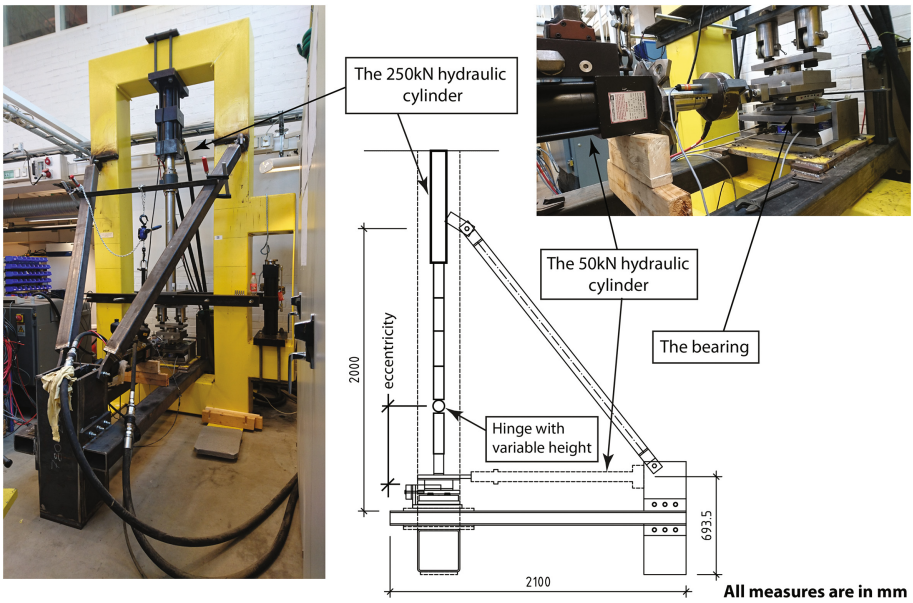

Fig. 2. Description of the test rig used for the laboratory tests.

The tested bearing (TOBE, Type E10) is shown in Fig. 3. The figure also shows how the bearing was instrumented with load cells and how we mounted the bearing in order to be able to measure the vertical force, the moment around the transversal axis, the horizontal displacement and the horizontal force over the bearing. The area of the PTFE plate was $A_{\mathrm{PTFE}} = 9859\,\mathrm{mm}^2$. Therefore, the maximum contact pressure is $p = 250\,\mathrm{kN}/A_{\mathrm{PTFE}} = 25\,\mathrm{MPa}$ although we chose to limit the applied vertical load to 200 kN. Typically, the PTFE stress is limited to around 25–30 MPa which is near the ultimate compressive stress for PTFE at room temperature. However, in the present context, where a serviceability limit state is considered, this is not a severe limitation.

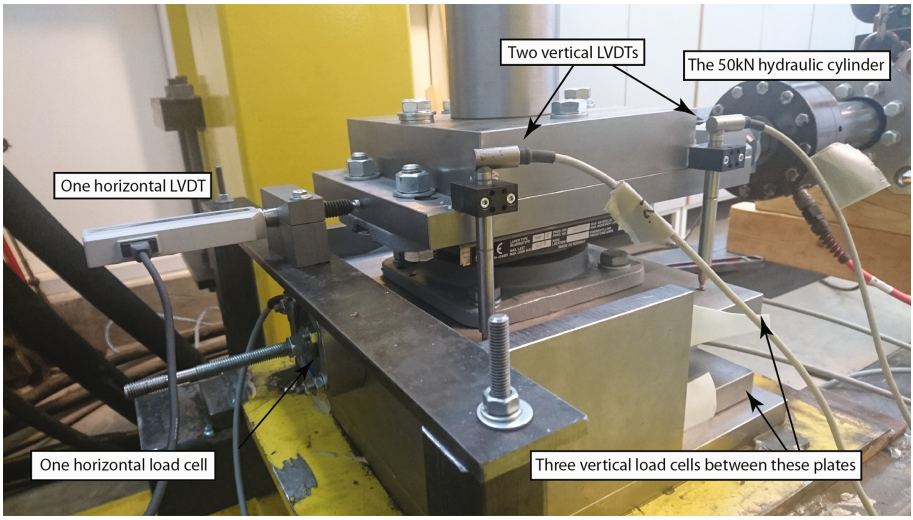

Fig. 3. A photograph of the bearing as mounted in the test rig.

The available pump could produce fairly consistent results for load frequencies $f < 5$ Hz. For faster motions, the pump required a large number of cycles to reach the programmed amplitude of the motion, as can be seen in Fig. 4.

Although limited in many ways, the tests were judged to provide us with the information we need to motivate further studies. Given the limitations in vertical load (contact pressure) and load frequency (sliding speed), a test series consisting of four discrete force values; 10, 50, 100 and 200 kN and 4 discrete load frequencies; 0.01, 1, 2 and 5 Hz was chosen. Thus sixteen combinations of vertical force and load frequency are obtained for each value of the eccentricity.

A uni-directional bearing is unstable in the direction of the bearing motion, since only the friction force in the bearing provides lateral support for the structure that applies the vertical load. This was dealt with by stabilizing the system using the horizontal cylinder that was used to apply the motion over the bearing. For the same reason, the test must be displacement-controlled.

The relation between the horizontal displacement and the rotation over the bearing is highly dependent on the eccentricity between the elastic line of the structure and the rotation center of the bearing. This distance is typically in the order of 1 m. If the eccentricity is small, the influence of the bearing friction on the dynamic properties of the bridge appears less pronounced than if the eccentricity is large [2]. In the tests performed this far, only one eccentricity has been studied, namely $e = 1$ m. The reason for this is that as the eccentricity increases, the bearing mechanisms approaches a linear sliding mechanism since the rotation for a given displacement amplitude is reduced. In the vertical section shown in Fig. 2, it is illustrated how the eccentricity of the bearing can be varied in the test rig.

Figure 4 shows one set of hysteresis loops obtained from the tests with the displacement amplitude 2 mm and an eccentricity of 1 m. The tests were performed twice,

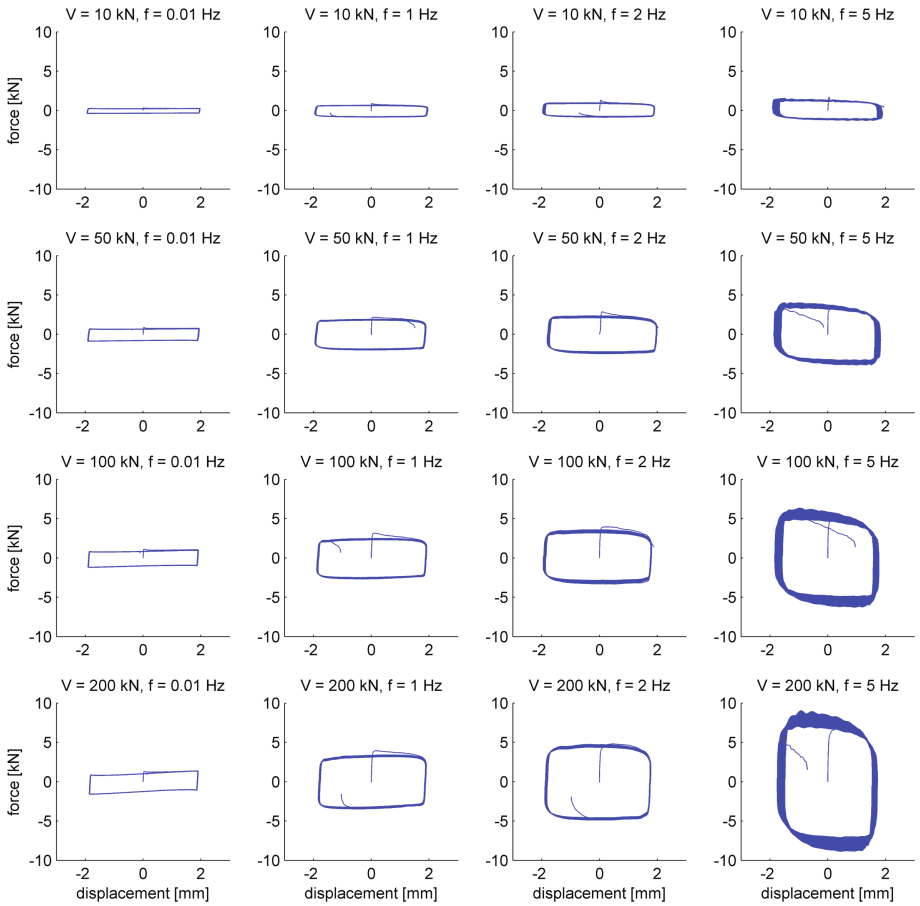

Fig. 4. Hysteresis loops for a uni-directional pot bearing.

directly after each other, for each parameter set (horizontal load frequency and vertical load), because the amount of break-away friction depends on the time between the tests (Fig. 5).

From the test performed by Dolce et al., we know how a linear sliding device based on a steel-PTFE contact behaves. The bearing has two features that differ from a linear sliding device; the rubber, which allows the sliding surface to rotate and a guide, which provides a uni-directional motion. The hysteresis loops of a linear sliding device are close to doubly symmetric (see Fig. 6.) if one ignores the break-away effect in the first cycle. The stick-slip behavior is not very strong. The results shown in Fig. 4 show that the rotation of the bearing leads to a small, approximately linear increase in the friction force, causing the loops to be sheared so that the part of the loop that resides in the first and the fourth quadrants move upwards, while the part of the loop that resides in the second and third quadrants move downwards. However, as the load frequency increases, the loops seem to be sheared in the opposite direction.

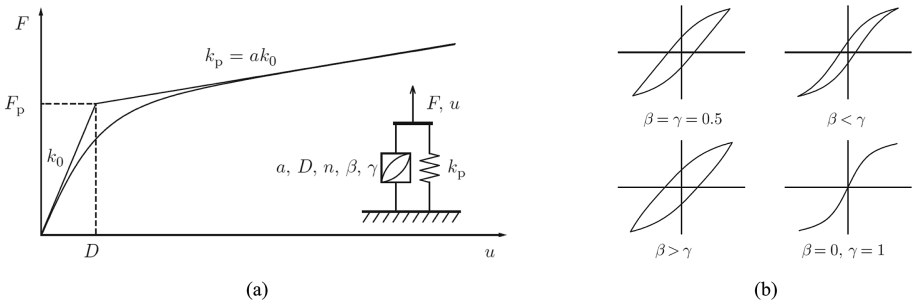

Fig. 5. The force-displacement relationship (a) and the loop shapes (b) of the Bouc-Wen model.

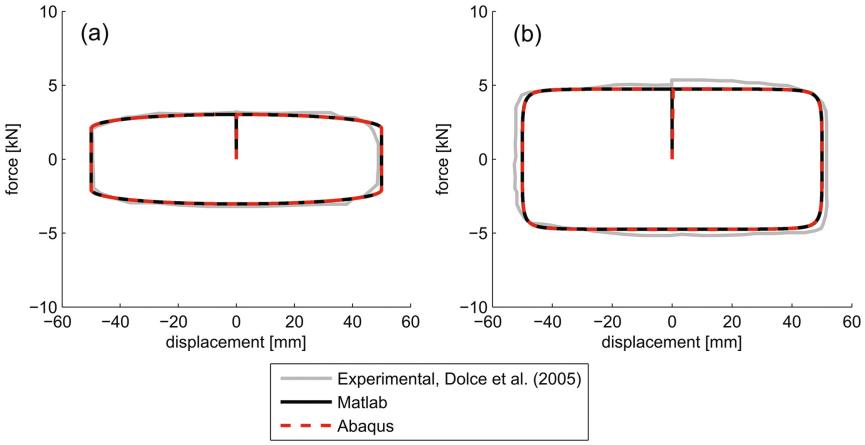

Fig. 6. Comparison between the Bouc-Wen-Dolce-model (black, solid lines: Matlab; red, dashed lines: Abaqus) and experimental results from Dolce et al. [7] (grey solid lines). (a) Maximum sliding speed 15 mm/s. (b) Maximum sliding speed 316 mm/s.

Increasing the load frequency increases the friction force, smoothens the shape of the loop and somewhere between 2 and 5 Hz, the effect of stick-slip becomes clear. However, since stick-slip is dependent on the flexibility of the sliding mechanisms and its surrounding structures, the observed stick-slip behavior must somehow be related to actual structural systems with pot bearings, i.e. this effect can be more or less pronounced in a bridge structure. As stick-slip is likely to increase wear, further studies along this line may improve bridge designs with respect to bearing maintenance.

At low sliding speeds, increasing the vertical load increases the friction force, the break-away friction and the slope of the plastic part of the hysteretic loops. The loops become sharper and the stick-slip becomes more apparent. At higher sliding speeds, assuming that the recorded loops are correct although the displacement amplitude does not reach the programmed value, the stick-slip effect is increased and the break-away friction becomes increasingly less pronounced.

4 Theoretical Modelling of Pot Bearings

Within this project, two types of theoretical models of pot bearings are studied; 3D finite element models are used to simulate the behavior of the bearings and to learn more about them and simple macro-elements are being developed in order to include the bearing mechanisms in models of structural systems. In the following, our progress in defining a macro element for bearing mechanisms is shortly described.

As the coefficient of friction is dependent on the sliding speed and the contact pressure, the classical models of friction i.e. the laws of Amonton and Coulomb need to be complemented to include these effects. The coefficient of friction decreases quite substantially with increasing contact pressure. Therefore a conservative model should consider the additional contact pressure from e.g. traffic loads. In modern railway bridges, the traffic load can be in the same order of magnitude as the dead weight.

Our own tests and the tests provided by Dolce et al. [7] clearly indicate that the difference between the static and the kinetic coefficients of friction give rise to break-away and stick-slip behavior (see for example [9] and the references therein). In the present context, it is assumed that the stick-slip effect can be neglected since it only causes some small ripples on the hysteresis loops, immediately after the sliding speed (or the force) changes sign. The effect of the break-away force would be to post-pone the motion slightly but typically, the horizontal reaction force resulting from a vertical load on a simply supported beam is considerably higher than the available friction force. As an example, consider the support moment M of a clamped beam with length L for a transversal point load P at the mid-point of the beam, $M = PL/4$. Given the eccentricity e, this moment (on the moveable end of the beam) can also be written $M = eF_\mu$, where F_μ is the friction force. In order for sliding to occur, we need $P(1 - 2\,\mu e/L) > 2\,\mu emg$. Here, m is the distributed mass of the beam and g is the gravitational constant. Clearly, since $e \ll L$ and $\mu \sim 0.1$, the influence of the external load is negligible. Furthermore, for short to medium span, single track railway bridges, the distributed mass $m \sim 20000$ kg/m. Assuming a coefficient of friction $\mu = 0.05$, the above reasoning gives $P > 2\,\mu emg \approx 2 \cdot 0.05 \cdot 1\ m \cdot 20000$ kg/m $\cdot$ 10 m/$s^2 = 20$ kN. Typical axle loads for passenger traffic on modern railways lie around 200 kN. Therefore, an additional break-away friction force of 20–30% will most likely have little effect. However, the dependency of the coefficient of friction on the sliding speed and the contact pressure seem to be highly important. The kinetic coefficient of friction can be modelled with an exponential function [10]

$$\mu = \mu_{\max} - (\mu_{\max} - \mu_{\min})e^{-\alpha v} \tag{1}$$

where $\mu_{\max}$ and $\mu_{\min}$ are the temperature and pressure dependent coefficients of friction at high and very low sliding speeds, respectively, α is a constant depending on temperature, pressure and the condition of the contact interface and v is the sliding speed. In the following, a generalization of the Bouc-Wen model, which accounts for the dependency on sliding speed and pressure, is proposed.

4.1 The Bouc-Wen Model

The Bouc-Wen model provides a convenient way of modelling hysteretic behavior. This model introduces an internal variable $z \in [-1, 1]$, which describes the hysteretic behavior. The internal variable is governed by a non-linear ordinary differential equation:

$$\dot{z} = \frac{\dot{u}}{D}[1 - (\beta + \text{sgn}(\dot{u}z)\gamma)|z|^n] \tag{2}$$

where $\beta + \gamma \neq 0$ and $n > 0$ are model parameters. In a single degree-of-freedom system based on the Bouc-Wen model, the force is given by

$$F = ak_0u(t) + (1 - a)Dk_0z(t) \tag{3}$$

Here, k_0 is the elastic stiffness, a is the ratio between the elastic stiffness and the plastic stiffness k_p and D is the plastic displacement limit.

4.2 A Generalization of the Bouc-Wen Model

The hysteretic behavior of the macro-elements is based on a generalization of the Bouc-Wen model. This generalization consists in including the effects of sliding speed and contact pressure in the Bouc-Wen model. For this purpose, we have been using data from Dolce et al. [7] and therefore, we have chosen to refer to this generalized Bouc-Wen model as the Bouc-Wen-Dolce model.

From the results of Dolce et al., we know that:

- The ratio between the elastic stiffness and the plastic stiffness $a = k_p/k_0 \approx 0$.
- $k_0 \gg k_p$.

If the initial stiffness k_0 is assumed to be fixed, the plastic limit displacement D will have to describe the coefficient of friction. These parameters are related to the plastic limit force $F_p = k_0D$ which in turn can be related to the friction force by

$$F_p = \mu(v, p) \cdot N = \mu(v, p) \cdot A_{PTFE} \cdot p \tag{4}$$

Thus,

$$D = \frac{F_p}{k_0} = \frac{\mu(v, p) \cdot A_{PTFE} \cdot p}{k_0} \tag{5}$$

We have implemented this in Matlab, using an explicitly integrated, single degree of freedom system and as a general 3D user-defined element in ABAQUS, with one Bouc-Wen element, i.e. a linear spring, a linear dashpot and a Bouc-Wen internal variable corresponding to each degree of freedom (3 translations and 3 rotations). A comparison with some of the data presented by Dolce et al. [7] is shown in Fig. 6 where we used $n = 1$, $\beta = 0.6$ and $\gamma = 0.4$, together with $a = 1 \cdot 10^{-12}$ and $k_0 = 30$ GN/m.

5 Discussion

This paper aimed at describing the current status of our project. We are beginning to finalize our laboratory tests and in terms of modelling, we have combined the data from Dolce et al. [7] with the friction model from Constantinou et al. [10] and the classical Bouc-Wen model. From the experimental results obtained this far, apart from the fact that more extensive tests on large bearings and also on other bearing types need to be performed, the following observations have been made; The shapes of the hysteresis loops do not vary so much for the studied contact pressures and sliding speeds; Break-away and stick-slip, i.e. effects related to static friction, do not seem very important in the context of studying the dynamic properties of structures. However, this needs to be further studied. When the laboratory tests have been completed, they will be described in a technical report and made public.

By using the Bouc-Wen-Dolce model as a starting point, the remaining steps in defining the sought model do not seem too distant. However, a number of issues remain to resolve in order to define a reliable model for practical purposes:

- Can the Bouc-Wen-Dolce model be adapted to the bearing tests without modification?
- Scale effects. It has to be ascertained that no relevant scale effects exist.
- Annual variations in temperature and freezing can be important factors in cold climates such as the Swedish.
- Other bearing types.
- The influence of the elasticity of the supports. The elasticity of the supports could lead to variations in the stick-slip behavior and reduces the sliding distance over moveable bearings.
- Validation of the model. Full scale testing of bridge structures at relevant amplitudes of vibration appears to be the most robust way to ascertain that the model is correct.

Acknowledgments. The authors gratefully acknowledge Tyréns AB and the Swedish Transport Administration for providing the financial support for this project.

References

1. Rebelo, C., Simões Da Silva, L., Pircher, M.: Dynamic behavior of twin single-span ballasted railway bridges—field measurements and modal identification. Eng. Struct. **30**(9), 2460–2469 (2008)
2. Ülker-Kaustell, M., Karoumi, R.: Application of the continuous wavelet transform on the free vibrations of a steel-concrete composite railway bridge. Eng. Struct. **33**, 911–919 (2011)
3. Ülker-Kaustell, M., Karoumi, R.: Influence of rate-independent hysteresis on the dynamic response of a railway bridge. Int. J. Railw. Transp. **1**(4), 237–257 (2013)
4. Ülker-Kaustell, M.: Essential modelling details in dynamic FE-analyses of railway bridges. TRITA-BKN Bulletin 120, KTH, Royal Institute of Technology (2013)

5. Bouc, R.: Forced vibration of mechanical systems with hysteresis. In: Proceedings of the Fourth International Conference on Nonlinear Oscillations, Prague, 5–9 September 1967
6. Wen, Y.K.: Method for random vibration of hysteretic systems. J. Eng. Mech. Div. ASCE **102**(2), 249–263 (1976)
7. Dolce, M., Cardone, D., Croatto, F.: Frictional behavior of steel-PTFE interfaces for seismic isolation. Bull. Earthq. Eng. **3**, 75–99 (2005)
8. Lomiento, G., Bonessio, N., Benzoni, G.: Friction model for sliding bearings under seismic excitation. J. Earthq. Eng. **17**(8), 1162–1191 (2013)
9. Nikfar, F., Konstantinidis, D.: Effect of the stick-slip phenomenon on the sliding response of objects subjected to pulse excitation. J. Eng. Mech. ASCE (2016). doi:10.1061/(ASCE)EM.1943-7889.0001183
10. Constantinou, M.C., Mokha, A., Reinhorn, A.M.: PTFE bearings in base isolation: modelling. J. Earthq. Eng. **116**(2), 455–472 (1990)

Full-Scale Dynamic Testing of a Railway Bridge Using a Hydraulic Exciter

Andreas Andersson[1,2(✉)], Johan Östlund[1,3], Mahir Ülker-Kaustell[1,3], Jean-Marc Battini[1], and Raid Karoumi[1]

[1] Division of Structural Engineering and Bridges, Royal Institute of Technology, Stockholm, Sweden
adde@kth.se
[2] The Swedish Transport Administration, Solna, Sweden
[3] Tyréns AB, Stockholm, Sweden

Abstract. This paper presents a full-scale dynamic testing on a simply supported railway bridge with integrated end-shields, by using a hydraulic exciter. Experimental frequency response functions are determined based on load controlled frequency sweeps. Apart from accurate estimates of natural frequencies, damping and mode shapes, the experimental testing also gives valuable information about the dynamic characteristics at resonance and amplitude dependent nonlinearities. Numerical models are used to simulate the dynamic response from passing trains which is compared to experimental testing of similar train passages. The results show that the bridge deck is partially constrained due to the interaction between the end-shields and the wing walls with the surrounding soil. Measurements at the supports also show that the flexibility of the foundation needs to be accounted for. An updated numerical model is able to accurately predict the response from passing trains. The response is lower than that predicted from the initial simulations and the bridge will fulfil the design requirements regarding vertical deck acceleration.

Keywords: Railway bridge · Dynamics · Full-scale test · Hydraulic exciter · Frequency response function

1 Introduction

The research field of railway bridge dynamics has gained increased interest due to the planning and construction of new high-speed lines around the world. For bridges on conventional lines, dynamic effects are commonly accounted for by factoring the static train load effect with a constant dynamic amplification factor. On high-speed lines however, long trains with equal axle spacing may induce resonant loading, which is not accounted for by the simplified amplification factors and normally requires extensive dynamic analyses of passing trains. Resonant loading can result in riding discomfort, track de-alignment, increased stresses in structural components and in worst case derailment or structural failure. Even for seemingly simple bridges, the dynamic manner of action may differ significantly compared to the corresponding static behavior. Experimental in-situ testing of existing bridges serve as an important input when developing models for more accurate predictions of the dynamic response.

© Springer International Publishing AG 2018
J.P. Conte et al. (eds.), *Experimental Vibration Analysis for Civil Structures*,
Lecture Notes in Civil Engineering 5, https://doi.org/10.1007/978-3-319-67443-8_30

In this paper, full-scale dynamic testing on a simply supported railway bridge is presented. A load-controlled hydraulic exciter is used to determine experimental frequency response functions (FRF), from which natural frequencies, damping and mode shapes are estimated. Numerical models are developed and the experimental data is used in a model updating procedure based on the experimental FRFs.

2 Experimental Testing

The case study bridge was tested during an experimental campaign that was conducted in October 2015. The results serve as input to an ongoing research project with the aim of better understanding the dynamic behavior of railway bridges, especially focusing on soil-structure interaction. The bridge is located along the Bothnia Line, a single track railway line in North of Sweden. The bridges along the line are designed for both freight trains (33 ton/axle) and high-speed trains (HSLM) with a design speed of 250 km/h.

2.1 Bridge Properties and Instrumentation

The case study bridge is designed as a simply supported concrete slab bridge with integrated end-shields. The span length is 24 m and the over-sail 1.7 m. A photo of the bridge during passage of an X62 commuter train is shown in Fig. 1. The end-shields are resting directly on the embankment, hence resulting in significant soil-structure interaction. This is a rather common bridge type in Sweden and it is often considered cost-effective to integrate the end-shields with the bridge deck instead of the abutment.

a) b)

Fig. 1. View of the case study bridge, (a) during train passage, (b) details of the exciter.

The load-controlled hydraulic exciter that was used is shown in Figs. 1b and 2. It consists of a 50 kN MTS hydraulic cylinder mounted on a 0.9 × 0.9 m support plate. It extends vertically to the bridge soffit by means of a module truss system. The hydraulic cylinder is connected to a 120 L oil pump with an integrated diesel engine. An MTS FlexTest SE controller assures a constant amplitude force, using a load cell on top of the truss as input. The controller is able to compensate for flexibility in the

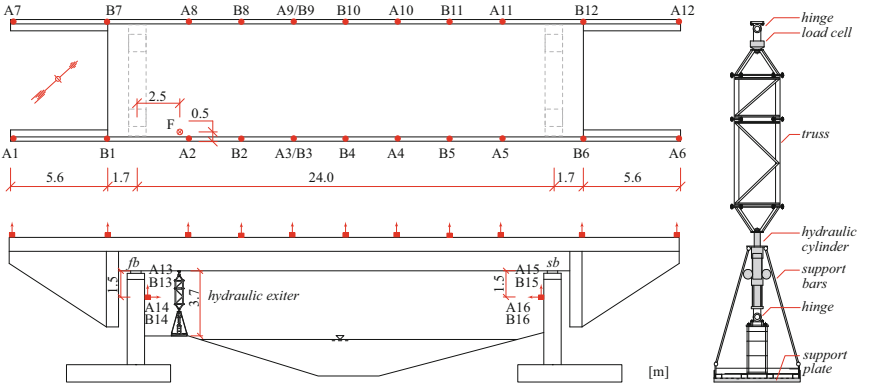

Fig. 2. Instrumentation illustrating the position of accelerometers in setup A (A1–A16) and setup B (B1–B16). Details of the hydraulic bridge exciter are shown to the right.

system, e.g., due to the truss system or the foundation. During the in-situ tests, the system was shown to work as intended up to at least 50 Hz. More details of the exciter system are found in [1].

The instrumentation layout is shown in Fig. 2. A total of 16 uniaxial SiFlex SF1500S accelerometers were used, distributed in two setups with notation A and B. Accelerometer in position 1–12 were mounted vertically on the edge beam and 13–16 centric on the support walls. Data was collected using a HBM MGCPlus data acquisition system. A sample frequency of 1200 Hz and an analogue LP-filter at 300 Hz was used.

The hydraulic exciter was positioned 2.5 m from the side with fixed bearing (*fb*) and 0.5 m from the edge. Tests with load amplitudes of 5, 10 and 20 kN were performed, to study potential amplitude-dependent nonlinearities. In each test, the load amplitude was held constant and a linear frequency sweep was performed at a sufficiently small rate to reach steady-state response. A constant pre-load larger than the dynamic load amplitude was applied, to assure that the exciter system was in compression at all times.

2.2 Forced Vibration Tests

A Fourier transform of the measured acceleration $a(t)$ and input force $F(t)$ results in complex-valued $A(\omega)$ and $F(\omega)$, from which the accelerance $H(\omega)$ is computed using to Eq. (1). The accelerance is hereafter referred to as the FRF and presented in m/s^2/kN.

$$\mathbf{A}(\omega) = \mathbf{H}(\omega)\mathbf{F}(\omega) \tag{1}$$

Within the studied frequency range, two bending modes and one torsional mode is detected. The FRF based on sensor A3 and A9 is shown in Fig. 3. By using the pair of sensors on each side of the bridge, the bending component is given by (A3 + A9)/2 and the torsional component by (A3 − A9)/2. This is especially useful when separating the second bending mode with the first torsional mode. FRFs with different load amplitudes are shown in Fig. 4. Increased load amplitude results in lower natural frequency

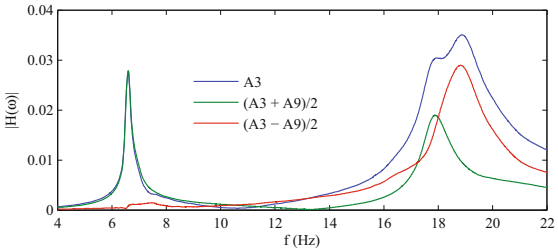

Fig. 3. Experimental FRF from sensor A3 and A9, load amplitude F = 5 kN.

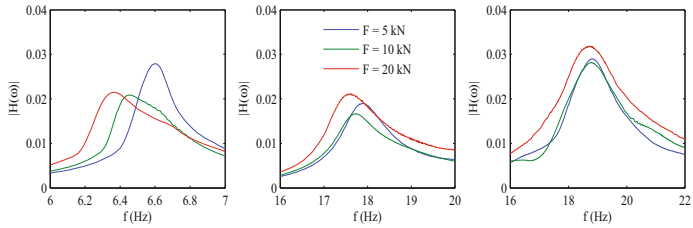

Fig. 4. Frequency response functions for sensor A3 and A9 for different load amplitudes.

and lower vibration amplitude, especially for the first mode. This may be due to decreased stiffness and increased damping. It shall be noted that for the case of F = 20 kN, the hydraulic exciter was positioned at 3.4 m from the support instead of 2.5 m, hence the FRFs are not fully comparable.

The mode shapes presented in Fig. 5 are estimated by combining setup A and B. At the supports, the bridge is assumed to move corresponding to sensor 13 and 15. Since the support sensors are mounted centric on the support wall, torsional effects are not included. It is clearly indicated that the end-shields contribute in restraining the end of the bridge deck.

The modal parameters estimated from the forced vibration tests are summarized in Table 1. The critical damping ratio is estimated using the Half-Power Bandwidth method. Similar to Fig. 4, it is seen that increased load amplitude results in decreased natural frequency and increased damping. It is further noted that the critical damping is significantly larger for the second bending mode and the first torsional mode, possibly partly due to increased soil-structure interaction.

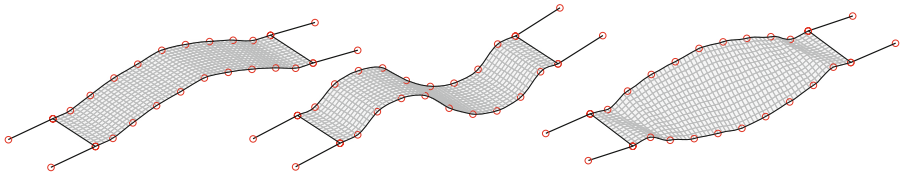

Fig. 5. Estimated mode shapes, (a) 1st bending, (b) 2nd bending, (c) 1st torsional mode. Based on experiment with F = 5 kN.

Table 1. Estimated modal parameters.

F (kN)	f_1 (Hz)	ζ_1 (%)	f_2 (Hz)	ζ_2 (%)	f_3 (Hz)	ζ_3 (%)
5	6.6	1.5	17.9	2.7	18.8	3.9
10	6.5	2.4	17.7	2.9	18.8	4.5
20	6.4	2.8	17.6	3.4	18.7	4.9

2.3 Train Passages

In addition to the forced vibration tests, the response from passing trains was recorded. Figure 6 shows the X62 train, also depicted in Fig. 1. The train consists of 10 axles in 5 bogies; the axle load is about 170 kN. The speed at the bridge site was estimated to 185 km/h. Since the train is rather short and the axle distances vary, full resonance behavior is not expected.

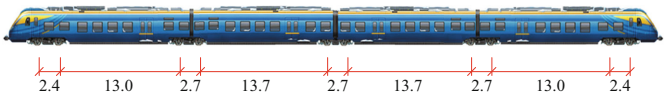

Fig. 6. Axle distances for commuter train X62.

The time response of the acceleration at position A3/A9 is shown in Fig. 7a. The first axle enters the bridge at about 0.5 s and the last axle leaves at about 2.5 s. Both bending and torsional modes are excited during train passage, but the following free vibrations are governed by the first bending mode. The resonance speed is calculated according to Eq. (2), where n_0 is the natural frequency and d the axle distance. For the first and the last car, the center distance between the bogies is about 15.5 m, corresponding to a critical speed of 185 km/h when n_0 = 6.6 Hz and i = 2. For the inner bogies however, the center distance is 16.4 m, resulting in a corresponding critical speed of 195 km/h. The torsional mode is likely excited by the axle distance within a bogie, d = 2.7 m and n_0 = 18.8 Hz gives a critical speed of 183 km/h.

$$v_{cr} = n_0 \lambda, \lambda = d/i, i = 1, 2, \ldots \tag{2}$$

In dynamic simulations where the train is idealized with moving point loads, the resonant response is often governed by the fundamental mode of vibration. Also, the design limits for vertical deck acceleration on ballasted tracks is often limited to a frequency range of 30 Hz. In Fig. 7b however, the peak accelerations from sensor A3 and A9 are presented as function of the cut-off frequency. An increased frequency range from 30 to 300 Hz results in a ten-fold increase in acceleration. This is probably due to high frequency components of the track and the train.

Based on the free vibration after the train passage, the critical damping for the first bending mode is estimated using the logarithmic decrement method. Based on consecutive cycles of vibration, both the natural frequency and critical damping can be expressed as function of the vibration amplitude. The results are shown as solid lines in

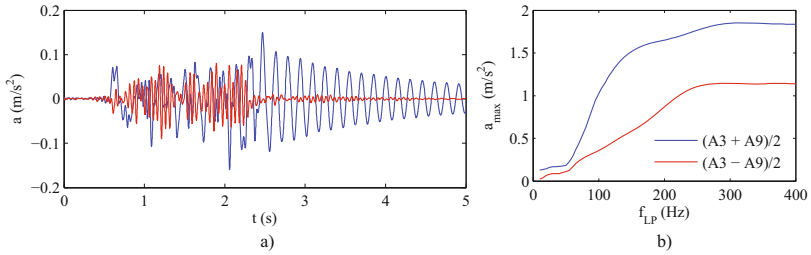

Fig. 7. Time response of vertical deck acceleration during train passage, (a) bending and torsional component of sensor A3 and A9 at 30 Hz low-pass filter, (b) influence of the filter limit on peak acceleration.

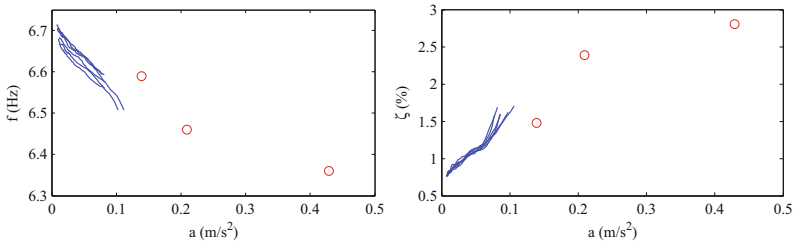

Fig. 8. Natural frequency and damping for the first bending mode as function of the vibration amplitude. Solid lines are based on free vibrations after train passage; circles are based on forced vibration tests.

Fig. 8, based on six X62 train passages running at similar speed, the circles indicate results from the forced vibration tests. The free vibration response show the same trend as the forced vibration tests with different amplitudes; decreased frequency and increased damping as a result of increased vibration amplitudes.

3 Numerical Results

In the following section, two different numerical models of the bridge are presented. The simplest approach is an SDOF-model with the experimental natural frequencies and critical damping as input. The second model is based on 2D beam theory where the boundary conditions are updated to fit the experimental FRFs. In both cases, only the first and second bending modes are included.

3.1 SDOF-Model

Although the mode shapes in Fig. 5 indicate partially constraint boundary conditions at the end-shields, a sine mode shape according to Eq. (3) gives a correlation of MAC > 0.98 and is therefore deemed sufficiently accurate. The modal mass $M = mL/2$ using Eq. (4), where m = 30 ton/m based on design drawings. The stiffness K and

damping C is obtained from Eqs. (5) and (6), using the experimental circular frequency ω_n and experimental critical damping ζ_n. Finally, the FRF for sensor j at position x_j due to a harmonic force at x_F is calculated according to Eq. (7).

$$\phi_n = \sin(n\pi x/L) \tag{3}$$

$$M_n = m\int_0^L \phi_n^2 dx \tag{4}$$

$$K_n = M_n\omega_n^2 \tag{5}$$

$$C_n = 2\zeta_n\sqrt{K_n M_n} \tag{6}$$

$$\mathbf{H}_j(\omega) = \sum_{n=1}^{modes} \frac{F(\omega)\phi_n(x_F)}{K_n} \frac{-\boldsymbol{\omega}^2\omega_n^2}{\omega_n^2 - \boldsymbol{\omega}^2 + 2i\zeta_n\boldsymbol{\omega}\omega_n}\phi_n(x_j) \tag{7}$$

3.2 2D Beam Model

The second model is based on a 2D Euler-Bernoulli beam on flexible supports, as depicted in Fig. 9. The system is discretized using a finite element approach with an element size of 0.1 m. The end-shield is assumed rigid and included as a lumped nodal mass m_1 = 90 ton at each end of the bridge. The over-sail L_1 = 1.7 m and the span length L = 24 m. The area moment of inertia I = 1.7 m^4 based on the geometry from the design drawings. The vertical support has a constant stiffness k_v and damping c_v. The interaction between the end-shield and the embankment is modelled with a vertical support k_{v1}, c_{v1} as well as a rotational support with k_r and c_r. Both supports are assumed to have the same boundary conditions. The concrete deck is assigned a constant structural damping ζ_c = 0.5% using the stiffness matrix K_c of the deck in Eq. (8), motivated by the damping of plain concrete. The remaining damping in the system is included by the boundary conditions.

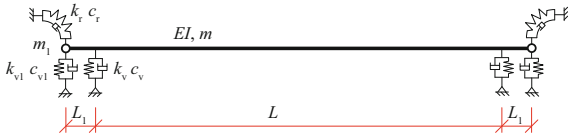

Fig. 9. 2D Euler-Bernoulli beam on elastic supports, with span length L and over-sail L_1.

Based on the assembled mass matrix M, damping matrix C and stiffness matrix K, the steady-state displacement x at each sensor position is obtained by solving Eq. (9) at each frequency ω. The FRF is then obtained using Eq. (10).

$$\mathbf{K}^* = \mathbf{K}_c(1 + 2i\zeta_c) \tag{8}$$

$$\mathbf{F}(\omega) = (-\omega^2\mathbf{M} + i\omega\mathbf{C} + \mathbf{K})\mathbf{x}(\omega) \tag{9}$$

$$\mathbf{H}(\omega) = \mathbf{x}(\omega)\boldsymbol{\omega}^2 \tag{10}$$

3.3 Model Updating

The pattern-search optimization algorithm available in MATLAB is used when updating the 2D beam model. The experimental FRFs H_{exp} are compared with the simulated counterpart H_{mod} using a shape correlation function χ_{s} and amplitude correlation function χ_{a} according to Eq. (11) [2]. The correlation functions $\chi \in \{0, 1\}$ where 1 is perfect correlation. The objective function is defined according to Eq. (12).

The updated parameters are presented in Table 2. Both the mass and the Young's modulus of the deck are in good agreement with expected values. The model is updated within the range 4–23 Hz and hence assuming constant parameters within that interval. The resulting correlation functions span from 0.850 to 0.997 indicating an overall good fit. Based on the results in Table 2, the updated model suggests that the end-shield is mainly constraint by a rotational stiffness k_{r}.

$$\chi_s = \frac{\left|\mathbf{H}_{exp}(\omega)^H\mathbf{H}_{mod}(\omega)\right|^2}{(\mathbf{H}_{exp}(\omega)^H\mathbf{H}_{exp}(\omega))(\mathbf{H}_{mod}(\omega)^H\mathbf{H}_{mod}(\omega))} \tag{11a}$$

$$\chi_a = \frac{2\left|\mathbf{H}_{exp}(\omega)^H\mathbf{H}_{mod}(\omega)\right|}{(\mathbf{H}_{exp}(\omega)^H\mathbf{H}_{exp}(\omega)) + (\mathbf{H}_{mod}(\omega)^H\mathbf{H}_{mod}(\omega))} \tag{11b}$$

$$f_{obj} = \sum_{j=1}^{sensors} \left(1 - \chi_{s,j}\right)^2 + \left(1 - \chi_{a,j}\right)^2 \tag{12}$$

A comparison between the experimental FRF, the SDOF model based on experimental input and the updated 2D beam model is shown in Fig. 10. The SDOF-model is found to be in even better agreement than the updated 2D beam model. The reason is that the SDOF-model is based on experimental natural frequencies and damping for

Table 2. Parameters for the 2D beam model, based on a model updating.

Bridge			Support stiffness			Support damping		
E	33.3	GPa	k_{v}	6.3	GN/m	c_{v}	18.6	MNs/m
m	29.6	ton/m	k_{v1}	7.4	GN/m	c_{v1}	5.3	MNs/m
			k_{r}	278	GNm/rad	c_{r}	945	MNms/rad

each mode, whereas the 2D beam model is based on constant boundary conditions for the whole frequency range. If instead using the optimization algorithm within a narrow frequency band for each mode, different parameters for the boundary conditions may be found. This would imply that the boundary conditions are frequency dependent, likely due to the dynamic characteristics of the soil. Further improvements involve coupling impedance functions for soil-structure interaction at the support and the end-shield with the bridge deck, using similar approach as reported in [3]. This would enable a model updating based soil parameters, e.g. shear wave velocity, instead of the discrete springs and dashpots.

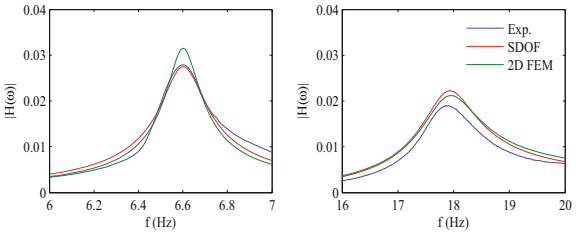

Fig. 10. Frequency response function, comparison between models and experiment, bending component of sensors A3/A9.

The response due to an X62 train running at 185 km/h is shown in Fig. 11. The 2D beam model is found to be in good agreement with the experimental results. The response is mainly governed by the first bending mode, as shown in Fig. 11b. It should be noted that the constraint due to the end-shields are of great importance. A corresponding simply supported beam would give $f_1 = 3.8$ Hz and $f_2 = 15.1$ Hz, resulting in significantly lower resonance speed for the train.

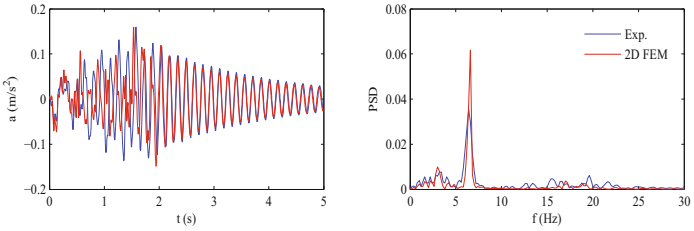

Fig. 11. Vertical deck acceleration based on sensor A3/A9 during passage of an X62 train at 185 km/h.

4 Conclusions

From the presented work on the case study bridge, the following is concluded:

- Using the hydraulic exciter, experimental FRFs are obtained with high accuracy.
- Accurate experimental estimates of natural frequencies, damping ratios and mode shapes are obtained.
- The natural frequencies and damping ratios are found to be amplitude dependent.
- The closely spaced second bending mode and first torsional mode are uncoupled and can be separated.
- The end-shields provide significant constraints, resulting in increased natural frequency and therefore increased critical resonance speed.
- Based on experimental modal parameters, a simple SDOF-model shows good agreement with experimental results.
- Good agreement is also found using a 2D beam model, where the boundary conditions are obtained using an optimization algorithm.

Acknowledgements. The development of the hydraulic exciter and the experimental campaign was performed by the first author together with Laboratory technicians *Mr. Stefan Trillkott* and *Mr. Claes Kullberg*, assisted by *Ph.D. student Hesham Elgazzar* and *Ph.D. student Abbas Zangeneh Kamali*. The work was co-funded by the Swedish Transport Administration and the KTH Railway Group.

References

1. Andersson, A., Ülker-Kaustell, M., Borg, R., Dymén, O., Carolin, A., Karoumi, R.: Pilot testing of a hydraulic bridge exciter. In: EVACES 2015. Empa, Dübendorf, Switzerland (2015)
2. Grafe, H.: Model updating of large structural dynamics models using measured response functions. Doctoral Thesis, Imperial College, London, England (1998)
3. Östlund, J.: Soil-structure interaction of end-frames for high-speed railway bridges. Master Thesis, Royal Institute of Technology, Stockholm, Sweden (2016)

A Practical Multi-cross-line Model for Simulating Nonlinear Cyclic Behavior of Reinforced Concrete Shear Wall in Super High-Rise Buildings

Baoyin Sun[1], Quan Gu[2(✉)], Peizhou Zhang[1], and Jinping Ou[1,3]

[1] School of Civil Engineering, Dalian University of Technology, Dalian, Liaoning, People's Republic of China
[2] School of Architecture and Civil Engineering, Xiamen University, Xiamen, Fujian, People's Republic of China
quangu@xmu.edu.cn
[3] School of Civil Engineering, Harbin Institute of Technology, Harbin, Heilongjiang, People's Republic of China

Abstract. Reinforced concrete (RC) shear walls are one of the most important components in tall buildings for resisting wind or earthquake loads. However it remains a challenging task to develop a model that can efficiently and accurately simulate the complicated nonlinear cyclic behaviors that the RC shear wall exhibits, and satisfactorily meet the requirement of the numerical stability for nonlinear dynamic analysis of super high-rise buildings. In this background, the paper presents a novel practical shear wall material model, namely, the multi-cross-line model (MCLM). The MCLM combines the advantages of accuracy in the existing micro models and the numerical stability of the macro models, therefore providing a practically ideal solution for such challenging problems. The newly developed MCLM has been implemented into a general finite element software platform, OpenSees. The model has been validated by using a RC shear wall specimens tested in laboratory and a realistic 32-story high-rise RC frame-shear wall building under cyclic loading conditions. The MCLM can accurately simulate the experimental results, simulating the main features of the stiffness reduction, strength deterioration and pinch effects. In addition, the Newton-Raphson (NR) process using MCLM converges systematically, demonstrating the good numerical stability of this model. The MCLM provides a practically important simulation tool for nonlinear analysis of realistic high-rise buildings.

Keywords: RC shear wall · Nonlinear finite-element model · High-rise building · Multi-cross-line model · Shell element

1 Introduction

Reinforced concrete (RC) shear walls play an essential role in lateral load resistance of high-rise buildings, e.g., wind or earthquake loads. Therefore, it is of significant importance to accurately and efficiently simulate the nonlinear behavior of the RC shear

© Springer International Publishing AG 2018
J.P. Conte et al. (eds.), *Experimental Vibration Analysis for Civil Structures*,
Lecture Notes in Civil Engineering 5, https://doi.org/10.1007/978-3-319-67443-8_31

walls during the seismic or wind analysis for tall buildings. In the past few decades, great efforts have been taken and various models have been developed for this purpose. These models can be classified into two categories, namely, micro-models and macro-models. The micro-model studies the constitutive behaviors of the RC share wall at material level (e.g., at Gauss point of a finite element), and the cracked concrete is simulated using continuous smeared-crack models; while the macro-models simulate the RC shear wall using a set of discrete components, e.g., trusses, frames and springs. Among the micro-models, the compression field theory (CFT) [1] and modified compression field theory (MCFT) [2] are widely used, in which the shear resistance is provided by concrete struts along the principal stress directions (i.e., the crack grow direction and its normal direction), and the compressive strength of the concrete struts deteriorates with the increasing tensile strain normal to the them for simulating the strength softening effect. Another set of widely used micro-models are presented by Hsu and coworkers, including the rotating-angle softened truss models (RA-STM) [3–6], the fixed-angle softened truss model (FA-STM) [7–9], the softened membrane model (SMM) [10, 11] and the cyclic softened membrane model (CSMM) [12–15]. These models assume that the direction of cracks is perpendicular to the direction of the principal tensile stress of concrete (RA-STM) or of the reinforced concrete (FA-STM, SMM, CSMM), while the state-dependent Poisson's effect (i.e., transformation between the biaxial strains and uniaxial strains) is ignored (RA-STM, FA-STM) or studied in great detail using a time-varying Hsu/Zhu ratio (SMM, CSMM). The current micro-models are able to accurately capture the complicated nonlinear behaviors (e.g., stiffness reduction, strength deterioration and pinch effects) of the shear walls, however cannot guarantee the numerical stability of the Newton-Raphson (NR) process when the models are used in large scale nonlinear analysis of realistic tall buildings. Particularly, the iterations used to find the crack grow directions (i.e., the principal stress direction) usually are computational expensive, therefore reducing the computational efficiency.

The second class of models is macro-models. Among these models, the three-vertical-line-element model (TVLEM) [16] simulates the bending and shearing behavior of shear panels using three vertical line (truss) elements, one horizontal truss element and one rotational spring element between two infinitely-rigid beams at top and bottom floor levels. The multi-vertical-line-element model (MVLEM) [17] employs a set of vertical truss elements and a horizontal spring element connecting with two rigid beams at the top and bottom floor levels. The panel-wall macro element (PWME) [18] modifies the TVLEM by replacing the horizontal and rotation truss elements with a plane element. The truss model (TM) [19] discretizes the RC shear wall components into a set of horizontal, vertical and diagonal truss elements, and the strength softening of the diagonal trusses is considered in the similar way as MCFT. Panagiotou and coworkers [20, 21] presented a cyclic beam-truss model for nonplanar reinforced concrete walls, in which a set of nonlinear Euler-Bernoulli fiber-section beam elements are used to model the mechanical behaviors along the vertical direction and nonlinear trusses for horizontal and diagonal directions (the softening effect is simulated similarly with the TM). The macro-models can simulate the nonlinear behavior of shear walls with reasonable accuracy and meet the requirement of numerical stability for nonlinear analysis, therefore is able to be used for large scale nonlinear analysis of high-rise RC buildings. However since the truss and beam

components are not physically based, it is not easy to build the FE model and determine the model parameters (e.g., determine the locations and areas of the trusses). Furthermore the micro behavior (e.g., micro-cracking or strain localization) cannot be simulated accurately unless the mesh size is small enough, which may lead to prohibitive computational cost.

Therefore, in spite of the various RC shear wall models in literatures, it remains a challenging task to accurately, efficiently and robustly simulate the complicated nonlinear behaviors of RC shear walls in super high-rise buildings. In this background, the paper presents a novel practical shear wall model, i.e., multi-cross-line model (MCLM), that is accurate, efficient and stable, providing a practically ideal solution for such challenging problems. The MCLM combines the concepts of micro and macro models by simulating the stress-strain relationship at "micro" material level (e.g., at a Gauss point) using a set of "macro" concrete bars or steel bars, and the two-dimensional (2D) membrane stress resultants at a material point are computed using an "equivalent stress" based on the forces of the bars. Furthermore, in order to apply MCLM to realistic three dimensional (3D) problems, a modified shell element is presented that simulates the in-plane nonlinear shearing behavior using the MCLM and out-plane force-deformation responses using linear elastic models. The newly developed MCLM has been implemented into a general finite element software platform, OpenSees (Open System for Earthquake Engineering Simulation), an open source finite element analysis software used to model structural systems and simulates their earthquake responses [22–24]. The efficiency and numerical stability of the newly developed MCLM is validated by using two RC shear wall specimens tested in laboratory and a realistic 32-story high-rise RC frame-shear wall building under cyclic loading conditions.

The novel MCLM has distinguishing features particularly for nonlinear seismic analysis of super high-rise buildings: (1) It is robust. The Newton-Raphson (NR) process using MCLM converges systematically, demonstrating the good numerical satiability of the model. (2) It is accurate and efficient. The main features of shear-flexural behavior of RC shear walls (e.g., stiffness reduction, strength deterioration and pinch effects) can be simulated with reasonable computational cost. (3) It is practical. The model setup and parameter selection are relatively easy, making the model practically useful in large scale nonlinear analysis of realistic super high-rise buildings.

2 The Multi-Cross-Line Model (MCLM)

2.1 Model Assumptions

The MCLM presented herein is a 2D plane stress model based on following assumptions:

(i) The 2D membrane stress resultant is computed by combining stresses from two uncoupled layers, i.e., a concrete layer and a reinforcing steel layer. The slippage between reinforcing bars (i.e., rebars) and concrete is not considered (see Fig. 1a). (ii) For the concrete layer, the shear stress is modeled by two physical diagonal concrete bars perpendicular to each other (Fig. 1b). The compressive strength of one concrete bar is reduced, or "softened", as the tensile strain of the other bar (normal to

this bar) increases. The horizontal and vertical normal stresses are computed independently based on the forces of a horizontal and a vertical concrete bars, respectively. (iii) The 2D stress of steel layer is computed from the forces of the rebars using a 1D smeared steel material model.

The MCLM can be considered as a modification or extension of existing micro models (e.g., CSMM model), however employs a set of "physically existing" discrete concrete bars or steel bars to get equivalent shear and normal stresses. The diagonal bars contribute only to shear resistance (i.e., have no contribution to normal stress), while the horizontal and vertical bars contribute to both normal stresses and shear stress. It is important to mention that the MCLM based on the above assumptions has distinguished features by combining the advantages of existing micro and macro models. Firstly, it has an advantage in macro models, i.e., the numerical stability. The MCLM employs four cross concrete bars to simulate concrete behaviors. The concrete bars do not rotate, therefore it avoids the rotation-induced stability problems, e.g., the possible non-convergence of NR process because that the principal stress angle changes sigh when close to horizontal or vertical directions, or because that the difference of the principal directions between the previous time step and current trial step is finite which leads to an abrupt jump of stress. Secondly, the MCLM is able to simulate the main features of shear-flexural behavior of RC shear walls (e.g., stiffness reduction, strength deterioration and pinch effects). The 'strength softening' is simulated using two coupled diagonal concrete bars, and the relationship between normal and shear stresses are considered explicitly using a correction factor. In addition, the MCLM can simulate the nonlinear behaviors or local damages of shear walls using moderate-fine mesh and at an acceptable computational cost, therefore is practically efficient. Thirdly, MCLM is a micro model built at material level describing the stress-strain relationships (as opposed to the macro model using a set of discretized beam or truss components), the FE model based on MCLM is relatively easy to build and the model parameters can be directly determined by experiments. There is no need to specify the parameters for each discrete component as in macro models.

2.2 Model Descriptions

According to the above assumptions, the stress resultant at a material (Gauss) point of a RC shear wall (i.e., the horizontal, vertical and shear stresses $[\sigma_l\ \sigma_t,\ \tau_{lt}]$ in Fig. 1(a) is calculated from two uncoupled layers, i.e., the stresses of reinforcing steel layer (i.e., $[\sigma_l^s,\ \sigma_t^s,\ \tau_{lt}^s]$ in Fig. 1(b) and the concrete layer (i.e., $[\sigma_l^c,\ \sigma_t^c,\ \tau_{lt}^c]$ in Fig. 1(c). The subscripts l and t denote the horizontal and vertical directions respectively, and the superscripts s and c denote the steel and concrete respectively. For the reinforcing steel layer, the stress is computed by transforming the stress of uniformly distributed reinforcement calculated using 1D smeared steel material model (i.e., $\rho_1 f_{\theta_{s1}}^s$ and $\rho_2 f_{\theta_{s2}}^s$ in Fig. 1b, where ρ_i and $f_{\theta_{si}}^s$ denote, respectively, the reinforcement ratio and stress along the i$^{\text{th}}$ direction, i = 1, 2). For the concrete layer (Fig. 1d), the shear stress τ_{lt}^c (Fig. 1e) is calculated using two cross diagonal bars perpendicular to each other and having 45 degree with horizontal, which are assumed to have no contribution to the normal stresses (i.e., setting $\sigma_t^{c'} = \sigma_l^{c'} = 0$ in Fig. 1e). The compressive strength of one diagonal bar is reduced by

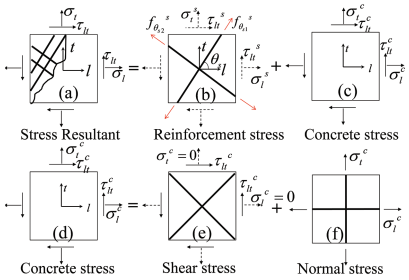

Fig. 1. The multi-cross-line model

tensile strain of the other bar. The normal stresses are calculated using two uncoupled concrete bars along normal directions (i.e., σ_t^c and σ_l^c in Fig. 1f).

2.3 Constitutive Equation of the MCLM

The 2D membrane stress resultant is computed by combing the stresses of concrete layer and reinforcing steel layer (see Fig. 1a–c), i.e.,

$$\begin{Bmatrix} \sigma_l \\ \sigma_t \\ \tau_{lt} \end{Bmatrix} = \begin{Bmatrix} \sigma_l^s \\ \sigma_t^s \\ \tau_{lt}^s \end{Bmatrix} + \begin{Bmatrix} \sigma_l^c \\ \sigma_t^c \\ \tau_{lt}^c \end{Bmatrix} \tag{1}$$

The stress of steel layer: the stress of steel can be computed from the stress of each steel bar using the uniform distribution assumption, as,

$$\begin{Bmatrix} \sigma_l^s \\ \sigma_t^s \\ \tau_{lt}^s \end{Bmatrix} = \mathbf{T}(-\theta_{s1}) \begin{Bmatrix} \rho_1 f_{\theta_{s1}}^s \\ 0 \\ 0 \end{Bmatrix} + \mathbf{T}(-\theta_{s2}) \begin{Bmatrix} \rho_2 f_{\theta_{s2}}^s \\ 0 \\ 0 \end{Bmatrix} \tag{2}$$

where $\mathbf{T}(\theta_{si})$ (i = 1, 2) is the coordinate transformation matrix, and θ_{si} (i = 1, 2) is the angle of the direction of the i$^{\text{th}}$ reinforcing steel with respect to horizontal direction ($l-$direction). The parameter ρ_i (i = 1, 2) in Eq. (2) is the reinforcement ratio along the i^{th} steel direction, and $f_{\theta,i}^s$ (i = 1, 2) is the stress of steel. A smeared uniaxial steel material model in literature (Mansour et al. [28]) is employed to compute the stress $f_{\theta,i}^s$ of the reinforcing bar based on the strain along the i^{th} direction (i.e., $\varepsilon_{\theta_{si}}^s$), which can be obtained by transforming the strain at the Gauss point (i.e., [ε_l, ε_t, γ_{lt}]), as,

$$\varepsilon_{\theta_{si}}^s = \begin{bmatrix} 1 & 0 & 0 \end{bmatrix} \mathbf{T}(\theta_{si}) \begin{Bmatrix} \varepsilon_l & \varepsilon_t & \gamma_{lt}/2 \end{Bmatrix}^T \tag{3}$$

The stress of concrete layer: the two diagonal bars contribute to shear stress only, therefore,

$$\begin{Bmatrix} \sigma_l^c \\ \sigma_t^c \\ \tau_{lt}^c \end{Bmatrix} = \begin{bmatrix} 0 & 0 & 0 \\ 0 & 0 & 0 \\ 0 & 0 & \zeta \end{bmatrix} \mathbf{T}\left(-\frac{\pi}{4}\right) \begin{Bmatrix} f_1^c \\ f_2^c \\ 0 \end{Bmatrix} + \begin{Bmatrix} \sigma_l^c \\ \sigma_t^c \\ 0 \end{Bmatrix} \tag{4}$$

Where f_1^c and f_2^c are the stresses of the concrete bars along two diagonal line directions, respectively. It is worth mentioning that the stresses of the two diagonal bars (i.e., f_1^c and f_2^c) are assumed to have no contribution to the normal stress (i.e., σ_l^c and σ_t^c) since the normal stresses are computed independently by using the horizontal and vertical concrete bars. The diagonal stress f_1^c and f_2^c are computed from the strains of the two diagonal concrete bars (i.e., ε_1^c and ε_2^c).

In this paper, a correction factor ζ is introduced (in Eq. 5) to consider the effective area of the bar and influence of the vertical compression on the shear strength, which is defined as a function of the maximum vertical compressive strain (i.e., $\varepsilon_{\max c}$), i.e.,

$$\zeta = \begin{cases} k_1 & \varepsilon_{\max c} \geq 0 \\ k_1 \exp(-k_2 \varepsilon_{\max c}) \leq 1 & \varepsilon_{\max c} < 0 \end{cases} \tag{5}$$

where k_1 and k_2 are suggested to take 0.25 and 1500 in this paper. The value k_1 is the correction due to the area reduction for the diagonal concrete bars. Considering that the MCLM combines the micro and macro models, i.e., simulating the stress-strain relationship by using macro concrete bars, the area reduction approach used in macro models need to be applied, i.e., the equivalent section area of the diagonal concrete bar resisting the shear stress is less than the diagonal section areas. This area reduction is considered in parameter k_1. On the other hand, the term $\exp(-k_2 \varepsilon_{\max c})$ in Eq. (5) considers the shear strength change due to the vertical compressive forces of the concrete. When the vertical forces (mainly caused by the self-weight) increase, the confinement grows and shear strength enlarges. The relationship between correction factor ζ and maximum vertical compressive strain (for $k_1 = 0.25$ and $k_2 = 1500$) is plotted in Fig. 2.

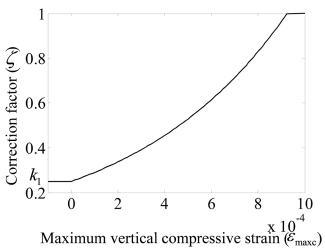

Fig. 2. The correction factor for area reduction and compression effect

Herein, a smeared concrete model [25] is used to model the nonlinear behavior of the concrete bars.

3 Application Examples

The newly developed MCLM has been implemented in a general finite element software framework, OpenSees. two application examples are used to validate the accuracy and numerical stability of the MCLM, including a RC shear wall specimen test (a flexural-shear specimen test) subjected to quasi-static cyclic loading conditions and a 32-story RC frame-shear wall building structure subject to seismic cyclic loading conditions.

3.1 Application Example 1

The second example is used to validate the MCLM under flexure-shear deformation. A RC frame shear wall specimen subjected to both vertical loading and horizontal pushover forces [26, 27] is re-examined as shown in Fig. 3. The frame elements (Fig. 3b) are modeled using nonlinear displacement-based Euler-Bernoulli elements and fiber sections with uniaxial concrete and steel material models (as shown in Fig. 3c). The constitutive behaviors of the unconfined and confined concretes are modeled using modified Kent-Park-Scott models (Park et al. 1982, see Fig. 3e), where the parameters of unconfined concrete are: compressive peak strength f_c = −42.8 MPa, ε_0 = −0.002, f_u = −8.2 MPa, ε_u = −0.004, f_t = 2.1 MPa, b = 0.1 and E_t = 3.0e3 MPa, while for confined concrete: f_c = −55.6 MPa, ε_0 = −0.006, f_u = −40.8 MPa, ε_u = −0.028, f_t = 2.6 MPa, b = 0.1 and E_t = 3.0e3 MPa. The constitutive behavior of the steel is modeled using a Giuffro-Menegotto-Pinto model (Menegotto and Pinto 1973, see Fig. 3f), where the elastic modulus E = 2.1e6 MPa, strength f_y = 395.2 MPa, and post to initial stiffness ratio b = 0.02. The top frame is modeled using rigid beam element, i.e., the elastic beam element with large elastic modulus. The shear wall is simulated using four-node quad elements with four Gauss points per element. The nonlinear behavior at each Gauss point is modeled using the newly developed MCLM model presented herein (see Fig. 3d). In the steel layer, the constitutive behaviors of reinforcement are simulated using a uniaxial reinforcing steel model [28] with elastic modulus E = 2.1e6 MPa and strength f_y = 448.2 MPa. The steel ratios in longitudinal and vertical directions are 0.32 and 0.32%, respectively. In the concrete layer, the modified smeared-crack concrete model used in MCLM has compressive strength f_c = −47.6 MPa and ε_0 = −0.0025. The strength softening is considered for the diagonal concrete bars.

After applying a uniformly distributed axial load of 378 kN (i.e., the axial compression ratio is equal to 0.07), a static pushover analysis is performed using displacement control method with the displacement increment of 0.1 mm. A tolerance of 1.0e−3 mm on the norm of the incremental displacement is used as the convergence criterion. The detail loading paths refer to [27].

The calculated hysteretic responses between the top displacement and the base shear force are plotted and compared with the experimental results to evaluate the accuracy of MCLM (see Fig. 4). The MCLM can simulate the nonlinear behavior of the shear wall under cyclic loading conditions, e.g., the stiffness degradation, strength reduction and the pinch effects, with reasonable accuracy. The Newton-Raphson iterative algorithm converging quadratically demonstrates the good stability of the MCLM presented herein. It is worth to mention that based on the study of many other

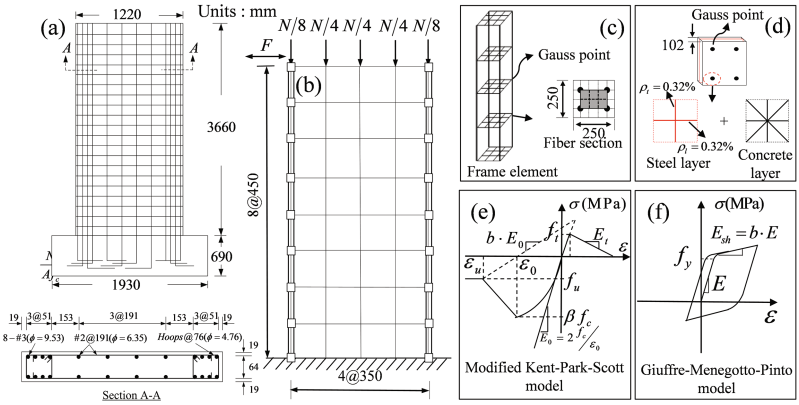

Fig. 3. The RC frame shear wall specimen in Example 2. (a) Geometry and reinforcement (b) FE model (c) Frame element and section properties (d) Quad element and section properties (e) Concrete constitutive model (f) steel constitutive model

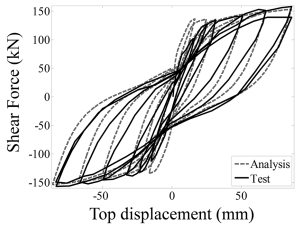

Fig. 4. Hysteretic curve between shear force and top displacement of the slender wall

experimental results using MCLM, it can be concluded that the numerical errors in term of compressive strength is usually less than 20%, and the numerical stability of the MCLM is practically acceptable.

3.2 Application Example 2: A Realistic 32 Story High-Rise Building

In order to verify the applicability of the MCLM in realistic tall building, a 129-m 32-story high-rise RC frame-shear wall building following GB 50011-2010 Code for Seismic Design of Buildings [29] (with seismic fortification intensity larger than 8 degree) subject to earthquake base excitation is studied. The height is 5.0 m in the first story and 4.0 m in the other stories. Both the length and width of the building are 48 m, and remain unchanged with altitude. The building consists of a core tube RC shear wall, outer steel-reinforced concrete frames, outer steel beam and steel braces. The details of component dimensions properties of the steel braces and beams, outer mega columns, shear walls, coupling beams and material properties refer to [30].

A FE model with 1920 nodes and 5696 elements is used to simulate the nonlinear seismic behavior of this tall building. Each shear wall in the core tube is modeled by one modified shell element using MCLM for modeling the in-plane behavior and linear

elastic model for the out-plane behaviors. After these loads are applied to the building using a quasi-static analysis, the 1940 EI-Centro earthquake record scaled by 0.19 (the peak ground acceleration, or PGA, is equal to 0.4 g) is employed as the base excitation input of the structural system. The Newmark-β integration scheme is employed with the parameters $\gamma = 0.5$ and $\beta = 0.25$, and a constant time step of 0.02 s is used. Rayleigh damping is applied to the system such that the damping ratio corresponding to the first frequency and third frequency is 0.025. A tolerance of 1.0e−5 mm on the norm of the incremental displacement is used as the convergence criterion. Figure 5 shows the displacement time histories of three representative floors and the magnitude of top displacement is 884.4 mm.

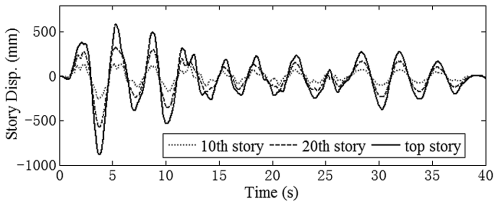

Fig. 5. Displacement time histories of three representative stories

The maximum drift ratio envelope of the building during the earthquake is illustrated in Fig. 6. The maximum drift ratio is 0.88%, occurring at the 12th floor. Form the Fig. 6, it is clear that the maximum drift ratio is below the limitation of drift ratio (i.e., 1%) according to the GB 50011-2010 Code for Seismic Design of Buildings.

Figure 7 shows the hysteretic relationship of the base shear force of frame shear wall, outer frame and shear wall with top displacement of the building. From this figure, it is observed that the magnitude of lateral resisting force of the frame shear wall, the frame and the shear wall are 1.883e4, 2.5504e5 and 2.5548e5 kN respectively. It is observed that the lateral resisting force is mainly contributed by the core shear wall. The maximum and minimum top displacements are 583.1 and −884.4 mm, respectively.

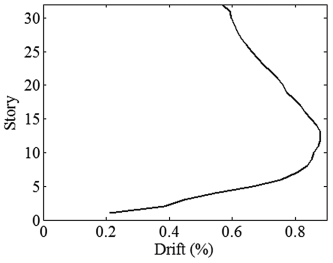

Fig. 6. Maximum drift ratio envelope of the building during the seismic load

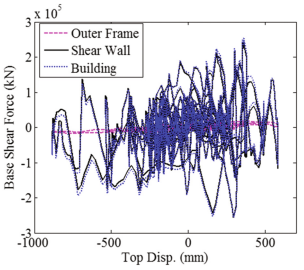

Fig. 7. Base shear forces of the frame-shear wall, the frame and the shear wall vs. the top displacement

The hysteretic responses of the shear forces versus drift ratios for representative shear walls at 1st, 12th, 20th and 30th floors are studied and plotted in Fig. 8 (a) to (d) respectively. It is observed that the maximum shear forces occur at bottom of the structure and the shear forces decrease with altitude. The drift ratios initially increase and then decrease with altitude, and the maximum drift ratio occurs at around 12th floor. Furthermore, the NR process using MCLM and modified shell walls exhibits good stability and converges systematically, indicating that the newly developed shear wall models (i.e., MCLM and modified shell element) are able to be applied to realistic complicated high-rise buildings.

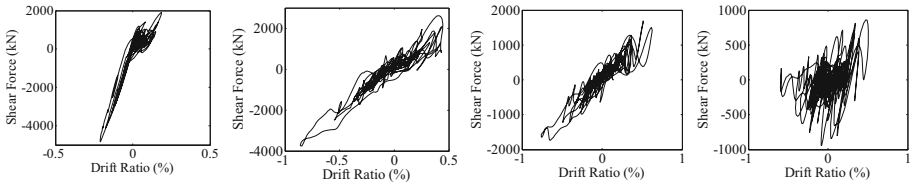

Fig. 8. Shear force versus drift ratio of shear walls in various floors (a) 1st floor (b) 12th floor (c) 20th floor (d) 30th floor

4 Conclusions

This paper presents a novel RC shear wall model, referred to as multi-cross line model (MCLM) for nonlinear seismic analysis of high-rise buildings. The MCLM combines the advantages of accuracy in the existing micro models and the numerical stability of the macro models, therefore providing a practically ideal solution for nonlinear seismic analysis of tall buildings. The newly developed MCLM has been implemented into a general finite element software platform, OpenSees, and validated by using two RC shear wall specimens tested in laboratory and a realistic 32-story high-rise RC frame-shear wall building under cyclic loading conditions. The MCLM can accurately simulate the experimental results, simulating the main features of the stiffness reduction, strength deterioration and pinch effects. In addition, the Newton-Raphson (NR) process using MCLM converges systematically, demonstrating the numerical satiability of this model. The MCLM provides a practically important simulation tool for nonlinear analysis of realistic high-rise buildings.

Acknowledgements. The authors acknowledge the financial supports from NSFC with Grant Nos. 51261120376, 91315301-12, and 51578473, as well as the valuable advices by Professor Yi-Lung Mo in University of Houston. Any opinions, findings, conclusions, or recommendations expressed in this publication are those of the authors and do not necessarily reflect the views of the sponsors.

References

1. Vecchio, F., Collins, M.P.: Stress-strain characteristic of reinforced concrete in pure shear. In: IABSE Colloquium, Advanced Mechanics of Reinforced Concrete, Delft, Final Report, International Association of Bridge and Structural Engineering, Zurich, Switzerland, pp. 221–225 (1981)
2. Vecchio, F.J., Collins, M.P.: The modified compression field theory for reinforced concrete elements subjected to shear. ACI J. **83**(2), 219–231 (1986)
3. Hsu, T.T.C.: Unified Theory of Reinforced Concrete, p. 329. CRC Press Inc., Boca Raton (1993)
4. Hsu, T.T.C., Belarbi, A., Pang, X.B.: A universal panel tester. J. Test. Eval. **23**(1), 41–49 (1995)
5. Belarbi, A., Hsu, T.T.C.: Constitutive laws of softened concrete in biaxial tension-compression. Struct. J. Am. Concr. Inst. **92**(5), 562–573 (1995)
6. Pang, X.B., Hsu, T.T.C.: Behavior of reinforced concrete membrane elements in shear. Struct. J. Am. Concr. Inst. **92**(6), 665–679 (1995)
7. Pang, X.B., Hsu, T.T.C.: Fixed-angle softened-truss model for reinforced concrete. Struct. J. Am. Concr. Inst. **93**(2), 197–207 (1996)
8. Hsu, T.T.C.: Toward a unified nomenclature for reinforced concrete theory. J. Struct. Eng. **122**(3), 275 (1996). doi:10.1061/(ASCE)0733-9445
9. Hsu, T.T.C., Zhang, L.X.: Tension stiffening in reinforced concrete membrane elements. Struct. J. Am. Concr. Inst. **93**(1), 108–115 (1996)
10. Zhu. R.H.: Softened membrane model for reinforced concrete elements considering poisson effect. Ph.D. Dissertation, Department of Civil and Environmental Engineering, University of Houston, Houston, TX (2000)
11. Hsu, T.T.C., Zhu, R.R.H.: Softened membrane model for reinforced concrete elements in shear. Struct. J. Am. Concr. Inst. **99**(4), 460–469 (2002)
12. Mansour, M.: Behavior of reinforced concrete membrane elements under cyclic shear: experiments to theory. Ph.D. Dissertation, Department of Civil and Environmental Engineering, University of Houston, Houston, TX (2001)
13. Mansour, M., Hsu, T.T.C.: Behavior of reinforced concrete elements under cyclic shear: I: experiments. J. Struct. Eng. **131**(1), 44–53 (2005). doi:10.1061/(ASCE)0733-9445
14. Mansour, M., Hsu, T.: Behavior of reinforced concrete elements under cyclic shear. II: theoretical model. J. Struct. Eng. **131**(1), 54–65 (2005). doi:10.1061/(ASCE)0733-9445(2005)
15. Hsu, T.T.C., Mansour, M.Y., Mo, Y.L., Zhong, J.: Cyclic softened membrane model for nonlinear finite element analysis of concrete structures. In: ACI SP-237, Finite Element Analysis of Reinforced Concrete Structures, American Concrete Institute, Farmington, MI, pp. 71–98 (2006)
16. Kabeyasawa, T., Shiohara, H., Otani, S., Aoyama, H.: Analysis of the full-scale seven story reinforced concrete test structure. J. Fac. Eng. Univ. Tokyo **37**(2), 431–478 (1983)
17. Vulcano, A., Bertero, V.V.: Analytical models for predicting the lateral response of RC shear walls, evaluation of their reliability. EERC Report No. UCB/EERC–87/19, Earthquake Engineering Research Center, University of California. Berkeley, California (1987)
18. Kabeyasawa, T.: Design of RC shear walls in hybrid wall system. In: Proceedings, Fourth Joint Technical Coordinating Committee, U.S.-Japan Cooperative Seismic Research on Composite and Hybrid Structures. Monterey, California (1997)
19. Park, H., Eom, T.: Truss model for nonlinear analysis of RC members subjected to cyclic loading. J. Struct. Eng. **133**(10), 1351–1363 (2007). doi:10.1061/(ASCE)0733-9445(2007)

20. Panagiotou, M., Restrepo, J.I., Schoettler, M., Geonwoo, K.: Nonlinear truss model for reinforced concrete walls. ACI Struct. J. **109**(2), 205–214 (2012)
21. Lu, Y., Panagiotou, M.: Three-dimensional nonlinear cyclic beam-truss model for reinforced concrete non-planar walls. J. Struct. Eng. **140**(3), 04013071 (2014). doi:10.1061/(ASCE)ST.1943-541X.0000852
22. McKenna, F.: Object-oriented finite element programming: frameworks for analysis, algorithms and parallel computing. Ph.D. Dissertation, University of California, Berkeley (1997)
23. McKenna, F., Scott, M.H., Takahashi, Y.: An object-oriented software environment for collaborative network simulation. In: Proceeding of the 13th World Conference on Earthquake Engineering, Vancouver, Canada, August (2004)
24. McKenna, F., Scott, M.H., Fenves, G.L.: Nonlinear finite element analysis software architecture using object composition. J. Comput. Civ. Eng. **24**(1), 95–107 (2010)
25. Belarbi, A., Hsu, T.T.C.: Constitutive laws of concrete in tension and reinforcing bars stiffened by concrete. ACI Struct. J. **91**(4), 465–474 (1994)
26. Thomsen IV, J.H.,, Wallace, J.W.: Displacement-based design of reinforced concrete structural walls: experimental studies of walls with rectangular and T-shaped cross sections. Report no. CU/CEE-95/06, Department of Civil and Environmental Engineering, Clarkson University, Potsdam, NY (1995)
27. Thomsen IV, J.H., Wallace, J.W.: Displacement-based design of slender reinforced concrete structural walls-experimental verification. J. Struct. Eng. **130**(4), 618–630 (2004). doi:10.1061/(ASCE)0733-9445
28. Mansour, M., Lee, J.-Y., Hsu, T.T.C.: Cyclic stress-strain curves of concrete and steel bars in membrane elements. J. Struct. Eng. **127**(12), 1402–1411 (2001). doi:10.1061/(ASCE)0733-9445
29. GB 50011-2010 Code for Seismic Design of Buildings. China Building Industry Press, Beijing (2010)
30. Goman, H., Hongchao, C., Rohin, C.: Summary of comparison for cases of nonlinear time history analysis for Sino-Japanese Conference. Build. Struct. **46**(16), 54–57 (2013). (in Chinese)

Dynamic Shake-Table Tests on Two Full-Scale, Unreinforced Masonry Buildings Subjected to Induced Seismicity

Gabriele Guerrini[1,2(✉)], Francesco Graziotti[1,2], Andrea Penna[1,2], and Guido Magenes[1,2]

[1] Department of Civil Engineering and Architecture (DICAr), University of Pavia, Pavia, Italy
gabriele.guerrini@unipv.it
[2] Masonry Structures Section, European Centre for Training and Research in Earthquake Engineering (EUCENTRE), Pavia, Italy

Abstract. This paper presents the results of an experimental campaign which is part of a wider research project, aimed at assessing the seismic vulnerability of buildings in the Groningen region of the Netherlands. The area, historically not prone to tectonic ground motions, has been subjected to seismic events induced by gas extraction during the last two decades. As part of this campaign, unidirectional dynamic shake-table tests were performed at the EUCENTRE laboratory on two full-scale, unreinforced masonry buildings, designed without specific seismic considerations or detailing. The first specimen simulated the end-unit of a two-story terraced house, built with unreinforced masonry cavity walls. These walls were composed of an inner load-bearing leaf, made of calcium silicate bricks supporting the floors, and an outer veneer, made of clay bricks with aesthetic and weather-protection function. The floors consisted of reinforced concrete slabs, providing rigid diaphragms; the pitched roof was made of longitudinal timber beams, supported by end gables perpendicular to the shaking direction, and wood boards. The second specimen represented a one-story detached pre-1940's house, built with double-wythe unreinforced clay masonry walls. The structure included large openings and a re-entrant corner, causing significant horizontal irregularities; the two façades perpendicular to the shaking direction simulated two common gable geometries. The first floor was made of timber beams and planks, resulting in flexible diaphragm; the steep-pitch roof consisted of timber trusses connected by wood purlins and boards. Two similar incremental dynamic tests were performed up to the near-collapse conditions of the two buildings; the selected input ground motions represented realistic scenarios of seismic events for the examined region. This paper summarizes the main characteristics of the two specimens and the shake-table experimental results, illustrating the evolution of the damage mechanisms and the hysteretic response of the structures.

Keywords: Cavity walls · Clay bricks · Induced seismicity · Shake-table test · Unreinforced masonry buildings

© Springer International Publishing AG 2018
J.P. Conte et al. (eds.), *Experimental Vibration Analysis for Civil Structures*,
Lecture Notes in Civil Engineering 5, https://doi.org/10.1007/978-3-319-67443-8_32

1 Introduction

The Groningen region of the northern Netherlands, historically not prone to tectonic earthquakes, during the last two decades has been interested by seismic events induced by gas extraction and reservoir depletion. The most severe event was a M_L 3.6 earthquake that occurred on August 16th, 2012 near Huizinge, above the central area of the Groningen gas field [1]. Local structures, not specifically designed for seismic actions, have been exposed to frequent low-intensity shaking during this period, with unreinforced masonry (URM) buildings representing almost 90% of the building stock.

Because of the limited available information on the seismic performance of Dutch building typologies, an experimental campaign has been launched in 2015, aimed at investigating the performance of structural components, assemblies, and systems. The experimental program includes in-situ mechanical characterization tests [2, 3] and laboratory tests, such as (i) characterization tests on bricks, mortar and small masonry assemblies; (ii) in-plane cyclic shear-compression tests [3, 4] and dynamic out-of-plane tests [3, 5] on full-scale masonry piers; and (iii) full-scale unidirectional shaking table tests on building prototypes. In particular, incremental full-scale shake-table tests were conducted on two building specimens at the EUCENTRE laboratory in Pavia, Italy, aimed at investigating the seismic response of two different URM building typologies: cavity-wall terraced houses [3, 6] and pre-1940's clay brick detached houses [3, 7].

Terraced houses represent more than 50% of the URM building stock of the region under consideration; they are usually two-story buildings with wide openings on two opposite sides, consisting of several side-by-side residential units. Most terraced houses are built with cavity walls, a technology that became popular after World War II, consisting of two leaves of bricks with insulating material sometimes inserted in between. The inner leaf has load-bearing function and is usually made of calcium silicate bricks, while the outer leaf is often a clay-brick veneer with only aesthetic and weather-protection function. The two leaves are typically interconnected by regularly distributed metal ties.

Adjacent units of a terraced house are generally separated by double-leaf transverse load-bearing walls, with discontinuous floor slabs resting only on the transverse wall leaves of the individual unit they belong to. Each unit is therefore completely self-supported by transverse walls and structurally independent from the adjacent units. The only shared walls are the outer non-load-bearing veneers. For this reason, only a representative portion (end unit) of an entire terraced house was tested on the shake table.

On the other hand, detached houses constitute another significant portion of the URM building stock of the Groningen region and comprises commonly one- or two-story buildings with irregular plan configurations, wide openings, and flexible floor and roof timber diaphragms. Solid clay-brick walls are generally found in this type of buildings, especially in those preceding World War II. Most detached houses are characterized by steep pitched roofs, with several combinations of external roof shapes and gable geometries.

This paper describes the geometric and mechanical characteristics of the two prototype buildings, the testing protocol, and the experimental results in terms of damage evolution and hysteretic responses.

2 Overview of the Specimens

2.1 Cavity-Wall Terraced House (CWTH)

This building specimen (Fig. 1a) was intended to represent the end unit of a 2-story unreinforced cavity-wall terraced house (CWTH) of the late 1970's, without specific seismic detailing according to the Dutch construction practice of the time [3, 6]. The specimen was built at full scale on a composite steel-concrete foundation attached to the shaking table of the EUCENTRE laboratory. This building typology is characterized by wide openings along the front and back longitudinal walls, while solid walls separate the units in the transverse direction; as a result, longitudinal walls are more vulnerable to in-plane seismic excitation than transverse ones. For this reason, the unidirectional shake-table test was performed in the longitudinal (North-South) direction. Figure 1b shows the specimen first-floor plan, with a red arrow indicating the positive shaking direction. Figure 2 shows elevation views of the CS inner leaves.

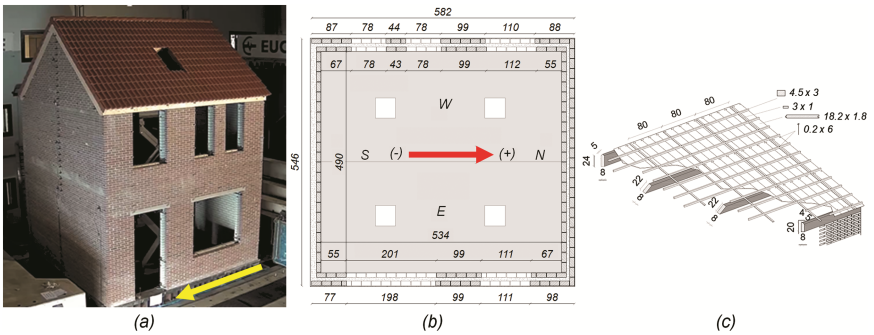

Fig. 1. Cavity-wall terraced house specimen: (a) N-W view of the full-scale building; (b) first-floor plan; (c) roof framing. Colored arrows indicate the positive direction of shaking. Units of cm.

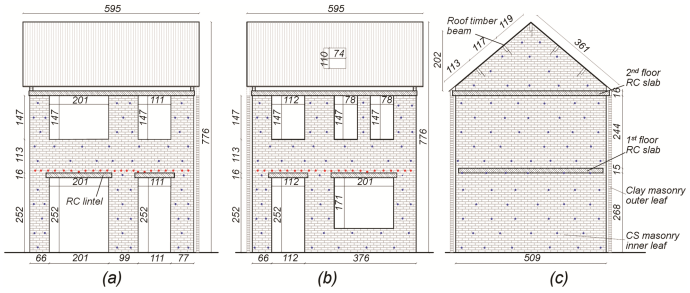

Fig. 2. Elevation views of the inner CS leaves of the CWTH specimen: (a) East side; (b) West side; (c)North and South sides. Blue dots represent ties between the two leaves (absent on the South side). Red dots represent wall-to-diaphragm connections. Units of cm.

The inner load-bearing leaf of the cavity walls was made of calcium silicate (CS) bricks, while the outer leaf was a clay brick veneer; both leaves were built with 10-mm-thick mortar bed joints. An 80-mm gap was left between the two walls as in common practice; 3.1-mm-diameter L-shaped steel ties provided connection between the two masonry leaves at the locations showed by blue dots on Fig. 2. The inner CS leaf ran around the entire perimeter, while the outer clay-brick veneer was not built on the South side, corresponding to an interior separation wall. At the first floor, precast reinforced concrete (RC) lintels were placed above the openings in both leaves.

RC slabs provided rigid diaphragms at the first and second floors. The slabs were supported by the transverse (North and South) inner CS leaves, while no gravity load was transferred to the longitudinal (East and West) walls under static conditions. Wall-to-diaphragm connection between the longitudinal CS leaves and first-floor slab was ensured by 6-mm-diameter rods at the locations indicated by red dots on Fig. 2. The second-floor slab extended over but was not directly supported by the longitudinal CS walls: a gap was left between the slab and the longitudinal inner leaves and was filled with mortar only after removal of temporary shoring. There was no direct connection between the longitudinal clay veneers and the two slabs.

The 43°-pitched timber roof frame (Fig. 1c) included (i) a ridge beam, (ii) two wall-plate beams at the base, connected to the second-floor slab but not supported by the longitudinal walls, and (iii) two girders on each side. Girders and ridge beam were supported by the transverse inner CS leaves (North and South sides, Fig. 2c), which extended above the second floor to form gables. The connection was improved by steel anchors. Timber boards were nailed to the longitudinal framing members. The roof was completed with the installation of clay tiles over a mesh of laths and counter battens nailed to the timber boards.

Masonry walls, first- and second-floor slabs, and finished roof provided masses of 31.9 t, 10.3 t, 11.0 t, and 2.8 t, respectively. The total mass of the building specimen resulted in 56 t.

A rigid steel frame was installed inside the building specimen. This structure served as a safety system, providing support in case of partial or global collapse of the specimen, and constituted a (approximately) rigid reference system for direct measurement of displacements relative to the shake-table. The frame was not in contact with the building, since its columns ran through four holes in the floor diaphragms (Fig. 1b), oversized to accommodate the specimen lateral displacements.

2.2 Clay-Brick Detached House (CBDH)

This building specimen (Fig. 3a) was designed to represent a pre-1940's unreinforced clay-brick detached house (CBDH) of the Groningen region, without specific seismic detailing according to the Dutch construction practice of the time [3, 7]. The specimen was built at full scale on a composite steel-concrete foundation attached to the shaking table of the EUCENTRE laboratory. The specimen was designed to include large asymmetrical openings on all sides and a reentrant corner, causing a discontinuity in one of the perimeter walls (Figs. 3, 4). The load-bearing structural system consisted of 208-mm-thick, double-wythe URM walls built with the Dutch cross brickwork bond. Lintels

were built above all openings which included a timber beam supporting the interior masonry wythe, and a brick flat arch below the exterior wythe.

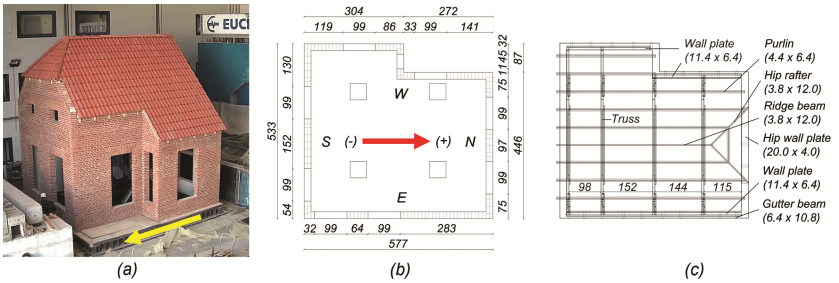

Fig. 3. Clay-brick detached house specimen: (a) N-W view of the full-scale building; (b) first-floor plan; (c) roof framing. Colored arrows indicate the positive direction of shaking. Units of cm.

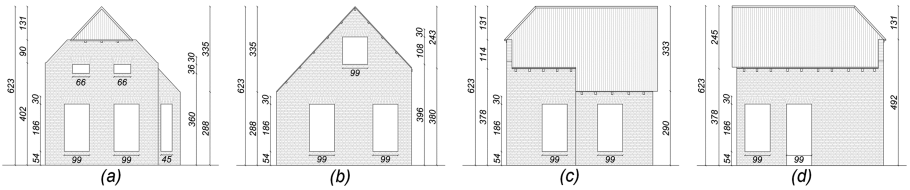

Fig. 4. Elevation views of the CBDH specimen: (a) North side; (b) South side; (c)West side; (d) East side. Units of cm.

The roof external shape was designed to combine two different end geometries: a half-hipped roof with clipped gable at the North façade and a full-height gable at the South façade. The perimeter walls extended above the first floor to form the 208-mm-thick gables. These elements are generally more vulnerable when subjected to out-of-plane excitation because of weak connections to the roof framing along this direction: for this reason, the unidirectional shaking table test was performed perpendicularly to the gables, as shown by the colored arrows on Fig. 3

The floor system consisted of timber floorboards, nailed perpendicularly to ten timber joists spanning between the longitudinal East and West walls, resulting in a flexible diaphragm. Connection between these walls and the floor diaphragm was improved by 14-mm-diameter L-shaped steel anchors attached to every other joist. A flat S-shaped steel anchor provided wall-to-diaphragm connection for each of the North and South façades, tying their midpoints to the first two floor joists and restraining them against out-of-plane mechanisms.

The roof structure consisted of four East-West timber trusses, supporting longitudinal North-South purlins and a ridge beam (Fig. 3c). The truss rafters were connected to wall plates and gutter beams resting above the longitudinal East and West walls and the North clipped gable. Mortar was placed below the wall plates on the longitudinal walls, but not on the North gable, as encountered in some pre-1940's Dutch houses. A

truss was placed back-to-back with the South gable, where the roof purlins protruded through the masonry wall; this resulted in almost no gravity load transferred to the South gable under static conditions. Two planks were nailed to the purlins beyond the South gable as common in Dutch practice for finishing reasons. It was observed that this detail was sufficient to restrain the out-of-plane gable displacements relative to the roof. Timber boards were nailed perpendicularly to the purlins above the roof framing. The roof was completed with clay tiles, supported by a mesh of laths and counter battens nailed above the timber boards.

Masonry walls, floor diaphragm, and finished roof provided masses of 28.96 t, 0.47 t and 1.87 t, respectively. An additional mass of 1.31 t was applied to the first floor by means of laminated rubber blocks, evenly distributed over the diaphragm. The total mass of the building specimen resulted in 32.61 t. A rigid steel frame was installed inside the building prototype as illustrated for the CWTH specimen.

2.3 Mechanical Properties of Materials and Components

A mechanical characterization campaign was performed on material samples, masonry wallettes, and structural components. Masonry material properties were obtained following the EN 772, EN 1015, and EN 1052 standards [8, 9], and the results are summarized in Table 1. The average pull-out and push-in strengths of the steel ties connecting the two leaves of the cavity walls were 1.5 kN and 1.1 kN, respectively [10], while the tensile strength of the ties was 4.3 kN. The concrete of the terraced house slabs had an average compressive strength of 29.5 MPa.

3 Instrumentation and Testing Protocol

Several sensors were installed on the buildings, in order to monitor their structural response. The instrumentation of the CWTH specimen [3, 6] consisted of 33 accelerometers, 10 wire potentiometers, and 20 linear variable displacement transducers (LVDTs). The CBDH specimen [3, 7] was instead equipped with 37 accelerometers, 21

Table 1. Material properties.

Material property [units]	CWTH		CBDH
	CS	Clay	Clay
Density of masonry [kg/m^3]	1835	1905	1984
Brick compressive strength [MPa]	17.18	32.45	47.00
Mortar compressive strength [MPa]	5.71	6.24	4.12
Mortar flexural strength [MPa]	1.78	1.48	1.20
Masonry compressive strength [MPa]	5.49	12.72	9.23
Masonry Young's modulus in compression [MPa]	1736	4742	8123
Masonry flexural bond strength [MPa]	0.056	0.15	0.23
Masonry (bed joint) initial shear strength [MPa]	0.03	0.11	0.15
Masonry (bed joint) shear friction coefficient [−]	0.50	0.68	0.55

wire potentiometers, 37 linear variable displacement transducers (LVDTs), and a 3-dimensional optical acquisition system.

The specimens were subjected to an incremental dynamic test, applying a series of shake-table motions of increasing intensity. A detailed study on the seismic hazard characteristics of the region [3] identified two main scenarios, with return periods of 50 and 500 years; accordingly, two smooth-response-spectra records SC1 and SC2 (Fig. 5) were generated. The acceleration amplitude of these two records was then scaled in order to obtain the desired incremental test protocol, summarized in Table 2 The buildings were subjected to random noise tests between those listed in Table 2.

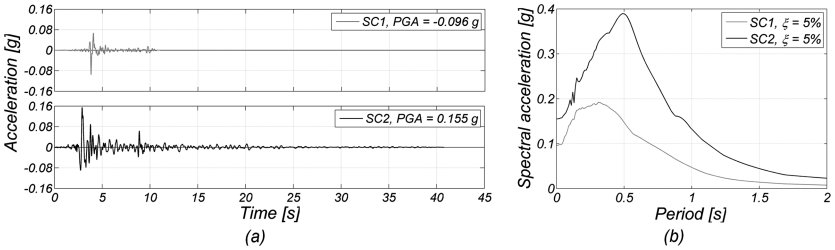

Fig. 5. Input ground motions: (a) acceleration time histories; (b) elastic acceleration response spectra.

Table 2. Summary of the testing sequence.

Test input	Scale factor [%]	Nominal PGA [g]	Recorded PGA [g]		Calculated PGV [m/s]	
			CWTH	CBDH	CWTH	CBDH
SC1	25	0.024	0.024	0.026	0.015	0.022
SC1	50	0.048	0.050	0.050	0.031	0.035
SC1	100	0.096	0.099	0.098	0.056	0.058
SC1	150	0.144	0.137	0.149	0.077	0.086
SC2	50	0.080	0.087	0.080	0.067	0.073
SC2	100	0.159	0.170	0.140	0.123	0.122
SC2	125*	0.199	0.194	–	0.133	–
SC2	150	0.239	0.243	0.227	0.164	0.186
SC2	200	0.318	0.307	0.293	0.218	0.241
SC2	250†	0.398	–	0.392	–	0.308
SC2	300†	0.477	–	0.500	–	0.365
SC2	400†	0.636	–	0.679	–	0.467

*Only for the CWTH specimen. †Only for the CBDH specimen. PGA = peak ground acceleration. PGV = peak ground velocity.

4 Test Results

The following sections illustrate the performance of the specimens reporting qualitative damage observations and significant hysteretic response plots. At the end of every shaking test, structural damage was surveyed in detail [3, 6, 7]. Videos of the testing sequences are available on the EUCENTRE webpage [3].

4.1 Cavity-Wall Terraced House (CWTH): Damage Evolution

During tests under SC1 input motions, scaled from 25% to 150% (PGA from 0.024 g to 0.137 g), the building did not experience any visible damage. After the EQ2 - 100% test (PGA = 0.170 g) some cracks were found at the base of the first-story inner-leaf corner piers, associated with their flexural response. Damage did not change significantly during the EQ2 - 125% test (PGA = 0.194 g). After the EQ2 - 150% test (PGA = 0.243 g) more cracks were observed at the top and/or bottom of several CS piers at both stories, indicative of their flexural-rocking response. One of these cracks extended diagonally into the adjacent spandrel. No damage was detected in the transverse walls and in the veneers up to this intensity level.

Damage spread significantly during the EQ2-200% test (PGA = 0.307 g). A global response of the structure was triggered, with the formation of new cracks or the elongation of pre-existing ones at the ends of all CS piers (Fig. 6). Extensive damage interested the CS spandrels, where wide diagonal cracks, mortar-joint sliding, and blocks decohesion were observed. In addition, residual sliding of 15 mm was measured on the horizontal cracks at the top of the second-story piers. 45° diagonal cracks (up to 1.2-mm

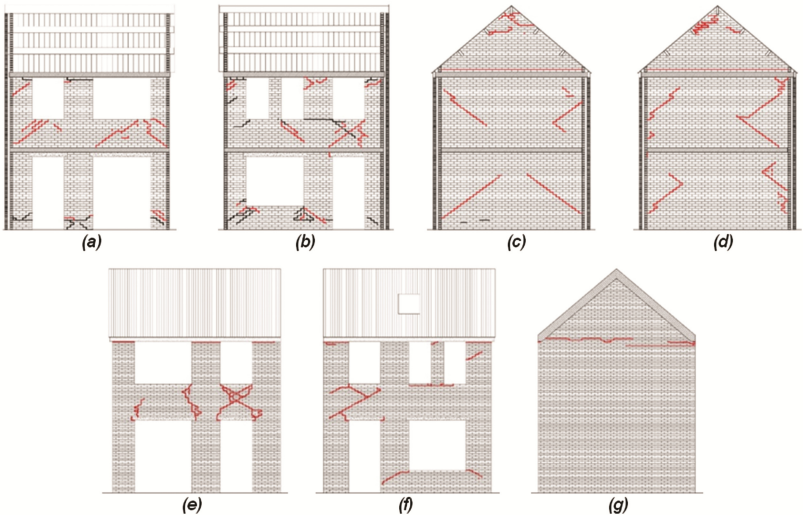

Fig. 6. Crack pattern on the CSTH specimen after the SC2-200% test: (a) East CS wall; (b) West CS wall; (c) North CS wall; (d) South CS wall; (e) East veneer; (f) West veneer; (g) North veneer. Cracks marked in black were pre-existing.

wide) were observed on the transverse walls, associated with the activation of a two-way out-of-plane bending mechanism. Horizontal cracks were visible at the base of the gables, also indicative of an out-of-plane overturning mechanism. Cracks due to interaction between roof beams and supporting CS gables were also found.

Visible cracks formed on the outer veneers only during the last test, EQ2-200% (PGA = 0.307 g). The long spandrel of the East façade developed a flexural mechanism with vertical cracks at both ends, whereas shorter spandrels presented X-shaped shear crack patterns. Most of the story drift was accommodated by sliding between the roof wall plates and the second story masonry piers. Horizontal cracks were observed along the entire base of the North veneer gable, due to out-of-plane overturning mechanism.

4.2 Clay-Brick Detached House (CBDH): Damage Evolution

During tests under SC1 input motions, scaled from 25% to 150% (PGA from 0.026 g to 0.149 g), the building did not experience any visible damage. Minor horizontal cracks became visible on the North gable during testing under SC2 - 150% (PGA = 0.227 g), at the interface between the timber lintels and the masonry just above the openings. The observed damage did not change significantly after testing under SC2-200% (PGA = 0.293 g). After the SC2-250% test (PGA = 0.392 g) horizontal cracks developed on the South façade, a few centimeters above the floor level; other cracks were observed at the bottom of the wider piers of the West façade, indicative of their rocking response. During shaking under SC2-300% (PGA = 0.500 g) a global response of the structure was triggered, with the activation of an out-of-plane mechanism on the South gable and in-plane flexural-rocking mechanisms in the longitudinal piers of the West façade.

After the SC2-400% test (PGA = 0.679 g) extensive damage was observed throughout the building (Fig. 7), which was deemed to have reached near-collapse conditions. An out-of-plane mechanism involved the upper portion of the North gable: residual sliding of the order of 20 mm and blocks de-cohesion were observed along a major horizontal crack located just above the openings. The out-of-plane overturning mechanism fully activated on the South gable causing an X-shaped crack pattern below the opening, mainly attributed to the restraining effect of the steel anchor at the floor level. Due to good interlocking between the intersecting walls, parts of the East and West façades participated in the out-of-plane response of the gables with the formation of stair-stepped cracks in the upper areas of the longitudinal walls.

The West piers exhibited pure flexural-rocking failure mechanisms, with widening and propagation of pre-existing cracks at their top and bottom ends, and severe damage to one of the flat-arch lintels. Visible cracks formed on the East squat pier only at this final stage of the test: a flexural-rocking mechanism developed under southward displacement, with subsequent sliding all along its base and a residual of about 0.2 mm. As the East squat pier was significantly stiffer and stronger than the West ones, the floor diaphragm was subjected to significant shear deformation, but its flexibility prevented overall torsional response of the building. No sliding or differential displacements were noted between roof and gables and between wall plates and longitudinal walls, despite weak connections.

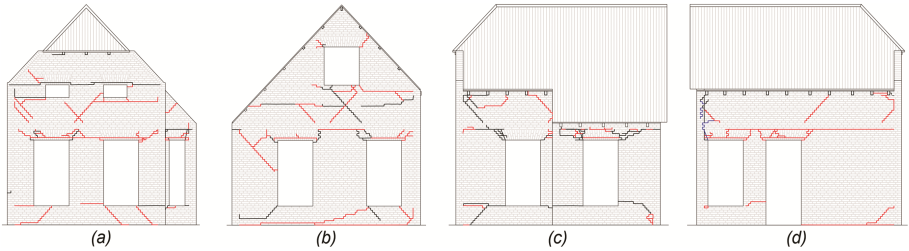

Fig. 7. Crack pattern on the CBDH specimen after the SC2-400% test: (a) North wall; (b) South wall; (c) West wall; (d) East wall. Cracks marked in black were pre-existing. Cracks marked in red were observed from inside, in blue from outside.

4.3 Hysteretic Responses

Figure 8a shows the hysteretic response of the two specimens in terms of base-shear coefficient (BSC) and global drift ratio (GDR) recorded during the final test. The BSC was computed as the sum of the products of each accelerometer reading times its tributary mass, lumped at the accelerometer location, divided by the total weight of the specimen. The GDR was defined as the second-floor displacement (relative to the base) divided by the second-floor height above the foundation for the CWTH building, or as the average first-floor displacement divided by the first-floor height for the CBDH prototype. Backbone envelopes are also shown for both specimens.

The first significant nonlinearity in the hysteretic response of the CWTH building was detected during the EQ2 - 150% test and was associated with diffuse flexural cracks in the inner CS walls; nonlinear behavior became significant during the EQ2-200% test due to widespread damage of the specimen. An ultimate GDR of 0.70% was achieved. Nonlinear response of the CBDH specimen was initially observed in the SC2-250% test and became rapidly pronounced under the two following tests; it was associated with flexural-rocking mechanisms in the West piers and out-of-plane behavior of the gables. The maximum recorded average first-floor drift ratio was 0.94%.

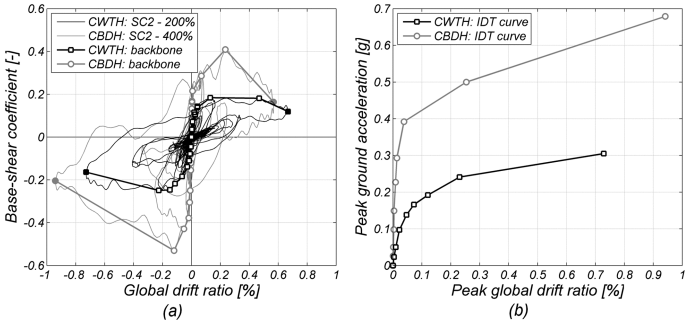

Fig. 8. Response of the two specimens: (a) hysteretic behaviors; (b) IDT curves.

The two specimens underwent similar GDRs when reaching near-collapse conditions. However, the CBDH specimen displayed a higher lateral strength with a BSC of about 0.53, compared to the CWTH building which reached 0.25. This is reflected also on the incremental dynamic test (IDT) plot of Fig. 8b, where the near-collapse limit state of the CBDH building is reached under more than twice the PGA resisted by the CWTH specimen.

5 Conclusions

This paper discussed the full-scale unidirectional shaking table test of two building specimens simulating a Dutch terraced house building with cavity walls and a clay-brick detached house. The specimens were subjected to incremental input motions representative of induced seismicity scenarios for the Groningen region in the Netherlands, characterized by smooth response spectra and short significant durations.

The terraced house specimen exhibited a box-type global response thanks to the rigid concrete slabs, which delayed the occurrence of local out-of-plane failure of the transverse walls and, engaging the longitudinal walls, allowed their in-plane capacity to be fully exploited. The building withstood the input motion with a PGA of 0.17 g with little damage and reached its near-collapse state at a PGA of 0.31 g. The response of the masonry piers was mainly governed by rocking, whereas sliding occurred at the top of masonry walls.

The detached house specimen suffered only minor damage under the input motion with PGA of 0.23 g and reached its near-collapse state at a PGA of 0.68 g. The building exhibited a box-type global response with prevailing damage on the gables perpendicular to the shaking direction, where local out-of-plane mechanisms occurred. Good interlocking between intersecting walls resulted in the participation of longitudinal wall portions to the gable mechanisms. Longitudinal masonry piers developed flexural-rocking in-plane mechanisms. Because of differential displacements between the two longitudinal walls, the flexible floor diaphragm underwent significant in-plane shear deformations. No significant sliding was observed between roof and masonry walls.

The detached house exhibited a lower seismic vulnerability compared to the cavity-wall building. In fact, it developed twice the base-shear coefficient and reached near-collapse conditions under more than twice the peak ground acceleration.

Acknowledgments. This work is part of the EUCENTRE project "Study of the vulnerability of masonry buildings in Groningen", within the research program framework on hazard and risk of induced seismicity in the Groningen region, sponsored by the Nederlandse Aardolie Maatschappij BV (NAM). The authors would like to thank all parties involved in this project: the DICAr Laboratory of the University of Pavia and the EUCENTRE Laboratory, which performed the tests; and partners NAM, Arup, and TU Delft. The valuable advice of R. Pinho is gratefully acknowledged. The authors would like to express their gratitude also to H. Crowley, A. Rossi, M. Mandirola, U. Tomassetti, B. Marchesi, S. Kallioras, E. Cenja, F. Dacarro, S. Peloso, F. Cuppari, and E. Mellia for their support during the experimental campaign.

References

1. Bourne, S.J., Oates, S.J., Bommer, J.J., Dost, B., van Elk, J., Doornhof, D.: A Monte Carlo method for probabilistic hazard assessment of induced seismicity due to conventional natural gas production. Bull. Seismol. Soc. Am. **105**(3), 1721–1738 (2015)
2. Tondelli, M., Graziotti, F., Rossi, A., Magenes, G.: Characterization of masonry materials in the Groningen area by means of in-situ and laboratory testing. Report, EUCENTRE, Pavia, Italy (2015)
3. EUCENTRE: Reports and test videos (2016). http://www.eucentre.it/project-nam/
4. Graziotti, F., Rossi, A., Mandirola, M., Penna, A., Magenes, G.: Experimental characterization of calcium-silicate brick masonry for seismic assessment. In: 16th International Brick and Block Masonry Conference, Padua, Italy (2016)
5. Graziotti, F., Tomassetti, U., Penna, A., Magenes, G.: Out-of-plane shaking table tests on URM single leaf and cavity walls. Eng. Struct. **125**, 455–470 (2016)
6. Graziotti, F., Tomassetti, U., Rossi, A., Kallioras, S., Mandirola, M., Penna, A., Magenes, G.: Full scale shaking table test on a URM cavity wall terraced house building. In: 16th World Conference on Earthquake Engineering, Santiago, Chile (2017)
7. Graziotti, F., Guerrini, G., Kallioras, S., Marchesi, B., Rossi, A., Tomassetti, U., Penna, A., Magenes, G. Shaking table test on a full-scale unreinforced clay masonry building with flexible diaphragms. In: 13th Canadian Masonry Symposium, Halifax, Canada (2017)
8. EN 1015-11, Methods of test for mortar for masonry. European Standards, CEN/TC (1999)
9. EN 1052-1,3,5, Methods of test for masonry. European Standards, CEN/TC (1998)
10. Esposito, R., Messali, F., Crielaard, R., Rots, J.: Tests for the Characterization of Replicated Masonry. Report, Delft University of Technology, Delft (2015)

Utilising an Advanced Technology of People Tracking in Vibration Serviceability Application

Ahmed S. Mohammed(✉) and Aleksandar Pavic

Vibration Engineering Section, College of Engineering, Mathematics and Physical Sciences, University of Exeter, Kay Building, North Park Road, Exeter EX4 4QF, UK
asm22l@exeter.ac.uk

Abstract. There is a continuous development in the facilities used for experimental measurements of human-induced vibrations due to walking of people in real-life structures. These facilities can be classified into three categories:

1. systems used to measure walking forces,
2. systems used to measure structural dynamic properties and vibration responses and
3. equipment required to locate the position of people within the structure.

In recent years, state-of-the-art technologies have enabled both direct and indirect measurement of walking forces and vibration responses with improved accuracy. However, determining people's position on the structure they occupy and dynamically excite is still a challenge, despite its importance. This is due to the limitations and lack of accuracy of existing systems used for this purpose.

This paper presents an advanced system based on the Ultra-WideBand (UWB) technology to track the position of multiple people within civil engineering structures. It is demonstrated that this system has the capability of providing measurements of people's positions in real-time, with around 50 cm accuracy, using wearable compact tags. In addition to the accuracy, the simple setting up and capability to track people's positions in different types of structures are advantages over other types of body location tracking systems. Incorporating the above mentioned systems to measure simultaneously walking-induced forces, realistic time-varying locations of these forces and the corresponding time-varying vibration responses has created an unprecedented opportunity to boost considerably research pertinent to human-induced vibration. This will be based on invaluable but, until now, difficult to conduct real-life simultaneous measurements of these three key time-varying walking-force parameters.

Keywords: Position tracking · Walking path · Vibration serviceability · Floors · Human-induced vibrations

© Springer International Publishing AG 2018
J.P. Conte et al. (eds.), *Experimental Vibration Analysis for Civil Structures*,
Lecture Notes in Civil Engineering 5, https://doi.org/10.1007/978-3-319-67443-8_33

1 Introduction

Vibration serviceability criteria due to human activities is increasingly becoming a critical factor in designing civil structures including building floors and footbridges [1–3]. This criterion is based on three key elements [4]:

- vibration source i.e. human-induced forces due to human activities, such as walking and jumping,
- vibration transmission path i.e. dynamic properties of the structure and
- vibration receiver i.e. sensitive equipment or perception of human occupants of the vibration responses.

While the dynamic properties can be identified using the currently available measurement facilities, recently, it became possible to measure human-induced forces and corresponding vibration responses simultaneously, with an acceptable accuracy [5, 6]. However, measuring the positions and walking routes of people, as dynamic exciters and vibration receivers, is still a challenge due to the technical limitations and lack of accuracy for relevant available measurement facilities [7].

This paper proposes utilising an advanced system of people tracking based on the Ultra-WideBand (UWB) technology to provide direct measurements of multiple-pedestrian walking locations on building floors. The unique UWB system can be easily set up, and measure people's locations with sub-meter accuracy. The system was tested by performing walking tests on a full-scale laboratory floor, while direct measurements of people's locations, their walking forces and the corresponding vibration responses were measured simultaneously.

2 Application of UWB Technology

UWB technology has a wide range of applications, including positioning, security and communications [8, 9]. For positioning, recent developments have made it possible to provide localisation in construction sites, hospitals and factories. The large bandwidth

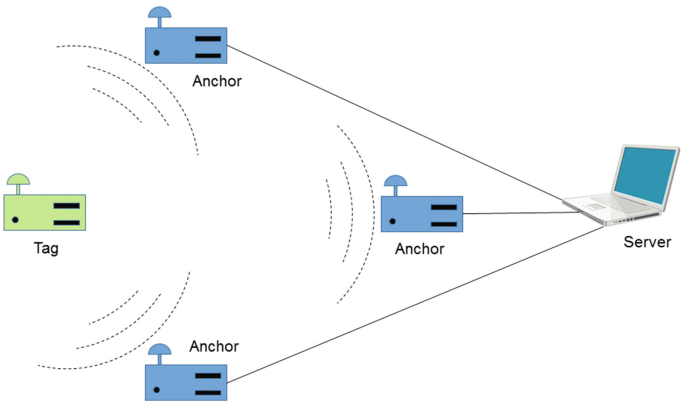

Fig. 1. Overview of UWB tracking system components.

of the UWB signal and its ability to mitigate the loss of energy in multipath environments are the main advantages of this technology [9].

In this paper, a system based on this technology is utilised in the context of vibration serviceability. It has been tested to track people's locations while walking forces and the corresponding vibration responses are measured simultaneously. The system comprises a wearable signal emitters (tags) which send pulses to signal receivers (anchors). A central server utilises the information of time and angle of arrival to estimate the positions using a triangularisation technique as shown in Fig. 1.

3 Experimental Test

The experimental work carried out in this paper utilises state-of-the-art facilities to extract the dynamic properties of a test structure and provide direct measurements of people's locations, their walking forces and the corresponding vibration responses.

3.1 Test Structure

The test structure is a full-scale laboratory floor located in the Structures Lab at the University of Exeter (Fig. 2). The floor is 7.5 m long and 5.0 m wide and it consists of Sandwich Plate System (SPS) plates supported by steel beams.

Fig. 2. Full-scale laboratory test structure

Multiple-input multiple-output (MIMO) modal testing was performed to identify the dynamic properties of the structure. Two APS400 [10] shakers were utilised to apply uncorrelated random excitation force to the floor and the forces were measured indirectly using Endevco 7754-1000 piezoelectric accelerometers [11] to measure the acceleration of the shakers' moving mass. Floor vibration responses were measured using 19 Honeywell QA750 accelerometers [12] on a 7.5 × 5.0 m grid as shown in Fig. 2. The frequency response functions (FRFs) were measured using a Data Physics DP730 24-bit spectrum analyser. The modal properties were identified using multiple

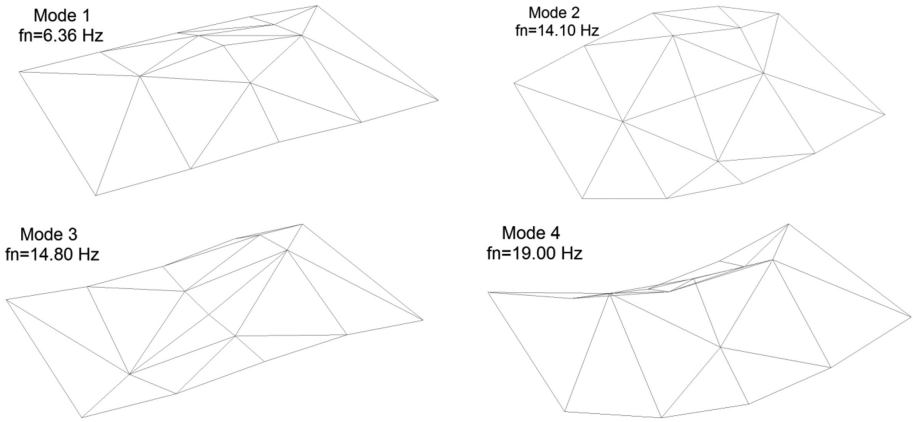

Fig. 3. Experimentally identified mode shapes of the 1st, 2nd, 3rd and 4th vertical bending modes

degree of freedom (MDOF) curve fitting tool available in the ME'Scope software [13]. A summary of the identified modes up to 20 Hz are shown in Fig. 3.

3.2 Walking Tests

Two test subjects (TSs) participated in the walking tests. To track their locations, each TS was instrumented with a compact wearable tag on his left hand wrist. Four anchors were deployed for the test and positioned just outside the four corners of the floor. The relative positions of the anchors were measured and used as input in the central server of the tracking system to calculate the positions of the tags.

The walking forces were measured indirectly [5] using two synchronised wireless APDM Opal™ [14] monitors (Fig. 4). The Opal™ monitors were attached to the seventh cervical vertebra (C7) at the lower neck of the TSs.

Fig. 4. APDM Opal™ monitor [14]

To measure the floor vibration responses, three accelerometers were positioned at the anti-nodes of the 1st, 2nd and 3rd vibration modes. The accelerometers were synchronised with the Opal™ monitors by shaking them manually after attaching them to each other so that their signals can be synchronised. A video camera was fixed at the top of the structure to compare the tracked with the real positions of the TSs. The data

acquisition starting times of the people tracking system, the Opal^{TM} monitors and the video camera were recorded to synchronise their data.

Two walking routes were selected for this test:

- diagonal route, where the TSs walk across the diagonal of the structure at the same time (Fig. 5a), and
- 8-shape walking route as shown in Fig. 5b.

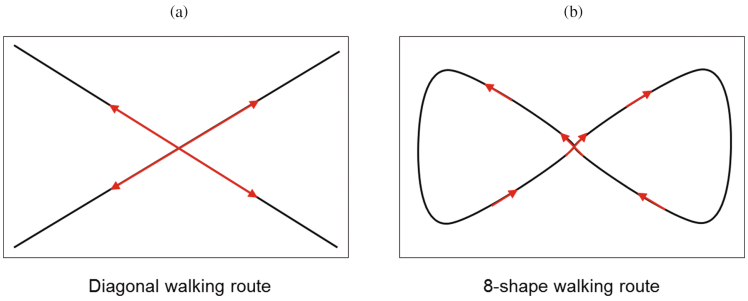

Fig. 5. (a) Diagonal and (b) 8-shape walking routes

The former walking route was chosen to compare the locations of the TSs with their corresponding vibration responses. The second walking route was used to test the performance of the tracking system for a more complex walking route.

4 Results and Discussion

The tracked and real positions of the TSs, their walking forces and the corresponding vibration response for one walking test in the diagonal route are presented in Fig. 6. The green and blue dots in Fig. 6a refer to the tracked positions of TS1 and TS2, respectively. The corresponding real locations of the TSs were extracted as images from the recorded video and merged for visualization purposes as shown in Fig. 6a. It is obvious that despite the tracked positions are not always accurate, they are consistent with the real locations, with good agreement between them most of the time.

Considering the mode shape of the first vibration mode (Fig. 3), the tracked positions of the TSs (Fig. 6a) are related to the measured vibration response (Fig. 6d). The maximum vibration response is obtained when the TSs were approximately walking in the middle of the floor, while lower vibration responses were recorded as TSs approach the corners (Figs. 6a and 6d).

Figure 7 shows the heat map, corresponding to the tracked positions in Fig. 6a, and its envelope for the two TSs, individually and collectively. The heat map is generated after the tracked positions were interpolated to obtain denser points. This plot can be used as an indication of the tracked positions and the corresponding proportion of time spent by TSs on the floor.

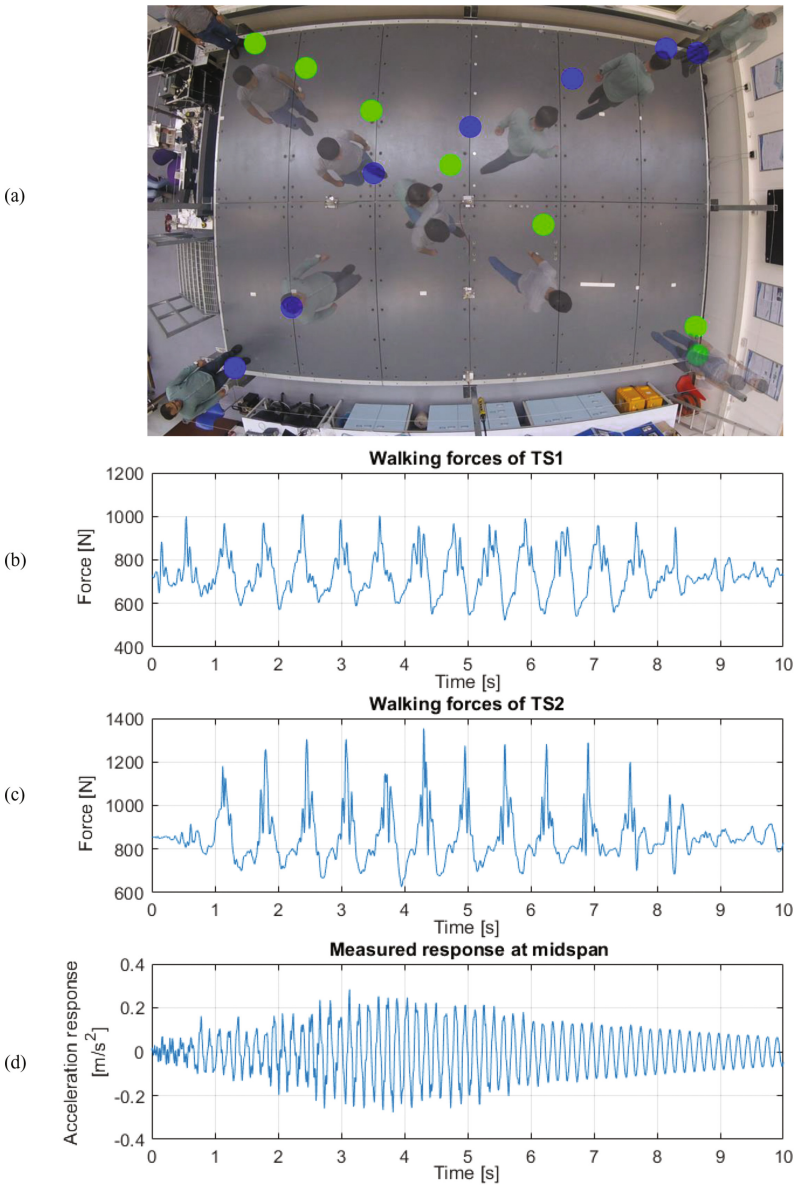

Fig. 6. (a) Tracked (green and blue dots) and real locations of TSs, (b) measured walking forces of TS1, (c) measured walking forces of TS2 and (d) the corresponding vibration response measured in the middle of the structure.

The heat map of tracked positions for the two TSs in the 8-shape walking route is presented in Fig. 8. It can be seen that there are relatively more tracked locations in the middle of the structure, which is consistent with the planned walking route (Fig. 5b).

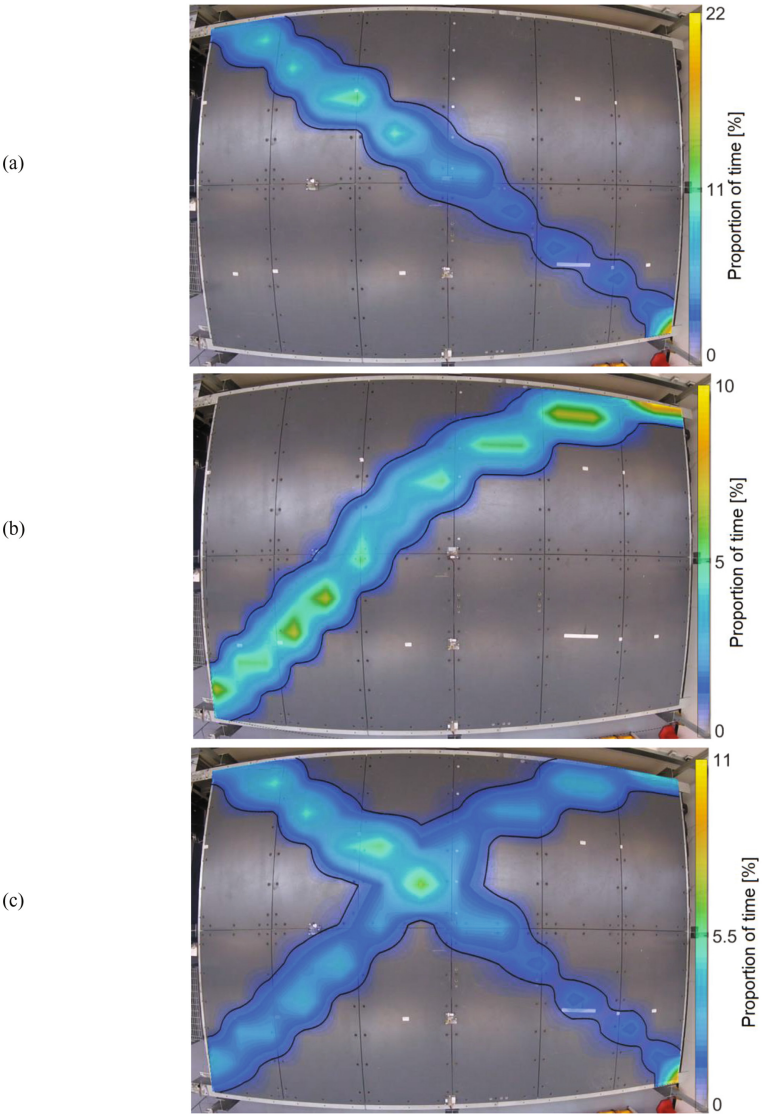

Fig. 7. The heat map of the tracked positions for (a) TS1 (b) TS2 and (c) both test subjects in a walking test in the diagonal walking route

The differences between the planned walking route (Fig. 5b) and the tracked positions (Fig. 8) could be explained by the inevitable errors of the tracking system and the natural inability of TSs to walk perfectly on the planned walking route with a constant speed.

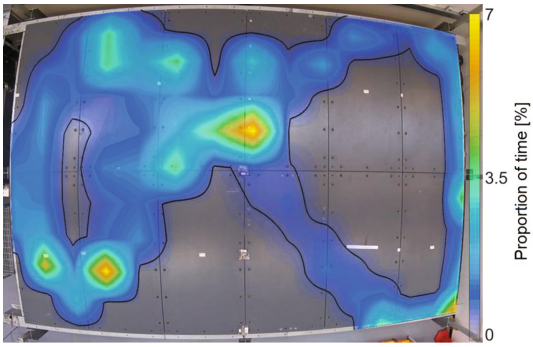

Fig. 8. The heat map of the tracked positions for the two TSs in a walking test in the 8-shape walking route

5 Conclusions

This paper proposes utilising a unique system based on the advanced technology of UWB to collect data regarding people's positions and movements in indoor building floors for vibration serviceability applications. To the best knowledge of the authors, this is the first attempt to monitor the people's locations in this context. The accuracy obtained by using this system and its easy implementation are promising for extensive use in future research. It has been shown that it finally became possible to measure directly the position of people, their walking forces and the corresponding vibration responses simultaneously, using state-of-the-art technology systems with an acceptable accuracy.

Acknowledgments. The authors are grateful for the College of Engineering, Mathematics and Physical Sciences in the University of Exeter for the financial support they provided for the first author and his PhD program. The authors would also like to acknowledge the financial support provided by the UK Engineering and Physical Sciences Research Council (EPSRC) for grant reference EP/K03877X/1 ('Modelling complex and partially identified engineering problems-Application to the individualised multiscale simulation of the musculoskeletal system').

References

1. Brownjohn, J.M.W., Pan, T.-C., Middleton, C.J., Tan, S.C., Yang, G.: Floor vibration serviceability in a multistory factory building. J. Perform. Constr. Facil. **30**, 4014203 (2014)
2. Chen, J., Zhang, M., Liu, W.: Vibration serviceability performance of an externally prestressed concrete floor during daily use and under controlled human activities. J. Perform. Constr. Facil. **30**, 4015007 (2015)
3. Reynolds, P., Pavic, A.: Reliability of assessment criteria for office floor vibrations. In: 50th United Kingdom Conference on Human Responses to Vibration, Southampton, UK (2015)
4. Pavic, A., Zivanovic, S.: Key elements for probabilistic framework for estimation of structural vibration due to human-structure dynamic interaction. In: 3rd International Conference Conference on Structural Engineering, Mechanics and Computation, Cape Town (2007)

5. Bocian, M., Brownjohn, J.M.W., Racic, V., Hester, D., Quattrone, A., Monnickendam, R.: A framework for experimental determination of localised vertical pedestrian forces on full-scale structures using wireless attitude and heading reference systems. J. Sound Vib. **376**, 217–243 (2016). Elsevier
6. Mcdonald, M.G., Stana, Ž.: Measuring ground reaction force and quantifying variability in jumping and bobbing actions. J. Struct. Eng. **143**, 4016161 (2016)
7. Teixeira, T., Dublon, G., Savvides, A.: A survey of human-sensing: methods for detecting presence, count, location, track, and identity. ACM Comput. Surv. **5**, 1–35 (2010)
8. Maalek, R., Sadeghpour, F.: Accuracy assessment of ultra-wide band technology in locating dynamic resources in indoor scenarios. Autom. Constr. **63**, 12–26 (2016). Elsevier
9. Alsindi, N., Alavi, B., Pahlavan, K.: Measurement and modeling of ultrawideband TOA-based ranging in indoor multipath environments. IEEE Trans. Veh. Technol. **58**, 1046–1058 (2009)
10. Instruction manual, Electro-seis, Model 400 Shaker. APS Dynamics, Inc., Carlsbad (2013)
11. Corporation, E. Endevco Model 7754A-1000 Datasheet. Rancho Viejo Road, San Juan Capistrano, CA, USA
12. Honeywell International, I. QA-750 Accelerometer Datasheet. Washington (2005)
13. Vibrant Technology Inc. ME'Scope VES 6.0 (2015)
14. Wearable Sensors—APDM. http://www.apdm.com/wearable-sensors/. Accessed 9 Dec 2016

Forced-Vibration Tests of the Daniel-Johnson Multiple-Arch Dam

O. Gauron[1], Y. Boivin[2], S. Ambroise[1], P. Paultre[1(✉)], J. Proulx[1], M. Roberge[3], and S.-N. Roth[3]

[1] Department of Civil Engineering, University of Sherbrooke, Sherbrooke, QC, Canada
patrick.paultre@usherbrooke.ca
[2] Tetra Tech, Sherbrooke, QC, Canada
[3] Hydro-Québec, Division Production, Direction Barrages et Infrastructures, Montreal, QC, Canada

Abstract. The Daniel-Johnson dam is a 1314-m long multiple-arch-buttress dam composed of 14 buttresses and 13 arches with a central arch of 214 m high. The upper part of the dam is composed of gravity dam supported by the arches. Its height, length and the 2 million cubic meters concrete used for its construction make it the largest dam of its type in the world. Hydro-Québec and the University of Sherbrooke carried out forced-vibration tests on the Daniel-Johnson dam that are presented in this paper. The tests aimed to determine the dynamic properties of the dam-reservoir-foundation (DRF) system to be used as a basis for the update of a 3D finite element model of the system. The outstanding size and the complex geometry of the dam are of great interest in this study, because they involved challenges in the experimental work not usually found for smaller dam of simpler geometry. The forced-vibration tests involved the use of an eccentric mass shaker generating forces up to 89 kN. The accurate modal identification of the dam required four different locations of the shaker, 52 measurement stations distributed along the crest of the dam and in the inspection galleries, and overall 13 tests configurations. These tests showed that it is possible to measure useful signals along the whole crest of a very large and massive concrete dam and as far as in the very lower inspection galleries, even with a relatively small excitation force. The analysis procedure of the experimental data were however quite complicated due to the numerous close local and global modes of the multiple-arch dam and their coupling. Twenty-two vibration modes were clearly identified. A 3D finite element model of the DRF system is briefly presented, and was correlated with the measured vibration modes.

Keywords: Modal analysis · Forced-vibration test · Multiple-arch dam · Eccentric mass shaker · 3D dam finite elements model

1 Introduction

In 2002, the Dam Safety Act came into effect for all dams of 1 m-high or more located in the province of Quebec. The main provisions of this Act apply to high capacity dams. The Dam Safety Act imposes a series of actions governing the construction, alteration

© Springer International Publishing AG 2018
J.P. Conte et al. (eds.), *Experimental Vibration Analysis for Civil Structures*,
Lecture Notes in Civil Engineering 5, https://doi.org/10.1007/978-3-319-67443-8_34

and operation of high-capacity dams. It requires that dam owners regularly maintain in good repair and monitor their structures. The Dam safety Regulation of the Act specifically requires that every high-capacity dams be designed and then be regularly verified to remain stable during the earthquake loading to which it may be subjected in the zone in which it is located. The work presented in this paper was carried out as part of a seismic safety evaluation of a unique multiple arch dam.

Hydro-Québec is a government-owned utility that owns and operates the majority of the hydroelectric powerplants in the province (more than 60). This includes the 2660 MW Manic-5 plant located on the Manicouagan River in northeastern Quebec and supplied by the high-capacity Daniel-Johnson dam (Fig. 1). This structure was constructed between 1959 and 1964 by Hydro-Québec and was inaugurated in 1969 with the hydroelectric plant. It is a multiple-arch-buttress dam composed of 14 buttresses and 13 arches with a central 214 m-high arch. The upper part of the dam is built like a 1314 m-long gravity dam that rests on top of the arches. Its height, its length and the 2 million cubic meters concrete used for its construction make it the largest dam of its type in the world. Most of the reservoir of the dam is located in a former meteor crater of about 197 000 hectares. Around 13 years were necessary to fill the 135 billion cubic meters water in the reservoir.

Fig. 1. Daniel-Johnson dam.

To support the seismic safety evaluation, Hydro-Québec decided to conduct an experimental program to evaluate the dynamic properties of the dam-reservoir-foundation (DRF) system, in collaboration with the Earthquake Engineering and Structural Dynamics Research Center (CRGP) at the University of Sherbrooke because of its experience in characterizing and modelling the dynamic behavior of large concrete dams [1–3]. The aim of this study was to get a 3D finite element model of the DRF system suitable for further seismic analyses.

The forced-vibration tests that were carried out on the Daniel-Johnson multiple-arch dam are the main focus of this paper. The tests aimed to determine the dynamic properties

of the DRF system in order to be used as a basis for calibration of a 3D finite element model of the system to be used as part of a seismic safety evaluation. The dynamic tests were carried out with an eccentric mass shaker and accelerations were recorded along the 1.3 km-long dam crest and in selected galleries of the 214 m-high central arch under harmonic loading. The test procedures and data processing are presented. The modal properties (frequencies, mode shapes and damping ratios), are then detailed together with the extraction procedure, which was complicated due to the coupling of the numerous global and local modes of such a complex structure. A 3D finite element model of the dam was finally developed using the computer program ANSYS [4]. It is briefly presented with the main steps that allowed to correlate with the measured dynamic properties.

2 Forced-Vibration Tests

2.1 Test Equipment

The equipment used for the forced-vibration tests of the Daniel-Johnson dam is presented below and includes an eccentric-mass shaker, accelerometers, a data acquisition system and a computer that controls and synchronizes the excitation of the shaker and the data acquisition in order to run the tests automatically.

The main objective of the forced-vibration tests was to measure acceleration responses of the DRF system subjected to a harmonic load acting on the dam crest in a desired direction. During the tests of the Daniel-Johnson dam, this force was provided by the MK-12.8A-4600 eccentric mass shaker (ANCO, Inc.) shown in Fig. 2a. Two sets of identical weights rotating in opposite directions about parallel vertical shafts generate a sinusoidal load in only one direction. The amplitude of the resulting force, which is proportional to the square of the rotation frequency, can be adjusted by varying the eccentricity of the weights (Fig. 2b). The maximal force amplitude that can be generated by the shaker is 89 kN, which limits the amount of eccentricity that can be used depending on the excitation frequency. The shaker is powered by a 3.7 kW computer-controlled electric motor at a maximum rotation frequency of 15 Hz.

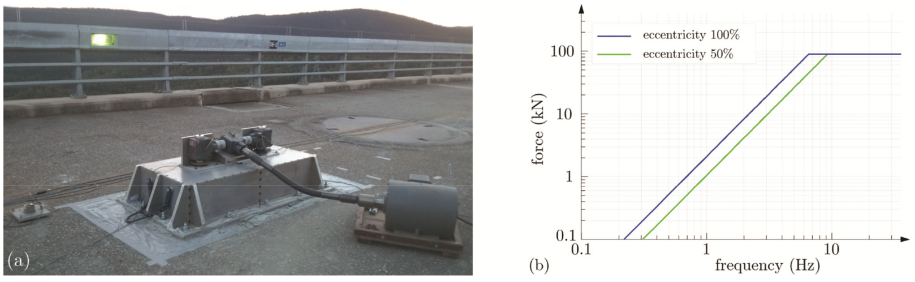

Fig. 2. (a) Eccentric mass shaker on the dam; (b) Generated excitation force.

The tests on the Daniel-Johnson dam were carried out within a frequency range of 1.0 Hz to 8.3 Hz in order to capture the desired modal frequencies determined with a preliminary numerical model of the dam structure. Considering the size of the dam and the need for a good signal to noise ratio even in the lowest frequencies of the test (where the generated harmonic force is the lowest), each sweep of the selected frequency range was completed in two steps using the maximum eccentricity (100%) for 1.0 Hz to 6.0 Hz (loads varying from 2 kN to 75 kN) and half eccentricity (50%) for 5.5 Hz–8.3 Hz (31–72 kN). The shaker was fixed to the dam crest with 12 anchor bolts and a cement grout was used to level the base plate and to ensure that the resulting force remained in a horizontal plane.

The horizontal dynamic responses of the dam excited by the harmonic force of the shaker were recorded by seven low-frequency uniaxial accelerometers with high sensitivity (50 V/g). These transducers allowed to clearly measure the harmonic acceleration responses of the dam with amplitudes ranging from as low as 10^{-5} g to 2×10^{-3} g. They were successively placed in different locations along the whole crest of the dam (measuring in a direction either parallel to, or perpendicular to the exciting force) as well as along two inspection galleries in the center arch (measuring in a direction perpendicular to the arch curvature).

Seven of the eight available acquisition channels were used to record the signals sent by the accelerometers and the last channel was used to record the pulse sent by the shaker once per rotation when the force was maximum. All signals were recorded simultaneously at a sampling rate of 1000 Hz using 20 Hz low-pass hardware filters. This high sampling frequency was required to correctly measure the excitation frequency, using an unfiltered channel. Hardware amplifiers (gain of 10 and 100) were used for the accelerometer channels to improve signal to noise ratios considering the very low level of the acceleration responses.

2.2 Test Procedure

The complete characterization of the modal properties of the Daniel-Johnson dam was carried out by using four different positions of the shaker along the crest. Figure 3 shows 3D views of the dam indicating each position used for the shaker along with the associated direction of the exciting force (red arrow) and associated positions and measurement directions of the accelerometers (yellow boxes). The *X* axis is along the longitudinal direction of the dam crest and the *Y* axis is along the transversal direction of the crest. Note that the buttresses of the dam are numbered from B1 to B14. In the following paragraphs, the arches of the dams will be named by using the number of each adjacent buttress, e.g. A6-7 for the center arch, located between buttresses B6 and B7.

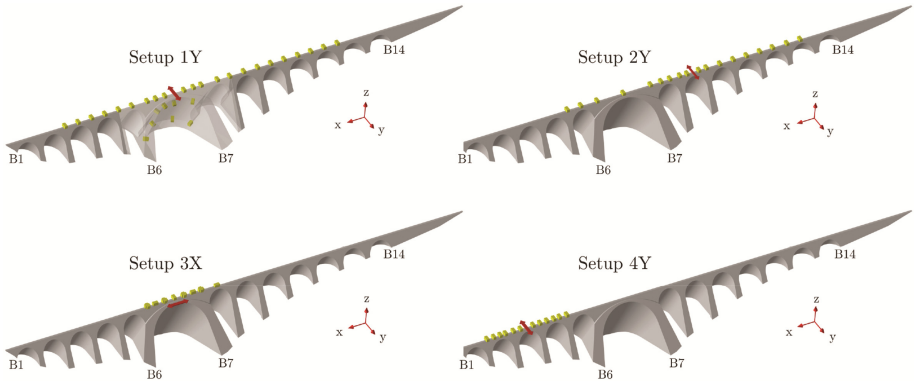

Fig. 3. Positions of the shaker and accelerometers for the four test setups.

The different positions of the excitation force were necessary to excite global modes of the structure (involving most of its 13 arches) as well as local modes (involving only few arches near the shaker) and to ensure that modes were not missed if the excitation force was located at a node of a particular mode shape. The four test setups (Fig. 3) were chosen by considering the results of a preliminary numerical analysis:

- Setup 1Y: the shaker was located at the center of the main arch (A6-7) and oriented to excite in direction *Y*; measurements were done along the crest in direction *Y*; additional measurements were done in inspection galleries 1011 and 800 of the center arch located 57 m and 122 m below the crest, respectively. This setup aimed to characterize most of the first global modes of the dam and the first local modes of the main arch and its adjacent arches A5-6 and A7-8. This position of the shaker was the most likely to produce measurable accelerations in the inspection galleries of the center arch.
- Setup 2Y: the shaker was located at the center of arch A8-9 and oriented to excite in direction *Y*; measurements were done along the crest in direction *Y*. This setup aimed essentially to get the global modes of the dam that have a node at the center of arch A6-7 and hence that were not excited during the tests of setup 1Y.
- Setup 3X: the shaker was located at the center of the main arch (A6-7) and oriented to excite in direction *X* (along the longitudinal crest axis); measurements were done only along the crest of arch A6-7 in directions *X* and *Y*. This setup aimed to characterize the global modes with a strong longitudinal component and the local modes of the center arch identified during the tests of setup 1Y that have a strong *X*-*Y* component coupling.
- Setup 4Y: the shaker was located at the center of arch A3-4 and oriented to excite in direction *Y*; measurements were done along the crest between buttresses B2 and B5 in direction *Y*. This setup aimed to characterize local modes involving the specific arch A3-4 for which a more refined 3D model was developed.

Overall, 36 measurement stations in direction *Y* were defined along the crest of the dam between buttresses B2 and B13 (some were used in several setups), 8 measurement

stations in direction *X* along the crest between buttresses B6 and B8 and 8 in the inspection galleries of the center arch (A6-7). The seven uniaxial accelerometers used were successively moved along the crest of the dam or the inspection galleries for each setup in order to record all locations presented in Fig. 3. A total of thirteen forced vibration tests were needed to complete the experimental study. For each setup, one accelerometer, referred to as the reference accelerometer, remained in the same location, next to the shaker, to ensure the compatibility of the frequency response functions (FRF) of two successive tests.

After having positioned the shaker on the crest and placed the transducers, the procedure for a complete test included a first low-frequency sweep between 1.0 Hz and 6.0 Hz, then a change of the eccentricity of the weights of the shaker, and finally a second high-frequency sweep between 5.5 Hz and 8.3 Hz. The common range of both sweeps (5.5 Hz to 6.0 Hz), was used to verify the compatibility of the FRF measured for both successive sweeps. An increment of 0.025 Hz was used throughout the tests. A complete frequency sweep involved 200 frequency increments for the low-frequency sweep and 113 increments for the high-frequency sweep. For each increment, the signals of the accelerometers and of the shaker pulse were recorded during 4 s, to ensure that the structure reached steady-state and to obtain a sufficient number of cycles for post processing.

2.3 Test Results

The data reduction process involves the computation of frequency response functions for each measurement station and for each test setup. For each frequency increment, a least-squares curve-fitting algorithm was used to calculate the harmonic amplitude and phase of each 4-second recorded time-history. The processing steps are as follows, for each frequency increment: (i) compute the exact excitation frequency from the recorded shaker pulse and calculate the amplitude of the shaker force generated at that frequency (Fig. 2b); (ii) extract the amplitude and phase for each measured response by harmonic curve fitting; (iii) correct the amplitudes and phases for the modifications brought upon by the individual transducers and the filters in the data acquisition unit; and (iv) normalize the response by dividing the amplitude by the excitation force. These steps were repeated during both sweeps of a test to get the complete frequency response curves of the DRF system. Figure 4a and b shows some frequency responses (FRs) obtained for setup 1Y (low-frequency sweep with full lines, high- frequency sweep with dotted lines). These figures show a nearly perfect overlap of the FRs in the common frequency range of both sweeps (5.5 Hz to 6.0 Hz), which validates the testing procedure for a complete sweep from 1.0 Hz to 8.3 Hz using two different eccentricities of the shaker weights. Figure 4b shows the FRs obtained for the reference accelerometer during three of the tests done to complete testing setup 1Y. Again, the nearly perfect overlap of the curves indicates the compatibility of the results of all measurement stations obtained from different sweeps for a specific position of the shaker. It should be noted that useful and significant acceleration responses were measured for all positions of the shaker and all measurement stations (some located almost 500 m away from the exciting force), as well as for stations inside the galleries located well below the crest.

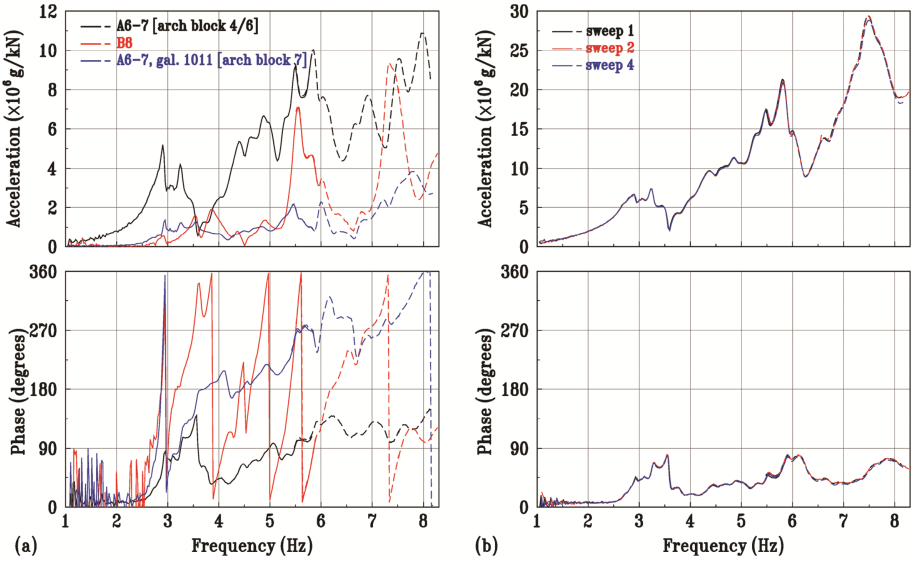

Fig. 4. Frequency responses for (a) setup 1Y (crest and galleries), (b) setup 2Y: reference accelerometer.

The identification of the resonant frequencies and associated mode shapes and damping ratios is usually straightforward using FRs obtained from forced vibration tests, if the tested structure only has well-separated modes in the tested frequency range. In the particular case of the 13-arch Daniel-Johnson dam with four testing setups, this task proved to be very difficult because of the coupling of several modes in the 1.0 Hz to 8.3 Hz range. The coupling of two close modes or more directly affects the time-history data used to compute the FRs as illustrated in Fig. 5. Figure 5a illustrates one second of a typical raw data recorded during test setup 1Y at 5.828 Hz, which is exactly the frequency of the identified mode #14 which is a relatively isolated mode. The harmonic curve fitting procedure calculated to match the recorded response is very accurate in this case. Figure 5b illustrates the same transducer response at 4.005 Hz, between both closely-spaced modes #5 and #6, where the effects of coupling of both modes are evident and where a decrease in the accuracy of the curve fitting process can be seen for this specific measurement station. As illustrated in Fig. 4a, the large number of vibration modes in the tested frequency range together with mode coupling resulted in FR amplitudes with many peaks having often poorly defined spectral bells and also in complicated evolutions of the calculated phase lags. All of these effects have several consequences on the modal identification process. It is first nearly impossible to trust the phase lag curves to identify the accurate frequency of a mode by finding the phase quadrature between the responses and the excitation force. Therefore, only the peak picking method can be used. Then, for two close modes of similar energy, mode coupling tends to provide FRs with amplitude at a given frequency resulting from a combination of both mode contributions. It can lead to either overestimated or underestimated amplitude values, which can greatly affect the accuracy of the corresponding identified mode shapes at

some measurement stations. In the case of coupled modes with a dominant contribution of one of them at a specific measurement station, the spectral bell of the mode of lesser energy will practically be canceled out by the dominant contribution of the other mode. In such a case, the concerned measurement station cannot be considered to identify the mode shape of the mode of lesser energy. These phenomena explain why the mode shapes of the dam could not be extracted systematically by just using the FRs amplitudes of each measurement station at an identified vibration frequency. Thus, the authors had to manually inspect each FR for all measurement stations, for each identified modal frequency, in order to accept or discard the corresponding station, resulting in identified mode shapes where some measurement stations are missing. Finally, the same reasons also explain why in Table 1 some modal damping ratios were not identified for modes that did not result in clear spectral bells on which to apply the half-bandwidth method.

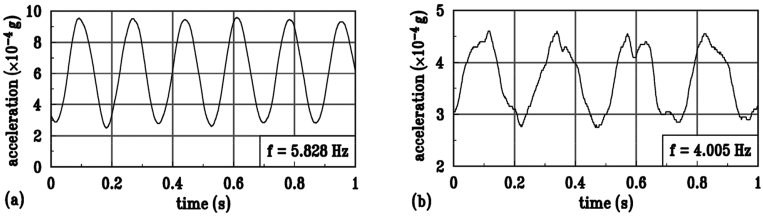

Fig. 5. Effect of mode coupling on the raw time-history response of a typical transducer in setup 1Y.

Table 1. Identified modal properties of the Daniel-Johnson dam used to calibrate the finite element model of the dam.

Mode	1	3	4			5		6		7	10		11
Test setup	3X	1Y	1Y	2Y	3X	1Y	2Y	2Y	3X	1Y	2Y	4Y	4Y
f (Hz)	2.918	3.256	3.535	3.552	3.555	3.868	3.812	4.089	4.069	4.240	4.840	4.793	5.252
σ(Hz)	0.009	0.013	0.038	0.021	0.014	0.056	0.028	0.036	0.035	0.024	0.032	0.012	0.009
ξ	1.31%	2.68%	2.04%	1.77%	1.43%	2.27%	2.94%	–	2.57%	2.11%	2.47%	–	1.63%

Considering previous remarks, the following procedure was applied for each test setup to extract the resonant properties of the dam: (i) extract all FRs peaks for each available measurement station; (ii) group all similar or identical resonant frequencies of the measurement stations to compute a mean resonant frequency f (considered as the identified modal frequency) and its corresponding standard deviation σ (considered as the experimental error); (iii) plot the resonant shapes of the dam for each resonant frequency using the amplitude and phase lag (with respect to the reference accelerometer close to the shaker) of each available measurement station; (iv) discard obviously inaccurate measurements resulting from coupling phenomena on the basis of the spectral bell definition for these specific transducers, of the appearance of the plotted mode shape and of the coherence of the resonant shapes obtained from different testing setups; (v)

compute the mean modal damping ratio ξ using the half-power bandwidth method for each available measurement station at each resonant frequency.

Twenty-two (22) resonant frequencies were identified for the Daniel-Johnson dam over the range 1.0 Hz to 8.3 Hz. For practical reasons, the properties of only the eight modes used to calibrate the numerical model of the dam described in the next section are presented in Table 1 and the shapes of only four of them in Fig. 8. These modes are also among the ones identified with the lowest uncertainties, considering the effect of mode coupling explained previously. Some of the identified mode shapes were obtained only from one test setup and others from several setups. In the latter case, the final resonant shapes were extracted by verifying the compatibility of the results from the different test setups and by adequately combining their shape if necessary. Figure 6a is an illustration of the very good coherence for the shapes of mode 4 identified from test setups 1Y and 2Y and justifies that a complete mode shape can be completed by using the results of different setups. Figure 6b shows the combination procedure applied for mode 6 to get a more complete and accurate shape by using the results of setup 3X for the central arch that were not available in test setup 2Y. In Figs. 6 and 8, the modes presented correspond to the lateral and longitudinal deformations of the dam crest. The available measurement stations used to plot the shapes are indicated by filled squares (with station number) that are connected together using a quadratic interpolation for a smoother illustration of the resonant shapes.

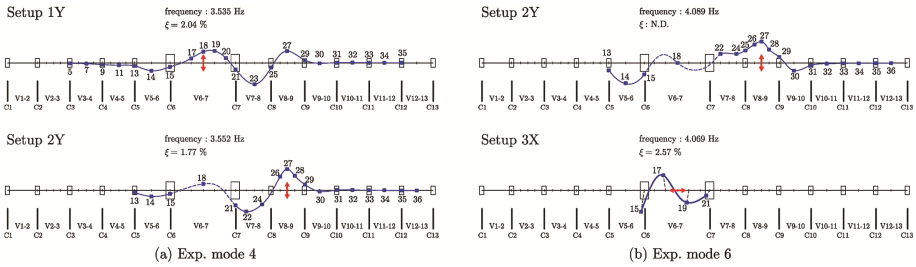

Fig. 6. Coherence and combination of mode shapes from different test setups.

3 Calibrated Numerical Model

The identified modal properties of the DRF system were used as a basis for the calibration of a finite element model of the DRF system developed with the finite element software ANSYS v14.5 [4]. The development of such a finite element model was not straightforward and included many steps to get the most appropriate model for time-history seismic analyses. The adequate model was selected based (i) on the accuracy of the modal properties compared to those measured experimentally; (ii) on the effective influence of some approximations on time-history results; and (iii) on the required computation time considering that numerous time-history calculations are required for a seismic evaluation.

Figure 7a presents the finite element model developed for the dam-foundation system. The model was developed by using the detailed 3D geometry of the dam meshed with 10-nodes quadratic tetra elements. The vertical contraction joints of the dam crest between the arches were accounted for by not connecting the nodes defining both faces of a joint. The surface rock of the foundation was represented in a realistic manner from in situ topographic data. The dam-foundation interface is made up of coincident surfaces between the dam and the foundation. The foundation dimensions were sized such that its side and bottom faces were located at a distance from the dam at least equal to the maximum dam height. Massless foundations were considered in order to simplify further seismic time-history analyses by avoiding deconvolution of the accelerograms [5]. Values of the elastic moduli for the dam concrete E_c and the rock E_r equal to 40 GPa were obtained from a preliminary parametric study.

(a)

Nb of elements	175 187
Nb of nodes	236 381
Dam-Foundation	Quadratic tetrahedron elements(SOLID 187)
Reservoir	Linear prism elements (FLUID 30)
Dam concrete	Linear elastic, E_c=44 GPa, ν_c=0.20, ρ_c=2400 kg/m^3
Rock	Linear elastic, E_r=40 GPa, ν_r=0.25, ρ_r=0 kg/m^3
Water	Incompressible, ρ_c=1000 kg/m^3, c=1.44×10^6 m/s
Bound. Cond. Reservoir	Zero gradient pressure on all sides of reservoir, except on dam-reservoir interface; zero pressure on the upper side of the reservoir.
Dam-Foundation	Fixed conditions in the three directions on all sides.

(b)

Fig. 7. Features of the calibrated finite element model of the dam-foundation-reservoir system.

A detailed analysis was carried out to select the appropriate modelling method for the impounded reservoir of the DRF system. Two widely used approaches were considered: the direct finite element modelling of the reservoir as well as the added mass approach [6]. For the finite element approach, fluid linear or quadratic prism elements were used to mesh the reservoir, with both compressible and incompressible water models. The added mass approach is a simplified modelling assumption of the reservoir that allows to greatly reduce the required calculations, compared to a complete finite element model of the reservoir, by significantly reducing the number of elements. However, it requires that the added masses be determined independently for each direction, and that time-history analyses be performed in each direction independently. Modal analyses and a benchmark seismic time-history analysis carried out on the DRF system for the different models of the reservoir showed that: (i) compressibility of water may affect the predicted vibration modes of the DRF system, but it has only a slight effect on the seismic time-history results; (ii) the use of linear fluid elements produces dynamic results similar to those obtained with quadratic ones, but with half the computation time; (iii) added mass models can provide satisfactory estimations of the maximum time history responses with significantly shorter computation times per analysis, but they are not the most appropriate for such a complex arch dam, because it requires that each direction be studied independently.

The authors concluded that the best approach in terms of accuracy of the dynamic behavior and of computation time was to model the reservoir by finite element with linear acoustic fluid elements with incompressible water. The resulting finite element model of the DRF system was finally refined by adjusting the preliminary calibrated value of the elastic modulus of the dam concrete to $E_c = 44$ GPa. All features of the final finite element model are given in Fig. 7b. The whole process allowed to efficiently correlate eight of the identified experimental modes (four modes illustrated in Fig. 8), including frequencies and mode shapes.

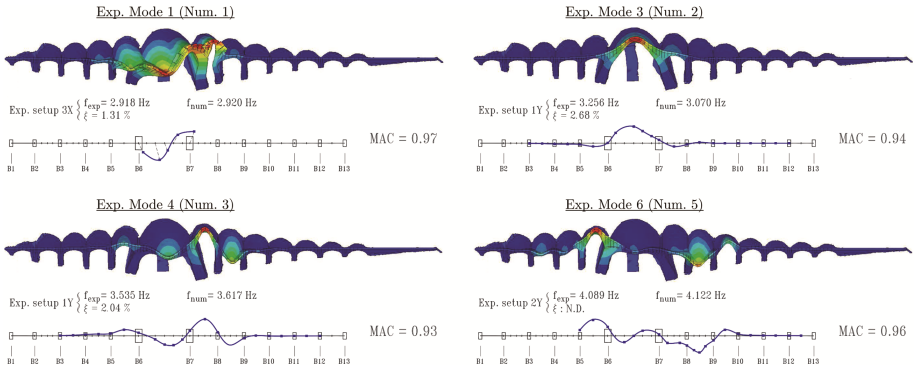

Fig. 8. Comparison of four of the eight experimental and numerical mode shapes used for model updating.

4 Conclusions

This paper presented the experimental modal analysis of the Daniel-Johnson multiple-arch concrete dam. This dam, composed of 14 buttresses and 13 arches with a 214 m-high central arch and a 1314 m-long crest is among the largest multiple-arch dams in the world. The outstanding size and the complex geometry of the dam lead to challenges in the experimental work. Forced-vibration tests were carried out on the dam, and involved the use of an eccentric mass shaker located at several positions along the crest of the dam in order to characterize the modal properties of the DRF system. These tests showed that it is possible to measure useful signals along the whole crest of a very large dam and as well as in the lowest inspection galleries, even with a relatively small excitation force. The analysis procedure of the experimental data were however quite complicated due to the numerous closely spaced local and global modes of the multiple-arch dam. Mode coupling provided difficulties in the analysis of the frequency response functions that could not be completed automatically. A particular modal extraction procedure was applied, including manual choices about the reliable measurement stations for each mode to extract accurate mode shapes. The results from the four different test setup corresponding to four different locations of the shaker were also combined for specific resonant frequencies to get complete mode shapes. Twenty-two

vibration modes were finally identified, including modal frequencies, mode shapes and modal damping ratios.

The identified modal properties of the DRF system were used as a basis for the calibration of a finite element model of the DRF system developed with ANSYS v14.5. The modelling work was carried out on the basis of a detailed 3D dam-foundation geometry. Different methods were considered to model the interactions of the dam-foundation system with the reservoir, including several finite element models of the reservoir and the added mass approach. From modal and time-history analyses, the authors concluded that a finite element model of the reservoir with incompressible water and linear elements was the most suitable model for the seismic analyses of the complex Daniel-Johnson dam, both in terms of accuracy and of computation time. The whole process allowed to efficiently correlate the model results with eight of the identified experimental mode shapes and frequencies, making the finite element model suitable for the subsequent seismic safety analyses.

Acknowledgments. The authors gratefully acknowledge the financial support of Hydro-Québec. Douglas Sparks, Head of Dam Safety Reviews at Hydro-Québec was the project leader. The authors wish to thank Claude Aubé and Jeason Desmarais, technicians at the University of Sherbrooke, who participated in the testing program.

References

1. Proulx, J., Paultre, P.: Experimental and numerical investigation of dam-reservoir-foundation interaction for a large gravity dam. Can. J. Civ. Eng. **24**(1), 90–105 (1997)
2. Proulx, J., Paultre, P., Rheault, J., Robert, Y.: An experimental investigation of water level effects on the dynamic behavior of a large arch dam. Earthq. Eng. Struct. Dyn. **30**(8), 1147–1166 (2001)
3. Paultre, P., Proulx, J., Carbonneau, C.: An experimental evaluation of ice cover effects on the dynamic behaviour of a concrete gravity dam. Earthq. Eng. Struct. Dyn. **31**(12), 2067–2082 (2002)
4. ANSYS Inc.: ANSYS Software v14.5. ANSYS Inc., Canonsburg, PA, USA (2012). http://www.ansys.com/
5. Léger, P., Boughoufalah, M.: Earthquake input mechanisms for time-domain analysis of dam foundation systems. Eng. Struct. **11**(1), 37–46 (1989)
6. Kuo, J.: Fluid-structure interactions: added mass computations for incompressible fluid. Report No. UCB/EERC-82/09, Earthquake Engineering Research Center, University of California, Berkeley, CA (1982)

Experimental Vibration Analysis of Composite Bridge Superstructure with Excessive Deformations

Mieszko Kużawa(✉) and Jan Bień

Department of Civil Engineering,
Wroclaw University of Science and Technology, Wrocław, Poland
mieszko.kuzawa@pwr.edu.pl

Abstract. The paper presents results of experimental vibration tests of dynamic susceptible composite, steel-concrete, multi-girder superstructure of highway bridge with excessive deformations. The whole structural system exhibit disproportionate, low-damped vibrations induced by normal traffic crossing the bridge. The presented series of dynamic tests under real traffic were performed for identification of the bridge dynamic characteristics important for future safety and fatigue analyses.

In the paper the tested bridge structure as well as procedure of the performed dynamic tests and applied measuring systems are described together with the numerical model developed during design of the experiment and analysis of the tests results. Measured strains, displacements and accelerations as well as calculated Dynamic Amplification Factors (DAF) are presented for various load scenarios caused by vehicles crossing the bridge. Conclusions regarding effectiveness of applied testing method in identification of the bridge dynamic condition are formulated.

Keywords: Composite bridge · Excessive deformations · Experimental vibration test · Dynamic characteristics

1 Bridge Structure and Objectives of Study

The investigated bridge structure over the Warta River (built in 1989) is a part of the highway A2, one of the main highways in Poland, going from Warsaw to Berlin, Germany. The bridge consists of two separated superstructures, each built of seven semi-continuous beam type spans. Every span is constructed of four steel plate girders, 2.5 m high, composed with typical RC slab of variable thickness. Theoretical length of each span is 41.0 m. The composite superstructure has in each span an excessive, permanent deflections, up to 10 cm, possibly resulting from creep and shrinkage of RC slab as well as design and construction faults. The structural form of the investigated bridge is presented in Figs. 1 and 2, as well as in Fig. 4.

The whole structural system exhibit excessive, low-damped vibrations induced by normal traffic crossing the bridge. The aim of the presented study was to evaluate the bridge dynamic behaviour in terms of its current serviceability and for future safety and

© Springer International Publishing AG 2018
J.P. Conte et al. (eds.), *Experimental Vibration Analysis for Civil Structures*,
Lecture Notes in Civil Engineering 5, https://doi.org/10.1007/978-3-319-67443-8_35

Fig. 1. Side view of investigated bridge – visible excessive permanent deflection of superstructure

Fig. 2. Investigated bridge: (a) bottom view of superstructure, (b) view of intermediate support area

fatigue analyses. Dynamic tests of the structure were executed according to recommendations specified in [1–5] and experience from previous similar tests, e.g. [6–12].

2 Testing Procedure

Evaluation of structural performance of the analyzed bridge was carried out in real traffic conditions during four whole-day experimental vibration tests carried out every month during the period of three months (June–September 2016). The detailed design of a measurement system were preceded by numerical analysis which enabled the most effective location of gauges during tests under regular traffic. Superstructure was modeled by means of one- and two-dimensional finite elements. One-dimensional, beam type elements, were utilized for representation of all steel components of superstructure, including stiffeners. Two-dimensional, shell type elements, were used for modelling of RC deck slab. Also non-structural joints were applied for connection of beams and shells together. For simplicity only two spans of one carriageway were considered in theoretical analysis. Applied finite element model of the structure (Fig. 3) was analyzed using ROBOT Structural Analysis system.

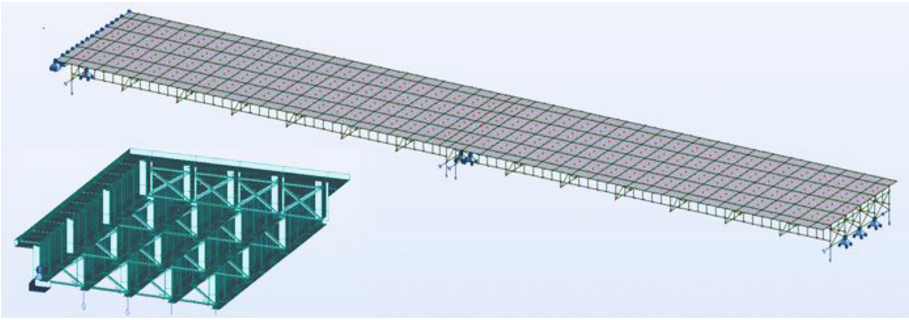

Fig. 3. Investigated bridge: (a) bottom view of superstructure, b) view of intermediate support area

The FEM analysis was carried out to discover how the superstructure behaves under theoretical loads representing heavy vehicles as well as for identification of its basic dynamic properties. In course of a preliminary linear-static analysis relatively low stiffness of multi-girder composite system was revealed - the maximum calculated deflection of span resulted from single 40-tonne vehicle crossing the bridge amounted for 7 mm. Theoretically obtained modal parameters revealed closely spaced bending and torsional vibration modes with associated relatively low frequencies (in a range of 2.0–2.5 Hz) indicating possible dynamic susceptibility. In addition, evaluation of stress ranges induced by the theoretical live load model FLM4 defined in Eurocode [13, 14] and recommended for fatigue analysis of existing road bridges in Europe [15], pointed out some critical spots of the steel superstructure with limited fatigue resistance and thus indicated the need of experimental verification.

On the basis of results of the preliminary structural analysis it was decided that precise assessment of bridge condition and its performance requires strain, displacement and acceleration measurements under real traffic loads. Selection of the bridge spans to examine were supported by detailed inspection of the bridge structure as well as by analysis of spans permanent deflections, which were measured by means of precise geodetic method every four years in previous 15 years of bridge operation. As a result of briefly described above preliminary evaluation two utmost adjacent spans (6–7 and 7–8) having the greatest permanent deflections were taken into consideration for experimental vibration analysis.

During consecutive four measuring sessions gauges arrangement scheme has been slightly modified according to current needs of the bridge evaluation. Exemplary gauges arrangement scheme applied during 4^{th} session is presented in Fig. 4. According to presented sensors layout during the last testing session the following physical quantities were measured:

- strains induced in lower flanges of steel girders in span 7–8 at the measuring points numbered from 00 to 06 shown in Fig. 4; measurement was conducted using a strain gauges – see Fig. 5a,

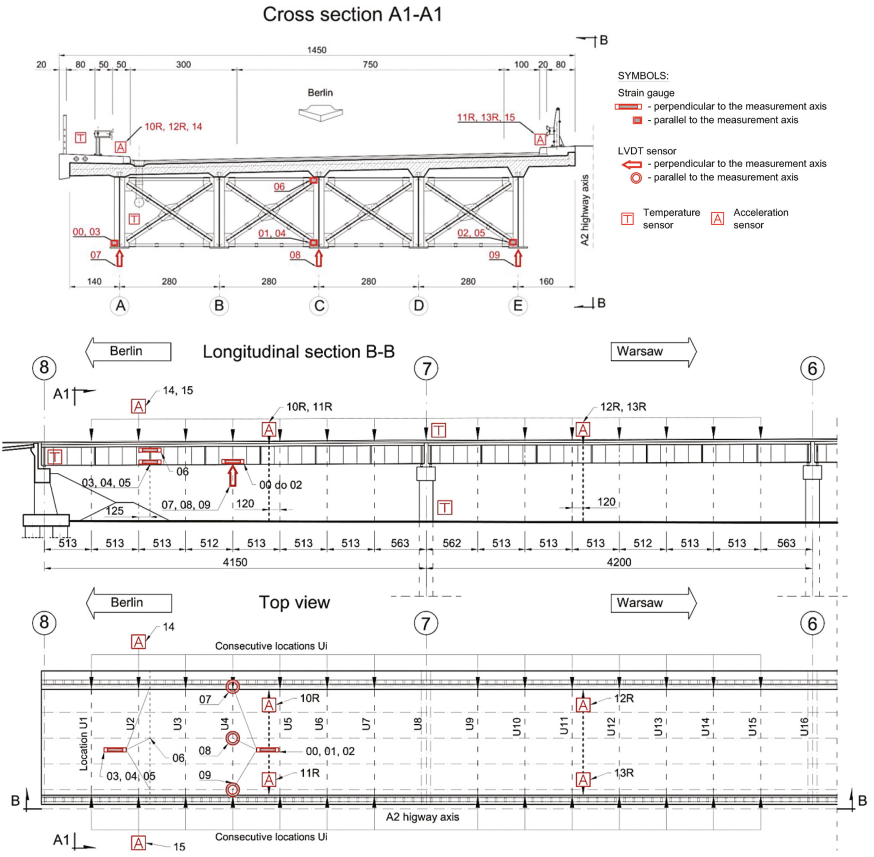

Fig. 4. Gauges arrangement scheme: (a) cross section, (b) longitudinal section, (c) top view

- vertical displacements in the middle section of span 7–8 at the measuring points numbered from 07 to 09; measurement was conducted using a LVDT sensors – see Fig. 5b,
- vertical accelerations at selected points of bridge deck numbered from 10R to 13R and 14 to 15 (shown in Fig. 4) located along both edges of single carriageway in spans 6–7, 7–8; measurement was conducted using a accelerometers – see Fig. 5c.

During whole-day measurements all vehicles crossing the bridge were registered using a camera and digital video recorder (DVR), for matching type of vehicles with the corresponding measured physical values. The temperature was controlled continuously in four specific areas of structure.

Fig. 5. Exemplary location of different types of measuring sensors in span 7–8: (a) strain gauge at point 00, (b) LVDT sensors at points 07–09, (c) accelerometer at point 10R

3 Results of the Vibration Tests

Measurements under service loads were made to get real-time information of the superstructure performance under normal traffic loads. During each measuring session between 20 and 25 measurements (10 min each) were carried out with the sampling frequency of 300 Hz. Selected results of the 4th testing session (September 14th, 2016) between 8.30 am and 18.00 pm are presented in Figs. 6, 7 and 8.

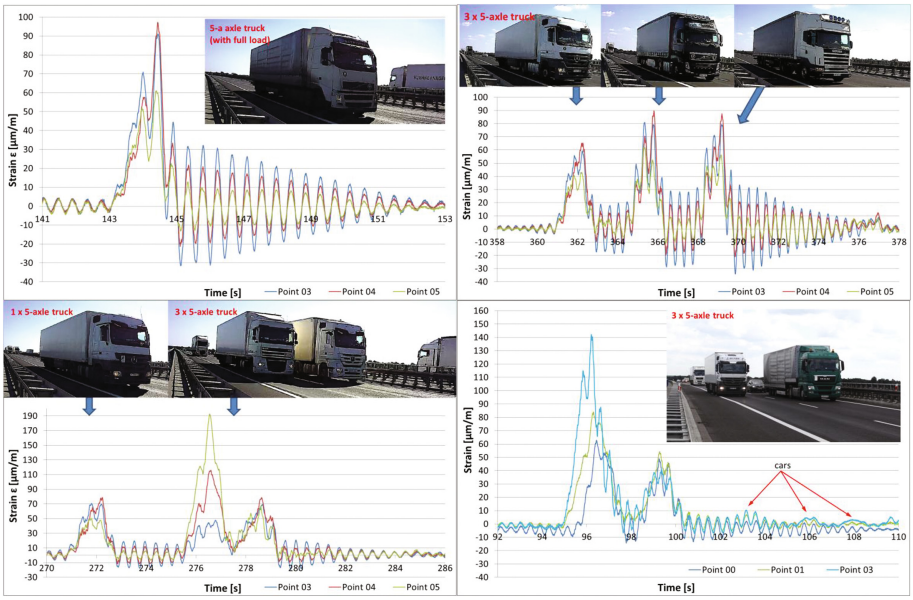

Fig. 6. History of strains induced in main girders by various schemes of 5-axle vehicles

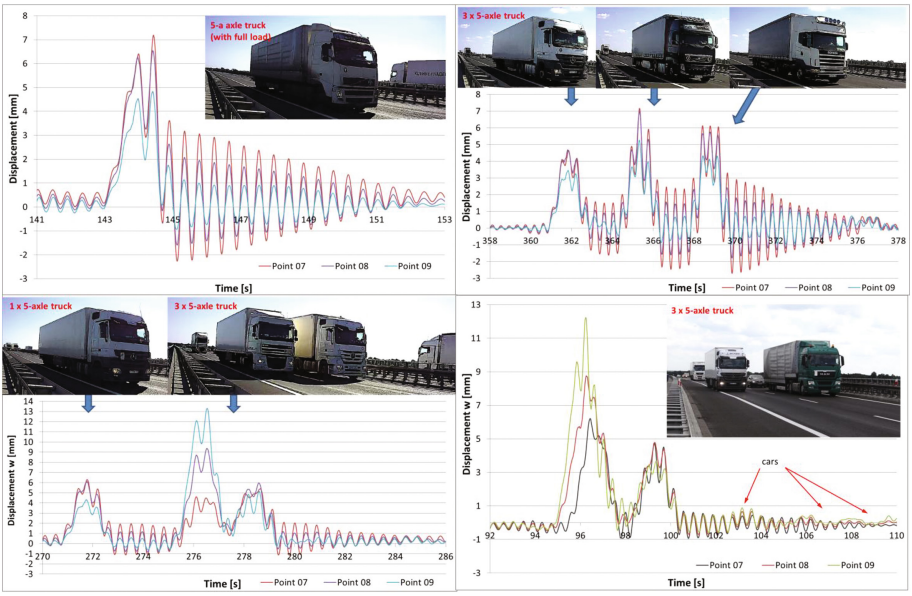

Fig. 7. History of main girders displacements induced by various schemes of 5-axle vehicles

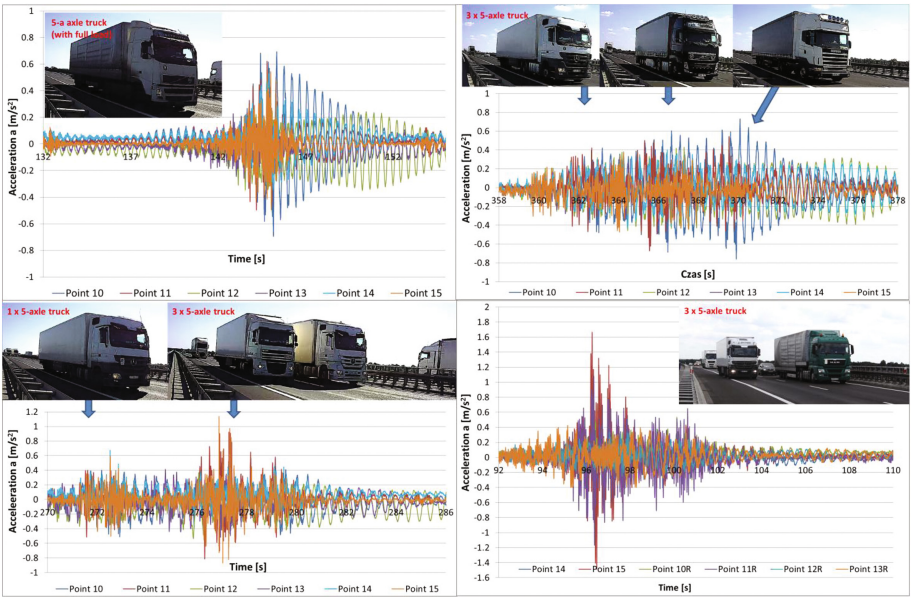

Fig. 8. History of main girders accelerations induced by various schemes of 5-axle vehicles

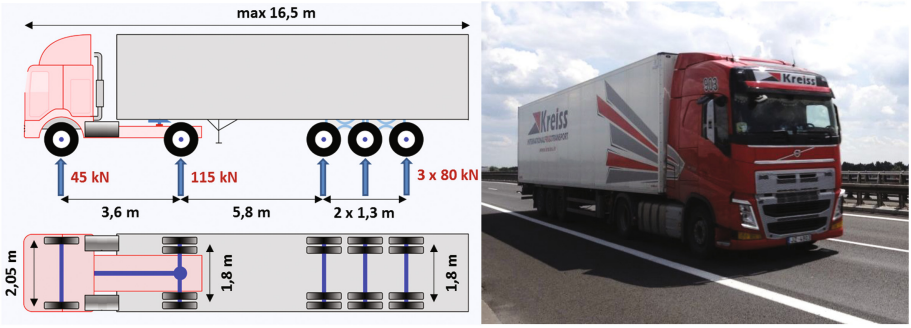

Fig. 9. Typical 5-axle trucks with a total maximum weight of 40 tones: (a) basic parameters – i.e. dimensions and axle loads, (b) general view of exemplary vehicle crossing analyzed bridge

Throughout the tests the traffic density was diversified, therefore it was possible to isolate structure response caused by various types of heavy single vehicles crossing the bridge. Measured values for heavy vehicles traveling in groups were also identified and registered – e.g. moving one by one along lane of slow traffic or moving simultaneously on both traffic lanes of highway. Recorded maximum strains, displacements and accelerations induced by various loading schemes during the last measuring session are presented in Figs. 6, 7 and 8. The analysis of the acquired results indicated that the highest values of measured physical quantities were caused by 5-axle lorries with total maximum weight of 40 tones, whose basic parameters (i.e. axle loads, dimensions) are shown in Fig. 9.

On the basis of analyzes of presented results it can be concluded that the whole structural system exhibit excessive, low-damped vibrations induced by typical cargo traffic crossing the bridge. Physical quantities caused by trucks are quite significant, clearly perceptible and visible to the naked eye. Even a single heavy vehicle generates considerable vibrations of bridge superstructure and the dynamic effects induced by those kind of trucks travelling in groups, especially moving simultaneously on both traffic lanes, are almost twice as large as caused by a single vehicle. The peak values of registered quantities shown in Figs. 6, 7 and 8 were as follows:

- for single 5-axle vehicle with total maximum weight of 40 tones crossing the bridge:
  - maximum strains (tension) of steel girder – ε_{max} = 98.16 μm/m (20.12 MPa),
  - maximum deflection of span – w_{max} = 7.16 mm,
  - maximum vertical acceleration of deck – a_{max} = 0.68 m/s^2,
- for pair of 5-axle vehicle with total maximum weight of 40 tones each, crossing the bridge simultaneously on both traffic lanes:
  - maximum strains (tension) of steel girder – ε_{max} = 190.82 μm/m (39.12 MPa),
  - maximum deflection of span – w_{max} = 13.20 mm,
  - maximum vertical acceleration of deck – a_{max} = 1.66 m/s^2.

The time required for total damping of vibrations is relatively long – about 10 s for span 7–8 and approximately 15 s for span 6–7. Calculated values of logarithmic

decrement of damping δ [−] are in the range 0,08–0,15. ratio ξ [%], defined as a percentage of critical damping, determined on the basis of δ [−] is between 1.3% and 2.1%.

In general, the vibrations magnitude, in terms of amplitudes of displacements, strains and accelerations, is greater for the external spans than for intermediate ones but the outmost spans cease to vibrate faster than the others. This is due to the beat phenomenon (e.g. see point 12R in Fig. 8a) observed which is caused by mutual amplification of vibrations caused by similar vibration frequencies of adjacent spans.

It was found that measured values of strain ranges caused by heavy vehicles, especially traveling in groups, in the light of current knowledge (e.g. according to [2, 3]) can affect fatigue life of steel main girders. Assuming for bridge plate girders with transverse stiffeners welded to lower flanges fatigue category 71 MPa according to [14], the corresponding fatigue cut-off limit below which micro-damages do not accumulate in material is 103 μm/m considering safety factor γ_M = 1.35 and 118 μm/m for safety factor γ_M = 1.15. While calculated maximum strain ranges from strain history depicted in Fig. 6 are the following:

- $D\varepsilon_{max}$ = 120.61 μm/m (24.72 MPa) resulted from a single 5-axle truck travelling along slow lane of traffic,
- $D\varepsilon_{max}$ = 196.34 μm/m (40.24 MPa) resulted from pair of heavy vehicles moving simultaneously on both traffic lanes.

Dynamic Amplification Factor (*DAF*) was calculated using the following formula, examined among other in [6, 7]:

$$DAF = \frac{R_{dyn}}{R_{dyn}^{fil}} \tag{1}$$

where R_{dyn} is a maximum dynamic response and R_{dyn}^{fil} is quasi-static response obtained by filtering the dynamic response, taken at the time when the maximum dynamic response occurs. Obtained values of DAF for selected measuring points are presented in Fig. 10. In the diagram the dynamic factor ϕ = 1.14 calculated according to the Polish Design Code [16] is also included. Polish Standard for bridge design [16] defines the dynamic factor ϕ as a partial safety factor calculated individually for every single component of superstructure using the formula:

$$\phi = 1.35 - 0.005 \cdot L_t = 1.35 - 0.005 \cdot 41.0\, m = 1.14, \tag{2}$$

where L_t is the average theoretical span length of the semi-continuous superstructure.

It can be clearly seen that maximum values of DAF obtained for all performed measurements in many cases exceed the code's assumed value of ϕ. The maximum calculated DAF amounted for 1.27. It has been found that for a single vehicles passing the bridge the value of DAF is close to 1.14, which is suggested by code's [16] formula. In the vast majority of cases greater values of DAF than 1.14 were obtained during passing through the bridge a group of vehicles, e.g. moving one by one in close proximity to each other.

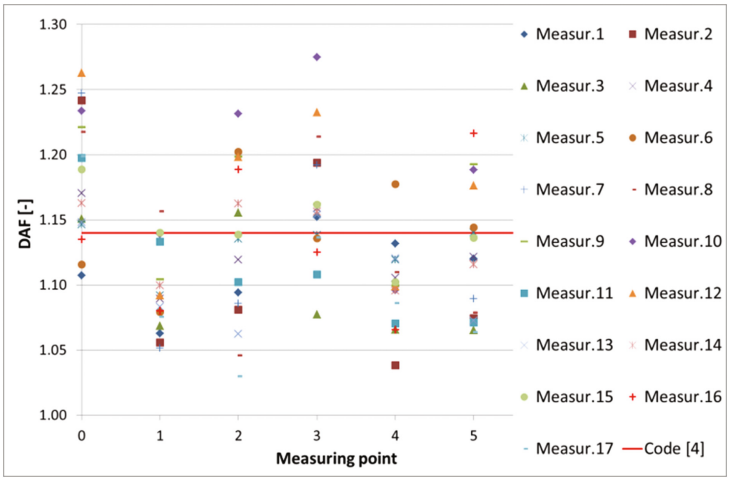

Fig. 10. Maximum values of Dynamic Amplification Factor (DAF) for consecutive measurements determined on the basis of experimental data

4 Conclusions

Evaluation of structural behavior of analyzed bridge was based on measured physical quantities (strains, displacements, accelerations) at various points of superstructure during four series of the whole-day dynamic tests carried out in real operational conditions. Presented results of the experimental vibration analysis of composite, steel-concrete, multi-girder superstructure of highway bridge with excessive deformations confirm relatively high dynamic sensitivity of the bridge. The main reasons of the situation can be listed as follows:

- the static system of superstructure which is in the form of semi-continuous beam – the adjacent spans are connected by the deck slab only (see Fig. 2),
- an excessive, up to 10 cm, permanent deflections of all spans and consequently – unevenness of the highway pavement,
- relatively low stiffens and mass of spans.

The applied method of testing planning and execution as well as measuring system confirmed practicability of the solutions in identification of dynamic characteristics of the structure. Video camera and recorder were very useful in documentation of the loads passing the structure during measurements.

The following general conclusions can be formulated on the basis of the collected and analysed experimental data:

- maximum vertical accelerations of the deck, in some cases, are over 1.6 m/s^2 and are negatively sensed by drivers and passengers of the vehicles passing the bridge,
- value of the Dynamic Amplification Factor in all measuring points is higher than the value accepted in the design code [16],

- time of vibration damping is relatively long and together with comparatively high level of normal stresses in the main girders increases hazard of fatigue cracks,
- the range of the collected experimental data is sufficient for assessment of the current serviceability of the bridge as well as for detailed analysis of potential fatigue hazard,
- dynamic characteristics of the considered bridge, obtained on the basis of live-load tests results, should be used in effective management of bridge operation and maintenance, including design of the structure rehabilitation.

Acknowledgments. Presented research has been partly carried out within the framework of the Project "Innovative resources and effective methods of safety improvement and durability of buildings and transport infrastructure in the sustainable development" financed by the European Union from the European Fund of Regional Development based on the Operational Program of the Innovative Economy.

References

1. Lee, Y.-S., Kim, S.-H., Skibniewski, M.J.: Analytical and experimental approach for assessing vibration serviceability of highway bridges due to heavy vehicle traffic. Baltic. J. Road. Bridge. Eng. (Vilnius: Technika) **4**(3), 123–133 (2009)
2. Alampalli, S.: Effects of testing, analysis, damage, and environment on modal parameters. Mech. Sys. Signal Process. **14**(1), 63–74 (2000)
3. Ewins, D.J.: Modal testing: theory, practice and application. Research Studies Press Ltd., Baldock (2000)
4. Cunha, A., Caetano, E., Magalhaes, F.: Output-only dynamic testing of bridges and special structures. Struct. Concr. **8**(2), 67–85 (2007)
5. Wenzel, H.: Health Monitoring of Bridges. Wiley, New Jersey (2009)
6. Adamcewicz, S., Banakiewicz, A., Bień, J., Rawa, P., Zwolski, J.: Comparison of DAF values based on displacement and strain measurements. In: 3rd International Conference on Experimental Vibration Analysis for Civil Engineering Structures "EVACES 2009", Wrocław, pp. 375–383 (2009)
7. Bień, J., Zwolski, J., Adamcewicz, S.: DAF for steel bridges based on experimental tests. In: 7th International Conference on Steel Bridges Proceeding, Guimaraes, Portugal, pp. 491–500 (2008)
8. Bień, J., Kamiński, T., Kużawa, M., Rawa, P., Zwolski, J.: Dynamic tests of two old masonry arch bridges over Odra River in Wrocław. In: 4th International Conference on Experimental Vibration Analysis of Civil Engineering Structures "EVACES 2011", Varenna, Italy, pp. 79–86 (2011)
9. Kużawa, M., Bień, J., Rawa, P., Kamiński, T., Zwolski, J.: Static and dynamic load tests of cable-stayed bridge over Odra River in Wrocław. In: 6th International Conference on Bridge Maintenance, Safety and Management "IABMAS", Stresa, Italy, pp. 3344–3351 (2012)
10. Bień, J., Kużawa, M., Zwolski, J., Banakiewicz, A., Rabiega, J., Rawa P., Adamcewicz, S.: Fatigue life assessment of Grunwaldzki Bridge based on experimental vibration tests. In: 3rd International Conference Experimental Vibration Analysis for Civil Engineering Structures "EVACES 2009", Wrocław, pp. 569–580 (2009)
11. Bień, J., Kużawa, M., Kamiński, T.: Validation of numerical models of concrete box bridges based on load test results. Arch. Civ. Mech. Eng. **15**(4), 1046–1060 (2015)

12. Kużawa, M., Bień, J.: Experimentally validated nonlinear analysis of bridge plate girders with deformations. Studia Geotechnica et Mechanica **37**(3), 53–61 (2015)
13. EN1991-2 (2003): Eurocode 1: actions on structures - Part 2: traffic loads on bridges. European Standard. CEN, Brussels (2003)
14. EN1993-9 (2003): Eurocode 3: design of steel structures – Part 9: fatigue. European Standard. CEN, Brussels (2003)
15. Kühn, B., Lukić, M., Nussbaumer, A., Günther, H.-P., Helmerich, R., Herion, S., Kolstein, M.H., Walbridge, S., Androic, B., Dijkstra, O., Bucak, Ö.: Assessment of existing steel structures: recommendations for estimation of remaining fatigue life. Background documents in support to the implementation, harmonization and further development of the Eurocodes prepared under the JRC – ECCS cooperation (2008)
16. PN-S-10030:1985 (Polish Standard). Bridges. Loads

Real-Time Structural Instrumentation as an Emergency Response and Business Continuity Tool

Erik Bishop[1(✉)], Kenny O'Neill[1], Drew Nielson[1], Dave Swanson[2], David Gonzalez[3], and Derek Skolnik[4]

[1] Reid Middleton, Inc., Everett, WA 98204, USA
ebishop@reidmiddleton.com
[2] Structural Engineering Group, Reid Middleton, Inc., Everett, WA 98204, USA
[3] Reid Middleton, Inc., San Diego, CA 92128, USA
[4] Kinemetrics, Inc., Pasadena, CA 91107, USA

Abstract. Structures worldwide have been instrumented with sensor systems (vibration accelerometers, strong-motion sensors, strain gauges, etc.) for the purpose of recording structural response data. Researchers, structural engineers, and seismologists use these data to further our understanding of actual building dynamic behavior and validate theories that lead to building code improvements. These same structural health monitoring (SHM) and instrumentation systems can also be utilized to report on the post-earthquake or disaster status of infrastructure to benefit building owners and public safety. First-hand experience from post-earthquake response efforts has indicated that the decisions to evacuate and reoccupy are difficult, especially under a state-of-emergency. These decisions can have dire consequences such as panic related injuries, lack of facility use, and significant financial and potential life loss due to unnecessary post-disaster closures and downtime. These potential consequences are heightened for essential facilities such as hospitals and emergency response facilities.

Although the concept of using strong-motion instrumentation to directly benefit the building owner has been discussed in the SHM community, a real, marketable solution built upon strong-motion monitoring, performance-based earthquake engineering principles, and standard-of-care post-disaster assessment protocols has yet to be put into practice until now. The real-time SHM systems of strong-motion accelerometers measure the acceleration at several levels/locations in a building, perform real-time double integration to calculate building displacements and drifts, and compare building drifts with pre-defined drift thresholds. The system utilizes intuitive onsite display, alerting, reporting, and remote notification tools to communicate results to building owners and facility managers throughout all phases of the post-earthquake response, inspection, and recovery process. Several case studies are presented describing how post-disaster real-time strong-motion instrumentation systems have been deployed in commercial applications for essential facilities to provide building owners and managers with real-time information to make knowledgeable decisions. This will improve disaster preparedness, the safety of building occupants, and ultimately the resiliency of communities.

Keywords: Business continuity · Structural health monitoring · Earthquake response planning · ATC-20 · PBEE

© Springer International Publishing AG 2018
J.P. Conte et al. (eds.), *Experimental Vibration Analysis for Civil Structures*,
Lecture Notes in Civil Engineering 5, https://doi.org/10.1007/978-3-319-67443-8_36

1 Introduction

1.1 Strong-Motion Instrumentation as an Emergency Response Tool

Hundreds, if not thousands, of buildings worldwide have been instrumented with strong-motion sensors for the sole purpose of recording structural response data. Earthquake engineers and seismologists use these data to further our understanding of actual building dynamic behavior, ultimately leading to building code improvements. Over time, the cost-bearing public (owners and residents) indirectly benefit from this work by owning and residing in safer structures. Competition among strong-motion instrumentation manufacturers has led to advances in both performance and economy. However, engineering and scientific utilization of data afforded by advancing technology has not necessarily kept pace with regards to the benefit of the public. Recent (and not so-recent) developments in commercial client-driven services has led to a new business continuity, which directly benefits owners and residents alike.

Although the concept of using strong-motion instrumentation to directly benefit the building owner is not necessarily new, it has, in the authors' opinion, only recently taken off and we attribute this to favorable circumstances, strategic academic and industrial partnerships, and wealth of experience. This paper introduces a real, viable business continuity solution built upon strong-motion monitoring, current principles of performance-based earthquake engineering, and standardized post-event assessment protocol.

1.2 Post-earthquake Evaluation Standard of Care

The Post-Earthquake Safety Evaluation of Buildings (ATC-20) is the standard of care for investigation, evaluation, and placarding the safety condition of buildings after a seismic event. Developed by the American Technology Council (ATC), the ATC-20 manual was first published about one month before the 1989 Loma Prieta Earthquake in Northern California [1]. The ATC-20 evaluation tool was used after this event, and the manual was subsequently improved based on the knowledge gained from its deployment after the Loma Prieta Earthquake. In 1995, the ATC issued ATC-20-2, an addendum to ATC-20, which includes updated safety evaluation procedures and revised red, yellow, and green placards to be posted to communicate the findings of the ATC-20 evaluation to the public. These placards, indicating "Unsafe," "Restricted Use," or "Inspected," communicate whether it is legal and safe to enter a building post-earthquake. In 2005, ATC revised the ATC-20 Field Manual [2], a condensed field manual that summarizes the latest ATC-20 procedures.

ATC-20 identifies various levels of safety evaluations based on the type, size, complexity, and occupancy of the building being evaluated. After a seismic event, the first responders from the authority having jurisdiction (AHJ) typically perform a "windshield survey" to determine the extent and breadth of the damage in order to deploy first responders and resources, accordingly. Based on the emergency response and services needed, engineers, architects, city inspectors, or other properly trained personnel may be deployed to conduct ATC-20 safety evaluations as soon as possible in order to determine the condition of the building infrastructure. The next phase of

evaluation as outlined in ATC-20 is the Rapid Evaluation, a cursory survey that typically includes the structure's interior and exterior. Depending on the complexity and configuration of the building, a Rapid Evaluation can usually be performed in 15–60 min per building. After the ATC-20 evaluation has been completed, inspectors complete evaluation forms that are based on the building's construction type (e.g. reinforced concrete, structural steel, masonry, and wood construction types) in order to identify the appropriate ATC-20 safety evaluation postings. The evaluators then determine the appropriate conclusion for the building occupancy and complete one of the following colored placards:

- Inspected (Green): signifies that the building is safe to occupy; there is no restriction on the type or use of building occupancy.
- Restricted Use (Yellow): signifies that the building may be occupied with some restrictions based on building use, extent, and duration or type of occupancy. Occupancy of a Yellow-tagged building is controlled by the tenant or owner of the building.
- Unsafe (Red): signifies that the building is not to be occupied due to its unsafe condition. Occupancy of a Red-tagged building is controlled by the jurisdiction.

Public facilities of high importance and critical facilities (e.g. hospitals, schools, high-occupancy buildings, and lifeline facilities), or buildings that were assigned a red or yellow placard in the Rapid Evaluation often require a Detailed Evaluation to ensure that they are safe for occupancy. The Detailed Evaluation is a more in-depth visual examination of the structure, including a more comprehensive evaluation of the structural system components. A Detailed Evaluation usually requires one to four hours, depending on the building's size, complexity and access, and also includes a more careful examination of the interior structure, in addition to exterior observation. Following the ATC-20 procedures, evaluators complete the specific Detailed Evaluation forms for the building's construction type in order to determine the appropriate occupancy classification for the building. If inspectors conclude that a Detailed Evaluation does not provide an adequate evaluation for the building, a more thorough Engineering Evaluation may be required. Conducted by a licensed engineer, an Engineering Evaluation usually takes much longer (days to months) and often includes more substantial computational analyses and record drawing reviews in order to determine the structural condition and occupancy of the facility.

2 The Problem

In the event of an earthquake, building occupants are advised to "Drop, Cover, and Hold On" for the extent of the shaking to shield themselves from immediate hazards in the building. When the shaking stops, occupants take their readily accessible valuables (e.g. phone, keys) and safely exit the building. People are then advised to wait until the building has been evaluated using ATC-20 evaluation procedures and has been posted with a Placard that signifies whether or not the building is safe and legal to occupy.

The ATC-20 evaluation procedure is the standard of care for evaluating buildings after disaster in order to protect public health, safety, and welfare. However, since the

AHJ is typically responsible for performing the ATC-20 evaluations after a major event, the demands on their resources greatly exceed their limits, even with the help of volunteers and paid engineering consultants. Consequently, access to buildings may be delayed for weeks or months, which can significantly impact an already-distressed community. This has motivated thousands of architects, engineers, and building officials throughout the United States to receive training in the ATC-20 procedures, so they can be deployed as volunteers to assist with ATC-20 safety evaluations promptly after a seismic event.

However, occupants in essential facilities such as hospitals, emergency operations centers, strategic military installations, critical financial institutions, and nuclear power plants, cannot easily evacuate immediately after an earthquake or wait for a detailed safety assessment to reoccupy the facility and resume operations. Hospitals and medical facilities, in particular, have a profound need to maintain operational status and function in the aftermath of strong earthquakes to allow continued care for current patients and also to receive new patients injured by the disaster [3]. Similarly, critical financial institutions cannot afford unnecessary evacuations following an earthquake as these eventually turn into losses due to downtime and business disruption. Therefore an emergency response tool is needed that can empower facility managers and decision-makers with knowledge of the real-time performance of the building in order to reduce uncertainty, avoid unnecessary evacuations, and self-perform post-earthquake building safety evaluations rather than waiting for the AHJ to continue critical facility operations.

3 The Solution

The solution consists of two primary components: the real-time structural health monitoring system (SHMS) coupled with a post-earthquake Rapid Evaluation & Assessment Program (REAP). When combined, this innovative post-disaster response program empowers facility management teams to perform faster, more accurate, and more reliable safety assessment of their facilities after a disaster (such as earthquake, wind event, or blast) in order to determine if they are safe and operational. Providing business continuity helps to minimize or avoid operational down-time, increase resiliency, improve disaster preparedness, and ultimately improve the safety of building occupants. Figure 1 provides a conceptualization of the SHMS and REAP integration.

3.1 Structural Health Monitoring System

A customized structural health monitoring system is required to continuously monitor important parameters that have influence on the performance and continued operation of the building and to rapidly disseminate critical information. The structural health monitoring system described here is the OASIS (On-line Alerting of Structural Integrity and Safety) system from Kinemetrics, Inc. See Fig. 3. The OASIS system is a flexible structural monitoring system that provides for the collection and processing of real-time acceleration, velocity, displacement, and inter-story drift data. The OASIS monitoring system consists of three major hardware subsystems; sensors, data acquisition, and the alarm and display cabinet.

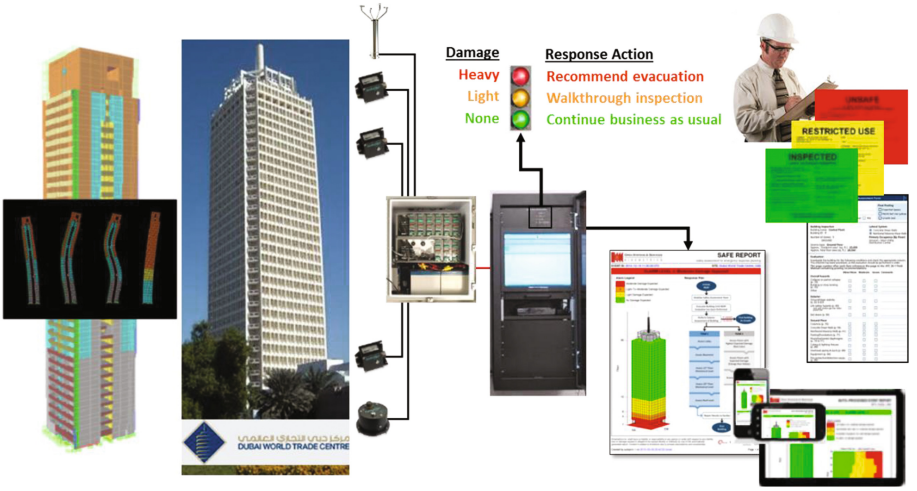

Fig. 1. Conceptualization of SHMS and REAP integration.

3.1.1 Sensors

Force-balance accelerometers are the sensor of choice due to their robustness, noise rejection and ease of installation. For buildings, inter-story drift is the critical response quantity, but since no sensor currently exists that can reliably capture relative story displacements [4], double numerical integration is performed on the real-time acceleration data. This difficult method requires several signal processes such as linear band-pass filtering and is one of the primary functions of the OASIS software described in the section SHM Software, Alarm and Display Cabinet.

In addition to accelerometers, almost any type of sensor (e.g. wind sensors, strain and displacement transducers, crack meters, etc.) can be integrated to address unique structural or specific monitoring objectives. For example, buildings with steel spires are subject to fatigue, which can be easily monitored with robust strain gages and cycle counting.

3.1.2 Data Acquisition Systems

Data recorders or digitizers provide the necessary tools for continuous real-time and event-driven data acquisition such as precise timing for synchronization, power supply and management, signal processing, analog-to-digital conversion, and data file formatting and archiving. They may also provide the necessary communication interfaces for display and alarm notification systems. In general, there are two types of recorder deployment layouts; central and distributed.

Central data recorders, in comparison to wireless distributed recorders, remain the best commercially viable solution for demanding applications requiring robust permanent systems. Although running long analog sensor cables can be expensive, wireless technology, while promising, is not yet mature enough. Wireless power, for example, is still in its technological infancy and probably will be for some time. Thus, replacing analog cabling with wireless technology (or distributed recorders) requires

local power supply at each sensor (or recorder) location which in-turn increases upfront costs in both hardware and implementation as well as in maintenance demand. This is especially true considering that sensors are typically located in difficult areas to access such as above ceiling tiles. Another challenge with wireless technology stems from the limited data buffering capacity at the sensor node, preventing packet re-transmission leading to permanent data gaps, which negatively impact overall results and real-time processes.

With the onset of IEEE 1588-2008 standard for Precision Time Protocol (PTP), a previously less-than-successful deployment layout has re-emerged as a potentially preferable alternative: wired distributed recorders. Previous attempts to use serial-based or NTP for digitizer clock synchronization over IP networks were not accurate enough for seismic applications, with observed errors on the order of few milliseconds. PTP-enabled digitizers on a PTP-compliant network will be able to synchronize their clocks to within a microsecond, comparable to GPS. As PTP-compliant network devices become ubiquitous, this deployment layout will certainly become a very attractive and economically competitive approach. The issue with distributed power sources can be resolved with Power over Ethernet injectors, with the one constraint being the 100 m length limitation of standard Ethernet protocol. The use of fiber optic media resolves the distance constraint for data, but not for power. However, for buildings, a nodal distance constraint of 100 m is rarely an issue.

3.1.3 SHM Software, Alarm and Display Cabinet

The alarm and display cabinet consists of an industrial server or computer running the necessary software, alarm panel, required network devices, and independent backup power. Real-time SHM software running on the server is responsible for controlling the alarm panel, performing real-time processes (e.g., double numerical integration), providing interactive and remote (web) display for user control, and sending message notifications (e.g., via email, SMS). An automatic processing and reporting tool (AutoPro) complements the real-time software to further process data and rapidly disseminate the acquired information. Highly customized SAFE Reports can be emailed to various facility management decision-makers and VIPs.

3.1.4 Performance-Based Earthquake Engineering Evaluation

The principal function of the SHM system is to compare the buildings measured response during an event to predetermined thresholds corresponding to various performance levels. See Fig. 2. That is, the objective of the system is to answer the questions: “How much did the building move?” and “How much movement is too much?”

In order to quantify movement, the parameter that best indicates building performance and potential for damage is interstory drift. For example, knowing that the top floor moved one meter is interesting, but does not indicate how much stress is in the building and how safe the building may be. Therefore, the purpose of the building evaluation is to calculate the levels of relative movement between measured floors at which safety is a concern. Therefore, for example, knowing that the building is leaning at 0.01% and that it can move 0.05% without concern provides building managers with knowledge of building safety and empowers them to make a more informed decision not to evacuate.

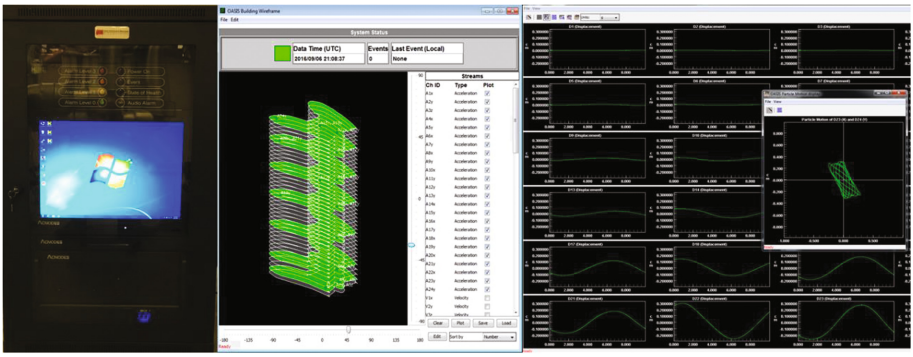

Fig. 2. SHM real-time display.

In reality, there is not a single value for the amount of movement the building can take, but rather a spectrum of performance levels. Therefore, in order to define these performance levels, a performance-based earthquake engineering (PBEE) methodology is employed to establish the three standard levels of performance: Immediate Occupancy, Life Safety, and Collapse Prevention. Where the building's response falls on this spectrum of performance ultimately guides the post-event response action for a particular event. However, the objective of this solution is not to simply identify the building's performance based on PBEE standards, but rather to provide guidance on an action plan for evaluating the post-earthquake safety of the building. Therefore, the PBEE performance limits of the building are merged with the ATC-20: Post-Earthquake Safety Assessment protocols to define building performance limits that best represent the post-earthquake safety of the building. As depicted in Fig. 3, several factors go into this process for determining the SHM performance limits, including PBEE standards, analytical modeling, past earthquake performance, component evaluations, and empirical research.

3.2 Rapid Evaluation and Assessment Program

The Rapid Evaluation and Assessment Program (REAP) is an innovative first-response tool invented by Reid Middleton structural engineers [4] that utilizes building-specific structural analysis techniques, custom design field evaluation manuals, and a structural monitoring system with customized software designed to provide building owners and facility managers with the ability to rapidly evaluate the post-earthquake condition of their facilities to ensure staff safety and business continuity. REAP includes inspection as well as structural and non-structural evaluation information and checklist tools tailored to each building. REAP is enhanced by the design and deployment of a real-time Seismic Monitoring System (SMS) that records and evaluates a building's forces, velocities, and displacement based on special algorithms developed through a performance-based structural analysis of each building. Corresponding performance-based earthquake engineering services are required to identify inter-story drifts corresponding to the building's seismic performance levels. It is essentially a data

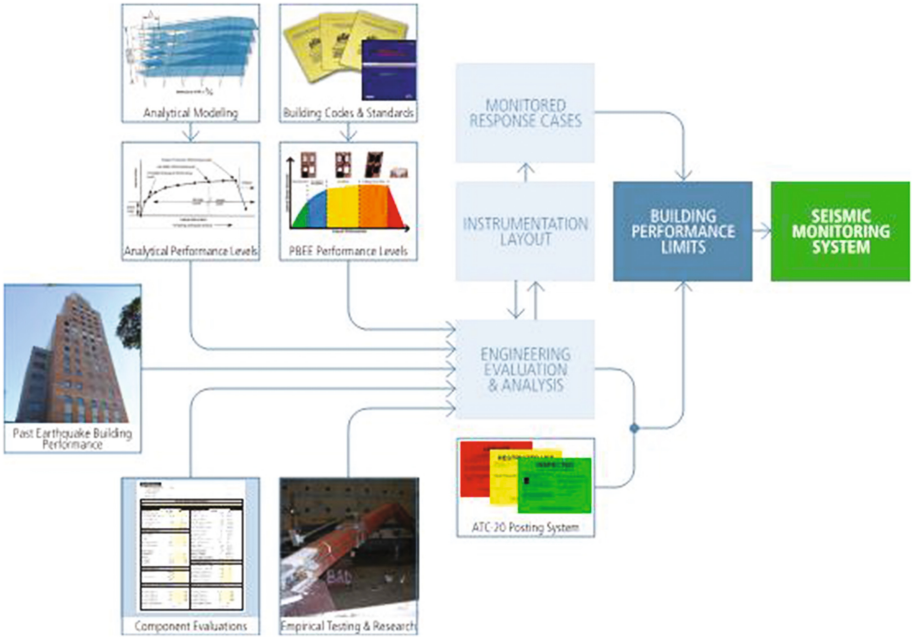

Fig. 3. Performance-based earthquake engineering evaluation process integration with post-earthquake building safety standards.

processing system and emergency response plan that transforms raw data into information and actionable knowledge for the building owners, Fig. 4.

A key aspect in the REAP process is the onsite safety inspection. Traditional visual-based inspections can impose high costs and inconvenience on building owners and occupants alike. For example, physical access to structural members usually requires the removal of non-structural components such as interior partitions and fireproofing. The post-earthquake detailed inspection requirements of welded steel moment frame buildings with pre-Northridge Earthquake style connections can be especially time consuming and costly to implement. Limited resources such as qualified inspectors may not be immediately available after a damaging event, especially for dense urban areas, prolonging expensive downtime. To streamline the response process and minimize conservatism, advanced structural health monitoring systems integrated within REAP empower onsite response teams to rapidly make critical decisions on evacuation and re-entry.

Additionally, it is important to note that it is the collapse of non-structural systems (e.g., interior partitions, HVAC, plumbing, windows, furniture, equipment, etc.) that pose the greatest risk to occupants and often cause buildings to shut down. However, it is impractical to model and measure how the multitude of non-structural systems dynamically move and perform in an earthquake. Therefore, an essential component of rapid post-earthquake safety evaluation is assessment of the performance of the non-structural systems.

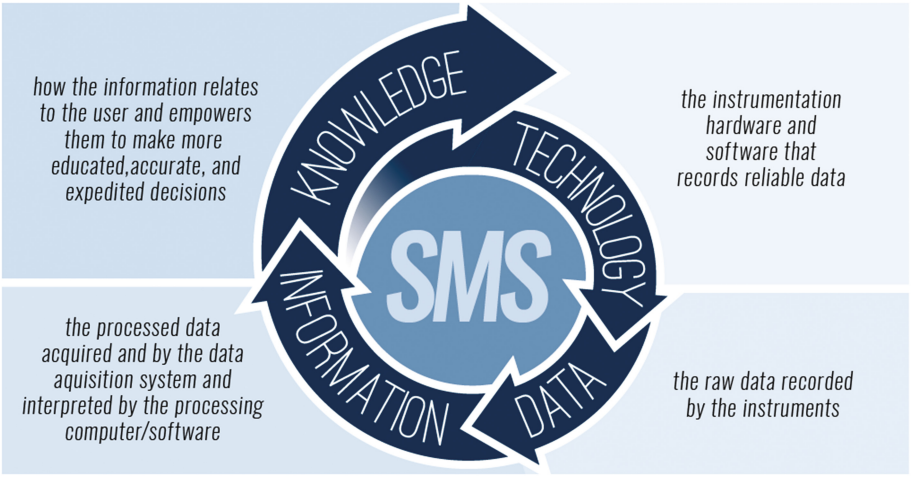

Fig. 4. Conceptualization of solution: technology-data-information-knowledge.

4 Case Studies

4.1 U.S. Military Hospitals: Installation at NMCSD

The SHM/REAP technology has been implemented at three United States Naval Hospitals, including the Naval Medical Center San Diego (NMCSD), the largest and most comprehensive military healthcare facility in the western United States. NMCSD has a staff of over 6,000 that provides health care for over 500,000 people (active duty, dependents, and retirees) in the San Diego area. It is one of about a dozen acute care hospitals in San Diego County and could be called on to serve an overall population of 1.2 million people after a disaster. It is the only military acute care medical facility in the area.

Figure 5 provides a summary of the locations of the seismic monitoring locations at NMCSD. After an earthquake, data from these monitors can be used to assist with the rapid building evaluation. The REAP flow chart, shown in Fig. 3, outlines the recommended post-earthquake building evaluation methodology that can be implemented to utilize the data provided by the SMS. Similarly, the flow chart outlines the steps that each building safety assessment team can take to arrive at an appropriate building safety evaluation posting. The building safety assessment plan provided in Fig. 5, illustrates the recommended exterior assessment routes that each team should follow to rapidly and effectively evaluate the NMCSD facilities.

4.2 Borrego Springs Earthquake

On June 10, 2016, a magnitude M5.2 earthquake occurred in Borrego Springs, located approximately 60 miles to the Northeast of San Diego, California. As depicted in Fig. 6, a peak ground acceleration (PGA) of approximately 13% g was measured near the epicenter, and a PGA of approximately 2% g was expected in the San Diego area.

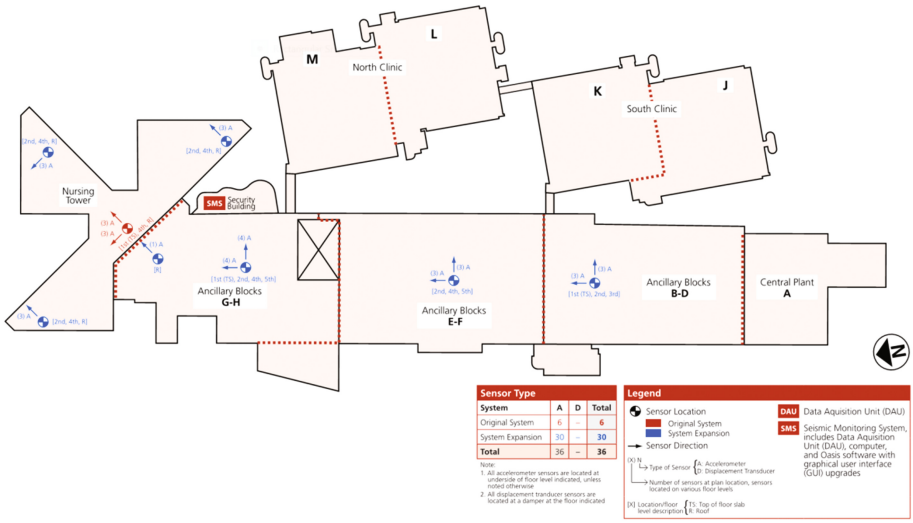

Fig. 5. Seismic monitoring system locations at NMCSD.

Additionally, the directly measured relative displacement across the 6th floor construction joint is represented in Fig. 7. For this relatively small earthquake, the NMCSD Safety Assessment for Emergency (SAFE) Response Planning Report, which was automatically created and sent to the hospital facility managers, indicated a uniform green-safe level of performance. Therefore, the hospital was not evacuated, but the small event allowed for the SMS/REAP response procedures to be executed and practiced.

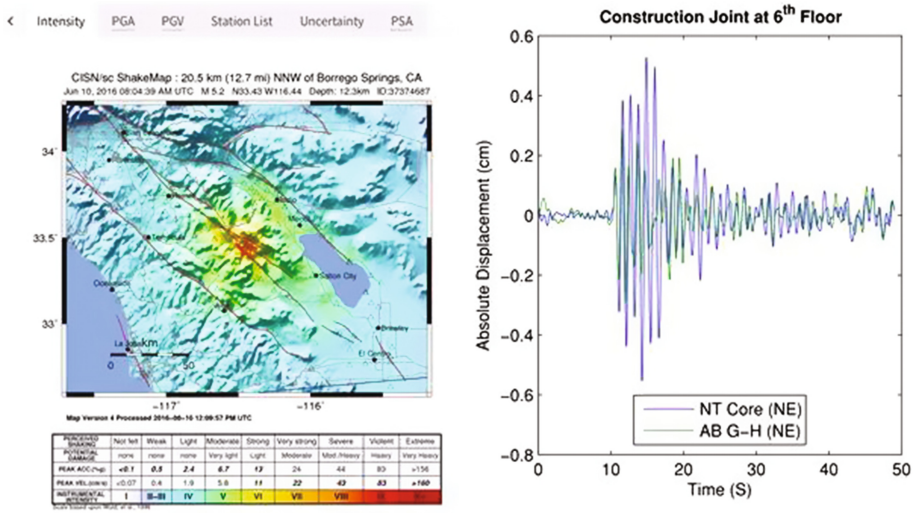

Fig. 6. Borrego Spring earthquake ShakeMap (courtesy of USGS), *left*; NMCSD measured construction joint displacement.

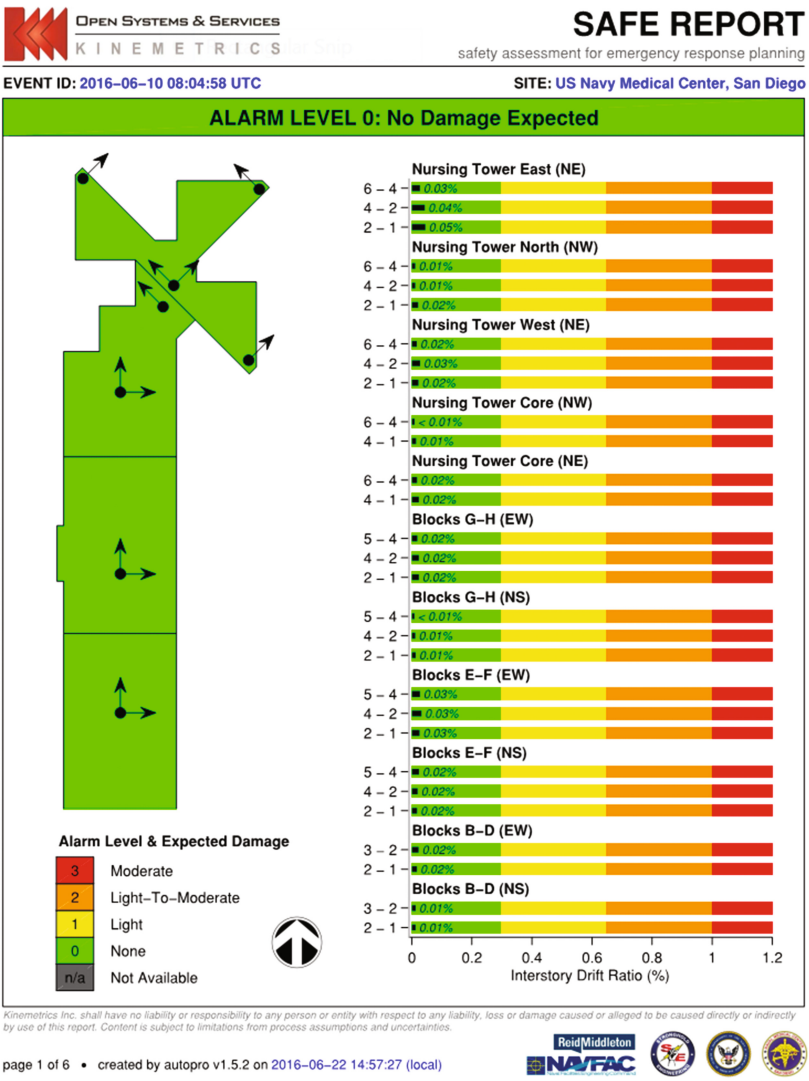

Fig. 7. NMCSD safety assessment for emergency (SAFE) response planning report.

5 Conclusions

Structural health monitoring systems, such as Kinemetrics OASIS, provide timely information that can be useful in all phases of post-event response if the information processing is well integrated within the overall earthquake response plan. Experiences gained through projects such as those presented as case studies here offer invaluable insight into what is required to implement a comprehensive response plan towards

enhanced rapid post-earthquake inspection and assessment. In general, the benefits of implementing a system like this can be summarized as follows:

1. Occupant confidence and safety is improved, avoiding panicked crowds.
2. Building Owners save money by reducing costly downtime and business interruption caused by unwarranted evacuations.
3. Facility Managers are better-equipped to make informed decisions on evacuation and reoccupation.
4. Policy Makers improve safety mandates for the public and showcase city's resilience and growth.

Acknowledgements. The authors would like to acknowledge the building owners who kindly agreed to allow us to present this work despite unavoidable disclosure of certain information regarding their facilities.

References

1. ATC-20: Procedures for Postearthquake Safety Evaluation of Buildings. Applied Technology Council, Redwood City, CA (1989)
2. ATC: ATC-20-1 Field Manual: Postearthquake Safety Evaluation of Buildings, 2nd edn. Applied Technology Council, Redwood City, CA (2005)
3. Wilson, D.R., Kent, R.D., Stanek, S., Swanson, D.: Rapid evaluation and assessment checklist program (REACH) – a case study at Naval Hospital Bremerton. In: Proceedings of the 13th World Conference on Earthquake Engineering, Canadian Association for Earthquake Engineering (2004)
4. Skolnik, D.A., Wallace, J.W.: Critical assessment of interstory drift measurements. ASCE J. Struct. Eng. **136**(12), 1574–1584 (2010)

A Comparison of Two Data Acquisition Techniques for Modal Strain Identification from Sub-microstrain FBG Data

Dimitrios Anastasopoulos(✉), Kristof Maes, Guido De Roeck, and Edwin Reynders

Structural Mechanics Section, Department of Civil Engineering, KU Leuven, Leuven, Belgium
dimitrios.anastasopoulos@kuleuven.be

Abstract. The identification of changes in the dynamic characteristics which are related to structural damage is the core principle of the vibration-based structural health monitoring (VBSHM). By addressing these changes, engineers can acquire valuable information about the condition of structures. Eigenfrequencies are influenced by environmental factors and this influence can be high enough to completely mask the effect of damage while they are also global structural characteristics and they cannot asses the location of the damage. A promising alternative is the monitoring of modal strains which offers the benefit of high sensitivity to local damage. However, current measurement techniques encounter difficulties in capturing the very small strain (sub-microstrain) levels that occur during ambient or operational excitation with sufficient accuracy and precision.

This research aims to accurately identify the modal strains of a steel I-beam from sub-microstrain data using Fiber-optic Bragg Grating (FBG) sensors. For this purpose, two measurement techniques are compared. In the first, an interrogator that measures all sensors simultaneously and saves the wavelength spectra for further processing is used. A novel signal processing algorithm that identifies the Bragg wavelength shift from low-resolution data with high accuracy and precision is used for processing the spectral data into strain values. In the second, an interrogator that scans each sensor individually with a high-speed sweep and therefore offers a high wavelength resolution is used. The peak-shifts from the reflected wavelength are identified with a built-in peak detection algorithm and subsequently converted into strains. The phase shift that is created between the various FBG sensors due to the sweep is resolved by implementing a novel synchronization technique.

The accuracy of both techniques in identifying the beam's dynamic characteristics is investigated through an experimental modal analysis. Two chains of multiplexed FBGs directly glued to the flanges of the beam are used as sensors. The beam is excited at low force amplitudes to explore the ability to identify dynamic characteristics from very low Signal-to-Noise-Ratio (SNR) data. Finally, the accuracy of the identified strain mode shapes from the two techniques is assessed by comparison with a validated finite element model.

Keywords: Modal strains · Fiber optic sensing · Operational modal analysis · Structural health monitoring · Peak-shift algorithms

© Springer International Publishing AG 2018
J.P. Conte et al. (eds.), *Experimental Vibration Analysis for Civil Structures*,
Lecture Notes in Civil Engineering 5, https://doi.org/10.1007/978-3-319-67443-8_37

1 Introduction

As many civil structures, such as bridges, dams and tunnels are reaching or even exceeding the last phase of their service life, reliable Structural Health Monitoring (SHM) techniques that provide the maintenance engineers with information about their structural condition are required [1]. Furthermore, SHM systems that continuously monitor structures from the beginning of their service life are introduced so that training data will be available and damage could be identified in an early stage [2]. Vibration-based structural health monitoring (VBSHM) can constitute a successful SHM approach for damage identification of civil structures [3]. There are though some drawbacks in the method; the eigenfrequencies suffer from low sensitivity to certain types of damage and especially to local damage of moderate severity [4]. Moreover, the influence of the environmental factors (e.g. temperature) on eigenfrequencies can be high enough to completely mask the presence of damage [5], while the eigenfrequencies constitute also a global structure characteristic and thus they cannot asses the location of damage. In contrast, modal characteristics obtained from dynamic strain measurements, such as modal strains and curvatures, are more sensitive in local damage [6]. The introduction of fiber-optic sensing systems, that can accurately measure dynamic strains while also offering ease of installation, resistance in harsh environment and long-term stability, contributed to an increased interest in adopting these systems for VBSHM applications [7]. In this context, the current paper reports about the accurate measurement of dynamic strains of very low (sub-microstrain) level, with the use of standard Fiber-optic Bragg Grating (FBG) strain sensors and two different data acquisition techniques.

The FBG strain sensors have gained ground in SHM applications over the past years due to the benefits that they offer, such as ease of installation, multiplexing, relatively low cost when compared with traditional accelerometers, electro-magnetic immunity and sensitivity to local damage. These advantages of the FBGs classify them as a good solution to the challenges that the VBSHM currently faces [8]. As a result, FBGs are used in a variety of structures for real-time monitoring, such as bridges [2] and railway infrastructure [9]. In these applications though, primarily the quasi-static strain levels are measured, while the dynamic strains that are needed for VBSHM have much lower amplitudes (in many cases ≤ 10 με).

The aim of this research is to measure dynamic strains of the sub-microstrain order which occur during ambient or operational excitation of civil structures, such as bridges, for dynamic system identification and damage localization. For this purpose, two measurement techniques that make use of standard FBG strain sensors are implemented. In the first technique, which is described in [10], a novel correlation algorithm, the Fast Phase Correlation algorithm (FPC) [11] is applied to obtain sub-microstrain accuracy and precision in wavelength-shift detection from a relatively low accuracy acquisition system with an absolute wavelength accuracy of ± 30 pm, the FBGS FBG-SCAN 700. The main advantage of the SCAN 700 system is that measures simultaneously all the sensors in the wavelength bandwidth. In the second technique, an acquisition system of relatively high absolute wavelength accuracy of ± 1 pm, the FBGS FAZT-I4, is used. The FAZT-I4 uses a built-in peak detection algorithm for the

identification of the Bragg wavelength shift while it does not simultaneously scan the various FBG sensors but instead makes a high-speed sweep scan of about 0.1 pm/ns along the wavelength bandwidth, achieving in this way high wavelength resolution. However, due to the sweep, a delay is introduced in the measurements which leads to a phase shift between the FBGs. A novel offline synchronization technique that is described in [12] is used to synchronize the FBGs. The technique makes use of the identified modal strains to calculate the time delay between the various FBGs and consequently corrects the modal strains.

Both methods are evaluated through an experimental modal analysis of a steel I-beam of type IPE 100. The beam is excited with a shaker at low force amplitudes and its response is monitored with two chains of multiplexed FBG sensors directly glued along its flanges and conventional uniaxial accelerometers. The offline synchronization technique is also applied to synchronize the identified displacement and strain mode shapes as a time delay is introduced between the strain and the accelerometer acquisition systems due to the way that the measurements are performed.

2 Experimental Setup

A steel I-beam of type IPE 100 of the European Standard Universal I-Beams serves as the test structure. The beam has a length of 3.0 m and steel rectangular plates are welded at its ends with dimensions 200 × 200 × 10 mm. The beam is suspended with flexible springs from fixed locations to approximate dynamic free-free boundary conditions (Fig. 1).

Uniaxial accelerometers and FBG strain sensors are used for recording the dynamic response of the beam to the input force (Figs. 3 and 4). An impedance head, which measures both the input force and the acceleration at the same location (location 17 in Fig. 3) is also used. The accelerometers measure the vertical acceleration of the beam (z-direction in Fig. 4) while the FBGs measure the longitudinal (horizontal) dynamic

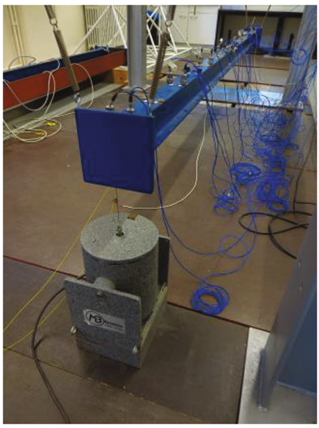

Fig. 1. The test setup

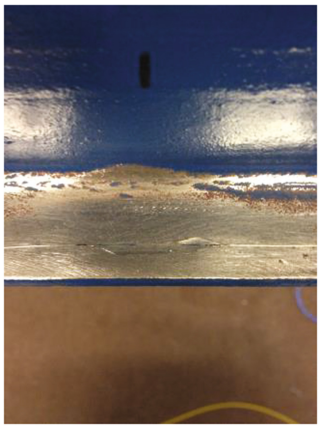

Fig. 2. FBG sensor detail

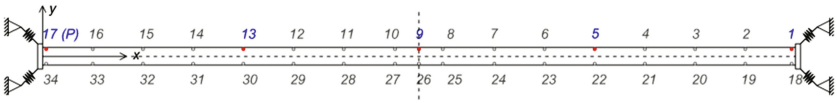

Fig. 3. Top view of the accelerometer setup. The locations of the sensors are denoted in red. 17 (P) denotes the location of the impedance head.

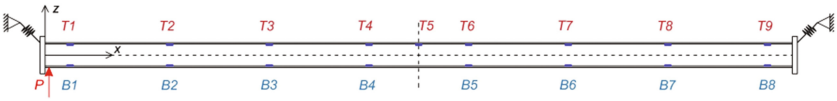

Fig. 4. Front view of the FBG sensor setup. The force is applied in the direction of the red arrow.

strains of the beam (x-direction in Figs. 3 and 4). The FBG sensors are directly glued on the flanges of the beam, with a distance of about 40 cm between them, to measure the local dynamic strains of the beam (Fig. 2). The structure is dynamically excited with an electrodynamic shaker for various force amplitudes of systematically decreasing level to investigate the identification accuracy for very low signal-to-noise-ratio (SNR) data. Several dynamic tests were conducted and the average root mean square (RMS) strain value for all FBG sensors varies from 2 με, for the test with the highest excitation amplitude, to 0.2 με for the test with the lowest excitation amplitude.

3 Methodology

The first methodology that makes use of optic algorithms for modal strain identification from low-amplitude strain data is fully developed and described in [10]. A comparison between this method and a new method that is proposed in this paper is performed. In the proposed method, an interrogator that offers high accuracy and precision for the purposes of this research is used, the FBGS-FAZ Technology I4. The absolute wavelength accuracy of the I4 is higher than ±1 pm, giving significantly higher accuracy than the interrogator that was used in [10], whose absolute wavelength accuracy is about ±30 pm. Therefore, the implementation of an optic algorithm for enhancing the modal strain identification is not required here. However, the I4 does not acquire the data from all FBG sensors simultaneously but instead makes a high speed linear sweep scan (~0.1 pm/ns) across its wavelength range, introducing a delay in the measurements (Fig. 5). This results in a phase shift between the sensors, which is important mainly for the high frequency modes (>300 Hz) although insignificant for the low frequency modes (0–20 Hz) that most of the real structures exhibit. By applying the offline synchronization method that is described in the next section, the delay can be calculated and the strain mode shapes can be corrected.

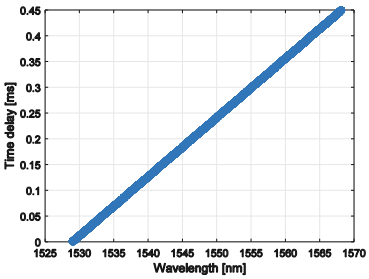

Fig. 5. Time delay – wavelength relationship due to the high-rate sweep of the FAZT I4 (~0.1 pm/ns) as provided from the manufacturer.

3.1 Offline Synchronization

Linear structures with proportional damping have real mode shapes. However, the identified mode shape vectors can be complex due to time delays that are introduced during asynchronous measurements. For instance, when several acquisition systems are used and a real-time synchronization is not applied (e.g. sampling of a common signal), then the occurring time delays should be accounted for.

In the described experiment first the acceleration acquisition system starts acquiring the data and then the FAZT I4, introducing in that way a time delay of a few seconds between the acceleration and the strain data. A rough estimation of this delay is obtained by calculating the cross-correlation between the acceleration and the strain time signals which is used to match specific events occurring in the channels. This event matches with a hammer impact that is given at the beginning of each recording. Since this estimation depends on the sampling frequency (f_s = 1000 Hz) and consequently on the time step (Δt = 1 ms), the time signals can be corrected with an accuracy of integer number of time steps. Figure 6 shows the cross-correlation between the acceleration time signal in location 9 (Fig. 3) and the strain time signal in location T5 (Fig. 4) and for the test with the lowest excitation amplitude. The time delay is estimated as δt = 4.56 s.

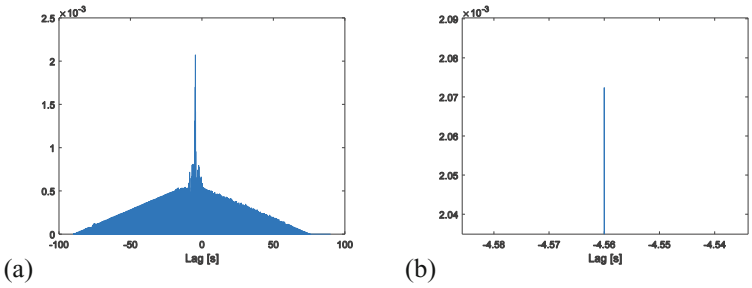

Fig. 6. (a) Cross-correlation of the acceleration (location 9) and the strain time history (location T5) for the test with the lowest excitation amplitude, (b) detail in the neighbor of the cross-correlation peak

A more accurate time delay estimation can then be obtained with the implementation of the offline synchronization technique that is described in [12]. This technique allows for time synchronization of data acquisition systems based on results obtained from system identification. The time synchronization is computed from the phase shift between the identified displacement and strain mode shapes, which results from the synchronization time delay. The accuracy of the time delay calculated with this method is not limited by the sampling frequency.

The time delay δt^* can be estimated by minimization of the objective function $f(\delta t)$ (Eq. (1)) that gives the average difference between the mean phases (MP) [13] of the complex mode shapes, Φ_{com}, and the reference mode shapes, Φ_{ref}, over all modes (n_m) [12]. The complex mode shapes are defined here as the mode shapes that need to be corrected (e.g. the strain mode shapes) with respect to the reference mode shapes (e.g. the displacement mode shapes).

$$\delta t^* = \arg\ \min f(\delta t) = \arg\ \min \frac{1}{n_m} \sum\nolimits_{m=1}^{n_m} \left| MP\left(\Phi_{com,m} e^{\lambda_{m1}\delta t}\right) - MP\left(\Phi_{ref,m}\right) \right| \quad (1)$$

The rescaling of the complex mode shapes is obtained by multiplying their components by a factor $A_m\psi$ which is defined as [12]:

$$A_m = e^{\lambda_{m1}\delta t^*} \quad (2)$$

where $\lambda_{m1} = -\omega_m \xi_m + i\omega_m \sqrt{1-\xi_m^2}$ is the pole corresponding to the natural frequency ω_m and modal damping ratio ξ_m of mode m. Before the implementation of the synchronization method, the results of the system identification and the modal analysis are presented.

4 Modal Analysis

The modal analysis of the beam is performed using both acceleration and strain data. The system identification is conducted with MACEC [14]. The data-driven Combined deterministic-stochastic Subspace Identification (CSI-data) [15] algorithm is used, where both the input force and the measured beam response (accelerations and strains) are used for the identification. The maximum model order and the half number of Hankel's block rows i that have to be defined in the algorithm are selected to be equal to 80 and 60 respectively. During data processing, the static or DC offset is removed from all measured signals. A 4th order Butterworth filter with a high-pass frequency of 2 Hz is applied to all channels to remove the influence of temperature fluctuations on the strain measurements. In the following, the results of the test with the lowest excitation amplitude are presented to demonstrate the high identification accuracy from low-excitation amplitude tests. Obviously, high identification accuracy is obtained as well from the other tests with the higher excitation amplitude.

4.1 Eigenfrequencies and Damping Ratios

Seven bending and torsion modes are identified in the frequency bandwidth of interest (0–500 Hz). All modes are selected from stabilization diagrams and their eigenfrequency, damping ratio and modal phase collinearity (MPC) [13] values are summarized in Table 1. The eigenfrequencies of a validated FEM [10] that was built in ANSYS are also provided for comparison. Most of the identified modes have relatively low MPC values which is an indicator of high complexity. Most probably, this is the result of the phase shift between the modal displacements vector and the modal strains vector, due to the time delay between the two acquisition systems. Moreover, the phase shift introduced in the modal strain vector components due to the sweep scanning of the FBGs from the FAZT-I4 further contributes to the complexity of the modes.

Table 1. Eigenfrequencies, damping ratios and MPC values of the beam modes (identified with the CSI-data algorithm). The eigenfrequencies of the validated FEM are also given. With 'T' are denoted the torsion and with 'B' the bending modes.

Mode	f [Hz] (FEM)	f [Hz] (CSI)	Damping ratio [%]	MPC
Mode 1 (T)	31.17	32.61	0.15	0.98
Mode 2 (B)	61.14	61.28	0.05	0.84
Mode 3 (T)	72.76	72.13	0.13	0.62
Mode 4 (T)	129.74	130.71	0.12	0.68
Mode 5 (B)	173.63	175.04	0.05	0.97
Mode 6 (T)	204.40	203.35	0.37	0.54
Mode 7 (B)	341.56	343.75	0.12	0.83

4.2 Strain Mode Shapes

A two-step procedure is applied to obtain corrected mass-normalized strain mode shapes. In the first step, the time delays originating from the sweep of the FAZT are accounted for. The sweep results in a phase shift of the identified strain mode shapes, as can be derived from Fig. 7, where the identified strain mode shapes are plotted in the complex plane. By applying Eq. (1) for all FBGs, their objective functions are obtained and consequently the time delay, with respect to the reference FBG is obtained. As reference sensor, FBG T1 is considered (Fig. 4), as it is the first sensor that is interrogated from the FAZT (being the sensor with the lowest wavelength value). After obtaining the time delays of all sensors, the strain mode shapes are rescaled, taking into account the scaling factor A_m in Eq. (2). The rescaled strain mode shapes are given in Fig. 8. The corrected strain mode shapes are highly collinear, although still complex due to the phase shift with the displacement mode shapes. Furthermore, in Fig. 9, the calculated time delays for all sensors of the two fibers are given. The time delay-wavelength relationship that is obtained is linear, which is in agreement with what it is expected since the I4 makes a linear high-rate sweep along its wavelength range (Fig. 5).

In the second step, the time delay between the strain and the displacement mode shapes is accounted for. The use of two different acquisition systems leads to

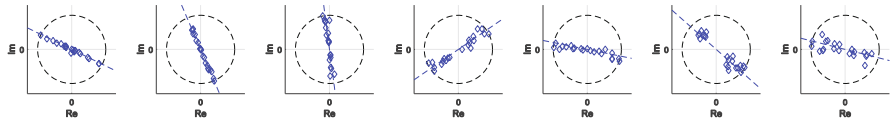

(a) Mode 1 (T) (b) Mode 2 (B) (c) Mode 3 (T) (d) Mode 4 (T) (e) Mode 5 (B) (f) Mode 6 (T) (g) Mode 7 (B)

Fig. 7. Representation of the strain mode shapes 1–7 in the complex plane, before the synchronization of the FBGs.

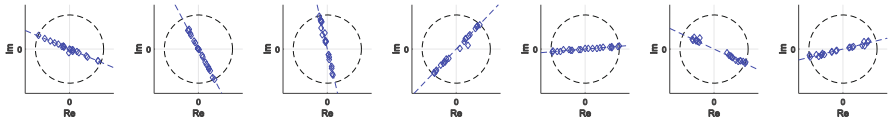

(a) Mode 1 (T) (b) Mode 2 (B) (c) Mode 3 (T) (d) Mode 4 (T) (e) Mode 5 (B) (f) Mode 6 (T) (g) Mode 7 (B)

Fig. 8. Representation of the strain mode shapes 1–7 in the complex plane, after the synchronization of the FBGs.

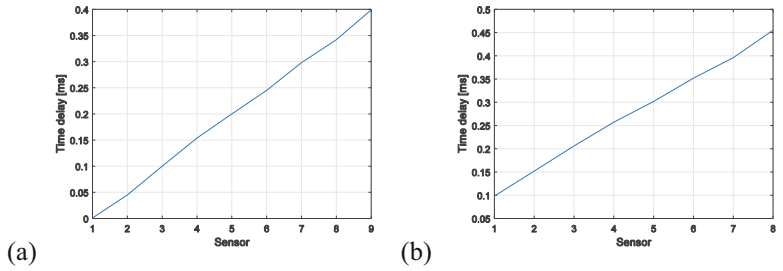

Fig. 9. Calculated time delays for all FBGs in ascending wavelength order. (a) Top flange fiber, (b) bottom flange fiber.

synchronization issues. The implementation of Eqs. (1) and (2) allows to calculate the time delay between the two acquisition systems and correct the strain mode shapes. The time delay that is obtained from the global minimum of the objective function is $\delta t^* = 2.85$ ms. In Fig. 10, the displacement and the strain mode shapes, after

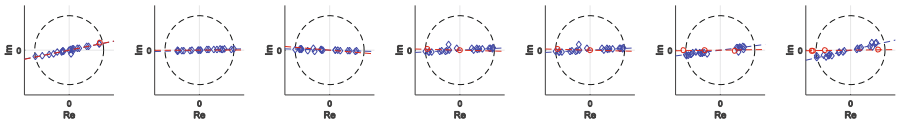

(a) Mode 1 (T) (b) Mode 2 (B) (c) Mode 3 (T) (d) Mode 4 (T) (e) Mode 5 (B) (f) Mode 6 (T) (g) Mode 7 (B)

Fig. 10. Representation of the displacement (red circles) and strain mode shapes (blue diamond) 1–7 in the complex plane, after the synchronization of the displacement and the strain modal vectors.

compensation for time delay $\delta t^* = 2.85$ ms, are given in the complex plane. It can be concluded that the combined displacement-strain modes are now almost real. This statement is further supported by calculating their MPC values which are approximating unity (>0.98). It should be mentioned here that modes 1 and 7 appear to be less corrected when compared to the other modes. This could be attributed to identification inaccuracies and/or violation of the inherent assumptions of the method, such as this of the proportional damping [12].

The final mass-normalized strain mode shapes, after compensation for all the hardware-induced time delays, are given in Fig. 11. As indicated by the high MPC values, the imaginary part of the strain mode shapes is rather small. Furthermore, the identification of the modal strains can be considered as accurate since their amplitude is well estimated when compared with the validated FEM. It should be mentioned here that the mass normalization is not affected by the synchronization since the accelerometers are used as the reference sensors.

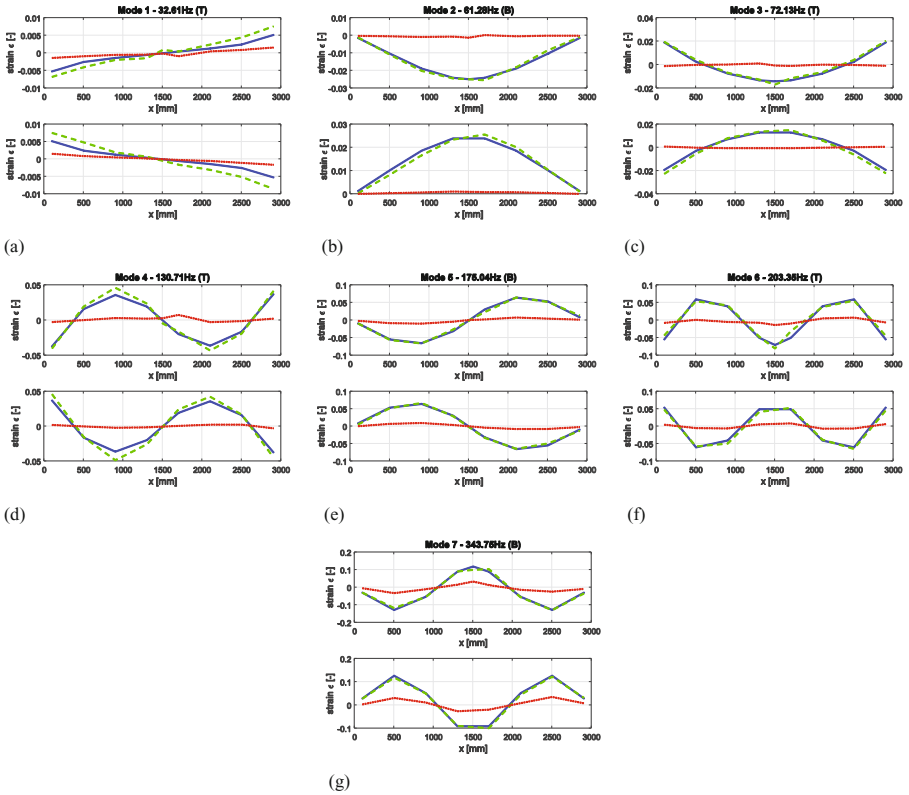

Fig. 11. Mass-normalized strain mode shapes. The top subplots correspond to the top flange fiber and the bottom to the bottom flange fiber. The green dashed line corresponds to the real part and the red dotted line to the imaginary part of the identified mode shapes (CSI-data). The continuous blue line corresponds to the FEM strain mode shapes.

5 Comparison of the Modal Strain Identification Techniques

In this section a comparison is made between two different methods that can be used to measure the very low-level dynamic strains occurring during ambient or operational excitation. The first method is the one described in the previous sections, where a high accuracy interrogator with an absolute wavelength accuracy of ±1 pm, the FBGS FAZT-I4, is used for dynamic strain measurements. The FAZT-I4 makes use of its own commercial internal peak-shift detection algorithm for detection of the Bragg wavelength shift. The drawback of the time delay in the data is solved with the proposed offline synchronization technique. The second method was extensively described in [10]. There, a relatively low accuracy interrogator with an absolute wavelength accuracy of ±30 pm, the FBGS FBG-SCAN 700 is used and the wavelength shifts are tracked with the implementation of two optic algorithms, a conventional peak-shift detection algorithm, the Maximum Detection Algorithm (MDA) and a phase correlation algorithm, the Fast Phase Correlation algorithm (FPC). In Fig. 12, the mass-normalized strain mode shapes as identified from the FAZT-I4 after offline synchronization, and from FBG-SCAN 700 after applying the MDA and the FPC algorithms are compared. The seventh mode is not presented here as it was not identified in [10] because it was out of the bandwidth of excitation (0–200 Hz). The comparison is conducted between the results of similar dynamic tests where the structure is excited with periodic random signals and an RMS input force of about 2.5 N which results in average RMS strain values of about 0.5 με. Finally, the modal assurance criterion (MAC) [13] is applied in

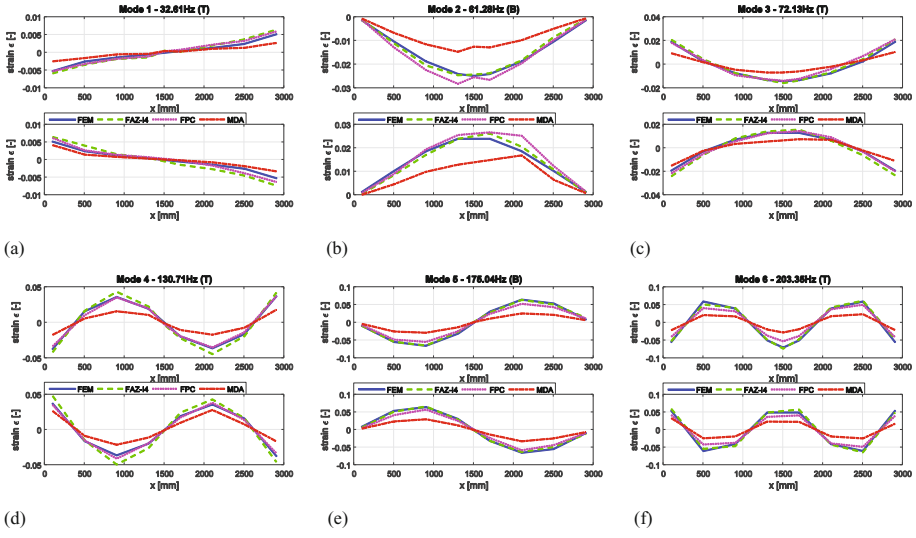

Fig. 12. Mass-normalized strain mode shapes. The top subplots correspond to the top flange fiber and the bottom to the bottom flange fiber. The continuous blue line corresponds to the FEM, the dashed green to the FAZT-I4, the pink dotted to the FPC and the dashed-dotted red to the MDA identified strain mode shapes.

comparison of the strain mode shapes (Fig. 13). The strain mode shapes of the validated FEM are used as the reference strain mode shapes.

The mass-normalized strain mode shape amplitude is well identified from both FAZT-I4 and the FPC algorithm. As it can be observed in Fig. 12, the amplitude inconsistencies of both techniques with the validated FEM are rather small, in contrast with the MDA algorithm, were an underestimation of the strain amplitude up to 80% is observed [10]. The strain mode shapes though are well identified from all techniques as indicated from the MAC values that are larger than 0.93 for all cases. However, higher accuracy must be attributed to the FAZT and the FPC as their MAC values are larger than 0.98.

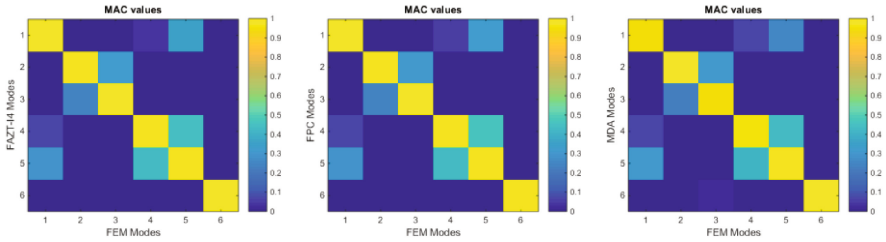

(a) FAZT-FEM (b) FPC-FEM (c) MDA-FEM

Fig. 13. MAC values

6 Conclusions

An experimental modal analysis of a steel I-beam of type IPE 100 is performed. Accelerometers and FBG strain sensors are used for measuring the dynamic response of the beam from low amplitude excitation tests. Due to the use of two acquisition systems, a time delay and consequently a phase shift is introduced between the displacement and the strain mode shapes which is corrected with the use of an offline synchronization technique. The same technique is used for correcting the strain mode shapes for the time delay introduced from the sweep of the FAZT. The identified strain mode shapes, after being corrected, are compared with the ones obtained from strain data processed with optic algorithms, which increase the identification accuracy of the wavelength shift. The obtained results from both methods are compared and the following conclusions can be drawn:

- The FBG sensors, as well the displacement and the strain mode shapes are successfully synchronized through the implementation of the offline synchronization technique.
- The mass-normalized strain mode shapes are well identified and their amplitude is well matching with the amplitude of the strain mode shapes obtained from a validated FEM (Fig. 11).

- Both the FAZT-I4 and the FPC are correctly identifying the mass-normalized strain mode shape amplitude, while the MDA highly underestimates it due to the peak locking effect [10].
- All techniques correctly identify the strain mode shapes (MAC values >0.93), even for tests with very low excitation levels where the RMS strain values are less than 1 με.

Acknowledgements. The research presented in this paper has been performed within the framework of the project G099014N "Identification and modeling of structural damage", funded by the Research Foundation Flanders (FWO), Belgium. Kristof Maes is a postdoctoral fellow of KU Leuven. The financial support of FWO and KU Leuven is gratefully acknowledged.

References

1. Farrar, C.R., Worden, K.: Structural health monitoring: a machine learning perspective. Wiley, West Sussex (2013)
2. Rodrigues, C., Félix, C., Lage, A., Figueiras, J.: Development of a long-term monitoring system based on FBG sensors applied to concrete bridges. J. Eng. Struct. **32**(8), 1993–2002 (2010)
3. Brownjohn, J.M.W., Stefano, A., Xu, Y.L., Wenzel, H., Aktan, E.: Vibration-based monitoring of civil infrastructure: challenges and successes. J. Civil Struct. Health Monit. **1**(3–4), 79–95 (2011)
4. Deraemaeker, A., Reynders, E., De Roeck, G., Kullaa, J.: Vibration-based structural health monitoring using output-only measurements under changing environment. J. Mech. Syst. Signal Process. **22**(1), 34–56 (2008)
5. Peeters, B., De Roeck, G.: One-year monitoring of the Z24-Bridge: environmental effects versus damage events. J. Earthquake Eng. Struct. Dynam. **30**(2), 149–171 (2001)
6. Unger, J.F., Teughels, A., De Roeck, G.: Damage detection of a prestressed concrete beam using modal strains. J. Struct. Eng. **131**(9), 1456–1463 (2005)
7. Glisic, B., Inaudi, D.: Fibre Optic Methods for Structural Health Monitoring. Willey, Chichester (2007)
8. Glisic, B.: Performance and health monitoring of civil structures and infrastructure using long-gauge and distributed fiber optic sensors. In: Proceedings of the 18th International Conference on Transparent Optical Networks (ICTON), Trento, Italy (2016)
9. Roveri, N., Carcaterra, A., Sestieri, A.: Real-time monitoring of railway infrastructures using fibre Bragg grating sensors. J. Mech. Syst. Sign. Process. **60–61**, 14–28 (2015)
10. Anastasopoulos, D., Moretti, P., Geernaert, T., De Pauw, B., Nawrot, U., De Roeck, G., Berghmans, F., Reynders, E.: Identification of modal strains using sub-microstrain FBG data. J. Mech. Syst. Sign. Process. **86**, 58–74 (2017)
11. Lamberti, A., Vanlanduit, S., De Pauw, B., Berghmans, F.: A novel fast phase correlation algorithm for peak wavelenght detection of fiber Bragg grating sensors. J. Optics Exp. **22**(6), 7099–7112 (2014)
12. Maes, K., Reynders, E., Rezayat, A., De Roeck, G., Lombaert, G.: Offine synchronization of data acquisition systems using system identification. J. Sound Vib. **381**, 264–272 (2016)

13. Reynders, E., Houbrechts, J., De Roeck, G.: Fully automated (operational) modal analysis. J. Mech. Syst. Signal Process. **29**, 228–250 (2012)
14. Reynders, E., Schevenels, M., De Roeck, G.: MACEC 3.3: A Matlab toolbox for experimental and operational modal analysis, User's manual, Report BWM-2014-06. Department of Civil Engineering, KU Leuven, Leuven, Belgium (2014)
15. Reynders, E., de Roeck, G.: Reference-based combined deterministic–stochastic subspace identification for experimental and operational modal analysis. J. Mech. Syst. Signal Process. **22**(3), 617–637 (2008)

Strong Motion Structural Monitoring in Practice

K. O'Neill[1(✉)], E. Bishop[1], D. Swanson[2], D. Aveyard[1], D. Skolnik[3], and M. Fraser[4]

[1] Reid Middleton, Inc., Everett, WA 98204, USA
koneill@reidmiddleton.com
[2] Structural Engineering Group, Reid Middleton, Inc., Everett, WA 98204, USA
[3] Kinemetrics, Inc., Pasadena, CA 91107, USA
[4] Naval Facilities Engineering Command Southwest, San Diego, CA 92132, USA

Abstract. Thousands of buildings, bridges, and structures worldwide have been instrumented with systems (including vibration accelerometers, strong-motion sensors, strain gauges, etc.) for the sole purpose of recording structural response data. Researchers, structural engineers, and seismologists use these data to further our understanding of actual building dynamic behavior, validate theories, and ultimately lead to building code improvements. However, these structural health monitoring and instrumentation systems are rarely implemented directly on real-world building projects. The objective of this paper is to present the following case studies on how structural instrumentation has been implemented and how these technologies have been executed. The case studies are intended to show the potential usefulness of leveraging measured data and stimulate further use of structural instrumentation technology in practice:

1. *California Hospital with Seismic Movements:* Each seismically separated hospital wing of the Naval Medical Center San Diego (NMCSD) is a pre-Northridge steel moment frame. The entire medical facility encompasses over 1 million square feet of space. One seismically separated wing of this building, the nursing tower, has some structural irregularities and some unique building properties. Additionally, recent structural analysis has been conducted on this building for the purposes of conducting seismic upgrades in addition to strong-motion accelerometers being installed in the building in 2015. The M5.2 Borrego Springs earthquake that occurred on June 10, 2016 was measured by the building's strong motion accelerometers and some of the measurement data is compared with other structural analysis calculations.
2. *Washington Hospital with Seismic Movements:* The hospital and clinic at Naval Hospital Bremerton (NHB) are pre-Northridge steel moment frame structures that represent 249,000 square feet of space used for essential medical services. In 1980, the building was instrumented with 12 channels of strong-motion accelerometers with an analog data recorder. After the 2001 M6.8 Nisqually Earthquake event, the data from this recording was digitized and allowed the nonlinear dynamic time-history analysis required for a seismic evaluation and upgrades design to be tuned to the actual dynamic characteristics of the building rather than the generalized assumptions provided by building standards.

Keywords: Strong motion · Modal analysis · Seismic response · Finite element analysis · Monitoring system

© Springer International Publishing AG 2018
J.P. Conte et al. (eds.), *Experimental Vibration Analysis for Civil Structures*,
Lecture Notes in Civil Engineering 5, https://doi.org/10.1007/978-3-319-67443-8_38

1 Introduction

Thousands of buildings, bridges, and structures worldwide have been instrumented with vibration accelerometers, strong-motion sensors, strain gauges, etc. for the sole purpose of recording structural response data. Researchers, structural engineers, and seismologists traditionally use these data to further our understanding of actual building dynamic behavior, validate theories, and ultimately lead to building code improvements. Concurrently, competition among instrumentation manufacturers has led to advances in both performance and economy of these technologies.

This paper describes two case studies that illustrate how strong motion accelerometers have been implemented and how these technologies can be potentially useful for understanding building behavior and can possibly be utilized to aid in the design of buildings and building retrofits.

2 Case Study 1 – Naval Medical Center San Diego

Naval Medical Center San Diego is the largest US Naval hospital in the world and includes more than 1 million square feet of medical space. The main hospital building includes several seismically separated wings and was built in the mid-1980s. The structural lateral system of each seismically separated wing is a pre-Northridge steel moment frame typical of the era when it was built. The building has relatively few lines of moment frame meaning that lateral forces are concentrated in these relatively few frame lines possessing relatively large and heavy frame sections. The beams of the moment frames are constructed using ASTM A36 steel and the columns are constructed using ASTM A572 steel. This configuration was typical at the time of the building's construction.

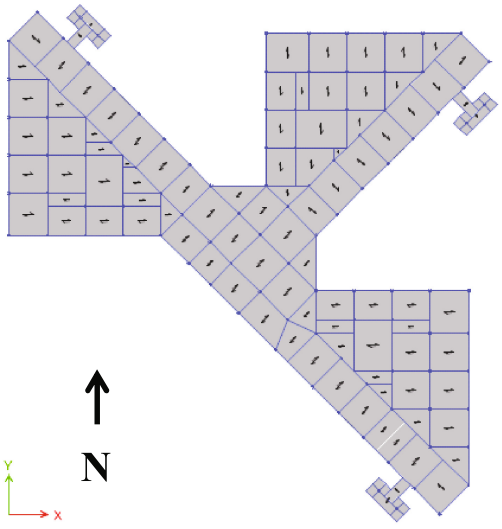

Fig. 1. Typical NMCSD nursing tower floor plate.

One seismically separated wing, the nursing tower, is a five story moment frame structure with some below-grade basement areas. The nursing tower has some structural irregularities including re-entrant corners, non-orthogonal lateral system and significant portions of the gross-diaphragm area are open. Figure 1 shows the typical floor plate of the structure.

The nursing tower has six channels of strong motion accelerometers installed in the core area near the center of the floor plate. (2) Channels of acceleration are measurement in the core area on Floor 1, Floor 4 and the Roof. The orientation of the accelerometers is the same on each level. One channel of the bidirectional sensor on each level measures acceleration in the NE-SW direction and the other channel measures acceleration in the NW-SE direction.

2.1 The 2016 Borrego Springs Earthquake

On June 10, 2016, an M5.2 earthquake occurred near Borrego Springs, California located approximately 96 km (60 miles) to the Northeast of San Diego, California. As depicted in Fig. 2, a peak ground acceleration (PGA) of approximately 13% g was measured near the epicenter, and a PGA of approximately 2% g was expected in the San Diego area. [1] Strong shanking lasted for approximately 10 s.

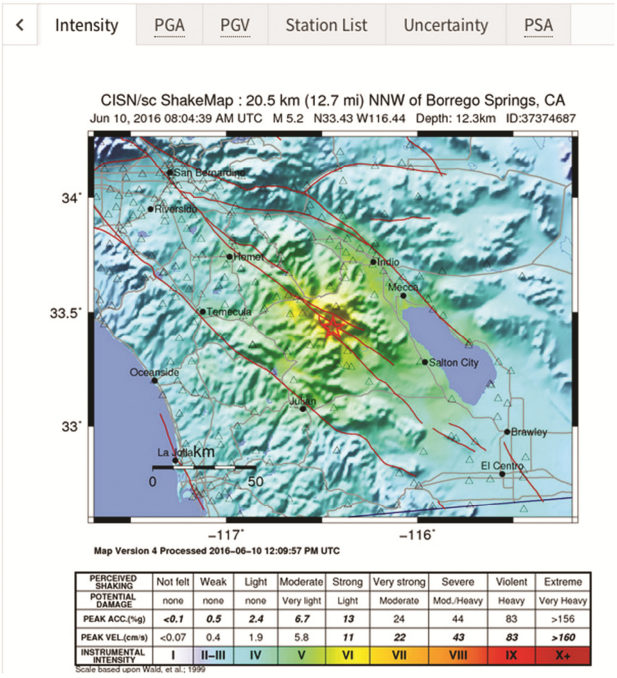

Fig. 2. Borrego springs earthquake USGS ShakeMap.

Even though the shaking in the San Diego area was classified at "light" by the USGS, some people at the hospital reported feeling the building move significantly and there were at least some initial concerns and speculation about building damage. Eventually it was determined that there was no observable damage to the structural or nonstructural components at the hospital due to this earthquake.

The strong motion accelerometers installed in the Nursing Tower recorded the motion of the earthquake. Figure 3 shows the acceleration measured at Floor 1 of the Nursing Tower in the NE–SW direction. This level is the ground level of the building, but the accelerometer is attached to an elevated slab (because there is a below-grade basement). The maximum acceleration experienced at Floor 1 is approximately 1.5% g. It is likely that the acceleration at Floor 1 is approximately equal to the ground acceleration (because they are at the same elevation and Floor 1 is directly connected into the foundation walls), though there may be some dynamic interaction between the structure and the surrounding soil.

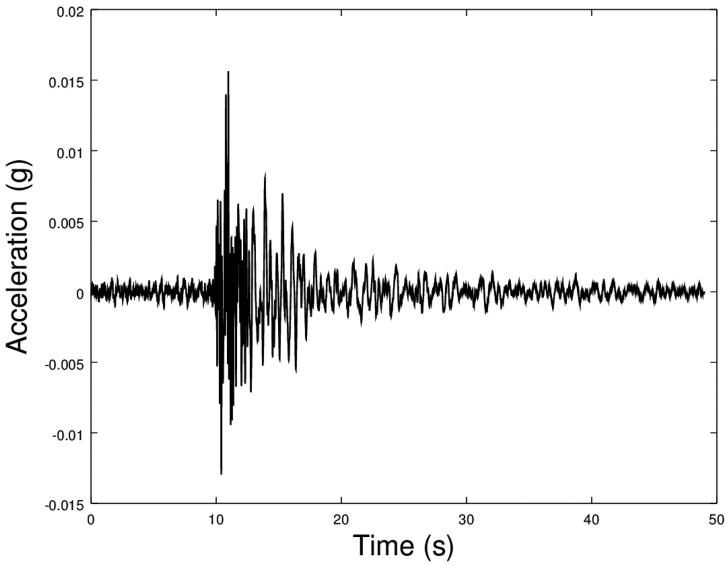

Fig. 3. Nursing tower Floor 1 absolute acceleration in NE-SW direction.

Figure 4 shows the relative displacement of the Roof compared to Floor 1 in the NE–SW direction. This plot was created by integrating the acceleration data at the Roof and Floor 1, then subtracting the Floor 1 displacement from the Roof. The maximum relative roof displacement was approximately 0.5 cm (0.2 in). The data was numerically integrated in the time-domain and the displacement (only) was filtered with a bandpass filter with a passband between 0.4–40 Hz (period of vibration between 2.5–0.025 s).

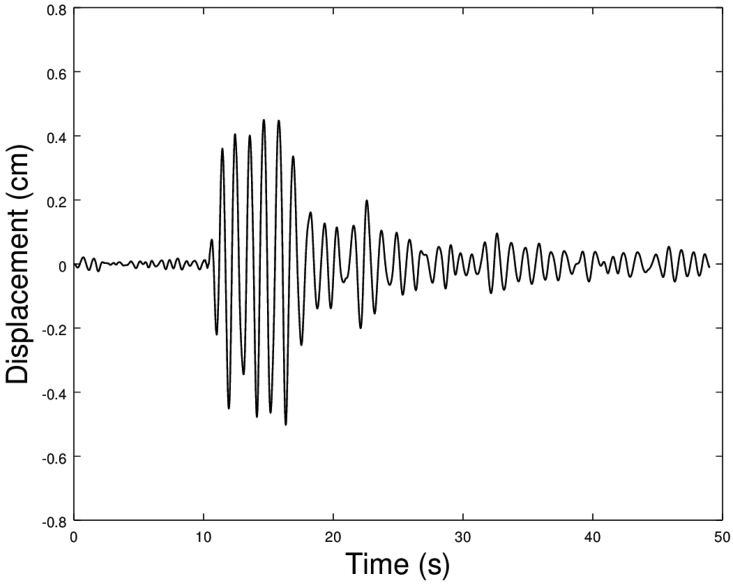

Fig. 4. Nursing tower roof relative displacement between roof and Floor 1.

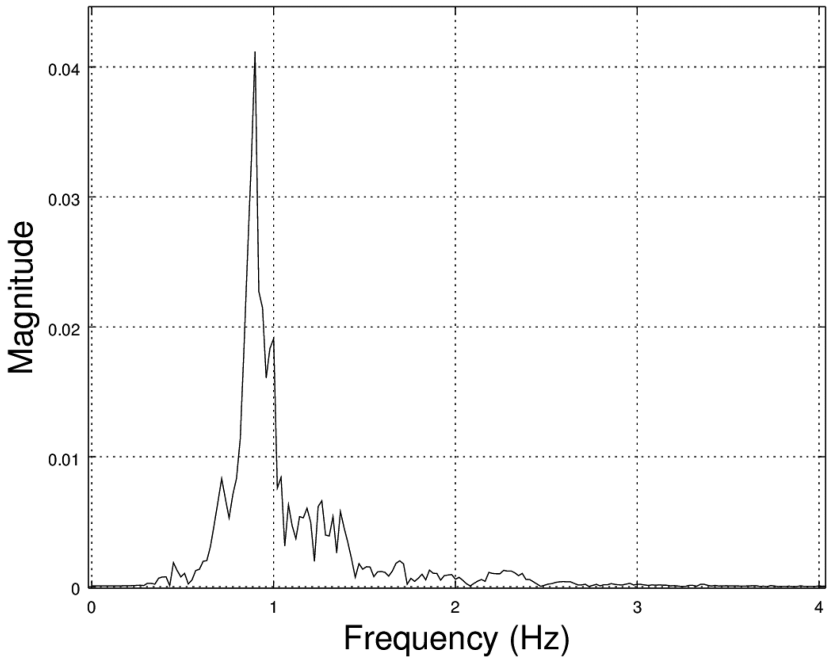

Fig. 5. Plot of fast Fourier transform of relative roof displacement.

Figure 5 shows the plot of the fast Fourier transform of the displacement plot shown in Fig. 4. This plot shows a significant contribution to the displacement magnitude coming from the vibration frequency around 0.9 Hz (~1.1 s period). This likely corresponds to the measured fundamental period of vibration of the structure in this direction or a combination of the contributing modes of vibration.

As previously mentioned, some recent structural analysis was conducted on the nursing tower building and a modal analysis was conducted in a structural finite element program. The participating mass ratios for the first three modes, as determined from the modal analysis, are listed in Table 1.

Table 1. Modal analysis results from structural analysis.

Mode	Period (s)	Ux	Sum Ux	Uy	Sum Uy	Rz	Sum Rz
1	1.91	0.22	0.22	0.37	0.37	0.22	0.22
2	1.74	0.55	0.77	0.05	0.41	0.21	0.42
3	1.55	0.04	0.81	0.39	0.80	0.37	0.79

Noticeably, the listed modal periods in Table 1 are significantly larger than the peak response period (~1.1 s) as shown in Fig. 5. There may be a few reasons for the difference: (1) The mass included in the structural model may be larger than the true structure, (2) The sensors are not oriented precisely in the same direction as the modes of vibration, (3) The ground motion may not have excited the larger structural periods as much as smaller periods, (4) Building nonstructural components may add to the stiffness of the structure, especially at relatively small displacements, that may not add significant stiffness if the structure were to displace to larger magnitudes. Although, it is possible that these reasons may not explain the entirety of the difference.

Another noticeable difference between the measured results and the finite element modal analysis is that the modal analysis indicates that there are several modes that contribute significantly to the building response. This includes significant torsional response (Rz) in each of the first three modes, and about 20% of the participating mass coming from modes higher than the third mode. Although not listed in Table 1, the next mode with participating mass larger than 2% is Mode 18 with a modal period of 0.66 s. In contrast, the plot of the fast Fourier transform shown in Fig. 5 appears to indicate that there is only one mode that contributes significantly to the building response in this direction, with possibly some lesser contribution from the range between 1–1.5 Hz (1–0.67 s period).

3 Case Study 2 - Naval Hospital Bremerton

The Naval Hospital Bremerton, with a staff of over 1200 personnel, provides health care for over 60,000 families (active duty, dependents, and retirees) in the area. It is one of only two hospitals in Kitsap County (the second most densely populated county in the state of Washington) and could be called on to serve an overall population of 250,000 people after a disaster. The hospital provides emergency services, surgery, obstetrics, and inpatient services as well as housing numerous outpatient clinics. These services

are needed without interruption, particularly following an earthquake or other catastrophic event. Damage to either the building structure or to the contents could result in the disruption of essential hospital functions for an indefinite time period.

3.1 The 2001 Nisqually Earthquake

Naval Hospital Bremerton is a 249,000-square–foot, nine-story building constructed in 1976 (see Fig. 6). On February 28, 2001, the Nisqually earthquake, with a magnitude 6.8, rocked the Puget Sound area of Washington State. The epicenter of the earthquake was approximately 30 miles away from the hospital, which experienced peak horizontal ground acceleration of approximately 0.11 g and a peak acceleration at the roof of approximately 0.47 g.

Fig. 6. 9-story, 249,000SF, Naval Hospital Bremerton.

The hospital structure experienced significant drifts during the earthquake– particularly on the upper floors. Figure 7 depicts recorded roof displacements during the 2001 Nisqually earthquake.

This displacement caused extensive nonstructural damage to the facility, including gypsum wall board damage, displacement of light fixtures in suspended ceiling, overturning of bookshelves, cabinets, and computer workstations, and the rupture of a fire sprinkler pipe in an elevator roof penthouse (the sprinkler leak was not located for over 30 min, which caused water intrusion from the elevator shaft on all levels of the hospital). The displacement also caused personnel to be thrown about. This, combined with the

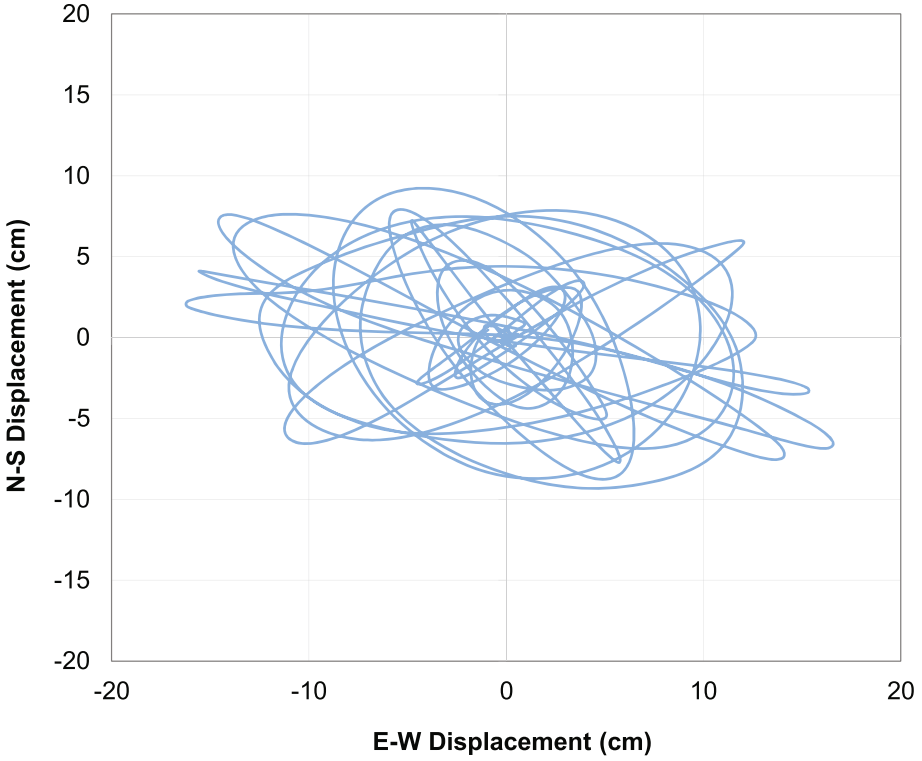

Fig. 7. Roof displacements recorded during the nisqually earthquake.

nonstructural damage, caused widespread confusion and chaos, even bordering on panic in some cases (refer to Fig. 8).

Luckily, the earthquake occurred during working hours and the Facility Management staff was present. However, most of the engineering staff was relatively new to the facility, and did not have a clear understanding of the type of building construction, nor were any of the staff familiar with post-earthquake evaluation protocols. The initial recommendations regarding immediate action came from the Fire Department, who recommended evacuation of the building. The Commanding Officer ordered non-essential personnel to evacuate the building, and some patients were evacuated to a nearby Mobile Field Hospital training site. Concurrently, the facility engineering and maintenance staff was frantically performing inspections, scouring files, and consulting with former staff members and area structural engineers to obtain information about the building construction and to determine the actual level of building damage and risk of building collapse. After approximately 6 h, enough information had been gathered to allow the hospital to be reopened for further operations, though it took several days for the utilities and systems to be fully restored, and several weeks for all repairs to be made.

Based on the experiences following the Nisqually earthquake, and because of the essential functions of the hospital, it was obvious that there was a need for a program to better evaluate the hospital for continued occupancy following a natural disaster.

Fig. 8. Typical effect on the contents of office space from the nisqually earthquake

3.2 Role of the Seismograph in Design and Response Plans

An analog seismograph with accelerometers in the basement, mechanical floor (approximately mid-height of building), and roof was installed at the hospital in 1980. The 1970s era instrument records strong motion accelerations on photographic film. After the earthquake, the accelerographs were processed and digitized for use in analytical work supporting detailed seismic evaluations and upgrades for the building. Information such as the length of the seismic event, peak acceleration, and general building response relative to the ground motion were obtained and this data was utilized to refine the 3-dimensional finite element model of the building structure. Furthermore, the original analog seismograph was upgraded to a digital seismograph that records accelerations and processes those in real time. This data is not only utilized for advanced computer modelling of the building, but also post-disaster safety evaluations of the facility.

4 Conclusion

Thousands of buildings, bridges, and structures worldwide have been instrumented with vibration accelerometers, strong-motion sensors, strain gauges, etc. for the sole purpose of recording structural response data. This data can be complex, but can provide insight for structure designers about the behavior of existing structures. In the past, there has been a lack of real-time building performance data of buildings during earthquakes. With more buildings being instrumented, there is an opportunity to analyze building performance following a strong motion earthquake event. It is even possible to use this

information to inform engineering decisions made about a structure for repair, upgrades or design.

The two case studies described in this paper indicate some of the possibilities for using structural response data to strong motion ground shaking to inform structural behavior and design. The results of the NMCSD case study indicate that the measured building response appears to be less modally complex than predicted by a finite element modal analysis, and the frequency of vibration of the modes appear to be smaller (larger period) than predicted by a finite element modal analysis. This smaller frequency (larger period) indicates that the existing building might be relatively stiffer than predicted by the finite element modal analysis, at least due to the displacement and ground motion experienced during the 2016 Borrego Springs Earthquake event.

The NHB case study indicates how earthquakes can cause significant nonstructural damage even when they do not cause structural damage. The chaos that occurs after an earthquake can make the emergency response difficult, and it is not always easy for emergency responders to make appropriate decisions about how and when to evacuate a facility. Ultimately, the strong motion NHB building response data measured during the 2001 Nisqually Earthquake was used in the design of seismic upgrades to qualify the expected post-upgrade behavior of the building.

Acknowledgements. The authors would like to acknowledge the building owners who kindly agreed to allow us to present this work despite unavoidable disclosure of certain information regarding their facilities.

Reference

1. M 5.2–20 km NNW of Borrego Springs, CA ShakeMap: (2016). Accessed 30 Jan 2017. http://earthquake.usgs.gov/earthquakes/eventpage/ci37374687#shakemap

A Bio-inspired Framework for Highly Efficient Structural Health Monitoring and Vibration Analysis

Maria-Giovanna Masciotta[1(✉)], Alberto Barontini[1], Luís F. Ramos[1], Paulo Amado-Mendes[2], and Paulo B. Lourenço[1]

[1] Department of Civil Engineering, ISISE, University of Minho, Guimarães, Portugal
mg.masciotta@gmail.com
[2] Department of Civil Engineering, ISISE, University of Coimbra, Coimbra, Portugal

Abstract. Civil engineering structures are continuously exposed to the risk of damage whether due to ageing effects, excessive live loads or extreme events, such as earthquakes, blasts and cyclones. If not readily identified, damage will inevitably compromise the structural integrity, leading the system to stop operating and undergo in-depth interventions. The economic and social impacts associated with such an adverse condition can be significant, therefore effective methods able to early identify structural vulnerabilities are needed for these systems to keep meeting the required life-safety standards and avoid the impairment of their normal function. In this context, vibration-based analysis approaches play a leading role as they allow to detect structural faults which lie beneath the surface of the structure by identifying and quantifying anomalous changes in the system's inherent vibration characteristics. However, although the considerable degree of maturity attained within the fields of experimental vibration analysis (EVA) and structural health monitoring (SHM), several technical issues still need to be addressed in order to ensure the successful implementation of these powerful tools for damage identification purposes.

The scope of this paper is to present a bio-inspired framework for optimal structural health monitoring and vibration analysis. After a critical overview on current methods and tools, three main sources of bio-inspiration are described along with the relative algorithms derived for SHM applications. It is shown how uncovering the general principles behind the functioning of selected biological systems can foster the development of efficient solutions to the technical conflicts of actual SHM architectures and lead to new sensing paradigms for optimal network topology and sensors location. A compatibility-matrix is proposed to help compare biological and SHM systems and discriminate desired from unwanted features. Such a framework will ultimately assist in seeking for the most suitable nature-inspired solutions for more accurate condition screening and robust vibration analysis.

Keywords: Structural health monitoring · Vibration analysis · Bio-inspired framework · Compatibility-matrix · Optimal network topology

© Springer International Publishing AG 2018
J.P. Conte et al. (eds.), *Experimental Vibration Analysis for Civil Structures*,
Lecture Notes in Civil Engineering 5, https://doi.org/10.1007/978-3-319-67443-8_39

1 Introduction

The potential for significant life-safety and economic benefits associated with structural health monitoring (SHM) methods has considerably boosted their implementation into the engineering practice [1]. Unlike traditional visual inspection methods, which can be subjective in nature and result insufficient when structural defects are not visible to human eyes, SHM systems may allow to catch even subtle structural changes, thereby allowing for more accurate condition screenings and continuous check-ups of the system health. Notwithstanding that, infrastructure managers often prefer experience-based solutions to SHM-weighed approaches, as the misuse and abuse of the latter can lead to inappropriate corrective actions and irremediably jeopardize the structural safety, resulting in considerable loss of economical and human resources. Hence the necessity to define new high-performance SHM strategies and to adopt a methodical framework for the successful implementation of such strategies in the engineering practice. Simultaneously, specific efforts have to be made to educate owners and raise their awareness about the consequences of poor structural health and the benefits that can be gained over time from the adoption of SHM-based preventive actions with respect to more invasive belated repair measures. In order to move forward in this direction, several problems associated with current SHM technologies must be overcome. To this end, in the last years, engineers have turned to biology for sources of inspiration, giving rise to new sensing paradigms for highly efficient SHM systems. Although the youth of this field, the amount of research related to bio-inspired systems is rapidly increasing both at academic and industrial levels. By reviewing what has been done so far in terms of bio-inspired SHM and by outlining a methodical framework for the development of new bio-inspired sensing patterns, the present paper wants to provide a useful contribution to the research community working on this topic.

2 Critical Appraisal of Current SHM Methods and Tools

2.1 General Overview of Traditional and Modern SHM Systems

The field of SHM is very wide and encompasses several techniques classified according to various criteria. In what concerns vibration-based SHM techniques, two categories can be distinguished: traditional and modern. Traditional techniques rely on tethered sensing systems which exploit a certain number of sensors (e.g. accelerometers, displacement transducers, strain gauges, and the like) distributed over the structure and wired back through coaxial cables to a centralized DAQ system for data storing and processing (Fig. 1a). Although reliable in communication, the use of cables drags behind various problems, in particular the high cost per sensing node channel and the considerable amount of time and manual work necessary to install and maintain dense sets of sensors. The large number of wires, fibre optic cables, or other physical transmission media may be prohibitive, especially in case of large-scale structures such as long-span bridges or tall buildings [2]. Moreover, wires need to be isolated from the harsh environment to avoid measurement corruption, tearing, rodent nibbling, thus causing a further increase in the cost and time of installation. These reasons explain

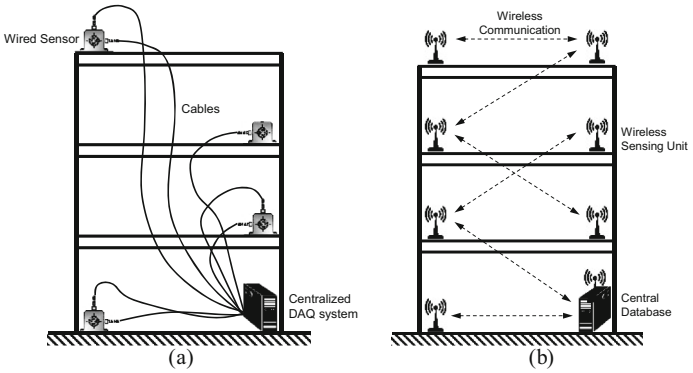

Fig. 1 Configuration of SHM systems: (a) tethered versus (b) wireless (adapted from [26]).

why tethered systems usually lack a high spatial density of sensors, which turns out to be very important for damage detection purposes as it allows to achieve greater monitoring fidelity.

The limitations of traditional monitoring techniques have led structural engineering researchers to seek for alternative and more modern approaches in order to perform many of the tasks associated with the health monitoring of civil structures. Such approaches are based on the use of sensing units that embody wireless communications and mobile computing elements so as to deliver a relatively inexpensive sensor platform [3] with distributed and no physically linked data acquisition nodes (Fig. 1b). Each wireless sensor is provided with an on-board computational core responsible for data collection, self-interrogation of measurement data and wireless communication within the sensor network. Thanks to the rapid advances in sensors technology and the decreasing cost of computing and communication systems, diverse wireless monitoring platforms have been designed and tested on different applications [3, 4]. Such systems feature a cheaper and quicker installation combined with a superior performance, thereby resulting valuable low-cost substitutes for tethered monitoring systems. In spite of that, several challenges and bottlenecks must still be overcome to fully realize the potential of wireless SHM architecture [3]. Hence, further research is required in this field.

2.2 Key Problems and Challenges

Among the wide number of issues to address are the over instrumentation and data inundation in SHM systems due to inappropriate sensors selection and location. In this regard, reliable algorithms for optimal sensors placement should be developed and lossless data compression techniques must be applied to reduce the flow of sensor information as well as face the limited capacity of wireless sensing units. Another issue to deal with is the data transmission within the wireless monitoring system which often results inaccurate and incomplete because of limited communication bandwidth, radio interference and path loss. The energy consumption and the operational life of the monitoring system are also key aspects that need to be tackled. The power supplies of

wireless sensors are indeed finite and the replacement of batteries in locations that are not easily accessible is often difficult. To trade off functionality and power consumption, the design of a flexible network management software combining sleep/wake cycles with threshold detection may be of great help. Although this would imply an *a priori* hierarchical planning of the wireless network topology, improving the entire Wireless Sensor Network (WSN) architecture before its implementation will ultimately upgrade the SHM system's performance and lead to a clever multi-level screening reducing both operation and maintenance costs. In addition, some extra efforts should be made to enhance the time synchronization of sensors in order to align data streams at different locations [5]. Last but not least issue is the influence of ambient factors and background noise on the vibration response of structures in operation conditions and the consequent necessity to provide wireless sensing units with computing procedures capable to autonomously spot and filter out these effects, which may otherwise risk to mask changes due to damage occurrence.

In light of the above considerations, it is clear that architectural and networking issues are not independent and cannot be addressed in isolation. A holistic approach, distinct from previous SHM strategies, is therefore needed.

3 Biomimicry and Structural Health Monitoring

3.1 Background on Biomimetic Concepts

To master imposing engineering challenges such as the ones mentioned previously, engineers have recently turned to biology for sources of inspiration, giving rise to a new field called biomimetics, biomimicry or bio-inspired engineering. From an etymological viewpoint, the term *biomimetics* comes from the Greek words *bios*, meaning life, and *mimesis*, meaning imitation. The name was coined in the 1950s by the polymath Otto Schmitt [6], whose doctoral research focused on the development of a physical device that explicitly mimicked the electrical action of a nerve. The chief idea of biomimetics is that Nature has already engineered superior, ingenious and sustainable systems which have benefited from millions of years of evolution and optimization and whose capabilities far surpass many of currently available technologies. Thus, the main scope of this new born discipline is to identify potential processes and mechanisms in biological systems and emulate them in order to develop innovative and efficient nature-inspired solutions in different fields and applications.

It is worth noting that mankind has been taking hints from biology for centuries. One of the earliest although unsuccessful attempt of biomimicry dates back to the 15th century, when Leonardo Da Vinci tried to build a "flying machine" based on the study of both anatomy and flying mechanisms of winged animals. Lately, with the technological progress and the integration of life and natural sciences with engineering and physical sciences, biomimetics has aroused interest across numerous disciplines and bio-inspired concepts have been assimilated into several areas, including material science, robotics and computer science. The most famous example of biomimicry is the hook-and-loop fastener, also known as Velcro [7], which was conceived in the late 1940s by the Swiss engineer George de Mestral after examining under a microscope the burs stuck to his

clothes and his dog's fur after returning from a hunting trip. Evidence of the benefits yielded by bio-inspired systems has been shown in various practical applications, including structures, aerodynamics of vehicles, highly efficient devices and apparatus [8–10]. Today, the word biomimetics is used in all contexts that involve the transfer of skills or information from biology to applied science.

3.2 Sources of Bio-inspiration in SHM and Relevant Algorithms

Given its success in many different areas of engineering, biomimetics is recently being explored for SHM purposes, guiding in the definition of nature-inspired sensing patterns for the development of highly efficient wireless sensor networks. So far, scientists seem to be particularly prone to investigate the processing mechanisms featured by biological sensory systems, due to the simplistic individual functional unit, the neuron, which forms sophisticated architectures with other units to convey information to the brain in real time [11]. This section gives a brief review of three of the main sources of bio-inspiration that have already found actuation in SHM (i.e. central nervous system, auditory system, and immune system) along with the most relevant bio-inspired algorithms derived for SHM applications. The goal is to identify the aspects upon which further research must be addressed for the advancement of the subject and to lead the way for the definition of a systematic framework for new bio-inspired sensing paradigms in the context of SHM.

3.2.1 Central Nervous System

The central nervous system (CNS) is one of the first sources of bio-inspiration that has been drawing the attention of engineers and mathematicians, especially in what concerns its adaptive architecture and parallel processing capabilities. The centre of the nervous system is the brain, which operates in combination with the spinal cord through a network of electrically excitable cells called neurons. Neurons can be of different types, but they all look alike in morphology and architecture. A typical neuron consists of three regions, namely the cell body, the axon and the dendrites. The cell body (or soma) analyses the incoming signals; the axon carries the signals to other neurons; and the dendrites receive the electrochemical signals from other cells' axons (Fig. 2). Note that neurons are not continuous, yet they communicate with one another through specific structures called synapses (from the Greek *synapsis*, meaning "conjunction"), each consisting of a presynaptic part located at the end of the axon and a postsynaptic part usually located upon another neuron's dendrite. Throughout life synapses can be subject to alterations, e.g. short-term physiological changes can modify the effectiveness of the synapses whereas long-term physiological changes can lead to modifications of the anatomy of the connection itself.

Each neuron is capable of encoding the information received from external input signals into all-or-none discrete electrochemical pulses called 'action potentials' or spike train, whose firing rate is linked to the amplitude and frequency of the input [12]. If the action potentials surpass a certain threshold, an impulse is sent down the axon's terminal cell, where neurotransmitters are released to transmit the impulse to the receptors located on the postsynaptic neurons. This yields a complete signal processing and information integration through complex networks of neurons which are able to

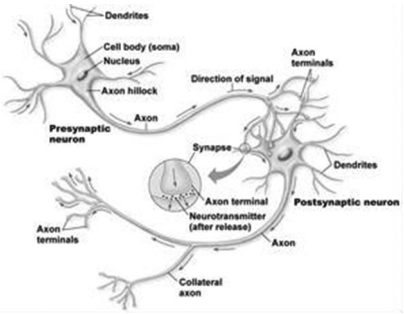

Fig. 2 Schematic architecture of two neurons (droualb.faculty.mjc.edu).

adapt over time depending on the input stimuli and to autonomously make sophisticated decisions [13]. It is remarked that the CNS enables high-speed simultaneous processing of analogous information either in different groups of neurons or in different neurons of the same pathway, being endowed with parallel processing capabilities. Furthermore, to minimize energy expenses while maintaining fast conduction, many neurons have insulating myelin sheaths around their axons. Not to mention the importance of the glial cells in providing support and nutrition to neurons, insulating them electrically, maintaining homeostasis, destroying pathogens and participating in the signal transmission within the nervous system. An extensive description of the physiology of the CNS can be found in [13].

Taking cue from nature, Artificial Neural Networks (ANNs) were developed in the early 1940's as an attempt to mathematically represent the basic physiology of a network of neurons for computer software purposes. The first mathematical model was developed by McCulloch and Pitts [14] who conceived the neuron as an extremely simplified processing unit firing only if the weighted sum of the inputs exceeded a certain threshold value α. Following this first work, several novel learning algorithms were conceived, leading to the development of numerous ANN-based methods [15, 16]. In what concerns SHM, the most used neural network architectures included the multilayer perceptron (MLP) with sigmoidal activation function [17], the counter propagation neural network [18], the probabilistic neural network [19], and the recurrent neural network [20]. Real applications of ANN for SHM purposes have been reviewed in literature [21], pointing out the efficiency of neural networks as non-model-based methods for damage identification in the presence of training sets (supervised learning). Nevertheless, neural networks have also shown good results in identifying damage patterns not belonging to training sets (unsupervised learning), which is essential for monitoring issues [22].

Beyond the achievements, it should be stressed that the original intent of ANNs was to mimic the processing mechanisms employed by the nervous system, but their evolution finally diverged from the primary source of inspiration. For instance, the architectural design of ANNs has no connection with the original human neural circuit and often ANNs are used in combination with other methods, further deviating from the initial biological principles.

3.2.2 Auditory System

Recently, a new source of inspiration for robust SHM has been chosen with the purpose of returning to the original principles of biological sensory systems. This is the mammalian auditory system, a subsystem of the sensory system, which boasts real-time spectral decomposition and high compression capabilities that render it an ideal source of inspiration for improving the performance of structural monitoring systems [23]. The mammalian auditory system relies on a few operational principles. The sound wave is received at the ear canal, or outer ear, is passed to the middle ear through the ear drum, and is transmitted to the inner ear by means of induced vibrations at the oval window, which is directly connected to the base of the cochlea, the main signal processing unit of the auditory system [24]. The cochlea is a snail-shaped tube partitioned in three fluid-filled cavities by two membranes, i.e. the Reissner's membrane and the basilar membrane (Fig. 3a–b). The basilar membrane features a geometric configuration and a mechanical stiffness that change across its length, therefore the natural frequency of this membrane also varies across its development. The deflections and resonant frequencies of the basilar membrane are correlated and tuned to the external sound wave [23]. Based on the vibrating subsections of this membrane (Fig. 3c), the cochlea instantaneously maps out the frequency content of the signal and conveys the perceived stimulus to higher levels of the auditory cortex via neural signals [25]. In detail, the stereocilia and associated inner hair cells (IHCs) of the organ of Corti, which runs on top of the basilar membrane, are responsible for encoding the membrane's motion into electrical spikes ('action potentials') which are transmitted to the CNS [24]. Being each electrical spike an all-or-none event, the spike will only fire if a threshold stimulus is reached and it will be part of a series of pulses that jointly encode information about the perceived stimulus. By using this unique method of spectral decomposition, the auditory system is able to attain an impressive auditory range while maintaining near real-time processing capabilities.

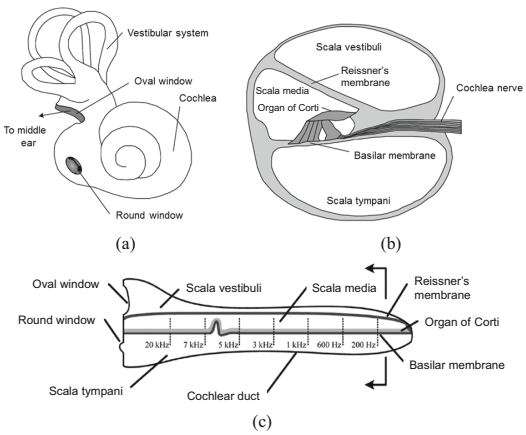

Fig. 3 Schematic representation of the mammalian auditory system: (a) inner ear; (b) cross-section of the cochlea; and (c) uncoiled cochlea indicating the vibrating subsections of the basilar membrane [25].

Based on the operational principles of the auditory system, Peckens and Lynch proposed a bio-inspired sensor [23] for structural monitoring applications. This sensor was conceived by mimicking the main processing mechanisms of the mammalian cochlea: (1) spectral decomposition by the basilar membrane; and (2) linear encoding of peak values and data compression by the inner hair cells. These mechanisms were translated into an engineered cochlea-inspired sensor system provided with a band-pass filter bank for frequency decomposition of the input signal and an ultralow power microcontroller for nearly real-time peak picking and linear encoding of the filtered signals [23]. The properties of the CNS, combined with the signal processing capabilities of the auditory system, were interpreted from an engineering viewpoint and their functionalities were ultimately applied for the enhancement of structural monitoring systems through the development of an efficient WSN architecture based on the biomimicry of the CNS. By emulating the interactions between neurons and muscles, a bio-inspired control algorithm was formulated and validated on a four-story shear mock-up [26].

The cochlea-inspired sensor did succeed in overcoming many of the technical limitations of traditional wireless sensor nodes, marking the beginning of a new era. However, there is still room for improvement, especially in terms of reduction of overhead information as well as learning and adaptability capabilities, characteristics seen within biological systems but not yet implemented. Additionally, a real application on a full scale structure is necessary to demonstrate the real-time monitoring and control capabilities of this bio-inspired technology in environments harsher than those afforded by controlled laboratory experiments.

3.2.3 Immune System

The human immune system is another source from which scientists are taking inspiration for building up optimal bio-inspired solutions in several fields. This system is formed by different biological structures and processes that aim at protecting the body against harmful microorganisms and infections. The first objective of the immune system is to differentiate between self and non-self entities. The former belong to the same organism of the immune system, whereas the latter are potential disease-causing agents, such as viruses, bacteria, parasites, etc., scientifically referred to as *pathogens*. The immune system operates by unfolding a multilevel defence of increasing specificity [27]: Level 1 – external and internal epithelial surfaces of the body; Level 2 – innate immune system; and Level 3 – adaptive immune system. The first two levels of defence are able to prevent most of infections, but when pathogens evade the innate immune response, the last level comes into play (Fig. 4). Vital for the adaptive response of the immune system are the lymphocytes, i.e. cells produced in the bone marrow that mature either within the thymus (T lymphocytes) or within the bone marrow itself (B lymphocytes). Each lymphocyte exhibits receptors able to recognize and bind with specific molecular patterns called *antigens* [27]. The strength of this bond is named ‘affinity’. Antigen specificity permits the generation of responses that are tailored to certain pathogens. In detail, to combat infections, B lymphocytes differentiate into effector B-cells producing antibodies, proteins able to identify and neutralize pathogens after binding to a specific antigen; whereas T lymphocytes differentiate into effector T-cells that kill infected cells or activate other cells. After defeating the disease, most of effector cells die, but the few cells that survive (‘memory cells’) memorize the tailored response

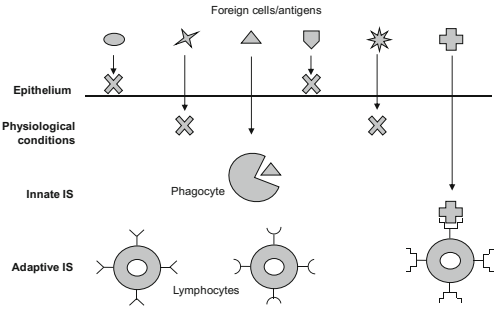

Fig. 4 Schematic representation of the multilevel defence structure of the immune system (adapted from [40]).

of the immune system ('immunological memory') so as to unfold a rapid and more effective response in case of a new contact with the same pathogen [27].

Inspired by immunology, several adaptive problem-solving methods, and consequently algorithms, have been developed and collected under the name of Artificial Immune Systems (AISs) [28]. Among the main algorithms are negative and positive selection algorithms, resulting from the evolution of the Self/Non-self discrimination theory formulated by Joshua Lederberg [29]. The main goal of this class of algorithms is to achieve a first identification of an emerging damage scenario, just by recognizing it as the cause of an abnormal pattern of features. Based on the clonal selection theory developed in the late 1970s by Burnet [30], de Castro and Von Zuben [31] proposed the first clonal selection algorithm, named CLONALG. Different approaches have been suggested over time to improve the reliability of the initial clonal selection algorithm. Detailed reviews of both classes of algorithms can be found in literature [32]. A considerable step forward in the development of a bio-inspired theory of the immune system was made by Jerne [33], who tried to formalize the interacting network of immune system cells by leveraging their ability to mutually recognize each other and to create a dynamic system of self-stimulated elements, even in the absence of external aggressions. The numerical formulation for activation/suppression of cells within the network was formalized into a model only some years later by Farmer et al. [34]. This model inspired the first Artificial Immune Network algorithm proposed by Ishida [35] in the 1990s.

AIS-based methods present several strengths, particularly in terms of flexibility, adaptability and learning capabilities. Indeed, the advantages of immune-inspired methods have fostered their use in different fields, such as Computer and Network Security, Fault Detection, Pattern Recognition, Data Mining Clustering and Filtering, Machine Learning, Function Optimization, and many others [36]. AIS architectures have also been developed and successfully applied in the field of mechanical engineering for condition monitoring purposes [37], but just a few works have extended the results to SHM applications in civil engineering. Some examples in the field of immune-inspired SHM are the Artificial Immune Pattern Recognition (AIPR) method formulated by Chen and Zang [38]; the damage detection model-based AIS algorithm with weighted attributes developed by Abbasidoust et al. [39]; and the very recent work

of Anaya et al. [40], who presented an active system for structural damage detection based on the use of piezoelectric transducers acting either as actuators or sensors. Being strongly reliable in tackling optimization problems, clonal selection and immune network theories have also inspired algorithms for improving the sensor deployment in the monitoring of civil engineering systems [41]. However, when dealing with damage identification problems, most of these algorithms allow to identify damage location and extent only if they are correctly trained to recognize the features of a given damage scenario or when, in case of supervised process, a label to the emerged damage is assigned for future recognition. This is one of the main issues to address to truly benefit from immune-inspired techniques for both supervised and unsupervised SHM.

Aiming at enhancing setting and effectiveness of the method, the evolution of AISs did ultimately deviate from the original source of inspiration, as seen for ANNs. For instance, in several cases, AIS-based algorithms are combined with non-bio-inspired models [42], preventing completely from the actuation of the initial bio-inspired paradigm.

4 A Framework for New Bio-inspired Patterns in SHM

As shown in the previous section, a few significant and successful contributions to the development of bio-inspired solutions have been produced in the last decade, aimed at overcoming most of the problems of actual SHM architectures. Still, several technical aspects remain not completely addressed. It is clear that by uncovering the general principles behind the functioning of selected biological systems, new sensing and control methods can be formulated from which current engineered monitoring systems may yet largely benefit. But, to pursue that, it is necessary to unfold a different strategy. Most bio-inspired paradigms have been conceived for reasons other than health monitoring and structural control. Hitherto, the main idea was to browse through biological literature and try to adjust some potential prototype for emulation into some artificial system which could likely turn out to be useful for SHM applications. On the contrary, a good strategy must first focus on the identification of all desirable properties and functions a robust SHM system must be provided with. Only after having a clear definition of the desired SHM features, one should look for functional analogies in biology in order to understand how nature has addressed similar instances, and eventually how to model an artificial system on a very complex natural prototype to imitate its functional principles as closely as possible.

Taking this into account and based on the critical appraisal emerged from the previous paragraphs, a holistic framework tailored to SHM requirements is defined. This framework embraces both architectural and networking issues and is materialized into a compatibility-matrix where the desired SHM system's characteristics are distributed along the top and the biological features - identified from the analysis of the three sources of bio-inspiration discussed in the paper – are arranged along the vertical axis (Table 1). Scope of the matrix is to help match analogous features between biological and SHM systems and to easily discriminate desired from unwanted nature-inspired characteristics. This pairing process will ultimately assist in the selection of the most

Table 1. Compatibility-matrix between biological and SHM systems (cells with dots indicate matching features).

			SHM system's features																													
			Signal Processing									Networking								Sensing Unit Architecture							Network Architecture					
	Biological features	Biological system	Real-time feature extraction	Signal encoding	Lossless data compression	Parallel & distributed computing	Noise reduction	Filtering env./operat. variations	Damage detection	Data fusion	Multi-layer sensor interaction	Mobile network supervision	Real-time data transmission	Time synchronization	Energy harvesting	Self-adaptability/organization	Homeostasis	Self-diagnostics & -repair	Learning/Pattern recognition	Threshold detection	Self-activation/shutdown	Power efficiency	Hierarchical topology	Multilevel clustering	Sensor placement optimization	Real-time decision making	Flexible management
CENTRAL NERVOUS SYSTEM	Signal processing & encoding	Nerve cells (soma)	●	●		●								●																	
	Threshold detection	Nerve cells (soma)																		●												
	Impulse transmission	Synaptic connection									●		●																			
	Information integration	Nerve fibers								●																						
	Learning and data mining	Nerve cells (soma)																	●													
	Metabolic expense reduction	Axons' myelin sheath																				●										
	Self-support and nutrition	Glial cells																				●										
	Adaptability to input	Synaptic connection														●																
	Optimal coverage	Neurons' number																							●							
	Real-time decision making	Brain																								●						
	Hierarc. Morphology/Physiology	Nervous system									●												●	●			●					
AUDSYS	Spectral decomposition	Basilar membrane	●																													
	Peak values encoding	Organ of Corti		●																												
	Data compression	Inner hair cells			●																											
	Data transmission	Hair-cell neurons											●																			
IMMUNE SYSTEM	Multilevel defence organisation	Skin-Inn.IS-Adap.IS						●								●								●		●	●					
	Alarm issue	Innate IS							●											●												
	Pattern recognition	Lymphocytes							●										●													
	Parallel actions	Lymphocytes				●					●			●																		
	Pathogen counteraction	Antibodies																●														
	Self/non-self discrimination	T lymphocytes						●	●																							
	Cells activation/suppression	T-cells																			●	●										
	Equilibrium restoration	Lymphocytes															●															
	Immunological memory	Memory cells																	●													

compatible functions to transfer from nature to structural monitoring system. The stronger the compatibility (analogy), the stronger the future solution (synthesis).

Although limited, the proposed matrix can be considered as the first attempt to systematize a framework for bio-inspired SHM. Hitherto, only a few bio-inspired analogies have found actuation in SHM. Most gaps still have to be filled, thereby calling for further research. The next step will entail increasing the order of the matrix by finding a wider range of functional analogies. The ones showing the closest fit will be thoroughly analysed for possible implementation into biomimetic engineered systems for optimal vibration-based SHM.

5 Conclusions

A critical analysis of the current state-of-the-art in the field of structural health monitoring has been provided in this paper, including an overview of the recent developments in the area of biomimetic engineering for SHM purposes. The work has revealed

that biomimetics still lacks a systematic approach. Apart from a few exceptions, most of bio-inspired paradigms and algorithms developed so far were conceived for reasons other than structural monitoring and they ultimately diverged from the primary source of inspiration. In order to go back to the original biological principles and overcome the conflicts of actual technologies, the authors have pointed out the need to tailor biomimetics to SHM requirements according to a holistic approach. To achieve that, a compatibility-matrix is outlined to assist in the identification of functional analogies between SHM systems and biological kingdom, and to guide in the selection of the best solutions for future implementation into real engineered systems for robust structural monitoring and vibration analysis.

Acknowledgments. This work was financed by FEDER funds through the Competitiveness Factors Operational Programme - COMPETE and by national funds through FCT – Foundation for Science and Technology within the scope of the project POCI-01-0145-FEDER-007633.

References

1. Brownjohn, J.M.W.: Structural health monitoring of civil infrastructure. Philos. Trans. R. Soc. Lond. A Math. Phys. Eng. Sci. **365**(1851), 589–622 (2007)
2. Spencer, B.F., Ruiz-Sandoval, M., Kurata, N.: Smart sensing technology for structural health monitoring. In: 13th World Conference on Earthquake Engineering, Vancouver, Canada (2004)
3. Lynch, J.P.: An overview of wireless structural health monitoring for civil structures. Philos. Trans. R. Soc. A Math. Phys. Eng. Sci. **365**(1851), 345–372 (2007)
4. Lynch, J.P., Loh, K.J.: A summary review of wireless sensors and sensor networks for structural health monitoring. Shock Vib. Dig. **38**(2), 91–130 (2006)
5. Lei, Y., Kiremidjian, A.S., Nair, K.K., Lynch, J.P., Law, K.H.: Algorithms for time synchronization of wireless structural monitoring sensors. Earthq. Eng. Struct. Dyn. **34**(6), 555–573 (2005)
6. Harkness, J.M.: A lifetime of connections—Otto Herbert Schmitt, 1913–1998. Phys. Perspect. **4**(4), 456–490 (2002)
7. Velcro, S.A.: Improvements in or relating to a method and a device for producing a velvet type fabric. Patent no. 721 338, Switzerland (1955)
8. Bechert, D.W., Bruse, M., Hage, W., Meyer, R.: Fluid mechanics of biological surfaces and their technological application. Naturwissenschaften **87**(4), 157–171 (2000)
9. Ayers, J., Witting, J.: Biomimetic approaches to the control of underwater walking machines. Philos. Trans. R. Soc. Lond. A Math. Phys. Eng. Sci. **365**(1850), 273–295 (2007)
10. Kennedy, J.: Particle swarm optimization. In: Sammut, C., Webb, G.I. (eds.) Encyclopedia of Machine Learning, pp. 760–766. Springer, New York (2010)
11. Bonser, R.H.: Patented biologically-inspired technological innovations: a twenty-year view. J. Bionic Eng. **3**(1), 39–41 (2006)
12. Bialek, W., Rieke, F., de Ruyter Van Steveninck, R.R., Warland, D.: Reading a neural code. Science **252**(5014), 1854–1857 (1991)
13. Kandel, C.E.R., Schwartz, J.H., Jessell, T.M.: Principles of Neural Science, 4th edn. McGraw-Hill, New York (2000)
14. McCulloch, W.S., Pitts, W.H.: A logical calculus of the ideas immanent in nervous activity. Bull. Math. Biophys. **5**(4), 115–133 (1943)

15. Hagan, M.T., Demuth, H.B., Beale, M.H., De Jesús, O.: Neural Network Design, 2nd edn. Martin Hagan (2014)
16. Anderson, J., Rosenfeld, E.: Neurocomputing: Directions for Research. MIT Press, Cambridge (1990)
17. Doebling, S.W., Farrar, C.R., Prime, M.B., Shevitz, D.W.: Damage identification and health monitoring of structural and mechanical systems from changes in their vibration characteristics: a literature review. Report LA-13070-MS. National Laboratory, Los Alamos (1996)
18. Hecht-Nielsen, R.: Applications of counter propagation networks. Neural Netw. **1**(2), 131–139 (1988)
19. Jiang, S., Fu, C., Zhang, C.: A hybrid data-fusion system using modal data and probabilistic neural network for damage detection. Adv. Eng. Softw. **42**(6), 368–374 (2011)
20. Butcher, J., Day, C., Austin, J., Haycock, P., Verstraeten, D., Schrauwen, B.: Defect detection in reinforced concrete using random neural architectures. Comput. Aided Civ. Infrastruct. Eng. **29**(3), 191–207 (2014)
21. Fan, W., Qiao, P.: Vibration-based damage identification methods: a review and comparative study. Struct. Health Monit. **10**(1), 83–111 (2011)
22. Manning, R.: Damage detection in adaptive structures using neural networks. In: 35th AIAA/ASME/ASCE/AHS/ASC Structures, Structural Dynamics, and Materials Conference, Hilton Head, SC, USA. American Institute of Aeronautics and Astronautics, Washington (1994)
23. Peckens, C., Lynch, J.P.: Utilizing the cochlea as a bio-inspired compressive sensing technique. Smart Mater. Struct. **22**(10), 105027 (2013)
24. Yost, W.A.: Fundamentals of Hearing: An Introduction, New York (1994)
25. Peckens, C., Lynch, J.P.: Resource-efficient wireless sensor network architecture based on bio-mimicry of the mammalian auditory system. J. Intell. Mater. Syst. Struct. **26**(1), 79–100 (2015)
26. Peckens, C.A.: Bio-inspired compressive sensing based on auditory neural circuits for real-time monitoring and control of civil structures using resource constrained sensor networks. Ph.D. thesis, University of Michigan, USA (2014)
27. Janeway Jr., C.A., Travers, P., Walport, M., Shlomchik, M.J.: Immunobiology: The Immune System in Health and Disease, 5th edn. Garland Publishing, New York (2001)
28. De Castro, L.N., Nunes, L., Von Zuben, F.J.: Artificial immune systems: Part I–basic theory and applications. Report TR-DCA 01/99. Universidade Estadual de Campinas, Brasil (1999)
29. Lederberg, J.: Genes and antibodies. Science **129**(3364), 1649–1653 (1959)
30. Burnet, F.M.: A modification of Jerne's theory of antibody production using the concept of clonal selection. CA Cancer J. Clin. **26**(2), 119–121 (1976)
31. De Castro, L.N., Von Zuben, F.J.: Learning and optimization using the clonal selection principle. IEEE Trans. Evol. Comput. **6**(3), 239–251 (2002)
32. Dasgupta, D., Yu, S., Nino, F.: Recent advances in artificial immune systems: models and applications. Appl. Soft Comput. **11**(2), 1574–1587 (2011)
33. Jerne, N.K.: Towards a network theory of the immune system. Ann. d'immunol. **125**(1–2), 373–389 (1974)
34. Farmer, D.J., Packard, N.H., Perelson, A.S.: The immune system, adaptation and machine learning. Phys. D Nonlinear Phenom. **22**(1), 187–204 (1986)
35. Ishida, Y.: Fully distributed diagnosis by PDP learning algorithm: towards immune network PDP model. In: 1990 IJCNN IEEE International Joint Conference on Neural Networks, San Diego, CA, USA (1990)

36. Aickelin, U., Dasgupta, D., Gu, F.: Artificial immune systems. In: Burke, E.K., Kendall, G. (eds.) Search Methodologies: Introductory Tutorials in Optimization and Decision Support Techniques. Springer, New York (2014)
37. Bayar, N., Darmoul, S., Hajri-Gabouj, S., Pierreval, H.: Fault detection, diagnosis and recovery using artificial immune systems: a review. Eng. Appl. Artif. Intell. **46**, 43–57 (2015)
38. Chen, B., Zang, C.: Artificial immune pattern recognition for structure damage classification. Comput. Struct. **87**(21), 1394–1407 (2009)
39. Abbasidoust, F., Lotfollahi-Yaghin, M., Sadeghi, M.H., Mojtahedi, A., Ettefagh, M.M., Hassanzadeh, Y.: A robust damage detection method developed for offshore jacket platforms using modified artificial immune system algorithm. China Ocean Eng. **26**(3), 379–395 (2012)
40. Anaya, M., Tibaduiza, D.A., Pozo, F.: A bioinspired methodology based on an artificial immune system for damage detection in structural health monitoring. Shock Vib. **2015**, 1–15 (2015)
41. Yi, T.H., Li, H.N., Zhang, X.D.: Health monitoring sensor placement optimization for Canton Tower using immune monkey algorithm. Struct. Control Health Monit. **22**(1), 123–138 (2015)
42. De Castro, P.A.D., Von Zuben, F.J.: A Bayesian artificial immune system for the effective handling of building blocks. Inf. Sci. **179**(10), 1426–1440 (2009)

Development of the UPRM Hybrid Simulation Facilities: Substructuring Techniques Coupled Numerical Simulations

Maria D. Cortes-Delgado[1(✉)] and Lemuel González Hernández[2]

[1] Department of Engineering Science and Materials,
University of Puerto Rico at Mayaguez, Mayaguez, Puerto Rico, USA
maria.cortes5@upr.edu
[2] Department of Civil Engineering and Surveying,
University of Puerto Rico at Mayaguez, Mayaguez, Puerto Rico, USA

Abstract. Hybrid simulation is an innovative experimental method currently being tested and utilized for the simulation of earthquake loads on structures. The reliability of this experimental method will be achieved as more research targeting realistic conditions of structures (e.g. subassemblages and structures at larger scales) with more complex configurations are conducted. Furthermore, these studies need to address the efficacy of hybrid testing to simulate the collapse of structures. The University of Puerto Rico at Mayaguez (UPRM) is developing a hybrid simulation facility with its first-stage consisting of a two channel MTS Flex Test 60 control system with quasi-static hybrid simulation capabilities. The main objective of the UPRM hybrid simulation facility is testing of more realistic models of prototypes subjected to dynamic loads. The research is also focused on substructuring techniques: development, implementation and error measurement. At first, the hybrid facility will be calibrated with the analysis and hybrid testing of a 3-story 2-bay moment resisting steel frame subjected to the Canoga Park time history. Hybrid simulation with substructuring allows the modeling of parts of the structure we can predict analytically and testing other parts of interest at the laboratory. In this case, only the exterior column of the first and second story column of our prototype will be tested at a 1:3 scale while the rest of the structure will be modeled analytically using the software OpenSees and OpenFresco. Coupled numerical simulations were conducted of current partitioning strategies including the conventional and pinned substructuring techniques. These numerical studies showed that there is a need for better partitioning methods. The problem with the studied substructuring techniques is that they approximate the response of the prototype when they do not fully enforce compatibility and/or equilibrium in all degrees of freedom at the boundaries of the partitioned structures trying to simplify the experimental substructure.

Keywords: Substructuring techniques · Hybrid simulation · Experimental methods · Coupled simulations · OpenFresco

© Springer International Publishing AG 2018
J.P. Conte et al. (eds.), *Experimental Vibration Analysis for Civil Structures*,
Lecture Notes in Civil Engineering 5, https://doi.org/10.1007/978-3-319-67443-8_40

1 Introduction

The probability of an extreme load event (e.g. wind, earthquake, man-made) continuously poses a threat to our infrastructure. The analytical tools developed to predict the behavior of structures to these extreme loads need to be validated by experimental work. Many simplifying assumptions are done in numerical simulations, therefore it is essential to validate these studies via experimental verification. The University of Puerto Rico at Mayagüez (UPRM) understands the importance of an adequate testing facility for conducting experimental research in the area of earthquake engineering in Puerto Rico. Not only is Puerto Rico located in a high seismicity zone but also as one of the top engineering minority serving institutions across the United States needs to stay at par with the new and innovative discoveries in science and technology.

2 Background

The Structural Laboratory at the Department of Civil Engineering and Surveying has facilities for testing of scaled complete structures under simulated loads, such as those produced by wind and earthquakes, as shown in Fig. 1. The small to medium size uni-directional shaking Table (2.28 m by 1.37 m) possess the capability to generate earthquake-like motion thus is able to test rate-dependent structural materials and structural devices. However, the prototypes and/or subassemblages to be tested have to be scaled (maximum scale being 1:4) due to size of the simulator. It has been proven that scaling affects the local response which is an important factor when evaluating the performance of the structure [1]. Hybrid simulation is an innovative technique that combines laboratory physical measurements and analytical models for evaluating the dynamic performance of structures, as explained by Eq. 1. The equation of motion for the combined experimental and analytical structure can be expressed as:

$$(\mathbf{M} \cdot \ddot{u})^A + (\boldsymbol{C} \cdot \dot{u})^A + (\boldsymbol{K} \cdot u)^A + r^E = \left(-M^t \cdot \boldsymbol{l} \cdot \ddot{u}_g\right)^A \tag{1}$$

Where (**M**, **C**, and **K)** are the mass, damping and stiffness matrices of the numerical substructure (analytical substructure), $(u, \dot{u}, \ddot{u})$ are the displacement, velocity and acceleration vectors, the restoring forces measured experimentally are ($\mathbf{r}^{\mathrm{E}}$), ($\mathbf{M}^{\mathbf{t}}$) is the total mass matrix and $(l, \ddot{\boldsymbol{u}}_g)$ are the influence and ground acceleration vectors. Quasi-static hybrid simulation applies the time history seismic event at a much slower rate than a real event which allows to evaluate elements that contribute stiffness and strength to the structure. A key advantage of this method is that it allows for larger specimens to be tested (depending on capacity of actuator), the local behavior can be captured and the test can be continuously monitored. On the contrary, error propagation is one of its disadvantages.

a. Earthquake simulator

b. Wind platform

Fig. 1. UPRM dynamic testing facilities.

3 UPRM Hybrid Simulation Facilities

The UPRM is developing a hybrid simulation facility with its first-stage consisting of a two channel MTS Flex Test 60 control system with quasi-static hybrid simulation capabilities, as shown in Fig. 2a. The proposed test-setup, shown in Fig. 2b, has been modified from previous validated test-setups utilized to conduct hybrid simulation studies [2]. The addition of the quasi-static hybrid simulation facilities will make the existing dynamic testing facilities able to test more realistic models of prototypes at larger scales reducing the errors associated with scaling and will be able to better track the local response of the prototypes. Furthermore, the hybrid simulation facility at the University of Puerto Rico at Mayagüez will be the first of its kind in Puerto Rico.

3.1 Objectives

The main objective of the UPRM hybrid simulation facility is testing of civil and military infrastructure subjected to dynamic loads. The UPRM hybrid simulation facility research project also encompasses the following objectives:

1. To test structures at larger scales and with more complex configurations (e.g. not only columns but one-and-half-bay by one-and-half story, others). Hybrid simulation with substructuring allows the modeling of parts of the structure we can predict analytically and testing other parts of interest at the laboratory at larger scales.

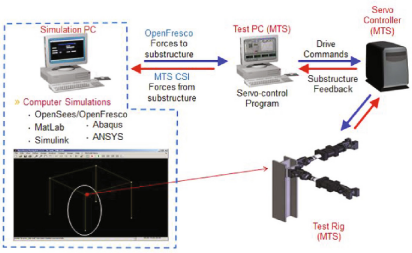

a. Hybrid simulation concept [3].

b. Proposed test setup for calibration of hybrid testing equipment [4].

Fig. 2. UPRM Hybrid simulation facility concept.

2. To contribute current substructuring techniques with the development of new strategies, and the implementation and error measurement of current and newly develop substructuring techniques. Hybrid simulations of more complex configurations requires the development of new and innovative substructuring techniques that addresses the boundary conditions at the interface of the analytical and experimental substructures.
3. These studies also need to address the safety margin against collapse of structures to breach the knowledge gap in predicting analytically this reserve.

The UPRM Hybrid simulation facilities will contribute, by means of these objectives, to the testing of the reliability of the hybrid simulation method. This paper will focus on the implementation and error measurement of current substructuring techniques by means of coupled numerical simulations.

4 Substructring Techniques: Coupled Numerical Simulations

The first-stage of the development of the UPRM hybrid simulation facility will be the installation and calibration of the equipment. At first, the hybrid facility will be calibrated with the analysis and hybrid testing of a 3-story 2-bay moment resisting steel frame subjected to the Canoga Park time history. In this case, only the exterior column of the first and second story column of our prototype will be tested at a 1:3 scale while the rest of the structure will be modeled analytically using the software OpenSees and OpenFresco. The initial substructuring analysis will consists of coupled numerical simulations comparing two strategies: the conventional substructuring technique (CS) and the "pinned" substructuring technique (PS) versus the response of the prototype without partitioning.

4.1 Prototype Description

The prototype is a 3-story 2-bay steel moment resisting frame with a longitudinal dimension (X) of 9.14 m per bay for a total width of 18.28 m. The typical story height

is 4.57 m for a total height of 13.71 m. Figure 3a shows the prototype's sections and dimensions. The prototype without partitioning is modeled with OpenSees with concentrated plasticity using modified IK deterioration model, modified by Lignos and Krawinkler [5]. Deterioration parameters are applied at all ends of beams and columns. The prototype is a previously studied and hybrid tested moment resisting frame [6] with modifications to accommodate our research project. The coupled numerical simulations utilize the NewmarkHSFixedNumIter integrator with average acceleration parameters and the test is FixedNumIter at 6 iterations. The time step of analysis is 0.001 s with a Rayleigh damping with a ratio of 5%.

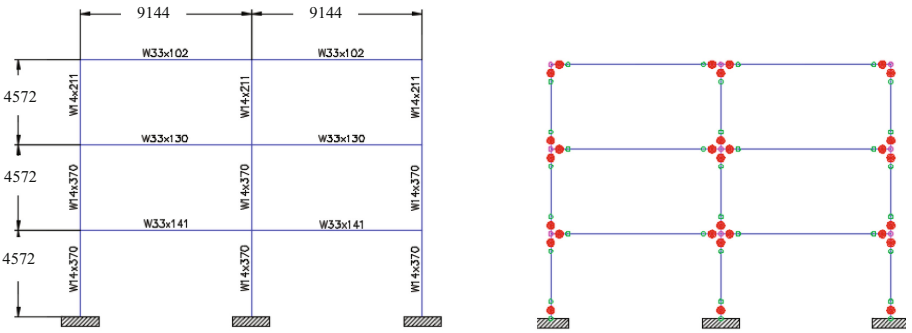

a. Dimension and sections. *b. Concentrated plasticity model*

Fig. 3. Description of prototype model in OpenSees (mm).

4.2 Substructuring Techniques

The prototype model is divided in two substructures: one numerical substructure and one experimental substructure. Both numerical and experimental substructures are modeled using OpenSees and coupled using OpenFresco. The numerical substructure will be referred as the master substructure and the "experimental" substructure as the slave substructure. OpenSees is a finite element program used for the numerical analysis. OpenFresco is a software that couples computer analysis software with laboratory control systems and/or other software to performed hybrid simulations. Two substructuring techniques (different partitioning strategies) are analyzed: the conventional substructuring technique and the pinned substructuring technique. For coupling the master and slave substructures four objects have to be defined in the master file. These objects are Experimental Element, Experimental Site, Experimental Setup and Experimental Control. Figure 4 illustrates the communication from the four different objects from the numerical to the "experimental" substructure [7]. An adapter element has to be defined on the slave file. The adapter element represents the actuator and applies nodal prescribed displacement to the slave file and return nodal reaction forces to the master file.

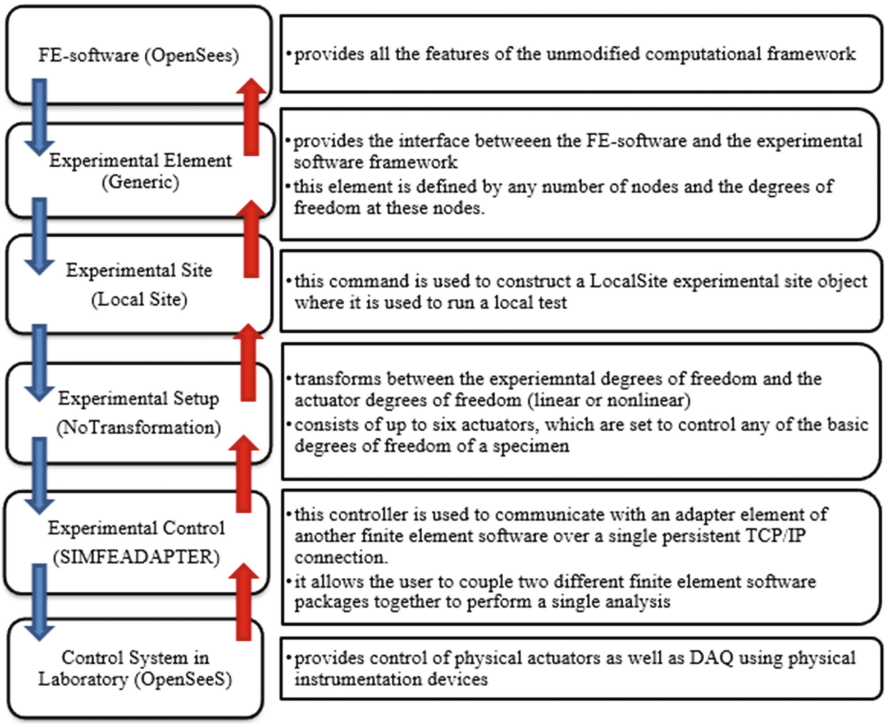

Fig. 4. OpenFresco experimental objects definitions utilized for these numerical simulations [modified from 7].

4.3 Conventional Substructuring Techniques (CS) Results

Figure 5a illustrates how the prototype was partitioned for the conventional substructuring technique (CS) coupled numerical simulation. This substructuring technique fully enforces compatibility and/or equilibrium in all degrees of freedom at the boundaries of the partitioned structures. For the first case, the horizontal and rotational degrees of freedom are transferred from the numerical and experimental substructure. On the master substructure, the node 32 is restricted only in 2-direction (vertical displacement) whereas node 032 on slave file is free in all directions. OpenFresco transmits the horizontal and rotational displacements of node 32 to node 032 through the adapter element.

The adapter element then in the slave file calculates the nodal reactions and these are sent back to node 32 on the master file. The generic element is defined for node 32 with stiffness value in direction 1 (horizontal) and 3 (rotation). The adapter element in slave file is defined for node 032 with a high stiffness matrix. Figure 5b shows the first story displacement time history of the numerical simulation where the response of the prototype without partitioning is represented by the blue curve and the CS technique is represented by the red curve. Furthermore, Fig. 5d also show a global response by the floor level response (first story shear versus story drift) with same legend. These global

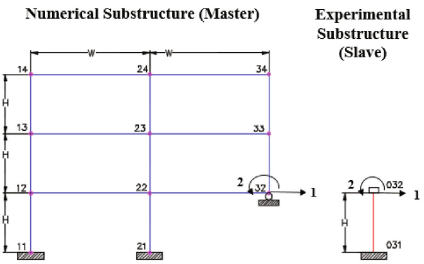

a. Conventional substructuring technique-Case1.

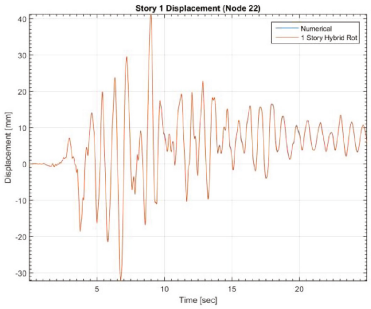

b. First story displacement time history (mm).

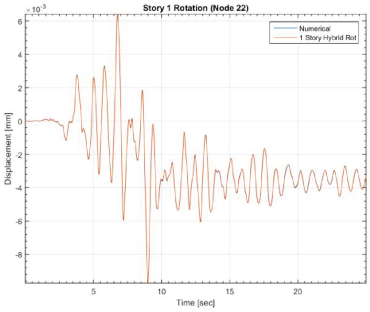

c. First story rotation time history (rad).

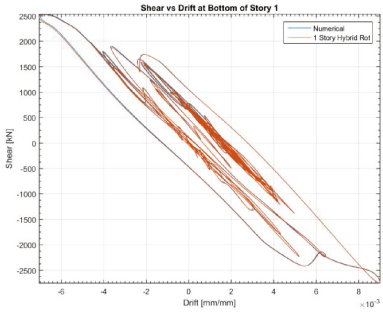

d. First story floor level response.

Fig. 5. Conventional substructuring techniques coupled simulation responses-Case 1.

results shows an excellent agreement between the two curves throughout the history of the plot. The local response was also measured by means of the rotation time history of the first story floor where the structure was partitioned, as displayed by Fig. 5c. The local response also show an excellent simulation of the response of the prototype without partitioning by the CS technique.

The second case that is studied, only the horizontal degree of freedom is transferred from the numerical and experimental substructure as shown in Fig. 6a. The master substructure is defined by the node 32 and only the 1-direction (horizontal displacement) is left unconstrained. The slave file is defined the same way as in the first case. Figure 6b, d shows the global response of the first story by means of the displacement time history and the floor level response (first story shear versus story drift). The global results shows only a small variation (over the maximum/minimum) of the peak responses between the two curves until they reached their positive and negative maximum responses on the time history plot. After the maximum and minimum response were achieved there is a big difference, due the residual displacements, between the two curves. Figure 6c, displays the first story rotations time history response for the second case where it can be seen the rotations for this case is approximately half of the previous case in the residual part of the plot.

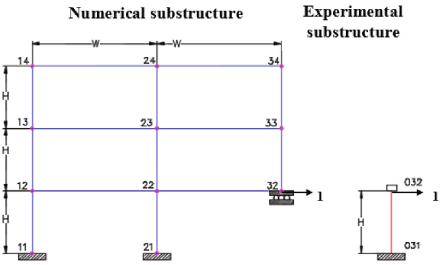

a. Conventional substructuring technique-Case 2

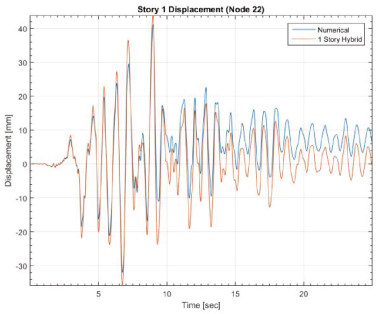

b. First story displacement time history (mm).

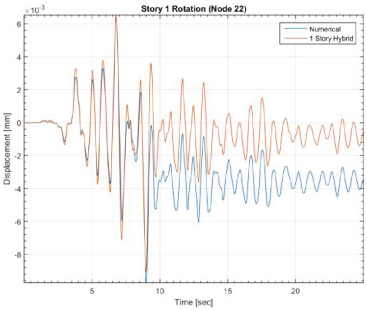

c. First story rotation time history (rad).

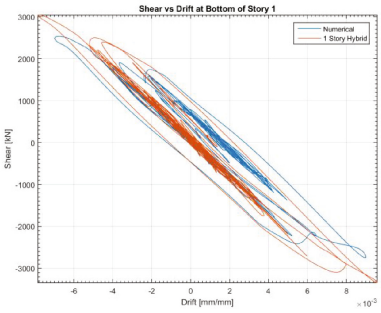

d. First story floor level response.

Fig. 6. Conventional substructuring techniques coupled simulation responses- Case 2.

4.4 Inelastic or Pinned Substructuring Techniques

Hybrid simulations of more complex configurations requires the development of new and innovative substructuring techniques that addresses the boundary conditions at the interface of the analytical and experimental substructures. The inelastic substructuring technique or "pinned" substructuring technique (PS) assumes pins at the points of inflection of the columns and beams thus simplifying the experimental substructure with small variations in the global response (drift) [8]. The boundaries between the analytical and experimental substructures are chosen to be the midpoint of the second story column. This point was selected assuming an inflection point at this location. This point of inflection needs to be validated by further studying the occurrence of the inflection points at each step in a dynamic analysis for the prototype and plotting histograms.

Figure 7a illustrates how the prototype was partitioned for the "pinned" substructuring technique (PS) coupled numerical simulation. In this case also, only the horizontal degrees of freedom are transferred form the numerical and experimental substructures. The master substructure, node 32 is restricted in directions 2 and 3 (vertical displacement and rotation) and node 325 only is restricted in the 2-direction.

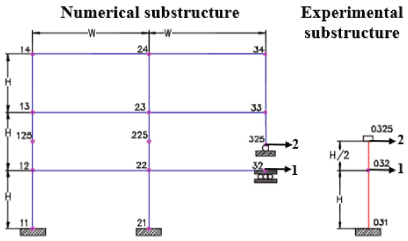

a. *Pinned substructuring technique.*

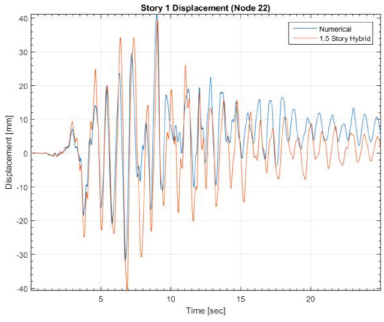

b. *First story displacement time history (mm).*

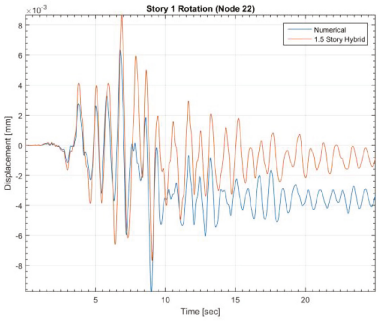

c. *First story rotation time history (rad).*

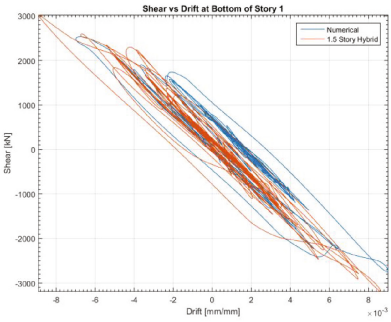

d. *First story floor level response.*

Fig. 7. Pinned substructuring techniques coupled simulation responses.

The nodes 032 and 0325 on the slave file are unconstrained. OpenFresco transmits the two horizontal displacements from nodes 32 and 325 on the master file to nodes 032 and 0325 on the slave file. The generic element is defined for nodes 32 and 325 with stiffness matrix 2 × 2 in 1-direction. The adapter element in the slave file is defined for nodes 032 and 0325. It has a stiffness matrix with high values in 1-direction.

Figure 7b, d shows the global response of the first story by means of the displacement time history and the floor level response. The global results shows there is a larger variation (over the minimum) of the peak responses between the two curves compared to the CS-Case 2 global responses. However, after the maximum and minimum responses were achieved there is a better agreement on the residual displacements than for CS-Case 2. Figure 7c, displays the first story rotations time history response for the PS where it is not shown a greater difference than the CS-Case 2.

5 Conclusions

The UPRM is developing a hybrid simulation facility with its first-stage consisting of a two channel MTS Flex Test 60 control system with quasi-static hybrid simulation capabilities. The addition of the quasi-static hybrid simulation facilities will make the

existing dynamic testing facilities able to test more realistic models of prototypes at larger scales reducing the errors associated with scaling and will be able to better track the local response of the prototypes. The substructuring techniques coupled numerical simulations of current partitioning strategies show that there is a need for better methods. The studied substructuring techniques approximate the response of the prototype when it does not fully enforce compatibility and/or equilibrium in all degrees of freedom at the boundaries of the partitioned structures, as does the conventional substructuring technique CS-Case 1. Hybrid simulations of more complex configurations requires the development of new and innovative substructuring techniques that addresses the boundary conditions at the interface of the analytical and experimental substructures while still maintaining a less complex experimental substructure (number of required actuators). The new strategies for partitioning the structure also entails the development of substructuring error indicators to better predict which method is best suited for different hybrid test using different prototype configurations and earthquake time histories.

6 On Going and Future Research

The overlapping domain substructuring technique (OL), where the boundaries of the physical substructures are extended to the mid-height of the second story columns, emerged to simplify the boundary conditions at the interface thus reducing the number of required actuators in the experimental test setup [9]. This substructuring technique is also being currently studied with coupled simulations. The UPRM Hybrid simulation facility will be installed and calibrated with the aforementioned prototype and the different strategies will be implemented. Error indicators will be evaluated with the data produced by the hybrid testing and the coupled simulations.

Acknowledgments. This project was supported by the Nuclear Regulatory Commission Faculty Development Award 2015; The University of Puerto Rico at Mayaguez Faculty Development Program: Structural Engineering for Nuclear Facilities – Experimental Research Initiative (NRC-HQ-84-15-G-0032).

References

1. Nakashima, M., MacCormick, J., Wang, T.: Hybrid simulation: a historical perspective. In: Saouma, V., Sevaselan, M. (eds.) Hybrid Simulation: Theory, Implementation and Applications, pp. 3–13. Taylor & Francis, London (2008)
2. Mehdi, A.: Real-time seismic hybrid simulation procedures for reliable structural performance testing. Ph.D. Thesis, University of New York at Buffalo, New York (2007)
3. Property of MTS System Corporation
4. Cortes-Delgado, M., Flores, C.: Development of hybrid simulation facilities: test setup design and initial calibration, Undergraduate Research Technical Poster, to be published (2016)
5. Lignos, D.G., Krawinkler, H.: Sidesway collapse of deteriorating structural systems under seismic excitations, Technical report 172, The John A. Blume Earthquake Engineering Research Center, Department of Civil Engineering, Stanford University, Stanford, CA (2009)

6. Del Carpio Ramos, M.: Hybrid simulation of the seismic response of a steel moment frame building structure through collapse. Ph.D. Thesis, University of New York at Buffalo, New York (2013)
7. Schellenberg, A., Huang, Y., Mahin, S.A.: Structural FE-software coupling through the experimental software framework, OpenFresco. In: Proceedings of 14th World Conference on Earthquake Engineering, Beijing, China (2008)
8. Schneider, S., Roeder, C.: An inelastic substructure technique for the pseudodynamic test method. Earthq. Eng. Struct. Dyn. **23**, 761–774 (1994)
9. Cortes-Delgado, M.: Hybrid simulation with distributed substructures including overlapping domains. Ph.D. Thesis, University of New York at Buffalo, New York (2014)

Shake-Table Testing and Performance Assessment of a Partially Grouted Reinforced Masonry Building

Andreas Koutras(✉) and P. Benson Shing

Department of Structural Engineering, University of California - San Diego, La Jolla, CA, USA
akoutras@ucsd.edu

Abstract. This paper presents a study on the seismic performance of partially grouted reinforced masonry buildings. Shake-table tests were conducted on a full-scale, one-story building that had ordinary partially grouted masonry shear walls. The building was designed according to the current practice and code provisions in the U.S. for areas of low to moderate seismicity. For the tests, a sequence of earthquake ground motions of increasing intensity was applied. The structure developed adequate base shear capacity and was able to resist ground motions with intensities twice the maximum considered earthquake without failures. However, it eventually failed in a brittle manner. To quantify the contribution of each shear wall to the overall lateral load capacity of the building, a nonlinear finite-element model was developed and calibrated with the experimental data obtained from the shake-table tests. The experimental and numerical results suggest that the shear strength equation of the current design code predicts reasonably well the base shear capacity of the building specimen.

Keywords: Shake table · Seismic performance · Full-scale testing · Reinforced masonry · Partial grouting · Finite-element model

1 Introduction

Reinforced masonry is commonly used in North America for low-rise buildings, such as residential, commercial, and school buildings. In these structures, walls are the main load-bearing elements resisting gravity loads, and lateral earthquake or wind loads. The walls are generally constructed of hollow, concrete masonry units. Vertical reinforcement is placed in continuous vertical cells, and horizontal reinforcement can be deformed bars placed in horizontal courses (bond beams) or steel wires embedded in the mortar joints. Masonry walls can be either fully grouted or partially grouted. In partially grouted walls, only the reinforced vertical and horizontal cells are filled with grout. The design provisions for reinforced masonry structures in the U.S. are provided in the masonry design code developed by the Masonry Standards Joint Committee (2013 MSJC) [1].

While a number of studies have been carried out to investigate the seismic performance of fully grouted reinforced masonry buildings, far less attention has been devoted to partially grouted masonry, although the latter constitutes most of the reinforced

© Springer International Publishing AG 2018
J.P. Conte et al. (eds.), *Experimental Vibration Analysis for Civil Structures*,
Lecture Notes in Civil Engineering 5, https://doi.org/10.1007/978-3-319-67443-8_41

masonry construction in the U.S. outside the West Coast. Experimental studies have shown that the behavior and failure modes of partially grouted walls strongly depend on the spacing of the grouted cells. Indeed, when the spacing is large (i.e., more than 1220 mm), partially grouted walls tend to respond similarly to reinforced concrete frames infilled with unreinforced masonry [2, 3]. For this situation, the shear strength equation in the MSJC code, which was developed based on experimental data on fully grouted masonry walls, does not represent well the behavior of partially grouted walls. Test data [4] have shown that the shear strength equation may significantly overpredict the shear strength of partially grouted walls as the spacing of the vertical grouted cells increases. Quasi-static tests conducted on shear walls with aspect ratios between 0.6 and 1, and vertical grouted cells spaced at 1830 mm on center, revealed that the shear capacity predicted by the code was 80% higher than the experimental capacity [3]. Nonetheless, the code equation appeared to be adequate for a wall assemblage that had a window opening, wall flanges, and a similarly wide spacing of vertical grouted cells [5]. The influence of different configurations of openings in partially grouted walls has been also investigated [6], but those walls were not subjected to axial load and had a much smaller spacing of grouted cells. All the aforementioned studies involved testing of single walls or wall assemblages under quasi-static, cyclic loading. The system-level response of partially grouted masonry buildings under real earthquake excitation was not studied before.

This paper presents the results and findings obtained from a full-scale, one-story, partially grouted, reinforced masonry building that was tested on the outdoor shake table at the University of California, San Diego. The objectives of the study were to investigate the seismic performance of partially grouted buildings with large spacing of vertical grouted cells and to assess the adequacy of the current design practice and code provisions. The tests have also provided data for the development and calibration of a nonlinear finite-element model that was employed to help interpret and extrapolate the experimental results.

2 Shake-Table Test Structure

2.1 Prototype Structure Configuration

The shake-table test structure was considered to be a part of a larger one-story, prototype building. The prototype building had a larger footprint than the test structure and had columns to carry most of the vertical loads of the roof. The building had partially grouted masonry walls arranged in four modules to resist the lateral seismic forces and also carry part of the gravity loads. The test structure (Fig. 1), represented one wall module of the prototype. In the prototype, the tributary seismic weight for each wall module was 1810 kN. That includes the corresponding tributary seismic weight of the roof and the self-weight of the masonry above the mid-height of the door opening. However, the total tributary gravity load carried by each wall module was only 338 kN, since in the prototype a significant portion of the roof weight was carried by the columns. The test structure was designed for the seismic weight of 1810 kN and for Seismic Design Category C_{max}, which corresponded to the short-period spectral

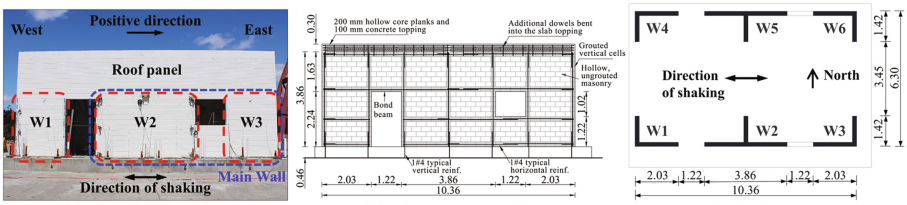

(a) south elevation view (b) reinforcement detail (c) plan view

Fig. 1. Design and configuration of the test structure (dimensions in meters).

acceleration parameter S_{DS} = 0.5 [7]. The partially grouted shear walls were classified as ordinary walls having spacing between the vertical grouted cells larger than 1220 mm. According to ASCE 7, the prescribed seismic response modification factor R = 2, implies that such wall systems are practically not allowed to develop inelastic deformations. The resulting design base shear was equal to 453 kN as calculated with the following equation given in ASCE 7: $V_b = \frac{S_{DS}}{R} W = \frac{0.5}{2} 1810\,\text{kN} = 453\,\text{kN}$.

As shown in Fig. 1, the wall system was symmetric in plan view about the center line in the east-west direction, which was also the direction of the shake-table motion. It had a door opening and a window opening on each of the north and south sides. The wall components separated by the openings are identified as W1, W2, and W3 on the south side, and W4, W5, and W6 on the north side, as shown in the figure. Wall components W2 and W3 along with the masonry below the window will be referred to as the Main Wall, whereas the masonry panel above the openings will be called the Roof Panel as shown in Fig. 1a.

2.2 Design of the Test Structure

The test structure was designed for a base-shear demand of 453 kN. For the given wall configuration, one or more of the piers next to the openings were expected to be shear-dominated. For ordinary walls, shear capacity-design ensuring flexure-dominated behavior is not required. Since a shear-dominated pier was expected to have little deformation capability to retain the plastic strength after reaching the peak shear resistance, the design was conducted with the assumption that the base-shear capacity of the structure would be reached when the shear demand in any of the shear-dominated piers reached its shear strength. The design was assisted with an elastic analysis, which will be described in the following section, based on this premise. The resulting reinforcement details for the test structure are illustrated in Fig. 1b. Both the vertical and horizontal reinforcement had Grade 60 #4 (129 mm^2) bars. The positions of the vertical bars satisfied the prescriptive requirements of the code in that there was vertical reinforcement of at least 129 mm^2 adjacent to the openings and at wall intersections and that the bar spacing did not exceed 3.05 m. Bond beams with horizontal reinforcement were cast in four masonry courses: the first course above the footing (Bond Beam 1), the course below and above the window (Bond Beams 2 and 3 respectively), and the topmost course (Bond Beam 4). The bond beams were extended into the wall flanges ensuring grout and reinforcement continuity at the web-flange intersections.

The roof system consisted of 200-mm-thick precast hollow-core planks with a 100-mm cast-in-place reinforced concrete topping. It was much thicker than that of the prototype to attain the targeted gravity load of 338 kN without the need to include the tributary roof area for the module represented by the test structure. The planks spanned along the north-south direction of the building and they were simply supported by the south and north walls. Eight-inch-wide hollow concrete masonry units were used and laid in a running bond pattern with face-shell mortar bedding. The resulted seismic weight of the test structure was 543 kN. That includes the self-weight of the roof and that of the masonry walls spanning above the mid-height of the piers. Complete drawings of the design details and the instrumentation plan can be found in [8].

2.3 Supporting Analysis

The reinforcement details were verified by analysis. Because of the symmetry of the structure, only the wall on the one side was considered. For the convenience of the discussion, this wall will be referred to as the South Wall. A linearly elastic plane-frame model was employed to calculate the seismic force demand in each of the wall components, W1, W2, and W3. In the model, the roof panel was treated as a very stiff beam and the portion of W3 below the window opening was assumed to be rigid. No horizontal reinforcement was considered in the calculation of the shear capacity of W3, whereas the reinforcement of Bond Beams 1 and 2 was accounted for in W1 and W2. For the design, the compressive prism strength of the ungrouted masonry was specified to be 12.6 MPa. Table 1 shows: the seismic load demands on the piers when the lateral load reached the design base shear of 453 kN, the load capacities of the piers calculated according to the code prescribed methods, and the corresponding capacity-to-demand ratios. It can be seen that all three piers were shear-dominated. The pier in W3 had a capacity-to-demand ratio barely greater than 1.0 whereas the other two piers had much higher ratios. Hence, W3 controlled the design. However, the actual base-shear capacity of the wall system could be higher because the piers might be able to develop some limited ductility so that the drop of the shear resistance after reaching shear strength would not be as rapid.

Table 1. Load demands on and load capacities of the wall piers in the negative and positive (west and east) directions.

Wall	Axial load (kN) neg./pos.	Seismic shear demand (kN) neg./pos.	Flexural capacity (kN) neg./pos.	Shear capacity (kips) neg./pos.	Capacity-to-demand ratio neg./pos.
W1	118.8/12.9	38.3/38.3	181.5/132.6	154.8/130.3	4.1/3.4
W2	90.3/56.6	82.7/83.2	453.3/408.8	242.4/239.8	2.9/2.9
W3	−0.9/135.7	105.4/104.5	274.0/422.6	112.5/113.9	1.1/1.3

3 Ground Motions and Scaling

The test structure was subjected to a sequence of 17 earthquake motions, which were historical records scaled to different intensity levels. The north-south component of the El Centro record from the 1940 Imperial Valley Earthquake (EC1940) was used in most of the tests. In addition, records obtained from earthquakes outside the West Coast were used, but they did not induce noticeable damage on the structure. After each earthquake motion, the structure was subjected to a white-noise excitation, which had a root-mean-square amplitude of 0.05 g, to identify any change in the natural period. The first white-noise test conducted before any earthquake test, identified a fundamental period of 0.043 s.

Since the actual seismic weight of the test structure was *Wspec* = 543 kN, while the design seismic weight was W = 1810 kN based on the prototype configuration, the seismic acceleration had to be scaled up by a factor of $S_{SA} = W/W_{spec} = 3.33$ and the time had to be compressed by a factor of $S_T = \sqrt{1/S_{SA}} = 0.55$ to satisfy the dynamic similitude with the prototype. This scaling was applied to the ground motion records. Figure 2 shows the acceleration time history and response spectrum of the strongest applied motion (Motion 17) and also the response spectrum of a motion (Motion 8) that had the intensity of a design-level earthquake (DE). The design spectra specified by the code are also included. The shake table was tuned with ground motions scaled to the DE with the procedure described in [9]. However, as the intensity of the motions increased, the table did not track the input motion closely, and the response spectra of the table motion showed a significant amplification in the frequency range of 10–20 Hz, which was around the oil column resonance frequency of the shale table. To quantify the intensity of the table motions in a meaningful manner, the ratio of the spectral acceleration of the motion to that of the Maximum Considered Earthquake (MCE) is used as an effective intensity measure (I_{eff}). The spectral acceleration is calculated as the average over the range of the structural period measured before and after the structure was subjected to the ground motion [10]. The MCE is defined as 1.5 times the DE.

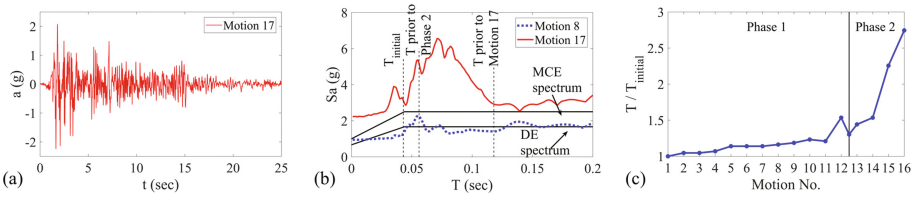

Fig. 2. (a) Acceleration time history (EC1940) of Motion 17 (recorded from table); (b) Acceleration response spectra; (c) Ratio of the structural period measured after each motion over the initial period.

4 Performance of the Test Structure

4.1 Global Response

The structure was tested in two phases. In the first phase, the structure was subjected to 12 motions, which had effective intensities I_{eff} ranging from 0.36 to 1.91. In this phase, the structure developed sliding at the base when the effective intensity of the applied motion reached the MCE level (i.e., when I_{eff} was around 1.0). The sliding measured at the base of the Main Walls was consistently larger than that of W1 and W4, reaching 6.2 mm during Motion 12. As a result, despite the high intensity of the motions, only minor damage was observed along the height of the Main Walls, whereas W1 and W4 had some fine diagonal cracks. In Phase 2, the sliding of the structure was restrained by casting concrete stoppers at the toes of the Main Walls and then Motions 13–17 were applied. Table 2 summarizes peak response quantities during Motions 11–17 as well as the effective intensities of the motions. The ground motions were derived from the 1940 El Centro record (EC1940). The percentage in the Test ID indicates the scaling applied to the original EC1940 record before the similitude scaling, whereas the letters correspond to different test trials conducted using the same excitation. In the calculation of the roof drift ratio, the sliding at the base of the Main Walls was subtracted from the roof displacement. Further details on the response of the test structure in Phase 1 can be found in [11]. The extent of damage after each motion is also indicated by the elongation of the fundamental period of the structure as shown in Fig. 2c. As shown, the structural period changed slightly during the Phase-1 tests, but it increased significantly during the motions of Phase 2. The decrease of the structural period at the beginning of Phase 2 was due to repairs conducted locally at the toes of the Main Walls.

Table 2. Summary of structural response during the shake-table tests.

Motion no.	Test ID	Phase	Structural period after test (sec)	Effective intensity (x MCE)	Peak roof disp. (mm)	Peak base sliding (mm) at W1/South Main Wall	Peak roof drift ratio (%)	Peak base shear (kN)
11	125%-C	1	0.052	1.46	4.1	1.3/2.3	0.05	974
12	164%-A		0.066	1.91	7.1	1.5/6.2	0.06	1054
13	125%-D	2	0.062	1.52	4.3	2.1/2.0	0.06	1076
14	164%-B		0.066	2.04	5.6	2.6/2.0	0.10	1174
15	188%-B		0.097	2.07	6.6	3.4/2.0	0.12	1205
16	202%		0.118	1.43	8.9	4.1/1.8	0.18	1232
17	214%		n.a.	1.17	87.4	7.0/1.7	2.25	1201

The structure exhibited a satisfactory load capacity and was able to resist two motions (Motions 14 and 15) with effective intensities twice the MCE level. It developed its maximum resistance, namely 1232 kN, during Motion 16 which mainly caused cracking along the mortar joints in the ungrouted panels as illustrated in Fig. 5a. However, during the final motion, the shear cracks propagated through the vertical grouted cells causing rapid load degradation before the structure reached 0.5% story

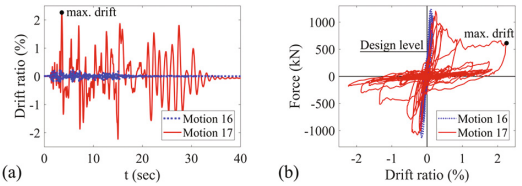

Fig. 3. Structural response during Motions 16 and 17: (a) roof drift ratio time history; (b) base shear-vs-roof drift ratio.

drift. During Motion 17, a maximum drift of 2.25% was reached, and was accompanied by the crushing and detachment of ungrouted masonry units. By the end of the motion, the weight of the roof was supported only by the wall flanges. The time histories of the roof drift ratio and the hysteresis loops obtained during Motions 16 and 17 are shown in Fig. 3. The state of the structure at the end of Motion 16, at the peak drift of Motion 17, and after Motion 17 is show in Fig. 4.

Fig. 4. State of structure prior to Motion 17 (southeast wall inside view), at peak drift of Motion 17, and after Motion 17.

4.2 Yielding of Reinforcement

The sequence of yielding of the reinforcing bars as detected by the strain gages is illustrated in Fig. 5b. For brevity, only the South Wall is shown since a similar yielding sequence occurred in the North Wall. The motion during which each strain gage registered yielding for the first time is indicated. Gages that did not record yielding as well as the faulty ones are also indicated. For conciseness, the sequence of yielding during different motions in the Phase-1 tests and during Motions 13 through 16 is not identified. During the Phase-1 tests, the vertical bars yielded along the base of the wall due to tension induced by base sliding. In the Phase-2 tests, most of the yielding occurred in Motion 17. However, yielding in the Bond Beam 2 of W2 and W3 was initially registered in Motion 16. The strains recorded during Motions 16 and 17 in Bond Beam 2 of W2 (Gage H1) and W3 (Gage H2) are plotted against the roof drift ratio in Fig. 6. It can be seen that the strains developed in Motion 16 barely exceeded the yield strain. However, during Motion 17 the strains in the bond beam of W3 increased dramatically up to the point the structure reached 0.5% drift. Beyond that drift level, the deformation of W3 localized in the masonry panel above Bond Beam 2. Figure 6 also shows the strains in the two vertical bars of W6 (GagesV1 and V2) right

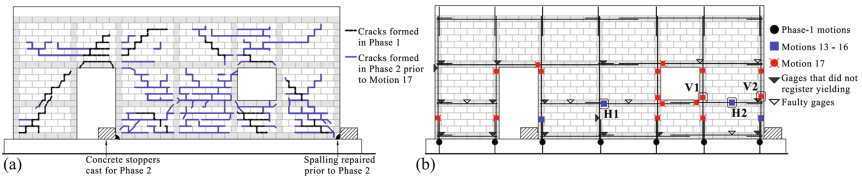

Fig. 5. (a) Crack pattern prior to Motion 17; (b) Yielding of reinforcement.

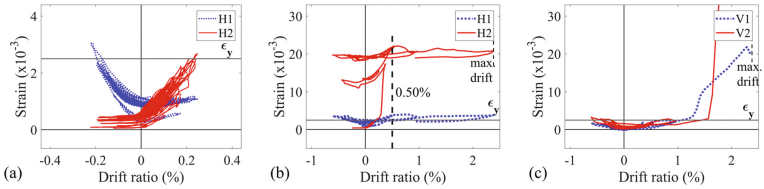

Fig. 6. Response of selected strain gages: (a) strains in Bond Beam 2 of W2 (Gage H1) and W3 (Gage H2) during Motion 16 and (b) during Motion 17; (c) strains recorded by Gages V1 and V2 in the vertical bars of W6 during Motion 17.

below the window opening in Motion 17. It can be seen that the vertical bars developed yielding after the failure of the vertical grouted cells occurred.

4.3 Distribution of Lateral Load Resistance

The design of the structure was proven to be conservative. Although the structure was designed for a base shear of 453 kN, it developed a maximum lateral resistance of 2.7 times that value. To investigate the source of this over strength, the shear strengths of the wall piers were calculated again using the MSJC shear strength formula and the actual material properties obtained from material sample tests. The compressive strength of masonry was 14 MPa based on prism tests and the yield strength of the reinforcing steel was 480 MPa. For the calculation, the wall piers were assumed to have fixed-fixed boundary conditions and they were subjected to gravity loads only. First, the height of the piers in W1/W4 and W2/W5 was assumed to be the same as the height of the door opening, and that of the piers in W3/W6 was the same as that of the window opening, as assumed in the elastic plane-frame model that was used for the design. Adding the shear strengths of all the piers resulted in a total base-shear capacity of 1379 kN. Similar total base-shear capacity, namely 1330 kN, was obtained when the height of W2/W5 was assumed to be the height of the window opening instead. These values are a little higher than the actual base-shear capacity of 1232 kN developed by the test structure. This could be attributed to the fact that the maximum shear strengths of the piers might not necessarily develop at the same time because of the disparity in the stiffness of the piers. Furthermore, the shear strength formula in the code might not be accurate for partially grouted walls. It should be mentioned that the total base-shear capacity calculated is not affected by the axial loads induced in the piers by the lateral

seismic forces as long as the total axial load on all the piers remains constant. To have a better understanding of the lateral load distribution in the piers, a nonlinear finite element analysis was conducted as presented in the following section.

5 Numerical Modeling

5.1 Modeling Scheme

To quantify the contribution of each wall pier to the base-shear capacity of the system and to assess the accuracy of the MSJC shear strength formula, a detailed finite-element model of the shake-table test structure was developed. The structure was modeled in three dimensions using a combination of smeared-crack shell elements and zero-thickness cohesive crack interface elements. A similar approach has been used for the modeling of reinforced concrete infilled plane frames [12, 13]. The grouted part is modeled with the discretization scheme shown in Fig. 7a, with each half masonry unit represented by 4 triangular smeared-crack shell elements and interface elements that simulate in a discrete fashion horizontal, vertical, or 45-degree cracks through the grouted masonry. The reinforcing bars are modeled with truss elements that have common nodes with the triangular shell elements. To allow for all the triangular elements to be connected to a reinforcing bar, each bar was equally divided into four truss elements. For the ungrouted part, each masonry unit was modeled with two quadrilateral smeared-crack shell elements which were connected through a vertical interface element to simulate possible splitting cracks in the units (Fig. 7b). The mortar joints were also modeled with interface elements as well. All the elements for the ungrouted panels were assigned a uniform thickness of 63.5 mm, which was equal to the total thickness of the two face shells of the units, whereas the elements for the grouted masonry had a thickness of 194 mm, which was the gross width of a masonry unit.

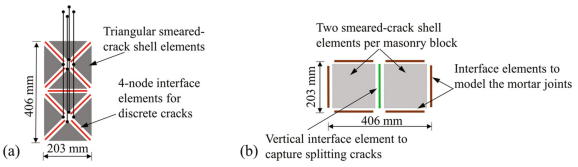

Fig. 7. Finite-element modeling scheme for: (a) the grouted masonry, (b) and the ungrouted masonry.

For the analysis, the finite-element software LS-DYNA was used. The smeared-crack material model used for the shell elements was Concrete EC2 [14], which is a concrete model but can be also used to accurately simulate the behavior of masonry such as crushing as well as crack opening and closing under cyclic loading. Although the material model does not account for the effect of the lateral stress on the compressive strength of the material, it was deemed adequate for the analysis of masonry walls, which normally do not have reinforcement for confinement. For the interface elements, the cohesive crack

material law that has been developed by [15] and extended by [16] for three-dimensional analyses was used. The model can simulate mixed-mode fracture, crack opening and closing, reversible shear dilatation, and joint compaction. The constitutive law has been implemented in LS-DYNA by the first author as a user-defined material model. For the truss elements representing the steel reinforcement, a bilinear material law with kinematic hardening was used. In addition, the dowel action of the reinforcing bars crossing a crack, was accounted for in a simplistic way by introducing a uniaxial dowel resistance – shear displacement law within the corresponding interface elements.

5.2 Model Validation

Because of the symmetry of the structure and loading, only the south half of the structure was modeled with appropriate boundary conditions. The wall along the loading direction (in-plane wall) was discretized with the scheme described above, while the walls orthogonal to the loading direction (out-of-plane walls) were modeled with less refinement with only horizontal interface elements. Nonetheless, vertical interface elements were used to connect the out-of-plane walls with the in-plane wall. The roof seismic mass was distributed over the area of roof, but the gravity load was applied as nodal forces only among the nodes of the in-plane wall, at the roof level, since the roof planks were supported only by the in-plane walls. The time-history analysis was performed using the Hilber-Hughes-Taylor time-intergration scheme [17]. This scheme has a desirable numerical damping characteristic to suppress spurious high-frequency modes, which could be generated by the sudden cracking of masonry. No other damping was specified. Prior to the time-history analysis, an eigenvalue analysis was performed revealing a 1st-mode period of 0.042 s, which was close to that identified in the first white-noise test of the structure.

Only the response in the Phase-2 tests was investigated with the finite-element model. It was assumed that the structure did not sustain any damage in Phase 1 during which the response was dominated by base sliding. Instead of explicitly modeling the sliding stoppers introduced in Phase 2, the interface connecting the walls to the footing was assigned a very high friction coefficient. The analysis started with Motion 14, since no major damage was observed before that motion. The roof displacement time history and the base shear-vs- roof displacement hysteresis curves obtained with Motion 14 are compared to the experimental results in Fig. 8. The deformed mesh at the instance of the peak roof drift is also shown. The base shear was calculated at the level of the bottom of the window opening by summing the shear forces developed in the horizontal interfaces. That was consistent with the method used to calculate the base shear with the experimental data in that only the seismic mass above that line was considered. It can be seen that the agreement between the numerical and experimental results is good. As expected, the numerical model has a stiffer response during the initial cycles of the motion since the actual test structure had suffered some damage in the previous motions. Furthermore, a portion of the roof displacement measured in the test was due to base sliding (see Table 2), which was not allowed to occur in the numerical model. Subtracting the base sliding component from the total displacement of the test structure results in a maximum story drift of 0.095%, while the drift from the finite element analysis was higher and equal to 0.166%. As shown in Table 2, the test structure

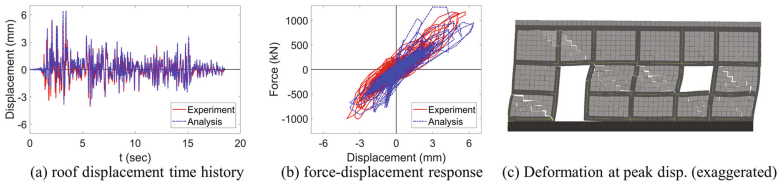

(a) roof displacement time history (b) force-displacement response (c) Deformation at peak disp. (exaggerated)

Fig. 8. Comparison of numerical and experimental results for Motion 14 and deformed mesh.

developed a drift ratio of 0.18% during Motion 16, indicating that the damage obtained in the analysis with Motion 14 was likely close to the damage observed during the test with Motion 16. Thus, in the numerical simulation, Motions 15 and 16 were omitted, and Motion 14 was immediately followed by Motion 17. The numerical and experimental results obtained for Motion 17 are compared in Fig. 9. The numerical model predicted the displacement response well for the first 10 s, but it under predicted the actual response afterwards, probably because the model did not account for the detachment of masonry blocks after severe cracking developed.

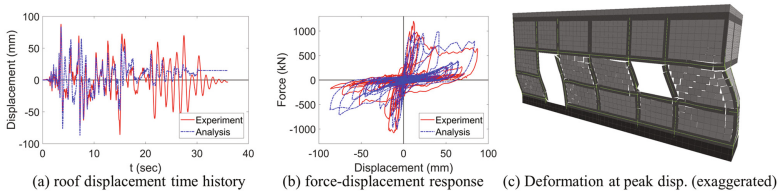

(a) roof displacement time history (b) force-displacement response (c) Deformation at peak disp. (exaggerated)

Fig. 9. Comparison of numerical and experimental results for Motion 17 and deformed mesh.

5.3 Response of Wall Piers

In the analysis, the structure reached its maximum lateral load capacity in the positive direction during Motion 14 and that in the negative direction during Motion 17. The maximum resistance of 1272 kN developed in the positive direction is only 3% larger than the experimental value, while the maximum resistance of 997 kN developed in the negative direction is 13% less than the experimental value. Figure 10 shows the shear force-vs-roof displacement curves obtained from the analyses for the three wall piers. The maximum resistance developed in each pier and the corresponding roof displacement (δ_{roof}) are summarized in Table 3 for the positive and negative directions of displacements. The results show the influence of the axial forces introduced into the piers by the horizontal seismic forces. Each pier developed a higher shear resistance in the direction in which it was subjected to a higher axial compressive force. However, the shear resistance developed by piers W2/W5 was much higher in one direction than the other. This contradicts the fact that those piers were near the middle of the walls and were therefore subjected to less variation in their axial forces. The much lower resistance in the negative direction could be caused by the damage induced in Motion 14 during which the structure experienced larger positive displacements.

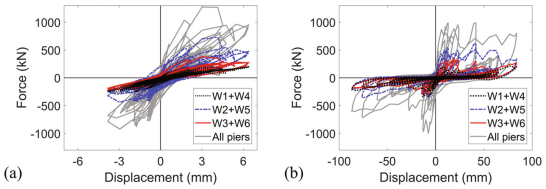

Fig. 10. Shear force-vs- roof displacement curves for the wall piers during: (a) Motion 14; (b) Motion 17.

The shear force developed in each wall pier at the time instance at which the base-shear capacity of the structure was reached is also shown in Table 3. It can be seen that the shear force developed in each pier was about 90 to 100% of the maximum shear strength of the pier. The only exception is the shear forces developed in the negative direction by piers W2/W5. Those piers suffered significant load degradation in the negative direction due to damage. Adding the maximum shear strengths of all the piers in the positive direction would result in a base-shear capacity of 1321 kN, which is close to that computed with the code formula. This analysis shows that the code formula is sufficiently accurate. However for a safe design, the base-shear capacity of the structure cannot be calculated as a simple sum of the shear strengths of the contributing piers because of the disparity in the stiffness and the brittle behavior of the piers.

Table 3. Summary of the maximum shear strengths developed in the wall piers in the analysis.

Piers	Max. shear (kN) pos./neg.	δ_{roof} (mm) at max. shear pos./neg.	Shear at base-shear capacity of the structure (kN) pos./neg.
W1 + W4	208/344	0.25/0.52	192/339
W2 + W5	730/441	0.16/0.12	700/360
W3 + W6	381/320	0.12/0.50	381/298
All Piers	1273/997	0.12/0.30	1273/997

6 Conclusions

This paper presents a study on the system-level response of a partially grouted reinforced masonry structure under earthquake loading. The structure had a single-story, and was designed for Seismic Design Category C_{max} as an ordinary wall system based on the 2013 MSJC provisions. It had widely-spaced vertical grouted cells and bond beams as it is commonly done in practice. In the Phase-1 tests, the structural response was dominated by base sliding. After sliding was restrained in Phase 2, the structural walls developed the ultimate load capacity showing cracking along the mortar joints and limited yielding in the bond beams. Under high intensity motions, the bond beam below the window opening was subjected to significant tension and helped to improve the resistance of the structure during the post-peak response. The structure exhibited a

sufficiently high lateral load capacity and was able to withstand repeated motions of intensities greater than the MCE. However, the structure failed in a brittle manner as soon as the vertical grouted cells above Bond Beam 2 failed in shear at 0.5% roof drift ratio. Determining the design base-shear capacity of the structure using an elastic analysis, as discussed here, was proven to be conservative. To investigate the contribution of the masonry piers in the walls to the base-shear capacity, a finite-element analysis was conducted. The analysis shown that the code formula for the shear strength is sufficiently accurate for the structure tested. However, the base-shear capacity of the structure cannot be calculated as a simple sum of the shear strengths of the contributing piers because of the disparity in the stiffness and the brittle behavior of the piers.

References

1. Masonry Standards Joint Committee: Building code requirements and specification for masonry structures. TMS 402-13, ACI 530-13, ASCE 5-13 (2013)
2. Minaie, E., Mota, M., Moon, F.L., Hamid, A.A.: In-plane behavior of partially grouted reinforced concrete masonry shear walls. J. Struct. Eng. ASCE **136**(9), 1089–1097 (2010)
3. Bolhassani, M.: Improvement of seismic performance of ordinary reinforced partially grouted concrete masonry shear walls. Ph.D. thesis, Department of Civil Engineering, Drexel University, Philadelphia, PA (2015)
4. Nolph, S.M., ElGawady, M.A.: Static cyclic response of partially grouted masonry shear walls. J. Struct. Eng. ASCE **138**(7), 864–879 (2012)
5. Johnson, C.A., Schultz, A.E.: Simulated seismic testing of partially-grouted masonry sub-assemblages. In: 10th U.S. National Conference on Earthquake Engineering, Anchorage, AK (2014)
6. Voon, K.C., Ingham, J.M.: Experimental in-plane strength investigation of reinforced concrete masonry walls with openings. J. Struct. Eng. ASCE **134**(5), 758–768 (2008)
7. ASCE/SEI 7-10. Minimum design loads for buildings and other structures. ASCE, Reston (2010)
8. Koutras, A., Shing, P.B.: Shake-table test of a partially grouted reinforced masonry building with separated single grouted cells. In: Seible, F. (ed.) Network for Earthquake Engineering Simulation, Dataset. University of California, San Diego (2015). doi:10.4231/D3W950P43
9. Luco, J.E., Ozcelik, O., Conte, J.P.: Acceleration tracking performance of the UCSD-NEES shake table. J. Struct. Eng. ASCE **136**(5), 481–490 (2010)
10. Stavridis, A., Koutromanos, I., Shing, P.B.: Shake-table testing of a three-story reinforced concrete frame with masonry infill walls. Earthq. Eng. Struct. Dyn. **41**, 1089–1108 (2011)
11. Koutras, A., Shing, P.B.: Shake-table tests of partially grouted reinforced masonry buildings. In: 12th North American Masonry Conference, Denver, CO (2015)
12. Stavridis, A., Shing, P.B.: Finite-element modeling of nonlinear behavior of masonry-infilled RC frames. J. Struct. Eng. ASCE **136**(3), 285–296 (2010)
13. Koutromanos, I., Stavridis, A., Shing, P.B., Willam, K.: Numerical modeling of masonry-infilled RC frames subjected to seismic loads. Comput. Struct. **89**(2011), 1026–1037 (2011)
14. LSTC. LS-DYNA Keyword User's Manual. Livermore Software Technology Corporation, Livermore, CA (2015)

15. Koutromanos, I., Shing, P.B.: Cohesive crack model to simulate cyclic response of concrete and masonry structures. ACI Struct. J. **109**(3), 349–358 (2012)
16. Kottari, A.: Horizontal load resisting mechanisms of external shear keys in bridge abutments. Ph.D. thesis, Department of Structural Engineering, University of California, San Diego, La Jolla, CA (2016)
17. Hilber, H.M., Hughes, T.J.R., Taylor, R.L.: Improved numerical dissipation for time integration algorithms in structural dynamics. Earthq. Eng. Struct. Dyn. **5**, 283–292 (1977)

Vibration Isolation and Control

Vortex-Induced Vibration of Stay Cables, Verification on the Footbridge

Shota Urushadze(✉) and Miroš Pirner

Institute of Theoretical and Applied Mechanics AS CR,
v. v. i, Prague, Czech Republic
urushadze@itam.cas.cz

Abstract. Long-span footbridges rank among engineering structures with a high social significance. Their architecture design must in general satisfy matters such as attractive look, reliability and light. These requirements predestinate the bridge to be sensitive to the wind effects and the assessment against the wind becomes crucial. One of the several wind phenomena occurring on such a type of structures is termed as the vortex shedding. This flow induced excitation lying in a periodic vortices separation may arise at low wind velocity on both the main parts of a bridge structure including bridge girder with pylons and additional members such as stay cables, hand railing, etc. According to the character and intensity of the excitations, the adequate treatment to reduce or avoid the oscillations should be given. It is also performed when the vortex induced oscillations do not influence the reliability of a footbridge, but the look at the amplitudes could start panic and could start vandal's action – increasing the amplitudes.

Keywords: Footbridge · Vortex-induced oscillations · Kármán vortex street · Vortex effect remedy

1 Introduction

The paper deals with vortex-induced oscillations of footbridge stay cables at a very low wind speed. The two-spans (2 × 50 m) reinforced concrete structure with the central pylon (25 m height) is designed as the harp system of stay cables with circular cross-section (see Fig. 1).

The stay cables consist of 3 ropes (∅ = 3 × 140 mm^2) which are covered by very smooth plastic tube (∅ 54 mm). The oscillations were observed at a wind speed around 2 m/s and the measured double amplitudes at loops exceeded 5 mm. The wind excited deformation shape corresponded to the 6th, 7th and 8th natural modes of a cables. The individual cables as well as their group were analysed to estimate the dynamic response, possible aeroelastic vibration and special interference or coupling effects. It also includes proposal for the elimination of the extensive vibration.

The suspended three-section bridge with the almost straight deck (see Fig. 2). The bearing structure consists of pre-fabricated sections of sufficiently pre-stressed concrete; in the first two sections, a two-beam profile is suspended on an "A"-shaped steel pylon.

© Springer International Publishing AG 2018
J.P. Conte et al. (eds.), *Experimental Vibration Analysis for Civil Structures*,
Lecture Notes in Civil Engineering 5, https://doi.org/10.1007/978-3-319-67443-8_42

Fig. 1. View of the footbridge

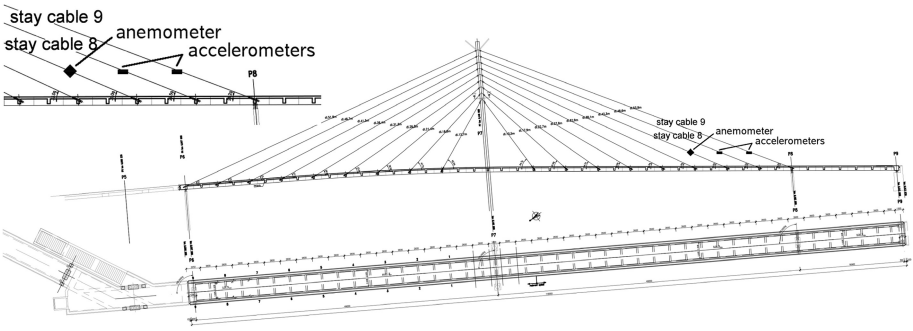

Fig. 2. Side and plan view of the footbridge

The distance between the axes of the 800 mm high beams is 3.3 m. The bearing structure is 3.9 m wide (see Fig. 3) The pre-fabricated section material is concrete [5].

The supports are V-shaped, made of steel tubes and are founded on the drilled piles. The supporting structure rest upon the roller bearings. The bearing structure is hanging on pairs of stay cables formed by three cables. The stay cables are strained up to 45 pct of their strength at maximum and 10 pct at minimum. Maximum amplitude of tension is 80 MPa at 1200 MPa. The stay cables are semi harp-type, exchangeable and rectifiable.

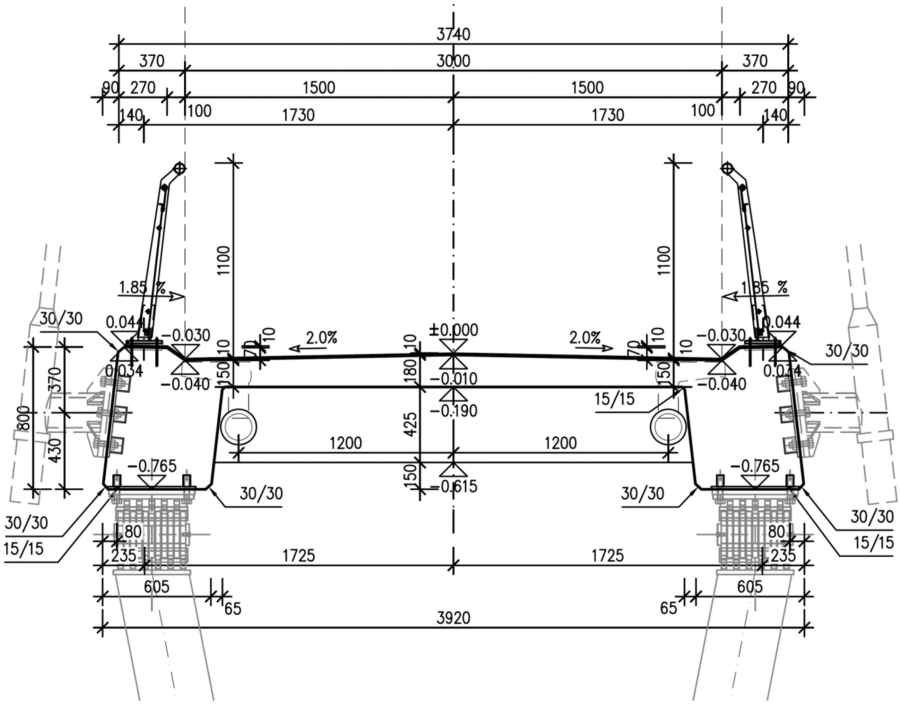

Fig. 3. Cross section of the footbridge

2 Phenomenon Monitoring

The vibrations of the 9th and 8th left stay cables (see Fig. 2) appeared at the relatively low wind speed (up to 3 m/s) when the wind direction was perpendicular to the footbridge axis.

We heard the witnesses, collected their findings and eliminated the subjective and distorted perceptions: vibration amplitudes, Česká zbrojovka (Czech Gun Factory) operations effects, effects of diesel-electric locomotives when shunting.

We stated that the "right" section (Fig. 1) is protected by buildings against winds from both sides; hence, the vibration effect does not appear.

Two pairs of ENDEVCO accelerometers type 86 measured dynamic response of the 9th and 8th cables. The sensor distance from the cables anchorage into the deck, projected onto the horizontal level, was 5 m. Table 1 shows the results of 60 s records for 9th and 8th cables during the wind excitation.

Figure 4 shows frequency analysis corresponding to the measurement recorded during the excessive vibrations (see Table 2), while Fig. 5 shows the time history of acceleration. On Table 2, there are amplitudes (in mm) of vertical and horizontal movements of stay cables in the sensor locations. Vertical means perpendicular to the catenary tangent, in the sensor location.

Table 1. Forced frequency of stay cables [Hz] and expected shapes of vibrations

Excitation	Frequency/natural mode 9th stay cable	Frequency/natural mode 9th stay cable	Frequency/natural mode 8th stay cable	Frequency/natural mode 8th stay cable
	Vertical	Horizontal	Vertical	Horizontal
Wind	12.8/6	10.01/5; 12.08/6; 14.10/7	9.70/4; 12.26/5; 17.29/7	9.68/4; 10.13/4; 12.19/5; 17.29/7
Wind	12.08/6; 16.26/8	10.01/5; 12.08/6; 16.26/8	9.70/4; 12.30/5; 14.80/6; 17.29/7	9.70/4; 12.30/5; 14.80/6; 17.29/7

Note: Vertical means perpendicular to the catenary tangent, in the location where the sensor is attached. Left and right side – see Fig. 1.

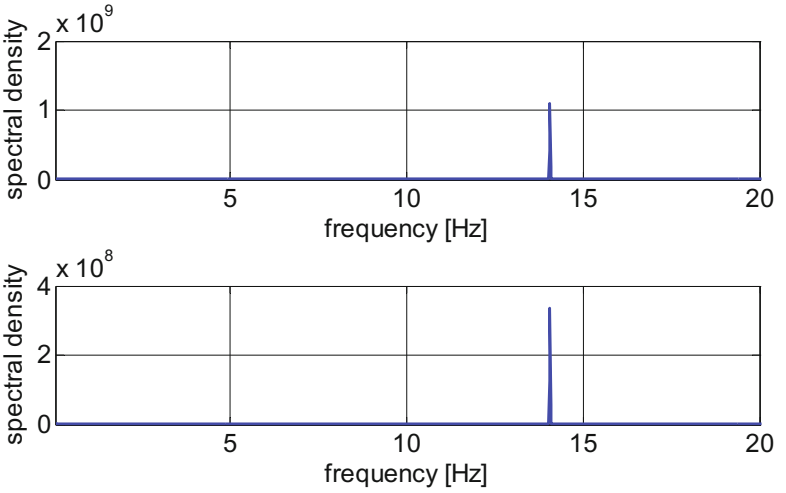

Fig. 4. Power spectral densities in vertical and horizontal directions of 9th stay cables.

Table 2. Amplitudes v [mm] in sensor location for left and right stay cables.

Excitation	9th stay cable		8th stay cable	
	Vertical	Horizontal	Vertical	Horizontal
Wind 1.75 ms^{-1}	$4.6 \cdot 10^{-2}$	$\approx 2.9 \cdot 10^{-2}$	$\approx 2.3 \cdot 10^{-2}$	$\approx 1.7 \cdot 10^{-2}$
Wind 2.2 ms^{-1}	$\approx 7.9 \cdot 10^{-2}$	$\approx 2.5 \cdot 10^{-2}$	$3.2 \cdot 10^{-2}$	$\approx 1.6 \cdot 10^{-2}$
Wind 2.0 ms^{-1}	Left: $1.9 \cdot 10^{-1}$ Right: 1.36	Left: $3.8 \cdot 10^{-2}$ Right: $7.4 \cdot 10^{-1}$	–	–
Wind 1.8 ms^{-1}	Left: $\approx 8.8 \cdot 10^{-2}$ Right: $1.45 \cdot 10^{-1}$	Left: $\approx 3.3 \cdot 10^{-2}$ Right: $6.6 \cdot 10^{-2}$	–	–
Wind 1.75 ms^{-1}	Left: $7.2 \cdot 10^{-2}$ Right: $3.0 \cdot 10^{-1}$	Left: $2.5 \cdot 10^{-2}$ Right: $1.8 \cdot 10^{-1}$	–	–

3 Evaluation

Vibration of stay cables investigated footbridge could be due to:

- wind
- Transfer of technological shocks of the adjacent Czech arms factory
- The transmission of shocks from rail traffic
- Sound pressure of the sounds of diesel - electric locomotives.

From the analysis of response of the 9th and 8th stay cables, footbridge section above the trackage, from the testimony of local citizens and from the video recording it is certain that the excitation is caused by the wind, the direction of which is perpendicular, or close to perpendicular, to the footbridge axis.

3.1 Selected Aeroelastic Effects

It has been concluded, from the analysis of the motion, that excessive vibration is not a wake galloping, since the stay cables distance is too large, ($L > 3$ m, $d = 0.054$ m). This phenomenon would happen when the wind sped exceed 15 m/s. Parameter L is the distance between the cables. Also, the geometric configuration excludes the so-called jet-switch mechanism [2].

We can also exclude the rain rivulets from the analysis, because the above mentioned vibration was observed also in dry conditions and the relation between the frequency of vibration of this type and wind speed is dramatically different from the frequency of separated vortices corresponding to the Strouhal effect.

Hence, the effect under examination is caused by a periodical vortices separation behind a smooth cylinder with the circular cross-section. The influence of the surface smoothness is testimonied by the by the fact that for example cable no. 9 vibrated with almost as double amplitude in the vertical direction as that one in the horizontal direction.

This is a typical effect of a periodical vortices shedding. In principle, the frequency of the separation is given by the Strouhal frequency:

$$f_{Sr} = S_r \cdot \frac{\bar{V}}{d} \tag{1}$$

where $\overline{V}$ is the mean value of speed of the wind, the direction of which is perpendicular to the cable axis, d is the cable diameter and 0.28 is Strouhal number S_r, [1] for the given Re number and intensity of turbulence. No higher frequencies have been considered for $S_r = 0.4, 0.6$.

Note: Reynolds numbers, characterising the circumfluence mode, are:

$$\mathrm{Re}_{12,08} \doteq 0,13 \cdot 10^5, \quad \mathrm{Re}_{14,10} \doteq 0,14 \cdot 10^5, \quad \mathrm{Re}_{16,26} \doteq 0,16 \cdot 10^5.$$

where lower subscript shows forced frequency.

Hence, this mode is called “critical”; some authors call it “transitional” [3, 4]. For this mode, the specified Reynolds numbers and turbulence intensity was

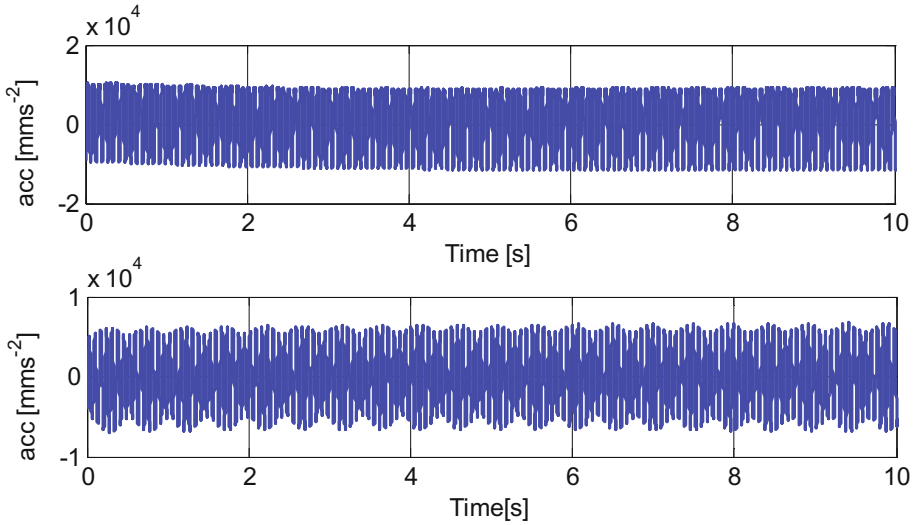

Fig. 5. Time history of the displacement of hanger 9 in the vertical and the horizontal directions.

$I_m = 9.1\%$ and $S_r = 0.28$. The 9th stay cable vibrated perpendicular to the wind direction with frequencies (see Table 1): 12.08; 14.10; 16.26 Hz.

Mean wind speeds correspond to those frequencies.

$$\bar{V}_{12.08} = 2.31 \text{ m/s}, \bar{V}_{14.10} = 2.72 \text{ m/s}, \bar{V}_{16.26} = 3.13 \text{ m/s}.$$

4 REMEDY

Stay cables 9 and 8 in the footbridge section above the bridge deck vibrate with higher shapes and clearly visible amplitudes under the load of the wind as slow as 1.75 to 2 m/s, if its direction is perpendicular to the footbridge axis.

Vibrations of the cables under the wind load are results from the periodical separation of vortices behind the stay cables with circular cross-section (Strouhal vibrations, Kármán vortex path). Theoretical calculation has indicated that:

Vibrations of the cables caused by wind load on the deck can be neglected.
The main cause of the unacceptable effect is the smoothness of the PE pipe surface affecting the flow regime.
The vibrations of the 9th and 8th stay cables caused by wind do not pose a threat to the footbridge structure (or cables, deck or pylon), so it would be possible to keep it in the original state.

However, the motion of the cables could lead to the discomfort or fear of some pedestrians and, in the case of a larger amount of people on the footbridge, even panic.

Therefore it is necessary to reduce the vibrations to the indistinctive level, or eliminate them.

In this case, there are three possibilities:

- To equip the 9th and 8th stay cables with Stockbridge dampers [4], the dampers there are doubled; (in our case single ones will do).
- Interlocking, by means of an additional cables, the 9th and 8th, perhaps also the 7th, stay cable and anchor them into an anchorage "block".
- Changing the flow regime by coarsening the stay cables surface through covering with (sticking) grains with diameter up to 5 mm onto the upper half of the circular cross-section.

The first possibility affects negatively the footbridge architecture. Despite that, the necessary masses of the dampers for the 9th stay cables are as follows: Total mass of 3 cables is 171.27 kg. The recommended ballast mass is 1/10 to 1/20 of the total cable mass, i.e., in the more efficient case, $m_{abs,tot} \doteq \sim 17$ kg.

The 9th stay cable vibrates in the 6th, 7th and 8th shape when subjected to the wind. The number of the vibration mode is identical with the number of antinodes and hence with the number of Stockbridge dampers.

The ballast mass, providing they are made of steel, would not exceed the stay cables diameter in order to maintain the visual aspects of the footbridge.

5 Conclusions

In this paper, unacceptable vibrations of the supporting stay cables are measured and investigated with respect to the pedestrian comfort. The examination includes a frequency analysis of the concerned stay cables with a determination of the origin of unstable behaviour.

From the records of the dynamic response of the cable No. 9 (Fig. 5), caused by vortex shedding, it was found that the tension in the cable reaches insignificant value. Only suggestive feelings diminish the comfort of pedestrians. The investor did not realised any of the methods, that are presented in section "REMEDY" of this paper.

Acknowledgments. The supports of grants GA CR 17-26353J are gratefully acknowledged. Identification code of research project of the Institute of Theoretical and Applied mechanics is AVOZ 6838297.

References

1. Anagnostopoulos, P.: Flow Induced Vibrations in Engineering Practice. WIT Press, Southampton (2002)
2. Dye, R.C.F.: Flow-induced vibration and noise with particular reference to heat exchanger tube systems. In: Proceedings of the Institution of Mechanical Engineers, Conference Proceedings, vol. 180, pp. 260–267, June 1965

3. Pirner, M.: Aeroelasticity of cylinder loaded by air stream, study, pp. 15–90. ČSAV (1990). (in Czech)
4. Pirner, M., Fischer, O.: Wind loads of buildings, Prague. ČKAIT (2003). (in Czech). ISBN: 80-86769-10-0
5. Static and dynamic design, SO 202 – Hanging footbridge. Stráský, Hustý and partners: Load Bearing Structure (2009). (in Czech)

Vertical Vibration Mitigation of a Bridge Cable Using a Non Smooth Absorber Under Gravity

Mathieu Weiss[1], Bastien Vaurigaud[2(✉)], A. Ture Savadkoohi[3], and C.-H. Lamarque[3]

[1] Service Technique des Remontées Mécaniques et des Transports Guidés, Saint-Martin d'Hères, France
[2] Cerema Sud Ouest, Pôle Sécurité et Durabilité des Ouvrages à Câbles, Bordeaux, France
bastien.vaurigaud@cerema.fr
[3] University of Lyon, ENTPE, LTDS UMR CNRS 5513, Vaulx-en-Velin, France

Abstract. Mainly nonlinear additional light attachments, named Nonlinear Energy Sink (NES), are widely studied for vibration mitigation of structures [1, 2]. Theoretical, numerical studies and finally preparation of design tools for a NES with cubic nonlinearity dedicated to mitigation of horizontal vibrations of a bridge cable have been studied already by the authors, and its efficiency demonstrated experimentally [3]. Nevertheless this cubic nonlinear absorber was unable to control vertical vibration of the cable because of gravity effects. The present study aims at controlling the vertical vibration of the same bridge cable under gravity effects using a different type of nonlinearity for the NES.

The theoretical study focuses on a non-smooth absorber with a free length. The 1st vertical mode of the cable, to be controlled, is coupled to the absorber, resulting in a 2 dof reduced system. Equations are analytically studied through modified complexification of variables and multiple scales expansion [4, 5]. The analytical results are confirmed by performing numerical integration of the 2 dof system.

Finally a prototype non-smooth NES is designed, built and set on the cable. Step released vertical excitations are performed on the cable with and without coupled NES. The efficiency of the non-smooth vertical NES prototype is demonstrated experimentally and quantified from measurements. Further calculations and experiments for periodic excitation are also discussed.

Keywords: Targeted energy transfer · Passive vibration mitigation · Cable bridge · Nonlinear Energy Sink (NES) · Non-smooth

1 Introduction

Nonlinear energy sink (NES) devices can be designed to perform strong vibration mitigation of principal structures thanks to their light mass and pure nonlinear nature [1, 2]. This paper deals with vibration mitigation of cables, which require controlling both of their vertical and horizontal vibrations. The conception, design and experiment

© Springer International Publishing AG 2018
J.P. Conte et al. (eds.), *Experimental Vibration Analysis for Civil Structures*,
Lecture Notes in Civil Engineering 5, https://doi.org/10.1007/978-3-319-67443-8_43

of a purely smooth cubic device dedicated to horizontal vibration control have been already achieved by the authors in [3]. Nevertheless this device was unable to control vertical oscillations of a cable since gravity destroys the pure smooth non linearity of the NES and as a result the targeted energy transfer phenomenon.

This study aims at performing vibration mitigation on vertical vibration of the bridge cable used in [3] using a different conception with a piecewise linear non smooth absorber with a clearance. This non smooth design allows keeping a strong nonlinear behavior of the NES despite the existence of the gravity. The first part focuses on the cable to be controlled and its modal properties, then an analytical analysis is performed using modified complex variables and time multiple scales [4, 5] analysis on a reduced 2 dof model of the overall system, in detail: 1st mode of the cable coupled to the NES. The resulting Slow Invariant Manifold (SIM) describes the underlying dynamic of the system. Physical parameters for an efficient device are determined using the SIM properties showing that the non-smooth design is able to perform efficient vibration energy localization despite the influence of gravity. Then the design is numerically tested for step released excitations. Finally, a NES prototype is built and experiments are performed on the cable mounted in a tensioning bench. Experiments under periodic excitations are also performed on the same device.

2 Description of the Cable

2.1 Physical Properties

The study focuses on a real cable tensioned on a bench. Physical properties of the cable are as it follows:
Length $L \approx 21.8$ m, diameter $D = 0.026$ m, area of steel $A = 0.76D^2/4\Pi = 4.04 \times 10^{-4}$ m^2, inertia $I = A^2/4\Pi = 2.243 \times 10^{-8}$ m^4, elasticity modulus $E = 160\,000$ MPa and linear mass $m_l = 3.35$ kg m^{-1}. The bench has several sensors including accelerometers, laser displacement sensors and a shaker for forced excitation.

2.2 Modal Analysis

Modal analysis [3] has been performed with hammer excitation and tension in the cable varying between 50 and 200 kN (which means span between ends varying between 21.67 and 21.72 m). The 9th first horizontal and vertical modes in terms of frequencies have been investigated for each tension. Experimentally identified frequencies have been compared with those obtained by theoretical results from an Irvine cable model [6]. The model has been fitted by reducing linear mass by 0.1 kg. Using modified mass $m_l = 3.25$ kg m^{-1} the error is under 3% for all modes for a tension in the vicinity of 100 kN. Damping of the first mode has been also evaluated during these experiments.

3 Dynamics of the System

3.1 General Equations

The design aims at controlling the first vertical mode of the cable. To simplify the equation and to perform the analytical study we work in the modal domain. To design the NES, we first reduce the behaviour of the cable to its first vertical mode, i.e. the mode to be controlled. After modal decomposition, the equation of motion of the first vertical mode of the cable without NES can be written as it follows in Eq. (1):

$$M\frac{d^2\bar{X}}{dt^2} + 2M\omega\xi\frac{d\bar{X}}{dt} + K\bar{X} = 0 \tag{1}$$

where $\bar{X}$ is the vertical displacement around the static equilibrium under gravity at the mid span of the cable. For design process reasons this displacement is reduced to its first mode, the mode to be controlled by the NES. The displacement at the mid span is specifically interesting as it is maximum during first mode, which means that if the NES is coupled to the cable at this point it will receive the maximum energy of the 1st vertical mode. *M, K,* ω and ξ are classical modal and damping parameters with M = 35.24 kg, K = 22807 N m^{-1}, $\xi = 10^{-3}$ and $\omega = \sqrt{\frac{K}{M}}$. These parameters are based on the Irvine model fitted from the experimental modal analysis for the cable under tension as T = 100 kN, which gives a frequency of 4.05 Hz for the first vertical mode.

Then the cable is coupled with a piecewise linear NES of mass m, damping ξ_1 and restoring force $C_1F(\ldots, A_1)$. The scheme of the 2 dof coupled system is represented Fig. 1. The nonlinear coupling function is made up of a piecewise linear behavior associated with the clearance $2A_1$ and a linear restoring force, this function F is multiplied by scalar C_1 standing for the rigidity. Function $F(\ldots, A_1)$ is represented Fig. 2. The dimensionless equations of the 2 dof system can be written as it follows:

$$\begin{aligned} \ddot{x} + \varepsilon\lambda\dot{x} + x + \varepsilon\lambda_1(\dot{x}-\dot{y}) + \varepsilon c_1 F(x-y, a_1) &= \varepsilon f sin(\omega\tau) \\ \varepsilon\ddot{y} - \varepsilon\lambda_1(\dot{x}-\dot{y}) - \varepsilon c_1 F(x-y, a_1) - \varepsilon p_m &= 0 \end{aligned} \tag{2}$$

where derivative $\dot{x}$ is associated to dimensionless time $\tau = \omega t$ such as $\dot{x} = \frac{dx}{d\tau}$. Small parameter ε is such as $\varepsilon = \frac{m}{M} \ll 1$ and p_m is the effects of gravity on the system. Displacements are also dimensionless with $x = \frac{\bar{X}}{X_{dim}}$ and $y = \frac{Y}{X_{dim}}$.

f is the amplitude of the force in the case of an external excitation, for step release tests $f = 0$. Following change of variable are introduced: $\varepsilon\lambda = 2\xi$, $\varepsilon\lambda_1 = 2\xi_1$, and $\varepsilon c_1 F(x-y, a_1) = \frac{C_1}{KX_{dim}} F(\bar{X} - Y, A_1)$. Then we obtain:

$$\begin{aligned} C_1 &= \varepsilon K c_1 \\ A_1 &= X_{dim} a_1 \end{aligned} \tag{3}$$

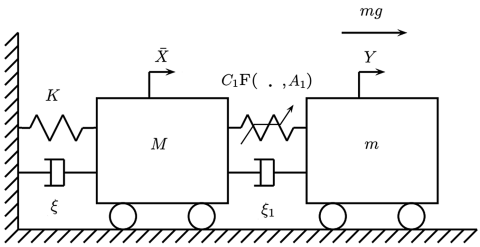

Fig. 1. Scheme of the 2-dof system, 1st cable mode coupled with a piecewise linear NES of rigidity C_1 and free-length A_1

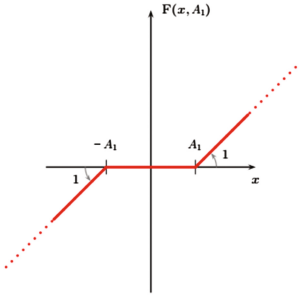

Fig. 2. Restoring force function with free-length $F(x,A_1)$.

3.2 General NES Design Calculations

Analytical calculations are performed on Eq. (2) based on change of variable $v = x + \varepsilon y$ and $w = x - y$ and modified complexification of variables as it follows:

$$\begin{aligned} iB_1 + \phi_1 e^{-i\tau} &= \omega(iv + \dot{v}) \\ iB_2 + \phi_2 e^{-i\tau} &= \omega(iw + \dot{w}) \end{aligned} \tag{4}$$

The system Eq. (2) is studied in the vicinity of 1:1 resonance using multiple scales time expansions, introduced in variables and their derivatives. The cable is considered acting as the master system, establishing its pulsation ω in the coupled system, this rescaled pulsation is equal to 1 in the dimensionless system.

System of equations similar to Eq. (2) have been studied by Weiss et al. [4] to design NES using the same analytical process. The multiple scales approach allows to separate the asymptotic behaviors of the system according to different time scales with fast time scale $\tau_0 = \tau$ and $\tau_j = \varepsilon^j \tau$ for $j = 1, 2,..$ as slow time scales. These analytical expansions are used to calculate the SIM of the system at fast time scale. The Slow Invariant Manifold (SIM) is expressed using variables N_1 and N_2 respectively $\phi_1 = N_1 e^{i\delta_1}$ and $\phi_2 = N_2 e^{i\delta_2}$. For small values of ε parameters N_1 and N_2 are dimensionless amplitudes respectively close to the amplitudes of the cable and the relative displacement between the cable and the NES. The SIM provides a good insight for tuning the NES as detailed

in [2, 3] for a purely cubic NES. In the case of a non-smooth piecewise linear NES, contrary to the case presented in [3], analytical formulation of the SIM and its extrema requires large analytical expansions and actuation of values at each point of the SIM. As a result for practical reasons SIM extrema calculations is obtained through numerical tools in this study. Finally the geometry of the SIM is slightly different from the system with NES with cubic nonlinearity, exhibiting globally 4 local extrema and 2 instable branches as already observed in [4] and depicted in Fig. 3

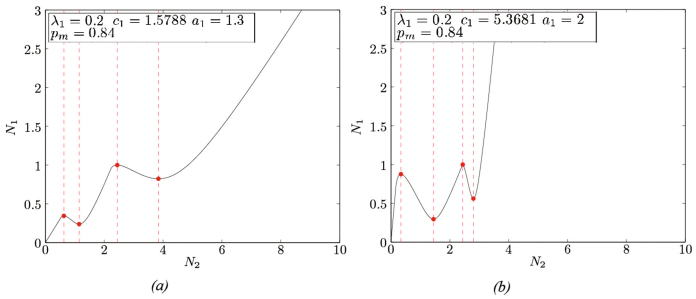

Fig. 3. Examples of Slow Invariant Manifold (SIM) of the cable first mode coupled with a piecewise linear NES

The NES design requires a defined displacement activation threshold X_{dim} of the passive absorber. Once this threshold is set, the design, under dimensionless calculations, aims to obtain a second extrema of the SIM equal to 1, with a set of parameters a_1 and c_1 physically relevant for a prototype. Several set of parameters of a_1 and c_1 can be suitable, the final choice has to take into account the more efficient shape of the SIM from a dissipation point of a view and from a displacement limitation consideration.

Finally the study of the invariant manifold gives a method to calculate approximated physical parameters for NES design. Even if the design is not totally accurate, especially because of wrong damping approximation, the approach allows to design an efficient device as presented in the following parts.

3.3 Applied Design for Bridge Cable

The NES is designed to be set in the center of the cable, which is the maximum displacement point for the first vertical mode shape. The total mass of the additional NES is chosen such as $\varepsilon = m/M = 0.01$, which gives $m = 0.3524$ kg. The mass m of the NES is approximately 0.5% of the total mass of the cable.

The activation threshold is chosen at $X_{dim} = 0.018$ m, then we obtain theoretical parameters for the NES prototype:

$$\begin{aligned} C_1 &= 1224\,\mathrm{N\,m^{-1}} \\ A_1 &= 0.036\,\mathrm{m} \end{aligned} \tag{5}$$

these values are introduced for numerical simulations with a NES damping estimated at $\xi_1 = 10^{-3}$.

4 Step Release Tests Numerical Simulations

Numerical simulation is set for a piecewise linear NES set vertically on the middle of the cable to perform vibration mitigation of the first vertical mode at 4.05 Hz. The NES device is designed to control displacement with activation threshold at 0.015 m at mid span.

Two step release tests are performed. First test is performed for a step at 0.01 m, which means 0.008 m below the theoretical design threshold. Second test is performed for a step at 0.025 m which means 0.007 m above the theoretical design threshold. Each test is performed twice, with and without the NES.

Numerical simulation results are represented in Fig. 4 from the SIM point of view and in Fig. 5 for the time domain. Figure 4 represents the theoretical SIM, obtained from numerical calculations on analytical expansions, is represented in colored dotted lines for several damping values. The SIM shape exhibits four extrema, also it can be noticed that the NES damping mainly influences the second extrema of the SIM. Position of the SIM extrema and numerical simulations are used to theoretically design the NES.

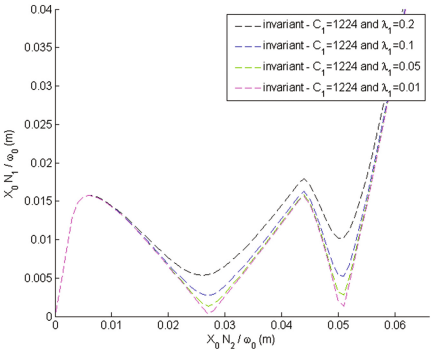

Fig. 4. Theoretical Slow Invariant Manifold (SIM) of the 2 dof reduced system in fast time scale for different NES damping values.

Numerical simulations, from the SIM point of view, underline that the NES is not activated and the system does not bifurcate through unstable branches for step releases test under the activation level. In this case the NES acts roughly as classical damping systems. For simulations with initial step release condition above activation threshold the NES is clearly activated with large amplitude and the behavior bifurcates several times through unstable branches.

These two different behaviors can be observed through direct integration of Eq. (1) by numerical tools in the time domain on Fig. 5. The red line represents the test with the NES installed on the cable, the blue line represents the test on the cable without NES.

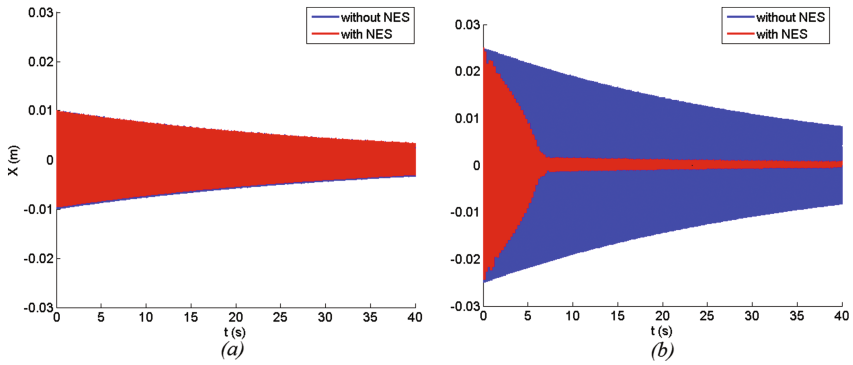

Fig. 5. Numerical simulation of cable time domain response under step release tests *(---)* with NES and *(---)* without NES coupled. (a) step release test below theoretical activation threshold (b) step release test above theoretical activation threshold.

On Fig. 5a no control is observed, the NES only add few damping to the coupled system. On the contrary Fig. 5b exhibits an efficient control of the NES: the amplitude of vibration strongly decreases in 5 s, and keeps the level of vibration at a very low level during the all test.

These numerical results validate the design process and the efficiency of the NES under gravity effect for vertical oscillations. As commonly admitted the NES is only efficient above a defined level of activation. The design process presented here is relevant to the choice of physical properties of the NES to perform efficient vibration control for a defined level of activation under step release excitations.

5 Experimental Results

A NES prototype is built from an oscillating mass between two springs separated via a clearance. The NES device is designed to control displacement at an activation threshold at 0.018 m at mid span with an approximate modal mass ratio $\varepsilon = m/M = 0.01$. The physical properties of the device are defined from previous part approximated design of Eq. (5). For spring and mass providing reasons the prototype is built with physical parameters slightly different for theoretical parameters. As a result parameters are as follows: spring rigidity $C_1 = 990\ N\ m^{-1}$ and additional mass $m = 0.3851$ kg. The free-length is set at $A_1 = 0.036$ m, same as in previous design and numerical examples.

The piecewise linear NES prototype is set vertically on the middle of the cable, tensioned at T = 100 kN with the bench. Sensors are used to quantify the vibration mitigation of the first vertical mode at 4.05 Hz.

5.1 Step Release Tests

Two step release tests are performed with the NES set on the cable, and two others without NES. The experimental results show good agreement with numerical simulations, from the SIM point of view as in the time domain. The NES design reveals very efficient and robust for step release tests above the 0.018 m threshold. Bifurcations and strong decrease of the response amplitude are observed. For small excitations below the threshold no effect is observed except a small additional classical damping.

5.2 Frequency Response Under Forced Excitation

In this part a shaker is added to deliver vertical forced excitations to the cable. For the test, the cable is excited in the vicinity of the first vertical mode, i.e. at frequency 4.05 Hz. Different experiments are performed at each frequency step between 3.9 and 4.1 Hz with increasing 0.02 Hz steps in the vicinity of the resonance peak, and 0.1 Hz out of this area. The same prototype is used, which means that the activation threshold is still close to 0.018 m at mid span. Forced tests are performed at 3 different levels of excitations.

First level L_1 is close to the activation threshold, levels L_2 and L_3 are respectively close to $2L_1$ and $3L_1$. Under level of excitation L_1no influence of the NES is observed on the amplitude, nevertheless the first frequency of the system is only reduced because of the additional mass of the NES acting as classical damper. Under excitation L_2 the efficiency of the NES allows to cut the resonance effect just above the design threshold at 0.018 m. The efficiency of the NES is clearly confirmed under forced excitation by this test. It can be noticed that the design is not totally accurate due to the rough estimation of NES damping. Experiment at amplitude L_3 underlines that despite the increase of the shaking excitation the NES is still efficient and still cut the resonance effect in the vicinity of the same activation level. As a result under harmonic excitation the NES maintains the amplitude of the coupled system under the theoretical level defined by the design process. These results confirm the accuracy of the design process and the efficiency of the NES for forced excitations. It can be noticed that the control above the activation level (in the vicinity of the resonance) is realized through a non periodic behavior, currently named Strong Modulated Response (SMR) [7] that allows efficiently dissipating the energy and interrupting the resonance phenomenon.

6 Conclusions

This work exhibits a design process for a piecewise linear nonlinear energy sink for vertical vibration mitigation of a bridge cable. The non-smooth nonlinearity allows the absorber to work efficiently despite the gravity effects, contrary to most classical absorbers with smooth nonlinearities. The analytical process allows determining physical properties of the non-smooth absorber using the geometry of the slow invariant manifold of a reduced equivalent system. The quality of the design is confirmed by numerical simulations and experiments on a real bridge cable. Experiments for step release and forced external excitations are performed. The results show good

agreement with analytical and numerical calculation in both cases. The high efficiency of the vertical piecewise linear absorber is confirmed for an additional mass of only 0.5% of full cable mass as the mass of the absorber, under transient and stationary regimes.

Acknowledgments. The authors would like to acknowledge the French Ministry of the Environment, Energy and the Sea for funding this work through a PhD grant.

References

1. Vakakis, A.F.: Inducing passive nonlinear energy sinks in vibrating systems. ASME J. Vib. Acoust. **123**, 324–332 (2001)
2. Vaurigaud, B., Ture Savadkoohi, A., Lamarque, C.-H.: Targeted energy transfer with parallel nonlinear energy sinks part I: design theory and numerical results. Nonlinear Dyn. **66**, 763–780 (2011)
3. Weiss, M., Vaurigaud, B., Ture Savadkoohi, A., Lamarque, C.-H.: Vibration mitigation of a bridge cable using a nonlinear energy sink: design and experiment. MATEC Web Conf. **24**, 06007 (2015). doi:10.1051/matecconf/20152406007
4. Weiss, M., Chenia, M., Ture Savadkoohi, A., Lamarque, C.-H., Vaurigaud, B., Hammouda, A.: Multi-scale energy exchanges between an elasto-plastic oscillator and a light non-smooth system with external pre-stress. Nonlinear Dyn. **83**, 109–135 (2016)
5. Nayfeh, A., Mook, D.: Nonlinear Oscillations. Wiley, New York (1979)
6. Irvine, M.: Cable Structures. Dover, New York (1981)
7. Starosvetsky, Y., Gendelman, O.V.: Strongly modulated response in forced 2DOF oscillatory system with essential mass and potential asymmetry. Physica D **237**, 1719–1733 (2008)

An Assessment of a Fractional Derivative Model Applied to Simulate the Dynamic Behavior of Viscoelastic Sandwich Beam

Waldir Felippe(✉) and Flavio Barbosa

Department of Applied Computational Mechanics,
Federal University of Juiz de Fora, Juiz de Fora, Brazil
waldir.felippe@gmail.com

Abstract. Viscoelastic materials can dissipate a large amount of energy when subjected to cyclic shear deformations. However, they have low bearing capacity. Therefore, they are often employed as damping layer in sandwich structures. These sandwich structures present a high damping ratio and simple application. In order to design sandwich structures, many aspects ranging from computer modelling to laboratory testing should be considered. In this paper, results from a test set of experiments are compared with a numerical fractional derivative based model, in order to establish a method to support viscoelastic sandwich beams design. In this way, starting from the dynamic properties of a viscoelastic material, a numerical model is used to evaluate the behavior of these structures. Comparisons with uncontrolled structures are also presented, showing the dissipative characteristics of this passive control.

Keywords: Viscoelastic sandwich beam · Fractional derivative model · Damping

1 Introduction

With the increasing use of flexible structures in civil engineering, it has become important to develop strategies to reduce the vibrations experimented by them. Because of the large flexibility, the vibrations amplitudes can grow to unwanted values. This leaded to an extensive research into active, semi-active and passive vibration control methods, where the latter ones standout due to no need of external energy source and its robustness.

Among these strategies, the passive control with viscoelastic materials (VEM) has shown reasonable efficiency. These materials have low bearing properties with high dissipative capacity when subjected to cyclic shear deformations. That is the main reason that justifies the wide application of VEM in sandwich layers with stiff elastic materials working as a passive control system. This type of vibration control has experienced a growth in practical applications also due to some benefits related to cost-effectiveness [1–3].

The differences between the behavior of viscoelastic and other materials are basically due to its frequency dependent rheological properties. Because of this and due to

© Springer International Publishing AG 2018
J.P. Conte et al. (eds.), *Experimental Vibration Analysis for Civil Structures*,
Lecture Notes in Civil Engineering 5, https://doi.org/10.1007/978-3-319-67443-8_44

the difficulties to establish models in time domain, time domain models are not as numerous as the frequency domain models. In view of the benefits that the time domain models may directly provide, such as the maximum displacement range, many researchers have been working on numerical methods to simulate the dynamical response of VEM in time domain.

Among the time-domain based methods for VEM, those that introduce extra dissipation coordinates or internal variables in a Finite Element Model have been applied in several applications, e.g. Golla-Hughes-McTavish (GHM) method [4, 5] and Anelastic Displacement Field model (ADF) [6, 7]. In recent years, time-domain models based on fractional derivative calculus [8–10] are attracting attention due to its advantages: the reduced computational memory consumption, precision on its results and easiness to curve fit experimental data.

Another advantage of fractional derivative (FD) models is its theoretical approach. That seems to be more suitable to model VEM than the GHM and ADF models. The actual mechanical behavior of a VEM is a function of its whole histories of stresses and strains experienced. In regard to this, it will be shown that the evaluation of fractional derivatives allows a direct approach to account these histories.

In this way, the present work presents a computational FD model and it is used to evaluate the behavior of viscoelastic sandwich beam. Comparisons between experimental and numerical results are also presented.

2 Viscoelastic Fractional Derivative Based Model

Traditionally, the behavior of linear viscoelastic materials may be represented by means of rheological models composed of linear elastic and linear viscous elements. These basic elements have their stress-strain relations well defined and they are given, respectively, by the following equations:

$$\sigma(t) = E\varepsilon(t) \text{ and} \tag{1}$$

$$\sigma(t) = \eta_v D\varepsilon(t), \tag{2}$$

where $\sigma(t)$ and $\varepsilon(t)$ are the stress and strain time dependent functions, E is the Young modulus, η_v is the viscosity and D is the first order derivative operator. Considering the concepts of fractional calculus one can write a general stress-strain relation as:

$$\sigma(t) = pD^{\alpha}\varepsilon(t), \tag{3}$$

where $\sigma(t)$ and $\varepsilon(t)$ are the stress and strain time dependent functions, p is a proportionality factor, α is the derivative order, with $\alpha \in [0,1]$, and D^{α} is the fractional derivative operator defined by Riemann-Liouville as:

$$D^{\alpha}x(t) = \frac{d^{\alpha}}{dt^{\alpha}}x(t) = \frac{1}{\Gamma(1-\alpha)}\frac{d}{dt}\int_0^t \frac{x(s)}{(t-s)^{\alpha}}ds, \tag{4}$$

with $\Gamma(t)$ being the gamma function.

In that way, when $\alpha = 0$ Eq. (3) becomes the linear elastic model ($\sigma(t) = p\varepsilon(t)$) and when $\alpha = 1$ this equation becomes the linear viscous model ($\sigma(t) = p\dot{\varepsilon}(t)$), or dashpot element. Therefore, as soon as α assumes values on interval [0,1], one has a model with intermediary behavior. A graphical interpretation of these three elements can be seen in Fig. 1.

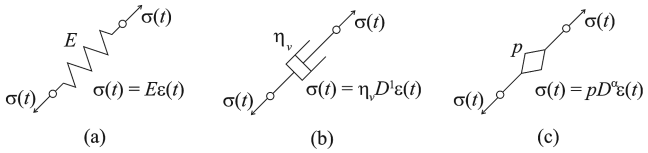

Fig. 1. Rheological elements used in viscoelasticity: (a) elastic, (b) dashpot and (c) fractional order elements

Considering the Standard Linear Solid rheological model, or Zener model, and its mathematical representation given by:

$$\sigma(t) + \tau\dot{\sigma}(t) = E_0\varepsilon(t) + \tau E_\infty\dot{\varepsilon}(t), \tag{5}$$

where τ is the relaxation time, E_0 is the relaxated Young modulus and E_∞ is the non-relaxated Young modulus. This model can be written using de fractional derivative operator, D^α, in the following way:

$$\sigma(t) + \tau^\alpha D^\alpha\sigma(t) = E_0\varepsilon(t) + \tau^\alpha E_\infty D^\alpha\varepsilon(t) \tag{6}$$

One challenge to implement a computational model with Eq. (6) is the numerical evaluation of fractional order derivatives. Diethelm et al. [11] present different ways to numerically evaluate the fractional derivatives. The Grünwald-Letnikov definition is the one that seems to be the most attractive one, since it is valid for any value of α and its easiness of computational implementation. The Grünwald-Letnikov definition is given by:

$$D^\alpha x(t) \approx \Delta t^{-\alpha}\sum_{j=0}^{N_t} A_{j+1}x(t - j\Delta t), \tag{7}$$

where Δt is the time step increment, N_t is the number of time steps considered to evaluate the fractional and A_{j+1} the Grünwald coefficients given by:

$$A_{j+1} = \frac{j - \alpha - 1}{j}A_j, \tag{8}$$

with $A_1 = 1$.

For illustrative purposes Table 1 presents some values of Grünwald coefficients for four values of α. As can be seen, the A_{j+1} coefficients take smaller values as j increases, when $j = 99$ the coefficients are lower than 10^{-3}. Therefore, it can be said that the

Table 1. Grünwald coefficients for different values of α and j

j + 1	α = 0.3	α = 0.5	α = 0.7	α = 0.9
1	1.0000	1.0000	1.0000	1.0000
2	−0.3000	−0.5000	−0.7000	−0.9000
3	−0.1050	−0.1250	−0.1050	−0.0450
5	−0.0402	−0.0391	−0.0262	-0.8663×10^{-2}
10	−0.0163	−0.0109	-0.5985×10^{-2}	-0.1608×10^{-2}
100	-0.5893×10^{-3}	-0.2875×10^{-3}	-0.9533×10^{-4}	-0.1542×10^{-4}
1000	-0.2914×10^{-4}	-0.8937×10^{-5}	-0.1863×10^{-5}	-0.1893×10^{-6}

contribution of first time instants becomes smaller as j increases. In this context, the full history of $x(t)$ need not to be computed.

Analyzing Eq. (7), one can observe that the numerical evaluation of $Dx^{\alpha}(t)$ depends on the functions history, $x(t - j\Delta t)$. Therefore, in order to numerically evaluate the model defined by Eq. (6) it is necessary to evaluate the derivatives and store the stresses and strains histories, $\sigma(t)$ and $\varepsilon(t)$. In order to reduce the computational cost of the model, Glaucio et al. [12] introduce an internal variable, $\bar{\varepsilon}(t)$, to eliminate the fractional derivative $D^{\alpha}\sigma(t)$. This variable is defined by the following expression:

$$\bar{\varepsilon}(t) = \varepsilon(t) - \frac{\sigma(t)}{E_{\infty}}. \tag{9}$$

Applying the Finite Element Method on Eqs. (6) and (9), one can show that is possible to write the following equation system for a discrete time instant $t = n + 1$:

$$\mathbf{M}\ddot{\mathbf{q}}_{n+1} + E_0\left(1 + c\frac{E_{\infty} - E_0}{E_{\infty}}\right)\mathbf{K}_v\mathbf{q}_{n+1} + cE_{\infty}\mathbf{K}_v\sum\nolimits_{j=1}^{N_t} A_{j+1}\bar{\mathbf{q}}_{n+1-j} = \mathbf{F}_{n+1}, \tag{10}$$

$$\bar{\mathbf{q}}_{n+1} = (1 - c)\frac{E_{\infty} - E_0}{E_{\infty}}\mathbf{q}_{n+1} - c\sum\nolimits_{j=1}^{N_t} A_{j+1}\bar{\mathbf{q}}_{n+1-j}, \tag{11}$$

where $\mathbf{M}$ is the mass matrix, $\mathbf{K}_v$ is the geometrical contribution of stiffness, $\mathbf{q}$ is the displacement vector, $\bar{\mathbf{q}}$ is an auxiliary displacement vector, $\mathbf{F}$ the force vector and $c = \frac{\tau^{\alpha}}{\tau^{\alpha} + \Delta t}$.

3 Experimental Data

In order to evaluate the viscoelastic model, experimental data was taken from literature. Huang et al. [13] performed a wide laboratory study. In these laboratory studies, a set of thirty sandwich beams were tested. The beams layer configuration consists in two elastic layers (base beam and clamped restraining layer) and one viscoelastic layer, as can be seen at Fig. 2.

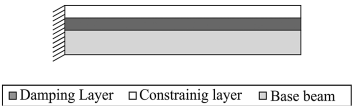

Fig. 2. An extract of the Finite Element mesh used to model the viscoelastic sandwich beams.

From this set two sandwich beams were selected, here called SB-1 and SB-2. These beams have rectangular cross section and 290 mm length; the base beam has 1.91 mm height; the viscoelastic layer of SB-1 has 1.0 mm height and 1.96 mm on SB-2; and the elastic constraining layers has 0.5 and 1.96 mm height for SB-1 and SB-2 beams, respectively.

The elastic material was aluminium and the viscoelastic material used was ZN-1, developed by Aerospace Research Institute of Materials & Processing Technology (ARIMT). Some mechanical properties of these materials are listed in Table 2.

Table 2. Mechanical properties of beam materials.

Properties	Aluminium	ZN-1
E (GPa)	69.9	–
v	0.30	0.49
ρ (kg/m^3)	2700.0	1010.0

These beams were excited under the action of a hammer impact and the transversal accelerations were measured and at the free end section. The experimental measurements in terms of natural frequencies, F_n, and damping ratios, ξ, for the first three vibration modes are presented in Table 3.

Table 3. Experimental results in terms of natural frequencies and damping ratios of SB-1 and SB-2 beams.

Vibration mode	SB-1 beam		SB-2 beam	
	Natural frequency (Hz)	Damping ratio (%)	Natural frequency (Hz)	Damping ratio (%)
1	25.3	10.52	31.5	21.12
2	130.3	13.59	142.5	18.86
3	347.3	14.97	351.8	17.01

Usually structural damping is in the order of 0.5% [14]. Analyzing the data from Table 3, one can see that this type of vibration control can improve significantly the damping ratios of original structures.

3.1 VEM Characterization

Huang et al. [13] present the results of VEM characterization test in terms of Young Modulus, $E^{'}(\omega)$, and Loss Factor, $\eta(\omega)$, for frequencies between 5 and 600 Hz. After the values of Complex Modulus are experimentally determined, one can adjust the curves of the real part of the Complex Modulus and the loss factor for the points obtained experimentally. In the case of the presented fractional derivative formulation, they are given, in terms of Shear Modulus, by:

$$E^{'}(\omega) = \frac{E_0 + (E_\infty + E_0)(\omega\tau)^{\alpha}\cos(\pi\alpha/2) + E_\infty(\omega\tau)^{2\alpha}}{1 + 2(\omega\tau)^{\alpha}\cos(\pi\alpha/2) + (\omega\tau)^{2\alpha}} \text{ and} \tag{12}$$

$$\eta(\omega) = \frac{(E_\infty + E_0)(\omega\tau)^{\alpha}\sin(\pi\alpha/2)}{E_0 + (E_\infty + E_0)(\omega\tau)^{\alpha}\cos(\pi\alpha/2) + E_\infty(\omega\tau)^{2\alpha}}. \tag{13}$$

where ω is the system's vibration frequency, defined in hertz.

Equations from (12) and (13) were used to determine the materials parameters. In this work, it was applied a Particle Swarm Optimization (PSO) algorithm based strategy [15] in order to curve fit the characterization equations.

Using the experimental data, the material parameters could be determined. These fitted values, defined in terms of Young modulus, are: $E_0 = 1.9 \times 10^5$ Pa, $E_\infty = 9.1318 \times 10^8$ Pa, $\tau = 2.1614 \times 10^{-7}$ s and $\alpha = 0.59088$. Figure 3 shows two graphics comparing the experimental values and the adjusted curves of $E^{'}(\omega)$ and $\eta(\omega)$.

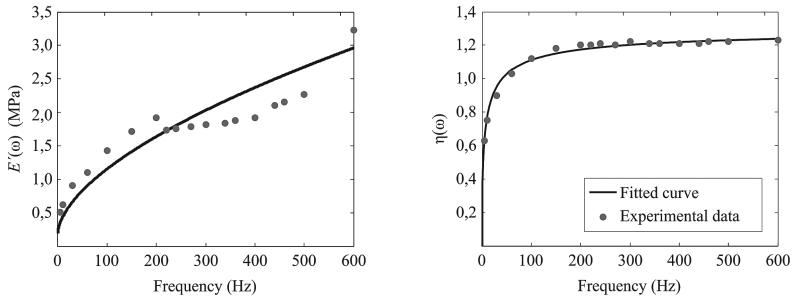

Fig. 3. Experimental values and fitted curves of $E^{'}(\omega)$ and $\eta(\omega)$.

4 Numerical Evaluation

In order to numerically simulate the dynamical behavior of the beams, the structures were discretized meshes as the ones stated by Barbosa and Farage [16]. Figure 4 presents an extract of the Finite Element mesh actually used to model SB-1 and SB-2 beams. This figure presents the Finite Element mesh and a representation of the beams layers overlapped. It also presents the dimensions of base beam, H_{bb}, damping layer, H_{dp}, and constraining layer, H_{cr}.

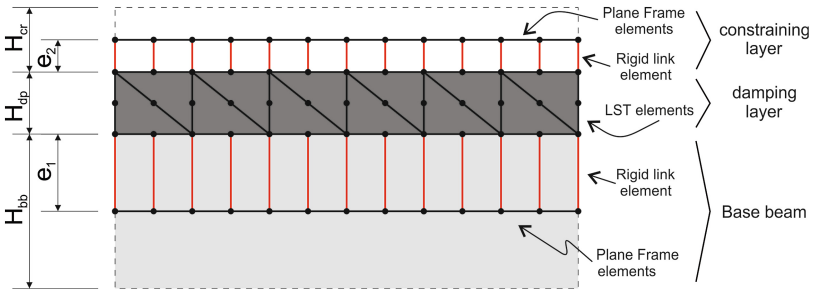

Fig. 4. An extract of the finite element mesh used to model the viscoelastic sandwich beams.

As can be seen, the elastic layers are modeled with Plane Frame elements and the damping layer with LST elements (quadratic triangular Finite Elements with 6 nodes). The elastic and damping layers are connected with rigid link elements in order to simulate the null line eccentricity of the elastic layers, e_1 and e_2. These elements are defined with plane frame elements with negligible mass and its Young modulus is 1000× the one of elastic layers. The final mesh was defined with 18240 LST elements and 2280 elements for each elastic layer; this mesh has 2079 nodes and 5346 dof. This configuration was achieved through a convergence analysis.

Once the mesh was defined, the value of the parameter N_t could be determined through another convergence analysis. The adopted value is $N_t = 402$ for SB-1 beam and $N_t = 355$ for SB-2 beam. The time step during the simulations was $\Delta t = 10^{-4}$ s.

The models were simulated under the action of a hammer impact at 72.5 mm from cantilever and the transversal displacements were observed along the time, at same point. With the models given by Eqs. (8) and (9), the time response of the beams could be obtained. Natural frequencies and damping ratios were extracted by means of an automatic Stochastic Subspace Identification algorithm as proposed by Cabboi et al. [17].

5 Results

Tables 4 and 5 list the natural frequencies and damping ratios numerically obtained for the analyzed sandwich beams. They also present the errors between experimental and numerical results.

Table 4. Comparisons of numerical and experimental evaluations of SB-1 beam in terms of natural frequencies and damping ratios.

Vibration mode	Frequencies (Hz)			Damping ratios (%)		
	Numerical	Experimental	Relative error (%)	Numerical	Experimental	Relative error (%)
1	24.9	25.3	−1.58	13.81	10.52	31.27
2	129.8	130.3	−0.38	12.22	13.59	−10.08
3	318.2	347.3	−8.38	10.40	14.97	−30.53

Table 5. Comparisons of numerical and experimental evaluations of SB-2 beam in terms of natural frequencies and damping ratios

Vibration mode	Frequencies (Hz)			Damping ratios (%)		
	Numerical	Experimental	Relative error (%)	Numerical	Experimental	Relative error (%)
1	28.2	31.5	−9.76	25.41	21.12	20.31
2	142.0	142.5	−0.35	17.79	18.86	−5.67
3	355.8	351.8	1.14	12.96	17.01	−23.81

6 Conclusions

This study evaluated a fractional derivative based model in order to establish a computational model to simulate viscoelastic materials acting as structural sandwich dampers. Based on experimental data available in literature, it was shown that this type of passive control significantly improve the damping rates, since the damping contribution of the elastic beams were close to zero and, after the damping treatment, the sandwich beams achieved significant values for damping ratio as shown in Table 3. As one can observe, beams with thicker viscoelastic layers present higher damping rate than those with thinner ones. Nevertheless, this behavior tends to vanish at high vibration modes.

Comparing the obtained responses of the computational FD viscoelastic model with of their experimental counterpart, it is possible to notice that natural frequencies identified with the numerical model have good agreement with the experimental counterpart for all tested beams. Despite the good agreement between the experimental characterization data and the fitted curves, the numerical model tends to under-evaluate ξ values for higher frequencies. Previous results [18] show that those differences are mostly due to the experimental dispersion observed in the VEM characterization data and in the damping ratios. Despite this, other factors such as: the methodology used on modal identification and the Finite Element discretization, also play a significant influence on numerical results.

Considering the difficulties on predicting damping ratios, the authors suggest that this model is accurate enough to be used to predict damping in current structures.

Acknowledgments. Authors would like to thank: CNPq (Conselho Nacional de Desenvolvimento Científico e Tecnológico); UFJF (Federal University of Juiz de Fora); FAPEMIG (Fundação de Amparo à Pesquisa do Estado de Minas Gerais) and CAPES (Coordenação de Aperfeiçoamento de Pessoal de Nível Superior) for financial supports.

References

1. Samali, B., Kwok, K.C.S.: Use of viscoelastic dampers in reducing wind- and earthquake-induced motion of building structures. Eng. Struc. **17**, 639–654 (1995)
2. Pant, D.R., Montgomery, M., Berahman, F., Baxter, R.P., Christopoulos, C.: Resilient seismic design of tall coupled shear wall buildings using viscoelastic coupling dampers. In: 11th Canadian Conference on Earthquake Engineering, Victoria, Canada (2015)
3. Banisheikholeslami, A., Behnamfar, F., Ghandil, M.: A beam-to-column connection with viscoelastic and hysteretic dampers for seismic damage control. J. Constr. Steel Res. **117**, 185–195 (2016)
4. Golla, D.F., Hughes, P.C.: Dynamics of viscoelastic structures - a time-domain, finite element formulation. J. Appl. Mech. **52**, 897–906 (1985)
5. McTavish, D.J., Hughes, P.C.: Modeling of linear viscoelastic space structures. J. Vib. Acoust. **115**, 13–110 (1993)
6. Lesieutre, G.A., Bianchini, E.: Time domain modeling of linear viscoelasticity using anelastic displacement fields. J. Vib. Acoust. **117**, 424–430 (1995)
7. Lesieutre, G.A., Govindswamy, K.: Finite element modeling of frequency-dependent and temperature-dependent dynamic behavior of viscoelastic materials in simple shear. Int. J. Solids Struc. **33**, 419–432 (1996)
8. Bagley, R.L., Trovik, P.J.: Fractional calculus - a different approach to analysis of viscoelastically damped structures. AIAA J. **21**, 741–748 (1983)
9. Bagley, R.L., Trovik, P.J.: Theoretical basis for the application of fractional calculus to viscoelasticity. J. Rheol. **27**, 201–210 (1983)
10. Bagley, R.L., Trovik, P.J.: Fractional calculus in the transient analysis of viscoelastically damped structures. AIAA J. **23**, 918–925 (1985)
11. Diethelm, K., Ford, N.J., Freed, A.D., Luchko, Y.: Algorithms for the fractional calculus: a selection of numerical methods. Comput. Methods Appl. Mech. Eng. **194**, 743–773 (2005)
12. Glaucio, A.C., Deü, J.F., Ohayon, R.: Finite element formulation of viscoelastic sandwich beams using fractional derivative operators. Comput. Mech. **33**, 282–291 (2004)
13. Huang, Z., Qin, Z., Chu, F.: Damping mechanism of elastic-viscoelastic-elastic sandwich structures. Compos. Struct. **153**, 96–117 (2016)
14. Mevada, H., Patel, D.: Experimental determination of structural damping of different materials. In: 12th International Conference on Vibration Problems - ICOVP 2015, Guwahati, India (2016)
15. Felippe, W., Barbosa, F.S.: Nature inspired curve fitting strategies for viscoelastic materials mechanical properties. Mec. Comput. **XXXIII**, 1557–1570 (2014)
16. Barbosa, F.S., Farage, M.C.R.: A finite element model for sandwich viscoelastic beams: experimental and numerical assessment. J. Sound Vib. **317**, 91–111 (2008)
17. Cabboi, A., Magalhaes, F., Gentile C., Cunha, A.: Automatic operational modal analysis: Challenges and practical application to a historical bridge. In: Conference on Smart Structures and Materials - SMART 2013, Torino, Italy (2013)
18. Felippe, W., Barbosa, F.S.: Dynamic properties comparisons between experimental measurements and nondeterministic numerical models of viscoelastic sandwich. In: Experimental Vibration Analysis for Civil Engineering Structures – EVACES 2015, Dübendorf, Switzerland (2015)

Modal Phase Compensation for Application of Direct Velocity Feedback to Active Control of Floor Vibration Under Impact Excitation

Kai Xue[1(✉)], Akira Igarashi[2], and Takahiro Kachi[3]

[1] Department of Urban Management, Kyoto University, Kyoto, Japan
xk5663279@gmail.com
[2] Disaster Prevention Research Institute, Kyoto University, Kyoto, Japan
[3] Sumitomo Riko Co. Ltd., Aichi, Japan

Abstract. The modal filtering approach has been investigated as a promising efficient implementation approach for control of human-induced vibration of building floors, so that the measured response of the floor is decomposed into modal responses. It is expected to achieve a simple and cost-effective framework, taking advantage of the mode-by-mode control approach. In this study, an automatic phase compensation technique and its implementation combined with modal filtering to vibration control of an impact-excited floor are presented. It has been observed that the phase-lag of electromagnetic actuators strongly affect the efficiency of the control performance of the vibration control as a result of the combined dynamics of the structure and the control system. Phase compensation can be implemented by a simple weighted linear combination of integration with the target modal control signal itself, which is similar to the proportional-integral (PI) technique. In this study, an automatic adjustment technique of the PI parameters when the modal frequency is known is developed and implemented to the control system. Verification experiments using a steel plate with all edges fixed and the developed control system are conducted to investigate the effectiveness of this method under impact loading. The control performance achieved by the developed system show the validity of this approach.

Keywords: Actuator dynamics compensation · Modal filtering · Direct velocity feedback control · Plate vibration suppression · Automatic control parameter adjustment

1 Introduction

Recently advancements in structural technology and modern trends in building layouts have resulted in unwanted vibration of structures due to less inherent damping under human excitation [1]. For the case of residential houses and buildings, the vibration problems caused by human-induced excitations spoil the environmental quality and the acoustical comfort for the occupants. Consideration for vibration suppression techniques is required so that the sound pressure level of the human-induced sound should be kept within allowable limits. Application of the active control using sensors,

© Springer International Publishing AG 2018
J.P. Conte et al. (eds.), *Experimental Vibration Analysis for Civil Structures*,
Lecture Notes in Civil Engineering 5, https://doi.org/10.1007/978-3-319-67443-8_45

actuators and controller can be a promising approach for this purpose because of its high potential vibration cancellation performance compared to the passive control methods.

Direct-output feedback (DOFB) controllers and model based (MB) controllers are often used to control the vibration of structures. In DOFB, the sensor outputs are multiplied by a gain matrix to produce the actuator commands and most previous research in the topic of the floor vibration suppression has been focused on this type mainly due to the ease of implementation [2]. The advantage of this controllers are its robustness to spillover effects due to residual modes because of the well-known interlacing property of poles and zeros of collocated systems and it is unconditionally stable in the absence of actuator and sensor dynamic. However, when the sensors and actuators are not collocated and their dynamics are considered, the interlacing property and unconditionally stable are no longer accomplished. Model-based controllers, on the other hand, are widely used in civil engineering for wind and seismic response cancellation. For the floor vibration control, these methods are not widely used mainly due to the higher processing power and higher level of difficulty in implementation compared with DOFB method [3].

A special model based technique called modal filtering can be used to control the vibration of floor system. Modal filtering utilizes the property that the dynamics response of any real floor is composed of summation of individual modal responses, each behaving as a single-degree-of-freedom (SDOF) system and each having a particular response shape [4]. The modal filtering approach applies a set of scalar, spatial weighting coefficients to responses measured by each sensor to extract these individual canonical modal responses from the global response of the floor [5]. Using this technique, the modal control forces can be independently designed for each mode through feedback control and applied by actuators. The final control force for multiple modes can be calculated by adding the control forces for individual modes. This approach allows controlling of the modes of interest rather than all the modes excited by the disturbance and easy implementation of phase compensation which would be introduced later.

It has been shown that the use of an actuator introduces a pair of high-damped poles that affect substantially the dynamics of structures [6]. This can be explain through the view of signal processing: when a control signal calculated by the controller go through the actuator which can be seen as a linear time invariant system in general, not only the amplitude but also the phase of the original signal are altered. In fact the change of phase might reduce the stability margins and the possible damping to be introduced when the direct velocity feedback control is used for each control mode.

Therefore, it is necessary to compensate for the phase lag caused by control actuator as well as other dynamics components that would cause phase change of the original signal such as ADC and low-pass filter so that a high damping and high stability margins can be achieved. An automatic phase compensation technique for individual modes which can be implemented by a simple weighted linear combination of integration of the target modal control signal with itself as long as the modal frequency is known is developed in this paper. A velocity feedback controller can be then constructed for each mode by multiplying the compensated velocity with a scalar feedback control gain.

2 Basic Control Background

2.1 Modal Filtering

The basis for modal filtering is the standard modal coordinate transformation to simplify the solution of the systems of linear differential equations. Since the eigenvectors are linearly independent, the signal measured by the sensors may be expressed as a linear combination of natural vibration modes as follows:

$$\mathbf{u}(t) = \sum_{n=1}^{N} A_n \boldsymbol{\Psi}_n \cos(w_n t - \gamma_n) = \sum_{n=1}^{N} q_n(t) \boldsymbol{\Psi}_n \tag{1}$$

where $\mathbf{u}(t)$ is the response measured by sensors represented as a vector, N is the number of natural modes to be considered, A_n is the real amplitude and $\boldsymbol{\Psi}_n$ is the modal shape vector, γ_n is the phase, w_n is the natural angular frequency and the subscript n denotes that the variable is for the nth mode. The symbol $q_n(t)$ represents the generalized coordinate of the nth mode.

It is assumed in this paper that the number of modes of the plate N is a finite integer because the higher frequency modes in floor system are harder to excite and have higher damping terms. For simplicity, Eq. (1) can be expressed in matrix-form:

$$\{u_S\} = [\Psi_{S\times N}]\{q_N\} \tag{2}$$

where the number of sensors is S, such that $S \geq N$. The goal of modal filtering is to apply a spatial filter to the measured response data to extract the modal coordinate responses $\{q_N\}$. From Eq. (2):

$$\{q_N\} = ([\Psi_{S\times N}]^T[\Psi_{S\times N}])^{-1}[\Psi_{S\times N}]^T\{u_S\} \tag{3}$$

Note that $([\Psi_{S\times N}]^T[\Psi_{S\times N}])^{-1}[\Psi_{S\times N}]^T$ is the pseudo inverse of the modal matrix $[\Psi_{S\times N}]$. Thus the pseudo inverse of the modal matrix yields a modal filter which can be used to extract modal coordinates from a vector of response information.

2.2 DVF Control Strategy

If the dynamics of the actuator are not considered in the real system, the DVF (Direct Velocity Feedback) control strategy can be a natural choice due to its readily established simple implementation. The DVF control indicates that the control force for the jth mode $f_j(t)(j = 1, 2\ldots)$ is defined to be proportional to the velocity of the jth response $\dot{q}_j(t)$ obtained by utilizing the modal filtering to the dynamic response $\mathbf{u}(t)$ measured by the sensors, as

$$f_j(t) = -\beta_j \dot{q}_j(t) \tag{4}$$

where the positive value β_j is the gain for the jth mode. The damping ratio of jth mode can be increased by this procedure. Therefore, the control force for multiple modes, denoted by $f(t)$, is calculated by:

$$f(t) = f_1(t) + f_2(t) + f_3(t) + \cdots = (-\beta_1 \dot{q}_1(t)) + (-\beta_2 \dot{q}_2(t)) + (-\beta_3 \dot{q}_3(t)) + \cdots \quad (5)$$

The response reduction effect for each mode is achieved by choosing optimal sufficiently large value of the control gain β_j. However, just as described above, dynamics of actuator or other dynamics components involved cannot be ignored in the whole control system, therefore the amplitude and phase of the response $\dot{q}_j(t)$ for each mode would be changed. The altered amplitude can be compensated by adjusting the value of β_j for each mode, however, the phase change might degrade the performance of this control strategy by reducing the stability margins as well as possible damping to be introduced. So a modified DVF controller designed to increase the closed-loop system stability and to make the system more amenable to the introduction of significant damping for each mode to be controlled through phase compensation is needed. In the next section, a simple technique would be introduced to compensate for the phase lag caused by the dynamics components for each control mode.

3 Phase Compensation

3.1 Problem Statement

As discussed above, after modal filtering, the filtered mode can be approximately seemed as a single-degree-of-freedom system, as

$$m_j \ddot{q}_j(t) + c_j \dot{q}_j(t) + k_j q_j(t) = f_{cj}(t) + f_{dj}(t) \quad (6)$$

where m_j, c_j and k_j are the modal mass, modal damping coefficient and modal stiffness of the jth mode, respectively, $f_{cj}(t)$ is the modal control force and $f_{dj}(t)$ is the modal disturbance. The modal coordinate $q_j(t)$ is in fact a damped sinusoidal response, which makes it easier to integrate the filtered response from acceleration to velocity. Since the control actuator, data-acquisition, filter and processing hardware are included in the feedback loop, the control signal would be deformed on both amplitude and phase using the described DVF controller, and then the second order linear differential equation can be written as:

$$m_j \ddot{q}_j(t) + c_j \dot{q}_j(t) + k_j q_j(t) = -\beta_j \alpha_j \dot{q}_j(t - t_{0j}) + f_{dj}(t) \quad (7)$$

where α_j and t_{0j} are the scaler of amplitude changed and phase lag of jth mode, respectively. By transforming both side of Eq. (7) into its Laplace domain, it can be expressed as:

$$s^2 m_j q_j(s) + s(c_j + e^{-st_{0j}} \beta_j \alpha_j) q_j(s) + k_j q_j(s) = f_{dj}(s) \quad (8)$$

This means that the damping ratio of the target mode would be increased when $t_{0j} = 0$. However, if $t_{0j} \neq 0$, the poles of the mode may lie in the right half-plane, implying instability.

Therefore, the problem is how to compensate for the phase lag involved so that a high damping ratio and high stability margins of the control modes can be achieved. The solution in this paper is simply using a weighted linear combination of integration of the target modal control signal with itself, which is similar to the proportional-integral (PI) technique. The procedure of the PI phase compensation for the *j*th mode is shown in Fig. 1. For simplicity, only the actuator is shown in Fig. 1 as the dynamics component.

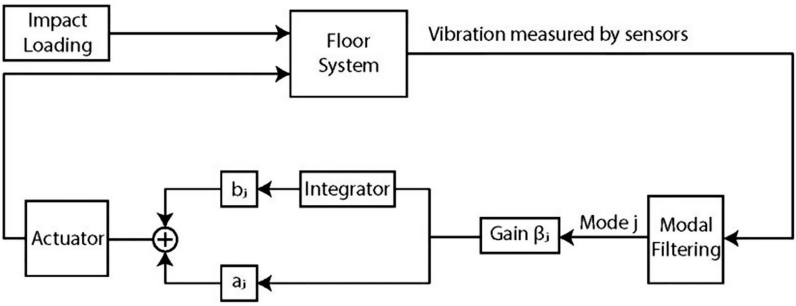

Fig. 1. Phase compensated active control of jth mode

It should be noted that the responses measured by sensors are assumed to be velocity in Fig. 1. The PI parameters are obtained by a set of real time experiments prior to the real time control. In order to search for the value of these parameters, four assumptions are introduced here:

(1) The digital signal processor (DSP) have the ability to generate signal by itself to active the actuator.
(2) The signals are assumed to be undamped during the PI parameter search, which means that the sinusoidal signals are considered in this phase compensation procedure.
(3) The delayed response signal can be detected by the sensor which is mounted on the mass of the actuator.
(4) All the components in the control loop are linear time invariant systems.

The DSP system used in the phase compensation and active control has six input channels and eight output channels that satisfy the assumption (1). The components of electromagnetic actuator which satisfy the assumption (3) are shown in Fig. 2.

According to the assumption (2), an undamped sinusoidal signal $y = Asin(wt)$ is supposed to be generated by output channel 1, which can be regarded as the filtered modal signal, where A is the amplitude (selected randomly) and w is the modal frequency that need to be controlled. While the sinusoidal signal is monitored through the input channel 1, it is provided to the feedback control loop to active the actuator and finally connect to input channel 2 to detect the response of the sensor mounted on the mass of the actuator, as shown in Fig. 3. Note that for simplicity, only three input channels and three out channels are draw in Fig. 3.

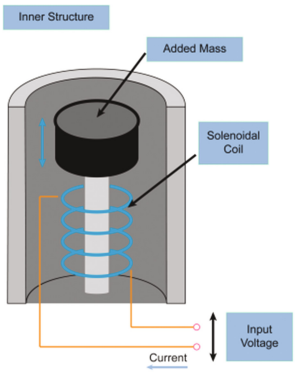

Fig. 2. Actuator for active control

From Fig. 3, since there are ADC and anti-aliasing filter inherent in the DSP, the signal measured by input channel 1 is digitalized and has a small phase lag t_1, which can be expressed as $y = Asin(wt - t_1)$. The signal measured by input channel 2 can be written as $y = \alpha Asin(wt - t_0)$ as discussed above.

In order to compensate the time lag t_0, a PI manipulation to the signal from input channel 1 through two parameters a and b is then applied, the synthesized signal generated at output channel 2 goes through the feedback control loop and measured by input channel 2 is as same as the original signal $y = Asin(wt)$. The process is shown in Fig. 4.

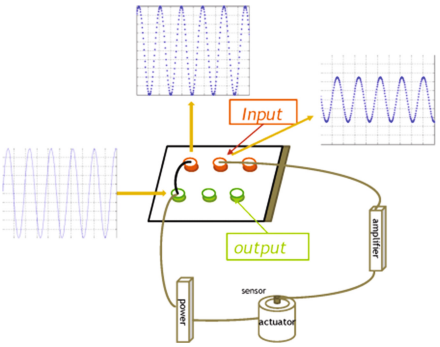

Fig. 3. Signal before phase compensation

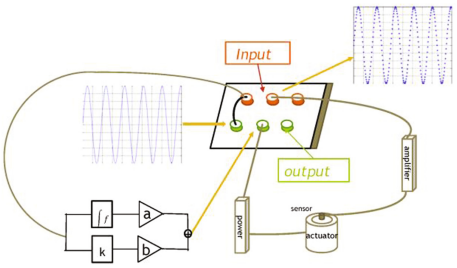

Fig. 4. Signal after phase compensation

The question now is how to find the parameters a and b. In the next sub-section, a technique would be introduced to automatically search for these parameters. Very little knowledge of the system is required to implement the PI phase compensation. The only information required is the modal frequencies of the modes to be controlled. No accurate model of the actuator are needed and no information regarding other dynamics components of control system is required.

3.2 Non-linear Regression and PI Parameter Design

Since the signals measured by input channels are recorded, in order to make a comparison among these signals, it is necessary to express the discrete data as a sinusoidal signal with the offset A_{off}, amplitude A_{amp} and phase φ by:

$$y = A_{off} + A_{amp}\sin(wt + \varphi) \tag{9}$$

Here, w is the nature frequency of the mode which is unchanged during all the process because of the linear time invariant characteristics of the system as assumed in the assumption (4). The identification of these three parameters is achieved by non-linear fitting with the Lebenberg-Marquardt algorithm (LMA). Since the identified A_{off} is extremely small during experiment, it will be neglected in the following illustration.

The process of phase compensation is shown in the following through several real time experimental steps:

Step 1: A sinusoidal signal with amplitude A is assumed to be generated by the output channel 1 for a short among of time, as shown in Fig. 4, that is $y = Asin(wt)$. Then the actuator is activated and the signals measured by input channel 1 and channel 2 are $y = Asin(wt - t_1)$ and $y = Bsin(wt - t_0)$, respectively. The amplitude A and B, the time lag t_1 and t_0 are found through LMA.

Step 2: A sinusoidal signal with amplitude B is then generated by output channel 1 for the same among of time, that is $y = Bsin(wt)$. The signals measured by input channel 1 and channel 2 are $y = Bsin(wt - t_1)$ and $y = Csin(wt - t_0)$, respectively, according to assumption (4).

Step 3: As shown in Fig. 4, $y = Bsin(wt)$ is assumed now as the signal to be compensated, in order to obtain the same signal from input channel 2, PI parameters a and b are now ready to apply to signal $y = Bsin(wt - t_1)$ which is obtain from input channel 1 in step 2. For the purpose of obtaining $y = Bsin(wt)$, from step 1, it is obvious that the signal generated by output channel 2 is $y = Asin(wt + t_0)$. The problem now is finding the parameters a and b so that:

$$a * Bsin(wt - t_1) + \mathrm{b{*}Int}(B\sin(wt - t_1)) = A\sin(wt + t_0) \tag{10}$$

where $\mathrm{Int}(\mathrm{Bsin}(\mathrm{wt} - t_1))$ implies the integration of discrete signal $B\sin(wt - t_1)$. Ideally, $\mathrm{Int}(B\sin(wt - t_1)) = -\mathrm{Bcos}(\mathrm{wt} - t_1)/\mathrm{w}$, therefore, Eq. (10) can be written as:

$$a * Bsin(wt - t_1) - \frac{\mathrm{b{*}B}}{w}\cos(\mathrm{wt} - t_1) = \mathrm{Asin}(\mathrm{wt} + t_0) \tag{11}$$

From the basic sine and cosine of sum identities, $a * B = Acos(t_0 + t_1)$ and $-\mathrm{b{*}}\frac{\mathrm{B}}{\mathrm{w}} = \mathrm{Asin}(t_0 + t_1)$. Therefore,

$$a = \frac{Acos(t_0 + t_1)}{B} \tag{12}$$

and

$$b = -\frac{A * wsin(t_0 + t_1)}{B} \tag{13}$$

The synthesized signal is then generated by output channel 2 and the amplitude and phase parameters of the signal measured by input channel 2 can be identified by LMA.

Step 4: In fact, there are more or less non-linear characteristics in the control system and the integrator used above is often chosen as a combination of an ideal integrator with a high-pass filter to constitute a robust integrator. As a result, the measured signal in step 3, in general, will not be the correct signal $y = Bsin(wt)$. Let us assume the measured signal in step 3 is $y = B_1 sin(wt - t_2)$. Thus, in this step, a new pair of parameters a and b is computed in the same manner described, and with it a new measured signal from input channel 2. The operation described is then repeated until the deviation of the phase measured by input channel 2 becomes sufficiently small. The final a and b calculated in this step can be used as the phase compensation parameters of the specified mode during the active control.

Step 5: The procedures described from step 1 to step 4 are then repeated to find PI parameters a and b for all the control modes as long as the modal frequencies are known.

3.3 Theory Behind Phase Compensation

Root locus analysis is developed here to explain the effect of phase compensation. Root locus analysis is a graphical method for examining how the roots of a system change with a control gain increasing from zero to infinity within a feedback system. From Eq. (6), the dynamic equation of the jth mode excited by the control force can be written as:

$$m_j \ddot{q}_j(t) + c_j \dot{q}_j(t) + k_j q_j(t) = f_{cj}(t) \tag{14}$$

The transfer function of the output velocity over control force is:

$$G_m(s) = \frac{\dot{q}_j(s)}{f_{cj}(s)} = \frac{s}{m_j s^2 + c_j s + k_j} \tag{15}$$

Without loss of generality, Eq. (14) can also be written as:

$$G_m(s) = \frac{\dot{q}_j(s)}{f_{cj}(s)} = \frac{s}{s^2 + 2\zeta_j w_j s + w_j^2} \tag{16}$$

in which w_j and ζ_j are the natural frequency and damping ratio of the jth mode.

The mass-spring electromagnetic actuator showed in Fig. 2 can be approximately described as a linear third-order system with the following transfer function:

$$G_A(s) = \frac{K_A s^2}{s^2 + 2\zeta_A w_A s + w_A^2}\left(\frac{1}{s+\varepsilon}\right) \tag{17}$$

in which K_A is a gain which relates the released inertial force $F_A(t)$ with the input voltage $V(t)$, ζ_A and w_A are the damping ratio and natural frequency of the actuator. A low-pass filter element is added in order to account for the dynamic property exhibited by actuator. The pole at $-\varepsilon$ provides the low-pass filtering property.

The PI phase compensation can be seen as a compensator written as:

$$G_p(s) = \frac{as+b}{s} \tag{18}$$

Thus the block diagram of the phase compensated velocity feedback control for each mode can be shown as Fig. 5. If the outputs of the system are structural acceleration, the integrator component must be used to obtain the velocity response.

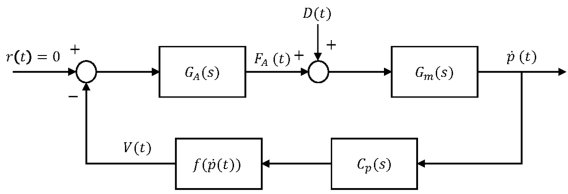

$r(t)$:	Reference command	$\dot{p}(t)$:	Mode velocity response
$D(t)$:	Mode disturbance	$V(t)$:	Control voltage
$F_A(t)$:	Actuator force of the mode	$f(\dot{p}(t))$:	Control gain

$G_A(s)$: Transfer function of the actuator

$G_m(s)$: Transfer function of the SDOF mode

$C_p(s)$: Transfer function of the compensator

Fig. 5. Control scheme for specified mode

The root locus of the DVF controller with a certain phase caused by the actuator is shown in Fig. 6. For the case of the illustration, the natural frequency and damping ratio of the mode to be controlled are assumed to be 97 Hz and 0.03, respectively. Identification of the actuator $G_A(s)$ utilized in the control were carried out using the System Identification Toolbox in MATLAB. $G_p(s) = 1$. The root locus shows that as the control gain increases, the damping ratio of the mode would not significantly change.

However, for the case of controller with phase compensation, the damping ratio would significantly increase as the control gain increases, as illustrated in Fig. 7.

Note that in Figs. 6 and 7, $(\times)$ and (o) denote the poles and zeros of the feedback system.

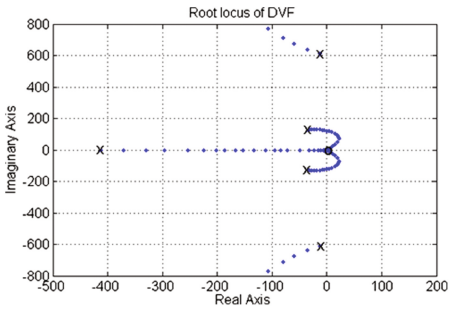

Fig. 6. Root locus using DVF.

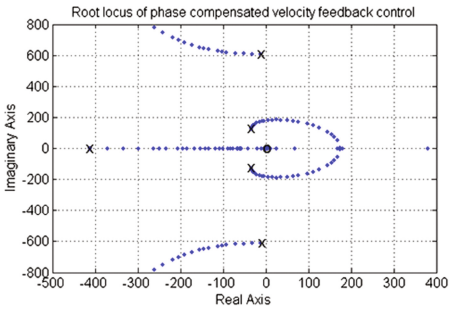

Fig. 7. Root locus after phase compensation.

4 Verification Test

This section presents the design and practical implementation of the phase compensated velocity feedback control system on a steel plate with all four edges clamped.

4.1 Test Setup

A series of experiments were conducted using a model of a square steel plate with all four edges clamped as shown in Fig. 8. The system consists of a 840 mm × 840 mm steel plate with a thickness of 4.5 mm. A square 9 × 9 grid mesh was defined to specify 81 sensor location candidates on the surface of the floor panel.

Experimental identification of the plate was performed to obtain the natural frequencies, modal damping ratios and complex modal shape vectors for the 81 grid mesh points. Acceleration response and transfer function at all the grid points were measured under the impact loading of a hammer, and four piezoelectric acceleration sensors were moved in consecutive measurements to cover the 81 grid points using an experimental identification software Mescope. The frequency range of recording is from 0 to 200 Hz. Five modes shown in Fig. 9 are identified by this process.

Based on the result of experimental identification, the total number of the modes to be considered in the test is selected to be 5. The $1st \sim 3rd$ modes were chosen as the control modes, and $4th \sim 5th$ modes were considered as the residual modes which will cause spillover effect to the control modes. The observation spillover would change the position of poles of residue modes and therefore instability of the system may be induced if the location of one pair of poles moves to the right half of the *s*-plane. The total number of the sensors used for the modal filtering of the first three modes as well as decreasing the spillover effect of the $4th \sim 5th$ modes is 4. A sensor placement design procedure to both enhance the separation performance of the control modes and reduction of the spillover effect of the truncated modes in modal filtering at the same time by combining the minimum spillover method, effective independence method (EFI) and modal assurance criterion (MAC) has been presented in another paper. The final sensor placement based on these methods are points 25, 31, 50, 61 as shown in Fig. 8.

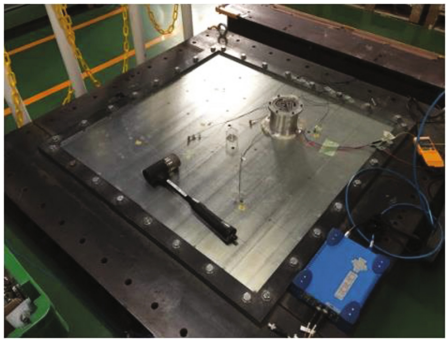

Fig. 8. Experiment set-up

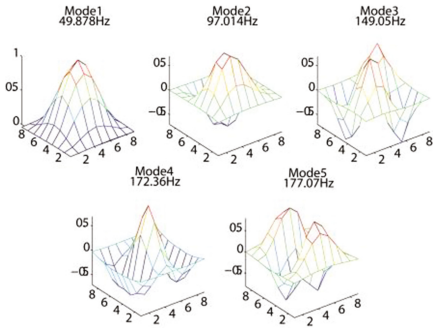

Fig. 9. Identified mode shape

4.2 Controller Design

Since the modal frequencies of the first three modes are identified as indicated in Fig. 9, the PI parameters a and b for phase compensation would be automatically found using the experimental technique described in Sect. 3.

The final step is choosing the control gains for the three modes. The test is done by first inducing an impact loading to the plate by a hammer, then the vibration of the plate is measured by the sensors which are connected to the controller. Gains of three modes are incrementally increased until the system is stable. When instabilities due to spillover effects occur, the test is stopped.

4.3 Experiment Result

The performance of the controlled floor using the DVF control under impact hammer loading is examined first. For the DVF approach, since acceleration sensors were used, an integrator combined with a high pass filter was used to obtain the filtered velocity response. The filtered velocity response was then multiply by the control gain directly to generate the control force. The transfer function of the sensor output at point 31 is compared for the case with and without the active control. The result of the second mode control of point 31 is shown in Figs. 10 and 11, respectively.

It can be observed from Fig. 10 that the control performance of the second mode by the simple DVF method is poor. This result can be explained through the root locus described in Sect. 3. As shown in Fig. 10, as the control gain increases, the modal frequency changed while with a small change of damping ratio as the control gain increases.

The performance of phase compensated velocity feedback control of the second mode is shown in Fig. 11. It is observed that after phase compensation of the second mode, significant reduction of the peak response of the second mode is achieved.

The final experiment is for the case of using phase compensated velocity feedback control to suppress the vibration of the first three modes. The final results are shown in Figs. 12 and 13, in which the transfer functions of points 25 and 31 sensor outputs are compared for the case with and without active control. Independent modal control

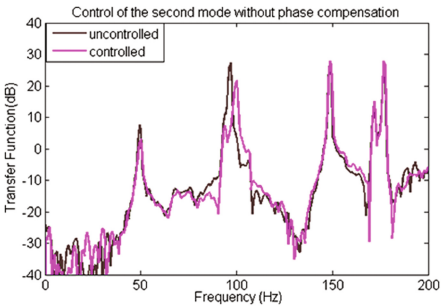

Fig. 10. Second mode control using DVF

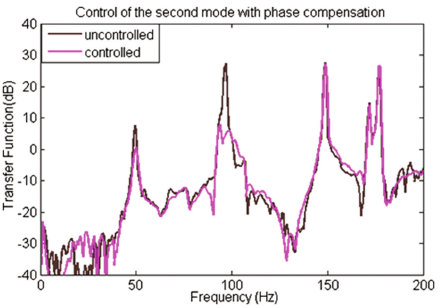

Fig. 11. Second mode control using PCV

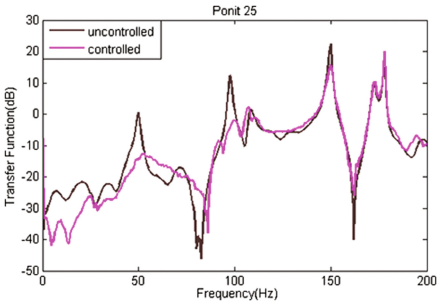

Fig. 12. Result of active control for point 25

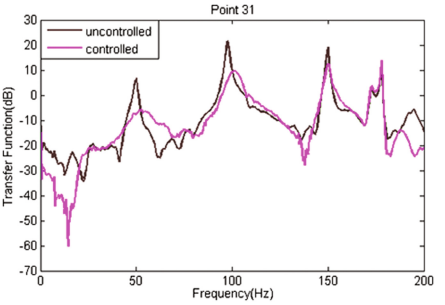

Fig. 13. Result of active control for point 31

allows to increase the modal damping of each controlled mode to effectively reduce the vibration of the floor, which can be observed from the figures that significant reduction of peak responses in the first 3 modes. Since the actuator is placed near the node of the 4th mode, the peak response of this mode did not significantly change. However, the peak of the 5th mode was increased because of the spillover effect.

5 Conclusions

The active control of floor vibrations induced by impact loading is considered. Since the existence of phase lag caused by the actuator or other dynamics components can spoil the performance of control cancellation, a technique of phase compensation using PI parameters for each control mode is put forward to achieve significant relative control system stability and damping for the filtered control modes. Through several experimental steps, the PI parameters were successfully found automatically as long as the modal frequency is known. Since little knowledge is required to implement this phase compensation technique, the method is more applicable for complex control system in which model identification of all the dynamics components is time consuming and error prone.

The performance of the proposed control scheme was verified by a series of tests using a square steel plate. Three modes were considered as the control modes and two as the residue modes. Sensor placement was first designed and then the effectiveness of the phase compensation is examined through the comparison of the control performance between the DVF controller and the controller with phase compensation for the second mode of the floor. For the first three modes control, significant reduction of the controlled modes was achieved using the proposed phase compensation method.

References

1. Reynolds, P.: On-off nonlinear active control of floor vibrations. Mech. Syst. Signal Process. **24**, 1711–1726 (2010)
2. Diaz, I.M., Reynolds, P.: Acceleration feedback control of human-induced floor vibrations. Eng. Struct. **32**(1), 163–173 (2010)
3. Hudson, M.J., Reynolds, P.: Implementation considerations for active vibration control in the design of floor structures. Eng. Struct. **44**, 334–358 (2012)
4. Zhang, Q., Allemang, R.J., Brown, D.L.: Modal filter: concept and applications. In: Proceedings of International Modal Analysis Conference, pp. 487–496 (1990)
5. Shelley, S.: Implementation of a modal filter on a five meter truss structure. In: Proceedings of the International Modal Analysis Conference, pp. 1036–1044 (1991)
6. Alkhatib, R., Golnaraghi, M.F.: Active structural vibration control: a review. Shock Vib. Dig. **35**(5), 367 (2003)

Application of a 240 Metric Ton Dual-Use Tuned Mass Damper System

Christian Meinhardt(✉)

GERB Vibration Control Systems, Berlin, Germany
christian.meinhardt@gerb.de

Abstract. The slender design of a 240 m tall tower structure requires additional structural damping to reduce vortex shedding induced vibrations. Wind tunnel tests indicate that wind speeds can produce critical accelerations at the observation deck on the tower's top level. The resulting displacements not only give concern regarding fatigue initiation at the concrete core of the tower, but would also lead to the discomfort to its visitors. To mitigate critical displacements a state of the art passive Tuned Mass Damping (TMD) system was chosen to be implemented. The primary use of the tower is not only to give visitors access to the observation deck but to serve as a test facility for equipment susceptible to building sway. To tests the equipment under real life conditions the TMD system is required to be either in passive mode or to artificially excite the tower in its fundamental mode of vibration and cause a significant controlled building sway in a defined direction. To satisfy these requirements a novel dual purpose active/passive TMD system was developed. This hybrid TMD is capable of suppressing the occurring vibration in one direction while with the aid of a control algorithm excites the tower's perpendicular direction. The following paper reports the design approach of the passive system and describes the control algorithm when switched into active mode. The initial optimization approach will be presented as well as in-situ results of vibration tests and a monitoring campaign of the tower. In addition the safety concept to avoid excessive displacements of the tower will be presented.

Keywords: Vibration monitoring tall building · Active control · Passive · Control · Excitation mode · Optimization

1 Introduction

The wind analysis for a 245 m tall and slender tower structure in Germany revealed that a resonant excitation of the structure can occur at wind speeds which correspond to ground values (height 10 m) in range of 55–60 km/h. It was expected that without additional damping this resonant excitation would cause top deflections of the tower of about ±750 mm which would not only cause discomfort for the occupants but also cause a significant fatigue loading for the concrete structure of the tower. To reduce the dynamic response to cross wind excitation, a passive Tuned Mass Damper System was implemented. Since the tower shall be used as a test tower for building sway sensitive equipment the owner was looking for a possibility to artificially excite the tower on calm days

© Springer International Publishing AG 2018
J.P. Conte et al. (eds.), *Experimental Vibration Analysis for Civil Structures*,
Lecture Notes in Civil Engineering 5, https://doi.org/10.1007/978-3-319-67443-8_46

– although with displacements that would not cause any fatigue issues. The requested level for the artificial sway motion was in range of approx. ±200 mm. This request gave the rare opportunity to implement a Hybrid Mass Damper (HMD) or since the design system deviates from other HMD systems that were introduced in the past, a so called DUAL USE TMD. The system shall be presented in the following chapters, including the optimization of the passive system, the design of the actuator mechanism, control algorithms and the safety concept.

2 Description of the Control System

The duality of the control system serves (a) the purpose of a reduced energy consumption for a normal operation to reduce the occurring vibrations (b) the purpose of reduced force requirements for the actuators since resonance effects can be used to excite the main TMD mass to achieve the actual reaction force. So compared to other control systems (see Fig. 1) the actuators connect the main structure and the TMD mass but are not used to control the TMD mass directly as it would be the case for an Active Mass Driver/Damper. For the implemented Dual Use TMD a reaction mass for the passive operation of 240 tons was chosen. For the excitation operation mode two linear drives – one in each main direction- are attached at the to the TMD mass with pivots near the center of gravity of the mass to avoid any torsional excitation. The linear drives can provide a force up to 40 kN within a stroke of max. ±600 mm (see Fig. 2). The linear drives can be detached so the entire passive mode will not be influenced by the bearings of the actuators for the unlikely event of bearing failure etc.

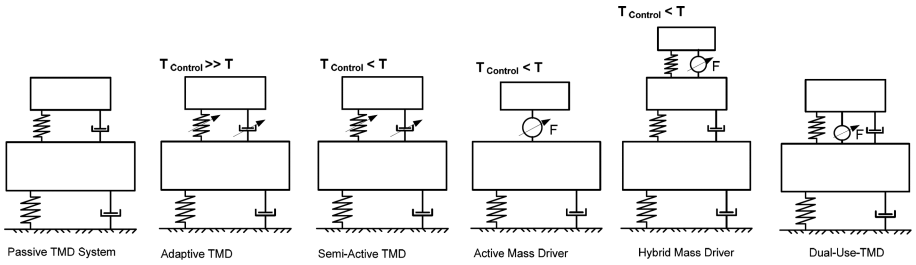

Fig. 1. Types of Control Systems – Dual Use TMD compared to passive, semi-active, active and hybrid systems

The reaction force that controls the building results from the displacement respectively the acceleration of the TMD mass which interacts with the tower through the pendulum rope support and damping devices of the TMD system. Since the actuators provide a sufficient force, the damping devices that are required for the passive system remain enabled during the active excitation mode so the force from the actuators works against the resisting damper force. The dynamic parameters of the passive damping devices were determined during work shop tests for which Force Deflection Tests were performed at a shaking table. The phase angle between the measured displacement and

Fig. 2. Left: Pendulum rope supported TMD mass – Right: Linear Motor as actuator

the reaction force of the damping device is approx. 70°. This value has to be considered for the dynamic stiffness of the damping devices and the force control signal timing.

The system is instrumented with 4 accelerometers (seismic K-Beam/MEMS) to determine the tower accelerations and the accelerations of the TMD mass. The acceleration signals are getting bandpass filtered for the frequency range of the towers fundamental natural frequencies (0.1–0.3 Hz) and integrated to obtain the tower deflections. In addition the integrated values can be compared with the displacement values of an additional Global Navigation Satellite System installed at the top and an initial correlation tests was performed accordingly. Furthermore the TMD displacements are monitored directly with string pot transducers and an inductive length measuring system integrated in the linear motor.

3 Optimization of the Passive Tuned Mass Damper System

The parameters of the passive TMD system had to be determined considering three different aspects – (a) to provide sufficient additional structural damping to reduce the dynamic response to vortex shedding excitation, (b) to limit the resulting TMD travel in the passive mode to a feasible value for the passive damping devices for gust and crosswind excitation and (c) to choose the TMD mass according to the energy input that is required for the desired tower deflection in the excitation mode based on the maximum force that can be generated by the actuators and the maximum stroke with they can perform. To optimize the TMD system a numerical model was used the represented the mass distribution of the tower, and mass moments of inertia as reported in the structural properties. The stiffness elements between the floors were tailored to match the mode shapes and natural frequencies in the provided structural properties. Figure 3 shows the mode shapes and natural frequencies of the analogous model. Figure 3 also shows the mode shapes of the analogous model compared to the detailed model prepared by the structural consultant. In addition the TMD has been discretely modeled as a pendulum system with its eccentric position at the tower.

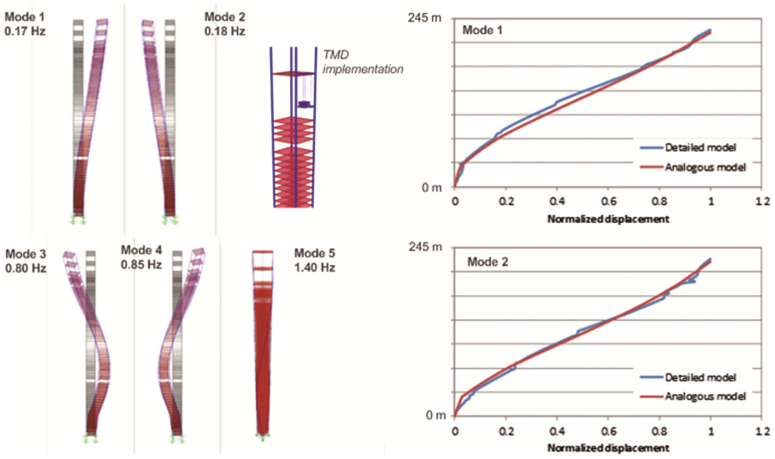

Fig. 3. Relevant modes and calculated natural frequencies for model calibration – mode shape comparison

The load characteristics for the governing load case – resonant excitation due to vortex shedding, are very similar to a harmonic excitation but the gust loading is a stochastic loading for which other optimization criteria apply than the well know DenHartog optimization criteria. In addition the relative displacements of the TMD mass are bigger for a stochastic then for a harmonic loading.

Since for the numerical determination of the TMD parameters a realistic loading should be considered, a time history was generated that included the stochastic gust loading (based on the Davenport Spectrum) and a resonant component for the crosswind excitation (see Fig. 4). The reduction that can be achieved with an optimized passive TMD system as well as the resulting TMD displacements are also shown in Fig. 4. Based on these results for an estimated inherent damping of $D = 0.8\%$ it was determined that a TMD mass of 240 t was required to keep the displacements within ± 650 mm while maintaining an optimum TMD damping ratio for the best TMD performance. An increase of the TMD damping could have reduced the travel while the efficacy would still be sufficient but this would have affected the actor force requirements. To determine the required forces for the optimum 240 t TMD setup the analogous model has also been used as well to verify that with a maximum force of 40 kN from the actuators tower deflections in range of ± 200 mm can be achieved. Figure 5 shows the results of a time domain analysis with the analogous numerical model for which the resulting tower and TMD mass deflections that are caused by the also shown force input are displayed.

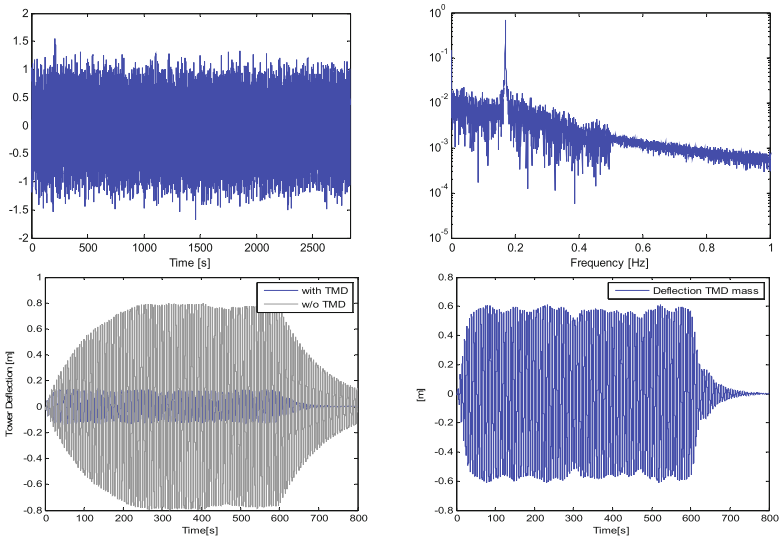

Fig. 4. Above: generated time history for the crosswind loading and resulting FFT spectrum – Below: Tower Displacement with and without optimized TMD and resulting TMD displacement

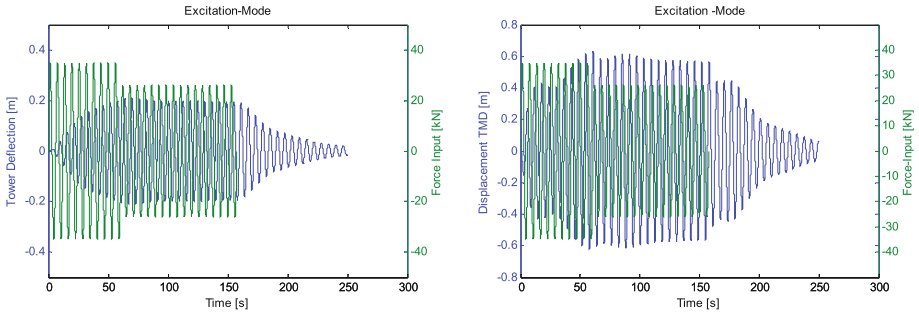

Fig. 5. Left: Numerical Time Domain Analysis – Left: Resulting tower deflections from the shown force input/Right: Resulting TMD mass displacements

4 Control Algorithm

The general control loop for the tower is shown in Fig. 6 which illustrates the general control sequence (closed-loop). The design of the control algorithm requires analytical models of the interaction Actuator-TMD mass to determine the required actuator input to achieved the necessary reaction force and an analytical model of the main structure itself that describe the buildings behavior.

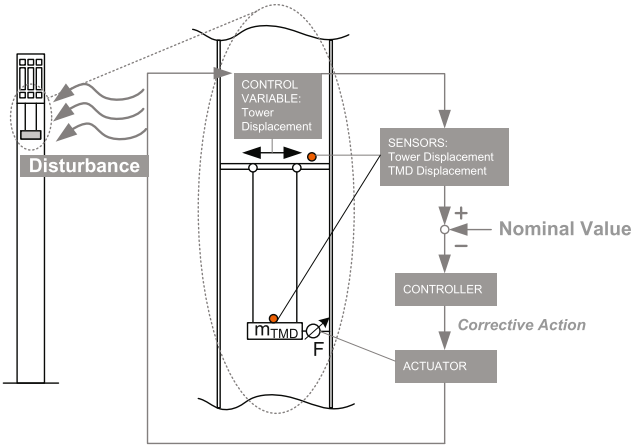

Fig. 6. Feedback control loop

Compared to control algorithms that were applied for other HMD applications as in [3, 6, 7] or theoretically investigated as in [4] the control algorithm for the test tower application had to consider a reduction in the direction perpendicular to the excitation and a controlled excitation in the main direction. Since the dominant dynamic response occurs in the fundamental modes linear feedback control with all its benefits to avoid instabilities could be applied.

The linear feedback control for reducing the towers dynamic response perpendicular to the excitation allows the force command to the actuator to be a specified weighted linear sum of the seven dynamic measurements of the program. The seven measurements are: TMD and tower acceleration, TMD and tower velocity, TMD and tower displacement, and TMD to tower relative displacement. It is important to note that the weighting factors are simple, positive or negative scalar values. The parametrization of the weighting factor is based on experimental dynamic tests of the tower. The actuator feedback is active is calculated instantaneously (50 Hz) and the weighting factors are scalars they are not using any form of frequency dependent transfer function. Also, the feedback is a linear combination of the dynamic property. There is no nonlinear manipulation or logic being used. The control design was implemented for a numerical simulation in the time domain (direct integration) so for each time step the force input to the TMD mass as actuator control could be adapted. Figure 7 shows the results from the simulation for vibration suppression – the tower displacements and the resulting travel of the TMD mass.

For the excitation mode the same control approach has been used in combination with an offset that represents the excitation of the tower to a desired displacement value. The offset is a sinusoidal function based on the detected fundamental frequency for each direction. The control output to counteract the variation of the top displacement due to the disturbance is then modulated on the sinusoidal offset function and the control value has to be adapted accordingly. For this offset a weighting factor was experimentally

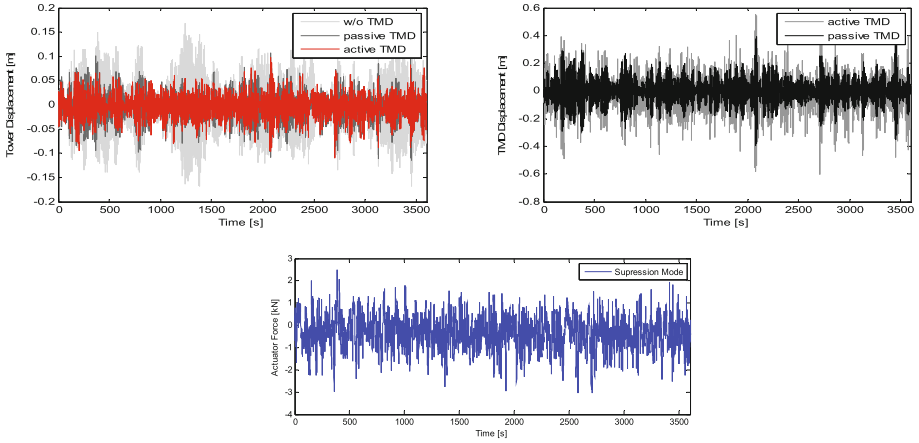

Fig. 7. Above: Time Histories of the calculated tower deflections, mass displacements and actuator force from the numerical time domain analysis to test the control algorithm for vibration suppression using the Dual Use TMD

determined. Figure 8 shows the numerical results with gust load disturbance for the excitation mode with a simple sinusoidal excitation and with applied control algorithm.

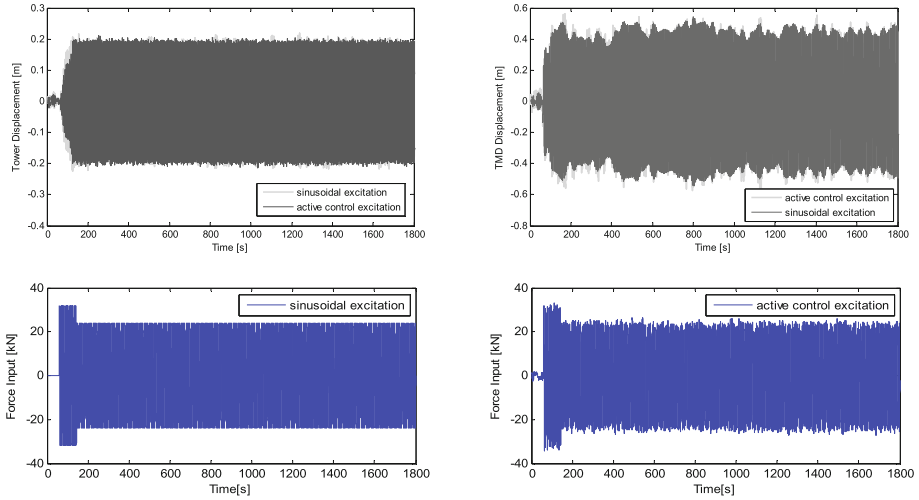

Fig. 8. Results for the excitation mode with gust load disturbance for the excitation mode with a simple sinusoidal excitation and with applied control algorithm

5 Safety Concept

Considering the force of ± 40 kN that can be provided by the linear drives that are used as actuators, a safety concept to ensure that the tower displacements do not exceed the

fatigue criterion is indispensable. Although the force output is not sufficient to cause top deflections bigger than the required ±200 mm. One approach to enhance the safety of the system was to increase the redundancy of the monitoring sensors which are observing the tower's top deflection. This can be best achieved by implementing an additional independent monitoring system that ideally uses different methods than the actual control hardware. For the herein presented project the control hardware used accelerometers and a defined acceleration threshold for a signal band-pass filtered for the band width in range of the relevant natural frequencies of the tower. The overriding superordinate monitoring system is a Global Navigation Satellite System (GNSS) with an accuracy of ±10 mm. The GNNS system requires a reference base station is processing the coordinate data to actual displacement values. If the towers top displacement exceeds a threshold during the artificial excitation mode due to additional wind excitation or other reasons a relay will switch the attendance signal to 0 V which will cause the abort of the excitation mode. In addition both monitoring systems are constantly checking the acquired data for faulty sensor signals which will also cause an abort of the excitation mode. The faulty acceleration/string pot signals will be detected by a peak picking criterion – only if peak picking in the relevant range is possible it can be assumed that the sensors provided a correct signal. The GNNS system analyzes the change of the coordinate data/if the sampled data does not change, a faulty signal has to be assumed.

6 Vibration Tests

Initial vibration tests of the tower were performed at the current stage where the tower is not completed yet so the fundamental frequencies of the tower at this stage are above the specified tuning range of the passive TMD system. The TMD is adjusted to the highest possible tuning frequency. Objective of the vibration tests was the determination of the fundamental frequencies of the tower with blocked TMD system as well as the inherent structural damping. In addition the dynamic behavior with engaged passive TMD system should be determined as well as the increase of structural damping due to the passive TMD system. To identify the fundamental natural frequencies of the tower the Averaged Normalized Power Spectral Density (ANPSD) Method [1] can be used. For this, the recorded time histories have to be separated into segments. These segments have to be transformed into the frequency domain. The resulting spectra need to be normalized, averaged and multiplied with the complex conjugated spectra. By doing so, all random vibration will be eliminated and only the recurring free vibrations of the structure will be displayed in the averaged spectrum, which now represents the dominantly excited natural frequencies of the tower. Figure 9 left shows the recorded time histories of the horizontal ambient vibrations in x- and y- directions with locked TMD. Figure 9 right shows the resulting averaged Auto Power Spectra for a segment length of 120 s. The spectra show that the tower shows a dynamic response at two dominant frequencies (0.225 Hz in x-direction and 0.245 Hz in y-direction).

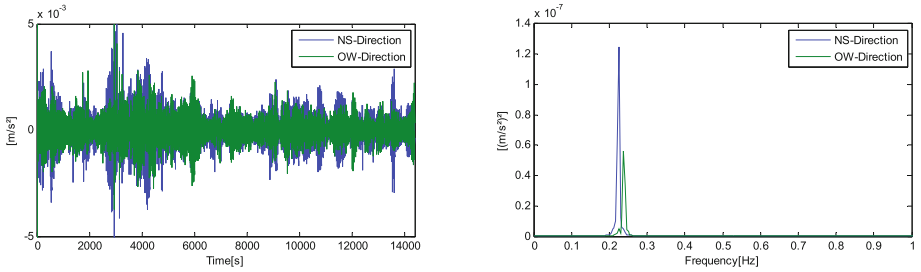

Fig. 9. Left: Time History of the measured acceleration at the top of the tower in the two main directions – Right: corresponding APS spectra

Further to the above described Averaged Power Spectrum Method – which assumes that the ambient excitation causes a sufficient dynamic response in the vibration modes of interest to gain stochastic security- the natural frequencies were determined using the commercial signal processing software ARTEMIS [1] which incorporates Enhanced Frequency Domain Decomposition and Stochastic Subspace Identification Methods. The Enhanced Frequency Domain Decomposition (EFDD) and the Stochastic Subspace Identification are widely used techniques for output-only modal parameter identification. The EFDD method relies on computation of response spectra. Long records are, therefore, required to keep low the error on spectrum estimation and to extract modal parameters in a reliable way. The stochastic subspace identification algorithm was applied to identify bridges using an output–only model. Stochastic Subspace Identification methods work in time domain and are based on a state space description of the dynamic problem. The system identification results at different model orders are compared to distinguish true structural modes from spurious modes in so-called stabilization diagrams. These diagrams are a popular way to select the identified system model, as the true structural modes tend to be stable for successive model orders, fulfilling certain stabilization criteria that are evaluated in an automated procedure. Figure 10 shows a resulting stability card for recorded ambient data, from which the

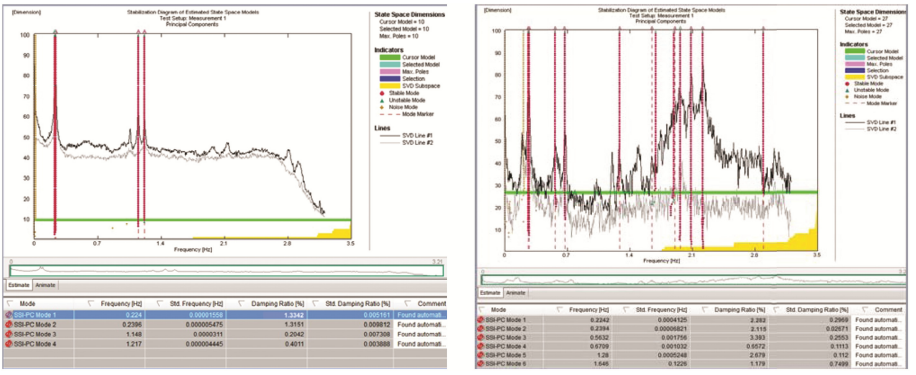

Fig. 10. Stability Cards for the ambient vibration record with blocked TMD (left) and activated TMD (right)

relevant modes could be determined. The identified modes and the determined damping ratios for each mode in the state with locked TMD (left) and the engaged TMD (right) are shown in Fig. 10 as well.

An increase of the structural damping can be noticed. The additional structural damping is in range of a theoretical value that can be determined from the theoretical model for which the detuned TMD setup was considered. In addition to the ambient vibration tests with the passive TMD system, preliminary tests with the active excitation mode were performed despite the detuned state of the TMD system. Figure 11 left shows the time history of the recorded accelerations at the tower top. After an initial sinusoidal excitation the algorithm for a steady acceleration level was enabled to experimentally determine the correlation between tower deflection and forced displacement of the TMD mass. The time history shown in Fig. 11 displays the two test scenarios in the excitation mode and the corresponding FFT spectra shows the clear response of the tower in its two fundamental frequencies (x- and y- direction). The green marked time section is a sinusoidal excitation of the mass with disabled active control which caused a dynamic response in both main directions. The resulting FFT spectrum displays the two peaks to identify the fundamental frequencies in these two directions. The blue marked time segment is for an excitation with enabled active control which caused a more steady tower displacement dominantly in one direction. The resulting vibration decay after the excitation mode was switched off was also used to determine the structural damping and determined to be D = 2.4%. This result correlates with the damping ratio determined with the SSI algorithms.

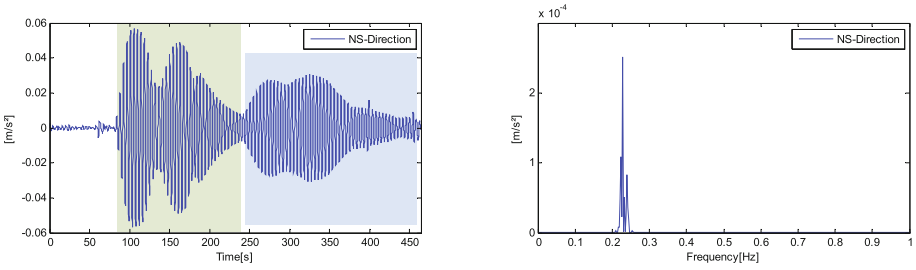

Fig. 11. Left: Time histories of the occurring accelerations at the tower top during the artificial excitation (marked green: sinusoidal excitation/marked blue: controlled excitation mode with suppression in one of the main axis – Centre: Corresponding FFT spectrum

7 Conclusion and Outlook

A Dual Use TMD has been installed at a 245 m tall test tower with the objective to purposely excite the tower to a controlled dynamic response in its fundamental frequencies. The objective of this excitation is to achieve a defined building sway in the two main directions of the tower. Based on numerical calculations it was found that a 240 t TMD mass was required to achieve the required supplementary damping for the passive mode and to generate the required control force to achieve a tower top displacement of ±200 mm. To create a steady displacement level for the excitation mode and to suppress

the displacements caused by wind and the forced vibration component in the perpendicular direction, a control algorithm was developed and tested with numerical simulations. After the installation of the passive pendulum type TMD system for which prefabricated concrete slabs were used as reaction mass, the actuators were commissioned and initial tests have been performed. The tests revealed that the inherent damping of the tower was higher than anticipated but all relevant modes could be determined clearly. The active excitation mode of the building is working and could be tested although not to the full extent to derive all operation parameters since the building is not entirely completed yet. Due to the premature state of the building the passive TMD could not be adapted to the determined fundamental frequencies.

As soon as the TMD system has been adapted, further tests of the building will be performed that will also include tests regarding amplitude dependent damping and the integrity of the safety concept.

Acknowledgements. The application of the Dual-Use TMD system was initiated by the R&D department of ThyssenKrupp Elevators. The development of the TMD system was supported by ThyssenKrupp Real Estates/Business Services.

References

1. Wenzel, H., Pichler, D., Schedler, R.: Ambiente Schwingungsmessungen zur System und Schadenserkennung an Tragwerken. Bauingenieur 74 (1991)
2. Döhler, M., Andersen, P., Mevel, L.: Operational modal analysis using a fast stochastic subspace identification method. In: Conference Proceedings of the Society for Experimental Mechanics Series (2012)
3. Soong, T.T., Spencer, J.R.: Active, semi-active and hybrid control of structures In: 12th World Conference for Earthquake Engineering (2000)
4. Ricciardelli, F., Pizzimenti, A.D., Mattei, M.: Passive and active mass damper control of the response of tall buildings to wind gustiness. Eng. Struct. **25**, 1199–1209 (2003)
5. Yang, N.Y., Agrawal, A.K., Samali, B., Wu, J.C.: Benchmark problem for response control of wind-excited tall buildings. J. Eng. Mech. **130**, 437–446 (2004)
6. Watakabe, M., Tohdp, M., Chiba, O., Izumi, N., Ebisawa, H., Fujita, T.: Response control performance of a hybrid mass damper applied to a tall building. Earthq. Eng. Struct. Dyn. **30**, 1655–1676 (2001)
7. Tan, P., Liu, Y., Zhou, F., Teng, J.: Hybrid mass dampers for canton tower. CTBUH J. **1**, 24–29 (2012)
8. Soong, T.T.: Active Structural Control: Theory and Practice. Wiley, New York (1990)
9. Preumont, A., Kazuto, S.: Active Control of Structures. Wiley, Padstow (2008)

Mitigate Seismic Response of Three-Span Bridge Using MR Damping System

G. Heo[1], C. Kim[1(✉)], S. Jeon[2], C. Lee[2], and S. Seo[3]

[1] Department of Civil Engineering, Konyang University, Nonsan-si, Chungcheong-do, South Korea
cg-kim@hanmail.net
[2] Department of Civil Engineering, Chungnam National University, Daejeon, South Korea
[3] Department of Civil Engineering, Chungnam State University, Cheongyang-gun, Chungcheong-do, South Korea

Abstract. In this paper, a mitigation of earthquake response is aimed at by constituting an MR damping system in a three-span bridge. It is a system where bridge spans are connected by means of an MR damper to control their vibration. A model structure of three-span bridge (12 m long) was built with an MR damper applied to connect each span, one between span A and B, the other between span B and C, and the MR damping system for this study was designed to work as a single unit with five components, that is, three spans and two MR dampers. Shaking table tests were carried out by inflicting a 40% load of Kobe earthquake to see how effective the system would be in mitigating seismic responses. All the tests were done under various conditions (un controlled, passive off, control algorithm) in order to closely examine and analyze under which condition mitigation could be maximized and how mitigation could be effected. As a result of the tests, it was found that the MR damping system was effective in reducing three spans from pounding each other and its active performance decreased the relative displacement of the bridge structure. Therefore, it was proven to be effective in attenuating the seismic responses of three-span bridge.

Keywords: Vibration control · Shaking table test · MR damper · Bridges · Control algorithm

1 Introduction

Bridge pounding occurs between spans or between a span and an adjoining structure. For instance, the 1989 Loma Prieta earthquake caused a severe damage on the southern section of an elevated bridge in China Basin, California by pounding its deck against the flank of its column [1, 2]. In 2001, again, due to the Bhuj earthquake in India, many cases of pounding between spans were observed in several bridges including highway [3].

Any pounding of bridge components against each other is so immensely destructive that brittle fracture becomes a great possibility in structure [4]. To prevent this type of seriously damaging pounding, researchers have been conducting various studies related to structural pounding [5]. However, the research on bridge pounding is relatively rare, compared to that of building [6]. An important study related to bridge pounding was

© Springer International Publishing AG 2018
J.P. Conte et al. (eds.), *Experimental Vibration Analysis for Civil Structures*,
Lecture Notes in Civil Engineering 5, https://doi.org/10.1007/978-3-319-67443-8_47

done by Tanabe et al., illuminating that pounding, caused by the earthquake of Hyogo-ken Nanbu in 1995, played a significant role in collapsing an elevated bridge, by analyzing a time history of the pounding of its upper spans which was idealized in nonlinear spring [7]. Another study of this kind was done by Kajita et al. who modeled the pounding of girders into an element with linear spring and damper, and conducted a time history analysis to analyze the response of an elevated bridge under the condition of virtual pounding among its adjoining superstructure [8].

However, while most of the existing studies seek to explain dynamic characteristics of structure when pounding occurs, it is hard to find any research related to active or semi-active control devices that would be congenial to particular structural characteristics [9]. Also, it should be noted that although the most typical way to check pounding is to secure a distance between adjoining structures, it cannot be applied in bridges where each structural component is to be closely adjoined.

Consequently, many recent studies have adopted MR-dampers, which had been already in use for vibration control, now for the prevention of pounding. Sheikh et al. conducted an analytic study on a MR-damper to verify its effect for the pounding prevention of Base-isolated RC Highway Bridge modeled by means of Matlab & Simulink [9]. Guo et al. also studied on the prevention of pounding by connecting two dampers, one to a span the other to a pier [10]. As such, there have been many studies which were concerned with the effectiveness of MR-damper for the control of seismic vibration [11]. However, all those studies were aimed at a prevention of two spans from pounding each other only, installing a MR-damper on each span individually; they were not concerned with pounding which could occur between spans and abutment.

This study, however, aims at a mitigation of pounding impact felt not only between spans but also between spans and other structural components, especially abutment, which allows for differentiation from other studies. Its uniqueness also lies in the vibration control by MR-dampers which are installed between spans and further in using it for the control of a whole structure by making both masses of span themselves and the MR-damper into a single system itself, what is called here a MR damping system. The purpose of this particular study is to prove its effectiveness. To validate the efficacy of the proposed system, shaking table tests were carried out by inflicting a seismic load of Kobe. They were conditioned under a un-controlled state, a passive-off state, a Lyapunov control state, and a clipped-optimal control to compare each response to the others. As a result, the suggested system was proven to effectively prevent the pounding of three-span bridge and mitigate the seismic response of the whole structure.

2 Three-Span Bridge and a MR Damping System

2.1 Physical Description

In this study, it is necessary to verify the effectiveness of the MR damping system for vibration control. For verification, a three-span bridge of 12 m in length was built for this study as in Fig. 1. The span A and Span C are made 1476 kg in weight, 2300 mm in length, and span B one 3492 kg, 6000 mm.

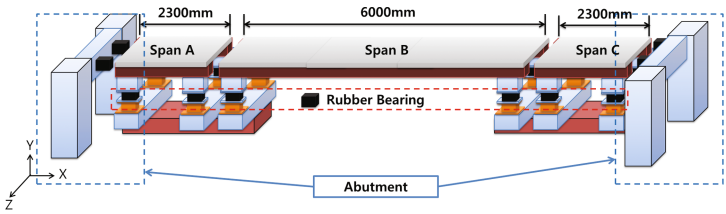

Fig. 1. Three span bridge.

As seen in Fig. 1, the bridge is composed of superstructure, substructure, and abutment. Its superstructure is made of RC slab and I-type beam to raise its mass, while its substructure is made up of short columns of I-type beam to minimize the effect of pier stiffness on structural vibration. A rubber bearing is fitted into each contact area of the superstructure with the substructure. Abutments are added on both ends of the bridge for the purpose of incurring clash against each span as well as preventing the superstructure from falling down. To complete the MR damping system, each MR damper was placed connecting span A and B, and also span B and C.

2.2 Feedback Control Theory

The MR damping system operates as a single unit for vibration control with thee spans and two MR dampers. To maximize its operation, it is necessary to embed a proper control algorithm into the system. In this particular study the Lyapunov stability-based control algorithm and the clipped-optional control algorithm are employed because they are related to the vibration control by means of a MR damping system [12, 13].

Lyapunov's direct approach was employed by Leitmann for the design of semi-active controller [12]. It is applicable for a variety of systems such as a linear, a nonlinear, a time-variant, and a time-invariant system. Lyapunov function for its application is as in Eq. (1).

$$V(z) = 1/2\|z\|_p^2 \tag{1}$$

Here, $\|z\|_p = \left\|\mathbf{z^T P z}\right\|^{1/2}$ refers to P-norm. After deriving $\|z\|_p$ using Lyapunov equation ($\boldsymbol{A}^T\mathbf{P} + \mathbf{PA} = -\boldsymbol{Q}_p$), an equation expressed as controllable is as follows:

$$V_i = V_{\max}\mathrm{H}((-\mathbf{z^T})\mathbf{PB}_i f_i) \tag{2}$$

Equation (2) shows a control theory in which Lyapunov control algorithm is applied. Here, V_i refers to the final input voltage supplied into a power device of MR-damper. V_{max} expresses the input voltage of power device allowed at maximum. $\mathrm{H}(\cdot)$ refers to Heaviside step function, $\dot{z}$ to an equation of state in the system, derived from that of motion, $\mathbf{P}$ to positive confirmation matrix found by Lyapunov equation, $\mathbf{B}_i$ to a row of i in B matric, and f_i to the control capacity of MR-damper for the same row i.

In the meantime, the clipped-optimal control algorithm is a method by which control force is calculated on the basis of the relationship between a force required for control and a force currently exerted by a control device. The required force is calculated as follows:

$$f_c = L\left\{-K_c(s)L\left\{\begin{matrix} y \\ f \end{matrix}\right\}\right\} \tag{3}$$

Where $L\{\cdot\}$ refers to Laplace Transformation, and $K_c(s)$ to a linear optimal control device. To make the current control force of MR-damper congruent to f_c (a control force required for the system control), it is necessary to modulate a control voltage v_i which MR-damper' working force depends on. Control voltage v_i can be modulated by Eq. (4) which refers to a control equation for a semi-active feedback vibration control system in which the clipped-optimal control algorithm is embedded.

$$v_i = V_{\max} H(\{f_{ci} - f_c\} f_i) \tag{4}$$

Where v_i signifies a control voltage which is to be input into each control device on the basis of the values calculated by Eq. (4), and V_{max} refers to a maximum voltage which can be input into a control device. Meanwhile, f_{ci} signifies a control force required for *ith* MR-damper, while f_i the one that is observed from *ith* MR-damper. When an MR-damper works well exerting a required control force, it must be supplied with control voltage to generate a particular control force which is congenial to a current state of structure. In the case of $f_{ci} = f_i$, its control voltage signals 0.

3 Experimental Test

3.1 Experimental Test Condition

For experimental tests on how effectively the MR damping system works to mitigate seismic responses, shaking tables were employed at the seismic simulation test center (Pusan University, Korea). As seen in Fig. 2, a span A and its columns were placed on a shaking table on the left of the picture below; meanwhile, span C and its columns on the other table. Also, the span B was placed between the span A and B. Then, Kobe earthquake load was inflicted equally on both tables by connecting them on an axis.

To repeat, the shaking table tests were aimed to examine under what condition the MR-damper would work most effectively, and so they were carried out under the following conditions: a un control condition (a structure without the MR damping system), a passive off one (with the MR damping system and 0–1 A electric current input into it), and a control algorithm condition (with the MR-damper supplied with the amount of electricity as allowed by the result of control algorithm).

In order to measure structural responses and analyze the measured data for control of the MR damping system, a DS 1103 PPC controller manufactured by dSpace Co. was employed. Electricity needs to be supplied to the MR-damper according to each voltage output from the controller, and for the purpose was also employed PMC 18-3A

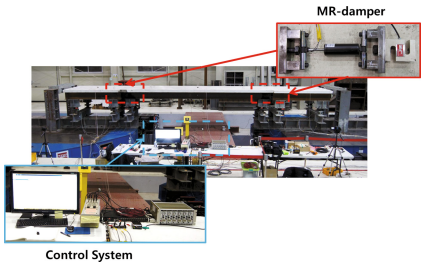

Fig. 2. Setup for shaking table test.

DC Power Supply made by KIKUSUI Co. The MR-damper adopted for the MR damping system here in this study was used RD-8040-1.

4 Experimental Results

The experiments about mitigation of seismic responses of the three-span bridge equipped with a MR damping system were carried out under three different conditions: the un controlled (without a MR damping system), the MR damping system & passive off condition (three spans connected by a MR-damper and supplied with 0A), and the MR damping system & control algorithm (supplied with electricity allowed according to control algorithm). As for earthquake load, it was 40% of Kobe seismic wave. The data acquired through experiments were all compared, especially the data pertaining to displacement which differed from each other according to each condition.

4.1 Control Performance: Passive Off

Experiments were carried out to examine the effect of the MR damping system under the un controlled and the MR damping system with no input of electricity. The data acquired from each condition were compared, and the result of comparison is expressed in the graph of Fig. 3 in which the black line refers to the un controlled state, and the red line to the passive off.

At first, the displacement did not vary too much at the span B, but the displacement between span A and span C was reduced thereafter as the MR damping system was applied as shown on Fig. 3(a). With regard to the acceleration response, the number of pounding was reduced after the MR damping system was applied as shown on Fig. 3 (b). However, the MR damping system was not able to mitigate most of pounding which could be harmful to structure under the condition of passive-off.

4.2 Control Performance: Lyapunov Control

Now, another test on the seismic response of the three-span bridge was performed, this time, inputting electricity adjusted by Lyapunov algorithm, into the MR damping system. The acceleration, displacement, and relative displacement from the test, with the Lyapunov control algorithm applied, are graphed in the following Fig. 4.

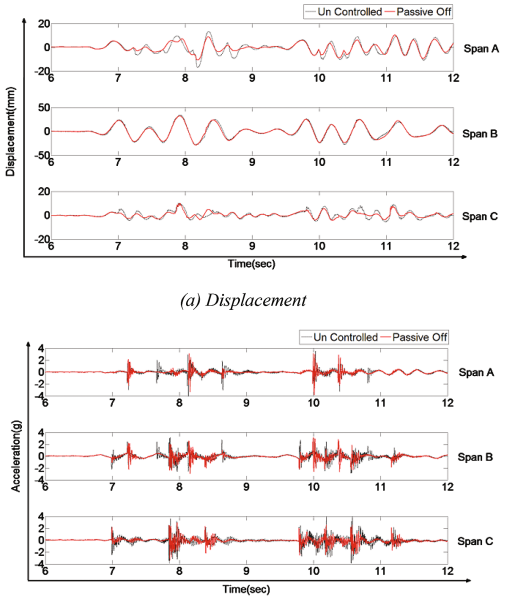

(a) Displacement

Fig. 3. Comparison of control performance: passive off.

In Fig. 4, the results coming from the test with Lyapunov control algorithm applied to the system was compared to those coming from the passive off. (a) and (b) graphs of Fig. 4 are displacement and acceleration of each span, and (c) the relative displacement of between spans. In the spans, the acceleration response was reduced more at the state with the Lyapunov control algorithm applied than at the passive off. As for displacement response, it did not decrease much under Lyapunov control algorithm, in comparison to passive off condition, but relative displacement did decrease.

4.3 Control Performance: Clipped-Optimal Control

In this section, the clipped-optimal control algorithm was applied to allow appropriate current into the MR damping system for the control of seismic response of the three-span bridge. The acceleration, displacement, and relative displacement from the test with the Clipped-optimal control algorithm applied are graphed in the following Fig. 5.

Figure 5 shows the graphs where the test result with the Clipped-optimal control algorithm applied was compared with that at passive off. When Clipped-optimal control algorithm was applied, acceleration, displacement, and relative displacement were found to be reduced in comparison to passive-off. As for displacement response in particular, it reduced to a greater extent than under Lyapunov control algorithm.

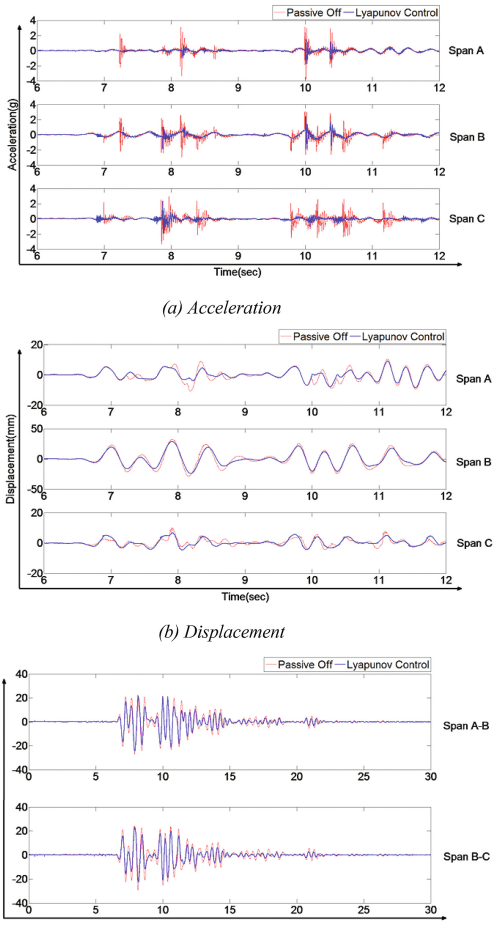

(a) Acceleration

(b) Displacement

(c) Relative displacement

Fig. 4. Comparison of control performance: Lyapunov control.

4.4 Summary of Comparison

So far, all the comparisons were made to examine how effective the MR damping system was, how differently it was affected depending each condition. Under various conditions, the experiments were carried out for the seismic response of the three-span bridge. They produced the data about acceleration, displacement, and relative displacement, and by graphing them all, each different performance of the system for its seismic control was compared under various conditions. To compare the results on the graph quantitatively, Tables 1, 2, and 3 show how the acceleration, displacement, and relative displacement response appear for each of 4 test conditions.

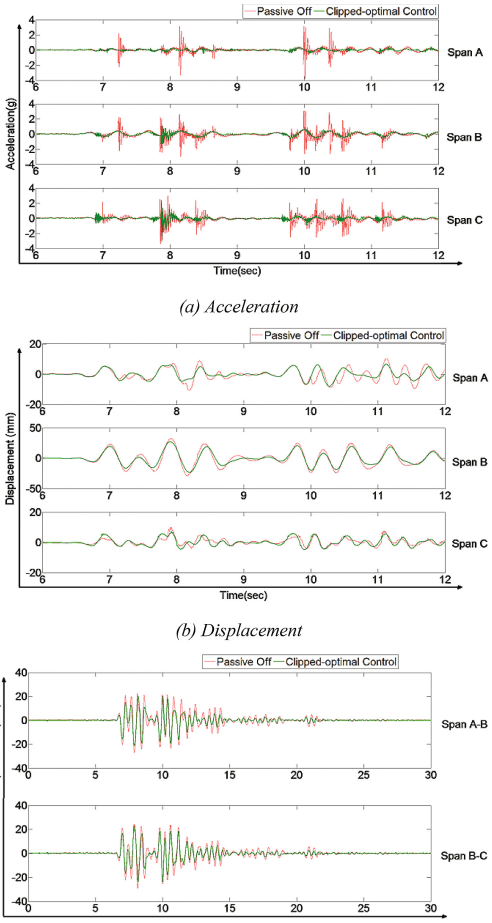

(a) Acceleration

(b) Displacement

(c) Relative displacement

Fig. 5. Comparison of control performance: Clipped-optimal control.

Table 1. Comparison of acceleration response per each span.

RMS value	Un-controlled	Passive off	Lyapunov control	Clipped-optimal control
Span A	0.1870	0.1510	0.0812	0.0548
Span B	0.2292	0.2197	0.1226	0.1094
Span C	0.2486	0.1965	0.0771	0.0914

Table 2. Comparison of displacement response per each span

RMS value	Un-controlled	Passive off	Lyapunov control	Clipped-optimal control
Span A	2.2957	1.8120	1.4353	1.4192
Span B	6.3961	6.1218	5.0762	4.8566
Span C	1.3371	1.0195	1.1647	1.2091

Table 3. Comparison of relative displacement response between spans

RMS value	Un-controlled	Passive off	Lyapunov control	Clipped-optimal control
Span A-B	5.6434	5.4901	4.6410	4.2042
Span B-C	5.9909	5.7830	4.4509	4.4601

The Tables 1, 2, and 3 present the relation between the acceleration, displacement and relative displacement at the state of un-controlled, passive off, Lyapunov control algorithm, and clipped-optimal control algorithm. As seen in Table 1, the MR damping system applied with control algorithm reduced acceleration response more effectively than with un-controlled and passive conditions. Compared to the un-controlled condition in particular, it showed 70% reduction at maximum and 45% at minimum. As for displacement response, it showed 35% reduction at maximum and 10% at minimum compared to uncontrolled state. When compared to passive off, responses reduced on span A and B while they increased about 20% more on span C. However, these results are about RMS, but other responses related to pounding generally decreased. Finally, the relative displacement (RMS value) decreased when control algorithm was applied more than under un-controlled and passive-off state. Since relative displacement is directly related to the pounding between spans, its decrease means that pounding as much decreases.

5 Conclusions

In this paper, a MR damping system was proposed for control of earthquake response in a three-span bridge, and its effectiveness for vibration control was verified by means of experiment. It was made as a single system composed of three spans and two MR dampers connecting each two spans. For an experimental validation of the MR damping system for the mitigation of seismic responses, a total of four tests were carried out under three conditions: a un-control, a passive, and a control algorithm applied condition. All the test results regarding acceleration, displacement, and relative displacement were compared each other to validate the effectiveness of the MR damping system for the control of seismic responses. The conclusions were as follows:

The MR damping system was experimentally proven effective for the mitigation of vibration under seismic load such as acceleration, displacement, and relative displacement so that it was found applicable to real bridges, although its performance could vary depending on experimental conditions.

The two control algorithms adopted to facilitate the performance of the MR damping system were proven remarkably effective in mitigating acceleration, displacement, and relative displacement.

As seen above, the MR damping system proposed in this study was proven excellent in the control of seismic response of the three-span bridge by effectively checking its vibration.

Acknowledgments. This research was supported by National Research Foundation of Korea through funding from the Ministry of Education (Project Nos: NRF-2016R1A2A1A05005499 and NRF-2016R1A6A3A11931945). Many appreciation and acknowledgements go to the National Research Foundation who made this research possible.

References

1. Kasai, K., Maison, B.F.: Building pounding damage during the 1989 Loma Prieta Earthquake. Eng. Struct. **7**(19), 195–207 (1997)
2. Priestly, M.J.N., Seibe, F., Calvi, G.M.: Seismic Design and Retrofit of Bridges. Wiley, New York (1995)
3. Muthukumar, S., DesRoches, R.: A Hertz contact model with non-linear damping for pounding simulation. Earthq. Eng. Struct. Dynam. **35**, 811–828 (2006)
4. Won, J.H., Mha, H.S., Kim, S.H.: Effects of the earthquake-induced pounding upon pier motions in the multi-span simply supported steel girder bridge. Eng. Struct. **93**, 1–12 (2015)
5. Fan, Y.C., Loh, C.H., Yang, J.N., Lin, P.Y.: Experimental performance evaluation of an equipment isolation using MR dampers. Earthq. Eng. Struct. Dynam. **38**(3), 285–305 (2009)
6. Choi, H.-S., Kim, J.-W., Gong, Y.-I., Cheung, J.-H., Kim, I.-T.: Pounding characteristics of a bridge superstructure on rubber bearings. J. Earthq. Eng. Soc. Korea **15**(4), 13–21 (2011)
7. Tanabe, T., Machida, A., Higai, T., Matsumoto, N.: General view of the reasons for seismic damages for bridge piers and columns of elevated bridges at Hyogoken-Nanbu earthquake. Structural Engineering World Congress, T153-4 (1998)
8. Kajita, Y., Sugiura, K., Tsumura, Y., Maruyama, T., Watanabe, E.: Numerical analysis on the scenario of girder fall-off of simple span elevated bridge during strong ground motions. Fifth Pac. Struct. Steel Conf. **1**, 583–588 (1998)
9. Sheikh, M.N., Xiong, J., Li, W.H.: Reducing of seismic pounding effect of base-Isolated RC highway bridge using MR damper. Struct. Eng. Mech. **41**(6), 791–803 (2012)
10. Guo, A.X., Li, Z., Li, H., Ou, J.: Experimental and analytical study on pounding reduction of base-isolated highway bridges using MR dampers. Earthq. Eng. Struct. Dyn. **38**, 1307–1333 (2009)
11. Heo, G., Kim, C., Lee, C.: Experimental test of asymmetrical cable-stayed bridges using MR-damper for vibration control. Soil Dyn. Earthq. Eng. **57**, 78–85 (2014)
12. Leitmann, G.: Semiactive control for vibration attenuation. J. Intell. Mater. Syst. Struct. **5**, 841–846 (1994)
13. Dyke, S.J., Spencer Jr., B.F., Sain, M.K., Carlson, J.D.: Experimental verification of semi-active structural control strategies using acceleration feedback. In: Proceedings of 3rd International Conference on Motion and Vibration Control, vol. 3, pp. 291–296 (1996)

An Analytic Comparison Regarding Steady-State Damping Performance Between the Twin Rotor Damper and a Dynamic Vibration Absorber

Richard Bäumer(✉), Richard Terrill, and Uwe Starossek

Structural Analysis and Steel Structures Institute, Hamburg University of Technology, Hamburg, Germany
richard.baeumer@tuhh.de

Abstract. A novel active mass damper, the twin rotor damper (TRD), was presented in previous research, including control algorithms for monofrequent vibrations. In this paper, the steady-state damping performance is evaluated by applying a harmonic excitation force to a single degree of freedom (SDOF) oscillator with and without the action of the damping device. Using the velocity of the SDOF oscillator as feedback, adequate steady-state damping performance can be achieved with the TRD by setting the control force of the TRD in antiphase to the velocity of the SDOF oscillator. An analytic solution describing the steady-state damping performance is derived. The analytic solution allows for the comparison with a dynamic vibration absorber (DVA) of comparable size (stroke) and control mass. The analytic comparison shows that the TRD achieves greatly better damping performance than the DVA.

Keywords: Twin rotor damper · Active vibration control · Closed-loop control · Steady-state damping performance · Frequency-ratio dynamic-amplification relation · Dynamic vibration absorber

1 Introduction

Damping devices can be classified into passive, semi-active and active ones. The use of passive devices is quite common, e.g. in bridges. A semi active mass damper was recently applied to a bridge exposed to wind-induced vibrations [1, 2]. Active mass dampers have also been implemented in other structures, see [3, 4].

The twin rotor damper (TRD) is an active mass damper which implements the centrifugal forces of two eccentric masses. In a preferred mode of operation, the continuous rotation mode, these eccentric masses rotate with a mostly constant angular velocity in opposite directions about two parallel axes. In previous research, control algorithms were presented ensuring that the TRD operates in the continuous rotation mode. In this mode, it was shown that the TRD can damp monofrequent vibrations in an power-efficient manner, see [5, 6].

The steady-state damping performance is evaluated with help of dynamic-amplification frequency-ratio relations. For the TRD, an analytic solution was found.

© Springer International Publishing AG 2018
J.P. Conte et al. (eds.), *Experimental Vibration Analysis for Civil Structures*,
Lecture Notes in Civil Engineering 5, https://doi.org/10.1007/978-3-319-67443-8_48

It allows for a direct comparison of the steady-state damping performance with a dynamic vibration absorber (passive device).

In the following chapter, the layout and equations governing the dynamics of the TRD along with the steady-state response of a single degree of freedom (SDOF) oscillator subjected to a harmonic excitation force are presented. This information summarizes previous publications [5, 6]. Subsequently, the analytic solution for the steady-state response of a SDOF oscillator subjected simultaneously to an excitation force and the force of the TRD is derived and analyzed [7]. To compare the steady-state response of the TRD with the one of a dynamic vibration absorber (DVA), a DVA is introduced including corresponding tuning rules. Both devices are of equal size and control mass and are compared with each other. Finally, conclusions are drawn.

2 SDOF Oscillator

2.1 Twin Rotor Damper for SDOF Oscillator

As shown in Fig. 1, the TRD consists of two eccentrically rotating masses $0.5m_c$. They are each hinged by a massless rod with length r to two separate parallel axes. A massless rod with an eccentric mass forms a rotor. The angular position $\varphi(t)$ defines the motion of both rotors. In the continuous rotation mode, both control masses rotate with a constant angular velocity $\dot{\varphi}$; creating a radial force drawing away from the center of the axis. The dot operator indicates the time derivative. If, as indicated in Fig. 1, the angular position is equal, the radial force components normal to the displacement coordinate $x(t)$ cancel each other out and a control force

$$f_c(t) = m_c r \dot{\varphi}^2 \cos \varphi(t) \tag{1}$$

in the displacement direction $x(t)$ is created. In the continuous rotation mode, $\varphi(t)$ increases linearly with a slope equal to $\dot{\varphi}$, consequently, the control force is harmonic.

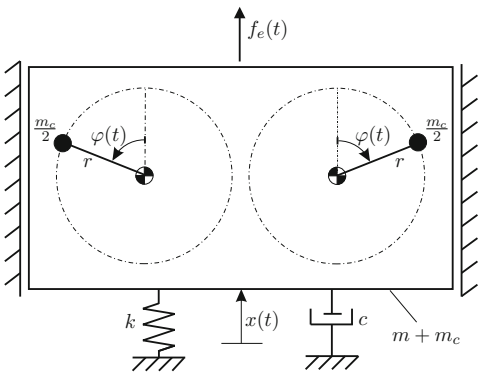

Fig. 1. Twin rotor damper for SDOF oscillator.

If the rotors are accelerated, tangential forces are additionally generated. In the continuous rotation mode, these tangential forces are to be kept as small as possible, for further information, see [5–7].

Applying the TRD to a SDOF oscillator, as shown in Fig. 1, the motion of the SDOF oscillator is governed by

$$(m+m_c)\ddot{x}(t)+c\dot{x}(t)+kx(t)=m_c r\dot{\varphi}\cos\varphi(t)+f_e(t) \tag{2}$$

in which $m+m_c$ is the total mass of the SDOF oscillator, c the damping coefficient, k the stiffness, $x(t)$ the displacement of the SDOF oscillator and $f_e(t)$ an excitation force. The forces on the left-hand side of Eq. (2) are referred to as system forces.

Dividing Eq. (2) by the total mass $m+m_c$ yields

$$\ddot{x}(t)+2\xi\omega_n\dot{x}(t)+\omega_n^2 x(t)=\mu_c r\dot{\varphi}^2\cos\varphi(t)+F_e(t) \tag{3}$$

in which the damping ratio ξ, the natural frequency ω_n, the mass ratio μ_c are given by the following relations [8, 9]:

$$c(m+m_c)^{-1}=2\xi\omega_n;\omega_n^2=k(m+m_c)^{-1};\mu_c=m_c(m+m_c)^{-1} \tag{4}$$

Furthermore, a normalized harmonic excitation force is given by

$$F_e(t)=F_0\cos(\omega_e t) \tag{5}$$

with the excitation frequency ω_e and the amplitude F_0 is assumed.

2.2 Uncontrolled Steady-State Response of SDOF Oscillator

Information regarding the uncontrolled steady-state response of SDOF oscillators can be found in many textbooks, see e.g. [8, 9]. A solution is presented here as it allows for a simple derivation of the steady-state response with the TRD. The particular displacement response, $x_p(t)$, of a SDOF oscillator under harmonic excitation is

$$x_p(t)=A_u\cos(\omega_e t-\theta) \tag{6}$$

in which A_u is the displacement amplitude and θ the phase the displacement lags behind the excitation. As shown in [8, 9], A_u and θ are as given by the following equation [8, 9]:

$$A_u=F_0\left[\left(\omega_n^2-\omega_e^2\right)^2+\left(2\xi\omega_n\omega_e\right)^2\right]^{-0.5};\theta=\operatorname{atan2}\left(2\xi\omega_n\omega_e,\omega_n^2-\omega_e^2\right) \tag{7}$$

Introducing the frequency ratio η and the (dimensionless) dynamic amplification D,

$$\eta=\omega_e\omega_n^{-1}D=A_u\omega_n^2F_0^{-1} \tag{8}$$

multiplying A_u of Eq. (7) with $\omega_n^2 F_0^{-1}$ and doing some rearrangements gives [8, 9]:

$$D = \left[\left(1-\eta^2\right)^2 + (2\xi\eta)^2\right]^{-0.5}; \theta = \text{atan2}\left(2\xi\eta, 1-\eta^2\right) \tag{9}$$

3 Controlled Steady-State Response

3.1 Analytic Derivation

In the following, the analytic solution for the controlled steady-state response is presented. This is a summary of a previous theoretical work [7]. Therefore, Eq. (3) is reconsidered and it is assumed that the angular velocity is constant and equal to the forcing frequency ω_e:

$$\dot{\varphi} = \omega_e \tag{10}$$

This assumption is further discussed in [7]. Inserting Eq. (10) into Eq. (3) gives:

$$\ddot{x}(t) + 2\xi\omega_n\dot{x}(t) + \omega_n^2 x(t) = \mu_c r\omega_e^2 \cos\varphi(t) + F_e(t) \tag{11}$$

The second term on the left-hand side of Eq. (11) is the normalized inherent damping force of the SDOF oscillator. This inherent damping force works in antiphase to the velocity of the SDOF oscillator. The control algorithm presented in [5] is used to ensure that the control force of the TRD is also in antiphase to the velocity of the SDOF oscillator. Taking this into consideration, the control force can be brought of the left-hand side of Eq. (11) as a function of the velocity $\dot{x}(t)$. This is done by, firstly, taking the time derivative of Eq. (6):

$$\dot{x}_p(t) = -A_c\omega_e \sin(\omega_e t - \theta_c) \tag{12}$$

in which A_u was replaced by the unknown controlled displacement A_c and θ by the unknown controlled phase θ_c. Both A_c and θ_c are derived further on. Secondly, dividing Eq. (12) by the absolute value of its amplitude $A_c\omega_e$ and multiplying it with the amplitude $\mu_c r\omega_e^2$ of the control force (first term on the right-hand side of Eq. (11)), the control force is now expressed as a function of the velocity on the left-hand side of Eq. (11), see the following equation:

$$\ddot{x}(t) + \left[2\xi\omega_n + \mu_c r\omega_e A_c^{-1}\right]\dot{x}(t) + \omega_n^2 x(t) = +F_e(t) \tag{13}$$

Equation (13) is only valid if a control algorithm is available ensuring that the control force and the velocity of the SDOF oscillator are in antiphase. Comparing the differential equations describing the uncontrolled and the controlled responses, see Eqs. (3) and (13), it becomes evident that the following substitution is needed:

$$2\xi\omega_n \rightarrow 2\xi\omega_n + \mu_c r\omega_e A_c^{-1} \tag{14}$$

Applying the substitution of Eq. (14) to the uncontrolled solution of Eq. (7) gives the following two expressions for the previously unknown controlled displacement amplitude A_c and the controlled phase θ_c [7]:

$$A_c = F_0\left[\left(\omega_n^2 - \omega_e^2\right)^2 + \left(2\xi\omega_n\omega_e + \mu_c r\omega_e^2 A_c^{-1}\right)^2\right]^{-0.5} \tag{15}$$

$$\theta_c = \operatorname{atan2}\left[\left(2\xi\omega_n + \mu_c r\omega_e A_c^{-1}\right)\omega_e, \omega_n^2 - \omega_e^2\right] \tag{16}$$

Note that θ_c is now a function of A_c. Therefore, Eq. (15) must be solved for first for A_c. Rearranging Eq. (15) yields:

$$\left[\left(\omega_n^2 - \omega_e^2\right)^2 + (2\xi\omega_n\omega_e)^2\right]A_c^4 + 4\xi\omega_n\omega_e^3\mu_c r A_c^3 + \left[\left(\mu_c r\omega_e^2\right)^2 - F_0^2\right]A_c^2 = 0 \tag{17}$$

The trivial solutions of Eq. (14) are not of interest. A quadratic equation remains. It provides two non-trivial solutions for A_c, which are

$$A_c = \left\{-2\xi\omega_n\omega_e^3\mu_c r \pm \left[F_0^2\left(\left(\omega_n^2 - \omega_e^2\right)^2 + (2\xi\omega_n\omega_e)^2\right) - \left(\mu_c r\omega_e^2\right)^2\left(\omega_n^2 - \omega_e^2\right)^2\right]^{0.5}\right\}\left[\left(\omega_n^2 - \omega_e^2\right)^2 + (2\xi\omega_n\omega_e)^2\right]^{-1} \tag{18}$$

As done for the uncontrolled steady-state response, the controlled dynamic amplification is introduced:

$$D_c = A_c\omega_n^2 F_0^{-1} \tag{19}$$

Multiplying Eq. (18) with $\omega_n^2 F_0^{-1}$, using Eq. (8) and doing some further rearrangements gives the expression for the controlled dynamic amplification [7]:

$$D_c = \left\{-2\xi\eta^3\omega_n^2\mu_c r F_0^{-1} \pm \left[\left(1-\eta^2\right)^2 + (2\xi\eta)^2 - \left(\mu_c r\omega_n^2\eta^2 F_0^{-1}\right)^2\left(1-\eta^2\right)^2\right]^{0.5}\right\}\left[\left(1-\eta^2\right) + (2\xi\eta)^2\right]^{-1} \tag{20}$$

3.2 Oscillator with Inherent Damping

In the following, the SDOF oscillator with inherent damping is considered. Introducing the dimensionless parameter

$$K_1 := \omega_n^2\mu_c r F_0^{-1} \tag{21}$$

Equation (20) can be written in a more compact form

$$D_c = \left(C_1 \pm C_2^{0.5}\right) C_3^{-1} \tag{22}$$

with the frequency-ratio dependent terms

$$\begin{aligned} &C_1 = -2\xi\eta^3 K_1, C_2 = \left(1-\eta^2\right)^2 + (2\xi\eta)^2 - \left(K_1\eta^2\right)^2\left(1-\eta^2\right)^2, \\ &C_3 = \left(1-\eta^2\right) + (2\xi\eta)^2 \end{aligned} \tag{23}$$

If $D_c > 0$, then $A_c > 0$ as $\omega_n > 0$ and $F_0 > 0$, see Eq. (21) [7]. For $A_c > 0$, the TRD contributes positive active damping, see second term on the left-hand side of Eq. (13). Otherwise, the control force of the TRD would be in phase with the velocity of the SDOF oscillator, consequently, the TRD would give negative active damping to the SDOF oscillator. To ensure that $D_c > 0$, Eqs. (22) and (23) must be analyzed further. As can be seen from Eq. (23), $C_1 < 0$. Therefore, the plus sign in Eq. (22) must be used to achieve that $D_c > 0$. However, it is still possible that the nominator of Eq. (22), $C_1 + C_2^{0.5}$, is negative if $C_2^{0.5} < C_1$ [7]. At $\eta = 0$, the nominator is equal to one. When η is increased, the nominator remains positive and real until the border frequency η_b is reached. It is assumed that η_b is reached when the control force amplitude $\mu_c r\omega_e^2$ is equal to the amplitude of the excitation force F_0 [7]. Note that $\mu_c r\omega_e^2$ increases with η, whereas F_0 is constant over η. Setting these amplitudes equal yields:

$$\mu_c r\omega_e^2 = F_0 \tag{24}$$

Rearranging Eq. (24) with Eqs. (8) and (21) and replacing η by the border frequency ratio η_b gives [7]:

$$\eta < \eta_b = K_1^{-0.5} \tag{25}$$

By varying the parameters according to the ranges given in the following equations

$$\eta < \eta_b, 0 < \xi < 1, K_1 > 0 \tag{26}$$

it can be shown numerically that the numerator of Eq. (22), $C_1 + C_2^{0.5}$, is greater than zero. Therefore, D_c is, as desired, greater than zero. By inserting the border frequency ratio of Eq. (25) into Eq. (23) and, subsequently, into Eq. (22), it follows: $D_c(\eta = \eta_b) = 0$. With help of Eqs. (8), (19) and (21), the controlled phase θ_c of Eq. (16) can be written as follows:

$$\theta_c = \operatorname{atan2}\left[2\xi\omega_n + K_1\eta^2 D_c^{-1}, 1-\eta^2\right] \tag{27}$$

The uncontrolled ($K_1 = 0$) and the controlled dynamic amplification D_c and corresponding phases θ_c are plotted in Fig. 2.

As $\eta \to \eta_b$, the phase θ_c approaches 0.5π and D_c goes to zero, see Fig. 2. If $D_c \to 0$, $A_c \to 0$. Consequently, the control force goes to infinite, see second term on

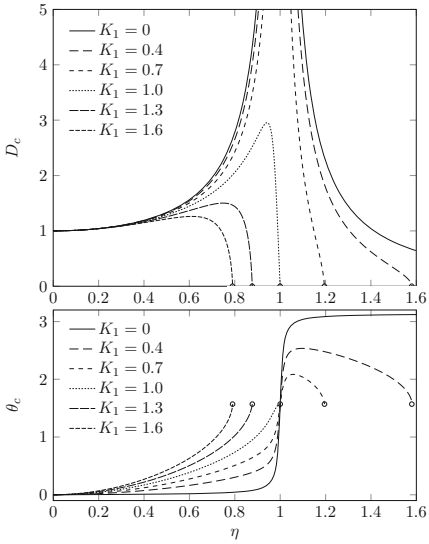

Fig. 2. Controlled dynamic amplification D_c and phase θ_c plotted against frequency ratio η for $\xi = 0.01$ and for several different values of K_1 [7].

the left-hand side of Eq. (13). As this corresponds to a non-realistic state, these points were excluded from the solutions shown in Fig. 2 [7]. The presented analytic solutions were validated experimentally in [7].

4 Comparison of Steady-State Damping Performance with Dynamic Vibration Absorber

In the following, the steady-state damping performance of the TRD is compared with the one of a dynamic vibration absorber (DVA). The DVA was invented by Frahm and is a passive damping device [19]. Its theory is explained briefly in the following; for more details, see [11, 12]. A SDOF oscillator equipped with a DVA as shown in Fig. 3 is considered. The main mass m is attached to the frame by a spring and a damping element. As before, k and c refer to the stiffness of the spring and the damping coefficient of the damping element, respectively. The coordinate $x(t)$ describes the motion of m. A control mass m_c is attached to the main mass by a spring with the stiffness k_2 and a damping element with the damping coefficient c_2. The control mass m_c with the spring and the damping element represents the DVA. The relative motion between m and m_c is described by $r_d(t)$. A harmonic excitation $f_e(t)$ acts on the mass m.

Establishing the dynamic equilibrium and performing some rearrangements yields the displacement amplitude A_{0d} of the main mass and the relative displacement amplitude A_{0r} [11, 12]. Normalizing these displacement amplitudes, as done for the TRD, yields the controlled dynamic amplification D_d of the DVA and $A_{0r}\omega_n^2 F_0^{-1}$

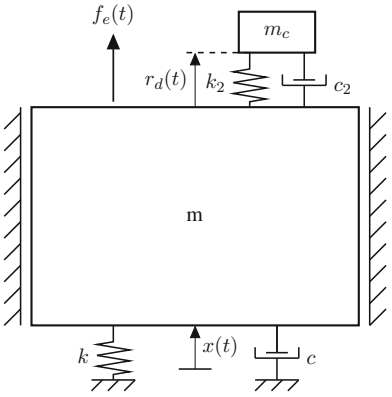

Fig. 3. Dynamic vibration absorber [11, 12].

$$D_d = A_{0d}\omega_n^2 F_0^{-1} = \left[\left(g_1^2 + g_2^2\right)\left(g_3^2 + g_4^2\right)^{-1}\right]^{0.5}, \quad A_{0r}\omega_n^2 F_0^{-1} = \left[\eta^4\left(g_3^2 + g_4^2\right)^{-1}\right]^{0.5} \tag{28}$$

with the following terms

$$g_1 = \eta^2 - \kappa^2, g_2 = 2\eta\kappa\xi_2 \tag{29}$$

$$\begin{aligned} g_3 &= \eta^4 - \eta^2\left(1 + \kappa^2 + \mu\kappa^2 + 4\kappa\xi\xi_2\right) + \kappa^2, \\ g_4 &= \eta\left[2\xi_2\left(\kappa^2 - \eta^2\right) + 4\kappa\xi_2\left(1 - \eta^2 - \mu\eta^2\right)\right] \end{aligned} \tag{30}$$

in which the frequency ratio κ, the damping ratio ξ_2, the mass ratio μ_2, the frequency ratio η and the damping ratio ξ are given by the following equations [11, 12]:

$$\kappa = \omega_2\omega_m^{-1} \text{ with } \omega_m = \left(km^{-1}\right)^{0.5}, \ \xi_2 = c_2(2m_c\omega_2)^{-1} \text{ with } \omega_2 = \left(k_2 m_c^{-1}\right)^{0.5} \tag{31}$$

$$\mu_2 = m_c m^{-1}, \eta = \omega_e\omega_m^{-1}, \xi = c(2m\omega_m)^{-1} \tag{32}$$

In Eq. (32), the frequency ratio η was surreptitiously set equal to the one introduced in Eq. (8), which considers ω_n according to Eq. (4) instead of ω_m according to Eq. (31). The difference is that ω_n considers the inertial forces induced by the total mass $m + m_c$, whereas ω_m considers only the inertial forces induced by the main mass m. As the control masses are usually small in comparison to the main mass, it can be assumed that $m \approx m + m_c$. Consequently, the frequency ratio η of Eqs. (8) and (31) are equal. The discussion for η also holds for ξ, see Eqs. (4) and (32).

The mass ratio μ_2 of Eq. (32) differs from the mass ratio μ_c of Eq. (4). By solving the mass ratio μ_2 for m_c and inserting this into Eq. (4), a relation between μ_2 and μ_c can be established:

$$\mu_c = \mu_2(1+\mu_2)^{-1} \tag{33}$$

According to [11, 12], the optimal frequency ratio κ_o and the optimal damping ratio $\xi_{2,o}$ are

$$\kappa_o = (1+\mu_2)^{-1}, \xi_{2,o} = \left\{3\mu_2\left[8(1+\mu_2)^3\right]^{-1}\right\}^{0.5} \tag{34}$$

Before discussing Fig. 4, the parameters forming the basis for the curves are explained. The damping ratio ξ and the mass ratio μ_2 are input parameters. With the given μ_2, the optimal values for κ and ξ_2 can be calculated according to Eq. (34). Using Eqs. (28) to (32), the dynamic amplification D_d and $A_{0r}\omega_n^2 F_0^{-1}$ can be computed for the DVA. The frequency ratio η is varied in the range in which D_d becomes relatively large. In the lower subdiagram of Fig. 4, the peak value for $A_{0r}\omega_n^2 F_0^{-1}$ can be read off. A_{0r} corresponds to half of the stroke required for the DVA. To ensure comparability regarding size between the TRD and the DVA, the peak value of A_{0r} is set equal to r, see Fig. 1. Therefore: $\max\left(A_{0r}\omega_n^2 F_0^{-1}\right) = r\omega_n^2 F_0^{-1}$. By calculating the mass ratio μ_c for the TRD according to Eq. (33), an equivalent parameter K_1 for the TRD can be calculated with Eq. (21). This equivalent parameter ensures that the TRD and the DVA have same size and control mass. D_c can then be calculated with Eq. (22) using the terms of Eq. (23).

Figure 4 shows that the TRD has a better steady-state damping performance than a DVA of comparable size and control mass. In addition, the TRD does not make the frequency range, in which relatively large dynamic amplification occurs, wider. However, by increasing the inherent damping, the advantage of the TRD over the DVA becomes less, see Fig. 5, in which D_d and D_c are shown for different damping ratios. Both figures show that the TRD lowers steady-state vibrations more effectively than a DVA of comparable size and control mass.

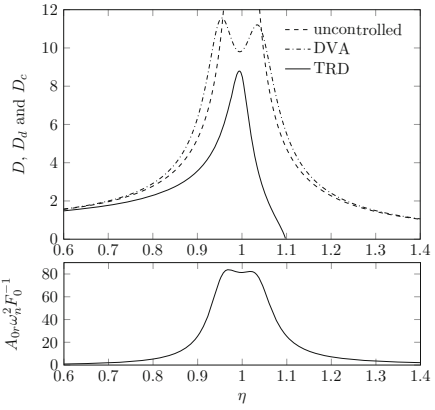

Fig. 4. Dynamic amplifications D_d (DVA) and D_c (TRD) and normalized relative displacement amplitude $A_{0r}\omega_n^2 F_0^{-1}$ in steady-state for $\mu_2 = 0.01$ and $\xi = 0.01$.

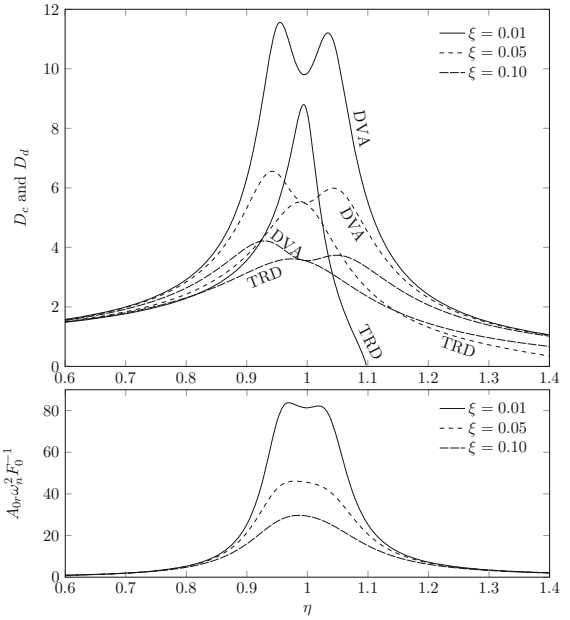

Fig. 5. Dynamic amplifications D_d (DVA) and D_c (TRD) and normalized relative displacement amplitude $A_{0r}\omega_n^2 F_0^{-1}$ in steady-state for $\mu_2 = 0.01$ for different ξ.

5 Conclusions

An active mass damper, the twin rotor damper (TRD), is presented. It consists of two eccentric control masses, which rotate in a preferred mode of operation with a constant angular velocity about two parallel axes in opposite directions. Each control mass creates a centrifugal force, which results, under some further constraints, into a harmonic control force. This harmonic control force is used to mitigate steady-state vibrations of a single degree-of-freedom oscillator, which is under harmonic excitation.

An analytic solution, which describes the steady-state damping performance of the TRD was found. It allows for a comparison with a dynamic vibration absorber (DVA) of comparable size (stroke) and control mass. If the DVA is used, the SDOF oscillator changes to a two-degree-of-freedom oscillator. This produces two lower peaks in the frequency-ratio dynamic amplification diagrams. In contrast to this, the TRD uses the inertial forces of two eccentrically rotating masses. It reduces the dynamic amplification over all frequencies. As the control force increases quadratically with frequency, the TRD can completely damp out vibrations above a certain ratio (border frequency ratio). The analytic comparison shows that the TRD achieves greatly better damping performance than a DVA of comparable size and control mass.

A DVA is usually tuned to a single frequency and this frequency cannot be altered easily. In contrast to this, the frequency ratio to which the TRD is tuned can be easily adapted.

References

1. Butz, C., Fobo, W.: Efficiency of passive and adaptive tuned mass dampers for Volgograd bridge. In: Proceedings of the 10th Japanese German Bridge Symposium, Munich, Germany (2014)
2. Benicke, O., Butz, C.: Volgograd-bridge: efficiency of passive and adaptive tuned mass dampers. In: Structural Engineering: Providing Solutions to Global Challenges, IABSE Conference Geneva, Switzerland (2015)
3. Kobori, T., Koshika, N., Yamada, K., Ikeda, Y.: Seismic-response-controlled structure with active mass driver system. Part 1: design. Earthq. Eng. Struct. Dyn. **20**(2), 133–149 (1991)
4. Kobori, T., Koshika, N., Yamada, K., Ikeda, Y.: Seismic-response-controlled structure with active mass driver system. Part 2: verification. Earthq. Eng. Struct. Dyn. **20**(2), 151–166 (1991)
5. Bäumer, R., Starossek, U.: Active vibration control using centrifugal forces created by eccentrically rotating masses. J. Vib. Acoust. ASME (2016). doi:10.1115/1.4033358
6. Scheller, J.: Power-efficient active structural vibration control by twin rotor dampers. Ph.D. Thesis, Hamburg University of Technology, Hamburg, Germany (2013)
7. Bäumer, R., Starossek, U.: Closed-form steady-state response solution of the twin rotor damper and experimental validation. J. Vib. Acoust. ASME (2016). doi:10.1115/1.4035134
8. Inman, D.: Engineering Vibration. Prentice Hall, Englewood Cliffs (1994)
9. Clough, R., Penzien, J.: Dynamics of Structures. McGraw-Hill, New York (2004)
10. Frahm, H. (1909). Device for damping vibrations of bodies, U.S. Patents No. 989958 A
11. Peterson, C.: Dynamik der Baukonstruktionen. Vieweg, Braunschweig (2000)
12. Den Hartog, W.: Mechanical Vibrations. McGraw-Hill, New York (1956)

Design of Test Setup for Prototype Testing of Base Isolators

Shiv Dayal Bharti[1(✉)], Mahendra Kumar Shrimali[1], Arnav Anuj Kasar[2], and Tushar Kanti Datta[2]

[1] Department of Civil Engineering, Malaviya National Institute of Technology, Jaipur, Rajasthan, India
sdbharti@mnit.ac.in
[2] National Center for Disaaster Mitigation and Management, Malaviya National Institute of Technology, Jaipur, Rajasthan, India

Abstract. A seismic isolation test facility is being developed at National Centre for Disaster Mitigation and Management in Malaviya National Institute of Technology Jaipur, India for characterisation of prototype elastomeric seismic isolation bearings. The maximum dimensions of bearings envisaged are 1000 mm × 1000 mm in plan and 700 mm height, subjected to constant compression and cyclic shear. The amplitude of vertical compression load may go up to 10,000 kN, while, for cyclic shear, it may go up to 1000 kN. The test specimen, that is, isolator, shall be subjected to the anticipated vertical load; to which it will be subjected due to the presence of superstructure. The test rig is designed as a self-equilibrating steel frame. The loads are to be applied using servo valve based hydro-electric actuators. Real time data acquisition system using electronic instrumentation system is to be used in order to acquire force and deformation readings. The force-deformation hysteresis curves, for characterisation of base isolation systems, are to be obtained for effective application of bearings. The test setup is capable to carry out characterisation of seismic bearings as per standard test protocols.

The system has been designed using mechanics based hand calculation, and also analysed using standard finite element analysis software packages. The controlling design parameters selected are- maximum elastic deformation and von Mises stresses. The analyses have been carried under various combinations of vertical (compressive) and horizontal (shear) forces. The test rig has been designed as stiffness controlled system. The designed members of the test rig include: horizontal beam member, column members and base box. The test rig is resting over a stiff concrete pedestal. The concrete base has been designed to resist the forces anticipated during the testing.

Further, a reliability analysis is performed considering the uncertainties in loading, material and geometry, to cater a few of the design uncertainties. The design is then optimized with respect to a certain specified reliability. Furthermore, the design has been carried out such that the frame may be used, in future, for cyclic testing of other specimens under vertical and horizontal loading.

Keywords: Base isolation · Prototype testing · Test rig · Self-equilibrating · Reliability

© Springer International Publishing AG 2018
J.P. Conte et al. (eds.), *Experimental Vibration Analysis for Civil Structures*,
Lecture Notes in Civil Engineering 5, https://doi.org/10.1007/978-3-319-67443-8_49

1 Introduction

Base isolation for seismic protection of buildings is now one of the most widely used passive devices and it has become one of the most proven technologies for seismic response control. Standard base isolation devices namely, Lead Rubber Bearing system (with or without lead core), friction Pendulum System etc. Friction isolators including simple friction devices are routinely manufactured, tested and employed for isolating all types of civil amenities. Most of the important buildings and specialty structures are currently provided with base isolation systems of one kind or the other. Seismic design codes of the USA, New Zealand, Europe and Canada provide clear guidelines for the design of base isolated buildings, which also provides the specifications for different types of isolators to be used. It is almost mandatory in all codes that the isolators to be used should be tested to conform to the guidelines prescribed in the codes, prior to their installation. As a consequence, industries manufacturing different types of isolation devices have prototype testing facilities integrated to their manufacturing process. Alternatively, the isolators may be prototype tested by National level testing facilities like National Centers for Earthquake Engineering and University testing Setup. Because of the development of sophisticated software, measurement devices and actuation units, the test facilities have high precision, adjustability and versatility. In India, current state of are of construction of base isolated buildings is to procure these base isolators, manufactured and tested abroad. With this background, and initiative has been taken up, in the National Center for Disaster Mitigation and Management at Malaviya National Institute of Technology Jaipur, to create a full scale base isolator testing facility which is indigenously manufactured in collaboration with identified industries in the country. For this purpose, the two-fold task at hand are the design of base isolators to be manufactured and the design of test rig, in which the test setup will be installed. Presently, Laminated Rubber bearing, with and without lead core, is in focus and test setup will be operating with servo-valve based hydraulic actuators. Real time data acquisition using electronic control system will be used to obtain force and deformation data. The testing will conform to international prototype test protocols.

In this paper, the design of test rig is presented. A brief outline of the complete test setup is also illustrated with the help of schematic diagrams. The system has been designed using mechanics based hand calculation and has also been analysed using standard finite element software package. Some of the international test facilities for base isolation devices are mentioned in Annexure-I. It can be seen from the existing test facilities that the self-equilibrating test rigs is most favored platform to support the actuation system.

1.1 Test Setup

In this paper, the design and analysis of a large capacity self-equilibrating integrated steel frame is presented, such that elastic deformations as well as stresses are within permissible limits. A stiffness base design procedure has been adopted for design stipulations. The rig comprises of one main girder, two vertical members, one stub member and base plate. The vertical members of the frame are designed to resist a force of 10 MN vertical direction without exceeding an axial deformation of 1 mm.

The main horizontal member of the frame has been designed to resist a horizontal force of 1 MN with the elastic transverse deformation limited to 1 mm. The excitation frequency of the frame has been limited to 25 Hz and the connections are designed to transfer the loads safely. The Table 1 below lists the various components of the test rig, and the nature of predominant forces, each of them will be subjected to.

Table 1. Primary components of test rig.

S. N.	Member	Function	Predominant force
1.	Vertical Member	Transfer Beam forces to Base	Axial and Flexure
2.	Horizontal Member	Vertical Load Application	Combined Flexure and Shear
3.	Connections	Transfer of forces	Axial and Shear
4.	Anchor bolts	Proper anchorage	Pull and Shear

1.2 Components of Test Rig

The dimension of the components of the test rig has been decided on the basis of the overall size of the frame along with the individual stiffness of the components of the frame. A thorough review of literature about the various test rigs installed in the major isolation testing centers (like Rockwell International Energy Technology Engineering Centre, Canoga, California; Dynamic Isolation System Inc. Berkeley; Earthquake Research Centre University of California Berkeley, Richmond, California) [1–6] has been carried out. For the design of load frames, primary consideration is to limit the deflections of the frame to the minimum, which requires that the members of the frame shall have sufficient stiffness. The loads considered for the sign of the members are 10000 kN in vertical directions and 5000 kN in horizontal direction.

The daylight space requirement has been estimated on the basis of the size of a full scale laminated rubber base isolator along with the length of actuators which are to be mounted in the frame. The typical dimensions of actuators and base isolators as obtained by the industry partners are used for estimation of dimensions of the frame. The schematic of the arrangement of the components of the test rig has been shown in Fig. 1. The preliminary design of the components of the frame has been carried out manually [7–9].

1.2.1 Horizontal Member

The span requirements of horizontal member is nearly 2.3 m. To keep the displacements of the member below 1 mm, the depth and width required for the member are 1 m and 1.5 m respectively. The connections are end connections are designed to safely transfer the reactions safely to the vertical member. The relationships used for estimation of deflection of the members considers both the flexural and shear deflections. The thicknesses of all the plates required are estimated to be 40 mm. The thickness estimation takes into consideration the prevention of local buckling of the member. To reinforce the joint between the horizontal member and the vertical members, Rib Plates are provided to smoothen the flow of forces between the two members. The total deflection of the member will be

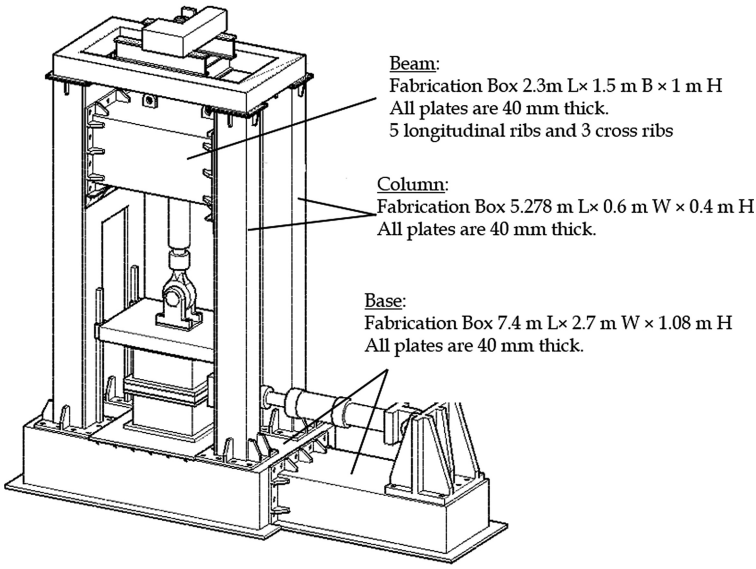

Fig. 1. Schematic view of test rig

$$\Delta = \frac{P'L^3(1+\alpha)}{24EI},$$

where, P' is the effective factored load acting on the beam, given as $P' = \left(\frac{P}{2} + \frac{WL}{2}\right)$, where P is the factored external (vertical) force anticipated on the member and W is the self-weight per unit run of the member, L' is the effective length of the member, and is equal to half of the span of the member, α is the shear deflection coefficient given by $\alpha = \frac{12EI}{GAL^2}$. The total deflection of the member under a vertical force of 10000 kN is 0.5 mm, which is well below the target deflection of the member. A schematic view of the horizontal member is shown in Fig. 2.

1.2.2 Vertical Member

The vertical member has been designed to support the vertical forces and transfer then safely to the base of the frame. The main horizontal member is designed to be supported by four vertical members. As the frame is designed to be self-equilibrating, these members plays a critical role in efficient functioning of the frame. The overall height requirements of the frame, as anticipated on the basis of dimensions of the equipment and specimen to be housed in the frame, is 5.2 m. This height is the effective length of the frame member. As the primary force in this member is axial in nature, the axial displacements of the frame serves as the design criteria. On the basis of modulus of elasticity and moment of inertia of the members, the cross-sectional dimensions of the members are estimated. The width and depth of each member as obtained through

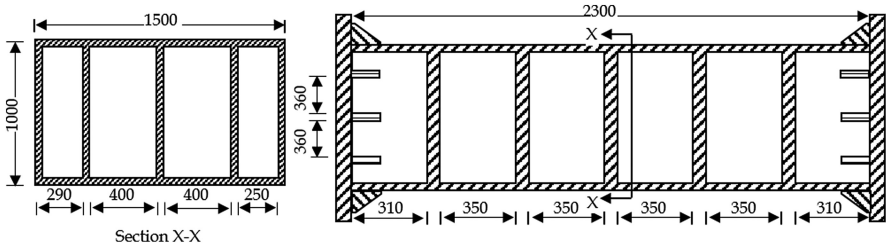

Fig. 2. Details of the primary horizontal member

manual design are 0.6 m and 0.4 m respectively. The thickness of the plates used for the members is 40 mm, to ensure safe transfer of forces. The deflections are checked using the elastic deflection criteria as

$$\Delta = \frac{RH}{A_s E},$$

where, R is half of the reactions from the horizontal member, H is the effective height of the member, A_s is the effective cross-sectional area of the member and E is the modulus of elasticity of the member.

On the basis of manual design calculations, the overall deflection of each vertical members is limited to 0.6 mm, which is well below the target deflection limit of 1.0 mm. The face of the vertical members towards the specimen are connected by a plate of 40 mm thickness. However, a cut out of 3 m × 0.8 m in the column plates (both sides) has been provided to house the horizontal actuator.

1.2.3 Base Box

The base box of the frame has been designed to support the various components of the loading frame. The primary function of the base box is to ensure effective and efficient distribution of forces among the members at all times. The base box is designed to undergo marginal deflection under the working loads and to maintain equilibrium among the members of the frame. The base T – slot arrangements in the bed (5 slots at 500 mm pitch). Figure 3 below gives the detailed drawing of the base box. The preliminary design of the base box has been carried out manually.

In order to assess the performance of the manually designed test rig, a finite element model pf the test rig has been generated, and a complete finite element analysis of the test rig has been generated in ABAQUS. A detailed finite element analysis of the test rig under the actual loading conditions has been carried out and the results of the analysis are presented here.

To determine the optimum design of the testing frame, Nonlinear Finite Element Analyses has been carried out for various design configurations. The basis for determination of design configurations is to attain minimum overall deformation of the testing frame. Finite Element Analysis software package ABAQUS is used to model the frame. The various structural components of the frame are independently modelled and assembled to generate the overall frame geometry. The model prepared is then

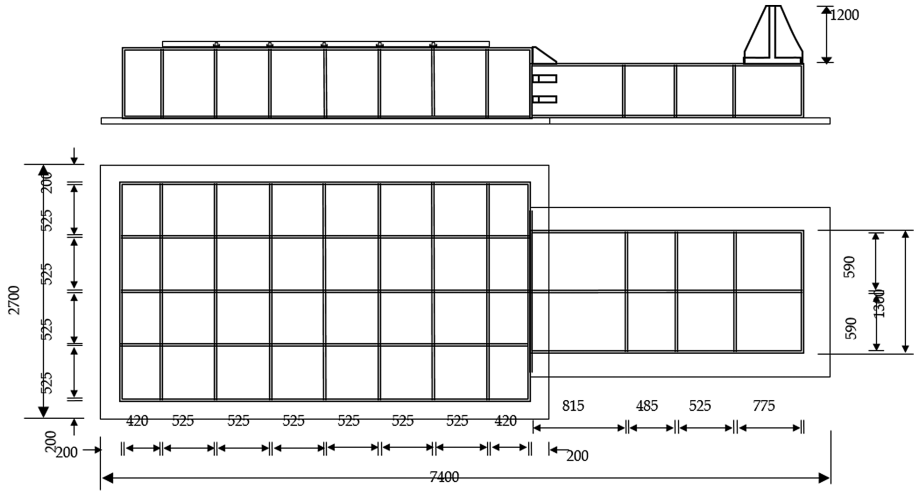

Fig. 3. Details of the base plate

meshed using the C3D8R (eight nodded linear brick elements with reduced integration) and C3D6 (six nodded liner triangular prism). The members are of ASTM A36 grade steel with isotropic hardening model (yield stress of 250 MPa and ultimate stress of 415 MPa). Welds between beam and column of subassemblage are modelled as Complete Joint Penetration (CJP) welds.

For both the materials, modulus of elasticity and Poisson's ratio are 200GPa and 0.260, respectively.

A classically isotropic plasticity model based on von Mises yield criteria and associated plastic flow is used to incorporate material nonlinearity. The number of triangular ribs was changed in each configuration to control the deformation in horizontal member and to provide more weld length so that we can reduce the size of weld. The total number of configuration analyzed was five with different number of triangular ribs which are shown in Fig. 3.

Loading: Pressure loading in different combination was applied at soffit of horizontal member over 1 sq. area in upward direction and the same load was applied on steel base plate in downward direction symmetrically. Pressure load was applied at 1.5 m height in lateral direction at column.

Frame is analyzed and designed for the considered loads and their combinations. Figure 4 shows the von Mises and Shear Stress contours of the analysed frame. The stresses generated are well within the elastic limit of the material. This shows that the designed sections are safe and are expected to perform satisfactorily. The maximum flexural stresses are developed in the horizontal member and is in the range of 38 MPa. However, the maximum shear stresses are developed at the junction of horizontal member and vertical member, and are of the order of 52kN. Initially sections are assumed as per IS code and they are analyzed statically using Abaqus The results were once again checked manually using conventional analysis procedures as per IS codes.

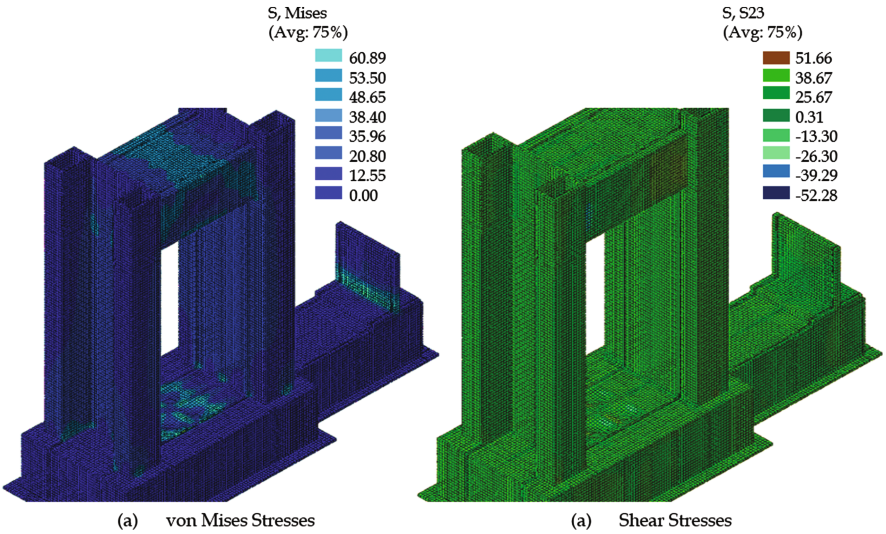

Fig. 4. Results of finite element analysis (Stress Contours) of the test rig

1.3 Reliability Analysis

A reliability analysis of the designed test rig is performed using first order second moment theory (A4SM). For the analysis the uncertainties in material, geometry and loading are considered. The uncertain parameters are assumed to be log-normally distributed. A probabilistic Risk Analysis (PRA) method developed by Sinhozuka is adopted for obtaining the probability of failure of the critical sections of test rig. The analysis has been carried out for the section having the highest concentration of stresses. It has been assumed the failure occurs when the stresses at any section is equivalent to the yield stress of the material (250 MPa, for steel). On the basis of the results of finite element analysis of the rig, the maximum stress occurs at the mid span of the main horizontal member of the rig. Assuming that R is the capacity of the structure (yield stress) and S is the response to an action (resultant stress), and also that both the yield and the resultant stresses are log-normally distributed, the probability of failure, as per PRA method is defined as:

$$p_f = P\left[\left(\frac{R}{S}\right) < 1\right]$$

If Z is the ratio of R and S in the log-normal space, then the probability of failure is defined as:

$$p_f = P[(Z) < 1] = \phi(\beta),$$

and $\beta = \frac{\ln(1/Z)}{\sigma_{\ln Z}}$.

Let $\tilde{Z}$ be the median and $\sigma_{\ln Z}$ be the standard deviation of *ln(Z)* which are defined as: $\tilde{Z} = \frac{\tilde{R}}{\tilde{S}}$ and $\sigma_{\ln Z} = \sqrt{\sigma_{\ln R}^2 + \sigma_{\ln S}^2}$,

where $\tilde{R}$ and $\tilde{S}$ are medians of distribution of R and S respectively. As, among the considered cases, the R values varies between *210* MPa and *300* MPa, while the S values varies between *30* MPa to *45* MPa, the value of variable β will be -3.33. Using the standard table for log-normal probability distribution, the probability of failure p_f is 4.834×10^{-4}.

Thus, the probability of failure of the most critical section will be of the order of approximately 10^{-3}.

2 Conclusions

A prototype testing facility for base isolators, indigenously manufactured in India is described. The design of the test rig supporting the actuation device is providing the specifications considered while designing the rig. Finite Element Analyses of the full scale model of test rig has been carried out to verify the design. It is shown that the maximum stresses developed in the designed rig under slow cycle testing of base isolators varies between 30 to 45 MPa, which is well within the elastic limit of material. A reliability analysis of the designed test rig shows that the probability of failure of the test rig is of the order of 10^{-3}.

Acknowledgments. The authors acknowledge the Department of Science and Technology – Technology Systems Development for providing financial support for the project entitled 'Indigenous Design and Development of Prototype Base Isolation Systems'. The kind technical inputs provided by our industry partners id also appreciated.

References

1. Rogerio, B., Vaz, C.: Shaking table testing of civil engineering structures—the LNEC 3D simulator experience. In: Proceedings of the 12th World Conference on Earthquake Engineering. Auckland, New Zealand, Paper, vol. 2129 (2000)
2. Kim, C.-H., Park, J.-H., Lee, D.-Y.: Development of a Safety I & C System for NPP. 2005 Spring Korea Nuclear Society meeting, Jeju, Korea (2005)
3. Gere, J.M., Timoshenko, S.P.: Mechanics of Materials Brooks, pp. 815–839. Pacific Grove, CA, Cole (2001)
4. Ray, W.C., Penzien, J.: Dynamics of structures. No. Monograph (1975)
5. IS 800: GENERAL Construction In Steel—Code of Practice. Bureau of Indian Standards (2007)
6. Michele, C.G.: Design of a large-scale dynamic and pseudo-dynamic testing facility. Dissertation, University of Pavia (2005)
7. Hemant, W., et al.: Experimental study of variation between quasi-static and dynamic load deformation properties of bovine medial collateral ligaments. No. 2009-01-0392. SAE Technical Paper (2009)

8. Cannon, R.W., Godfrey, D.A., Moreadith, F.L.: Guide to the design of anchor bolts. Concrete International, Farmington Hills (1981)
9. Capéran, P.: Seismic Engineering Research Infrastructures for European Synergies
10. Luis, A., Saito, T.: Seismic risk and damage cost evaluation of base isolated buildings
11. Datta, T.K.: A state-of-the-art review on active control of structures. ISET J. Earthq. Technol. **40**(1), 1–17 (2003)

Comparison of State-of-the-Art Methods of Estimating & Controlling Floor Vibrations

Austin Devin[1(✉)] and Paul J. Fanning[2]

[1] Skidmore, Owings & Merrill, 224 S Michigan Avenue, Chicago, IL, USA
austin.devin@som.com
[2] University College, Dublin, Ireland

Abstract. Vibration serviceability is often a governing factor in the design of steel framing systems. The increasing availability of sophisticated Finite Element programs and widespread experimental modal testing of floors has resulted in a second edition of the AISC Design Guide on 'Vibrations of Steel-Framed Structural Systems Due to Human Activity'. This guide broadens the permissible design methods that designers can utilize in designing efficient steel framing systems.

This paper investigates the accuracy and sensitivity of this extended method based on previous research carried out to account for the effects of non-structural components on the modal response of floor systems. This newly published method is compared to that recommended by the Steel Construction Institute of the UK. It is shown that, whilst this guide is a positive step forward, further research is still required to ensure that such methods prescribed can be replicated accurately and repeatable results can be produced using this method.

Keywords: Floor vibrations · Walking excitation · Modal analysis · Steady-state analysis · Transient analysis · Steel composite floors · Non-structural elements · Frequency response functions

1 Introduction

Specific consideration of the serviceability limit state for floor vibration in new and renovated buildings is becoming increasingly necessary. The move towards more open floor systems, with fewer supporting columns, and lighter composite systems for floor structures results in reduced natural frequencies, less damping, and hence greater potential for floor excitation that could adversely impact on the structural integrity of the floor itself and also on the comfort of those using the building.

The relatively high stiffness, inertia and damping associated with reinforced concrete floors meant that such floors did not generally suffer from vibration serviceability issues [1]. Their frequencies were high relative to those associated with excitation forces and their inertia was such that excitation was difficult to achieve for the level of loading experienced. Modern design is driven by the need for more open-plan and flexible floor layouts. Composite construction techniques and post-tensioned systems enable longer spans with more slender structural components. However, these more lightweight solutions can be more prone to vibration serviceability issues [2–4] and

© Springer International Publishing AG 2018
J.P. Conte et al. (eds.), *Experimental Vibration Analysis for Civil Structures*,
Lecture Notes in Civil Engineering 5, https://doi.org/10.1007/978-3-319-67443-8_50

specific attention is required to their dynamic response. Where vibration is identified as a problem, the approaches used to achieve compliance with acceptable limits usually involve methods seeking to increase floor stiffness, reduce mass, or provide additional active, passive [5–8] or viscoelastic damping [9].

Tuning the natural frequency of a floor to avoid frequencies associated with an excitation source, minimizes the potential for resonance [10]. However, the accurate prediction of a floor's modal characteristics at the design stage is difficult, as many parameters, including for example partitions considered to be non-structural, have been shown to have a significant effect on dynamic response [11–17].

In construction, the most economical and beneficial stage to alter a building's design is as close to its inception as possible, before decisions with large cost implications have been made [18, 19]. Therefore, to enhance any project, it is vital that structural engineers can utilize innovative and practical solutions to floor vibration issues in the design stage. Figure 1 illustrates how decisions made at different stages of the construction process have a diminishing ability to have a significant effect on cost as a project progresses. In addition to impact, any decisions made later in the process or at the end of process will have an increasing impact on increasing costs.

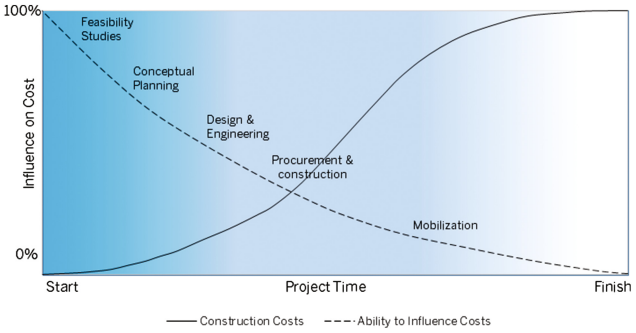

Fig. 1. Graph of construction project time history

In an aim to aid this problem solving, the American Institute of Steel Construction (AISC) has recently issued the second edition of the Design Guide 11: 'Vibrations of Steel-Framed Structural Systems Due to Human Activity' [20]. This new edition of the Design Guide is a result of continuous research conducted by Murray at Virginia Polytechnic Institute [21–23]. The most significant addition to this guide was a more comprehensive guide to using finite element analysis and steady state analysis to estimate vibration serviceability of floors. This paper compares this recent method to the method described in the Steel Construction Institute's Guide - 'Design of Floors for Vibration: A New Approach' [24] investigated previously [13].

2 Case Study Building

A composite construction (steel-concrete) building analyzed following guidelines provided in the European Committee for Standardization (CEN) Eurocode No. 4 [25] was investigated. For the purposes of this study a four-story building with dimensions typical of those used in modern office buildings was considered – Fig. 2 shows the floor layout and it is noted that this is the same for all floor levels.

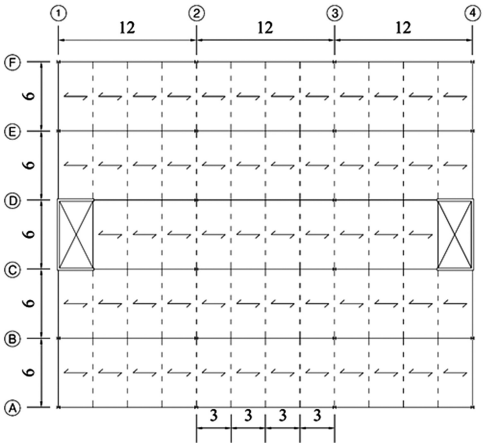

Fig. 2. Case study building – floor layout investigated.

The characteristics of the floor system were set as being consistent to those of a steel-composite slender floor typical of those likely to be susceptible to excitation due to human occupancy [2, 3, 26, 27].

The building was modelled using ANSYS V14 [28] and SAP2000 V18 [29], the ANSYS model is shown in Fig. 3. All composite slabs and shear cores were modelled using shell elements. Orthotropic material properties were assigned to the slab shell

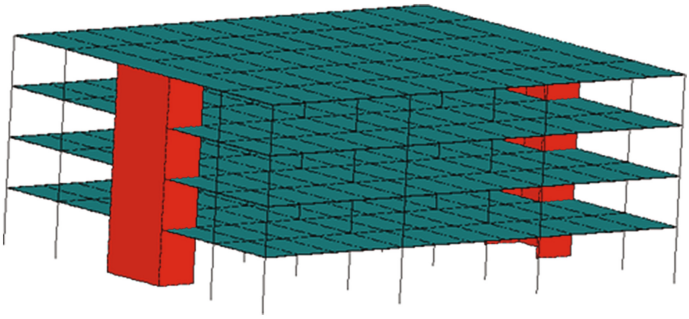

Fig. 3. Three-dimensional finite element model (ANSYS model).

elements with a reduced Young's modulus assigned in the direction perpendicular to the beams acting compositely with the slab to account for the 'strong' and 'weak' directions of the metal deck. Primary floor beams were included as beam elements in the models.

3 Methods for Estimating Human-Induced Response

This paper compares two procedures for estimating the dynamic response of floors to walking excitation, the Steel Construction Institute method [30] and the recently published AISC Design Guide 11 method [20].

3.1 Steel Construction Institute (SCI P354) Method

To evaluate the vibration serviceability of the composite floor system a series of transient analyzes was carried out. In each case the floor was subjected to forces representing excitation due to walking at four different locations. The vertical load model used is given in Eq. 1 – current vibration serviceability procedures [24] define the cyclical walking force (F_p) using the following equation:

$$F_p(t) = G + G\alpha_1 \cos\left(2\pi f_p t\right) + G\alpha_2 \cos\left(4\pi f_p t\right) + G\alpha_3 \cos\left(6\pi f_p t\right) + G\,\alpha_4 \cos(8\pi f_p t) \tag{1}$$

Where G = weight of the human walker (taken as 784.5N);
f_p = pacing frequency (taken as 2.1 Hz);
t = time; and α_i = attenuation factor for each of the four harmonics (taken as 0.5, 0.2, 0.1 and 0.05 respectively).

Then Response Ratio Factor (R), defined as the ratio between the weighted RMS acceleration and the threshold of human perception (Eq. 2), is used to evaluate the vibration serviceability of floors due to human excitation.

$$R = \frac{a_{w,rms}}{0.005} \tag{2}$$

Where $a_{w,\ rms}$ = weighted RMS acceleration response, expressed in m/s^2 due to the walking excitation applied.

Where the response factor is 4.0 or lower a floor is deemed meet the serviceability limit state for vibration [24]. The analysis results are presented by way of a response factor contour plot. A grid of 275 points (2 m × 1.5 m) was established initially with interpolation used between these points to produce smooth contours for the response factor plots.

3.2 AISC (Design Guide 11) Method

The AISC Design Guide 11 [20] presents a finite element analysis procedure using steady-state analysis of the floor at certain locations, using frequency response functions and simple formulas to compare the estimated accelerations induced by walking excitation. The predicted peak sinusoidal acceleration due to walking is defined as a_p, as shown in Eq. 3.

$$a_p = FRF_{Max}\alpha Q_\rho \tag{3}$$

Where FRF_{max} = maximum Frequency Response Function magnitude at frequencies below 9 Hz, (%g/lb)
Q = Bodyweight = 168 lb
α = dynamic coefficient
ρ = resonant build-up factor.

For a given floor to be considered satisfactory, a_p, must be below 0.05%g for a given test. To estimate the FRF_{max}, a steady-state analysis is completed on the floor. The research which produced this method, predominately utilized SAP2000, a commercial software by CSi. A Frequency Response Function is a plot of a structure's steady-state response due to a sinusoidal load with unit amplitude vs frequency.

4 Discussion of Results

Two finite element models were produced to study the two different methods of evaluating the dynamic response of floors using transient analysis and steady-state analysis. First modal analysis was conducted, the first three mode shapes of these models are shown in Fig. 4.

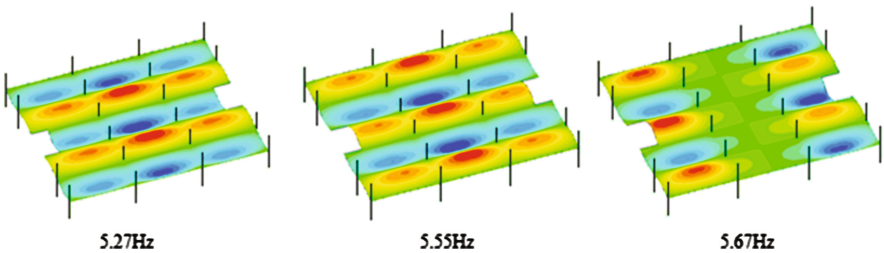

Fig. 4. First three mode shapes of the case study floor extracted from the finite element model (ANSYS model).

4.1 Steel Construction Institute (SCI P354) Method

The method outlined in [30], provides an output of acceleration response of the floor for a defined time period. A sample acceleration response time history is shown in Fig. 5 for the bare frame case study building. From this acceleration time history, the weighted root mean square (RMS) acceleration response due to the walking excitation is calculated and in turn this value is input into Eq. (2). This procedure was followed for a response location and a detailed response contour plot was created by interpolating between them. A sample response factor contour plot can be seen in Fig. 6. As can be seen from the plot, a significant portion of the floor does not have a satisfactory

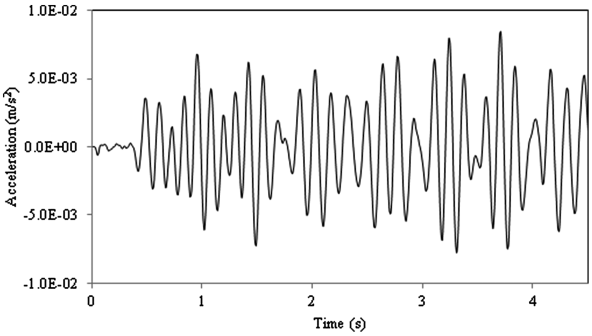

Fig. 5. Typical acceleration response from walking-induced excitation from the bare frame FE model.

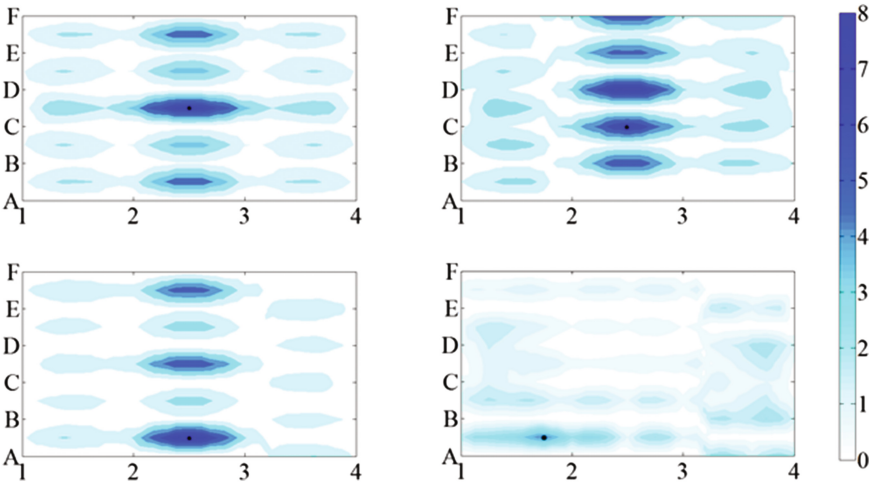

Fig. 6. Response factors shown as gradient calculated due to walking excitation at four different locations (marked with a black dot) on the bare frame FE model, with a maximum response factor of 8.

acceleration response – indicated by the dark blue values which are above the recommended value of 4.

4.2 AISC (Design Guide 11) Method

The method outlined in [31], provides an output of a frequency response function which allows an estimation of the permissible excitation which would occur due to human-induced excitation of the tested floor. Figure 7 below presents a sample FRF, the peaks indicate the frequencies of the natural frequencies of the floor and are the first two peaks occur at identical frequencies of the first two mode shapes shown in Fig. 4. Using Eq. (3) defined above the estimated acceleration caused by walking is estimated.

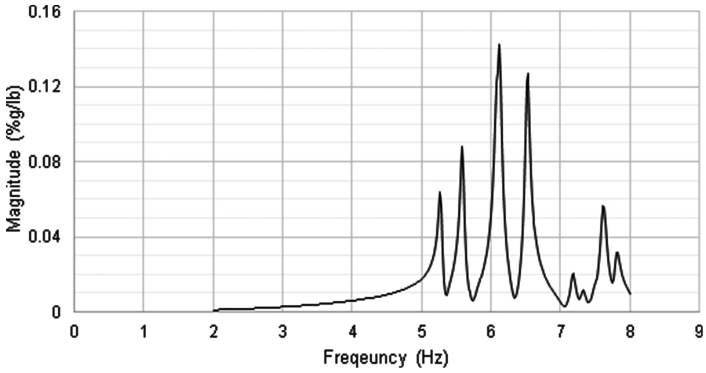

Fig. 7. Sample FRF extracted from steady-state analysis.

5 Conclusions

The ability to complete a comprehensive, accurate vibration serviceability estimate of a floor system is highly beneficial at the design stage of buildings. However, such a procedure is still in the realm of specialized engineering and not carried out or is not comprehensively understood by the average structural engineer.

Two recent design guides, from the Steel Construction Institute in the UK and the American Institute of Steel Construction endeavor to outline straightforward methods of analysis, utilizing the finite element method, to evaluate the vibration serviceability of composite steel-concrete floor systems. This paper investigates how these two methods differ. While both methods would still be considered relatively complex to the average engineer, both methods have a definitive procedure and can be achieved in commercially available software, ANSYS and SAP2000 were the packages utilized in this case. Such procedures shall extend the number of new and existing building structures that can be readily evaluated for vibration serviceability, which shall broaden understanding of the parameters which affect the dynamic response of floors, enhancing the ability of structural engineers to produce economical and practical floor systems.

Acknowledgments. The authors wish to express their gratitude to the following: (1) the Chicago Structures Team of Skidmore, Owing & Merrill for allowing this research to be published and (2) the Irish Research Council for Science, Engineering and Technology (IRCSET) Grant No. RS2000810.

References

1. Pavic, A., Reynolds, P., Waldron, P., Bennett, K.J.: Critical review of guidelines for checking vibration serviceability of post-tensioned concrete floors. Cem. Concr. Compos. **23** (1), 21–31 (2001)
2. Pavic, A., Miskovic, Z., Reynolds, P.: Modal Testing and Finite Element model updating of a lively open-plan composite building floor. J. Struct. Eng. **133**(4), 550–558 (2007)
3. Nyawako, D., Reynolds, P., Hudson, M.: Findings with AVC design for mitigation of human induced vibrations in office floors. Topics Dyn. Civil Struct. **4**, 37–44 (2013)
4. Pavic, A., Widjaja, T., Reynolds, P.: The use of modal testing and FE model updating to investigate vibration transmission between two nominally identical building floors. In: Proceedings of the International Conference on Structural Dynamics Modeling-Test, Analysis, Correlation and Validation, pp. 347–355 (2002)
5. Alkhatib, R., Golnaraghi, M.: Active structural vibration control: a review. Shock Vib. Dig. **35**, 367 (2003)
6. Yang, J., Soong, T.: Recent advances in active control of civil engineering structures. Prob. Eng. Mech. **3**(4), 179–188 (1988)
7. Soong, T., Costantinou, M.: Passive and Active Structural Vibration Control in Civil Engineering. Springer, New York (1994)
8. Datta, T.: A state-of-the-art review on active control of structures. ISET J. Earthq. Technol. **40**(1), 1–17 (2003)
9. Saidi, I., Gad, E., Wilson, J., Haritos, N.: Development of passive viscoelastic damper to attenuate excessive floor vibrations. Eng. Struct. **33**(12), 3317–3328 (2011)
10. Brownjohn, J.M.W., Pavic, A.: Vibration control of ultra-sensitive facilities. Proc. ICE Struct. Build. **159**(5), 295–306 (2006)
11. Devin, A., Fanning, P., Middleton, C., Pavic, A.: Structural dynamic parameter identification and the effect of test techniques. In: Proceeding of the International Modal Analysis Conference (IMAC 2013) (2013)
12. Devin, A., Fanning, P.J.: Non-load bearing elements and their contribution to a structure's dynamic response. In: Experimental Vibration Analysis for Civil Engineering Structures (EVACES 2011), pp. 667–674 (2011)
13. Devin, A., Fanning, P.J., Pavic, A.: Nonstructural partitions and floor vibration serviceability. J. Archit. Eng. **22**(2002), 1–9 (2016)
14. Reynolds, P.: The effects of raised access flooring on the vibrational performance of long-span concrete floors. Ph.D. thesis, University of Sheffield (2000)
15. Miskovic, Z., Pavic, A., Reynolds, P.: Effects of full-height nonstructural partitions on modal properties of two nominally identical building floors. Can. J. Civ. Eng. **36**(7), 1121–1132 (2009)
16. Devin, A., Fanning, P.J.: The evolving dynamic response of a four storey reinforced concrete structure during construction. Shock Vib. **19**(5), 1051–1059 (2012)
17. Devin, A., Fanning, P.J., Pavic, A.: Modelling the effect of non-structural elements on floor modal properties of buildings. Eng. Struct. **91**, 58–69 (2014)
18. Vickroy, J.O.C.: Control of construction project scope (1986)

19. Oberlender, G.D., Trost, S.M.: Predicting accuracy of early cost estimates based on estimate quality. J. Const. Eng. Manag. **127**(3), 173–182 (2001)
20. Murray, T.M., Allen, D.E., Ungar, E.E., Davis, D.B.: AISC Design Guide 11: Vibrations of Steel Framed Structural Systems due to Human Activity, 2nd edn. AISC (2016)
21. Perry, J.D.: A study of computer modeling techniques to predict the response of floor systems due to walking. Doctoral dissertation, Virginia Tech (2003)
22. Davis, D.B.: Finite element modeling for prediction of low frequency floor vibrations due to walking. Doctoral dissertation, Virginia Tech (2008)
23. Barrett, A.R.: Dynamic testing of in-situ composite floors and evaluation of vibration serviceability using the finite element method. Virginia Polytechnic Institute and State University Blacksburg (2006)
24. Smith, A., Hicks, S., Devine, P.: Design of Floors for Vibration: A New Approach, 2nd edn. Berkshire, Assot (2009)
25. Eurocode: Eurocode 4: design of composite steel and concrete structures part 1-1: general rules and rules for buildings. Control, pp. 1–117 (2004)
26. Díaz, I., Pereira, E., Reynolds, P.: Integral resonant control scheme for cancelling human-induced vibrations in light-weight pedestrian structures. Struct. Control Heal. Monit. **19**, 55–69 (2012)
27. Díaz, I., Pereira, E., Hudson, M., Reynolds, P.: Enhancing active vibration control of pedestrian structures using inertial actuators with local feedback control. Eng. Struct. **41**, 157–166 (2012)
28. ANSYS Inc., ANSYS Parametric Design Language Guide, 14.5, vol. 15317. Canonsburg, PA, October 2012
29. C. & Structures: CSI Analysis Reference Manual, April 2009
30. The Steel Construction Institute, Smith, A.: Design of Floors for Vibration: A New Approach, Revised edn., February 2009
31. Murray, T.M., Allen, D.E., Ungar, E.E., Davis, D.B.: Vibrations of Steel-Framed Structural Systems Due to Human Activity, 2nd edn., p. 130 (2016)

Optimal Design of Active Tuned Mass Dampers for Mitigating Translational–Torsional Motion of Irregular Buildings

Mohsen Azimi[1], Hong Pan[1,2], Mehdi Abdeddaim[3], and Zhibin Lin[1(✉)]

[1] Department of Civil and Environmental Engineering, North Dakota State University, Fargo, ND, USA
zhibin.lin@ndsu.edu
[2] College of Civil Engineering, Tongji University, 1239 Siping Rd, Shanghai, China
[3] Department of Civil Engineering and Hydraulics, Mohamed Khider University, Biskra, Algeria

Abstract. The active tuned mass dampers (ATMDs) are accepted as effective energy dissipating devices to effectively reduce structural dynamic response when subjected to seismic loads. The conventional design of these devices, however, may not be applicable to high-rise buildings with irregularity in plan and elevation, where significant torsional motions could be dominant during a strong earthquake. This study is to develop a new approach using the ATMD for reducing the torsional motion as well as resisting the lateral translational displacements. Three actuators are used to apply the control forces to the twin-TMD system in two directions, while the optimal control forces were determined using linear quadratic regulator (LQR) algorithm. In addition, instead of using two independent mass dampers in two directions, a single damper system was used to minimize the displacements and rotation simultaneously. To demonstrate the performance of the system, the final design was applied to an irregular ten-story building subjected to near- and far-field earthquakes. The results indicate that the proposed design approach is more cost effective as compared to the design with independent pairs of dampers in two directions. Further, the system exhibits higher reliability under different ground accelerations in two directions than conventional ones.

Keywords: LQR control · Irregular building · Tuned mass damper (TMD) · Active tuned mass damper (ATMD) · Twin tuned mass damper (TTMD)

1 Introduction

During recent years, seismic response control of structures has gained a significant attention due to the life safety requirements and the tragic events related to major earthquakes [1, 2]. Reviewing the literature reveals the fact that several historic earthquakes such as 1940 El Centro, 1971 San Fernando, 1989 Loma Prieta, 1994 Northridge, 1995 Kobe, and 1999 Chi-Chi caused severe damages in civil structures

© Springer International Publishing AG 2018
J.P. Conte et al. (eds.), *Experimental Vibration Analysis for Civil Structures*,
Lecture Notes in Civil Engineering 5, https://doi.org/10.1007/978-3-319-67443-8_51

[2–5]. Even though seismic provisions are revised each year based on the new findings in seismic performance design of structures, which may require existing building to be retrofitted according to the current design criteria [6], they do not guarantee the minimum damage due to the future unknown seismic events [7, 8]. Significant levels of damage to the structures with asymmetric design demands development of effective methods for protection of existing and new structures for a safer environment for humans [9].

The majority of researchers have concentrated on seismic performance of structures under unidirectional seismic loads using independent shear frame models in two directions; however, the fact is that earthquakes have indeed arbitrary direction, that can be described by a bidirectional excitation [10]. In addition, the nature of buildings is asymmetric, which cause torsion coupling (TC) vibration with simultaneous torsional–translational oscillation under bidirectional ground motion.

Bidirectional seismic loads can cause severe structural damage due to translation–torsion coupled vibrations, that is ignored in the shear frame models, and needs to be taken into consideration [11], particularly, for those structures with irregularity in plan and elevation [12, 13]. For instance, the axial forces in the corner columns are different when subjected to bidirectional or unidirectional ground motions [14]. Also, the border members—the transverse elements—can behave nonlinearly under bidirectional earthquakes [15].

The traditional approaches for reinforcing the structures tend to introduce additional stiffness and damping to the substandard structures [6]. Passive tuned mass dampers (TMD) are one of the attractive mass vibration absorbers for reducing the structural responses that consist of a mass, spring, and dashpot. TMDs have been employed in a large number of structures around the world [16, 17]. TMDs counteract the movement of floor when they are stretched or compressed. Although TMDs are theoretically high-performance devices, application of passive TMD systems are limited to a narrow frequency band and needs to be tuned according to the main structure. Therefore, they cannot be effective for such structures with closely spaced natural frequencies [18].

One of the variables in tuning a TMD is the mass ratio (μ) that is usually within the range of 1–10%. Using the mass ratio, μ, researchers used different optimal designs; the formulation for classic TMD designs are listed in [19]. However, the estimated natural frequency and mass can differ from the real ones due to estimation errors. Those effects will result in a suboptimal TMD tuning or even a mistuning, and thereby a loss of damping in the controlled structure [20].

Active-TMD and active mass driver (AMD) do not have the limitations of passive TMDs, they are considered as one of the most efficient control devices, due to their stability and high adaptability to seismic loading variations [21]. Such damping system requires a controller to drive the mass through an actuator. The design of a proper controller is as much important as the tuning for passive TMDs.

Although several proposals have been presented for designing TMD systems for 3D buildings under bi-directional earthquake loads, only limited studies have considered the torsional motion in their designs; therefore, an integrated system with optimum cost and performance needs to be developed. In this study, a new approach is presented for the optimal design of passive and active tuned mass dampers. The proposed twin tuned mass damper (TTMD) system is designed to reduce the translational movements

of irregular buildings and also resist the torsional motion. The performance of the proposed TTMD and active-TTMD (ATTMD) is evaluated for a 10-story irregular building under bidirectional ground motions.

2 Optimal Vibration Control Using TTMD

2.1 Configuration of TTMD System

As shown in Fig. 1, the twin tuned mass damper (TTMD) system includes two masses, M_1 and M_2, that are connected to each other with a rigid bar; while the bar is restrained in the x-direction at midpoint, it can move in the y-direction and rotate about the midpoint O. Three springs and dashpots are used to stabilize the system. For the active-TTMD system, three actuators apply the controlling forces in two directions as well as the moment for suppressing the translational–torsional vibration. For simplicity, properties of each twin dampers are selected identical, and the optimal values were obtained through an optimization algorithm. The length of the connecting rigid bar is assumed to be 10 m.

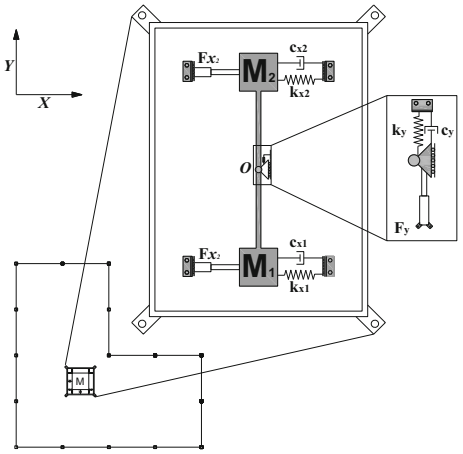

Fig. 1. Schematic diagram of the active twin tuned mass damper (ATTMD) installed on the roof level.

2.2 Optimal Design Using Particle Swarm Optimization (PSO) Algorithm

Intelligent algorithms are used extensively in structural engineering [22–25]. Since the optimization problem is continuous in this study, the particle swarm optimization (PSO) algorithm is used for the optimal design of TTMD parameters. The procedure is based on the PSO algorithm [26] that takes the parameters of the TTMD as the design variables and determines them to meet the objectives. The design objectives can be

varied; in this study, in order to maintain the integrity of the building, the optimization problem is expressed as:

$$\begin{aligned} &\text{Find}: \ C_{x1,x2,y_{TTMD}}, K_{x1,x2,y_{TTMD}} \\ &\text{Minimize}: \ X_{\max} = \max\left|x_{roof}(t)\right| \\ &\text{Subjected to}: \ 0 < K < K_{\max}; 0 < C < C_{\max}; \end{aligned} \tag{1}$$

where C and K are the damping and stiffness of each dashpot and spring in both directions, respectively.

2.3 Governing Equations of the Controllable System Using TTMD and ATTMD

The governing equation of motion for a controlled nDOF system under seismic ground acceleration load, $\ddot{x}_g$, can be condensed and described as:

$$[\boldsymbol{M}]\{\ddot{x}(t)\} + [\boldsymbol{C}]\{\dot{x}\} + [\boldsymbol{K}]\{x\} = [\boldsymbol{\gamma}]\{u(t)\} + \{\boldsymbol{\delta}\}\ddot{x}_g(t), \tag{2}$$

where $\boldsymbol{M}$, $\boldsymbol{C}$, and $\boldsymbol{K}$ are $(3n \times 3n)$ matrices of mass, damping, and stiffness, and $\{x\}, \{\dot{x}\}$, and $\{\ddot{x}\}$ are the $(n \times 1)$ displacement, velocity and acceleration vectors, respectively and relative to the base of the building [27]. $\{u(t)\}$ is the control force vector, and $\{\boldsymbol{\delta}\}$ is the coefficient vector for earthquake ground acceleration $\ddot{x}_g(t)$. $[\boldsymbol{\gamma}]$ is the controller location matrix that also represents the influence of each actuator on the other DOFs. Damping matrix of the system, C_{-s}, is determined using the Rayleigh method based on the mass and stiffness matrices [28, 29], and an inherent damping of 5% is assumed for the first and fourth modes of vibration. The equation of motion can be solved by rewriting it in state-space form as:

$$\left\{\dot{Z}(t)\right\} = [\boldsymbol{A}]\{Z(t)\} + [\boldsymbol{B_u}]\{u(t)\} + \{\boldsymbol{B_r}\}\ddot{x}_g(t), \tag{3}$$

where

$$\begin{aligned} \{Z(t)\} &= \begin{Bmatrix} x(t) \\ \dot{x}(t) \end{Bmatrix}; \quad \boldsymbol{A} = \begin{bmatrix} [\boldsymbol{0}] & \boldsymbol{I} \\ -\boldsymbol{M}^{-1}\boldsymbol{K} & -\boldsymbol{M}^{-1}\boldsymbol{C} \end{bmatrix}; \quad \{\boldsymbol{B_u}\} = \begin{bmatrix} [\boldsymbol{0}] \\ \boldsymbol{M}^{-1}[\boldsymbol{\gamma}] \end{bmatrix}; \\ \{\boldsymbol{B_r}\} &= \begin{bmatrix} \{\boldsymbol{0}\} \\ [\boldsymbol{M}]^{-1}\{\boldsymbol{\delta}\} \end{bmatrix}. \end{aligned} \tag{4}$$

The control forces for the active systems are calculated using the linear quadratic regulator (LQR). The LQR controller has recently gained significant importance, and it has been used for controlling the vibration of buildings with asymmetric plans in order to reduce the lateral-torsional responses [30].

2.4 Numerical Example: Ten-Story Irregular Steel Moment Frame

Inspired by the research carried out by Kaveh et al. [31], a ten-story irregular building frame was selected for numerical simulations. The 3D and plan views of the model are

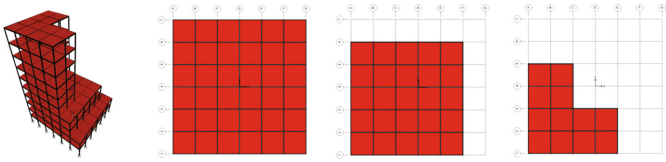

Fig. 2. 3D and plan views of the ten-story irregular building.

shown in Fig. 2. Following assumption are made in order to idealize the numerical model of the example: all the column members have the same symmetric cross section and height; each floor acts as a rigid diaphragm and all the columns are fixed at both ends. Therefore, the stiffness of each column in this model can be estimated as $k = 12EI/h^3$, where h is the story height, E is the modulus of elasticity of the steel material, and I is the moment of inertia in the x- and y-direction.

2.5 Modal Analysis

For an irregular building, higher modes of vibration may participate as well as the primary first modes during an earthquake. Since the model is neither symmetric nor has the same center of mass for all the stories, the modal analysis of the system was carried out in order to study the mode shapes (Fig. 3). From the mode shapes, it can be expected that the torsional motion of the building is inevitable under the bi-directional ground motions. Therefore, for such buildings with irregularity, it is necessary that the earthquake ground motion is applied in both directions simultaneously, and the influence of dimension, location and other properties of a TMD need to be considered in evaluating the performance of the system. In this study, the influence of the location of the TMD is not investigated; thus, it is assumed that it is located at the center of mass of the roof level.

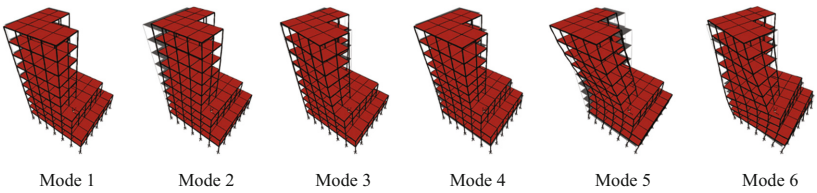

Fig. 3. Mode shapes of the building.

2.6 Optimization Problem Results

The optimum parameters for the typical TMD systems, for minimizing the roof displacement, can be obtained using the equations given in Table 1. The optimum design parameters of the traditional TMD system for different mass ratios can be obtained by using the equations in this table, which are basically developed for unidirectional earthquake excitation without considering the eccentricities. For three mass ratios of 1%, 3%, and 5%, the mass, damping, and stiffness of the TMD are given in Table 2.

Table 1. The optimal parameters for a TMD attached to a building [32].

Minimizing item	Frequency ratio	Damping ratio
Displacement	$\frac{1}{1+\mu}$	$\sqrt{\frac{3\mu}{8(1+\mu)^3}}$

Table 2. Optimum parameters of TMD using the traditional method (in one direction).

Criterion	μ	M_d (kg)	C_d (N/m/s)	K_d (N/m)
Displacement	1%	77,925	7763	53,119
	3%	233,775	37,662	147,336
	5%	389,625	75,761	227,379

The main concern about the traditional design of TMDs is that they do not consider the torsional motion of irregular buildings, however, they are proved to be effective for symmetric structures. Figure 4 shows the roof displacement of the 10-story building under the El Centro and Northridge earthquakes. It can be seen that by considering the torsional motion of the story levels, the maximum displacement at the corners of each floor are greater, which are neglected in the unidirectional design approach.

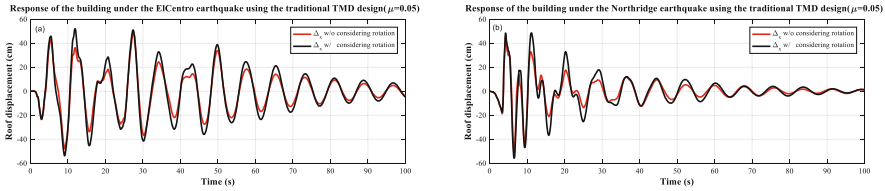

Fig. 4. Displacement response of the irregular building in x-direction with and without considering the torsional motion under the (a) El Centro and (b) Northridge earthquakes.

Therefore, the traditional approaches for the optimal design of TMD parameters for irregular buildings do not guarantee the superior performance of the system under bidirectional earthquake loads. In this study, the particle swarm optimization (PSO) algorithm is used in order to find the optimum design parameters of the proposed TTMD system. For this purpose, the 10-story irregular building is subjected to bidirectional random excitation that is obtained by filtering a white noise through a linear filter—known as Kanai–Tajimi filter—which represents the surface ground [19].

Figure 5 shows the number of PSO algorithm iterations vs. the best cost which is the displacement of the roof level in this study. Since irregular buildings have different configurations, it is preferable to find the optimum design parameters for the TTMD using the powerful metaheuristic algorithms. The procedure is repeated for three different mass ratios: μ = 1%, 3%, and 5%.

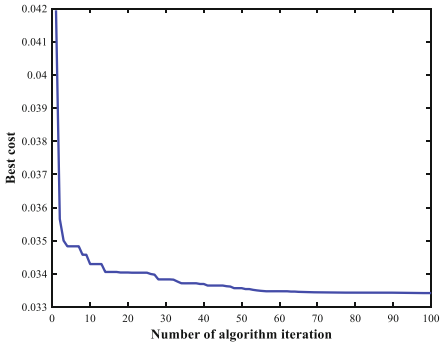

Fig. 5. The best design history of the controlled 10-story building with TTMD using PSO algorithm ($\mu = 0.05$).

2.7 Performance of the Designed TTMD and ATTMD Under Historic Earthquakes

While the TTMD parameters are designed using the white noise excitation (Fig. 6), three historic earthquake records are selected in this research to evaluate the performance of the TTMD and ATTMD control systems under different ground excitations. The characteristics of the selected earthquakes are given in Table 3.

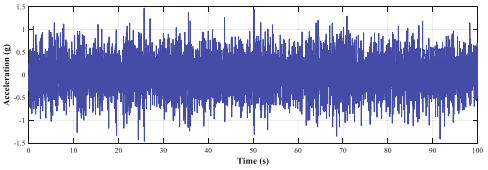

Fig. 6. Filtered white noise excitation.

Table 3. Characteristics of the historic earthquake records.

Earthquake*	Station and direction	Magnitude (M_w)	PGA (g)	PGV (cm/s)
1940 El Centro	El Centro Array #9 270°	7.2	0.21	30.2
	El Centro Array #9 180°	7.2	0.28	31.0
1994 Northridge	Sylmar - Olive View Med FF 360°	6.7	0.84	129.6
	Sylmar - Olive View Med FF 090°	6.7	0.61	77.53
1995 Kobe	H1170546.KOB 090°	7.2	0.63	76.6
	H1170546.KOB 000°	7.2	0.83	91.13

*Source: http://ngawest2.berkeley.edu/

The torsional motion of the building is considered in the proposed control system; for the proposed ATTMD, the actuators generate a moment in addition to the forces in two directions. The moment counteracts the torsional motion; therefore, the overall displacements in both directions, particularly for those columns in the corners, are reduced. Figure 7 shows the maximum displacement response of the building at the roof level—the corner columns—as well as the roof rotation using the three control systems, TMD, TTMD, and ATTMD. It is evident that by using the proposed design approach for TTMD system, both translational and torsional responses of the irregular building is reduced significantly compared to the traditional TMD system with the same mass ratios. In addition, the active form of the TTMD system (ATTMD) considerably reduces the response of the building during the excitation time. For example, from the displacement responses, by using the ATTMD control system there is no noticeable displacement after 50th second of the ground excitations. The maximum responses for each scenario are given in Table 4. In this table, $x_{\max}$ and θ_{roof} are the maximum displacement and rotation at the roof level, respectively.

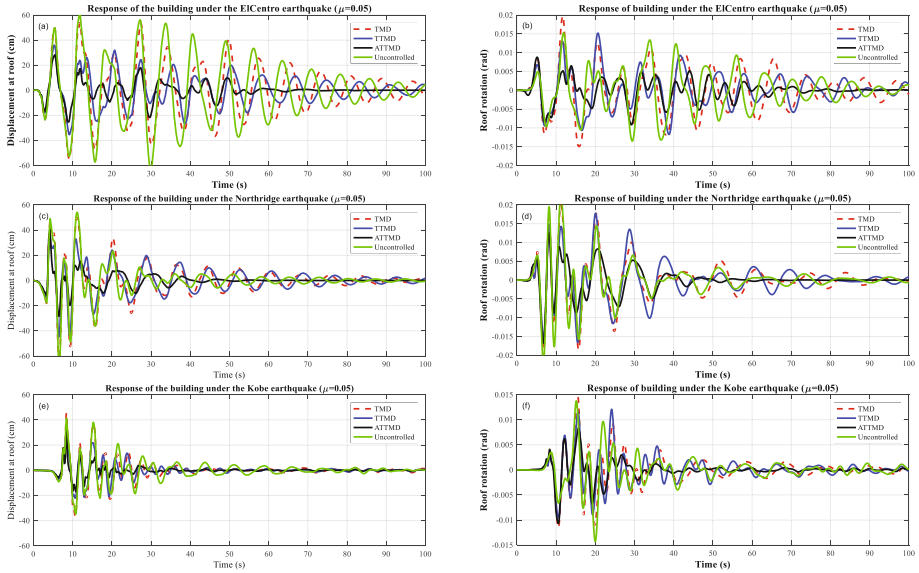

Fig. 7. Displacement and rotation responses at roof level under the El Centro, Northridge, and Kobe earthquakes.

From Table 4, it can be seen that the traditional optimal design does not guarantee the maximum reduction of response in the irregular 10-story building. For example, by using the TMD system with 5% mass ratio, the maximum reduction in the displacement response obtained under the El Centro earthquake (21%), however, the same design increases the displacement and the rotation at roof level by 7% and 1%, respectively. On the other hand, the proposed TTMD system offers significant response reduction for all the mass ratios and under all three earthquake records. The maximum response

Table 4. Maximum responses of the uncontrolled building and the response reduction percentage for each control technique.

μ	Earthquake	Response	Uncontrolled	TMD	TTMD	ATTMD
1%	El Centro	x_{max}	69.4 cm	−7%	−32%	**−65%**
		θ_{roof}	0.0210 rad	−1%	−25%	**−44%**
	Northridge	x_{max}	72.3 cm	−5%	−30%	−45%
		θ_{roof}	0.0204 rad	−1%	−25%	−11%
	Kobe	x_{max}	42.4 cm	**+7%**	−16%	−23%
		θ_{roof}	0.0145 rad	**+1%**	−19%	−26%
3%	El Centro	x_{max}	69.4 cm	−16%	−44%	**−60%**
		θ_{roof}	0.0210 rad	−4%	−33%	**−48%**
	Northridge	x_{max}	72.3 cm	−7%	−30%	−44%
		θ_{roof}	0.0204 rad	−1%	−25%	−13%
	Kobe	x_{max}	42.4 cm	**+7%**	−16%	−26%
		θ_{roof}	0.0145 rad	**+0%**	−20%	−26%
5%	El Centro	x_{max}	69.4 cm	**−21%**	**−48%**	**−59%**
		θ_{roof}	0.0210 rad	**−6%**	**−40%**	**−56%**
	Northridge	x_{max}	72.3 cm	−8%	−38%	−53%
		θ_{roof}	0.0204 rad	−1%	−28%	−31%
	Kobe	x_{max}	42.4 cm	**+7%**	−19%	−25%
		θ_{roof}	0.0145 rad	**+1%**	−31%	−37%

reduction is for the TTMD design with 5% mass ratio under El Centro earthquake by 48%. Although for the building controlled by TMD, greater mass ratios result in more reduction, for the active-TTMD, the maximum reduction in the response is achieved using the least mass ratio, μ = 1%. Differences between the reduction percentages suggest that it is more appropriate to optimize the design case-by-case and separately, and avoid using set of equations for all configurations. Particle swarm optimization (PSO) algorithm is a powerful tool in finding the optimal design parameters of the proposed TTMD for buildings with irregularities in plan and elevation.

3 Conclusions

A new structural control approach is introduced in designing the active tuned mass dampers (ATMDs) for irregular high-rise buildings. The optimal parameters of the proposed twin tuned mass damper (TTMD) systems are obtained through the particle swarm optimization (PSO) algorithm using a filtered white noise as the ground acceleration. The performance of the proposed system is evaluated for a 10-story irregular building under three historic earthquakes that are applied bi-directionally to the system. The results confirm that, despite the traditionally designed TMDs, the proposed TTMD is more effective in reducing the translational–torsional motion of irregular structures. In addition, the active-TTMD (ATTMD) control system is also investigated in this study, which significantly decreases the responses by using the

linear quadratic regulator (LQR) for determining the optimal control forces. The results of this study may lead to introduce new design criteria for designing of tuned mass damper systems for irregular buildings.

Acknowledgements. The authors gratefully acknowledge the financial support provided by Ozbun Economic Development Award, ND NSF EPSCoR (FAR0022364) and US DOT (FAR0025913). The results, discussion, and opinions reflected in this paper are those of the authors only and do not necessarily represent those of the sponsors.

References

1. Abdeddaim, M., Ounis, A., Djedoui, N., Shrimali, M.K.: Pounding hazard mitigation between adjacent planar buildings using coupling strategy. J. Civ. Struct. Health Monit. **6**(3), 603–617 (2016)
2. Mosleh, A., Rodrigues, H., Varum, H., Costa, A., Arêde, A.: Seismic behavior of RC building structures designed according to current codes. Structures **7**, 1–13 (2016)
3. Mosleh, A., Jara, J., Varum, H.: A methodology for determining the seismic vulnerability of old concrete highway bridges by using fragility curves. J. Struct. Eng. Geo-Tech. **5**(1), 1–7 (2015)
4. Mosleh, A., Razzaghi, M.S., Jara, J., Varum, H.: Seismic fragility analysis of typical pre-1990 bridges due to near- and far-field ground motions. Int. J. Adv. Struct. Eng. (IJASE) **8**(1), 1–9 (2016)
5. Mosleh, A., Varum, H., Jara, J., Razzaghi, M.S.: Development of fragility curves for RC bridges subjected to reverse and strike-slip seismic sources. Earthq. Struct. **11**(3), 517–538 (2016)
6. Ghodrati Amiri, G., Azimi, M., Darvishan, E.: Retrofitting I-beam to double-I built-up column connections using through plates and T-stiffeners. Sci. Iran. Trans. A Civ. Eng. **20** (6), 1695 (2013)
7. Gerist, S., Maheri, M.R.: Multi-stage approach for structural damage detection problem using basis pursuit and particle swarm optimization. J. Sound Vib. **384**, 210–226 (2016)
8. Gerist, S., Naseralavib, S.S., Salajegheh, E.: Basis pursuit based genetic algorithm for damage identification. Int. J. Optim. Civ. Eng. **2**(2), 301–319 (2012)
9. Lin, J.L., Tsai, K.C.: Seismic analysis of two-way asymmetric building systems under bi-directional seismic ground motions. Earthq. Eng. Struct. Dynam. **37**(2), 305–328 (2008)
10. Heo, J.S., Lee, S.K., Park, E., Lee, S.H., Min, K.W., Kim, H., et al.: Performance test of a tuned liquid mass damper for reducing bidirectional responses of building structures. Struct. Des. Tall Spec. Build. **18**(7), 789–805 (2009)
11. Zhang, J., Zeng, K., Jiang, J.: An optimal design of bi-directional TMD for three dimensional structure. In: Computational Structural Engineering, pp. 935–941. Springer, Berlin (2009)
12. Yanik, A., Aldemir, U., Bakioglu, M.: A new active control performance index for vibration control of three-dimensional structures. Eng. Struct. **62**, 53–64 (2014)
13. Nigdeli, S.M., Boduroğlu, M.H.: Active tendon control of torsionally irregular structures under near-fault ground motion excitation. Comput. Aided Civ. Infrastruct. Eng. **28**(9), 718–736 (2013)
14. Cruz, E.F., Cominetti, S.: Three-dimensional buildings subjected to bi-directional earthquakes. Validity of analysis considering uni-directional earthquakes. In: Proceedings of the 12th World Conference on Earthquake Engineering (2000)

15. Correnza, J., Hutchinson, G., Chandler, A.: Effect of transverse load-resisting elements on inelastic earthquake response of eccentric-plan buildings. Earthq. Eng. Struct. Dynam. **23**(1), 75–89 (1994)
16. Matta, E.: Effectiveness of tuned mass dampers against ground motion pulses. J. Struct. Eng. **139**(2), 188–198 (2012)
17. Sladek, J.R., Klingner, R.E.: Effect of tuned-mass dampers on seismic response. J. Struct. Eng. **109**(8), 2004–2009 (1983)
18. Farghaly, A.A., Salem Ahmed, M.: Optimum design of TMD system for tall buildings. ISRN Civ. Eng. **2012**, 13 (2012)
19. Soto, M.G., Adeli, H.: Optimum tuning parameters of tuned mass dampers for vibration control of irregular highrise building structures. J. Civ. Eng. Manag. **20**(5), 609–620 (2014)
20. Weber, F., Maślanka, M.: Frequency and damping adaptation of a TMD with controlled MR damper. Smart Mater. Struct. **21**(5), 055011 (2012)
21. Nishimura, I., Kobori, T., Sakamoto, M., Koshika, N., Sasaki, K., Ohrui, S.: Active tuned mass damper. Smart Mater. Struct. **1**(4), 306 (1992)
22. Khademi, F., Jamal, S.M.: Estimating the compressive strength of concrete using multiple linear regression and adaptive neuro-fuzzy inference system. Int. J. Struct. Eng. **8**(1), 20–31 (2017)
23. Behfarnia, K., Khademi, F.: A comprehensive study on the concrete compressive strength estimation using artificial neural network and adaptive neuro-fuzzy inference system. Iran Univ. Sci. Technol. **7**(1), 71–80 (2017)
24. Khademi, F., Behfarnia, K.: Evaluation of concrete compressive strength using artificial neural network and multiple linear regression models. Iran Univ. Sci. Technol. **6**(3), 423–432 (2016)
25. Azimi, M., Li, M.: Estimating the displacement in reinforcement concrete building using artificial neural network modelling. J. Struct. Eng. (JSTE) **5**(3), 1–6 (2016)
26. Kennedy, J., Eberhart, R.: Particle swarm optimization. In: Proceedings of the IEEE International Conference on Neural Networks, 1995, vol. 4, pp. 1942–1948 (1995)
27. Cheng, F.Y., Jiang, H., Lou, K.: Smart Structures: Innovative Systems for Seismic Response Control. CRC Press, Boca Raton (2008)
28. Chopra, A.K.: Dynamics of Structures: Theory and Applications to Earthquake Engineering. Prentice Hall, Englewood Cliffs (2012)
29. Azimi, M., Rasoulnia, A., Lin, Z., Pan, H.: Improved semi-active control algorithm for hydraulic damper-based braced buildings. Struct. Control Health Monit. (2016)
30. Chandiramani, N.K., Motra, G.B.: Lateral-torsional response control of MR damper connected buildings. In: ASME 2013 International Mechanical Engineering Congress and Exposition, 2013, p. V04BT04A056 (2013)
31. Kaveh, A., Bakhshpoori, T., Azimi, M.: Seismic optimal design of 3D steel frames using cuckoo search algorithm. Struct. Des. Tall Spec. Build. **24**(3), 210–227 (2015)
32. Den Hartog, J.P.: Mechanical Vibrations. Courier Corporation, Chelmsford (1985)

Active Vibration Control of a Three Degree of Freedom Oscillator Using Two Eccentrically Rotating Masses

R. Terrill(✉), R. Bäumer, and U. Starossek

Structural Analysis and Steel Structures Institute,
Hamburg University of Technology, Hamburg, Germany
richard.terrill@tuhh.de

Abstract. An active mass damper utilizing rotating masses to damp the vibrations of an oscillator with two translational degrees of freedom in a horizontal plane and one rotational degree of freedom about a vertical axis is presented along with a corresponding closed-loop control algorithm. The damper consists of two masses rotating about a single vertical axis, powered by two actuators. In a preferred mode of operation, these masses rotate with a nearly constant and equal angular velocity in opposite directions, thus producing a harmonic control force in a single horizontal direction. By varying the relative angular position of the rotating masses, this control force can be directed in an arbitrary direction and used to damp the translational motion. In previous research, a control algorithm was derived for this purpose. The rotational degree of freedom can additionally be controlled by producing a moment by imposing angular accelerations on the rotating masses. In this paper, the previous control algorithm is augmented such that the rotational degree of freedom is additionally controlled. The augmented control algorithm is verified with help of numerical simulations.

Keywords: Three degree of freedom oscillator · Active damping · Twin rotor damper · Centrifugal forces · Closed-loop control

1 Introduction

In previous research, it has been shown that an active mass damping device implementing the centrifugal forces of two rotating masses can effectively control the motion of an oscillator with two translational degrees of freedom in a plane perpendicular to gravity [1, 2]. The purpose of this active mass damping device is to solve vibration-induced problems in structures such as high-rise buildings or monopile wind turbine towers. The first vibration mode determines the motion of such cantilever structures. Now an additional degree of freedom, the rotation about the oscillator's center of gravity is considered. When damping the translational motion of an oscillator, the damping device operates in a preferred mode of operation. In this mode of operation, the angular velocity of the control masses is approximately constant. In order to control the rotational vibrations of the now three degree of freedom oscillator, a moment must be created about its center of gravity. A moment induced by the angular accelerations of the control masses can be used to control the additional rotational

© Springer International Publishing AG 2018
J.P. Conte et al. (eds.), *Experimental Vibration Analysis for Civil Structures*,
Lecture Notes in Civil Engineering 5, https://doi.org/10.1007/978-3-319-67443-8_52

degree of freedom. Numerical simulations are performed to illustrate how two control algorithms, one for the translational degrees of freedom according to [2] and one for the rotational degrees of freedom which is derived here, can be combined to control the motion of the three degree of freedom oscillator.

2 Three Degree of Freedom Oscillator and Damping Device

2.1 Three Degree of Freedom Oscillator

The three degree of freedom oscillator considered in this paper is shown in Fig. 1. The two translational degrees of freedom, x and y, are used to define the translational motion of the oscillator in a plane perpendicular to gravity. ψ is used to describe the rotational degree of freedom about the center of gravity of the oscillator. The oscillator has a total mass $m + m_c$ and a moment of inertia I_o. The oscillator is supported in the X and Y directions by springs with the stiffness k_x and k_y, respectively. The rotational degree of freedom is restrained by a torsional spring with the stiffness k_r. Neglecting all types of damping, the equation of motion for the translational and rotational degrees of freedom is as given in Eqs. (1) and (2) in which the dot operator indicates the derivative with respect to time [3].

$$(m+m_c)\ddot{x}(t)+k_x x(t)=0 \quad (m+m_c)\ddot{y}(t)+k_y y(t)=0 \tag{1}$$

$$I_o\ddot{\psi}(t)+k_R\psi(t)=0 \tag{2}$$

Assuming that the spring stiffnesses k_x and k_y are equal, the indices are dropped and the natural circular frequency ω_n in both the X and Y directions is given by Eq. (3). With this assumption, the response of the three degree of freedom oscillator becomes equivalent in both directions. As a consequence, the control algorithms implemented

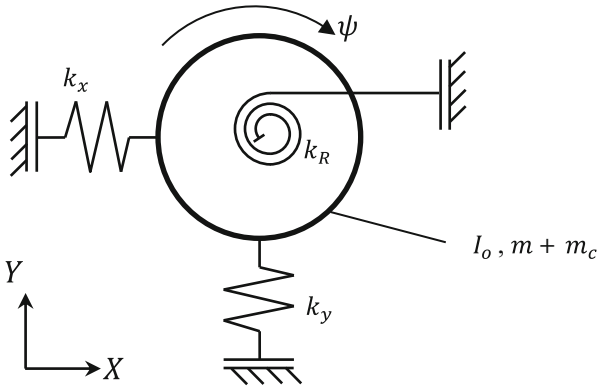

Fig. 1. Oscillator with two translational and one rotational degree of freedom.

and derived in this paper are confined for such systems. The natural circular frequency of the rotational degree of freedom, ω_r, is given by Eq. (4).

$$\omega_n = \sqrt{\frac{k}{m + m_c}} \tag{3}$$

$$\omega_r = \sqrt{\frac{k_r}{I_o}} \tag{4}$$

2.2 Damping Device

The vibrations of the three degree of freedom oscillator are controlled using the active mass damping device shown in Fig. 2. Two rotors, each consisting of a control mass, $0.5m_c$, and a massless rigid rod with the length r_c, are connected to a single axis at the center of gravity of the oscillator. Each rotor can move independent from one another.

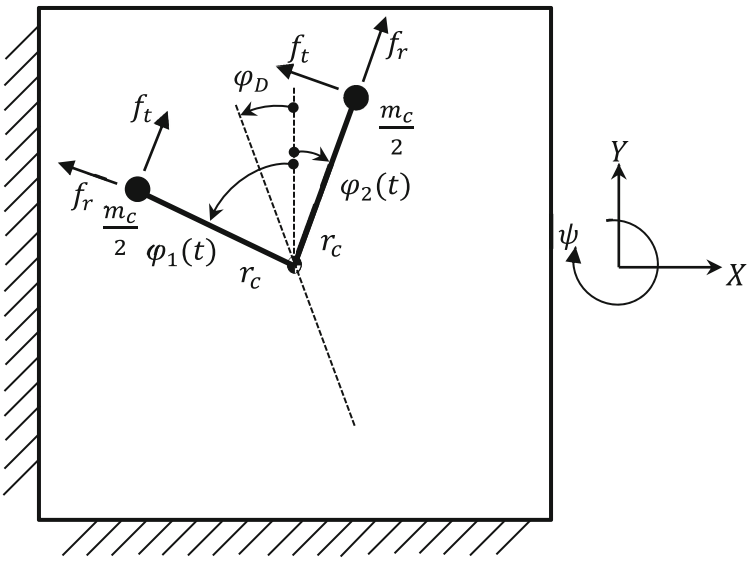

Fig. 2. Damping device

The time-dependent angular position of each rotor, $\varphi_1(t)$ and $\varphi_2(t)$, is measured from the positive y-axis and given in Eq. (5), in which the index 0 is used to refer to the initial conditions. The rotational motion of the rotors produces time varying radial and tangential forces, $f_r(t)$ and $f_t(t)$, respectively, see Eq. (6).

$$\varphi_1(t) = \dot{\varphi}_1(t)t + \varphi_{01} \qquad \varphi_2(t) = \dot{\varphi}_2(t)t + \varphi_{02} \tag{5}$$

$$f_r(t) = \frac{m_c}{2} r_c \left(\dot{\varphi}_1(t)^2 + \dot{\varphi}_2(t)^2 \right) \qquad f_t(t) = \frac{m_c}{2} r_c (\ddot{\varphi}_1(t) + \ddot{\varphi}_2(t)) \tag{6}$$

In [4], the vibrations of a single degree of freedom oscillator are damped using a similar device. This is done by operating the damping device in a preferred mode of operation in which the angular velocity, $\dot{\varphi}(t)$, of both rotors is constant and equal to the natural frequency of the oscillator. With a constant angular velocity, the angular accelerations, $\ddot{\varphi}(t)$, are equal to zero and therefore only radial forces are produced by the damping device. This mode of operation is referred to as the continuous rotation mode. The radial forces superimpose to a harmonic control force in a single direction. The direction of this control force,φ_D, solely depends on the initial angular positions, see Eq. (7).

$$\varphi_D = \frac{\varphi_1(t) - \varphi_2(t)}{2} \tag{7}$$

For the single degree of freedom oscillator the angular positions of the rotors are equal and the relative angular position between the rotors is constant. Therefore, the damping direction is also constant. However, in order to damp the vibrations of an oscillator with two translational degrees of freedom, the control force must be able to assume an arbitrary direction. This can be done by slightly varying the angular velocities of the rotors, therefore allowing for angular accelerations. In [1, 2], two control algorithms are presented for continuously calculating the time varying damping direction, $\varphi_D(t)$, such that the control force, f_c, always damps the translational motion of a two degree of freedom oscillator similar to the one here. Note this control force will be referred to in the following sections.

To damp the rotational vibrations of the oscillator is Fig. 1, the tangential forces are used to create a moment, M_c, about the center of gravity of the oscillator, see Eq. (8). The moment of inertia of each rotor, I_r, is equal to $0.5 m_c r_c^2$.

$$M_c = I_r(\ddot{\varphi}_2(t) - \ddot{\varphi}_1(t)) \tag{8}$$

Tangential forces are only produced by accelerating the rotors. In the continuous rotation mode, the angular velocity is approximately constant. Therefore, the tangential forces produced by the rotors are small. By allowing for larger changes in the angular velocity (angular accelerations) and simultaneously operating in the continuous rotation mode, the translational degrees of freedom will be damped and tangential forces can be used to create the moment, M_c, to damp the rotational degree of freedom of the oscillator.

3 Control Algorithms

3.1 Translational Degrees of Freedom

In [1, 2], control algorithms were derived and shown to be effective for damping the vibrations of a two-degree of freedom oscillator in an arbitrary direction. In [1], an energy approach is used to minimize the work done by the control force of the rotors on the oscillator to damp the translational degrees of freedom. The major drawback of this control algorithm is that when the trajectory of the two translational degrees of freedom oscillator becomes circular, damping efficiency could no longer be maintained. Therefore, further research was done and in [2] a control algorithm based on continuously determining the damping direction of the two degree of freedom oscillator is derived. This control algorithm is implemented here. In the following, a short summery is presented for completeness. For further information regarding the control of the two translational degrees of freedom, see [1, 2].

In order to damp the vibrations of an oscillator with two translational degrees of freedom, it is essential to determine the damping direction, $\varphi_D(t)$. This is done by observing the translational states of the oscillator and continuously calculating the amplitude, $A(t)$, of the oscillator's translational trajectory. Doing so, the major axis of the, in general, elliptical trajectory of the oscillator can be tracked and its direction, $\theta(t)$, determined, see Fig. 3. Using $\theta(t)$ the target angular position of each rotor, φ_{1T} and φ_{2T}, can be calculated such that a control force, which at all times opposes the velocity along the major axis, can be calculated [2].

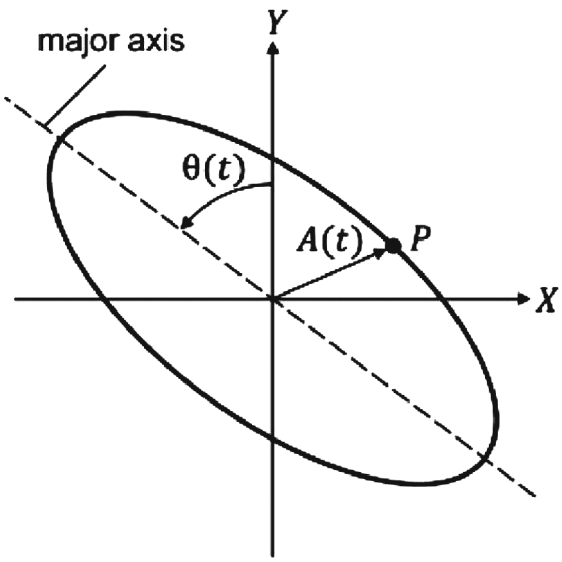

Fig. 3. Direction of the major axis [2]

3.2 Rotational Degree of Freedom

The equation of motion for the rotational degree of freedom of the oscillator, Eq. (2), can be modified by dividing by I_o and inserting Eq. (4) into Eq. (2). Taking the influence of the moments induced by the tangential forces produced by the rotors around the center of gravity of the oscillator into account, Eq. (9) is derived.

$$\ddot{\psi}(t) + \omega_r^2 \psi(t) = \frac{I_r}{I_o}(\ddot{\varphi}_2(t) - \ddot{\varphi}_1(t)) \tag{9}$$

The inertial forces due to the acceleration of the oscillator in the X and Y directions are assumed to be small and therefore neglected.

In order to derive a state space model incorporating the dynamics of the actuators, it is first assumed that the dynamics of the actuators can be simulated using the strictly proper transfer functions $G_1(s)$ and $G_2(s)$, see Eq. (10) [5].

$$G_1(s) = \frac{\varphi_1(s)}{U_1(s)} = \frac{a}{s^2 + bs} \qquad G_2(s) = \frac{\varphi_2(s)}{U_2(s)} = \frac{c}{s^2 + ds} \tag{10}$$

Note a, b, c, and d are constant values and $U_1(s)$ and $U_2(s)$ are the total control efforts. Transforming the transfer functions into the time domain, a differential equation to express the motor dynamic is derived, see Eq. (11).

$$\ddot{\varphi}_1(t) = a u_{r,1}(t) - b\dot{\varphi}_1(t) \qquad \ddot{\varphi}_2(t) = c u_{r,2}(t) - d\dot{\varphi}_2(t) \tag{11}$$

In Eq. (11) $u_1(t)$and $u_2(t)$ are replaced by $u_{r,1}(t)$ and $u_{r,2}(t)$ as, in this section, only the control effort required to damp the rotational degree of freedom is considered. Inserting Eq. (11) into Eq. (9) a state space model of the form

$$\dot{\mathbf{z}}(t) = \mathbf{A}\mathbf{z}(t) + \mathbf{B}\mathbf{u}(t) \tag{12}$$

whereas the state vector $\mathbf{z}(t)$, the system matrix $\mathbf{A}$, the input matrix $\mathbf{B}$, and the input vector $\mathbf{u}(t)$ are given in Eq. (13), [5].

$$\mathbf{z}(t) = \begin{bmatrix} \dot{\varphi}_1(t) \\ \varphi_1(t) \\ \dot{\varphi}_2(t) \\ \varphi_2(t) \\ \dot{\psi}(t) \\ \psi(t) \end{bmatrix}, \quad \mathbf{A} = \begin{bmatrix} -b & 0 & 0 & 0 & 0 & 0 \\ 1 & 0 & 0 & 0 & 0 & 0 \\ 0 & 0 & -d & 0 & 0 & 0 \\ 0 & 0 & 1 & 0 & 0 & 0 \\ -\frac{I_r}{I_o} b & 0 & \frac{I_r}{I_o} d & 0 & 0 & -\omega_r^2 \\ 0 & 0 & 0 & 0 & 1 & 0 \end{bmatrix}, \quad \mathbf{B} = \begin{bmatrix} a & 0 \\ 0 & 0 \\ 0 & c \\ 0 & 0 \\ \frac{I_r}{I_o} a & -\frac{I_r}{I_o} c \\ 0 & 0 \end{bmatrix},$$
$$\mathbf{u}(t) = \begin{bmatrix} u_{r,1}(t) \\ u_{r,2}(t) \end{bmatrix} \tag{13}$$

Using this state space model, a controller is designed using the Linear-quadratic regulator (LQR) design technique. For the LQR design, the cost function

$$J = \int_{t_0}^{t_{end}} \mathbf{z}^T(t)\mathbf{Q}\mathbf{z}(t) + \mathbf{u}^T(t)\mathbf{R}\mathbf{u}(t)dt \tag{14}$$

is minimized, where t_0 and t_{end} refer to the start and end times, respectively, and T is used to signify the transposition of a vector [5]. The weighting matrix of the LQR controller output $\mathbf{Q}$ is chosen such that only the rotational degree of freedom, $\psi(t)$ and $\dot{\psi}(t)$, are penalized. This ensures that this controller is not in conflict with the controller ensuring that the rotors operate in the continuous rotation mode for the damping of the translational degrees of freedom. Furthermore, the weighting matrix of the LQR controller output $\mathbf{R}$ is tuned by hand such that the inputs $u_{r,1}(t)$ and $u_{r,2}(t)$ are small and simultaneously provide sufficient damping for the rotational degree of freedom $\psi(t)$. The LQR design was performed using the program MATLAB.

3.3 Closed-Loop Control Algorithm for Three Degree of Freedom Oscillator

The closed-loop control algorithm for the three degree of freedom oscillator is shown in Fig. 4. It is assumed that the states, $x(t)$, $\dot{x}(t)$, $y(t)$, $\dot{y}(t)$, $\psi(t)$, and $\dot{\psi}(t)$, are available from the oscillator. The states, $x(t)$, $\dot{x}(t)$, $y(t)$, $\dot{y}(t)$ from the oscillator and $\varphi_1(t)$ and $\varphi_2(t)$ from the motor dynamics are fed into the controller for the translational degrees of freedom producing the control efforts $u_{t,1}(t)$ and $u_{t,2}(t)$ according to [2]. Simultaneously, the state vector $\mathbf{z}$ is fed into the LQR controller described in the previous section, producing the control efforts $u_{r,1}(t)$ and $u_{r,2}(t)$. The total control effort for each actuator is then calculated as

$$u_1(t) = u_{r,1}(t) + u_{t,1}(t) \qquad u_2(t) = u_{r,2}(t) + u_{t,2}(t) \tag{15}$$

and fed into the transfer functions $G_1(s)$ and $G_2(s)$, producing the state variables of the rotors. These states are then used to produce the control force $f_c(t)$ and the control moment $M_c(t)$ which act on the three degree of freedom oscillator.

3.4 Numerical Simulations

Numerical simulations were performed with the closed-loop control algorithm introduced in the previous section. The required variables and initial conditions, x_0, y_0, and ψ_0, of the oscillator were chosen as shown in Table 1. The additional variables for the controller and transfer functions were set to: $a = c = 60$ and $c = d = 20$. For simplicity, the natural circular frequency of the translational degrees of freedom is assumed to be equal to 2π. The natural circular frequency of the rotational degree of freedom, ω_r, is assumed to be twice as large as ω_n. The unitless ratios $m_c(m+m_c)^{-1}r_c x_o^{-1}$ and $I_r I_o^{-1}$ determine the decay of the vibrations in the translational and rotational degrees of freedom, respectively. For the LQR controller a $\mathbf{Q} = \mathrm{diag}(10^{-6}, 10^{-6}, 10^{-6}, 10^{-6}, 1, 1)$

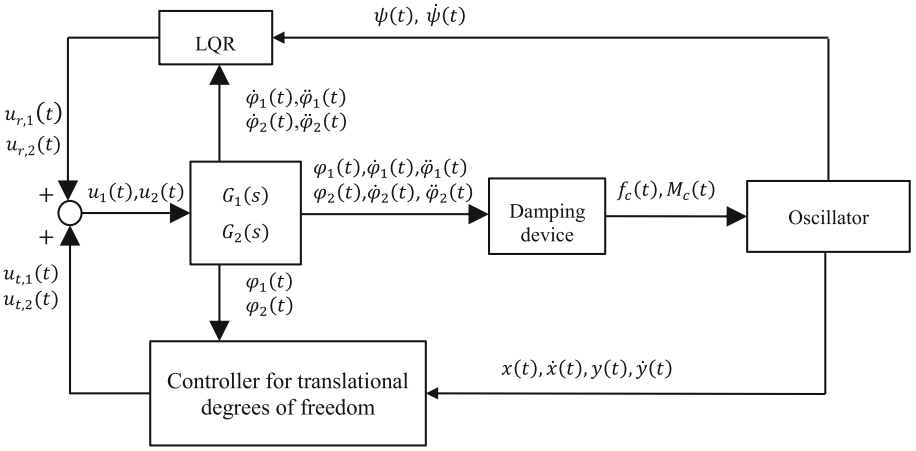

Fig. 4. Closed-loop control algorithm.

Table 1. Assumed simulation parameters.

$\omega_n = 2\pi$	$\omega_r = 2\omega_n$	$\frac{I_r}{I_o} = 0.025$	$\frac{m_c}{m+m_c} r_c x_o^{-1} = 0.06$	$y_o = 0.5x_o$	$\psi_0 = 0.1745$ rad (10°)

and a $\mathbf{R} = \text{diag}(7, 7)$ are chosen, where diag is used to denote the entries of the diagonal matrices **Q** and **R.**

In Figs. 5 and 6, respectively, the responses of the three degree of freedom oscillator and the angular velocities of the rotors are shown for a length of $10T_n$, whereas $T_n = \omega_n(2\pi)^{-1}$. Three numerical simulations scenarios are performed: uncontrolled, control of the translational degrees of freedom, and control of the translational and rotational degrees of freedom.

In Fig. 5, the vibrations of the oscillator in each degree of freedom are shown for each simulation scenario. The top two diagrams show the translational vibrations for each simulation scenario normalized by x_o. From these diagrams, it can be seen that the translational vibrations are effectively damped with and without controlling the rotational degree of freedom. The difference in the damping performance, when additionally damping the rotational degree of freedom, is minimal. This verifies that the tangential forces created by the rotor accelerations, $\ddot{\varphi}_1(t)$ and $\ddot{\varphi}_2(t)$, do not interfere with the control force used to damp the translational degrees of freedom in the continuous rotation mode. The third diagram shows the uncontrolled and controlled rotational vibrations normalized by ψ_0. In this diagram, it can be seen that the rotational vibrations are effectively damped. Therefore, the control algorithm introduced in the previous section used in combination with the control algorithm from [2] effectively damps all three degrees of freedom.

In Fig. 6, the rotor velocities, $\dot{\varphi}_1(t)$ and $\dot{\varphi}_2(t)$, are shown normalized by ω_n when controlling the translational degrees of freedom and all three degrees of freedom. In this diagram, it can be seen that both rotors are in the continuous rotation mode when only the translational degrees of freedom are controlled as both rotors have an approximately

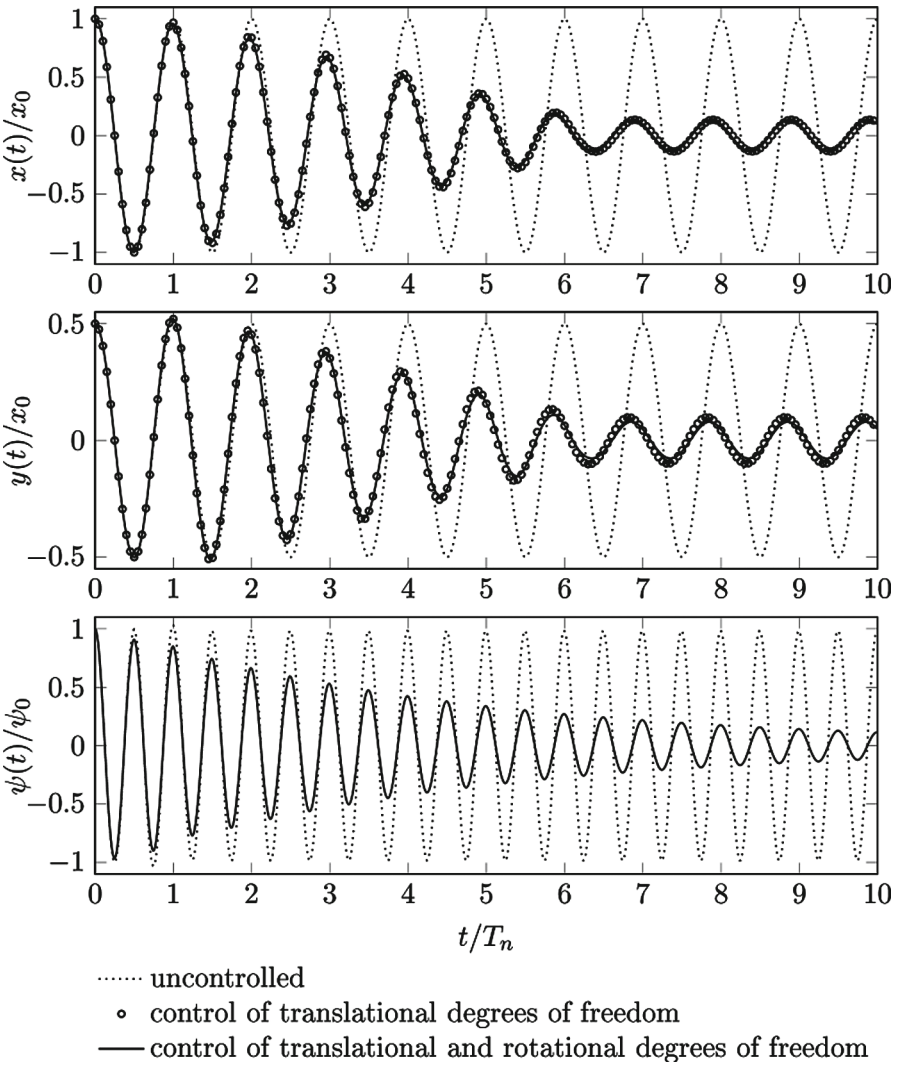

Fig. 5. Three degree of freedom oscillator vibrations, uncontrolled and controlled

constant angular velocity. $\dot{\varphi}_1(t)$ and $\dot{\varphi}_2(t)$ reach ω_n at different times. This is a secondary effect of the control algorithm used for the translational degrees of freedom [2]. When controlling the translational degrees of freedom, the angular velocities fall suddenly to zero after approximately $6T_n$. At this point in time the vibration amplitudes are considered to be sufficiently small and the control algorithm for the translational degrees of freedom is turned off. This is done to prevent re-excitation. For further information regarding the control of the translational degrees of freedom, see [2].

Now considering the angular velocities in which the translational and rotational degrees of freedom are controlled, it can be seen that the angular velocities are at no

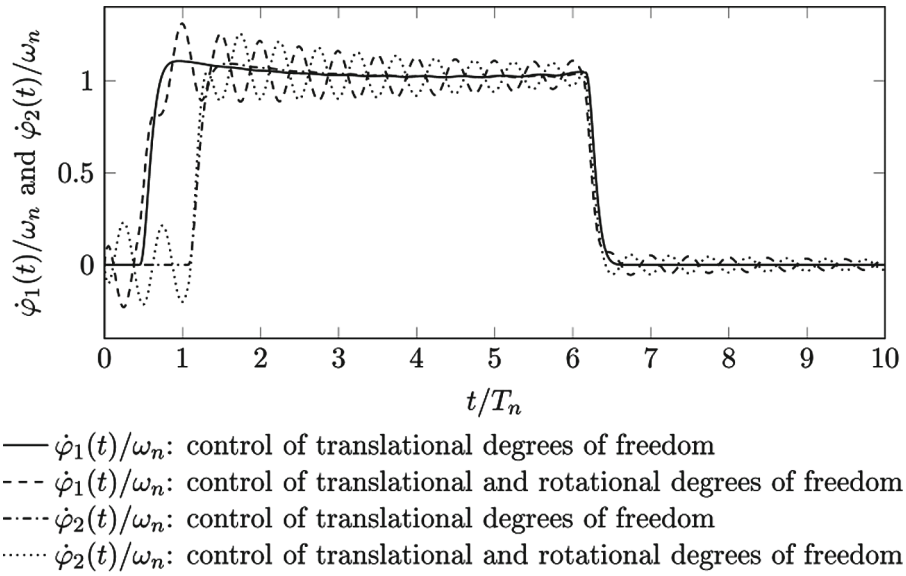

Fig. 6. Rotor angular velocities

time near constant. The angular velocities of both rotors oscillate with the natural frequency of the rotational degree of freedom counter-phase of one another. Inspecting Eq. (8), it can be seen that a positive $\ddot{\varphi}_2(t)$ and a negative $\ddot{\varphi}_1(t)$ are required to produce a positive moment; hence the counter-phase of the angular velocities. In the numerical simulation, a positive initial rotation, ψ_0, is given, therefore at the start of the simulations, $\dot{\varphi}_2$ and $\dot{\varphi}_1$ become positive and negative, respectively. At the start of the simulations, the discrepancy between the angular velocities when damping the translational degrees of freedom and all degrees of freedom is largest. This is a result of the large rotational vibration at the start of the simulation. The angular velocities never reach zero as the rotational vibrations are damped throughout the entire simulation.

From Figs. 5 and 6, it can be concluded that is it possible to simultaneously control the translational and rotational degrees of freedom of the presented three degree of freedom oscillator. These diagrams also indicate that the control algorithm used for controlling the translational degrees of freedom is robust. This can be seen by noting that this control algorithm is based on operating in a mode of operation with an approximately constant angular velocity. In order to damp the rotational vibrations, angular accelerations are required leading to a non-constant angular velocity. Nonetheless, the translational degrees of freedom are damped with only a nominal difference in the damping performance.

4 Future Work

Numerical simulations have been used to show the effectiveness of the combined control algorithms. The next step is to evaluate their effectiveness experimentally. This has been done in [2] for the control algorithm for the translational degrees of freedom using the test setup shown in Fig. 7. The test setup consists of an oscillating body suspended by three steel wires to a stiff frame. Two actuators with rotors consisting of a control mass and steel rod are attached to the center of gravity of the oscillating body. Displacement transducers are used to continuously measure the displacement of the oscillating body in both translational directions. The test setup is currently being altered such that the rotational degree of freedom can be continuously measured. This will allow for the experimental evaluation of the control algorithm for the rotational degree of freedom.

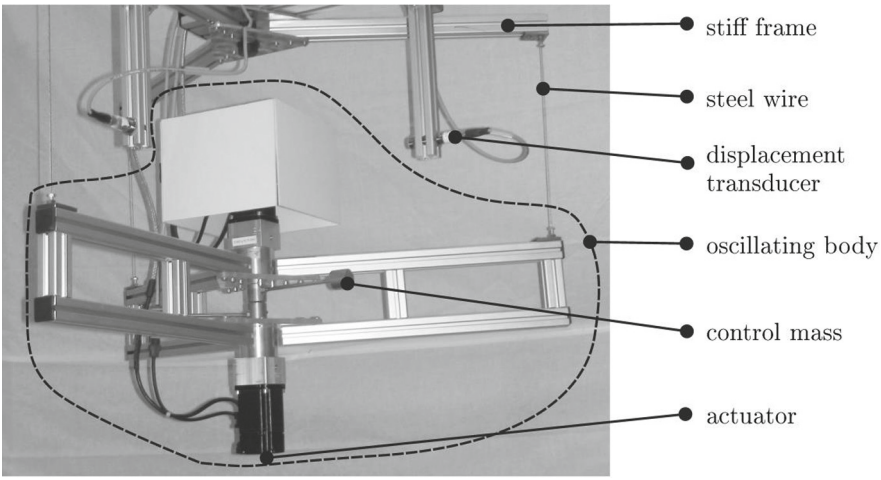

Fig. 7. Test setup according to [2]

5 Conclusions

An active mass damper implementing the centrifugal forces produced by the rotation of two control masses about a single axis for the vibration control of an oscillator with two translational and one rotational degree of freedom is presented. In previous research, a control algorithm is derived for the control the translational degrees of freedom. The translational degrees of freedom are controlled in a mode of operation in which the angular velocities of the control masses are approximately constant; therefore the angular accelerations are small. The more the rotors are required to accelerate the larger the energy required by the actuators becomes. Therefore, the continuous rotation mode is, due to the small accelerations, an energy efficient mode of operation. However, when it is wished to additionally damp the rotational degree of freedom, accelerations are required. Here a control algorithm implementing the tangential forces created by the angular accelerations of the control masses is shown to be effective for the control of

the rotation of the oscillator about its center of gravity. By combining the control algorithm presented here and the control algorithm for the translational degrees of freedom, all three degrees of freedom can be damped. The continuous rotation mode loses some of its advantages, but an additional degree of freedom is controlled. Numerical simulations of the combination of the control algorithm for the translational degrees of freedom and the control algorithm for the rotational degrees of freedom are performed. It is shown that all three degrees of freedom can be effectively controlled.

References

1. Bäumer, R., Terrill, R., Starossek, U.: An energy approach for the active vibration control of an oscillator with two translational degrees of freedom using two auxiliary rotating masses. J. Phys. Conf. Ser. **744**, 012230 (2016). doi:10.1088/1742-6596/744/1/012230
2. Bäumer, R., Starossek, U.: Active vibration control of an oscillator with two translational degrees of freedom using centrifugal forces created by two eccentrically rotating masses. Int. J. Dyn. Control (2016). doi:10.1007/s40435-016-0280-8
3. Clough, R.W., Penzien, J.: Dynamics of Structures, 2nd edn. McGraw-Hill, New York (1993)
4. Bäumer, R., Starossek, U.: Active vibration control using centrifugal forces created by eccentrically rotating masses. J. Vib. Acoust. **138**(4), 041018 (2016). doi:10.1115/1.4033358
5. Franklin, F.F., Powell, J.D., Emami-Naeini, A.: Feedback Control of Dynamic Systems, 4th edn. Prentice Hall, Upper Saddle River (2002)

System and Modal Identification

Experimental Evaluation of the Effect of Geometric Nonlinearities on Structural Resonances

Reyolando M. Brasil[1(✉)] and Alexandre M. Wahrhafitg[2]

[1] Aerospace Engineering, Federal University of ABC, São Bernardo, SP, Brazil
reyolando.brasil@poli.usp.br
[2] Federal University of Bahia, Salvador, BA, Brazil

Abstract. In this research paper, we intend to study the effects of geometric nonlinearities on vibrations of rotating machinery support structures. Dynamic characteristics of structures depend on their stiffness and mass. With those, we determine their natural frequencies and modes of free vibrations. Nevertheless, the initial stiffness of a structure, computed in its unloaded state, is affected by the applied forces, the so-called geometric stiffness. Compressive forces usually reduce the stiffness and the frequencies and may lead to buckling, for zero frequencies. In the other hand, tractions loads tend to increase stiffness and frequencies, a phenomenon resorted upon by the so-called tensile structures.

Classes of structures of economic-strategic importance are bases of machines, excited by vibrations induced by the supported equipment. These vibrations may affect the structures but, in general, may generate damage to the suspended equipment and the quality of the production. They may also render inadequate human working conditions. Almost all industrial branches are subjected to this problem, including highly sensitive ones such as petrol, wind and atomic energy generation areas.

Although machine support structures are, as a rule, very bulky, and thus little affected by geometric stiffness considerations, the tendency of modern structural engineering is towards slender members, due to more efficient materials and more powerful analysis tools. In this research paper, we study these effects via mathematical and experimental methods. Both laboratory essays and numerical models are developed. Our structure is a metal beam under pretension supporting a rotational machine. We suppose the original design have provided for natural frequencies away from the excitation frequency. Nevertheless, the presence of large axial compressive force will reduce the beam stiffness and natural frequencies leading to unexpected potentially dangerous resonance states.

Keywords: Experimental vibration analysis · Geometric nonlinearity · Resonance · Machine foundations · Pretension

1 Introduction

In this paper, we study the effects of geometric nonlinearities on vibrations of a motor metal beam support structure under large compressive axial loading. This will reduce the stiffness of the beam due to the so called geometric nonlinearity. In consequence,

© Springer International Publishing AG 2018
J.P. Conte et al. (eds.), *Experimental Vibration Analysis for Civil Structures*,
Lecture Notes in Civil Engineering 5, https://doi.org/10.1007/978-3-319-67443-8_53

natural frequencies will be reduced. We suppose the original design have provided for natural frequencies away from the excitation frequency. Nevertheless, the presence of the geometric nonlinearity due to the large axial force may lead to unexpected potentially dangerous resonance states. Previous mathematical modeling and simulation about the effect on geometric nonlinearity on the frequencies of structures are to be found in [1], in the context of mode localization in quasi periodic structures, and [2], for portal framed support structures.

The studied problem is represented in schematic form in Fig. 1. It is a simply supported aluminum beam with thin walled (thickness t = 2.5 mm) square 4″ × 4″ cross section. The material elastic modulus is E = 72 GPa, density ρ = 2700 kg/m^3, and yielding stress 127 MPa. The span is L = 3 m. At middle section a motor and its fixtures of mass M = 5.385 kg is mounted. The variable compressive axial load P is applied by a 15 mm diameter steel rod, 1.44 kg/m, stretched by a hydraulic jack.

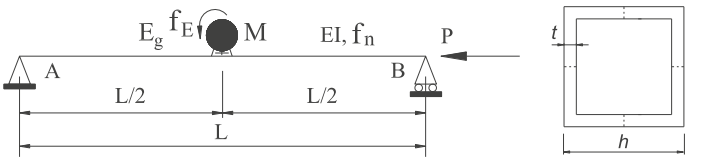

Fig. 1. The motor support beam model.

2 The Mathematical Model

2.1 Rayleigh's Method

John William Strutt, 3rd Baron of Rayleigh, presented, in "The Theory of Sound" [3], a simplified method to access the dynamic properties of structures. In the case of horizontal beams, the transverse vertical vibration displacement of the axis, as shown in Fig. 2, is a function of both a spatial x coordinate and time, may be written as

$$v(x,t) = \phi(x)\, q(t) \tag{1}$$

where $\phi(t)$ is a *shape function*, that must satisfy the geometric boundary conditions and assume unitary value where the $q(t)$ generalize coordinate is chosen. In our model, that is the center section of the beam, where the motor is mounted.

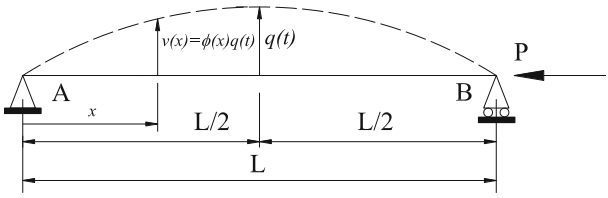

Fig. 2. Rayleigh's method hypothesis.

For a prismatic, simply supported, homogeneous beam, the best such function is a simple sine half wave

$$\phi(x) = \sin \frac{\pi}{L} x \tag{2}$$

The resulting equivalent elastic stiffness is

$$k_0 = EI \int_0^L (\phi'')^2 dx = \frac{\pi^4 EI}{2L^3} \tag{3}$$

the equivalent geometric stiffness is

$$k_g = P \int_0^L (\phi')^2 dx = \frac{P\pi^2}{2L} \tag{4}$$

and the equivalent lumped mass is

$$m_0 = \bar{m} \int_0^L (\phi'')^2 dx = \frac{\bar{m}L}{2} \tag{5}$$

where $\bar{m}$ is the mass of the beam per unity length. Of course, the motor mass M must be added to the value given by Eq. (5).

Table 1 displays results of the first natural frequency for a series of possible compressive axial loads, using Rayleigh's method. One must observe that axial loads more than 140 KN will cause yielding of the material, aluminum. Zero frequency correspond to Euler's bucking load 128.38787 KN.

Table 1. First natural frequency results for variable P compressive axial load, Rayleigh's method.

P (KN)	Frequency (Hz)	Frequency (RPM)
0	23.299	1397.957
20	21.408	1284.464
40	19.332	1159.920
60	17.005	1020.285
80	14.304	858.223
100	10.956	657.352
120	5.955	357.320
128.38787	0.000	0.000

2.2 The Finite Element Method

A recent enhancement of Rayleigh's method is the finite element method, FEM, [4, 5]. Here, the problem domain is discretized in many small but finite sub domains, called *elements*, and shape functions are adopted in such a way as to be different from zero only inside of the element and assume unity value in only one of the *nodes* of the element.

In Fig. 2 we present a very coarse two elements discretization of the studied beam.

In Eqs. (6) to (11) L is now the length of the element, not of the complete beam (Fig. 3).

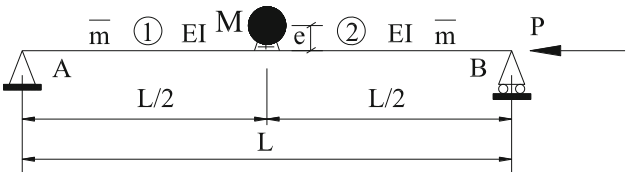

Fig. 3. A two elements FEM model.

The prismatic homogeneous beam element linear elastic stiffness matrix, adopting cubic polynomial shape functions is given by Eq. (6).

$$\mathbf{k_0} = \begin{bmatrix} \frac{12EI}{L^3} & \frac{6EI}{L^2} & -\frac{12EI}{L^3} & \frac{6EI}{L^2} \\ & \frac{4EI}{L} & -\frac{6EI}{L^2} & \frac{2EI}{L} \\ & & \frac{12EI}{L^3} & -\frac{6EI}{L^2} \\ & & & \frac{4EI}{L} \end{bmatrix} \tag{6}$$

The beam element linear geometric stiffness matrix is

$$\mathbf{k_G} = P \begin{bmatrix} \frac{6}{5L} & \frac{1}{10} & -\frac{6}{5L} & \frac{1}{10} \\ & \frac{2L}{15} & -\frac{1}{10} & -\frac{L}{30} \\ & & \frac{6}{5L} & -\frac{1}{10} \\ & & & \frac{2L}{15} \end{bmatrix} \tag{7}$$

The beam consistent mass matrix is

$$\mathbf{m} = \begin{bmatrix} \frac{156\bar{m}L}{420} & \frac{22\bar{m}L^2}{420} & \frac{154\bar{m}L}{420} & -\frac{13\bar{m}L^2}{420} \\ & \frac{4\bar{m}L^3}{420} & \frac{13\bar{m}L^2}{420} & -\frac{3\bar{m}L^3}{420} \\ & & \frac{156\bar{m}L}{420} & -\frac{22\bar{m}L^2}{420} \\ & & & \frac{4\bar{m}L^3}{420} \end{bmatrix} \tag{8}$$

Next, we assemble the structure global elastic stiffness, geometric stiffness and mass matrices, as follows.

$$\mathbf{K_0} = \begin{bmatrix} \frac{24EI}{L^3} & 0 & -\frac{6EI}{L^2} & \frac{6EI}{L^2} \\ & \frac{8EI}{L} & \frac{2EI}{L} & \frac{2EI}{L} \\ & & \frac{4EI}{L} & 0 \\ & & & \frac{4EI}{L} \end{bmatrix} \tag{9}$$

$$\mathbf{K_G} = P \begin{bmatrix} \frac{12}{5L} & 0 & -\frac{1}{10} & \frac{1}{10} \\ & \frac{4L}{15} & -\frac{L}{30} & -\frac{L}{30} \\ & & \frac{2L}{15} & 0 \\ & & & \frac{2L}{15} \end{bmatrix} \tag{10}$$

$$\mathbf{M} = \begin{bmatrix} \frac{312\bar{m}L}{420} + M & 0 & \frac{13\bar{m}L^2}{420} & -\frac{13\bar{m}L^2}{420} \\ & \frac{8\bar{m}L^3}{420} + Me^2 & -\frac{3\bar{m}L^3}{420} & -\frac{3\bar{m}L^3}{420} \\ & & \frac{4\bar{m}L^3}{420} & 0 \\ & & & \frac{4\bar{m}L^3}{420} \end{bmatrix} \tag{11}$$

Table 2 displays results of the first natural frequency for a series of possible compressive axial loads. Even though we have only two elements, FEM computed values are reasonably close to those predicted by Rayleigh's method in Table 1. As expected, frequencies are slightly higher, as the method theoretically converge to exact values from above, that is, fewer elements result a stiffer model.

Table 2. First natural frequency results for variable P compressive axial load, two element FEM model.

P (KN)	Frequency (Hz)	Frequency (RPM)
0	23.813	1428.8
20	21.898	1313.9
40	19.798	1187.9
60	17.444	1046.7
80	14.718	883.1
100	11.352	681.1
120	6.409	384.5

3 Experimental Vibration Analysis

3.1 The Experimental Setup

Figure 4 is a photograph of the experimental setup. As mentioned, it is a simply supported aluminum beam with thin walled (thickness t = 2.5 mm) square 4″ × 4″ cross section. The material elastic modulus is E = 72 GPa, density ρ = 2700 kg/m^3, and yielding stress 127 MPa. The span is L = 3 m. At middle section a motor and its

Fig. 4. Photograph of the experimental setup.

fixtures of mass $M = 5.385$ kg is mounted. The variable compressive axial load P is applied by a 15 mm diameter steel rod, 1.44 kg/m, stretched by a hydraulic jack, shown in Fig. 5.

Fig. 5. Hydraulic jack applied to the experimental setup.

Commercial accelerometers are mounted under the motor position and standard vibration data acquisition hardware and software were used.

The experimental measurements were performed at the Laboratories of the Structural Engineering Department of the Federal University of Bahia, Salvador City, Bahia, Brazil.

3.2 Experimental Results

Table 3 displays resulting measured first natural frequencies for a series of axial loads applied by the hydraulic jack.

Table 3. Experimentally measured first natural frequency results for variable P axial load.

P (KN)	Frequency (Hz)	Frequency (RPM)
0	23.299	1397.94
20	22.337	1340.22
40	20.878	1253.88
60	19.045	1142.70
80	16.592	995.52

Due to the presence of imperfections in the position of the axial load, that is, accidental eccentricities, for a value of axial force somewhat above 90 KN the beam failed because of additional flexural stresses, as shown in Fig. 6.

One should note, in Table 3, that the measured initial frequency, for zero axial load it is almost the same provided by the mathematical models in Tables 1 and 2. As the pretension forces are applied, due to the presence of imperfections, the values of the

Fig. 6. Flexural failure of beam due to accidental eccentricities of the axial load.

first natural frequency decreases as expected, but vary considerably from the predicted by the mathematical models.

4 Conclusions

We presented both mathematical and experimental analysis of a simply supported aluminum beam carrying a rotating electric motor and subjected to a large axial compressive load applied by a hydraulic jack. This force, due to geometric nonlinearity, reduces the structure stiffness and consequently its natural frequencies. This effect may be used to avoid resonances.

Experimental and mathematical results agree very closely for zero axial force. As the pretension forces are applied, due to the presence of imperfections, the values of the first natural frequency decrease as expected, but vary considerably from those predicted by the mathematical models. Beam failure from flexural stresses is also observed.

A new series of measurements are being carried out with very careful attention to the elimination of initial eccentricities to check mathematical predictions. Traction axial forces are also being applied leading to increase in frequency values.

Acknowledgments. The authors acknowledge support by FAPESP, CNPq and CAPES, all Brazilian research funding agencies.

References

1. Brasil, R.M.L.R.F., Mazzilli, C.E.N.: Influence of loading on mode localization in periodic structures. Appl. Mech. Rev. **48**, 132–137 (1995)
2. Mazzilli, C.E.N., Brasil, R.M.L.R.F.: Effect of static loading on the nonlinear vibrations of a three time redundant portal frame: analytical and numerical studies. Nonlinear Dyn. **8**, 347–366 (1995)
3. Rayleigh, J.W.S.: The Theory of Sound, 2nd edn. Dover Publications, New York (1945)
4. Clough, R.W., Penzien, J.: Dynamics of Structure, 2nd edn. McGraw-Hill, New York (1993)
5. Cook, R., Malkus, D.S., Plesha, M.E.: Concepts and Applications of Finite Element Analysis, 4th edn. Wiley, New York (2002)

The Selection of a Dynamic Model of a RC Chimney Based on In Situ Research

Tadeusz Tatara(✉) and Bartłomiej Ratajewicz

Faculty of Civil Engineering,
Cracow University of Technology, Kraków, Poland
ttatara@pk.edu.pl

Abstract. This paper refers to the dynamic in situ investigation of a RC chimney and the choice of an appropriate numerical model in order to evaluate it. The first part of the study deals with the evaluation of the dynamic characteristics of a typical RC industrial chimney which belongs to a heating plant. In the investigation, different sources of excitation were used in order to better assess the structure's free vibrations. In this investigation, wind gusts and rhythmic, human-induced swaying were used as sources of excitation in order to better assess the structure's free vibrations. The following three pieces of measuring apparatus were used in order to record the structure's movement: electro-dynamical strain gauges; piezoelectric accelerometers; a Doppler laser vibrometer. Power-spectral density (PSD), cross-spectral density (CSD) and fast Fourier transform (FFT) algorithms were applied to determine the natural frequencies of the structure. The second part of the study involves the determination of the calculated dynamic characteristics of the selected RC chimney. A FEM model was built and important structural factors were used in its determination. Ground properties under the foundation of the structure were applied and variations in concrete characteristics due to carbonation and decay were factored in as were geometrical imperfections of the structure. By using natural vibration excitation sources, the lowest frequency of free vibration of the structure was determined. The third part of the paper focuses on the evaluation of the accuracy of the applied models resulting in the identification of the most valuable FEM model of the chimney. Different element types and varying levels of material modelling precision were used. The results of experimental studies were used as a basis for the verification and rating of the proposed models. The most accurate model was chosen – this was defined on the basis of it being the most capable of being successfully applied in further calculations of the dynamic response of the structure.

Keywords: RC chimney · Structural health monitoring · Carbonation · Concrete deterioration · In situ dynamic investigation · Source of vibration · FEM analysis · Geometrical imperfection · Ground properties · Measuring apparatus

B. Ratajewicz — Ph. D. Student at Faculty of Civil Engineering, Cracow University of Technology, Kraków, Poland

© Springer International Publishing AG 2018
J.P. Conte et al. (eds.), *Experimental Vibration Analysis for Civil Structures*,
Lecture Notes in Civil Engineering 5, https://doi.org/10.1007/978-3-319-67443-8_54

1 Introduction

Industrial chimneys are an important element of technical infrastructure and industrial facilities such as power plants, steel mills, waste incinerators and petrochemical plants. They are divided into various types based on the material used for their construction (concrete, steel, ceramic) and the construction of the flue (single, multi) [1, 2]. Depending on the material and design, they have completely different dynamic properties – a steel smoke stack will behave differently to a reinforced concrete stack [1, 2]. The single-flue reinforced concrete chimneys which are analysed in this paper consist of a reinforced concrete shaft, a ceramic lining inside the flue duct and a thermo-insulation layer [2, 3]. During their operation, the structures are exposed to adverse weather conditions and aggressive chemical fumes containing acidic compounds (*e.g.* sulphur or chlorine) which corrode the concrete shaft [1–4], the lining, the thermal insulation layer and often, chimney accessories such as maintenance galleries or access ladders. In some cases, due to production cycle changes and additional installations, the chimneys are not adapted to cope with the volumes of discharged gases, their temperature, humidity, or chemical composition – this causes a significant increase in the intensity of chimney corrosion [3, 4]. The long-term operation of industrial chimneys causes changes to the strength properties of materials used for their construction. Acidification of concrete causes creeping carbonation which changes the material characteristics of the concrete and lowers the pH value [3, 4]. Low pH may cause the concrete to cease protecting the rebar steel from corrosion. This leads to the formation of corrosive *substances* around the rebar elements and the further degradation of the concrete chimney shaft. Under the influence of exhaust gases, the ceramic flue lining ceases to serve its protective function over time causing further penetration of the chemically aggressive exhaust to the concrete chimney shaft and the thermo-insulating layer, often completely destroying the latter [3, 4]. Industrial chimneys are the subject of numerous in-situ experimental studies [1, 3–5]. These studies can be divided into static tests (indicating changes to material properties and general condition) and dynamic tests used to determine the dynamic properties of the structure, such as eigenfrequencies, mode shapes, damping coefficients and dynamic response [1, 5]. This paper is devoted to the experimental and numerical analysis of a 120-metre-tall, single-flue, reinforced-concrete chimney. This chimney is part of a power plant in southern Poland. In this study, the dynamic properties of the chimney were evaluated using in-situ dynamic testing; the results were used to verify the numerical (FEM) models of the chimney.

2 Case Study

2.1 Description of the Selected Structure

A 120-metre-tall, reinforced-concrete chimney with a ceramic-lined single flue was chosen (Fig. 1); this chimney can be considered to be typical of this type of structure. The chimney was designed in 1975 and fully commissioned in 1982; it is founded upon a circular reinforced concrete foundation block with a diameter of 24 m.

The chimney's shaft is made of reinforced concrete. Its outer diameter is 8.7 m at the base and 5.5 m at the outlet (at 120 m). The shaft ends with a reinforced concrete

Fig. 1. Mode shapes of the building.

slab forming the narrowed section of the chimney outlet. The wall thickness of the chimney shaft is 0.5 m at its base and 0.18 m near the top. The ceramic lining of the chimney's flue duct is made of 15 cm-thick ceramic bricks with a compressive strength of 25 MPa. Between the lining and the concrete shaft, an 8 cm-thick thermo-insulation layer of mineral wool is installed. The chimney is equipped with three steel maintenance galleries at heights of 40 m, 80 m and 117 m, and an arrangement of steel access ladders over its entire height. The chimney's concrete shaft and the steel fittings were renovated in phases from 1999 to 2003. The outer surface of the shaft is in good condition, with the only damage being local cracking, point scaling and pop-outs The condition of the chimney's ceramic flue duct lining is good.

2.2 Material Analysis

According to the original design, the chimney was built of C16/20 class reinforced concrete with a compressive strength of 20 MPa, reinforced with A-0 class steel (tensile strength of 220 MPa). From 1997 to 2011, the chimney was repeatedly examined in numerous technical surveys. Chemical tests of samples taken from the concrete shaft show the contamination of the concrete in the outer and inner layers. In 1997, SO_4^{2-} ions on the inner layer of the shaft constituted 3.1–4.2% of the concrete binder weight, and 4.0–5.5% in the year 2011 [3, 4]. At the level of the first gallery, the contamination occurs both on the internal and external layers. At the level of the second gallery, the concrete of the shaft is highly contaminated with sulphates and chlorides in its inner layer; however, its pH indicates that it still offers corrosion protection to the rebar elements. At the third gallery's level, the contamination covers only in the inner layer to a thickness of around

2 cm. Laboratory tests on samples Φ = h = 100 mm and in-situ Schmidt hammer tests show an increase in the compressive and tensile strength of the shaft's concrete. According to the 2011 data,
the measured compressive strength of the shaft's concrete is f_{ck} = 37.5 MPa. For comparison, in 1997 the laboratory studies determined the average compressive strength of concrete to be f_{ck} = 25 MPa; therefore, an increase in the average compressive strength of the shaft's concrete due to carbonation is clearly visible.

2.3 Geometry

Geodetic measurements have indicated that the top of the chimney is tilted towards the south east. In 2005, the deflection was 226 mm and in 2011, this had increased to 246 mm (±5 mm). Tilt measurements according to the data for 2011 are shown in Fig. 2a, and projections on X and Y axes are shown in Figs. 2b and c, respectively.

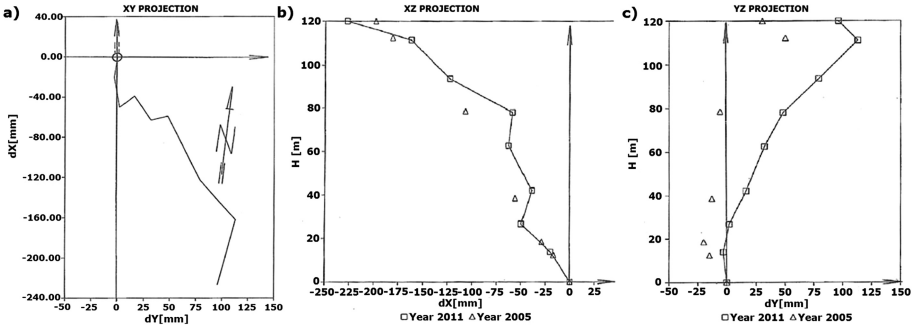

Fig. 2. The chimney's axial tilt. (a) XY projection, (b) XZ projection, (c) YZ projection.

3 Dynamic Testing

Dynamic tests focused at measuring natural frequencies and damping factors of the chimney. Wind-gusts and human swaying were used as vibration sources. Wind gust speed, according to a local meteorological station, was 24 km/h during the time of testing. Figure 3 shows a sketch indicating the chimney sections and sensors used in the research. The following three types of sensors were used for measurement: piezoelectric accelerometers; a laser vibrometer; strain gauges.

3.1 Piezoelectric Accelerometers

PCB model 393B12 piezoelectric accelerometers were placed in pairs at heights of 40 m, 80 m and above 117 m level. These devices allow for the measurement of accelerations of the structure to which they are attached. The measurement was performed in the X and Y axis of the chimney. Accelerometers were mounted to aluminium blocks fixed to the chimney's shaft.

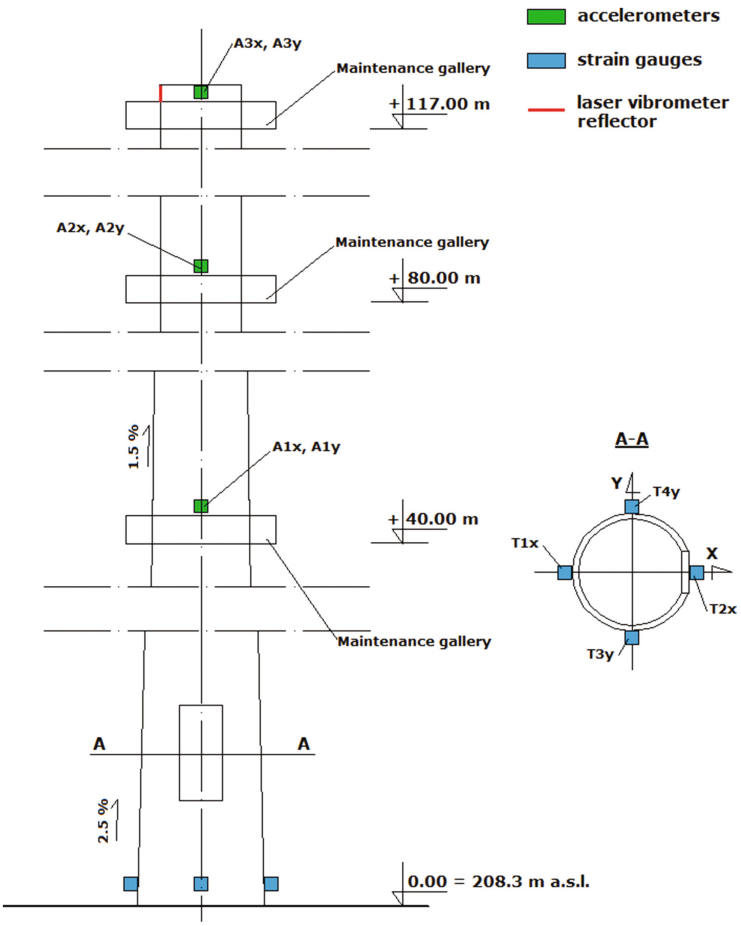

Fig. 3. Sketch of the structure, deployment of chosen sensors.

3.2 Laser Vibrometer

A Polytec RSV-150 laser vibrometer was used in this investigation – this is a dual laser Doppler interferometer with a sensor capable of measuring displacement and velocity at distances of over 100 m. The measurement is performed through the laser illumination of a reflector mounted on a vibrating surface. The frequency of the reflected wave of the laser light is modulated due to the Doppler effect and measured by the interferometer inside the device which converts the incoming signal into an electrical signal to determine the speed or displacement of the structure. The reflective surface was fitted above the third gallery at a height of 118 m.

3.3 Strain Gauges

Philips 100 mm strain gauges were mounted at a height of 1.5 m in four spots on the main axes of the chimney, in the zone where major strains of the concrete shaft were expected. Four sets of strain gauges were used to measure the deformation of the chimney's shaft resulting from the shaft's vibration (see Fig. 4).

Fig. 4. Strain gauges, location and example measuring point.

3.4 Analysis of the Results

Figure 5 shows example time-history plots of the recorded vibrations of the chimney's shaft which were induced by the movement of a group of people at the highest level gallery (above 117 m) using accelerometers, strain gauges and the laser vibrometer at selected measuring points. Vibration data was filtered using a low-pass filter with a value of 10 Hz. Figure 6 depicts the results of the FFT analysis of the time-history of vibrations along the X axis induced by the movement of a group of people at the highest gallery level (see Fig. 3). The FFT spectra according to Fig. 6 show that the frequency of the chimney's first mode of resonance vibration is 0.365 Hz according to the accelerometric measurement, 0.388 Hz according to strain gauge measurement and 0.375 Hz as measured with the laser vibrometer. Figure 7 depicts example FFT spectra of measured acceleration and velocity in the X axis, determining the chimney's second resonance vibration as 1.567 Hz according to accelerometric measurement and 1.563 Hz as measured using a laser vibrometer. Table 1 shows a summary list of the measured free vibration frequencies (considered here to be identical to eigenfrequencies due to low damping factors) of the chimney in both X and Y axes for each measurement method used. Table 2 shows the values of the damping coefficient ξ obtained using the recorded time-histories of acceleration, velocity and strains in the X (ξ_{1x}) and Y (ξ_{1y}) axes corresponding to a first frequency of resonant vibration of the chimney (see Fig. 6). Calculated values indicate very low vibration damping of the structure. Tables 3 and 4 show example comparisons of relative errors of the f_{1x} and f_{2x} values of the resonant vibration frequencies of the chimney in the X axis for the three types of measurement devices used. The comparison of error values listed in Tables 3

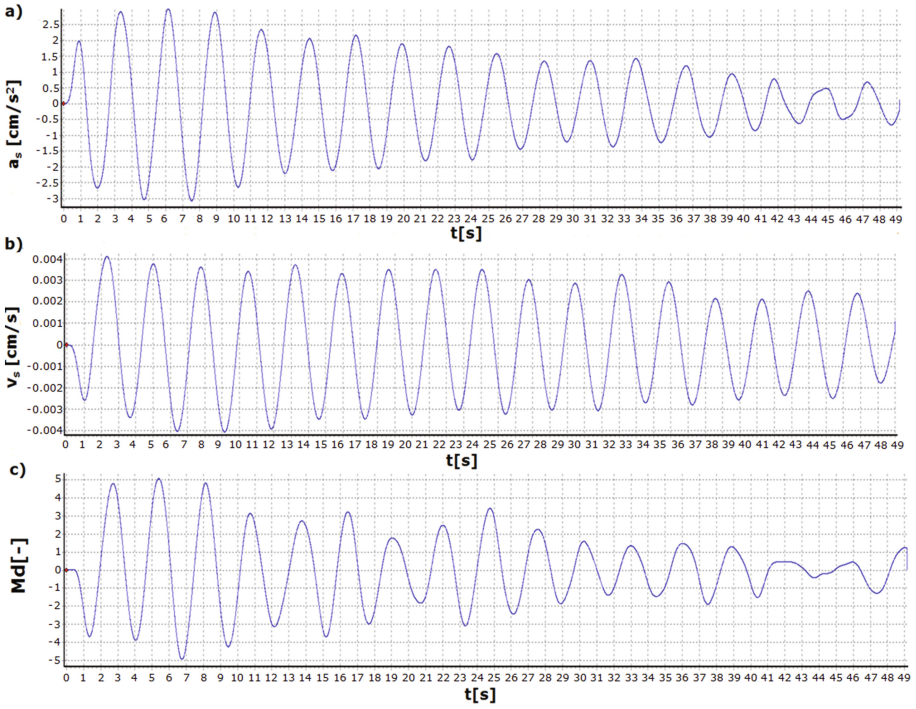

Fig. 5. Example time-history plots for the measured vibration of the chimney's shaft using accelerometers (a), laser vibrometer (b) and strain gauges (c), X-axis.

and 4 indicates that the relative error values do not exceed 6% for the first measured natural frequency and do not exceed 10% for the second frequency. Similar results are observed for the first and second resonant frequencies of the chimney in the Y axis; it can therefore be concluded that each of the devices used for testing give comparable and satisfactory results.

4 Numerical Analysis

4.1 FEM Models

Three numerical models of the chimney were created using the structure's blueprints and post-construction geodetic measurements performed from 1997 to 2011.

- Model A – built of two-dimensional plate finite elements with the flue duct lining and fittings (maintenance galleries and ladders) modelled as masses added to the shell (Fig. 8a).
- Model B – built of three-dimensional solid finite elements with the flue duct lining and fittings modelled as masses added to the shell (Fig. 8b).

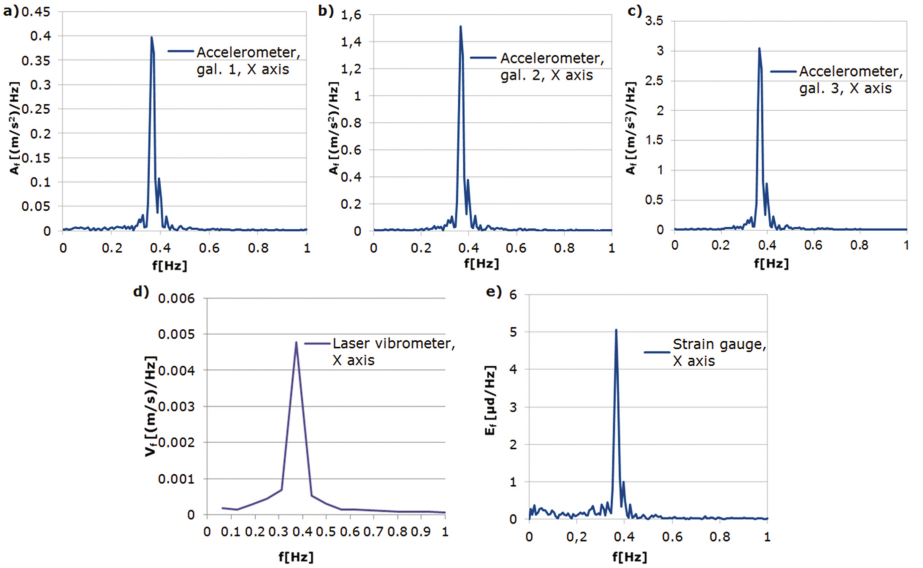

Fig. 6. FFT spectra for recorded time-history of measured vibrations using accelerometers (a), (b) and (c), laser vibrometer (d) and strain gauges (e), X axis.

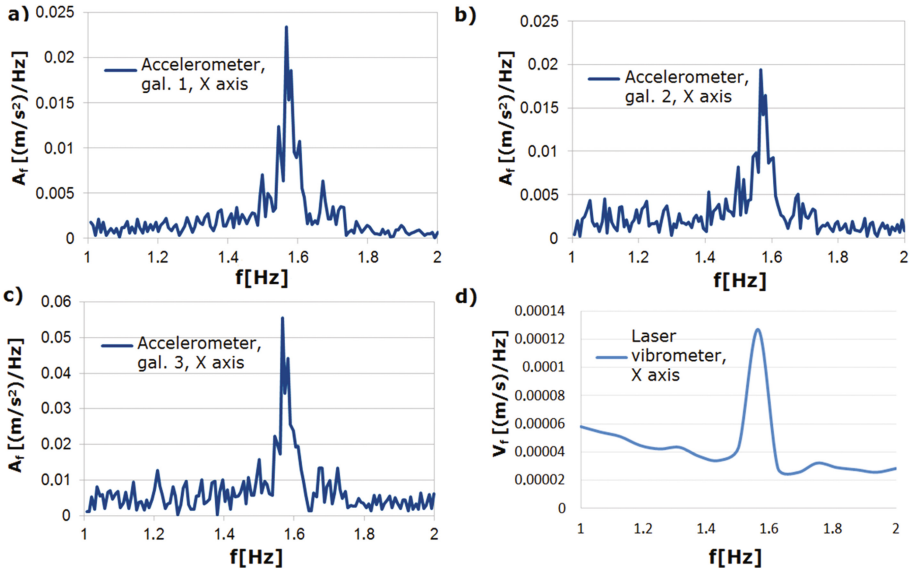

Fig. 7. FFT spectra for recorded time-history of measured vibrations using accelerometers (a), (b) and (c) and laser vibrometer (d), X axis, frequency range 1–2 Hz.

Table 1. Values of the first and second eigenfrquency based on in-situ measurements.

Vibration mode	Accelerometer [Hz]	Strain gauge [Hz]	Laser vibrometer [Hz]
f_{1x}	0.365	0.388	0.375
f_{1y}	0.365	0.366	0.375
f_{2x}	1.567	1.418	1.563
f_{2y}	1.566	1.418	1.562

Table 2. Values of critical damping ξ, X and Y axis.

	ξ_{1x}	ξ_{1y}
Accelerometer	1.7%	1.6%
Strain gauge	2.2%	2.2%
Laser vibrometer	1.2%	1.3%

Table 3. Result comparison, first natural frequency, X axis.

	Frequency [Hz]	Error in relation to accelerometer [%]	Error in relation to laser vibrometer [%]	Error in relation to strain gauge [%]
Accelerometer	0.365	–	3	6
Strain gauge	0.388	6	3	–
Laser Vibrometer	0.375	3	–	3

Table 4. Result comparison, second natural frequency, X axis.

	Frequency [Hz]	Error in relation to accelerometer [%]	Error in relation to laser vibrometer [%]	Error in relation to strain gauge [%]
Accelerometer	1.567	–	0.3	10.5
Strain Gauge	1.418	9.5	9	–
Laser Vibrometer	1.563	0.3	–	10

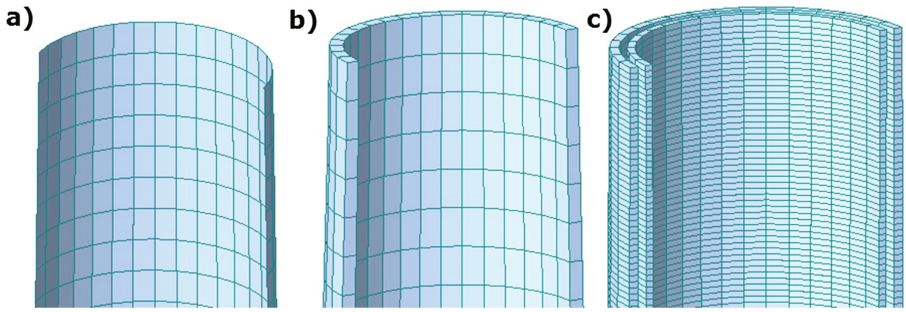

Fig. 8. FEM model cross-sections, (a) – Model A, (b) – Model B, (c) – Model C.

- Model C – built of three-dimensional solid finite elements with the flue duct lining and maintenance galleries fully modelled (Fig. 8c).

The structure's foundation was fully modelled using spring supports applied in three directions (x, y, z and φ_x, φ_y, φ_z) on the ground-foundation contact surface. The stiffness of the springs was set to match the properties of the soil at the location of the object. Each model uses strength characteristics for concrete and rebar elements based on the 2011 material study of the chimney. In addition, the geometry of the models was adjusted in accordance with the shaft imperfection data and geodetic measurements performed in 2011. In the case of model A, the thickness parameter of the used plate elements was adjusted according to the data contained in the archive documentation and subsequent case studies of the object. For models B and C, the thickness of the used elements was also adjusted in accordance with the aforementioned documentation and data. Model C assumed a resilient connection between the flue duct lining and the reinforced concrete cantilevers protruding from the inner surface of the chimney shaft. For models A and B, the ceramic lining was represented as masses added to the concrete cover of the chimney.

4.2 Comparison of Calculations Results and In-Situ Measurement Data

Eigenfrequency analysis was performed for all three models (A, B & C). Results of the calculations corresponding to the first and second mode shapes of the chimney are displayed in Table 5. The calculations show minor differences between the calculated natural frequencies of the assumed models.

Table 5. First and second eigenfrequency calculated for selected numerical models.

Vibration mode	Model		
	A	B	C
f_{1x}	0.348 Hz	0.359 Hz	0.411 Hz
f_{1y}	0.353 Hz	0.361 Hz	0.427 Hz
f_{2x}	1.405 Hz	1.444 Hz	1.611 Hz
f_{2y}	1.430 Hz	1.470 Hz	1.671 Hz

Numerical calculation results and in-situ measurement results were compared and *a strong consistency* was observed between them for the first and second eigenfrequencies of the smoke stack. Tables 6 and 7 display example calculated and measured frequencies in the X axis including relative errors.

Observed differences between the calculated and measured frequencies are in the range of 1–16% for the first eigenfrequency and 1–18% for the second eigenfrequency. The strongest consistency was observed for the B model for which the relative error between the measured and calculated frequencies was the smallest. It can therefore be assumed that the created FEM models have a high level of accuracy.

Table 6. Comparison of FEM frequency analysis results with in-situ measurement results, first eigenfrequency, X axis.

	Frequency [Hz]	Error in relation to accelerometer [%]	Error in relation to laser vibrometer [%]	Error relation to strain gauge [%]
Accelerometer	0.365	–	3	6
Strain gauge	0.388	6	3	–
Laser vibrometer	0.375	3	–	3
Model A	0.348	5	7	10
Model B	0.359	2	4	7
Model C	0.411	13	10	6

Table 7. Comparison of FEM frequency analysis results with in-situ measurement results, second eigenfrequency, X axis.

	Frequency [Hz]	Error in relation to accelerometer [%]	Error in relation to laser vibrometer [%]	Error relation to strain gauge [%]
Accelerometer	1.567	–	3	6
Strain gauge	1.418	6	3	–
Laser vibrometer	1.563	3	–	3
Model A	1.405	10	10	1
Model B	1.444	8	2	8
Model C	1.611	3	13	3

5 Conclusions

The chosen reinforced concrete smoke stack was subjected to dynamic testing. In recent years, many material studies and technical condition assessments were conducted. During the dynamic testing, three types of sensors were used to determine the vibration frequencies of the chimney. The chosen excitation methods were wind gusts and human-swaying on the highest maintenance gallery (*above* 117 m). In-situ measurements indicate that the fundamental frequencies of natural vibrations (here identified as eigenfrequencies) obtained using the different measurement devices are comparable. Based on recorded time-history vibrations, the first and second eigenfrequencies was calculated. Differences between the results obtained using the different sensors did not exceed 6% for the first, and 10% for the second natural frequency. Based on the recorded time-history of vibration, fractions of critical damping of vibrations in the X and Y axis of the chimney were calculated. The calculated critical damping fractions are in the range of 1.2–2.2%, depending on the measuring equipment used. Numerical analysis using three different models built using different types of finite element geometry and mass distributions was performed. The model labelled as B, built of three-dimensional solid finite elements with the flue duct lining and

fittings modelled as masses added to the shell, was found to most accurately reflect the dynamic characteristics of the analysed chimney. The differences between the results of the in-situ measurements and the numerical analysis for this model were found to not exceed 7% for the first and 8% for the second eigenfrequency. Larger differences were observed comparing the results of the numerical analysis for models A and C. In both cases, those differences did not exceed 13% for the first and 18% for the second frequency, thus suggesting these models to be accurate representations of the dynamic behaviour of the structure. The numerical models represent the analysed structure well and can be used for further accurate dynamic calculations of the chimney.

References

1. Oruba, R.: Analiza wpływu uszkodzeń na sztywność i właściwości dynamiczne żelbetowych kominów przemysłowych. Praca Doktorska, Politechnika Krakowska, Kraków (1994)
2. Oruba, R.: Oddziaływanie środowiska przemysłowego i eksploatacji górniczej na bezpieczeństwo żelbetowych kominów przemysłowych, Rozprawy Monografie 211. Wydawnictwa AGH, Kraków (2010)
3. Kańka, S.: Materiałowe i eksploatacyjne uwarunkowania trwałości żelbetowych kominów przemysłowych. Praca Doktorska, Politechnika Krakowska, Kraków (2012)
4. Fiertak, M., Kańka, S.: Postęp destrukcji betonu trzonu komina energetycznego. W XII Konferencja Naukowo–Techniczna KONTRA'2000, pp. 85–92. Warszawa – Zakopane (2000)
5. Chmielewski, T., Górski, P.: Analiza dynamiczna odpowiedzi wysokiego komina żelbetowego na działanie wiatru. Inżynieria Bud. **5**, 279–282 (2005)

A New System Identification Method Operated in the Pole Domain

Qianying Cao[1(✉)], Bin Gao[2], Huajun Li[1], and Sau-Lon James Hu[2]

[1] College of Engineering, Ocean University of China, Qingdao, Shandong, China
cao_qianying@outlook.com
[2] Department of Ocean Engineering, University of Rhode Island, Narragansett, RI, USA

Abstract. A recent article [1] showed that the poles and residues of responses could be easily obtained from those of the loadings and system functions. Following the same theoretical principle, a new system identification method operated in the pole domain has been developed and tested in this article. In this method, the poles and residues associated with the input signals and output signals were first extracted by using the multi-signal Prony-SS method. Sequentially, the system poles were simply the output poles minus the input poles. The remaining work was to compute each corresponding system residue, which in theory is equal to the output residue (at the system pole location) divided by a quantity obtained from the input function calculated at the system pole location in the Laplace domain. In the numerical study, a 5-DOF shear building model was chosen to demonstrate the effectiveness of the proposed method. Two kinds of loading were investigated: (1) a sinusoidal decay signal, and (2) a signal composed of two sinusoidal components. From both scenarios, one concluded that the proposed method could accurately identify the system poles and residues, and thus the corresponding system transfer function.

Keywords: System identification · Poles · Residues · Prony-SS method · FRF

1 Introduction

Traditional methods to perform the system identification for linear dynamic systems can be classified into two groups: frequency domain methods and time domain methods. Strictly speaking, this paper proposes a new system identification method which is neither a frequency domain method nor a time domain method. The newly proposed system identification method is a "pole domain" method which is operated in the complex plane. As shown in Hu et al. [1], the output poles are the system poles plus the input poles. In turn, the system poles are the output poles minus the input poles. From the system poles, one can obtain modal frequencies and damping ratios of the system.

An efficient pole-residue method for computing the dynamic response of a multi-degree-of-freedom (MDOF) system has been developed in a recent article [1]. It showed that the poles and residues of dynamic responses can be easily obtained from those of excitations and system functions. Once the poles and residues of a response are

© Springer International Publishing AG 2018
J.P. Conte et al. (eds.), *Experimental Vibration Analysis for Civil Structures*,
Lecture Notes in Civil Engineering 5, https://doi.org/10.1007/978-3-319-67443-8_55

available, the corresponding response signal is readily obtained. Following the same theoretical principle of the pole-residue method for computing dynamic response, a system identification method can be developed based on that the poles and residues of system functions can be obtained from those of excitations and dynamic responses. Once the poles and residues of a system function are known, the corresponding system transfer function (TF), complex frequency response function (FRF) or unit impulse response function (IRF) can be obtained.

In the proposed pole-residue system identification method, the poles and residues associated with the input signals and output signals will be extracted simultaneously by using the multi-signal Prony-State-Space (Prony-SS) method [2]. To process output signals together with input signals is for ensuring that the common poles of the input and output signals are extracted. From the magnitudes of residues, one can discern the input poles from the output poles.

A 5-DOF (degree-of-freedom) damped shear building model will be chosen for the numerical studies. Two scenarios of testing loading will be considered: (1) a sinusoidal decay signal, and (2) a signal composed of two sinusoidal components. Response signals are generated by invoking a Matlab function to the testing loadings. In addition to clean response signals, noisy response signals will also be employed to test the proposed system identification method, where a noisy signal is generated by adding Gaussian white noise to the original clean response signal.

2 Preliminaries

This section reviews background materials which are of essential importance to this article; it also intends to acquaint the reader with the notation convention to be used.

2.1 Time, Frequency and Laplace Domains

Throughout this paper, functions depending on time t are in lower cases; their Laplace transforms on s denoted by the same letters with a tilde, and their Fourier transforms on ω denoted by the same capital letters. For example, $\tilde{y}(s)$ and $Y(\omega)$ denote the Laplace transform and Fourier transform of $y(t)$, respectively.

It is easy to show that $\alpha\, exp(\lambda t)$ and $\frac{\alpha}{s-\lambda}$ form a Laplace transform pair. In turn, for the sum of complex exponent functions

$$y(t) = \sum_{\ell=1}^{L} \alpha_\ell \exp(\lambda_\ell t) \tag{1}$$

one shows

$$\tilde{y}(s) = \sum_{\ell=1}^{L} \frac{\alpha_\ell}{s - \lambda_\ell} \tag{2}$$

Equation 2 in the Laplace domain is often called a *partial fraction* form, or *pole-residue* form, with poles λ_ℓ and the corresponding residues α_ℓ. When one sets the real

part of the complex variable s to zero, that is, substitutes s by $i\omega$ in Eq. 2, it yields the corresponding Fourier transform function:

$$Y(\omega) \equiv \tilde{y}(s = i\omega) = \sum_{\ell=1}^{L} \frac{\alpha_\ell}{i\omega - \lambda_\ell} \tag{3}$$

which is essentially the frequency domain representation of $y(t)$.

2.2 Equation of Motion

The equation of motion for a linear N-DOF system is written in the form [3]:

$$\mathbf{M}\ddot{\mathbf{x}}(t) + \mathbf{C}\dot{\mathbf{x}}(t) + \mathbf{K}\mathbf{x}(t) = \mathbf{p}(t) \tag{4}$$

where $\mathbf{M}, \mathbf{C}, \mathbf{K} \in R^{N\times N}$ are the mass, damping and stiffness matrices, respectively, $\mathbf{x}(\mathrm{t}) \in R^{N\times 1}$ the displacement vector, and $\mathbf{p}(\mathrm{t}) \in R^{N\times 1}$ the excitation vector. Let the system be initially at rest, that is, $\dot{\mathbf{x}}(0) = \mathbf{0}$ and $\mathbf{x}(0) = \mathbf{0}$. In the Laplace domain, Eq. 4 becomes:

$$\tilde{\mathbf{p}}(s) = \mathbf{Z}(s)\tilde{\mathbf{x}}(s) \tag{5}$$

where

$$\mathbf{Z}(\mathrm{s}) = \mathbf{M}s^2 + \mathbf{C}s + \mathbf{K} \tag{6}$$

or

$$\tilde{\mathbf{x}}(s) = \mathbf{T}(s)\tilde{\mathbf{p}}(s) \tag{7}$$

where

$$\mathbf{T}(s) = \mathbf{Z}^{-1}(\mathrm{s}) = (\mathbf{M}s^2 + \mathbf{C}s + \mathbf{K})^{-1} \tag{8}$$

The *transfer function* matrix $\mathbf{T}(s)$ is an $N \times N$ matrix, and the (j, k) entry $T_{jk}(s)$ of $\mathbf{T}(s)$ denotes the transfer function of the displacement at coordinate j due to the excitation at coordinate k. When $\mathbf{M}$, $\mathbf{C}$ and $\mathbf{K}$ are symmetric, $T_{jk}(s)$ can be written in its pole-residue form [1]

$$T_{jk}(s) = \sum_{n=1}^{2N} \frac{\beta_{jk,n}}{s - \mu_n} \tag{9}$$

where μ_n are the system poles which are jk-independent and always appear in complex conjugate pairs, and the corresponding residues $\beta_{jk,n}$, which are jk-dependent and also appear in complex conjugate pairs, are related to the nth mode shape ϕ_n:

$$\beta_{jk,n} = \frac{\phi_{k,n}\phi_{j,n}}{a_n} \tag{10}$$

in which $\phi_{k,n}$ and $\phi_{j,n}$ are the kth and jth components of ϕ_n.

The natural frequency ω_n and damping factor ς_n can be computed from the pole μ_n as

$$\omega_n = |\mu_n| \quad \varsigma_n = \frac{-\mathrm{Re}(\mu_n)}{|\mu_n|}, \tag{11}$$

where $\mathrm{Re}(\mu_n)$ means the real part of μ_n.

2.3 Multi-signal Prony-SS Method

A signal $y(t)$ can often be decomposed into a finite number of exponential components as shown in Eq. 1 by Prony's method [4]. As an improvement over Prony's method, the Prony-State-Space (Prony-SS) method has been proposed recently [5]. In the Prony-SS method, a high-order difference equation used in Prony's method has been replaced by a state-space model so that the ill-conditioned problem of solving the roots of a high-order polynomial required in Prony's method can be avoided. The so-called multi-signal Prony-SS method [2], which processes multiple signals simultaneously, is an extension of the Prony-SS method. In this paper, the poles and residues of an excitation signals and the corresponding response signal are extracted simultaneously by the multi-signal Prony-SS method. The purpose is to numerically guarantee that the poles of the input signal will also appear at those of the output signal.

3 Pole-Residue Method

This section provides the theoretical basis to compute the dynamic response of a linear system and develops a new system identification approach in the pole domain by the pole-residue operations.

3.1 Forward Dynamic Analysis

The displacement response at coordinate j to the load at k in the time domain can be expressed as

$$x_{jk} = \int_0^t h_{jk}(t-\tau)p_k(\tau)d\tau \tag{12}$$

where $h_{jk}(t)$ is the unit impulse response function associated with coordinates j and k. In the Laplace domain, one has

$$\tilde{\mathrm{x}}_{jk}(s) = T_{jk}(s)\tilde{p}_k(s) \tag{13}$$

As shown in [1], the poles and residues of $\tilde{\mathrm{x}}_{jk}(s)$ can be obtained from those of $\tilde{p}_k(s)$ and $T_{jk}(s)$. For simplifying notations, subscripts j and k of the residues of $\tilde{p}_k(s)$

and $T_{jk}(s)$ are omitted in the remaining derivation. When $\tilde{p}_k(s)$ and $T_{jk}(s)$ are written in their pole-residue forms

$$\tilde{p}(s) = \sum_{\ell=1}^{L} \frac{\alpha_\ell}{s - \lambda_\ell} \tag{14}$$

and

$$T_{jk}(s) = \sum_{n=1}^{2N} \frac{\beta_n}{s - \mu_n} \tag{15}$$

respectively. Substituting Eqs. 14 and 15 into 13 leads to

$$\tilde{\mathrm{x}}_{jk}(s) = \left(\sum_{n=1}^{2N} \frac{\beta_n}{s - \mu_n} \right) \left(\sum_{\ell=1}^{L} \frac{\alpha_\ell}{s - \lambda_\ell} \right) = \sum_{m=1}^{2N+L} \frac{\gamma_m}{s - \upsilon_m} \tag{16}$$

It is evident that the poles υ_m of the response $\tilde{\mathrm{x}}_{jk}(s)$ consist of L excitation poles λ_ℓ and $2N$ system poles μ_n. Let the first L poles of $\tilde{\mathrm{x}}_{jk}(s)$ be the excitation poles λ_ℓ, namely, $\upsilon_m = \lambda_m$ for $m = 1, \ldots, L$, and the last $2N$ poles of $\tilde{\mathrm{x}}_{jk}(s)$ be the system poles μ_n, namely, $\upsilon_{m+L} = \mu_m$ for $m = 1, \ldots, 2N$. The residue γ_m corresponding each υ_m can be computed by

$$\gamma_m = \lim_{s \to \upsilon_m} (s - \upsilon_m) \tilde{x}_{jk}(s) = \lim_{s \to \upsilon_m} (s - \upsilon_m) \tilde{p}_k(s) T_{jk}(s) \tag{17}$$

Consequently, the first L residues γ_m (for $m = 1, \ldots, L$) of $\tilde{\mathrm{x}}_{jk}(s)$ at the excitation poles λ_ℓ are

$$\gamma_m = \lim_{s \to \upsilon_m} (s - \upsilon_m) \left(\sum_{\ell}^{L} \frac{\alpha_\ell}{s - \lambda_\ell} \right) T_{jk}(s) = \alpha_m T_{jk}(\lambda_m) \tag{18}$$

and the last $2N$ residues γ_{m+L} (for $m = 1, \cdots, 2N$) of $\tilde{\mathrm{x}}_{jk}(s)$ at the system poles μ_n are

$$\gamma_{m+L} = \lim_{s \to \upsilon_{m+L}} (s - \upsilon_{m+L}) \tilde{p}_k(s) \left(\sum_{n=1}^{2N} \frac{\beta_n}{s - \mu_n} \right) = \beta_m \tilde{p}_k(\mu_m) \tag{19}$$

Equations 18 and 19 show that all residues of $\tilde{\mathrm{x}}_{jk}(s)$ can be computed from simple operations of the poles and residues of the excitation $\tilde{p}_k(s)$ and the system transfer function $T_{jk}(s)$.

3.2 System Identification

The dynamic analysis by the pole-residue method represents a simple relationship among the loading, system and response. If the poles and residues of two of them are known, those of the third one can be easily computed by simple algebraic manipulations. Following the same theoretical principle of the pole-residue method for computing dynamic response, a system identification method operated in the pole domain

can be developed. For simplicity, the following presentation will focus on the single-input single-output (SISO) system identification. However, the same principle and approach can be applied to multi-input multi-output (MIMO) system identification cases as well.

In this system identification method, the poles and residues associated with the input signal $p_k(s)$ and output signal $x_{jk}(s)$ are first extracted by using the multi-signal Prony-SS method. By using this multi-signal method to process the input and output signals simultaneously, it numerically guarantees that the poles of the input signals will also appear at those of the output signals. The outcomes of this multi-signal method include both the poles and residues associated with the input and output signals. After discerning the input poles from the output poles, the system poles μ_n (see Eq. 15) are simply the output poles υ_m (see Eq. 16) minus the input poles λ_ℓ (see Eq. 14).

If the transfer function $T_{jk}(s)$ is desired, the remaining work is to compute the residue β_n corresponding to each system pole μ_n in Eq. 15. In accordance with Eq. 19, the computed β_m (for $m = 1, \ldots, 2N$) is equal to the output residue γ_{m+L} (at the system pole μ_m) divided by a quantity obtained from the input function calculated at the system pole location $\tilde{p}_k(\mu_m)$, that is,

$$\beta_m = \frac{\gamma_{m+L}}{\sum_{\ell=1}^{L} \frac{\alpha_\ell}{\mu_{m-\lambda\ell}}}, m = 1, \ldots, 2N \tag{20}$$

Note that the input pole λ_ℓ and residue α_ℓ, together with the output residue γ_{m+L} and the system pole μ_m in Eq. 20, have already been obtained through the multi-signal Prony-SS method.

Once the system poles μ_n and the residues β_n associated with $T_{jk}(s)$ are available, one can also numerically compute the corresponding unit impulse response function

$$h_{jk}(t) = \sum_{n=1}^{2N} \beta_n \exp(\mu_n t) \tag{21}$$

and the complex frequency response function (FRF)

$$H_{jk}(\omega) = \sum_{n=1}^{2N} \frac{\beta_n}{i\omega - \mu_n} \tag{22}$$

4 Numerical Studies

The structure chosen for the numerical studies is a 5-DOF (degree-of-freedom) shear building model, which is equivalent to the mass-spring-dashpot system shown in Fig. 1. The displacement vector is denoted by $\mathbf{x} = [x_1, x_2, x_3, x_4, x_5]^{\mathrm{T}}$, where "T" is the transpose operator, with x_1 being the displacement at the fixed end (see Fig. 1). The

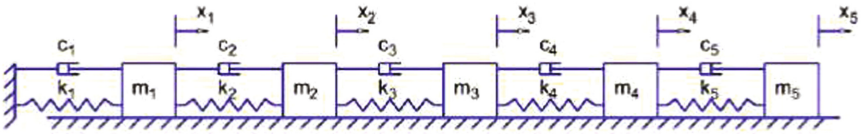

Fig. 1. 5-DOF mass-spring-dashpot system.

mass matrix $\mathbf{M}$ of the structure is a diagonal matrix with diagonal components $m_n, n = 1, \cdots, 5$. The stiffness matrix $\mathbf{K}$ can be obtained as

$$\mathbf{K} = \begin{bmatrix} k_1 + k_2 & -k_2 & 0 & 0 & 0 \\ -k_2 & k_2 + k_3 & -k_3 & 0 & 0 \\ 0 & -k_3 & k_3 + k_4 & -k_4 & 0 \\ 0 & 0 & -k_4 & k_4 + k_5 & -k_5 \\ 0 & 0 & 0 & -k_5 & k_5 \end{bmatrix} \tag{23}$$

The damping matrix $\mathbf{C}$ shares the same form as $\mathbf{K}$, but replacing k_n by the corresponding c_n. In the following numerical investigation, one has $m_n = 50\,\text{kg}$, $c_n = 1000\text{N} \times s/m$ and $k_n = 2.9 \times 10^7 \text{N}/m$, for $n = 1, \cdots, 5$. Listed in Table 1 are the computed system poles μ_n, together with the corresponding modal frequencies $f_n = \omega_n/2\pi$ and damping ratios ζ_n obtained from Eq. 11.

In all numerical examples below for the system identification of this 5-DOF model, only the single-input single-output identification with excitation at $k = 5$ and displacement at $j = 2$ is considered. The corresponding residues β_n of the transfer function $T_{25}(s)$ are also listed in Table 1. From Eq. 22, the frequency response function $H_{25}(\omega)$ can be easily obtained.

Table 1. Analytical poles, modal frequencies, damping ratios and residues of T_{25}.

n	Pole μ_n ($\times 10^3$)	Frequency f_n (Hz)	Damping ratio ζ_n (%)	Residue β_n of T_{25}
1	$-0.0008 + 0.2168i$	34.4996	0.3737	$2.4897 \times 10^{-18} - 8.9772 \times 10^{-6}i$
2	$-0.0008 - 0.2168i$	34.4996	0.3737	$2.4897 \times 10^{-18} + 8.9772 \times 10^{-6}i$
3	$-0.0069 + 0.6327i$	100.7039	1.0909	$5.1633 \times 10^{-18} + 5.1748 \times 10^{-6}i$
4	$-0.0069 - 0.6327i$	100.7039	1.0909	$5.1633 \times 10^{-18} - 5.1748 \times 10^{-6}i$
5	$-0.0172 + 0.9973i$	158.7498	1.7197	$-9.6025 \times 10^{-19} - 7.7634 \times 10^{-7}i$
6	$-0.0172 - 0.9973i$	158.7498	1.7197	$-9.6025 \times 10^{-19} + 7.7634 \times 10^{-7}i$
7	$-0.0283 + 1.2810i$	203.9347	2.2092	$3.6125 \times 10^{-18} - 1.1598 \times 10^{-6}i$
8	$-0.0283 - 1.2810i$	203.9347	2.2092	$3.6125 \times 10^{-18} + 1.1598 \times 10^{-6}i$
9	$-0.0368 + 1.4610i$	232.5980	2.5198	$-4.3063 \times 10^{-19} + 6.3786 \times 10^{-7}i$
10	$-0.0368 - 1.4610i$	232.5980	2.5198	$-4.3063 \times 10^{-19} - 6.3786 \times 10^{-7}i$

Two scenarios of the loading p_5(t) will be included: (1) a sinusoidal decay excitation, and (2) an excitation being the sum of two harmonic components.

4.1 Scenario 1: Sinusoidal Decay Excitation

The first scenario considers the sinusoidal decay excitation with the specific form

$$p_5(t) = 5\exp(-0.1t)\sin(480\pi t) \tag{24}$$

The excitation has a frequency 240 Hz, which is close to the fifth modal frequency of the system (see Table 1).

Table 2. Common poles and corresponding residues of the $p_5(t)$ in Eq. 24 and $x_2(t)$.

m	Pole v_m ($\times 10^3$)	Input residues α_m	Output residues γ_m
1	$-0.0008 + 0.2168i$	$2.7157 \times 10^{-16} + 2.3703 \times 10^{-17}i$	$4.1657 \times 10^{-12} - 3.0163 \times 10^{-8}i$
2	$-0.0008 - 0.2168i$	$8.1984 \times 10^{-16} - 1.0389 \times 10^{-16}i$	$4.1657 \times 10^{-12} + 3.0163 \times 10^{-8}i$
3	$-0.0069 + 0.6327i$	$7.7442 \times 10^{-15} + 2.8115 \times 10^{-15}i$	$-9.4936 \times 10^{-11} + 2.0665 \times 10^{-8}i$
4	$-0.0069 - 0.6327i$	$7.7267 \times 10^{-15} - 3.4758 \times 10^{-15}i$	$-9.4936 \times 10^{-11} - 2.0665 \times 10^{-8}i$
5	$-0.0172 + 0.9973i$	$2.6493 \times 10^{-14} - 1.9248 \times 10^{-15}i$	$1.2059 \times 10^{-10} - 4.5365 \times 10^{-9}i$
6	$-0.0172 - 0.9973i$	$2.7611 \times 10^{-14} - 2.0850 \times 10^{-15}i$	$1.2059 \times 10^{-10} + 4.5365 \times 10^{-9}i$
7	$-0.0283 + 1.2810i$	$9.0705 \times 10^{-14} + 3.9270 \times 10^{-14}i$	$1.5420 \times 10^{-9} - 1.3520 \times 10^{-8}i$
8	$-0.0283 - 1.2810i$	$9.2062 \times 10^{-14} - 3.9569 \times 10^{-14}i$	$1.5420 \times 10^{-9} + 1.3520 \times 10^{-8}i$
9	$-0.0368 + 1.4610i$	$-3.2103 \times 10^{-15} + 5.2305 \times 10^{-13}i$	$-1.6342 \times 10^{-8} + 2.1443 \times 10^{-8}i$
10	$-0.0368 - 1.4610i$	$-9.9430 \times 10^{-16} - 5.2446 \times 10^{-13}i$	$-1.6342 \times 10^{-8} - 2.1443 \times 10^{-8}i$
11	$-0.0001 + 1.5080i$	$-0.0000 - 2.5000i$	$1.4770 \times 10^{-8} - 1.0256 \times 10^{-8}i$
12	$-0.0001 - 1.5080i$	$-0.0000 + 2.5000i$	$1.4770 \times 10^{-8} + 1.0256 \times 10^{-8}i$

Throughout this paper, for the simulation of a discrete signal, the sampling rate 5×10^3 Hz is always taken, that is $\Delta t = 2\times10^{-4}$ s. First, a clean discrete signal of $x_2(t)$ is computed by using the Matlab function lsim [6]. In implementing the multi-signal Prony-SS method for $p_5(t)$ and $x_2(t)$ together, the model order associated with these signals must be determined, which can be achieved by analyzing the normalized singular values of a block Hankel matrix from these signals. The interesting reader is referred to [7] for the detailed information. In this example, the model order has been determined to be 12. Listed in Table 2 are the common poles and the corresponding residues of $p_5(t)$ and $x_2(t)$ extracted by the multi-signal Prony-SS method. The input poles, namely the poles of $p_5(t)$, can be identified by observing the corresponding input residues. As shown in Table 2, only the residues at the 11th and 12th poles, $-0.0001 + 1.5080i$ and $-0.0001 - 1.5080i$, are not negligibly small, thus only these two poles are the input poles. From the theoretical derivation, the system poles are the response poles minus the input poles, thus all other poles are system poles. Afterwards, the residues of the transfer function $T_{25}(s)$ can be computed by using Eq. 20. In this paper, symbols with and without a hat are utilized to distinguish, respectively, the parameters obtained from the proposed method and those from the analytical solution. For instance, μ_n and $\hat{\mu}_n$ are the analytical poles and the corresponding estimated poles, respectively. Table 3 shows the relative errors of poles $(|\hat{\mu}_n| - |\mu_n|)/|\mu_n|$ and residues $(\left|\hat{\beta}_n\right| - |\beta_n|)/|\beta_n|$. Since those relative errors are practically zero, it suggests that the proposed method can accurately identify all system parameters.

In view of the fact that real measurements are often contaminated by noise, a noisy response signal for $x_2(t)$ has also been simulated. The noisy $x_2(t)$ has been generated by adding Gaussian white noise to the original clean response signal. The level of the additive white noise is quantified as 5%, where the stated percentage is defined as the ratio of the standard deviation of the white noise to that of the clean signal. Similar to Tables 3 and 4 presents the relative errors of both poles and residues for the noisy $x_2(t)$ and these relative errors are still very small. The comparison between the estimated $|H_{25}(\omega)|$ and the analytical one is shown in the Fig. 2, which indicates that there is virtually no difference between them.

Table 3. Relative errors of poles and residues associated with the clean response in Scenario 1.

n	$(\lvert\hat{\mu}_n\rvert - \lvert\mu_n\rvert)/\lvert\mu_n\rvert$	$(\lvert\hat{\beta}_n\rvert - \lvert\beta_n\rvert)/\lvert\beta_n\rvert$
1	0.7146×10^{-12}	−0.0076
2	0.7146×10^{-12}	−0.0076
3	8.3142×10^{-12}	−0.0076
4	8.3142×10^{-12}	−0.0076
5	-1.7854×10^{-12}	−0.0076
6	-1.7854×10^{-12}	−0.0076
7	-0.6420×10^{-12}	−0.0076
8	-0.6420×10^{-12}	−0.0076
9	1.3658×10^{-12}	−0.0076
10	1.3658×10^{-12}	−0.0076

Table 4. Relative errors of poles and residues associated with the noise response in Scenario 1.

n	$(\lvert\hat{\mu}_n\rvert - \lvert\mu_n\rvert)/\lvert\mu_n\rvert$	$(\lvert\hat{\beta}_n\rvert - \lvert\beta_n\rvert)/\lvert\beta_n\rvert$
1	2.2882×10^{-4}	0.0005
2	2.2882×10^{-4}	0.0005
3	2.9699×10^{-4}	−0.0175
4	2.9699×10^{-4}	−0.0175
5	-4.9041×10^{-4}	0.0251
6	-4.9041×10^{-4}	0.0251
7	0.1455×10^{-4}	−0.0328
8	0.1455×10^{-4}	−0.0328
9	-5.8059×10^{-4}	−0.0071
10	-5.8059×10^{-4}	−0.0071

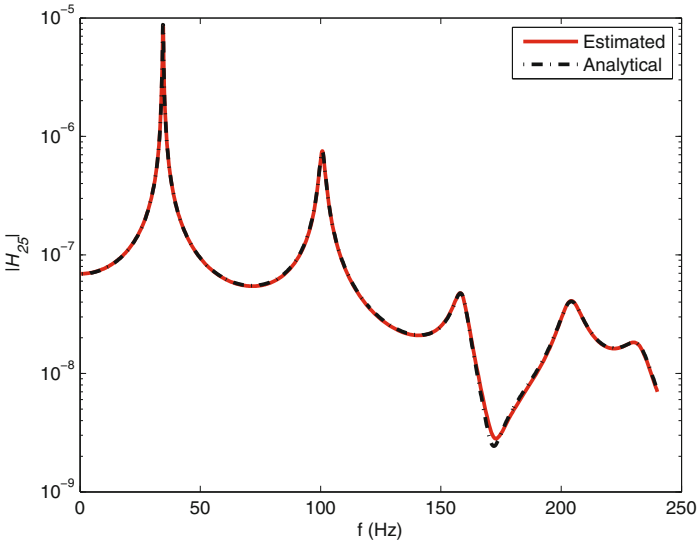

Fig. 2. The analytical and estimated $|H_{25}|$ associated with the noisy response in Scenario 1.

4.2 Scenario 2: An Excitation Signal Composed of Two Sinusoidal Components

The second scenario considers the excitation

$$p_5(t) = 5\sin(320\pi t) + 5\sin(480\pi t) \tag{25}$$

This excitation contains two frequencies: 160 Hz and 240 Hz. These two frequencies are close to the third and fifth modal frequencies of the system, respectively. The model order chosen for the multi-signal Prony-SS method is 14. From Table 5, one concludes that the poles of $m = 11 - 14$ are the input poles, and all other poles are the system poles. The corresponding residues of the transfer function $T_{25}(s)$ can be computed by using Eq. 20. The relative errors of poles $(|\hat{\mu}_n| - |\mu_n|)/|\mu_n|$ and residues $(\left|\hat{\beta}_n\right| - |\beta_n|)/|\beta_n|$ are listed in Table 6, which suggests that the proposed method can accurately identify all system parameters.

A 5% noisy response signal for $x_2(t)$ has also been simulated. Shown in Table 7 is the comparison between the analytical poles/residues of $T_{25}(s)$ and those estimated by the proposed method using the noisy $x_2(t)$. The relative errors of poles and residues are still small. The comparison between the estimated $|H_{25}(\omega)|$ and the analytical one is shown in Fig. 3. Overall, the proposed method performs well even under the noisy situation.

Table 5. Common poles and corresponding residues of the $p_5(t)$ in Eq. 25 and $x_2(t)$.

m	Pole v_m ($\times 10^3$)	Input residues α_m	Output residues γ_m
1	$-0.0008 + 0.2168i$	$-1.5346 \times 10^{-14} + 4.9564 \times 10^{-15}i$	$8.9497 \times 10^{-12} - 5.9053 \times 10^{-8}i$
2	$-0.0008 - 0.2168i$	$-1.3591 \times 10^{-14} - 3.6412 \times 10^{-15}i$	$8.9497 \times 10^{-12} + 5.9053 \times 10^{-8}i$
3	$-0.0069 + 0.6327i$	$-6.6807 \times 10^{-14} - 3.2638 \times 10^{-14}i$	$-1.7874 \times 10^{-10} + 4.0164 \times 10^{-8}i$
4	$-0.0069 - 0.6327i$	$-6.7370 \times 10^{-14} + 3.1078 \times 10^{-14}i$	$-1.7874 \times 10^{-10} - 4.0164 \times 10^{-8}i$
5	$-0.0172 + 0.9973i$	$-2.4391 \times 10^{-13} - 1.0416 \times 10^{-13}i$	$2.1660 \times 10^{-10} - 8.6394 \times 10^{-9}i$
6	$-0.0172 - 0.9973i$	$-2.3880 \times 10^{-13} + 9.9095 \times 10^{-14}i$	$2.1660 \times 10^{-10} + 8.6394 \times 10^{-9}i$
7	$-0.0283 + 1.2810i$	$-7.7843 \times 10^{-13} - 6.5279 \times 10^{-13}i$	$2.4978 \times 10^{-9} - 2.4358 \times 10^{-8}i$
8	$-0.0283 - 1.2810i$	$-7.7286 \times 10^{-13} + 6.4602 \times 10^{-13}i$	$2.4978 \times 10^{-9} + 2.4358 \times 10^{-8}i$
9	$-0.0368 + 1.4610i$	$2.1673 \times 10^{-12} - 5.1228 \times 10^{-12}i$	$-2.0688 \times 10^{-8} + 3.4869 \times 10^{-8}i$
10	$-0.0368 - 1.4610i$	$2.1822 \times 10^{-12} + 5.1097 \times 10^{-12}i$	$-2.0688 \times 10^{-8} - 3.4869 \times 10^{-8}i$
11	$0.0000 + 1.5080i$	$0.0000 - 2.5000i$	$1.4775 \times 10^{-8} - 1.0214 \times 10^{-8}i$
12	$0.0000 - 1.5080i$	$0.0000 + 2.5000i$	$1.4775 \times 10^{-8} + 1.0214 \times 10^{-8}i$
13	$-0.0000 + 1.5708i$	$0.0000 - 2.5000i$	$3.3682 \times 10^{-9} - 4.8658 \times 10^{-9}i$
14	$-0.0000 - 1.5708i$	$0.0000 + 2.5000i$	$3.3682 \times 10^{-9} + 4.8658 \times 10^{-9}i$

Table 6. Relative errors of poles and residues associated with the clean response in Scenario 2.

n	$(\lvert\hat{\mu}_n\rvert - \lvert\mu_n\rvert)/\lvert\mu_n\rvert$	$(\lvert\hat{\beta}_n\rvert - \lvert\beta_n\rvert)/\lvert\beta_n\rvert$
1	0.7181×10^{-12}	-0.0050
2	0.7181×10^{-12}	-0.0050
3	8.3117×10^{-12}	-0.0048
4	8.3117×10^{-12}	-0.0048
5	-1.6461×10^{-12}	-0.0035
6	-1.6461×10^{-12}	-0.0035
7	-0.7405×10^{-12}	-0.0135
8	-0.7405×10^{-12}	-0.0135
9	1.4128×10^{-12}	-0.0079
10	1.4128×10^{-12}	-0.0079

Table 7. Relative errors of poles and residues associated with the noise response in Scenario 2.

n	$(\lvert\hat{\mu}_n\rvert - \lvert\mu_n\rvert)/\lvert\mu_n\rvert.$	$(\lvert\hat{\beta}_n\rvert - \lvert\beta_n\rvert)/\lvert\beta_n\rvert$
1	0.3894×10^{-3}	0.0098
2	0.3894×10^{-3}	0.0098
3	0.4321×10^{-3}	-0.0186
4	0.4321×10^{-3}	-0.0186
5	-0.1932×10^{-3}	0.0184
6	-0.1932×10^{-3}	0.0184
7	-2.5358×10^{-3}	0.0783
8	-2.5358×10^{-3}	0.0783
9	-1.8747×10^{-3}	0.0115
10	-1.8747×10^{-3}	0.0115

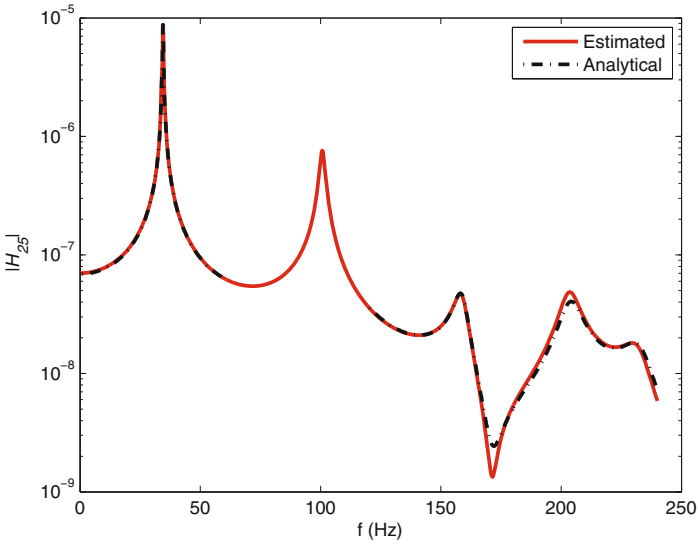

Fig. 3. The analytical and estimated $|H_{25}|$ associated with the noisy response in Scenario 2.

5 Conclusions

An efficient system identification method based on pole-residue operations has been proposed and tested in this paper. After the poles and residues of the loading and response signals were extracted from carrying out the multi-signal Prony-SS method, the poles and residues of a system transfer function could be easily obtained from those of the loading and response signals. From the numerical studies of a 5-DOF (degree-of-freedom) damped shear building model, it was found that: (1) the proposed method could correctly identify all modal frequencies and damping ratios when the structure was subjected to very simple testing excitations, and (2) the proposed method performed well even when response signals were significantly contaminated.

Acknowledgments. The work was financially supported by the National Natural Science Foundation of China (Grant Nos. 51490675) and the 111 Project B14028.

References

1. Hu, S.-L.J., Liu, F., Gao, B., Li, H.: Pole-residue method for numerical dynamic analysis. J. Eng. Mech. **142**(8) (2016)
2. Su, L.: Finite element model updating of piezoelectric transducers. Ph.D. thesis (2016)
3. Craig, R.R., Kurdila, A.J.: Fundamentals of Structural Dynamics. John Wiley & Sons, Hoboken (2006)
4. de Prony, B.G.R.: Essai éxperimental et analytique: sur les lois de la dilatabilité de fluids élastique et sur celles de la force expansive de la vapeur de lalkool, a différentes températures. J. de lécole polytechnique **1**(22), 24–76 (1795)

5. Hu, S.-L.J., Yang, W., Li, H.: Signal decomposition and reconstruction using complex exponential models. Mech. Syst. Signal Process. **40**(2), 421–438 (2013)
6. The MathWorks. Control System Toolbox Users' Guide. The MathWorks Inc., Natick, MA, USA (2004)
7. Hu, S.-L.J., Yang, W., Liu, F., Li, H.: Fundamental comparison of time-domain experimental modal analysis methods based on high-and first-order matrix models. J. Sound Vib. **333**(25), 6869–6884 (2014)

Discussion of Several "RSID" Algorithms to Linear Time-Varying System and System with Abrupt Change of Joint Failure

Chin-Hsiung Loh(✉) and Jun-Da Chen

Department of Civil Engineering,
National Taiwan University, Taipei 10617, Taiwan
lohc0220@ccms.ntu.edu.tw

Abstract. Tracking modal parameters and estimating the structural current state from building seismic response measurement can provide useful information for building safety assessment, therefore, on-line or recursive identification technique needs to be developed for building seismic response monitoring. In this paper, three recursive subspace identification algorithms are developed. One is the recursive subspace identification with Bona-fide LQ renewing algorithm (RSI-BonaFide), one is recursive subspace identification based on matrix inversion lemma algorithm (RSI-Inversion) either with oblique projection technique or with orthogonal projection technique. A forgetting factor is introduced in the RSI-Inversion to emphasize the latest state of the time-varying system in this method. Two different sets of building seismic response data are used to verify the applicability of the proposed methods. One is the 3-story steel structure with abrupt change of story stiffness shaking table test in laboratory, the other is the seismic response analysis of a 9-story mid-story isolation building.

Keywords: Data-driven recursive subspace identification · Bona fide algorithm · Forgetting factor · Building seismic response

1 Introduction

The subspace method can be classified into the Subspace Identification (SI) algorithm which uses both input and output data, and the Stochastic Subspace Identification (SSI) algorithm which is an output-only identification algorithm. Good recent overview papers that of the whole class of subspace identification algorithms can be found in the reference [1–4]. Several well-known algorithms, include CVA, N4SID, MOESP and IV-4SID [5–7], had been developed. In recent years, various versions of subspace method have been used to identify the state space model of linear systems. The basic concept of subspace identification (SI) algorithm is the exploitation of the state as a finite-dimensional interface between the past and the future. Since the traditional subspace identification method is not suitable for online computations due to the computational complexity of SVD as well as the ability to detect the time-varying system. Therefore, several recursive subspace identification (RSI) algorithms have been proposed. [8, 9] proposed an algorithm by updating the projection matrix. [10] proposed RSI based on instrumental variable unconstrained. [11] proposed the recursive

© Springer International Publishing AG 2018
J.P. Conte et al. (eds.), *Experimental Vibration Analysis for Civil Structures*,
Lecture Notes in Civil Engineering 5, https://doi.org/10.1007/978-3-319-67443-8_56

4SID-based identification algorithm with fixed input-output data size developed the RSI algorithms to avoid the use of repetitive LQ decomposition. A recursive update algorithm of PI-MOESP (Past-Input/Past Output Multivariable Output-Error State sPace) was proposed by [12] to determine order and parameter of time-varying system. In this study two recursive subspace identification algorithms are developed: RSI-BonaFide algorithm and RSI-Inversion algorithm with forgetting factor. Comparison on these two algorithms to a 3-story steel frame structure with abrupt change of stiffness is made. Besides, tracking the time-varying modal properties using building seismic response data is also discussed. Finally, based on the identified system matrix, damage detection on the experimental structure is also conducted. Through the identified change of stiffness and flexibility, the damage location and quantification of the structure can be successfully assessed.

2 Recursive Subspace Identification Algorithm

There are several data driven subspace identification algorithms (SI-DATA) available to obtain system matrices of the state space equations for identifying modal parameters. Past-Input/Past Output Multivariable Output-Error State sPace (PO-MOESP) is the most commonly utilized algorithm. First, a data Hankel matrix including both input and output measurements is defined:

$$\mathbf{H}_{1:j} \equiv \begin{bmatrix} \mathbf{U}_f \\ \mathbf{\Xi}_p \\ \mathbf{Y}_f \end{bmatrix} = [\,\mathbf{h}_{k-j+1} \quad \mathbf{h}_{k-j+2} \quad \cdots \quad \mathbf{h}_k\,] \in R^{2(m+l)i\times j} \tag{1}$$

where $\mathbf{h}_n = [\hat{\mathbf{u}}_{f,i}(n)\ \hat{\varepsilon}_{p,2i}(n)\hat{\mathbf{y}}_{f,i}(n)]^T$, $\hat{\mathbf{u}}_{f,i}(n) = [\mathbf{u}_{n-i+1} \quad \mathbf{u}_{n-i+2} \quad \cdots \quad \mathbf{u}_n]$, and $\widehat{\mathbf{y}}_{f,i}(n) = [\mathbf{y}_{n-i+1} \quad \mathbf{y}_{n-i+2} \quad \cdots \quad \mathbf{y}_n]$

$$\hat{\varepsilon}_{p,2i}(n) = [\mathbf{u}_{n-2i+1} \quad \mathbf{u}_{n-2i+2} \quad \cdots \quad \mathbf{u}_{n-i} \quad \mathbf{y}_{n-2i+1} \quad \mathbf{y}_{n-2i+2} \quad \cdots \quad \mathbf{y}_{n-i}],$$
$$n = k-j+1,\, k-j+2,\, \ldots k$$

The goal of PO-MOESP is to compute oblique projection between each data Hankel matrices (i.e. $(\mathrm{Y}_f/_{U_f}\Xi_p)/\mathrm{U}_f^{\perp}$) to acquire observability matrix and following system matrices (i.e. **A**, **C**) for system identification. It is significant to note that there are two different ways to calculate oblique projection in PO-MOESP algorithm: one is LQ decomposition, and the other uses direct expansion of the oblique projection with matrix inverse lemma.

To detect the time-varying modal properties, Recursive Subspace Identification (RSI) algorithm needs to be developed. It is important to point out that the selection of user-defined parameters in RSI plays an important role in the estimation of modal dynamic properties. First, the number of row "i" needs to be at least $2 \times i \geq$ fundamental period of the structure. The window length (data points) "r" is defined as $r = 2(m + l + 1)i - 1$ where m and l are the number of input and output, respectively. There are three different ways to determine the subspace deciding criteria: Fixed Order

(assign a value which is equal to or more than Model order), or Ced value (decide the position to truncate based on a ratio to maximum singular value), or LOGed (It is aimed to automated estimate the position where an obvious drop of Eigen-value occurs from which the modal order was determined). Besides, criteria to remove the spurious modes are also required (e.g. Comac: Output Modal Amplitude Correlation and Cwpe: Weighted Phase Error [13]). In this study four different approaches on RSI are proposed and discussed using seismic response data of two building structures (one is experimental data and the other is the building seismic response data).

2.1 RSI with Bona-Fide LQ Renewing Algorithm (RSI-BonaFide)

The RSI-BonaFide algorithm is derived from LQ decomposition applied in PO-MOESP to estimate system matrices and modal parameters on each time instant recursively. By conducting LQ decomposition on the arranged data Hankel matrix as shown in Eq. (2), the outcome of oblique projection can be obtained, which is equal to $\mathbf{L}_{32}\,\mathbf{Q}_2^{\mathrm{T}}$. Then, after applying singular value decomposition (SVD) on $\mathbf{L}_{32}\,\mathbf{Q}_2^{\mathrm{T}}$, or eigenvalue decomposition (ED) on $\mathbf{L}_{32}\,\mathbf{L}_{32}^{\mathrm{T}}$, the observability matrix and following system matrices can be derived for identifying dynamic characteristics.

$$\begin{bmatrix}\mathbf{U}_f\\ \mathbf{\Xi}_p\\ \mathbf{Y}_f\end{bmatrix} = \begin{matrix}mi\\ (m+l)i\\ li\end{matrix} \begin{bmatrix}\overset{mi}{\mathbf{L}_{11}} & \overset{(m+l)i}{0} & \overset{li}{0}\\ \mathbf{L}_{21} & \mathbf{L}_{22} & 0\\ \mathbf{L}_{31} & \mathbf{L}_{32} & \mathbf{L}_{33}\end{bmatrix} \begin{bmatrix}\overset{j}{\mathbf{Q}_{11}^T}\\ \mathbf{Q}_{21}^T\\ \mathbf{Q}_{31}^T\end{bmatrix} \tag{2}$$

When a new set of input and output data is obtained, RSI-BonaFide is applied to update $\mathbf{L}_{32}\,\mathbf{L}_{32}^{\mathrm{T}}$ for the next time instant, which is based on a moving window technique that keeps the window size of input and output data as a constant, which is as presented in Eq. (3).

$$\left[\begin{array}{c:c}\mathbf{U}_f(k|k-j+1) & \mathbf{u}_f(k+1)\\ \mathbf{\Xi}_p(k|k-j+1) & \boldsymbol{\varepsilon}_p(k+1)\\ \mathbf{Y}_f(k|k-j+1) & \mathbf{y}_f(k+1)\end{array}\right] = \left[\begin{array}{c:c}\mathbf{u}_f(k-j+1) & \mathbf{U}_f(k+1|k-j+2)\\ \boldsymbol{\varepsilon}_p(k-j+1) & \mathbf{\Xi}_p(k+1|k-j+2)\\ \mathbf{y}_f(k-j+1) & \mathbf{Y}_f(k+1|k-j+2)\end{array}\right] \tag{3}$$

Perform the LQ-decomposition of the data matrix at the step "k" and "k + 1" and substitute computed LQ elements into the left- and right-hand side of Eq. (3), then through mathematical operation, L_{32}(k + 1) L_{32}^T(k + 1) can be solved [11]. Through the eigenvalue decomposition of L_{32}(k + 1) L_{32}^T(k + 1), the system matrices can be identified. Repeat the above-mentioned procedures as time goes along with k = 0, 1, 2,… The crucial idea of this method is to update and down-date a couple of input and output data in order to keep the data size to be constant, and then L_{32}(k + 1) for the system identification on the next window can be derived (Table 1).

2.2 RSI with Matrix Inversion Lemma Renewing Algorithm (RSI-Inversion-Oblique)

The core concept of PO-MOESP is that by computing the oblique projection with I/O data Hankel matrix on the LHS of Eq. (4), one can estimate the observability matrix of the structural system either by eigenvalue decomposition (ED) of $\mathbf{L}_{32}\,\mathbf{L}_{32}^{\mathrm{T}}$ as shown in the middle of Eq. (5), which is already described in RSI-BonaFide algorithm, or it can be achieved by, on the other hand, direct expansion of oblique projection formula as the one on the RHS of Eq. (5), which is defined as a compressed I/O data matrix [8].

$$(\mathrm{Y_f}/_{U_f}\Xi_p)/\mathrm{U_f^{\perp}} = L_{32}Q_2^T = \mathrm{Y_f}\Pi_{U_f}^{\perp}\Xi_p^T(\Xi_p\Pi_{U_f}^{\perp}\Xi_p^T)^{-1}\Xi_p\Pi_{U_f}^{\perp} \tag{4}$$

$$[(\mathrm{Y_f}/_{U_f}\Xi_p)/\mathrm{U_f^{\perp}}][(\mathrm{Y_f}/_{U_f}\Xi_p)/\mathrm{U_f^{\perp}}]^T = L_{32}L_{32}^T = \mathrm{Y_f}\Pi_{U_f}^{\perp}\Xi_p^T(\Xi_p\Pi_{U_f}^{\perp}\Xi_p^T)^{-1}\Xi_p\Pi_{U_f}^{\perp}Y_f^T \tag{5}$$

After appending a new set of input and output data, the RSI-Inversion algorithm based on compressed I/O data matrix was derived to estimate system matrices and modal parameters on each time instant recursively [14].

It keeps the same data window with RSI-BonaFide only for the initial identification, and then appends the following data points to identify modal parameters for the whole excitation time history; a forgetting factor λ less than 1 is thus introduced to emphasize the latest state of system in this method. Even though some round-off error might exhibit numerically poor performance sometimes by expanding the projection operation, a forgetting factor can be only introduced by matrix inversion lemma. To demonstrate how forgetting factor is added into the recursive algorithm, one term of the compressed I/O data matrix is taken out as presented in Eq. (6). Since each data Hankel matrix can be divided into several vectors that corresponds to time instant from $k - j + 1, k - j + 2 \ldots$ to k as previously shown in Eq. (1), original multiply operation in Eq. (6) between different data matrices can be decomposed into a summation of time related matrices generated from product of these vectors, and exponential-type forgetting factor can thus be added as presented in Eq. (6). When the new pair of input and output measurement from the next instant is available, new vectors appending original data Hankel matrices can be constructed and applied in RSI-Inversion algorithm for deriving compressed I/O data matrix on next step.

$$\begin{aligned}\mathrm{Y_f}\Pi_{U_f}^{\perp}\Xi_p^T = Y_f\Xi_p^T - Y_fU_f^T\left(U_fU_f^T\right)^{-1}U_f\Xi_p^T = \left[\sum_{n=k-j+1}^{k}\lambda^{k-n}\hat{y}_{f,i}(n)\hat{\varepsilon}_{p,2i}^T(n)\right] \\ -\left[\sum_{n=k-j+1}^{k}\lambda^{k-n}\hat{y}_{f,i}(n)\hat{u}_{f,i}^T(n)\right]\times\left[\sum_{n=k-j+1}^{k}\lambda^{k-n}\hat{u}_{f,i}(n)\hat{u}_{f,i}^T(n)\right]^{-1}\times\left[\sum_{n=k-j+1}^{k}\lambda^{k-n}\hat{u}_{f,i}(n)\hat{\varepsilon}_{p,i}^T(n)\right]\end{aligned} \tag{6}$$

where $\Pi_{U_f}^{\perp} = I - U_f^T(U_fU_f^T)^{-1}U_f$.

2.3 Discussion on RSI-Inversion-Oblique, RSI-Inversion-Orthogonal and RSI-EIVPAST-Orthogonal

Since the extended observability matrix can be estimated by either oblique projection or orthogonal projection to obtain system matrices for identification, as shown in Eqs. (4) and (5), with the above mentioned concepts, two recursive subspace identification algorithms can be derived. RSI-Inversion-Oblique algorithm is derived from the oblique projection with eigenvalue decomposition (ED) for obtaining subspace representing extended observability matrix, while RSI-Inversion-Orthogonal algorithm is based on the orthogonal projection with singular value decomposition (SVD) for required subspace. Matrix inversion lemma is then utilized on both of these RSI algorithms to explicitly expand the operation of matrix projection, and a series of recursive formula for these two methods can be built [8, 12, 14]. It is observed that recursive computing formula of RSI-Inversion-Orthogonal are completely included in RSI-Inversion-Oblique algorithm, the difference comes from two assumptions on eliminating noise matrix appearing in the previously mentioned input-output equation. RSI-EIVPAST-Orthogonal utilizes the same orthogonal projection formula mentioned above to estimate extended observability matrix; however, it is noted that computing subspace of the compressed I/O data matrix can be also achieved by using the concept of EIV-PAST method that is proposed by [15], and thus avoids re-calculating the entire SVD at each step of identification, which accelerates the speed of recursive computation.

Table 1. List of four different RSI algorithms and show the major features on the application of these methods.

	RSI-BonaFide-Oblique	RSI-Inversion-Oblique	RSI-Inversion-Orthgonal	RSI-EIVPAST-Orthgonal
Formula of Projection	$[(Y_f/_{U_f}\Xi_p)/U_f^\perp][(Y_f/_{U_f}\Xi_p)/U_f^\perp]^T = L_{32}L_{32}^T$	$[(Y_f/_{U_f}\Xi_p)/U_f^\perp][(Y_f/_{U_f}\Xi_p)/U_f^\perp]^T = Y_f\Pi_{\hat{U}_f^\perp}\Xi_p^T(\Xi_p\Pi_{\hat{U}_f^\perp}\Xi_p^T)^{-1}\Xi_p\Pi_{\hat{U}_f^\perp}Y_f^T$	$Y_f/_{U_f}\Xi_p^T = Y_f\Pi_{\hat{U}_f^\perp}\Xi_p^T$	$Y_f/_{U_f}\Xi_p^T = Y_f\Pi_{\hat{U}_f^\perp}\Xi_p^T$
Type of Compressed I/O Matrix	Oblique Projection multiplied by its transverse matrix	Oblique Projection multiplied by its transverse matrix	Orthgonal Projection	Orthgonal Projection
Dimension of Compressed Matrix	(#. of Output*i) x (#. of Output*i)	(#. of Output*i) x (#. of Output*i)	(#. of Output*i) x (#. of Input&Output*i)	(#. of Output*i) x (#. of Input&Output*i)
Type of Recursive Window	Moving window on Time History	Enlarging window on Time History	Enlarging window on Time History	Enlarging window on Time History
Window Length/Window Size	Fixed as a constant	Keep appending new arrived data points	Keep appending new arrived data points	Keep appending new arrived data points
Forgetting Factor	No fading factor is involved	With a fading factor less than 1	With a fading factor less than 1	With a fading factor less than 1
Type of Recursive Computation	LQ factorization with bona-fide algorithm	Explicit computation with matrix inversion lemma	Explicit computation with matrix inversion lemma	EIVPAST with RLS-like algorithm
Type of Decomposition	Eigenvalue Decomposition	Eigenvalue Decomposition	Singular Value Decomposition	No Numerical Decomposition
Estimation of Model Order	Distribution of Eigenvalues	Distribution of Eigenvalues	Distribution of Singular values	Assign a Fixed Order
Computation Time	3rd	4th (Slowest)	2nd	1st (Fastest)

Recursion on step-1: Forming a Compressed Matrix (or L32*trans(L32)) on every time instant

Recursion on Step-1 & Step-2: SVD on every time instant

3 Experimental Verification of RSI Algorithms

To verify the proposed four RSI algorithms on the ability of system identification, two different structures are used: one is the 3-story steel frame designed with the abrupt change of member stiffness and test it on the shaking table, the other one is seismic response data of a 9-story mid-story isolation building.

3.1 A 3-Story Steel Frame with Abrupt Change of Stiffness

A three-story full-scale steel structure is constructed. As shown in Fig. 1a, the three-story structure consists of a single bay with a 3 m × 2 m floor area and 3 m tall stories. It is constructed using H150 × 150 × 7 × 10 steel I-beam elements with each beam-column joint designed as a bolted connection. The dead load of each floor is about 6,000 kg (deployed with concrete blocks on each floor diaphragm). A lock-up system which connected the stiffener and the floor base with a steel rod is designed. This lock-up system can be released at any instant of time in the 1st floor during the base excitation to simulate the abrupt change of inter-story stiffness. The identified natural frequencies corresponding to the first three modes of the structure using low-level white noise base excitation are 1.08 Hz, 3.25 Hz, and 5.06 Hz, respectively, and the identified stiffness for the stiffener structure is: 2692 kN/m for the 1st floor, 1346 kN/m for the 2nd floor and 3rd floor (the first story is connected an extra stiffness by adding a stiffener to increase the stiffness of the 1st floor from 1346 kN/m to 2692 kN/m). In the shaking table test, this structural system was subject to the El Centro earthquake ground motion normalized to 100 gal on shaking table, and the steel rod was assigned to release the 1st floor stiffness at t = 14.75 s to simulate the abrupt change of floor stiffness. The recorded acceleration response of the 3-story structure is shown in Fig. 1b.

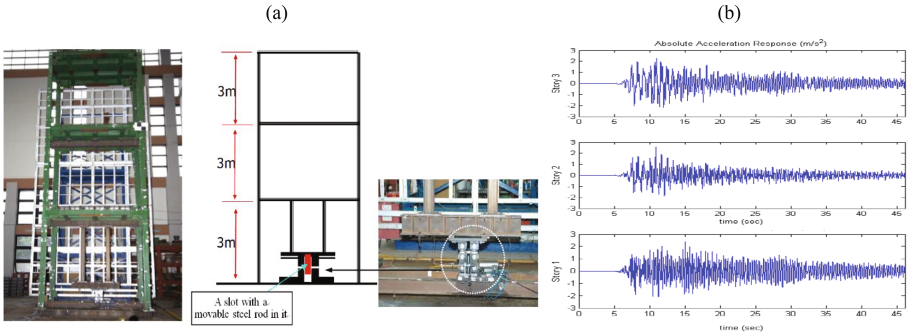

Fig. 1. (a) Test structure on NCREE shaking table and the schematic diagram of a frame structure with stiffened first story is also shown; (b) Recorded acceleration responses under earthquake excitation.

The user-defined parameter for RSI algorithms for this test case needs to be dre-cribedas: Data was down-sampled to 50 Hz and considered the number of row in Hankel matrix as $i = 25$. For the economic size of Hankel matrix "r" is determined as $r = 2(m + l + 1)i - 1 = 2(1 + 3 + 1) \times 25 = 250$, and the window length is $r \times (sampling\ rate) = 5$ s. A shift length means the period of recursive conduction after its first identification, and it is set to be 0.1 s. Since the system has 3 DOFs, model order is fixed to be 6. Forgetting factors used in RSI-Inversion are is 0.98. Criteria for filtering out spurious modes are also utilized in this study, i.e. Comac = 0.95, Cwpe = 0.5. The identified structural frequencies derived from the proposed fur RSI methods are shown in Fig. 2a. It is observed that these four algorithms provide similar results of identification on modal frequencies. The change of modal frequencies at time t = 14.75 s is not so clear due to the abrupt change of stiffness in the first floor. But RSI-Inversion algorithm with adequate forgetting factor demonstrates the robustness to identify the degradation of frequencies (particularly the 2nd mode). RSI-Inversion using forgetting factor can track the appearance of 4th mode at an earlier time than RSI-BonaFide. From the RSI-Inversion algorithm it is faster to identify the change of stiffness. To enhance the rapid identification on the abrupt change of stiffness in the 1st floor, different forgetting factors can also be used in RSI-Inversion. Smaller value of forgetting factor indicated a quick (For example: forgetting factors 0.98 will provide a quick identification on the abrupt change of floor stiffness that forgetting factor 0.99 in RSI-Inversion algorithm).

By using the identified modal frequencies and mode shapes from the RSI algo-rithms, the damage detection algorithms based on stiffness matrix are applied and the results are presented in Fig. 3. It is important to note that using a forgetting factor of 0.98 the RSI-EIVPAST can identify the degradation of stiffness faster than RSI-BonaFide because of the implementation of forgetting factor.

3.2 Seismic Response of a 9-Story RC Building with Mid-Story Isolation

Seismic response data of a 9-story pre-cast reinforced concrete structure building with mid-story isolation system is used to identify the dynamic characteristics of the structure. The layout of the isolators and the location of accelerometer (AC - 63 accelerometer with resolution of 10^{-5} g) in the building and the isolation floor area are shown in Fig. 4a, b [16]. A total of 19 isolators were put underneath each column location. Besides the isolators, six viscous dampers were also installed in this isolation floor. An earthquake event, 2009/7/13 (UT), with magnitude of M = 6.0, depth 18.1 km, epicenter distance 130.05 km trigger the building seismic monitoring. The PGA in transverse direction is 21.69 gal and in longitudinal direction is 24.41 gal. RSI algorithms will be applied to the collected seismic response data to study the dynamic characteristics of the structure and the isolation system.

To conduct the RSI from the seismic response measurement, the user-define parameter must be determined. First, low-pass filter with 25 Hz as corner frequency was applied and then data was down sampled to 50 Hz. Considered the number of row in Hankel matrix as $i = 15$ and window length WL = 7.0 s ($>2i + 2i\ (m + l) = 330$). The sliding window is set to 0.2 s. RSI-Inversion the forgetting factor is set 0.993. Figure 4c shows the identified time-varying modal frequencies of the building. It is observed that

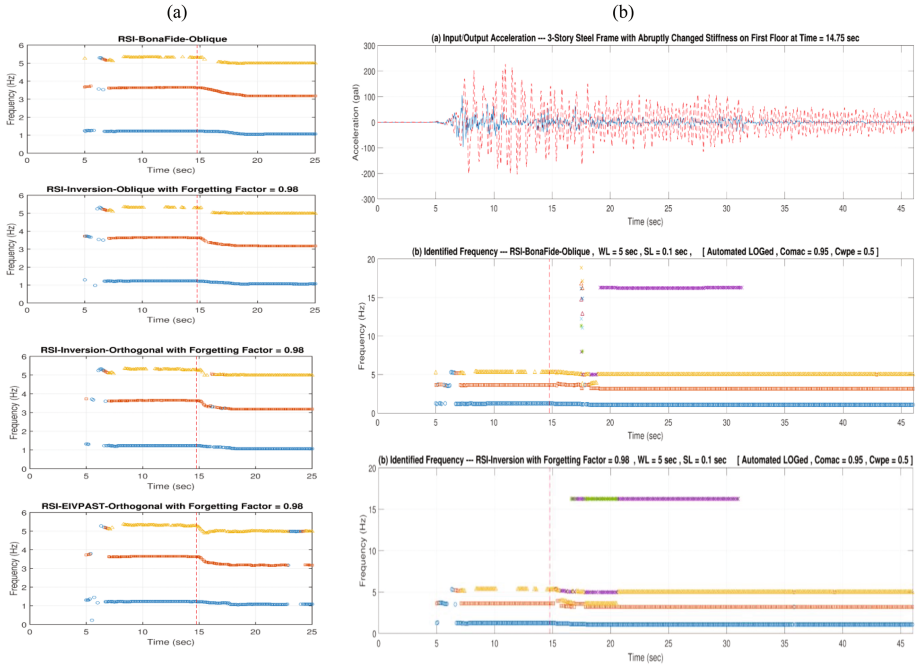

Fig. 2. (a) Comparison on the identified modal frequencies using four different RSI algorithms, RSI-BonaFide algorithm and RSI-Inversion algorithm, respectively.

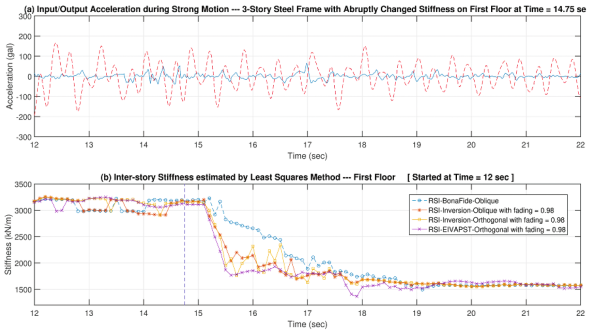

Fig. 3. Comparison on the identified the change of stiffness in the first floor, during 12.0 s and 22.0 s, using two different forgetting factor in RSI-Inversion method.

the RSI-Inversion (orthogonal) can provide a stable identification on the fundamental frequencies while higher modes are more difficult to identify (not stable). Among the proposed four RSI methods the RSI-BonaFide, RSI-Inversion (Oblique) and RSI-Inversion (Orthogonal) adopt LOGed to determine the order, while the RSI-EIVPAST (orthogonal) used the fixe order. Comparison on the RSI computation time among these four methods is shown in Table 2. By checking the analysis time per identification of

Table 2. Comparison on the total computation time among different RSI algorithm. Computation time required for each sliding time window is also shown.

Unit : second		RSI-BonaFide-Oblique	RSI-Inversion-Oblique	RSI-Inversion-Orthogonal	RSI-EIVPAST-Orthogonal	check with SL
SL = 0.2 sec	# of id. = 466	6.57	6.83	3.74	3.03	
Analysis Time / identification		0.01410	0.01466	0.00803	0.00650	< SL = 0.2 s
SL = 0.1 sec	# of id. = 931	10.5	10.5	6.26	4.73	
Analysis Time / identification		0.01128	0.01128	0.00672	0.00508	< SL = 0.1 s
SL = 0.02 sec	# of id. = 4652	48	39.02	26.27	17.64	
Analysis Time / identification		0.01032	0.00839	0.00565	0.00379	< SL = 0.02 s

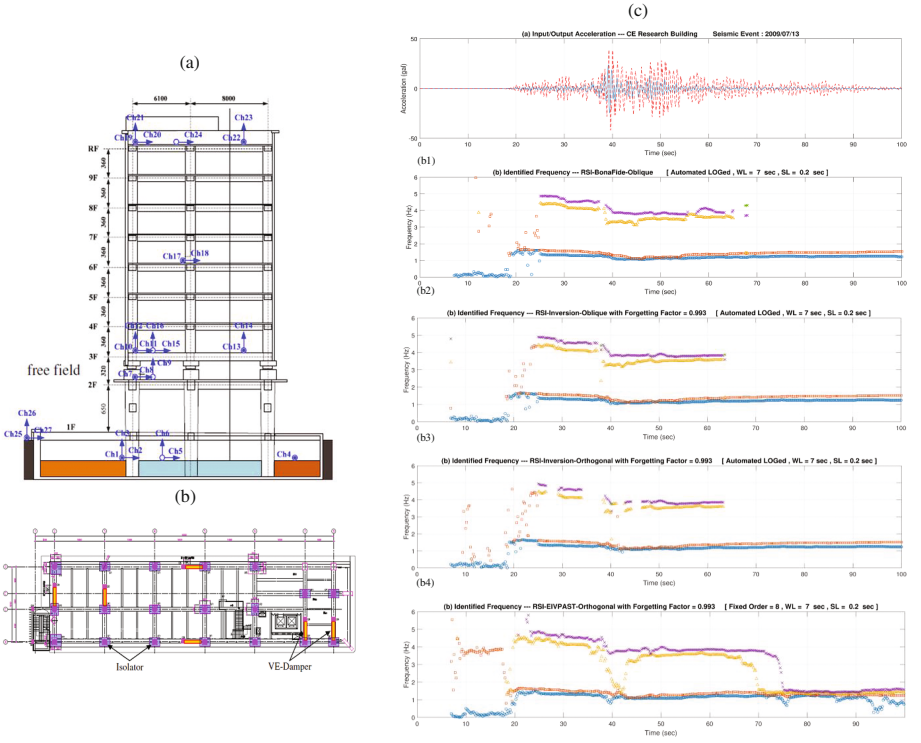

Fig. 4. (a) Location of accelerometers in the NTU-CE Research Building, (b) Location of isolators and viscous dampers in the isolated floor, (c) Identified time-varying modal frequencies using four different RSI algorithms.

each method, it is noted that every analysis on system identification can be done before next time's conduction. The computational time for each analysis is even less than the sampling period 0.02 s. It indicated that the online and real time identification can be done from these proposed system identification algorithms.

By using the identified modal frequencies and mode shapes obtained from the RSI algorithms with the concept proposed by Caicedo et al. (2004), a least squares

optimization to estimate stiffness of each DOF can be derived. Since the selected earthquake data for this analysis is very small (PGA less than 30 gal), because of the isolation system, the time-varying modal frequencies can be identified. Under the assumption of simplified model (as shown in Fig. 5) the change of stiffness in the isolation floor can be detected (assume the super structure remain elastic). Procedures to determine the equivalent linear stiffness of each story in the isolation building are described as follows: *Step 1*: Determine the inter-story stiffness of the upper structure using initial small earthquake response. Assume that the story stiffness is equally distributed along the height of the upper structure. In this analysis, the identified dominant frequencies of the upper structure from small earthquake event will be used as the criteria for optimization between the analytical model and the experimental data. *Step 2*: Identify the stiffness of the lower structure by using the identified stiffness of the upper structure from step 1 and also determine the initial stiffness of the isolator from the performance test of the isolator. The dominant frequencies (identified from the ambient vibration measurements) of the building are considered as an objective of the optimization process to identify the stiffness of the lower structure. *Step 3*: It is assumed that the stiffness of the lower and upper structures remained unchanged during small earthquake excitations. The stiffness of the isolator can be identified using finite element model updating method to match the natural frequencies that were identified from steps 1 and 2. Table 3 shows the identified modal frequencies as well as the stiffness of the isolation system (assumed as an equivalent linear system) at time t = 25 s, t = 45 s and t = 60 s. It is observed that at the time which the strong motion appears, the stiffness of the isolation system will reduce to 22 $\sim$ 30%. Since the yield displacement of the isolator is very small (about 0.4 mm), therefore under a small earthquake excitation, the isolation system will go into the inelastic range.

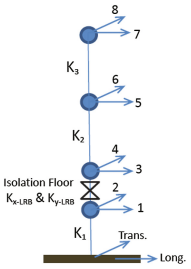

Fig. 5. Structural model (mid-isolation building)

Table 3. Identified change of stiffness in the isolation floor and the modal frequencies at time t = 25 s, t = 45 s and t = 60 s under earthquake Event-2009/7/13 excitation.

Reference State: at time=25.0 sec	
	Updated Member Stiffness (kN/m)
X-LRB	432413*19
Y-LRB	431261*19
Modal Data	
Mode	Natural Freq. (Hz)
1	1.38 (Transverse)
2	1.62 (Longitudinal)
3	4.44 (Transverse)
4	4.87 (Longitudinal)
Derived Parameter Results through the procedure	
α	1.000
β	1.000

Identified State : At time = 45 sec	
	Updated Member Stiffness (kN/m)
X-LRB	α*490500*19 (Iterated)
Y-LRB	β*490500*19 (Iterated)
Modal Data	
Mode	Natural Freq. (Hz)
1	1.07 (Transverse)
2	1.14 (Longitudinal)
3	3.11 (Transverse)
4	3.79 (Longitudinal)
Derived Parameter Results through the procedure	
α	0.2205
β	0.3075

Identified State : At time = 60 sec	
	Updated Member Stiffness (kN/m)
X-LRB	α*490500*19
Y-LRB	β*490500*19
Modal Data	
Mode	Natural Freq. (Hz)
1	1.20 (Transverse)
2	1.38 (Longitudinal)
3	3.58 (Transverse)
4	4.08 (Longitudinal)
Derived Parameter Results through the procedure	
α	0.5060
β	0.4600

4 Conclusions

In this study four different RSI algorithms and damage identification of stiffness reduction were discussed using two different test data. For the 3-story steel frame with abrupt change of stiffness in the 1st floor during earthquake excitation, it is observed that both of these four proposed algorithms derive similar identified results of modal frequencies, the only difference appears right after the occurrence of abrupt change of stiffness where RSI-Inversion with adequate forgetting factor demonstrates the method can rapidly identify the decay of frequencies. Besides, orthogonal projection methods such as proposed RSI-EIVPAST and RSI-Inversion can be successfully applied on the identification of structure with abrupt change of stiffness faster than RSI-BonaFide because of the fading memory less undamaged data were used. Besides, using forgetting factor in RSI-Inversion (or in RSI-EIVPAST) one can quickly identify the drop of stiffness, also, RSI-EIVPAST has the advantage of high speed of recursive computation since it avoids complex operation of SVD, especially when matrix dimension is large and shift length is small. However, the SVD provides a tool to choose model order at every computation point that can derive stable results which is shown above. Based on the seismic response data collected from the mid-isolation building, no matter which method was used, one can identify the time-varying modal frequencies of the system. Besides, the computational time for each system identification is even less than the sampling period 0.02 s. It is important to pointed out that the identified results coming from a higher model order might contain noise modal frequency, a reference mode assigned on the beginning of strong motion is used to filter out those noise modes by the consistency of MAC.

Acknowledgments. The research was supported by the Ministry of Science & Technology (Taiwan) under grant No. MOTC-CWB-05-E-04 and No. MOST 104-2221-E-002-113, respectively. Data provided by the Central Weather Bureau (CWB, Taiwan) and National Center for Research on Earthquake Engineering is also acknowledged.

References

1. Rao, B., Arun, K.S.: Model based processing of signals: a state space approach. Proc. IEEE **80**(2), 283–309 (1992)
2. Van Der Veen, A., Deprettere, E.F., Swindlehurst, A.L.: Subspace-based signal analysis using singular value decomposition. Proc. IEEE **81**(9), 1277–1308 (1993)
3. Viberg, M.: Subspace methods in system identification. In: Proceedings of SYSID 1994, Copenhagen, Denmark, pp. 1–12, July 1994
4. Van Overschee, P., De Moor, B.: Subspace Identification for Linear Systems: Theory-Implementation - Applications. Kluwer Academic Publishers, Dordrecht (1996)
5. Larimore, W.E.: The optimality of canonical variate identification by example. In: Proceedings of SYSID 1994, Copenhagen, Denmark, vol. 2, pp. 151–156, 4–6 July 1994
6. Van Overschee, P., De Moor, B.: N4SID: subspace algorithms for the identification of combined deterministic-stochastic systems. Automatica **30**(1), 75–93 (1994)
7. Verhaegen, M.: Identification of the deterministic part of MIMO state space models given in innovations from input-output data. Automatica **30**(1), 61–74 (1994)

8. Oku, H., Kimura, H.: A recursive 4SID from the input-output point of view. Asian J. Control **1**, 258–269 (1999)
9. Oku, H., Kimura, H.: Recursive 4SID algorithms using gradient type subspace tracking. Automatica **38**, 1035–1043 (2002)
10. Mercère, G., Lecoeuche, S., Lovera, M.: Recursive subspace identification based on instrumental variable unconstrained quadratic optimization. Int. J. Adapt. Control Signal Process. **18**, 771–797 (2004)
11. Kameyama, K., Ohsumi, A., Matsuura, Y., Sawada, K.: Recursive 4SID-based identification algorithm with fixed input-output data size. Int. J. Innov. Comput. Inform. Control **1**(1), 17–33 (2005)
12. Tamaoki, M., Akizuki, K., Oura, K.: Order and parameter estimation of time-varying system by subspace method. Electr. Eng. Jpn. **157**(2), 57–64 (2006)
13. Weng, J.-H., Loh, C.-H.: Recursive subspace identification for on-line tracking of structural modal parameter. Mech. Syst. Signal Process. **25**, 2923–2937 (2011)
14. Oku, H., Nijsse, G., Verhaegen, M., Verdult, V.: Change detection in the dynamics with recursive subspace identification. In: Proceedings of the 40th IEEE CDC, Orlando, Florida, pp. 2297–2302 (2001)
15. Gustafsson, T.: Instrumental variable subspace tracking using projection approximation. IEEE Trans. Signal Process. **46**(3), 669–681 (1998)
16. Loh, C.-H., Weng, J.-H., Chen, C.-H., Lu, K.-C.: System identification of mid-story isolation building using both ambient & earthquake response data. Struct. Control Health Monit. **20**, 139–155 (2013)

Dynamic Characteristics of a 55-Story Building Before and After Retrofit

Mehmet Çelebi[1(✉)], Toshihide Kashima[2], S. Farid Ghahari[3], Shin Koyama[2], Ertuğrul Taciroğlu[3], and Izuru Okawa[2,4]

[1] Earthquake Science Center, USGS, Menlo Park, CA 94025, USA
celebi@usgs.gov
[2] Building Research Institute, Tsukuba, Japan
[3] University of California, Los Angeles, CA 90095, USA
[4] Tokyo Soil Research Co. Ltd, Tokyo, Japan

Abstract. A sparsely instrumented 55-story building in Osaka, Japan, recorded unprecedented severe and long-duration, long-period resonant responses during the March 11, 2011, **M**9.0 Tohoku earthquake that occurred at 767 km distance. Thereafter, studies of the records resulted in implementation of a significant retrofit design, comprising dampers and buckling restrained braces (BRBs). The responses of the retrofit building were subsequently recorded during the April 24, 2016, **M**7.3 Kumamoto earthquake that occurred 478 km away, but at an azimuth nearly opposite to that for the Tohoku event. The earthquake records and ambient response data analyzed in this study represent a rare opportunity to assess the impact of retrofitting on an instrumented tall building subjected to strong long-period shaking from distant earthquakes. As expected, the fundamental frequency and critical damping ratio of the building increased, albeit by small amounts, after the retrofit. Increased damping percentage is a positive finding, and suggests that even larger percentages might be attained for shaking stronger than occurred following the 2016 event. The records indicate that the building still experiences significant resonance and torsion, as well as a beating effect.

Keywords: Building instrumentation · Frequency · Damping · BRB · Dampers

1 Introduction

The motivation for this paper is to investigate possible changes in the behavior and performance of a unique, 55-story tall instrumented building located on a reclaimed island near Osaka, Japan, that was (a) subjected to the wrath of long-period motions during the mainshock and aftershocks of the March 11, 2011 **M**9.0 Tohoku earthquake at an epicentral distance of 767 km, (b) retrofitted in 2013–2014, and (c) severely shaken again during the April 16, 2016, **M**7.3 Kumamoto earthquake and its foreshocks

Data Source and Disclaimer:Japan data from http://www.kyoshin.bosai.go.jp (last visited April 21, 2016). Any use of trade, firm, or product names is for descriptive purposes only and does not imply endorsement by the U.S. Government.

© Springer International Publishing AG 2018
J.P. Conte et al. (eds.), *Experimental Vibration Analysis for Civil Structures*,
Lecture Notes in Civil Engineering 5, https://doi.org/10.1007/978-3-319-67443-8_57

at epicentral distances of ~475 km. The map in Fig. 1 shows the relative locations of the building and the epicenters of the Tohoku and Kumamoto events (marked as e_i, where i corresponds to the event index in Table 1). The event data used in this study are summarized in Table 1, which includes peak accelerations at the top and 1st floor of the building. Figure 2 shows vertical sections, plan view, orientation of the building and its major axes, and the distribution of the tri-axial accelerometers along the height of the building. The building is 256-m tall, vertically irregular, and has a steel-moment frame (55 stories plus 3-story basement). There are no shear walls around the several elevator shafts that, if present, would have added to the lateral stiffness of the building. The building is founded on end-bearing piles that are approximately 60–70 m long (~63 m below ground surface and resting on a diluvial gravel layer). The pile designs include friction in the upper alluvial clay layers of the subsurface. The construction of the building was completed in 1995 and was designed according to pre-1995 codes (before the **M**6.9 Kobe earthquake of 16 January 1995) [1].

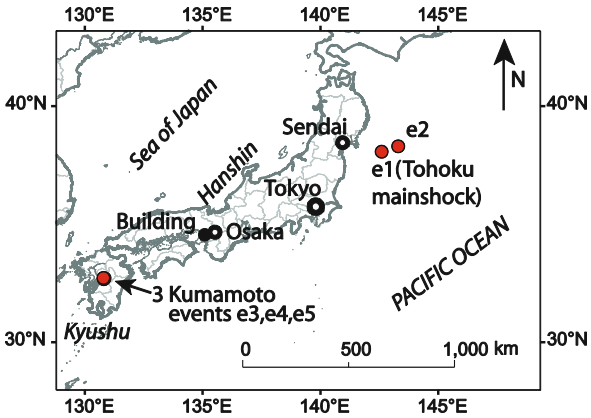

Fig. 1. Map of Japan, epicenters of events and major cities

Records from both Tohoku and Kumamoto earthquakes show how structures sensitive to long-period motions are affected by events from distant sources. During the Tohoku earthquake, the building resonated for a long time, with more than 100 cycles of motion at its fundamental frequency (period) of ~0.15 Hz (6.67 s) (e.g., [1]). As a result of several subsequent studies of the building response records (*e.g.* [2, 3]), the building was retrofitted with dynamic response modification features (Kashima, pers. comm., July 2016). Then, after the retrofit, the building was subjected to strong motions from the **M**7.3 Kumamoto mainshock of April 16, 2016, and its two significant foreshocks. Response records reveal how the building responded during the Tohoku mainshock and aftershocks, which led to the decision to retrofit between late 2013 and June 2014, and how the retrofit building responded during the Kumamoto mainshock and its foreshocks.

Table 1. Events before and after retrofit in this study [Building coordinates: 34°38′17″N, 135° 24′52″E, h(depth [km]), D = epicentral distance (km)]

Event	Time, (local time)	Name of event and epicenter coordinates	Mag (JMA)/ depth (km)	Dist. (km)	Largest peak acc. (gals) 1stFL/52ndFL
Tohoku events before retrofit					
e1	2011/03/11 14:46	Tohoku mainshock 38°06′11”N, 142° 51′36”E	9.0/24	769	34/130
e2	2011/07/10/0957	Off Sanriku 38° 01′54″N, 143° 20′24″E	7.3	816	1.5/13
a1	2011/12/31	Ambient			0.14/0.23
Kumamoto events after retrofit					
e3	2016/04/14 21:26	Kumamoto (foreshock) 32°44′ 30″N, 130°48′29″E	6.5/15	475	0.7/2.2
e4	2016/04/15 00:03	Kumamoto (foreshock) 32°42′ 00″N, 130°46′36″E	6.4/7	480	0.5/2.9
e5	2016/04/16 01:25	Kumamoto (mainshock) 32°45′ 11″N, 130°45′42″E	7.3/12	478	6.6/71.1
a2	2016/01/01	Ambient			0.10/0.22

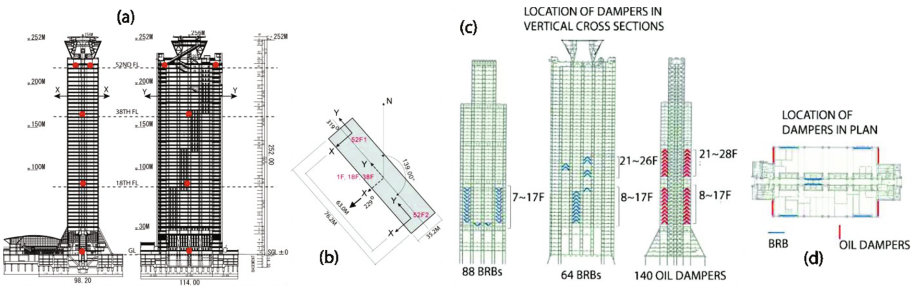

Fig. 2. (a) Vertical sections and general dimensions of the building showing locations (red dots) of the tri-axial accelerometers deployed along the height of the building at the ground level (first floor) and at the 18th, 38th and 52nd floors. (b) Orientations of the building and its principal axes. On the 52nd floor, 1 and 2 denote north and south locations of the two tri-axial sensors F52 N and F52S, respectively. Azimuths clockwise from North of X and Y axes are 229 and 319 degrees, respectively. (c and d) Distribution of dynamic response modification elements (BRBs and oil dampers) [acquired from T. Kashima, pers. Comm., 2016 and modified]. The instruments were installed by Building Research Institute (http://smo.kenken.go.jp/).

To the best knowledge of the authors and others, there are no retrofitted buildings taller than 50 stories in the United States (C. Poland, *pers. comm*. 2016 and F. Naeim, *pers. comm*., 2016).

In performing the analyses, spectral analyses methods [4] and system identification methods in Matlab [5] are used.

Although finite element models and analyses are precluded because of the unavailability and propriety of the blue-prints of the building, the fundamental frequencies for the two principal horizontal directions (X and Y) and torsion were computed during the design/analyses process to be 0.17 Hz, 0.18 Hz and 0.27 Hz, respectively.

In prior studies [1] the fundamental site response characteristics were determined using transfer functions computed by (a) using the depth-shear wave velocity (Vs) profile of the nearby KIKNET station OSKH02 (www.kik.bosai.go.jp/, last visited 16 September 2011), and (b) spectral ratios using actual downhole (at 1550 m depth) and surface data recorded at OSKH02 during the 2011 Tohoku event. Both methods yielded a fundamental site frequency of $\sim$0.13–0.17 Hz. Not reported in detail, the spectral ratios computed for OSKH02 using the Kumamoto 2016 mainshock data confirm repeatability of the previous results.

2 Retrofit

Following the Tohoku event, and as a result of poor behavior expressed by the prolonged and resonating response of the building during the event, an extensive retrofit program for the building was implemented during 2013–2014 (we note that the proprietary analyses and resulting designs that led to the retrofit were unavailable for inclusion here). Dynamic response-modification members (140 oil dampers and 114 buckling restrained braces [BRB]) were installed at several floors up to the 21st level and within several bays as shown in Fig. 4. After the retrofit, and between April 14–16, 2016, the Kumamoto earthquake sequence occurred on the island of Kyushu, approximately 475 km southwest of the building. Significant shaking was recorded during the April 16, 2016, Kumamoto mainshock (**M**7.3) and its two large foreshocks on April 14, 2016 (**M**6.5) and April 15, 2016 (**M**6.4)[1]. These valuable records provide a rare opportunity to investigate how the building response to long-period shaking was modified by the retrofit.

[1] Wikipedia (https://en.wikipedia.org/wiki/2016_Kumamoto_earthquakes) reports "The 2016 Kumamoto earthquakes are a series of earthquakes, including a magnitude 7.0 mainshock which struck at 01:25 JST on April 16, 2016 beneath Kumamoto City of Kumamoto Prefecture in Kyushu Region. It killed at least 49 people and injured about 3,000 others in total. Severe damage occurred in Kumamoto and Ōita Prefectures, with numerous structures collapsing and catching fire. More than 44,000 people have been evacuated from their homes due to the disaster"
.

3 Recorded Earthquake and Ambient Responses

Figure 3 shows comparisons of acceleration time-histories in both X and Y orientations for all five earthquakes. Immediately evident in these acceleration time-histories are the prolonged motions lasting for 200 s or more, which indicate a lightly damped system with beating in the response. Both of these aspects are discussed below.

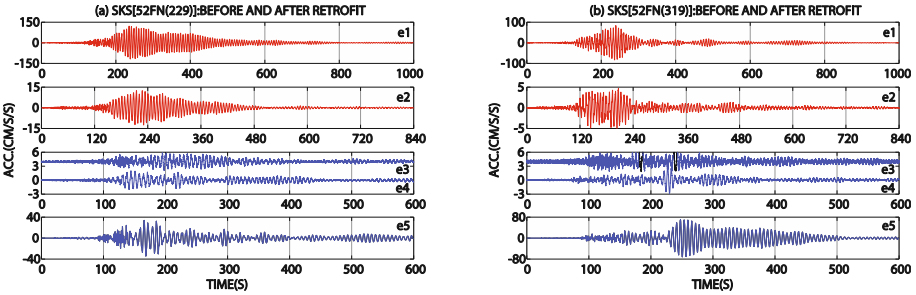

Fig. 3. For all five events, acceleration time-histories are plotted for both the (a) X and (b) Y orientations. Each frame is plotted with a different vertical scaling to better resolve the amplitudes of the time-histories, and with a different horizontal scaling determined by the total duration of the record. The two events that occurred before retrofit are in red, while the three post-retrofit events are in blue.

In Fig. 4, normalized amplitude spectra and spectral ratios of accelerations for all five earthquakes (e1–e5) are presented. In both the spectra and spectral ratio plots the first two modes in each principal direction are generally shifted to slightly higher frequencies (in the ~0.02–0.10 Hz range) after retrofit. Although this might seem to be insignificant, this is not the case for buildings with such low-frequencies (e.g. tall buildings) when changes in the overall stiffnesses (k) are computed (e.g., an increase in fundamental frequency from 0.16 Hz before retrofit to 0.17 Hz after retrofit implies or, at least, is quantified roughly as at least ~13% [$(k_{after}/k_{before}) \sim (f^2_{after}/f^2_{before}) \sim 0.17^2/0.16^2 \sim 1.1289$]). The changes to the critical damping percentages as a result of retrofit will be examined later by other methods. Similar comparisons are made later using ambient data from the pre- and post-retrofit epochs. For the 2nd mode, the differences of frequencies in Y direction are larger (~0.04 Hz) for the Kumamoto mainshock and even larger for its two foreshocks. Since torsional effects can be computed only at the 52nd floor, spectral ratios cannot be obtained. Therefore, only amplitude spectra of torsional motions are shown in Fig. 4c. The torsional amplitude spectra shown in Fig. 4c are more reliable since the distance between channels in the X direction is much larger than that of the Y direction. The fundamental torsional frequency before and after retrofit are ~0.21 Hz and 0.23 Hz for the mainshocks, respectively.

During low-amplitude ambient shaking of the structure the influence of ground motions is generally considered to be negligible, but if it exists, then, when spectral ratios are computed with respect to ground level, the ratios should be ~1. Therefore, the intent is to make a comparison of frequencies and inferred stiffnesses computed

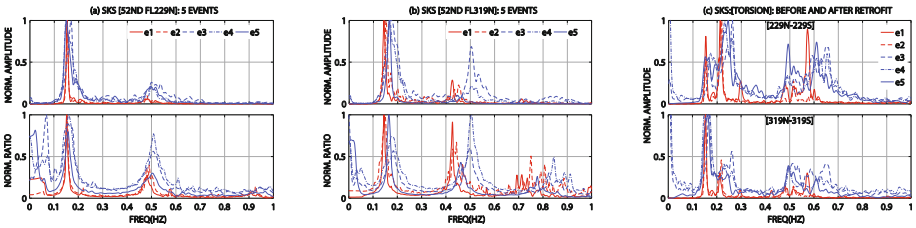

Fig. 4. Normalized amplitude spectra of accelerations and spectral ratios at 52nd floor for (a) X and (b) Y and (c) torsional orientations for all five events. Color indicates before (red) and after (blue) retrofit events and individual events are distinguished by line pattern. Spectral ratios are computed with respect to first floor. Peaks at frequencies lower than about 0.08 Hz likely reflect ground motion inputs rather than building responses.

from ambient data retrieved from pre- and post-retrofit epochs, as well as between earthquakes. As seen in Figs. 5a and b there are no significant differences between the translational frequencies identified from the computed amplitude spectra as compared to those from the spectral ratios. However, for the fundamental mode of both translation directions there is a small shift ($\sim$0.01 Hz) to longer frequencies after the retrofit. Even larger shifts to higher frequencies can be observed for higher modes. Likewise, the amplitude spectra for torsion shows a $\sim$0.04 Hz shift to a higher frequency for the fundamental mode after the retrofit. Specifically, in Fig. 5a, amplitude spectra of ambient accelerations "before" and "after" retrofit regimes of the building are presented. Both translational and torsional fundamental frequencies are identified. Compared to e1 (Tohoku event) the ambient data computed frequencies are higher and also the post-retrofit ones are higher (0.17 Hz, 0.19 Hz and 0.26 Hz for X, Y and torsional response) also higher than those of the Kumamoto (e5) event (for which the corresponding fundamental frequencies are 0.16 Hz, 0.16 Hz and 0.23 Hz, respectively). Figure 5b shows spectral ratios only for translational responses and confirm the same observation as those from amplitude spectra.

4 System Identification (SID)

Spectral analyses methods are powerful for identifying modal frequencies from amplitude spectra, spectral ratios and cross-spectra, as shown above, but these particular applications are not generally useful in estimating modal critical damping percentages (ξ) and mode shapes. In order to obtain critical damping percentages and mode shapes, in addition to modal frequencies, we use numerical algorithms for Subspace State Space System Identification [6, 7] refined by the Prediction Error Method (PEM) [8, 9]. Spectral analyses show that none of the natural frequencies observed in spectra from mid-height and roof levels are observed in the spectra from the first floor, thus leading to the conclusion that there is no inertial soil-structure interaction effect. Hence, an input-output identification technique can be used for the identification purpose. N4SID is coded in Matlab [5].

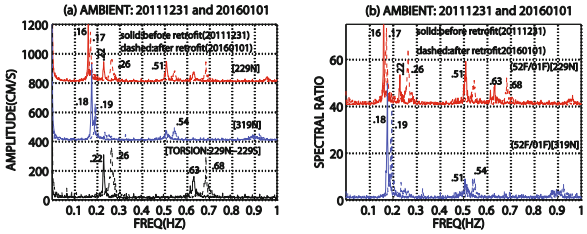

Fig. 5. Ambient data from pre- and post-retrofit epochs. (a) Amplitude spectra of translational and torsional accelerations. (b) Spectral ratios of amplitude spectra for translational accelerations. Line pattern (solid or dashed) indicates pre- and post-retrofit epochs, resp. Line color corresponds to motion: red for X, blue for Y, and black for torsion.

We first identify an initial estimation of the system through N4SID [6] and then refine the model using PEM. Furthermore, identification techniques applied to flexible buildings with such sparse instrumentation need crucial pre-processing steps because the presence of higher modes can cause spatial aliasing and thus produce errors in identifying lower modes. To remove these unfavorable effects, we filtered out frequencies above 2.5 Hz. This will also help by allowing a smaller model order for the system – which is the most important factor in any parametric identification method like N4SID or PEM. To obtain reliable results, we repeated the identification process for a range of model orders from 10 to 60 and selected stable model order through a stability diagram [10]. Relative frequency and damping errors less than 2% and 20%, respectively, along with Modal Assurance Criterion (MAC) index greater than 0.95, were used for detecting stable model order. Table 2 shows the identified natural frequencies and damping ratios for both translational directions for the two mainshocks (e1 and e5). For comparison, we identified the same modal characteristics for the two ambient data sets listed as events a1 and a2; t.

Table 2. Identified natural frequencies (Hz) and damping percentages (%).

Event	Frequency (Hz)						Damping (%)					
	X (229) Direction			Y(319) Direction			X (229) Direction			Y(319) Direction		
	1	2	3	1	2	3	1	2	3	1	2	3
e1	0.152	0.481	0.905	0.145	0.427	0.729	0.94	1.41	1.16	1.64	1.51	2.31
a1	0.160	0.506	0.957	0.176	0.512	0.894	1.11	1.41	0.55	1.51	0.48	1.94
a2	0.170	0.538	1.007	0.194	0.541	0.916	1.56	1.09	1.46	1.46	1.12	1.36
e5	0.155	0.500	0.947	0.163	0.461	0.762	3.44	4.27	3.81	1.58	1.78	1.79

As expected, for the same structure and within the same epoch (either pre- or post-retrofit) the natural frequencies identified from earthquake data are always shorter than those identified from ambient data (e.g. [11]). For the building in this study such differences are more significant in the Y direction. Also as expected, (i) due to

amplitude-dependency, damping ratios identified from earthquake data are higher, and (ii) the level of damping in the "after" retrofit event e5 is much higher than "before" retrofit event e1. This is due to added dampers (but not due not excitation intensities because the higher level of energy dissipation is only observed in the X(229) direction while similar levels of damping are observed in the Y(319) direction). Another important observation is the difference between natural frequencies "before" and "after" retrofit. As seen, for both ambient or earthquake pairs, the building is stiffer after retrofit. However, we cannot quantify such differences because amplitude-dependency is implicitly included in earthquake data and the differences of frequencies identified from ambient data are small.

The identified mode shapes are normalized and presented in Fig. 6. While there are minor differences in mode shapes from event to event (emphasized by keeping largest amplitude +1), to see such variations are not surprising considering the sparsely sampled mode shapes that are less sensitive to local changes in the building.

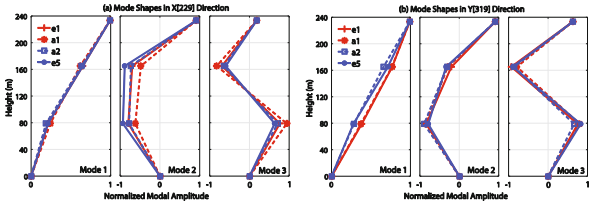

Fig. 6. Identified mode shapes in X(229) and Y(319) directions.

5 Accelerations, Displacements and Average Drift Ratios

Figure 7 compares the time histories of acceleration and displacement for each of the principal building directions, X and Y, and includes only the records for the 2011 Tohoku (e1) and 2016 Kumamoto (e5) mainshocks. Note that the waveforms of acceleration and displacement for a given event and orientation are remarkably similar due to the fact at the fundamental frequency ($f \sim 0.17$ Hz), $\omega \sim 1$. The time-histories distinctly display persistent beating before and after retrofit.

Next, in Fig. 8, time histories of average drift ratios for several combinations of instrumented floors are shown. For the Tohoku event (e1), the maximum average drift ratio is $\sim$0.6–0.7% in the X and $\sim$0.5% in the Y direction. These values are near the threshold where damage might be expected according to Japanese practice [12]. For the Kumamoto mainshock (e5), the maximum average drift ratios, $\sim$0.25–0.3% in both X and Y directions, are lower due to the lower shaking amplitudes both in acceleration and displacements.

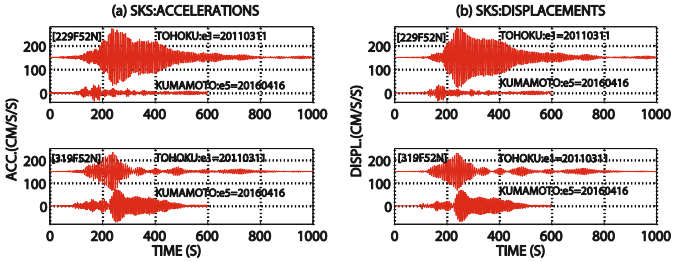

Fig. 7. Comparison of time histories at the 52nd floor for each of the principal building directions X (upper panels) and Y (lower panels) of accelerations (a) and displacements (b). Within each plot the vertical scaling of both traces is the same, but they are offset for clarity; the upper trace shows the data for 2011 Tohoku (e1) mainshock and the lower trace shows the 2016 Kumamoto (e5) mainshock. Note the shorter duration of the record from the Kumamoto event.

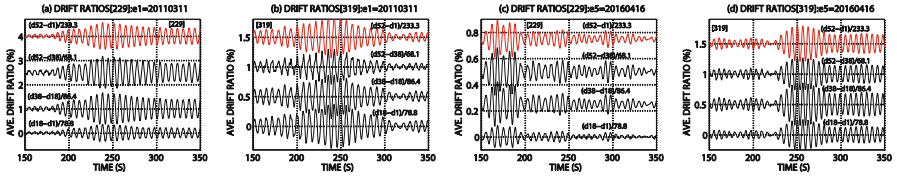

Fig. 8. Drift ratios as a function of time for windows of equal duration. Within each plot the vertical scaling is the same, but traces are offset for clarity. From top to bottom within each plot the traces correspond to drift rations computed using floors 52 and 1, 52 and 38, 38 and 18, and 18 and 1. The two left plots show data for the Tohoku mainshock, with (a) and (b) corresponding to principal building directions X and Y. Similarly, the two plots on the right, (c) and (d), show data for the Kumamoto mainshock.

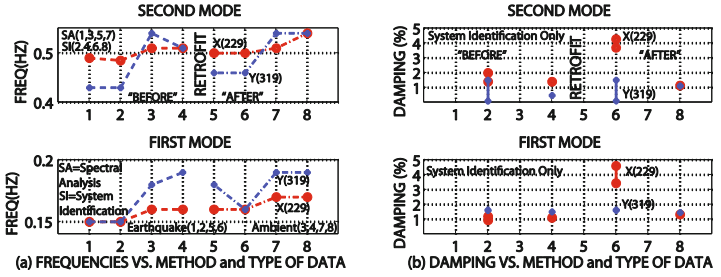

Fig. 9. Comparison of 1st and 2nd modal (a) frequencies and (b) damping identified for "before" and "after" retrofit epochs by method of analyses of earthquake and ambient data.

6 Discussion and Conclusions

Figure 9 displays the trend in changes of the (a) first and second modal frequencies and (b) damping percentages for pre- and post-retrofit epochs. Distinctions are made between values identified by analyses of (i) earthquake and ambient responses, and (ii) spectral or system identification methods of analyses of those responses. The modal frequencies after retrofit identified from earthquake and ambient data are higher than those from prior to retrofit, even though the retrofit structural elements were added only up to the 21st floor, about 2/5 of the building height. This observation is expected since the BRB's or dampers provide some level of increase in stiffness (as demonstrated by considering even a small 0.01 Hz increase in frequency). And for both pre- and post-retrofit epochs, modal frequencies determined using ambient data are higher than those using earthquake data. Damping ratios increased from 1.2% to 4.6% in the X direction (where dampers are installed) following the retrofit. This is a desirable outcome. At higher shaking levels, the damping ratios in the X direction could increase more, as the dampers are expected to be more effective when subjected to larger displacements. On the other hand, in the Y direction, where only BRB's are installed, damping decreased from 1.60% to 1.31%. This also makes sense as the structure became stiffer after the retrofit.

Time histories of acceleration and displacement do not indicate any improvements in combating beating effects as a result of the retrofit.

Due to the sparse instrumentation, only average drift ratios can be computed. The average drift ratios are higher, as expected, for the Tohoku mainshock than for the Kumamoto mainshock.

In conclusion, this study of recorded responses of this sparsely instrumented building for the pre- and post-retrofit epochs clearly indicates improved dynamic characteristics (e.g. higher damping and stiffness) for better performance following the retrofit. However, the trends do not show reduction of beating effects, nor any discernable decrease in the effects of site response on the building response.

Acknowledgements. Data used in this paper was provided for cooperative studies between USGS and Building Research Institute of Japan as part of activities of Wind and Seismic Effects Panel of United States Japan Panel on Natural Resources. The authors thank USGS internal reviewers Chris Stephens and Kishor Jaiswal for their valuable comments.

References

1. Çelebi, M., Okawa, I., Kashima, T., Koyama, S., Iiba, M.: Response of a tall building far from the epicenter of the March 11, 2011 Mw 9.0 Great East Japan earthquake and its aftershocks. Wiley J. Struct. Des. Tall Spec. Build. **23**, 427–441 (2014)
2. Okawa, I., Kashima, T., Koyama, S., Iiba, M., Çelebi, M.: Summary of recorded building responses during t the 2011 off the Pacific Coast of Tohoku earthquake with some implications to design motions. In Proceedings of the International Symposium on Engineering Lessons Learned from the Giant Earthquake—One year the 2011 Great East Japan Earthquake, 1–4 March, 2012, Kenchiku–Kaikan, Tokyo Japan. [CD-ROM Proceedings] (2012)

3. Kashima, T., Koyama, S., Okawa, I., Iiba, M.: Strong motion records in buildings from the 2011 great east Japan earthquake. Paper no. 1768, In: Proceedings of the 15th World Conference on Earthquake Engineering, Lisbon, Portugal (2012)
4. Bendat, J.S., Piersol, A.G.: Engineering Applications of Correlation and Spectral Analysis. Wiley, New York (1980)
5. Mathworks and previous versions. Matlab and Toolboxes, South Natick, MA (2013)
6. Van Overschee, P., De Moor, B.: N4SID: Subspace algorithms for the identification of combined deterministic-stochastic systems. Automatica **30**(1), 75–93 (1994)
7. Van Overschee, P., De Moor, B.: Subspace Identification for Linear Systems. Kluwer Academic Publishers, Dordrecht (1996)
8. Ljung, L.: System Identification: Theory for the User. Prentice Hall, Englewood Cliffs (1987)
9. Ljung, L.: Prediction error estimation methods. Circ. Syst. Signal Process **21**, 11–21 (2002)
10. Bodeux, J., Golinval, J.: Application of ARMAV models to the identification and damage detection of mechanical and civil engineering structures. Smart Mater. Struct. **10**, 479–489 (2001)
11. Çelebi, M.: On the variation of fundamental frequency (period) of an undamaged building—a continuing discussion. In: Proceedings Experimental Vibration Analysis for Civil Engineering Structures, pp. 317–325, Porto, Portugal (2007)
12. Kubo, T., Hisada, Y., Murakami, M., Kosuge, F., Hamano, K.: Application of an earthquake early warning system and a real-time strong motion monitoring system in emergency response in a high-rise building. Soil Dyn. Earthq. Eng. **31**, 231–239 (2011)

Time-Frequency Analysis of Suspension Bridge Response for Identification of Vortex Induced Vibrations

Daniel Cantero(✉), Ole Øiseth, and Anders Rønnquist

Department of Structural Engineering, Norwegian University of Science and Technology NTNU, Trondheim, Norway
daniel.cantero@ntnu.no

Abstract. It is increasingly more frequent to install continuous monitoring systems on large bridges around the world. These systems are then used to monitor the loading and structural behavior, which generally translates into continuous estimates of the bridges' modal properties. Because of practical reasons, in general only the lower frequency range of the signals is stored and analyzed, and only a limited number of sensors can be installed. This means that for the particular case of suspension bridges it is not feasible to instrument each hanger. This paper shows that it is possible to detect vortex induced vibrations on hangers indirectly by monitoring the accelerations at the deck. The study is based on the acceleration signals collected by a permanent monitoring system installed on the deck and pylons of the Hardanger suspension bridge (1310 m span) in Norway. Additionally, the temporary measurements of some of the hangers are used to assess the validity of the predictions. The signals are analyzed in time-frequency domain by means of Short-Term Fourier Transform and Continuous Wavelet transform. The paper includes some discussion on the advantages and disadvantages of both methods for the task at hand. The results clearly show the presence of frequencies associated to vortex shedding on the hangers and how these frequencies change with wind speed. The ideas reported in this study should allow owners of large bridges to obtain more information from their existing monitoring systems.

Keywords: Vortex-induced vibrations · Signal processing · Time-frequency analysis · Suspension bridge · Monitoring · Hanger

1 Introduction

Cable-stayed and suspension bridges are large, expensive and critical elements of the transport infrastructure. In recent times, bridge owners are more willing to invest additional money to install and run continuous monitoring systems. Collections of examples of large bridge projects with such systems can be found in [1–3]. One possible use for the information gathered with these systems is the vibration based monitoring [1], which has been proven to be useful for characterization of the bridge response under different loading conditions, structural performance evaluation, validation and correction of design models and as a source of structural updating information.

© Springer International Publishing AG 2018
J.P. Conte et al. (eds.), *Experimental Vibration Analysis for Civil Structures*,
Lecture Notes in Civil Engineering 5, https://doi.org/10.1007/978-3-319-67443-8_58

In order to perform a correct analysis of the recorded responses it is required to have a good understanding of all the underlying phenomena of the structural behavior.

In the design of long-span bridges, wind loading is one of the most important aspects to consider [4]. Among the many possible wind related phenomena, vortex induced vibrations (VIV) is one of the most frequent, in particular for low to medium wind velocities. When a bluff body, like a cable, separates the wind stream it results in a Von Karman vortex trail that produces a harmonic oscillation in the wake of the structural member. The frequency of that oscillation is called the vortex shedding frequency f_{vs} (Eq. (1)) where u is the wind velocity, St the Strouhal number and D the diameter of the cylinder [5]. In practical applications for a cylinder shaped element, the value of St can be taken as 0.2. When the excitation frequency is close or matches one of the cable frequencies the so-called lock-in phenomenon appears, which effectively is a synchronization of the load and the response. Additional information on vortex shedding and VIV can be found in [6, 7] that provide good overviews on recent developments on these topics.

$$f_{vs} = \frac{u\,St}{D} \tag{1}$$

Even though the nature of VIV is self-exciting, it is also a self-limiting phenomenon where vibrations rarely attain half the cable diameter [5]. However, these vibrations are of concern because they potentially induce additional stresses and lead to cumulative fatigue in the cables themselves and in the connections. Furthermore, these vibrations affect the whole structure and are present in the signals recorded by the monitoring systems. Therefore, the main goal of this paper is to show that it is possible to distinguish these vibrations by correlating them with the changing wind velocity using appropriate time-frequency domain methods. Section 2 describes the particular bridge used in this study, the existing permanent monitoring system as well as the temporary measurements performed directly at the hangers. This is followed by an introduction to time-frequency analysis tools in Sect. 3 supported by several numerical examples that clarify various aspects and compares different possibilities. Finally, in Sect. 4, recorded acceleration signals from the hangers and the bridge deck are compared to the associated vortex shedding frequency showing clear correlations.

2 Bridge Instrumentation

The Hardanger Bridge (Fig. 1) in Norway is a suspension bridge with a central span of 1310 m opened to traffic in 2013. A permanent monitoring system was installed then to record the wind loading and the dynamic structural behavior. The system comprises of 20 triaxial accelerometers and 8 ultrasonic anemometers distributed along the deck and pylons as shown in Fig. 2. The signals are stored locally but are also send wirelessly to a server on-line where they can be downloaded and processed from any computer.

In order to perform a detailed investigation of the VIV of the bridge hangers, an additional temporary measurement campaign was performed. This consisted on the measurement of the accelerations directly from the hanger. Several ambient vibration

Fig. 1. Hardanger Bridge

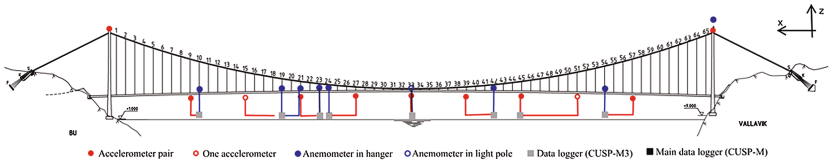

Fig. 2. Permanent instrumentation layout

tests of 1 h duration were performed on the two longest hangers near the North pylon. During the tests the loading of the hangers consisted of passing traffic and blowing wind. Measurements were repeated for different days with different weather conditions, for wind velocities ranging from almost perfectly still up to 15 m/s (Figure 3).

Fig. 3. Temporary hanger instrumentation

3 Time-Frequency Signal Processing

As seen in Eq. (1), the excitation frequency f_{vs} is directly proportional to the wind velocity. But, because of the fluctuating nature of wind, the excitation and therefore the response will be nonstationary, i.e. the frequency changes in time. The Fourier transform is generally used to transform a signal into frequency domain. However, this is not appropriate for studying a nonstationary process. One possible solution is to subdivide the signal into overlapping portions by means of a window of a certain length and perform the Fourier transform on each. This offers a representation of the energy content in time-frequency domain in what is generally called Short-Term Fourier Transform (STFT). Alternatively, one might use the Continuous Wavelet Transform (CWT) that essentially compares scaled and shifted versions of a given function (basis) to the signal resulting also in a time-frequency map. Both tools have advantages and disadvantages [8, 9] and should not be used as exclusive solutions but rather as complementary tools.

To highlight the differences between tools, a synthetic numerical signal is analyzed in Fig. 4. The signal (Fig. 4a) consists of two sinusoidal components. One is stationary with a constant frequency of 12 Hz, amplitude of 1 and goes from 5 to 25 s. The second component is nonstationary with a linearly increasing frequency from 5 to 20 Hz and constant amplitude of 1. The CWT of the signal using the Morlet basis, which is probably the most commonly used basis, leads to a time-frequency energy map shown in Fig. 4b. Choosing the appropriate basis for the problem at hand is not trivial and can vary depending on the signal or on the intended use of the result. For visualization purposes of bridge acceleration signals it is convenient to adopt the Modified Littlewood-Paley (MLP) basis, which was successfully used in [10] to

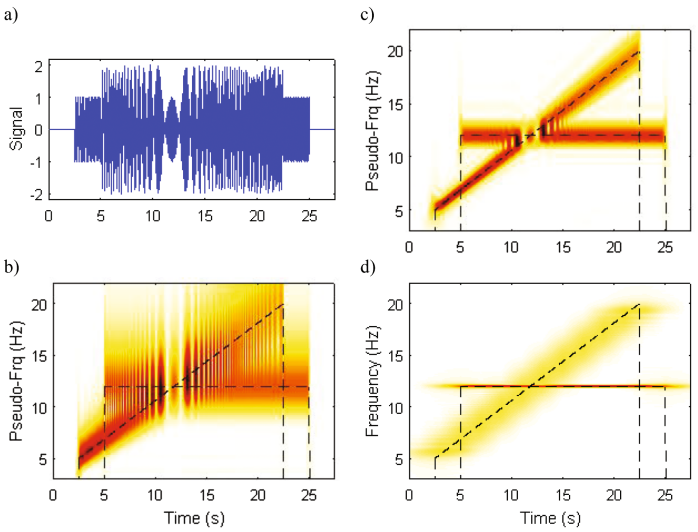

Fig. 4. First numerical example; (a) Nonstationary signal; (b) CWT and Morlet basis; (c) CWT and MLP basis; (d) STFT

analyze the response of a railway bridge during train passages. The energy map obtained with the MLP basis (Fig. 4c) offers a much clearer and sharper representation of the signal's frequency evolution in time. Finally, Fig. 4d is the STFT for a Hamming window of 10 s duration and an overlap of 80%. It is clear that it is possible to obtain a very sharp representation of the stationary part of the signal, whereas the nonstationary part is more ambiguous. Additionally, the high frequency resolution obtained in Fig. 4d comes with a cost, a lower resolution in time.

A particular issue that we encounter during the analysis of bridge acceleration signals in time is the alternating presence and absence of vehicles. When a vehicle crosses the bridge, higher acceleration levels are recorded. Inevitably the time-frequency energy map will be dominated by the short time instances when vehicles are passing near the sensor. To illustrate this, a second numerical signal is analyzed. Now the signal has varying amplitude with a short duration peak (Fig. 5a) and linearly increasing frequency (Fig. 5b), resulting in the signal shown in Fig. 5c. Performing the time-frequency analysis by means of CWT and MLP basis produces the energy map displayed in Fig. 5d. As expected, the representation is dominated by the part of the signal with higher amplitude, making it difficult to clearly track the evolution of the frequency. It is therefore convenient to normalize the results from the CWT by the instantaneous energy, which can be obtained as the sum of all CWT coefficients for a given time. This normalization, see Fig. 5e, offers a clearer picture of the changing frequency.

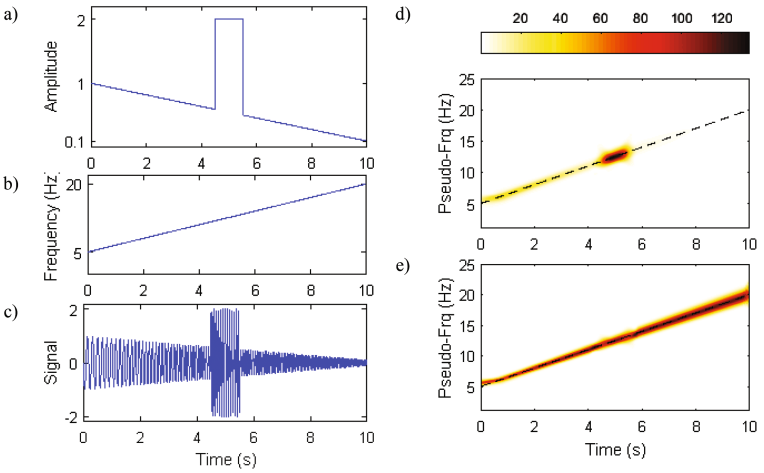

Fig. 5. Second numerical example; (a) Amplitude; (b) Frequency; (c) Nonstationary signal; (d) CWT with MLP basis; (e) CWT with MLP basis normalized by instantaneous energy

4 Structural Response Analysis

In this section we analyze in time-frequency domain the acceleration signals recorded at the Hardanger Bridge. First, it is interesting to study in detail a short duration interval (10 s) of the horizontal accelerations measured at one of the hangers during ambient vibration. The signal is presented in Fig. 6a, which perfectly illustrates the typical behavior of the hanger. Holding the hanger with the hands during VIV, one can feel a pulse-like response that could be interpreted as a travelling wave going up and down the hanger. The energy distribution map obtained with CWT analysis, shown in Fig. 6b, indicates that the energy is mostly concentrated around a band near 20 Hz. Note that the small variation in frequency observed here is an artifact of the normalization by the instantaneous energy. On the other hand, performing the STFT of the same signal (Fig. 6c) offers a much clearer picture of the frequency components of the signal. The energy is clearly concentrated around certain fixed frequencies that correspond to some of the cable's frequencies. More precisely the excited frequencies correspond to 19.8 Hz and 20.7 Hz. A vibration composed of two sinusoidal components with closely spaced frequencies produces the familiar beat-like response, where the envelope of the beat has a frequency equal to the difference in frequencies. This corresponds namely to 0.9 Hz, or a period of 1.11 s, which clearly matches the response observed in Fig. 6a. This example shows that for sufficiently long stationary VIVs, the STFT together with a long duration window offers a good description of the phenomena.

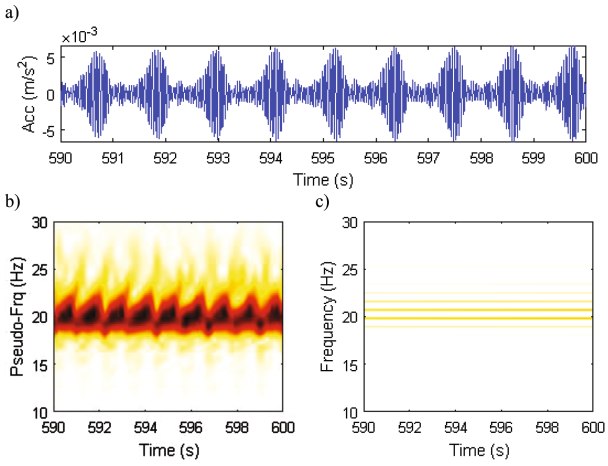

Fig. 6. Beating phenomenon; (a) Acceleration signal; (b) CWT with MLP; (c) STFT

However, due to the variable nature of wind, sudden changes in wind velocity are expected leading to nonstationary excitations and responses. As shown in the first numerical example it is appropriate then to study the nonstationary signals with a tool that is able to capture this varying nature. Performing the CWT with the MLP basis on

a 3000 s long acceleration signal recorded directly at the hanger gives the energy map shown in Fig. 7b. The vortex shedding frequency associated to the 60 s average wind velocity is indicated by a black solid line superimposed to the energy map. The correspondence between wind and energy content is remarkable. The result shows an approximately constant frequency band near 20 Hz from 0 s to 1000 s, even though the recorded wind indicates that the vortex shedding frequency varies between 17 Hz and 23 Hz. This might correspond to the lock-in phenomenon known to occur when the excitation frequency is near one of the excited structure's frequencies. After that, the energy distribution in time seems to follow closely the vortex shedding frequency estimated with Eq. (1) and the 60 s average wind velocity. For reference, the acceleration signal recorded directly at the hanger is shown in Fig. 7a.

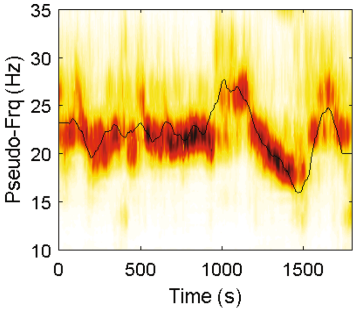

Fig. 7. (a) Hanger acceleration; (b) CWT of hanger acceleration; (c) CWT of deck acceleration. (Black solid line = 60 s average vortex shedding frequency) (Color figure online)

Furthermore, these VIV hanger vibrations can also be identified on the deck. Figure 7c shows the CWT analysis of the recorded deck accelerations during exactly the same time period as shown in Fig. 7b. There is not an exact match between hanger and deck vibrations but their similarity is striking. The same lock-in phenomena and frequency variability can be monitored on the deck and is also directly correlated to the calculated vortex shedding frequency. Therefore, it is possible to monitor the VIV of the bridge hangers indirectly by analyzing the acceleration signals recorded elsewhere on the bridge deck. It is worth noting that this strong correlation is observed in many of the recorded signals obtained during the bridge's operational life and is not the result of an isolated loading situation. For instance, Fig. 8 shows the CWT of a deck acceleration signal prior to the mounting of the temporary measurement system. Thus, no information is available about the particular vibrations of any of the hangers. But the time-frequency analysis shows that a significant amount of energy is concentrated close to the vortex shedding frequency predicted for cylinders with the same dimensions as the hangers. Therefore, it is possible to conclude that at least one of the hangers is vibrating induced by the blowing wind.

The results showed here open a wide range of possibilities. A clear physical interpretation is given to one significant portion of the energy content in deck accelerations. Knowing the source of these vibrations facilitates the correct postprocessing

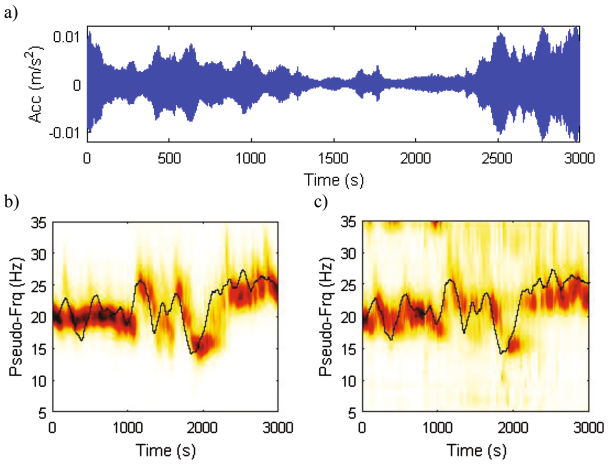

Fig. 8. CWT of deck acceleration (Black solid line = 60 s average vortex shedding frequency) (Color figure online)

of the acceleration signals. Furthermore, this also offers the possibility of assessing the effect of VIV on the hangers. It is generally not feasible to monitor every single hanger. The time-frequency analysis of the deck accelerations can offer a preliminary tool to evaluate the need of additional and targeted investigations on the VIV responses of the hangers.

5 Conclusions

This paper has investigated the Hardanger Bridge response monitored through a permanent and a temporary system. It clearly shows the convenience of analyzing the recorded signals using time-frequency tools. In particular, this investigation evaluates the Short-Term Fourier Transform and the Continuous Wavelet Transform together with the Modified Littlewood-Paley basis, highlighting that these are complementary tools that can offer useful information. In order to remove, to some extent, the contribution of traffic loading, a normalization of the time-frequency results by the total instantaneous energy is suggested. The analysis of the hanger accelerations shows that there is a direct correspondence with the vortex shedding frequency associated to the 60 s average wind velocity. It is shown that these hanger VIV can be identified also on the acceleration signals of the bridge deck. Therefore, this paper offers a physical explanation on some of the major components present in deck acceleration signals. Furthermore, it shows that it is possible to monitor the VIV of the bridge hangers indirectly by analyzing the acceleration signals recorded elsewhere on the bridge deck.

Acknowledgments. The research presented in this manuscript was possible thanks to the financial support of The Fjord Crossing research program for the Coastal Highway Route E39.

References

1. Brownjohn, J.M.W., De Stefano, A., Xu, Y.L., Wenzel, H., Aktan, A.E.: Vibration-based monitoring of civil infrastructure: challenges and successes. J. Civil Struct. Health Monit. **1**, 79–95 (2011)
2. Andersen, J.E., Vesterinen, A.: Structural health monitoring systems. COWI A/S and Futurtec OY. (2006). http://www.shms.dk
3. Wong, K.Y.: Instrumentation and health monitoring of cable-supported bridges. Struct. Control Health Monit. **11**, 91–124 (2004)
4. Larsen, A., Larose, G.L.: Dynamic wind effects on suspension and cable-stayed bridges. J. Sound Vib. **334**, 2–28 (2015)
5. Caetano, E.: Cable Vibrations in Cable-Stayed Bridges. ETH Hönggerberg, Zürich (2007)
6. Wu, T., Kareem, A.: An overview of vortex-induced vibration (VIV) of bridge decks. Front. Struct. Civ. Eng. **6**(4), 335–347 (2012)
7. Williamson, C.H.K., Govardhan, R.: Vortex-induced vibrations. Annu. Rev. Fluid Mech. **36**, 413–455 (2004)
8. Nagarajaiah, S., Basu, B.: Output only modal identification and structural damage detection using time frequency & wavelet techniques. Earthq. Eng. Eng. Vib. **8**, 583–605 (2009)
9. Gonzalez, I., Karoumi, R.: Analysis of the annual variations in the dynamic behavior of a ballasted railway bridge using Hilbert transform. Eng. Struct. **60**, 126–132 (2014)
10. Cantero, D., Ülker-Kaustell, M., Karoumi, R.: Time–frequency analysis of railway bridge response in forced vibration. Mech. Syst. Signal Process. **76–77**, 518–553 (2016)

Dynamic Characteristics of Layered Stone Pagoda System

Byeong Hwa Kim(✉)

Department of Civil Engineering,
Kyungnam University, Changwon, South Korea
bhkim@kyungnam.ac.kr

Abstract. For the dynamic behavior of a layered stone pagoda system, the continuous cantilever beam model or discrete shear building model are often considered as a numerical model. However, the validations of such models have not been fully examined yet. A modal testing and analysis of a layered stone pagoda system reveals that there exist a set of closely placed double modes and the time delay of a shear wave occurs through friction surfaces. Moreover, the modal parameters of aforementioned numerical models do not agree with those of real pagoda structure. This work newly proposes a numerical model that can explain such peculiar dynamic characteristics of the layered stone pagoda system. The validation of the proposed model has been examined through the various experiments.

Keywords: Modal analysis · Numerical modelling · Stone pagoda · Stick-slip · Rigid block rocking

1 Introduction

The studies on ancient stone pagoda have been mainly conducted in terms of humanities and sociology, and approaches from the aspect of engineering have been attempted recently. Initial studies [1, 2] of stone pagoda from the aspect of structural engineering mostly attempted to identify the behavior characteristics of layered stone structures and construct structural analysis models with a view to utilizing the models in frequency based safety diagnoses.

Although the structural types of stone pagoda cultural properties are diverse by period and regions, stone pagoda cultural properties commonly have layered discontinuous faces. Stone pagoda cultural properties show complicated structural behavior patterns according to not only the forms of inner foundations of stone pagodas but also overburden loads on interlayer discontinuous faces and bump shear properties [2]. In engineering analysis, the layered stone pagodas are numerically modeled as cantilever beams which are a continuum or often modeled as shear buildings. However, the suitability and accuracy of those analysis models have not been verified yet. Since the structural behavior modes of stone pagodas, which are complex systems, not only natural frequencies but also mode shapes should be measured and identified. However, most structural engineering studies of stone pagoda cultural properties utilized analysis

© Springer International Publishing AG 2018
J.P. Conte et al. (eds.), *Experimental Vibration Analysis for Civil Structures*,
Lecture Notes in Civil Engineering 5, https://doi.org/10.1007/978-3-319-67443-8_59

models in which only actually measured natural frequencies were matched without measuring or identifying actually measured mode shapes.

For dynamic behavior of an ancient layered stone pagoda system, the few numerical models such as the stick-slip model [3] and rocking model [4, 5] are available in literature. However, no experimental verifications have been reported yet.

A recent experimental study [6] for the modal testing and analysis of a layered stone pagoda reveals that there exist a set of double modes. Moreover, the modal parameters of real pagoda do not agree with those of the small deflection theory models. This work proposes a simple numerical model that could explain the peculiar double mode mechanism. The simulated results from the proposed model are compared with those from a real mock-up structure of stone pagoda system.

2 Modal Testing

2.1 Test Setup

As shown in Fig. 1, a set of modal testing have been conducted for a five-story stone pagoda mock-up. Horizontal excitation of the roof stone of the stone pagoda was implemented using a model impact hammer. To collect acceleration time histories of the stacked rigid blocks, a total of 5 accelerometers were installed horizontally as shown in Fig. 1. The data were collected at 2 kHz using the RDAS program of NewConsTech. Inc.

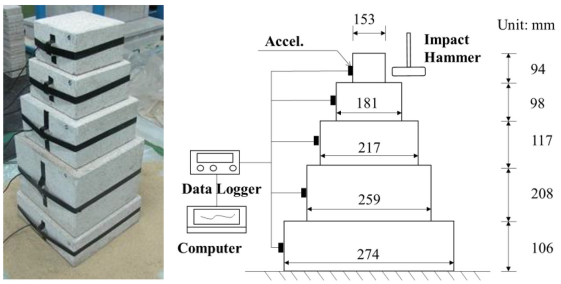

Fig. 1. Test setup

2.2 Modal Analysis

Figure 2 shows the horizontal acceleration response signals and their power spectral densities, when the fifth story stone was horizontally excited 49 times by using the impact hammer. The largest horizontal deflection occurs at the fifth story. It is also observed that the first three lower modes are strongly excited, while a few higher modes are weekly excited. The natural frequencies and mode shapes of the pagoda mock-up are extracted by the TDD technique [7]. The extracted mode shapes are shown in Fig. 3. Among extracted four modes, the first two lower modes are similar to

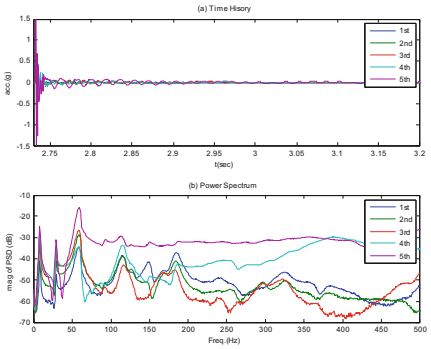

Fig. 2. Measured time histories and power spectral densities.

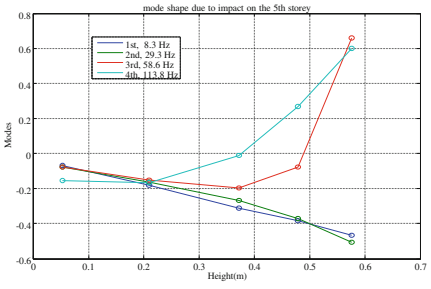

Fig. 3. Extracted modes

the first modes of typical continuum cantilever beam. And the other two modes are similar to the second modes of the typical shear building models.

3 Modelling

The two major difficulties in modelling lie in the contact surfaces between two layered stones. Firstly, the asperity in the friction surface are very irregular and unpredictable. This can be resolved by introducing a simple horizontal spring. Secondly, each rigid block has large contacting surface area. This fact implies that the horizontal deflection of upper stone is affected by the rotation of lower blocks.

A close inspection of double mode shapes suggests that both shear modes and flexural modes are combined. The shear modes may be generated by the horizontal translation of the rigid blocks, while the flexural modes are owing to the rotation of neighbor blocks. As shown in Fig. 4, the contacting surface could be modelled by a horizontal spring and a rotational spring.

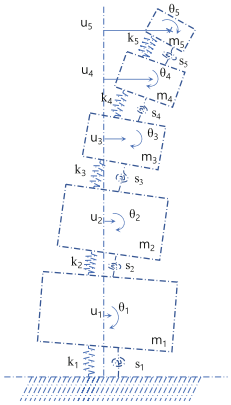

Fig. 4. Numerical model.

For the shear modes, the application of the Newton's 2nd law, $\sum \mathbf{F} = \mathbf{M}\ddot{\mathbf{u}}$, to a free body diagram of a block yields

$$\mathbf{M}\ddot{\mathbf{u}} + \mathbf{C_t}\dot{\mathbf{u}} + \mathbf{K}\mathbf{u} = \mathbf{f} \tag{1}$$

where $\mathbf{u} = [\,u_1 \quad u_2 \quad u_3\ u_4 \quad u_5\,]^T$ denotes the horizontal translation of gravity center of blocks. The vector $\mathbf{f}$ denotes a forcing vector in the horizontal direction, while matrices, $\mathbf{M}, \mathbf{C}_t, \mathbf{K}$ denote mass, damping and stiffness matrix, respectively.

For the rotational modes, the application of the Newton's 2nd law, $\sum \mathbf{M} = \mathbf{I_G}\ddot{\boldsymbol{\theta}}$, to a free body diagram of a block yields

$$\mathbf{I_G}\ddot{\boldsymbol{\theta}} + C_\mathbf{r}\dot{\theta} + \mathbf{S}\theta = \mathbf{p} \tag{2}$$

where $\boldsymbol{\theta} = [\,\theta_1 \quad \theta_2 \quad \theta_3\ \theta_4 \quad \theta_5\,]^T$ denotes the rotational degree of gravity center of blocks. The vector $\mathbf{p}$ denotes a forcing vector in the rotational direction, while matrices, $\mathbf{I_G}$, $\mathbf{C_r}$, $\mathbf{S}$ denote mass moment of inertia, rotational damping and rotational stiffness matrix, respectively.

It can be shown that total translation output, $\mathbf{y}$, of gravity center of blocks is

$$\mathbf{y} = \mathbf{u} + \mathbf{H}\theta \tag{3}$$

where the matrix $\mathbf{H}$ denotes the contribution of rotation of lower blocks on the horizontal translation of upper blocks.

4 System Identification

For the measured four modes of the stone pagoda mock-up system, the sensitivity-based System Identification(SI) algorithm [8] has been applied. Here, the mass matrix and the mass moment of inertia matrix are supposed to be known.

The only independent system variables that are supposed to be identified are five horizontal spring constants and five rotational stiffness. Then, the identification variable vector can be defined as

$$\mathbf{x} = [k_1 \;\; k_2 \;\; k_3 \;\; k_4 \;\; k_5 \;\; s_1 \;\; s_2 \;\; s_3 \;\; s_4 \;\; s_5]^T \tag{4}$$

Then the ith natural frequencies β_i can be described by a function of the identification variable vector in Eq. (4). Next, the application of variation theory results in the following sensitivity equation.

$$\mathbf{z} = \mathbf{G}\alpha \tag{5}$$

where the 4×1 vector $\mathbf{z}$ is the variation of the natural frequency denoted by

$$\mathbf{z} = \left[\frac{\delta\beta_1}{\beta_1} \quad \cdots \quad \frac{\delta\beta_N}{\beta_N} \right]^T \tag{6}$$

The 10×1 vector $\boldsymbol{\alpha}$ is denotes the fractional change in the identification variables denoted by

$$\boldsymbol{\alpha} = \left[\frac{dk_1}{k_1} \quad \cdots \quad \frac{\delta s_5}{s_5} \right]^T \tag{7}$$

The 4×10 vector $\mathbf{G}$ is denotes sensitivity matrix denoted by

$$\mathbf{G} = \begin{bmatrix} \frac{\partial\beta_1}{\partial k_1}\frac{k_1}{\beta_1} & \cdots & \frac{\partial\beta_1}{\partial s_5}\frac{s_5}{\beta_1} \\ \vdots & \ddots & \vdots \\ \frac{\partial\beta_4}{\partial k_1}\frac{k_1}{\beta_4} & \cdots & \frac{\partial\beta_4}{\partial s_5}\frac{s_5}{\beta_4} \end{bmatrix} \tag{8}$$

The unknowns in Eq. (4) can readily be identified by solving the overdetermined sensitivity equations by applying the iterative solution procedure.

5 Simulation

Using a set of the identified stiffness constants, the numerical simulation has been conducted to obtain time responses shown in Fig. 5. Here, the Rayleigh damping matrices are assumed for damping ratio of 5% for all modes. The identified modes are compared in Table 1.

The numerical simulation has been conducted in linear state space. The system matrices are defined as follows.

$$\dot{\mathbf{v}} = \mathbf{A}\mathbf{v} + \mathbf{B}\mathbf{q} \tag{9}$$

$$\mathbf{y} = \mathbf{C}\mathbf{v} + \mathbf{D}\mathbf{q} \tag{10}$$

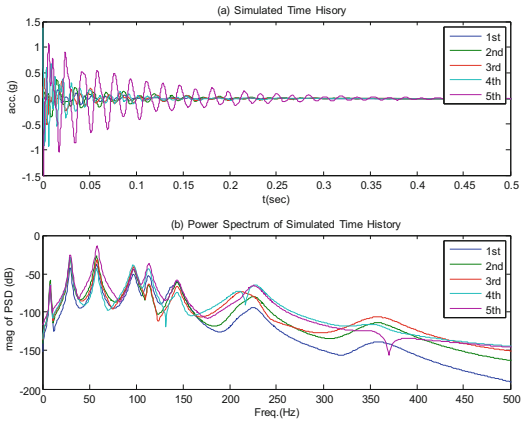

Fig. 5. Simulated time responses and power spectral densities.

Table 1. Comparison of frequencies

Mode no.	Measured freq. (Hz)	Simulated freq. (Hz)
1	8.3008	8.9061
2	29.2969	29.3447
3	58.5938	58.0608
4	113.7695	122.0082

where, $\mathbf{v} = [\mathbf{u} \quad \boldsymbol{\theta}]^T$, and $\mathbf{q} = [\mathbf{f} \quad \mathbf{p}]^T$,

$$\mathbf{A} = \begin{bmatrix} \mathbf{O} & \mathbf{I} & \mathbf{O} & \mathbf{O} \\ -\mathbf{M}^{-1}\mathbf{K} & -\mathbf{M}^{-1}\mathbf{C_t} & \mathbf{O} & \mathbf{O} \\ \mathbf{O} & \mathbf{O} & \mathbf{O} & \mathbf{I} \\ \mathbf{O} & \mathbf{O} & -\mathbf{I_G}^{-1}\mathbf{S} & -\mathbf{I_G}^{-1}\mathbf{C_r} \end{bmatrix}, \tag{11}$$

$$\mathbf{B} = \begin{bmatrix} \mathbf{O} & \mathbf{O} \\ \mathbf{M}^{-1} & \mathbf{O} \\ \mathbf{O} & \mathbf{O} \\ \mathbf{O} & \mathbf{I_G}^{-1} \end{bmatrix}, \tag{12}$$

$$\mathbf{C} = \begin{bmatrix} -\mathbf{M}^{-1}\mathbf{K} & -\mathbf{M}^{-1}\mathbf{C_t} & -\mathbf{H}\mathbf{I_G}^{-1}\mathbf{S} & -\mathbf{H}\mathbf{I_G}^{-1}\mathbf{C_r} \end{bmatrix}, \tag{13}$$

$$\mathbf{D} = \begin{bmatrix} \mathbf{M}^{-1} & \mathbf{H}\mathbf{I_G}^{-1} \end{bmatrix} \tag{14}$$

The simulated spectrum in 5(b) could be compared with the measured spectrum in Fig. 2b. A good agreement is observed in the lower four modes, while there exists a little discrepancy in higher modes.

6 Conclusions

It is experimentally observed that the stacked rigid stone blocks have dual modes. The proposed simple numerical model with translation and rotational springs provides a way to explain the peculiar double mode mechanism of the layered stone pagoda system.

There is still room for improvement of the proposed simple numerical model. More delicate numerical model with the less parameters and higher accuracy is expected in near future.

Acknowledgments. This research was supported by Basic Science Research Program through the National Research Foundation of Korea (NRF) funded by the Ministry of Education (NRF-2015R1D1A1A01059055).

References

1. Kim, J.K., Ryu, H.: Seismic test of a full-scale model of a five-story stone pagoda. Earthq. Eng. Struct. Dyn. **32**, 731–750 (2003)
2. Lee, S., Park, H., Kim, H., Kim, S., Lee, S.: Change of dynamic characteristics of stone masonry structures according to number of layers of granite brick. J. Archit. Inst. Korea **17**(6), 3–10 (2001). (In Korean)
3. El-Raheb, M.: Dynamics of a gravity stonewall. Int. J. Solids Struct. **47**(9), 1196–1208 (2010)
4. Spanos, P.D., Roussis, P.C., Politis, N.P.A.: Dynamic analysis of stacked rigid blocks. Soil Dyn. Earthq. Eng. **21**, 559–578 (2001)
5. Kounadis, A.N.: On the rocking-sliding instability of rigid blocks under ground excitation: some new findings. Soil Dyn. Earthq. Eng. **75**, 246–258 (2015)
6. Kim, B.H., Moon, D.J., Lee, D.H.: Extracting modal parameters of a layered stone pagoda using TDD technique. J. Earthq. Eng. Soc. Korea **19**(3), 103–108 (2015)
7. Kim, B.H., Park, T., Stubbs, N.: A New method to extract modal parameters using output-only responses. J. Sound Vib. **282**, 215–230 (2005)
8. Stubbs, N.: A general theory of non-destructive damage detection in structures. In: Proceedings of the Second International Symposium on Structural Control, pp. 694–713. University of Waterloo, Ontario, Canada, Martinus Nijhoff Publishers, Dordrecht, Netherlands (1985)

Identification of Symmetrical Structures with Fabrication and Damage Induced Asymmetry

Abhineet Gupta[1(✉)], Wei Zhao[2], Chris Regan[1], Peter Seiler[1], and Rakesh K. Kapania[2]

[1] Department of Aerospace Engineering and Mechanics, University of Minnesota, Minneapolis, MN, USA
guptal65@umn.edu
[2] Kevin T. Crofton Department of Aerospace and Ocean Engineering, Virginia Polytechnic Institute and State University, Blacksburg, VA, USA

Abstract. Experimental vibration testing is a common technique employed to identify modal frequencies, mode shapes, and at times, modal damping. The identified data can then be used for updating the structural dynamic models, e.g. those obtained by using approaches like the finite element method. It can also be used to identify any damage in the structure. For many symmetric structures like buildings, large shells such as cooling towers, bridges, and aircraft, conventional flexible modes are often separated into symmetric and anti-symmetric modes. This leads to significant reduction in computing both the natural modes and frequencies, and the resulting dynamic responses. However, in practice, during fabrication and manufacturing of these structures, or due to damage during their operation, it is often observed that the structure can develop significant asymmetry. As a result, for real structures, the often assumed separation into symmetric and antisymmetric modes no longer holds. The modes start to possess both symmetric and antisymmetric components in the same mode, which then poses a significant challenge for both modal identification and FEM modeling. Furthermore, it can significantly change the dynamic response of structures. This paper describes the process of ground vibration test, modal identification and FEM modeling for an asymmetrical aircraft. Details of the best practices for incorporating the asymmetry during the model updating process is discussed and the results of the GVT and FEM updating procedure for the aircraft are described. The FEM update procedure successfully identifies the source of the asymmetry. The suitability of the FEM update procedure for characterizing the source of asymmetry is discussed.

Keywords: Ground vibration test · Modal analysis · FEM updating · FEM modeling · Damage-induced asymmetry · Fabrication-induced asymmetry

1 Introduction

In order to reduce the weight and increase the fuel efficiency, many modern aircraft are utilizing flexible, light weight material for aircraft construction. But, as the flexibility of the airframe increases, the interaction between the structural dynamics, aerodynamics and control system also increases. The effects of this increased interaction, also known

© Springer International Publishing AG 2018
J.P. Conte et al. (eds.), *Experimental Vibration Analysis for Civil Structures*,
Lecture Notes in Civil Engineering 5, https://doi.org/10.1007/978-3-319-67443-8_60

as aero-servo-elastic phenomena, can cause a degradation in handling qualities and in extreme cases, can result in catastrophic failure of the aircraft due to flutter [1, 2]. Therefore, advanced aero-servo-elastic control system are required to control such aircraft and suppress these aero-servo-elastic instabilities [1, 3–6]. In order to design and test these control system, low order mathematical models are required. These simple models can be obtained either by model reduction of complex fluid/structure models [3, 7], or using a flight dynamics approach [8, 9]. In either case, a suitable structural dynamics model of the aircraft is required. A common methodology employed to model the structural dynamics of a flexible aircraft is to develop a finite element method (FEM) based model.

To ensure that the FEM model represents the actual structural dynamics of the aircraft, the FEM model is validated and updated against experimental data [10–13]. Ground Vibration Tests (GVT) can be conducted to obtain such experimental data. Several considerations go into designing a suitable GVT [12, 14]. The obtained data can be processed to obtain modal vibration data like mode shapes and modal frequencies [14]. The modal data can then be used to update the finite element model of the aircraft [13, 15].

For a symmetric structures including symmetric aircraft, bridges and circular disks, the vibration modes can be categorized into symmetric and anti-symmetric modes. This separation of the modes can result in significant reduction in computational cost for obtaining the natural modes, frequencies and the resulting dynamic responses of the structure. But, for real structures, this symmetry might not hold for various reasons. Small deviations in the manufacturing process might cause an asymmetry in the structure. Damage to the structure, either due to normal operation or due to an unintentional cause, might also result in loss of symmetry in the structure. Due to this loss in symmetry, the modes can no longer be classified into symmetric and anti-symmetric modes [16, 17]. As the structure becomes more asymmetric, the modes change from being perfectly symmetrical or anti-symmetrical to symmetric or anti-symmetric dominated. In case of circular disks, it has been observed that as the asymmetry increases, some of the modes split into two separate modes [18–20].

Several methods have been implemented to detect, locate and estimate the source of the asymmetry. These methods include using modal frequencies [21–23], mode shapes [16, 17, 23, 24], and the frequency response functions [25, 26] for detecting, locating as well as estimating the severity of the asymmetry. Finite element model updating [27] and changes in the flexibility matrix [28] have also been used for the same purpose.

This paper describes the process of conducting GVT, FEM modeling and FEM updating of an asymmetrical aircraft. The process is used for identifying and quantifying the fabrication induced asymmetry in the aircraft. The details of the aircraft, including the dimensions and mass properties are presented in the next section. The following section contains the details of the experiment conducted on the aircraft. The result of the static tests conducted to obtain equivalent stiffness properties of the wings are described. The setup and procedure of the GVT and the identified modal frequencies and mode shapes are also described. The next section gives an overview of the FEM modeling and updating procedure and results are presented. Finally conclusions are drawn about the effectiveness of the FEM updating procedure in identifying and isolating the fabrication induced asymmetry in the aircraft.

2 Aircraft Details

Performance Adaptive Aero-elastic Wing (PAAW) program is a research project whose objective is to tackle the challenges associated with flying a flexible aircraft [29]. Moreover, it also aims to develop an aircraft that continuously optimizes its shape according to the current flight conditions and aircraft configuration. Possible applications of this concept could be to maximize lift for takeoff, minimize fuel consumption in cruise, or maximize lift and drag for landing. As part of this research, the Uninhabited Aerial Vehicle (UAV) laboratories at University of Minnesota has built several aircraft and wing-sets to act as a testbed for the research conducted as part of the program [30].

This paper focuses on the latest aircraft of the mAEWing1 series of aircraft developed as part of the PAAW project. This aircraft configuration is named as 'Geri + Wingset4' to distinguish it from the other aircraft in the mAEWing1 series. The aircraft dimensions are shown in Fig. 1. The mass properties of the aircraft are shown in Table 1.

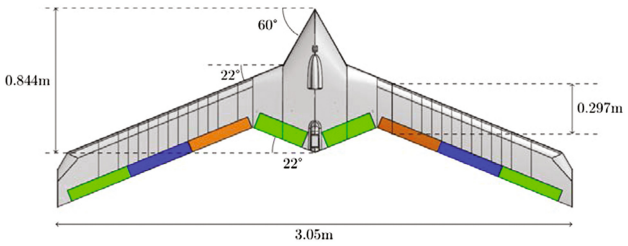

Fig. 1. Aircraft dimensions

Table 1. Mass properties of the aircraft

Mass (kg)	CG position (m from nose)	Roll inertia (I_{xx}) (kg-m^2)	Pitch inertia (I_{yy}) (kg-m^2)	Yaw inertia (I_{zz}) (kg-m^2)
6.24	0.60	2.74	0.46	3.17

The wings are designed such that a single spar, spanning the entire length of the wing, is the main load carrying structure in a wing. A foam and composite-based aerodynamic shell is fabricated over the spars to a suitable aerodynamic shape to the wings. The foam shell also provides some structural integrity to the wings [30].

3 Experiments Conducted

3.1 Static Tests

Static tests are conducted on the both the left and right spars and the wings to find the equivalent beam stiffness properties. This data is used in the first step of the FEM updating procedure. The results of the test are given below in Table 2.

Table 2. Equivalent stiffness properties of the spars and wings

Structure	EI (N-m^2)	GJ (N-m^2)
Left spar	119.30	96.08
Right spar	119.47	86.18
Left wing	359.29	299.34
Right wing	304.76	261.90

3.2 Dynamics Tests: GVT

In order to obtain the experimental data to be used for modeling the structural dynamics of the aircraft, Ground Vibration Test (GVT) are conducted. The raw data obtained from the GVT is used to identify the mode shapes and the modal frequency of the aircraft. The identified modal data is later used to synthesize a finite element method based structural model of the aircraft. The general procedure of the GVT are described here. Further details about the GVT conducted on mAEWing1 series of aircraft, including the details of the hardware used and the post-processing algorithm for identification of modal data can be found in [14]. A detailed discussion of the general considerations that go into designing a suitable vibration experiment are described in [12, 14].

3.3 GVT Setup and Procedure

The setup for the ground vibration test is shown in Fig. 2. The aircraft is suspended from a wooden frame which provides a rigid support for the test setup. The aircraft is suspended using a flexible spring which is attached to the center of gravity (CG) of the aircraft as shown in the left part of Fig. 2. This allows the aircraft to remain approximately horizontal throughout the test. The spring is chosen to be of sufficiently high flexibility (k = 130 N/m) so that the aircraft experiences free-free vibration condition. As the mass of the aircraft is 6.24 kg, the natural frequency of the mass/spring oscillation is 0.72 Hz. This is well below the expected fundamental vibration frequency

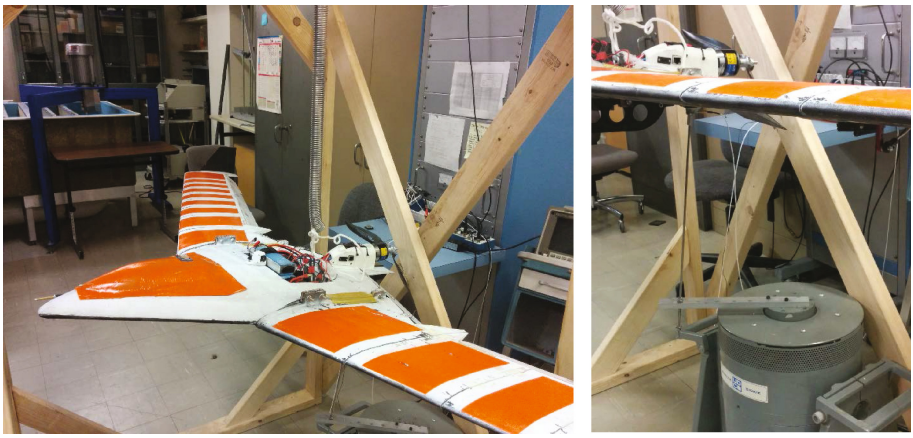

Fig. 2. GVT setup

of the aircraft which is around 8 Hz. Thus, the mass/spring oscillation is well separated from the flexible modes and should not interfere with the identification of the flexible modes.

The excitation is provided using an Unholz-Dickie, model 20 electro-dynamic shaker in the form of a continuous chirp input. The shaker transmits the force to the aircraft using a stinger mechanism as shown in the right part of Fig. 2. A stinger is attached to the shaker. A force transducer is attached to the other end of the stinger. The force transducer is then attached to the aircraft using hot glue. The hot glue is chosen so that the surface of the aircraft does not get damaged while conducting the test. The force transducer measures the exact force being transmitted from the shaker to the aircraft via the stinger. This force measurement acts as an input for the dynamic test (GVT). The stinger is used as a transmission mechanism as it permits the transmission of only the perpendicular component of the force and eliminates the transmission of any transverse force. This is important for a complex structure like aircraft because transverse forces might interfere with the excitation of a particular mode of interest. Using a stinger also ensures the force is only applied in the single axis measurable by the uniaxial force transducer.

The excitations are provided at both a symmetric excitation point on the longitudinal axis and to an asymmetric point off this axis one at a time in a series of tests. The excitation points are chosen carefully so that both bending and torsion modes are excited. As the aircraft is vibrated using the shaker, the accelerations at various points on the aircraft are measured using accelerometers. The accelerations are measured at 28 locations across the aircraft for both the symmetric and asymmetric excitations. The symmetric and asymmetric excitation locations as well as the locations of the 28 output points are shown in Fig. 3. The input force and the output accelerations are measured for each pair of input & output in a series of tests. Thus, total 48 data sets are obtained containing time series information of the input force and output acceleration. This data is processed to obtain the modal frequencies and mode shapes using two different methods described below.

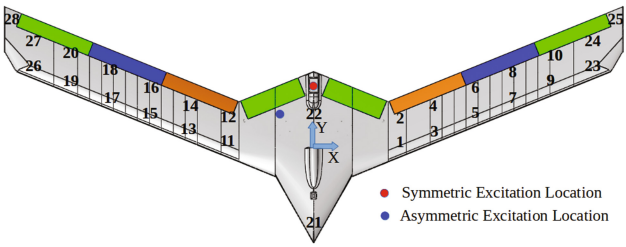

Fig. 3. Force excitation input and acceleration output location

3.4 Post-processing of Experimental Data

The data obtained from the experiment is in the form of 48 data sets containing time series information of the input force, measured by the force transducer and the output acceleration, measured by the accelerometers. Two different methods are employed to

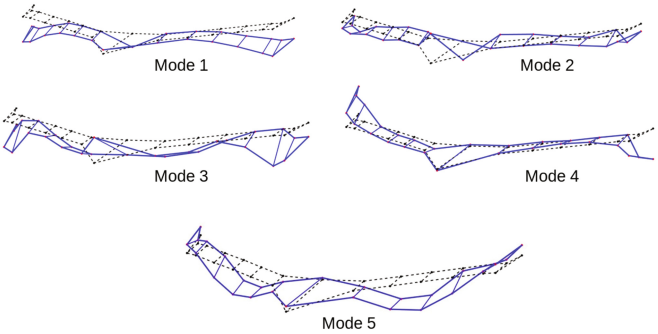

Fig. 4. Mode shapes identified by GVT

Table 3. Properties of the buildings.

Mode #	Frequencies (Hz)	Dominant modes
1	7.94	1st symmetric bending
2	9.20	-
3	16.10	1st symmetric torsion
4	18.54	1st anti-symmetric bending
5	31.22	2nd symmetric bending

obtain the modal data from the time domain data: Quadrature response method and Curve-fitting Frequency Domain Decomposition method. The details of these two method can be found in [14]. Both modal frequencies and mode shapes are identified using both the methods. The identified mode shapes are shown in Fig. 4 and the identified modal frequencies are shown in Table 3.

It should be noted that the identified modes are not perfectly symmetric or anti-symmetric but were dominated by symmetric or anti-symmetric modes. The 2nd mode at 9.20 Hz could not be categorized. The fact that the modes do not exhibit symmetric and anti-symmetric behavior implies that the aircraft is not a symmetric structure. The results of the static tests in Table 2 also suggest an asymmetry. As the two wings have similar mass distribution and both spars have exhibit similar elastic properties, the static test suggests that the cause of the asymmetry is the foam and composite shell. But the location and the extent of this asymmetry cannot be inferred from the test data alone.

4 Finite Element Model Updating

The finite element model for the aircraft is developed in NASTRAN [13]. A few different approaches are used to determine the cross section stiffness and mass properties of the structure. One approach is to use the equivalent stiffness and mass properties of the beam obtained from the static tests to create the finite element model. Another approach uses the cross-sectional analysis for an accurate span-wise stiffness and mass distribution for the

wing. A three-step subcomponent-based optimization approach is employed to update the mass and stiffness distributions for use in the finite element model. Steps I and II update the mass distribution for the center-body and the individual wing of the aircraft, respectively, to match the test article's mass properties. The updated finite element models for the center-body and the wing are then assembled as the initial finite element model for the full aircraft model, in Step III. This initial finite element model is updated to match both the test article's mass properties and the GVT modal results for the full model. The mass properties for both the individual wing and the center-body obtained from the full aircraft finite element model updating in Step III are then compared against the test data. Once the difference between the mass properties for the updated finite element models and the available test data is less than a given allowance criterion, the program is terminated and a near best finite element model is output. The process of the FEM update is described in Fig. 5 below. The details of this approach, including the details of the cross sectional analysis and the cost function for optimization can be found in [13].

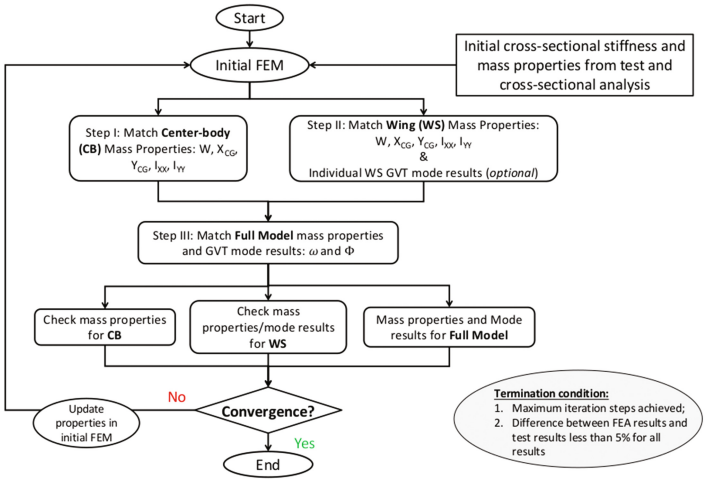

Fig. 5. Work flow of FEM update

A total of 39 design variables are chosen for the full aircraft model updating. Table 4 lists these design variables along with their final value identified by the optimization. It can be seen that the final identified values for stiffness properties of the wing foam and composite cover show significant difference between left and right wing. Thus, the FEM update procedure is able to identify and quantify the source of the asymmetry in the aircraft.

The updated FEM model has modal frequencies and mode shapes quite close to those derived by the GVT as shown in Table 5. Here, the modal assurance criteria (MAC) is a metric used to compare mode shapes. An MAC value of 1 indicates perfect matching. The iteration history of the optimization for the weights of different components and the modal frequencies of a few modes are shown in Fig. 6. It can be clearly seen that the optimization is converged.

Table 4. Design variables for FEM update

DV #	Property	Unit	Initial value	Lower bound	Upper bound	Identified value
1	Flight computer, weight	lb	1.000	0.500	2.000	0.986
2	Flight computer, CG	in	9.06	4.06	14.06	8.88
3	Propulsion battery, weight	lb	1.205	1.000	3.000	2.197
4	Propulsion battery CG	in	19.28	14.28	24.28	18.96
5	Propulsion battery, Moment of inertia, I_{xx}	lb-in^2	1.00	0.00	5.00	0.00
6	Propulsion battery, Moment of inertia, I_{yy}	lb-in^2	1.00	0.00	5.00	3.32
7	Engine motor, weight	lb	1.000	0.500	2.000	1.109
8	Engine motor, CG	in	32.32	27.32	37.32	32.33
9	Foam + cover, distributed weight	lb/in	0.036	0.010	0.100	0.0810
10	Foam + cover, X_{CG} offset	in	0.000	−2.000	2.000	−0.105
11	Foam + cover, Y_{CG} offset	in	0.000	−2.000	2.000	0.075
12	Foam + cover, mass moment of inertia, I_{xx}	lb-in^2	0.50	0.00	5.00	0.00
13	Foam + cover, mass moment of inertia, I_{yy}	lb-in^2	5.00	0.00	10.00	9.99
14	Outer wing cross-sectional area	in^2	10.27	0.00	15.00	3.88
15	Inner wing cross-sectional area	in^2	4.96	4.00	15.0	11.60
16	Material density	lb/in^2	6.23E−3	4.00E−3	1.00E−2	6.14E−3
17	Inner wing, X_{CG} offset	in	−0.050	−1.350	1.350	0.441
18	Inner wing, Y_{CG} offset	in	−0.024	−1.350	1.350	−0.031
19	Outer wing, X_{CG} offset	in	−0.269	−1.350	1.350	−0.093
20	Outer wing, Y_{CG} offset	in	−1.105	−1.350	1.350	−0.274
21	Outer wing, X_{CG} offset*	in	−0.200	−1.350	1.350	−0.635
22	Outer wing, Y_{CG} offset*	in	0.419	−1.350	1.350	0.129
23	Nodal mass moment of inertia, I_{xx}	lb-in^2	32.23	0.00	50.00	30.10
24	Nodal mass moment of inertia, I_{yy}	lb-in^2	15.33	0.00	20.00	12.70
25	Left Outer foam + cover, Young's modulus	psi	1.153E+6	1.00E+4	1.00E+7	**1.701E+6**
26	Left Inner foam + cover, Young's modulus	psi	1.497E+6	1.00E+4	1.00E+7	**9.098E+4**
27	Left Outer foam + cover, Shear modulus	psi	1.153E+5	1.00E+4	1.00E+7	**2.821E+5**
28	Left Inner foam + cover, Shear modulus	psi	1.497E+5	1.00E+4	1.00E+7	**8.482E+4**
29	Right Outer foam + cover, Young's modulus	psi	1.153E+6	1.00E+4	1.00E+7	**2.222E+6**
30	Right Inner foam + cover, Young's modulus	psi	1.497E+6	1.00E+4	1.00E+7	**2.065E+5**
31	Right Outer foam + cover, Shear modulus	psi	1.153E+5	1.00E+4	1.00E+7	**1.141E+6**
32	Right Inner foam + cover, Shear modulus	psi	1.497E+5	1.00E+4	1.00E+7	**1.460E+5**

(*continued*)

Table 4. (*continued*)

DV #	Property	Unit	Initial value	Lower bound	Upper bound	Identified value
33	Outer foam + cover, Torsional constant	in^4	3.018E−3	1.000E−5	1.000	1.065E−1
34	Inner foam + cover, Torsional constant	in^4	3.066E−3	1.000E−5	1.000	2.400E−2
35	Outer foam + cover, Area Inertia	in^4	1.026E−3	1.000E−5	1.000	1.770E−1
36	Inner foam + cover, Area Inertia	in^4	8.251E−3	1.000E−5	1.000	4.894E−1
37	Solid spar material, Young's modulus	psi	3.254E+5	2.929E+5	3.579E+5	2.929E+5
38	Solid spar material, Shear modulus	psi	8.025e+4	7.223e+4	8.828e+4	7.223E+4

Table 5. Comparison of GVT and FEM results.

Mode #	GVT frequencies (Hz)	FEM frequencies (Hz)	% Diff in frequencies
1	7.94	7.81	−1.64%
2	9.20	10.0	8.70%
3	16.10	14.73	−8.51%
4	18.54	19.72	6.36%
5	31.22	32.44	3.91%

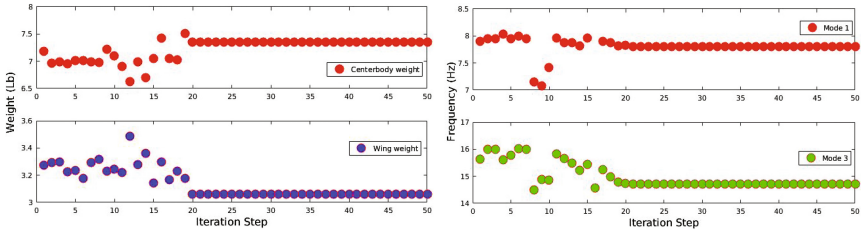

Fig. 6. Iteration history of optimization

5 Conclusions

Static and dynamic tests are conducted on a flexible aircraft. The mode shapes obtained from the dynamics test show that the modes cannot be categorized into symmetric and anti-symmetric modes indicating the presence of an asymmetry. The static test results suggest that the most likely candidate of the asymmetry is the foam and composite shell of the wings. But the degree of the asymmetry cannot be ascertained by the test results alone. An FEM model is obtained by applying the FEM update procedure. The optimized design variables, which include the stiffness properties of the foam and the composite shell, confirm that the cause of the asymmetry is the difference in the elastic properties of the foam and the composite shell.

Acknowledgments. The authors acknowledge the NASA NRA NNX14AL36A, Lightweight Adaptive Aeroelastic Wing for Enhanced Performance Across the Flight Envelope, Mr. John Bosworth (Technical Monitor) and Mr. Dan Moerder (acting Technical Monitor) for funding this research. The authors also acknowledge the PAAW research group for their continued support and suggestions which were critical in the success of the research.

References

1. Beranek, J., Nicolai, L., Buonanno, M., Burnett, E., Atkinson, C., Holm-Hansen, B., Flick, P.: Conceptual design of a multi-utility aeroelastic demonstrator. In: 13th AIAA/ISSMO Multidisciplinary Analysis Optimization Conference, vol. 3, pp. 2194–2208 (2010)
2. Lind, R., Brenner, M.: Robust Aeroservoelastic Stability Analysis: Flight Test Applications. Springer Science & Business Media, London (2012)
3. Danowsky, B.P., Thompson, P.M., Farhat, C., Lieu, T., Harris, C., Lechniak, J.: Incorporation of feedback control into a high-fidelity aeroservoelastic fighter aircraft model. J. Aircr. **47**(4), 1274–1282 (2010)
4. Burnett, E., Atkinson, C., Beranek, J., Sibbitt, B., Holm-Hansen, B., Nicolai, L.: Ndof simulation model for flight control development with flight test correlation. In: AIAA Modeling and Simulation Technologies Conference, vol. 3, pp. 7780–7794, August 2010
5. Patil, M.J., Hodges, D.H.: Flight dynamics of highly flexible flying wings. J. Aircr. **43**(6), 1790–1799 (2006)
6. Theis, J., Pfifer, H., Seiler, P.: Robust control design for active flutter suppression. In: AIAA Atmospheric Flight Mechanics Conference, p. 1751 (2016)
7. Nguyen, N., Tuzcu, I.: Flight dynamics of flexible aircraft with aeroelastic and inertial force interactions. In: AIAA Atmospheric Flight Mechanics Conference, vol. 6045, August 2009
8. Schmidt, D.: Modern Flight Dynamics. McGraw-Hill Higher Education, New York (2012)
9. Waszak, M.R., Schmidt, D.K.: Flight dynamics of aeroelastic vehicles. J. Aircr. **25**(6), 563–571 (1988)
10. Mottershead, J.E., Friswell, M.I.: Model updating in structural dynamics: a survey. J. Sound Vib. **167**(2), 347–375 (1993)
11. Zárate, B.A., Caicedo, J.M.: Finite element model updating: multiple alternatives. Eng. Struct. **30**(12), 3724–3730 (2008)
12. Ewins, D.J.: Modal Testing: Theory and Practice, vol. 15. Research Studies Press, Letchworth (1984)
13. Zhao, W., Muthirevula, M., Kapania, R.K., Gupta, A., Regan, C., Seiler, P.: A subcomponent-based finite element model updating for a composite flying wing aircraft. In: Proceedings of the AIAA SciTech Conference, Grapevine, TX (2017)
14. Gupta, A., Seiler, P., Danowsky, B.: Ground vibration tests on a flexible flying wing aircraft. In: Proceedings of the AIAA SciTech Conference, San Diego, CA (2016)
15. Gupta, A., Moreno, C., Pfifer, H., Taylor, B., Balas, G.: Updating a finite element based structural model of a small flexible aircraft. In: Proceedings of the AIAA Science and Technology Forum, Kissimmee, Fl (2015)
16. Dilena, M., Morassi, A.: Dynamic testing of a damaged bridge. Mech. Syst. Signal Process. **25**(5), 1485–1507 (2011)
17. Wahab, M.A., De Roeck, G.: Damage detection in bridges using modal curvatures: application to a real damage scenario. J. Sound Vib. **226**(2), 217–235 (1999)
18. Yu, R.C., Mote, C.D.: Vibration and parametric excitation in asymmetric circular plates under moving loads. J. Sound Vib. **119**(3), 409–427 (1987)

19. Stange, W.A., MacBain, J.C.: An investigation of dual mode phenomena in a mistuned bladed disk. J. Vib. Acoust. Stress Reliab. Des. **105**(3), 402–407 (1983)
20. Honda, Y., Matsuhisa, H., Sato, S.: Modal response of a disk to a moving concentrated harmonic force. J. Sound Vib. **102**(4), 457–472 (1985)
21. Salawu, O.S.: Detection of structural damage through changes in frequency: a review. Eng. Struct. **19**(9), 718–723 (1997)
22. Hearn, G., Testa, R.B.: Modal analysis for damage detection in structures. J. Struct. Eng. **117** (10), 3042–3063 (1991)
23. Kim, J.T., Ryu, Y.S., Cho, H.M., Stubbs, N.: Damage identification in beam-type structures: frequency-based method vs mode-shape-based method. Eng. Struct. **25**(1), 57–67 (2003)
24. Pandey, A.K., Biswas, M., Samman, M.M.: Damage detection from changes in curvature mode shapes. J. Sound Vib. **145**(2), 321–332 (1991)
25. Hwang, H.Y., Kim, C.: Damage detection in structures using a few frequency response measurements. J. Sound Vib. **270**(1), 1–14 (2004)
26. Sampaio, R.P.C., Maia, N.M.M., Silva, J.M.M.: Damage detection using the frequency-response-function curvature method. J. Sound Vib. **226**(5), 1029–1042 (1999)
27. Jaishi, B., Ren, W.X.: Damage detection by finite element model updating using modal flexibility residual. J. Sound Vib. **290**(1), 369–387 (2006)
28. Pandey, A.K., Biswas, M.: Damage detection in structures using changes in flexibility. J. Sound Vib. **169**(1), 3–17 (1994)
29. Performance adaptive aeroelastic wing. https://www.paaw.net
30. Regan, C., Taylor, B.: mAEWing1: design, build, test. In: Proceedings of the AIAA SciTech Conference, San Diego, CA (2016)

Experimental Incremental System Identification Method Using Separate Time Windows on Basis of Ambient Signals

Simon Schleiter(✉), Okyay Altay, and Sven Klinkel

Chair of Structural Analysis and Dynamics,
RWTH Aachen University, Aachen, Germany
schleiter@lbb.rwth-aachen.de

Abstract. Experimental system identification methods, such as Frequency Domain Decomposition (FDD), Autoregressive Moving Average Model (ARMA), Autoregressive Models with eXogenous input (ARX), Kalman Filter and Stochastic Subspace Identification (SSI), are commonly used in civil engineering to determine dynamic parameters of existing structures. Basis for these methods are in-situ measurements, which can be very time-consuming and cost-intensive depending on the complexity of the structure. This paper investigates the possibility to reduce the in-situ measurement effort by introducing a new method, which bases on incremental measurements by using only a single sensor in separate time windows. The proposed incremental identification method (IIM) requires stationary ergodic response signals of the structure induced by ambient vibrations with white noise density. Therefore, after each incremental measurement a quality-check of the response signal should be conducted to verify the applicability of the theory. This approach ensures the comparability of the input signals with each other and thus the reproducibility of the identified dynamic behavior. For this purpose, a signal evaluation criterion is defined. For low-quality data, which cannot satisfy this criterion, special signal processing methods have to be applied. With the signals, which already accomplish the evaluation criterion, the identification of the system parameter can then be carried out by using one of the above mentioned system identification methods, such as FDD. The IIM is applied so far both on numerical and experimental examples. In this paper the validation of the IIM is reached by identifying the parameters of the IASC-ASCE Structural Health Monitoring Benchmark Problem for different ambient simulated input signals.

Keywords: System identification · Ambient signal · In-situ measurement · Incremental identification method · Operational modal analysis

1 Introduction

The determination of the parameters of structures by Operational Modal Analysis (OMA) has become one of the emerging technologies of civil engineering. For the corresponding system identification methods, such as FDD, ARMA, ARX, Kalman Filter and SSI, the measurement of the output-only data is generally sufficient.

© Springer International Publishing AG 2018
J.P. Conte et al. (eds.), *Experimental Vibration Analysis for Civil Structures*,
Lecture Notes in Civil Engineering 5, https://doi.org/10.1007/978-3-319-67443-8_61

Thus OMA obviously reduces the temporal as well as the cost effort for the measurement in comparison to the experimental modal analysis (EMA). For the EMA it is necessary to excite the structures using auxiliary exciters or others. Thus the measuring effort for civil engineering structures, such as buildings and bridges, is huge in comparison to OMA. But even OMA requires a lot of logistics, equipment and certainly time due to the reason that so far the output data has to be measured simultaneously by multiple sensors for a precise identification of the system parameter. Since the data is assumed time dependent it is a necessary fact to use multiple sensors.

The FDD is a common method used for OMA to identify natural frequencies and modal shapes by only using input-signals with constant frequency content. With this assumption for input-signals a calculation of modal parameters using the power spectral density (PSD) is possible without exciting the structure. Until now the FDD applications are carried out by simultaneous signals without the analysis of the sample quality. For good conditioned samples, with a consistent frequency distribution, theoretically the identification should be also possible by using signals, which are measured incrementally in different time frames. Thus it should be possible to get results from the OMA by measuring all necessary points by only one sensor successively.

2 Incremental Identification Method

The Incremental Identification Method (IIM), which can reduce the measurement efforts of the OMA civil engineering applications for the future, focuses on the conditioning and choice of the suitable system response signals. The identification of system parameters from these signals can be conducted by common methods, such as FDD, with minor modifications in the corresponding algorithms. As a first step this paper presents a general concept for assessing the signal quality, which is necessary for the IIM. An assessment criteria based on the power spectral density function of the signals is proposed, which analyses in several frequency intervals, the sufficiency of the inherent energy. Depending on the results the required measuring time of the sample is determined. If a minimum request of energy is fulfilled, the sample can be utilized for system identification, otherwise signal conditioning methods can be applied to improve the sample quality. This sample quality analysis can be carried out online during the measurements, to determine the required sample time.

The planned process of the IIM is shown as a flowchart in Fig. 1. The measurement starts with the measurement at the first point. From this measurement the natural frequencies and damping ratios of the structure can be determined. By using the frequency response function, the input signal can be recalculated based on fundamental principles of structural dynamics. This input signal is assessed afterwards with regard to the power density. If the inherent energy is lower than a certain tolerance value η, the measurement has to be repeated or continued, till an increased measuring duration is reached. Otherwise an application of the IIM is impossible and a conventional method using simultaneous signals has to be used. If the assessment of the signal is sufficient the procedure can be applied at the next measurement point. Afterwards all signals can be evaluated together in one data set by using common identification methods, such as FDD, ARMA, SSI.

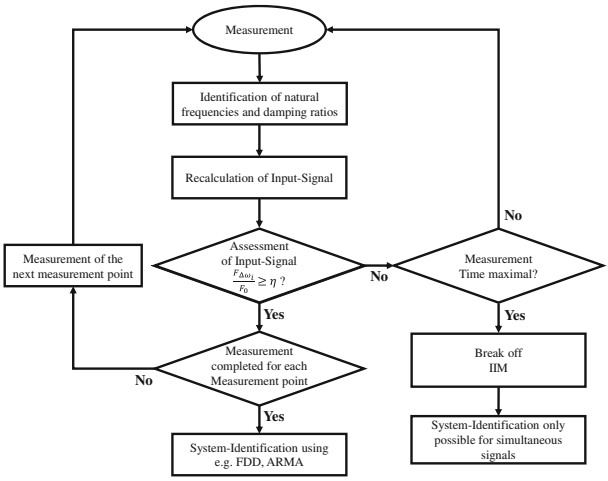

Fig. 1. Flowchart for the proposed Incremental Identification Method (IIM)

2.1 Calculation of Input-Signals for Output Only Systems

Once a measurement is done one can easily transfer the output time signal into the frequency domain and compute the power density spectrum or the frequency spectrum. Hereby also the natural frequencies and damping values can be estimated. By using these parameters the frequency response function $\mathbf{H}(\omega)$ can be calculated. In the frequency domain the general key equation between input and output signals is given as:

$$\mathbf{Y}(\omega) = \mathbf{H}(\omega) \cdot \mathbf{X}(\omega) \tag{1}$$

By transforming this formula, it is possible to recalculate the unknown input signal from the measured output signal and the frequency response function $\mathbf{H}(\omega)$ as shown below.

$$\mathbf{X}(\omega) = \mathbf{H}^{-1}(\omega) \cdot \mathbf{Y}(\omega) \tag{2}$$

For this recalculation of the input signal $\mathbf{X}(\omega)$ the frequency response function $\mathbf{H}(\omega)$ can be applied as a frequency filter, as shown in Fig. 2. The determined Frequency Response Function can be calculated in a simplified way for a SDOF, as described in He [4], where the corresponding function is given by:

$$H(\omega) = \frac{\frac{1}{m}}{\omega_0^2 - \omega^2 + 2iD\omega_0\omega} \tag{3}$$

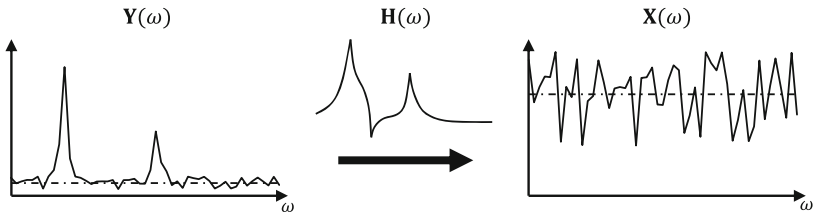

Fig. 2. Recalculation of the input-signal

2.2 Assessment of Input-Signals

For the application of the IIM the input signals have to fulfill some conditions. The assessment criteria for the IIM is defined over the power spectral density (PSD) function of the input signal. Since it has to be guaranteed, that all frequencies are excited in the same extend, it has to be proved that the signal is consisting of white noise. Thus the mean value and the standard deviation of the power spectral density can be calculated by the frequency increments $\Delta\omega_i$, the PSD illustrated by S_{xx} and the spectrum length n as follows.

$$\bar{S}_{xx} = \frac{1}{n}\sum_{i=1}^{n} S_{xx}(\Delta\omega_i) \tag{4}$$

$$\sigma(S_{xx}) = \sqrt{\frac{1}{n}\cdot\sum_{i=1}^{n}\left(S_{xx}(\Delta\omega_i) - \bar{S}_{xx}\right)^2} \tag{5}$$

If the standard deviation lays in the defined borders of the tolerance value η, the signal can be assumed to be as ambient:

$$\sigma(S_{xx}) \leq \eta \tag{6}$$

To identify dynamic responses, the corresponding frequency excitation has to be high enough for every frequency increment $\Delta\omega$. If the frequency excitation is low, the signal cannot ensure that every mode shape is inherent.

An example for the PSD assessment is to be found in Fig. 3. The frequency signal is divided in increments of size $\Delta\omega$. For the given increments the PSD is averaged. This value can be referred to the mean value and afterwards compared to a free defined minimum threshold. The assessment would be as following:

$$\frac{S_{xx}(\Delta\omega_i)}{\bar{S}_{xx}} \geq \eta \tag{7}$$

In Table 1 an example assessment corresponding to Fig. 3 is carried out for a tolerance value η of 70%, which shows that the input signal fulfills the criteria.

A change of tolerance up to 90% would lead to an insufficient signal for the second frequency range $\Delta\omega_2$ and thus for the whole signal (see Table 2). At this case there are two possibilities (corresponding to Fig. 1): Either the measurement should be repeated

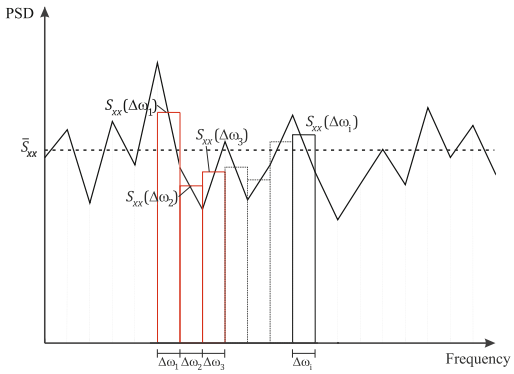

Fig. 3. Power density assessment of the input signal

Table 1. Assessment of an input signal

Frequency range	Mean value	$S_{xx}(\Delta\omega_i)$	Tolerance value	Condition fulfilled
$\Delta\omega_1$	$\bar{S}_{xx}$	$1.2 \cdot \bar{S}_{xx}$	$\eta = 0.7$	✓
$\Delta\omega_2$		$0.8 \cdot \bar{S}_{xx}$		✓
$\Delta\omega_3$		$0.9 \cdot \bar{S}_{xx}$		✓
Overall assessment				✓

Table 2. Assessment of an input signal

Frequency range	Mean value	$S_{xx}(\Delta\omega_i)$	Tolerance value	Condition fulfilled
$\Delta\omega_1$	$\bar{S}_{xx}$	$1.2 \cdot \bar{S}_{xx}$	$\eta = 0.9$	✓
$\Delta\omega_2$		$0.8 \cdot \bar{S}_{xx}$		✖
$\Delta\omega_3$		$0.9 \cdot \bar{S}_{xx}$		✓
Overall assessment				✖

with longer time durations or conditioned using signal processing. If the signal cannot be improved anymore, it would lead to the classical system identification methods using simultaneous measurements.

After all signals are assessed as sufficient, the amplitudes of the recalculated input signals should be compared with each other. If the amplitudes show high variance, an evaluation of the data is not favorable, as the analysis would weight them differently and the modal shapes would be calculated inaccurately. The natural frequencies and damping ratios of the structure can still be determined.

2.3 Stepwise Investigation of Output-Signals for Separate Time Windows

The main idea of the IIM is the use of stationary ergodic signals, which exhibits same statistical properties independent of time. Figure 4 compares IIM with other conventional system identification methods. On the left side a typical signal composition of the

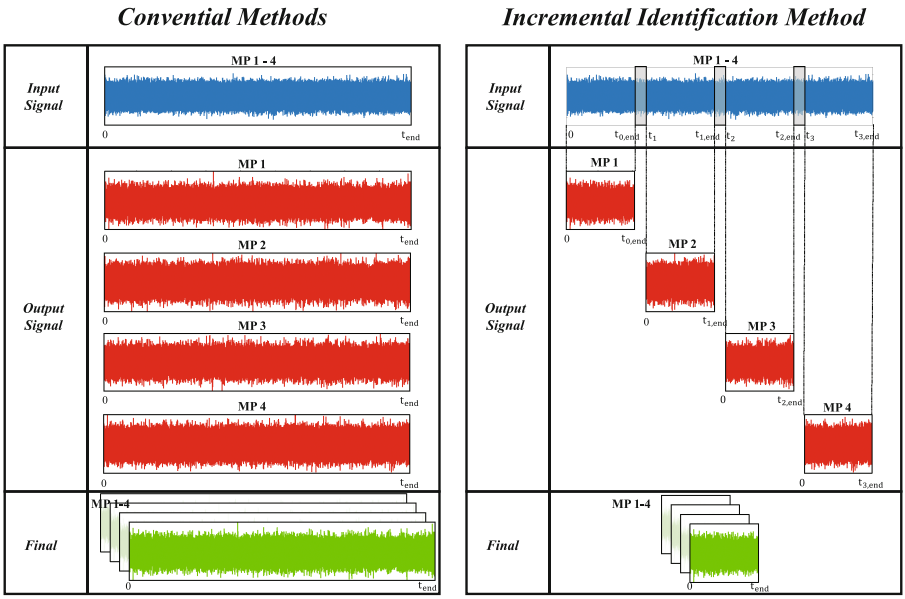

Fig. 4. Comparison measurements for conventional system identification methods (left) with the measurements for the Incremental Identification Method (right)

state of the art is shown. Here each measurement point is measured simultaneously for an identical input signal. Afterwards the system identification can be done with the output signals (MP 1–4) from 0 to t_{end}.

The output signals for the IIM however can be gathered from time independent signals, as shown in Fig. 4 on the right side. Here the first measurement is done from 0 to $t_{1,end}$. The second measurement could be started to a completely random time t_2 with a corresponding measurement duration $t_{2,end}$. For the remaining measuring points, the same procedure can be repeated, so that at the end all output signals can be summarized to a matrix of one data. The central requirement of this method is the similarity of the input signal, which means the same mean value and a similar standard deviation as well as the existence of the ambient signals.

From the theoretical background the IIM can be applied with FDD or other common identification methods. The FDD requests only the existence of an ambient behavior of the signals. Brincker [3] shows as the central equation for the FDD the relation between the power spectral density (PSD) of the input and the output:

$$\mathbf{S_{yy}}(j\omega) = \mathbf{H}^{*}(j\omega)\mathbf{S_{xx}}(j\omega)\mathbf{H}^{\mathbf{T}}(j\omega) \tag{8}$$

In the special case of ambient signals, the PSD for the input signal can be reduced to a constant matrix as following:

$$\mathbf{S_{xx}}(j\omega) = \mathbf{C} = const. \tag{9}$$

Thus one can simplify Eq. (8) to:

$$\mathbf{S_{yy}}(j\omega) = \mathbf{H}^{*}(j\omega)\mathbf{C}\mathbf{H}^{\mathbf{T}}(j\omega) \tag{10}$$

Further description of the application and functionality of the FDD can be found in several references (Brincker et al. [1], Rainieri et al. [2]). Based on the constant input matrix **C** the application is transferred to the IIM, which assumes similar input signals with the same statistical properties. In this case however it must be analyzed that the independent input signals fulfill previously mentioned conditions and assessment criteria.

3 Investigations of Benchmark Building IASC-ASCE

The IIM is applied so far both on numerical and experimental examples [7]. The application of the IIM is validated using the benchmark building IASC-ASCE. As shown in Fig. 6 it is a four story high structure consisting of columns and braces without bending stiffness. The building with 3.6 m height has a quadratic floor of 2.5 × 2.5 m, where the floors can be assumed as rigid slabs in the present case. Thus for each floor three degrees of freedoms (x, y and θ) are relevant with the relevant masses of 3.2 t for the first floor, 2.4 t for the second and third floor and 1.6 t for the top floor. The building material is steel with a yielding stress of 300 MPa. A detailed floorplan with the used sensors can be found in Fig. 5. For detail information of the

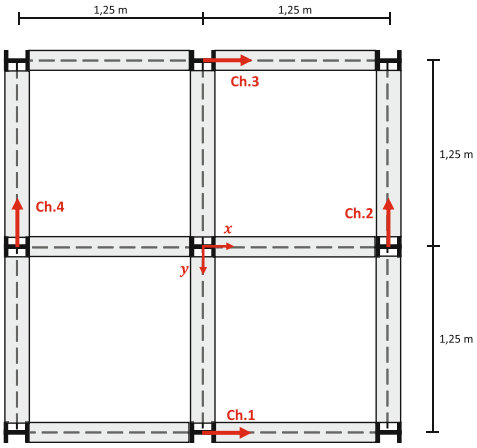

Fig. 5. Floor plan of benchmark building

Fig. 6. Benchmark structure [5]

benchmark structure the lecture of Johnson [5] and Dyke [6] are recommended. The benchmark studies offer besides experimental data a data generator to simulate user-defined time signals. For the data analysis the data generator inherent in the benchmark studies is employed. For the validation the standard benchmark structure setup was chosen, which has a symmetric mass and stiffness distribution. Thus a 2D respectively decoupled dynamic behavior is to be expected. In the benchmark structure furthermore a variation of damage patterns consisting of brace distribution would be possible as well as asymmetric mass distributions.

The excitation forces were applied in both horizontal directions (x- and y-direction) at the top floor. For every story the data generator simulates four signals. The signal directions (Ch. 1–4) can be seen in Fig. 5. With the distribution of these sensors the bending mode shapes as well as torsional mode shapes can be caught. Due to the horizontal excitation mentioned as above only bending mode shapes can be excited. Therefore, for the validation of the method only the bending mode shape in y-direction of the structure are evaluated.

The signal setup for the data generator was chosen as 900 s length with a sample rate of 500 Hz. For the noise level, which is defined over the RMS in the generator, a value of 10 has been chosen. The damping of the structure was assumed as 2% and the force intensity of the excitation was chosen to 150 kN. There were no filters applied to the signals.

As mentioned before for the FDD the output signals of the structure were generated due to one generated input-signal of 900 s. As explained in Fig. 4 on the left side for the FDD it is requested, that all output signals were measured simultaneously. According to this single input signal the FDD can be applied. In Fig. 7 the identified first two normed modal shapes from the FDD analysis are shown. The standardization of the modal shapes is effected to one. The natural frequencies of the structure can be found in Table 3. The results agree with the given modal shapes in Johnson et al. [5].

The IIM was conducted with four incrementally generated signals (for each story one signal data) of each 900 s length. As described in Fig. 4 on the right side all four signal data can be summarized to one data set afterwards. By doing so the previously mentioned signal assessment has to be conducted. Hence Table 4 shows the statistical

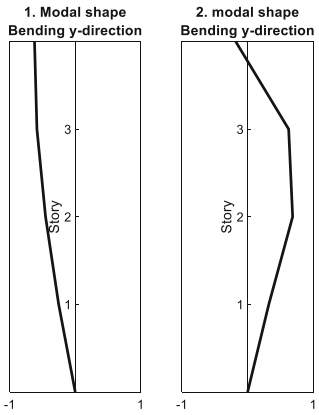

Fig. 7. Modal shapes identified from simultaneous measurements with FDD

Table 3. Natural frequencies of the benchmark structure

Eigenmode	FDD	IIM
1	9.52 Hz	9.52 Hz
2	25.56 Hz	25.53 Hz

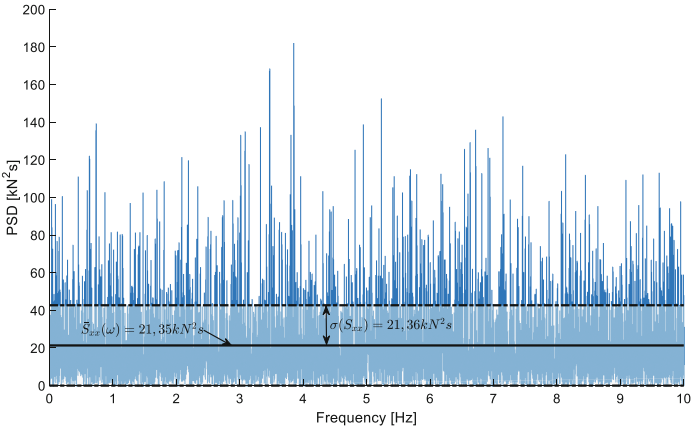

Fig. 8. Power spectral density function of the input signal for the first floor in the frequency range of 0–10 Hz

properties of the PSD of the corresponding input signals for all four stories. It is obvious that the mean values of every floor are very similar to each other as well as the standard deviation.

Table 4. Statistical properties of input signals

Story	Mean value	Standard deviation
1	21.35	21.36
2	21.35	21.42
3	21.49	21.50
4	21.42	21.40

For assessment of the input signal the PSD values are investigated according to the previously described approach. Figure 8 shows the example 0 to 10 Hz PSD-spectra belonging to the input signal of the first floor. The previously mentioned tolerance value η has to be chosen below 86.6%. This result is calculated for a frequency decrement of 1 Hz. For smaller frequency steps the tolerance value needs to be reduced. The calculation of the mean values of frequency increment gave a minimum value of 18.62 kN^2s. Due to the relation of this minimum and the meanvalue of 21.35 kN^2s the assessment can be done:

$$\frac{\min(S_{xx}(\Delta\omega_i))}{\bar{S}_{xx}} = \frac{18.62}{21.49} = 86.6\% \geq 85\% \tag{11}$$

After this assessment the system identification of the summarized data is carried out. The results of the modal shapes are given in Fig. 9. Compared to the modal shapes identified from the simultaneous measurements the results of IIM show a good convergence. In both applications the natural frequencies of the system can be determined very accurately, s. Table 3. For the first natural frequency of 9.52 Hz there are no differences only for the second one of 25.56 Hz there are a negligible deviation of 0.03 Hz.

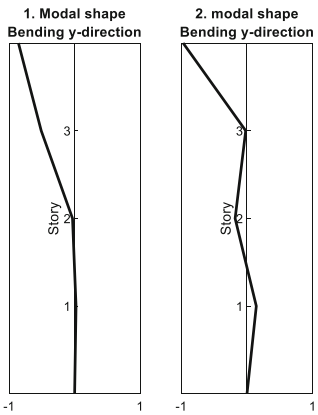

Fig. 9. Modal shapes of IIM

4 Conclusions

The present paper shows the proposed IIM, which is applied on stationary ergodic response signals induced by ambient vibrations. For the measurement effort in practical it would mean, that every measurement point can be measured separately independent from time using one sensor. The idea and the single steps of the approach are summarized in this paper including recalculation of the input signals, signal assessment and afterwards the system identification. For the validation an application of the IIM as well as a pure FDD on the benchmark building IASC-ASCE is conducted. The identified system parameters show a good convergence with the results acquired using conventional methods.

5 Future Work

The numerical and experimental examples investigated so far have used ambient input signals with almost perfect white noise density. As the time dependent fluctuation of the frequency content can disturb especially the identification of the modal shapes, the future work is going to enlarge the evaluation of the power density of the input signal both in time and frequency domain. This approach contents also the development of further signal conditioning procedures, which are necessary for the application of IIM on real civil engineering structures.

Acknowledgement. The authors gratefully acknowledge the financial support of the Daimler and Benz foundation.

References

1. Brincker, R., Ventura, C.E.: Introduction to Operational Modal Analysis. Wiley, Chichester (2015)
2. Rainieri, C., Fabbrocino, G.: Operational Modal Analysis of Civil Engineering Structures: An Introduction and Guide for Applications. Springer, Heidelberg (2014)
3. Brincker, R., Zhang, L., Andersen, P.: Modal identification of output-only systems using frequency domain decomposition. Smart Mater. Struct. **10**(2001), 441–445 (2000)
4. He, J., Fu, Z.F.: Modal Analysis. Butterworth Heinemann, Boston (2001)
5. Johnson, E.A., Lam, H.F., Katafygiotis, L.S., Beck, J.L.: The phase I IASC-ASCE structural health monitoring benchmark problem using simulated data. ASCE J. Eng. Mech. **130**, 3–15 (2002)
6. Dyke, S.J., Bernal, D., Beck, J.L., Ventura, C.: An experimental benchmark problem in structural health monitoring. In: 3rd International Workshop on Structural Health Monitoring, Stanford, CA, USA (2001)
7. Schleiter, S., Altay, O., Klinkel, S.: Experimental identification of an elasto-mechanical multi-degree-of-freedom-system using stochastic signals. In: Acta Polytechnica CTU Proceedings, vol 1. ExNum 2016 (2017)

Effect of Cross-Section and Discontinuities on Damping Enhancement in Composites: An Experimental Study

Komal Chawla[1(✉)] and Samit Ray. Chaudhuri[2(✉)]

[1] Department of Civil Engineering, Indian Institute of Technology, Kanpur, India
komalc@iitk.ac.in
[2] Indian Institute of Technology, Kanpur, India
samitrc@iitk.ac.in

Abstract. Damping in structures is an important aspect from the vibration control and dynamic stability point of views. These days, significant emphasis is placed on the damping in composite structures due to involvement of different mechanisms for controlling damping at micro (fibre-matrix interface, fibre orientation etc.) and macro levels (fibre orientation, stacking sequence etc.) under dynamic loading. This study scrutinizes the specimen cross-sectional effect on the damping capacity of hollow tubes. For this purpose, carbon fibre reinforced tubes of square and hexagonal cross-sections were investigated. To improve the damping capacity further, circular holes were drilled at different positions along the tube. Free vibration and base excitation tests were performed to induce vibration in tubes and responses at different locations (i.e., along the tube length) were recorded using accelerometers and strain gauges. It is observed from the experimental results that the damping ratio increases in presence of holes in tube specimens. Further, damping enhancement is found to be more for tubes containing smaller holes (owing to more localized stresses) in comparison to the tubes containing larger holes. Typically, damping of hexagonal tubes is found to be slightly less in comparison to the square tube.

Keywords: Carbon fibre reinforced hollow tube · Damping · Cross-section · Circular hole

1 Introduction

The vibration response of a structure under dynamic loading is controlled by various parameters such as inertia, stiffness and damping. The first two parameters relate to the material properties and geometric configurations of a system. The last one, i.e., the damping, may vary from one system to another due to involvement of various mechanisms. For example, in composite structures, damping is high owing to several mechanisms involved at micro (fibre-matrix interface, fibre orientation etc.) and macro level (fibre orientation, stacking sequence etc.) This leads to higher energy dissipation and ultimately reduces the vibration amplitude [1, 2].

© Springer International Publishing AG 2018
J.P. Conte et al. (eds.), *Experimental Vibration Analysis for Civil Structures*,
Lecture Notes in Civil Engineering 5, https://doi.org/10.1007/978-3-319-67443-8_62

Mead [3] measured the damping constants as well as damping capacity of solid cylindrical specimens consisted of different material (i.e., cast iron, copper and steel) under random excitation. A mathematical expression was derived between the energy dissipation and surface shear strain. Damping constants were evaluated using experimental results and the derived expression of the energy dissipation. Since damping contributes a significant role towards the reduction in vibration amplitude of a system under dynamic loading, various approaches have been adopted in past for its enhancement. Mallik and Ghosh [4] performed an analytical study and introduced solid and annular (ring-type) elastic inserts in the structural member to improve its damping capacity. Elastic inserts were (a) welded to the member and (b) inserted into the holes by press-fit. It has been found that application of elastic inserts increased the damping capacity of member with a negligible loss in the static rigidity. However, its pronounced effect is found more in case of press-fit method of introducing inserts in a member. This study was further extended by Mallik and Ghosh [5] for the analyses of damping in composite and porous materials. High damping was observed in case of composite (with addition of very small inclusions) and porous materials. Further, experiments were conducted on cantilever strips with solid and annular inserts of different materials by Rahmathulla and Mallik [6]. It was observed that, damping capacity can be significantly increased by using proper insert shape and materials.

Rajoria and Jalili [7] studied the damping improvement in carbon nanotube-epoxy reinforced composites. Composites were prepared using different proportions of single and multi-walled nanotube reinforcements. Free and forced vibration tests were performed. A significant enhancement in damping ratio was observed in case of multi-walled nanotube reinforced composites. Further, DeValve and Pitchumani [8] dispersed carbon nanotubes of different aspect ratios, types and weight fractions in composite matrix and observed the similar results of damping enhancement.

It is clear from the aforementioned studies that several techniques were adopted in past to evaluate and enhance the damping characteristics of a structure. As per author's knowledge, literatures are not available on the specimen geometry/cross-section effect on the damping characteristics. Vibration response of a structure (under dynamic loading) depends on the inertia which is also a function of the geometry of a member. Hence, specimen geometry might contribute a significant role towards the improvement in damping characteristics [9]. In this study, the effect of specimen cross-sections on the damping characteristics is analysed. For this purpose, carbon fibre reinforced hollow tubes of different cross-sections (square and hexagonal) were considered. Further, to improve damping characteristics, discontinuities (i.e., circular holes) were introduced in tube specimens. A free vibration and base excitation tests were performed to induce vibration in specimen and responses at various locations are captured using piezoelectric accelerometers. In addition, strain gauges were applied on the opposite side of the accelerometer to obtain the strain response at different locations. Based on these responses, modal and damping characteristics of hollow tubes were estimated. Further, these results were also validated with the theoretical formulations.

2 Experimental Study

2.1 Specimen Details and Configurations

Experiments were conducted on different cross-sectional carbon fibre reinforced hollow tubes to understand how the geometric configurations influence the damping characteristics. Figure 1 shows the square and hexagonal hollow tubes considered for this study. The geometric dimensions of these tubes are enlisted in Table 1. Further to understand the effect of discontinuities on damping capacity, circular holes were drilled at different locations in tubes.

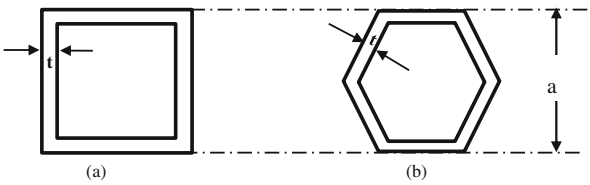

Fig. 1. Carbon fiber reinforced hollow tubes of (a) square and (b) hexagonal cross-sections

Table 1. Geometric details of carbon fiber reinforced hollow tubes

Cross-section	a (mm)	t (mm)	Length (m)
Square	25	2	1
Hexagonal	26	2.5	1

2.2 Experimental Set-Up and Instrumentations

Figure 2(a) shows the experimental set-up considered for this study. One end of the tube was clamped on shake table to act as a cantilever support (see Fig. 2(b)). Sinusoidal harmonic base excitations of varying amplitudes (i.e., 0.5 mm to 1 mm) were applied to the tube specimens through the shake table. For capturing the vibration responses, accelerometers were installed at different positions along the length of tube (see Fig. 2(a)). For collecting the strain responses, strain gauges were also mounted on the opposite side of accelerometers (see Fig. 2(c)). All these responses were recorded using data acquisition system and LabVIEW software.

Number of cases (enlisted in Table 2) was studied for understanding the dynamic characteristics of tubes while subjected to free vibration and base excitation. For each case, hollow tubes were initially subjected to free vibration by imparting an initial excitation at its free end and responses were recorded at different locations using accelerometer, strain gauges and data acquisition systems. Further, tubes were also subjected to a sweep harmonic base excitation of frequency ranges varying from 10 Hz to 30 Hz using shake table (See Fig. 2(a)) and responses were captured. Based on the peak response and natural frequency, base excitation tests were performed on tube specimens for some discrete frequencies ranging from 16 Hz to 22 Hz with an interval of 0.5 Hz.

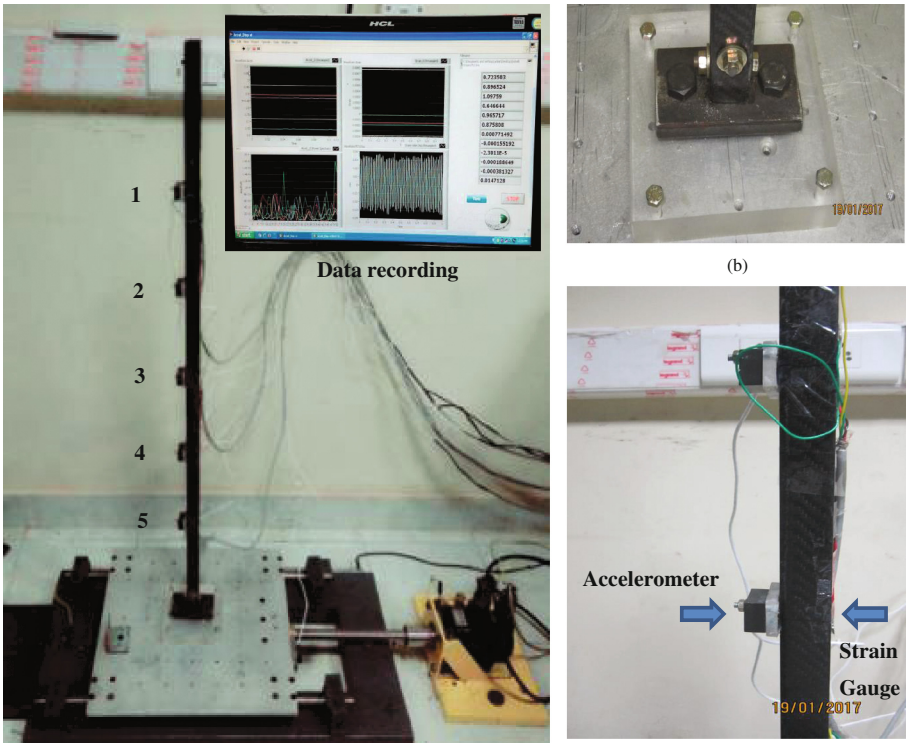

Fig. 2. (a) Experimental set-up for vibration testing of a square tube, (b) close view of the fixed end of tube i.e., cantilever support, connected with shake table and (c) close view of accelerometers and strain gauges

Table 2. Different cases studied for the dynamic properties of carbon fiber reinforced hollow tubes

Tubes/case	I	II	III	IV	V
Square	Without hole	5 circular holes of 2 mm ϕ (one side)	5 circular holes of 2 mm ϕ (both side)	5 circular holes of 4 mm ϕ (both side)	5 circular holes of 4 mm ϕ (both side) + 5 circular holes of 2 mm ϕ (one side)
Hexagonal	Without hole	5 circular holes of 2 mm ϕ (one side)	5 holes of 2 mm ϕ (both side)	–	–

3 Results and Discussions

The dynamic properties of square and hexagonal hollow tubes are investigated under free vibration and base excitation. At first, vibration responses of a square tube (without any holes) under free vibration and base excitation tests are discussed. Figure 3(a) shows the response amplitude for a square tube subjected to free vibration. From this, a peak in the response amplitude can be observed, which corresponds to a frequency of 19 Hz. Hence, the fundamental natural frequency of the square tube is considered as 19 Hz. In addition, response near the free end of tube is found to be much higher (i.e., accelerometer 1) in comparison to the bottom end (i.e., accelerometer 5) for the very obvious reason (see also Fig. 2(a)). Figure 3 (b) shows the similar observation for vibration response of a square tube subjected to a sweep harmonic base excitation of 0.5 mm amplitude and applied frequency ranges varying from 10 Hz to 30 Hz. Similarly, the fundamental frequency of hexagonal tube was found as 17.80 Hz.

In addition, natural frequencies of square and hexagonal tubes were also calculated theoretically. Table 3 shows the experimental and theoretical values of natural frequencies for mode 1, mode 2 and mode 3. Since each of the accelerometers were having a non-negligible mass (almost 8% of the total mass of tube), theoretical values of natural frequencies were calculated by: (i) without considering the accelerometer masses and (ii) considering the accelerometer masses. For the former case, theoretical formulations available in Meirovitch [10] (for free and forced vibration of a cantilever beam) were used. Based on these, Table 3 shows the overestimated values of the fundamental natural frequencies when compared with its experimental values for square and hexagonal tubes. For the latter case, tubes were analyzed by assuming proportionate lumped mass at accelerometers positions and at the tube ends. Rayleigh Ritz method was used to estimate the natural frequencies of square and hexagonal tubes. Using this approach, a good comparison can be observed between the experimental and theoretical values of natural frequencies (see Table 3). To corroborate

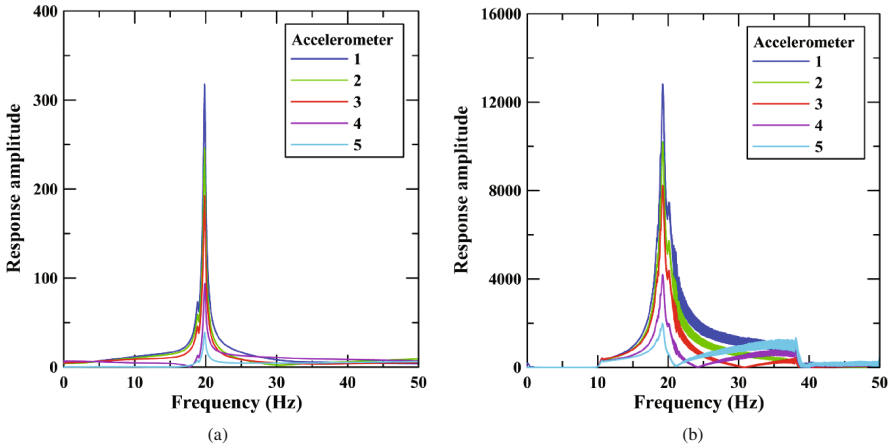

Fig. 3. Vibration response of square hollow tube specimen while subjected to (a) an initial excitation (i.e., free vibration) and (b) base excitation

Table 3. Experimental and theoretical values of natural frequencies for square and hexagonal tubes

	Natural frequency (Hz)				
Cross-section	Mode	Experimental	Theoretical		Numerical (ANSYS)
			Without consideration of accelerometer mass	With consideration of accelerometer mass using Rayleigh Ritz method	With consideration of accelerometer mass
Square	Mode 1	**19.05**	25.85	**21.43**	**22.00**
	Mode 2	–	161.93	127.55	136.05
	Mode 3	–	453.52	338.20	381.02
Hexagonal	Mode 1	**17.80**	25.38	**21.51**	–
	Mode 2	–	159.01	127.96	–
	Mode 3	–	445.34	339.34	–

further, square hollow tube with accelerometer masses was modelled in ANSYS [11] under sweep harmonic excitation as shown in Table 3.

Figure 4(a) shows the frequency response curve based on accelerometers data for a square tube under constant amplitude base excitation (i.e., 0.5 mm). The vertical and horizontal axes represent the normalized response amplitude and excitation frequency, respectively. Similarly, Fig. 4(b) shows the frequency response curve for the similar tube based on the strain data. From these figures, a peak in the response amplitude can be noted as 19 Hz, which was also found in earlier observations. These data (accelerometers and strains) were fitted with polynomial as shown in Fig. 4(a) and (b). Furthermore, the response is found to be much higher at top end of the tube (accelerometer 1).

Figure 5(a) shows the fundamental mode shape of a square tube obtained from the normalized maximum response ratios of the accelerometers data (at different locations along the tube length). Similar observations were also found for the hexagonal tube. Further, damping ratio was estimated using frequency response curve and half power bandwidth method. Figure 5(b) shows the damping ratio (along the tube length) obtained for different cases as explained in Table 2. Damping ratios obtained from accelerometers and strain gauges were found almost equal. Damping ratios along with the percentage enhancement are enlisted in Table 4. One can note the higher damping ratio for case II (i.e., square tube containing 5 circular holes at one side) due to stress

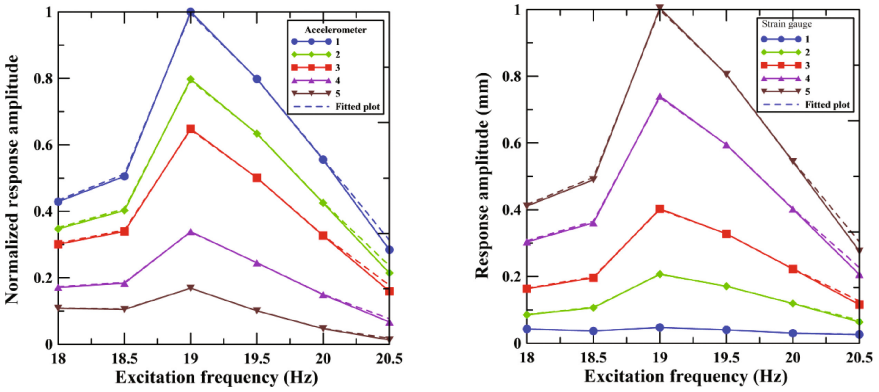

Fig. 4. Normalized vibration response of a square tube based on (a) accelerometers and (b) strains data

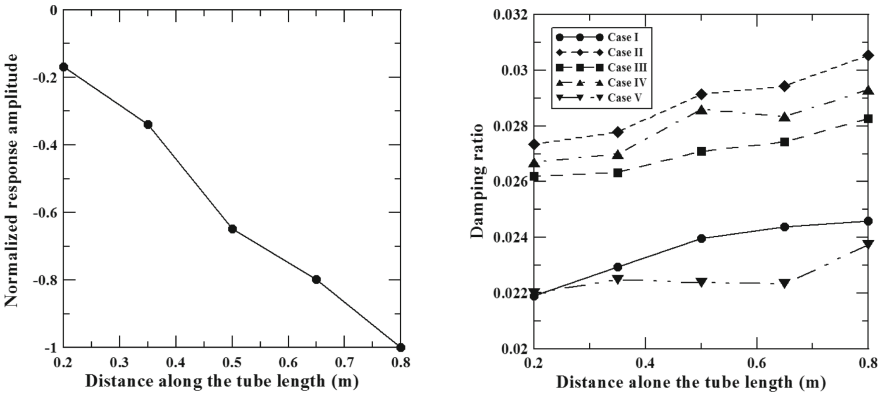

Fig. 5. (a) Fundamental mode shape of a square tube and (b) damping ratios obtained for the different cases

concentration around holes. However, these values got slightly reduced when holes are present on both side of the tube i.e., for case III. In addition, with increase in hole sizes i.e., case IV (square tube containing 5 circular holes of 4 mm size on both sides), damping is increased although it is comparatively lesser than the damping obtained for case II. The reason might be the presence of more localized stresses in case of smaller hole size compared to the larger hole size. One can also observe that (for case V), with further increment in the number of holes, damping starts to decrease.

Similarly, vibration response of a hexagonal tube is analyzed for the different cases explained in Table 2. Similar steps were followed for hexagonal tube to obtain the

Table 4. Damping ratios of square and hexagonal tubes for its different cases

Case	Square tube		Hexagonal tube	
	Damping ratio	% Enhancement	Damping ratio	% Enhancement
I	0.0246		0.0214	
II	0.0305	23.98%	0.0247	15.40%
III	0.0283	15.04%	0.0241	12.61%
IV	0.0293	19.10%	–	–
V	0.0237	–	–	–

natural frequencies, mode shapes and damping ratios. Table 4 shows the damping ratios of square and hexagonal tubes obtained for the different cases. It can be observed that, for the similar case study, square tube shows comparatively higher damping than the hexagonal tube.

4 Conclusions

This study deals with the damping ratio of square and hexagonal hollow tubes under free vibration and base excitation. Further to enhance damping, a few circular holes of different sizes were drilled at different locations along the tube length. Different cases were studied for the influence of varying number of holes and hole-sizes on damping in square and hexagonal tubes. It was found that the presence of holes in tubes increases its damping ratio up to 24% owing to stress concentration around the holes. However, this increase was found to be more in case of tubes containing holes of smaller sizes due to comparatively more localized stress effect. In addition to hole size, damping was also found to be dependent on their locations and number of holes in tubes. With increase in number of holes in a tube, the damping ratio starts to decrease Furthermore, damping of a square tube was found to be slightly higher compared to a hexagonal tube.

Acknowledgments. The authors would like to thank lab technicians and staff of Indian Institute of Technology, Kanpur for their help and guidance during the work. This work was supported by Indian Space Research Organization (ISRO) through ISRO-IITK Space Technology Cell.

References

1. Chandra, R., Singh, S.P., Gupta, K.: Damping studies in fibre-reinforced composites: a review. Compos. Struct. **46**, 41–51 (1999)
2. Finegan, I.C., Gibson, R.F.: Recent research on enhancement of damping in polymer composites. Compos. Struct. **44**, 89–98 (1999)
3. Mead, D.J.: Material damping under random excitation. J. Sound Vib. **45**, 487–494 (1976)
4. Mallik, A.K., Ghosh, A.: Improvement of damping characteristics of structural members with high damping elastic inserts. J. Sound Vib. **27**, 25–36 (1973)
5. Mallik, A.K., Ghosh, A.: Damping characteristics of composite and porous materials. J. Compos. Mater. **8**, 207–211 (1974)

6. Rahmathulla, R., Mallik, A.K.: Damping of cantilever strips with inserts. J. Sound Vib. **66**, 109–117 (1979)
7. Rajoria, H., Jalili, N.: Passive vibration damping enhancement using carbon nanotube-epoxy reinforced composites. Compos. Sci. Technol. **65**, 2079–2093 (2005)
8. DeValve, C., Pitchumani, R.: Experimental investigation of the damping enhancement in fibre-reinforced composites with carbon nanotubes. Carbon **63**, 71–83 (2013)
9. Mallik, A.K.: Principles of Vibration Control. East-West Press Private Limited, New Delhi (2010)
10. Meirovitch, L.: Fundamentals of Vibration. McGraw-Hill, New York (2001)
11. ANSYS: ANSYS mechanical user's guide, Version 15.0. ANSYS, Inc., Canonsburg (2013)

Modal Strain Energy Based Structural Parameter Identification from Limited Vibration Measurement

D. Bandyopadhyay[1(✉)] and J.S. Ali[2]

[1] Department of Construction Engineering, Jadavpur University, Kolkata, India
dban65@yahoo.com
[2] Department of Civil Engineering, Aliah University, Kolkata, India

Abstract. Structural parameter identification is significantly important for condition assessment and health monitoring to ensure safety, future usefulness and to adopt effective retrofit & repair measure. System identification techniques, using inverse dynamic approach, are important tool to improve the mathematical models for structural parameter identification. However, techniques using frequency, mode shape or their derivatives are quite sensitive to the measurement noise. An analysis methodology is proposed for the structural parameter identification of the framed structure in the framework of finite element model with limited dynamic responses. The proposed dynamic responses are not feasible in all degrees of freedom. Dynamic condensation technique is adopted to take care of the limited dynamic responses measured at selected degrees of freedom experimentally. The structural properties viz. bending rigidity and mass density per unit length parameters are identified at the parameter level in the updated models of the system. Damage at the element level may be identified, by comparing the identified structural parameters of the system with those of the undamaged state. The proposed model is suitable for practical problem as it is able to identify the structural parameters with limited modal data of first few modes, assumed at selected degrees of freedom. Numerical example with various damage scenarios is exploded to demonstrate the applicability of the proposed model. The model is able to identify the structural damage with great accuracy from the noisy dynamic responses. Experimental studies establish the potential of the proposed method for its practical application in the field of structural parameter identification.

Keywords: Damage · Parameter identification · Modal strain energy · Structural health monitoring

1 Introduction

Civil engineering structures often experience different forms of distress within its design life due to its aging, improper design, inferior construction, environmental action, accidental loading etc. Natural disaster of different types such as earthquake, flood, cyclone etc. leaves behind their sign on structures in terms of damages. Monitoring of health for assessing the condition of age-old structures, disaster driven

© Springer International Publishing AG 2018
J.P. Conte et al. (eds.), *Experimental Vibration Analysis for Civil Structures*,
Lecture Notes in Civil Engineering 5, https://doi.org/10.1007/978-3-319-67443-8_63

damaged structures has become an essential requirement for the safety of structures. Monitoring of structural health, particularly the integrity of existing structures, is useful in improving the structural safety and helpful for better utilization of the structure, for appropriate maintenance strategy and avoidance of catastrophic failure. The benefits of SHM include optimal maintenance cost and constant reliability instead of increasing maintenance cost and decreasing reliability.

Structural health monitoring technique based on dynamic responses seems to be a better proposition as the assessment is carried out in a global manner. It is presumed that the damage changes the structural characteristics considerably, so that the dynamic responses are influenced by the changed parameters. System identification techniques, adopting inverse dynamic approaches, are important tools to monitor structural health. The objective of system identification in structural dynamics is to update the mathematical models of the dynamics of structure by using measured responses. The uncertainties in measured data might lead to unreliable identification. System identification techniques using statistical approach with probabilistic concepts may prove better to account for the uncertainties associated with the limited observations, assumed model and other environmental and operational variations in structural health monitoring.

Different approaches have been attempted by several researchers to address the problem of structural health monitoring based on dynamic responses. These attempts may be classified based on various parameters. In most of the system identification approaches (Adam et al. 1978; Sanayi and Onipede 1991; Casas and Aparicio 1994; Liu 1995) the uncertainties were not adequately addressed. A few have also considered the availability of dynamic response data, measured at a few selected degrees of freedom (Wang and Haldar 1994; Sanayi et al. 1999) considering the feasibility of practical application. In recent times, statistical system identification approaches are employed in structural health monitoring (Katafygiotis et al. 1998; Beck and Au 2001; Xia and Hao 2003; Yuen et al. 2006) with due consideration of the uncertainties associated with the measured data (Lim and Kashangaki 1994). Stubbs et al. (1992) presented a pioneering work of using modal strain energy for damage localization. The MSE of a structure on the rth mode can be demonstrated as $MSR_r = \frac{1}{2}\Phi_r^T K \Phi_r$ where K is the stiffness matrix of a structure. Stubbs and Kim (1996) verified the feasibility of a practical modal strain energy method for damage localization and severity estimation with only the post-damage information available. Carrasco et al. (1997) discussed using modal strain energy change to find damage location and extent for a space truss model and claimed that the magnitude change of the indicator is related with the damage's overall magnitude. Result of the test showed that this method works well at locating damaged elements. Also, Park et al. (2002) examined another damage index using modal strain energy. The index was extracted from the periodical measurement data of the prior visually inspected cracks on a concrete box-girder bridge. They found that the environmental factors are likely to affect the accuracy of the proposed. Wang et al. (2010) studied MSE as a correlation indicator, called modal strain energy correlation (MSEC) to identify damage for truss bridge structures. The MSE to- damage sensitivity was derived from theory. The capacity of MSEC was verified through several damage scenarios. It was found that the method has high

computational efficiency, however, when measurement noise is considered, the method may report false alarms. Cornwell (1999) examined the application of a modal strain energy method on a plate-like model. The method only requires mode shape data before and after damage. From the experimental validation, the method is effective even for the damage whose extent is as low as 10%.

The objective of the present investigation is to develop a structural health monitoring technique based on limited experimental modal noisy dynamic responses, measured at selected degrees of freedom. In the present investigation modal strain energy based damage identification technique is employed with limited modal data (both natural frequency and mode shape) to identify the damage existence. The identification of structural damage, which is mainly local reduction of stiffness and/or mass, is evaluated. The efficiency of the damage identification algorithm depends on the accuracy of the finite element model and the measured dynamic responses. There are several uncertainties associated with the assumed FE model and in the measured data. On the other hand, noise in measurement is inevitable. This may lead to unreliable identification of damage in structures.

1.1 Theoretical Formulation

The dynamic equilibrium equation of motion of finite element model can be expresses as,

$$[\mathrm{m}]\{\ddot{\mathrm{u}}\} + [\mathrm{k}]\{\mathrm{u}\} = \{\mathrm{f}\} \tag{1}$$

Where [k] and [m] are the stiffness and consistent mass matrices of the element respectively. {u} and {f} are the nodal displacements and force vectors. Assembling the element equations and applying boundary conditions, one can obtain the following equilibrium equation for the undamped forced vibration shall be

$$[\mathrm{M}]\{\ddot{\mathrm{U}}\} + [\mathrm{K}]\{\mathrm{U}\} = \{\mathrm{F(t)}\} \tag{2}$$

$$\left([\mathrm{K}] - \omega^2 [\mathrm{M}]\right)\{\varphi\} = \{0\} \text{ i.e.} [\mathrm{K}]\{\varphi\} = \lambda[\mathrm{M}]\{\varphi\}, \text{ where } \lambda = \omega^2. \tag{3}$$

Equation (3) is a generalized eigenvalue problem that can be solved for λ and $\{\varphi\}$. The eigenvector $\{\varphi\}$ is the mode shape and eigenvalue λ is the square of the associated natural frequency in radians per seconds.

Elemental modal strain energy (MSE) is defined as the product of the elemental stiffness matrix and the second power of its mode shape component (Shi et al. 1998). For the jth element and ith mode, the elemental MSE before and after the occurrence of damage are given as

$$MSE_{ij} = \Phi_i^T \mathrm{K}_j \Phi_i, \quad MSE_{ij}^d = \Phi_i^{dT} \mathrm{K}_j \Phi_i^d, \tag{4}$$

Where MSE_{ij} and MSE_{ijd} = jth elemental modal strain energy corresponding to the ith mode shape for the undamaged and damaged states, respectively; K_j = jth elemental stiffness matrix, and ϕ = the ith mode shape. The superscript d denotes the damaged

state. Since the damage elements are not known, the undamaged elemental stiffness matrix K_{ji}s used instead of the damaged one as an approximation in MSE_{ij}^{d}.

The elemental modal strain energy change ratio (MSECR) has been verified to be a good indicator for damage localization and is defined as (Shi et al. 1998).

$$MSECR_{ij} = \frac{\left|MSE_{ij}^{d} - MSE_{ij}\right|}{MSE_{ij}} \tag{5}$$

A structural damage often causes a loss of stiffness in one or more elements of a structure but not a loss in the mass. In the theoretical development that follows, damage is assumed to affect only the stiffness matrix of the system. When damage occurs in a skeletal structure, it can be represented by a small perturbation in the original system. Thus, the stiffness matrix K^{d}, the ith modal eigenvalue λ_i^d, and the ith mode shapes ϕ_i^d of the damaged system can be expressed as follows:

$$K^{d} = K + \sum_{j=1}^{L} \Delta K_j = K + \sum_{j=1}^{L} \alpha_j K_j, (-1 < \alpha_j < < 0) \tag{6}$$

$$\lambda_i^d = \lambda_i + \Delta\lambda_i \tag{7}$$

$$\Phi_i^d = \Phi_i + \Delta\Phi_i \tag{8}$$

where α_j = coefficient defining a fractional reduction in the jth elemental stiffness matrices; and L = total number of elements in the system.

The elemental modal strain energy change (MSEC) for the jth element in the ith mode is expressed as

$$MSEC_{ij} = \Phi_i^{dT} K_j \Phi_i^d - \Phi_i^T K_j \Phi_i \tag{9}$$

So, the $MSEC_{ij}$ becomes

$$MSEC_{ij} = 2\Phi_i^T K_j \Delta\Phi_i \tag{10}$$

For a small perturbation in an undamped n-DOFs dynamic system, the equation of motion becomes

$$[(K + \Delta K) - (\lambda_i + \Delta\lambda_i)M](\Phi_i + \Delta\Phi_i) = 0 \tag{11}$$

Neglecting second-order terms, Eq. (11) leads to

$$(K - \lambda_i M)\Delta\Phi_i = \Delta\lambda_i M\Phi_i - \Delta K\Phi_i \tag{12}$$

$\Delta\Phi_i$ in Eq. (12) can be expressed as a linear combination of mode shapes of the original system (Fox and Kapoor 1968)

$$\Delta\Phi_i = \sum_{k=1}^{n} d_{ik}\Phi_k \tag{13}$$

Where d_{ik} = scalar factors and n = total number of modes of the original system

Substituting Eqs. (12) into (13), and pre multiplying Φ_r^T to both sides of Eq. (12), we have

$$\sum_{k=1}^{n} d_{ik}\Phi_r^T(K-\lambda_i M)\Phi_k = \Delta\lambda_i\Phi_r^T M\Phi_i - \Phi_r^T\Delta K\Phi_i \tag{14}$$

With the orthogonal relationship, Eq. (14) can be simplified into the following when r is not equal to i:

$$d_{ir} = -\frac{\Phi_r^T\Delta K\Phi_i}{\lambda_r - \lambda_i}, where, r \neq i \tag{15}$$

For the case of $r = i$, d_{rr} equals 0.0 from the orthogonal relationship $\Phi_i^T M\Phi_i = I$. Therefore, Eq. (13) can be written as

$$\Delta\Phi_i = \sum_{r=1}^{n} -\frac{\Phi_r^T\Delta K\Phi_i}{\lambda_r - \lambda_i}\Phi_r, where, r \neq i \tag{16}$$

Substituting Eqs. (16) into (10), the MSECij becomes

$$MSEC_{ij} = 2\Phi_r^T K_j\left(\sum_{r=1}^{n} -\frac{\Phi_r^T\Delta K\Phi_i}{\lambda_r - \lambda_i}\Phi_r\right), where,\ r \neq i \tag{17}$$

And finally we obtain.

$$MSEC_{ij} = \sum_{p=1}^{L} -2\alpha_p\Phi_i^T K_j\sum_{r=1}^{n}\frac{\Phi_r^T K_p\Phi_i}{\lambda_r - \lambda_i}\Phi_r, where,\ r \neq i \tag{18}$$

In absence of a more realistic representation, a simple model with uniformly–distributed noise will be used here:

$$d_{ij}' = (1+\sigma\%)d_{ij} \tag{19}$$

where d and d' are the noise free and polluted values by random noise. is a random number that varies between zero and maximum expected error, typically 5%–10% depending on the type of structure that is being used.

1.2 Numerical Example-1

A cantilever beam of 500 mm span length is prepared from 50 mm wide and 15 mm thick rectangular mild steel strips. Table 1 shows the detail properties of the damaged beam. Different damages have been introduced in the beam to check the accuracy of the proposed method.

Table 1. Properties of the damaged cantilever beam

Element number	Length (mm)			Width (mm)			Thickness (mm)			Cross sectional area (mm^2)			Moment of inertia ($10^4 \times mm^4$)			Modulus of elasticity (E) (GPa)		
Damaged condition	UD	1D3	2D34	UD	1D3	2D34	UD	1D3	2D34	UD	1D3	2D34	UD	1D3	2D 34	UD	1D3	2D34
1	100	100	100	50	50	50	15	15	15	750	750	750	1.40	1.406	1.406	210	210	210
2	100	100	100	50	50	50	15	15	15	750	750	750	1.40	1.406	1.406	210	210	210
3	100	**100**	**100**	50	**45**	**45**	15	**15**	**15**	750	**675**	**675**	1.40	**1.265**	**1.265**	210	**210**	**210**
4	100	100	**100**	50	50	**45**	15	15	**15**	750	750	**675**	1.40	1.406	**1.265**	210	210	**210**
5	100	100	100	50	50	50	15	15	15	750	750	750	1.40	1.406	1.406	210	210	210

UD = Undamaged Beam; 1D1 = Single Element Damage at element 3; 2D34 = Double Element Damage at element 3 and 4

Damage identification is performed based on the mode shapes and the frequency and the true and predicted parameters are listed below for different damage scenario for different noise conditions.

Tables 2, 3 and 4 clearly indicate that using analytical frequency, mode shapes and modal strain energy one can easily identify structural parameters with higher accuracy

Table 2. True and predicted bending rigidity (EI) using analytical mode shapes of cantilever beam for undamaged case

Member	Base value ($10^3 \times mm^4$)	Without noise ($10^3 \times mm^4$)	5% noise ($10^3 \times mm^4$)	10% noise ($10^3 \times mm^4$)
1	3.5	3.485923	3.485907	3.485937
2	3.5	3.485923	3.485907	3.485937
3	3.5	3.485923	3.485907	3.485937
4	3.5	3.485923	3.485907	3.485937
5	3.5	3.485923	3.485907	3.485937

Table 3. True and predicted moment of inertia (I) using analytical mode shapes of cantilever beam for 1D3 (10% damage)

Member	Base value ($10^3 \times mm^4$)	Without noise ($10^3 \times mm^4$)	5% noise ($10^3 \times mm^4$)	10% noise ($10^3 \times mm^4$)
1	3.5	3.462791	3.462937	3.462954
2	3.5	3.462791	3.462937	3.462954
3	**3.15**	**3.112931**	**3.113077**	**3.113094**
4	3.5	3.462791	3.462937	3.462954
5	3.5	3.462791	3.462937	3.462954

Table 4. True and predicted moment of inertia (I) using analytical mode shapes of cantilever beam for 2D34 (2.5% damage)

Member	Base value ($10^3 \times mm^4$)	Without noise ($10^3 \times mm^4$)	5% noise ($10^3 \times mm^4$)	10% noise ($10^3 \times mm^4$)
1	3.5	3.476811	3.476737	3.476791
2	3.5	3.476811	3.476737	3.476791
3	**3.4125**	**3.389346**	**3.389272**	**3.389326**
4	**3.4125**	**3.389346**	**3.389272**	**3.389326**
5	3.5	3.476811	3.476737	3.476791

even if analytically noise is introduced up to 10%. Experimentation has been performed with the same cantilever beam. One edge of the beams is rigidly fixed with four numbers of bolts to the supporting frame. The bolts are tightened to the maximum extent to ensure adequate rigidity. The statistical variations in length, width and thicknesses are measured. The specimens are intentionally not machined perfectly to have the variations as expected in the structures in practice. Similar specimens with damage at single and multiple locations are prepared. The damage is introduced with 10% reduction of stiffness and mass parameters in those elements. The detail of the damaged test specimen with single element number 3 and double damage (element 3 and 4) as damaged is shown in Fig. 1.

Four no. of sensors are connected to the cantilever beams as shown and responses are recorded by The A4404 – SAB which is a pocket sized 4 channel vibration analyzer

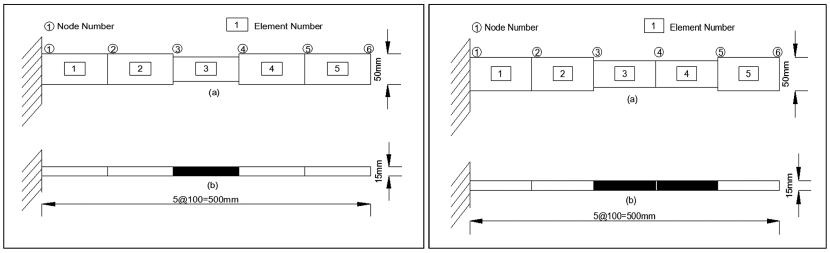

Fig. 1. Schematic damaged beam (a) single damage, (b) double damage as prepared for analysis and experiment

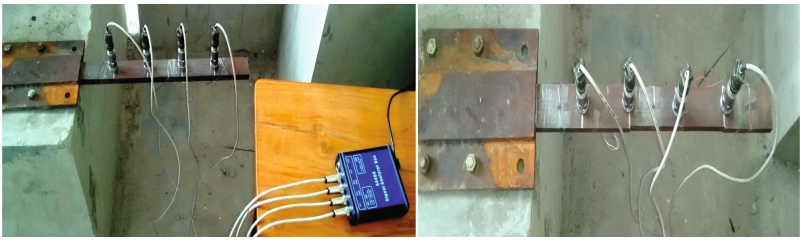

Fig. 2. Actual damaged beam (a) single damage, (b) double damage during experiment

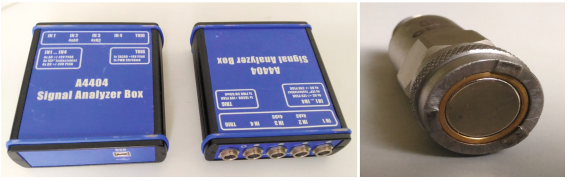

Fig. 3. Data accusation system (a) and acceleration transducer (b)

(Fig. 2). Responses are recorded through a data accusation system as shown in Fig. 3 and then further processed to get the mode shapes and natural frequencies using **ARTeMIS** Modal Pro (Fig. 4).

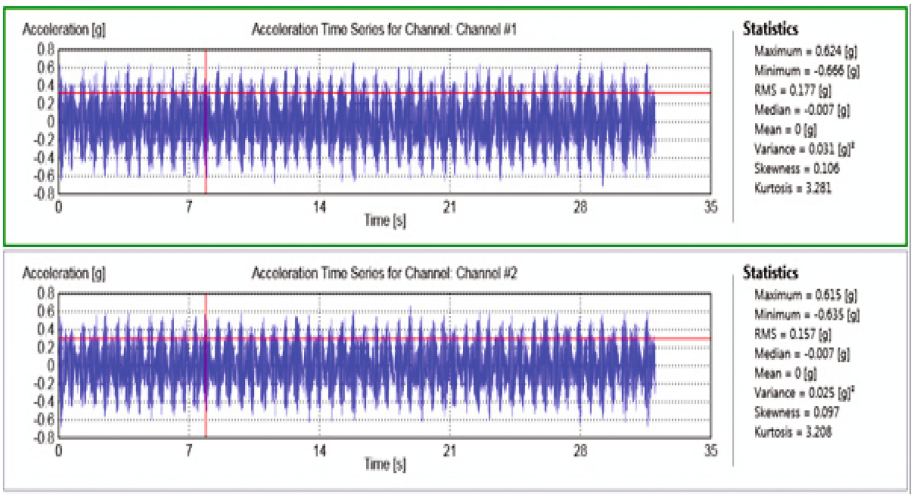

(a)

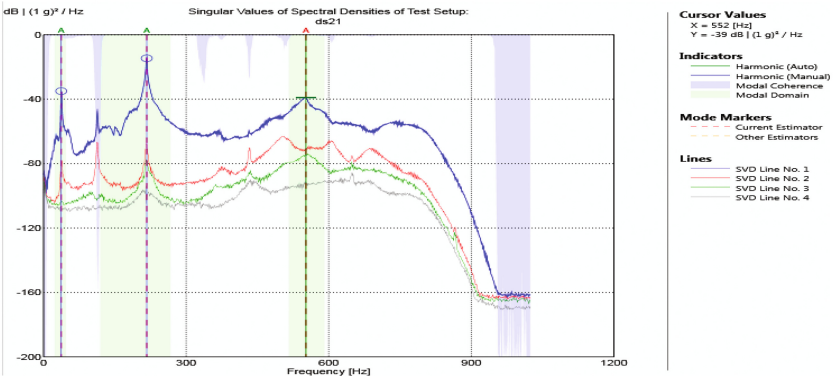

(b)

Fig. 4. (a) Typical signals recorded at transducers, (b) The FDD results from ARTeMIS Modal Pro for single damage case

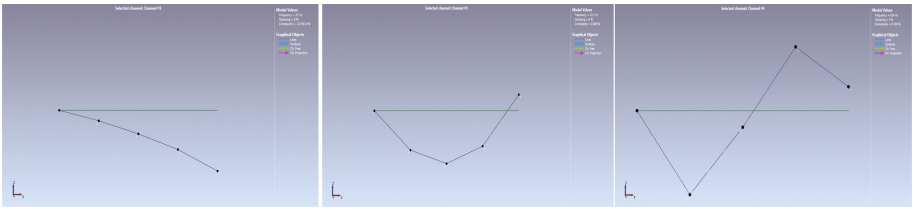

Fig. 5. Measured first (a), second (b) and third mode (c) shapes of the cantilever beam for 10% damage in element 3

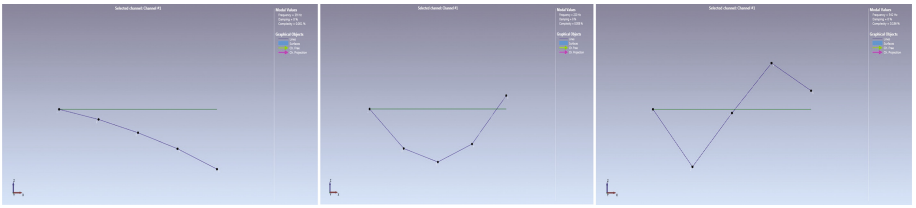

Fig. 6. Measured first (a), second (b) and third mode (**c**) shapes of the cantilever beam for 10% damage in element 3 and 4

The measured first three mode shapes for single element damage and double element damages are shown in Figs. 5 and 6 and also the damaged first three measured natural frequencies are shown in the Table 5. From the above measured mode shapes

Table 5. Measured first three natural frequencies (Hz) for 10% damage in single and double element damage

Modes	Natural frequency (Hz)		
	Undamaged	Single damage	Double element damage
First	38	37	39
Second	235	217	220
Third	556	552	542

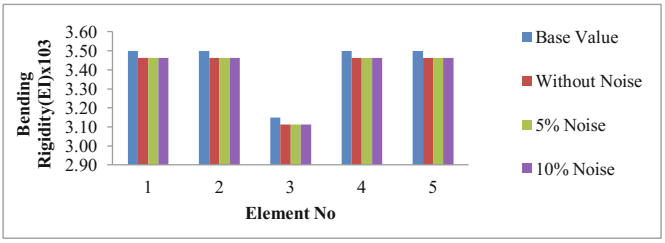

Fig. 7. True and the identified parameter (bending rigidity) (EI) for the damaged cantilever beam (10% single damage at element-3) for different noises using measured mode shapes, frequencies and modal strain energy

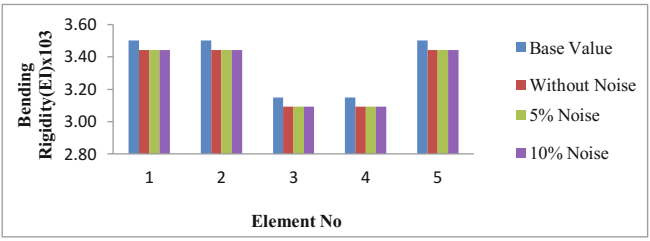

Fig. 8. True and the identified parameter (bending rigidity) (EI) for the damaged cantilever beam (10% double damage at element 3 and 4) for different noises using measured mode shapes, frequencies and modal strain energy

and the frequencies and modal strain energy damage identification is performed using inverse dynamic approach and shown in the Figs. 7 and 8.

2 Conclusions

The present investigation is focused on the structural health monitoring aspect, particularly the diagnosis of damage in terms of reduction of structural parameters of axial rigidity, bending rigidity and mass density using limited dynamic response data measured at a few selected locations. Equation error approach is employed in a finite element framework adopting statistical system identification technique. The uncertainty associated with the measurement is duly considered and the parametric study of the noise level, number of measurements etc. on the accuracy of the identification parameter is carried out. The damage at the element level is identified in a probabilistic manner by comparing the distributions of the identified structural parameters at the initial or undamaged and damaged states. Computational algorithms are developed and numerical examples are presented to establish the efficacy of the proposed method. An experimental study is also carried out to have an insight on a few basic aspects of modal testing and subsequent extraction of the modal data. The proposed method of structural health monitoring is validated with the experimentally obtained data. Based on the results of example studied, a few important conclusions may be drawn.

The proposed method is able to accurately identify the damage from limited number of noisy data. The condition of each element may be updated and monitored continuously as the measured data are available. It is noted that the accuracy of the proposed models increases with the increase of the number of measured modes and decreases with the increase of noise level. The experimental study with cantilever beams validates the proposed method and demonstrates the potential of the numerical model for its practical implementation.

References

Adam, R.D., Clawley, P., Pye, C.J., Stone, B.J.: A vibrating technique for non-destructively assessing the integrity of structures. J. Mech. Sci. **20**(2), 93–101 (1978)

Beck, J.L., Au, S.-K.: Monitoring structural health using a probabilistic measure. Comp.-Aided Civil and Infrastructural Engrg. **16**, 1–11 (2001)

Casas, J.R., Aparicio, A.P.: Structural damage identification from dynamic-test data. J. Struct. Engrg., ASCE **120**(8), 2437–2450 (1994)

Cornwell, P., Doebling, S.W., Farrar, C.R.: Application of the Strain Energy Damage Detection Method to Plate-Like Structures. (Anon, Ed.) J. Sound Vib. **224**(2), 359–374. (1999). doi:10.1006/jsvi.1999.2163, SEM, Bethel, CT, United States

Fox, R.L., Kapoor, M.P.: Rates of change of eigenvalues and eigenvectors. AIAA J. **6**(12), 2426–2429 (1968)

Katafygiotis, L.S., Papadimitriou, C., Lam, H-F.: A probabilistic approach to structural model updating. Soil Dyn. Earthquake Engrg. **17**, 495–507 (1998)

Sanayi, M., Onipede, O.: Damage assessment pf structures using static test data. AIAA J. **29**, 1174–1179 (1991)

Sanayi, M., McClain, J., Wadia-Fascetti, S., Santini, E.: Parameter Estimation Incorporating Modal data and Boundary Conditions. J. Struct. Engrg., ASCE **125**(9), 1048–1055 (1999)

Stubbs, N., Kim, J.-T.: Damage localization in structures without baseline modal parameters. AIAA J. **34**(8), 1644–1649 (1996)

Park, S., Kim, Y., Stubbs, N.: Nondestructive damage detection in large structures via vibration monitoring. Electron. J. Struct. Eng. **2**, 59–75 (2002)

Wang, D., Haldar, A.: Element-level system identification with unknown input. J. Eng. Mech. ASCE **120**(5), 159–176 (1994)

Xia, Y., Hao, H.: Statistical damage identification of structure with frequency changes. J. Sound Vib **263**, 853–870 (2003)

Yuen, K., Beck, J.L., Katafygiotis, L.S.: Efficient model identification and health monitoring methodology using incomplete modal data. J. Struct. Control Health Monit. **13**, 91–107 (2006)

Shi, Z.Y., Law, S.S., Zhang, L.M.: Structural damage localization from modal strain energy change. J. Sound Vib. **2185**, 825–844 (1998)

Carrasco, C.J., Osegueda, R.A., Ferregut, C.M., Grygier, M.: Damage localization in a space truss model using modal strain energy. In: Proceedings-SPIE the International Society for Optical Engineering, Orlando, FL, pp. 1786–1792 (1997)

Experimental Modal Properties of a Steel Arch Bridge During the Static Load Test

Fabrizio Gara[1(✉)], Vanni Nicoletti[1], Davide Roia[1], and Andrea Dall'Asta[2]

[1] Department of ICEA, Università Politecnica delle Marche, Ancona, Italy
f.gara@univpm.it
[2] School of Architecture and Design, University of Camerino, Ascoli Piceno, Italy

Abstract. This paper deals with the identification of the dynamic properties of a steel arch bridge located on the No. 77 main road, close to Macerata in central Italy. The main span of the bridge, of about 115 m, is formed by two inclined steel tubular arches that sustain the steel-concrete composite bridge deck by means of couples of hangers. During the static load test, before opening the bridge to traffic, an accelerometer array was installed over the bridge deck to evaluate the dynamic characteristics of the structure under different load conditions, in particular for bridge unloaded (before and after the load test) and for bridge loaded according to different load configurations obtained by positioning trucks over the bridge deck. Measurements of ambient vibrations, and operational modal analysis, were performed to estimate modal properties of the deck, namely natural frequencies and mode shapes. These experimental modal parameters determined at different loading phases were compared with the numerical ones obtained with the structural finite element model of the bridge. The dynamic interaction between bridge and trucks was also investigated by modeling the trucks as dynamic systems, i.e., not only in terms of added mass but also including their vertical and transversal stiffness. The obtained results show a good agreement between theoretical and experimental results, in terms of frequencies and mode shapes, both in the unloaded and loaded configuration; the first results on how different strategies of modelling trucks influence the modal parameters of the bridge are also discussed.

Keywords: Bridge dynamic testing · Modal identification · Operational modal analysis · Steel arch bridge · Truck-structure interaction

1 Introduction

Steel arch bridges are complex engineering structures that need to be designed and built with utmost care and accuracy due to their importance in the transportation network. In the recent years, in order to obtain a thorough assessment of these structures dynamic-based methods are increasingly used in conjunction with traditional static tests. These evaluations can be based on comparisons between experimental modal parameters and those predicted by the finite element (f.e.) structural models. In such a contest, in situ dynamic tests, based on ambient vibration measurements, are increasingly used to

© Springer International Publishing AG 2018
J.P. Conte et al. (eds.), *Experimental Vibration Analysis for Civil Structures*,
Lecture Notes in Civil Engineering 5, https://doi.org/10.1007/978-3-319-67443-8_64

identify the experimental values of the modal parameters of structures, namely the natural frequencies and mode shapes, which can be used for the validation of the structural f.e. model and for its calibration and updating. Updated models can be used for many purposes, among which the prediction of dynamic responses under new load scenarios, for damage identification, to design structural health monitoring systems, as well as for improved remaining life-time predictions [1–4]. However, the model updating procedures are not without uncertainties, since the hypotheses made on the structural model are manifold, e.g., those on geometry and on mechanical properties of materials. Uncertainties may greatly reduce if the updating procedures are based on several data set relevant to the same structure subjected to loading conditions enough different to produce significant differences of the dynamic properties. In this sense, in the case of bridges, static load tests required for opening to traffic represent a good opportunity to carry out the dynamic tests of the bridge under different loading conditions; in fact, in terms of mass, the maximum load can reach 10–15% of the bridge mass inducing therefore significant reductions of natural frequencies of the bridge and also differences in the relevant mode shapes. Obviously, dynamic tests carried out during the static load test, are also very useful to get real time monitored the structure during the load application so that any anomaly of the dynamic response can be soon observed and, eventually, the load test interrupted.

In this paper, the dynamic behavior of a half-through steel arch bridge during the standard static load test, is investigated. At first, a brief description of the structure is presented; then the dynamic properties of the main bridge are determined by means of ambient vibration tests and operational modal analysis (OMA) that allow the estimation of the natural frequencies and the relevant mode shapes. These experimental tests, which are basically focused on the characterization of the overall dynamic behavior of the main bridge deck, are performed during different phases of the static load test, in detail in the unloaded configuration and in some loaded configurations obtained by positioning trucks over the bridge deck. The experimental values of resonant frequencies and mode shapes are compared with the theoretical ones obtained from the f.e. model of the bridge developed for design purposes and then modified to take into account the real conditions of the bridge during the static and dynamic tests. The last part of the paper deals with the dynamic interaction between bridge and trucks used for the loading test. The trucks are modelled in terms of masses and stiffnesses on the basis of the results of vibration measurements carried out on a real truck. The analytical results, in terms of frequencies and mode shapes, obtained considering only the mass of the trucks are compared with those obtained including the stiffness of the trucks.

2 Bridge Description

The half-through steel arch bridge case study is located in the central of Italy, on the No. 77 main road, close to Macerata. The structure of the main bridge is composed by two inclined steel coupled arches and a steel-concrete composite deck 115 m long. The span is supported by couples of inclined pre-tensioned hangers that connect the arches with the transverse beams of the deck, which are wider than the concrete slab of the deck. Along the upstream side of the bridge there is a pedestrian walkway with

Fig. 1. (a) Main arch bridge; (b) approaching viaducts.

curvilinear shape. The bridge is supported by rubber bearings placed over four reinforced concrete basements founded on piles (Fig. 1a).

Two approaching viaducts connect both sides of the main bridge with the road. Each viaduct is 85 m long and consists of three spans, realized with a steel-concrete composite deck supported by two intermediate piers based on pile foundations and an abutment at the end (Fig. 1b).

The decks of the bridge and viaducts are formed by variable deep reinforced concrete slabs supported on two main longitudinal steel beams with double T cross section and variable height.

Figure 2 shows a global bridge layout with some construction details. For more details, please refer to [5].

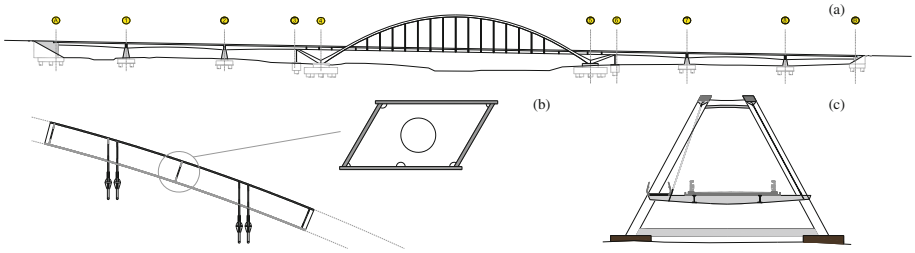

Fig. 2. (a) Global view of the structure; (b) rhomboidal cross section of steel arches; (c) transversal section of the structure.

3 Dynamic Tests During Static Load Test

The monitoring of the dynamic properties of the structure, namely natural frequencies and mode shapes, during the different load phases of the static load test, may be useful to understand how the dynamic behavior of the structure changes as a function of the applied load; it can also be useful to reveal the presence of damages due to the load application. Furthermore, by comparing the experimental modal parameters, obtained before, during and after the static load test, with the numerical ones it can be possible to

verify the reliability of the finite element model developed for the bridge design as well as the correct construction of the structure.

The dynamic tests performed consist of ambient vibration measurements of the deck of the arch bridge; the modal parameters of the deck are assessed through OMA based on the measured accelerations. These tests were performed under several load configurations, but, in this paper, only the result of ambient vibration tests in the unloaded structure (U) and the load configuration 1 (C1) (Fig. 3a), are discussed. The latter configuration was obtained by positioning ten fully loaded trucks on the upstream side of the bridge. Figure 3b shows a global view of the bridge during the load configuration C1.

Figure 4 displays the arrangement of the sensors along the deck of the arch bridge:

- three sensors positioned in transverse direction;
- four sensors on the upstream side and four sensors on the downstream side of the bridge placed in vertical direction;
- one sensor in half of the bridge span positioned in longitudinal direction.

Fig. 3. (a) Layout of the load configuration C1; (b) load configuration C1 during static load test.

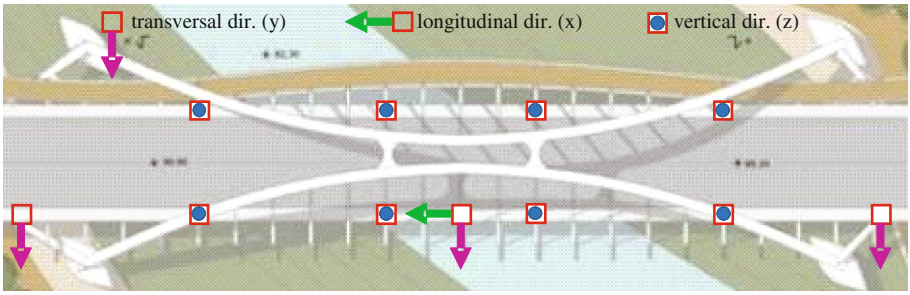

Fig. 4. Arrangement of the accelerometers along the bridge deck during static load test.

4 Numerical Modelling

The dynamic analyses of the bridge are performed using a three-dimensional finite element model developed with SAP2000 software [6] (Fig. 5). This model includes the arch bridge and both the approaching viaducts.

The arches, hangers, bracings, transverse beams and the two main longitudinal beams are modelled with elastic beam elements. To reproduce the actual length of deformable section of each beam element, rigid elements are introduced at their ends.

The reinforced concrete (r.c.) slabs of the deck of bridge, viaducts and pedestrian walkway are modelled in their real position by means of shell elements having different thickness, according with the design requirements. The barycentric axis of the longitudinal beams and the barycentric plane of the slabs have an eccentricity in height; therefore, to connect these elements, rigid frame elements are introduced. The concrete stiffness is calculated considering the uncracking condition and increasing the mean value of the elastic modulus, of about 10%, to take into account the dynamic properties of the material.

Furthermore, also the stiffness contribution given by the asphalt concrete is considered by further increasing the elastic modulus of the r.c. slabs.

Piers and foundations are not modelled and therefore the steel arches and the deck of the approaching viaducts are restrained by means of vertical supports; to model the horizontal stiffness of the seismic isolator, two elastic springs are introduced in each support, one in transverse direction and another one in longitudinal direction.

The masses of the non-structural elements are calculated and then considered like added masses, while the masses of the elements modelled are automatically taken into account by the software, depending on their material properties and geometry.

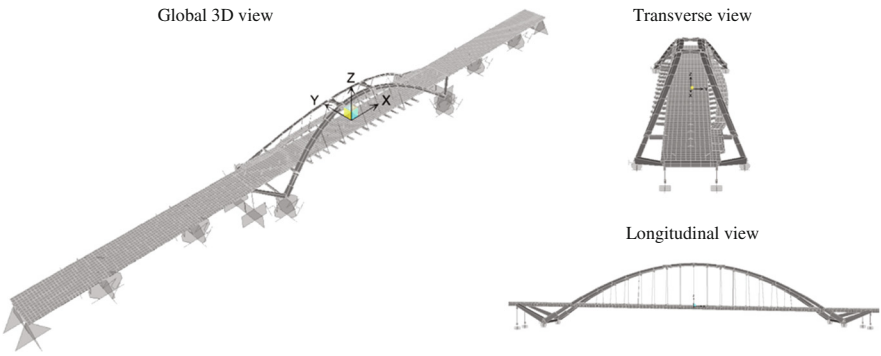

Fig. 5. Three-dimensional finite element model of the bridge.

5 Results

In this section the experimental and the numerical results, in terms of frequencies and mode shapes, are reported and compared, by considering the unloaded configuration (U) and the load configuration C1. In particular, for the loaded configuration C1, the trucks are considered only in terms of added masses, neglecting their stiffness, as usual in the practice.

To get the modal parameters of the bridge, a modal analysis with eigen-vectors is carried out.

In Table 1 the experimental and numerical resonance frequencies pertinent to the structure under two different load configurations (unloaded configuration and load configuration 1) are reported. In Fig. 6 the first six analytical mode shapes (the first three bending mode shapes, the first torsional mode shape and the first two transversal mode shapes) are displayed, considering the same load configurations previously mentioned. In the same figure the experimental values are also reported to facilitate a comparison between theoretical and experimental results.

Table 1. Experimental and numerical resonance frequencies for the unloaded configuration U and the load configuration C1.

Natural frequencies (Hz)				Shape
Unloaded config. (U)		Load config. (C1)		
Experimental	Numerical	Experimental	Numerical	
1.18	1.19	1.03	1.07	1st bending
1.45	1.57	1.43	1.45	1st transverse
1.89	1.94	1.76	1.67	2nd bending
2.22	2.20	2.09	2.10	3rd bending
/	3.07	2.37	2.97	1st torsion
2.81	2.81	2.71	2.77	2nd transverse

As expected, due to the added mass of the trucks, the experimental and the numerical values of the frequencies relevant to the loaded configuration are lower than those relevant to the unloaded bridge; the differences are higher for bending modes than for transverse modes.

In order to compare the mode shapes identified experimentally with those obtained numerically, for both the configuration U and C1, the modal assurance criterion (MAC) index is calculated. This index indicates how well the analytical mode shapes fit the experimental ones [7]; the closer the value approaches 1, the more similar are the mode shapes. Figure 7 portrays the MAC values between the experimental and numerical mode shapes for the unloaded configuration U and the load configuration C1, respectively. The corresponding modes (diagonal entries) have high MAC values, indicating a very good agreement between experimental and numerical mode shapes.

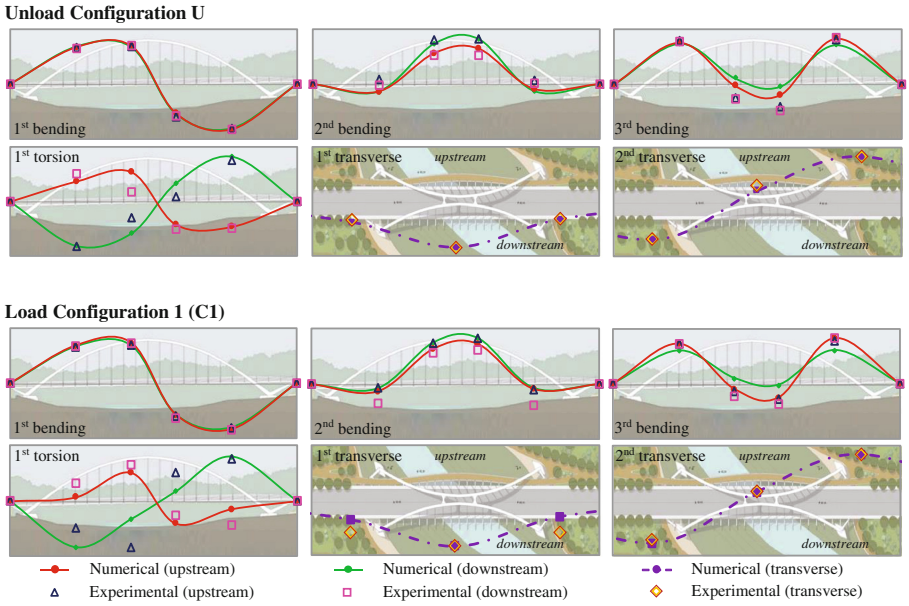

Fig. 6. Analytical and experimental mode shapes for the unloaded configuration U and the load configuration C1.

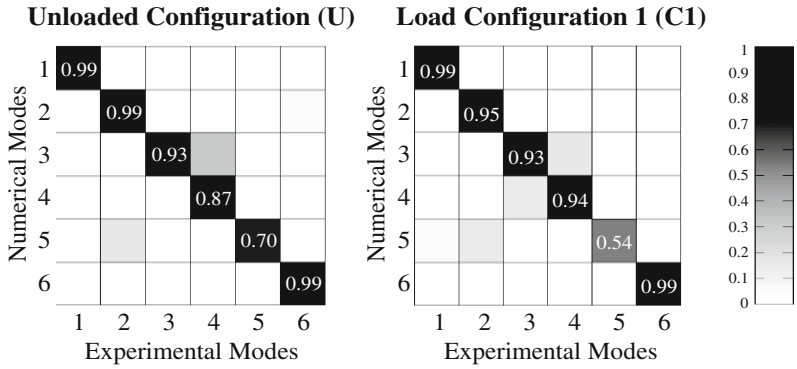

Fig. 7. MAC between the experimental and numerical mode shapes for the unloaded configuration U and the load configuration C1.

6 Refined F.E. Model Considering the Dynamic Interaction Between Bridge and Trucks

Modeling the dynamic vehicle-bridge interaction is very complex; the system is composed of two dynamic sub-systems interacting with each other via the contact between the vehicle wheels and the bridge surface. Moreover, being the first natural

frequencies of the bridge and the truck close together, this interaction may be significant. To investigate this topic, a simplified model of the truck is developed starting from a general model obtained from that proposed in [8]. A truck can be modelled with a dynamic system having several degrees of freedom: a vertical displacement for each wheel (or couples of wheels) and the displacements of the body, namely the bounce, the pitch, the roll and the transverse one. The mass of the wheels and axle assembly have to be considered as well as the body mass, supported on a suspension over the axle assembly, and the two rotational moments of inertia for body pitch and roll. The stiffness and damping due to suspensions should be considered as well as the stiffness of each tire that can be modelled with one vertical spring and one horizontal spring. However, considering that during the static load test the trucks are still and the energy level of the measured vibrations is very low, some simplifying assumptions on the dynamic behavior of a truck can be assumed. In particular, the damping provided by the shock absorbers can be neglected.

To better understand the dynamic behavior of a truck and to determine the spring stiffness of the suspensions and the tires, an experimental test on a single truck was carried out. The truck studied had similar features to the typical truck used for the static load test of the arch bridge. Two accelerometers were positioned inside the rim of a rear wheel, one in vertical direction and one in horizontal direction (Fig. 8). The modal parameters of the vehicle were estimated by means of OMA based on vibration measurements of the truck and, from the data obtained with these tests it was possible to estimate the first natural frequencies of the vehicle for vertical and transverse displacements, that are 2.93 and 3.79 Hz, respectively (Fig. 9).

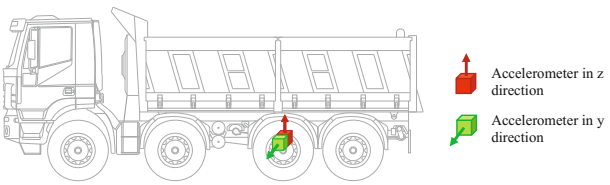

Fig. 8. Location of the accelerometers on the truck.

To investigate the dynamic interaction between bridge and trucks, these latter are modelled into the f.e. model not only in terms of added masses, but also considering their stiffness. The single truck is modelled by means of four lumped masses representing the left and right loading imprints in correspondence of the two front axles and the two rear axles. Each lumped mass is connected to the deck of the bridge through two elastic links, one in vertical direction and the other one in horizontal direction, representing the portion of the stiffness of the truck in both directions. Only one spring is considered in the vertical direction, instead of two, to simplify the numerical model and to have a smaller number of variables. To estimate the stiffness of the springs simulating the truck stiffness in vertical and transverse direction, the simple formula of the natural frequency for one d.o.f. systems is used.

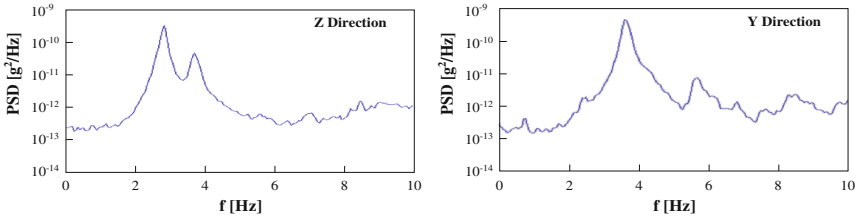

Fig. 9. Power spectral density (PSD) of signals registered by the two sensors located over the rim of the truck rear wheel.

Table 2 shows the comparison between the first six values of resonance frequencies obtained experimentally and numerically with the model above described for the load configuration C1; Fig. 10 displays the relevant mode shapes and Fig. 11 the MAC. The comparison shows a good agreement; it can be noted that this agreement is better for some natural frequencies and worse for some other frequencies than in the case of the model considering trucks only as masses. However, it is interesting to observe that a significant difference, in terms of both natural frequencies and mode shapes, is obtained with the two f.e. models. A more refined modeling of the trucks and a better calibration of the bridge should be considered to better investigate the phenomena involved.

Table 2. Analytical and experimental natural frequencies: load configuration C1.

Natural frequencies (Hz)		Shape
Experimental	Numerical	
1.03	1.05	1st bending
1.43	1.43	1st transverse
1.76	1.59	2nd bending
2.09	2.01	3rd bending
2.37	2.67	1st torsion
2.71	2.74	2nd transverse

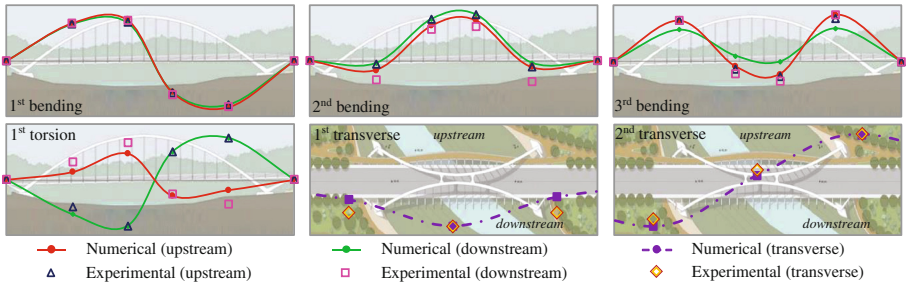

Fig. 10. Analytical and experimental mode shapes for the load configuration C1.

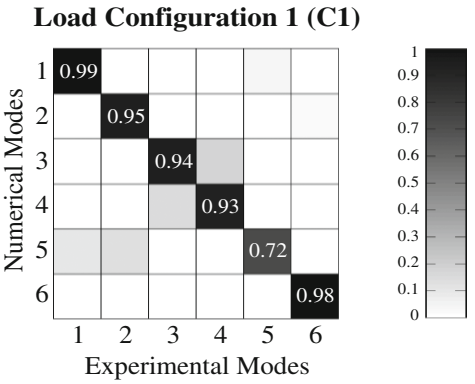

Fig. 11. MAC between the experimental and numerical mode shapes for the load configuration C1.

7 Conclusions

This paper deals with the dynamic identification of a steel arch bridge with couples of hangers that sustain a steel-concrete composite bridge deck. Based on ambient vibration tests, the frequencies and the mode shapes of the first six global modes of vibration of the main bridge have been identified.

Thanks to these dynamic tests it is possible to observe how the added masses over the span of the bridge produce some modifications on the modal parameters of the structure. Of particular interest is the reduction of the frequencies due to the mass addition.

The numerical modal parameters relating the unloaded bridge (U) are in good accordance with the experimental ones determined using the data acquired before the static load test. It follows that the f.e. model developed for the bridge design and then upgraded, is reliable for the prediction of the dynamic behavior of the structure.

Regarding the load configuration C1, obtained considering the trucks only in terms of added masses, the numerical frequencies and mode shapes match quite well the experimental ones, the latter obtained during the static load test. This good agreement was crucial, from a practical point of view, for the final judgment on the bridge behavior that must be asserted on the basis of the final load test.

To consider the truck-bridge interaction, a refined model of the bridge including the trucks not only in terms of masses but also in terms of stiffness has been developed, based on an experimental test carried out on a real truck. The numerical results relevant to the loaded bridge are in good agreement, even if still not perfect, with those obtained experimentally. The most interesting aspect is that significant differences between theoretical frequencies and mode shapes are obtained with two f.e. models; this means that the effects of the dynamic interaction between bridge and trucks can not be negligible when the results of static load tests have to be accurately interpreted.

References

1. Brownjohn, J., Xia, P.: Dynamic assessment of curved cable-stayed bridge by model updating. J. Struct. Eng. **126**(2), 252–260 (2000)
2. Cunha, A., Caetano, E., Magalhães, F., Moutinho, C.: Recent perspectives in dynamic testing and monitoring of bridges. Struct. Control Health Monit. **20**(6), 853–877 (2012)
3. Ribeiro, D., Calçada, R., Delgado, R., Brehm, M., Zabel, V.: Finite element model updating of a bowstring-arch railway bridge based on experimental modal parameters. Eng. Struct. **40**, 413–435 (2012)
4. Dezi, L., Gara, F., Roia, D., Leoni, G.: Experimental and numerical modal analysis of a historical masonry bridge. In: 16th International Brick and Block Masonry Conference, Padova (2016)
5. Gara, F., Nicoletti, V., Roia, D., Dezi, L., Dall'Asta, A.: Dynamic monitoring of an isolated steel arch bridge during static load test. In: Proceedings of IEEE Workshop on Environmental Energy and Structural Monitoring Systems (2016)
6. SAP2000 advanced (v14.1.0): Static and Dynamic Finite Element Analysis of Structures. CSI Computer & Structures Inc., Berkeley (2009)
7. Friswell, M., Mottershead, J.E.: Finite Element Model Updating in Structural Dynamics. Kluwer Academic Publishers, Dordrecht (1995)
8. Prendergast, L.J., Hester, D., Gavin, K.: Determining the presence of scour around bridge foundations using vehicle-induced vibrations. J. Bridge Eng. **21**(10), 04016065 (2016)

Evaluation of Vibration Problems in Existing Office Buildings

Matthew A. Pavelchak(✉)

Diagnostics Group, Walter P Moore and Associates, Inc.,, Houston, TX, USA
mpavelchak@walterpmoore.com

Abstract. Commercial office buildings are subject to many significant modifications over their design life. These modifications often include revisions to architectural features, changes in occupancy, and replacement of mechanical systems and are typically completed without formal consideration of vibration performance. These ongoing modifications impact the vibration level of service experienced by the occupants and can cause significant owner and tenant frustrations.

Architectural renovations and changes in tenant build out can significantly alter the nature of walking excitation and system damping. The detailing of tenant build out partitions has a big impact not only on the system damping but also the susceptibility of vibration induced noise within the partition systems. Changes in occupancy or intensity of use can also impact user expectations and comfort within the built environment. The degradation of existing building mechanical systems or the replacement of these systems can also greatly impact the vibration level of service within an existing structure. These impacts often catch building owners and facility managers off guard due to a lack of knowledge regarding vibration performance. The objective of this paper is to explore the process of vibration source detection, system evaluation, and rehabilitation through recent case studies. These case studies will explore the onsite evaluation procedure used including client interviews, testing, and evaluation of excitation sources as well as considerations used for detailing of remedial measures.

Keywords: Vibration testing · Source detection · System evaluation · Human perception · Rehabilitation

1 Introduction

A commercial office building may experience dozens of build outs, renovations, and divisions over its service life. The generic office floor plate can be fitted out for high density occupancies such as call centers, or low density uses such as law offices. Within many commercial buildings the tenant finishes vary widely in terms of function, style, and weight. Building owners and managers are always seeking to maximize the flexibility of their commercial space to appeal to the broadest range of potential tenants. The overarching trend for most businesses is toward open concept office spaces and digital offices. In many industries compression of office spaces to increase employee density and thereby minimize costs is also a major trend.

© Springer International Publishing AG 2018
J.P. Conte et al. (eds.), *Experimental Vibration Analysis for Civil Structures*,
Lecture Notes in Civil Engineering 5, https://doi.org/10.1007/978-3-319-67443-8_65

All of these factors related to how commercial office spaces are finished and utilized can impact the perceived vibration performance by the building occupants. Often these building modifications are made without any thought or knowledge related to the properties of the structural system or the potential vibration performance issues. However, the properties of the underlying structural system can have an important impact on the potential success of various office fit outs. This paper documents some important considerations when planning, evaluating, or troubleshooting bothersome vibration performance in office occupancies.

2 Factors Effecting Vibration Performance

2.1 Structural System

The most fundamental aspect which will impact the vibration performance of a potential office layout is the structural system within the underlying building and its inherent properties. A wide variety of systems have been used over time in different regions but the most common systems are:

- Steel joists supporting concrete slabs;
- Composite steel framing systems;
- Concrete slab and beam systems; and
- Concrete pan-joist systems.

While vibration performance can vary widely within each system type, the systems are generally listed above from lowest to highest level of service for typical configurations. When considering office renovations is it important to document the nature of the existing structural framing which can provide some insight into the types of concerns that may arise with different office configurations.

2.2 Partition Design

After the inherent properties of the structural system, the design and detailing of partitions is often the next most important aspect of how a space may be perceived by future tenants. Partition type and density varies widely in different office configurations from modular cubicles to full height partitions. Increasingly offices may have a combination of several different partition types within the same space. Partition design is important because they can have a significant impact on system damping and on vibration generated noise. One of the common causes of tenant vibration perception complaints is poor partition detailing and construction.

As detailed in the case studies to follow, the combination of lively floor slabs and flimsy partitions can cause quick and widespread tenant complaints. Modular or custom partitions which are loosely fitted and where individual members can move under floor motions often cause noise emission under low to moderate floor vibrations and can be an important driver in both tenant perception and complaints. This can be particularly bothersome for systems that involve glass either as a divider on the top of cubicle walls

or built into drywall assemblies. The introduction of audible noise can amplify human perception and annoyance with even low level vibration events.

Another important consideration in partition design is the level of damping that it can provide to the overall system. This level of damping contribution is highly dependent on the detailing of the partition systems. Generally, drywall partitions which extend the full story height (slab to slab) will provide the most damping to the system and can partially mobilize the slab on the level above during vibration events. As we continue to see more open concept office spaces, older office spaces are often remodeled without consideration of the impact that removal of partitions will have on the overall system performance. The author has been involved in several recent investigations where owners ended up restoring a portion of the full height partitions when satisfactory performance could not be achieved with the initial open concept design.

2.3 Raised Access Flooring

Raised access flooring is almost ubiquitous in data center applications but is also used in some open concept office environments. It can add significant flexibility in the routing of utilities within the field of the floor and is sometimes used as a plenum for the supply forced air service. While the use of raised access flooring alone does not present a concern, in the author's experience, the commonly installed systems tend to amplify the underlying structural vibrations slightly. It is important to keep this behavior in mind, particularly when dealing with lively floor systems.

3 Case Study: Open Concept Office with Steel Joist Support Framing

3.1 Background

The tenants of a low-rise office building in Tampa, Florida began complaining of bothersome floor vibrations shortly after moving into a new office space on the second level of an existing office building. The building was constructed in 1984 and the building management had not recorded any complaints in the first twenty years of service. The building interior had been renovated prior to the current tenants moving in. The renovation scope of work did not include an evaluation of the building structural system for vibration performance. The tenant complaints were related to both perception of bothersome vibrations attributed to footfall excitation but also in relation to vibration induced noise in the partition systems.

Review of the completed project revealed that the typical office building floor system consisted of steel joists with concrete slab on metal deck. The renovated office layout consisted of an open floor plan in the main field of the floor with modular cubical workstations throughout and isolated clusters of managerial offices and conference rooms in select areas. Complaints had been received throughout, but the most frequent complaints came from the occupants of the modular workstations. The building management wanted options for improving the vibration performance without significantly modifying the new interior design.

3.2 System Evaluation

The original (1984) interior design featured full height partitions throughout. While the original partitions could not be observed, the contractor indicated that they had extended from slab-to-slab with the studs and drywall in firm contact with the slab above. The new design featured some partition walls which extended to the top of the suspended ceiling system and typically had intermittent braces to the slab above for lateral stability but were classified as partial height partitions. Throughout the typical floor plate modular workstations were used with occasional accent "spine" walls. A typical workstation layout is shown in Fig. 1.

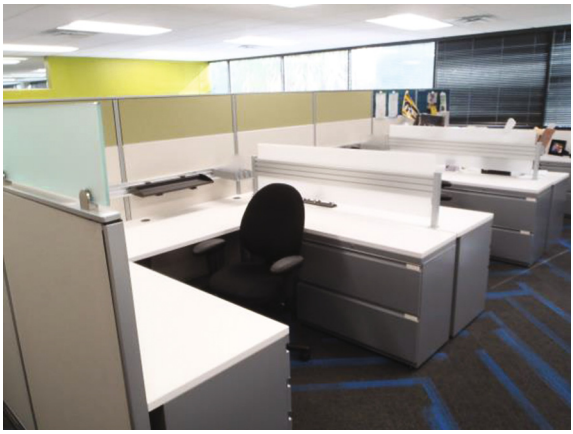

Fig. 1. Typical office layout.

3.3 Testing and Results

Accelerometers were installed at three locations throughout the floor (two locations in the open concept areas, and one location near managerial offices with partial height partitions). Data was recorded at each of the locations during ambient tenant walking excitation, coordinated walking exercises and during coordinated bobbing. It was immediately evident that the floor was lively under footfall excitation. Typical walking induced vibration results with two walkers are shown in Fig. 2 along with the American Institute of Steel Construction (AISC) Design Guide 11 (DG11) [1] criteria for offices and residences. While the vibrations were perceptible the noise emissions from the partition systems greatly added to the level of perceptibility and annoyance throughout the day. The partitions contained a number of loosely held metal and glass components which were easily excited by the floor movements.

The natural frequency of the floor bays was found to vary between 6.0–6.5 Hz at the locations tested. Analysis of the coordinated bobbing excitation events was utilized to estimate the system damping using the logarithmic decrement method evaluated over eight successive oscillations (Fig. 3). This allowed for comparison of the damping characteristics of open concept areas and areas with partial height partitions. The results

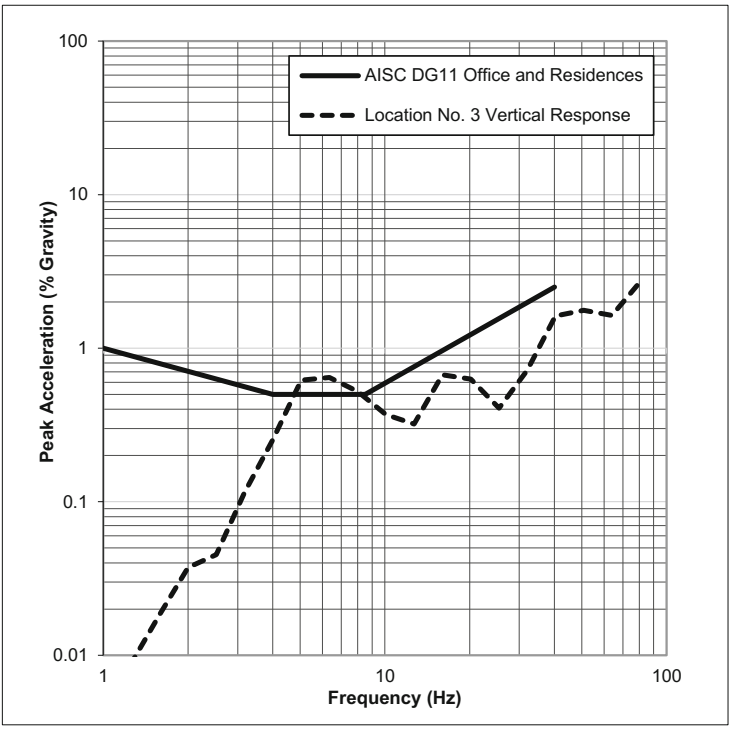

Fig. 2. Representative walking excitation response (2 walkers).

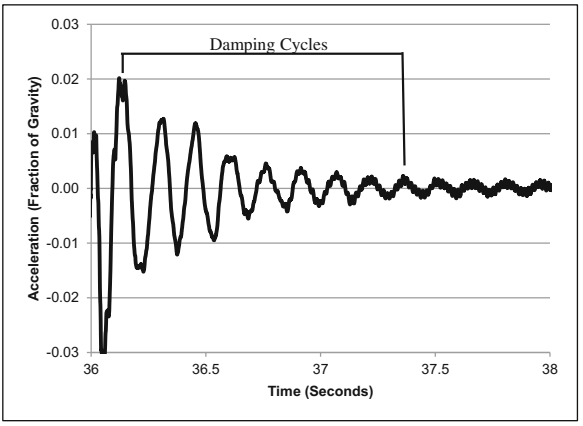

Fig. 3. System damping.

Table 1. Comparison of vibration characteristics.

	Peak response with two walkers	Natural frequency	Damping ratio
Location with partial height partitions	0.59%g	6.5Hz	4.75%
Open concept area	0.64%g	6.0Hz	2.80%

of this study are included in Table 1. The partial height partitions significantly increased the inherent system damping by 1.7 times that of the open concept areas. While the performance was not acceptable anywhere on the floor plate, the results were used to demonstrate the importance of partitions.

3.4 Summary and Discussion

A number of potential interventions were considered in order to address the tenant complaints including stiffening the floor system, adding dampers, modifying the walking paths throughout the space, and modifying the partitions. Based on the relative cost and disruption associated with each alternate, the building management elected to modify the existing partitions to increase the inherent damping of the floor system and improve overall performance. This was accomplished through modification of the existing partial height partitions into full height partitions (with no visual impact since the existing partitions extended to the suspended ceiling system) and replacement of select modular cubical walls with full height partitions. Through these modifications the building management was able to achieve satisfactory performance for their tenants.

This case study highlights the importance of partition design and layout to the overall performance of an office space and the significant impact partitions can have on inherent damping within the floor system.

4 Case Study: Aging Mechanical Systems

4.1 Background

The tenants of a high-rise office tower in Houston, Texas began reporting bothersome vibrations in select office workstations and in portions of the women's restroom on Level 28. The building was constructed in the mid 1980's and did not have a record of bothersome vibrations. The tenant reports were inconsistent about the return interval of the vibrations events and their typical duration but it was believed the events were closely spaced and lasted up to 1 h. Additionally, the two principal areas of where complaints were being generated were not adjacent to one another.

4.2 System Evaluation

The typical floor framing within the tower was composite steel framing with concrete on metal deck and the existing tenant interior build out was estimated to be more than 10 years old. In the proceeding months the tenant office manager and the building manager had worked to try to identify likely sources of vibrations within the space but were unable to determine the source(s). Two of the office occupants were complaining regularly of vibration events while others were unaffected and many employees had reported feeling intermittent vibrations within the women's restroom.

4.3 Testing and Results

Accelerometers were initially installed within the two offices where events had been reported as well as one additional location where not complaints had been reported. Testing over several typical days indicated that both office spaces where complaints had been received were experiencing significant intermittent vibration events with high frequency content as shown in Fig. 4 which includes the AISC DG11/ISO curve for steady state vibrations [1]. The frequency content and duration of the measured events pointed to a mechanical source of vibration. Interestingly, the third accelerometer which had been installed between the two areas where complaints were received did not indicate the presence of any excessive vibration events.

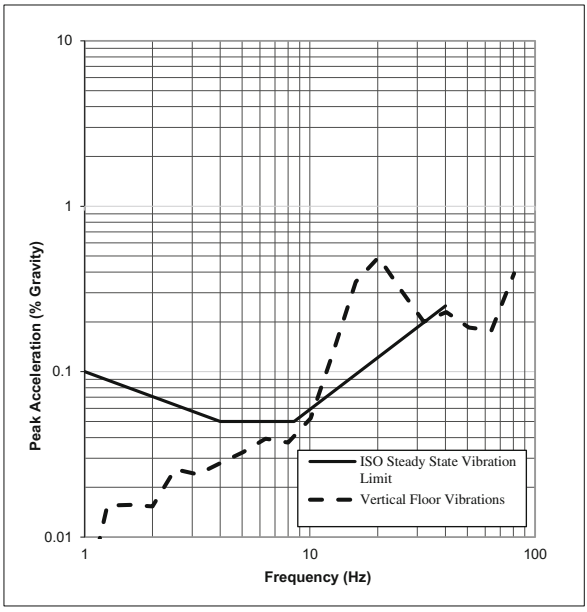

Fig. 4. Representative floor vibration results.

Since the two areas of complaints were not located in close proximity and because the vibration events at each location did not occur simultaneously, the possibility of two independent vibration sources was considered. Working with the building management, the mechanical equipment on the floor was systematically evaluated and two separate excitation sources were identified within the floor; water pumps supplying the upper floors and a door mounted server rack air conditioning unit owned by the tenant. Each was producing vibrations which were transmitted to one of the offices where complaints were reported.

Additional vibration data was collected at each location to evaluate the level of vibration transmission from the mechanical equipment into the underlying structure. Accelerometers were placed on a typical pump base plate and on the structural floor directly adjacent as shown in Fig. 5. Similar testing was performed on the frame of the server rack and the adjacent floor slab. The results of this testing allowed for documentation of the transmissibility of the mechanical vibrations through the existing isolators as shown in Fig. 6 and Table 2 for the pump.

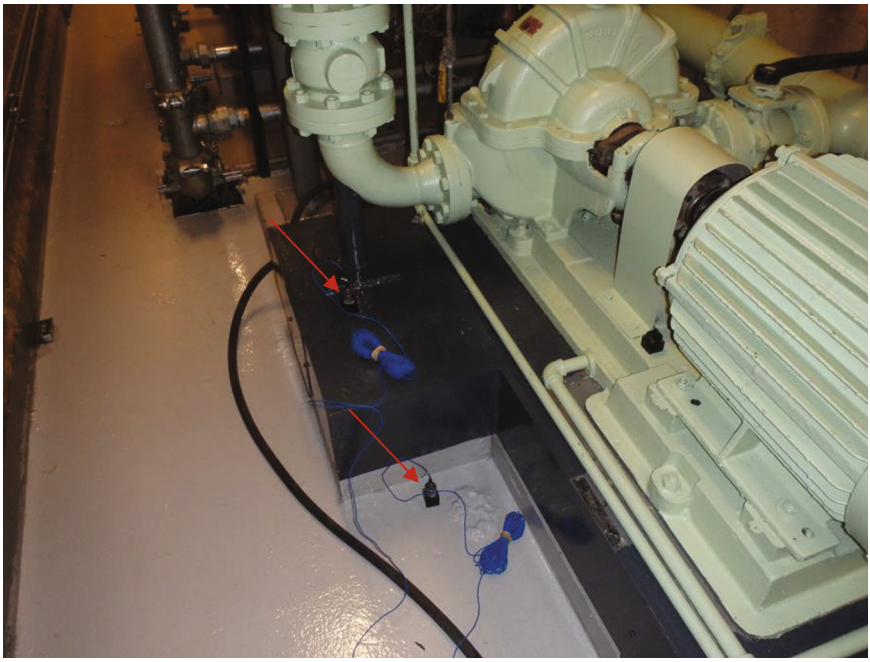

Fig. 5. Transmissibility testing at the pump housing.

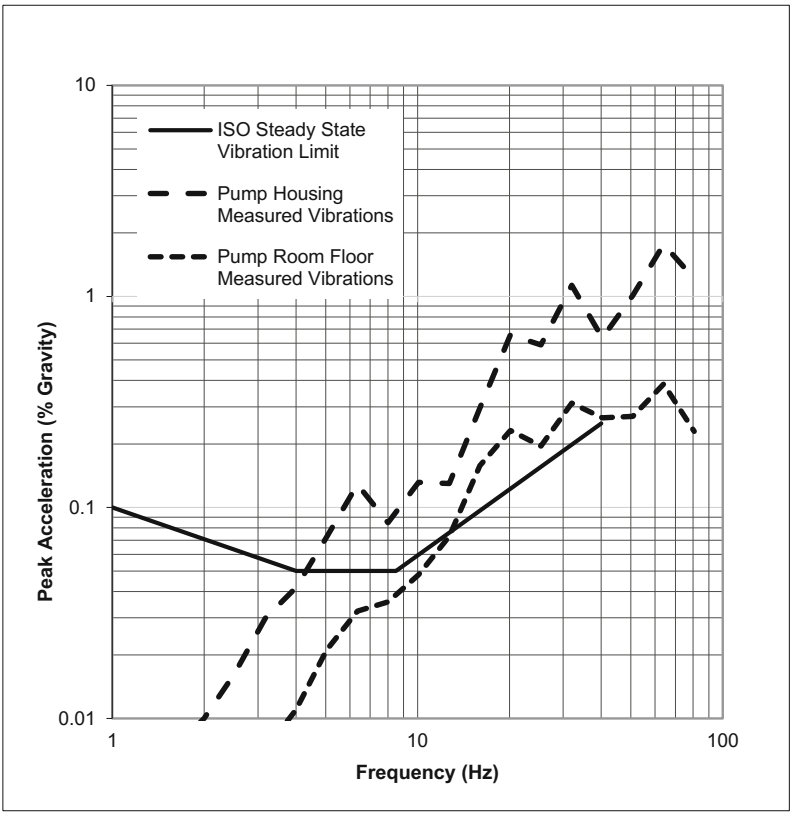

Fig. 6. Vibration data from transmissibility test.

4.4 Summary and Discussion

The transmissibility data prepared for both the water pumps and the air conditioning unit were then used to direct improvements to the existing systems. A mechanical electrical and plumbing (MEP) engineer was retained to recommend steps to overhaul the aging pumps to minimize their vibration excitation while specifying a more robust base isolation system. The tenant took similar steps to address the vibration excitation caused by their air conditioning unit.

This case study highlights the role that aging mechanical systems can have in generating bothersome vibrations as well as the complexity of troubleshooting vibration complaints within building environments which contain many different possible excitation sources.

Table 2. Transmissibility of pump housing vibration to the structural floor.

Frequency band (Hz)	Pump housing peak acceleration (% Gravity)	Pump room floor peak acceleration (% Gravity)	Percent transmissibility
1	0.002	0.001	31%
1.26	0.004	0.001	30%
1.59	0.007	0.003	40%
2	0.010	0.004	40%
2.52	0.016	0.005	30%
3.17	0.030	0.007	24%
4	0.042	0.011	26%
5.04	0.072	0.021	29%
6.35	0.129	0.032	25%
8	0.085	0.036	42%
10.08	0.131	0.048	36%
12.7	0.130	0.073	56%
16	0.296	0.158	53%
20.16	0.659	0.232	35%
25.4	0.589	0.195	33%
32	1.131	0.312	28%
40.32	0.636	0.266	42%
50.8	1.010	0.270	27%
64	1.764	0.384	22%
80.63	1.214	0.229	19%

5 Conclusions

These case studies explore important concepts in understanding the long term performance of office buildings. These structures are often subject to vibration excitation sources which vary significantly overtime as mechanical systems are added, modified, and age in place. Additionally the functional and build out changes which are common for these properties can materially impact the level of service imparted to tenants. The presence of many excitation sources within each level can further complicate identification and analysis of bothersome vibration events.

Reference

1. Murray, T.M., Allen, D.E., Ungar, E.E.: Design Guide 11: Floor Vibrations due to Human Activity. American Institute of Steel Construction Inc., USA (2003)

Post-earthquake Field Measurement-Based System Identification and Finite Element Modeling of an 18-Story Masonry-Infilled RC Building

Mohammed A. Mohammed[1], Hanshun Yu[2], Andre Furtado[3], Andre R. Barbosa[1(✉)], Babak Moaveni[2], Humberto Varum[3], Hugo Rodrigues[4], Nelson Vila-Pouca[3], and Richard L. Wood[5]

[1] School of Civil and Construction Engineering, Oregon State University, Corvallis, USA
andre.barbosa@oregonstate.edu
[2] Department of Civil and Environmental Engineering, Tufts University, Boston, USA
[3] CONSTRUCT-LESE, Faculty of Engineering (FEUP), University of Porto, Porto, Portugal
[4] RISCO, School of Technology and Management, Polytechnic Institute of Leiria, Leiria, Portugal
[5] Department of Civil Engineering, University of Nebraska-Lincoln, Lincoln, USA

Abstract. This paper describes the system identification and finite element modeling of an 18-story unreinforced masonry infilled reinforced concrete building that was damaged following the 2015 M7.8 Gorkha Earthquake, Nepal, and subsequent aftershocks. The identification is performed using the ambient vibration data collected using broadband seismometers and accelerometers. The new apartment building was seismically designed using Indian Codes and Standards. At the time of the earthquake mainshock, its construction was complete as the building was being finalized for handover to the clients. Following the earthquake mainshock and aftershocks, most of the damage to the building was observed in the non-structural masonry infill walls, while minor damage was observed in the diaphragms and elevator core link beams on lower stories. The ambient vibration response of the damaged building was recorded using either: (1) fifteen accelerometers at different setups, or (2) three seismometers. The dynamic characteristics of interest are the modal parameters of the first few lateral and torsional vibration modes. The modal identification results from the two measurement systems are compared to provide insight into the uncertainty of the results. In addition, two finite element models of the structure are developed from the information provided in the design documentation of the building. The models are tuned to match the identified modal parameters and compared with each other. Special attention is placed on the stiffness of structural and non-structural elements.

Keywords: Ambient vibration testing · Finite element modeling · Gorkha earthquake · Structural health monitoring · System identification

© Springer International Publishing AG 2018
J.P. Conte et al. (eds.), *Experimental Vibration Analysis for Civil Structures*,
Lecture Notes in Civil Engineering 5, https://doi.org/10.1007/978-3-319-67443-8_66

1 Introduction

A M7.8 shallow earthquake hit Nepal on April 25, 2015 with the epicenter located 80 km Northwest of Kathmandu, which is the capital of Nepal. More than hundred aftershocks occurred after the mainshock (Fig. 1), including M7.3 and M6.3 earthquakes on May 12, 2015 [1]. The mainshock ground motion accelerograms (Fig. 2a, b) were recorded at USGS station in Kathmandu (KATNP, 27.71N, 85.31E), and the recorded horizontal peak ground acceleration was 0.164 g in the North–South direction. Figure 2c shows the response spectrum of the two horizontal components of the recorded ground motion. As it can be seen in the figure, the spectral acceleration of the horizontal component is more than 0.6 g in the short period range, and there is a large spectral magnification in the long period range. This earthquake killed more than 8000 people and destroyed more than 500,000 buildings and many more were damaged to different levels of damage [1, 2].

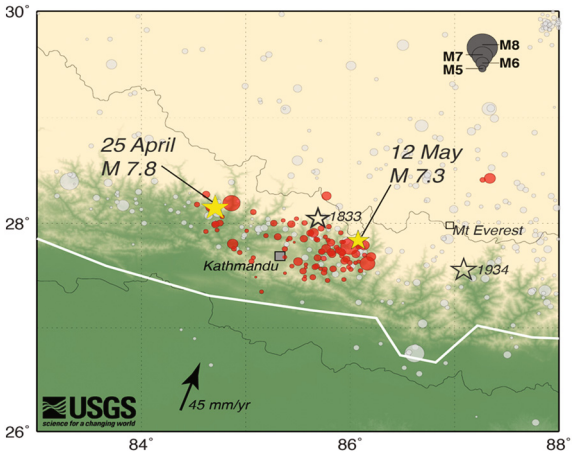

Fig. 1. Nepal 25 April 2015 earthquake and aftershock earthquakes distribution.

Structural identification is an important tool to estimate the dynamic properties of structures and to predict the changes that can occur over time in aging structures. Using multiple recorded responses of full scale structures that have been damaged by real natural disasters is an essential and effective way to validate the different methods of structural identification [3]. System identification by using measured vibration data is a method used with increased frequency in the recent years to evaluate the performance of existing structures and as part of the basic information needed for finite element model updating. The ambient vibration test is considered as one of the most attractive techniques to carry out the system identification of structures, this mainly because of the low economical cost and fast installation of the system that can be used to perform the test in the field.

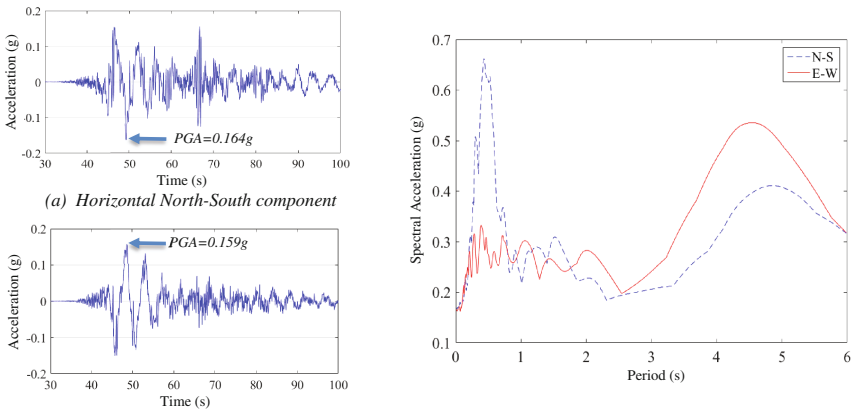

Fig. 2. Horizontal acceleration time histories and response spectra of the KATNP (27.71°N, 85.31°E) during the M7.8 Gorkha 2015 Nepal earthquake.

The main purpose of this paper is to describe the system identification that was performed on an 18-story building that was damaged during the Gorkha 2015 Nepal earthquake. The system identification for the building is carried out using two groups of ambient vibration data that were collected using two systems independently: (1) accelerometers, or (2) seismometers. A comparison between the results of the modal parameters (natural frequencies and damping ratios) by the two measurements is presented to improve our understanding on the differences in the results of the two systems. Moreover, two linear elastic finite element (FE) models are developed to predict the dynamic characteristics of the building. The dynamic characteristics are then compared with the ones identified from the ambient vibration testing. Lastly, the numerical models are calibrated by assigning different reduction factors for the masonry infill walls to account for the damage that was observed following the earthquake.

2 Description of the 18-Story Masonry Infilled RC Building

2.1 Structural Details

The structural system of the 18-story reinforced concrete (RC) building (Fig. 3) (17-stories above grade and a basement level) consists of RC frames with shear walls located in the core area of the building around the elevators. There are two staircases located to the north and south of the middle part of the building. Unreinforced masonry walls with different size of openings, thicknesses and heights are used as partitions along the height of the building.

(a) *Front view of the building* *(b) Typical floor plan*

Fig. 3. 18-story RC building.

2.2 Seismic Damage

The infill walls were moderately damaged after the earthquake. Minor to no damage was observed in the structural elements of the building. Crushed corners, diagonal and horizontal cracks are some of the damage that were observed in the masonry infill walls, and most of this damage was heavily concentrated in the lower stories of the building. Shear and flexural cracks can be seen clearly in the coupling beams that connect the elevator cores. Figure 4 shows different types of damage that was observed in the infill walls during a site visit 6 weeks after the mainshock.

(a) Interior wall diagonal cracks *(b) Interior wall sliding cracks* *(c) Exterior wall diagonal and sliding cracks*

Fig. 4. Observed infill wall damage in the 18-story building after the earthquake.

3 Instrumentation for the Ambient Vibration Test

Two systems were used to collect ambient vibration data. The first was a system consisting of fifteen accelerometers and the second was a system that made use of three seismometers. Details of the two systems are provided below.

3.1 Accelerometers

A network of 15 accelerometers with two different setups of sensors were used to collect the ambient vibration data. For setup A1, the sensors were installed on floor 9, 12, and 15. For setup A2, the sensors were installed on floor 3, 6, and 9. For both setups A1 and A2, the accelerometers were installed in the center, as well as the northwest and southeast corners of each specific floor to measure the acceleration in two perpendicular directions. The accelerometers were fixed on brackets that were distributed over the locations illustrated in Fig. 5a. Then, the sensors were wired to a National Instruments compact DAQ by BNC cables of upto 50 m in length. Figure 5b shows the setup for the installed accelerometers. Table 1 shows the sensors layout for setup A1. Approximately 1 h of ambient vibrations were recorded for each setup.

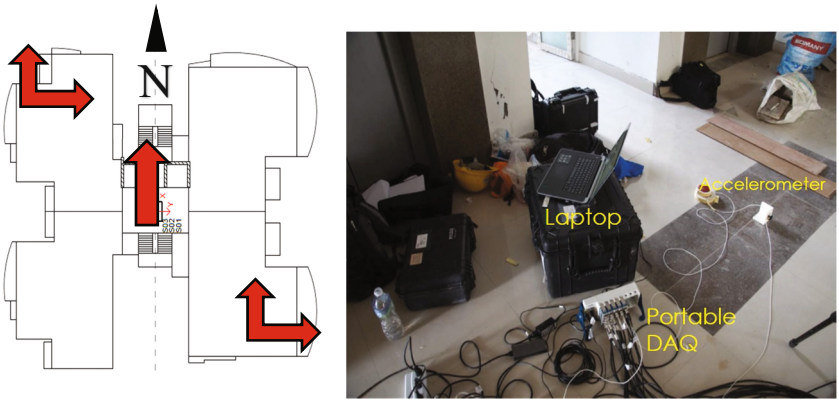

(a) Layout of sensors *(b) Setup for the ambient vibration test*

Fig. 5. Ambient vibration testing setup.

3.2 Seismometers

In the present work, the ambient vibration test was performed using three portable triaxial macro seismographs GSR from GeoSIG [4] (see Fig. 6). Each macro-seismograph allows for the recording of acceleration signals in three orthogonal directions under specific conditions of trigger, reading, and sampling rates. Series of 900 s duration were considered with a sampling rate of 250 Hz. Time series lengths adopted for each setup were essentially limited by restrictions for the tests' duration, and counting the expected relevant natural frequencies. Each macro-seismograph was set to work independently, avoiding the use of cables and minimizing labor associated with test preparation. This was made possible resorting to internal clock synchronization. The tests consisted in successive vibration measurements in building locations, corresponding to several locations on the building plan (at the top story) and along the building height. The vibration data are collected with the macro-seismographs in four

Table 1. Sensors layout for setup A1.

Sensor no.	Floor	Corner	Dir.
1	9	SE	N
2	9	SE	E
3	12	SE	N
4	12	SE	E
5	9	M	N
6	9	NW	N
7	9	NW	E
8	15	SE	S
9	15	SE	E
10	15	M	N
11	15	NW	W
12	15	NW	S
13	12	NW	N
14	12	M	N
15	12	M	E

setups. A reference seismograph (S03) was placed in the center close to the elevators core on level 15 for all setups, which was not moved for the duration of testing for all setups. In the first setup S1, seismographs S01 and S02 were placed on floor 15 in the South–West side of the building to capture the local torsional mode. In the second setup S2, two sensors were placed at two opposite corners on floor level 15 to capture the global torsional mode of the building. Finally, in the third and fourth setup, all seismographs were installed in the center of the building along the same vertical alignment as the reference seismograph S03. For setups S3 and S4, seismograph S01 and S02 were placed on floor levels 9 and 12, and floor levels 3 and 6, respectively. Figure 7 shows the floors layout for all setups.

Fig. 6. Macro-seismograph GeoSIG, model GSR-18.

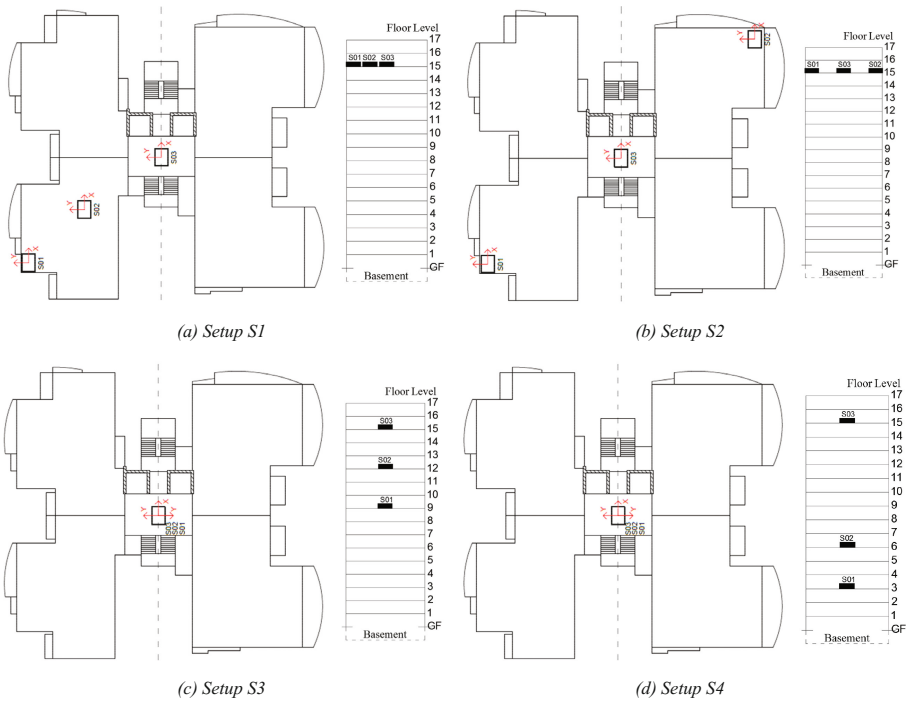

Fig. 7. Layout for the ambient vibration test using seismographs.

4 System Identification

4.1 Using Ambient Vibration Data Collected by Accelerometers

The modal parameters of the building are estimated using the NExT-ERA method [5, 6]. For both setups A1 and A2, the reported ambient vibration data is divided into 6 sets depending on the length of the available data. Each data set is approximately a 9 min long ambient vibration accelerogram. However, the last set of data of setup A1 are only 6 min long. A cleaning process was used to eliminate any noise from the recorded data before using it for system identification. The data cleaning process is carried out as follow: (1) filter the data in the frequency range of interest (0.2–10 Hz), (2) down-sample from 2048 Hz to 256 Hz for computational efficiency, and (3) remove voltage spikes in the time domain [7]. After examining the acceleration time history and power spectral density plots, measurements from some specific sensors were removed from the system identification process due to the high level of noise in the recorded data. Figure 8 shows the power spectral densities of the cleaned data for the first dataset in setup A1. Figure 9 plots the sample stabilization diagrams of the natural frequencies for modes 1–3. In the stabilization diagram of the natural frequency, the frequencies that are repeatedly identified at increasing orders are considered to be “stable”. Vertical thick (red) lines indicate the stable frequencies of interest in this study. The statistics (mean and standard deviation) of the identified natural frequencies and damping ratios for

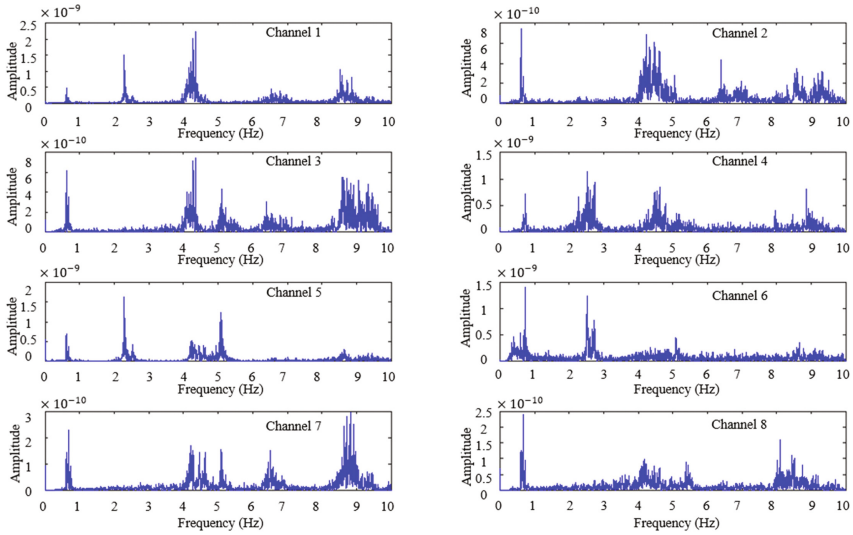

Fig. 8. Sample power spectral densities after data cleaning (setup A1 and dataset 1).

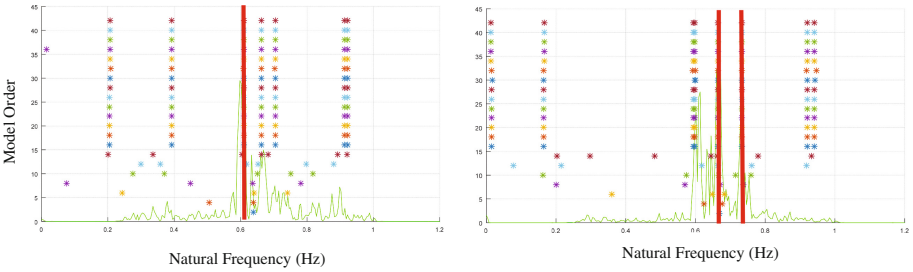

(a) *Mode 1* *(b) Modes 2 and 3*

Fig. 9. Sample stabilization diagram for the first three modes.

Setups A1 and A2 are reported in Table 2. Comparing the mean values of natural frequencies for the two setups, there is an excellent agreement between the two setups with a maximum error of 0.8% for mode 3. The damping ratios show larger variability across different datasets, but they are still reasonable.

4.2 Using Ambient Vibration Data Collected by Seismometers

The determination of the frequencies and vibration mode shapes of the building in this section is based on the acquisition of the acceleration measurements using the seismographs. For this purpose the ARTeMIS [8] software for analysis and signal processing is used. In the ARTeMIS software, the natural frequencies and the vibration mode shapes can be found by using the peak peaking and the frequency domain decomposition (FDD) techniques. Concerning the peak peaking technique, natural

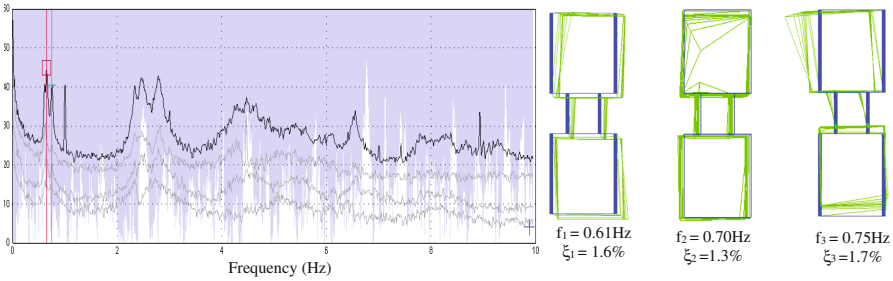

(a) *Normalized single values of spectral density matrices* (b) *Vibration modes*

Fig. 10. Spectral density and vibration modes.

frequencies are identified from the peaks of the normalized average power spectra of the measured accelerations in each section, assuming that the dynamic output in resonance is due only to one vibration mode shape. The modal identification is performed through the application of the enhanced frequency domain composition method (EFDD). From the spectral density information illustrated in Fig. 10a, it can be observed that the natural frequencies of the building are 0.61 Hz, 0.70 Hz, and 0.75 Hz with the corresponding identified modes shown in Fig. 10b. It is possible to observe that the next level of natural frequencies of the building are between 2.3–3 Hz.

4.3 Comparison Between the Modal Parameters Obtained Using the Two Different Systems

Table 2 lists the identified natural frequencies and the damping ratios of the building that were obtained from the system identification when using ambient vibration data collected using accelerometers and seismometers. It can be seen that the natural frequency of the first mode is same by both measurements. In addition, there is a resonable match between the values of the natural frequency of the third mode with a difference of 2.7%. However, for the second mode, the difference is 4.4% between the two measurements. Considering the different equipment and setups, the authors consider that there is a very good match overall between the first three identified natural frequencies. For the damping ratios, however, the difference between the two measurments is approximately 30% for the first three modes.

Table 2. Comparison of identified frequencies by two measurements.

Mode	Natural frequencies (Hz)		Difference (%)	Damping ratios (%)		Difference (%)
	Accelerometers	Seismometers		Accelerometers	Seismometers	
1	0.61	0.61	0.0	2.4	1.6	33.3
2	0.67	0.70	4.4	1.9	1.3	31.5
3	0.73	0.75	2.7	1.3	1.7	30.7

5 Finite Element Models

Two linear elastic finite element models of the 18-story building (Fig. 11) were developed using the SAP2000 software [9]. The two models were developed by two teams independently, one at Oregon State University (model 1) and the other at the University of Porto (model 2) without any interaction between teams, not to bias the modeling approaches and assumptions used by the two teams. For the both models, linear elastic shell elements are used to model the shear walls, without any reduction factor for the flexural rigidity. The RC beams and RC columns are modeled using linear elastic frame element with flexural rigidity as follows: (1) for model 1, $EI_{effective} = 0.7\ EI_{gross}$ for columns, and $EI_{effective} = 0.3\ EI_{gross}$ for beams, and (2) for model 2, $EI_{effective = 0.4\ EIgross}$ for columns, and $EI_{effective} = 0.6\ EI_{gross}$ for beams. The dimensions of the RC columns are obtained from the design drawings. The building has a typical 3 m story height with 125 mm thickness for the slabs. For all RC elements in the model, a compressive strength of 30 MPa is used as a typical value based on Schimdt hammer testing performed on the site. A compressive strength of 4.5 MPa and elastic modulus equal to 2400 MPa are used as material properties for the infill walls [10]. Two types of infill walls are used: (1) 120 mm thick for interior walls, and (2) 240 mm thick for exterior walls. Stiffness reduction factors with values ranging from 0.3 to 0.7 are used to account for openings with different sizes and locations [11]. Additional reduction factors are used to simluate the observed damage following the earthquake. For model 1, the equivalent diagonal strut method is used to model the masonry infill walls. In this method, the infill wall is replaced with two compression struts. The thickness of the struts is equivalent to the thickness of the infill walls. FEMA 356-2000 procedures [12], which are based on the work of Stafford-Smith and Carter [13], are used to calculate the width of the compression struts. The equivalent diagonal strut method requires the infill walls to be confined with columns on both sides. Because of this requirement, only the

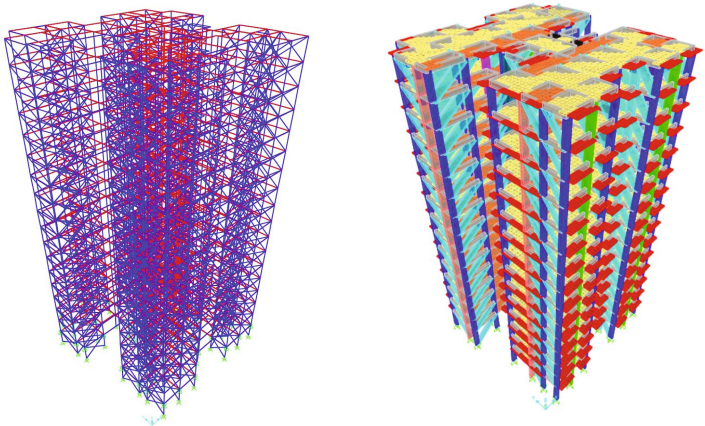

(a) Model 1 *(b) Model 2*

Fig. 11. FE models

Table 3. Summary of obtained natural frequencies from FE models.

Mode	Natural frequencies (Hz)		Difference (%)
	Model 1	Model 2	
1	0.64	0.70	9.3
2	0.72	0.77	6.9
3	0.85	00.84	1.1

walls with columns at both ends are modeled and the walls with only one column at one side are not modeled in model 1. For model 2, the equivalent diagonal strut method is also used to model the infill walls. However, the width of the diagonal strut is based on the work of Priestley et al. [14]. Then, the dynamic parameters of the two models are obtained by performing linear modal analysis. Table 3 shows the natural frequencies obtained from the two FE models. It can be observed that the natural frequencies of model 1 are very close to the ones obtained from model 2. The maximum difference between the obtained natural frequencies by the two FE models is less than 10%. Comparing results in Tables 2 and 3, it can be inferred that the errors between the natural frequencies estimated from the ambient vibration tests and the ones obtained from the FE models range between 4.5% and 15%, even with simple FE models.

6 Conclusions

The system identification and modeling of an 18-story masonry-infilled RC building that was damaged during the 2015 Gorkha earthquake are described in this paper. The ambient vibration test of the building is executed using two different measurement systems, including: (1) 15 accelerometers, or (2) 3 seismometers. The system identification of the building is performed by using the collected ambient vibration to extract the modal parameters of the building. The natural frequencies are accurately identified using the two sets of collected vibration data. Moreover, there is a good agreement between the first three natural frequencies that are identified using the two measurements, even though differences were observed for the identified modes 2 and 3. Two linear elastic FE models are developed adopting the equivalent strut method. A stiffness reduction factor with different values is used to simulate the observed damage in the masonry infill walls of the building after the earthquake. There is a reasonable match between the obtained natural frequencies from the two models and the identified frequencies for the first three modes, suggesting that these models with minor modifications, can be used for post-earthquake response prediction. Nonetheless, in the experimental systems used, it is worth noting that little to no variation was observed in the estimation of Mode 1, while Modes 2 and 3 showed differences ranging from 5% to 10%, which was not expected. Further investigation is sought to clarify reasons that can explain these differences and how they can be avoided with appropriate system setups.

Acknowledgments. Partial support of this study by the National Science Foundation Grants 1254338, 1545632, and 1545595 is gratefully acknowledged. The authors express their gratitude to the building owners who provided access to the buildings and thank Mr. Rajendra Soti, Mr. Supratik Bose, Dr. Daniel Gillins, Mr. Patrick Burns, and Mr. Matthew Gillins for their assistance in the collection of data. The third author would like to acknowledge the financial support of "FCT—Fundação para a Ciência e Tecnologia", Portugal, through the research project P0CI-01-0145-FEDER-016898 — Safety Evaluation and Retrofitting of Infill masonry enclosure Walls for Seismic demands. The opinions, findings, and conclusions expressed in this paper are those of the authors and do not necessarily represent the views of the organizations and collaborators involved or funding in this project.

References

1. Briggs, R., Jaiswal, K., McNamara, D., Wald, D., Benz, H., Hearn, M., , Earle, P.: The April–May 2015 Nepal Earthquake Sequence. Earthquake Educational Slides, US. Geological Survey, National Earthquake Information Center (2015). http://earthquake.usgs.gov/learn/topics/Nepal_Slides.pdf
2. Brando, G., Rapone, D., Spacone, E., Barbosa, A., Olsen, M., Gillins, D., Soti, R., Varum, H., Arede, A., Vila-Pouca, N., Furtado, A., Oliveira, J., Rodrigues, H., Stavridis, A., Bose, S., Fagella, M., Gigliotti, R., and Wood, R.: Reconnaissance report on the 2015 Gorkha Earthquake effects in Nepal. XVI Convegno Anidis, L'Aquila, Italy (2015)
3. Todorovska, M., Trifunac, D.: Impulse response analysis of the Van Nuys 7-storey hotelduring 11 earthquakes and earthquake damage detection. Struct. Control Health Monit. **15**(1), 90–116 (2008)
4. Grob, J.: GeoSIG GSR-12/16/18. Operation Manual. GeoSIG AG, Switzerland (2009)
5. James, G., Carne, T., Lauffer, J.: The natural excitation technique for modal parameters extraction from operating wind turbines." Sandia National Laboratories, SAND92-1666, UC-261, Sandia, New Mexico, USA (1993)
6. Juang, J., Pappa, R.: An eigensystem realization algorithm for model parameter identification and model reduction. J. Guid. Control Dyn. **8**(5), 620–627 (1985)
7. Yu, H., Mohammed, M., Mohammadi, M., Moaveni, B., Barbosa, A., Stavridis, A., Wood, R.: Structural identification of an 18-Story RC building in Nepal using post-earthquake ambient vibration and lidar data. Front Built Environ. **3**, 11 (2017)
8. ARTeMIS: "ARTeMIS Extractor Pro. Structural Vibration Solutions ApS, ed., Aalborg (2009)
9. Computers and Structures Inc. (2013). SAP2000 V.16 software
10. Pradhan, P.: Composite actions of brick infill wall in RC frame under in-plane lateral load. Dissertation, Tribhuvan University (2009)
11. Al-Chaar, G., Issa, M., Sweeney, S.: Behavior of masonry-infilled nonductile reinforced concrete frames. J. Struct. Eng. **128**(8), 1055–1063 (2002)
12. FEMA-356: Prestandard and Commentary for the Seismic Rehabilitation of Buildings. Federal Emergency Management Agency, Washington, D.C. (2000)
13. Stafford, S., Carter, C.: A method for the analysis of infilled frames. Proc. Inst. Civ. Eng. **44**, 31–48 (1969)
14. Paulay, T., Priestley, M.J.N.: Seismic Design of Reinforced Concrete and Masonry Buildings. Wiley, New York (1992)

Study of the Environmental Influence on the Dynamic Behavior of Adobe Walls: Preliminary Test in Laboratory Specimens

Rick Delgadillo[1], Giacomo Zonno[1], Rubén Boroschek[2], Paulo B. Lourenço[3], and Rafael Aguilar[1(✉)]

[1] Department of Civil Engineering, Pontificia Universidad Católica del Perú - PUCP, Lima, Peru
raguilar@pucp.pe
[2] Department of Civil Engineering, University of Chile, Santiago, Chile
[3] Department of Civil Engineering, ISISE, University of Minho, Guimarães, Portugal

Abstract. The shift of modal parameters induced by temperature and humidity effects may mask the changes of vibration properties caused by structural damage because the dynamic properties are often sensitive to changing environmental conditions. Furthermore, temperature and humidity are generally non-uniform and time-dependent variables, and therefore, their simple record in air or at a specific surface cannot be sufficient to obtain useful models to understand the relationship between the dynamic properties and environmental effects.

The present paper aims at presenting preliminary findings in the task of quantifying the effects of environmental conditions (variations in temperature and humidity) on the dynamic properties of earthen constructions with a laboratory test campaign. The first stage of the research consisted on the analysis of a real structural system and for this three 1:1 scale adobe walls were built in the laboratory. This stage considered the performance of a long-term monitoring program recording environmental conditions, the surface and inner walls variation of temperature and humidity and the dynamic behaviour of the walls. The second stage consisted on the understanding the correlation between dynamic properties and environmental parameters. In particular, linear auto-regressive models with exogenous variables (ARX) and multiple linear regression models (MLRM) were built and compared. The paper presents the results of the measurements and shows that is possible to distinguish the changes of dynamic properties due to environmental effects in adobe walls.

Keywords: Adobe masonry · Structural health monitoring · Environmental effects · Hygro-thermal monitoring · Laboratory tests

1 Introduction

Long term structural health monitoring systems are finding increased use in many fields, including preservation of historic structures. Many researches are being developed in the field of the Structural Health Monitoring (SHM) for implementing

© Springer International Publishing AG 2018
J.P. Conte et al. (eds.), *Experimental Vibration Analysis for Civil Structures*,
Lecture Notes in Civil Engineering 5, https://doi.org/10.1007/978-3-319-67443-8_67

structural damage detection protocols and for this reason a diversity of damage detection methods are being implemented for different types of structures. Among them, vibration-based methodologies are prevalent and are being used more frequently for modern and historical constructions. The vibration-based method is used to monitor the structural condition and identify structural damage, because dynamic properties such as natural frequencies, mode shapes and modal damping are functions of the physical parameters of the structural mass, damping, and stiffness [1]. However, the vibration properties of real structures are not only affected by structural damages (earthquakes or by other types of dynamic loadings); environmental factors also cause changes in dynamic properties [2]. Several studies have reported that changes in structural responses due to temperature and humidity variation could be more significant than the changes due to structural damage [3]. In [4] the authors presented the variation of the dynamics properties due to the environmental effects of the Central Tower in Chile showing a decrease in the frequencies of about 0.7% when the external temperature is in the range of 20.5 °C and 21.5 °C. The continuous monitoring system on the Dowling Hall Footbridge reported a variation of about 4–8% of natural frequencies due to a temperature range variation between −14 °C to 39 °C [5]. It is accepted that the temperature can change the modulus of elasticity in an inverse relationship and also the boundary conditions can be dependent on the temperature variation [6]. Furthermore, the temperature distribution in a structure needs to be investigated because it is generally non-uniform and time-dependent. In [7] the researchers showed the correlation between environmental and internal temperature and dynamic properties of a RC slab and the non-uniform and time-dependent temperature distribution in the structure.

On the other hand, vibration-based structural health monitoring (SHM) techniques are being used increasingly for structural evaluation of historical buildings, such as bell tower [8], churches [9] and rammed earth structures [10]. This is due to its completely non-destructive character and for the respect of international standards to protect cultural heritage. [11] Shows a complete monitoring system for two historical structures with the objective of detecting structural damage and estimating the severity of damage.

This paper presents an extensive study of temperature-humidity internal distribution of a full-scale adobe wall built in the laboratory with a specific focus on the environmental effects on the dynamic properties. The adobe wall was placed outside the laboratory and the dynamic parameters and environmental factors (internal temperature and humidity, air temperature and relative humidity) were monitored for more than four months. Correlations between modal frequencies and environmental parameters are investigated in detail. In addition, multiple linear regression models (MLRM) and linear auto-regressive models with exogenous variables (ARX) are established.

2 Methodology

Monitoring data were locally recorded and subsequently processed. For processing purposes, the authors have developed a code in LabVIEW [12] to automatically obtain the dynamic properties of the studied systems. Linear auto-regressive models with exogenous variables (ARX) and multiple linear regression models (MLRM) are

developed in Matlab [13] and they are adopted to obtain correlations between environmental parameters and natural frequencies in the studied walls.

The dynamic properties are obtained with an automated procedure using the Data-Driven Stochastic Subspace Identification method together with a new automatic analysis process for cleaning the stabilization diagram and selecting dynamic properties with the application of soft and hard validation criteria [14] and the hierarchical clustering methodology [15]. Subsequently, an algorithm for the automatic choice of the most representative values of the estimated parameters is developed with the use of the modal shape complexity criteria.

To calculate predictions considering previous recorded data of the dependent parameters, dynamic autoregressive models were used. These models have the advantage of being generated rapidly, as they are obtained experimentally when the input-output relationships of the system can be identified [16]. Firstly, the ARX model was used and it consists in the description of the output as an Auto-Regressive variable and the input as an eXogeneous one [17]. In this case, the input of the model corresponds to the environmental parameters, while the output corresponds to dynamic properties such as, the natural frequencies, damping and modal shape. Subsequently, Multiple Linear Regression (MLR) was used and it is a statistical technique that can be used to analyze the relation between a single dependent variable and several independent ones [18]. In this study, regression analysis were developed from a set of dependent variables (natural frequencies) and a set of independent variables (environmental factors such as temperature and humidity). The main objective of regression analysis is to develop a model that, with an initial tracking period, provides a good fit between the observations (input) and the calculated values of the dependent variable provided by the model [19]. These are usually obtained through the least squares method, which minimizes the sum of the squared errors.

3 Description of Experiment

Adobe blocks (320 × 220 × 120 mm) were built and dried for seven weeks approximately. Subsequently, the full-scale wall was built in the laboratory and was continuously monitored for more than 4 months. The dimensions of the adobe wall are 1660 × 2000 × 220 mm and a concrete plinth was considered as foundation to avoid the filtration of water through ground.

3.1 Equipment and Test Setups

The temperature and humidity monitoring systems were designed to monitor the internal temperature and humidity of adobe walls and the air temperature and humidity. Internal temperature data of adobe walls were collected through a system of sensors type LM35 [20] and the internal humidity through a system of sensors type FC28 [21] (Fig. 1a and b). The measurement range of both are from −55 °C to 150 °C and 5% to 95% respectively. A UX100-011 HOBO digital temperature and humidity sensor [22] was chosen to monitor the air temperature and humidity (Fig. 1c). Its air temperature range is between −55 °C and 150 °C and relative humidity range is between 0% to

99% with a temperature resolution of 0.024 °C and humidity resolution of 0.05%. The LM35 and FC28 sensors were connected to two data acquisition devices, NI USB 6225 (16-bit resolution, 80 analog inputs and 250 kS/s maximum rate) and NI USB 6003 (16-bit resolution, 8 analog inputs) [23] (Fig. 1d). Furthermore, the accelerometers installed on site were PCB 393B12 uni-axial sensors model with 10 V/g sensitivity, with a frequency range of 0.15–1000 Hz and a weight of 210 g (Fig. 2a). These sensors include a thermal jacket for major outdoor protection [24]. The accelerometers were connected to two multi-channel systems, cDAQ-9234 (24-bit resolution, 102 dB dynamic range and anti-aliasing filters) [25] (Fig. 2b).

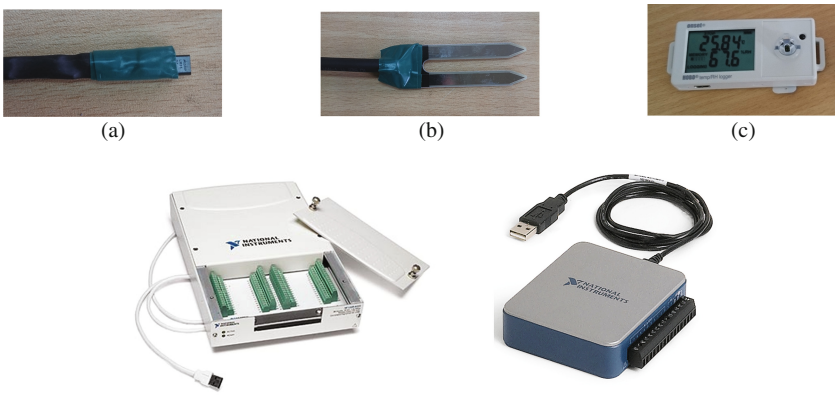

Fig. 1. Environmental equipment (a) LM35 – internal temperature sensor (b) FC28 – internal humidity sensor (c) UX100-011 environmental sensor (d) NI USB 6225 and NI USB 6003data acquisition devices

Fig. 2. Acceleration monitoring equipment (a) PCB 393B12 - accelerometer sensor (b) cDAQ-9234 acquisition system.

To monitor the temperature and humidity inside the adobe wall, sensors were placed along four cross sections at the top, middle, down and foundation. Specific layouts of temperature and humidity sensors are shown in Fig. 3. Temperature and humidity sensors were placed in the plane of foundation to evaluate humidity gradients. The external environmental sensor was located close to the wall. The two visible transversal sections of the wall were coated to prevent moisture transmission in the

East-West direction (black layers in Fig. 4). For a better quantification of the environmental conditions, the number of sensor were as follows: 10 temperature sensors (9 embedded sensors and 1 air temperature sensor) and 17 humidity sensors (16 embedded sensors and 1 relative humidity sensor). Data from internal and external sensors were acquired every 1 h since September 2016.

The dynamic monitoring system consisted in placing three accelerometers for measuring out of plane (two sensors) and in plane (one sensor) behavior of the wall. Data from the accelerometers was acquired every 1 h considering a 256 Hz sampling rate with 600 s of recorded data since September 2016. Figure 4 shows the adobe wall and the continuous monitoring system installed.

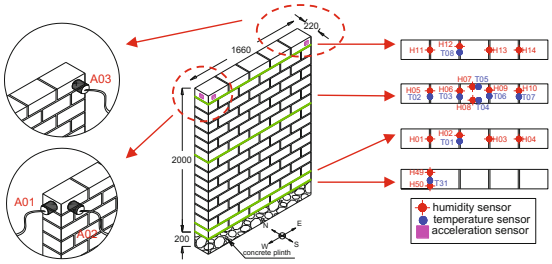

Fig. 3. Sketch of the monitoring system with sensors positions of the adobe wall (A, H, T denote acceleration, humidity and temperature sensors respectively, dimensions in mm).

Fig. 4. Place of installation and continuous monitoring center of three adobe walls.

4 Temperature and Humidity Internal Distribution

The temperature-humidity distribution in the adobe wall is non-uniform and time depending not only in the horizontal cross sections (in both the directions) but also along the height of the wall. In particular, the non-uniform distributions dependent on the several factors such as air temperature and humidity, solar radiation and the thermal inertia of earthen constructions. Figure 5a shows the different internal temperatures recorded from the sensors T01 and T08, respectively at down and top sections. Furthermore, a similar behaviour is present with the other sensors (Fig. 5b). The significant

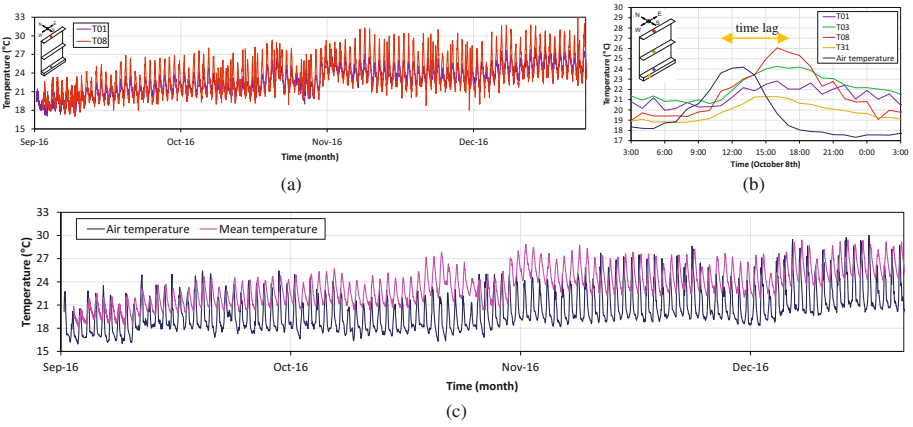

Fig. 5. Temperature variations of the adobe wall (a) comparison between the temperature at top and down section (b) comparison between temperature in different points (c) comparison between the air temperature and mean temperature

differences of temperatures at the same time demonstrate the non-uniform temperature distribution inside the adobe wall during a day. A time lag of 3 h between air temperature and temperature inside the wall was also registered, probably due to the adobe wall property to absorb solar energy and to transfer it later as heat, as referenced by [26]. Figure 5c shows the difference between the air temperature and the internal mean one, calculated by averaging the data of all the internal sensors.

The data of the humidity sensors shows the evolution of the moisture content since the walls' construction stage (Fig. 6). At the very beginning, a humidity close to 90% was recorded for the wet joints, and subsequently, the moisture content decreased until reaching a value of about 11% in the internal cross-sections. Due to the contact between concrete and adobe, the humidity at foundation is around of 7.2, which shows a no negligible influence between the two different materials. Furthermore, Fig. 6 shows the evolution of the air humidity and its daily variation.

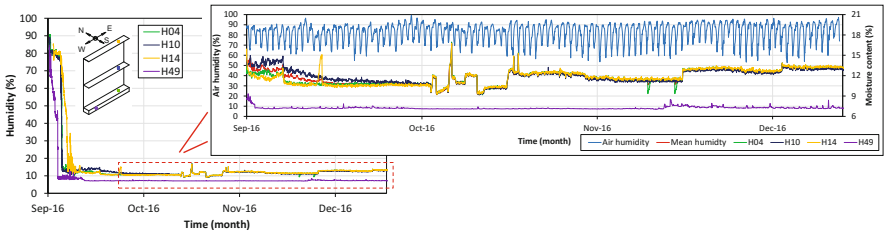

Fig. 6. Humidity variation of the adobe wall.

To evaluate moisture and temperature variation inside the wall, the humidity and temperature at cross section at half height of the wall were analysed. Figure 7 presents the temperature and moisture profiles of November 1, 2016 at 2:00 pm in the East-West section. There is a point where the temperature increases faster (the reverse case occurs with moisture), probably due to the solar radiation and the presence of the waterproof layers.

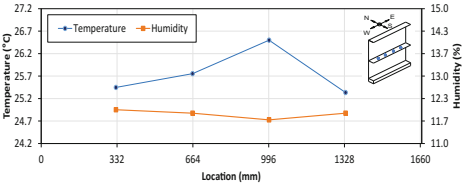

Fig. 7. Internal temperature and humidity variation along the cross-section (November 1, 2016 at 2:00 pm).

5 Analysis of Environmental Effects on Dynamic Properties

The wall was analyzed to quantify the effects of environmental conditions on the dynamic properties of earthen constructions. The first four frequencies were investigated and correlated with the environmental parameters and regression models were developed to obtain accurate prediction results.

5.1 Variations of Modal Frequencies

Figure 8 shows the first four natural frequencies of the adobe wall. The results show a clear influence of daily temperature and humidity variations on modal frequencies. In the first month of data, it is evident the variation of the frequencies during the hardening process of the wall, and, in particular, the upward trend of the frequencies because the joints between the adobe blocks were hardening and, therefore, the rigidity of the wall tends to increase.

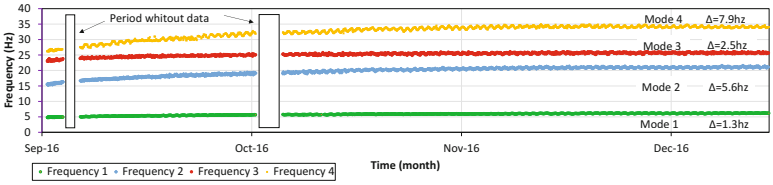

Fig. 8. Variation of the identified natural frequencies during the monitoring period of the adobe wall.

5.2 Correlation Between Identified Natural Frequencies and Measured Environmental Parameters

The external temperature and humidity and the internal mean temperature and humidity were considered to perform the correlation analysis with frequencies. Mean values are obtained by averaging the data from all the sensors placed along the three cross-sections at the top, middle and down (T01–T08) in the adobe wall. Figure 9 shows the evolution in time of the frequencies and the environmental parameters from November 17 to November 25, 2016. Figure 9a shows that the modal frequencies change significantly with the variation of mean temperature and, moreover, each frequency decreases when the mean temperature increases, instead, the relationship with the air temperature does not show a similar behaviour with the presence of a time lag between frequency and measured air temperature. Figure 9b shows the comparison between the frequency and the air and internal mean humidity. Both humidities have a weak relationship with the frequencies. To quantitatively analyse the correlations between the monitored parameters, coefficients of determination (R^2) were calculated and listed in the Table 1. It is found that the R^2 between frequencies and internal mean temperature are larger than air temperature and humidity. Therefore, the relationship between modal frequencies and environmental parameters in earthen constructions cannot be properly developed using the air temperature and humidity.

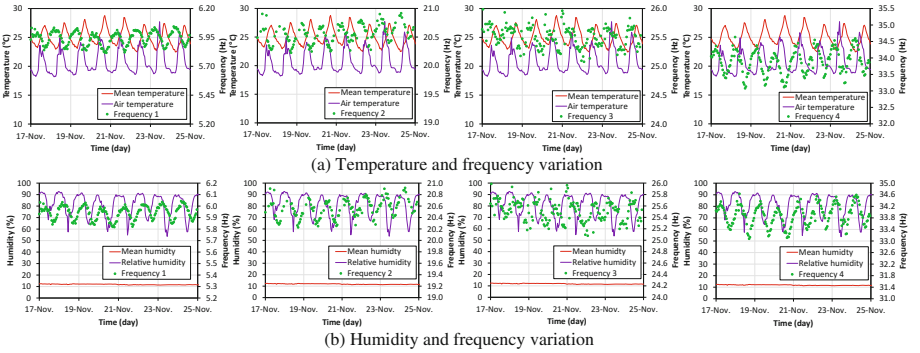

(a) Temperature and frequency variation

(b) Humidity and frequency variation

Fig. 9. Correlation between modal frequencies and environmental parameters.

Table 1. Coefficient of determination (R^2) between modal frequencies and environmental parameters for wall type I.

Environmental parameters	Mode			
	1	2	3	4
Mean temperature	0.88	0.81	0.16	0.82
Air temperature	0.04	0.02	0.01	0.02
Mean humidity	0.03	0.02	0.01	0.02
Air humidity	0.12	0.14	0.10	0.15

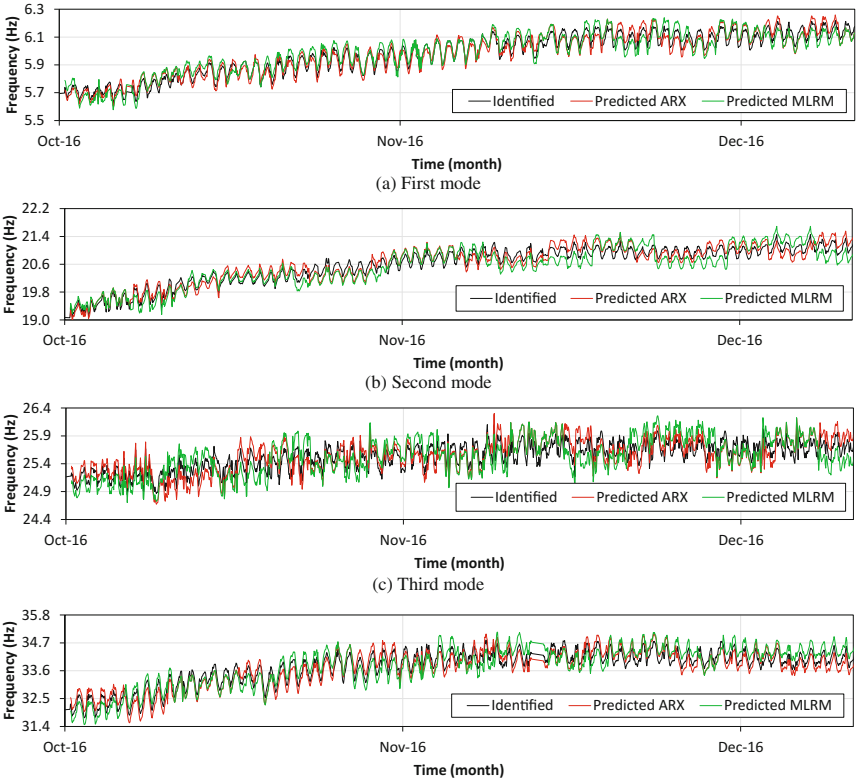

Fig. 10. Identified and statistically predicted modal frequencies for the adobe wall.

5.3 Multiple Linear Regression (MLRM) and Linear Auto-Regressive Model with Exogenous Variables (ARX)

A set of data from October 2016 to January 2017 was considered to develop the ARX and MLRM models and to predict the modal frequencies in function of the internal temperature. In the case of MLRM model, the internal temperature data recorded by all the sensors placed along the three-cross sections at the top, middle and down (T01–T08) in the adobe wall was considered, and in the case of ARX the internal temperature data was calculated by averaging the data from all the sensors of the same cross-sections. The input and output variables were divided into two subgroup, the first 50% of data was selected for estimating the parameters and the other 50% for the validation. MLRM and ARX models are developed considering the mathematical formulation given by Eqs. (1) and (2) respectively. Figure 10 shows identified and predicted frequencies in the monitoring period using the two statistical techniques (MLRM and ARX model). Subsequently, the coefficients of determination (R^2) are calculated between the identified and predicted frequencies. In the case of ARX model are: 0.91, 0.88, 0.68 and 0.89 and in the case of MLRM model are: 0.84, 0.80, 0.61 and

0.80 for the first four frequencies of the adobe wall. This indicates that ARX can achieve a more favorable quantification of temperature influence on natural frequencies, even if the difference is small. However, the high coefficients of determination show a good fitting performance of both models that are able to predict the trend and magnitude of the identified modal frequencies.

$$f_n = \beta_0 + \beta_1 T_{01} + \beta_2 T_{02} + \beta_3 T_{03} + \beta_4 T_{04} + \beta_5 T_{05} + \beta_6 T_{06} + \beta_7 T_{07} + \beta_8 T_{08} \quad (1)$$

$$A(z)y(t) = B(z)u(t) + e(t) \quad (2)$$

6 Conclusions

In this paper, an adobe wall was built and placed outside the laboratory to continually monitor the dynamic properties and environmental conditions (temperature and humidity). The paper proposes to analyze the temperature and humidity non-uniform variation in the earthen constructions and to quantify the influence of environmental effects on modal frequencies through preliminary test in laboratory specimens. In contrast to the conventional studies that use only air temperature or temperatures at a few points of the structure, the paper aims to obtain the internal thermal distribution of the entire structure through continuous monitoring. Consequently, the relation between the modal frequencies and the temperature and humidity at the whole structure is established.

During the monitoring period, the variation range of first four natural frequencies of the adobe wall is between 1.3 Hz and 7.9 Hz, while air temperature changes from 16 °C to 27 °C. This frequency variation is mainly correlated with the hardening period of the wall.

The determination coefficients show that it is useful to consider the correlation between the frequencies and temperatures measured in the internal sections of the wall. Therefore, the non-uniform temperature distribution within an earthen structure is necessary to consider in the correlation between dynamic parameters and environmental parameters.

MLRM and ARX models were developed to correlate the modal frequencies with internal temperature. The proposed procedure makes it possible to obtain models with a good fitting performance. Finally, both models adequately predict the behavior of the modal frequencies under the effect of environmental conditions with coefficients of determination between 0.91 and 0.65.

Acknowledgments. The present work was developed thanks to the funding provided by the program Cienciactiva from CONCYTEC in the framework of the Contract No. 222-2015. The first author acknowledge FONDECYT for the scholarship in support of graduate studies (Contract No. 027-2015-FONDECYT). The second author gratefully acknowledge ELARCH program for the scholarship in support of his PhD studies (Project Reference number: 552129-EM-1-2014-1-IT-ERA MUNDUS-EMA21).

References

1. Zhou, G.D., Yi, T.H.: A summary review of correlations between temperature and vibration properties of Long-Span bridges. Math. Probl. Eng. **2014**(638209), 19 (2004)
2. Xia, Y., Hao, H., Zanardo, G., Deeks, A.: Long term vibration monitoring of an RC slab: temperature and humidity effect. Eng. Struct. **28**(3), 441–452 (2006)
3. Yan, A.-M., Kerschen, G., De Boe, P., Golinval, J.-C.: Structural damage diagnosis under varying environmetal conditions-Part I: A linear analysis. Mech. Syst. Signal Process. **19**, 847–864 (2005)
4. Boroschek, R., Tamayo, F., Aguilar, R.: Evaluacion de los efectos ambientales en un edificio de media altura. XI Congreso Chileno de Sismología e Ingeniería Sísmica (ACHISINA), Universidad de Chile (2015)
5. Moser, P., Moaveni, B.: Environmental effects on the identified natural frequencies of the Dowling Hall Footbridge. Mech. Syst. Signal Process. **25**, 2336–2357 (2011)
6. He, X:. Vibration-based damage identification and health monitoring of civil structures. Ph. D. Thesis, University of California, San Diego (2008)
7. Xia, Y., Xu, Y.-L., Wei, Z.-L., Zhu, H.-P., Zhou, X.-Q.: Variation of structural vibration characteristics versus non-uniform temperature distribution. Eng. Struct. **33**(1), 146–153 (2011)
8. Ubertini, F., Comanducci, G., Cavalagli, N.: Environmetal effects on natural frequencies of the San Pietro bell tower in Perugia, Italy, and their removal for structural performance assessment. Mech. Syst. Signal Process., Math. Probl. Eng. **82**, 307–322 (2016)
9. Ramos, L., Aguilar, R., Lourenço, P.B., Moreira, S.: Dynamic structural health monitoring of Saint Torcato church. Mech. Syst. Signal Process. **35**, 1–15 (2013)
10. Bui, Q.-B., Hans, S., Morel, J.-C., Do, A.-P.: First exploratory study on dynamic characteristics of rammed earth buildings. Eng. Struct. **33**, 3690–3695 (2011)
11. Morrison, T.: Advanced numerical tool to analyze monitoring data. Master's Thesis, University of Minho, Portugal (2008)
12. National Instruments. LabVIEW 2015, United States (2016)
13. The MathWorks, I.: MATLAB R2013a. Natick, Massachusets, United States (2012)
14. Boroschek, R., Bilbao, J.: Evaluation of an automatic selection methodology of model parameters from stability diagrams on a damaged building. In: 6th International Operational Modal Analysis Conference, IOMAC, Gijon, Spain, pp. 12–14 (2015)
15. Magalhães, F., Cunha, A., Caetano, E.: Online automatic identification of the modal parameters of a long span arch bridge. Mech. Syst. Signal Process. **23**(2), 316–329 (2009)
16. Ljung, L.: System identification: theory for the user. Prentice Hall, New Jersey (1999)
17. Peeters, B., De Roeck, G.: One-year monitoring of the Z24-Bridge: environmental effects versus damage events. Earthquake Eng. Struct. Dynam. **30**(2), 149–171 (2001)
18. Johnson, R.A., Wichern, D.W.: Applied Multivariate Statistical Analysis. Prentice Hall, Upper Saddle River (1992)
19. Magalhães, F.: Operational modal analysis for testing and monitoring of bridges and special structures. Ph.D. thesis, Faculty of Engineering, University of Porto, Porto (2010)
20. National semiconductor corporation. Temperature sensor LM35 (2016). national.com. http://www.fasttech.com
21. FC-28 Soil humidity detection sensor module. Humidity sensor (2016). amazon.com. http://www.fasttech.com
22. ONSET. Data logger (2015). ONSET.com. http://www.onsetcomp.com
23. National Instrument. NI USB-6225,6003 (2016). http://www.ni.com/datasheet/pdf/en/ds-10

24. PCB Piezotronics. Accelerometer 393B12 (2016). http://www.pcb.com/Products.aspx?m=393B12
25. National Instrument. Daq NI 9234 (2016). http://www.ni.com/datasheet/pdf/en/ds-316
26. Torres, I., Peixoto de Freitas, V.: The influence of the thickness of the walls and their properties on the treatment of rising damp in historic buildings. Constr. Build. Mater. **24**, 1331–1339 (2010)

Assessing the Performance of a Heavy Haul Railway Viaduct Through Monitoring Traffic Loads and Dynamic Effects

Fulvio Busatta(✉) and Pilate Moyo

Department of Civil Engineering,
University of Cape Town, Cape Town, South Africa
fulvio.busatta@uct.ac.za

Abstract. South Africa is one of the leading countries in heavy haul railway freight transport. At present, it operates the longest freight train in the world, 4.1 km long and consisting of 342 wagons, to export iron ore. Moving loads induced by trains on bridges are repetitive in nature thus leading to possible excitation of the deck, and a very long sequence of wagons with identical wheelset distance may magnify this effect. The paper presents an ongoing monitoring program of the Olifants River Viaduct, a large-scale multi-span bridge crossed by the long freight train. Focus is given to both monitoring of traffic loads and dynamic effects.

Keywords: Monitoring · Operational modal analysis · Heavy haul · Railway viaduct · Weight-in-motion

1 Introduction

In recent decades, numerous viaducts have been constructed to serve the modern railway infrastructure around the world for high speed (HS) passenger and heavy haul (HH) freight transport. The former, mostly active in Europe/Eastern Asia, operates trains consisting of hi-tech cars running at high speed, thus offering a fast and sustainable alternative to aircraft to travel between major cities. The latter is a special type of freight transport active in the BRICS countries, in USA, Canada, Australia and Sweden/Norway, that operates the heaviest and longest trains in the world to convey large amounts of bulk commodities from mines to dedicated export terminals. A comparison between HS and HH in terms of train parameters, as collected by the authors from major railway manufacturers, owners and operators worldwide, is provided in Table 1.

Either built as a sequence of simply-supported beams or through continuous girders, viaducts are typically multi-span and repetitive bridge structures. Similarly, the loading induced by a moving train on a bridge is repetitive in nature due to a sequence of cars/wagons, with identical wheelset distance, moving on the bridge deck. Thus, certain frequencies of excitation are likely to be imposed on the bridge during the passage of a train. Hence, the investigation of both the natural dynamic properties of repetitive bridges and the effects induced on these structures by the rail moving loads

© Springer International Publishing AG 2018
J.P. Conte et al. (eds.), *Experimental Vibration Analysis for Civil Structures*,
Lecture Notes in Civil Engineering 5, https://doi.org/10.1007/978-3-319-67443-8_68

Table 1. Comparison between high speed and heavy haul trains.

Train Parameter	High Speed	Heavy Haul
Car/Wagon Axle Load (kN)	150–180	250–400
Operational Speed (km/h)	200–400	50–80
Number of Cars/Wagons	8–16	100–350
Car/Wagon wheelset distance (m)	18–20	5–10
Length (m)	150–300	1500–4000

has recently become an attractive research topic in the scientific community working on dynamics of railway bridges [1–4].

Within this context, the paper aims to present the dynamic investigations and monitoring of both traffic loads and dynamic effects of the Olifants River Viaduct (ORV), a 23-span, 1 km long bridge in South Africa [4]. At present, the ORV is crossed by the longest HH train in the world (4.1 km long) with a very long sequence of 342 wagons. The viaduct girder has been equipped with (i) a Wheel-Impact-Monitoring & Weight-In-Motion (WIM-WIM) system by the owner to estimate the railway loading; (ii) a multi-sensor monitoring system by the authors to investigate the dynamic effects on the girder.

The paper is organized as follows: the section "The Olifants River Viaduct" introduces the bridge and summarizes the natural dynamic properties of the viaduct girder. Subsequently, the section "The Monitoring System of the Viaduct" briefly presents how the viaduct girder is equipped in terms of sensors and data acquisition (DAQ) system. The section "Monitoring of the Traffic Loads" focuses on the HH railway traffic by providing some information on train configuration, speed, and dynamic axle load as extracted from the WIM-WIM files. Finally, selected results from continuous monitoring of the dynamic effects on the viaduct are presented and discussed in the section entitled "Performance Monitoring of the Viaduct Girder".

2 The Olifants River Viaduct

2.1 Description of the Structure

The ORV (Fig. 1) is located near Vredendal, in the Western Cape Province of South Africa. It was constructed in 1974–75 and has been serving the 861 km long Iron Ore Export "Sishen-Saldanha" Line since 1976. The line connects the mining areas in Sishen, Northern Cape Province, to the Saldanha Bay Commercial Harbor, Western Cape Province. Transnet SOC Ltd owns, manages and operates the line through the operational division Transnet Freight Rail (TFR).

The most relevant features of the ORV are summarized as follows (Fig. 2):

- The viaduct consists of a single box prestressed concrete (PSC) girder, 1 035 m long, on 23 spans equally spaced, supported by 22 reinforced concrete (RC) piers 45 m apart.

Fig. 1. General view of the Olifants River Viaduct.

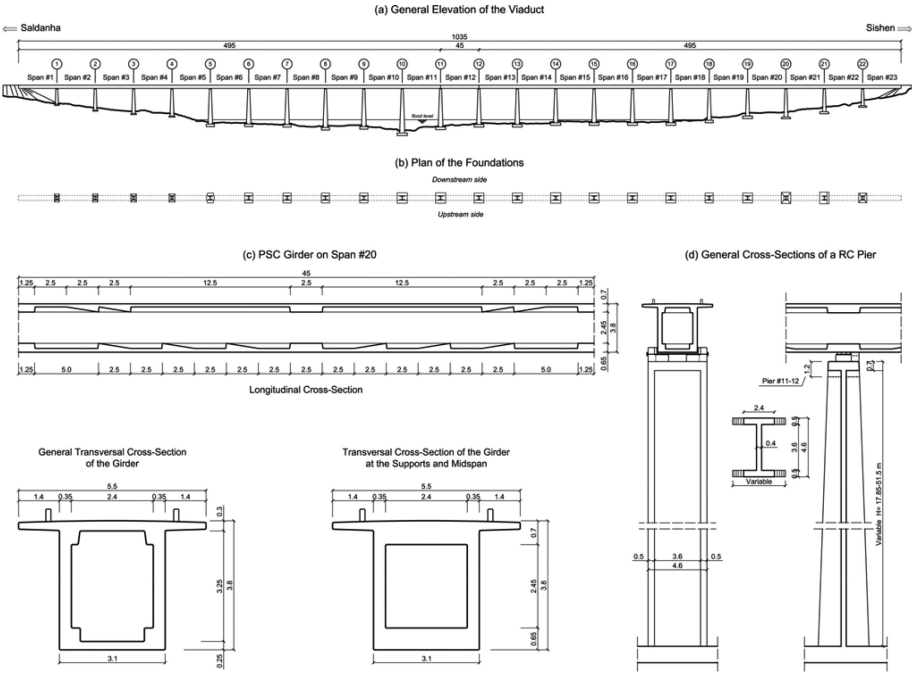

Fig. 2. The Olifants River Viaduct: (a) general elevation; (b) plan of the foundations; (c) cross-sections of the PSC girder on span #20 and (d) cross-sections of a typical RC pier (dimensions in m).

- Two expansion joints are located at piers #11–12 so that three structural members result: two large continuous girders, 495 m long, on spans #1–11 and #13–23, respectively, and a short simply supported beam, 45 m long, on span #12.
- The two large girders are fixed at the Saldanha/Sishen abutments. Fixed reinforced neoprene bearings are positioned at piers #1–4, 11–12 (under the simply supported beam) and 18–22, while sliding bearings are located at piers #5–10, 11–12 (under the large girders) and 13–17. Transverse bearings are positioned between girder webs and pier caps to transfer wind loads and train-induced transversal actions to the piers;

- The 23-span girder was constructed, span by span, by the incrementally launching method to contain the construction time of this structural member to within 9 months. Consequently the girder has a continuous layout and its outer cross-section is uniform with overall depth of 3.80 m, so that the girder "depth-to-span length" ratio is approximately 1/12;
- Disregarding the track and the ballast, each 45 m long precast beam has a self-weight of 6000 kN (600 t) so that the self weight of the 23-span viaduct girder is approximately 138000 kN (13800 t);
- The deck is 5.50 m wide and hosts a single track ballasted line with a narrow rail gauge of 1065 mm;
- The girders are longitudinally post-tensioned and transversally reinforced members. In addition, the girder webs were vertically prestressed by a set of 26 mm diameter bars to increase the shear strength under train impact loads;
- Transverse prestressing was not applied and the girders do not have transverse diaphragms;
- Bottom and top girder slabs are of thickness 0.25 m and 0.30 m, respectively. They increase to 0.65 m and 0.70 m at supports and mid-span to accommodate the prestressing tendon anchorages. Consequently, cross-section area and second moment of area (involved in the vertical bending) are 4.91 m^2 and 9.52 m^4, and 6.45 m^2 and 12.70 m^4, respectively;
- The RC piers have a tapered H-type cross-section with flanges oriented along the longitudinal axes of the viaduct. Due to the topography of the Olifants River Valley where the viaduct is located, piers have a different height ranging from 17.85 m (pier #1) to 51.50 m (pier #10). The pier width is uniform (4.60 m), hence the pier "width-to-height" ratio ranges from approximately 1/4 (pier #1) to 1/11 (pier #10).

2.2 Dynamic Characterization of the Viaduct Girder

The first ambient vibration test (AVT) on the ORV was performed in October 2014 on half-span #19, span #20 and half-span #21 in order to identify the natural dynamic properties of the viaduct girder on the Sishen side. Full results from Operational Modal Analysis (OMA) in the vertical and transversal directions of the ORV are reported in [4].

A second more comprehensive AVT was carried out in December 2016. Six spans of the viaduct girder (#18–23), were investigated through a multi-setup AVT, deploying 20 force-balance current-driven accelerometers, 8 of which were reference sensors. The identified modes in the transversal and vertical directions are illustrated in Figs. 3 and 4, respectively. Figure 3 shows the twenty-one transversal bending (TB) modes identified in the frequency range 0–6 Hz, from signals 3200 s long, originally sampled at 256 Hz, by the Frequency Domain Decomposition (FDD) technique [5] as implemented in the SVS ARTeMIS Modal Pro V5.1 software.

Through this second more extensive AVT, the first 3 low-frequency TB modes, seemingly involving the entire 23-span viaduct girder, were identified more clearly. The fundamental natural frequency equals 0.80 Hz, revealing a flexible structure in the transversal direction. In addition, it is worth mentioning that some pairs of closely spaced modes, exhibiting similar mode shapes, such as #1–2, 9–10, 11–12, 16–17 and 19–20 characterize the dynamic behavior of the ORV.

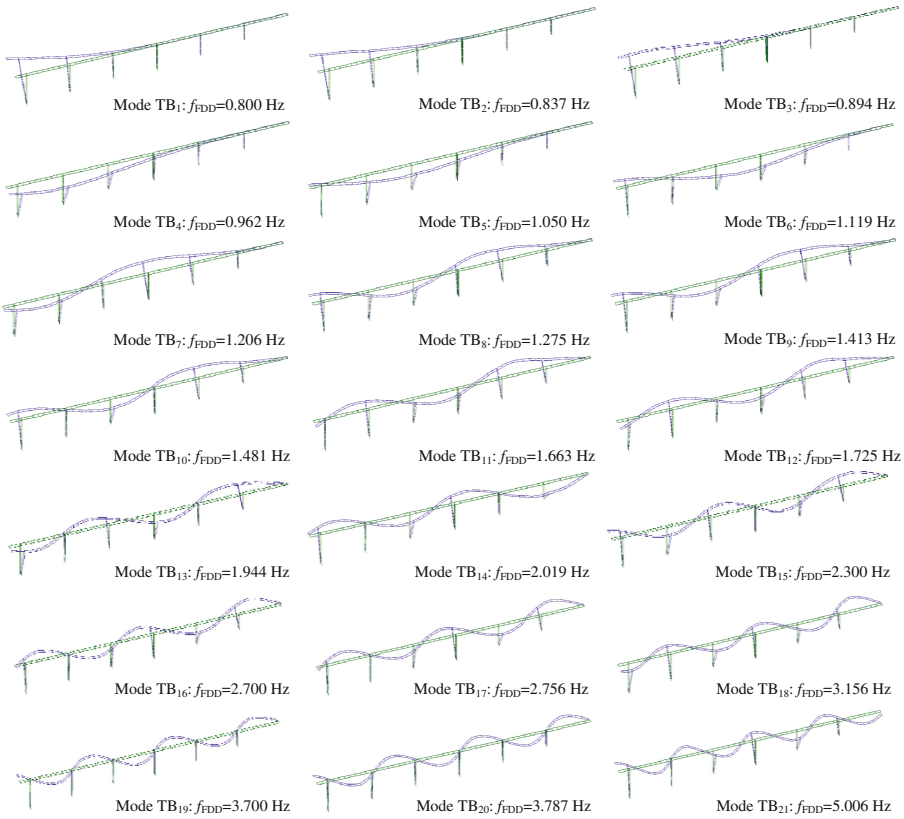

Fig. 3. Transversal bending modes identified through the AVT carried out in December 2016 (spans #18–23).

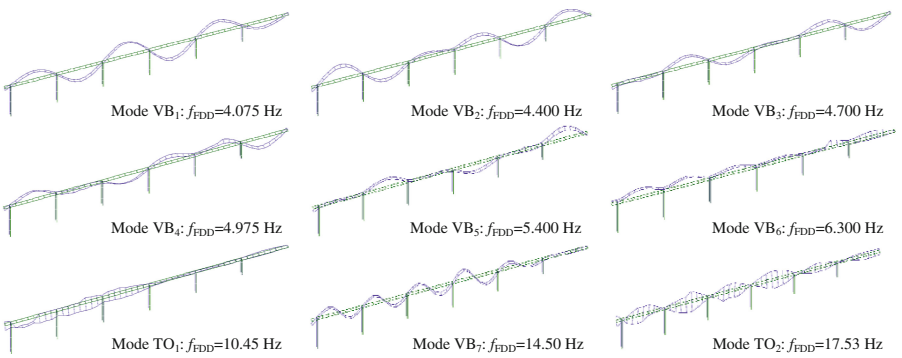

Fig. 4. Vertical bending and torsion modes identified trough the AVT carried out in December 2016 (spans #18–23).

Figure 4 shows the seven vertical bending (VB) modes and two torsion (TO) modes identified in the frequency range 0–20 Hz from signals 3000 s long, sampled at 256 Hz. In this regard, two additional VB modes, denoted as VB_2 and VB_5 in Fig. 4, were identified in addition to the previous AVT due to the very small modal amplitudes of those modes at the spans tested in 2014. The first vertical natural frequency equal to 4.075 Hz, for a 45 m long span, reveals a stiff girder in the vertical direction.

3 The Monitoring System of the Viaduct

The ORV is currently equipped with (a) WIM-WIM system located on the rail at span #21, installed and managed by TFR; (b) a monitoring system located at span #20 installed and managed by the Concrete Materials and Structural Integrity Research Unit (CoMSIRU) of the University of Cape Town (UCT).

The former system consists of 32 strain gauges welded on the rail and a dedicated computer-based DAQ system inside the viaduct girder in order to weigh the train as well as detect excessive wheel irregularities and incorrectly loaded wagons. The latter, installed in late March 2016, is based on the National Instruments CompactRIO (NI cRIO) technology (Fig. 5). An 8-slot NI cRIO-9081 system is located inside the girder, at the support on pier #20, while an 8-slot NI 9149 Ethernet expansion chassis is placed at the mid of span #20. The cRIO hosts five 4-channel NI DAQ modules to acquire signals from 8 strain gauges (SGs), 8 thermocouples (TCs) and 2 crack gauges (CGs). The expansion chassis hosts four 4-channel NI DAQ modules to record signals from 8 accelerometers (AMs), and 8 SGs. The cRIO carries out the DAQ through the Real-Time controller and FPGA module which refer to a dedicated NI operating system to ensure continuous data logging. It is worth mentioning that both continuous

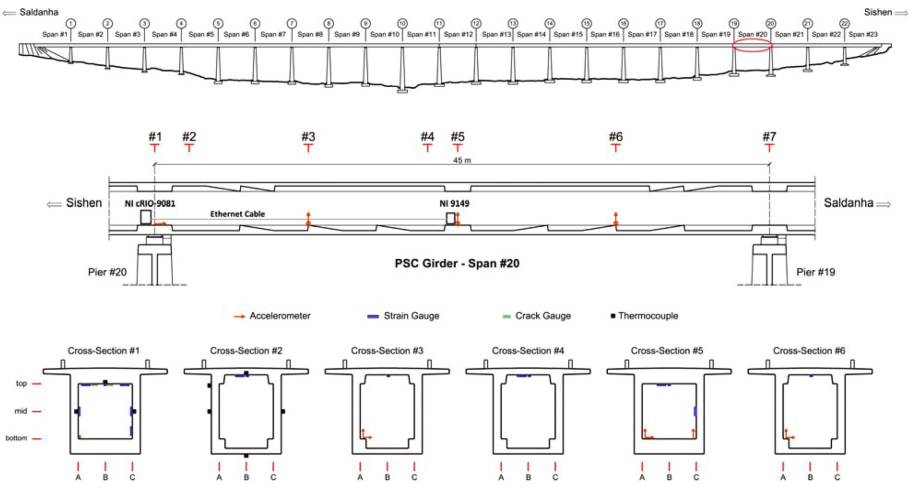

Fig. 5. Schematic of the monitoring system installed on the ORV.

monitoring (CM) and event monitoring (EM) are carried out, the latter to record train signals at higher sampling frequency.

4 Monitoring of the Traffic Loads

4.1 Train Configuration

The typical configuration of the 4.1 km long freight train crossing the Iron Ore Line consists of 4 Locomotive Consists (LC) and 342 Wagons (W) distributed in 3 rakes of 114 cars as follows: LC"A" + 114 W + LC"B" + 114 W + LC"C" + 114 W + LC"D". Details on the 6-axle electric/diesel locomotives and the 4-axle wagon can be found in [4].

The WIM-WIM system provides information of the actual train configuration of both the empty trains moving from the port to the mines and the loaded trains which leave Sishen to reach the commercial harbor in Saldanha. Statistics on the train configuration, as extracted from 503 empty/loaded trains running on the Iron Ore Line from March, 20th 2016 to April, 30th 2016, is shown in Fig. 6. The most frequent train configuration includes 6 locomotives, distributed within the LC "A"–"D" mentioned above, and 342 wagons resulting in a total number of 1404 axles. Short-length trains consisting of 24–38 wagons and medium-length trains of around 200 cars have been operating as well.

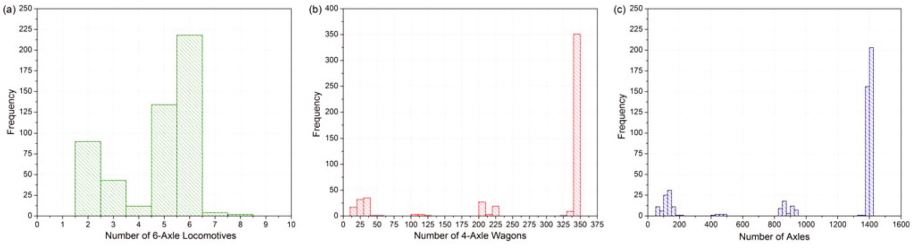

Fig. 6. Statistics on the train configuration: (a) Number of locomotives, (b) Number of wagons and (c) Number of axles.

4.2 Statistics on Heavy Haul Train Speed and Axle Load

A comparison in terms of rail traffic and capacity of the Iron Ore Line over 40 years of operation (1976–2016), is reported in [6], highlighting a significant increase in all the traffic parameters. The 4-axle wagon used in the Sishen-Saldanha train has a nominal axle load equal to 50 kN when empty, 300 kN when loaded. The latter value (30 t/axle) was assumed at the design stage to compute the live load and an impact allowance of 29% was adopted [6]. Taking into account that up to 18 axles can simultaneously load a single span (see Fig. 7) due to the short wheelset distance of the wagon (6.49 m), the live load can reach 5400 kN (540 t) per span, a value very close to the beam self weight (600 t) mentioned in the description of the ORV (disregarding not only the additional dead load due to track and ballast but also the dynamic load amplification).

Fig. 7. The heavy haul freight train crossing the Olifants River Viaduct.

Figure 8 shows statistics on the actual railway moving loads as extracted from the 503 trains mentioned earlier. Min and Max denote the minimum and maximum values of the entire sequence of axle values estimated for the investigated train (e.g. min and max of the 1404 values estimated for a 6-locomotive and 342-wagon train) or related to wagons only. The Mean value comes from the average of all the axle values. As shown in Fig. 8, it is worth noting that the operational speed is sometimes greater than the limit value of 50 km/h on the ORV, with upper values of 60–65 km/h. However, the mean speed generally complies with the limit. The maximum wagon's dynamic axle load is often greater than 400 kN while the mean value is around 330–340 kN. Thus, traffic load monitoring and its integration with the monitoring of the dynamic effects of the viaduct girder can be valuable tools to investigate the actual performance of the ORV under those repetitive moving loads.

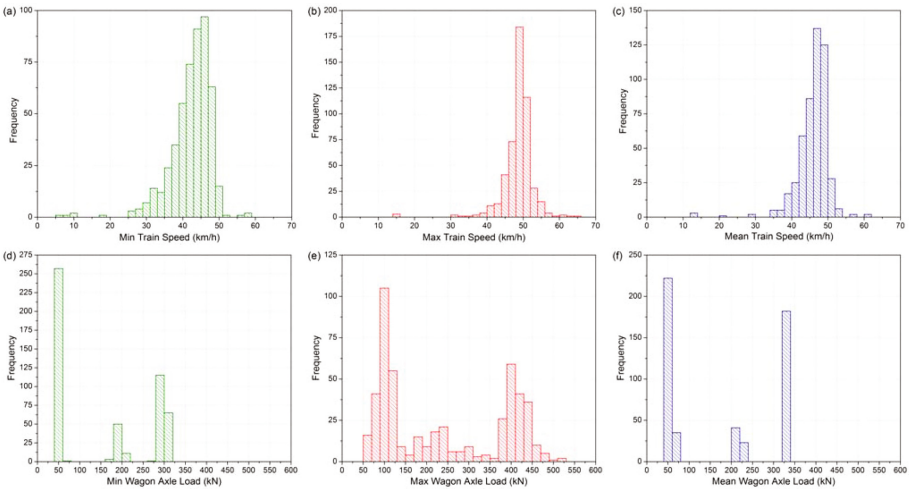

Fig. 8. Statistics on (a–c) minimum, maximum and mean train speed; (d–f) minimum, maximum and mean wagon axle load.

5 Performance Monitoring of the Viaduct Girder

In this section, some selected results from the analysis of CM files, by using in-house NI LabVIEW software, are presented and discussed. In the following, each sensor is denoted according to the schematic of the monitoring system shown in Fig. 5. In this regard, suffix -V/-T/-L stands for "Vertical/Transversal/Longitudinal" direction of the sensor (measuring vector or tensor quantities) with respect to the ORV axes; t/m/b denotes "at the top/mid/bottom" of the cross-section for those sensors distributed at different heights in the cross-section. For example, **3A** AM-V denotes the accelerometer located at cross-section #3, row A, in vertical direction; **1B** TC-t refers to the thermocouple at cross-section #1, row B, positioned at the top.

5.1 Concrete and Ambient Temperature

Temperature monitoring has been performed to support the investigation of the thermal effects on the behavior of the viaduct girder on the Sishen side. This appears of great interest due to (i) the box cross-section and continuous layout of the PSC girder, (ii) the large length of the girder (495 m) and (iii) the influence of the ballasted track with continuous welded rails placed over the entire viaduct deck and abutments. In this regard, 8 TCs were installed on the ORV, 4 sensors inside the girder, embedded in the concrete of girder webs and top slab, and 4 outside (see Fig. 5). Figure 9(a) shows a selected tracking of the concrete temperature in April 2016 at 2 TCs embedded in the webs. The plot clearly shows a daily recurrent trend with the heat due to solar radiation reaching the inner surface of the 350 mm thick webs around midnight with (daily peak). Figure 9(b) shows the evolution of the ambient temperature as recorded through the **2B** TC-b positioned outside, under the girder, during the recent summer season in Vredendal.

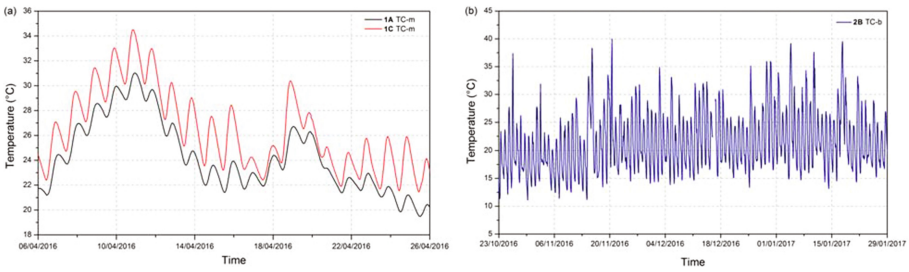

Fig. 9. Tracking of the (a) concrete temperature on the webs; (b) ambient temperature above the girder.

5.2 Natural Frequencies of the Girder

The CM of the natural frequency (f_n) of the vibration modes of the girder aims to investigate their variation over time and related causes. Figure 10(a) shows the tracking of the VB/TO modes identifiable at span #20 over the first six months of CM (20 March 2016-30 September 2016) generally showing an increasing scattering as the

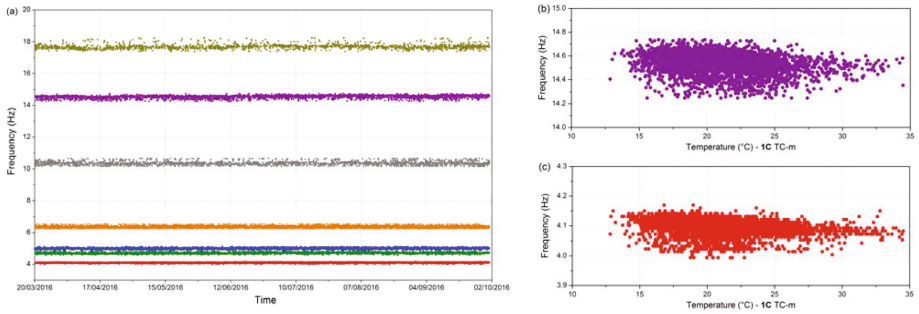

Fig. 10. Selected VB/TO modes: (a) Tracking of natural frequencies; (b–c) Correlation concrete temperature - f_n.

mode order increases. This has been observed also through the AVTs, for example mode VB_1 was identified at 4.075 Hz both in 2014 and 2016 while VB_6 was identified at 6.45 Hz in 2014, 6.30 Hz in the latest test. Figure 10(b–c) shows the correlation "concrete temperature-f_n" for the modes denoted as VB_1 and VB_7 in Fig. 4, highlighting as a decrease in temperature results in a stiffer girder.

5.3 Train-Induced Dynamic Effects on the Viaduct Girder

A preliminary investigation of the train-induced response (see e.g. Figure 11(a)) was performed through the a^{p}_{RMS} function (Fig. 11(b)). The function computes the RMS over each second of the acceleration signal recorded at each p-*th* accelerometer. Figure 11(c) shows the tracking of the mean value of the a^{p}_{RMS} function, at position **3A**, for the 503 trains mentioned earlier. A larger response in the transversal direction than the vertical one has been generally observed.

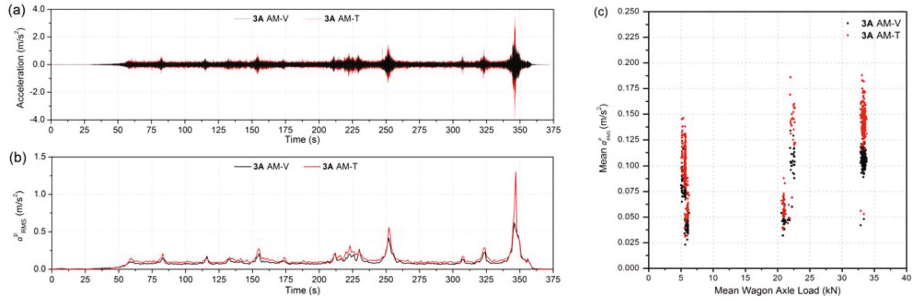

Fig. 11. Example of (a) train time histories; (b) a^{p}_{RMS} functions; and (c) Tracking of the mean a^{p}_{RMS}.

6 Conclusions

The paper presented and discussed the latest dynamic investigation performed on the ORV as well as some selected results from the WIM-WIM and the monitoring systems installed on the railway bridge.

Two large continuous girders characterize the ORV due to the use of the incrementally launching method. As a consequence, dynamic coupling between the girder spans occurs, making the execution of AVT and subsequent OMA challenging as shown for the girder on the Sishen side. Notwithstanding the expansion joints at piers #11–12, a few low-frequency TB modes apparently involving the entire 23-span girder were identified due to the continuous ballasted track over the viaduct. Several closely spaced TB modes and VB modes with very different modal amplitudes from span to span characterize the ORV.

Due to the importance of the ORV and type of rail traffic, a monitoring program of the viaduct girder has been performing since late March 2016 supported by an existing WIM-WIM system. In terms of dynamic behavior, on the one hand, the goal is to investigate the variation of the natural frequencies of the girder over time. On the other hand, the monitoring of train signals aims to detect possible dynamic amplifications of the deck response. In this regard, a preliminary investigation through RMS functions generally showed larger responses in the transversal direction of the ORV than in the vertical one.

Acknowledgments. The Authors gratefully thank Transnet SOC Ltd for financing the research on the ORV and CoMSIRU for the installation of the monitoring system and assistance in conducting the dynamic tests. The first Author gratefully thanks CoMSIRU and the University Research Committee of the UCT for financing his postdoctoral research program.

References

1. Rui Calçada, R., Delgado, R., Campose Matos, A. (eds.): Dynamics of High-Speed Railway Bridges. CRC Press, London (2008)
2. Liu, K., Lombaert, G., DeRoeck, G.: Dynamic analysis of multi-span viaducts with weak coupling between adjacent spans. J. Bridge Eng. ASCE **19**(1), 83–90 (2014)
3. De Roeck. G.: Diagnosis performance of vibration-based structural identification and health monitoring In: 9th International Conference on Structural Dynamics (EURODYN 2014), Porto, PT (2014)
4. Busatta, F., Moyo, P.: Vibration Monitoring of a Large Scale Heavy Haul Railway Viaduct. In: 6th International Conference on Experimental Vibration Analysis of Civil Engineering Structures (EVACES 2015), Dübendorf, CH. MATEC Web of Conferences, 24(04007) (2015). http://dx.doi.org/10.1051/matecconf/20152404007
5. Brincker, R., Ventura, C.E.: Introduction to Operational Modal Analysis. Wiley, Chichester (2015)
6. Busatta, F., Moyo, P.: Performance monitoring of a prestressed concrete railway viaduct: implementation of a system and first results. In: Proceedings of the fib Symposium 2016, Cape Town, RSA (2016)

Specific Dynamic Properties of SFRC Based on Waste Ceramic Aggregate

Jacek Katzer[1(✉)] and Jacek Domski[2]

[1] Koszalin University of Technology, Koszalin, Poland
jacek.katzer@tu.koszalin.pl
[2] Laboratory of Structures and Strength of Materials, Koszalin University of Technology, Koszalin, Poland

Abstract. Red waste ceramics (RWC) is getting increasing popularity as a raw material for coarse aggregate production. Aggregate obtained from RWC is characterized by very high water absorptivity. Therefore traditional concrete mix designing methods are not suitable for mixes based on RWC aggregates and a new approach is required. Replacing traditional coarse aggregates by RWC aggregate significantly influences the homogeneity of properties of hardened concrete and properties themselves. The conducted research programme addressed these technological obstacles through steel fibre reinforcement and the process of internal curing. Fibres were used in volumes of 0.0%, 0.5%, 1.0% and 1.5%. Specimens were in a form of: cubes, cylinders (used for strength tests), prisms (used for LOP test), circular plates (used for impact tests). During the impact tests, deflection and propagation of cracks were followed. Created fibre reinforced RWC concrete is characterized by values of residual flexural strengths enabling substitution of conventional reinforcement.

Keywords: Concrete · Fibre · SFRC · Waste · Aggregate

1 Introduction

Red waste ceramic (RWC) is playing an increasingly important role as a raw material for production of aggregate. In Europe, the volume of construction and demolition waste is usually dominated by red ceramics [1]. Therefore more and more attention is given to different recycling technics of RWC. Harnessing RWC as coarse aggregate for concrete production is becoming the main aim of numerous research programmes. All the testing and research activities focused on harnessing RWC in construction industry have been only partially successful so far. There are some examples of creating and using concretes based on RWC but these concretes are characterized by lesser mechanical performance. The most common application of such concretes are pavement slabs [2, 3]. Utilizing RWC as a coarse aggregate instead of a natural aggregate is associated with multiple technological challenges. The key problems are: workability of fresh mix and compressive strength of hardened concrete. RWC is porous and characterized by extremely high water absorptivity in comparison to natural aggregate. This phenomenon influences the amount of water needed for creation of concrete mix. Traditional concrete mix designing methods used for creation of ordinary concrete

© Springer International Publishing AG 2018
J.P. Conte et al. (eds.), *Experimental Vibration Analysis for Civil Structures*,
Lecture Notes in Civil Engineering 5, https://doi.org/10.1007/978-3-319-67443-8_69

compositions are not suitable for mixes based on RWC. Issues with maintaining water content in fresh RWC concrete mix result in relatively small homogeneity of mechanical properties of hardened concrete. While analysing mechanical performance of RWC based concretes one has to remember that compressive strength of RWC usually ranges from 10 MPa to 12 MPa. In ordinary concrete based on natural aggregate, aggregate is the "strongest" part of concrete volume. The destruction of an ordinary concrete element happens due to failure of a cement mortar not coarse aggregate. Using RWC (characterized by very limited compressive strength) as coarse aggregate significantly influences overall mechanical characteristics of RWC concrete. To overcome limited mechanical performance of RWC based concretes, one can simultaneously utilize fibre reinforcement and the process of internal wet curing [4]. Engineered steel fibre were successfully used for enhancing limited mechanical characteristics of concretes based on varied waste aggregates [5–7]. Therefore achieving similar improvement in case of RWC based concretes is very likely. The efficiency of fibre addition would be influenced by irregular size and shape of the RWC aggregate impacting fibre spacing [8, 9], but the overall mechanical efficiency should be satisfactory. Internal wet curing would be based on pre-saturation of RWC and using its large absorptivity as a "storage" of extra water for extended and thus very efficient curing process. The main aim of the planned experimental programme was to achieve, RWC based and modified by fibre, concrete with mechanical properties enabling its full structural application. The developed concrete would be characterized by non-conventional properties allowing using it for dynamically loaded structural elements. Successful merging RWC, fibre reinforcement and internal wet curing process would result in creating sustainable concrete for construction industry.

2 Research Programme

2.1 Materials and Mix Proportioning

During the research programme RWC obtained from construction debris was used. This raw RWC consists of different types of broken and crushed ceramic wall blocks, hollow and wire-cut bricks. This kind of RWC which is partially contaminated by cement mortar is very common in Europe [2]. It emerges during multiple civil engineering activities starting from the very production of elements, through transportation to execution of construction etc. [1]. The creation of RWC aggregate was a two-stage process. Stage number 1 covered grinding raw RWC using an electric industrial grinder with 21 steel spheres (from 1343 g to 2650 g) [10]. At the end of grinding the all-in-aggregate was achieved. Stage number 2 covered sieving all-in-aggregate to separate fractions characterized by a diameter larger than 32.0 mm and smaller than 1.0 mm. Granular properties of RWC aggregate were established with the help of rectangular sieve set described by EN 933-1:2012 [11]. Properties of RWC aggregate after two stages of preparation process are presented in Table 1.

Natural sand of post-glacial origin washed from all-in-aggregate during hydro-classification process was used as fine aggregate. The main mineral components of this sand are quartz and granite. For creation of all mixes Portland cement CEM I

Table 1. Properties of RWC aggregate after two stages of preparation process.

Bulk density		Absorptivity by weight	Fineness modulus			Median diameter
Loose	Bulk		by Hummel	by Abrams	by Kuczyński	
[kg/m^3]	[kg/m^3]	[%]	[-]	[-]	[-]	[mm]
948	1170	22	213.4	7.1	8.2	7.4

42.5 which complies with EN 197-1:2011 [12] was utilized as a binder. The mixes were modified by admixture of 1% of silica fume FM superplasticizer characterized by density of 1.45 g/cm^3. Tap water fulfilling the requirements of EN 1008:2002 [13] was the last ingredient of the mix.

Engineered steel fibre was preliminary selected as fibre reinforcement. From all commercially available engineered steel fibre, hooked fibre is the most commonly used for production of fibre reinforced concrete. The chosen hooked fibre was characterized by a circular cross-section. The main geometrical and mechanical properties of the fibre are presented in Table 2.

Table 2. Properties of the engineered steel fibre.

Length - L [mm]	Diameter - d [mm]	L/d [-]	FIER[d] [-]	Hook [mm]	R_m[a] [MPa]	Ductility[b] [№ bends]	Steel[c] [-]
60	0.75	80	321.04	5.75	1040	9.0	Group I

a- EN ISO 6892-1:2009 [14]
b- EN 10218-1:2012 [15]
c- EN 14889-1:2006 [16
d- Fibre intrinsic efficiency ratio proposed by Naaman [17]

RWC aggregate was fully saturated before the use. The full saturation stabilized properties of the fresh mixes during all stages of handling, mixing and casting. Traditionally calculated mix composition was adjusted to take into account water absorbed by RWC aggregate. This extra water influences both the properties of fresh mix and the curing process through internal wet curing process. The adjustment of water amount was conducted by basic "trial and error method" due to unknown proportions of water influencing consistency and curing. Mix proportions of cast concrete are presented in Table 3.

Table 3. Mix proportions in kg.

Saturated RWC aggregate	Water trapped in RWC aggregate	Oven dry sand	Cement	Water	Admixture
830.0	182.6	652.0	307.0	92.0	3.1

The total mass of one cubic meter of fresh RWC concrete mix was equal to 1884.1 kg. There were cast five mixes. One was without fibre, four other ones were modified by fibre addition of 0.0%, 0.5%, 1.0% and 1.5% (by volume).

The specimens were cast in two layers in laboratory conditions. Each layer was compacted on a vibrating table. For the first 24 h after casting the specimens were kept in moulds covered with polyethylene sheets. After 24 h specimens were removed from moulds and placed in a tank with water characterized by temperature +21 °C ± 1 °C. Total time of curing was equal to 28 days.

2.2 Specimens and Tests

The degree of compactability method defined by EN 12350-4:2009 [18] was used for assessing the consistency of all fresh mixes. There were cast cube, cylinder, prism and plate specimens. Density checks were conducted on all available specimens. The compressive and splitting tensile strength were tested on cube and cylinder specimens. During the compressive strength tests, stress–strain relations of cylinder specimens were followed and static modulus of elasticity was established. Prisms were used for flexural strength tests based on CMOD method and establishing values of all residual strengths. Circular plates were tested on the tailored lab stand designated for impact tests. The conducted test programme and prepared specimens are summarized in Table 4.

Table 4. Tests and specimens

Test		Specimen	
Property	Standard	Type	Size [mm]
Consistency	EN 12350-4:2009 [18]	Fresh mix	-
Compressive strength splitting tensile strength	EN 12390-3:2009 [19] EN 12390-6:2009 [20]	Cube	b = 150, h = 150, l = 150
Compressive strength static modulus of elasticity	EN 12390-3:2009 [19] EN 12390-13:2013 [21]	Cylinder	φ = 150, h = 300
Flexural tensile strength shear strength	EN 14651:2005 [22] JCI-SF6:1984 [23]	Prism	b = 150, h = 150, l = 700
Impact tests	Tailored lab stand [24]	Circular plate	φ = 1000, h = 100

The tailored lab stand designated for impact tests was built from steel modular elements of high load carrying capacity. The stand was mounted on a massive concrete block structurally separated from the rest of the testing hall and equipped with multiple mounting pockets. The concrete block with dimensions of 8.00 m • 10.00 m • 1.45 m is able to support vertical and horizontal loads up to 50 tonnes. Tested plates were installed on the three massive supports located on the circumference. During the test, the plate has been loaded by the free fall of 40 kg mass from the 1.0 m height. After each impact

Fig. 1. The tailored lab stand for impact tests (left), mounted slab during the test and three supports (right).

deflection of the plate and cracks width were measured. The deflection was measured in 17 locations and cracks width was measured on the bottom surface of a slab. The tailored lab stand is presented in Fig. 1 [24].

3 Results

All prepared mixes were characterized by consistency class C2 according to EN 206:2013 [25], thus there were no doubts considering quality of casting and compaction. Testing density of all available specimens played a role of a partial quality control. A large number of achieved results enabled full statistical analysis. The full density characteristics of tested concretes is presented in Table 5.

Table 5. Density characteristics of hardened concretes

Volume of fibre [%]	Density [kg/m^3]	Standard deviation [kg/m^3]	Volatility ratio [%]
0.0	2001	23.14	1.16
0.5	2006	29.29	1.46
1.0	2048	28.36	1.38
1.5	2096	32.58	1.55

Static modulus of elasticity (E) of RWC concrete with no fibre was equal 22 GPa. All fibre reinforced RWC concretes were characterized by $E = 23$ GPa. Strength properties of tested concretes are presented in Fig. 2. All strengths are growing along the increasing volume of added fibre. RWA concrete with no fibre is characterized by "cube" compressive strength of 39.1 MPa and "cylinder" compressive strength of 27.9 MPa. Concrete reinforced by $V_f = 1.5\%$ is characterized by "cube" compressive strength of 50.6 MPa and "cylinder" compressive strength of 34.4 MPa. In cases of both compressive strengths RWC concrete reinforced by $V_f = 1.5\%$ performed better than the unreinforced one by 29.4% and 23.3% respectively. It is worth noticing that differences between cylinder and cube compressive strengths of RWC concretes are higher than those described by EN 206:2013 [25] for ordinary concrete. The RWC concrete with no fibre fulfills strength requirements for class C25/30. Theoretical strength difference is 5 MPa, but in reality it is equal to 9 MPa. The RWC concrete with 1.5% of fibre volume fulfills strength requirements for class C32/40. Theoretical strength difference is 8 MPa, but in reality it is equal to 16 MPa. In assigning both strength classes the value of cylinder strength was critical and thus cube strength was significantly underestimated. Therefore the strength classes dedicated for ordinary concrete are subjected to large inaccuracy in case of describing RWC fibre reinforced concrete. Shear strength of tested concretes ranges from 5.0 MPa for unreinforced concrete to 11.6 MPa for the concrete reinforced by $V_f = 1.5\%$ (improvement of 133%). The values of tensile strength range from 3.1 MPa for RWC concrete with no fibre to 5.4 MPa for concrete reinforced by $V_f = 1.5\%$ (see Fig. 2). It gave the 74% improvement of tensile strength.

Flexural characteristics of tested RWC concretes are presented in Fig. 3. During the tests both force-deflection and force-CMOD relation were recorded and calculation of residual strengths (f_{LOP}, $f_{R,1}$, $f_{R,2}$, $f_{R,3}$, $f_{\mathrm{R},4}$) was enabled. All tested RWC fibre

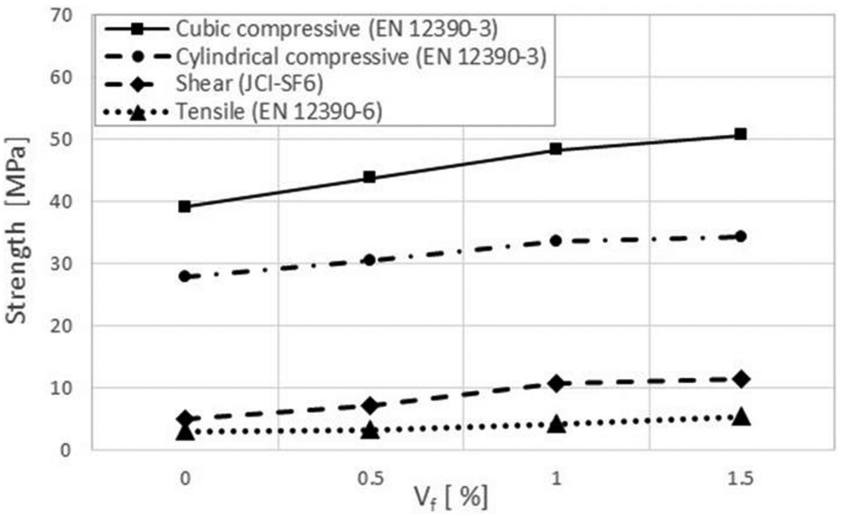

Fig. 2. Compressive, shear and tensile strength of tested fibre RWC concretes.

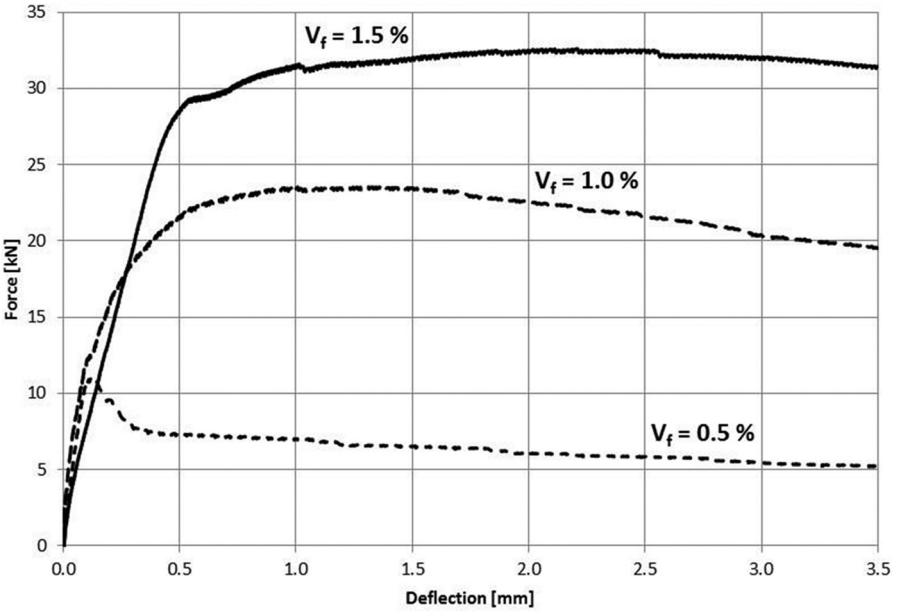

Fig. 3. Flexural performance of tested RWC fibre concretes.

reinforced concretes are characterized by significantly larger than the required minimum values of residual strengths $f_{R,1}$ and $f_{R,4}$. Residual strengths $f_{R,1}$ and $f_{R,3}$ are commonly assumed to characterize service (SLS) and ultimate (ULS) conditions respectively. There were also computed values of two factors: $f_{R,3}$ /$f_{R,1}$ and $f_{R,1}$ /f_{LOP} for

Table 6. Residual strengths and strength class of tested fibre RWC concretes

Property	Unit	Value		
V_f	[%]	0.5	1.0	1.5
f_{LOP} (limit of proportionality according to EN 14651)	[MPa]	3.3	2.9	1.9
f_{R1} (residual flexural strength corresponding with $CMOD_1$)	[MPa]	2.4	6.4	8.7
f_{R2} (residual flexural strength corresponding with $CMOD_2$)	[MPa]	2.3	7.5	10.1
f_{R3} (residual flexural strength corresponding with $CMOD_3$)	[MPa]	2.1	7.5	10.4
f_{R4} (residual flexural strength corresponding with $CMOD_4$)	[MPa]	1.9	7.2	10.4
f_{R3}/f_{R1} (>0.5)	[-]	0.88	1.16	1.19
f_{R1}/f_{LOP} (>0.4)	[-]	0.7	2.2	4.6
Conventional reinforcement substitution	[-]	enabled	enabled	enabled
Strength class according to *fib* Model Code 2010	[-]	2b	6d	8d

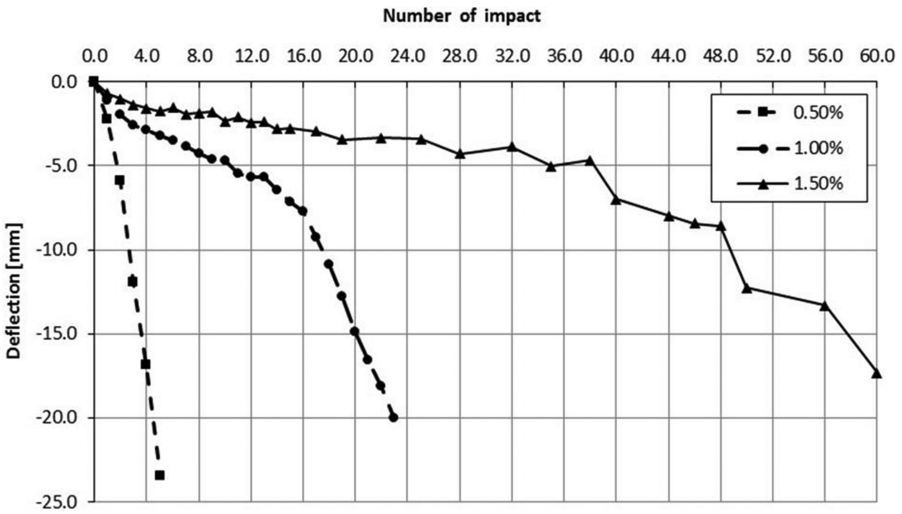

Fig. 4. Deflection of RWC fibre concretes slabs after impacts

all tested concretes. The values of the factors were used to assign strength classes according to Model Code 2010 [26]. The possible substitution of traditional rebar/stirrup reinforcement was assessed. Residual strengths, strength class and enabled conventional reinforcement substitution of tested fibre RWC concretes are presented in Table 6.

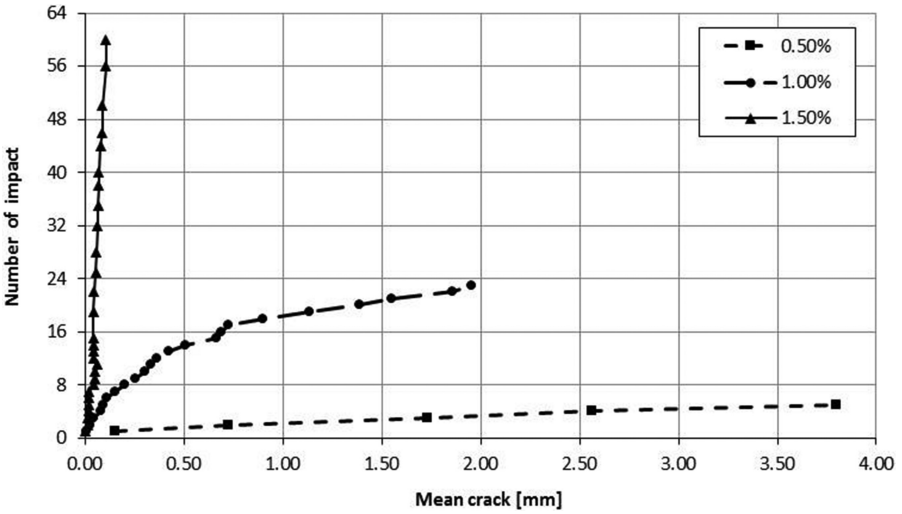

Fig. 5. Mean crack opening after varied number of impacts

The results of the circular slab impact test are presented in Figs. 4 and 5 in a form of relations impacts-deflection and impacts-mean crack opening respectively. When the deflection (δ) of a slab was reaching 20 mm it was considered as destroyed. The slab with no fibre was brittle and ultimately destroyed after the first impact. Slabs reinforced by V_f equal to 0.5, 1.0 and 1.5% were characterized by $\delta \leq 15$ mm after 4, 21 and 60 impacts respectively. When deflection reaches 15 mm crack mouth openings are much wider than the limit of 0.4 mm defined by EN1992-1:2004 [27]. In case of dynamic loadings serviceability limits are of secondary interest [28].

4 Conclusions

Using strength class of ordinary concrete to describe RWC fibre reinforced concretes is doubtful.

Flexural characteristics of RWC fibre reinforced concretes allowed to classify them as 2b, 6d and 8d.

Tested RWC fibre reinforced concretes are characterized by mechanical properties enabling substitution of traditional rebar/stirrup reinforcement.

The largest changes in strength associated with fibre addition were observed during the shear test.

Tests performed on the entire set of plates show that the presence of fibres in RWC concrete significantly influences a dynamic response to impact loads.

References

1. Correia, J.R., et al.: Effects on concrete durability of using recycled ceramic aggregates. Mater. Struct. **39**, 169–177 (2006)
2. De Brito, J., et al.: Mechanical behaviour of non-structural concrete made with recycled ceramic aggregates. Cement Concr. Compos. **27**, 429–433 (2005)
3. Hendriks, C.F., Janssen, G.M.T.: Use of recycled materials in construction. Mater. Struct. **36**, 604–608 (2003)
4. Suzuki, M., et al.: Use of porous ceramic waste aggregates for internal curing of high-performance concrete. Cem. Concr. Res. **39**, 373–381 (2009)
5. Domski, J.: Long-term study on fibre reinforced fine aggregate concrete beams based on waste sand. Rocznik Ochrona Srodowiska **17**, 188–199 (2015)
6. Katzer, J.: Properties of precast SFRCC beams under harmonic load. Sci. Eng. Compos. Mater. **15**(2), 107–120 (2008)
7. Łapko, A., Grygo, R.: Effectiveness of the use of recycling aggregate concrete for sustainable building structures. Rocznik Ochrona Srodowiska **16**, 627–638 (2014)
8. Maidl, B.R.: Steel Fibre Reinforced Concrete. Ernst & Sohn, Berlin (1995)
9. Johnston, C.D.: Fibre Reinforced Cements and Concretes. Gordon and Breach Science Publishers, Amsterdam (2001)
10. Domski, J., et al.: Load-CMOD characteristics of fibre reinforced cementitious composites based on waste ceramic aggregate. Rocznik Ochrona Srodowiska **14**, 69–80 (2012)
11. EN 933-1 Tests for geometrical properties of aggregates. Determination of particle size distribution. Sieving method, 18 p. (2012)

12. EN 197-1 Cement. Composition, specifications and conformity criteria for common cements, p. 38 (2011)
13. EN 1008 Mixing water for concrete. Specification for sampling, testing and assessing the suitability of water, including water recovered from processes in the concrete industry, as mixing water for concrete, p. 19 (2002)
14. EN ISO 6892-1 Metallic materials. Tensile testing. Method of test at room temperature, p. 71 (2009)
15. EN 10218-1 Steel wire and wire products. General Test methods, p. 12 (2012)
16. EN 14889-1 Fibres for concrete. Steel fibres. Definitions, specifications and conformity, p. 25 (2006)
17. Naaman, A.E.: Engineered steel fibres with optimal properties for reinforcement of cement composites. J. Adv. Concr. Technol. **1**, 241–252 (2003)
18. EN 12350-4 Testing fresh concrete. Degree of compactability, p. 10 (2009)
19. EN 12390-3 Testing hardened concrete. Compressive strength of test specimens, p. 20 (2009)
20. EN 12390-6 Testing hardened concrete. Tensile splitting strength of test specimen, p. 13 (2009)
21. EN 12390-13 Testing hardened concrete. Determination of secant modulus of elasticity in compression, p. 16 (2013)
22. EN 14651 Test method for metallic fibered concrete – measuring the flexural strength (limit of proportionality (LOP), residual), p. 17 (2005)
23. JCI-SF6 Method of test for shear strength of fibre reinforced concrete, 3 p. (1984)
24. Katzer, J., Domski, J.: Characteristics of concrete based on red waste ceramics and reinforced by steel fibre. In: Fourth International Conference on Sustainable Construction Materials and Technologies SCMT4, Las Vegas, Nevada, USA, 7–11 August 2016
25. EN 206 Concrete. Specification, performance, production and conformity, p. 95 (2013)
26. Model Code First complete draft. International Federation tor Structural Concrete (*fib*), Bulletin 55 (2010)
27. EN 1992-1-1 Design of concrete structures. General rules and rules for buildings, p. 209 (2004)
28. Cichocki, K., Adamczyk, R., Ruchwa, M.: Material modelling for structures subjected to impulsive loading. Comput. Assist. Mech. Eng. Sci. **6**(2), 231–244 (1999)

Parametric Estimation of Wave Dispersion for System Identification of Building Structures

Hamed Ebrahimian(✉), Monica Kohler, Anthony Massari, and Domniki Asimaki

Department of Mechanical and Civil Engineering, Caltech, Pasadena, CA, USA
hebrahim@caltech.edu

Abstract. The linear-elastic response of a building structure subjected to an earthquake base excitation can be approximated as the response of a continuous, spatially inhomogenous, dispersive, viscoelastic solid subjected to vertically incident plane shear waves. The frequency-dependent phase velocity and attenuation of seismic energy at different wavelengths, together with the inertial properties of the multilayer solid characterize the response of the building structure. The objective of this study is to identify the structural system by estimating the parameters that characterize the propagation of seismic waves in an equivalent multilayer viscoelastic solid. To pursue this objective, first, the measured dynamic responses of a building structure are used to derive the frequency response functions (FRFs) of the floor absolute acceleration with respect to the base excitation using a seismic interferometry approach. The FRFs obtained from the measured structural responses are then compared with the FRFs estimated using analytical models for one-dimensional shear wave propagation in a multilayer Kelvin-Voigt dispersive medium. Through a recursive Bayesian estimation approach, the parameters characterizing the phase velocity and damping ratio of the multilayer medium are estimated. This study provides a step forward in seismic interferometric identification of building structures by proposing a new method for parametric estimation of shear wave velocity and damping dispersion at the story level of a building structure. The estimated shear wave velocities before and after a damage-inducing event can be used to identify permanent loss of effective lateral stiffness of the building structure at the story level, thus can provide an alternative method for structural health monitoring and damage identification.

Keywords: Wave inversion · Dispersion · Bayesian estimation · Interferometry · Structural system identification

1 Introduction

The linear-elastic response of a building structure subjected to an earthquake base excitation can be approximated by modeling the propagation of seismic waves through a continuous, layered, viscoelastic solid. The velocity of shear waves, which are induced by seismic base excitation and propagating along the building height, can be estimated from the impulse response functions (IRFs) of the building structure, e.g., [1–6] to name only a few. Considering that the shear wave velocity is related to the

© Springer International Publishing AG 2018
J.P. Conte et al. (eds.), *Experimental Vibration Analysis for Civil Structures*,
Lecture Notes in Civil Engineering 5, https://doi.org/10.1007/978-3-319-67443-8_70

lateral stiffness of the building structure, several studies have been able to detect structural damage in terms of loss of effective lateral stiffness by comparing estimated shear wave velocities from the pre- and post-damage IRFs (e.g., [7–9]).

In this study, an advanced sequential Bayesian estimation method for parametric estimation of wave dispersion in a continuous, multilayer, viscoelastic solid is proposed. While the proposed approach in this study is general and can be applied to other wave inversion problems, it is validated using a structural system identification case study. In this case study, a building structure is identified as a layered, dispersive, Kelvin-Voigt model, in which each layer represents a story or group of stories. Empirical functions are defined to characterize the dispersion of phase velocity and damping ratio at each layer. The parameters characterizing phase velocity and damping ratio as a function of frequency, and mass density profile along the building height are estimated and their estimation uncertainties are quantified by minimizing the discrepancies between the measured and predicted FRFs.

2 Parametric Estimation of Seismic Wave Dispersion

2.1 One-Dimensional Wave Propagation in a Multilayered Kelvin-Voigt Model

To analyze the seismic wave propagation in a building structure, the building is modeled as a horizontally layered shear beam on a rigid base excited by vertically incident plane shear waves (Fig. 1). The shear force-deformation response of each layer of the shear beam is characterized by a Kelvin-Voigt viscoelastic material model. The solution to the vertically propagating SH-wave in a layered shear beam for a harmonic motion of frequency f can be expressed as [10]

$$\boldsymbol{u}(z,t) = \boldsymbol{A}\, e^{\boldsymbol{i}(2\pi f t + k^* z)} + \boldsymbol{B}\, e^{\boldsymbol{i}(2\pi f t - k^* z)} \tag{1}$$

in which $\boldsymbol{A}, \boldsymbol{B}$ = constants representing the amplitude of the waves travelling in $-z$ and $+z$ (upward and downward) directions, respectively, and $\boldsymbol{k}^* = 2\pi \boldsymbol{f}/\boldsymbol{V}^*$ is the complex wave number. The term $\boldsymbol{V}^* = \boldsymbol{V}\sqrt{1+2\boldsymbol{i}\xi}$ is the complex shear wave velocity and $\xi = \pi\eta \boldsymbol{f}/\boldsymbol{G}$ is the damping ratio, where η denotes the viscosity and $\boldsymbol{G}$ denotes the shear modulus of the Kelvin-Voigt material model.

By introducing a local coordinate system for each layer as shown in Fig. 1, the displacement and force compatibility at each layer interface yields the following two equations.

$$\boldsymbol{u}_{\boldsymbol{m}+1}(\boldsymbol{h}_{\boldsymbol{m}+1}, \boldsymbol{t}) = \boldsymbol{u}_{\boldsymbol{m}}(0, \boldsymbol{t}) \;\Rightarrow\; \boldsymbol{A}_{\boldsymbol{m}+1} e^{-\boldsymbol{i}k^*_{\boldsymbol{m}+1}\boldsymbol{h}_{\boldsymbol{m}+1}} + \boldsymbol{B}_{\boldsymbol{m}+1} e^{-\boldsymbol{i}k^*_{\boldsymbol{m}+1}\boldsymbol{h}_{\boldsymbol{m}+1}} = \boldsymbol{A}_{\boldsymbol{m}} + \boldsymbol{B}_{\boldsymbol{m}} \tag{2}$$

$$\begin{aligned} \tau_{\boldsymbol{m}+1}(\boldsymbol{h}_{\boldsymbol{m}+1}, \boldsymbol{t}) = \tau_m(0, \boldsymbol{t}) \;\Rightarrow\; & G^*_{\boldsymbol{m}+1} k^*_{\boldsymbol{m}+1} \left(\boldsymbol{A}_{\boldsymbol{m}+1} e^{-\boldsymbol{i}k^*_{\boldsymbol{m}+1}\boldsymbol{h}_{\boldsymbol{m}+1}} - \boldsymbol{B}_{\boldsymbol{m}+1} e^{-\boldsymbol{i}k^*_{\boldsymbol{m}+1}\boldsymbol{h}_{\boldsymbol{m}+1}} \right) \\ & = G^*_{\boldsymbol{m}} k^*_{\boldsymbol{m}} (A_{\boldsymbol{m}} - B_{\boldsymbol{m}}) \end{aligned} \tag{3}$$

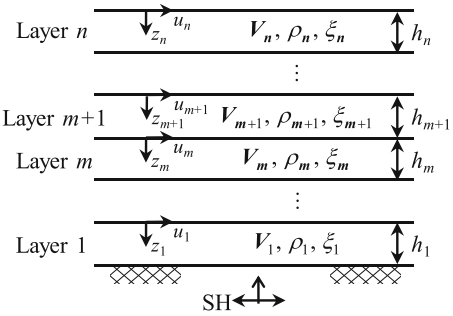

Fig. 1. Multilayer Kelvin-Voigt shear beam model on a rigid base.

where $\boldsymbol{u_m(z, t)}$ and $\boldsymbol{\tau_m(z, t)}$ represent the displacement and shear stress of layer m, respectively, and the shear stress is defined as $\tau_m = G_m^* \partial u_m / \partial z$, in which the complex shear modulus is expressed as $G_m^* = G_m(1 + 2i\xi_m)$. Equations (2) and (3) can be solved to find the wave amplitude factors at layer m as a function of those at layer $m + 1$.

$$\begin{bmatrix} A_m \\ B_m \end{bmatrix} = \frac{1}{2} \begin{bmatrix} (1+\alpha_{m+1})\, e^{ik^*_{m+1}h_{m+1}} & (1-\alpha_{m+1})\, e^{ik^*_{m+1}h_{m+1}} \\ (1-\alpha_{m+1})\, e^{-ik^*_{m+1}h_{m+1}} & (1+\alpha_{m+1})\, e^{ik^*_{m+1}h_{m+1}} \end{bmatrix} \begin{bmatrix} A_{m+1} \\ B_{m+1} \end{bmatrix} \tag{4}$$

in which $\alpha_{m+1} = \frac{\rho_{m+1} V^*_{m+1}}{\rho_m V^*_m}$ is the complex impedance ratio between layer $m + 1$ and m, ρ_m is the mass density of layer m, and $V_m^* = \sqrt{G_m^*/\rho_m}$. By considering a stress-free surface at the top of layer n (i.e., $\tau_n(0, t) = 0$), it can be concluded that $A_n = B_n = A$, where A is a constant. Therefore, the recursive solution shown in Eq. (4) can be used repeatedly to find the following relationship between the amplitude of the travelling waves in layer m and layer n, i.e., the top layer.

$$A_m = \alpha_m(\boldsymbol{\theta}, f)\, A, \;\; B_m = \beta_m(\boldsymbol{\theta}, f)\, A \tag{5}$$

where $\alpha_m(\boldsymbol{\theta}, f)$ and $\beta_m(\boldsymbol{\theta}, f)$ are scalar valued functions of frequency and the wave model parameter vector, which is denoted by $\boldsymbol{\theta}$. The wave model parameter vector consists of shear wave velocity, density, and damping ratio of the layers. The absolute displacement (or acceleration) FRF (or transfer function) at the top of layer m with respect to the displacement (or acceleration) input at the base is denoted as $H_m(\boldsymbol{\theta}, f)$ and is derived as

$$H_m(\boldsymbol{\theta}, f) = \frac{u_m(0, t)}{u_1(h_1, t)} = \frac{\alpha_m(\boldsymbol{\theta}, f) + \beta_m(\boldsymbol{\theta}, f)}{\alpha_1(\boldsymbol{\theta}, f)\, e^{ik^*_1 h_1} + \beta_1(\boldsymbol{\theta}, f)\, e^{ik^*_1 h_1}} \tag{6}$$

2.2 Dispersive Model Parametrization

The shear wave propagation in building structures is known to be dispersive, i.e., shear waves of different wavelength propagate at different velocities. The flexural and flexural-shear modes of deformation are most likely the main reason for dispersion of shear waves in a building structure [11, 12]. In order to account for the dispersion, an empirical function is proposed in this study to characterize the shear wave phase velocity as a function of frequency at each layer as

$$\boldsymbol{V_m}(\boldsymbol{f}) = \frac{\boldsymbol{a_m^V}\left(\frac{\boldsymbol{f}}{\boldsymbol{f}_{\max}}\right)}{\boldsymbol{b_m^V}\left(\frac{\boldsymbol{f}}{\boldsymbol{f}_{\max}}\right)^2 + \boldsymbol{c_m^V}\left(\frac{\boldsymbol{f}}{\boldsymbol{f}_{\max}}\right) + 1} \tag{7}$$

in which $\boldsymbol{f}_{\max}$ is the maximum frequency to be considered in the estimation (i.e., $0 \leq \boldsymbol{f} \leq \boldsymbol{f}_{\max}$). The phase velocity function has three degrees of freedom; thus, it can be fully characterized by determining the slopes at $\boldsymbol{f} = 0$ and $\boldsymbol{f} = \boldsymbol{f}_{\max}$, and the phase velocity at $\boldsymbol{f} = \boldsymbol{f}_{\max}$. To ensure a smooth positive phase velocity function, monotonically increasing with a negative curvature, the following constraints are defined for the phase velocity parameters at each layer.

$$\boldsymbol{a_m^V} > 0, \quad \boldsymbol{b_m^V} < 1, \quad \boldsymbol{c_m^V} > 0, \quad \boldsymbol{b_m^V} + \frac{1}{2}\boldsymbol{c_m^V} > 0 \tag{8}$$

Therefore, the phase velocity parameter vector to be estimated for layer m is defined as $\boldsymbol{\theta_m^V} = \left[\boldsymbol{a_m^V}, \boldsymbol{b_m^V}, \boldsymbol{c_m^V}\right]$. Consequently, the phase velocity parameter vector for the multilayer model shown in Fig. 1 is defined as $\boldsymbol{\theta^V} = \left[\boldsymbol{\theta_1^V}, \boldsymbol{\theta_2^V}, \ldots, \boldsymbol{\theta_n^V}\right]$.

2.3 Sequential Bayesian Estimation of Wave Model Parameters Using FRFs

The frequency domain is discretized into N sampling points with frequency spacing $\Delta\boldsymbol{f} = \boldsymbol{f}_{\max}/\boldsymbol{N} - 1$. At each sampling point, the FRFs are estimated from the analytical model and measurement data. The predicted FRF from the analytical model at the top of layer m at the k^{th} frequency sampling point is denoted as $\boldsymbol{H_{mk}}(\boldsymbol{\theta}) = \boldsymbol{H_m}(\boldsymbol{\theta}, (\boldsymbol{k}-1)\times \Delta\boldsymbol{f}) = \boldsymbol{H_{mk}^R} + i\boldsymbol{H_{mk}^I}$, where $\boldsymbol{H_{mk}^R}$ and $\boldsymbol{H_{mk}^I}$ are the real and imaginary parts of $\boldsymbol{H_{mk}}$, respectively, and i denotes the imaginary unit. The values of the estimated FRFs can be stacked in a tall vector, as

$$\hat{\mathbf{y}}_k(\boldsymbol{\theta}) = \left[\left[\left[H_{11}^R \;\; H_{11}^I\right] \;\; \left[H_{12}^R \;\; H_{12}^I\right] \;\; \cdots \;\; \left[H_{1k}^R \;\; H_{1k}^I\right]\right] \;\; \cdots \;\; \left[\left[H_{n1}^R \;\; H_{n1}^I\right] \;\; \left[H_{n2}^R \;\; H_{n2}^I\right] \;\; \cdots \;\; \left[H_{nk}^R \;\; H_{nk}^I\right]\right]\right]^T \tag{9}$$

in which $\hat{\mathbf{y}}_k \in \mathbb{R}^{(2\boldsymbol{kn})\times 1}$ $(1 \leq \boldsymbol{k} \leq \boldsymbol{N})$ is the predicted FRF vector, and n depicts the number of layers. Similarly, the measured FRFs are estimated at the same frequency sampling points and stacked in the measured FRF vector, $\mathbf{y}_k$, as

$$\mathbf{y}_k(\boldsymbol{\theta}) = \left[\left[\begin{bmatrix}\hat{\hat{G}}_{11}^R & \hat{\hat{G}}_{11}^I\end{bmatrix}\ \begin{bmatrix}\hat{\hat{G}}_{12}^R & \hat{\hat{G}}_{12}^I\end{bmatrix}\ \cdots\ \begin{bmatrix}\hat{\hat{G}}_{1k}^R & \hat{\hat{G}}_{1k}^I\end{bmatrix}\right]\ \cdots\ \left[\begin{bmatrix}\hat{\hat{G}}_{n1}^R & \hat{\hat{G}}_{n1}^I\end{bmatrix}\ \begin{bmatrix}\hat{\hat{G}}_{n2}^R & \hat{\hat{G}}_{n2}^I\end{bmatrix}\ \cdots\ \begin{bmatrix}\hat{\hat{G}}_{nk}^R & \hat{\hat{G}}_{nk}^I\end{bmatrix}\right]\right]^T \tag{10}$$

in which $\hat{\hat{\mathbf{G}}}_{mk}$ is the estimated transfer functions (or FRF) between the output measurements at the top of layer m and the input excitations at the k^{th} frequency sampling point. The FRFs are estimated as

$$\hat{\hat{\mathbf{G}}}_{\boldsymbol{m}}(\boldsymbol{f}) = \frac{\hat{\hat{\Phi}}_{\boldsymbol{a_m a_g}}(\boldsymbol{f})}{\hat{\hat{\Phi}}_{\boldsymbol{a_g a_g}}(\boldsymbol{f})} \tag{11}$$

where $\hat{\hat{\Phi}}_{\boldsymbol{a_m a_g}}(\boldsymbol{f})$ = cross spectral density between the floor absolute acceleration response measured at level m of a building structure, $\boldsymbol{a_m(t)}$, and the ground acceleration input, $\boldsymbol{a_g(t)}$, and $\hat{\hat{\Phi}}_{\boldsymbol{a_g a_g}}(\boldsymbol{f})$ = auto spectral density estimate of $\boldsymbol{a_g(t)}$. The auto/cross spectral densities are estimated using the Welch's method [13].

The unknown wave model parameter vector, $\boldsymbol{\theta}$, is modeled as a random vector (denoted by $\boldsymbol{\Theta}$), whose values are uncertain and their uncertainties are characterized by a probability distribution function (pdf). The prior knowledge about the wave model parameter vector is modeled as a prior pdf. The prior pdf of $\boldsymbol{\Theta}$ can be updated to posterior pdf by extracting information from the discrepancies between the predicted and measured FRFs through the Bayes' rule. The discrepancy between the predicted and measured FRFs is modeled as

$$\mathbf{y}_k = \hat{\mathbf{y}}_k(\boldsymbol{\theta}) + \mathbf{v}_k(\boldsymbol{\theta}) \tag{12}$$

in which $\mathbf{v}_k$ = simulation error vector, which is modeled herein as an independent and identically distributed Gaussian white noise. Assuming that the prior pdf of the wave model parameter vector is Gaussian, the posterior pdf can be derived as [14]

$$\boldsymbol{p}(\boldsymbol{\theta}|\mathbf{y}_k) = \frac{1}{\boldsymbol{p}(\mathbf{y}_k)} \times \frac{\boldsymbol{e}^{-\frac{1}{2}(\mathbf{v}_k(\boldsymbol{\theta}))^T \mathbf{R}_k^{-1}(\mathbf{v}_k(\boldsymbol{\theta}))}}{(2\pi)^{kn}\,|\mathbf{R}_k|^{1/2}} \times \frac{\boldsymbol{e}^{-\frac{1}{2}\left(\boldsymbol{\theta}-\hat{\theta}^-\right)^T\left(\hat{\mathbf{P}}^-\right)^{-1}\left(\boldsymbol{\theta}-\hat{\theta}^-\right)}}{(2\pi)^{n_\theta/2}\,\left|\hat{\mathbf{P}}^-\right|^{1/2}} \tag{13}$$

where $\mathbf{R}_k \in^{(2kn)\times(2kn)}$ = covariance matrix of the simulation error vector $\mathbf{v}_k$; $\hat{\theta}^-$ is the prior mean vector, and $\hat{\mathbf{P}}^- \in \mathbb{R}^{n_\theta \times n_\theta}$ is the prior covariance matrix of the wave model parameter vector. Since $\mathbf{v}_k$ is modeled as an independent and identically distributed Gaussian white noise, $\mathbf{R}_k$ will be a diagonal matrix.

Equation (13) results in a non-Gaussian distribution for the posterior pdf of wave model parameter vector. To simplify the mathematical derivations, the posterior pdf can be gaussianized using a first-order approximation. The first order Taylor series expansion of $\mathbf{v}_k(\boldsymbol{\theta})$ with respect to $\boldsymbol{\theta}$ at $\hat{\theta}^-$ can be expressed as

$$\mathbf{v}_k(\boldsymbol{\theta}) = \mathbf{y}_k - \hat{\mathbf{y}}_k(\boldsymbol{\theta}) \cong \mathbf{y}_k - \hat{\mathbf{y}}_k\left(\hat{\theta}^-\right) - \mathbf{C}\left(\boldsymbol{\theta} - \hat{\theta}^-\right) \tag{14}$$

in which $\mathbf{C} = \frac{\partial \hat{\mathbf{y}}_k(\boldsymbol{\theta})}{\partial \boldsymbol{\theta}}\Big|_{\boldsymbol{\theta}=\hat{\theta}^-}$ is the model response sensitivity matrix and can be computed by analytically differentiating Eq. (6) with respect to $\boldsymbol{\theta}$. Substitution of Eq. (14) into Eq. (13) results in the following equations to update the mean vector and covariance matrix of the gaussanized posterior pdf of $\boldsymbol{\Theta}$.

$$\hat{\theta}^+ = \hat{\theta}^- + \mathbf{K}\left(\mathbf{y}_k - \hat{\mathbf{y}}_k\left(\hat{\theta}^-\right)\right), \hat{\mathbf{P}}^+ = \left(\mathbf{C}^T\mathbf{R}_k^{-1}\mathbf{C} + \left(\hat{\mathbf{P}}^-\right)^{-1}\right) \tag{15}$$

in which $\mathbf{K}$ is the Kalman gain matrix and can be expressed as [15]

$$\mathbf{K} = \left(\mathbf{C}^T\mathbf{R}_k^{-1}\mathbf{C} + \left(\hat{\mathbf{P}}^-\right)^{-1}\right)^{-1}\mathbf{C}^T\mathbf{R}_k^{-1} \tag{16}$$

The posterior estimates obtained from Eq. (15) should be corrected to satisfy the constraints shown in Eq. (8). For this purpose, the posterior Gaussian pdf that is resulted from Eq. (15) is truncated at the constraint edges. The constrained posterior mean vector and covariance matrix are then calculated using the truncated pdf. To this end, the wave model parameter space is transformed into a new space to decouple the constraints, so that each constraint equation will involve only one parameter in the transformed space. Then, the pdf of the transformed single parameter is truncated to correct for constraints and the corrected mean and variance (obtained from the truncated pdf) are transferred back to the wave model parameter space. More details about constrained recursive estimation can be found in[15, 16].

3 Numerical Case Study

The benchmark building used for this case study is a 52-story building structure, instrumented as a part of the community seismic network (CSN) project [17, 18]. A detailed three-dimensional linear-elastic model of the structural system has been developed in the structural analysis software ETABS [19] based on the available structural drawings [20]. The model is used to generate simulated structural response data for the purpose of validating the wave model parameter estimation method presented in this study. As mentioned before, each layer in the multilayer Kelvin-Voigt shear beam model represents a single story or group of stories of the building structures. In this case study, two different layering configurations are considered as presented in Table 1. In the first layering configuration, which is referred to as Case #1 model, the building structure is modeled as a 51-layer shear beam model. The basement and penthouse stories are combined together and modeled as a single layer. Every two layers between layers #2 and #49 have the same phase velocity and damping ratio parametrization. Therefore, 27 sets of phase velocity and damping ratio parameters, or $27 \times (3 + 2) = 135$ unknown parameters, characterize Case #1 model. In contrast, Case #2 model consists of a 51-layer shear beam model, in which each layer has an

independent parametrization to characterize the phase velocity and damping ratio. Therefore, Case #2 model has $51 \times (3 + 2) = 255$ unknown phase velocity and damping ratio parameters. Both Case #1 and Case #2 models have the same parametrization for mass density, as listed in the last column of Table 1. Since the mass distribution along the height of the building structure is piecewise uniform, many layers are expected to have similar mass densities. Furthermore, following Eqs. (5) and (6), it can be concluded that the analytical FRFs depend on the relative mass density of the layers. To simplify the estimation process, the mass density of the top layer (i.e., layer #51) is set as a unit constant (i.e., $\rho_7 = 1$). Thus, six unknown mass density parameters (i.e., ρ_1 to ρ_6) are used to characterize the mass distribution for both Case #1 and Case #2 models. In fact, each mass density parameter represents the relative mass density of the corresponding layer with respect to layer #51. The last three columns in Table 1 list the labels for parameter sets that characterize phase velocity (and damping ratio) and mass density.

Table 1. ETABS model parameters and layering configurations used for multilayer Kelvin-Voigt dispersive shear beam model identification.

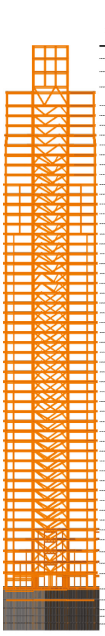

ETABS Structural Model			Multilayer Shear Model			
			Parameter Set Label			
Level	Height (m)	Story Mass (x 10^3 kg)	Layer Label	Case #1 $V_{s,\frac{1}{2}}$	Case #2 $V_{s,\frac{1}{2}}$	Case #1&#2 ρ
Roof	5.0	240.4				
52	5.5	301.6	51	27	51	7
51	5.8	314.4				
50	7.6	1024.2	50	26	50	6
49	4.0	770.5	49	25	49	5
48	4.0	765.5	48	25	48	5
47	4.0	775.2	47	24	47	5
46	4.0	817.0	46	24	46	5
45	4.0	838.0	45	23	45	5
44	4.0	838.1	44	23	44	5
43	4.0	838.9	43	22	43	5
42	4.0	840.1	42	22	42	5
41	4.0	894.1	41	21	41	5
40	4.0	895.8	40	21	40	5
39	4.0	895.9	39	20	39	5
38	4.0	897.1	38	20	38	5
37	4.0	898.2	37	19	37	5
36	4.0	961.3	36	19	36	4
35	4.0	937.2	35	18	35	4
34	4.0	938.8	34	18	34	4
33	4.0	940.4	33	17	33	4
32	4.0	942.1	32	17	32	4
31	4.0	945.9	31	16	31	4
30	4.0	941.0	30	16	30	4
29	4.0	941.2	29	15	29	4
28	4.0	942.8	28	15	28	4
27	4.0	944.4	27	14	27	4
26	4.0	945.8	26	14	26	4
25	4.0	948.0	25	13	25	4
24	4.0	950.9	24	13	24	4
23	4.0	953.4	23	12	23	4
22	4.0	955.2	22	12	22	4
21	4.0	957.5	21	11	21	4
20	4.0	966.2	20	11	20	4
19	4.0	961.8	19	10	19	4
18	4.0	966.4	18	10	18	4
17	4.0	968.4	17	9	17	4
16	4.0	973.5	16	9	16	4
15	4.0	976.9	15	8	15	4
14	4.0	982.4	14	8	14	4
13	4.0	988.4	13	7	13	4
12	4.0	993.3	12	7	12	4
11	4.0	996.1	11	6	11	4
10	4.0	1000.9	10	6	10	4
9	4.0	1005.3	9	5	9	4
8	4.0	1010.1	8	5	8	4
7	4.0	1012.3	7	4	7	4
6	4.0	1032.5	6	4	6	4
5	4.6	1072.3	5	3	5	3
4	4.6	1103.1	4	3	4	3
3	4.3	1009.8	3	2	3	3
2	6.1	1100.8	2	2	2	2
1	4.6	3524.7				
A	3.6	5830.9				
B	3.0	3472.5	1	1	1	1
C	3.0	3303.5				
D	3.0	3302.3				

3.1 Structural System Identification

A 240-seconds long, 5% g root-mean-square (RMS) Gaussian white noise acceleration time history sampled at 50 Hz is used as the base acceleration time history to simulate

the floor absolute acceleration responses of the building structure. Although such a long broadband base excitation is unrealistic in the real-world, it has been considered herein to provide an ideal condition for a proof-of-concept study to validate the performance of the proposed wave model parameter estimation method. The time histories of the floor absolute acceleration response in the direction of base motion are computed at the geometric center of the floors. No artificial measurement noise is added to the simulated responses. Spectral analysis method based on the Welch's averaging method [21], is used to find the FRF of the floor absolute acceleration responses with respect to the input base acceleration. The acceleration time histories are divided into five estimation windows with 50% overlap. Each window is weighted by a Hann function. The auto/cross spectra densities are estimated across each window and averaged over the five estimation windows. The FRFs are estimated in the frequency range of 0 to 6 Hz, with a frequency spacing of $\Delta f \cong 0.0244$ Hz.

The sequential Bayesian estimation algorithm described earlier is used to estimate the wave model parameters. The initial values for the phase velocity and damping ratio parameters are the same for all layers in both Case #1 and Case #2 models. The initial value for the phase velocity parameter vector is selected as $\boldsymbol{\theta}^{V}_{m,initial} = [12000, -7, 46]$ for each layer. The initial values for the relative mass densities can be selected based on the prior information about the mass distribution along the building height. Here, they are initialized based on the story masses defined in the model as $\boldsymbol{\theta}^{\rho}_{m,initial} = [\rho_1, \rho_2, \ldots, \rho_6, \rho_7] = [16.0, 3.4, 4.5, 4.6, 4.0, 2.5, 1.0]$, where $\rho_7 = 1.0$ is constant. Other different initial values for the wave model parameters have also been investigated to check the consistency of the estimation results. The prior wave model parameter covariance matrix is defined as a diagonal matrix, where the diagonal entries are selected by assuming a uniform 20% prior coefficient of variation (COV) for each wave model parameter.

The wave model parameters are estimated considering both dispersive and nondispersive models. For the nondispersive system identification, the dispersive relation in Eq. (7) is simplified as $\boldsymbol{V}_m(f) = \boldsymbol{a}^{V}_{m}$ where $\boldsymbol{a}^{V}_{m}$ denotes the constant (nondispersive) phase velocity for layer m. The same estimation procedure is used for the nondispersive identification. The initial values for the phase velocity and damping ratio for the nondispersive model are selected as $\boldsymbol{\theta}^{V}_{m,initial} = 275.9$ m/s and $\boldsymbol{\theta}^{\xi}_{m,initial} = 2.1\%$, respectively, which are equivalent to the initial phase velocity and damping ratio of the dispersive model at $f = 3$ Hz.

Figure 2 compares the measured, initial, and estimated FRFs for Case #1 model at two layers: layers #1, and #33. The real and imaginary parts of the FRFs are plotted separately. As can be observed, the initial FRFs are significantly different from the measured FRFs, while the estimated FRFs using the dispersive model match the measurements with good accuracy. The identified dispersive model captures correctly all the mode shapes in the frequency range considered for estimation. This verifies the correct performance of the estimation algorithm in steering the initial model to reduce its prediction discrepancies with the measurements. The estimated FRFs are plotted for both the dispersive and nondispersive models. It can be concluded that the FRFs of the identified dispersive model match the measurements better than the nondispersive model and the identified dispersive model provides a better prediction of the measured FRFs.

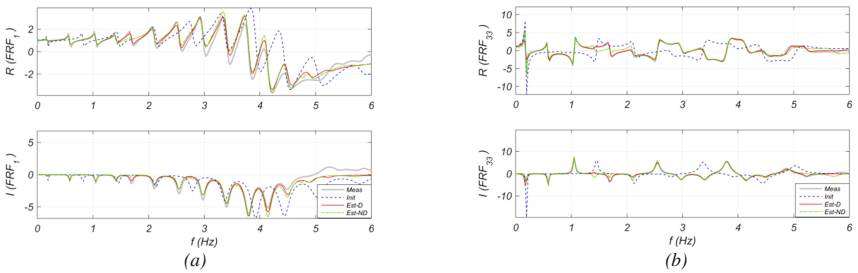

Fig. 2. Comparison of the measured (Meas), initial (Init), and estimated (Est) real (R) and imaginary (I) parts of the FRFs for Case #1 model at two layers: (a) layer #1, (b) layer #33. The estimated FRFs are plotted for both the dispersive (Est-D) and nondispersive (Est-ND) models.

Figure 3 compares the estimation results for Case #1 and Case #2 dispersive models. This figure compares the final estimates of the phase velocity (Fig. 3(a)) and damping ratio (Fig. 3(b)) – both evaluated at $f = 3$ Hz – the relative mass density profile (Fig. 3(c)), and the relative root mean square errors (*RRMSE*) of the estimated FRFs (Fig. 3(d)). The phase velocity and relative mass density estimates for the two models are comparable along the height of the building. Nevertheless, the damping ratio estimates show non-negligible differences. The inconsistency in the identified damping ratios is most likely due to the weak identifiability of the damping parameters. The *RRMSE* for the estimated FRF at level m is defined as

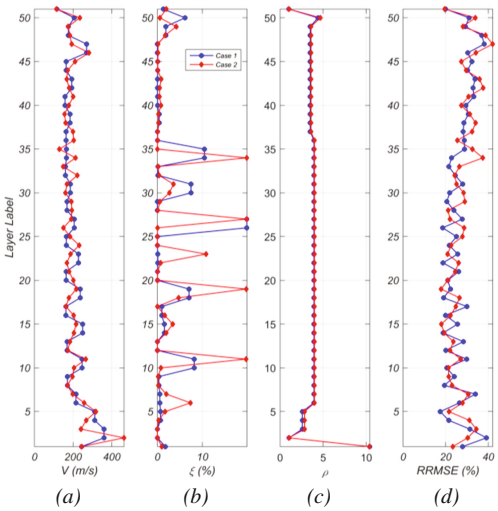

Fig. 3. Comparison of estimation profiles for Case #1 and Case #2 models; (a) final estimates of phase velocity at **f** = 3 Hz; (b) final estimates of damping ratio at **f** = 3 Hz; (c) final estimates of relative mass density; (d) relative root mean square error (RRMSE) of the estimated FRFs.

$$\boldsymbol{RRMSE_m}\ (\%) = \sqrt{\frac{\sum_{k=1}^{N}\left|\boldsymbol{H_{mk}}\left(\hat{\boldsymbol{\theta}}\right)-\hat{\hat{\mathbf{G}}}_{\boldsymbol{mk}}\right|^2}{\sum_{k=1}^{N}\left|\hat{\hat{\mathbf{G}}}_{\boldsymbol{mk}}\right|^2}}\times 100 \tag{17}$$

Figure 3(a) shows an unphysical fluctuation pattern in the phase velocity estimates along the building height, especially at lower and upper levels. The reason for this pattern can be justified by considering the estimation bias and the effects of model uncertainty. Obviously, the response behavior of the structural model is physically different from a multilayer dispersive Kelvin-Voigt model, no matter how the wave model parameters are tuned. The difference is more dominant where there are sudden changes (or discontinuities) in the lateral stiffness along the height of the building. The 52-story building model has stiffness contrasts at the lower levels, where the upper ground braced frame structure connects to the basement shear wall structure, and at the penthouse location. These contrasts result in a mismatch between the response behavior of the structural model and the dispersive shear beam model, which in turn, results in biased and unphysical estimation of phase velocities. Figure 3(a) shows that the fluctuation pattern is more significant in the lower and upper levels of the building than the middle levels (i.e., layer #30 to #40), where the response behavior of the structural system is close to a shear beam model. It should be noted that by including higher modes in the estimation (i.e., considering larger frequency estimation range) the estimation bias will most likely be reduced, but will never be eliminated completely due to the effects of model uncertainties.

4 Conclusions

This study proposed a sequential Bayesian estimation algorithm for estimating the parameters characterizing the propagation of seismic waves through a continuous, spatially non-homogenous viscoelastic solid. These parameters include those that characterize the phase velocity and damping ratio as a function of frequency, and the relative mass densities of a multilayer Kelvin-Voigt model. While the proposed Bayesian estimation method is general and can be applied to other waveform inversion problem, it was validated using a building system identification problem in this study. The case study showed the correct performance and accuracy of the proposed structural system identification approach, which can potentially be used for detection and localization of structural damage at the story level of building structures.

Acknowledgments. Support of this research provided by the Terrestrial Hazard Observation and Reporting (THOR) Center at Caltech is gratefully acknowledged.

References

1. Şafak, E.: Wave-propagation formulation of seismic response of multistory buildings. ASCE J. Struct. Eng. **125**(4), 426–437 (1999)
2. Todorovska, M.I., Ivanović, S.S., Trifunac, M.D.: Wave propagation in a seven-story reinforced concrete building: I. Theoretical models. Soil Dyn. Earthq. Eng. **21**(3), 211–223 (2001)
3. Kawakami, H., Oyunchimeg, M.: Normalized input-output minimization analysis of wave propagation in buildings. Eng. Struct. **25**(11), 1429–1442 (2003)
4. Snieder, R., Şafak, E.: Extracting the building response using seismic interferometry: theory and application to the Millikan library in Pasadena, California. Bull. Seismol. Soc. Am. **96** (2), 586–598 (2006)
5. Kohler, M.D., Heaton, T.H., Bradford, S.C.: Propagating waves in the steel, moment-frame factor building recorded during earthquakes. Bull. Seismol. Soc. Am. **97**(4), 1334–1345 (2007)
6. Todorovska, M.I., Rahmani, M.T.: System identification of buildings by wave travel time analysis and layered shear beam models—spatial resolution and accuracy. Struct. Control Health Monitor. **20**(5), 686–702 (2013)
7. Todorovska, M.I., Trifunac, M.D.: Earthquake damage detection in the imperial county services building III: analysis of wave travel times via impulse response functions. Soil Dyn. Earthq. Eng. **28**(5), 387–404 (2008)
8. Todorovska, M.I., Trifunac, M.D.: Impulse response analysis of the Van Nuys 7-Storey Hotel during 11 earthquakes and earthquake damage detection. Struct Control Health Monitor. **15**(1), 90–116 (2007)
9. Rahmani, M., Todorovska, M.I.: Structural health monitoring of a 54-story steel-frame building using a wave method and earthquake records. Earthq. Spectra **31**(1), 501–525 (2015)
10. Kramer, S.L.: Geotechnical Earthquake Engineering. Pearson Education, India (1996)
11. Ebrahimian, M., Rahmani, M., Todorovska, M.I.: Nonparametric estimation of wave dispersion in high-rise buildings by seismic interferometry. Earthq. Eng. Struct. Dyn. **43**(15), 2361–2375 (2014)
12. Ebrahimian, M., Todorovska, M.I.: Wave propagation in a Timoshenko beam building Model. ASCE J. Eng. Mech. **140**(5), 04014018 (2014)
13. Alessio, S.M.: Digital Signal Processing and Spectral Analysis for Scientists: Concepts and Applications. Springer, Switzerland (2016)
14. Ebrahimian, H., Astroza, R., Conte, J.P., de Callafon, R.A.: Nonlinear finite element model updating for damage identification of civil structures using batch Bayesian estimation. Mech. Syst. Signal Process. (2016). doi:10.1016/j.ymssp.2016.02.002
15. Simon, D.: Optimal State Estimation: Kalman, H-Infinity, and Nonlinear Approaches. Wiley, Hoboken, NJ (2006)
16. Simon, D., Dimon, D.L.: Constrained Kalman filtering via density function truncation for turbofan engine health estimation. Int. J. Syst. Sci. **41**(2), 159–171 (2010)
17. Clayton, R.W., et al.: Community seismic network: a dense array to sense earthquake strong motions. Seismol. Res. Lett. **86**(5), 1354–1363 (2015)
18. Clayton, R., Heaton, T., Chandy, M., Krause, A., Kohler, M., Bunn, J., Guy, R., Olson, M., Faulkner, M., Cheng, M.-H., Strand, L., Chandy, R., Obenshain, D., Liu, A., Aivazis, M.: Community seismic network. Ann. Geophys. **54**(6), 37–747 (2011)

19. Computers and Structures Inc.: Extended Three Dimensional Analysis of Building Systems, ETABS Ver. 15.2, Berkeley, CA (2015)
20. Kohler, M., Massari, A., Heaton, T.H., Kanamori, H., Hauksson, E., Guy, R., Clayton, R.W., Bunn, J., Chandy, K.M.: Downtown Los Angeles 52-story high-rise and free-field response to an oil refinery explosion. Earthq. Spectra (2016). doi:10.1193/062315EQS101M
21. Tangirala, A.K.: Principles of System Identification: Theory and Practice. CRC Press, Boca Raton, FL (2015)

Coupled Dynamical Systems (Includes Human-Structure, Vehicle-Structure and Soil-Structure Interaction)

Experimental Testing of Soil-Steel Railway Bridge Under Normal Train Loads

Damian Beben(✉)

Faculty of Civil Engineering and Architecture,
Opole University of Technology, Opole, Poland
d.beben@po.opole.pl

Abstract. The paper presents the experimental tests under normal train loads that were conducted on a soil-steel railway bridge. Up to now, the dynamic testing of soil-steel bridges and culverts were conducted in limited range. The load-carrying structure was constructed as pipe-arch shell assembled from corrugated steel plate sheets, designed with a corrugation depth of 0.05 m, pitch of 0.15 m and plate thickness of 0.003 m. Inductive gauges, strain gauges and accelerometers were used to measure deflections, unit strains and accelerations of this bridge, respectively. Deflections, unit strains and accelerations were registered for all trains during a 24 h. The largest deflections and unit strains were measured at the shell crown and quarter points, respectively. Greater strains (compressive) were mainly measured at the top of wave and lower at the bottom (tensile). This is related with the joint effect of thrust and bending, and also unequal load distribution on the perimeter of the structure. American and Australian codes suggest that the loads should be taken into account as a uniform pressure at the level of the structure crown, which is contrary to the received testing results in this paper. The maximum bridge and ballast accelerations were equal to 0.71 and 1.31 m/s^2, respectively, and they did not exceed the Eurocode limit value of 3.5 m/s^2. On the basis of the registered deflections, a Discrete Fourier Transform method was implemented to determine the frequencies of bridge (dominant frequencies were 0.3 and 1.25 Hz). The natural frequencies of the bridge were 0.25 and 1.3 Hz, and they corresponded to approximately two first dominant frequencies extracted from the forced vibration tests (live loads). The damping ratios were about 9% (using the ambient vibration testing), and 50% (the forced vibration testing).

Keywords: Dynamic testing · Soil-steel bridge · Displacement · Strain · Acceleration

1 Introduction

Testing of bridges are conducted usually in order to validate structural requirements or for planning of the bridge maintenance. In this study, the experimental tests were carried out in order to acquaint with the behavior of soil-steel railway bridge under dynamic live loads. Soil-steel bridges are an effective alternative for short-span bridges. The span of bridge is usually from 3 to 25 m. These type of bridges fulfill the same design and safety requirements as for typical steel and concrete bridges, simultaneously

© Springer International Publishing AG 2018
J.P. Conte et al. (eds.), *Experimental Vibration Analysis for Civil Structures*,
Lecture Notes in Civil Engineering 5, https://doi.org/10.1007/978-3-319-67443-8_71

at lower maintenance costs. Therefore, the soil-steel bridges are recently more often used in transportation projects.

The paper [1] presents the maximum dynamic displacements of soil-steel bridges and culverts which were smaller than the static ones. The displacement ratio was in the range from 0.7 to 0.9 for most bridges. The typical dynamic testing of soil-steel bridges and culverts was presented by Flener and Karoumi [2], Manko and Beben [3], Beben [4]. Initial testing results of a soil-steel railway culvert under passage of a cargo train over were presented by Flener et al. [5]. An experimental study on dynamic amplification factors (DAF) for soil-steel railway bridge using was conducted by Beben [6]. Beben [7] presents the experimental results of railway soil-steel bridge with double shells.

The main design and construction rules for railway culverts and bridges are included in the Manual for Railway Engineering elaborated by the American Railway Engineering and Maintenance-of-Way Association (AREMA [8]) and in the Australian Standard (AS 3703.2-1989 1989 [9]). The AREMA proposes that the steel culverts can be designed to carry the Cooper's E-80 Railroad live loading with diesel impact. This 355 kN axle load may be distributed laterally a distance of 0.91 m, plus a distance equal to the depth from structure grade line to the base of rail, on each side of centerline of single tracks. The steel culverts located under the railroad should have a minimum height of soil cover of 1.68 m counting from the base of rail. The Australian railway code [9] suggests that the minimum soil cover over the steel culverts with small corrugations should be greater than 0.70 m. The railway load can be calculated as a uniform pressure at the level of the crown of culvert.

The analysis of the railway bridges and culverts require the fulfillment of special design criterions (the serviceability state, e.g. accelerations levels, displacements, end-rotations etc.). The acceleration and deflection criteria are decisive for most bridges. The cause of the acceleration and deflection criteria is mostly to avoid ballast instability with resulting de-alignment of the train. The Eurocode [10] gives that: (i) the vertical bridge deck acceleration is limited to 3.5 m/s^2, (ii) the vertical bridge deflection caused by the live loads should not exceed 8 mm.

This paper presents a study of the dynamic behavior of soil-steel railway bridge under the normal train loads. The deflections and unit strains were registered during the normal passages of trains. The ballast and bridge accelerations were also taken into account. The discrete Fourier transform (DFT) method was applied to determine the bridge frequencies. The ambient vibration tests were also conducted (before the basic bridge testing). The Half Power Bandwidth method [11] was used to estimate the damping ratio. Deflections, unit strains and accelerations of the soil-steel bridge were registered continuously for all trains during a 24 h. Axial thrusts and bending moments were calculated using the measured unit strains and based on the corrugation plate characteristics.

2 Soil-Steel Bridge Description

The tested soil-steel railway bridge in the cross section has pipe-arch profile with span of 4.73 m and height of 2.87 m (Fig. 1). The load-carrying structure was assembled from corrugated steel plate (CSP) sheets, designed with a corrugation depth of 0.05 m, pitch of 0.15 m and plate thickness of 0.003 m (please see a detail in Fig. 1).

The individual CSP sheets were connected together using high strength bolts $\varnothing$ = 0.02 m. The formed steel shell was covered by backfill that was properly compacted (in the Proctor Normal scale in the range of 0.95–0.98), allowed to install the double rail tracks laying on the ballast (broken stone base). The soil cover over the steel shell structures (including ballast, blanket and backfill) equals 1.45 m. The width of the bridge at the top is 13.20 m, whereas at the bottom it is 19.00 m. In the plan view, the longitudinal axis of bridge is situated perpendicularly to the railway line. On the bridge, two rail tracks are arranged: the first (track no. 1) is electrified, and the second (track no. 2) is designed for non-electrified rolling stock (Fig. 1).

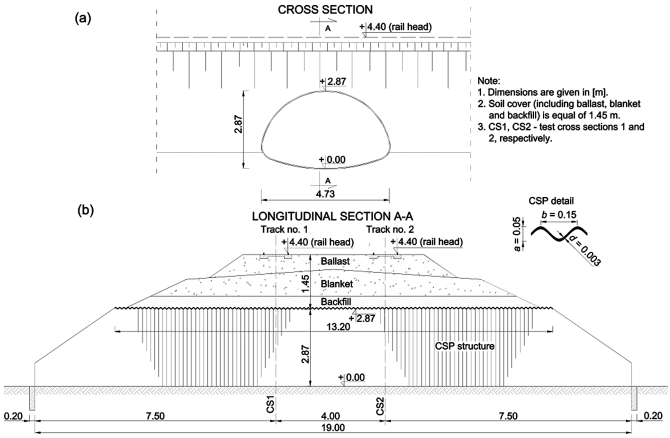

Fig. 1. The soil-steel railway bridge: (a) cross section, (b) longitudinal section A–A.

The bridge was designed in compliance with the Polish bridge codes, i.e. PN-85/S-10030 [12]; PN-82/S-10052 [13]; and PN-88/B-02014 [14]. Besides, the railway bridge structures had to fulfill the requirements for the railway engineering structures specified by the Polish Railway Lines [15]. For this bridge, four pressure axes (4 × 250 kN) with a pitch of 1.60 m, symmetrically situated on a distance of 6.40 m were used. At the same time, uniformly distributed loads (80 kN/m) on both sides of the point loads on the unlimited lengths should be applied. In addition, the load caused by soil cover (ballast, blanket and backfill) should be also taken into account. Before the testing the technical condition of bridge was thoroughly checked and no signs of cracks, deformation, puncture, perforations, flattening, spreading of the CSP sheets were noted. Joints defects were also not noted. In some places, the beginning of the corrosion was observed. Taking into account the field inspection [16], bridge rating was “sufficient”.

3 Measurements Methodology

Deflections and strains of the soil-steel railway bridge under the dynamic live loads were registered with using inductive and strain gauges, respectively. All these sensors were situated inside the bridge shell. Situation of sensors in the steel shell of the bridge

is shown in Fig. 2. Generally, two main testing cross-sections (CS1 and CS2) were selected for the bridge at a distance of 4.0 m from each other. The CS1 and CS2 testing sections were situated underneath the track axes (Fig. 2b). Testing section CS1 had five measurement points MP1–MP5, i.e. MP1 $x = 0$ (haunch); MP2 $x = L/4$ (quarter point); MP3 $x = L/2$ (crown); MP4 $x = 3L/4$ (quarter point) and MP5 $x = L$ (haunch). Whereas, the section CS2 included only one measurement point for the reason that the rail traffic on this railway line was slight. Two strain gauges were situated in each of the measurements points to register strains in longitudinal direction (y-axis) of the shell (at the top and at the bottom of the wave), which gives 10 strain gauges (E1-1–E5-10) for testing section CS1 and 2 strain gauges (E3'-5–E3'-6) for testing section CS2 (Fig. 2). Furthermore, at measurement points MP2, MP3 and MP4 (testing section CS1), 3 inductive gauges (I1, I2 and I3) were mounted to register deflections (Fig. 3). Next, in testing section CS2 (MP3'), 1 inductive gauge (I4) was installed. Inductive gauges I1 and I4 were situated at the shell crown, and sensors I2 and I3 at the quarter points of the bridge shell. Additionally, 2 accelerometers (A1 and A2) were applied to monitoring the of the ballast and bridge acceleration. Accelerometers were placed both on the bridge crown (A1) and on ballast (A2) – on the railway embankment between the sleepers of track no. 1 directly over the bridge crown (Fig. 2). The registered signals were filtered by means of the Butterworth low-pass filter with cut-off frequency at the level of 30 Hz. This allowed to reduce interference coming from the power generator feeding the inductive gauges.

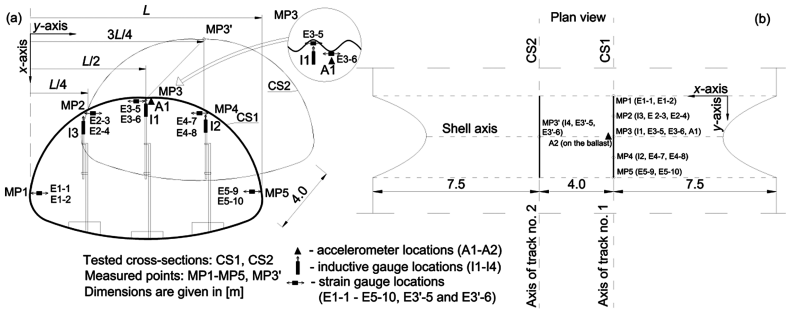

Fig. 2. Arrangement of sensors on the CSP shell: (a) cross section, (b) plan view.

4 Results of Measurements and Their Analyses

4.1 General Remarks

The field testing were conducted after ten years of service of this bridge structure. The experimental tests were carried out continuously for 24 h. Forty-five trains were registered, i.e. seventeen passenger trains; twenty freight; eight others (service trains, locomotives and handcars). The global loading of tested soil-steel bridge reached: passenger trains 31 967 kN; freight trains 171 014 kN; others 6 198 kN. It is very important to add that the maximum weight of a passenger train (MMPE) amounted to 3 346 kN,

and the freight train (TGZE) 17 857 kN (Table 1). The maximum length of the passenger train was 178 m, and the freight train equaled 535 m. The maximum train speed was 45 km/h for freight trains (TGRE) and 130 km/h for passenger trains (MMPE).

4.2 Bridge Deflections

The maximum deflection is determined as the allowable vertical displacement of the bridge that cannot exceed the value received based on the three specifications, namely: (i) CHBDC [17], i.e. 0.5% of the bridge span (in this case 22 mm), (ii) CSPI [18], i.e. 2% of the bridge span (88 mm), (iii) Eurocode [10], i.e. 8 mm for bridge located on the railway line.

Figure 3 shows the deflection course of the crown of bridge (gauge I1) during passage of express train (MMPE) at a speed of 130 km/h. The impact of each axle of the express train can also be observed from the deflection versus time plots. Three major phases of deflections were highlighted. The first phase reveals effect of the locomotive, and the maximum deflection equaled −0.54 mm. The second phase refers to the impact of four wagons. At this stage, the maximum deflection amounted to −0.25 mm. The third phase refers to the vibration damping after the passage of the express train. The deflections at the quarter point are strongly smaller than at the crown, and they do not exceed −0.25 mm. Generally, the maximum deflections of the soil-steel bridge do not exceed −0.65 mm. Taking into consideration the testing period (24 h), the largest deflections of the soil-steel bridge are related to the effect of locomotives (mainly for freight trains). The effect of wagons is fairly small in comparison to the locomotive effect. It is related to the locomotive weight.

The largest deflection amplitudes depend on train weight, especially the locomotive. The effect of train speeds appears to have a smaller significance. This is visible during the express train passing (v = 130 km/h, weight 3346 kN). This train induced lower deflection than during passing the heavy freight train (weight ca. 18000 kN) at a low speed v = 40 km/h. Table 1 shows the maximum deflections obtained during testing under live loads.

The deflections peaks are located directly under the axles of locomotives and wagons. Dynamic loading time (DLT) depends on the train lengths. However it is

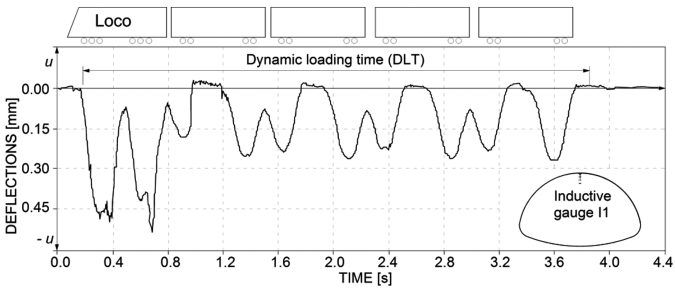

Fig. 3. The deflections of the soil-steel bridge crown during passage of express train at the speed of 130 km/h.

Table 1. The maximum deflections, strains and frequencies as well as the characteristics of trains passing over the soil-steel bridge.

Type of train	Weight of train (kN)	Approx. speed (km/h)	Max deflections (mm)	Characteristic frequency (Hz)	Max strain (μm)
TGRE	14074	45	0.49	2.6	−44
TGZE	17857	40	0.65	2.8	−58
MMPE	3135	120	0.53	5.1	−40
TGRE	13123	45	0.49	2.6	−42
TMZS	14164	40	0.54	2.8	−48
TGRE	16573	40	0.58	2.9	−50
MMPE	3346	130	0.54	4.9	−44

Notes: TGZE, TGRE – international freight train; MMPE – international passenger express train; TMZS – national freight train. The speeds were estimated in approximately ±5 km/h.

important to note the effect of wagons in comparison to locomotives is negligible. The soil-steel bridge reacts with quite high sensitivity to changes of live loads. As indicated on Fig. 3 (after the train passage over the structure - stage three), the CSP shell recovered to its original shape (without the permanent deflections). The deflections decrease immediately after the passage of trains, and it results from the flexible nature of the CSP shell. Relatively small deflections are also likely caused by the large depth of soil cover over the shell structure (the backfill constitutes a vibration damper). It should be noted that the slight bridge deflections are caused also by the positive arching effect appearing locally over the crown zone of the CSP shell.

It is also evident that the condition given by the Eurocode [10] is more restrictive than the overall requirements for the soil-steel bridges and culverts. As demonstrated in the research, the maximum CSP structure deflections (0.65 mm) is strongly lower than the limit values received from the standards. In case of the first two requirements, it is caused by a conservative approach to establish the limit values (the soil-structure interaction was not take into consideration). While, the Eurocode condition concerns to the all type of railway bridge structures (the code is not take into account the specific behavior of the CSP bridges, for example their flexibility).

4.3 Bridge Strains

The largest values of bridge strains were registered at the quarter points of the shell (MP2 and MP4, strain gauges E2-3 and E4-7 are located on the top of wave, respectively): $\varepsilon_{2\text{-}3} = 49$ μm, $\varepsilon_{4\text{-}7} = -58$ μm. They were measured during passage of a freight train (TGZE) with a weight of over 17800 kN with a speed of 40 km/h. Table 1 shows the maximum unit strains obtained from testing under live loads. The unit strains in other measurement points (crown and haunches) were strongly lower and did not exceed 25 μm. It is very important to emphasize, that the shell sides (quarter points) are both in the compression and tensile states. This demonstrates unequal loads distribution on the circumference of the CSP structure. Probably it may be caused by the various backfill stiffness around the CSP structure.

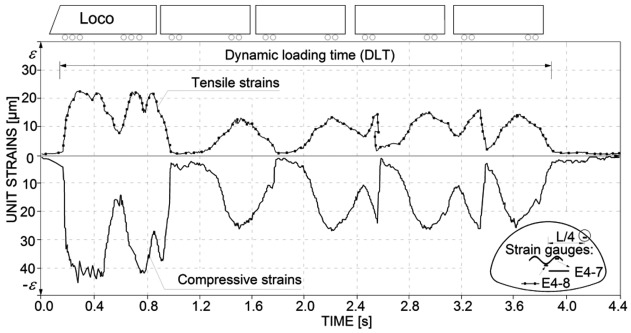

Fig. 4. The compressive (top of wave) and tensile (bottom of wave) strains at quarter point during passage of the express train at the speed of 130 km/h.

Figure 4 presents that the compressive strains at the wave top (sensor E4-7, $\varepsilon = -43$ μm) and the tensile strains at the bottom of the corrugation (sensor E4-8, $\varepsilon = 23$ μm) are different. This shows that the neutral axis is not located in the middle of the wave and the load distribution on the CSP shell circumference is unequal. Similar results were received by other authors during static and dynamic testing [5, 7, 19, 20]. This mainly results from the combined effect of thrust and bending as well as curvilinear form shell structure, and it causes dislocation of the neutral axis of wave. It is important to add that in the case of the second quarter point (measurement point MP2), the compressive strains are located at the wave bottom, and the tensile strains are situated at the corrugation top. This is in contrary to the quarter point (measurement point MP4).

4.4 Bridge and Ballast Accelerations

Big vibrations of railway bridges can induce failures of structures such as ballast instability leading to changes in the geometry of the rail track and in the worst accident, to the train derailment. So, it is very interesting to register the ballast and bridge accelerations to verification their safety. As referred to the first part of the paper, the European code [9] gives a limit value of vertical deck acceleration (3.5 m/s^2). It is to guarantee safety against ballast instability. So, the vertical ballast and bridge accelerations were also measured during the testing at two various points. First point is situated on the track (between the sleepers), about 1.45 m from the shell crown and the second one is located at the crown of bridge. Table 2 presents the maximum vertical ballast and bridge accelerations for various trains. The results demonstrate very low acceleration levels (both ballast and bridge), much lower than the Eurocode limit of 3.5 m/s^2. The results visibly show that in the case of this bridge there are no ballast instability problems.

The results showed in Table 2 indicate that the train speed is one of the most significant elements influencing on the acceleration, i.e. if the train speed growths, the bridge and ballast accelerations also growth. The maximum peak bridge and ballast accelerations are 0.71 m/s^2 and 1.31 m/s^2, respectively. Other trains induced lower accelerations.

Table 2. Maximum ballast and bridge accelerations for various type of trains.

Train type	Maximum vertical acceleration (m/s^2)		Relative difference (%)
	Bridge crown	Ballast	
Passenger (slow), 70 km/h	0.41	0.71	42.25
Passenger (express), 130 km/h	0.71	1.31	45.80
Freight, 40–45 km/h	0.26	0.48	45.83
Other, 35–55 km/h	0.37	0.69	46.37

Moreover it can be noted that the vertical acceleration of the bridge crown is significantly smallest (42–46%) than the ballast acceleration. The diminish level of acceleration at the bridge crown can be caused by a drop of the wave speed in the soil and a significant soil depth over the shell crown. Beben [7] and Andersson et al. [21] received an acceleration reduction of 38% and 45%, respectively. It should be added that in these bridges, the depth of the soil cover at the shell crown amounted to 1.90 m and 2.40 m, respectively.

4.5 Discrete Fourier Transform (DFT) Method

To extract the frequencies of the soil-steel bridge, all data sets were processed using the Discrete Fourier Transform (DFT) method [22]. More complex engineering problems can be solved using the Fast Fourier Transform [23].

Figure 5 presents the DFT of the recorded deflections from which the peaks associated with the dominant frequencies of the soil-steel bridge are distinguished. Overall, the dominant frequency of the bridge is in the range of 0.3–1.25 Hz, which corresponds to an angular frequency (ω = 1.88–7.85 rad/s) and a vibration period (T = 0.8–3.33 s). Less dominant frequencies were also registered ranging from 1.8 to 3.0 Hz (ω = 11.30–18.84 rad/s and T = 0.33–0.55 s). Train type do not effects on the dominant frequency of the bridge. As it can be seen the case of the express train passage with a speed 130 km/h, the bridge frequency has two intervals (0.3–1.25 Hz and 1.8–3.0 Hz). Almost identical frequency intervals were obtained during passage of other trains. In general, the forms of the power spectra are related to the character of excitations (speed and weight of trains). In case of this bridge, the factor most influencing the forms of the PSDs is the train weight (Fig. 5). The freight train induced the biggest the PSD (Fig. 5b).

Before the primary testing of the soil-steel bridge, the ambient vibration testing was also carried out. It was done in order to extract the natural frequencies of tested bridge. The PSD of the registered crown deflection without loading is shown on Fig. 6. The first two natural frequencies of the soil-steel bridge are distinctly visible for both the ambient vibration (Fig. 6) and the live load testing (Fig. 5). The first natural frequency is establish approximately at 0.25 Hz from the ambient vibration test and at 0.3 Hz from the live load testing. The smaller frequency is partly related to the additional mass of the train, especially the locomotive.

It is very interesting to assessment the damping ratio of the first mode of vibration. It was done using the Half Power Bandwidth method [11]. The damping ratios for the

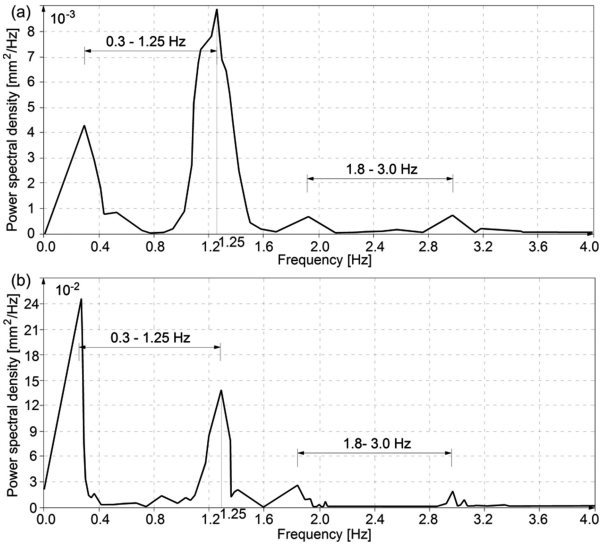

Fig. 5. PSD of registered deflections for the passing trains: (a) passenger train, (b) freight train.

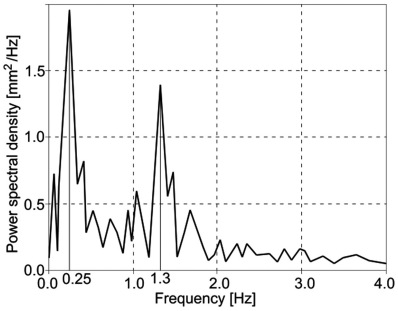

Fig. 6. PSD of registered deflections at the bridge crown during the ambient vibration testing.

ambient vibration test (Fig. 6) and for the forced vibration test (Fig. 5) are about 9 % and 50%, respectively. The cause for so big difference are: (i) the effect of the activation of the soil-structure interaction when the soil-steel bridge is loaded, (ii) the increased friction damping in the backfill when loaded and (iii) the additional damping coming from the locomotive.

5 Conclusions

As a result of the experimental tests conducted on the soil-steel railway bridge during live loads, the following general conclusions can be drawn:

1. The maximum deflections did not exceed −0.65 mm, and unit strains −58 μm, at loading by a freight train with weight of almost 18000 kN and passing with speed of 40 km/h. The largest deflections and unit strains were measured in the bridge crown and quarter points, respectively. The registered deflections were definitely smaller than the calculated based on the three bridge design codes. The relatively small effort of the soil-steel bridge is related to the soil cover depth over the CSP shell (1.45 m). The positive arching appearing in the backfill also influences on the low level of CSP deformations.
2. The received ballast and bridge accelerations do not exceed the limit value of 3.5 m/s^2 (the Eurocode requirement). The bridge crown accelerations were strongly smaller than the ballast accelerations (42–46%). The reduced energy at the bridge crown may be induced by a drop of the wave speed in the soil and an ample soil depth over the CSP shell. In addition, the testing results indicated that if the train speed growths, the bridge and ballast accelerations also growth.
3. The dominant frequencies of the soil-steel bridge were 0.3 and 1.25 Hz, which correspond to angular frequencies of 1.88–7.85 rad/s and vibration periods of 0.8–3.33 s. The first two natural frequencies of the bridge (from the ambient vibration testing) were 0.25 and 1.3 Hz; what roughly corresponds to the dominant frequencies received from the forced vibration tests (live load). The damping ratios were about 9 and 50% for the ambient vibration tests and the forced vibration tests, respectively. The cause for so big difference is the activation of the soil-structure interaction when the CSP structure was loaded.
4. The largest strains (compressive) were mainly measured at the wave top and smallest at the corrugation bottom (tensile). This is caused with the joint effect of thrust and bending, and also unequal load distribution on the perimeter of the CSP structure (probably, the neutral axis of the CSP structure is not situated at the central part of wave). The codes [8, 9] suggested that the railway loads should be assumed as a uniform pressure at the bridge crown. It is contrary to the received testing results.
5. The highest impact on the tested bridge was caused mainly by the passage of freight trains (TGZE) and express trains (MMPE). Other trains (slow passenger trains, maintenance trains, locomotives) have not a meaningful effect on soil-steel bridge. Test results show that the deformations of the soil-steel bridge are depends more on the weight of trains than on their speed.

References

1. Yeau, K.Y., Sezen, H., Fox, P.J.: Load performance of in situ corrugated steel highway culverts. J. Perform. Construct. Facil. ASCE **23**(1), 32–39 (2009)
2. Flener, E.B., Karoumi, R.: Dynamic testing of a soil-steel composite railway bridge. Eng. Struct. **31**(12), 2803–2811 (2009)
3. Manko, Z., Beben, D.: Dynamic testing of a corrugated steel arch bridge. Can. J. Civ. Eng. **35**(3), 246–257 (2008)
4. Beben, D.: Field performance of corrugated steel plate road culvert under normal live load conditions. J. Perform. Constr. Facil. ASCE **27**(6), 807–817 (2013)

5. Flener, E.B., Karoumi, R., Sundquist, H.: Field testing of a long-span arch steel culvert during backfilling and in service. J. Struct. Infrastruct. Eng. **1**(3), 181–188 (2005)
6. Beben, D.: Experimental study on the dynamic impacts of service train loads on a corrugated steel plate (CSP) culvert. J. Bridge Eng. ASCE **18**(4), 339–346 (2013)
7. Beben, D.: Corrugated steel plate (CSP) culvert response to service train loads. J. Perform. Construct. Facil. ASCE **28**(2), 376–390 (2014)
8. AREMA: Manual for Railway Engineering, Chapter 1. American Railway Engineering and Maintenance-of-Way Association, Washington, DC (2012)
9. AS 3703.2-1989. Long-Span Corrugated Steel Structures. Part 2: Design and Installation. Standards Association of Australian. Homebush, NSW (1989)
10. CEN, EN 1991-2. Eurocode 1. Actions on Structures, Part 2: Traffic Loads on Bridges. European Committee for Standardization, Brussels (2002)
11. Sustainable Bridges SB-5.2-S2. Guideline for Estimating Structural Damping of Railway Bridges. Prepared by Sustainable Bridges—A Project Within EU FP6 (2007)
12. PN-82/S-10052. Polish Bridge Standards: Bridges. Steel Structures. Design (1982)
13. PN-85/S-10030. Polish Bridge Standards: Bridge Structures. Loads (1985)
14. PN-88/B-02014. Polish Standards: Actions on Building Structures. Soil Loading (1988)
15. SFRES: Specifications for Railway Engineering Structures. The Polish National Railways, Warsaw (1998)
16. SFRES: Specifications for Railway Engineering Structures, Part IV. The Polish Railway Lines, Warsaw (2005)
17. CHBDC: Canadian Highway Bridge Design Code. CAN/CSA-S6-06, Canadian Standards Association International, Mississauga, Ontario (2006)
18. CSPI: Handbook of Steel Drainage & Highway Construction Products. American Iron and Steel Institute; Corrugated Steel Plate Institute, Canadian Edition, Ontario (2007)
19. Beben, D., Manko, Z.: Dynamic Testing of a Soil-Steel Bridge. Struct. Eng. Mech. **35**(3), 301–314 (2010)
20. Sezen, H., Yeau, K.Y., Fox, P.J.: In-situ load testing of corrugated steel pipe-arch culverts. J. Perform. Construct. Facil. ASCE **22**(4), 245–252 (2008)
21. Andersson, A., Sundquist, H., Karoumi, R.: Full scale tests and structural evaluation of soil-steel flexible culverts for high-speed railways. In: 2nd European Conference on Buried Flexible Steel Structure, Rydzyna, Poland (2012)
22. Smith, J.O.: Mathematics of the Discrete Fourier Transform (DFT) with Audio Applications, 2nd edn. W3K Publishing (2007)
23. Yang, Y.B., Chang, K.C.: Extracting the bridge frequencies indirectly from a passing vehicle: Parametric study. Eng. Struct. **31**(10), 2448–2459 (2009)

Analysis of Records from Downhole Arrays

Erdal Şafak(✉) and Eser Çaktı

Kandilli Observatory and Earthquake Research Institute,
Bogazici University, Istanbul, Turkey
erdal.safak@boun.edu.tr

Abstract. The paper presents an approach to identify characteristics of layered soil media from the records of vertical downhole arrays. It is assumed that the behavior of soil is linear and it is subjected to vertically propagating shear waves. The approach is based on discrete time formulation of wave propagation in terms of up-going and down-going waves in the layers. It is shown that the upgoing and downgoing waves in any layer can be expressed as a linear combination of the time-shifted and scaled forms of the excitation. For identification, we first model the surface record as the response of an IIR filter (i.e., an auto-regressive random process) subjected to Gaussian white-noise input. We convert the IIR filter into a lattice filter, defined by its reflection coefficients. We then divide the soil into fictional thin layers, whose two-way travel times are equal to the sampling interval. Starting from the top layer next to the surface, we calculate the motions at each fictional layer interface by using the surface record and the reflection coefficients. When the calculated interface response matches the recorded response by one of the downhole sensors, we conclude that the layers above the matching interface represent the layers between the surface and the downhole sensor.

Keywords: Downhole arrays · System identification · Layered soil media

1 Introduction

The amplification of seismic waves by near-surface soil layers (i.e., site amplification) is a critical factor influencing the level of shaking experienced on ground surface. One of the most accurate ways to identify site amplification is to record motions synchronously at different depths below the surface. Such arrays are known as vertical downhole arrays.

In the literature, majority of data analyses from such arrays are based on the spectral ratio approach, in which the surface to downhole Fourier spectral ratios of records are used to identify soil characteristics. Spectral ratio approach should not be used for downhole arrays, because the downhole sensors do not only record the waves coming from below, but also the waves reflected from the surface, as well as the layer interfaces. These reflections make the input and output in the spectral ratio coupled, and can give very misleading results [1]. For the correct identification of site amplification, the effects of multiple reflections in the downhole sensors should be eliminated before taking spectral ratios.

© Springer International Publishing AG 2018
J.P. Conte et al. (eds.), *Experimental Vibration Analysis for Civil Structures*,
Lecture Notes in Civil Engineering 5, https://doi.org/10.1007/978-3-319-67443-8_72

This paper presents an alternative approach based on discrete-time formulation of wave propagation in layered media. It is assumed that the site can be modeled as a one-dimensional elastic media, subjected to vertically propagating plane shear waves. We model the surface record as the response of an IIR (Infinite Impulse Response) filter, modeled in lattice form and subjected to a Gaussian white-noise input. We assume that the soil medium is composed of horizontal layers, whose thicknesses are defined by equal travel times. By using the reflection coefficients of the filter, we can calculate the sub-surface response at each layer interface from the surface record, and compare it to the record at the downhole sensor. When they match, we say that the layers identified up to that point represent the layers between the sensor and the surface.

1.1 Discrete-Time Wave Propagation in Layered Media

Consider an *m*-layered media with input *X* and the output *Y*, as shown in Fig. 1. It will be assumed that the layer $m + 1$ has infinite depth and the reflected waves from interface $m + 1$ do not come back. The propagation of waves is defined by the wave travel times in the layers, and the wave reflection and transmission coefficients at each interface.

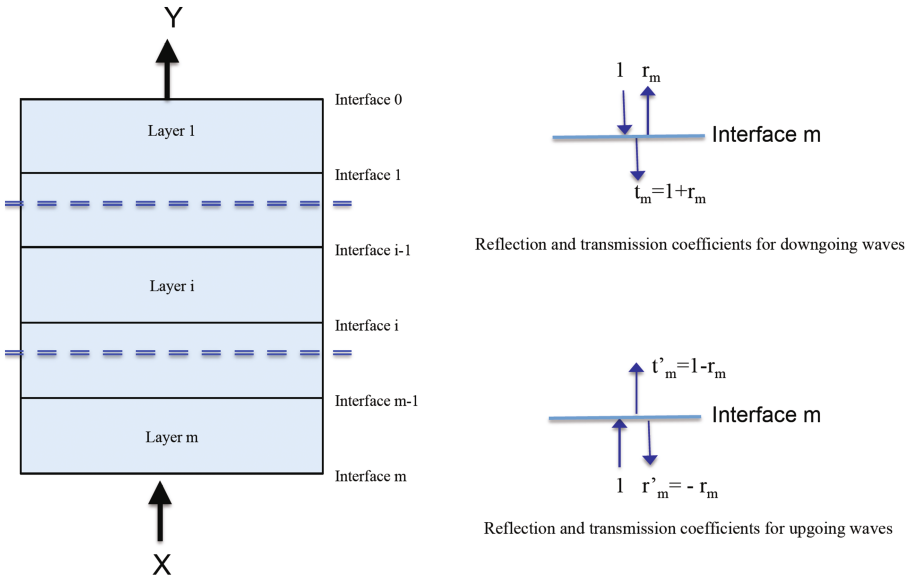

Fig. 1. Notation for a layered medium, and the definition of reflection and transmission coefficient.

From the conservation of energy, the reflection and transmission coefficients for downgoing waves, r_i and t_i, at interface i can be calculated as [2]:

$$r_i = \frac{(\rho V)_i - (\rho V)_{i+1}}{(\rho V)_i + (\rho V)_{i+1}} \quad \text{and} \quad t_i = \frac{2(\rho V)_i}{(\rho V)_i + (\rho V)_{i+1}}$$

The term ρV is called the impedance of the layer, where ρ is the mass density and V is the shear wave velocity in the layer. The corresponding coefficients, r'_i and t'_i, for the upgoing waves are:

$$r'_i = \frac{(\rho V)_{i+1} - (\rho V)_i}{(\rho V)_i + (\rho V)_{i+1}} \quad \text{and} \quad t'_i = \frac{2(\rho V)_{i+1}}{(\rho V)_i + (\rho V)_{i+1}}$$

Note that, $t = 1 + r$, $r' = -r$, and $t' = 1 + r' = 1 - r$. These expressions are valid whether the waves represent accelerations, velocities, or displacements, but not for stresses.

To develop the equations for wave propagation, we will separate the waves in each layer into upgoing and downgoing waves, and denote them at the top of the layer by U_i, and D_i, and at the bottom of layer by U'_i, and D'_i, as shown in Fig. 2.

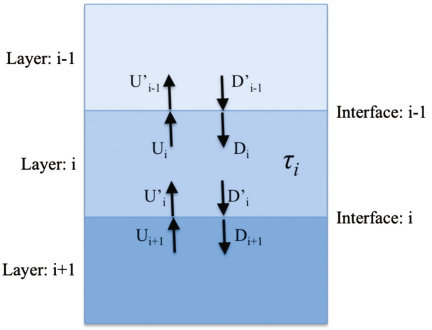

Fig. 2 Upgoing and downgoing waves for layer i.

For simplicity, we will not consider the damping in the layers. Damping can be incorporated in the formulation by adding a complex part to the velocity, which makes the reflection and transmission coefficients complex-valued quantities.

From Figs. 1 and 2, we can write the following equations:

$$D_{i+1}(t) = r'_i \cdot U_{i+1}(t) + t_i \cdot D'_i(t)$$
$$U'_i(t) = t'_i \cdot U_{i+1}(t) + r_i \cdot D'_i(t)$$

The first equation states that the downgoing wave at the top of layer $i + 1$ is composed of the reflected portion of the wave at the top of the same layer, plus the transmitted portion of the downgoing wave at the bottom of the layer above. Similarly, the second equation states that the upgoing wave at the bottom of layer i is composed

of the transmitted portion of the upgoing wave at the top of the layer below, plus the reflected portion of the downgoing wave at the bottom of the same layer. Also note that the relationship between the upgoing and dongoing waves at the bottom and the top of layer i can be expressed by the following equations:

$$U_i'(t) = U_i(t - \tau_i) = q^{-\tau_i} \cdot U_i(t)$$
$$D_i'(t) = D_i(t + \tau_i) = q^{+\tau_i} \cdot D_i(t)$$

where τ_i denotes the wave travel time in the layer and q is the backward shift operator, defined as $q^{-k}\, x(t) = x(t - k)$.

From the equations above, and also by using the relationships between the reflection and transmission coefficients for the upgoing and downgoing waves shown in Fig. 1, we can write the relationship between the upgoing and downgoing waves at the top of the layer $i + 1$ and layer i:

$$\begin{Bmatrix} U_{i+1}(t) \\ D_{i+1}(t) \end{Bmatrix} = \frac{1}{1 - r_i} \cdot \begin{bmatrix} q^{-\tau_i} & -r_i \cdot q^{+\tau_i} \\ -r_i \cdot q^{-\tau_i} & q^{+\tau_i} \end{bmatrix} \begin{Bmatrix} U_i(t) \\ D_i(t) \end{Bmatrix} = T_i \cdot \begin{Bmatrix} U_i(t) \\ D_i(t) \end{Bmatrix}$$

where

$$T_i = \frac{1}{1 - r_i} \cdot \begin{bmatrix} q^{-\tau_i} & -r_i \cdot q^{+\tau_i} \\ -r_i \cdot q^{-\tau_i} & q^{+\tau_i} \end{bmatrix} = \frac{q^{-\tau_i}}{1 - r_i} \cdot \begin{bmatrix} 1 & -r_i \cdot q^{+2\tau_i} \\ -r_i & q^{+2\tau_i} \end{bmatrix}$$
$$= \frac{q^{-\tau_i}}{1 - r_i} \cdot \begin{bmatrix} 1 & -r_i \cdot q^{+2\tau_i} \\ -r_i & q^{+2\tau_i} \end{bmatrix}$$

T_i is known as the transfer matrix for layer i, for it transfers the waves from layer i to $i + 1$.

Since we do not know the layer interfaces, we will divide the media into superficial layers whose two-way travel time is equal to the sampling interval of the records; that is $2\tau_i = \Delta$, where Δ is the sampling interval. With this, the transfer matrix for layer i now becomes:

$$T_i = \frac{q^{-\Delta/2}}{1 - r_i} \cdot \begin{bmatrix} 1 & -r_i \cdot q^{\Delta} \\ -r_i & q^{\Delta} \end{bmatrix} = \frac{q^{-\Delta/2}}{1 - r_i} \cdot \begin{bmatrix} 1 & -r_i / q^{-\Delta} \\ -r_i & 1/q^{-\Delta} \end{bmatrix}$$

Since the reflection coefficient for the surface (soil-air interface) is -1 for the downgoing waves, and $+1$ for the upgoing waves, we can write the upgoing and downgoing waves at the top of the first layer $U_1 = Y/2$ $D_1 = Y/2$, as shown in Fig. 3.

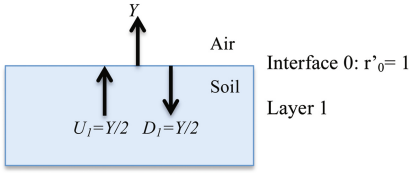

Fig. 3 Upgoing and downgoing waves at the top of layer 1 (soil-air interface).

With this, the relationship between the upgoing and downgoing waves at layer m (i.e., the bedrock-soil interface) and layer 1 (i.e., soil-air interface) can be written as:

$$\begin{Bmatrix} X(t) \\ 0 \end{Bmatrix} = T_1 \cdot T_1 \cdot \cdots T_m \cdot \begin{Bmatrix} Y(t)/2 \\ Y(t)/2 \end{Bmatrix}$$

where we assumed that there are no upgoing waves at the bedrock soil interface (interface m).

1.2 Identification of Layers Between the Downhole Sensors

With the assumption that the media is composed of layers, in each of which the two-way travel time is equal to one sampling interval, it can be shown by multiplying the transfer matrices from layer 1 to layer m, that the relationship between *X(t)* and *Y(t)* is equivalent to an IIR (Infinite Impulse Response) filter of the following form:

$$Y(t) = \frac{b_0}{1 + a_1 q^{-1} + a_1 q^{-2} + \cdots + a_n q^{-n}} \cdot X(t)$$

where, for convenience, we have assumed that the sampling interval is $\Delta = 1$ (i.e., $q^{-1} = q^{-\Delta}$).

It is reasonable to approximate the bedrock input waves, *X(t)*, as a Gaussian white-noise random process. With this assumption, the equation above represents an auto-regressive polynomial (AR) model for *Y(t)*. The coefficients a_k in the denominator can be calculated by various methods available in the literature [e.g., 3]. It is possible to convert these coefficients into reflection coefficients and represent the AR model in the form of a cascade of lattice filters [4, 5]. Each lattice filter represents the transfer matrix of a layer. By using the lattice filters, we can calculate the upgoing and downgoing waves for each successive layer, starting from layer 1, as shown below.

$$\begin{Bmatrix} U_2(t) \\ D_2(t) \end{Bmatrix} = \frac{q^{-0.5}}{1 - r_1} \cdot \begin{bmatrix} 1 & -r_1/q^{-1} \\ -r_1 & 1/q^{-1} \end{bmatrix} \begin{Bmatrix} Y/2 \\ Y/2 \end{Bmatrix}$$

$$\begin{Bmatrix} U_3(t) \\ D_3(t) \end{Bmatrix} = \frac{q^{-0.5}}{1 - r_2} \cdot \begin{bmatrix} 1 & -r_2/q^{-1} \\ -r_2 & 1/q^{-1} \end{bmatrix} \begin{Bmatrix} U_2(t) \\ D_2(t) \end{Bmatrix}$$

$$\cdots \quad \cdots \quad \cdots$$

The recorded motion $Y_i(t)$ at interface i is the sum of the upgoing and down going waves at the top of the layer $i + 1$, that is:

$$Y_i(t) = U_{i+1}(t) + D_{i+1}(t)$$

Therefore, as we go down calculating the upgoing and downgoing waves at each layer, we also calculate the total response $Y_i(t)$ at each interface, and compare it with the recorded response *S(t)* by the downhole sensor. When they match (by minimizing the difference in the least square sense), we conclude that the layers above the matching

interface represent the layers between the surface and the downhole sensor. That is, we calculate the error ε_k at each interface by using the following equation, and find the k value that minimizes ε_k.

$$\varepsilon_k = \sum_t [U_{k+1}(t) + D_{k+1}(t) - S(t)]^2 \text{ for } k = 1, 2, \cdots, m-1$$

2 Conclusions

We presented a discrete-time wave propagation approach to analyze records from vertical downhole arrays. The methodology is based on the identification of a lattice filter with Gaussian white noise input to represent the recorded surface motion. By dividing the soil media into imaginary layers, whose two-way travel times are equal to sampling interval of the record, we can calculate the response at each layer interface, starting from the surface. When the calculated interface response matches the recorded response by a downhole sensor, we conclude that the layers above the matching interface represent the layers between the surface and the downhole sensor.

References

1. Safak, E.: Models and methods to characterize site amplification from a pair of records. Earthq. Spectra EERI **13**(1), 97–129 (1997)
2. Ewing, W.M., Jardetsky, W.S., Press, F.: Elastic Waves in Layered Media. Mc Graw-Hill Book Co., New York (1957)
3. Burg, J.P.: A new analysis technique for time series data. In: Childers, D.G. (ed.) Modern Spectrum Analysis. NATO Advanced Study Institute of Signal Processing with Emphasis on Underwater Acoustics. IEEE Press, New York (1968)
4. Levinson, N.: The Wiener RMS error criterion in filter design and prediction. J. Math. Phys. **25**, 261–278 (1947)
5. Todd, R.M, Cruz, J.R.: Frequency estimation and QD method. In: Computer Techniques and Algorithms in Digital Signal Processing. Academic Press, pp. 1–78 (1996)

Effect of Soil-Structure Interaction on Low to Medium-Rise Steel Frames Through Shake Table Experiments

B. Vivek and Prishati Raychowdhury(✉)

Department of Civil Engineering, Indian Institute of Technology, Kanpur, India
prishati@iitk.ac.in

Abstract. The present study investigates the effect of soil-structure interaction on the dynamic response of low to medium-rise steel-moment-resisting-frame (SMRF) structures supported by isolated shallow footings resting on loose dry Ganga sand bed. A series of shake table experiments is conducted on three-dimensional steel models of a 3-storey and a 6-storey building for this purpose. The model frames are placed in a laminar container filled with dry Ganga sand of 36% relative density and subjected to a number of base excitations. Further, the same structures are tested under the fixed base conditions (i.e., clamped with the base plates) in order to isolate the effect of soil-structure interaction. Various engineering demand parameters such as storey displacement, base moment and foundation rocking are emphasized. It is observed that SSI causes significant increase in the storey displacement and reduction in the base moment of the building. The roof displacement is observed to increase up to twice for the 3-storey structure and up to 37% for the 6-storey structure for structure being placed on the Ganga sand bed compared to its fixed-base position. On the contrary, a reduction in base moment up to 65% and 90% is observed due to SSI effect for the 3-storey and 6-storey structure, respectively. The energy dissipations due to rocking movement are estimated up to about 36% and 42.6% for the 3-storey and 6-storey structure, respectively.

Keywords: Soil-structure interaction · Shallow footings · Shake table experiment · Laminar container

1 Introduction

Rocking, sliding and settlement of foundations during an earthquake-induced vibration may significantly alter the seismic behavior of the superstructure. The flexibility of the foundations may increase the natural period of the system, whereas the inelastic deformations at the soil-foundation interface may increase the damping of the system. Although a number of previous studies have utilized shake table facility to experimentally investigate the effect of rocking shallow foundations on structural responses (e.g., Ishimura et al. [1], Pitilakis et al. [2], Anastasopoulos et al. [3] and Biondi et al. [4]), most of them had considered single-degree-of-freedom (SDOF) structures. However, SDOF systems may not adequately represent the dynamic characteristics of a multi-storey building, especially during high frequency vibrations, where possibility of

© Springer International Publishing AG 2018
J.P. Conte et al. (eds.), *Experimental Vibration Analysis for Civil Structures*,
Lecture Notes in Civil Engineering 5, https://doi.org/10.1007/978-3-319-67443-8_73

higher mode contribution may increase. In the present study, the effect of seismic SSI is evaluated through a series of shake table test on three-dimensional models of a 3-storey and a 6-storey frame building under fixed and flexible base conditions. The following subsections describe the details of the experimental program, instrumentation, loading protocol, and experimental observations from the study.

2 Experimental Program

A 3-storey and a 6-storey steel moment-resisting frame with rigid beam-column joints are fabricated for this study (as shown in Fig. 1). The model structures have storey heights of 30 cm and bay width of 60 cm. The beams and columns of the structures are made with solid square mild steel sections with dimensions 10 mm × 10 mm and 12 mm × 12 mm, respectively. The columns are supported by isolated square footings of size 10 cm × 10 cm × 1 cm. The models are scaled-down representative of typical low to medium-rise buildings of India. The details of prototype buildings and scaling justifications can be found in Vivek and Raychowdhury [5].

(a) (b) (c)

Fig. 1. Model structures: (a) 3-storey fixed base, (b) 6-storey fixed base and (c) 3-storey on Ganga sand

The superstructure masses are assigned through steel plates of 1 cm thickness and lead blocks installed at each floor level in such a manner that the centre of mass coincides with the centre of the stiffness to avoid any torsional movement. Mass at each floor level has been kept the same except the top floor, which has a mass of 0.85 times of that of any other floor. The amount lumped floor mass has been chosen to create an adequate model such that the scaled structure-foundation soil model provides similar

dynamic characteristics such as frequency, time period and mode shapes to the model as that of the prototype during dynamic excitation.

A laminar soil box of inner dimension 110 cm × 160 cm × 76.5 cm is used to hold the soil and simulate an elastic half-space with minimum boundary effect. This laminar soil box comprises of 15 individual lamina (with a 2 mm clearance between each lamina), supported independently on multiple roller bearings guided through a guide channel (Fig. 2a). The outer frame connected to the guide rods transfers the self-weight of each lamina off the shake table.

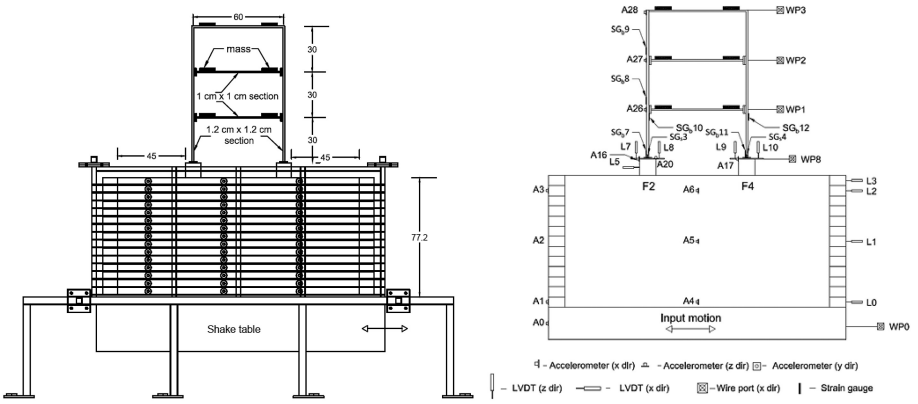

(a) (b)

Fig. 2. (a) Schematic of the experimental set-up and (b) instrumentation of the 3-storey structure [all dimensions in cm]

Uniformly-graded dry Ganga sand is used to prepare the soil bed. The geotechnical properties of the sand are provided in Table 1. In order to maintain the desired relative density of 36%, the sand is layered inside the container through the well-established rainfall pouring technique by hand hopper. To obtain the uniformity of the soil bed, the hand hopper is swung back and forth like a pendulum, keeping a constant height of fall of 15 cm after Shubham et al. [6]. In order to assure the uniformity of sand deposition while filling, a dynamic cone penetrometer is employed at different location along the horizontal direction.

The structures and foundations are instrumented with a number of accelerometers, displacement transducers and strain gauges to record the dynamic characteristics of the mentioned frames of the structure under the dynamic load. Figure 2(b) shows the schematics of one of the completely instrumented frame of the 3-storey moment resisting structure. Note that both frames showed nearly same response, and thus response of one frame can be considered as the representative of the entire structure. The accelerometer, A0 measures the input acceleration of the shake table. The wire ports WP0 attached to the shake table measures the shake table displacement. This displacement transducer is used to monitor, whether the measured displacement from shake table matches the targeted displacement. The wireports, WP1-WP3 in 3-storey

Table 1. Physical properties of Ganga sand

Property	Value
Specific gravity, G_s	2.67
Uniformity coefficient, C_u	2.06
Coefficient of curvature, C_c	1.01
Effective size, D_{10} (mm)	0.15
Max. unit wt. γ_{max} (kN/m^3)	15.59
Min. unit wt. γ_{min} (kN/m^3)	13.29
Max. void ratio, e_{max}	0.97
Min. void ratio, e_{min}	0.68

and WP1-WP6 in 6-storey records the storey displacements in the translational direction. The wireports WP7 and WP8 in footing F3 and F4 as well as the LVDT's L4 and L5 in footing F1 and F2 measures the footing translation or the foundation sliding. Two LVDT's each (L7-L12) positioned vertically and connected to footing F1, F2 and F4 respectively measures the foundation rotations. At each mentioned footings, two LVDT's are positioned at a distance of 150 mm c/c of pin head. This LVDT's are vertically positioned over a rigid perplex block attached to the top of the footing. The strain gauges connected each at the base column measures the base moment and base shear. All the instruments such as the accelerometers, displacement transducers and strain gauges are connected directly to the data acquisition (DAq) system. This is an integrated module programmed through the LabView system design software to automate continuous data collection during each experiment.

The model structure-foundation-soil system is excited with uniaxial harmonic excitations tuned to the natural frequency of the structure-foundation system. The fundamental frequencies of the model structure-foundation-soil system obtained

Table 2. Details of experiment conducted

Sl No.	Experiment Number	Model Structure	Base condition	Predominant frequency (Hz)	Peak acceleration, A_{max} (g)
1	S3-HM1	3-storey	Ganga sand	5.02	0.05
2	S3-HM2		Ganga sand	5.02	0.1
3	S3-HM3		Ganga sand	5.02	0.2
4	S3-HM7		Fixed base	6.85	0.05
5	S3-HM8		Fixed base	6.85	0.1
6	S3-HM9		Fixed base	6.85	0.2
7	S6-HM1	6-storey	Ganga sand	2.75	0.036
8	S6-HM2		Ganga sand	2.75	0.072
9	S6-HM3		Ganga sand	2.75	0.14
10	S6-HM7		Fixed base	3.85	0.036
11	S6-HM8		Fixed base	3.85	0.072
12	S6-HM9		Fixed base	3.85	0.14

through impact hammer tests (Vivek and Raychowdhury [5]) are chosen as harmonic excitations with varying amplitudes. The harmonic excitations for 3-storey model structure with SSI and fixed base have frequencies of 5.02 and 6.85 Hz, respectively with peak acceleration amplitude of 0.05, 0.1 and 0.2 g. For the 6-storey structure with SSI and fixed base, excitations of frequencies of 2.75 and 3.85 Hz, respectively, with peak acceleration 0.04, 0.072 and 0.14 g are used. The duration of cyclic loading is adopted is between 8 and 10 s. Table 2 provides the details of experiment conducted.

3 Results and Discussion

Figures 3 and 4 show the variation of the peak displacement of the 3-storey and 6-storey structure with fixed base and SSI base for varying base excitation intensity. The peak displacement demands of both the structures increase with increase in flexibility of the structure as well as the increase in base excitation. It can be observed that the peak roof displacement of the 3-storey structure increases up to twice from fixed base to flexible base. For the 6-storey structure, the peak roof displacement shows an increase of about 16–37% from fixed base to flexible base condition.

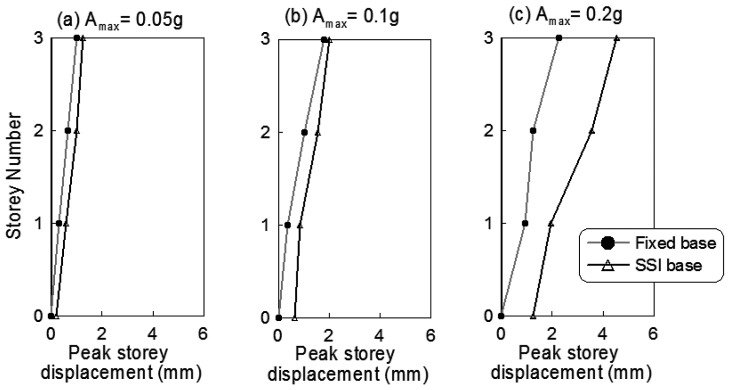

Fig. 3. Effect of base fixity to the peak storey displacement of 3-storey structure for base excitation amplitude.

The base moment and foundation rotation are two important parameters for soil-foundation interface behavior of rocking shallow foundations. Hence, some typical experimental time history observations of the base moment and the foundation rotation for the *S3-HM3* (SSI Case, 3-storey building) experiment case are presented in Fig. 5. Note that the peak base moment is about 8.65 N-m and the peak foundation rotation is about 0.004 rad.

The inelastic SSI attributed to hysteretic energy dissipation is observed through the moment-rotation hysteresis loops provided in Figs. 6 and 7. It can be observed that as the input loading intensity increases, the amount of rotational displacement as well as

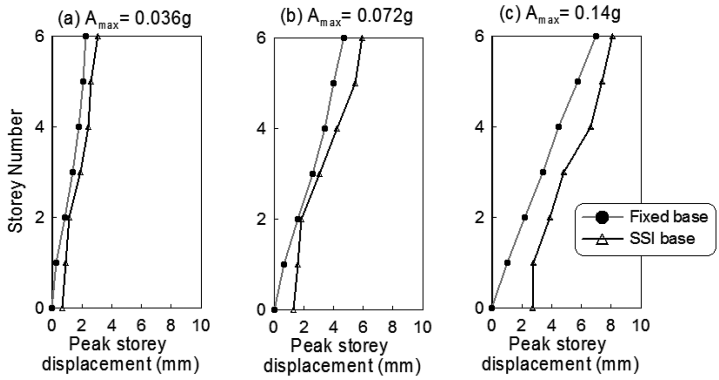

Fig. 4. Effect of base fixity to the peak storey displacement of 6-storey structure for base excitation amplitude.

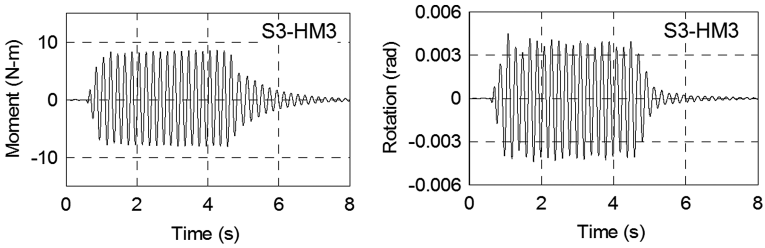

(a) Base moment(b) Foundation rotation

Fig. 5. (a) Base moment time history and (b) foundation rotation time history of the 3-storey structure with SSI base for experiment case S3-HM3

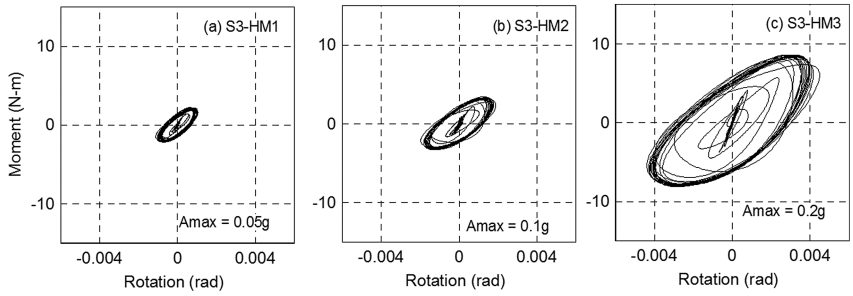

Fig. 6. Rotation-moment relationship of the 3-storey structure for different tests on Ganga sandbed

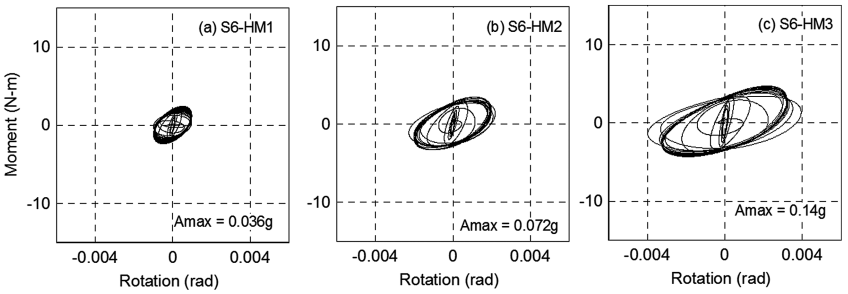

Fig. 7. Rotation-moment relationship of the 6-storey structure for different tests on Ganga sandbed

the area under the hysteresis loops increase. This indicates larger energy dissipation at higher load intensities caused from yielding of supporting soil. Note that the moment-rotation behavior of only SSI base cases is presented herein, as the foundations in the fixed base conditions are restricted against any movement.

To quantify the amount of hysteretic energy dissipation through foundation rocking, the equivalent viscous damping is estimated as follows [7]:

$$\varsigma_{eq} = \frac{1}{4\Pi}\left[\frac{A_{M-\theta}}{1/2\theta_{\max}.M_{\max}}\right] \tag{1}$$

where, $A_{M-\theta}$ is the area of $M-\theta$ hysteresis loop, and $M_{\max}$ and $\theta_{\max}$ are the corresponding maximum moment and rotation of a particular loop as shown in Figs. 6 and 7. Table 3 provides the peak rotations as well as the estimated values of equivalent viscous damping due to foundation rocking. The equivalent damping due to rocking is observed to be up to 36% for the 3-storey structure and 42.6% for the 6-storey structure, indicating significant energy dissipation due to rocking movement at the foundation level. It may also be noted that damping increases with increasing excitation intensity, indicating yielding of larger extend of soil at the foundation base at high intensity excitations. The relationship between the amount of rotation and damping due to rocking movement is examined in Fig. 8. It is noticed that a linear correlation can be established between the two parameters.

Table 3. Peak rotation and estimated equivalent viscous damping due to foundation rocking

Sl No.	Experiment case	A_{max} (g)	θ_{max} (rad)	$\zeta_{rocking}$ (%)
1	S3-HM1	0.05	0.0011	27.48
2	S3-HM2	0.10	0.0022	34.02
3	S3-HM3	0.20	0.0044	36.01
4	S6-HM1	0.036	0.001	39.49
5	S6-HM2	0.072	0.002	40.16
6	S6-HM3	0.14	0.004	42.62

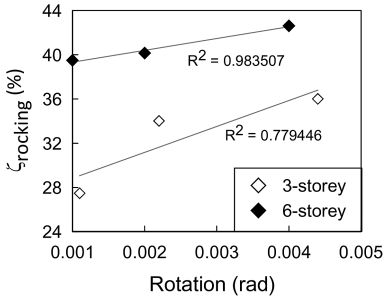

Fig. 8. Relationship between peak rotation and energy dissipation due to rocking

Table 4 summarizes the effect of SSI on structural response focusing on base moment and roof drift demand. The peak values of base moment and roof drift for all experimental cases are provided herein. Moreover, the effect of SSI is extracted by providing the ratio of the base moment and roof drift of the structure on Ganga sand with respect to the fixed base structure (e.g., $\delta_{SSI}/\delta_{fixed}$and M_{SSI}/M_{fixed}). It is observed that increase in peak roof drift due to SSI is 1.12 times to 2 times for the 3-storey structure and 1.19–1.37 times for the 6-storey structure. Conversely, the peak base moment is observed to reduce when the structure is supported by the soil bed compared to its fixed base condition. The reduction in base moment is up to 65% for the 3-storey structure and up to 90% for the 6-storey structure.

Table 4. Summary of effect of SSI on the structural response

Sl No.	Experiment Number	Model Structure	Base condition	Peak roof drift, δ (mm)	Base Moment, M (N-m)	Effect of SSI	
						$\delta_{SSI}/\delta_{fixed}$	M_{SSI}/M_{fixed}
1	S3-HM1	3-storey	SSI	1.25	2.23	1.24	0.35
2	S3-HM2			2.01	3.45	1.12	0.36
3	S3-HM3			4.55	8.65	2.00	0.37
4	S3-HM7		Fixed base	1.01	6.30	1	1
5	S3-HM8			1.79	9.60	1	1
6	S3-HM9			2.27	23.20	1	1
7	S6-HM1	6-storey	SSI	3.06	2.34	1.37	0.17
8	S6-HM2			5.94	3.44	1.26	0.13
9	S6-HM3			8.28	4.73	1.19	0.10
10	S6-HM7		Fixed base	2.24	13.70	1	1
11	S6-HM8			4.70	26.00	1	1
12	S6-HM9			6.96	46.00	1	1

4 Conclusions

The present study investigates the effect of dynamic SSI on structural response through a series of shake table experiments. The following key observations are made from the study:

1. The roof displacement is observed to increase up to twice for the 3-storey structure and up to 37% for the 6-storey structure for structure being placed on the Ganga sand bed compared to its fixed-base position.
2. The base moment reduces significantly when the base condition is changed from fixed to sand bed. A reduction ranging 63–65% for the 3-storey structure and 83–90% for the 6-storey structure is observed in this study.
3. Significant energy dissipation in the rocking mode is observed. The equivalent viscous damping values for the highest intensity excitations are estimated as 36% and 42.6% for the 3-storey and 6-storey structure, respectively. A linear relationship between the amount of rocking and energy dissipated can be established for the chosen cases.

Acknowledgments. The research is funded by the Department of Science and Technology (DST), India, under the *FastTrack Grant for Young ScientistsScheme* (Award Number: SERB/CE/20130058). The above financial support is greatly appreciated. Any opinions, findings, and conclusions expressed in this paper are those of the authors, and do not necessarily reflect those of the sponsoring organization.

References

1. Ishimura, K., Ohtsuki, A., Yoloyama, K., Koyanagi, Y.: Sway-rocking model for simulating nonlinear response of sandy deposit with structure. In: Proceedings of the Tenth World Conference on Earthquake Engineering, Rotterdam, pp. 1897–1903 (1992)
2. Pitilakis, D., Dietz, M., Wood, D.M., Clouteau, D., Modaressi, A.: Numerical simulation of dynamic soilstructure interaction in shaking table testing. Soil Dyn. Earthq. Eng. **28**(6), 453–467 (2008)
3. Anastasopoulos, I., Loli, M., Georgarakos, T., Drosos, V.: Shaking table testing of rocking-isolated bridge pier on sand. J. Earthq. Eng. **17**, 1–32 (2013)
4. Biondi, G., Massimino, M.R., Michele, M.: Experimental study in the shaking table of the input motion characteristics in the dynamic SSI of a SDOF model. Bull. Earthq. Eng. **13**(6), 1835–1869 (2015)
5. Vivek, B., Raychowdhury, P.: Influence of SSI on Period and Damping of Buildings Supported by Shallow Footings on Cohesionless Soil. Int. J. Geomech. (ASCE) (2016). in Press
6. Shubham, S., Srinivasan, V., Ghosh, P.: Effective utilization of dynamic penetrometer in determining the soil resistance of the reconstituted sand bed. In: The 15th Asian Regional Conference on Soil Mechanics and Geotechnical Engineering, Fukuoka, Japan (2014)
7. Chopra, A.K.: Dynamics of Structures: Theory and Application to Earthquake Engineering. Prentice Hall, Englewood Cliffs (2006)

Natural Vibration Characteristics and Seismic Response Analysis of Train-Bridge Coupling System in High-Speed Railway

Zhi Liu[1,2,3(✉)], Hui Jiang[1,2,3], Lanfang Zhang[4], and Endong Guo[5]

[1] Guangdong Earthquake Administration, Guangzhou, China
liuzhi8725@126.com
[2] Key Laboratory of Earthquake Monitoring and Disaster Mitigation Technology, CEA, Guangzhou, China
[3] Key Laboratory of Earthquake Early Warning and Safety Diagnosis of Major Projects, Guangzhou, China
[4] Hefei University of Technology, Hefei, China
[5] Institute of Engineering Mechanics, CEA, Harbin, China

Abstract. In order to study the natural vibration characteristics and dynamic response of the train-bridge coupling system during an earthquake, based on recent research production, a more accurate and reasonable finite element model of train-bridge coupling system for high-speed railway was established, a single bridge model without considering train-bridge coupling effect was also set up for comparison. The dynamic characteristics and seismic response under the action of typical ground motion were calculated, and the diversity of the single bridge model and train-bridge coupling model was compared, the acceleration amplification factor of these two models was also obtained. The results showed that, the natural vibration characteristics were obviously different between train-bridge model and single bridge model which could directly affect the dynamic response and running safety of the train. Finally, seismic response results comparison at typical seismic motions has further validated the differences between train-bridge model and single bridge model, and spectrum characteristic analysis results indicated that the characteristics of earthquake motions have significant influence on the seismic acceleration response of the trains and bridges.

Keywords: High-speed railway · Vibration characteristics · Train-bridge coupling system · Seismic response · Acceleration amplification factor

1 Introduction

As the basement and carrier of high-speed railway, bridges have hold a high percentage in large rate of the railway mileage. Bridges have occupied about 30% of the Shinkansen mileage in Japan [2], the high railway mileage has reached to more than 8000 km in Chinese passenger dedicated railway line [1], which covers more than half of the whole high-speed railway mileage. Take Wuhan Guangzhou high-speed railway for example, the rate of bridge/railway mileage has reached to 48.1%, which is up to 80.5% for Beijing-Shanghai high-speed railway [3].

© Springer International Publishing AG 2018
J.P. Conte et al. (eds.), *Experimental Vibration Analysis for Civil Structures*,
Lecture Notes in Civil Engineering 5, https://doi.org/10.1007/978-3-319-67443-8_74

China is an earthquake-prone country located in the world's two largest seismic zone [4]. As the wide use of high-speed railway bridges, the property of the rail train running on bridges will substantially increases when an earthquake occurs, seismic safety of the running train becomes more and more concerned [5]. Vibration characteristics are very important for the seismic response analysis of railway bridges. Structural system performance will change when the high-speed train runs through the bridge, so the natural frequency of the railway bridge can not accurately reflect true vibration characteristics of the train-bridge coupling system, and the seismic response is also different from the single bridge.

Researches on dynamic interaction of train-bridge coupling system start late in China, however, a wealth of practical consequences, from the moving load theory of single bridge model progressively extend to vibration analysis of train-bridge coupling system, have been obtained [6–8]. In the 1970s, Flexure torsion vibration theory of the truss beam was proposed by professor Li Guohao. From 1980s to 1990s, field measurement and calculation analysis of truss bridge transverse vibration excited by trains has been carried out, many useful research findings have been obtained. Professor Zhai Wanming and Xia He as well as their research team have done systematic researches on dynamic response of high-speed rail bridges and running safety of trains [9]. In the previous finite element analysis and research of seismic response of bridges, train-bridge coupling effect was rarely considered in the finite element model, as well as the comparison between single bridge model and train-bridge coupling model (hereinafter referred to as 'single model' and 'coupling model' for short). Based on the existing research results, finite element method has been used, combined with practical engineering, a more accurate and reasonable train-bridge coupling model has been established, the vibration characteristics as well as seismic response between single model and coupling model have been compared, the acceleration amplification factors of the bridge deck have been obtained. These researches have laid foundations for further study of earthquake threshold and running safety of high-speed train.

1.1 Train-Bridge Coupling Model

Competent flexural and torsional rigidity are required in the superstructure of high-speed rail bridge with specific applied force, and convenient for standardized production [3]. By far, simply-supported box girder is widely used in the high-speed rail bridges, span length is mainly 24 m and 32 m. A multi-span simply-supported beam bridge in practical engineering has been chosen to set up the research model in this paper. Eight span single bridge model and train-bridge coupling mode are separately established. The span length is 32 m, single room and equal-height box girder are adopted in the beam section, beam width is 12 m, and section height is 3.05 m, basin rubber support is used in the bridge bearing. Double-column rectangular pier which is widely used in the rail bridge is chosen in the model with a pier height of 10 m. Entity unit is used in the finite element model to simulate the bridge beam and column. Concrete C50 and C30 are respectively used in the bridge beam and column (Fig. 1).

The high-speed locomotive with eight compartments is selected to set up the train model [5–7]. The train body is simplified to rigid body with equivalent mass and stiffness, transverse and vertical springs, damping as well as tangential sliding friction

Table 1. Rail passenger high-speed locomotive model parameter

Parameters	Value	Unit	Parameters	Value	Unit
Train mass	34000	kg	Transverse spring	2e8	N/m
Bogie mass	3000	kg	Vertical spring	1e8	N/m
Wheel set mass	1400	kg	Sliding friction factor	0.3	–
Half of train distance	9	m	Half of bogie distance	1.2	m

are used to simulate contact relation between the train and track. Parameter values are listed in Table 1.

Based on the parameters above, the final train-bridge coupling model has been established (Fig. 2).

Fig. 1. Train-bridge coupling system

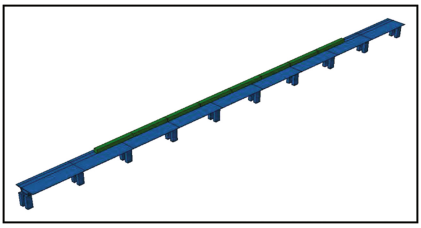

Fig. 2. Train-bridge coupling model

Compared with previous finite element models, this mode has made some improvement:

(1) Plastic relation has been considered.
(2) Train-bridge coupling effect has been taken into account, contact relation and constraint condition between train and bridge have also been considered.
(3) A single bridge model has been set up for comparison.

Boundary constraint and contact relation of the model are as follows. Horizontal spring restraint with a stiffness equal to bridge deck system has been set at the joint of simply supported beam. The contact relation between train and track has been simplified, horizontal and vertical springs have been set, the stiffness value of which are obtained by Hertz nonlinear theory. The friction factor value between the wheel and track is set as 0.3.

1.2 Natural Vibration Characteristics Analysis

In order to study the influence of natural vibration characteristics, vibration comparison between single model and coupling model has been progressed. Subspace iteration method is a usual modal analysis method, which can easily solve eigenvalue problems of large sparse banded matrix in the vibration analysis. However, considering the complexity and large number of modal, Lanczos algorithm has been adopted instead of subspace iteration method for higher computational efficiency. Using Lanczos

Table 2. Natural vibration period comparison between single bridge and train-bridge coupling system

Period/s				$\Delta T = \frac{T_2 - T_1}{T_2}$ (%)	Direction
Mode	T_1 (single model)	Mode	T_2 (coupling model)		
1	0.35	1	0.38	6.79	Transverse
9	0.226	4	0.227	0.15	Longitudinal
18	0.15	11	0.17	11.76	Vertical
2	0.31	2	0.37	11.11	Torsional

algorithm method, the first 50 natural modes have been picked up. Natural frequencies and modes of four direction have been obtained (Table 2).

Corresponding to the basic vibration modes, the first order mode of single mode and coupling mode is transverse direction, which indicate that the transverse stiffness of the bridge is respectively weak. The comparison results of the first order mode of the two models are listed in Table 2. Results shows that, the first order vibration period at each direction of the single model is less than the coupling model. In contrast with the single bridge, the biggest difference Δt of coupling model is about 11.76% at vertical direction. Overall, the integral rigidity of coupling model is weaker than single bridge model, considering the vibration differences, train-bridge coupling effect cannot be ignored in the structure response analysis.

1.3 Seismic Response Analysis of Train-Bridge Coupling System

In order to study the seismic response analysis difference between the single model and coupling model, the comparison analysis of seismic acceleration response is obtained [6]. Typical earthquake records at different sites of Class I, II and III have been selected (Table 3), and the peak acceleration have been adjust to 0.1 g. Finally, the seismic response of single model and coupling model have been calculated, the response acceleration values at the mid-span, bottom center and edge of the box girder have been picked up. The maximal acceleration values are screened for comparison.

Corresponding to the response analysis results of the single model and coupling model, the maximum values of acceleration response are picked up, time history curves of the deck acceleration are obtained. Figures 3 and 4 show the deck acceleration curves of Qianan wave and El-centro wave respectively. In order to formulate clearly, these curves cut out parts of the response time history which include peak acceleration.

Comparing with the initial earthquake excitation, the deck acceleration responses of the single model and coupling model are obviously enlarged and lagged. Meanwhile, the acceleration response are different between the single model and coupling model. Table 4 and Fig. 5 shows the comparison results of peak transverse accelerations and amplification factors of the deck for single model and coupling model.

According to the calculated results, the deck acceleration responses have varied for different earthquake inputs. The peak response values and amplification factors calculated at long-periodic earthquake at site of Class II and III is obvious bigger than that at site of Class I, which indicated that the seismic response of the deck is closely related to the natural period of the earthquake.

Table 3. Selection of seismic motion

No.	Earthquake name	Year	Site classification	Dominant period (s)	Peak acceleration (g)
1	Qianan	1976	I	0.07	0.1
2	Superstition Mountain	1979	I	0.15	0.1
3	Hayward CSUH	1980	I	0.20	0.1
4	TAR	1987	II	0.31	0.1
5	Kobe	1995	II	0.35	0.1
6	Wen Chuan-Wolong	2008	II	0.42	0.1
7	El-centro	1940	II	0.56	0.1
8	TOPANGA	1994	III	0.60	0.1
9	CHICHI-CHY006	1999	III	0.62	0.1
10	CHICHI-CHY015	1999	III	0.67	0.1

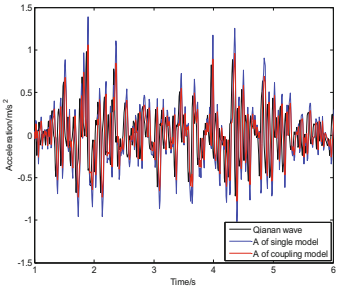

Fig. 3. Maximum acceleration response of deck under Qian-an wave

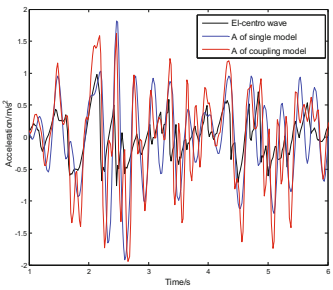

Fig. 4. Maximum acceleration response of deck under El-centro wave

Most of the acceleration response amplification factors fall in the interval [1.5, 2.5], which are consistent with the research results of seismic response for high-speed rail bridges by Gao Qilang in 2013 [10].

Amplification factors are different between the single model and coupling model at the same earthquake input. Take Qianan wave for example, the amplification factors differences of these two models come to 23%, which can greatly affect the safety evaluation results. Therefore, it is necessary to consider train-bridge coupling effect in seismic response analysis of high-speed rail bridge to reduce assessment risk.

1.4 Influence of Seismic Spectral Characteristics

In order to study the influence of seismic spectral characteristics to the response acceleration of the deck, according to the piecewise linear interpolation based accurate method of response spectrum by N.C. Nigam and P.C. Jennings, Matlab programs have been written, Response spectrum curves have been obtained for 10 typical earthquake

Table 4. Comparison of peak transverse accelerations and amplification factors of the deck

No.	Earthquake record	Peak acceleration (g)	Single model		Coupling model		$\Delta\alpha = \frac{\alpha_2 - \alpha_1}{\alpha_2}$ (%)
			Peak value (g)	Amplification factor α_1	Peak value (g)	Amplification factor α_2	
1	Qianan	0.1	1.42	1.39	1.08	1.06	−23.74
2	Superstition Mountain	0.1	1.17	1.19	1.14	1.17	−1.68
3	Hayward CSUH	0.1	1.68	1.71	1.59	1.62	−5.26
4	TAR	0.1	1.96	2.00	2.12	2.16	8.00
5	Kobe	0.1	1.58	1.62	1.61	1.64	1.23
6	Wenchuan-Wolong	0.1	2.10	2.14	2.12	2.17	1.40
7	El-centro	0.1	1.92	1.96	1.95	1.99	1.53
8	TOPANGA	0.1	2.10	2.27	2.22	2.56	12.78
9	CHICHI-CHY006	0.1	2.22	2.27	2.04	2.08	−8.37
10	CHICHI-CHY015	0.1	2.51	2.56	2.44	2.49	−2.73

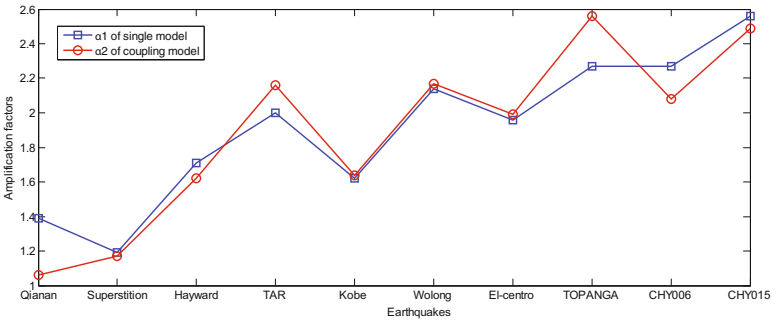

Fig. 5. Acceleration amplification factor of the deck of single bridge and train-bridge coupling system

inputs (Fig. 8). Figures 6 and 7 show the response spectrum curve of Qianan and El-centro waves. The structure damping ratio is 5%.

From the response spectrum curve of Qianan and El-centro waves in Figs. 6 and 7, the amplitudes of the coupling model are greatly varied, and the structure periods corresponding to the amplitudes are also different. It indicate that the frequency characteristics of the deck acceleration response time history have changed. Therefore, in order to evaluate the earthquake alarm thresholds of the coupling model more reasonably in the further study, the deck acceleration response data is more suitable as the input excitation than the initial seismic acceleration data.

The first order natural vibration period of the coupling model is 0.38 s, according to the spectra curves in Fig. 8, around this period, the peak response spectrum acceleration values of typical earthquakes in site of Class I are less than those of Class II and III, which further validate the conclusion: the peak response values and amplification

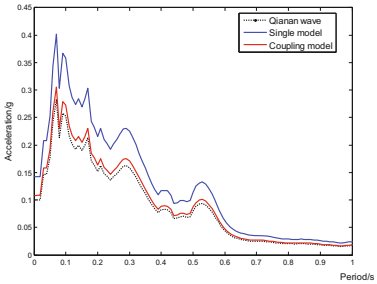

Fig. 6. The response spectrum curve of Qian-an wave and deck acceleration

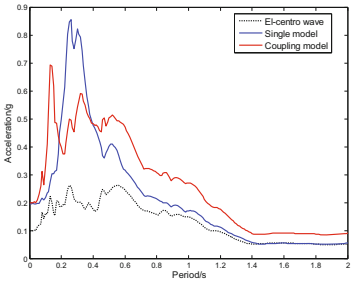

Fig. 7. The response spectrum curve of El-centro wave and deck acceleration

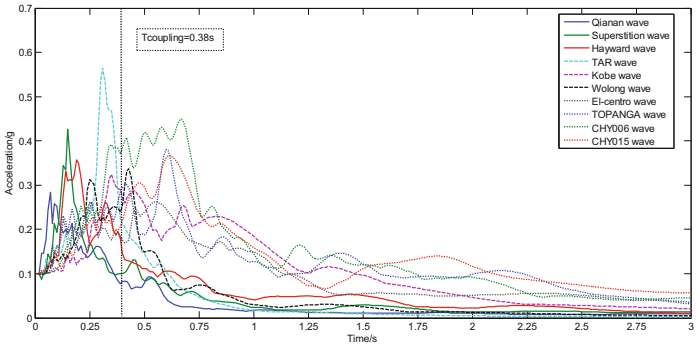

Fig. 8. The summary response spectrum curve of the input seismic motion

factors obtained at long-periodic earthquake at site of Class II and III is obvious bigger than that at site of Class I.

Meanwhile, there are some differences of the period corresponding to the peak value of deck acceleration spectra curves between the single model and coupling model. Take El-centro wave for example, these periods are 0.26 and 0.38 s respectively for the single model and coupling model, the deviation is up to 46.1%. It obviously more reasonable and correct to use coupling model for seismic response analysis than the single model.

2 Conclusions

Based on the previous seismic response analysis and research productions of high-speed rail bridges, finite element method has been used, combined with practical engineering, a more accurate and reasonable train-bridge coupling model has been established.

Seismic responses and amplification factors are different between the single model and coupling model under typical earthquake inputs. It is necessary to consider

train-bridge coupling effect in seismic response analysis of high-speed rail bridge to ensure the running safety of the high-speed train.

The seismic response analysis results shows that, amplification factors of the deck acceleration response have varied for different earthquake inputs. In some cases, the amplification factors calculated may be greater than the statistical average values 2.55 of typical structure include railway bed and bridge in China, it is more reasonable to use the deck seismic response data as the input in the train safety evaluation.

There are closely relation between the deck acceleration response and input earthquake data, reasonable and adequate typical earthquake records should be chosen for the seismic response analysis and earthquake alarm threshold research of the high-speed rail bridge. Meanwhile, Structural vibration characteristics, site condition and seismic spectral characteristics should also be considered.

References

1. Ministry of Transport: Railway working conference. Report (2013)
2. Wanming, Z.: Vehicle-track Coupling Dynamics, 3rd edn. Science Press, Beijing (2007)
3. Shuli, S.: High-Speed Railway Bridge Design and Application. China Railway Publishing House, Beijing (2011)
4. Wanming, Z., He, X.: Train-Track-Bridge Dynamic Interaction; Theory and Engineering Application. Science Press, Beijing (2011)
5. Chunguang, L.: Seismic Response and Performance Analysis of Bridge. China Architecture and Building Press, Beijing (2009)
6. Yufei, M.: Comprehensive Study on Seismic Emergency Handling Technology. Institute of Engineering Mechanics, CEA, Guangzhou (2011)
7. Guanglei, H.: Research on Threshold Value of Seismic Urgent Handling System of High-Speed Railway. Institute of Engineering Mechanics, CEA, Guangzhou (2013)
8. Renfei, G.: Seismic Response Analysis of High-Speed Train and Bridge Coupling System. Institute of Engineering Mechanics, CEA, Guangzhou (2014)
9. Xianting, D., Xia, H., Zhu, Yu.: Study on the input of seismic ground motion in the dynamic interaction analysis of train-bridge system. China Railway Sci. **32**(6), 34–41 (2011)
10. Qilang, G.: Earthquake Response Analysis and Amplification Factor Study of High-Speed Railway Viaduct. Institute of Engineering Mechanics, CEA, Guangzhou (2013)

Simulation of Human Induced Vibration of a Lively Footbridge

Eleonora Lai and Maria G. Mulas(✉)

Department of Civil and Environmental Engineering,
Politecnico di Milano, Milano, Italy
mariagabriella.mulas@polimi.it

Abstract. In the last years, the need for structures able to link the functional and aesthetic role has led to the design of new flexible footbridges. The low ratio between permanent and variable loads makes them more sensitive to dynamic loads, such as the forces transmitted by pedestrians.

During the human walking, the pedestrian moves on a flexible structure adapting his gait to the bridge motion. The interaction between pedestrian and footbridge takes place at contact points, where the pedestrian transmits contact forces to the bridge that, in turn, imposes a set of displacements and velocities to the pedestrian's feet. The description of the human being as a mechanical system allows for the derivation of the equation of motion of the bridge-pedestrian coupled system. In this work a previously developed bipedal pedestrian mass-spring-damper (MSD) model is adopted. The analytical formulation of the human-structure interaction, involving the derivation of the bridge-pedestrian coupled equations of motion, has been implemented in a numerical code, named INTER2.0. The bridge is modelled using a commercial FE code and its geometry is fully described. The code reads in input both the bridge structural matrices and the pedestrian dynamic properties needed to assembly the MSD matrices or the feet forces.

The present contribution investigates the effect, on a lively footbridge response, of a few parameters: distance between pedestrians and pedestrians' trajectory. The results due to groups of pedestrians walking along different eccentric trajectories have highlighted the relation between the bridge mode excited and the pedestrians' position. As it was expected, the eccentric transit induces a torsional behavior. In addition, the spatial distribution affects the bridge response: the vertical accelerations rise if the longitudinal distance among pedestrians increases, although this trend is not linear with the distance.

Keywords: Pedestrian mechanical model · Pedestrian induced vibration · Coupled footbridge-pedestrian analysis · Case study · Lively footbridge

1 Introduction

In the last years the new footbridge design, moved by aesthetics requirements, has sprouted challenging bridges characterized by greater slenderness, longer spans, low damping and light materials [1]. As a consequence, their structural systems, with a low ratio between permanent and live loads, exhibit natural frequencies very close to the

© Springer International Publishing AG 2018
J.P. Conte et al. (eds.), *Experimental Vibration Analysis for Civil Structures*,
Lecture Notes in Civil Engineering 5, https://doi.org/10.1007/978-3-319-67443-8_75

range of frequencies of human walking [2]. When the bridge accelerations exceed the limit perceived as comfortable and safe by humans, the utilization of the structure can be highly impaired. Thus, the design requires a greater care regarding vibration phenomena and the vibrations produced by human-induced loads are to be assessed within the class of serviceability limit states [3]. The vibration serviceability under human-induced dynamic forces is the governing criterion for the design of these slender structures.

During footbridge vibrations, some form of human-structure interaction (HSI) occurs, playing an important role in the structural dynamic response. HSI (a complex and inter-disciplinary issue) can be subdivided into two key areas [4]. One concerns the influence of structural vibration on forces induced by human occupants; the other the effect of pedestrians on the dynamic properties of civil engineering structures. This paper focuses on the second aspect.

The correct modeling of pedestrians represents an important issue into the study of HSI. A large research effort in the last 15 years has led to the development of both analytical expressions for the walking force and procedures to determine the footbridge response. Following the first simplified models, the increasing sophistication of the proposed expressions did not lead to significant improvements in numerical estimates of the response under pedestrian flows [5]. A mechanical model considers the mass, stiffness and damping of the pedestrian, all of which can interact with the structure [6]. Furthermore, the bridge response accounting for the human-structure interaction depends on both reliable estimates of expected loading scenarios and the accuracy of the models representing pedestrian.

Aim of this work is the study of the dynamic response of a footbridge accounting for the human-structure interaction (HSI) in the vertical direction. A mass-spring-damper (MSD) pedestrian model, developed in a previous work [7], has been adopted. The mechanical model is able to reproduce the correct human gait. Numerical analyses have been carried out with an ad-hoc numerical code, based on an uncoupled analytical formulation recently proposed [7]. The modeling and analysis approach is inherently uncoupled when forces are considered. Due to the pedestrian motion, the structural matrices of the coupled system are time-dependent and should be modified whenever the pedestrian's foot position on the bridge changes. The proposed alternative solution strategy is based on the forced uncoupling of the system, based on the key assumption that the contact points between pedestrian and bridge deck are massless. The uncoupled formulation considers the footbridge and the pedestrian as two separate sub-systems (the former subjected to contact forces transmitted by the pedestrian, the latter excited by the bridge motion), reducing the computational burden associated to the time-varying properties of the matrices of the coupled system.

Numerical analyses are computed with the objective of evaluating the effect, on the bridge response, of a few parameters: pedestrians' trajectory and distance between pedestrians. First, analyses with six pedestrians, walking in a single line, are carried out to study how transits, with the same spatial distribution but different eccentricity, affect the bridge response, highlighting the relation between the bridge mode excited and the pedestrians' position. Secondly, analyses with nine pedestrians, placed on a uniform grid, investigate the variation of maximum accelerations when the mutual distance among pedestrians increases. Eight spatial distributions are considered, with an

increasing value of the longitudinal distance among two subsequent pedestrians' rows, in a range between a lower value of 1 m and an upper one of 4.5 m.

2 Seriate Footbridge

The Seriate footbridge in Fig. 1a, 63.75 m long, connects two cycle routes in the Serio Park (near to Milan, Italy). The width of the timber deck on a steel grid (Fig. 1b) ranges between 2.5 m at the entrance and 5 m at mid-span. The slightly curved longitudinal steel girders have a rise of 1.3 m. The transverse beams of the steel grid (Fig. 1b) are spaced 1 m apart and are subdivided in main and secondary elements. Main girders have a tapered section and are connected to the hangers. Secondary beams have an IPE 120 cross-section. The stringers are a pair of IPE 330 beams at the edges, and a central beam with a circular section (ϕ = 298.5 mm), deemed to stabilize the deck on the horizontal plane.

Fig. 1. Seriate footbridge: (a) overall view; (b) footbridge deck, detail of longitudinal and transverse beam.

A series of X-braces (Fig. 1b) connects the main transverse girders providing stiffness in the horizontal plane. The timber deck (Fig. 1b) has only a minor structural role, providing the walking surface. The ends of the transverse main girders are crossed by stabilizing cables, whose sliding in the longitudinal direction is allowed by the interposition of a polymeric layer between the two contact surfaces.

The suspension system is composed of: (a) steel main pylons, slightly inclined with respect to the vertical plane, supporting the suspension system and the backstays cables as shown in Fig. 1a; (b) 2 main suspension cables (ϕ = 60 mm), supporting the longitudinal girders through 42 vertical hangers (ϕ = 16 mm); (c) backstays cables (ϕ = 60 mm), connecting the pylons top to the ground; (d) two stabilizing cables of opposed curvatures ϕ = 40 mm.

The suspension system is symmetric neither about the vertical plane crossing the longitudinal bridge axis nor about the vertical plane crossing the mid-span. All the cables were pre-tensioned during construction.

The dynamic behavior of the footbridge was investigated through a dynamic test. The bridge response under ambient excitation was recorded with conventional accelerograms. With output-only techniques typical of the operational modal analysis, 14 vibration modes were identified in the frequency range 0–10 Hz. The frequency of the fundamental mode was 1.03 Hz. Figure 2 depicts four mode shapes, whose natural frequency is into the walking load critical range, identified using the FDD method.

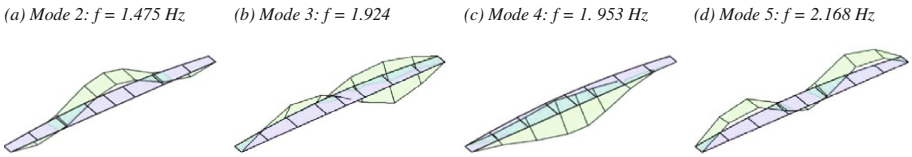

Fig. 2. Mode shapes identified: (a) mode 2; (b) mode 3; (c) mode 4; (d) mode 5

A finite element model of the bridge, based on the original drawings, was set up within the ANSYS framework and a modal analysis was carried out in order to obtain the numerical dynamic properties. The agreement between experimental and numerical values is fully satisfactory. Further details on the derivation of the FE model are found in [8].

3 Pedestrian Mechanical Model

A mechanical system is the most accurate pedestrian modelling in the analytical study of human-structure interaction. In this work, reference is made to a bipedal mechanical model recently proposed [7], capable to simulate the human locomotion, characterized by the alternate sequence of single support phase (SSP) and double support phase (DSP) of the typical human gait cycle (Fig. 3a). SSP begins when the leading foot hits the ground and the trailing foot is off the ground, moving through the air towards the next position. DSP starts when the trailing foot hits the ground becoming the leading foot and both feet are in contact with the bridge deck.

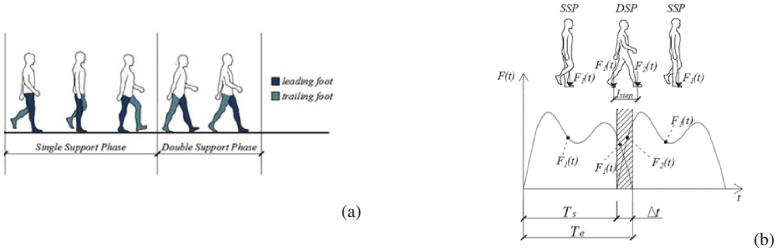

Fig. 3. Human gait cycle: (a) sequence of SSP and DSP; (b) single foot force model.

The pedestrian is modelled as a SDOF mass-spring-damper mechanical system. Its equation of motion takes into account the interaction with the bridge and the biomechanical force acting on it. The MSD system has two spring-damper legs (Fig. 4), capable to reproduce the correct human gait (SSP and DSP in a sequence). The legs parameters follow the data provided by Kim & Park [9]. The mass, lumped at the centre of gravity of the body, oscillates in the vertical direction only. A fictitious bio-mechanical force F_b excites the MSD system. By solving an inverse problem, in this work F_b has been derived as the force that, applied on the system moving on a rigid surface, produces a ground reaction force (transmitted by each leg) matching the single foot force model in Fig. 3b.

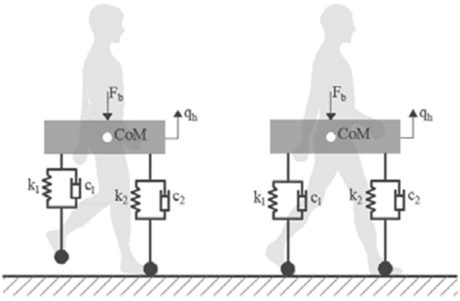

Fig. 4. MSD model: left, only one leg is in contact, right, both legs are in contact.

4 Equations of Motion for the Coupled System

The coupled equations of motion governing the HSI are written for the overall system composed of the bridge and the pedestrian mechanical system, where the bridge is discretized with the FE method. Hence, the problem has a finite number of coordinates. The two systems interact at contact points exchanging a vertical contact force: the bridge, due to its flexibility, oscillates and applies a motion at the base of pedestrian's feet. The walking pedestrian, excited by the biomechanical force and the motion applied by the bridge, transmits to the bridge deck a set of contact forces (leg internal forces). The coupled equations are first forcibly uncoupled and then solved via an iterative procedure [7, 10]. The pedestrian model and the uncoupled algorithm are implemented in a research code named INTER 2.0 [7].

4.1 Pedestrian Traffic and Spatial Configuration in INTER 2.0

Inter 2.0 can consider either a single pedestrian or a group of pedestrians. In both cases the pedestrian's trajectory is a straight line parallel to the bridge axis, not necessarily coinciding with a line of nodes. The groups of pedestrians can be distributed according to three different spatial configurations: uniform grid (Fig. 5a), "chessboard" (Fig. 5b) and "random-like" distribution (Fig. 5c). Pedestrians move with the same step velocity and their mutual (deterministic) distance do not change during the analysis.

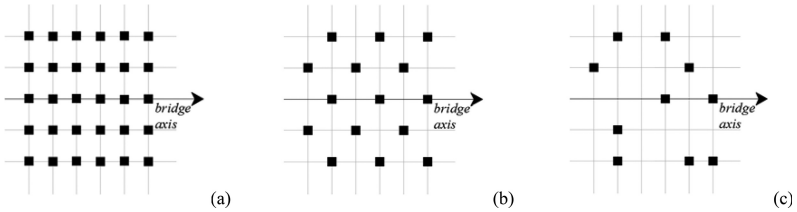

Fig. 5. Pedestrians' spatial configuration: (a) uniform grid; (b) "chessboard" grid; (c) "random-like" grid.

Three types of synchronization have been considered: full, partial and no synchronization, the only compatible with the probabilistic approach. A total synchronization takes place if *n* identical pedestrians walk perfectly in phase. Partial synchronization means in-phase walking along rows and uncorrelated phases among rows. No synchronization means that a group of *n* pedestrians walks with completely uncorrelated phases. The degree of synchronization is independent of the spatial configuration.

5 Numerical Results

The relevant response parameters adopted in this work are the maximum vertical accelerations and the time histories of vertical displacements. Both accelerations and displacements are evaluated in seven transverse sections of the deck for three points: two are placed at the base of handrails and the third one is on the longitudinal axis of the footbridge deck (Fig. 6).

The analyses have been performed with a staggered approach, without introducing the iteration process since, as the time step decreases, the solutions are convergent. The integration time step Δt is 0.005 s, quite smaller than 1/10 of the period of the 14th mode, and sufficient to discretize accurately the forcing term. The Rayleigh damping matrix is computed for a 1% damping, a value experimentally identified, on the first and fourth mode, and the Newmark's coefficient β and γ are respectively 0.25 and 0.5 (constant acceleration method). Finally, a velocity of 1.3 m/s, normal distribution mean value [11], is considered for each pedestrian.

Numerical analyses are computed with the objective of evaluating the effect, on the bridge response, of a few parameters: distance between pedestrians, degree of synchronization, correlation in terms of step frequency and spatial distribution.

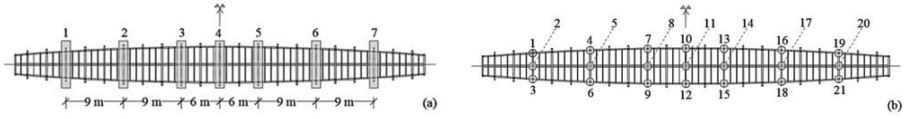

Fig. 6. (a) Bridge cross sections, (b) corresponding points nodes considered in the analysis.

5.1 Six Pedestrians with Different Trajectories

The six people are placed in a single line, parallel to the bridge axis, with a mutual distance of 2 m. Each of the three analyses is characterized by a different value of the eccentricity of the rectilinear trajectory from the longitudinal axis. In the first one, the pedestrians are walking on the left side of the deck, with an eccentricity of 1 m. In the second one, the eccentricity is the same, but the pedestrians are walking on the right side. Finally, the last configuration provides six pedestrians walking along the bridge longitudinal axis.

The six MSD pedestrians are considered uncorrelated and unrestricted. They have their own step frequency (f_1 = 1.843 Hz, f_2 = 2.057 Hz, f_3 = 1.675 Hz, f_4 = 1.776 Hz, f_5 = 1.634 Hz, f_6 = 1.799 Hz) drawn from a normal distribution, and no synchronization has been taken into account. The pedestrians have a common weight and height of 700 N and 1.70 m, respectively. Each pedestrian crosses the bridge about in 49 s and the last pedestrian exits the bridge about 8 s after the first.

Figure 7a–c show, respectively, the comparison between the displacement time-histories of nodes 16, 17 and 18 (at section #6, at ¾ of the span), for the cases of people walking along the left, right and central side, respectively. The comparison highlights that eccentric transits induce a torsional behavior, which could be amplified by the configuration of the bridge suspension system, which is not-symmetric respect to both the bridge longitudinal axis and the mid-span.

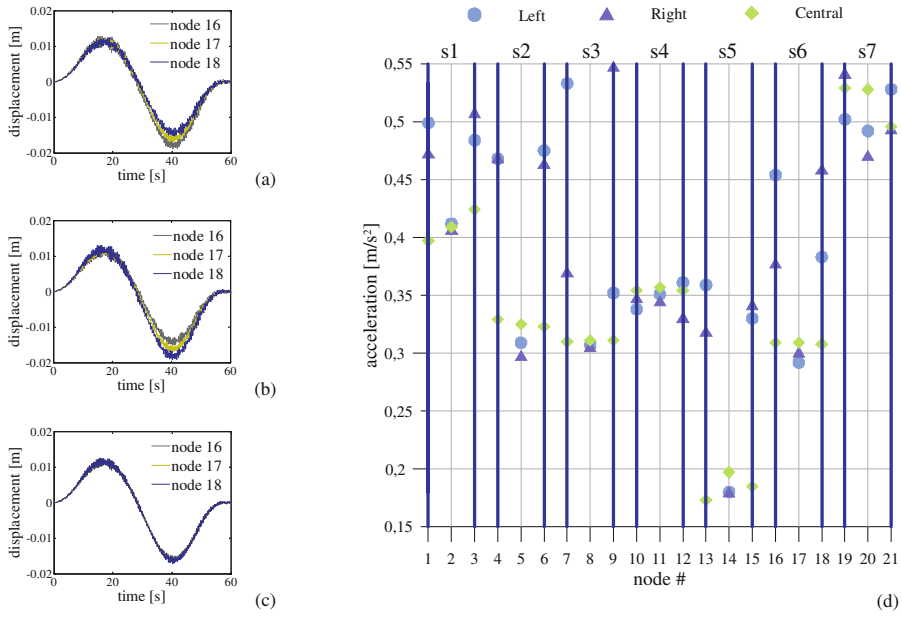

Fig. 7. Displacement time-history of nodes at Sect. 6 for the pedestrians with: (a) left; (b) right and (c) no eccentricity. (d) Maximum vertical accelerations with six pedestrians having different eccentricity, for all nodes (s# identifies the section).

The analysis of plots in Fig. 7a and b highlights that the torsional behavior becomes larger when the pedestrians cross the section at study. Obviously, nodes closer to the pedestrians' trajectory, i.e. node 16 for a left eccentricity and node 18 for a right one, experience displacements larger than those of the node on the opposite side. On the other hand, the pedestrians walking along the longitudinal axis do not induce a torsional effect. In fact, in Fig. 7c (same nodes of Fig. 7a, b), the displacement histories are overlapped during the whole time interval.

Figure 7d shows the maximum vertical acceleration attained at each of the nodes in Fig. 6b for the three analyses at study. As a general trend, at each section the eccentric transits produce larger accelerations than a centered load, with the exception of nodes at Sections 4 and 7, where the results are similar for the three load configurations. In addition, it can be noticed that, as for the displacement response, the lateral nodes of each section experience the largest acceleration with the first two load configurations, while a central trajectory does not produce a considerable difference on the nodes belonging to the same section. This finding can be explained with the modal shape of the third mode, a torsional mode with a node around midspan.

The vertical accelerations, produced by different transits, have been further analyzed by comparing, at each node, the corresponding Fourier spectra. From the analysis of the results, the following statements can be inferred:

- Fourier spectra due to eccentric transits, computed for lateral nodes, both on the left and right side, have a common pattern, different from that induced by pedestrians walking along the longitudinal axis (Fig. 8). However, the lateral nodes at mid-span show the same trend and frequency content (results not reported here for the sake of brevity);
- central nodes, along the longitudinal axis, are not influenced by the pedestrians' position. In fact, at each node, the comparison among the three Fourier spectra shows a common pattern (Fig. 9). This behavior is coherent with the shape of the 8th mode, a torsional one, which has nodes close to the bridge axis [8].

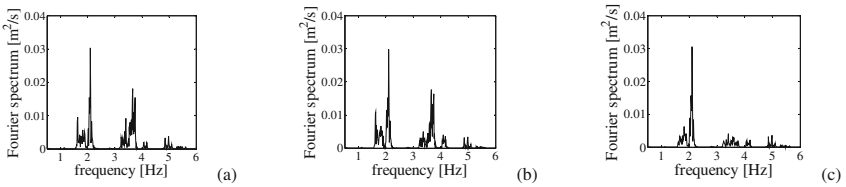

Fig. 8. Fourier spectrum of vertical acceleration at node 9 (Sect. 3): (a) left eccentricity, (b)right eccentricity, (c) no eccentricity.

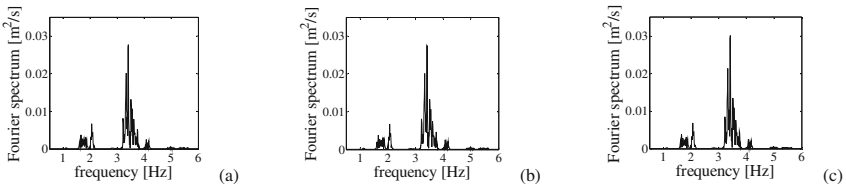

Fig. 9. Fourier spectrum of vertical acceleration at node 11 (Sect. 4): (a) left eccentricity, (b) right eccentricity, (c) no eccentricity.

5.2 Nine Pedestrian with Different Spatial Distributions

This section investigates the effect of pedestrians' spatial distribution on the bridge response. The goal has been pursued by modifying the longitudinal distance among pedestrians, while the transverse one, equal to 0.75 m, remains constant. Analyses have been carried out by adopting nine pedestrians with a uniform distribution on three rows. The center of gravity of the group is on the longitudinal bridge axis. Eight spatial distributions have been considered, characterized by an increasing value of the longitudinal distance d among two subsequent pedestrians' rows, equally spaced in a range between a lower value of 1 m and an upper one of 4.5 m. The pedestrians have a common step frequency, a common weight and a common height of 1.7 Hz, 700 N, and 1.70 m, respectively. Each pedestrian walks with a step velocity of 1.3 m/s. Pedestrians are not synchronized.

As a general trend, the comparison among the results of the eight analyses shows that the maximum accelerations tend to increase with the distance. However, the increment is more pronounced in the interval between 1.0 m and 2.5 m, becoming null or negligible when d exceeds 2.5 m. A few nodes, i.e. node 11, experience a slight decrease after 3 m. On the contrary, the accelerations at Sects. 3 and 5 increase when d varies from 1 m to 1.5 m and then tend to decrease. These two opposite behaviors are shown in Fig. 10a and b, respectively.

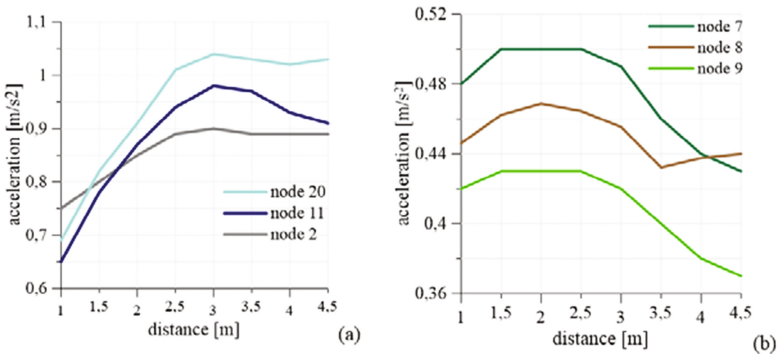

Fig. 10. Plot of maximum accelerations as a function of distance d: (a) nodes 2, 11 and 20, (b) nodes 7, 8 and 9.

This behavior (larger accelerations associated to a larger distance) could be explained with the fact that pedestrians with a larger mutual distance excite the footbridge for a longer time than pedestrians close to each other. Also an effect of the mode shapes could have played a role.

On the other hand, the different pattern (some nodal accelerations increase while others decrease) could be related to the modal damping. In fact, by analyzing the Fourier spectra of acceleration of each node, it can be noticed that the maximum peak is not always in the same frequency range. Thus, the response of the seven sections at study could be affected by different modes, having different modal damping.

In this case, the Fourier spectra of nodes at Sects. 1, 2, 4, 6 and 7 have a maximum peak about the frequency describing the 2nd harmonic of the load (3.4 Hz), while the nodes at Sects. 3 and 5 experience accelerations whose Fourier spectrum has a maximum peak about the step frequency (1.7 Hz). Nodes on the same section are characterized by the same Fourier spectra. This pattern is common for the eight analyses.

Figure 11a and b show the Fourier spectrum of acceleration at node 8 and 11, respectively, while Fig. 11c and d show the time-history of vertical acceleration at node 20 (Sect. 7). The pattern of Fourier spectrum is common for the eight analyses highlighting that, whatever the longitudinal distance, the modes that are excited are always the same. As for the Fourier spectra, the eight acceleration histories, even though with different amplitudes, have a common pattern characterized by a beat phenomenon. Thus, it can be stated that the increase of distance induces only a variation in the acceleration amplitude, without modifying the trend of the time-history or the frequency content of Fourier spectrum.

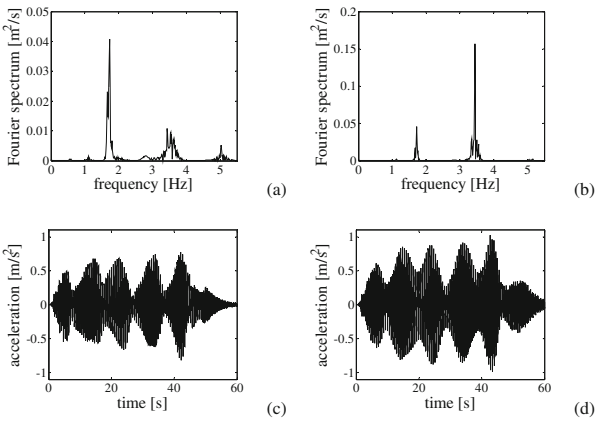

Fig. 11. Fourier spectrum of vertical acceleration at node 8 (Sect. 3): (a) d = 1.5 m, (b) d = 3.5 m. Acceleration time history at node 20 (Sect. 7): (c) d = 1.5 m, (d) d = 3.5 m.

6 Conclusions

In this paper the response of a lively footbridge to walking pedestrians is computed with an uncoupled approach. The bridge is modeled with the Finite Element Method. The pedestrian is represented by a mechanical bipedal model, simulating the sequence of SSP and DSP, typical of the human gait. The two systems interacts at contact points that are not necessarily coincident with bridge mesh nodes.

The case study is a lively footbridge, whose dynamic behavior has been extensively analyzed both experimentally and numerically. The results of the numerical analyses, computed with the objective of evaluating the effect on the bridge response of a few parameters (distance between pedestrians and spatial distribution) can be summarized as it follows:

- The numerical response is coherent with (and determined by) the dynamic properties of the bridge. In fact, the pattern of maximum acceleration follows the bridge modes excited by pedestrians' walking.
- Acceleration time histories show a beat phenomenon. This fact can be explained by observing that the bridge has nine frequencies within the walking frequency range 1–4 Hz (considering also the second harmonic of the load).
- The effect of the second harmonic of the load (biomechanical force with a MSD model) on the response of the bridge at study is not negligible.
- Eccentric transits produce larger accelerations than those induced by a group of pedestrian walking without eccentricity. Moreover, as it was expected, the eccentric transit induces a torsional behavior in the bridge response.
- In general, the vertical accelerations increase with the longitudinal distance among pedestrians, although this is not a linear trend. In fact, the acceleration increment tends to become negligible or null for distances exceeding 3 m.

It is important to note that the analytical formulation and its numerical implementation are not restricted to the footbridge at study or to the mechanical model proposed. In fact, the generality of the uncoupled approach allows taking into account both different footbridges and different mechanical systems.

Acknowledgments. The financial contribution of MIUR (Italian Ministry of Higher Education) under grant PRIN 2015-2018 "*Identificazione e diagnostica di sistemi strutturali complessi*" is gratefully acknowledged.

References

1. Ingólfsson, E.T., Georgakis, C.T., Jönsson, J.: Pedestrian-induced lateral vibrations of footbridges: a literature review. Eng. Struct. **45**, 21–52 (2012)
2. Van Nimmen, K., Lombaert, G., De Roeck, G., Van den Broeck, P.: Vibration serviceability of footbridges: evaluation of the current codes of practice. Eng. Struct. **59**, 448–461 (2014)
3. Živanović, S.: Benchmark footbridges for vibration serviceability assessment under the vertical component of pedestrian load. J. Struct. Eng. **193**, 1193–1202 (2012)

4. Sachse, R., Pavic, A., Reynolds, P.: Human-structure dynamics interaction in civil engineering dynamics: a literature review. Shock. Vib. Digest. **35**, 3–18 (2003)
5. Jimenez-Alonso, J.F., Sáez, A., Caetano, E., Magalhãe, F.: Vertical crowd-structure interaction model to analyze the change of the modal properties of a footbridge. J. Bridge Eng. **21**, C4015004 (2016)
6. Toso, M.A., Gomes, H.M., De Silva, F.T., Pimentel, R.L.: Experimentally fitted biodynamic models for pedestrian-structure interaction in walking situations. J. Mech. Syst. Signal Process. **72–72**, 590–606 (2016)
7. Lai, E.: Pedestrian-footbridge dynamic interaction: un-coupled analysis using a MSD model, PhD. Thesis. Department of Civil and Environmental Engineering, Politecnico di Milano, Milan (2016)
8. Lai, E., Gentile, C., Mulas, M.G.: Experimental and numerical serviceability assessment of a steel suspension footbridge. J. Constr. Steel Res. **132**, 16–28 (2017)
9. Kim, S., Park, S.: Leg stiffness increases with speed to modulate gait frequency and propulsion energy. J. Biomech. **44**, 1253–1258 (2011)
10. Feriani, A., Mulas, M.G., Lucchini, G.: "Vehicle-bridge interaction analysis: an uncoupled approach". In: Proceedings of ISMA, Leuven, Belgium (2008)
11. Pachi, A., Ji, T.: Frequency and velocity of people walking. Struct. Eng. **83**, 36–40 (2005)

Vibrations in Multilayered Soils: A Simplified and Robust Prediction Equation

Abdul Karim Jamal Eddine(✉), Luca Lenti, and Jean-Francois Semblat

Université Paris-Est, GERS, SV, IFSTTAR, F-77447 Marne-La-Vallée, France
abdul-karim.jamal-eddine@ifsttar.fr

Abstract. Wave propagation in soil is controlled by both attenuation and amplification laws. The former is due to geometrical and material damping, while the latter is mainly due to velocity contrasts between the various layers and possibly some geometrical/topographic effects. In the field of seismology and earthquake engineering, several factors are considered to describe the site properties and predict the amplifications features, such as average velocity V_{s30} and velocity-gradient-based coefficients. The reliability of these factors is questioned in the case of vibration problems, for which surface sources generated frequency components are much higher than in earthquake engineering. With this aim, considering various sites typologies, this paper suggests a set of relevant parameters for predicting vibration away from the vibratory source. Starting from numerical results (FEM), correlations between the proposed factors and the estimated displacements are discussed. These simple prediction equations are shown to be relevant and robust.

Keywords: Vibration · Amplification · Gradient · Wave propagation · Prediction equation

1 Introduction

While ground motion prediction equations are an important research domain since many decades in earthquake engineering, the necessity of similar approaches for vibration prediction is on the rise. Similarly to the seismic case, attenuation and site effects due to the presence of waves trapped in weaker soils over stiffer soils play an important role in the determination of vibration levels [1].

In the domain of earthquake engineering, V_{s30} which is the harmonic average shear wave velocities in the first 30 m of soil is usually taken as the main parameter of analysis and classification [2, 3].

The doubts about the capability of the V_{s30} factor to predict the site amplification, and therefore predict precisely the ground displacement, led to the suggestion of more or alternative factors for the analysis. Such suggestions are, but not limited to, the use of the soil fundamental frequency f_0 along with V_{s30} [4, 5]. Another suggestion is the use of the gradient of the shear-wave velocity profile factor B_{30} [6] that describes the variation of soil impedance in the first 30 m.

© Springer International Publishing AG 2018
J.P. Conte et al. (eds.), *Experimental Vibration Analysis for Civil Structures*,
Lecture Notes in Civil Engineering 5, https://doi.org/10.1007/978-3-319-67443-8_76

In the present study, the aim is to suggest prediction equations for vibration from surface sources using adapted parameters capable of describing specific site properties.

2 Parameters Suggestion

For the purpose of analyzing the soil behavior under higher frequencies excitation originating from surface sources, the existing parameters used in earthquake engineering should be modified. The modifications aim to consider the peculiar aspects of the wave propagation for these kinds of sources. Higher frequencies are associated with smaller wavelength, since wavelength is inversely proportional to frequency. This will intuitively mean that the parameters in the higher frequencies vibration cases will be associated with shallower depths.

Unlike the seismic cases where the waves come from below the surface of earth, the soil surface response from higher frequencies surface sources is mainly dominated by Rayleigh waves/surface waves (R-waves). The dominance of surface waves in the case of vibration will eliminate the idea of using factors describing the shear wave velocity at higher depths, for instance V_{s30} and V_{s20}.The alternative will be the use of a parameter capable of describing the very top layer of a complex soil system where the R-waves will be dominant. In order to find such parameter, an approximation should be adopted that fits the best possible the wide range of soil types encountered by civil engineers. Thus this study is focalized on three soil types representing the range of soils usually encountered in shallow depths (as surface layers). The three chosen soil types are characterized by Vs = 100 m/s, 200 m/s, 400 m/s. The frequency content of pulses used to analyze the soils was chosen to cover the range 0–120 Hz in which most of the vibration from urban surface sources fall within.

The average of these frequencies which is 60 Hz and the average of the Rayleigh wave speed over the chosen range of soils are the main defining parameters. The most suitable average depth which will fulfill the description of the required dominance of Rayleigh waves at the surface is then calculated.

The Rayleigh wave velocities for the soils are calculated assuming a constant value of $v = 0.3$ and using the following Eq. (1):

$$V_R = \frac{0.862 + 1.14v}{1 + v} \times V_S \tag{1}$$

The associated wavelength using the average Rayleigh wave speed of the three soils and a 60 Hz frequency as mean frequency of the source is then calculated as follows:

$$\lambda_R = \frac{V_R}{f} \simeq 3.5\,\mathrm{m} \tag{2}$$

A wavelength of 3 m was finally adopted and the factor V_{s3} will be used in order to characterize the effective part of soil that controls the effects of the R-waves.

For the purpose of measuring the heterogeneity of the soil (the change of impedance with depth) the most pertinent factor used and previously suggested in measuring

soil properties in the seismic domain is the gradient of the shear-wave velocity profile. The effect of soil heterogeneity will be manifested through the amplification caused from reflected and refracted waves.

Measuring the heterogeneity (the change of impedance with depth) of different sites will be done using gradients for different depths. Gradients B_Z are found through a linear regression using the following equation:

$$log_{10}V_{s(Z)} = B_Z \times log_{10}(z) + A_Z \tag{3}$$

where Z is the depth of the soil section taken, A_Z is the origin ordinate of the regression and $V_{s(Z)}$ the shear wave velocity at the given depth Z. Figure 1 shows an example of a soil column with a simplified representation of the gradient physical meaning.

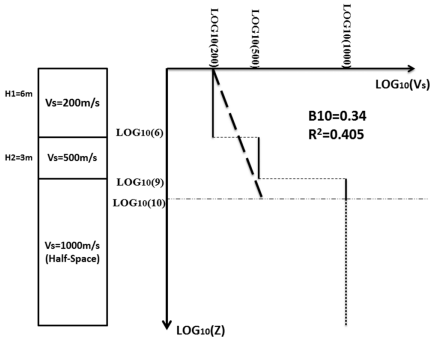

Fig. 1. A simplified representation of the definition of a gradient (B_{10} in this case)

Working with a wide range of high frequencies, and therefore a wide range of wavelengths associated with them, makes it theoretically challenging to find the most relevant depth which influences the vibration prediction at the surface. Moreover in different sites, the soil types are changing and different soils are vulnerable to different frequencies. Thus three types of gradients are suggested for the study describing different depths: B_{20}, B_{15} and B_{10}.

Gradients were chosen to describe values smaller than 30 m and the three gradients will be studied to examine which one correlates better with the numerical predictions of displacement.

3 Computation and Data Selection

For the purpose of the present study, finite elements models were executed using CESAR-LCPC software. A surface displacement was applied as the source where a pulse is injected. Absorbing layers were applied at the boundaries to avoid spurious waves reflected at the model artificial boundaries.

Varying simulations were done taking into account four factors: a varying V_{s3}, a varying depth of the top layer, a varying depth of the bedrock and a wide variation of gradient values in the range between 0 and 1 (the minimum and the maximum).

4 Results

In order to quantify the efficiency of the suggested parameters, a comparison between the multilayered cases and the homogeneous case was done. The comparison considered normalized peak displacement values as a function of distance from source. For the homogeneous cases (half-space) normalized attenuation laws were established for the three types of soils as shown in Fig. 2.

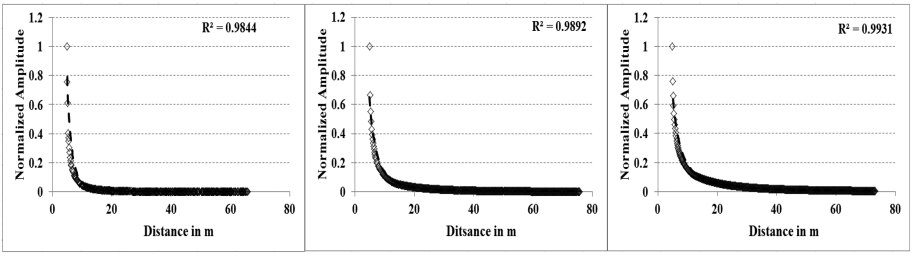

(a) (b) (c)

Fig. 2. Attenuation laws for homogeneous soils (a) Vs = 100 m/s, (b) Vs = 200 m/s, (c) Vs = 400 m/s

The attenuation equations for the homogenous cases are summarized as following:

$$Attenuation\ Level\ AL = 10.53 \times (d+5)^{-1.75} \text{ for Vs} = 400\,\text{m/s} \tag{4a}$$

$$Attenuation\ Level\ AL = 19.15 \times (d+5)^{-2.16} \text{ for Vs} = 200\,\text{m/s} \tag{4b}$$

$$Attenuation\ Level\ AL = 54.53 \times (d+5)^{-3.02} \text{ for Vs} = 100\,\text{m/s} \tag{4c}$$

where the *Attenuation Level* is the normalized level of vibration after attenuation in respect to the value at the source (smaller than 1) and d is the distance from source.

For each case of V_{s3}, the amplification factor will be calculated as shown in Eq. (5). The amplification factor describes the difference between the total maximum displacement in the multilayered case and the homogeneous case normalized with the latter.

$$Amplification\ factor\ AF = \frac{PGD(Multilayered) - PGD(Homogeneous)}{PGD(Homogeneous)} \tag{5}$$

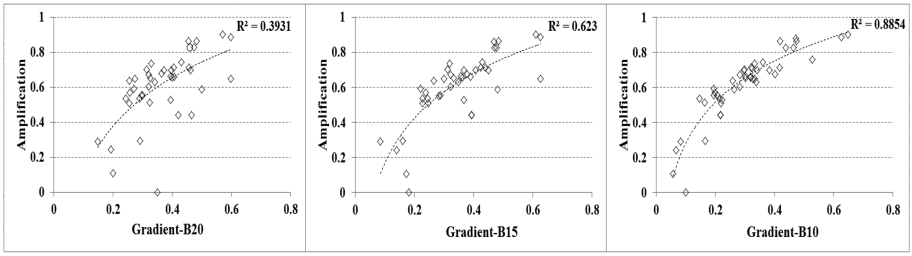

(a) *(b)* *(c)*

Fig. 3. Amplification factors for Vs = 400 m/s versus gradient (a) B_{20} (b) B_{15} (c) B_{10}.

The amplifications are then averaged for different segments of distance from the source and tested with different gradients. The correlation of the calculated values of each group plotted against the varying gradient indicates the efficiency of the chosen gradient in detecting the amplification. Figure 3 illustrates the correlation variability of peak displacement values averaged for the first 20 m next to the source for different gradients (B_{20}, B_{15} and B_{10}) for the case of V_{s3} = 400 m/s. The B_{10} case shows a very coherent distribution of amplification factor versus the ascending gradient. Similarly for the case of V_{s3} = 200 m/s and 100 m/s (Figs. 4 and 5), the best correlation is seen for the B_{10} gradient.

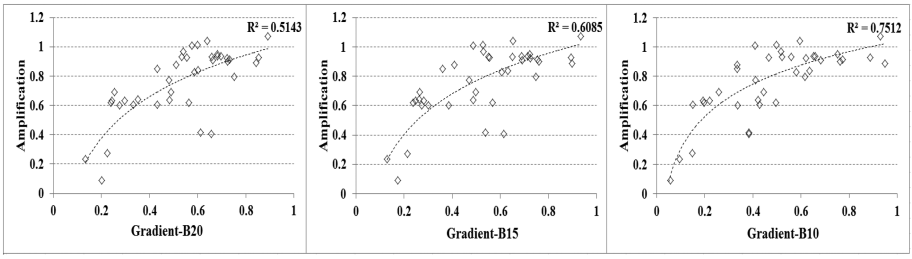

(a) *(b)* *(c)*

Fig. 4. Amplification factors for Vs = 200 m/s versus gradient (a) B_{20} (b) B_{15} (c) B_{10}.

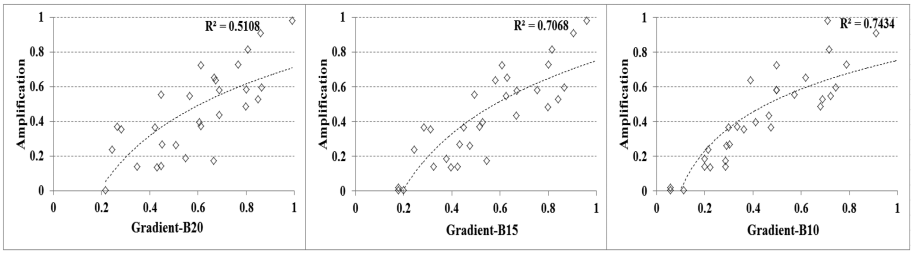

(a) *(b)* *(c)*

Fig. 5. Amplification factors for Vs = 100 m/s versus gradient (a) B_{20} (b) B_{15} (c) B_{10}.

The amplification equations are summarized as following (using B_{10} for the first 20 m from source):

$$Amplification\,factor\,AF = 0.34 \times \ln(\mathrm{B}_{10}) + 1.06 \text{ for } \mathrm{Vs} = 400\,\mathrm{m/s} \tag{6a}$$

$$Amplification\,factor\,AF = 0.314 \times \ln(\mathrm{B}_{10}) + 1.05 \text{ for } \mathrm{Vs} = 200\,\mathrm{m/s} \tag{6b}$$

$$Amplification\,factor\,AF = 0.323 \times \ln(\mathrm{B}_{10}) + 0.75 \text{ for } \mathrm{Vs} = 100\,\mathrm{m/s} \tag{6c}$$

In order to summarize, using Eqs. (4a)–(4c) and (6a)–(6c) the final prediction equation will be in the following form:

$$Final\,Vibration\,Amplitude = AL + AL \times AF \tag{7}$$

where AL and AF are respectively the attenuation level and the amplification factor as previously defined.

Changing the segment of distance from the first 20 m to the first 35 m for example, shows that the consistency continues to be present as shown in Fig. 6 but with a small reduction in the correlation fitting value. The rather quick drop of vibration amplitudes away from source as previously seen in Fig. 2 imposes the necessity of being prudent when choosing the size of window in which the values are chosen to be analyzed.

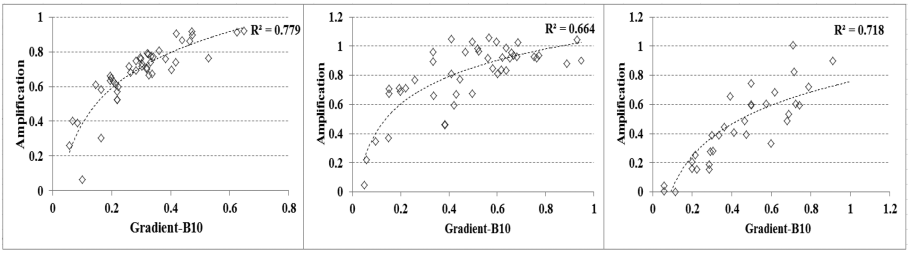

(a) (b) (c)

Fig. 6. Amplification factors averaging the first 35 m using B_{10} for (a) Vs = 400 m/s (b) Vs = 200 m/s, (c) Vs = 100 m/s.

Enlarging excessively the window of distance from source will increase the imprecision due to averaging values from a very different range of amplitudes. In other words, enlarging excessively the window will start underestimating the values near the source where the most influential amplification are present in terms of ground displacement, while clearly conserving the same pattern of amplification.

4.1 Mid and Far-Field

While the near field displacement was shown to be well correlated with the variation of the gradient, it is still of clear importance to check for mid-field (20–40 m from source)

and far-field responses (40–60 m from source). No precise correlation could be established when taking soil segment **disrupted** from the source. For the mid-field most of the amplification seems rather constant independently from the gradient. In the far-field, similarly to the mid-field, a clear correlation could not be established but it is noted that the amplifications started to move toward the lower gradients. Hence the lower gradients affect more the far field than the high gradients. An example showing the amplification in a $V_{s3} = 200$ m/s soil for 20–40 m and 40–60 m from source segments (representing mid-field and far-field) are respectively shown in the Fig. 7.

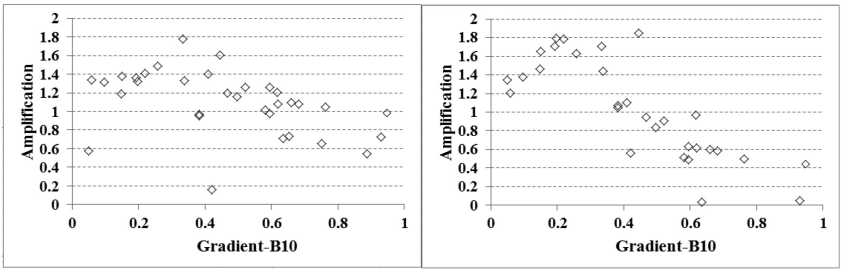

(a) (b)

Fig. 7. Amplification factors for $V_{s3} = 200$ m/s soils using B_{10} for (a) 20–40 m segment (b) 40–60 m segment

It is very important to indicate that the chosen windows to define the mid and far field response are chosen independently of the properties of the site. In other words changing the soil properties whether it is the V_{s3} or the gradient will influence the frequency response and therefore the wavelengths. Wavelengths will play a pivotal role in defining the response of soil in relation with distance. For instance, weaker soils and smaller gradients will be associated with bigger wavelengths/lower frequencies and therefore the distance segments choice does not represent the wavelength dependency.

The response of a site where $V_{s3} = 200$ m/s with two different gradients in the frequency domain are shown in Fig. 8. The comparison shows that for the case of near field (0–20 m segment), the vibration is quite dominated by the higher frequencies and the effect of higher gradients is strongly manifested as shown in Fig. 8(a). For the far field (40–60 m segment) window the peak displacement caused in the lower gradient case is higher than that of the higher gradient with a dominance of lower frequencies/ larger wavelengths as shown in Fig. 8(b).

However the aim is to get a formulation capable of predicting peak vibration levels not only for the near field, without neglecting the fact that away from source, levels of vibration become unimportant as shown in Fig. 2. Moreover that the most important amplifications are present near the source and the amplification pattern is clearly dominated by it (as clearly shown previously in the comparison between results from the first 20 and 35 m).

In order to check the validity in the far field of the equations which are derived from the first 20 m, few tests were carried out using the formulation in Eqs. (4a)–(4c),

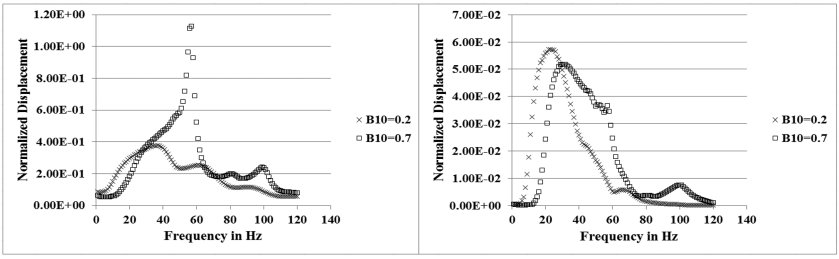

Fig. 8. Normalized displacement for V_{s3} = 200 m/s-in frequency domain for (a) 0–20 m segment (b) 40–60 m segment

(6a)–(6c) and (7). Results from equations were then compared with FEM results between 5 m and 60 m from the source.

Figure 9(a) shows the results of the standard deviation ratio between the results of FEM models and those found by the prediction equations for three different sites with different gradients where V_{s3} is equal to 400 m/s. The results from the prediction equation shows a good agreement with the FEM results since most of the predicted values are within 20% precision even at far distances (beyond 40 m). Figure 9(b) shows the same for V_{s3} = 100 m/s. The deviation shows a less coherent agreement than the V_{s3} = 400 m/s case but the deviation is still within an acceptable range for varying distances. As a consequence, the formulas are reliable also for distances larger than 20 m (i.e. mid-field and far-field).

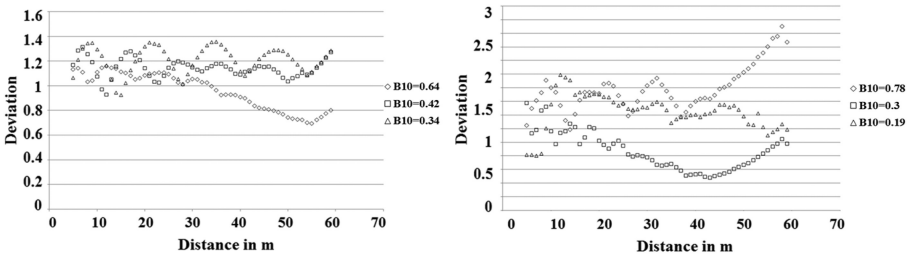

Fig. 9. Deviation ratio between FEM and prediction equations results for different sites (gradients) where (a) V_{s3} = 400 m/s (b) V_{s3} = 100 m/s

5 Conclusions

The scope of this study is to establish a set of formulation that serves as a prediction method for vibration levels in the civil engineering area. For this purpose results obtained from FEM models were analyzed in relation to the relevantly introduced parameters. The proposed parameters (V_{s3}, B_{10}) showed a very good efficacy in

describing the attenuation and the amplification for a given site. A well correlated formula was developed for the prediction of vibration near the source which also showed a good reliability far from the source. The B_{10} factor, particularly, showed to be very reliable especially that it is calculated via a linear regression that does not correlate well constantly. A further and more advanced analysis, in the frequency domain, is still needed but was beyond the scope of this paper. Such analysis will help to refine the results and establish a more efficient prediction method for vibration levels induced by surface sources.

References

1. Semblat, J.-F., Pecker, A.: Waves and Vibrations in Soils: Earthquakes, Traffic, Shocks Construction Works. IUSS Press, Pavia (2009)
2. Borcherdt, R.: Estimates of site-dependent response spectra for design (methodology and justification). Earthq. Spectra **10**(4), 617–653 (1994)
3. Eurocode 8: Design of Structures for Earthquake Resistance, Part 1: General Rules, Seismic Actions and Rules for Buildings EN 1998-1, European Committee for Standardization (CEN), Brussels (2004)
4. Luzi, L., Puglia, R., Pacor, F., Gallipoli, M.R., Bindi, D., Mucciarelli, M.: Proposal for a soil classification based on parameters alternative or complementary to VS30. Bull. Earthq. Eng. **9**, 1977–1998 (2011)
5. Cadet, H., Bard, P.-Y., Duval, A.-M., Bertrand, E.: Site effect assessment using KiK-net data: part 2—site amplification prediction equation based on f0 and VSZ. Bull. Earthq. Eng. **10**(2), 451–489 (2012)
6. Régnier, J., Bonilla, L.F., Bertrand, E., Semblat, J.F.: Influence of the VS profiles beyond 30 m depth on linear site effects: assessment from the KiK-net data. Bull. Seismol. Soc. Am. **104**(5), 2337–2348 (2014)

The Effect of Traffic Modeling on Damage Detection Procedure of Bridges

A.H. Hadjian Shahri(✉) and A.K. Ghorbani-Tanha

School of Civil Engineering, College of Engineering,
University of Tehran, Tehran, Iran
amir_hajian@ut.ac.ir

Abstract. One of the most important issues in the damage detection procedure of the real bridges is to detect damage at its early stages during the presence of heavy traffic on bridges. The identified damage extent is of high importance in bridge management. The bridge may put out of service if it becomes necessary. Herein, the effect of traffic modeling on damage detection of bridges is studied through numerical simulation. A simply supported beam has been considered; and, the traffic is modeled as a Poisson arrival process. The mass of traffic is considered as ratios of total mass of the bridge ranging from 0.05 to 0.20. The vibrations of beam have been simulated considering moving mass effect of the vehicles passing the bridge. Using only vertical accelerations responses, modal features of the structure have been extracted by the frequency domain decomposition (FDD) method. Modal strain energy method with incomplete mode shapes have been employed to identify the extent of damage for different damage and traffic scenarios. Damage(s) have been introduced to the beam elements as stiffness reduction in three single and multiple scenarios with different extents of damage ranging from 0.10 to 0.30. According to the results, it is visible that heavy traffic did not have any outstanding effect on mode shapes and the damage(s) at mid-span of the modeled beam are more likely to be indicated and quantified.

Keywords: Damage detection · Bridges · Traffic effect · Poisson arrival process · Modal strain energy · Moving mass

1 Introduction

Health monitoring of structures has been emerged in the last decades; and, it is one of the most challenging and complex fields of study in civil and mechanical engineering. Bridges are one of the most important structures which are used for transportation purposes. One of the challenges in dealing with health monitoring of these structures is the effect of traffic on the structure. Among all traffic conditions, heavy traffic has the most negative effect on the structure. Due to random and stochastic nature of the traffic, numerical simulations and real studies should be done in order to understand the effects of heavy traffic on bridges.

Traffic simulations are usually carried out according to the statistical distribution of the different parameters involved (e.g. distribution of vehicles weight, distribution of

© Springer International Publishing AG 2018
J.P. Conte et al. (eds.), *Experimental Vibration Analysis for Civil Structures*,
Lecture Notes in Civil Engineering 5, https://doi.org/10.1007/978-3-319-67443-8_77

headway, and etc.). In the previous studies, researchers used Poisson arrival process or similar arrival processes due to lack of information about statistical properties of the traffic [1, 2]. However, recent studies have investigated the traffic statistical properties by using weigh-in-motion (WIM) systems that are installed on the highway bridges and utilizing micro-simulation techniques [3, 4]. These measurements might be used for more accurate modeling of traffic in the case of real structures [5]. In the present study, it is decided to model traffic current by making use of the Poisson arrival process.

The traffic exerts loads on the structures and may change the dynamical properties of bridges. According to the quantity of vehicles which pass the bridge, traffic is roughly categorized into two main groups: Congested, and Free Flow. In the present study, only congested traffic condition is considered in numerical simulations. It has been shown that a moving vehicle on the bridge can affect the mass, damping, and stiffness matrices of the structure [6]. Moreover, it is shown that in the range of low velocities, the effect of damping, and stiffness changes are negligible in the bridge responses [7]. Vehicles in the congested traffic condition are likely to have low velocity. Hence, it is decided to model vehicles as moving masses on the bridge by considering the effect of vehicle-bridge interaction without making any change in damping and stiffness matrices.

It is important to study the feasibility of damage detection method in congested traffic condition. In the presence of damage, the bridge may put out of service. By doing so, further damage on the bridge and the occurrence of catastrophic events may be avoided.

In this paper, a simply supported beam is considered which represents a simply supported real bridge. The simulation is carried out by using a dimensionless quantity which is used in past studies [8, 9].

Considering the location of damaged element(s), three different damage scenarios are selected in this study and the extent of damage for each damage scenario varies in the range of 10% to 30%. The ratio of the total mass of vehicles that are present on the bridge to mass of the bridge is decided to vary in the range of 0.05 to 0.20. The acceleration signals are generated for each damage case and the effect of noise is considered by the superposition of Gaussian white noise of different levels to each generated signal. Then, the FDD method [10] is applied to the generated time histories and the modal properties of the simulated simply supported beam are extracted. Finally, by making use of closed-form modal strain energy based sensitivity matrix technique [11], the damage location and extent for different damage, mass, and noise scenarios are calculated.

2 Simply Supported Beam Similitude

The similitude method is applied to approximate dimensions of a real bridge to simulate the representative numerical model. Simulation is based on a dimensionless quantity presented below

$$\alpha = \frac{f.l}{v} \tag{1}$$

where α, f, l, and v represent dimensionless quantity, first natural frequency of the real structure, length of the real bridge and velocity of the passing vehicle in the real bridge, respectively.

The geometry of real bridge is assumed to be 50 m length and 20 m width. The first natural frequency of the real bridge is assumed to be around 1 Hz. The vehicles velocity is considered to be 5.55 m/s (20 km/h) in the real structure and constant for the sake of simplicity in modeling and simulation purposes. By making use of parameter α and assuming the geometrical ratio of 0.04, and the first natural frequency of 5 Hz for model, the vehicles passage velocity value in the model will be 1.25 m/s (4.5 km/h).

3 FEM Model

The governing mathematical model of the bridge in its traffic free state is modeled using FEM method. The geometrical and mechanical properties of the structure is shown in Table 1.

Table 1. Geometrical and mechanical properties of the simply supported beam

Young's modulus (GPa)	Density (kg/m^3)	Length (mm)	Width (mm)	Thickness (mm)
200.00	7850.0	2000	400	10

The numerical 2D model of simply supported beam consists of eight Euler-Bernoulli beam elements with 18 vertical and rotational DOFs which are considered for simulation purposes. In the formulation of damage detection technique [11], full mode shapes are used while in dealing with the case of real structures, only vertical mode shape values are available from experimental tests. Hence, in the numerical simulations, it is assumed that in each node only vertical mode shape values are available. Therefore, System Equivalent Reduction Expansion Process (SEREP) method proposed by O'Callahan et al. [12] is applied to numerical models in order to remove the rotational DOFs and to consider only vertical DOFs. It is useful to note that reduced form of system matrices have been used only in damage detection procedure.

4 Traffic Simulation

The traffic flow is generated by using Poisson arrival process and only considered in one lane in the congested condition. The headway of traffic is assumed to be 6 m. Therefore, with a simple calculation using geometrical ratio, headway of traffic, and the velocity of vehicles in the model, passage time of vehicles in the model will be approximately 0.2 s/vehicle; and hence, the rate of entering cars to the model will be 5 vehicle/s. The Poisson probability distribution function is defined as follows

$$f(n|\lambda) = \frac{\lambda^n}{n!} e^{-\lambda}; n = 0, 1, 2, \ldots, \infty \tag{2}$$

where λ and n represent the mean value of the entering rate of vehicles to the bridge and the randomly generated number, respectively. By considering the Poisson probability distribution function for traffic in each time interval, the number of approaching cars to the bridge are generated via random number function in MATLAB environment.

The mass of each vehicle is considered to be deterministic and its value is calculated as below

$$\text{vehicle's mass} = \beta\left(M \times \frac{hw_p}{l_p}\right) = \beta\left((7850 \times 2.0 \times 0.4 \times 0.01) \times \frac{6}{50}\right) \approx 7.5\beta$$

where β represents the ratio of total mass of vehicles which are present on the bridge to the structural mass of the bridge. Moreover, M, hw_p, and l_p stand for structural mass of the model, headway, and length of the bridge in the prototype, respectively. The values of β vary in the range of 5.0% to 20.0%. The value of 5.0% corresponds to concrete bridges and 20% corresponds to light structures which are built using steel deck.

5 Moving Mass Problem

According to the literature, VBI effect can be applied to the bridge FEM model by making use of simple assumptions like no-jump condition and a versatile element [6]. It is useful to note that in the range of low velocities, the dynamic amplification factor value is near to 1. This indicates that the vehicle influences the beam statically and only added mass influences the system matrices. The moving mass effect is considered via versatile finite element model to consider VBI effects [6]. The system matrices are updated in each time step according to the location of each car that is present on the bridge. The responses of the system are calculated by the Newmark-Betta numerical method. The acceleration responses of the vertical DOFs in the simply supported beam are stored in order to apply FDD method to them and extract modal properties of the structure.

6 Damage Detection Method

Initial simulations show that traffic can affect the natural frequencies with a significant value and the mode shapes are less affected by the moving mass effect of vehicles. Therefore, it is decided to use a method which utilizes only mode shapes for damage detection purposes. Mode shape curvature and modal strain energy based methods are two kinds of methods that only utilize mode shapes of the structure in the damage identification process. Herein, it is assumed that nearly accurate model exists for the structure which represents real dynamic behavior of the modeled bridge. Therefore, it will be more accurate to use modal strain energy (MSE) method. Sensitivity matrix of the MSE method is obtained according to the paper published by Yan et al. [11] and their

proposed method is utilized in this study. The only difference here is that first two modes of vibration is used here for better numerical stability in solving damage equations.

7 Damage and Noise Scenarios

The effect of traffic on three different damage scenarios is investigated through this study. Three different damage scenarios related to the location of damage are presented in Table 2. The extent of damage in these scenarios is decided to be in the range of 10% to 30%.

Table 2. Damage scenarios based on location and extent of damage

Damage scenarios		Damaged element(s)	Damage extent		
DS1	Single damage	No. 1	10%	20%	30%
DS2	Double damage	No. 1	10%	20%	30%
		No. 3	10%	20%	30%
DS3	Triple damage	No. 2	10%	20%	30%
		No. 4	10%	20%	30%
		No. 5	10%	20%	30%

Due to random nature of noise and its adverse effect on the extracted modal features, Gaussian white noise with different signal-to-noise ratios are superposed to the records. For each noise scenario, 100 simulations have been carried out in MATLAB environment using the obtained accurate vertical acceleration signals including moving mass effect. Different noise scenarios are presented in Table 3. It is useful to note that these Gaussian white noises are imposed on the obtained signals via AWGN function in MATLAB environment with measured signal power and specified noise power according to Table 3.

Table 3. Noise scenarios to investigate noise effect

Noise scenarios	Noise RMS to signal ratio (NRSR)	Signal to noise ratio (dB)
NS1	1.0%	40
NS2	3.0%	30
NS3	5.0%	26

Statistical assessment of these data is carried out by the coefficient of variance (COV) as it is used in past studies [11]. This parameter is a powerful unit-less measure in dealing with uncertainty quantification involved within the problem. COV is defined as below

$$\mathrm{COV} = \frac{\bar{\sigma}}{\bar{m}} \tag{3}$$

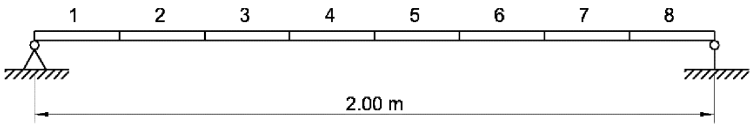

Fig. 1. Discretization of the simply supported beam

where $\bar{\sigma}$ and $\bar{m}$ are the standard deviation and the mean value of the damage indices in 100 simulations, respectively (Fig. 1).

8 Results and Discussions

Damage detection procedure is carried out and the results of different damage scenarios are presented here. For the sake of brevity, results of the mean damage indices are provided here only for 10% damage extent scenarios. However, the COV results are reported for all considered damage scenarios. Figures 2, 3 and 4 demonstrate the mean damage indices in different damage scenarios under the influence of different noise scenarios.

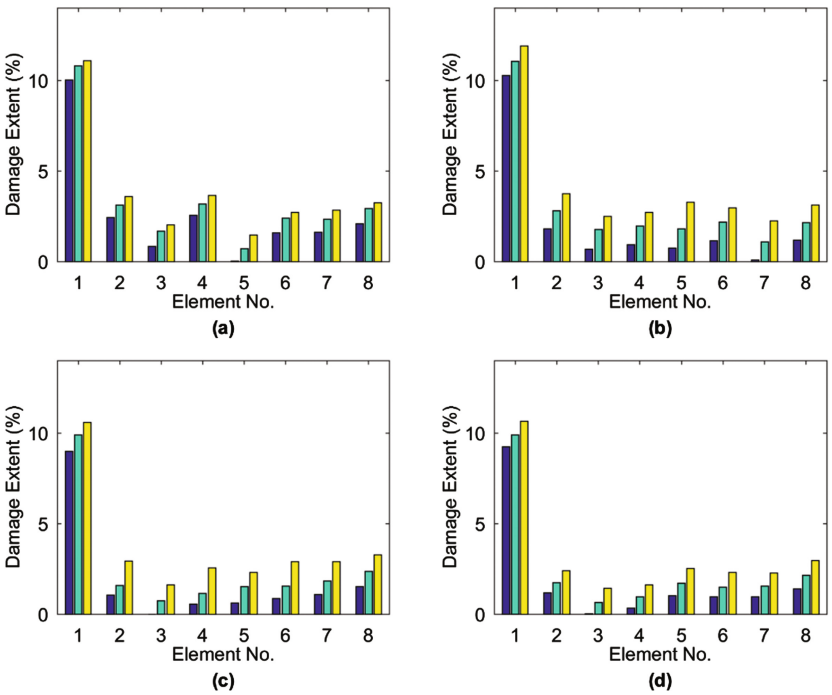

Fig. 2. Mean damage indices in DS1 for values of (a) $\beta = 0.05$, (b) $\beta = 0.10$, (c), $\beta = 0.15$, and (d) $\beta = 0.20$.

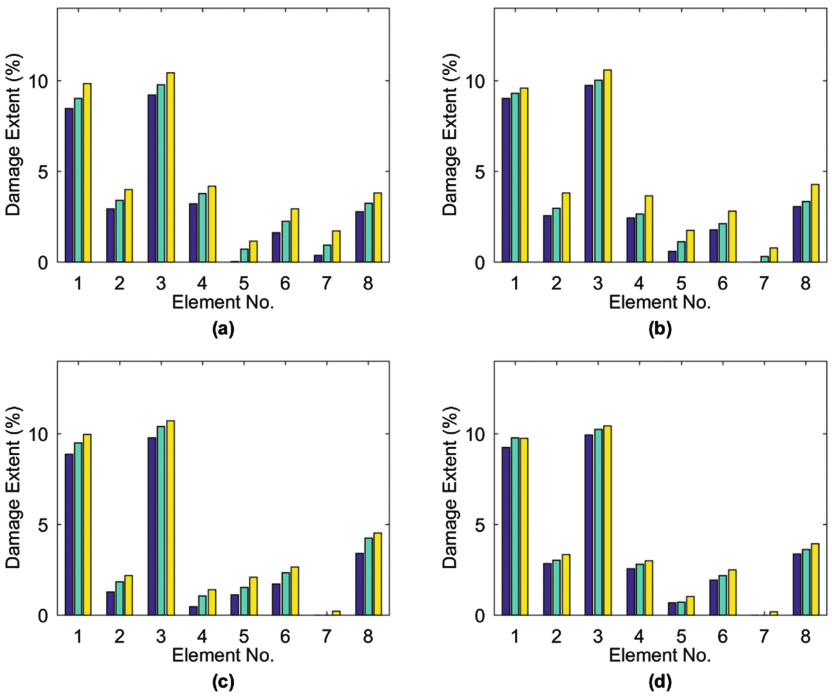

Fig. 3. Mean damage indices in DS2 for values of (a) $\beta = 0.05$, (b) $\beta = 0.10$, (c), $\beta = 0.15$, and (d) $\beta = 0.20$.

It is important to note that in the Figs. 2, 3 and 4 the color of the bars indicate the level of imposed noise on the acquired signal. The colors blue, green, and yellow indicate the 1.0%, 3.0%, and 5.0% NRSR, respectively.

In the presented results, it is obvious that with an increase in noise percentage (NRSR) the results tend to deviate from real values. Moreover, the results are with acceptable accuracy in all damage scenarios. However, false alarms are shown in the first and third element in DS3, and eighth element in DS2. These are due to the fact that mode shape based methods usually do not yield favorable results near supports of the structure. It is important to note that in practice and experiments damage indices less than 5% are neglected and they are considered as computational or noise terrors.

One of the other parameters that is considered in this study is β which is defined before. By looking at the Mean damage indices, it becomes evident that the parameter β does not have any outstanding influence on the results of damage detection procedure. However, it seems that with an increase in the value of β, the false alarms tend to be alleviated slightly.

The second group of results is COV values for damaged elements. These are shown in Figs. 5, 6 and 7 and it is worth noting that colors blue, red and green refers to 10%,

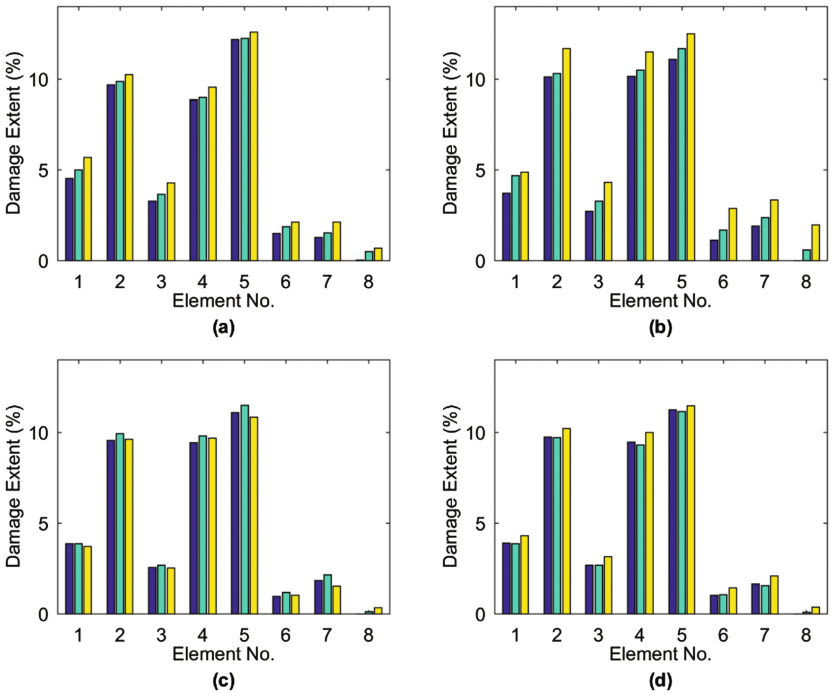

Fig. 4. Mean damage indices in DS3 for values of (a) $\beta = 0.05$, (b) $\beta = 0.10$, (c), $\beta = 0.15$, and (d) $\beta = 0.20$.

20%, and 30% damage extent in the damaged element(s). Moreover, solid, dotted, and dashed lines represent the first, second and third damaged element in different damage scenarios.

Figures 5, 6 and 7 reveal the fact that COVs are mainly dependent on two factors; first, the damage extent of the damaged element; and, second, the location of the damaged element. A quick glance at Fig. 5 shows that with an increase in damage extent the uncertainty of damage value in the first element reduces notably. Moreover, it is obvious in Figs. 6 and 7 that most of the green lines which correspond to 30% damage extent are lower than the others. Therefore, it is true to say that as damage increases in an element, uncertainty of damage quantification reduces.

The other factor in damage quantification uncertainty is the location of damaged element as mentioned before. To study this factor, damage extents are decided to be equal for different elements in different damage scenarios. In Fig. 6 the COV of the third element (dotted line) is significantly lower than the first element; and, this results, because MSE based sensitivity matrix depends mostly on the first mode of vibration in beam-like structures [11]. Considering the first mode of vibration for the simply supported beam, it is obvious that the first element displacements are much lower than that

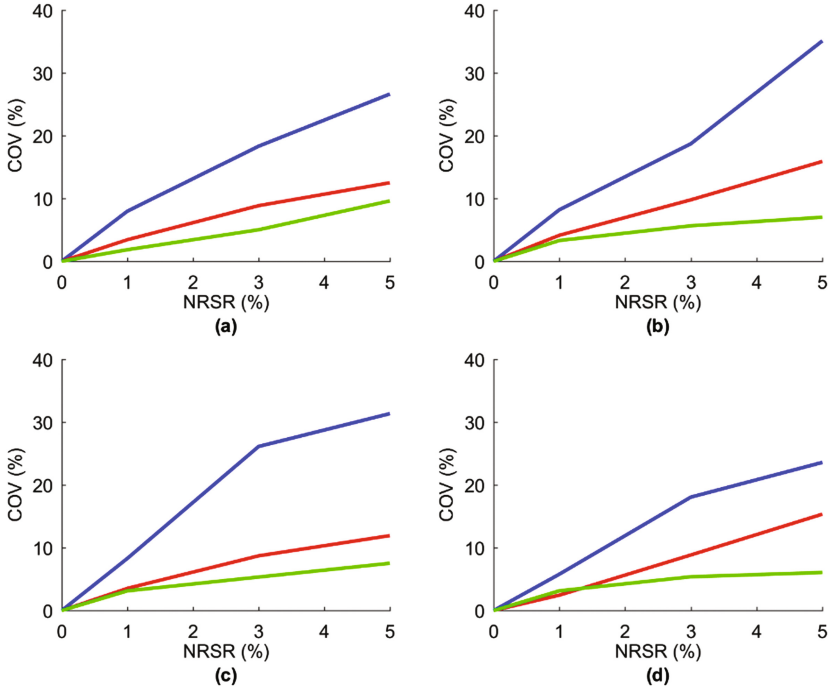

Fig. 5. COVs' in DS1 for values of (a) $\beta = 0.05$, (b) $\beta = 0.10$, (c), $\beta = 0.15$, and (d) $\beta = 0.20$.

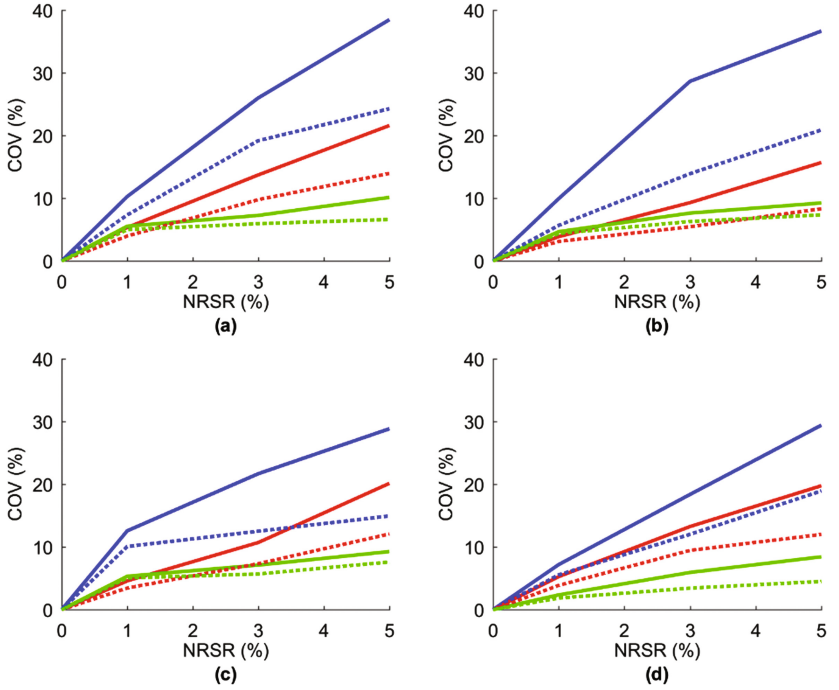

Fig. 6. COVs' in DS2 for values of (a) $\beta = 0.05$, (b) $\beta = 0.10$, (c), $\beta = 0.15$, and (d) $\beta = 0.20$.

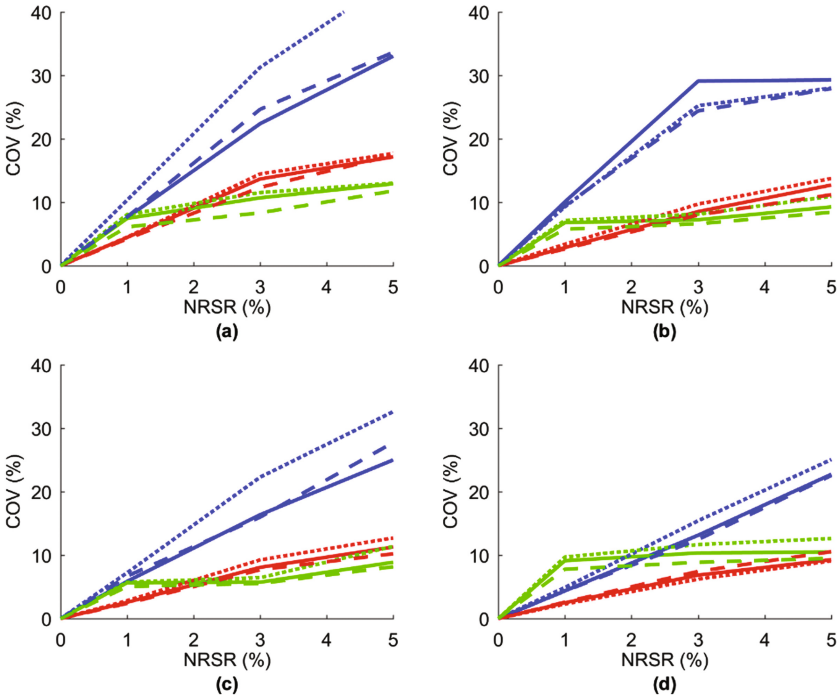

Fig. 7. COVs' in DS3 for values of (a) $\beta = 0.05$, (b) $\beta = 0.10$, (c), $\beta = 0.15$, and (d) $\beta = 0.20$.

of the third element. Therefore, its contribution to the MSE sensitivity matrix is much smaller than the third element and this fact explains the reason behind lower uncertainty in the damage quantification of third element.

Feasibility and reliability of this method in different traffic conditions is related to the COV values. It seems that for 2% Gaussian white noise imposed on the signal, damage(s) of extent 10% can be located and quantified with 90% confidence interval with maximum deviation of 40% from the mean value. Furthermore, the results show that in the severe noise conditions (5% NRSR), the damage(s) with the extent of 30% can be quantified with the 90% confidence interval and maximum deviation of 20% from mean in all investigated damage scenarios.

The effect of traffic mass (parameter β) on the uncertainty involved in the damage values has shown that with an increase in parameter β, COV values are slightly reduced. Therefore, it is more likely to indicate and quantify damage in lightweight bridges in comparison to concrete bridges. This is an outstanding result of this study and justifies the need to be studied in more accurate and realistic simulations of traffic flow and also more complicated bridges.

9 Conclusion

In this study the effect of traffic on damage detection of beam-like structures is investigated. The traffic is modeled as a Poisson arrival process and different mass ratios are considered. Results show that in the presence of traffic, damage(s) that are located far from nodal points in the first mode of vibration are more likely to be identified and quantified. Moreover, as the extent of damage increases, the uncertainty involved in the damage quantification process reduces notably. This justifies the need to develop methods that can quantify damage in all elements of the bridge with equal or near to equal uncertainty.

It has been shown that traffic mass does not have any outstanding effect on mode shapes; but, as the mass ratio of traffic (β) increases, the uncertainty involved in the damage detection procedure tends to reduce in all investigated damage scenarios. This is a surprising effect and justifies the need to carry out more complex simulations considering real traffic conditions through micro-simulation methods and to consider more complicated bridge structures.

References

1. Chen, Y., Tan, C.A., Feng, M.Q.: Physics-based traffic excitation models for highway bridges. In: Smart Structures and Materials. International Society for Optics and Photonics, pp. 377–388, July 2004
2. Chen, Y., Feng, M.Q., Tan, C.A.: Bridge structural condition assessment based on vibration and traffic monitoring. J. Eng. Mech. **135**(8), 747–758 (2009)
3. Mei, G., Qin, Q., Lin, D.J.: Bimodal renewal processes models of highway vehicle loads. Reliab. Eng. Syst. Saf. **83**(3), 333–339 (2004)
4. Lipari, A., O'Brien, E.J., Capriani, C.C.: A comparative study of a bridge traffic load effect using micro-simulation and Eurocode load models. In: Bridge Maintenance, Safety, Management, Resilience and Sustainability, Stresa, Italy, pp. 3420–3427. CRC Press, 8–12 July 2012
5. Enright, B., O'Brien, E.J.: Monte Carlo simulation of extreme traffic loading on short and medium span bridges. Struct. Infrastruct. Eng. **9**(12), 1267–1282 (2013)
6. Yang, Y.B., Wu, Y.S.: A versatile element for analyzing vehicle–bridge interaction response. Eng. Struct. **23**(5), 452–469 (2001)
7. Humar, J.L., Kashif, A.M.: Dynamic response of bridges under travelling loads. Can. J. Civ. Eng. **20**(2), 287–298 (1993)
8. Lee, J.W., Kim, J.D., Yun, C.B., Yi, J.H., Shim, J.M.: Health-monitoring method for bridges under ordinary traffic loadings. J. Sound Vib. **257**(2), 247–264 (2002)
9. Kwon, S.D., Kim, C.Y., Chang, S.P.: Change of modal parameters of bridge due to vehicle pass. In: Proceedings of 23rd International Modal Analysis Conference on Structural Dynamics, Society for Experimental Mechanics, Orlando, FL, 31 January–3 February 2005
10. Brincker, R., Zhang, L., Andersen, P.: Modal identification of output-only systems using frequency domain decomposition. Smart Mater. Struct. **10**(3), 441 (2001)
11. Yan, W.-J., Huang, T.-L., Ren, W.-X.: Technical papers: damage detection method based on element modal strain energy sensitivity. Adv. Struct. Eng. **13**(6), 1075–1088 (2010)
12. O'Callahan, J., Avitabile, P., Riemer, R.: System equivalent reduction expansion process (SEREP). In: Proceedings of the Seventh International Modal Analysis Conference, February 1989

Soil-Foundation Compliance Evidence of the "Chiaravalle Viaduct"

Marco Regni[1(✉)], Fabrizio Gara[1], Francesca Dezi[2], Davide Roia[1], and Sandro Carbonari[1]

[1] Department of Civil and Building Engineering and Architecture, Università Politecnica delle Marche, Ancona, Italy
m.regni@pm.univpm.it
[2] Department of Economics and Technology, University of San Marino, San Marino, Italy

Abstract. This paper focuses on the contribution of the soil-foundation compliance on the measured dynamic response of the Chiaravalle viaduct subjected to ambient excitations. The viaduct, linking the SS76 with the airport of Ancona (in Central Italy), is 875 m long and is constituted by four kinematic chains separated by expansion joints. The r.c. deck is formed by three V-shaped beams supported by column bent piers characterized by circular cross-sections. The piers foundation is constituted by a group of six concrete piles. Ambient vibration measurements have been performed to evaluate the actual natural frequencies and mode shapes of the bridge and data have been used to calibrate a numerical model that was adopted to design the bridge seismic retrofit. Experimental modal properties are evaluated by means of the Operational Modal Analysis; due to the great length of the viaduct, different configurations of sensors placed on the deck are used to study the overall behavior of the viaduct and the Pre Global Estimation Re-scaling method is adopted to merge mode shapes obtained from each configuration. Furthermore, with reference to the transverse behavior, some tests are performed in correspondence of one pier, measuring accelerations of the foundation cap (both translational and rotational components) and the pier bent, in order to identify contribution to the transverse modal displacement due to the elastic deflection of the pier and the foundation rocking. Test results are compared with those obtained from a 3D Finite Element model of the viaduct, including or not the Soil-Structure Interaction problem. The numerical model on compliant restraints is able to capture the foundation rocking, experimentally detected, and provides modal parameters in good agreement with experimental ones.

Keywords: r.c. viaduct · Soil-structure interaction · Dynamic identification · Operational modal analysis · Finite element model

1 Introduction

Dynamic identification tests are nowadays a recognized tool to develop reliable finite element models of existing structures [1–4] that can be used to assess the seismic vulnerability and/or to design retrofitting works. In addition, the structural monitoring

© Springer International Publishing AG 2018
J.P. Conte et al. (eds.), *Experimental Vibration Analysis for Civil Structures*,
Lecture Notes in Civil Engineering 5, https://doi.org/10.1007/978-3-319-67443-8_78

during repairing or retrofitting works (i.e. identification tests performed at different stages of the works) is often considered an efficient strategy to assess the effectiveness of interventions. Modal parameters, evaluated from the monitoring activities, are usually compared with those obtained from finite element models of the structure, which progressively account for the works progress. In the case of bridges, above considerations are of particular validity since the structural dynamic behaviour is very little influenced by non-structural components so that any change in the bridge dynamics is essentially due to variations of mass and stiffness of structural elements.

This work focuses on the dynamic identification of the Chiaravalle viaduct, performed through ambient vibration measurements. The viaduct is located in Central Italy and links the SS76 to the Raffaello Sanzio airport in Falconara. The experimentally estimated modal properties of the viaduct have been used to calibrate a Finite Element (FE) model of the structure that was crucial for the design of the seismic retrofit of the bridge. In particular, the paper deals with some interesting aspects concerning the contribution of the foundation compliance on the dynamic measured response of the structure subjected to ambient vibrations. Some aspects of the performed ambient vibration tests are discussed, focusing on the measurement approach, which required acquisitions of data from more than one configuration of the sensors. The Enhanced Frequency Domain Decomposition (EFDD) approach and Pre Global Estimation Re-scaling (PreGER) technique are adopted to get the Operational Modal Analysis (OMA). Modal parameters obtained from the OMA are finally compared with those obtained from refined 3D finite element models of the bridge. In particular, both a conventional finite element model of the viaduct, based on the fixed base assumption, and a more accurate finite element model on compliant restraints (i.e. including the SSI problem), are developed.

2 Viaduct Description

The "Chiaravalle Viaduct" in Central Italy connects the SS76 road to the "Raffaello Sanzio" airport (Fig. 1a). The viaduct has a total length of 875 m and is constituted by four Kinematic Chains (KC#), as reported in Fig. 1b, separated by structural joints (Fig. 2a). Kinematic chains from 1 to 4 are constituted by 13, 10, 3 and 5 spans, respectively, having length of 27.5 m (Fig. 2b).

The deck is 12.10 m wide and is constituted by three simply supported V-shaped r. c. beams underlying a 0.6 m thick concrete slab. The viaduct is characterized by 7.6 m high column bent piers constituted by two circular columns with diameter of 1.4 m. It is worth mentioning that only one pier of the whole viaduct (the 5th of KC2 from the left in Fig. 1b) is different, characterized by a single column with a rounded rectangular cross section.

The foundation of each pier is constituted by six r.c. piles, having length of 30 m and diameter of 1 m. Piles are connected at the head by a rigid cap of dimensions 5 m $\times$ 9 m $\times$ 1.70 m.

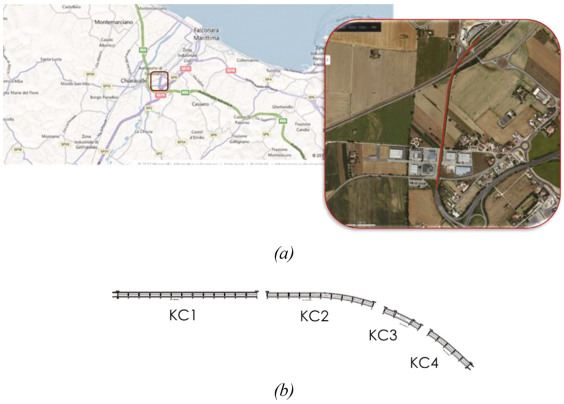

Fig. 1. Plan view of the viaduct: (a) geographical position; (b) schematic layout of kinematic chains.

Fig. 2. (a) Structural joint between kinematic chains; (b) view of the deck intrados and of the column bent pier.

3 Overall Performed Ambient Vibration Tests

Ambient vibration tests are performed with two main objectives: (*i*) to estimate the overall transverse, torsional and vertical vibration modes and frequencies of the whole viaduct and (*ii*) to capture possible Soil-Structure Interaction (SSI) effects on the bridge response.

All acquisitions are obtained with low noise piezoelectric accelerometers connected to a 24-bit data acquisition system through coaxial cables; the acquisition system is finally connected to a portable PC for storage of data (Fig. 3).

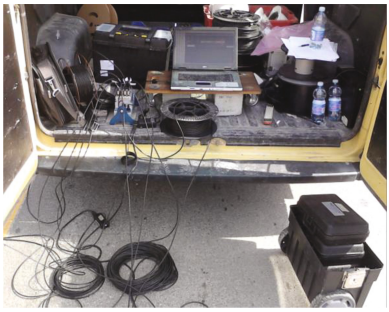

Fig. 3. Equipment.

3.1 Tests for the Evaluation of the Overall Transverse, Torsional and Vertical Vibration Modes

Due to the limited availability of sensors, different configurations are adopted to measure vibrations of most of the KCs. As well known, in these cases, experimental tests have to be replicated in different times, moving the available sensors to get different configurations and cover the entire length of the structure. The merging operation of data recorded from the different configurations is guaranteed by the presence of reference sensors (i.e. sensors common to all acquisitions) that allow to scale data acquired from the roving sensors (i.e. from sensors that change their position). As an example, Fig. 4 shows, the position of reference and roving sensors for the different configurations adopted to measure the ambient vibrations of the KC1. In particular, configuration 1 and 2 are adopted to catch the transverse dynamic response of the KC (involving the in-plane flexural behavior of the deck) and foresees unidirectional accelerometers located at each deck supports and oriented in the transverse direction of the bridge (Fig. 4a); configurations 3, 4, 5 and 6 are adopted to capture the out-of-plane flexural behavior as well as the torsional behavior of the deck and thus foresees sensors located at each mid-span at both side of the deck and oriented in the upward direction (Fig. 4b). 500 s long records sampled at a rate of 2048 Hz are acquired; the registration length assures a satisfactory frequency resolution and allows for a precise estimation of the modal parameters [5].

In this paper, asynchronous data acquired from the different sensors configurations are analyzed through the PreGER approach, which allows for an overall estimation of the modal parameters since asynchronous data are correlated and scaled starting from reference sensors [6, 7].

Before executing the modal analyses every recorded data are elaborated with standard signal processing techniques; data are firstly carefully controlled in order to cut all parts characterized by anomalous behaviors (signal clipping, intermittent noise, spikes and so on) due to measurement errors or due to signal saturation. Subsequently, experimental data are corrected, to eliminate the contribution of spurious trends, and filtered, to eliminate contribution of higher frequencies. In details, a Butterworth low pass filter of order 4 and cut-off frequency of 20 Hz is used. Finally, signals are

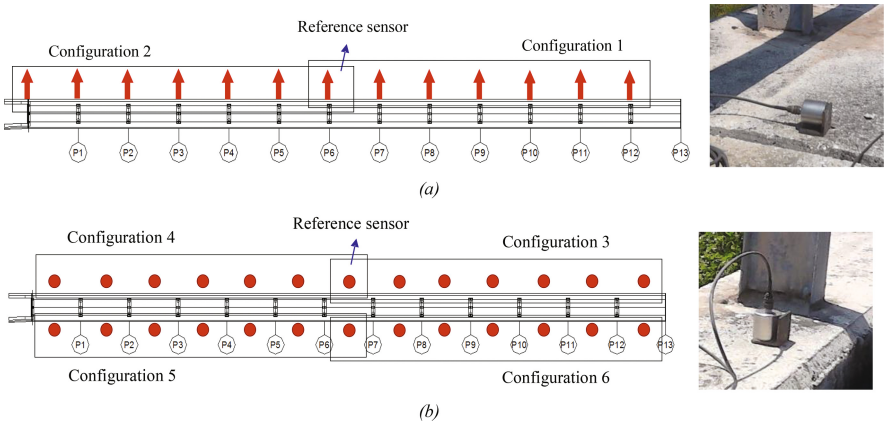

Fig. 4. Sensors configurations for the evaluation of: (a) the transverse behavior and (b) the vertical behavior of the deck

down-sampled at 51.2 Hz in order to reduce the amount of data, making numerical analyses faster.

The EFDD method [9, 10], implemented by the authors in a Matlab routine [8], is adopted to get the experimental modal parameters (natural frequencies, damping ratios and modal shapes). The method consists on a simple processing of spectral acceleration matrices: the peak picking technique is used to select modes from the Singular Value Decomposition (SVD) of the spectral density matrices and, for each mode, a frequency band in a neighborhood of the peak is selected through the evaluation of the Modal Assurance Criterion (MAC). Parts of spectral matrices with a MAC lower than 0.9 are set to zero. Through the Inverse Discrete Fourier Transform an approximation of the correlation function of the SDOF system is achieved for each selected peak. Crossing time and logarithmic decrement are used to estimate natural frequency and damping ratio, respectively, while the singular vector, for each peak, represents an approximation of the mode shape.

3.2 Tests for the Evaluation of the Soil-Foundation Compliance Effects

In addition to tests carried out for the overall identification of the structure, experimental investigations are performed to evaluate possible contributions of the soil-foundation compliance on the dynamic response of the bridge. For this purpose, pier 3 of the KC1 is selected (Fig. 1b), and some tests are performed with the aim of identifying the foundation translation and rocking. In particular, the instrumentation layout reported in Fig. 5 is considered to capture translational and rotational accelerations of the foundation cap and the pier bent. In details, accelerometer 1 catches the transverse displacement of the foundation cap while accelerometers 2 and 3 are positioned to capture the rocking of the cap. Furthermore, accelerometers 4, 5 and 6 are necessary to evaluate displacements due to the pier deflection.

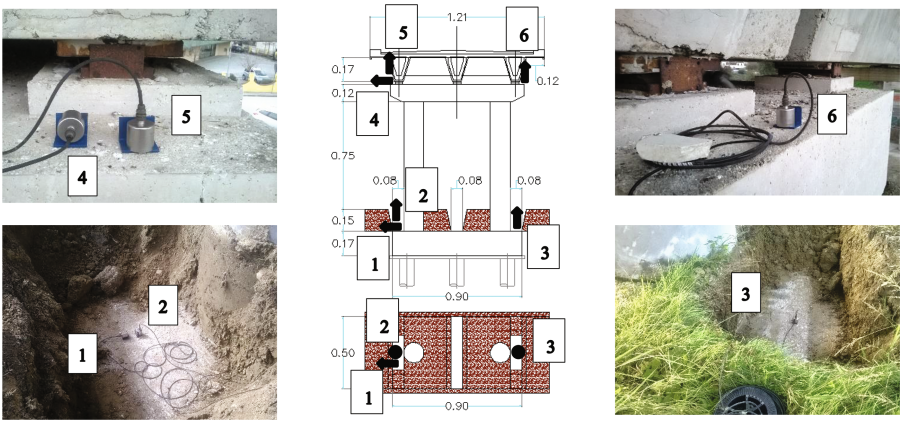

Fig. 5. Accelerometers layout at pier 3 (with photos of sensors positions).

4 Results of Experimental Tests

In this section, some results of experimental tests performed to evaluate the overall dynamic behavior of the viaduct are reported. Figure 6b shows the plan view of the first six transverse mode shapes relevant to KC1, to which the pier suitably instrumented to evaluate effects of soil-foundation compliance belongs. Table in Fig. 6a collects the modal frequencies relevant to the plotted model shapes.

Concerning results of tests performed on pier 3, aimed at evaluating the contributions SSI on modal displacements, Table 1 reports the experimental fundamental frequencies and modal displacements identified by means of EFDD method. These frequencies correspond to those of the 4th, 5th and 6th transverse modes of the deck, respectively (Fig. 6a). It is worth noting that lower transverse modes, characterized by very small displacements in correspondence of pier 3, cannot be captured with the adopted instrumentation; on the other hand, for logistic reasons, it was not possible to perform tests on a different pier. Modal displacements reported in Table 1 are normalized with respect to the maximum displacement, always occurring at the pier top (sensor 4). The overall displacement at the pier head is due to both the rigid motion of the foundation (Fig. 7a) and the elastic deflection of the structural members constituting the pier (Fig. 7b); in particular, the 6% of the total displacement is due to the foundation translation, the 13% is produced by the foundation rocking while the remaining 81% of the displacement is due to the pier deflection. Finally, it can be observed that normalized modal displacements are the same for all the identified frequencies, i.e. frequencies are not associated to superior modes of the pier.

Mode	OMA (EFDD)
	f[Hz]
1	1,61
2	1,81
3	2,05
4	2,21
5	2,45
6	2,72

(a)

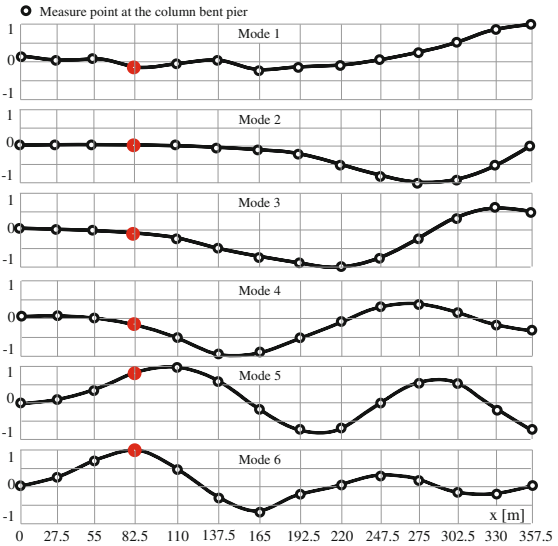

(b)

Fig. 6. (a) Frequencies of KC1 from experimental tests and (b) identified transverse mode shapes.

Table 1. Experimental frequencies and normalized modal displacements identified from tests on pier 3.

OMA (EFDD)	Modal displacements					
f [Hz]	1	2	3	4	5	6
2.23	−0.05	0.05	−0.05	−1.00	0.18	−0.19
2.48	0.06	−0.05	0.05	1.00	−0.18	0.18
2.75	−0.05	0.06	−0.04	−1.00	0.19	−0.18

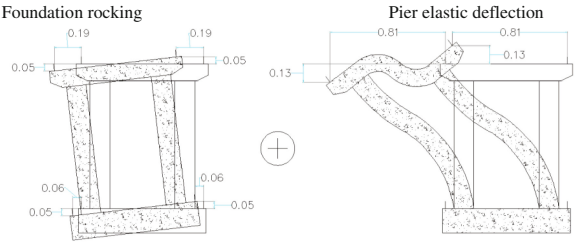

(a) (b)

Fig. 7. Contributions to the modal displacements: (a) foundation rigid translation and rocking and (b) pier deflection.

5 Finite Element Model of the Viaduct

Results of operational modal analysis are compared, in terms of fundamental frequencies and mode shapes, with those obtained from 3D refined numerical models of the viaduct, developed within the SAP2000 code [11]. Both the deck and piers are schematized with 2-node elastic frame elements and mechanical properties of materials estimated from results of experimental tests are implemented.

The model was calibrated to reproduce experimental results by slightly changing material properties (considering the elastic dynamic modulus of materials) and by implementing interactions between KCs. The latter are simulated through the use of suitably calibrated elastic springs at the level of the expansion joints.

A conventional fixed base model (Fig. 8a) as well as a more refined model incorporating the SSI problem (Fig. 8b) are developed. The soil-foundation compliance is taken into account in the latter model by introducing piles, modeled as elastic beam elements on a Winkler type soil medium, connected at the head by thick shell elements that simulate the piles cap. Stiffness constants of the Winkler's springs are obtained from indications available in the technical literature [12] taking into account the local stratigraphic conditions. The soil-pile cap interaction is included through springs located in the cap centroid, evaluated according to expressions available in the literature [13].

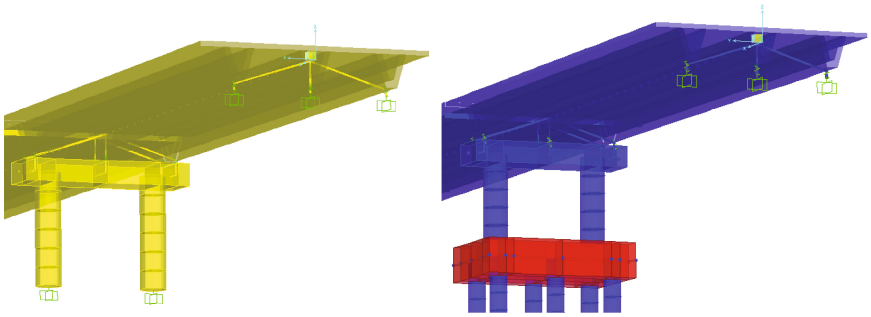

Fig. 8. FE models: (a) model with pier fixed at the base, (b) model including SSI.

With only reference to KC1, table in Fig. 9a reports the first six transverse experimental and analytical fundamental frequencies while Fig. 9b compares the relevant analytical and experimental mode shapes. The compliant base model is able to capture the measured dynamic behavior with a high accuracy.

Table 2 collects modal displacements, obtained from both the numerical models in correspondence of sensors 1 to 6 at pier 3 of KC1; displacements are normalized with respect to the maximum value attained at the pier head. For the model disregarding SSI effects, displacements in correspondence of sensors 1, 2 and 3 are set to 0. It can be observed that the local behavior of the pier 3, obtained from the numerical model

Mode	Model without SSI	Model with SSI	OMA (EFDD)	Mode shape
	f[Hz]	f[Hz]	f[Hz]	
1	1,91	1,68	1,61	1st transverse
2	2,11	1,87	1,81	2nd transverse
3	2,37	2,05	2,05	3rd transverse
4	3,03	2,46	2,21	4th transverse
5	3,35	2,66	2,45	5th transverse
6	3,76	2,91	2,72	6th transverse

(a)

(b)

Fig. 9. Comparison between the experimental and analytical results: (a) transverse frequencies and (b) transverse mode shapes.

incorporating SSI, is practically coincident with the registered one, as demonstrated by the normalized modal displacements evaluated at the sensors positions, which are nearly equal to those obtained experimentally. The almost perfect agreement of numerical and experimental data demonstrates the reliability of the developed model (used for the bridge retrofit design) as well as the significance of the SSI phenomena on the bridge dynamics, even for input actions of very low intensities.

Table 2. Experimental frequencies and normalized modal displacements from the analysis of numerical results at pier 3.

Model with SSI	Modal displacements					
f [Hz]	1	2	3	4	5	6
2.46	0.06	−0.10	0.10	1.00	−0.18	0.18
2.66	0.06	−0.10	0.10	1.00	−0.18	0.18
2.91	−0.06	0.10	−0.10	−1.00	0.18	−0.18
Model without SSI	Modal displacements					
f [Hz]	1	2	3	4	5	6
3.03	0.00	0.00	0.00	1.00	−0.12	0.12
3.35	0.00	0.00	0.00	−1.00	0.12	−0.12
3.76	0.00	0.00	0.00	−1.00	0.12	−0.12

6 Conclusions

Some notable aspects concerning the contribution of Soil-Structure Interaction (SSI) on the measured dynamic response of the Chiaravalle viaduct subjected to ambient excitations have been shown in this paper. Ambient vibration tests are performed on the viaduct in order to evaluate the actual modal properties of the structure to be used for the calibration of a reliable numerical model for the retrofit design of the bridge. Besides conventional tests aimed at evaluating the overall transverse, torsional and vertical vibration modes of the deck, un-conventional identification tests have been performed on a selected bridge pier in order to assess the contribution of SSI on the modal displacements. It was found that SSI sensibly affects the dynamics of the bridge, even for low intensity actions, contributing to the 18% of the overall modal displacement of the deck.

Results of tests, in terms of fundamental frequencies and mode shapes, have been compared with those resulting from a 3D refined finite element model of the bridge. In order to accurately capture the measured response a numerical model incorporating SSI phenomena was necessary; the model, suitably calibrated was able to accurately predict the dynamic behavior of the bridge subjected to ambient vibrations.

References

1. Butt, F., Omenzetter, P.: Seismic response trends evaluation and finite element model calibration of an instrumented RC building considering soil–structure interaction and non-structural components. Eng. Struct. **65**, 111–123 (2004)
2. Roia, D., Gara, F., Speranza, E., Gioiella, L., Dezi, L.: Operational modal analysis on a R.C. building for the evaluation of the dynamic changes due to retrofitting. In: Proceedings of Environmental, Energy and Structural Monitoring System, Trento, Italy (2015)
3. Brownjohn, J., Xia, P.: Dynamic assessment of curved cable-stayed bridge by model updating. J. Struct. Eng. **126**, 252–260 (2000)
4. Dezi, L., Gara, F., Roia, D., Leoni, G.: Experimental and numerical modal analysis of a historical masonry bridge. In: 16th International Brick and Block Masonry Conference, Padova, Italy (in press, 2016)
5. Cantieni, R.: Experimental methods used in system identification of civil engineering structures. In: Proceedings of the 1st International Operational Modal Analysis Conference, Copenhagen, Denmark, pp. 249–260 (2005)
6. Parloo, E.: Application of frequency-domain system identification techniques in the field of operational modal analysis. Ph.D. Thesis, Vrije Universiteit Brussel, Belgium (2003)
7. Parloo, E., Guillaume, P., Cauberghe, B.: Maximum likelihood identification of non-stationary operational data. J. Sound Vib. **268**, 971–991 (2003)
8. MathWorks: MATLAB, version 7.9 (R2009b). The MathWorks, Inc., Natick (2009)
9. Brincker, R., Ventura, C.E., Andersen, P.: Damping estimation by frequency domain decomposition. In: Proceedings of 19th International Modal Analysis Conference, Kissimmee, FL, USA, pp. 698–703 (2001)
10. Jacobsen, N.J., Andersen, P., Brincker, R.: Eliminating the influence of harmonic components in operational modal analysis. In: Proceedings. of 25th International Modal Analysis Conference, Orlando, FL, USA (2007)

11. SAP2000 Advanced (v14.1.0) Static and Dynamic Finite Element Analysis of Structures. CSI Computer & Structures, Inc., Berkeley (2009)
12. Gazetas, G., Makris, N.: Dynamic pile-soil-pile interaction, Part II: lateral and seismic response. Earthq. Eng. Struct. Dyn. **21**, 145–162 (1992)
13. Mylonakis, G., Nikolaou, S., Gazetas, G.: Footings under seismic loading: analysis and design issues with emphasis on bridge foundations. Soil Dyn. Earthq. Eng. **26**, 824–853 (2006)

Experimental Analysis of Arroyo Bracea II Bridge in Madrid – Sevilla High-Speed Railway Line: Dynamic Response of the Structure and Effect of Soil Properties

Pedro Galvín[1], Antonio Romero[1], Emmanuela Moliner[2], and María D. Martínez-Rodrigo[2(✉)]

[1] Escuela Técnica Superior de Ingeniería, Universidad de Sevilla, Sevilla, Spain
[2] Mechanical Engineering and Construction Department, Universitat Jaume I, Castellón, Spain
mrodrigo@uji.es

Abstract. Traffic induced vibrations in railway bridges has become an issue of main concern among scientists and engineers due to the extensive construction of new High-Speed railway lines and the upgrading of existing lines for higher operating velocities [1, 2]. In this context, short to medium-span bridges (10–25 m) composed by simply-supported elements are especially critical, due to their usually associated low masses, and may experience considerably high vertical acceleration levels at the platform area [3]. As a result, the transverse acceleration in such structures is one of the most demanding Serviceability Limit States according to present regulations [4]. As a consequence, there is a need to realistically predict the behavior of railway structures in the design phase and along the bridge's life. In this contribution the authors include results and conclusions from an experimental and numerical analysis of Arroyo Bracea II railway bridge, located in the Madrid-Sevilla High-Speed railway line in Spain. This structure is monitored due to its short length and typology, which make it susceptible to experience high transverse vibration levels. During the experimental campaign the soil properties at the site were obtained. Also, the response of the structure under the circulation of railway convoys travelling at speeds over 260 km/h was measured at several points of the deck and at the abutments. From the experimental measurements the modal parameters of the bridge are identified. Finally the experimental results are compared to those provided by a finite element numerical model in the time and frequency domains. Conclusions are extracted regarding the structure performance and the adequacy of the numerical model implemented for the particular soil and loading conditions.

Keywords: Railway bridges · Experimental measurements · Traffic induced vibrations · Bridge dynamics · Soil-structure interaction

1 Introduction

The evaluation of the dynamic effects caused by modern railway transportation systems on railway infrastructures is a key factor to guarantee structural integrity and travelling comfort. At circulating speeds above 200 km/h, resonance effects caused by the regular

© Springer International Publishing AG 2018
J.P. Conte et al. (eds.), *Experimental Vibration Analysis for Civil Structures*,
Lecture Notes in Civil Engineering 5, https://doi.org/10.1007/978-3-319-67443-8_79

nature of train axle loads may entail harmful consequences on railway bridges, such as ballast destabilization, passenger discomfort or a raise in the maintenance costs of the line. Especially critical in this regard are short-to-medium span simply-supported (S-S) bridges with usually low associated structural damping and mass, which may experience considerably high vertical accelerations at the deck level [1, 2, 6]. In these structures the Serviceability Limit State of vertical acceleration is one of the most demanding specifications for their design or upgrading. These facts point out the importance of developing accurate numerical models, able to realistically predict the vibration levels in the bridge with reasonable computational costs. In this regard, the calibration of these models with in situ dynamic testing becomes crucial. With this purpose a number of researchers have performed experimental campaigns on railway bridges in the past [7–10]. In these studies, usually performed on structures of long spans, the attention is focused on the dynamic response of the bridge deck under ambient or train induced vibrations, with the aim of identifying its modal properties.

However, as indicated in [11], the dynamic response of short-to-medium span S-S railway bridges is difficult to predict during the design or upgrading stages, since the influence of the environment and the super-structure components (rails, ballast) can be significant and it is not well known. Despite the high vibration levels that such structures may experience, the number of reported experimental campaigns is low. In [11] the authors perform in situ dynamic testing in short-to-medium span S-S slab bridges belonging to a conventional railway line to be upgraded for higher operating speeds. Despite that some studies reveal that soil-structure interaction (SSI) may significantly affect the bridge dynamic response [12], especially in short S-S structures, the properties of the soil are seldom measured during the tests nor included in the numerical FE models. Only when the interaction between the super-structure and the soil is more evident due to the bridge typology, as it is the case of portal frames or soil-steel composite railway bridges [13, 14], the SSI is taken into account.

In this work the results and conclusions from an experimental campaign performed on a short S-S bridge belonging to a high-speed line in Spain are included. This bridge is particularly interesting as (i) the structure has a skew angle of 45º with a span length similar to the deck width, therefore its dynamic response substantially differs from that of a "beam-like" structure; and (ii) in a preliminary numerical evaluation [3], using a three dimensional finite element (FE) model that follows the main simplifications adopted by practitioners in accordance with the European Standards [4, 15], an important transverse vibration response was predicted at the deck level. Conclusions are extracted regarding the structure performance and the adequacy of the numerical model implemented for the particular soil and loading conditions.

2 Structure Description

The structure under study, designated as Arroyo Bracea II bridge, is a railway bridge composed of two identical S-S bays of 15.25 m equal spans. The bridge belongs to the Madrid-Sevilla high-speed railway, which was the first high-speed line in Spain opened in 1992. The structure crosses the Bracea stream with a 45° skew angle as shown in Fig. 1. Each deck consists of a 25 cm thick, 11.6 m width concrete slab resting over

Fig. 1. Arroyo Bracea II Bridge. Experimental campaign images (from left to right): S102 Talgo 350 train passage at v = 263 km/h and S103 ICE 350 train passage at v = 279 km/h.

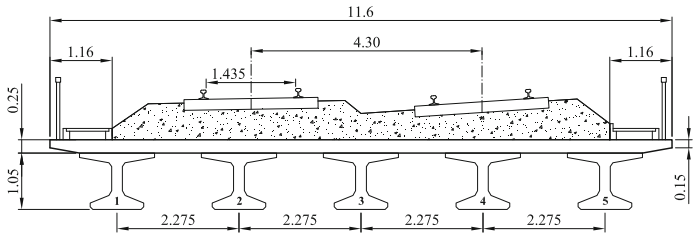

Fig. 2. Arroyo Bracea II bridge deck cross section.

five 1.05 m height pre-stressed concrete I girders. The girders lean on the supports through laminated rubber bearings. The slab carries two ballasted tracks with an equal eccentricity of 2.15 m from its longitudinal axis, two sidewalks and handrails (Fig. 2). As per the substructure, the bridge deck is supported on reinforced concrete abutments in its outermost sections and the inner sections of both bays lean on a pile foundation.

3 Numerical Model Description

A finite element numerical model of the bridge is used in order to compare the predicted response with the experimental measurements that will be described later on. Figure 3 shows the main features of the model, which are the following: (i) the deck behavior is simulated by means of an orthotropic thin plate discretised in Linear Varying Curvature FEs. These are C^1 compatible triangular elements with 12 degrees of freedom [5]; (ii) the laminated rubber bearings of the deck girders are included in the model as an equivalent vertical stiffness uniformly distributed along the supports lines; (iii) different mass density elements are employed in order to concentrate the weight of the ballast, sleepers and rails at the central portion of the plate; (iv) a point load model is adopted for the railway excitation, therefore neglecting vehicle-structure interaction effects. As the track rigidity is not included in the numerical model and in order to avoid un-realistic high-frequency modal contributions when a load enters or exits the bridge due to the presence of the elastic bearings, the gradual nature of the wheel loads application

process close to the abutments due to the distributive effect of rails, sleepers and ballast, is simulated. To this end, the value of each axle load is modulated at the deck entrance and exit vicinity applying a function based on the Zimmerman-Timoshenko solution for an infinite beam on Winkler foundation [3]. Finally, the dynamic equations of motion are transformed into modal space and numerically integrated by the Newmark-Linear Acceleration algorithm taking into account the first 20 natural modes of the structure. Initially, the plate orthotropic constants, mass and the supports flexibility are obtained from the bridge geometry and mechanical properties. Subsequently the model properties are updated to reproduce the proof load test performed on the structure prior to its opening [3]. In a first approach and due to the soil properties that are measured at the site, SSI is not included in the model. In the following sections, conclusions regarding its effect under resonant and not-resonant conditions of the structure will be exposed.

4 Experimental Campaign

The experimental program, carried out in July of 2016, included a dynamic characterization of the structure and of the soil at the bridge site. The acquisition equipment was a portable system LAN-XI of Brüel and Kjaer. The acquisition system fed the accelerometers and the impact hammer used in the tests, and also performed the Analog/Digital conversion (A/D). The A/D was performed at a high sampling frequency and aliasing effect was avoided applying a low-pass filter with constant cut-off frequency to the digital signals. The sampling frequency was f_s = 4096 Hz. The acquisition equipment was connected to a laptop for data storage.

The dynamic characterization of the soil was done by the seismic refraction and the spectral analysis of surface waves (SASW) tests. The seismic refraction test allowed the identification of the P-wave velocity (C_p) of the soil layers. The SASW test was used to determine the S-wave velocity (C_s) and the material damping ratio of the soil layers [16].

The measurements were performed in 2 setups. In each setup, 100 impacts were applied to a 50 cm × 50 cm × 8 cm aluminium foundation anchored to the soil surface (Fig. 4). The instrumented hammer was a PCB 086D50 force sensor. The vertical free field response was recorded by means of accelerometers anchored to the soil surface

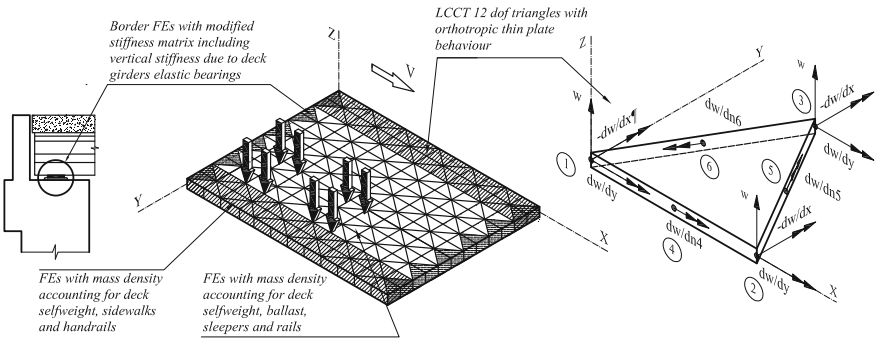

Fig. 3. Finite Element model main features.

Fig. 4. SASW test: impact hammer, foundation and accelerometers set-up.

every 2 m, (2 to 68 m distant from the foundation). Steel stakes of cruciform section and 0.3 m length were driven into the ground for mounting each of the accelerometers.

After each impact, a time signal of 16,348 samples (4 s) was stored. The force channel was used as a trigger, with a trigger level of 10 N, a pre-trigger of 4096 samples (or 1 s), and a post-trigger of 12,288 samples (or 3 s). The signals were decimated (order 4), filtered with a third-order Chebyshev filter with a high-pass frequency of 5 Hz and with a third-order Chebyshev filter with a low-pass frequency of 100 Hz. Figure 5 shows the resulting dispersion curve. The maxima in the spectrum are due to the Rayleigh waves. On the right hand side of the figure, the soil properties are included obtained from the resolution of the inverse problem. The profile is consistent with that provided by a geotechnical analysis performed at the site prior to the bridge construction [17].

The acceleration response of the structure was measured at 11 points of the lower flange lower horizontal face of the pre-stressed concrete girders (points 1–11 in Fig. 6) and at the pile abutment upper horizontal surface, close to the girders support (point 12 in Fig. 6). Endevco model 86 piezoelectric accelerometers were used (Fig. 7) with a nominal sensitivity of 1000 mV/g and a low frequency limit of approximately 0.1 Hz. The sensors were attached to the deck using circular aluminum plates of 0.09 m diameter and 0.006 m thickness glued with epoxy resin to the girders.

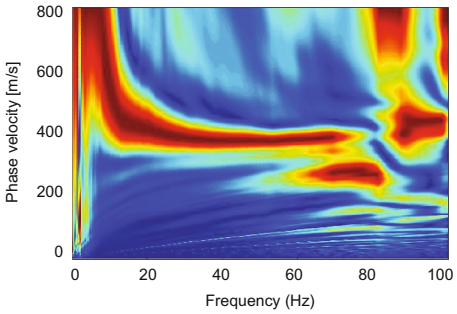

Layer	Depth (m)	C_p (m/s)	C_s (m/s)
1	2	900	250
2	∞	1750	430

Fig. 5. Dispersion curve and soil properties.

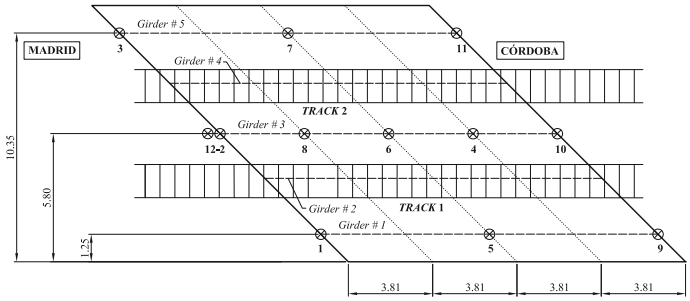

Fig. 6. Sensor locations.

Fig. 7. Accelerometers set up.

The ambient vibration response was acquired in 4184 s per channel. Data were decimated (order 16) to carry out data analysis in the frequency range of interest (0 to 30 Hz). The signals were filtered applying two third-order Chebyshev filters with high-pass and low-pass frequencies of 1 Hz and 30 Hz, respectively.

During the recording time, several trains crossed the bridge with circulating velocities in the range [100, 280] km/h. In the next section the response of the structure is presented for two of these trains: a Talgo 350 with an axle scheme as that shown in Fig. 8a and a coach distribution type L-1-10 $\times$ 2-1-L, and an ICE 350 (Fig. 8b) with a coach distribution $1 - 6 \times 2 - 1$. These two cases have been selected as both

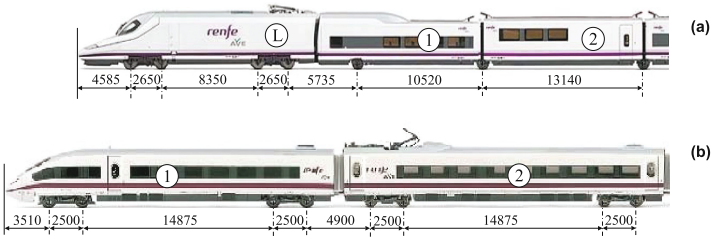

Fig. 8. Talgo 350 and ICE 350 trains coach distribution and axle distances.

circulated at speeds higher than 260 km/h and, as it will be shown later on, the former leads to a non-resonant response of the structure and the latter to a resonant response.

5 Experimental vs. Numerical Results

5.1 Modal Parameters

First, the modal parameters of the bridge are identified from ambient vibration data by state-space models using MACEC software developed by the Structural Mechanics Section of KU Leuven [18]. The deck presents five modes in the frequency range [0, 30] Hz, where the lowest ones in frequency order correspond to the first longitudinal bending, first torsion and first transverse bending modes. In Table 1 the identified natural frequencies and the damping ratios are included for the first five modes. The numerical natural frequencies provided by the FE model are included as well. The correlation between numerical and experimental mode shapes according to the MAC values [19] is also indicated.

Table 1. Experimental and numerical natural frequencies, experimental modal damping and AutoMAC values

#	f_{exp} (Hz)	f_{num} (Hz)	ζ_{exp} (%)	A_MAC (-)	#	f_{exp} (Hz)	f_{num} (Hz)	ζ_{exp} (%)	A_MAC (-)
1	9.25	9.19	3.64	0.98	4	17.94	17.20	0.80	0.96
2	10.63	10.34	1.66	0.96	5	24.58	24.81	0.95	0.98
3	12.75	12.65	1.30	0.97					

The experimental vs. numerical mode shapes are represented in Fig. 9 for the first four natural frequencies. The correspondence between numerical and experimental results is reasonably accurate. The identified damping for the fundamental mode reaches 3.64%, a higher value than that prescribed by standards for design purposes [15, 21] for this length and bridge typology.

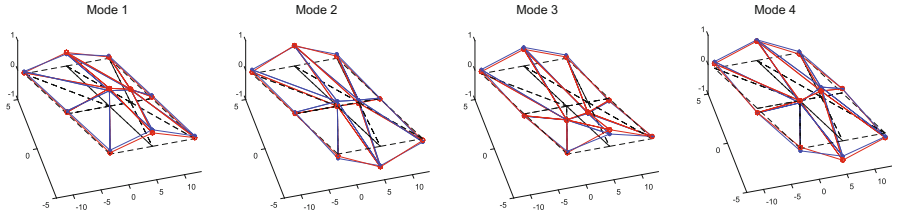

Fig. 9. Experimental (blue) vs. numerical (red) first four identified mode shapes. Undeformed shape (black).

5.2 Transient Structure Response Under the Circulation of High-Speed Trains

In Figs. 10 and 11 the vertical acceleration time history response and its frequency contents are represented at sensors 4, 5, and 6 (see Fig. 6) for two train passages: Renfe S102 (Talgo-350) at v = 263 km/h and Renfe S103 (ICE-350) at v = 279 km/h. Only the load passage excitation is considered in the numerical model as it dominates the response at the track [20] (other sources of excitation as rail irregularities are not included in the model). The computed results show a reasonably good agreement with those experimentally recorded. In the frequency domain peaks coinciding with the bogie passing frequency $f_b = v/L_b$ Hz (L_b is the characteristic distance between bogies), the axle passing frequency $f_a = v/L_a$ Hz (L_a is the characteristic distance between axles) and at the natural frequencies of the structure may be detected. It should be noted that the circulation of Talgo-350 train does not induce resonance in the bridge deck. In this case, several modal contributions are responsible for the deck response below 30 Hz, and the first longitudinal bending and first torsion modes are both very relevant to the total acceleration at some points (see Fig. 10 sensor 5). In this particular case, where no clear resonance takes place the experimental measurements are slightly higher than the numerical prediction.

On the other hand, train ICE-350 travelling at 279 km/h induces a third resonance of the fundamental mode of the bridge at a theoretical velocity of $v_{res,3} = 3.6 \cdot d_{car} \cdot f_1 / 3 = 275$ km/h associated to the length of the cars repetitive distance (d = 24.775 m). Although for this particular train this situation is not associated to excessively high acceleration levels, it can be detected in the progressively increasing response of the structure with the axles passage. In this case, the peak associated to the resonant mode (fundamental) predominates in the frequency response (see Fig. 11) and the

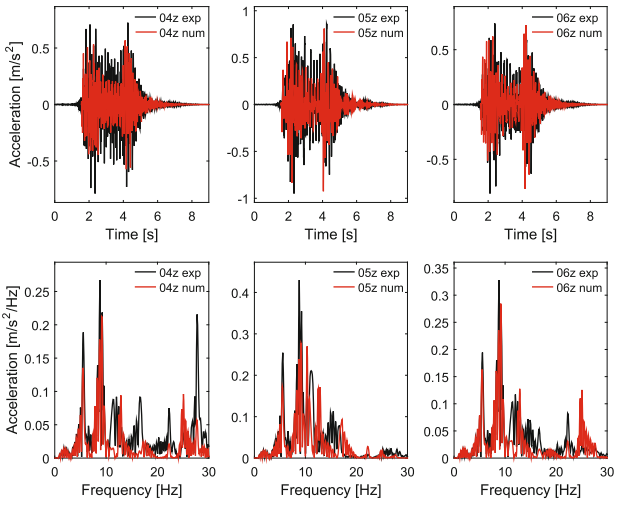

Fig. 10. Acceleration response in time and frequency domains under the passage of a S102 Talgo 350 train at v = 263 km/h.

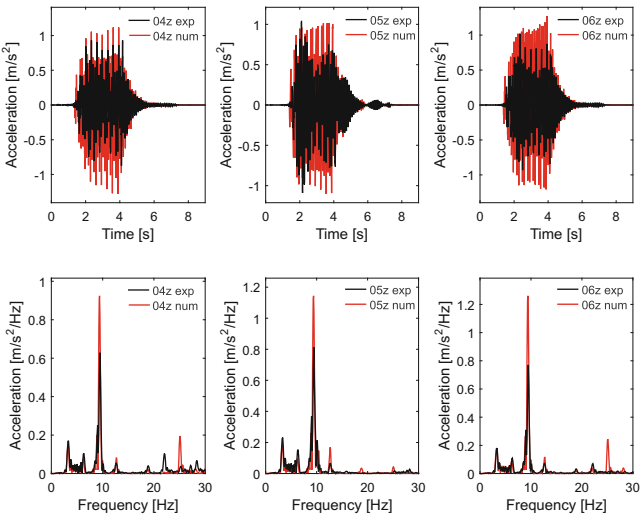

Fig. 11. Acceleration response in time and frequency domains under the passage of a S103 ICE 350 train at v = 279 km/h.

contribution of other frequency contents is less relevant in comparison. It should be noted that even though the correspondence between experimental and numerical results is even better in this case, the numerical model overestimates the real response, and specially at the fundamental frequency of the structure, associated to the resonant response. This is consistent with the fact that the effect of wave radiation exerted by the soil is especially noticeable at resonant velocities [22], where soil structure interaction effects become particularly relevant.

6 Conclusions

The experimental dynamic response of a short S-S railway bridge under high-speed traffic belonging to the Spanish railway network is presented and compared to numerical predictions. The structure modal parameters are identified from ambient vibration measurements showing a reasonably good correspondence with numerical parameters. Due to the deck dimensions and skew angle the deck dynamic response substantially differs from that of a "beam-like" structure and the participation of modes different from the first longitudinal bending one show an important participation. The response of the bridge under the circulation of a Talgo 350 train travelling at 263 km/h and an ICE 350 travelling at 279 km/h are shown. In the former case, the train does not induce resonance on the bridge deck, therefore the response is not dominated by a predominant modal contribution. Also, in this case the numerical model predicts quite accurately the experimental response of the bridge, being experimental amplitudes slightly higher than numerical. In the second case, the train ICE 250 induces a third resonance of the fundamental mode of the structure. The phenomenon is evident both

in the experimental response and in the numerical predictions. In this case even though the prediction is good, the FE model overestimates the real response, specially at the first mode natural frequency undergoing resonance. This is consistent with the fact that the effect of wave radiation exerted by the soil is especially noticeable at resonant velocities, where soil structure interaction effects become particularly relevant.

Acknowledgments. The first two authors would like to acknowledge the financial support provided by the Spanish Ministry of Economy and Competitiveness (Ministerio de Economía y Competitividad) under the research project [BIA2013-43085-P]. The authors also wish to acknowledge the support provided by the Andalusian Scientific Computing Centre (CICA). The third and fourth authors would like to acknowledge the financial support provided by Universitat Jaume I under the research project [P1-1B2015-54]. This work falls within the initiation of research project BIA2016-75042 coordinated between Universidad de Sevilla and Universitat Jaume I and financed by the Spanish Ministry of Economy and Competitiveness.

References

1. ERRI D214: Rail bridges for speeds >200 km/h. Final report. Part A. Synthesis of the results of D 214 research. European Rail Research Institute (1999)
2. Le, R., Ripke, B., Zacher, M.: Influence of bridge dynamics on ballast deterioration on high-speed lines. In: World Congress on Railway Research, Edinburgh, Scotland (2003)
3. Martínez, M.D., Lavado, J., Museros, P.: Dynamic performance of existing high-speed railway bridges under resonant conditions retrofitted with fluid viscous dampers. Eng. Struct. **32**, 808–828 (2010)
4. CEN/TC250: Eurocode: basis of structural design. Annex A2: application for bridges. European Committee for Standardisation (2002)
5. Felippa, C.A.: Refined finite element analysis of linear and nonlinear two dimensional structures. Ph.D. thesis, University of California, Berkeley (1966)
6. Frýba L.: Dynamic behaviour of bridges due to high-speed trains. In: Workshop Bridges for High-Speed Railways, Porto (2004)
7. Álvarez, R., Diaz, J., Moreno, C., Santos, J., Santos, F.: Conclusiones de los ensayos realizados en el Viaducto sobre el río Tajo en la línea de alta velocidad Madrid-Sevilla. Consideraciones para el proyecto de obras de paso en FF.CC. de alta velocidad. Hormigón y acero **214**, 131–140 (1999)
8. Liu, K., Reynders, E., De Roeck, G., Lombaert, G.: Experimental and numerical analysis of a composite bridge for high-speed trains. J. Sound Vib. **320**, 201–220 (2009)
9. Ribeiro, D., Calçada, R., Delgado, R., Brehm, M., Zabel, V.: Finite element model updating of a bowstring-arch railway bridge based on experimental modal parameters. Eng. Struct. **40**, 413–435 (2014)
10. Malveiro, J., Ribeiro, D., Calçada, R., Delgado, R.: Updating and validation of the dynamic model of a railway viaduct with precast deck. Struct. Infrastruct. Eng. **10**(11), 1489–1509 (2014)
11. Rebelo, C., Simoes da Silva, L., Rigueiro, C., Pircher, M.: Dynamic behaviour of twin single –span ballasted railway viaducts. Field measurements and modal identification. Eng. Struct. **30**, 2460–2469 (2008)
12. Romero, A., Solís, M., Domínguez, J., Galvín, P.: Soil-structure interaction in resonant railway bridges. Solid Dyn. Earthq. Eng. **47**, 108–116 (2013)

13. Ülker-Kaustell, M., Karoumi, R., Pacoste, C.: Simplified analysis of the dynamic soil-structure interaction of a portal frame railway bridge. Eng. Struct. **32**, 3692–3698 (2010)
14. Mellat, P., Andersson, A., Pettersson, L., Karoumi, R.: Dynamic behavior of a short span soil-steel composite bridge for HS railways. Field measurements and FE-analysis. Eng. Struct. **69**, 49–61 (2014)
15. CEN: Eurocode 1: actions on structures—part 2: traffic loads on bridges. European Committee for Standardisation (2008)
16. Badsar, S.A., Schevenels, M., Haegeman, W., Degrande, G.: Determination of the material damping ratio in the soil from SASW tests using the half-power bandwidth method. Geophys. J. Int. **182**(3), 1493–1508 (2010)
17. Ministerio de transporte, turismo y comunicaciones. Gobierno de España: Nuevo acceso ferroviario a Andalucía. Proyecto de infraestructura y vía. Estudio geológico y geotécnico. Tramo Mascaraque-El Emperador (1987)
18. Reynders, E.: System identification methods for (operational) modal analysis: review and comparison. Arch. Comput. Methods Eng. **19**(1), 51–124 (2012)
19. Allemang, R.J., Brown, D.L. Correlation coefficient for modal vector analysis. In: Proceedings of the 1st International Modal Analysis Conference (IMAC I), Orlando, Florida (1983)
20. Lombaert, G., Degrande, G.: Ground-borne vibration due to static and dynamic axle loads of InterCity and high-speed trains. J. Sound Vib. **319**, 1036–1066 (2009)
21. Ministerio de Fomento: IAPF 2010: Instrucción de acciones a considerar en puentes de ferrocarril (2010)
22. Doménech, A., Martínez-Rodrigo, M.D., Romero, A., Galvín, P.: On the basic phenomenon of soil-structure interaction on the free vibration response of beams: application to railway bridges. Eng. Struct. **125**, 254–265 (2016)

Dynamic Modeling of Train and Bridge with Stepped-Beam Cross-Sections

Hani Nassif[1], Yingjie Wang[2], and Peng Lou[1(✉)]

[1] Department of Civil and Environmental Engineering, Rutgers, The State University of New Jersey, Piscataway, NJ, USA
penglou@rutgers.edu
[2] Beijing Jiaotong University, Beijing, China

Abstract. Railway systems are critical in many regions and facilitate large volume of freight movement cost-effectively. In North America, the majority of railway bridges were built at the beginning of the twentieth century. With the recent increase of railcar weight limits from 1170 kN to 1272 kN, concerns are raised regarding the condition and dynamic behavior of these bridges. This study focuses on the dynamic response of stepped beam under moving trains. The train is composed of a certain number of railcars, and each railcar is consisted of oscillators with three masses representing the railcar body, bogie and wheel sets, respectively. The connects among components is simulated by spring and dashpot units. Meanwhile, finite element method with Euler-Bernoulli beam element is used to model the stepped beam with variational sections. The contact force between the wheel and rail is simulated by the Hertzian spring. The interaction of train-bridge system is assumed to be nonlinear and is solved by an iterative algorithm. At last the developed model is verified using the data from field testing.

Keywords: Vehicle-bridge system · Stepped beam · Field testing · Beam resonance

1 Introduction

Bridge vibration caused by the moving trains has caused more concern for railway industry especially regarding the new introduced high-speed railway. Comprehensive study about train-bridge (track) interaction have been previously presented [1–3]. In Cheng et al.'s study [4], the train was modeled as a series of oscillators including spring and dashpot units. The beam was modeled as track beam element (upper) and girder beam element (lower) to take the effect of tracks and beams into consideration. A new iterative solution algorithm was introduced by Jo et al. [5]. A discrete element technique was presented by Ziaei-Rad et al. [6]. In Ziaei-Rad et al.'s study, the beam was modeled as Timoshenko beam. Although lots of previous studies have established their own train-bridge interaction models, steel bridge structures were usually modeled as constant cross section beam elements, which is not practical in real design. In addition, the wheel sets were assumed to be in fully contact with the beam elements at all time and the nonlinear forces between wheel and rail was not considered. However, most of

© Springer International Publishing AG 2018
J.P. Conte et al. (eds.), *Experimental Vibration Analysis for Civil Structures*,
Lecture Notes in Civil Engineering 5, https://doi.org/10.1007/978-3-319-67443-8_80

the dynamic responses of both bridge and train are caused by the contact forces between the wheel sets and the rail.

Freight industry in New Jersey uses a portion of the passenger railway network, mainly New Jersey Transit (NJT), to complete their trips. The national freight network has push the weight limits of freight railcar from the previous standard of 1170 kN to 1272 kN. This caused concern for the bridges in passenger lines in New Jersey since these bridges were not originally designed for the higher loads. In addition, the dynamic load effect of the proposed heavier railcar remains unknown. In this study, one of the selected bridges operated by New Jersey Transit was tested under the dynamic loading. It was built in 1906 and has a total length of 890 m. It is consisted by one steel-truss swing span, Fig. 1(a), and twenty-eight simply supported steel-deck girder spans, Fig. 1(b).

(a) Steel-truss swing span *(b) Simply supported steel-deck girder spans*

Fig. 1. Tested bridge

In this paper, a new train-bridge interaction model considering the nonlinear contact forces between wheel sets and rail is proposed to simulate the dynamic responses of the bridge under the moving train. The bridge structure is regarded as Euler-Bernoulli beam elements in order to take the variational cross sections into consideration. The Hertzian spring is used to simulate the contact forces between the wheel sets and the rail. An iterative procedure is used to solve for the dynamic response of the bridge and lastly the developed model is verified by the data from field testing.

2 Dynamic Modeling of Train Bridge Interaction

In order to simplify the formulation of the dynamic interaction, following assumptions have been made in the model:

(1) Only the vertical vibration of the bridge is considered;
(2) Linear elastic Bernoulli-Euler beam element is used to model the bridge girders with variational cross sections.
(3) A sequence of mass-spring-damper units each with three Degree of Freedom are used to simulate the train loading running on the stepped beam.

(4) No rail surface roughness is considered.
(5) The contact force between wheel sets and rail is simulated by Hertzian spring.

2.1 Equations of Motion for Train Model

The train is modeled as a series of oscillators with a distance of d traveling at the speed of v. Each oscillator has three components with mass of m_c, m_b, and m_w to represent the car-body, bogie and wheel-sets, respectively. Spring-dashpot systems are used to simulate vehicle's primary and secondary suspension systems. In Fig. 2, the stiffness of spring and the damping coefficient of the dashpot for the secondary suspension system are denoted as k_s and c_s, while the stiffness of spring and the damping coefficient of the dashpot for the primary suspension system are denoted as k_p and c_p. The equations of motion for car-body, bogie, and wheel-sets are shown in Eqs. (1), (2) and (3), respectively.

$$m_c\ddot{Z}_c(t) + c_s\dot{Z}_c(t) - c_s\dot{Z}_b(t) + k_sZ_c(t) - k_sZ_b(t) = m_cg \tag{1}$$

$$\begin{aligned} m_b\ddot{Z}_b(t) + \left(c_s + c_p\right)\dot{Z}_b(t) - c_s\dot{Z}_c(t) - c_p\dot{Z}_w(t) \\ + \left(k_s + k_p\right)Z_b(t) - k_sZ_c(t) - k_pZ_w(t) = m_bg \end{aligned} \tag{2}$$

$$m_w\ddot{Z}_w(t) + c_p\dot{Z}_w(t) - c_p\dot{Z}_b(t) + k_pZ_w(t) - k_pZ_b(t) = m_wg - f(t) \tag{3}$$

where,
$Z_c(t)$, $Z_b(t)$, and $Z_w(t)$ represent the vertical displacement of car-body, bogie and wheel-sets, respectively, and $f(t)$ = the contact force which is illustrated in Eq. (4).

$$f(t) = \begin{cases} C_H[Z_w(t) - u(x,t)]^{3/2} & Z_w(t) - u(x,t) > 0 \\ 0 & Z_w(t) - u(x,t) \le 0 \end{cases} \tag{4}$$

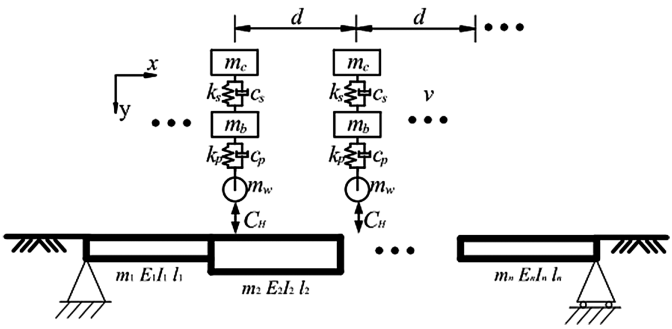

Fig. 2. Developed model of train-bridge interaction

where,

$u(x, t)$ = the vertical displacement of the beam where the kth oscillator is located on,

C_H is the Hertzian constant, and is assumed as 9.37×10^{10} N/m$^{3/2}$ in this study.

The equation of motion of all oscillators using multi-body system dynamics can be assembled as Eq. (5).

$$[M_v]\{\ddot{U}_v\} + [C_v]\{\dot{U}_v\} + [K_v]\{U_v\} = \{F_v\} \tag{5}$$

where,

$[M_v]$, $[C_v]$ and $[K_v]$ represent the mass matrices, damping matrices and stiffness matrices, respectively,

$\{\ddot{U}_v\}$, $\{\dot{U}_v\}$, and $\{U_v\}$ represent the accelerations matrices, velocities matrices and displacements matrices, respectively, and

$\{F_v\}$ represent the external force vector acting on oscillators.

2.2 Development of Beam Model

The stepped beam with variational sections is divided into n sections with different section properties. The mass, stiffness, and length are denoted as m_i, I_i and L_i for each section. The finite element method is used to develop the equations of motion for the stepped beam. A two-dimensional beam element is assumed for each cross section with one translations and one rotations (total four DOFs) for with each of the two ends of the element, i and j. The vectors of displacement for the beam element is shown in Eq. (6). Meanwhile, the mass matrix and stiffness matrix of the element are shown in Eqs. (7) and (8).

$$\{u_b\} = \{y_i\ \theta_i\ y_j\ \theta_j\}^T \tag{6}$$

$$[m_b] = \frac{mL}{420}\begin{bmatrix} 156 & 22L & 54 & -13L \\ 22L & 4L^2 & 13L & -3L^2 \\ 54 & 13L & 156 & -22L \\ -13L & -3L^2 & -22L & 4L^2 \end{bmatrix} \tag{7}$$

$$[k_b] = \frac{EI}{L^3}\begin{bmatrix} 12 & 6L & -12 & 6L \\ 6L & 4L^2 & -6L & 2L^2 \\ -12 & -6L & 12 & -6L \\ 6L & 2L^2 & -6L & 4L^2 \end{bmatrix} \tag{8}$$

where,

L = the length of element, and

m = the mass per unit length.

The assumption of Rayleigh damping is made for the damping matrix as shown in Eqs. (9) and (10).

$$[C_b] = a_0[M_b] + a_1[K_b] \tag{9}$$

$$\begin{aligned} a_0 &= \frac{2(\xi_1\omega_2 - \xi_2\omega_1)}{\omega_2^2 - \omega_1^2}\omega_1\omega_2 \\ a_1 &= \frac{2(\xi_2\omega_2 - \xi_1\omega_1)}{\omega_2^2 - \omega_1^2} \end{aligned} \tag{10}$$

where

ω_1, ω_2 represent the first and second natural frequencies of the beam, and
ξ_i, ξ_j represent the damping coefficients.

Then both the stiffness matrices and mass matrices of beam elements are assembled into the equation of motion for the entire beam as illustrated in Eq. (11), as well as the damping matrix from Eq. (9).

$$[M_b]\{\ddot{U}_b\} + [C_b]\{\dot{U}_b\} + [K_b]\{U_b\} = \{F_b\} \tag{11}$$

where,

$[M_b]$, $[C_b]$ and $[K_b]$ represent the mass matrix, damping matrix and stiffness matrix of the beam, respectively,
$\{\ddot{U}_b\}$, $\{\dot{U}_b\}$ and $\{U_b\}$ represent the accelerations, velocities and displacements of the beam, respectively, and
$\{F_b\}$ represents the force vector applied on the beam.

2.3 Train-Bridge Interactive Model Using Iterative Algorithm

The contact force between the wheel sets and the beam is simulated using Hertzian spring. Thus, the interaction of entire train-bridge system is nonlinear. An iterative algorithm shown in Fig. 3 is proposed [7] to solve the Eqs. (5) and (11) simultaneously. The convergence criterion, presented in Eqs. (12) and (13), needs to be satisfied for the equations of motion of the train and bridge in Eqs. (5) and (11). The allowable tolerance of the convergence criterion is equal to 10^{-6}.

$$\left\|{}^{t+\Delta t}_{n+1}U_b - {}^{t+\Delta t}_{n}U_b\right\| \le CC, \left\|{}^{t+\Delta t}_{n+1}\dot{U}_b - {}^{t+\Delta t}_{n}\dot{U}_b\right\| \le CC, \left\|{}^{t+\Delta t}_{n+1}\ddot{U}_b - {}^{t+\Delta t}_{n}\ddot{U}_b\right\| \le CC \tag{12}$$

$$\left\|{}^{t+\Delta t}_{n+1}U_v - {}^{t+\Delta t}_{n}U_v\right\| \le CC, \left\|{}^{t+\Delta t}_{n+1}\dot{U}_v - {}^{t+\Delta t}_{n}\dot{U}_v\right\| \le CC, \left\|{}^{t+\Delta t}_{n+1}\ddot{U}_v - {}^{t+\Delta t}_{n}\ddot{U}_v\right\| \le CC \tag{13}$$

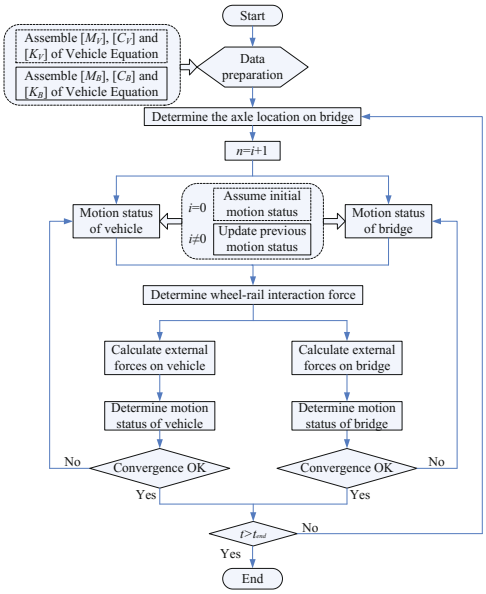

Fig. 3. Flowchart of the iterative algorithm

3 Field Instrumentation and Testing

The Structural Testing System (STS), as shown in Fig. 4, is used to capture the strain response of the tested bridge. It is a modular data acquisition system manufactured by Bridge Diagnostics, Inc. The system is consisted of three components, strain transducers, junction nodes, and the main unit. The strain transducers are mounted to the structural elements with C-clamps and wired connected with junction nodes, each with a unique identification number and a microchip to help the system to identify it. The main unit is wireless connected with junction nodes and field laptop to transfer real-time data. The instrumentation focused mainly on girders in Span 26 with a span length of 26.4 m, one of the twenty-eight spans since this span has the lowest load rating factor. The plan view of the selected span as well as the sensor locations are shown in Fig. 5. The cut off points in the Fig. 5 refer to the location where section changes. The cross sections of the girder near the support and at mid-span is shown in Fig. 6. The section properties of the bridge are shown in Table 1.

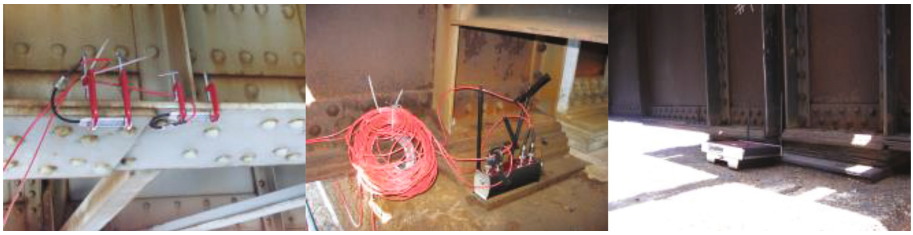

(a) Strain transducers *(b) Junction node* *(c) Main unit*

Fig. 4. STS system

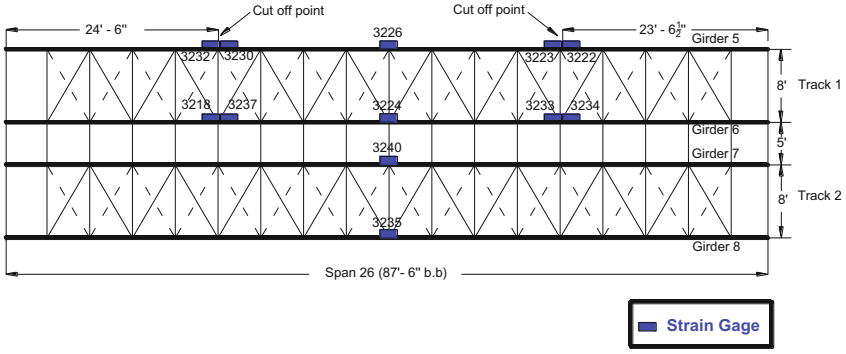

Fig. 5. Locations of installed strain transducers

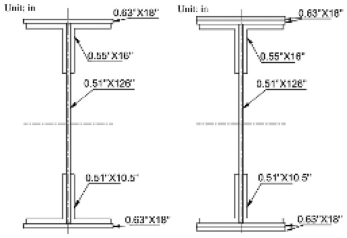

(a) Near support (b) Mid span

Fig. 6. Cross sections of girders

Table 1. Detail information of the tested bridges

Span length (m)	Girder spacing (m)	Girder height (m)	Section area (m^2)		2nd moment of area (m^4)		Tested natural freq.
			Near support	Mid-span	Near support	Mid-span	
25.9	2.44	2.591	0.07299	0.09348	0.08463	0.10708	7.9

4 Model Validation Using Data from Field Tests

The model then is validated using the testing data (Fig. 7). The tested train was running at 22.6 km/h. The following value of parameters are assumed for the bridge: 2.87×10^6 kN/m^2 for Young's modulus, 2.5% for damping ratio, 5750 kg for the sprung mass, and 1595 kN/m for spring constant.

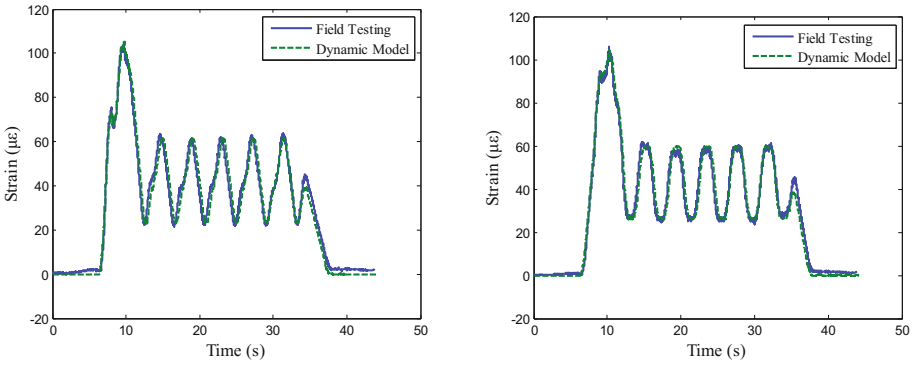

(a) Cut off location *(b) Mid-span*

Fig. 7. Model validation at cut off location and mid-span

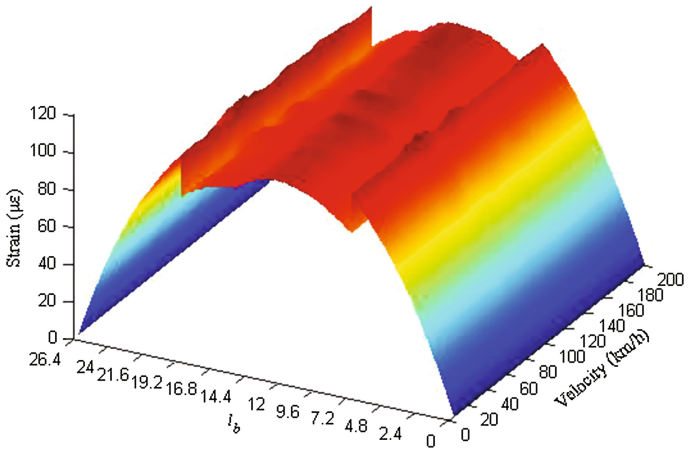

Fig. 8. Max strain of left girder along girder length with different velocities

5 Results and Discussions

In numerical study, the maximum strain along the girder length with different velocities are computed. Figure 8 show the three-dimensional plot for the maximum strain of the beam. The maximum strain doesn't change a lot under different velocities. The dynamic influence on the steel girder is low. There is a shift of maximum strain at the cut off location. This is can be attributed to the variable cross section parameters due to plate girder cut off design. The maximum strain values at the cut off location are close to that at the mid-span, in the range of 100–110 $\mu\xi$. Usually for the girder with constant section, mid span is usually concerned where the max strain occurs. For the girder with cut off design, the mid span and cut off locations should be considered together.

References

1. Frýba, L.: Vibration of Solids and Structures Under Moving Loads, vol. 1. Springer, New York (2013)
2. Frýba, L.: Dynamics of Railway Bridges. Thomas Telford Publishing, London (1996)
3. Yang, Y.B., Yau, J.D., Wu, Y.S.: Vehicle-Bridge Interaction Dynamics: With Applications to High-Speed Railways. World Scientific, London (2004)
4. Cheng, Y.S., Au, F.T.K., Cheung, Y.K.: Vibration of railway bridges under a moving train by using bridge-track-vehicle element. Eng. Struct. **23**(12), 1597–1606 (2001)
5. Jo, J.S., Jung, H.J., Kim, H.: Finite element analysis of vehicle-bridge interaction by an iterative method. Struct. Eng. Mech. **30**(2), 165–176 (2008)
6. Ziaei-Rad, S., Ariaei, A., Imregun, M.: Vibration analysis of Timoshenko beams under uniform partially distributed moving masses. Proc. Inst. Mech. Eng. Part K J. Multi-body Dyn. **221**(4), 551–566 (2007)
7. Zhang, N., Xia, H., De Roeck, G.: Dynamic analysis of a train-bridge system under multi-support seismic excitations. J. Mech. Sci. Technol. **24**(11), 2181–2188 (2010)

Nonlinear Stay Cable – Bridge Deck Interaction

Benedikt Weber(✉)

Empa, Swiss Federal Laboratories for Materials Science and Technology,
8600 Dübendorf, Switzerland
Benedikt.Weber@empa.ch

Abstract. Nonlinear coupling between stay cables and bridge deck can cause internal resonance. This coupling is due to the length change of the cables when vibrating. During one cycle of transverse motion, the cable length is reduced twice, once for the positive and once for negative displacement. This internal resonance occurs when the natural frequency of the deck is twice the natural frequency of the cable. It is thus also called 2:1 resonance.

Tests have been performed at Empa on a full-size model bridge in the laboratory. The cable frequency has been tuned to half of the deck frequency by attaching additional masses. The bridge was excited by an electromechanical shaker with a frequency near the resonance frequency of the deck.

Some interesting phenomena can be observed: (1) Internal resonance only occurs if the natural frequency of the cables is about half the natural frequency of the deck. (2) Internal resonance only occurs for excitation frequencies near the resonance frequency of the deck. Outside a certain frequency range, the cables mainly act as flexible supports for the deck. (3) The transition from one regime to the other takes place at different frequencies for an ascending or a descending frequency sweep. (4) Internal resonance only occurs above a critical level of excitation. (5) Increasing the excitation force above the critical value mainly increases the displacement of the cables while the deck movement is hardly affected (saturation phenomenon).

To better understand this unexpected behavior, the system is modelled as a two-degree-of-freedom system including nonlinear coupling. For the steady-state case, this nonlinear system is then solved by perturbation methods. Although the mathematics are a bit involved, the analytical solutions are very helpful for understanding and interpreting the experimental results, which otherwise appear strange sometimes.

Keywords: Internal resonance · Nonlinear dynamics · Perturbation methods · Cable-stayed bridges · Saturation phenomenon

1 Introduction

Most civil engineering structures behave essentially linear. Even if they exhibit some nonlinearities, they can usually still be analyzed with linear models but with amplitude-dependent parameters. It is typically observed that the damping increases with displacement amplitudes while natural frequencies decrease. When analyzing such

© Springer International Publishing AG 2018
J.P. Conte et al. (eds.), *Experimental Vibration Analysis for Civil Structures*,
Lecture Notes in Civil Engineering 5, https://doi.org/10.1007/978-3-319-67443-8_81

structures, the superposition principle applies and when excited with a harmonic force, all quantities respond with that very same frequency. Modes with higher frequencies are only excited by higher frequency components of the exciting force. This linear behavior is the basis of all modal analysis and system identification methods.

The nonlinearities we present in this paper are completely different. Geometric nonlinearities can introduce coupling between modes having natural frequencies with a ratio of 2:1. Although such nonlinearities are still considered weak, they can lead to quite unexpected behavior. An example of internal coupling in a cable-stayed steel bridge has been reported in [1].

The internal resonance can be explained intuitively by the idealized example sketched in Fig. 1. The model consists of a mass on a spring to which a vertical cable is connected. When the cable is displaced to either side, it pulls up the mass, whereas in the neutral position, the force on the mass is released. Thus, one cycle of cable motion corresponds to two cycles of the mass movement.

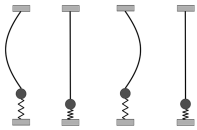

Fig. 1. Sketch for visualizing the 2:1 internal resonance.

Cable vibrations in bridges have been investigated in the literature to some extent. Some investigations only considered one-degree-freedom systems of a cable with a prescribed support motion but including sag [2, 3]. These systems typically show an instability region in the frequency-amplitude diagram where infinite displacements occur. Two-degree-of-freedom systems with out-of-plane motion have been studied in [4, 5]. In contrast to the in-plane motion, the out-of-plane motion of an inclined cable has no linear coupling with the bridge deck but the principal behavior is similar to the one considered here. Theoretical results on different kinds of nonlinear interactions are presented in [6]. Besides the internal resonance considered in this paper, the reference also treats nonlinear coupling due to angle variation.

References [3–5] also include experimental results, but only on small-scale laboratory systems. Tests on real bridges are rare. In [7], a large cable-stayed bridge was analyzed experimentally and cables with natural frequencies of half the deck frequency were identified. However, the authors conclude that the amplitudes were too low for internal resonance. First results of the experiments described in this paper have been presented previously [8].

2 Experimental Results

Experimental investigations have been performed on a cable-stayed laboratory bridge at Empa, shown in Fig. 2. The bridge is 20 m long and 2.5 m wide with a pylon of 7.5 m height. The deck is made of GFRP-profiles. A pair of cables, 9.25 m long, connects the

deck to the pylon. To adjust the cable frequency to half of the deck frequency, masses were added to the cables every 0.4 m. To force the cables to vibrate in their vertical plain, guides have been installed as shown in Fig. 2(b). An excitation force was applied to the deck by an electromechanical shaker. The shaker was placed near the cable support. By slightly changing its position, it was possible to fine-tune the deck frequency. The bridge deck was excited harmonically varying the frequency or the amplitude of the force in several steps. For each step, a sample of 60 s was registered. This period was sufficient to reach steady-state conditions. Accelerations were measured on the deck at both cable supports and on both cables at mid-length. The shaker force has been calculated from the accelerations of the shaker and the acceleration of the moving mass. Other quantities have been measured but are not reported here.

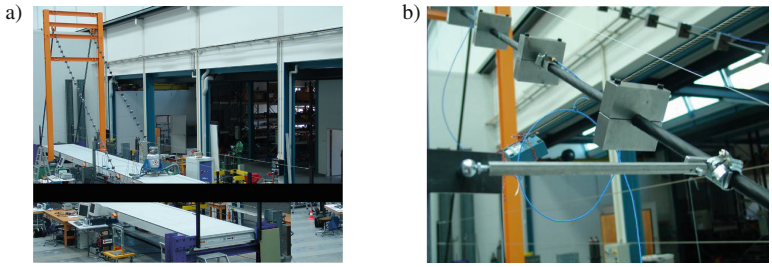

Fig. 2. (a) Laboratory bridge, (b) cable with added mass and guide.

As described above, internal resonance can occur when the cable frequency is close to half the deck frequency. When applying a harmonic force with a frequency close to the deck frequency, the deck vibrates with the excitation frequency, whereas, due to the nonlinear coupling, the cable vibrates with half the excitation frequency. However, due to the inclination of the cable, there is also a linear coupling exciting the cable directly with the motion of the deck, and the deck with the motion of the cable. To make the analysis more clear, the responses due to the linear coupling are filtered out in all plots. Thus, for the deck, always the harmonic corresponding to the excitation frequency (denoted as mode 1) is shown, and for the cables, the harmonic corresponding to half of the excitation frequency (denoted as mode 1/2) is plotted.

The amplitudes of the deck and the cables are plotted in Fig. 3. For the deck (Fig. 3a), the amplitudes at the centerline are plotted, calculated from the mean acceleration between the two cable supports. For the cables, one needs to be careful with the definition of the amplitudes. Since the cables vibrate sometimes in phase, sometimes out of phase, the amplitude of the mean is zero for the out-of-phase motion, whereas the mean of the amplitudes always gives a positive value without considering the phase between the two cables. Note that the out-of-phase motion of the cables is coupled with torsion of the deck, but with the frequency of the cable, not with the frequency of the deck. In Fig. 3(b), we show the mean of the two amplitudes. For ascending frequencies, internal resonance starts occurring at 3.85 Hz and ends at 4.2 Hz. Outside this frequency range, the cables have no harmonic contribution with

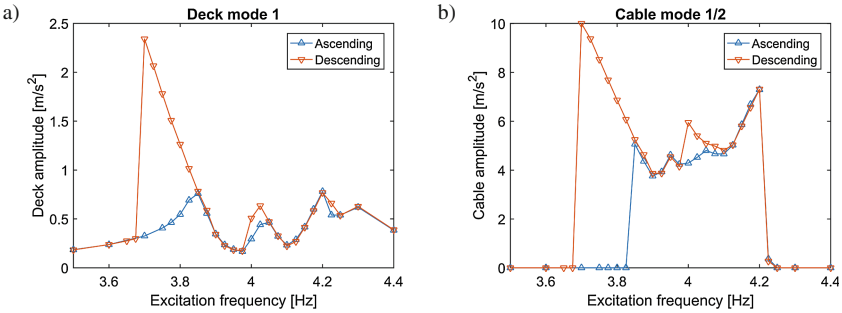

Fig. 3. Frequency response of (a) deck and (b) cables, due to harmonic excitation with amplitude 120 N.

half the excitation frequency. The deck amplitude shows two valleys in this range. For descending frequencies, the range of internal resonance extends down to 3.7 Hz. Observing this difference between ascending and descending excitation frequencies for the first time can be quite confusing.

To distinguish the in-phase and the out-of-phase motion of the cables, we can also look at the mean and half the difference of the two cable accelerations. The amplitudes of these values are plotted in Fig. 4(a), (b) for ascending and descending excitation frequencies, respectively. For the in-phase motion, without torsion of the deck, the difference is zero, whereas for the out-of-phase motion, with torsion of the deck, the mean is zero. Clearly, the cross-over frequency is around 4 Hz. Below this frequency, the cables vibrate in phase; above this frequency, they vibrate out of phase. The amplitudes, either in-phase or out-of-phase show the same picture as in Fig. 3(b).

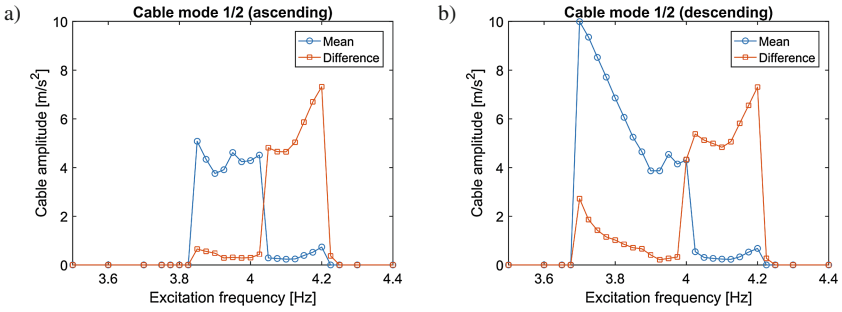

Fig. 4. Frequency response of cables with (a) ascending and (b) descending excitation frequency.

To complete the picture, experiments were also conducted with varying the amplitude of the excitation force while keeping the frequency constant. The most interesting results are for excitation frequencies 3.9 Hz and 4.1 Hz. The acceleration amplitudes of the deck and the cables are shown in Fig. 5. For a low level of the excitation force, the deck amplitude increases linearly, while the cables have no

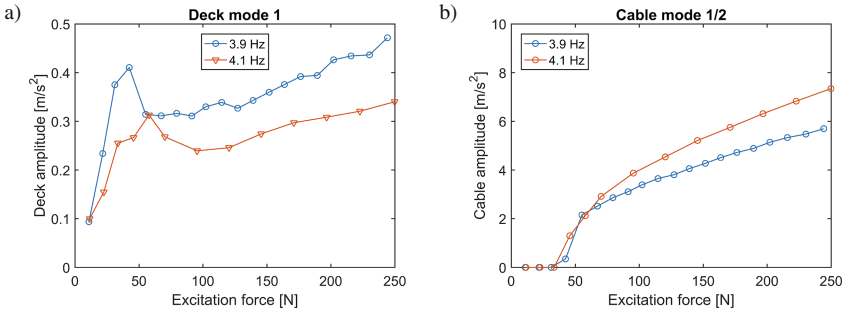

Fig. 5. Amplitude response of (a) deck and (b) cables at two selected frequencies.

harmonic contribution with a frequency of half the excitation frequency. Once the critical value of the excitation force has been reached, the deck amplitude decreases and then recovers slowly with increasing excitation force. Most of the energy goes into the cables. This is called the saturation phenomenon.

3 Theory

For the formulation of the differential equations describing the combined motion of the deck and the cable, we use Lagrange's equations of motion [9], similarly as in [3, 4]. The basic layout of the deck-cable system is sketched in Fig. 6. The geometry is defined by the length ℓ of the cable and the inclination angle θ. The deck is represented by the mass M and the spring with stiffness K. The properties of the cable are the stiffness EA and the distributed mass m. The initial tension of the cable is N_0.

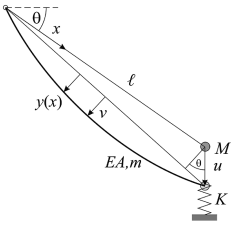

Fig. 6. Layout of deck-cable system

The displacement of the deck is described by the variable u, the displacement of the cable is described by the function $y(x)$ measured from the chord, which itself is moving with the deck. Not included in this idealized model are the flexibility of the pylon and the cable sag, which modify the cable frequency [10]. These effects are considered indirectly by taking the measured eigenfrequencies in the numerical model.

The potential energy of the cable depends on the stretching of the cable, which is due to the elongation of the chord when the deck moves down and due to the lateral

movement of the cable. Assuming a cable shape measured from the chord as $y = v\sin\pi x/\ell$, the cable stretching is given as

$$\Delta\ell = u\sin\theta + \int_0^\ell \sqrt{1-y'}dx - \ell \approx u\sin\theta + \frac{1}{2}\int_0^\ell y'dx = u\sin\theta + \frac{v^2\pi^2}{4\ell} \tag{1}$$

Considering the initial cable tension N_0, the potential energy of the deck and the cable is

$$\begin{aligned} V &= N_0\Delta\ell + \frac{1}{2}\frac{EA}{\ell}\Delta\ell^2 + \frac{1}{2}K_{deck}u^2 - uN_0\sin\theta \\ &= N_0\frac{\pi^2}{4\ell}v^2 + \frac{1}{2}\frac{EA}{\ell}\left(u\sin\theta + \frac{\pi^2}{4\ell}v^2\right)^2 + \frac{1}{2}K_{deck}u^2 \end{aligned} \tag{2}$$

Note that, in the potential energy, the initial cable tension gives rise to linear terms with respect to the cable elongation and the deck displacement. The kinetic energy is

$$\begin{aligned} T &= \frac{1}{2}\int_0^\ell m\left(\dot{y}(x) + \frac{x}{\ell}\dot{u}\cos\theta\right)^2 dx + \frac{1}{2}M\dot{u}^2 \\ &= \frac{m}{2}\left(\frac{\ell}{2}\dot{v}^2 + 2\cos\theta\frac{\ell}{\pi}\dot{u}\dot{v} + \cos^2\theta\frac{\ell}{3}\dot{u}^2\right) + \frac{1}{2}M\dot{u}^2 \end{aligned} \tag{3}$$

Introducing the Lagrangian defined by $L = T - V$, the equations of motion are

$$\frac{d}{dt}\left(\frac{\partial L}{\partial\dot{u}}\right) - \frac{\partial L}{\partial u} = Q \quad \text{and} \quad \frac{d}{dt}\left(\frac{\partial L}{\partial\dot{v}}\right) - \frac{\partial v}{\partial u} = 0 \tag{4}$$

Applying Eq. (4) to the kinetic and potential energy and neglecting third-order terms, the equation of motion becomes:

$$\begin{bmatrix} M + \cos^2\theta\frac{m\ell}{3} & \cos\theta\frac{m\ell}{\pi} \\ \cos\theta\frac{m\ell}{\pi} & \frac{m\ell}{2} \end{bmatrix}\begin{bmatrix}\ddot{u}\\ \ddot{v}\end{bmatrix} + \begin{bmatrix} K_{dec} + \sin^2\theta\frac{EA}{\ell} & 0 \\ 0 & N_0\frac{\pi^2}{2\ell} \end{bmatrix} + \begin{bmatrix}u\\ v\end{bmatrix} + \sin\theta\frac{\pi^2 EA}{4\ell^2}\begin{bmatrix}v^2\\ 2uv\end{bmatrix} = \begin{bmatrix}F\cos\Omega t\\ 0\end{bmatrix} \tag{5}$$

Notice how the Lagrange equations automatically yield all linear and nonlinear coupling terms, which would be difficult to obtain directly. From Eq. (5) we see that the deck mass and stiffness are augmented by cable contributions and there is a mass coupling between deck and cable. More interesting are the nonlinear contributions: The term v^2 in the deck equation stems from the longitudinal cable force due to the cable displacement. The term uv in the cable equation takes into account the variability of the cable tension due the movement of the deck.

The linear coupling due to the inclination of the cable can be removed by the usual transformation into modal coordinates:

$$\begin{bmatrix} u \\ v \end{bmatrix} = \begin{bmatrix} P_{11} & P_{12} \\ P_{21} & P_{22} \end{bmatrix} \begin{bmatrix} q \\ r \end{bmatrix} \tag{6}$$

Pre-multiplying by the transposed transformation matrix, the mass and the stiffness matrix can be uncoupled:

$$\mathbf{P}^T\mathbf{M}\mathbf{P} = \mathbf{I} \quad \text{and} \quad \mathbf{P}^T\mathbf{K}\mathbf{P} = \mathbf{diag}(\omega_1, \omega_2) \tag{7}$$

For the nonlinear terms, the transformation introduces all possible quadratic combinations of the variables q and r:

$$\begin{aligned} \ddot{q} + \omega_1^2 q + d_1 q^2 + d_2 qr + d_3 r^2 &= P_{11} F \cos\Omega t \\ \ddot{r} + \omega_2^2 r + d_4 q^2 + d_5 qr + d_6 r^2 &= P_{12} F \cos\Omega t \end{aligned} \tag{8}$$

For a vertical cable ($\theta = \pi/2$), there is no linear coupling and $u = q$ and $v = r$. It is thus convenient to refer to the first modal equation as to the deck equation and to the second equation as to the cable equation. In this case, ω_1 is the larger frequency and $\omega_2 \approx 1/2\omega_1$ is the smaller frequency. The excitation frequency is near the deck frequency: $\Omega \approx \omega_1$.

It is shown in Nayfeh [11] that the additional quadratic terms in Eq. (8) introduced by the linear transformation do not contribute to the internal resonance and only the term with qr in the first equation and the term r^2 in the second equation need to be retained. Also the excitation force in the second equation does not contribute since its frequency Ω is not close to the eigenfrequency ω_2. Basically, the cable inclination does not introduce any important nonlinear coupling terms and we only need to discuss the case of a vertical cable. The inclination just changes the values of the parameters but not the form of the equations.

Equation (8) can be solved by perturbation methods [11]. For small amplitudes, the quadratic terms are small relative to the linear terms. If we also assume the exciting force to be small and add a small damping, Eq. (8) can be written as

$$\begin{aligned} \ddot{q} + \omega_1^2 q + \varepsilon\left(2\mu_1 \dot{q} + d_3 r^2\right) &= \varepsilon f \cos\Omega t \\ \ddot{r} + \omega_2^2 r + \varepsilon(2\mu_2 \dot{r} + d_5 qr) &= 0 \end{aligned} \tag{9}$$

where ε is an unspecified small parameter. The modal damping values are $\varepsilon\mu_1 = \xi_1\omega_1$ and $\varepsilon\mu_2 = \xi_2\omega_2$. The force parameter is $\varepsilon f = P_{11}F$ and the coefficients for the nonlinear terms are $\varepsilon d_3 = (P_{11}P_{22} + 2P_{12}P_{21}P_{22})\sin\theta \cdot \pi^2 EA/4\ell^2$ and $\varepsilon d_5 = 2\varepsilon d_3$.

The classical method for solving Eq. (9) is the method of Multiple Scales [11]. This method is quite involved and will not be explained here. Instead we present a more intuitive method, which also shows how the nonlinear coupling introduces internal resonance. This is the method of Harmonic Balance [11] which is only applicable to

periodic solutions. We are looking at the case $\omega_1 \approx 2\omega_2$ and $\Omega \approx \omega_1$ and thus define the detuning parameters ρ and σ

$$\omega_1 = 2\omega_2 + \varepsilon\rho \quad \text{and} \quad \Omega = \omega_1 + \varepsilon\sigma \tag{10}$$

Expressing ω_1 and ω_2 in Eq. (9) in terms of the excitation frequency Ω and the detuning parameters ρ and σ yields

$$\begin{aligned} \ddot{q} + \Omega^2 q + \varepsilon\left[2\mu_1\dot{q} - 2\Omega\sigma q + d_3 r^2\right] &= \varepsilon f \cos\Omega t \\ \ddot{r} + \tfrac{1}{4}\Omega^2 r + \varepsilon\left[2\mu_2\dot{r} - \tfrac{1}{2}\Omega(\rho+\sigma)r + d_5 qr\right] &= 0 \end{aligned} \tag{11}$$

These equations already show how the deck degree of freedom q is vibrating with the excitation frequency Ω and the cable degree of freedom r is vibrating with half the excitation frequency. We thus assume solutions of the following form

$$\begin{aligned} q &= a_1 \cos\Omega t + a_2 \sin\Omega t \\ r &= b_1 \cos\tfrac{1}{2}\Omega t + b_2 \sin\tfrac{1}{2}\Omega t \end{aligned} \tag{12}$$

These solutions satisfy the order ε^0 equations identically. For the order ε^1 we need to expand the quadratic terms. Multiplication of sine and cosine functions produces sine and cosine function of sums and difference of the argument. Thus, squaring sine and cosine functions with argument $1/2\Omega t$ produces sine and cosine functions with argument Ωt plus constants. Likewise multiplying sine and cosine functions with arguments $1/2\Omega t$ and Ωt produces sine and cosine functions with arguments $1/2\Omega t$ and $3/2\Omega t$. More explicitely:

$$\begin{aligned} r^2 &= \tfrac{1}{2}b_1^2(1+\cos\Omega t) + b_1 b_2 \sin\Omega t + \tfrac{1}{2}b_2^2(1-\cos\Omega t) \\ qr &= \tfrac{1}{2}(a_1 b_1 - a_2 b_2)\cos\tfrac{3}{2}\Omega t + \tfrac{1}{2}(a_2 b_1 + a_1 b_2)\sin\tfrac{3}{2}\Omega t + \tfrac{1}{2}(a_1 b_1 + a_2 b_2)\cos\tfrac{1}{2}\Omega t + \tfrac{1}{2}(a_2 b_1 - a_1 b_2)\sin\tfrac{1}{2}\Omega t \end{aligned} \tag{13}$$

Since the cable frequency is half of the deck frequency, the cable produces a force on the deck with the deck frequency (double cable frequency) and the deck produces a force with the cable frequency (deck frequency minus cable frequency). These relations are responsible for the internal resonance. Note also that constant terms and terms with frequency $3/2\Omega$ (deck frequency plus cable frequency) occur, which do not contribute to the internal resonance. Additional terms with other frequencies would also occur if we had included all quadratic combinations from Eq. (8). It can easily be seen that these additional terms would also not contribute to internal resonance, which justifies their omission.

The method of Harmonic Balance requires that the order ε^1 terms do not excite the system to resonance. Thus the terms containing harmonics of frequency Ω in the deck equation and the terms containing harmonics of frequency $\Omega/2$ in the cable equation

have to vanish. In this way we obtain two conditions for the coefficients a_1, a_2, b_1, b_2 from each equation, one from sine-terms and one from cosine terms:

$$\begin{array}{ll} \mu_1 a_1 + \sigma a_2 - \frac{d_3}{2\omega_1} b_1 b_2 = 0 & \mu_1 a_2 - \sigma a_1 + \frac{d_3}{4\omega_1}\left(b_1^2 - b_2^2\right) = \frac{f}{2\omega_1} \quad \text{(deck equation)} \\ \mu_2 b_1 + \frac{1}{2}(\rho+\sigma) b_2 + \frac{d_5}{4\omega_2}(a_1 b_2 - a_2 b_1) = 0 & \mu_2 b_2 - \frac{1}{2}(\rho+\sigma) b_1 + \frac{d_5}{4\omega_2}(a_1 b_1 + a_2 b_2) = 0 \quad \text{(cable equation)} \end{array} \tag{14}$$

Note that in these equations, the frequency Ω has been changed back to the eigenfrequencies ω_1 and ω_2 using Eq. (10).

Since we are interested in the amplitudes of the motion, the form assumed in Eq. (12) to has to be converted to the form

$$q = A\cos(\Omega t - \alpha) \qquad \text{and} \qquad r = B\cos\left(\frac{1}{2}\Omega t - \beta\right) \tag{15}$$

where the amplitudes are given by $A^2 = a_1^2 + a_2^2$ and $B^2 = b_1^2 + b_2^2$. Equation (14) have two solutions for the amplitudes [11]. One is the trivial solution corresponding to a deck motion without cable movement. This is the solution of the linear problem:

$$A = \frac{F}{2\omega_1\sqrt{\mu_1^2 + \sigma^2}} \qquad B = 0 \tag{16}$$

The other solution is the one with internal resonance

$$\begin{array}{l} A = \dfrac{2\omega_2}{d_5}\sqrt{4\mu_2^2 + (\rho+\sigma)^2} \qquad B^2 = E \pm \sqrt{\left(\dfrac{2f}{d_3}\right)^2 - F^2} \\ \text{where} \quad E = \dfrac{8\omega_1\omega_2}{d_3 d_5}(\sigma(\rho+\sigma) - 2\mu_1\mu_2) \quad \text{and} \quad F = \dfrac{8\omega_1\omega_2}{d_3 d_5}(\mu_1(\rho+\sigma) + 2\sigma\mu_2) \end{array} \tag{17}$$

It is a remarkable result that the deck amplitude in this case is independent of the applied force. Therefore, increasing the load does not increase the deck response but only the cable response. This is called the saturation phenomenon.

A more detailed solution based on the method of multiple scales is provided in [11]. This book also discusses the stability of the solutions. Stability conditions are not derived here, but the unstable solutions are given in the plots by dashed lines.

4 Discussion

The results of the perturbation solutions can now be used for the interpretation of the experimental results. First recall that the two cables moved symmetrically near an excitation frequency of 3.9 Hz but changed to an antisymmetric pattern near an excitation frequency of 4.1 Hz. Since the model presented here includes only one cable, it cannot reproduce both of these modes. Instead, we consider two models, one with a cable frequency near 3.9 Hz and one with a cable frequency near 4.1 Hz. The higher

frequency is attributable to the additional torsion stiffness mobilized in this mode. The amplitudes of the deck and the cables are compared to the perturbation solutions of the two models in Fig. 7. As before, the harmonic corresponding to the excitation frequency is shown for the deck and the harmonic corresponding to half of the excitation frequency is shown for the cable. This representation filters out the response due to linear coupling. The measured amplitudes can well be interpreted by the perturbation solutions. Not only can the two valleys be interpreted, but also the different behavior for a test with ascending and descending excitation frequencies can be explained.

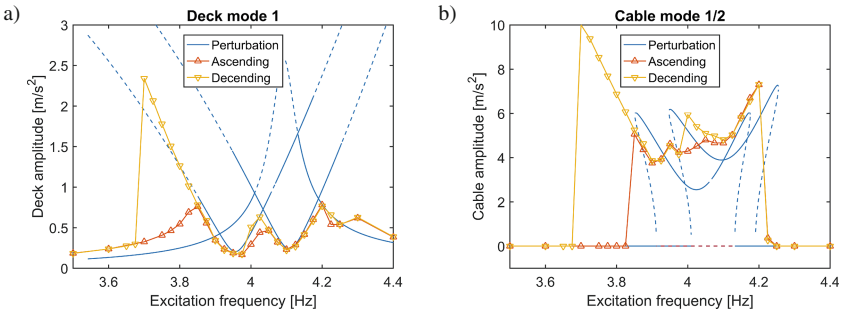

Fig. 7. Frequency response of (a) deck, (b) cable.

For the analytical model, mass and stiffness properties were taken from the physical model as much as possible. However, since the results depend heavily on the correct frequencies, these properties have been adjusted to the measured response. The cable frequencies of the two models correspond directly to the valleys of the deck response. Since the deck frequency is completely hidden by the internal resonance, some additional measurements have been performed omitting internal resonance. This has been done once by applying a low level excitation force (Fig. 8a) and once by restraining the cable motion by wires connecting the center of the cables with the floor (Fig. 8a). The response due to a low excitation has been scaled to the normal level. The two linear frequency responses look quite similar, although there is some difference due to the different amplitudes. The deck frequency can be estimated from the main peak around 4.1 Hz. Besides the deck mode, the response also exhibits the second cable mode, which has not been included in the analytical model. Since the cables are tuned to half the deck frequency, their second mode (with a node at the center) is close to the deck frequency. Therefore the secondary peak in these figures is close to the first valley with internal resonance (around 3.9 Hz).

The case of varying amplitude of the excitation force is shown in Fig. 9. Although not all details are represented exactly by the perturbation solution, the general behavior is clearly captured. After a linear branch of the deck response with no contribution of the cable response, the deck amplitude remains more or less constant while the cable amplitude increases with increasing force amplitude.

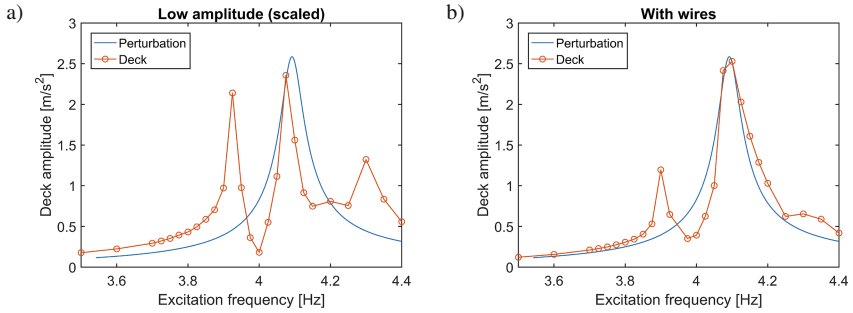

Fig. 8. (a) Frequency response of deck (a) due to low level excitation (scaled up), (b) with restrained cable motion.

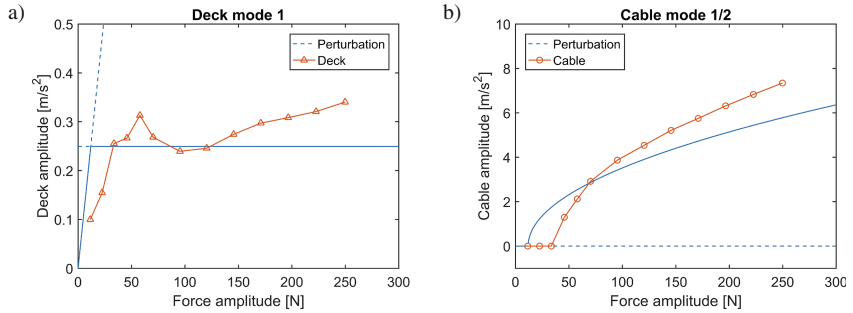

Fig. 9. Response for varying excitation amplitude at 4.1 Hz: (a) deck response, (b) cable response.

5 Conclusions

Dynamic tests on a laboratory bridge have been performed to investigate the effect of internal resonance between stay cables and bridge deck. Internal resonance leads to some unusual effects which cannot be explained by the classical modal analysis. The most striking phenomenon is the coupling of two modes with different frequencies. Internal resonance only occurs when the cable frequency is tuned to half of the deck frequency. A further requirement is that the forcing function is large enough and also has a frequency close to the deck frequency.

All principal phenomena can be explained with a simple model of an inclined cable connected to a spring-mass system. The equations of motion can be derived with Lagrange's equations, which automatically yield the linear and nonlinear coupling terms. These nonlinear equations have been solved approximately by perturbation methods.

References

1. Hamm, P.: Nicht-lineares Zusammenwirken von Brückendeck und Abspannseilen bei Fußgängerbrücken. Institut für Baustoffe und Konstruktion, Technische Universität München (2007)
2. Cai, Y., Chen, S.S.: Dynamics of elastic cable under parametric and external resonances. J. Eng. Mech. **120**(8), 1786–1802 (1994)
3. Pinto da Costa, A., Martins, J.A.C., Branco, F., Lilien, J.L.: Oscillations of bridge stay cables induced by periodic motions of deck and/or towers. J. Eng. Mech. **122**(7), 613–622 (1996)
4. Perkins, N.C.: Modal interactions in the non-linear response of elastic cables under parametric/external excitation. Int. J. Non-Linear Mech. **27**(2), 233–250 (1992)
5. Fujino, Y., Warnitchai, P., Pacheco, B.M.: An experimental and analytical study of autoparametric resonance in a 3DOF model of cable-stayed-beam. Nonlinear Dyn. **4**(2), 111–138 (1993)
6. Gattulli, V., Lepidi, M.: Nonlinear interactions in the planar dynamics of cable-stayed beam. Int. J. Solids Struct. **40**(18), 4729–4748 (2003)
7. Caetano, E., Cunha, A., Gattulli, V., Lepidi, M.: Cable–deck dynamic interactions at the International Guadiana Bridge: on-site measurements and finite element modelling. Struct. Control Health Monit. **15**(3), 237–264 (2008)
8. Weber, B., Hamm, P.: Nonlinear cable-deck interaction in cable-stayed footbridges. In: Footbridge, Third International Conference, Porto (2008)
9. Meirovitch, L.: Elements of Vibration Analysis. McGraw-Hill, New York (1975)
10. Irvine, H.M.: Cable Structures. Dover Publications, New York (1992)
11. Nayfeh, A.H.: Nonlinear Interactions: Analytical, Computational, and Experimental Methods. Wiley, New York (2000)

Author Index

A
Abdeddaim, Mehdi, 586
Aguilar, Gerardo, 179
Aguilar, Rafael, 758
Aktan, Emin, 104
Ali, J.S., 714
Altay, Okyay, 694
Alves, Vinicius N., 94
Amado-Mendes, Paulo, 455
Ambroise, S., 397
Anastasopoulos, D., 3
Anastasopoulos, Dimitrios, 432
Andersen, Palle, 306
Andersson, Andreas, 354
Anigacz, Wojciech, 331
Argyris, Costas, 38
Asimaki, Domniki, 791
Aveyard, D., 445
Azarbayejani, Mohammad, 283
Azari, Hoda, 104
Azimi, Mohsen, 167, 586

B
Bakhshi, Ali, 156
Balduccini, Marcello, 104
Bandyopadhyay, D., 714
Barbosa, Andre R., 746
Barbosa, Flavio S., 94
Barbosa, Flavio, 514
Barontini, Alberto, 455
Barrett, Anthony R., 126
Bartoli, Ivan, 104
Bartolini, Andrew, 17
Battini, Jean-Marc, 354
Bäumer, Richard, 557, 597
Beben, Damian, 331, 805
Benson Shing, P., 480
Bhaiya, Vishisht, 146
Bharti, Shiv Dayal, 146, 568
Bień, Jan, 237, 409
Bishop, Erik, 420, 445
Boivin, Y., 397
Boroschek, Rubén, 758
Boschmonar, Gabriel F., 343
Bradley Davis, D., 126
Braley, John, 104
Branscomb, James, 118
Brasil, Reyolando M., 611
Busatta, Fulvio, 770

C
Çaktı, Eser, 816
Cantero, Daniel, 667
Cao, Qianying, 631
Carbonari, Sandro, 871
Casas, Joan Ramon, 249
Çelebi, Mehmet, 656
Chadha, Mayank, 317
Chalouhi, Elisa Khouri, 200
Chatzi, Eleni N., 261
Chaudhuri, Samit Ray., 705
Chawla, Komal, 705
Chen, Jun-Da, 644
Choi, Jaemook, 62
Chung, Junyeon, 62
Cortes-Delgado, Maria D., 469
Cury, Alexandre A., 94

D
Dall'Asta, Andrea, 725
Damkilde, Lars, 306
Danforth, McKenzie, 118
Datta, Tushar Kanti, 146, 568
De Roeck, Guido, 3, 432
Delgadillo, Rick, 758
Dertimanis, Vasilis K., 261

© Springer International Publishing AG 2018

J.P. Conte et al. (eds.), *Experimental Vibration Analysis for Civil Structures*,
Lecture Notes in Civil Engineering 5, https://doi.org/10.1007/978-3-319-67443-8

Devin, Austin, 577
Dezi, Francesca, 871
Domski, Jacek, 781

E
Ebrahimian, Hamed, 791
Ellenberg, Andrew, 104
Esfandiari, Akbar, 156

F
Fallais, Dominik, 225
Fanning, Paul J., 577
Farid Ghahari, S., 656
Felippe, Waldir, 514
Fraser, M., 445
Furtado, Andre, 746

G
Galvín, Pedro, 882
Gao, Bin, 631
Gara, Fabrizio, 725, 871
Gauron, O., 293, 397
Gentile, Carmelo, 200
Geweth, C.A., 138
Ghorbani-Tanha, A.K., 860
Gonzalez, David, 420
González, Ignacio, 73, 200
Graziotti, Francesco, 376
Gres, Szymon, 306
Gu, Quan, 364
Guerrini, Gabriele, 376
Gui, Guoqing, 167
Guo, Endong, 831
Gupta, Abhineet, 683

H
Hadjian Shahri, A.H., 860
Heo, G., 547
Hernández, Lemuel González, 469
Hu, Sau-Lon James, 631
Huerta-Carpizo, Carlos H., 179

I
Igarashi, Akira, 523
Isusi, Pablo B., 343
Iwasaki, Eiji, 192

J
Jamal Eddine, Abdul Karim, 851
Jeon, S., 547
Jiang, Hui, 831
Johansen, Rasmus Johan, 306
Judd, Johnn, 118
Jung, Michael, 118

K
Kachi, Takahiro, 523
Kamiński, Tomasz, 237
Kapania, Rakesh K., 683
Karoumi, Raid, 73, 200, 343, 354
Kasar, Arnav Anuj, 568
Kashima, Toshihide, 656
Katzer, Jacek, 781
Kerkeling, C., 138
Kijewski-Correa, Tracy, 17
Kim, Byeong Hwa, 676
Kim, C., 547
Kim, Kiyoung, 62
Klinkel, Sven, 694
Kohler, Monica, 791
Kontsos, Antonios, 104
Koo, Gunhee, 62
Koutras, Andreas, 480
Koyama, Shin, 656
Kullberg, Claes, 343
Kużawa, Mieszko, 237, 409
Kwiatkowski, Jacek, 331

L
Laflamme, J.-F., 293
Lai, Eleonora, 839
Lamarche, C.-P., 293
Lamarque, C.-H., 505
Leander, John, 73
Lee, C., 547
Lenti, Luca, 851
Li, Huajun, 631
Lin, Zhibin, 167, 586
Liu, Zhi, 831
Loh, Chin-Hsiung, 644
Lorenz, Werner, 212
Lou, Peng, 893
Lourenço, Paulo B., 455, 758
Lourens, Eliz-Mari, 225
Luong, Hoa T.M., 212

M
Maes, Kristof, 432
Magenes, Guido, 376
Mahendra, N.V.D., 85
Marburg, S., 138
Martínez-Rodrigo, María D., 882
Masciotta, Maria-Giovanna, 455
Massari, Anthony, 791
Masuya, Hiroshi, 273
Mazzotti, Matteo, 104
Meinhardt, Christian, 536
Miyashita, Takeshi, 192
Moaveni, Babak, 746

Mohammed, Ahmed S., 388
Mohammed, Mohammed A., 746
Moliner, Emmanuela, 882
Moon, Franklin, 104
Moughty, John James, 249
Moyo, Pilate, 770
Mulas, Maria G., 839
Murià-Vila, David, 179
Murray, Thomas M., 126

N
Nagai, Masatsugu, 192
Nassif, Hani, 893
Neves, A.C., 73
Nicoletti, Vanni, 725
Nielson, Drew, 420

O
Øiseth, Ole, 667
O'Neill, K., 445
O'Neill, Kenny, 420
Okawa, Izuru, 656
Östlund, Johan, 354
Ou, Jinping, 364
Ou, Yaowen W., 261

P
Pan, Hong, 167, 586
Panetsos, Panagiotis, 38
Papadimitriou, Costas, 38
Paultre, P., 293, 397
Pavelchak, Matthew A., 736
Pavic, Aleksandar, 388
Penna, Andrea, 376
Pirner, Miroš, 497
Proulx, J., 397

R
Rahai, Mohammad, 156
Ramos, Luís F., 455
Rao, Putti Srinivasa, 85
Ratajewicz, Bartłomiej, 619
Raychowdhury, Prishati, 822
Regan, Chris, 683
Regni, Marco, 871
Reynders, Edwin, 3, 432
Roberge, M., 397
Rodrigues, Hugo, 746
Rohrmann, Rolf G., 212
Roia, Davide, 725, 871
Romero, Antonio, 882
Rønnquist, Anders, 667
Roth, S.-N., 397

S
Saati Khosroshahi, F., 138
Şafak, Erdal, 816
Said, Samir, 212
Saidou Sanda, M., 293
Sánchez, Abraham R., 179
Schleiter, Simon, 694
Schmidt, Richard, 118
Seiler, Peter, 683
Semblat, Jean-Francois, 851
Seo, S., 547
Sepahvand, K., 138
Shrimali, Mahendra Kumar, 146, 568
Sjoblom, Kurt, 104
Skolnik, Derek, 420, 445
Sohn, Hoon, 62
Starossek, Uwe, 557, 597
Sun, Baoyin, 364
Swanson, Dave, 420, 445

T
Taciroğlu, Ertuğrul, 656
Talbot, M., 293
Tatara, Tadeusz, 619
Terrill, Richard, 557, 597
Todd, Michael D., 317
Torres, Alan S., 94
Trillkott, Stefan, 343
Turcotte, N., 293
Ture Savadkoohi, A., 505

U
Ülker-Kaustell, Mahir, 343, 354
Ulriksen, Martin Dalgaard, 306
Urushadze, Shota, 497

V
Varum, Humberto, 746
Vaurigaud, Bastien, 505
Vila-Pouca, Nelson, 746
Vivek, B., 822

W
Wahrhafitg, Alexandre M., 611
Wang, Yingjie, 893
Weber, Benedikt, 902

Weiss, Mathieu, 505
Wood, Richard L., 746

X
Xu, Chen, 273
Xue, Kai, 523

Y
Yan, Fei, 167
Ye, Shi, 104
Young, Charles, 104
Yu, Hanshun, 746

Z
Zabel, Volkmar, 212
Zhang, Lanfang, 831
Zhang, Peizhou, 364
Zhao, Wei, 683
Zonno, Giacomo, 758